

JAYCOR

AD-A274 323



12

**Research In Pulsed Power
Plasma Physics**

Final Report

November, 1993

Prepared
by:

David Hinshelwood
David Rose

Prepared
for:

Naval Research Laboratory
4555 Overlook Avenue, SW
Washington, DC 20375-5000

S DTIC
ELECTE
JAN 03 1994
A

93-31142

Contract Number: N00014-89-C-2134

93 12 22 243

1608 Springhill Road • Vienna, Virginia 22182-2270 • (703) 847-4000

JAYCOR

**Research In Pulsed Power
Plasma Physics**

Final Report

November, 1993

Prepared
by:

David Hinshelwood
David Rose

Prepared
for:

Naval Research Laboratory
4555 Overlook Avenue, SW
Washington, DC 20375-5000

Contract Number: N00014-89-C-2134

1608 Springhill Road • Vienna, Virginia 22182-2270 • (703) 847-4000

Contents

Section 1:	Overview	1
Section 2:	Intense Ion Beam Generation	2
2.1	"Standard" and "Backless" Diode Development	2
2.2	PBFA II Equatorial Pinch Reflex Diode Development	2
2.3	Magnetically Insulated Diode Development	3
2.4	Active Anode Development	3
2.5	List of Papers	4
Section 3:	Intense Ion Beam Transport and Ion Beam Applications	111
3.1	Ballistic Transport of Intense Light-Ion Beams	111
3.2	Z-Discharge Transport of Intense Light-Ion Beams	111
3.3	Effects of Time-of-Flight-Bunching on Transport Systems for LMF	112
3.4	Wall-Stabilized Discharge Channel Development	112
3.5	Current Neutralization of Intense Ion Beams	113
3.6	Light-Ion Beam Induced Nuclear Activation	113
3.7	Soft X-ray Simulation With Light Ion Beams	114
3.8	Pulsed Ion Beam Evaporation for Thin-Film Deposition	114
3.9	List of Papers	114
Section 4:	Plasma Opening Switches	373
4.1	Facility Development	373
4.2	Conduction Phase Studies	374
4.3	Switch Opening Model	375
4.4	Switch Optimization	376
4.5	Plasma Source Evaluation	376
4.6	List of Papers	377
Section 5:	System Study for Inductive Storage Generator	605
5.1	System Study	605
5.2	List of Papers	605

Accession For	
NTIS CRA&I	<input checked="" type="checkbox"/>
DTIC TAB	<input type="checkbox"/>
Unannounced	<input type="checkbox"/>
Justification	
By	
Distribution /	
Availability Codes	
Dist	Avail and/or Special
A-1	

THIS DOCUMENT IS UNCLASSIFIED

SECTION ONE

OVERVIEW

This final report covers work performed by JAYCOR under Contract N00014-89-C-2134 for the Naval Research Laboratory (NRL) over a period of 36 months from May 10, 1989 to June 9, 1992. No-cost extensions of the contract were granted on April 25, 1990, January 23, 1991, and January 30, 1992.

The research was conducted on-site at NRL by JAYCOR as part of NRL's programs in support of light-ion-driven inertial confinement fusion (ICF) for the Department of Energy (DOE), and nuclear weapon effects simulation (NWES) for the Defense Nuclear Agency (DNA). The work performed under this contract included research in several areas. The emphasis of the work shifted during the period of performance as the needs of the NRL program changed. The original Statement of Work comprised 12 research areas: (1) ion beam transport; (2) ion beam focusing; (3) 30-MV opening switch development; (4) microsecond-conduction-time opening switch investigation; (5) plasma flow switch development; (6) plasma flow switch/plasma opening switch coupling; (7) rep-rated switch development; (8) opening switch/diode coupling; (9) plasma radiation source investigation; (10) plasma source optimization for x-ray lasers; (11) plasma source development; and (12) inductive generator system study. The statement of work was modified on January 21, 1991 to reduce the rate of spending. This modification explicitly eliminated tasks (3), (7), (9), (10), and (11) above. Further direction from the COTR resulted in tasks (5) and (6) being dropped. The elimination of effort in submicrosecond and multimicrosecond opening switch development was offset by a significantly increased level of effort in microsecond opening switch development, as the DNA interest became focused on this time scale of switch operation. As requested by NRL, effort in the field of ion beam technology was expanded to include several schemes of ion beam transport, development of a new ion diode, and nuclear weapon effects simulation.

Results of the JAYCOR effort under this contract significantly aided NRL in accomplishing its objectives. Accomplishments related to ion beams include: development of a practical backup approach to ion beam transport; the first studies of ion-beam interaction with a neutral gas; initial investigations of a promising industrial application of ion beam technology; and detailed theoretical evaluation of several different ion beam transport schemes. Major accomplishments relating to opening switches include: the first direct measurement of the electron density in an opening switch; detailed studies of switch conduction-time scaling; evaluation of several different switch plasma sources; and extensive studies of switch performance into diode loads, leading to the development of a new (and now generally accepted) model of switch behavior.

In this final report, all aspects of the work performed under the contract are presented. Section Two addresses Task (2) and related work on ion beam diode development. Section Three describes work in support of Task (1) and efforts in new areas of ion beam applications. Section Four addresses Tasks (4) and (8), and Task (12) is addressed in Section Five

SECTION TWO

INTENSE ION BEAM GENERATION

Research on ion beam generation involved characterizing and developing several versions of ion beam extraction diodes. This Section discusses the development of pinched-beam ion-extraction diodes on GAMBLE II (Section 2.1), equatorial pinch-reflex diodes on PBFA II (Section 2.2), and the magnetically insulated diode (MID) on GAMBLE II (Section 2.3). This effort was closely coupled with the ion beam transport and applicator efforts discussed in Section 3. Section 2.4 discusses the development of an active anode source for the MID. This Section is concluded with a list of publications and reports.

2.1 "Standard" and "Backless" Diode Development

Pinched-beam extraction diodes, under development as loads for pulsed power generators, produce high-current ion beams employed in a variety of research areas (see, for example, Sec. 3 of this report). Efforts over the past few years have been directed at characterizing the ion beam produced by pinch-reflex diodes on the NRL GAMBLE II pulsed power accelerator. These diodes comprise a hollow cylindrical cathode located opposite a thin planar anode foil. During operation, electrons from the cathode reflex (pass back and forth) through the anode foil, vaporizing the foil and liberating ions that are then accelerated toward the cathode. Typically a solid backplate is located behind the anode foil. A low debris version of the pinch-reflex diode, referred to as the "backless" diode, excludes this back plate. A virtual cathode is assumed to form near the same axial position as the original anode plate, enabling the reflexing of electrons much the same as the "standard" configuration.

Characterization of the ion beams produced by these diodes included a determination of the beam microdivergence resultant from the diode. A detailed, three-dimensional numerical calculation was performed, employing a model for the time-dependent focusing in the anode-cathode gap. Measured diode electrical characteristics, such as net ion current and corrected voltage, were used in the code. For the "standard" configuration pinched-beam diode of radius 6.0 cm, a microdivergence of approximately 125 mrad was found. This result is in agreement with previous calculations performed for 3.0 cm radius diodes. A similar analysis for the 6.0 cm "backless" pinched-beam diode was performed, yielding approximately 175 mrad of microdivergence. This increase in source divergence for the "backless" over the "standard" diode is attributed to the tenuous formation of a virtual cathode in the vacuum region of the original anode plate location. The high source divergence of the "backless" diode has been exploited in low-debris, low-fluence experiments (see Sec. 3.7).

2.2 PBFA II Equatorial Pinch Reflex Diode Development

The equatorial pinch reflex diode (EPRD) is a barrel shaped version of the pinched-beam diode described above. This diode is a possible load for the Particle Beam

Fusion Accelerator II (PBFA II) located at Sandia National Laboratories, Albuquerque, NM. A study was carried out to examine the total power density delivered to an inertial-confinement-fusion (ICF) target. A transmission code, previously developed at NRL by JAYCOR personnel, was employed to analyze and predict EPRD produced proton power density on target. This work utilized experimentally obtained values for the source microdivergence, gap spacing, etc. The results obtained included an estimate of approximately 25 TW/cm² of proton power density deliverable onto an ICF target for realistic constraints. Similarly, results for deuteron beams indicate that about 10 TW/cm² may be achievable.

2.3 Magnetically Insulated Diode Development

During the contract period, an extraction magnetically insulated ion diode, built by Sandia National Laboratories, was installed in the NRL GAMBLE II pulsed power accelerator. This diode uses two pairs of magnetic field coils, located behind the anode and cathode, to produce a radial magnetic field in the diode gap. Currents through each of the four coils are varied independently to obtain the desired field configuration. JAYCOR personnel participated in the characterization and optimization of this diode. Initially, a passive, flashover anode source, consisting of a set of concentric, epoxy-filled grooves, was used. An optimum magnetic field configuration will allow a small number of electrons to cross the gap and trigger the formation of an anode plasma, while insulating most of the electron flow from the anode and thus giving a high ion current efficiency. These experiments represented the first operation of this diode on a low-impedance generator. Partially successful results were obtained although the diode exhibited a relatively long delay before the onset of ion current. This delay resulted in an early, high impedance phase of the diode and an inefficient coupling to the generator.

2.4 Active Anode Development

In order to improve operation of the diode, an active anode plasma source was adapted to this diode. The EMFAPS (Exploding Metallic Foil Anode Plasma Source) consists of a thin metallic film on the anode surface. Several tens of kA are driven through this foil at the start of the generator pulse. This current vaporizes the foil, leading to the formation of an anode plasma. In this way, anode plasma formation is decoupled from the electron flow in the diode. In principle, a rapid onset of ion current is possible, and the ion current can be a very large fraction of the total current. In the first experiments on Gamble II, a plasma opening switch was used to divert the early part of the generator pulse through the foil. This approach suffered from the difficulty in synchronizing the plasma sources to the generator. Subsequently, an external pulser was used to drive the foil current. This pulser was triggered from the generator in such a way as to minimize the jitter between the pulser and the generator. Both of these approaches showed encouraging results, and work in this area is ongoing.

2.5 List of Papers

- 2.5.1 "Ion Beam Microdivergence for the Standard Pinch Reflex Diode," D.V. Rose, and P.F. Ottinger, Pulsed Power Physics Technote 92-07 (1992).
- 2.5.2 "Experimental Study of the "Backless Anode" Pinch-Reflex Diode as an Ion Source," S. J. Stephanakis and V.E. Scherrer, Pulsed Power Physics Technote 91-01 (1991).
- 2.5.3 "Experimental Study of the "Backless Anode" Pinch-Reflex Diode as a Bremsstrahlung Radiator," S.J. Stephanakis, J.R. Boller, J.C. Kellogg, W.F. Oliphant, V.E. Scherrer, and B.V. Weber, Pulsed Power Physics Branch Technote 91-09 (1991).
- 2.5.4 "Focused Proton Power Density Prediction For PBFA II Using an EPRD Diode," P.F. Ottinger, J.R. Boller, D. Rose, D.D. Hinshelwood, S.J. Stephanakis, and G. Cooperstein, Pulsed Power Physics Technote 91-02 (1991).
- 2.5.5 "Initial Results with an EMFAPS on GAMBLE II," D. Hinshelwood, Pulsed Power Physics Technote 93-03 (1993).
- 2.5.6 "Initial Pulser-Driven EMFAPS Results," D. Hinshelwood, R. Fisher and J. Neri, Pulsed Power Physics Technote 93-03 (1993).

PULSED POWER PHYSICS TECHNOTE NO. 92-07

TITLE: ION BEAM MICRODIVERGENCE FOR THE STANDARD PINCH REFLEX
DIODE

AUTHORS: D.V. Rose, and P.F. Ottinger

DATE: 12 March 1992

ABSTRACT: A determination of the average microdivergence for
the standard pinch reflex ion diode is described.
Results are in agreement with previous calculations
done for smaller radius standard diodes.

THIS REPORT REPRESENTS
UNPUBLISHED INTERNAL
WORKING DOCUMENTS AND
SHOULD NOT BE REFERENCED
OR DISTRIBUTED

Ion Beam Microdivergence for the Standard Pinch Reflex Diode

D. V. Rose and P. F. Ottinger

March 12, 1992

Abstract

A determination of the average microdivergence for the standard pinch reflex ion diode is described. Results are in agreement with previous calculations done for smaller radius standard diodes.

Recent ion beam shots on GAMBLE II were taken to characterize the average microdivergence, Θ_μ , for the large radius (anode radius ~ 6.0 cm), "backed" pinch reflex ion diode (standard PRD). Previous work determined the microdivergence on small radius (~ 3.0 cm), "backed" [1] and large radius "backless" [2] diodes. The results presented here are consistent with this earlier work and point to $\Theta_\mu \sim 125$ mrad.

The GAMBLE II diode is modeled as having a radial bending angle Θ_b which acts to focus ions towards the axis after leaving the diode plane. Previous investigations have indicated the presence of a "pimple" forming on axis [3]. A simple model has been used to investigate the effects of this feature on focusing. This is represented in the total bending angle as

$$\Theta_b = \Theta_{bo} + \Theta_{bp} \quad (1)$$

where the normal bending angle component is

$$\Theta_{bo} = \frac{\omega_c \Delta}{v_z} \quad (2)$$

and the bending due to the pimple is

$$\Theta_{bp} = \frac{r\delta}{r_m^2} \exp\left(-\frac{r^2}{2r_m^2}\right) \quad (3)$$

In the above equations, ω_c is the ion cyclotron frequency and is given as (in MKS units)

$$\omega_c = \frac{\mu_o e I_d Z_d}{2\pi m_i R}, \quad (4)$$

with R being the radius of the anode (6.0 cm). For this work δ is given as $\delta_o t(ns)/60$ and δ_o is 1 or 2 mm for normal and double height pimples respectively.

This model is incorporated into a computer code [4] that uses the corrected voltage and ion current traces from GAMBLE II shots 5259, 5261, and 5262. The first shot is a full aperture shot to determine the total yield produced by the full ion beam (6257 cpm). The last two shots give the yield produced by the beam after passing through an aperture at 19 cm (shot 5261, 1220 cpm) and 27 cm (shot 5262, 1260 cpm) from the anode surface. Ions are launched from the Kimfol surface at radial angle Θ_b and randomly placed within a microdivergence cone of half-angle Θ_μ about Θ_b . Code runs were carried out for microdivergences ranging from 25 to 150 mrad.

Ions are projected through the aperture onto a LiF target where the total time-integrated yield is calculated by a subroutine described previously [4] for comparison with the measured yield. Energy loss due to classical stopping in a gas over the transport distance of each ion is also accounted for (1 torr air).

In order to determine the microdivergence, a set of code runs were conducted over a range of Θ_μ with and without a pimple. These runs are listed in Table 1. In this and other tables, the yield due to the full-target shot is referred to as 'A', and the yields due to the apertured shots are referred to as 'B' (19 cm shot) and 'C' (27 cm shot). Ratios of full-target to apertured shots are given in Table 2 and plotted in Fig. 1. By plotting the ratio B/A against the ratio C/A, a parameter space that gives calculated yield ratios is set up. Calculated results give ratios that do not pass through the experimental value, but do clearly establish that a microdivergence of ~ 125 mrad gives the best fit. Note that the inclusion of a pimple has little effect on the yield ratios at this microdivergence. Previous work gave ~ 125 mrad for small radius (3 cm) "backed" diodes [1] and ~ 175 mrad for large radius "backless" diodes [4,5].

One further point to note is the similarity in values for the two experimental target ratios. By examining the tabulated differences in the yield ratios (B/A - C/A), a microdivergence value of ~ 50 mrad seems to best fit the experimental data. However, this yield difference value should be

Shot	Θ_μ mrad	Yield (arb. units)		
		$\delta_o=0$	$\delta_o=1$ mm	$\delta_o=2$ mm
5259	25			4.7650145
5261	"			2.6100777
5262	"			3.0324174
5259	50	4.76722	4.7638	4.7645005
5261	"	2.2980001	2.847313	2.5156202
5262	"	2.257623	2.937469	2.6131206
5259	75			4.7620474
5261	"			2.2027619
5262	"			1.8342304
5259	100	4.7695864	4.7650411	4.7679105
5261	"	1.6567697	1.9043686	1.7221816
5262	"	1.1581413	1.3047639	1.2548963
5259	125	4.7640603	4.7620402	4.7689924
5261	"	1.3144046	1.4247432	1.3269813
5262	"	0.8513496	0.9077793	0.8758495
5259	150	4.7658366	4.7650733	4.7676346
5261	"	1.0624954	1.0825868	1.0064719
5262	"	0.630675	0.6602545	0.6228485

Table 1: Matrix of computer runs and resultant yields.

$\Theta_{\mu}(mrad)$	$\delta_o(mm)$	B/A	C/A	(B-C)/A
Experiment	-	.195	.201	-.006
25	2	.548	.636	-.089
50	0	.482	.474	.008
"	1	.598	.617	-.019
"	2	.528	.548	-.020
75	2	.463	.385	.077
100	0	.347	.243	.105
"	1	.400	.274	.126
"	2	.361	.263	.098
125	0	.276	.179	.097
"	1	.299	.191	.109
"	2	.278	.184	.095
150	0	.223	.132	.091
"	1	.277	.139	.089
"	2	.211	.131	.080

Table 2: Experimental and calculated yield ratios.

considered a qualitative indication of the experimental error associated with the experimental measurement.

References

- [1] D. Mosher, *private communication*.
- [2] S. J. Stephanakis et. al., "Experimental Study of the 'Backless Anode' Pinch-Reflex Diode as an Ion Source," *NRL Pulse Power Physics Branch Technote 91-01, unpublished*.
- [3] D. Mosher, et. al., *Bull. Am. Phys. Soc.*, 33 1864(1983).
- [4] D. V. Rose, et. al., "Orbit Calculations for Z-Discharge Transport Experiments on Gamble II," *NRL Pulse Power Physics Branch Technote 91-07, unpublished*.

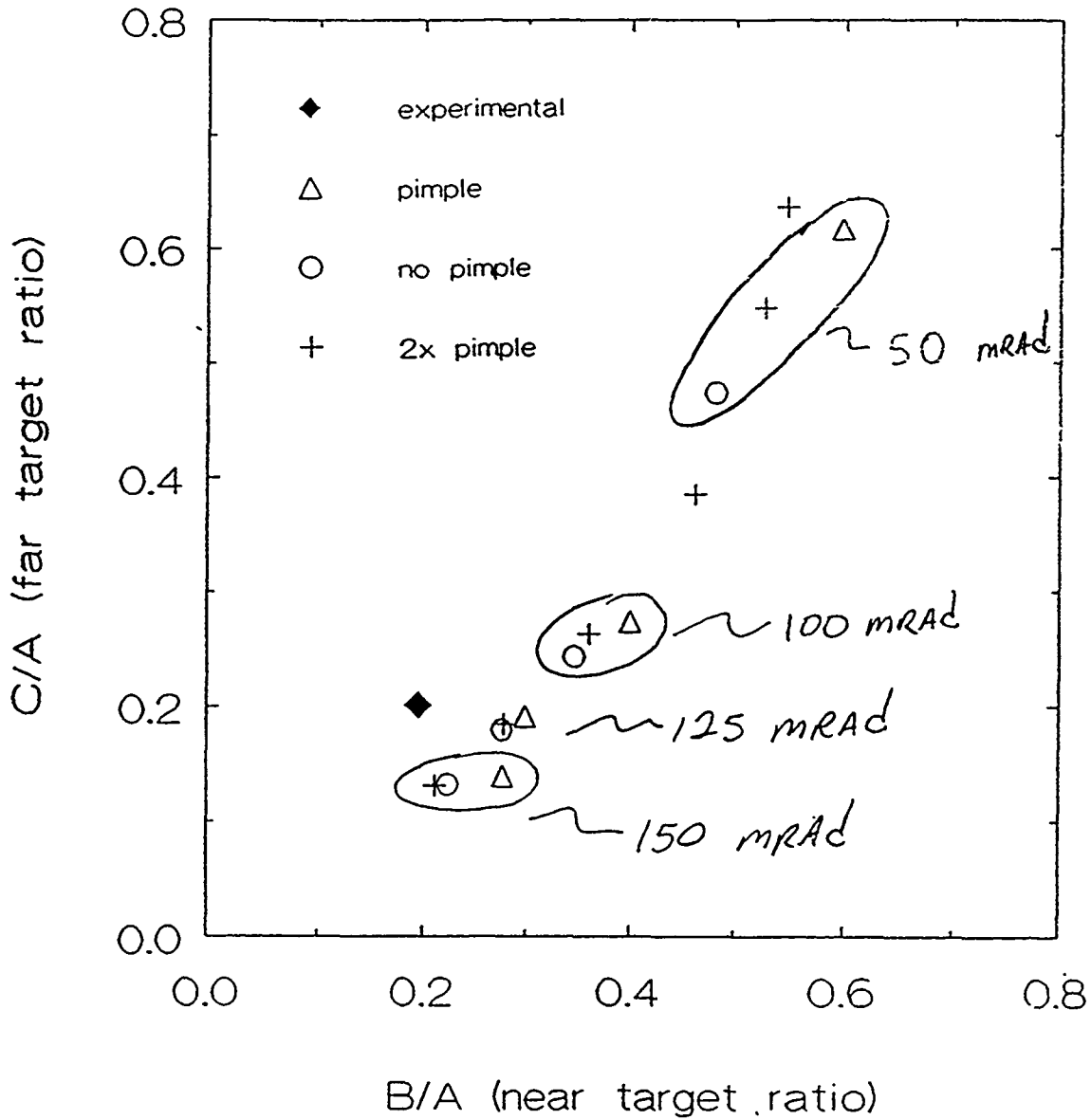


Figure 1: Graphical representation of the data in Table 2. Increasing θ_μ brings calculated results near to experimentally determined yield ratios.

- [5] J. M. Neri, et. al., "Experimental Demonstration of Z-Discharge Plasma Channel Transport of Intense Ion Beams," *to be submitted to Phys. Fluids B.*

PULSED POWER PHYSICS TECHNOTE NO. 91-01

TITLE: EXPERIMENTAL STUDY OF THE "BACKLESS ANODE" PINCH-REFLEX DIODE AS AN ION SOURCE

AUTHOR(S): S.J. Stephanakis and V.E. Scherrer

DATE: 2 January 1991

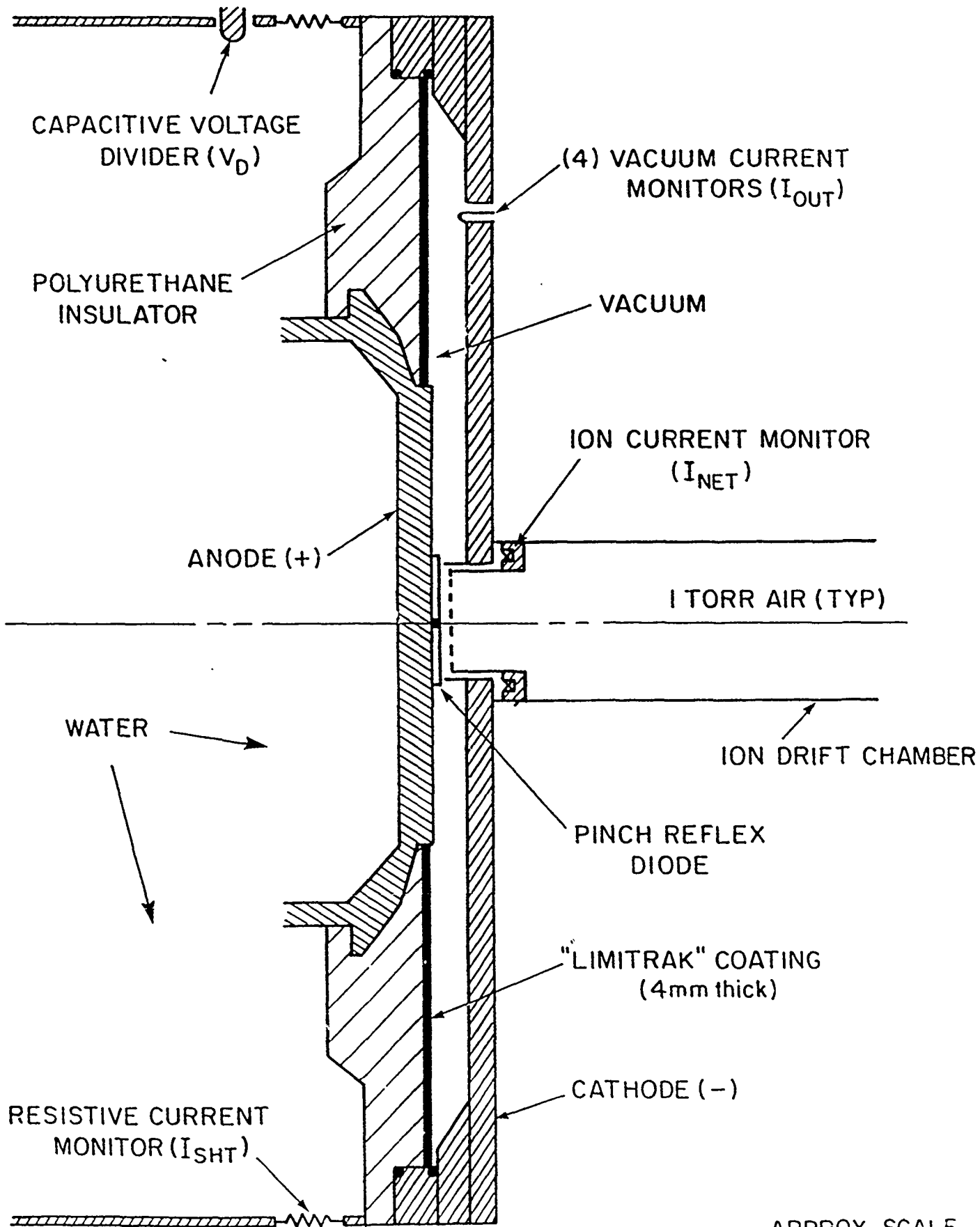
ABSTRACT: The "backless anode" pinch-reflex diode was invented to meet the need for a minimal-debris ion source suitable for material response studies, downstream of the diode. In this technote the electrical characteristics of such a diode will be presented and compared with those of the standard (backed) pinch-reflex diode. In addition, results will be presented of an optimization study undertaken in order to determine the thinnest usable (plastic) reflexing foil and metallic annular ring across from the cathode tip.

THIS REPORT REPRESENTS
UNPUBLISHED INTERNAL WORKING
DOCUMENTS AND SHOULD NOT BE
REFERENCED OR DISTRIBUTED

1. INTRODUCTION

Pinch reflex diodes have been used by our group for the efficient production of proton beams since the mid-1970's. The typical experimental arrangement for such a diode in the context of the Gamble II front end is shown in Figure 1. The cathode is a hollow cylinder ~12 cm in diameter with a radial width of ~3 mm. A second ~11 cm dia. cylinder is located coaxially within the cathode with its tip typically 8 mm downstream of the cathode tip. The front of this interior cylinder is usually covered with a stretched, vacuum-tight polycarbonate foil (Kimfol) of 2 μm thickness to allow proton transmission through it. The return electron current due to the ions traversing the Kimfol is monitored with a Rogowski coil as shown in the figure. The Kimfol also separates the evacuated diode region from the ion drift region which is typically filled with 1 Torr air for charge- and current-neutralization of the ion beam. The anode consists of a stretched, 102 μm thick polyethylene foil which is held along its perimeter by a plastic or metal ring and is connected to the positive electrode at the center through a 6.3 mm dia., 5 mm long solid carbon cylinder. An annular, 178 μm thick aluminum washer is placed in contact with the polyethylene foil to define an equipotential surface across the cathode tip. The inner diameter of this washer is 1-2 mm smaller than the inner diameter of the cathode cylinder. The anode-cathode gap is typically 5 mm. The operation of this diode is understood to proceed as follows. Electrons are emitted from the cathode tip and the total current drawn is determined initially by the Child-Langmuir relation. When the current increases beyond the critical-current limit, the electron flow becomes essentially radial, the anode foil surface-flashes making positive ions available leading to a tight pinch at the center. The electrons that transverse the anode foil are "reflexed" back into the anode-cathode region due to the azimuthal magnetic field behind the anode foil created by the current flowing through the central support ("button").

The configuration shown in Figure 1 has served us well for satisfying both our DOE and DNA sponsor requirements over the past decade or so, in that it has proven a very efficient, reproducible ion source for ICF-related research. In the last couple of years however, a new application for ion beams has emerged, namely material-response studies using such beams. After a few experimental sessions in this new field, it became clear that although the ion beams themselves were more than adequate in terms of spectrum, fluence magnitude and distribution, the considerable debris that accompanied the ion beams, albeit delayed in time, interfered with the diagnostics and made evaluation of permanent ion beam effects on the materials under study very difficult or impossible. We thus undertook to determine the source of that debris. We very quickly established that the Kimfol and the fill gas in the drift chamber contributed very little to the debris and that almost all of it was due to the melting and vaporization of the materials that constitute the anode structure. We thus proceeded to reduce



APPROX. SCALE

1/5

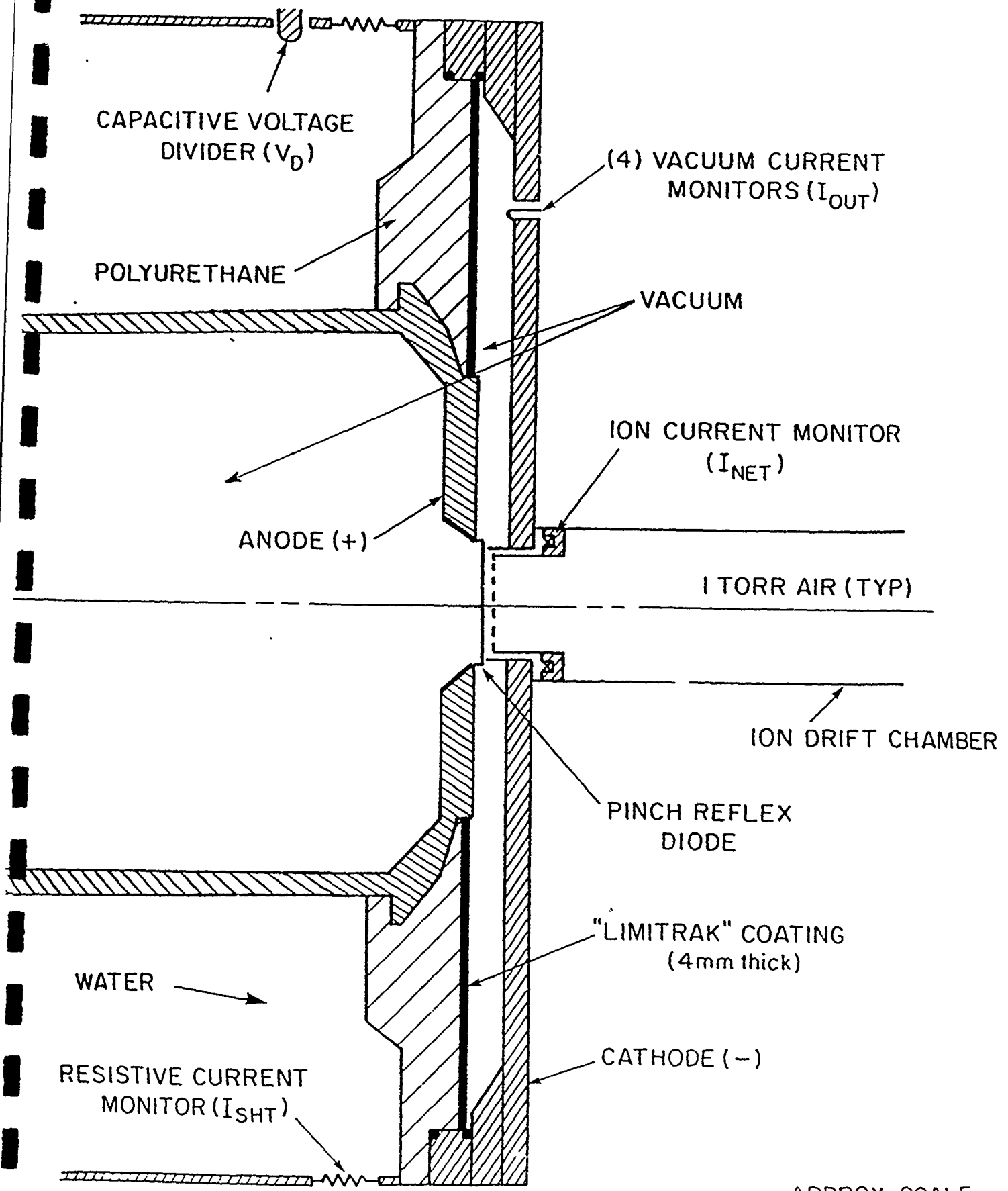
Figure 1

the mass of the anode structure to the extent possible by decreasing the thickness of the anode foil and essentially eliminating all the structure behind the foil as shown in Figure 2. The effect on the debris downstream of the diode was dramatic especially when a debris-expansion chamber was used for the little debris that was left. This is illustrated clearly in Figure 3. The effect of this total re-structuring of the anode on the electrical characteristics and ion-producing ability of the diode is the subject of this technote. It should be emphasized that obviously the physics of electron reflexing, foil flashover, etc. must be assumed to be different in this "backless" geometry since there is not longer a $B\theta$ -producing button at the center; instead there is an essentially-infinite vacuum space upstream of the anode foil in which electrons follow paths the nature of which one can only speculate upon at this time.

2. RESULTS

All the data which will be presented were taken with Gamble II operating in positive polarity and the Marx generator charged to ± 36 kV. The cathode was as described above with its tip aerodagged. The I_{NET} structure was placed so that the Kimfol front was 8 mm downstream of the cathode tip in all cases. The drift region downstream of the Kimfol was filled with 1 Torr air in all cases. A shadowbox was in place immediately behind the Kimfol for evaluation of ion beam bending angle and divergence changes. No such changes were detectable on the shadowbox witness plates for any of the anode configurations tried. A Bremsstrahlung pinhole camera and photodiode were viewing the anode axially from a distance of about 2 meters. The photodiode signals were generally weak (~ 0.5 v) primarily due to shielding by the massive (brass and steel) shadowbox in the line of sight. The shapes of the photodiode signals were consistent with the electron power ($I_{et}V_{cor}$). The pinhole pictures showed very faint images for backless anodes even with the fastest films while the pinch was easily discernible in the cases of carbon-backed anodes. The nature of Bremsstrahlung production will be discussed in detail in an upcoming technote dedicated to the subject.

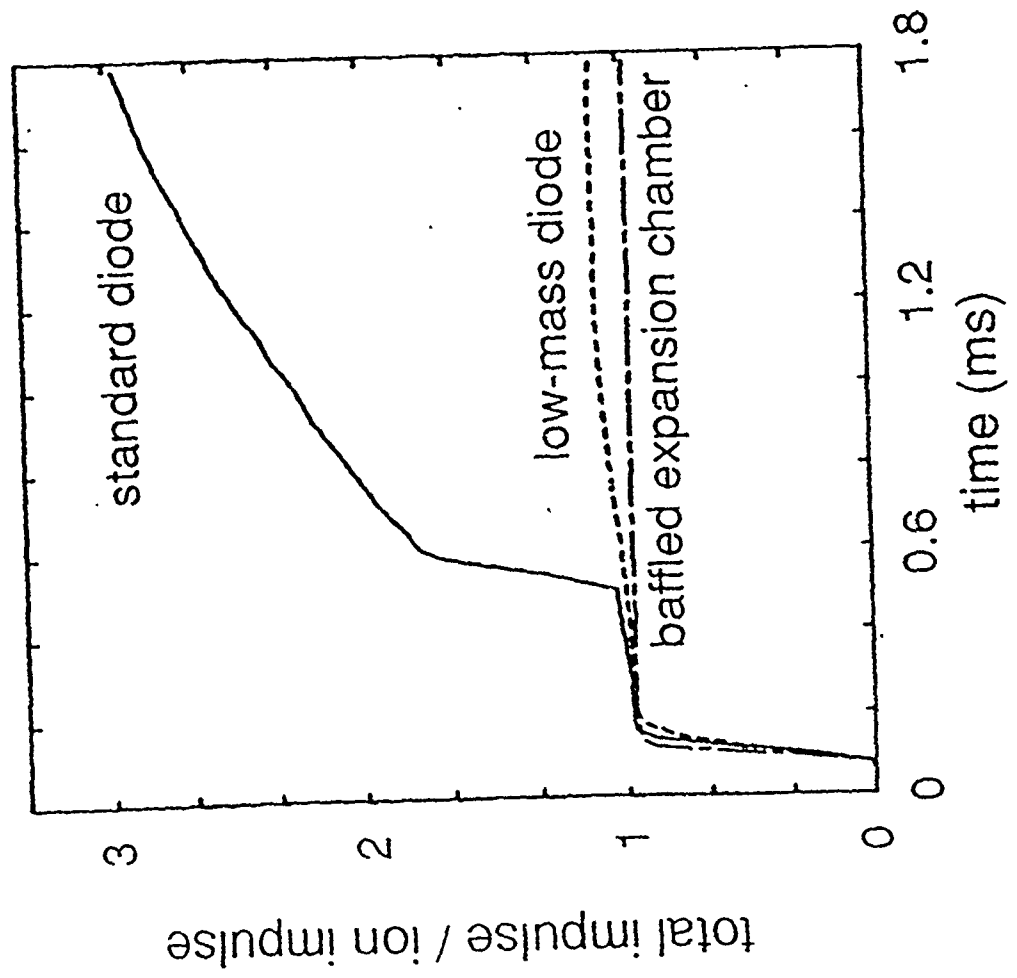
The discussion of the electrical results will proceed as follows. First, data will be presented from shots used to evaluate the optimum reflexing foil thickness for backless anodes. In these shots, the annular ring thickness was kept constant at $178 \mu\text{m}$. Second, the effect of annular ring thickness will be evaluated with the reflexing foil thickness kept constant at $12.7 \mu\text{m}$. Finally, once the optimum reflexing foil and annular ring thicknesses are chosen, the comparison will be made between backed and unbacked anodes using the chosen foils and aluminum annuli.



APPROX. SCALE
1/5

Figure 2

Debris Impulse Measurements



- ≤ 300 taps with low-debris diode
- immeasurable ≤ 50 taps with baffled expansion chamber
- 0.5 ms debris arrival time

Figure 3

2a. Effect of reflexing foil thickness

The data shown in Figures 4, 5, 6, and 7 compare three shots where the reflexing foil thickness was changed from 102 μm (#4707) to 12.7 μm (#4705) to 1.8 μm (#4709). Figure 4 compares the impedance histories for the three cases. No significant difference is apparent. Figure 5 compares the ion production efficiency (defined as the ratio of ion current to total diode current for the three cases). It is seen that although at late times all three reach about 58%, the two thinner foils are more efficient producers of ions at earlier times with no significant difference between the 1.8 μm and 12.7 μm foils. As a result of this early-time difference, the ion power (Figure 6) and ion energy (Figure 7) for the two thinner foils is seen to be 15-20% higher than it is for the 102 μm thick foil. The one caveat about this data is that, due to material availability, the 1.8 μm foil was non-aluminized polycarbonate (Kimfol, $\text{C}_{16}\text{H}_{14}\text{O}_3$; $\rho = 1.36$) while the other two foils were polyethylene (CH_2 ; $\rho = 1$). Due to different chemical composition of the two materials there is some question as to how similar they are in terms of flashover properties and/or the proton content of the resulting ion beam.

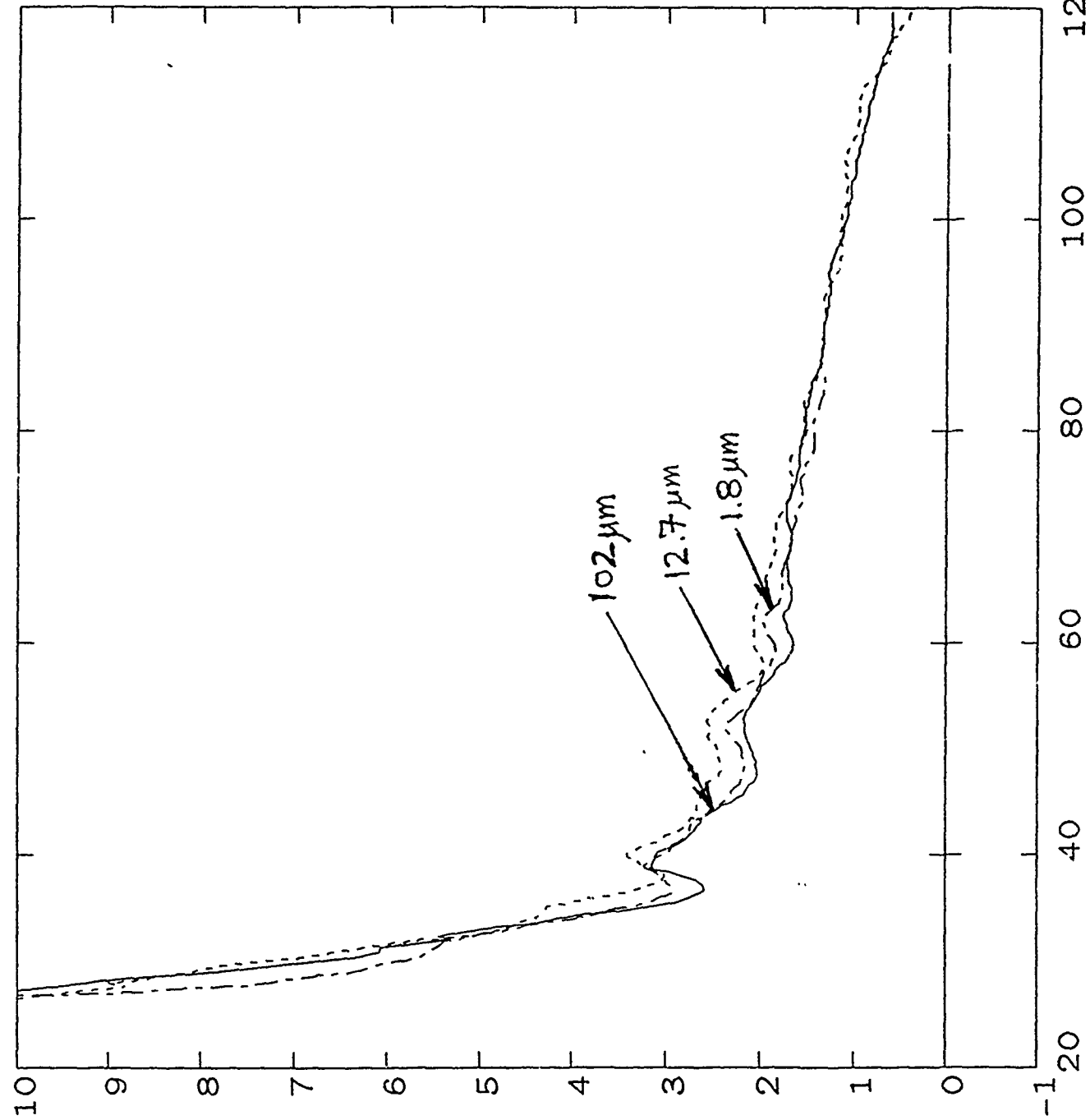
2b. Effect of annular ring thickness

The data shown in Figures 8, 9, 10 and 11 compare three shots where the anode annular ring across from the cathode tip was absent (#4715), was 178 μm thick (#4705) and was 1.6 mm thick (#4710). The four figures compare impedances, ion production efficiencies, ion powers and ion energies as in Figures 4-6. Note that for the case of no annular ring, the impedance drops significantly faster than in the other two cases and flattens out at the 1.5 Ω level for the full pulse. When annular rings are present on the other hand, the impedance drop occurs later in time and the impedance is on average, higher. The speculation here is that in the case of no metallic annulus, ions are produced faster across from the cathode tip and thus cause the immediate drop in impedance. This speculation is not reflected in the efficiency curves of Figure 9, however this could be due to the fact that ions produced directly across from the cathode tip may not be intercepted by the I_{NET} structure which has a smaller acceptance diameter than the cathode itself. Despite this apparent advantage of not having an annulus at all, it is seen from Figures 9-11 that in terms of late time efficiency, power and total energy the anodes with an annulus in place are superior. In addition, it is speculated that the presence of a metallic equipotential surface across the cathode tip tends to lead to more predictable symmetric pinching of the electron beam and thus a better-centered ion beam.

2c. Backed vs. unbacked anode

Based on the arguments put forward in 2a and 2b and on Figures 4-11, the anode of choice for minimum debris production and maximum ion power is clearly one where the reflexing foil is about 12.7 μm thick with a 178 μm thick annular metallic ring

Shot 4707 UNBACKED -- FOIL DELTA - IMPEDANCES



----- Z
Units: 1.00E+00 OHMS
Max: 1.00E+01
Ts(ns): 0.00E+00

----- Z4705 OHMS
Units: 1.00E+00
Max: 1.00E+01
Ts(ns): 0.00E+00

----- ZT4709 OHMS
Units: 1.00E+00
Max: 1.00E+01
Ts(ns): 0.00E+00

Shot 4707 UNBACKED - FOIL DELTA - ION EFFICIENCIES

IEFF Amps
Units: 1.00E-01
Max: 1.00E+00
Ts(ns): 0.00E+00

IEFF4705 Amps
Units: 1.00E-01
Max: 1.00E+00
Ts(ns): 0.00E+00

IEFF4709 Amps
Units: 1.00E-01
Max: 1.00E+00
Ts(ns): 0.00E+00

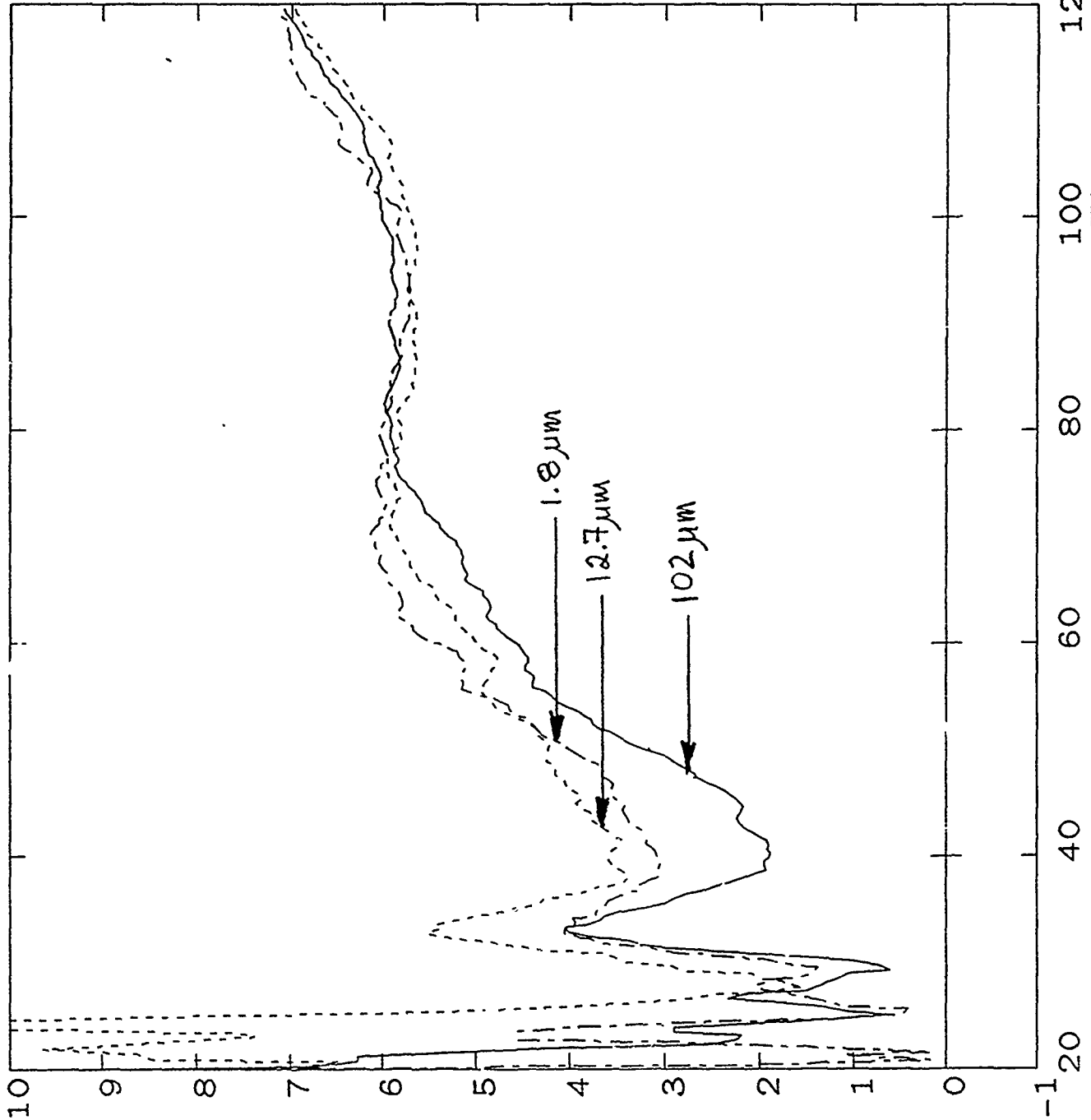


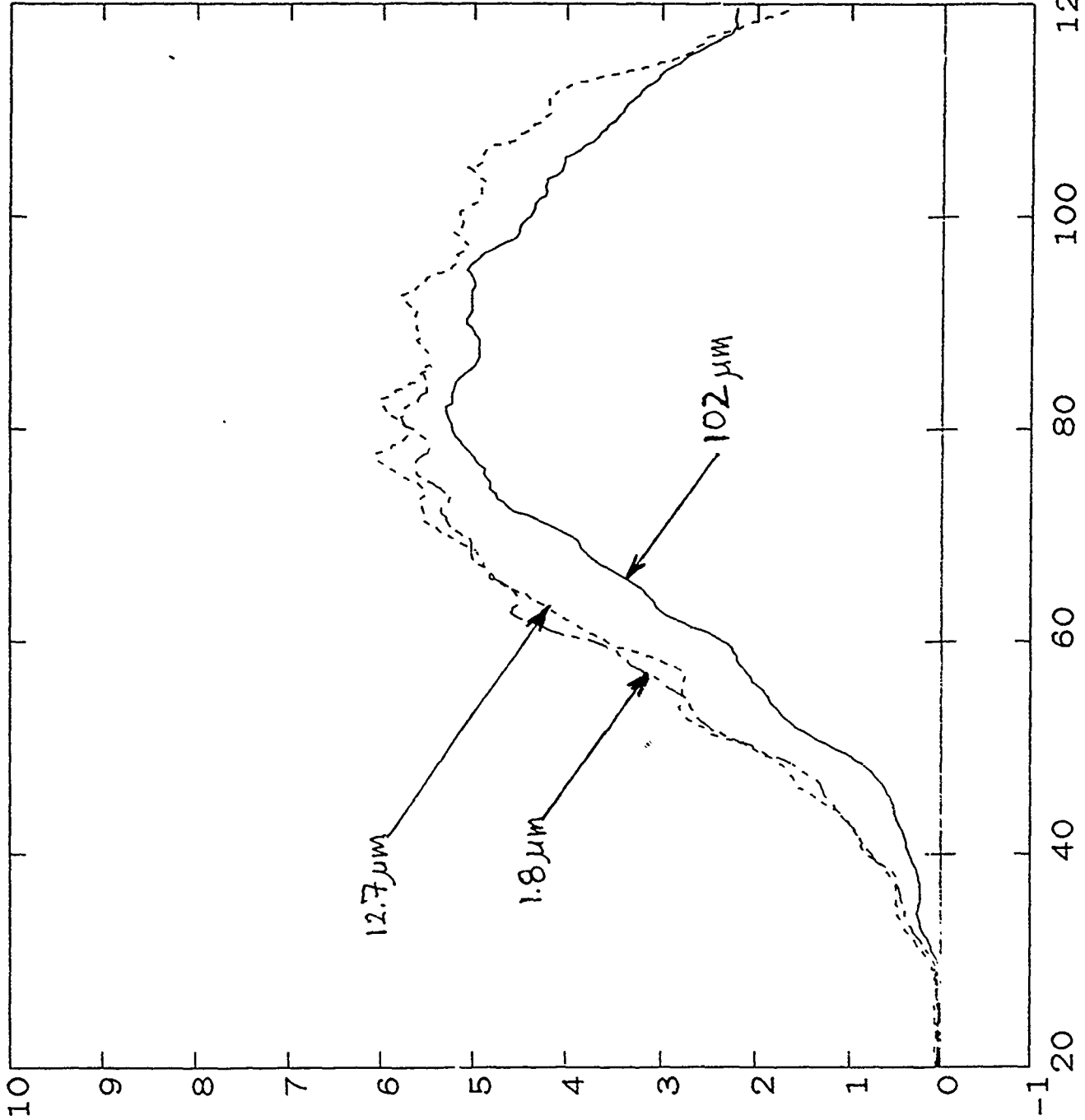
Figure 5

Shot 4707 UNBACKED - FOIL DELTA - ION POWERS

--- PION WATTS
 Units: 1.00E+11
 Max: 5.29E+11
 Ts(ns): 0.00E+00

----- PION4705 WATTS
 Units: 1.00E+11
 Max: 6.06E+11
 Ts(ns): 0.00E+00

----- PION4709 WATTS
 Units: 1.00E+11
 Max: 5.78E+11
 Ts(ns): 0.00E+00



Timescale: Nanoseconds

Figure 6

Shot 4707 UNBACKED - FOIL DELTA - ION ENERGIES

EION WATTS
Units: 5.00E+03
Max: 2.83E+04
Ts(ns): 0.00E+00

----- EION4705 WATTS
Units: 5.00E+03
Max: 3.41E+04
Ts(ns): 0.00E+00

----- EIUN4709 WATTS
Units: 5.00E+03
Max: 2.63E+04
Ts(ns): 0.00E+00

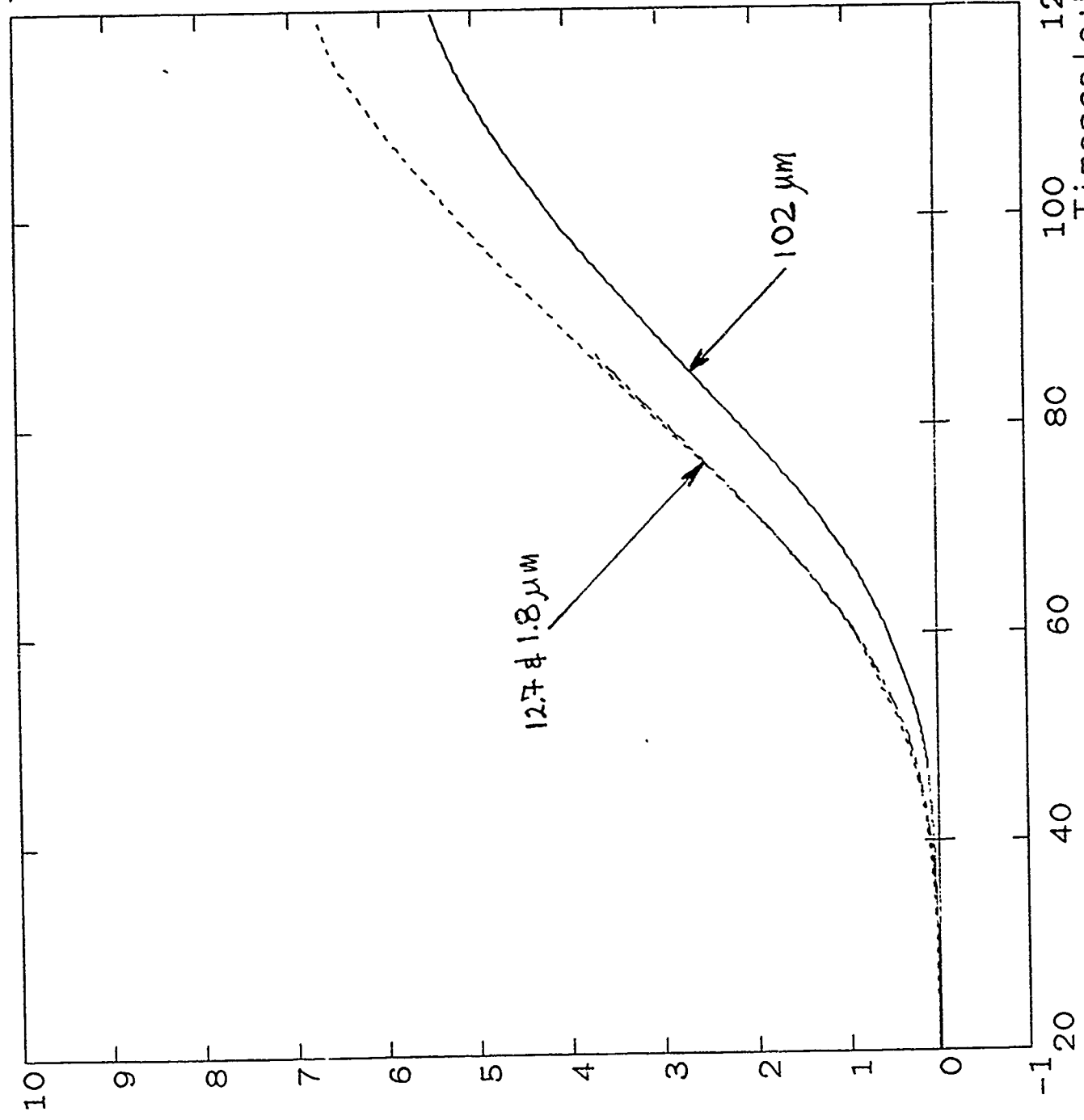
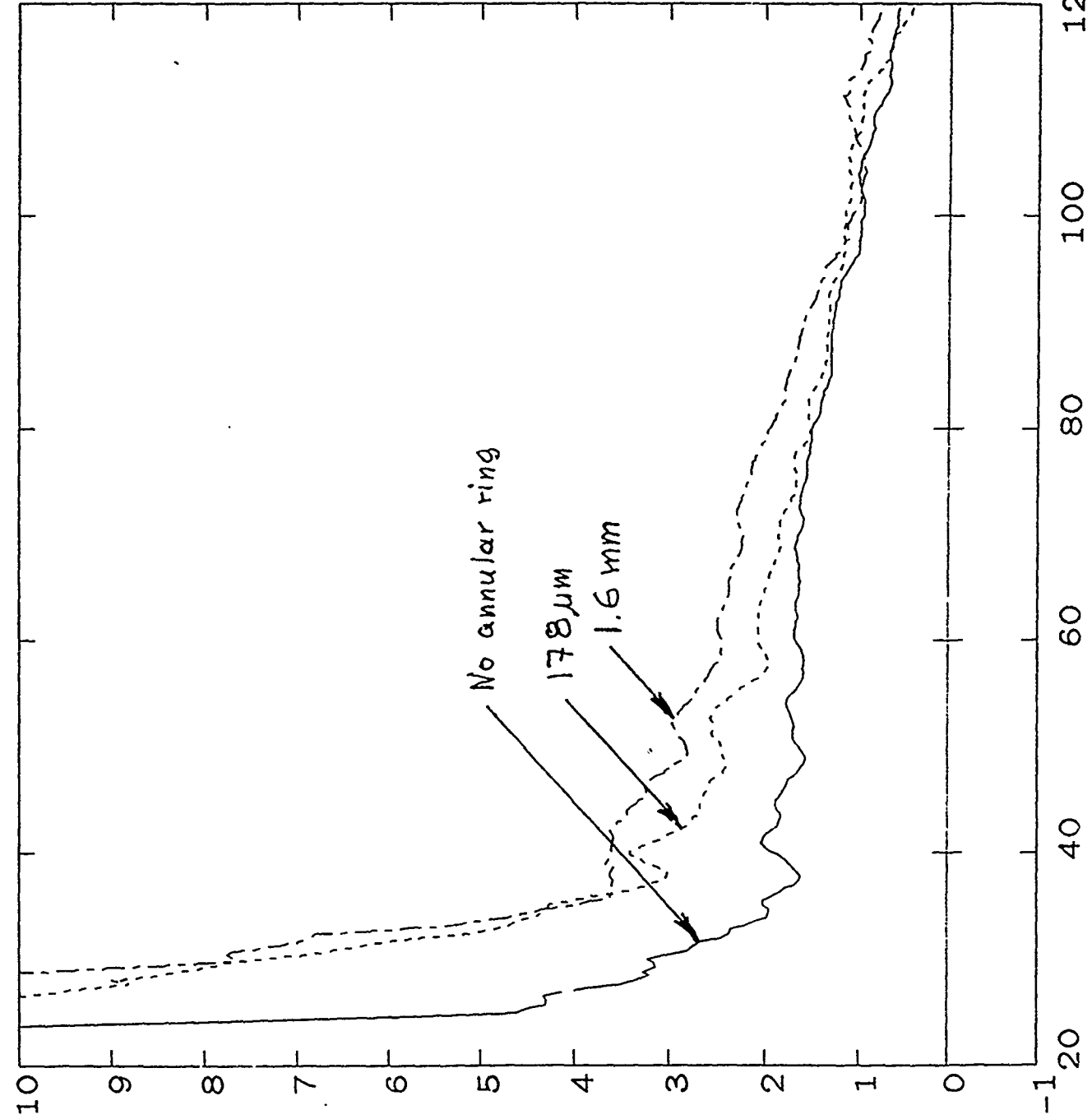


Figure 7 Timescale: Nanoseconds

Shot 4715 UNBACKED - ANNULAR RING - IMPEDANCES



Z DHMS
 Units: 1.00E+00
 Max: 1.00E+01
 Ts(ns): 0.00E+00

----- Z4705 DHMS
 Units: 1.00E+00
 Max: 1.00E+01
 Ts(ns): 0.00E+00

----- Z4710 DHMS
 Units: 1.00E+00
 Max: 1.00E+01
 Ts(ns): 0.00E+00

Timescale: Nanoseconds

Shot 4715 UNBACKED - ANNULAR RING - ION EFFICIENCIES

IEFF Amps
 Units: 1.00E-01
 Max: 1.00E+00
 Ts(ns): 0.00E+00

IEFF4705 Amps
 Units: 1.00E-01
 Max: 1.00E+00
 Ts(ns): 0.00E+00

IEFF4710 Amps
 Units: 1.00E-01
 Max: 1.00E+00
 Ts(ns): 0.00E+00

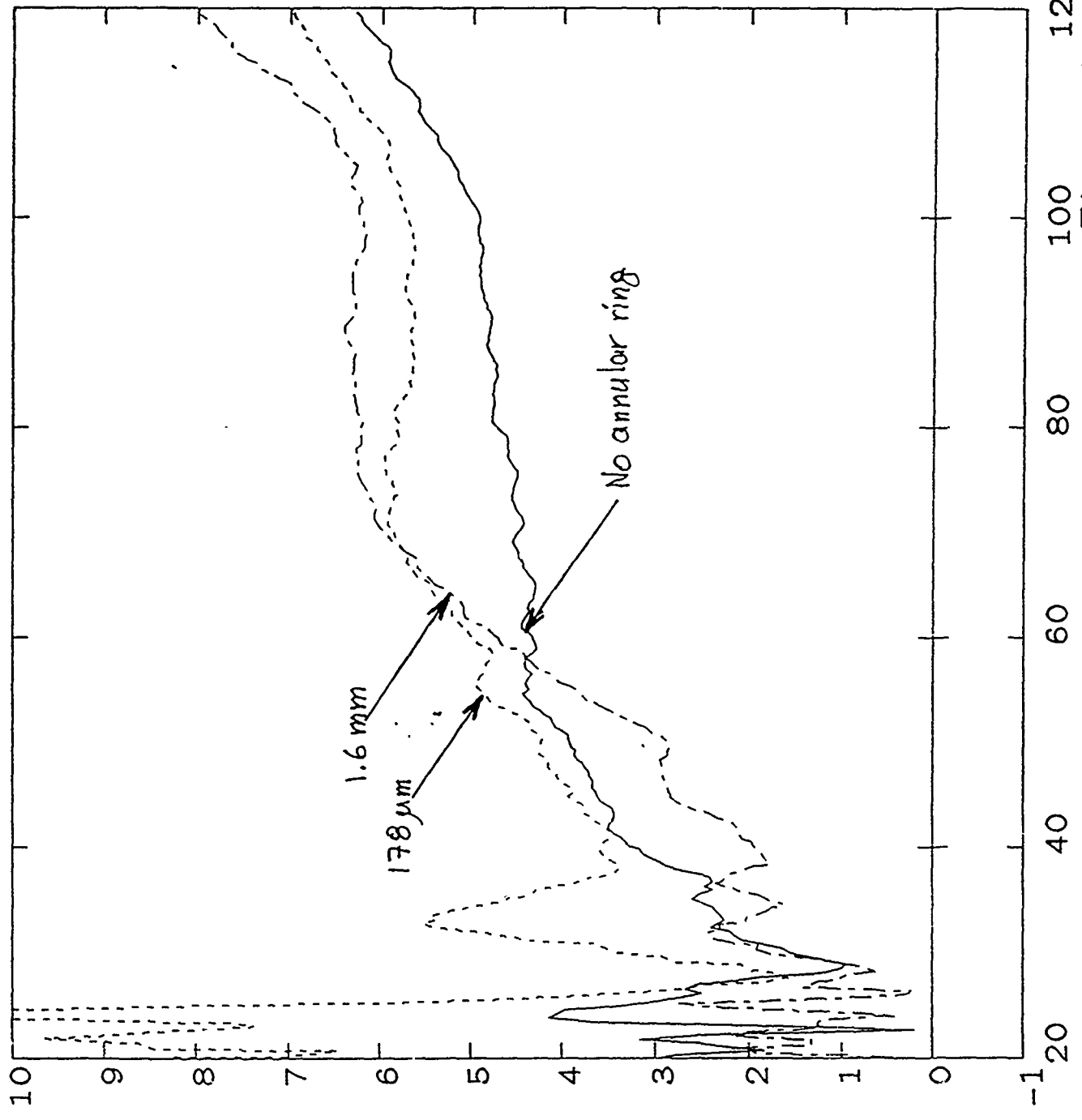


Figure 9 Timescale: Nanoseconds

Shot 4715 UNBACKED - ANNULAR RING - ION POWERS

--- PION WATTS
 Units: 1.00E+11
 Max: 5.05E+11
 Ts(ns): 0.00E+00

----- PION4705 WATTS
 Units: 1.00E+11
 Max: 6.06E+11
 Ts(ns): 0.00E+00

----- PION4710 WATTS
 Units: 1.00E+11
 Max: 6.41E+11
 Ts(ns): 0.00E+00

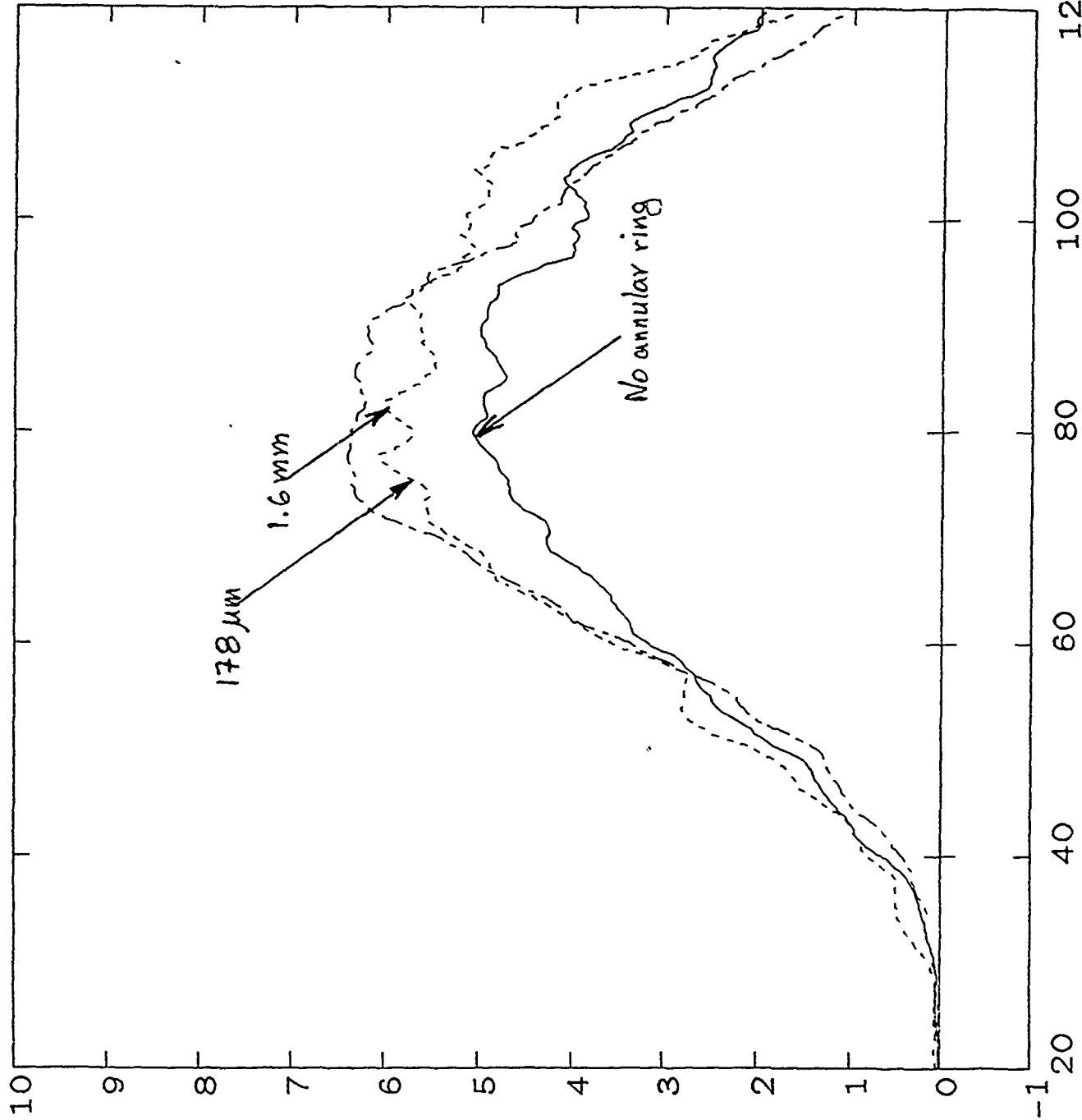


Figure 10 Timescale: Nanoseconds

Shot 4715 UNBACKED - ANNULAR RING - ION ENERGIES

— EION WATTS
 Units: 5.00E+03
 Max: 2.87E+04
 Ts(ns): 0.00E+00

----- EION4705 WATTS
 Units: 5.00E+03
 Max: 3.41E+04
 Ts(ns): 0.00E+00

----- EION4710 WATTS
 Units: 5.00E+03
 Max: 3.17E+04
 Ts(ns): 0.00E+00

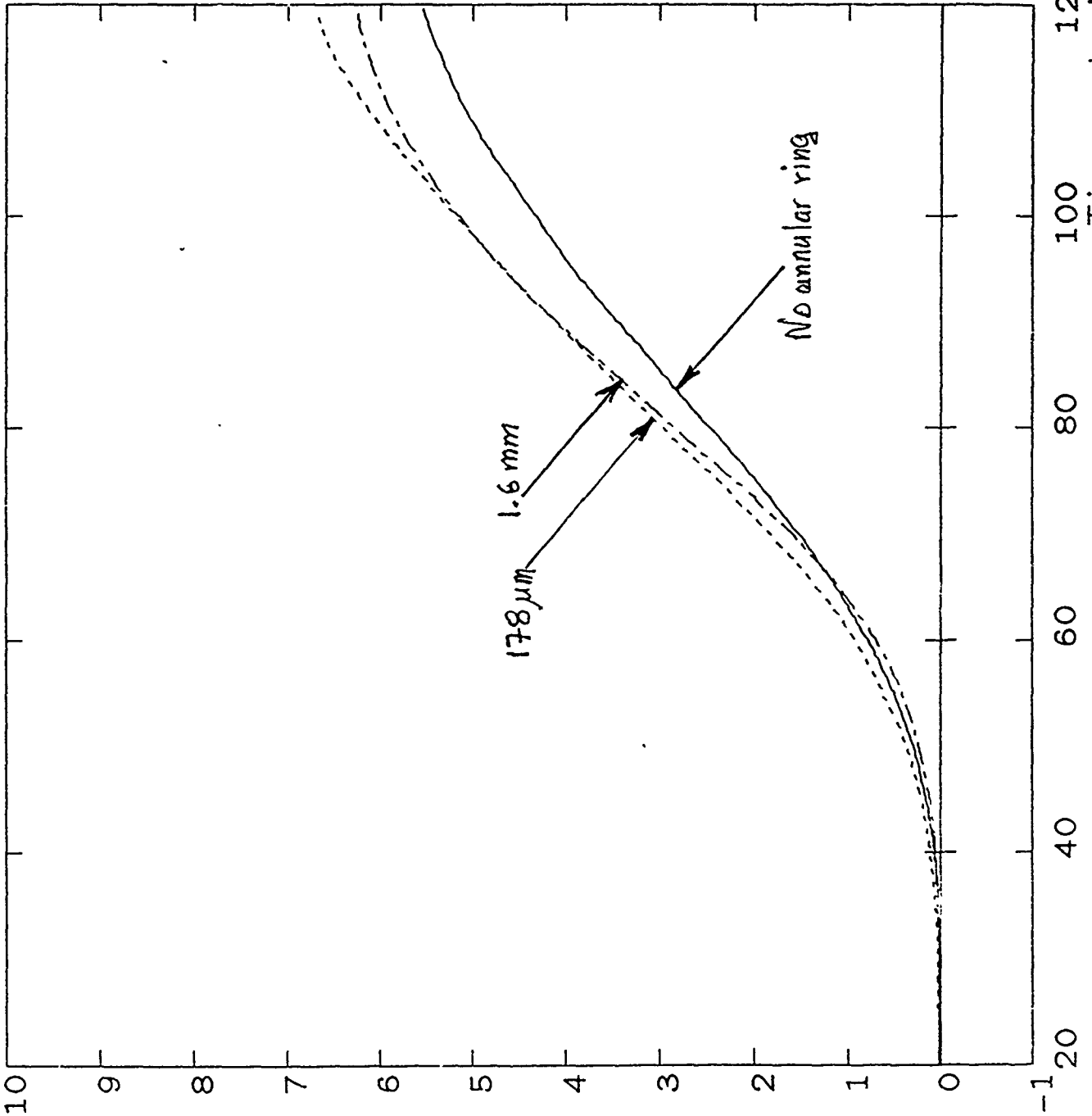


Figure 11 Timescale: Nanoseconds

across the cathode tip. So now the question remaining to be answered is whether such a diode behaves similarly to the "standard" backed-anode diode and, if not, can we live with the differences. The answer to that question is illustrated in Figures 12-15. Again, these figures display the same quantities that were shown in Figures 4-7 and 8-11. The two curves in each figure represent the "backed-anode" (#4704) and "unbacked-anode" (#4705) cases. The impedance time history (Figure 12) for the two cases looks very similar although it could be argued that the one for the unbacked tends to be a little lower especially at early times. The similarities however end there as Figure 13 clearly demonstrates. The ion efficiency is significantly higher in the unbacked case at early times and for the duration of the rising portion of the ion power pulse. Figure 14 shows that power pulse for the two cases. Note that for both cases the peak power is the same the difference being that in the unbacked case there is a 10-15% increase in the width of the power pulse which of course is reflected in the energy curves of Figure 15.

3. SUMMARY AND CONCLUSIONS

We have experimentally arrived at an anode design for the pinch reflex diode which minimizes diode debris while maintaining (actually, slightly improving) the high ion production efficiency necessary for material response studies downstream of the diode. We speculate that if further debris reduction is desired, an even thinner polyethylene reflexing foil can be used with no detrimental effects on the electrical properties of the diode. In addition, a thinner metallic annulus can be used provided it can be made smooth enough and flat enough for flush attachment onto the anode surface. More detailed studies of the bending angle distribution, microdivergence and ion specie content of the ions extracted from such a diode are needed but are not anticipated at this time due to funding limitations. Suffice it to say, that radial ion fluence maps taken in the ion drift region at various axial locations do not indicate large differences in bending angles between the unbacked- and backed-anode designs.

The physics of the electron reflexing orbits through the unbacked thin-foil anode is not known at this time. There is experimental evidence that a portion of the electron beam (probably accompanied by ions) propagates several 10's of centimeters upstream of the anode foil and strikes a "dump plate" primarily near the center. The Theory and Analysis Section (Code 4771) has undertaken a PIC code simulation of the "unbacked" geometry. This theoretical effort is progressing slowly, again due to funding limitations, but it is hoped it will give us a better physics understanding of the operation of the backless diode.

Experiments using the backless anode design have also been performed with tantalum reflexing foils in both positive and negative polarities in order to evaluate their usefulness as Bremsstrahlung sources. The results of these studies are very interesting and will be reported in detail in a future technote.

Shot 4704 BACKED VS UNBACKED IMPEDANCES

Units: 1.00E+00
Max: 1.00E+01
Ts(ns): 0.00E+00

----- Z4705 OHMS
Units: 1.00E+00
Max: 1.00E+01
Ts(ns): 0.00E+00

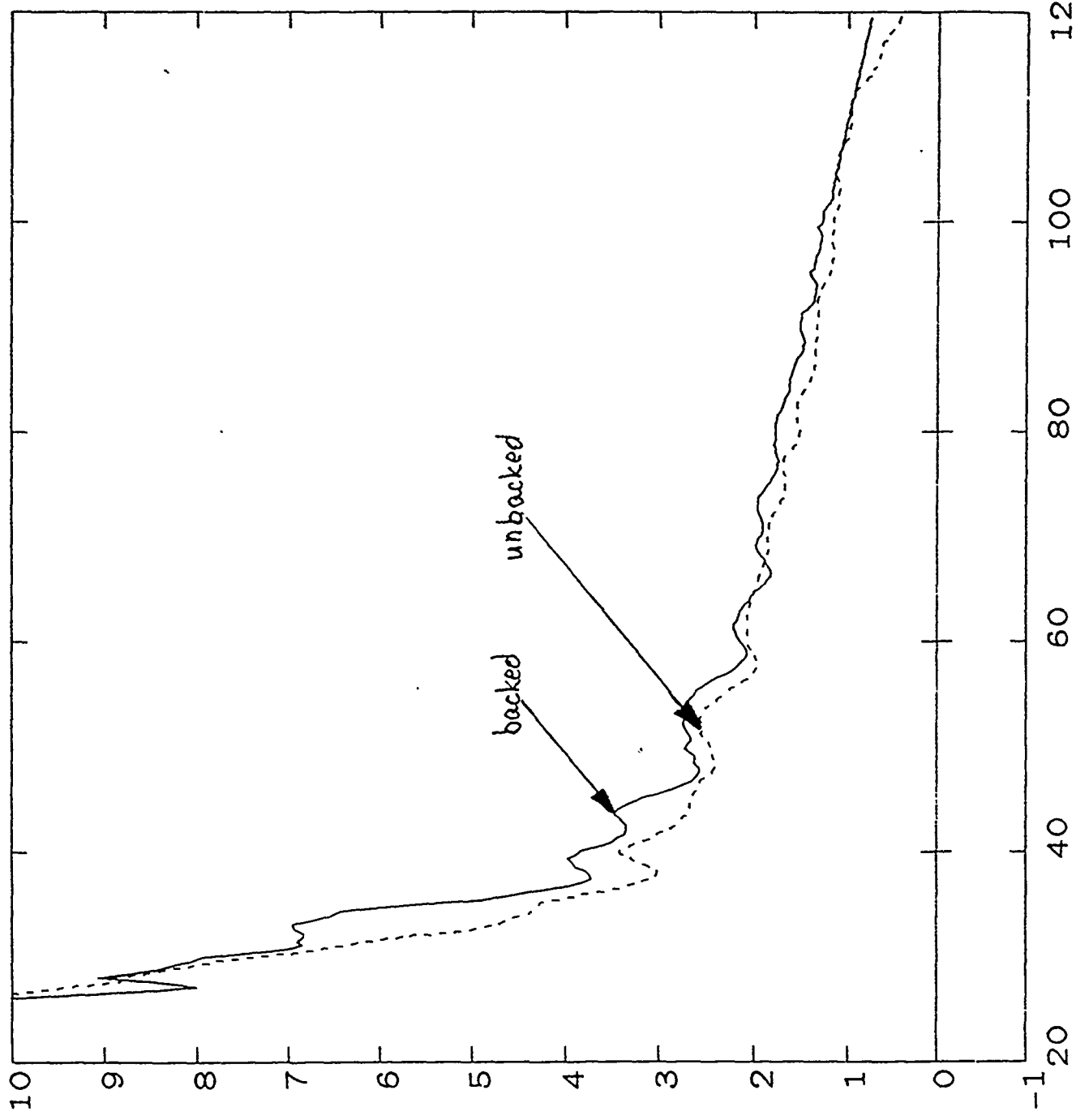


Figure 12

Shot 4704 BACKED VS UNBACKED — ION EFFICIENCIES

IEFF Amps
Units: 1.00E-01
Max: 1.00E+00
Ts(ns): 0.00E+00

----- IEFF4705 Amps
Units: 1.00E-01
Max: 1.00E+00
Ts(ns): 0.00E+00

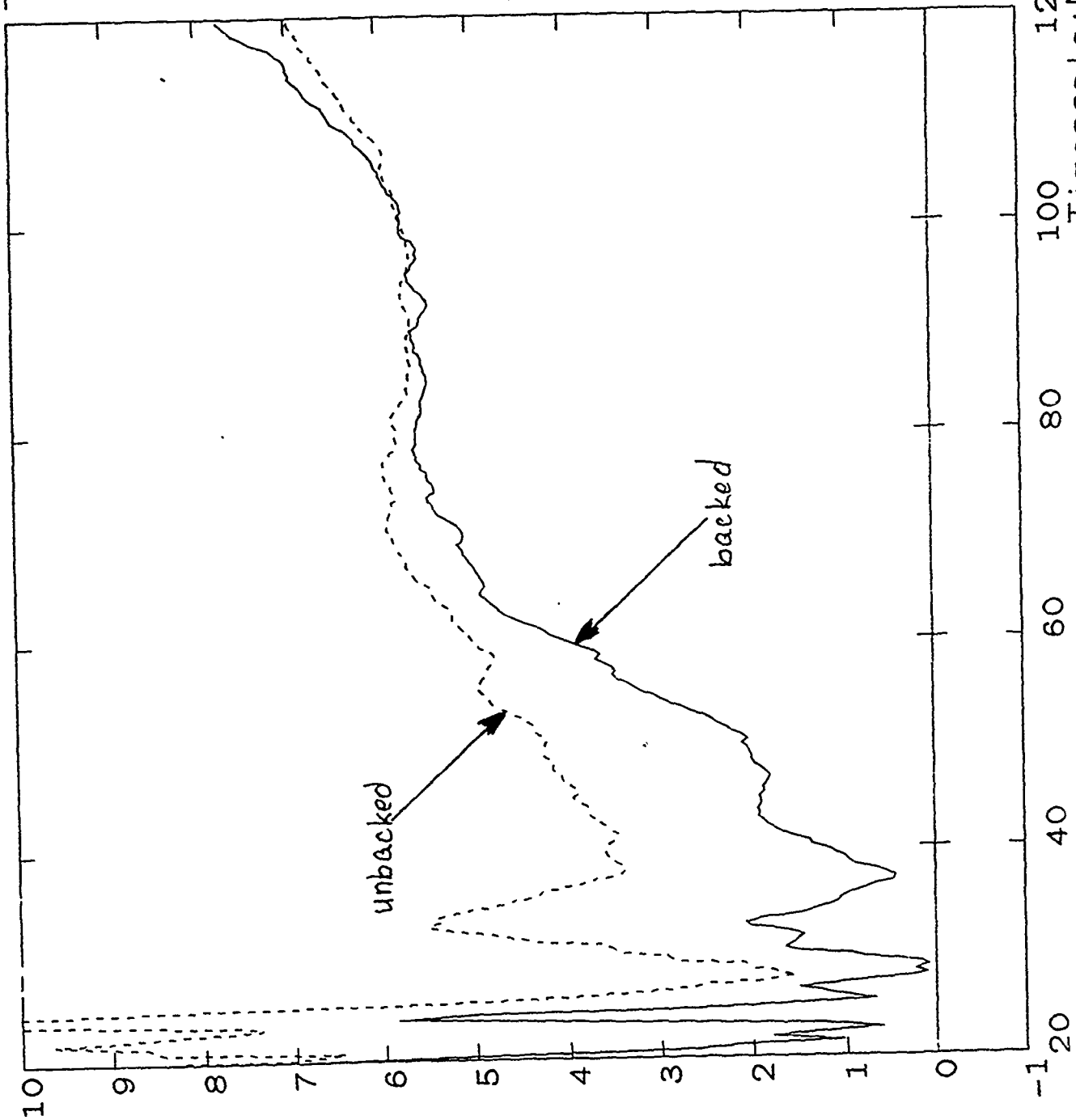
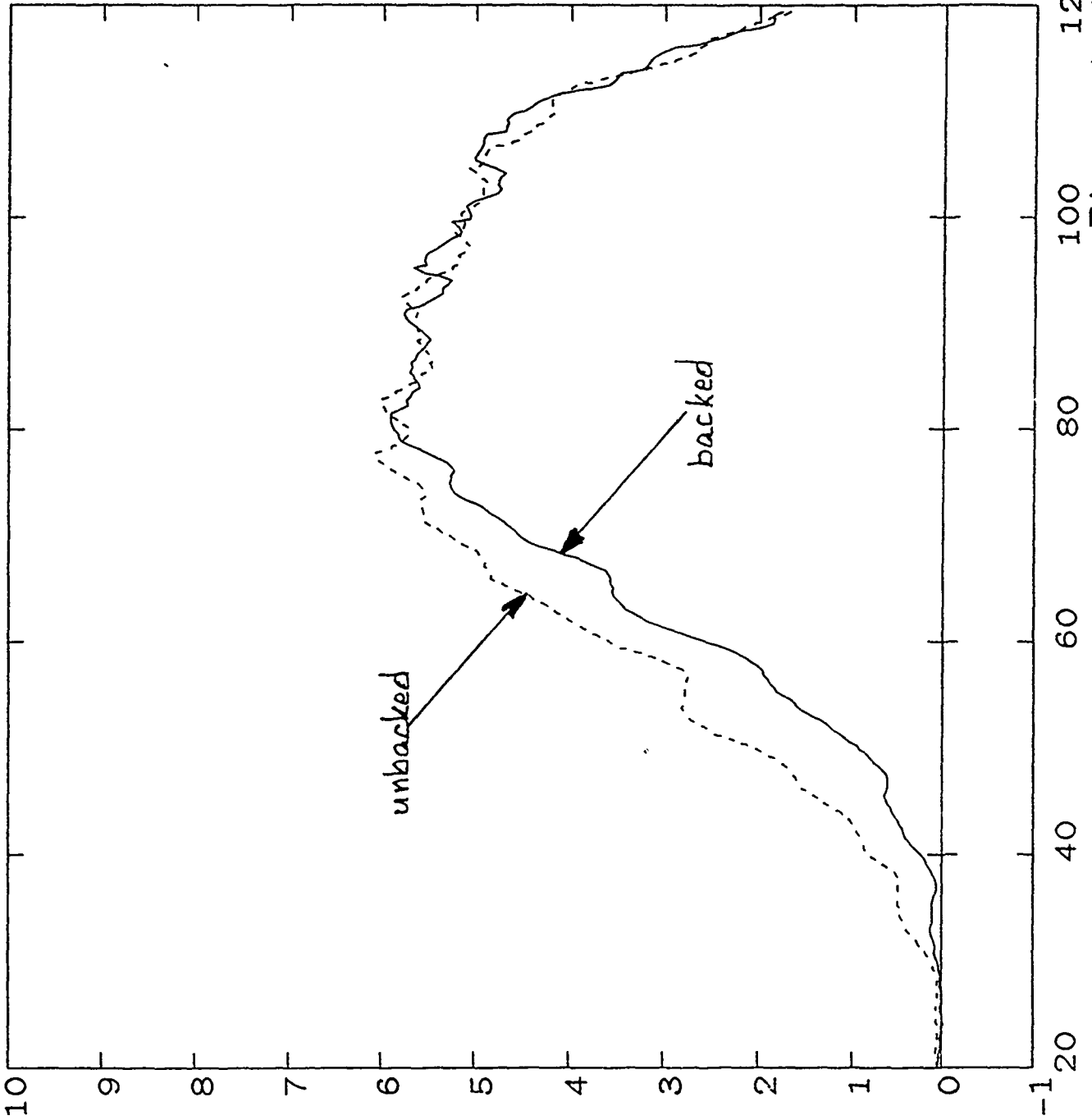


Figure 13

Shot 4704 BACKED VS UNBACKED ION POWERS

----- PION WATTS
Units: 1.00E+11
Max: 5.90E+11
Ts(ns): 0.00E+00

----- PION4705 WATTS
Units: 1.00E+11
Max: 6.06E+11
Ts(ns): 0.00E+00

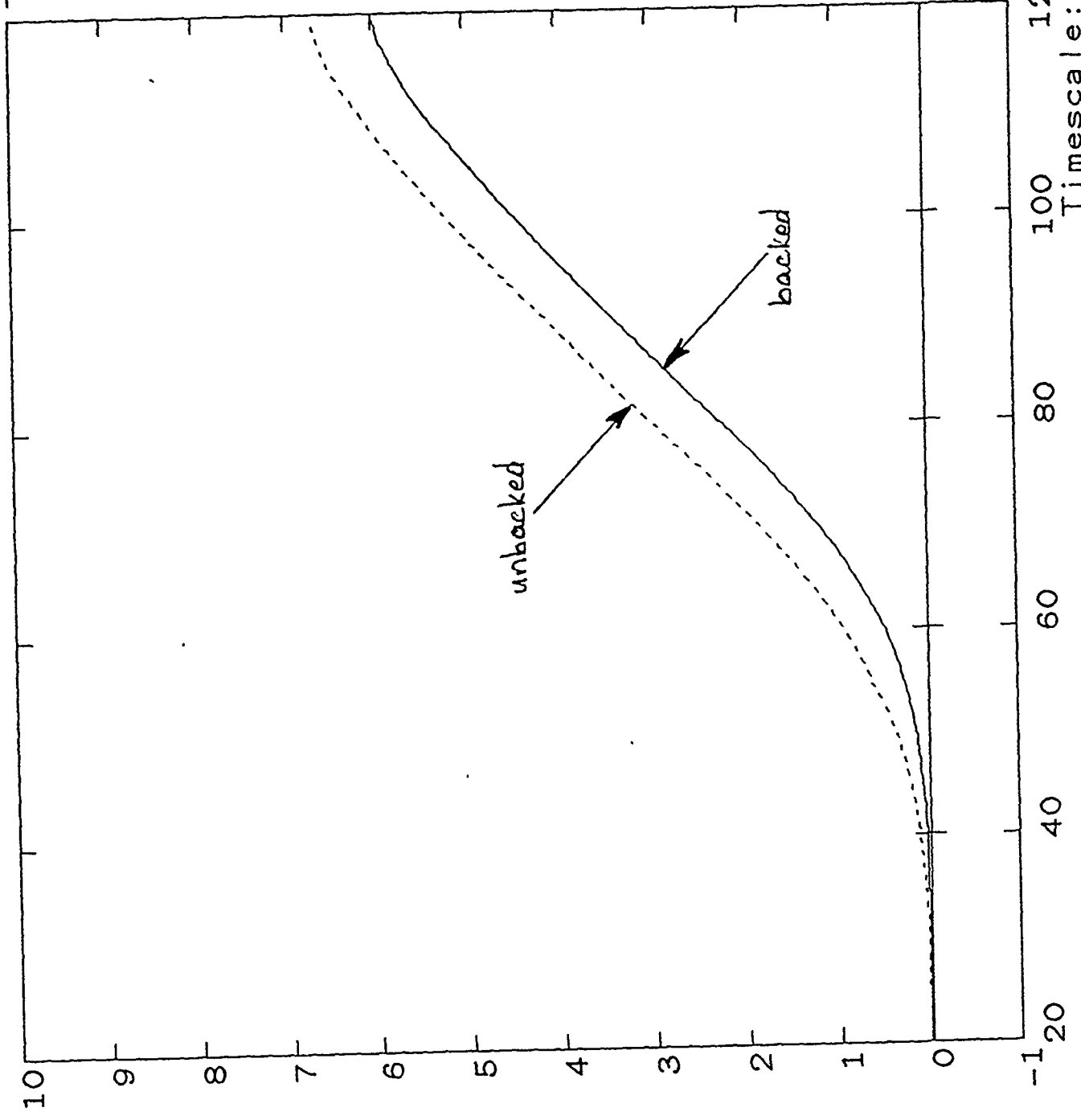


Timescale: Nanoseconds
Figure 14

Shot 4704 BACKED VS UNBACKED -- ION ENERGIES

EION WATTS
Units: 5.00E+03
Max: 3.06E+04
Ts(ns): 0.00E+00

----- EION4705 WATTS
Units: 5.00E+03
Max: 3.41E+04
Ts(ns): 0.00E+00



igu 5

PULSED POWER PHYSICS TECHNOTE NO. 91-09

TITLE: EXPERIMENTAL STUDY OF THE "BACKLESS ANODE" PINCH-REFLEX DIODE AS A BREMSSTRAHLUNG RADIATOR

AUTHOR(S): S.J. Stephanakis, J.R. Boller, J.C. Kellogg, W.F. Oliphant, V.E. Scherrer, and B.V. Weber

DATE: 26 March 1991

ABSTRACT: This is a follow-up report to Technote No. 91-01 which dealt with the "backless anode" diode as an ion source. When the plastic anode foil, used for these experiments, is replaced with a high Z (typically Ta) foil, a Bremsstrahlung-emitting diode results which may have advantages over the conventional converter Bremsstrahlung diodes used to date. The study was undertaken on Gamble II in two short experimental sessions one in positive and one in negative polarity. These experiments confirm that electron reflexing through high Z anode foils does occur and should be seriously considered for future Bremsstrahlung diode designs. Such reflexing can be significantly enhanced by the presence of a metallic insert in the interior of the hollow cathode at the expense however of copious ion current emission which in turn depresses the late-time Bremsstrahlung radiation. Ways to overcome such drawbacks and optimize the diode design for Bremsstrahlung radiation will be discussed.

THIS REPORT REPRESENTS
UNPUBLISHED INTERNAL
WORKING DOCUMENTS AND
SHOULD NOT BE REFERENCED
OR DISTRIBUTED

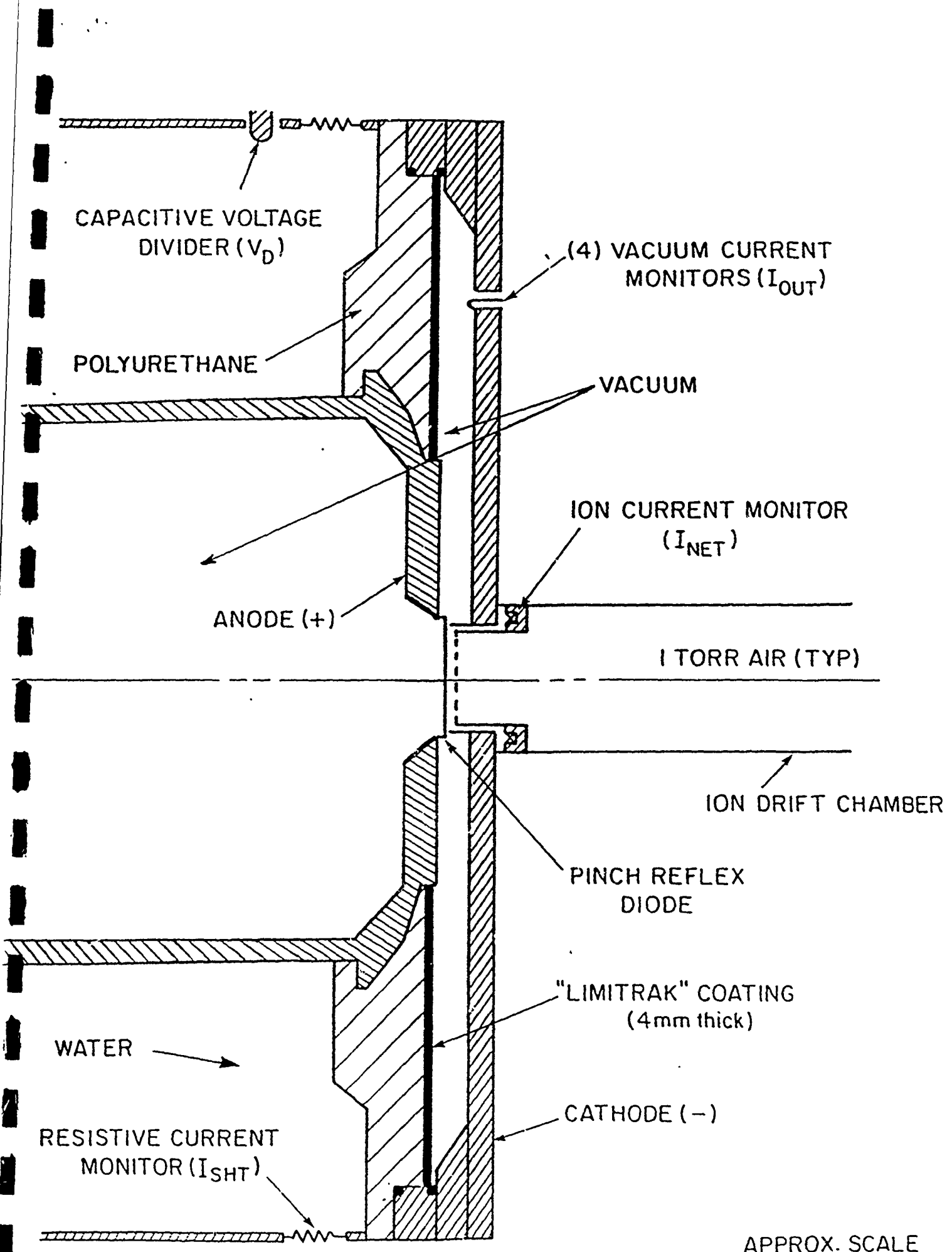
1. INTRODUCTION

All the experiments described herein were performed on the Gamble II generator with the Marx charged to ± 36 kV for both polarities. The transit time isolator was not used thus allowing the full available power at this charging voltage to reach the load. The cathode in all cases was the standard -12 cm diameter, -3 mm tip width, hollow cylinder with aerodagged tip.

The results will be presented separately for the two polarities in Sections 2 and 3 since the two experimental sessions were separated in time by several months and the diagnostics (photodiode and TLD's) were located differently and filtered differently in the two sessions. Thus, direct comparison of absolute values of the radiation output is not possible for the two polarities. However, some physics observations concerning the two configurations and their similarities and differences can and will be made in the Summary and Conclusions Section.

2. POSITIVE POLARITY RESULTS

The diode geometry used for the positive polarity tests is shown in Fig. 1. Note that this figure is essentially identical to the second figure of Technote No. 91-01 the only difference being the atomic number of the anode reflexing foil. The $2\mu\text{m}$ Kimfol covering the I_{NET} monitor was in all cases located 8 mm downstream of the cathode tip and 13 mm from the anode (5 mm A-K gap). The drift chamber was filled with 1 Torr air (as for the ion shots) and a photodiode was viewing the anode end-on from about 2 m away. The first striking observation made from the outset of this experimental run was that, for the geometry shown in Fig. 1, Ta anodes are copious emitters of ions (probably protons from desorbed gases on the surface of the Ta). As illustrated in Figures 2 and 3, the ion current from a 0.5 mil thick backless Ta anode starts 25 nsec later than for the 0.5 mil thick backless CH_2 anode. However, once the ion current is



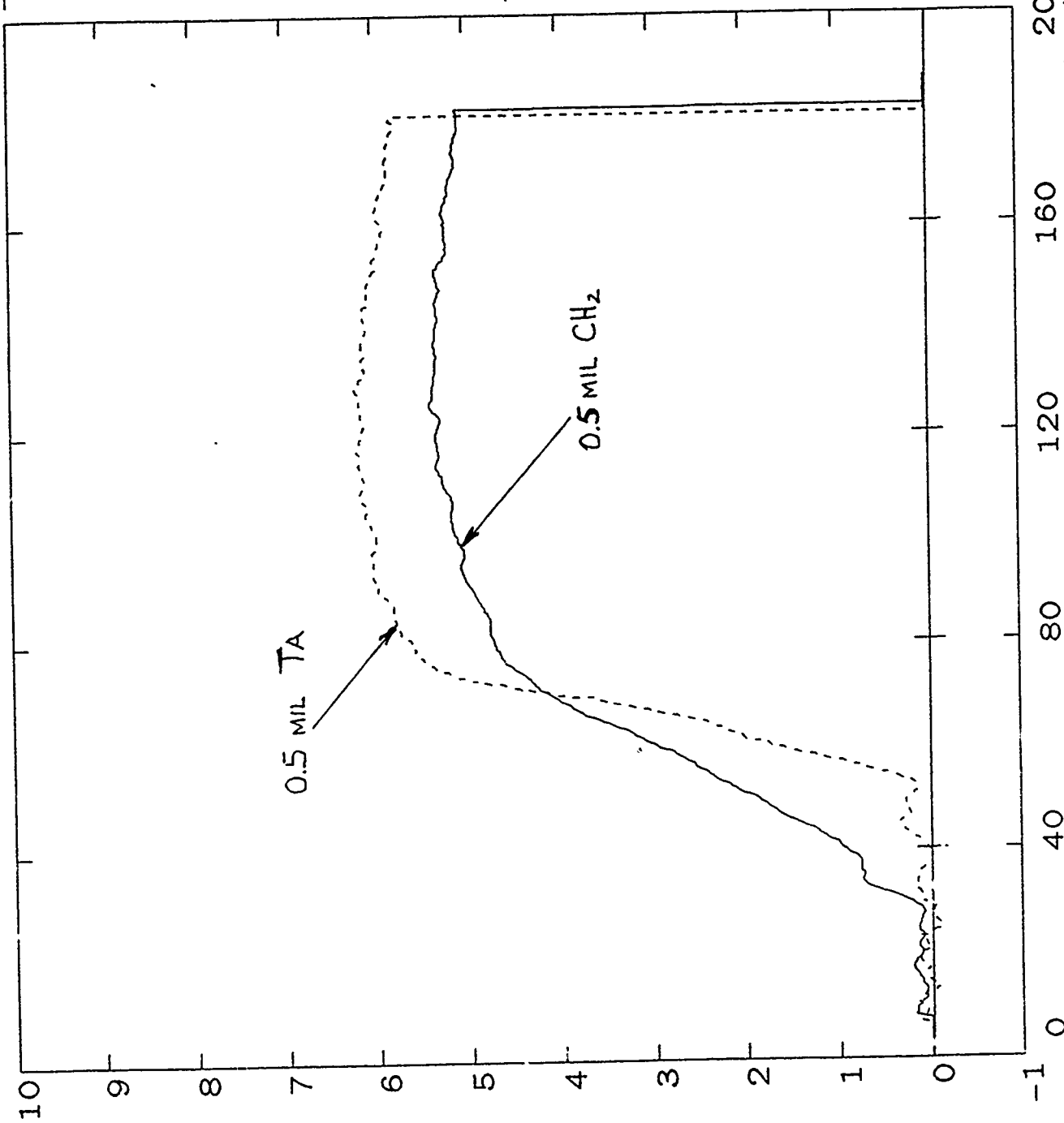
APPROX. SCALE

Figure 1

Shot 4705 ION CURRENTS CH2 VS TA ANODE

INET Amps
Units: 1.00E+05
Max: 5.38E+05
Ts(ns): 0.00E+00

INET4711 Amps
Units: 1.00E+05
Max: 6.21E+05
Ts(ns): 0.00E+00



Shot 4705 ION EFFICIENCIES CH2 VS TA ANODE

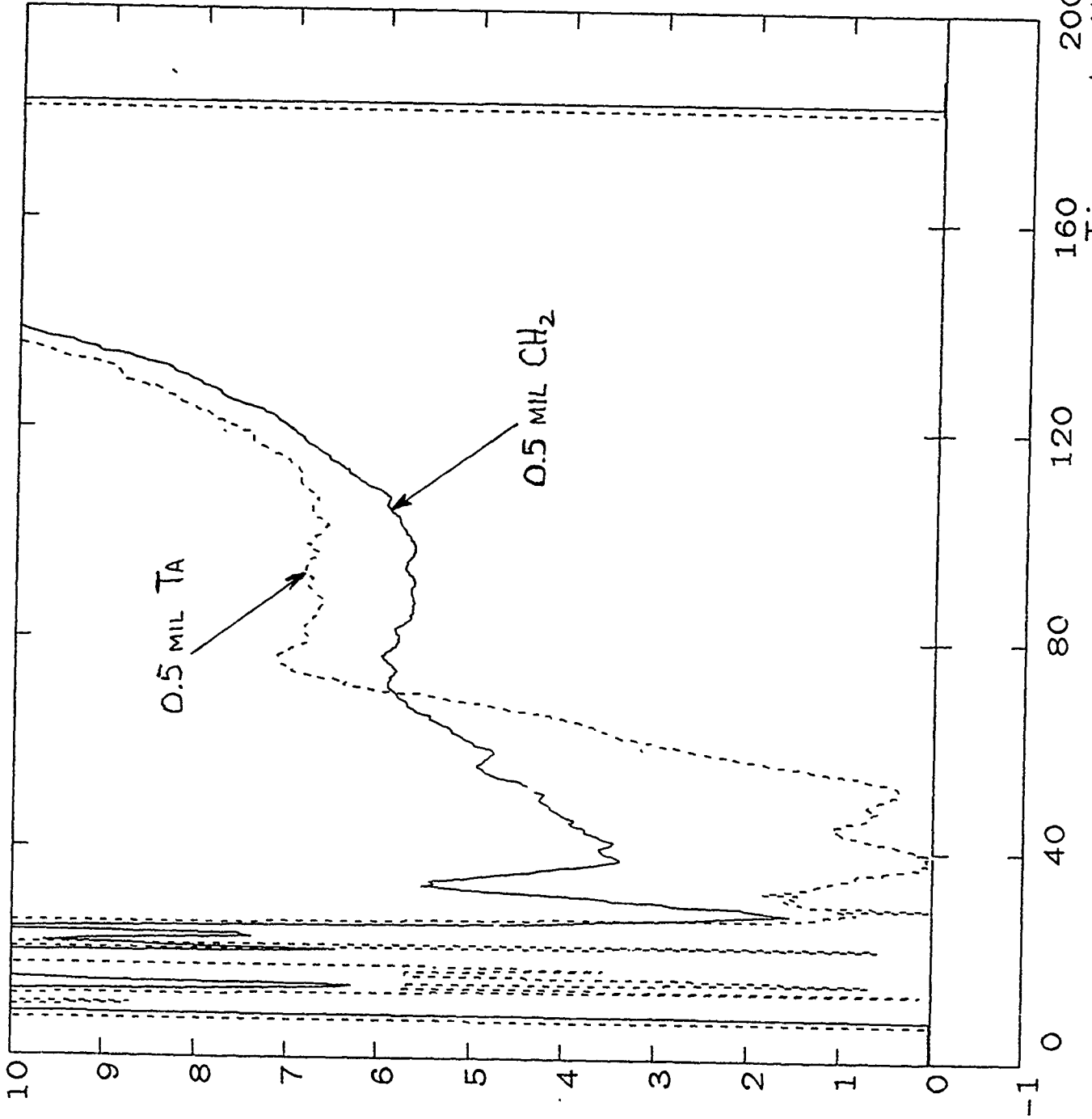


Figure 3

initiated, it reaches its peak in about half the time of that required for CH₂ anodes. In addition, the ion current and ion efficiency (defined as I_{NET}/I_{OUT}) are actually higher for the Ta anode than for the CH₂ anode at the time of peak power which occurs at ~80 - 90 nsec for both shots. Furthermore, aerodagging of the Ta foil (on both sides) made no difference whatsoever in the ion emitting ability of the anode as is clearly illustrated in Fig. 4. By backing the 0.5 mil Ta foil with a solid block of carbon or by increasing the foil thickness to 4 mils we were able to reduce the ion current slightly (~15%) and further delay its onset by 4 - 5 nsec.

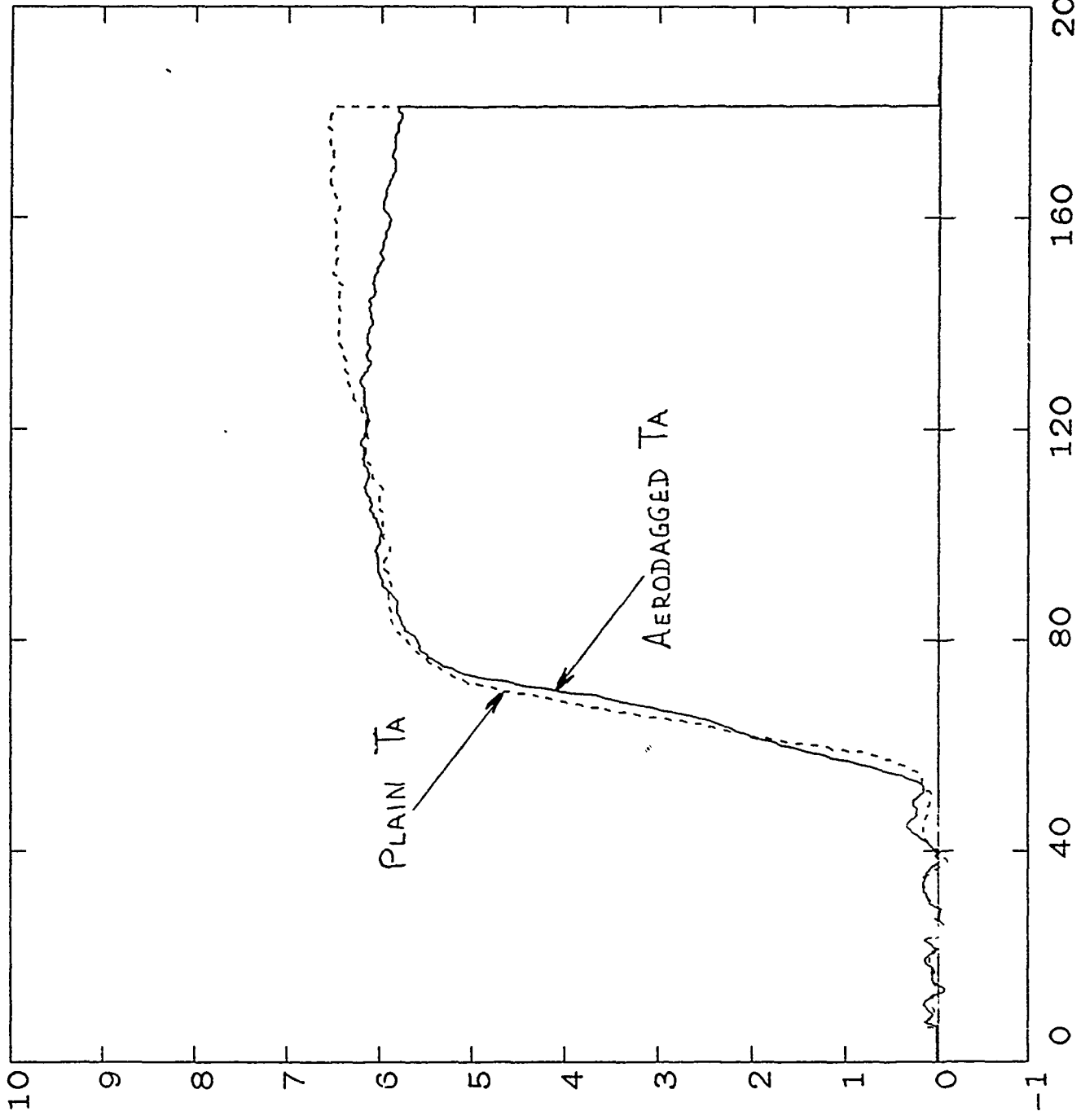
The radiation pulses for the anode configurations studied are shown in Fig. 5. The two shots labeled "0.5 mil Ta (reflexing)" had 0.5 mil Ta anodes with no backing whatsoever. The shot labeled "0.5 mil Ta, non-reflexing" had an anode consisting of 0.5 mil Ta foil in contact (on the upstream side) with a solid backing of 1/4" thick graphite. Finally, the shot labeled "4 mil Ta (reflexing?)" had an anode configuration identical to what is used routinely in negative polarity for Bremsstrahlung production, i.e., a 4 mil Ta foil backed, after a ~2cm vacuum gap, by a debris catcher consisting of 1/8" thick melamine covered (on the e-beam side) by 1/8" thick boron carbide tiles. Note that the non-reflexing case produces about 2.5X less radiation than the reflexing cases for the same thickness Ta foil. In addition, the 0.5 mil Ta reflexing anodes produce almost as much radiation as the "standard" Bremsstrahlung converter. At this point, it is not known to what extent reflexing occurs in the 2cm vacuum gap behind the 4 mil foil; it is possible that if the 4 mil Ta anode were totally backless even more radiation would have been observed. On the other hand, if the 4 mil Ta were to be backed by solid carbon we speculate that the x-ray yield would drop. These possibilities should be studied in a more systematic series of experiments in the future.

A peculiarity of the radiation pulses shown in Fig. 5 is that they all exhibit a two-hump shape. Such a shape is not observed in negative polarity with the standard 4 mil Ta x-ray converter.

Shot 4711 HALF MIL TA ANODE PLAIN VS AERODAGGED

INET Amps
Units: 1.00E+05
Max: 6.21E+05
Ts(ns): 0.00E+00

----- INET4713 Amps
Units: 1.00E+05
Max: 6.55E+05
Ts(ns): 0.00E+00



Timescale: Nanoseconds

Figure 4

Positive polarity PD signals reflexing vs non-reflexing

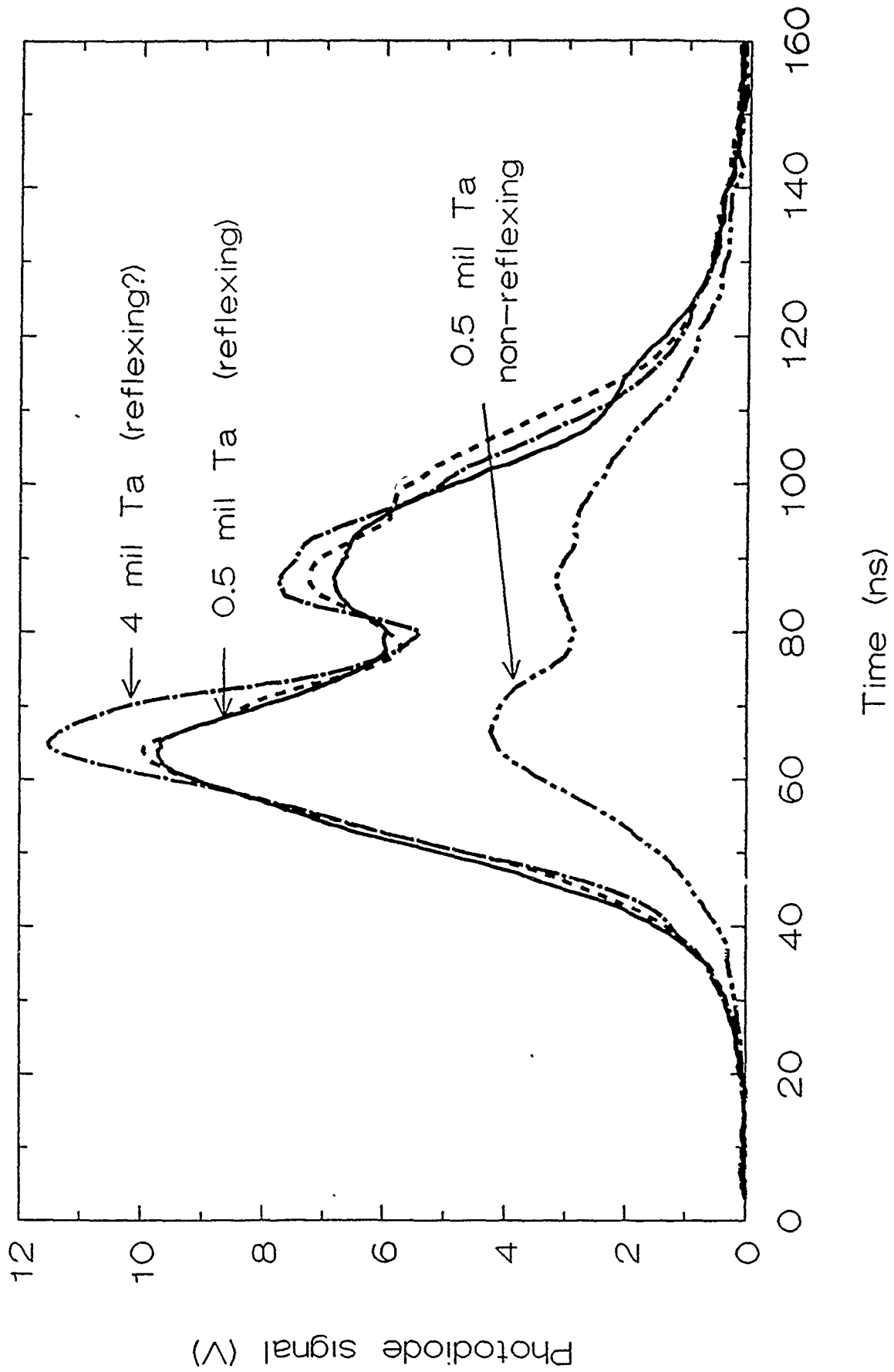


Figure 5

The reason for this becomes apparent when one examines the voltage, current and impedance waveforms of any one of the shots. Typical such waveforms are shown in Fig. 6. Note the sudden drop in impedance at the time of ion current onset and the accompanying drop in voltage and photodiode signal while, at the same instant in time, the total diode current increases rapidly consistently with the factor-of-two drop in impedance. Thus it is rather apparent that the double-humped behavior of the x-ray pulse is associated with the onset of significant ion current and the two-tier impedance behavior. This effect is not as obvious when plastic anodes are used because, as is shown in Fig. 2, the ion current onset in that case occurs more than 24nsec earlier in time and thus the effect of such an onset on the impedance is obscured by the fact that the impedance is dropping rapidly at that time from its infinite open-circuit value.

Matching the x-ray shapes of Fig. 5 to the product IV^n proved to be difficult partly because of the need to deduce the electron current (I_e) component of the total current (I_{OUT}). This requires the subtraction of the ion current trace (I_{NET}) from I_{OUT} and the shape of I_{NET} once it reaches the plateau (crowbar?) is not known with a high degree of confidence. Suffice it to say, that the reflexing shots (0.5 mil Ta and 4 mil Ta) produce an x-ray pulse more closely resembling $V_{cor}I_{el}$ as illustrated in Fig. 7. As expected, no match could be found when I_{OUT} was used rather than I_{el} . A similar exercise performed for the shot with no reflexing resulted in no match whatsoever in either overall pulsewidth or ratio of hump amplitudes. It is speculated that since the backing for the 0.5 mil Ta foil for this shot was thick graphite the resulting Bremsstrahlung pulse is due to a combination of high energy electrons passing once through the Ta foil, the same electrons stopping in graphite and lower energy electrons being stopped by the Ta foil. Thus the pulse amplitude would be a function of voltage as well as Z at different times and consequently cannot be modeled by a single simple expression involving voltage and electron current.

Shot 4716 POS POL BREMS DIODE TRACES AND X RAYS

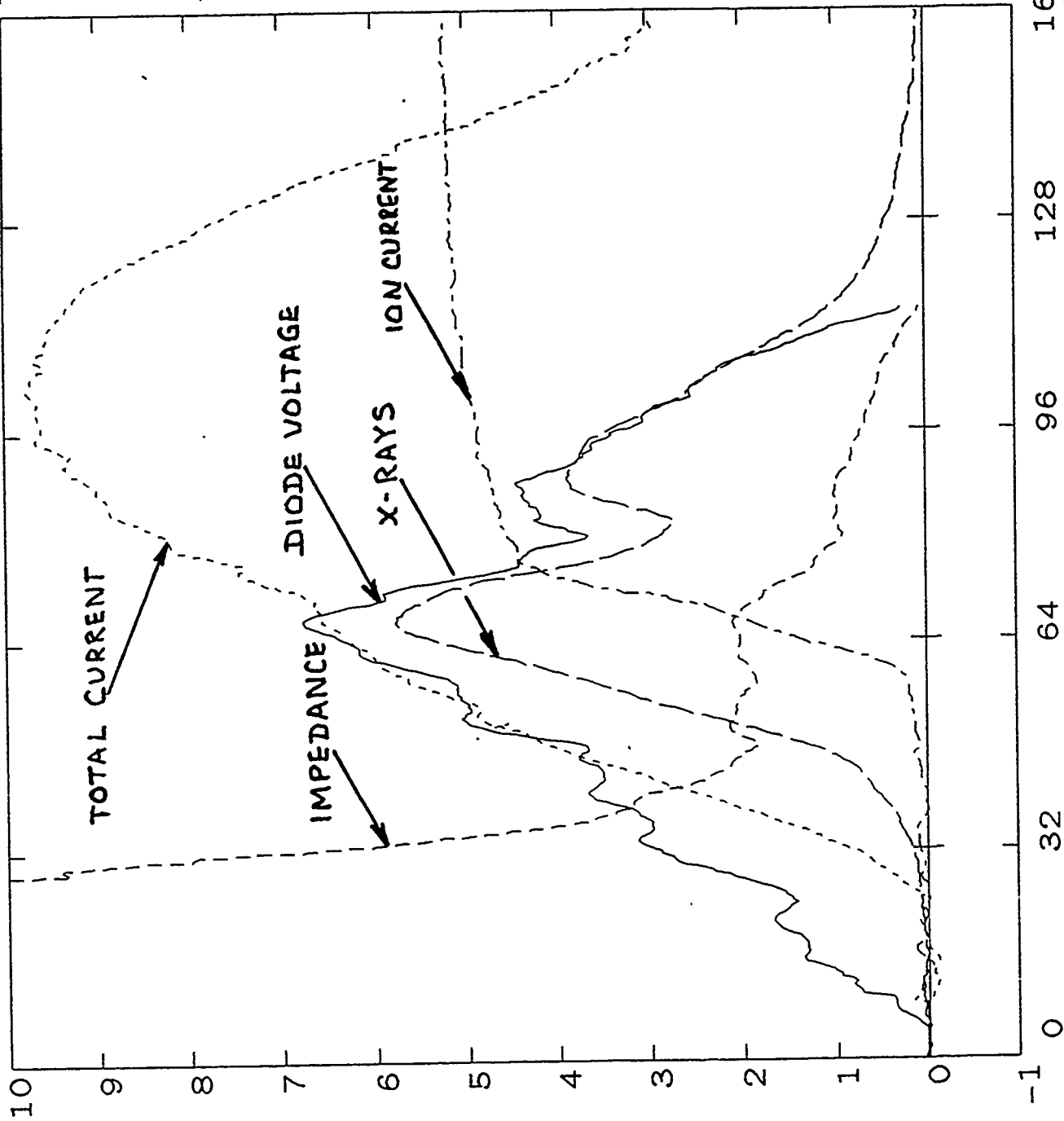
VCOR Volts
 Units: 2.00E+05
 Max: 1.35E+06
 Ts(ns): 0.00E+00

IOUT Amps
 Units: 1.00E+05
 Max: 9.76E+05
 Ts(ns): 0.00E+00

INET Amps
 Units: 1.00E+05
 Max: 5.26E+05
 Ts(ns): 0.00E+00

ZT OHMS
 Units: 1.00E+00
 Max: 9.41E+00
 Ts(ns): 0.00E+00

PDT Volts
 Units: 2.00E+00
 Max: 1.15E+01
 Ts(ns): -2.59E+01



Timescale: Nanoseconds

ATTEMPT TO MATCH BREMS. EMISSION WITH IV^n

Positive polarity - 0.5 mil Ta backless anode w/ions

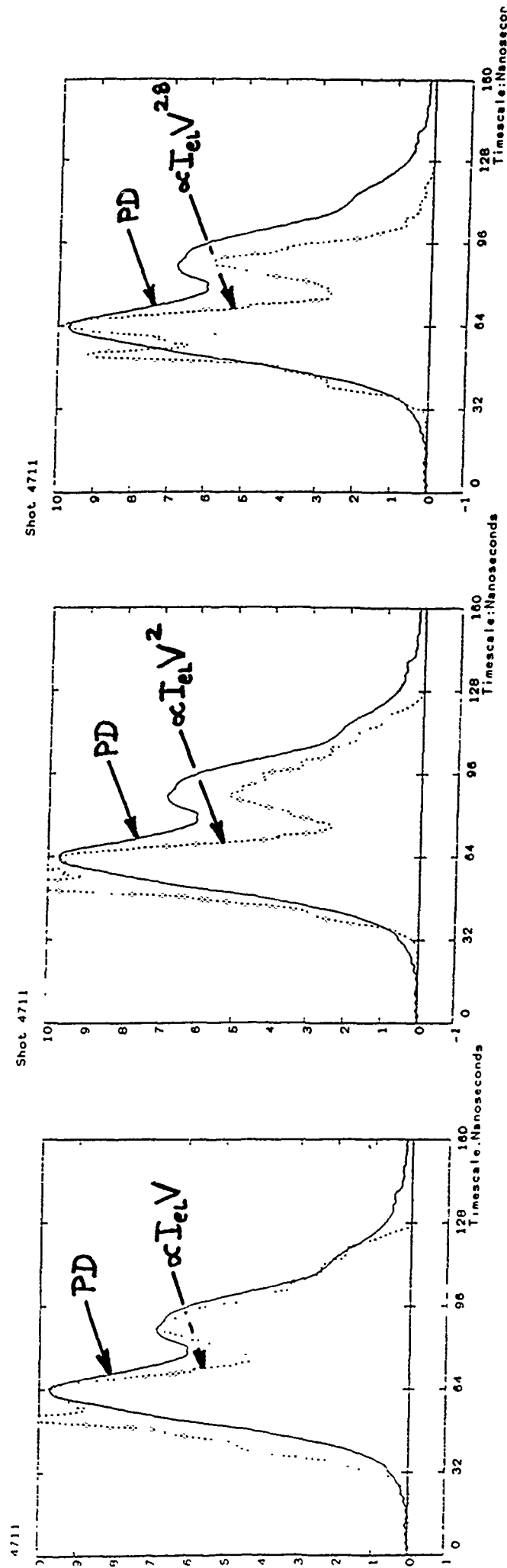


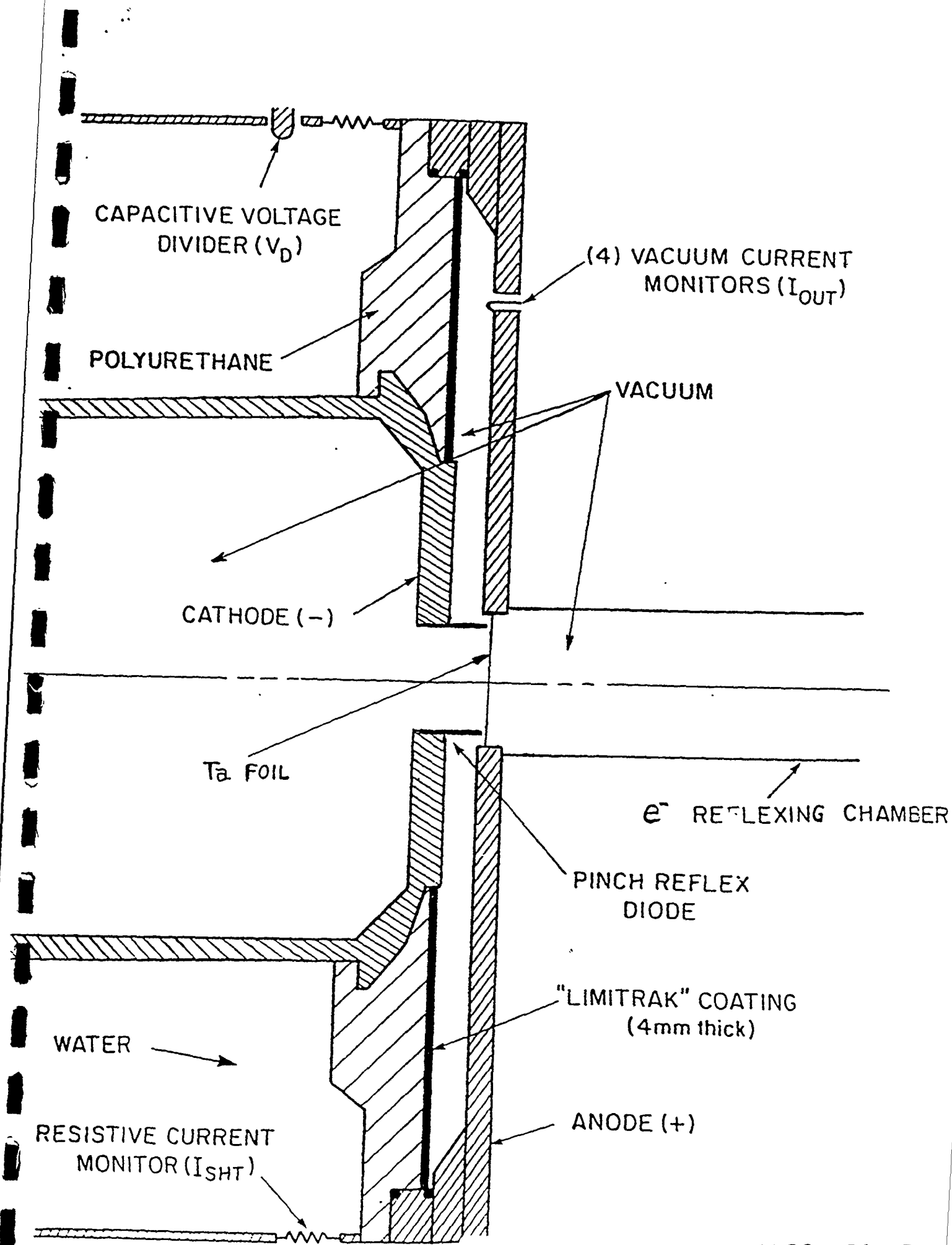
Figure 7

3. NEGATIVE POLARITY RESULTS

The diode geometry used for the negative polarity tests is shown in Fig. 8. It is essentially a mirror image of Fig. 1 except that for most shots the cathode was totally hollow. No ion current measurements were possible in this geometry. Additionally, the photodiode was again looking end-on from a distance of ~4.4m from the downstream side of the anode. In some shots TLD's were fielded in addition to the photodiode to provide absolute dose measurements and to check consistency from shot to shot. The anode-cathode gap for this experimental series was 5.9mm (rather than the 5mm in positive polarity) which is the gap routinely used for efficient Bremsstrahlung production.

The first tests made in this configuration had the purpose of establishing a data baseline and re-certifying the ability of Gamble II to produce the advertised radiation. Thus, the anode consisted of a 4 mil Ta foil followed (downstream) by a ~2cm vacuum gap and a boron-carbide-covered melamine debris catcher. The 1/8" thick melamine served as the vacuum seal. An array of five, equally-spaced CaF₂ TLD's were arranged along a diameter of a 6" circle at a distance of 12.5cm from the anode converter. The average dose over the 150 - 200cm² covered by the TLD's was 9.5 ± 1.3 kRad Si (11.0 kRad Si @ the center) which is consistent with the advertised doses in the DNA Radiation Facilities booklet (2nd Edition) as well as in the internally-generated package that we provide potential Gamble II users. Two more shots with this anode configuration were fired with the only difference being the location of the TLD array, this time at 95cm from the anode. The radiation dose in this case for the two shots was 178 ± 8 Rads Si and 196 ± 6 Rads Si respectively which follows approximately the anticipated $1/d^2$ scaling with distance from the source when compared to the dose @ 12.5cm.

The next set of shots used a purely reflexing anode configuration with a free-standing 0.5 mil Ta foil anode followed by a 95-cm long evacuated 6" chamber. The end of the chamber was



vacuum-sealed by the usual melamine/boron-carbide end-plate so that the overall x-ray attenuation as viewed by the end-on-looking photodiode was the same for all shots. The x-ray yield for these shots, as monitored by the photodiode, dropped by about a factor of 3 relative to the 4 mil shots. Furthermore, the TLD array at the 95cm position actually increased dramatically (instead of decreasing as anticipated from the photodiode signals) to a value of 464 ± 150 Rads Si (!). The erratic TLD readings (as indicated by the ± 150 Rads variation along the 6" diameter) plus their unexpected high value leads us to believe that the TLD readings are primarily due to diode electrons which traversed the whole 95cm distance without reflexing and impinged on the BC target which was within 2cm of the TLD's. Based on the photodiode signals the dose should have been ~ 65 Rads Si. Taking this expected dose into account as well as the ratio in Z's between Ta and BC (~ 13) and the distances involved, we can make the following estimate. If X electrons interacted with the Ta anode producing ~ 65 Rads Si at the TLD position then it would only take $0.035X$ electrons of the same energy interacting with the BC target to produce the extra 400 Rads Si observed. The photodiode signal is not affected at all ($<0.5\%$) by radiation from the BC because of its location at 4.4m from the anode and 3.5m from the BC and the relative strength of the two x-ray sources (367:1).

The 0.5 mil Ta , fully-reflexing shot was repeated with a 6.5" long, 12" dia tube followed by a 20" long, 20" dia tube replacing the 6" tube shown in the figure to test the possibility that the reflexing chamber diameter had an effect on the physics of electron reflexing and thus altered the radiation properties of the backless-anode diode. The result of this test was clear-cut in that the two shots were identical in all respects.

At this point in the experimental session, one observation was becoming very apparent. The photodiode signals from the shots described above, were all well-behaved, single-humped and

belljar-shaped in obvious contrast with the double-humped photodiode signals observed in the positive polarity shots (see Fig. 5). We had already concluded from the data taken in positive polarity that the drop in the photodiode signal creating this double-hump effect was due to the sudden onset of ion current. Thus we attempted to simulate the exact geometry used in positive polarity by inserting a solid conductive plate inside the cathode, 8mm upstream of the tip as per the Kimfol location in positive polarity. The results of this test were dramatic. Not only did the double-hump nature of the photodiode signal reappear but the first hump was more than a factor of 2 higher in amplitude than the peak of the 0.5 mil Ta backless shots and within 25 - 30% of the peak amplitude of the 4 mil Ta shots. We speculate that if 4 mil Ta shots were to be fired with the cathode plate insert, the 0.5 mil Ta and 4 mil Ta radiation pulses would be very similar in shape and amplitude in agreement with the positive polarity results. All the radiation pulses from the negative polarity experiments are presented in Figure 9 where the above observations can be confirmed. The abnormally high photodiode amplitude (~30V) and the late flashover (sudden drop in signal at -80nsec) for one of the two 4 mil Ta shots is attributed to an inadvertently larger than normal A-K gap setting.

Figures 10, 11 and 12 compare the electrical characteristics of diodes with hollow and non-hollow cathodes. Note the similarity of shot #5004 with the positive polarity shots shown in Fig. 6. Another observation concerning the presence of the cathode plate insert is worth mentioning. The TLD arrays placed at the 95cm position no longer give erratic and abnormally high doses as they did for the hollow-cathode case. For the two shots shown on Fig. 9 they gave doses of 125 ± 2 Rads Si and 128 ± 4 Rads Si respectively, which compare favorably with the -190 Rads Si recorded for the 4 mil Ta given the differences in photodiode signals for the two cases. This implies that even fewer electrons, if any at all, are reaching the BC end-target when the cathode plate insert is used. This observation, coupled with the

Negative polarity PD signals reflexing vs non-reflexing

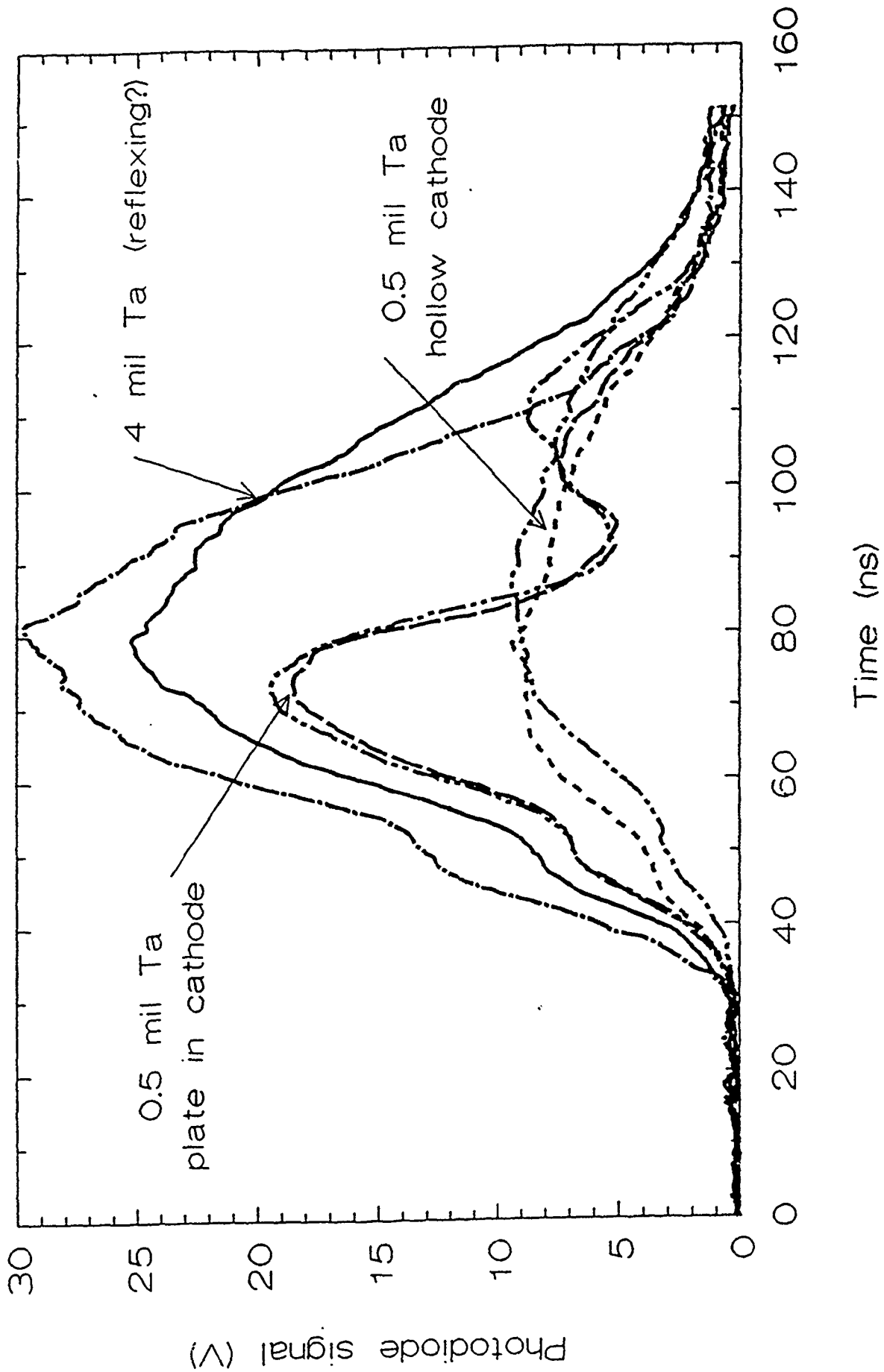


Figure 9

Shot 4999 CORRECTED DIODE VOLTAGES NEG POL

VCOR Volts
 Units: 2.00E+05
 Max: 1.86E+06
 Ts(ns): 0.00E+00

VCOR5006 Volts
 Units: 2.00E+05
 Max: 1.69E+06
 Ts(ns): 0.00E+00

VCOR5004 Volts
 Units: 2.00E+05
 Max: 1.75E+06
 Ts(ns): 0.00E+00

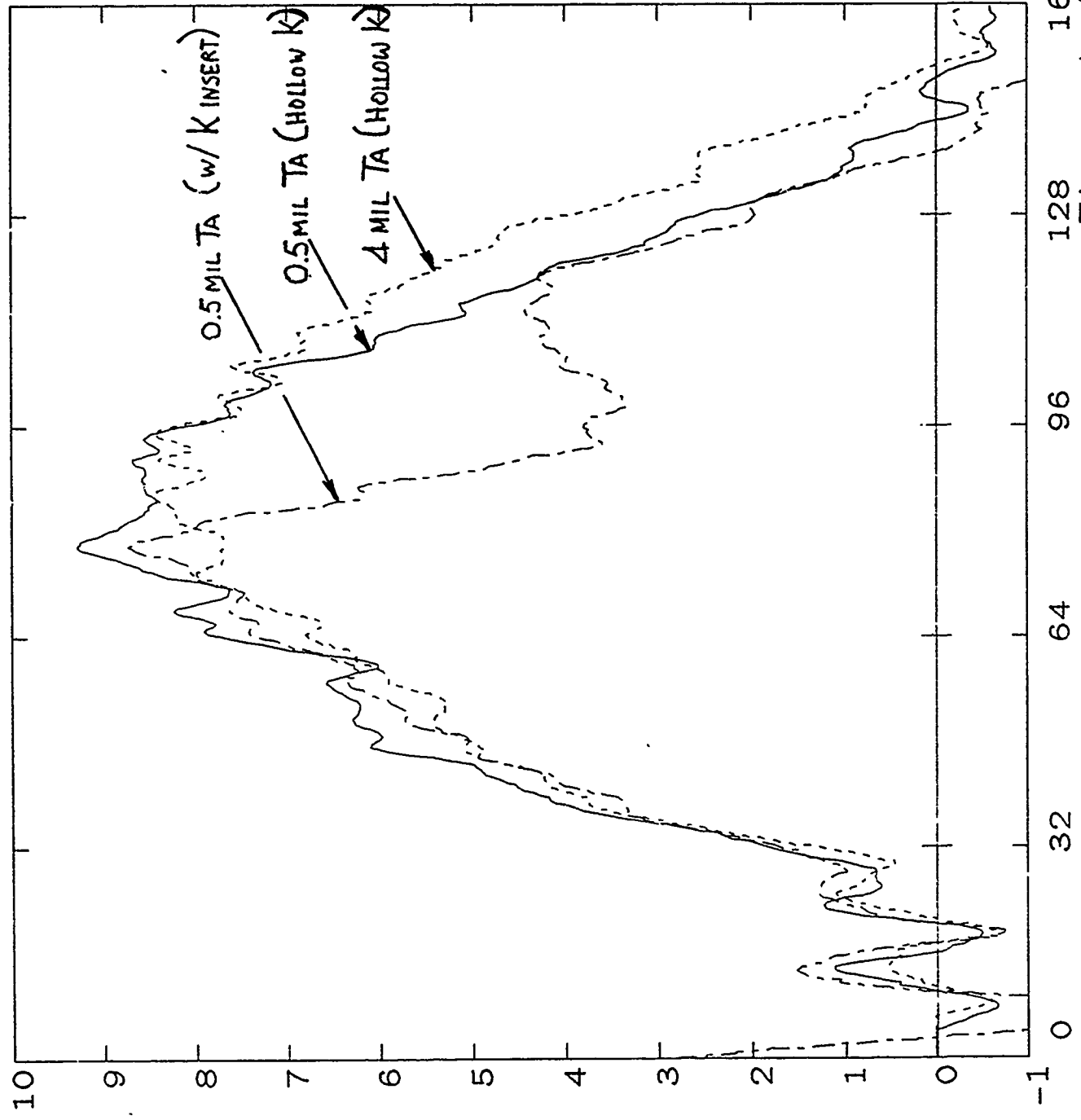
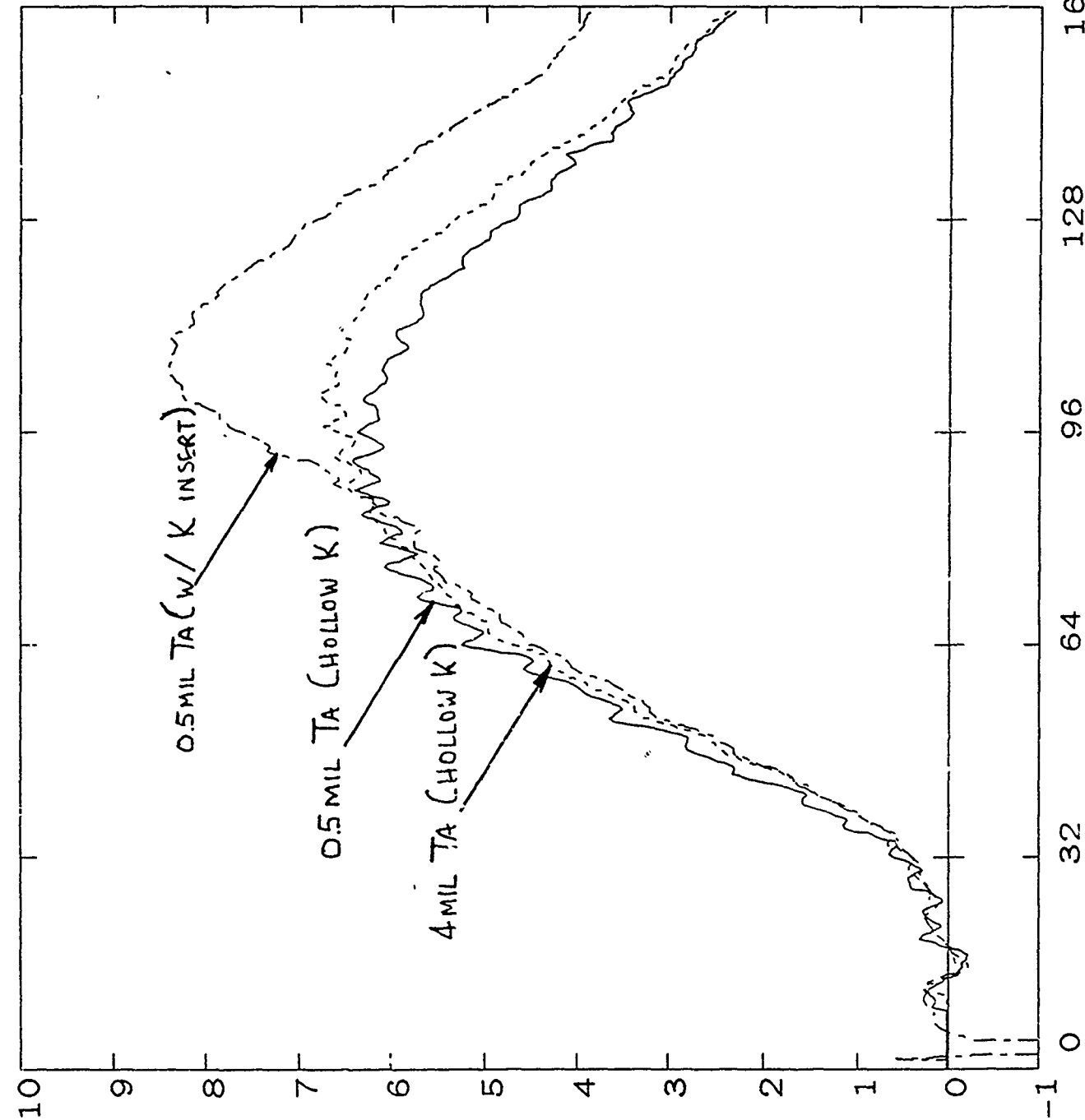


Figure 10

Shot 4999 DIODE CURRENTS NEGATIVE POLARITY



--- IOUT Amps
 Units: 1.00E+05
 Max: 6.41E+05
 Ts(ns): 0.00E+00

----- IOUT5006 Amps
 Units: 1.00E+05
 Max: 6.79E+05
 Ts(ns): 0.00E+00

----- IOUT5004 Amps
 Units: 1.00E+05
 Max: 8.41E+05
 Ts(ns): 0.00E+00

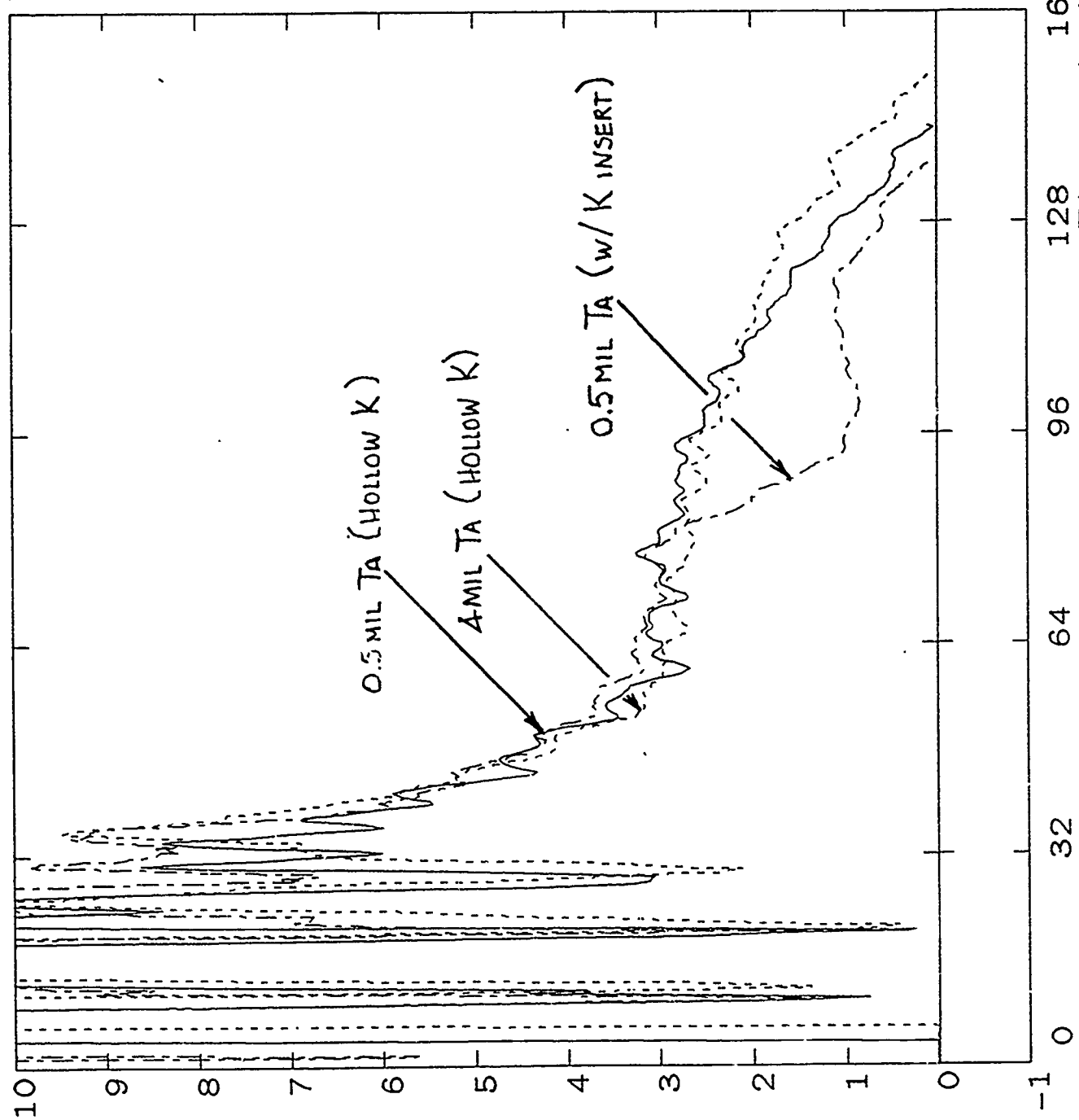
128 160
 Timescale: Nanoseconds

Shot 4999 DIODE IMPEDANCES · NEGATIVE POLARITY

Z Ohms
 Units: 1.00E+00
 Max: 1.00E+01
 Ts(ns): 0.00E+00

----- Z5006 Ohms
 Units: 1.00E+00
 Max: 1.00E+01
 Ts(ns): 0.00E+00

----- Z5004 Ohms
 Units: 1.00E+00
 Max: 1.00E+01
 Ts(ns): 0.00E+00



Timescale: Nanoseconds

Figure 12

increase of the first hump of the x-ray pulse suggests that the cathode plate insert (Kimfol) helps make for more efficient electron reflexing through the Ta anode foil.

Further confirmation that the presence or absence of ion current is directly dependent on the presence or absence of a cathode insert is illustrated in Figures 13 and 14. Figure 13 shows that for a totally hollow cathode, we can adequately match the experimental photodiode signal shape by the product of the diode voltage and the total diode current, implying that if there is any ion current at all, it is very small compared to the electron current. Furthermore, as was the case for positive polarity, the shapes of $I_T V^2$ and $I_T V^{2.8}$ do not match the experimental FWHM of the PD. Figure 14, on the other hand, clearly shows that no match to the experimental trace can be found without taking into account the ion current (which in negative polarity was not measured).

4. SUMMARY AND CONCLUSIONS

Despite the limited number of shots taken in this preliminary study, several conclusions can be drawn with potentially important implications for future advanced Bremsstrahlung converters.

(a) Tantalum anodes, whether bare or aerodagged, reflexing or non-reflexing, are copious emitters of ions (most likely protons from absorbed surface contaminants). These ions are emitted later in time than ions from plastic anodes but early enough to drastically affect the impedance characteristics of the diode and the resulting radiation pulse.

(b) This large ion current from the anode is only observed when the cathode interior is covered with an insert such as the Kimfol (positive polarity) or a metal plate (negative polarity). Totally hollow cathodes serve to suppress or eliminate this ion current probably due to space charge effects in the cathode interior.

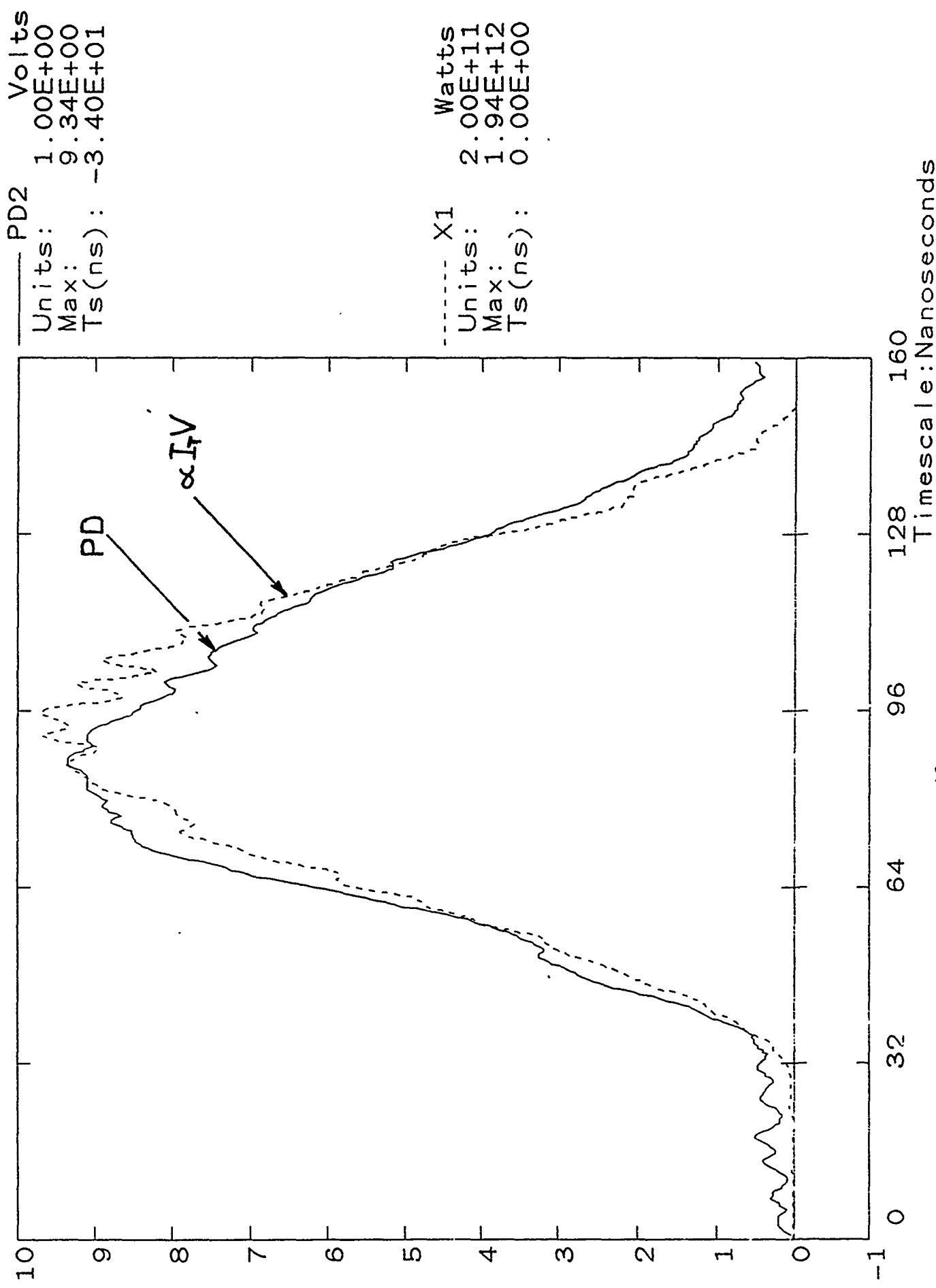


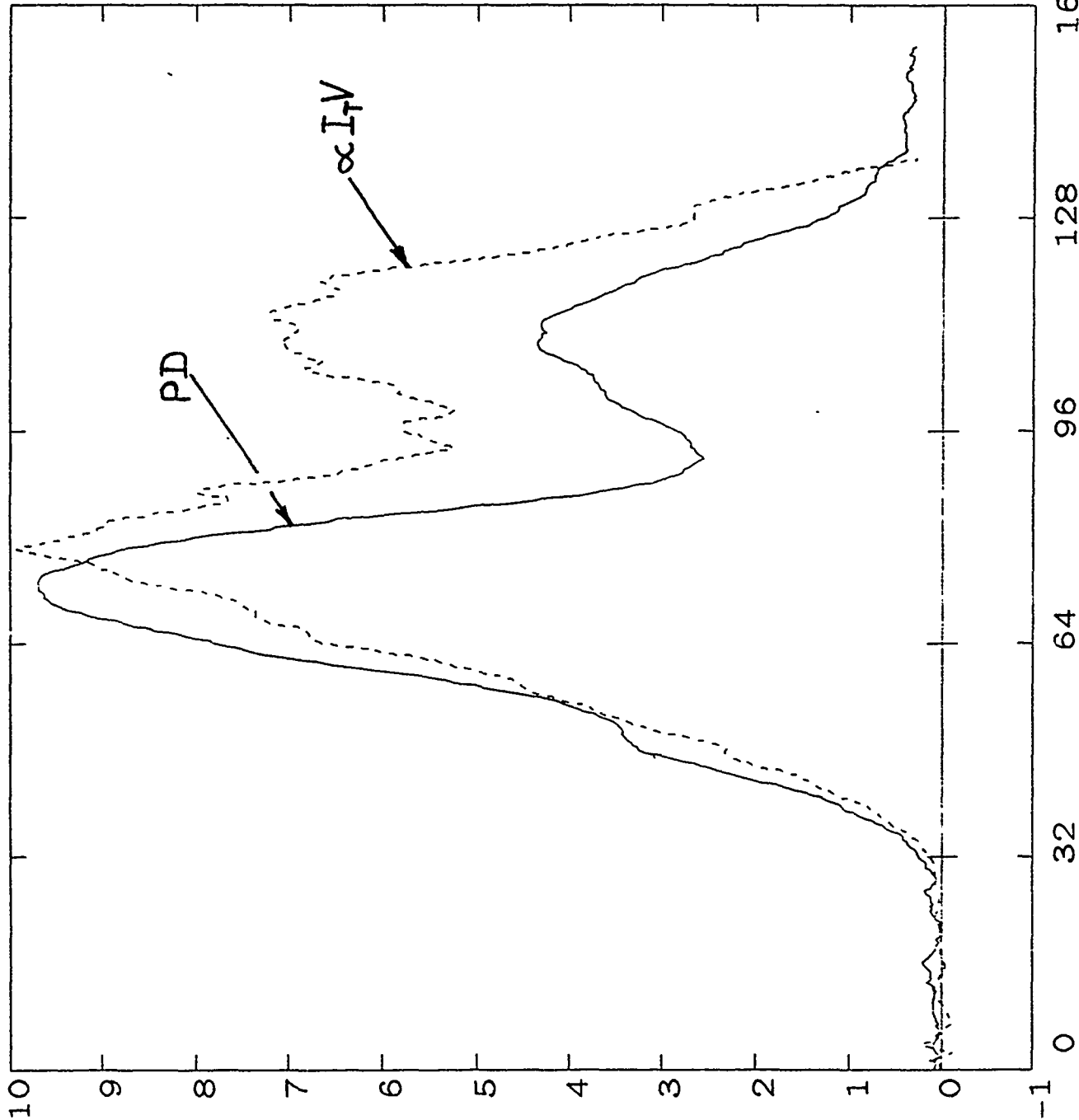
Figure 13

NEG. POLARITY - W/ CATHODE INSERT - NO MATCH

Shot 5004

PD
Units: 2.00E+00 Volts
Max: 1.94E+01
Ts(ns): -3.40E+01

X1
Units: 1.00E+11 Watts
Max: 9.94E+11
Ts(ns): 0.00E+00



Timescale: Nanoseconds

Figure 14

(c) In the presence of ions, 0.5 mil Ta backless anodes produce almost as much radiation as 4 mil Ta anodes in the standard Bremsstrahlung geometry. They produce about 2.5 times more radiation than 0.5 mil Ta backed anodes. This is clear evidence that reflexing is real and beneficial to Bremsstrahlung production.

(d) In the absence of ions, the 4-mil Ta, "standard" configuration is the best x-ray emitter (~3 times better than the 0.5 mil Ta, backless configuration).

(e) The presence of a cathode insert significantly enhances the electron reflexing process as evidenced by the fact that, prior to ion turn-on, the radiation from a 0.5 mil Ta backless anode is twice as intense when a cathode insert is used than when the cathode is totally hollow.

The current thinking is that an optimized Bremsstrahlung diode should probably be designed for positive polarity operation. The main reason for this is that, with the electron beam directed away from the test object, a much thinner debris-catcher/vacuum-air interface could be used allowing for a large portion of the soft component of the spectrum to be available to the test object. In view of the results presented above, optimization of such a diode should include further study of the role of the cathode insert such as its optimum location relative to the cathode tip for maximum electron reflexing and minimum ion contamination. Ion emission could be presumably diminished or eliminated by pre-baking or in-situ heating of the anode. The Ta foil thickness should be optimized (minimized) for maximum radiation and minimum debris. As has been suggested before, electron reflexing can probably be optimized by replacing the virtual cathode, which for these experiments is probably diffuse and varying in location and time, by a well-defined plane (metallic or otherwise) at some well-chosen position upstream of the anode. Finally, the debris-catcher/vacuum-air interface should be optimized and absolute dose and spectrum measurements should be made in positive polarity.

PULSED POWER PHYSICS BRANCH TECHNOTE NO. 91-02

TITLE: FOCUSED PROTON POWER DENSITY PREDICTION FOR PBFA II USING AN
EPRD DIODE

AUTHOR(S): P.F. Ottinger, J.R. Boller, D. Rose, D.D. Hinshelwood, S.J.
Stephanakis, and G. Cooperstein

DATE: 10 January 1991

ABSTRACT: The Equatorial Pinch Reflex Diode (EPRD) is a barrel shaped version of the pinch reflex diode and is suitable for fielding on PBFA II. In this technote proton/deuteron power density on target is estimated for an EPRD on PBFA II. Because the appropriate range proton for ICF is only about 5 MeV, no POS is included in the circuit. Results indicate that about 25 TW/cm² may be achievable using protons at 8.8 MeV with a 6.5-cm radius, 5-cm half height EPRD (assuming a microdivergence half angle of about 35 mrad). For ions with energies close to their proper range for ICF, this is reduced to about 22 TW/cm² for 3.3 MV protons and about 21.5 TW/cm² for 5.7 MeV deuterons, again with the 6.5-cm radius diode.

THIS REPORT REPRESENTS
UNPUBLISHED INTERNAL WORKING
DOCUMENTS AND SHOULD NOT BE
REFERENCED OR DISTRIBUTE

INTRODUCTION

The Equatorial Pinch Reflex Diode (EPRD)¹ is a barrel shaped version of the pinch reflex diode and is suitable for fielding on PBFA II. Figure 1 shows a schematic of a full EPRD which is fed from top and bottom. Here R is the diode radius (distance to the center line), H is the half height of the diode (height of the top or the bottom), and D is the initial AK gap. The NRL transmission line code, BERTHA², was used to analyze and predict EPRD performance on PBFA II, in particular, in regard to estimating proton or deuteron power density on target. Because the appropriate range proton (deuteron) for ICF is only about 3.8 MeV (5.4 MeV) (compared with 30 MeV for ⁷Li³⁺), no POS is included in the circuit. If some pulse sharpening is needed, a POS could be added to the circuit in future calculations. Figure 2 shows the equivalent circuit used to model one half of PBFA II. The open circuit voltage waveform, which was used in the analysis, was provided by Gary Rochau and is based on SHOT 2338 with a peak open circuit voltage of 23.9 MeV. Thus, results are being calculated for typical machine operation at the 3/4 power level. Losses in the vacuum feed are modeled by 5 consecutive MITL circuit elements.

Data from previous experiments at both NRL¹ and SNL³ were used to arrive at a reasonable diode model for the EPRD. The model includes a electric field threshold for turn-on (E_b), a diode turn-on phase (t_o), a space charge limited flow phase (I_s), a critical current phase (I_c), an enhanced ion flow turn-on phase (t_i), ion enhancement factor due to electron reflexing (α), and AK gap closure (v_c). For the runs considered here, the values used for the fixed parameters were $E_b = 0.1$ MV/cm, $t_o = 8$ ns, and $v_c = 2.5$ cm/ μ s. The ion turn-on time, t_i , was varied from 15 to 30 ns, and the ion enhancement factor, α , was varied from 1 to 2. Enhanced ion flow begins when the critical current is reached with

$$I_c = 1.6 (8500) \beta \gamma R / (D - v_c t) \quad , \quad (1)$$

and

$$\frac{I_i}{I_e} = \alpha \left(\frac{m_e \gamma + 1}{m_i \frac{2}}{2} \right)^{1/2} \frac{H}{D - v_c t} f(t) \quad , \quad (2)$$

where $f(t)$ represents the turn-on of the ion enhancement. Here it is assumed that $f(t)$ increases linearly from D/H to 1 during the ion turn-on time t_i . The factor of 1.6 in Eq. (1) is a scaling parameter determined from fitting experimental data and verified by numerical simulation. The ion efficiency is calculated as

$$\eta_i = \frac{I_i}{I_i + I_e} \quad . \quad (3)$$

For a focusing diode of radius R and microdivergence θ_μ , the ion power

density on target can be estimated as

$$P_i = \frac{(2I_i)V}{4\pi(R\theta_\mu)^2} \quad (4)$$

where $2I_i$ is the full machine current, so that P_i is the peak power density for the full PBFA II (top and bottom). For the EPRD, the best values to date for θ_μ have been measured to be about 35 mrad. This ion diode model and all the parameter values used here are consistent with data presented in Refs. 1 and 3.

It should be noted that, unlike the PRD, the EPRD has good focusing characteristics. Since there is a line pinch for the EPRD, rather than the point pinch of the PRD, the ion current density is uniform. Thus, the self magnetic field of the diode increases linearly in z away from the diode midplane, leading to a natural focus. Strong focusing over a short distance will require anode shaping to augment this natural focusing.

RESULTS

Six runs were made to scope out parameter space. All results presented assumes the ions are protons. For deuterons (or other species) results need to be scaled properly [e.g. I_i/I_0 is reduced by $2^{1/2}$ for deuterons and η_i is then appropriately reduced using Eq. (3)]. Shot 1000 used an initial AK gap appropriate for a matched load impedance of about 4.4 Ω at peak power in order to draw the maximum amount of energy from the machine. The peak load voltage of about 8.8 MV, however, is too high for the proper range proton or deuteron. The initial AK gaps for Shots 1001 and 1002 are reduced to provide load impedances of about 2.2 Ω and 1.1 Ω respectively at peak load power. The peak load voltage of Shot 1001 (1002) corresponds roughly to that required for the proper range deuteron (proton). In Shots 1010, 1011, and 1012 a matched load impedance of about 4.4 Ω was again used. In order to study the effect of longer ion turn-on time, t_i was increased from the 15 to 30 ns for Shot 1010. In addition to longer t_i , α was also decreased from 2 to 1 in Shot 1011, in order to study the effect of reduced ion enhancement from reflexing. The data in Ref. 3 suggests t_i is as long as 30 ns and α is as small as 1 (corresponding to Shot 1011), while Ref. 1 suggests the shorter t_i and the larger α (corresponding to Shot 1000). Finally, the diode radius R is decreased from the usual value of 13 cm for PBFA II to 6.5 cm in order to demonstrate the decoupling of ion efficiency (scales with H/D) and diode impedance (scales with R/D). In addition, the smaller R will provide larger power density on target for the same θ_μ (see Eq. (4)).

Figures 3-20 shows the data from the runs and Table I summarizes the results. There are three figures for each Shot with four plots on each figure. The plots show the voltage (VOL06), current (CUR06), and energy (ENR06) at point A (see Fig. 2) upstream of the MITL section and at the load (VOL20, CUR20, ENR20), the ion current (ION07), the open circuit voltage (VOC01), the load impedance (ZL), the ion power (PION), the ion energy (EION) and finally the ion efficiency (IEFF). The voltage, current and energy are plotted upstream of the MITL section in order to illustrate

the losses in the MITL's. High voltage runs show energy losses as much as about 19%, while lower voltage runs show only 6% losses. Voltage, current, power, and ion efficiency values quoted in Table I are peak values. In addition, the values of power density on target, \overline{P}_i , quoted in Table I are peak values assuming $\theta_\mu = 35$ mrad and no steering errors. Note that the last column lists the power density for the full diode on PBFA II (top and bottom), while all other columns in Table I and the data in the plots (Figs. 3-20) refer to 1/2 of PBFA II.

Shots 1000, 1001, and 1002 show that although the diode as a whole couples best at the matched load value of 4.4Ω (Shot 1000), the ion power is reasonable over the full range of load voltages (impedances) because of improved η_i at lower impedance. In fact, the largest P_i occurs for Shot 1001, which corresponds to the voltage appropriate for deuterons. Shot 1010 shows that a slow ion enhancement turn-on time does not significantly degrade the performance. Shot 1011, however, shows that reduced reflexing can degrade performance. Shot 1012 demonstrates two effects. First, it shows an improvement of η_i from 31% (Shot 1000) to 47% (Shot 1012). This results from a decoupling of diode impedance from ion efficiency; R/D was adjusted to provide the same impedance at the smaller radius, leading to a larger H/D enhancement of the ion current. Second, for the same θ_μ better focusing is obtained at smaller R. Although Shot 1002 (1001) with a voltage appropriate for a proper range proton (deuteron) was not repeated here with a smaller radius diode, results comparable to Shot 1012 can be scaled from the results of Shots 1000-1002 yielding about 26.8 TW/cm^2 on target at about 5.7 MV and 22.3 TW/cm^2 on target at about 3.3 MV for protons. Scaling down the 5.7 MV case to account for the higher mass of the deuterons yields about 21.6 TW/cm^2 on target for deuterons.

Results for the small radius diode are promising but it should be pointed out that they assume that the microdivergence half angle is 35 mrad, that the enhancement factor for ion efficiency due to electron reflexing is 2 and that ion steering errors are negligible. Microdivergence half angles as small as 35 mrad have been measured at both NRL and SNL but this will need to be demonstrated on PBFA II. There is good evidence from NRL experiments that reflexing does provide the factor-of-two enhancement in ion efficiency, while SNL experiments on PBFA I did not confirm this. In principle, steering errors can be adjusted for, while in practice this will also need to be demonstrated. On the other hand, improvement in these results is also possible. H has been restricted to 5 cm in these runs. [Note that H should be interpreted as the arc length along the anode surface (the electron path length) and not the perpendicular height of the diode.] Increasing H will linearly increase the ion efficiency, and thus the ion power density on target. However, H will be limited by diagnostic access through the top and bottom openings in the diode. Electrons, reflexing along the anode foil, will also eventually run out of energy and thus limit H.

A few words should be added concerning the use of a POS. With a POS, lower energy losses in the MITL's would be traded off against energy losses in coupling the POS to the load. In the low voltage regime studied here for protons/deuterons, no voltage multiplication is required, only pulse sharpening. In addition, the low load impedance ($1.1\text{-}4.4 \Omega$) favors good POS/load coupling. The EPRD also has no applied magnetic fields to affect power flow in the feed which again favors good POS/load coupling. Thus,

it is not expected that including a POS in the circuit for pulse sharpening will significantly degrade the results presented here.

In summary, this technote provides estimates of proton/deuteron power density on target for an EPRD on PBFA II. Because the appropriate range proton for ICF is only about 5 MeV, no POS is included in the circuit. Results indicate that about 25 TW/cm² may be achievable with protons at 8.8 MV for PBFA II at typical 3/4 power operation with a 6.5-cm radius, 5-cm half height EPRD assuming a microdivergence half angle of about 35 mrad. The results in Table I can be applied to other species and parameters by adjusting the results according to the scalings provided in Eqs. (1)-(4). For ions with energies close to their proper range for ICF, the ion power density on target is reduced to about 22 TW/cm² for 3.3 MV protons and about 21.5 TW/cm² for 5.7 MeV deuterons, again with the 6.5-cm radius diode.

REFERENCES

1. G. Cooperstein, et al., in Laser Interaction and Related Plasma Phenomena, Vol. 6, edited by H. Swartz, H. Hora, M Lubin, and B. Yaakobi, (Plenum Press, NY, 1984), p. 957.
2. D.D. Hinshelwood, NRL Memorandum Report 5185 (Nov. 1983).
3. J.N. Olsen, et al., J. Appl. Phys. 55, 1254 (1984).

Shot #	half diode											full diode
	R cm	D cm	α	t_i ns	V_L MV	I_L MA	E_L kJ	I_i MA	P_i TW	E_i kJ	η_i %	$\frac{P_i}{TW/cm^2}$
1000	13	1.75	2	15	8.80	2.00	785	0.62	5.47	226	31	4.20
1001	13	1.00	2	15	5.68	2.49	657	1.03	5.83	254	41	4.48
1002	13	0.60	2	15	3.27	2.87	439	1.48	4.84	214	52	3.72
1010	13	1.75	2	30	8.77	1.99	779	0.62	5.41	221	31	4.16
1011	13	1.75	1	30	8.8	2.00	785	0.37	3.24	131	19	2.50
1012	6.5	0.95	2	15	8.72	1.98	772	0.94	8.18	344	47	25.16

Table I - Results of BERTHA runs assuming ions are protons, $E_p = 0.1$ MV/cm, $t_o = 8$ ns, $v_c = 2.5$ cm/ μ s, and $\theta_\mu = 35$ mrad. Note that the last column list the power density for the full diode on PBFA II (top and bottom), while all other columns and data in plots (Figs. 1-18) refer to 1/2 of PBFA II.

SHEPERD DIODE

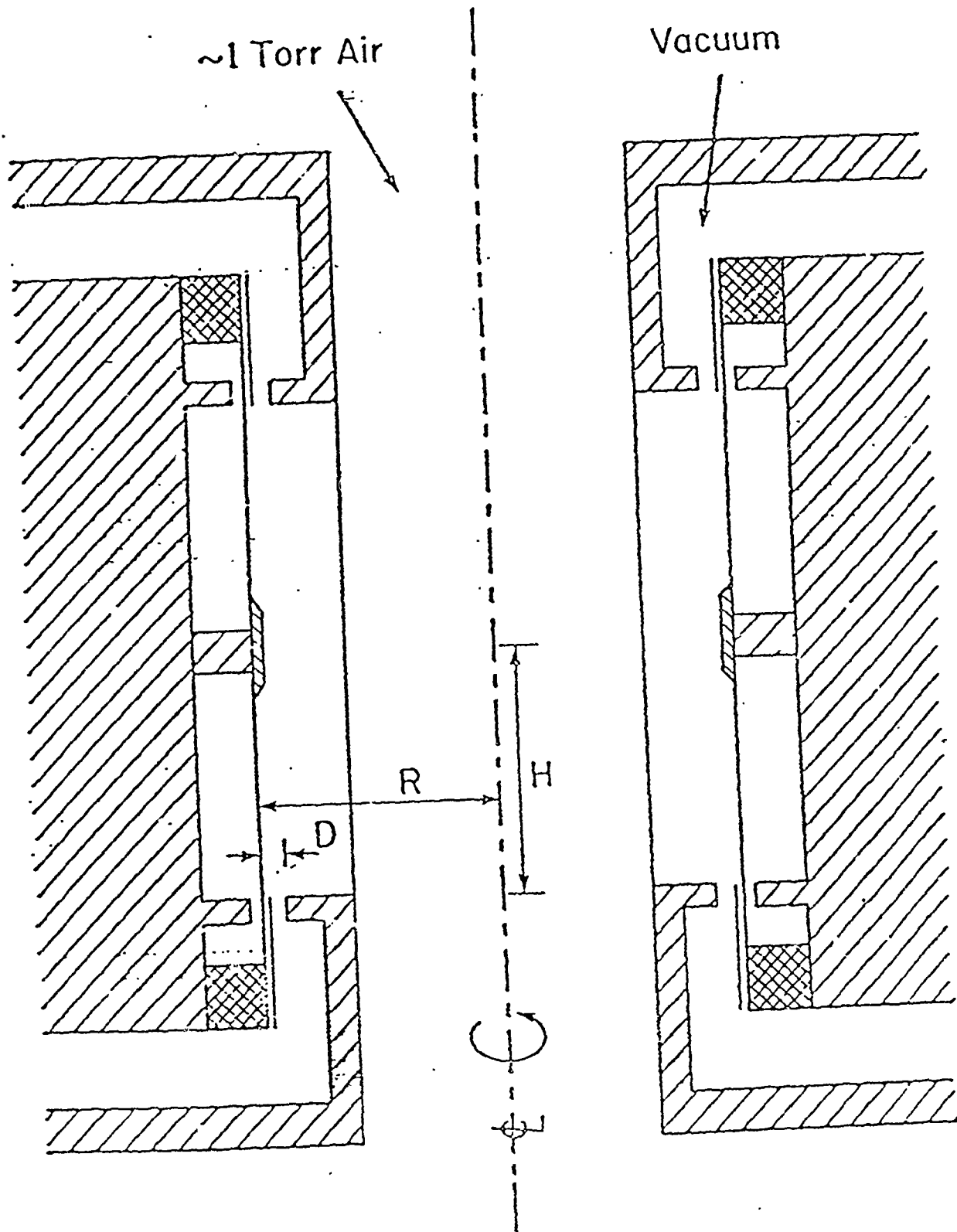


Fig. 1

PBFA II (1/2 machine)

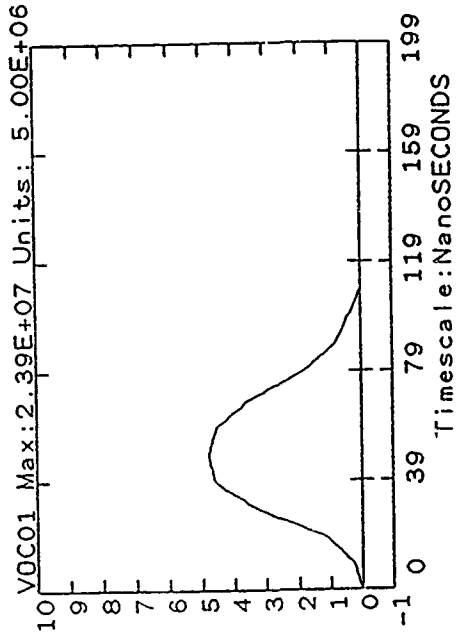
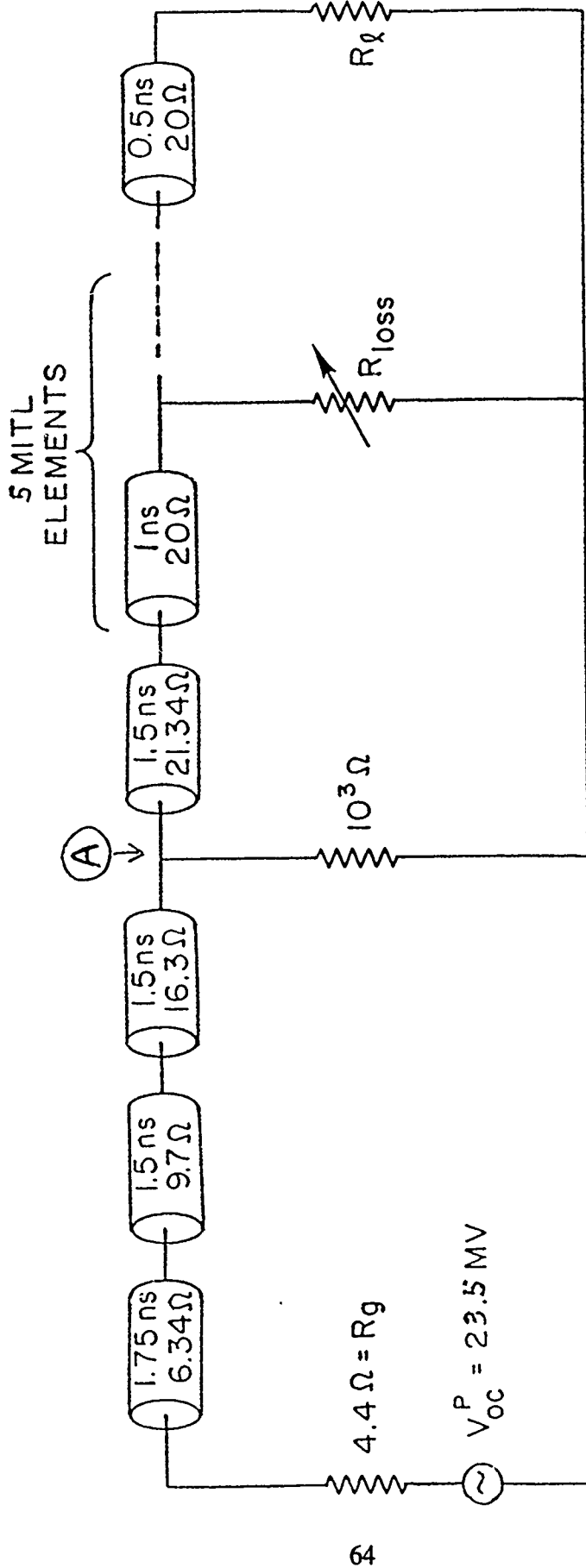
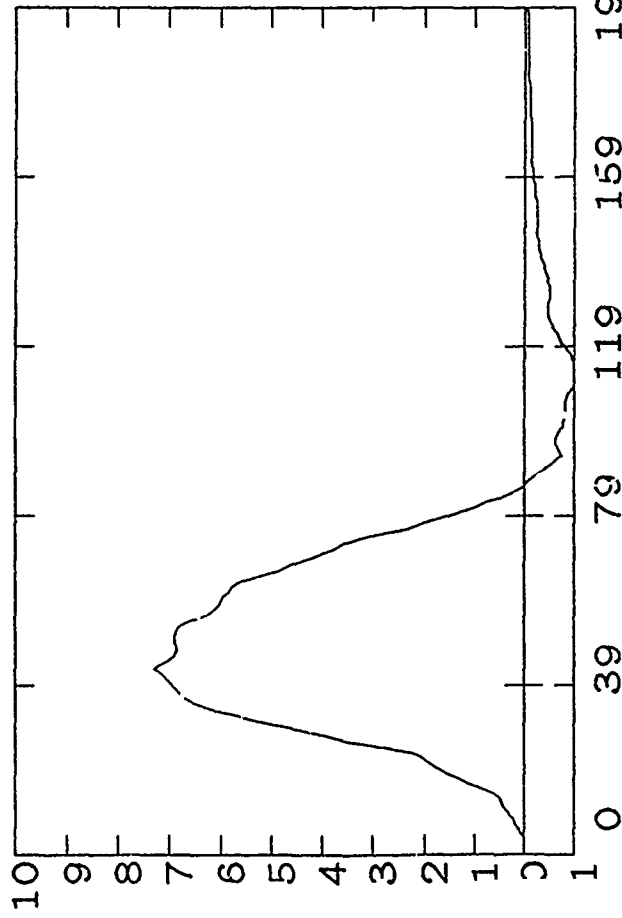


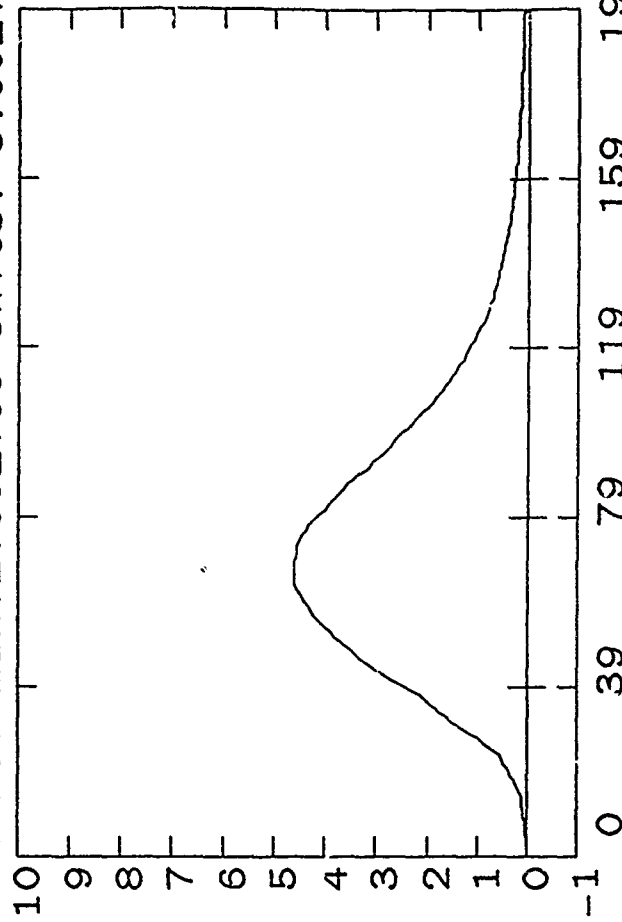
Fig. 2

Shot 1000

VOL06 Max:1.46E+07 Units: 2.00E+06

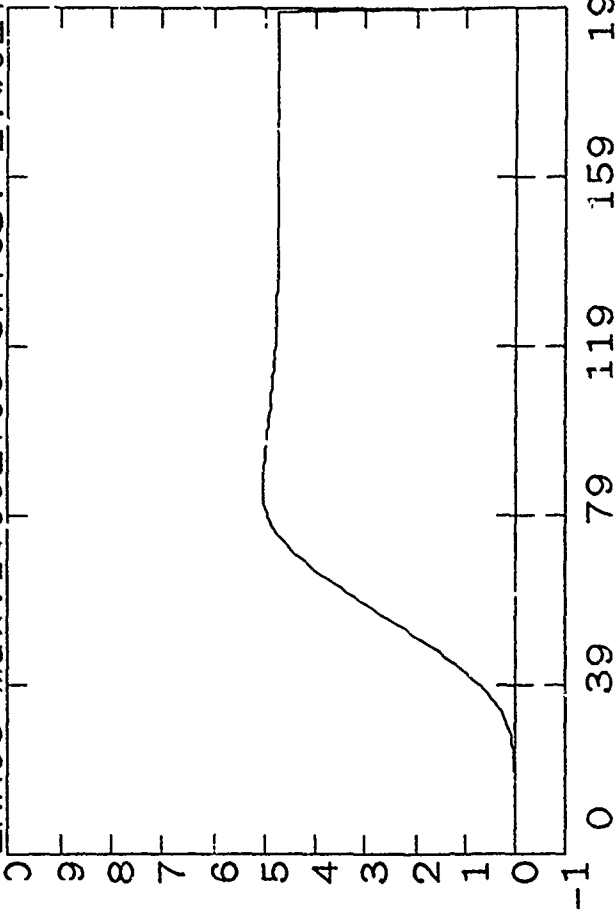


CURJ6 Max:2.30E+06 Units: 5.00E+05



5

ENRO6 Max:1.00E+06 Units: 2.00E+05



VOL20 Max:8.80E+06 Units: 1.00E+06

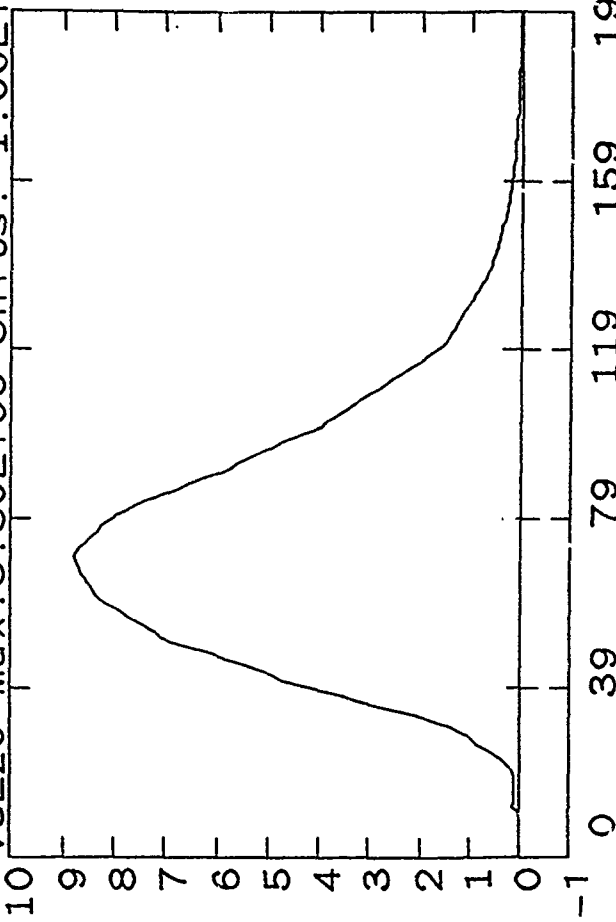
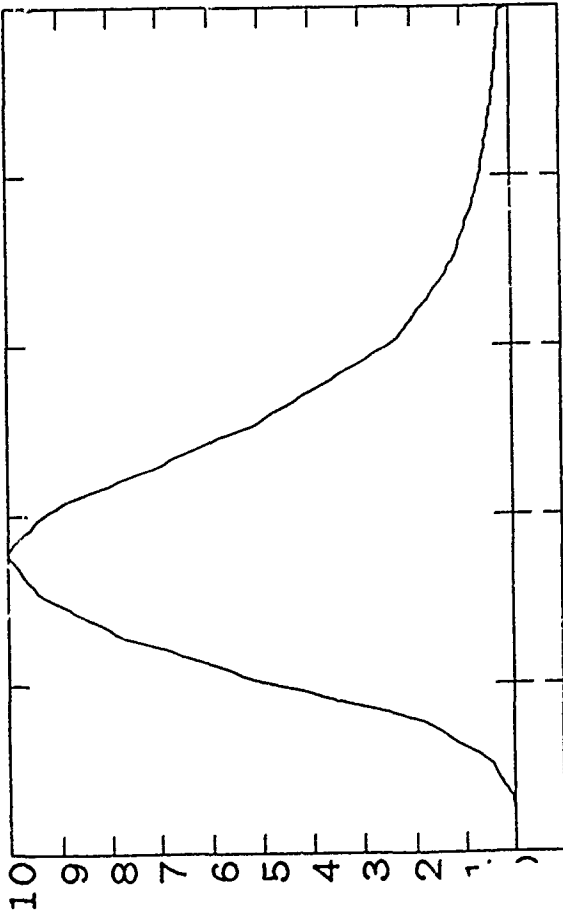


Fig. 3

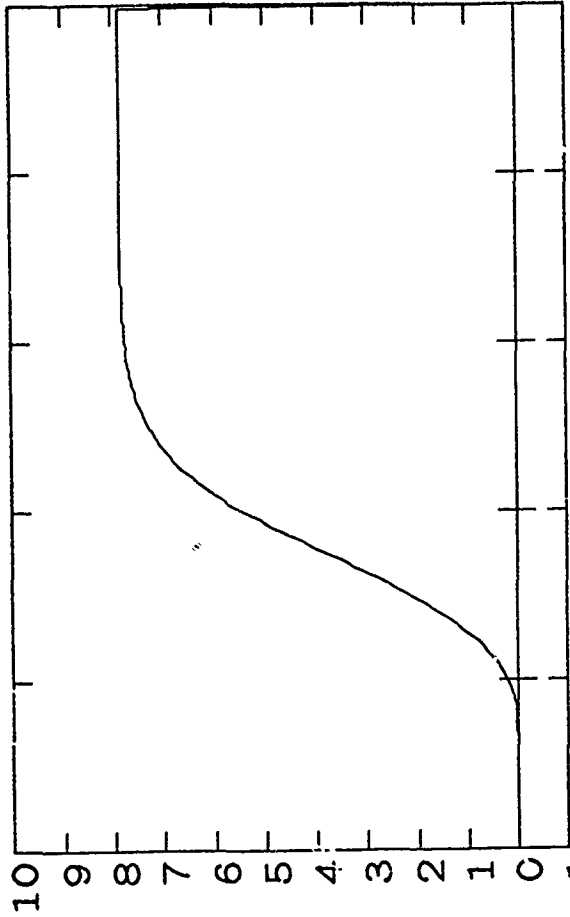
Shot 1000

CUR20 Max: 2.00E+06 Units: 2.00E+05



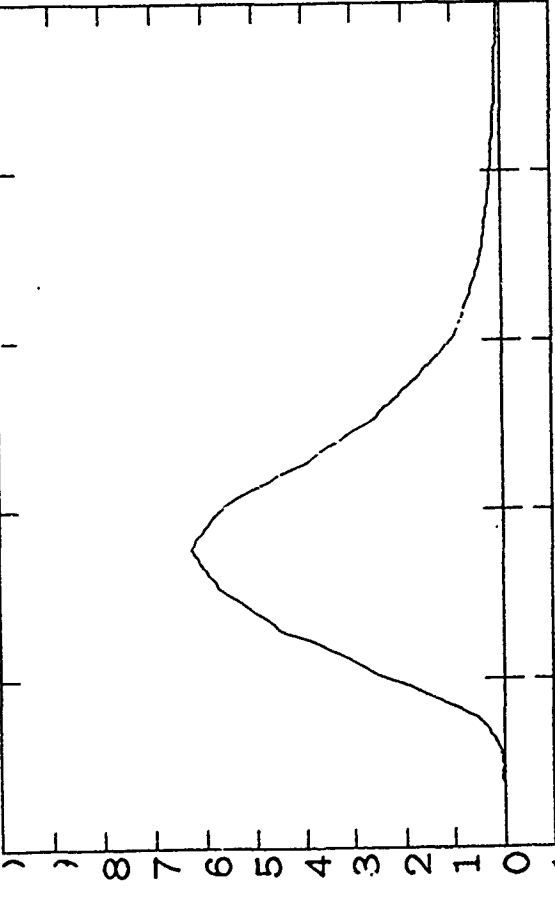
Timescale: NanoSECONDS

ENR20 Max: 7.85E+05 Units: 1.00E+05



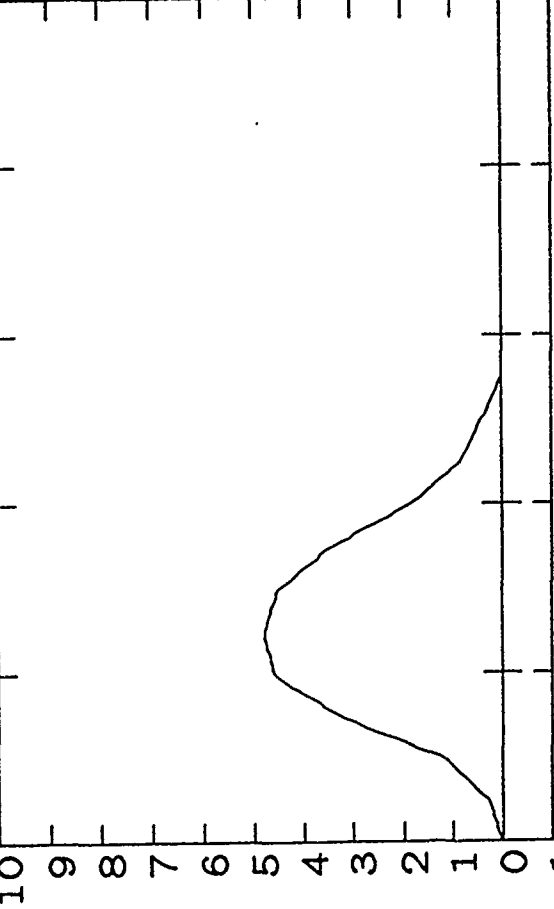
Timescale: NanoSECONDS

ION07 Max: 6.21E+05 Units: 1.00E+05



Timescale: NanoSECONDS

VOC01 Max: 2.39E+07 Units: 5.00E+06

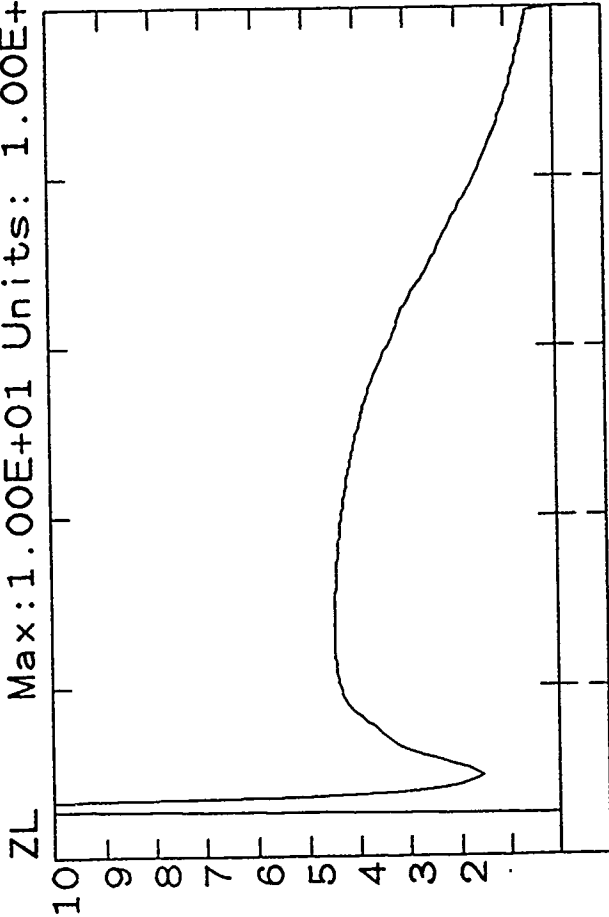


Timescale: NanoSECONDS

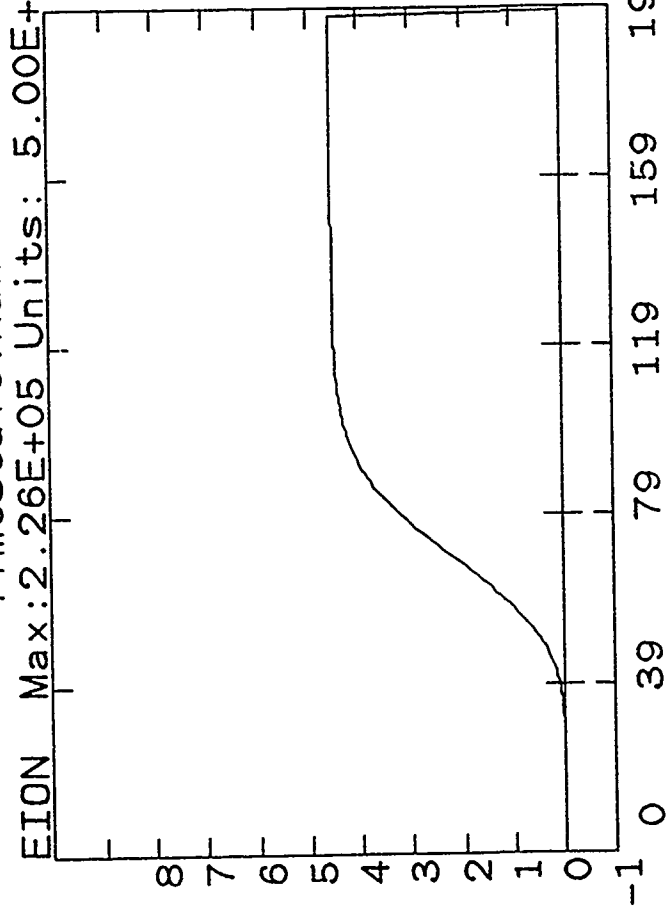
Fig. 4

Shot 1000

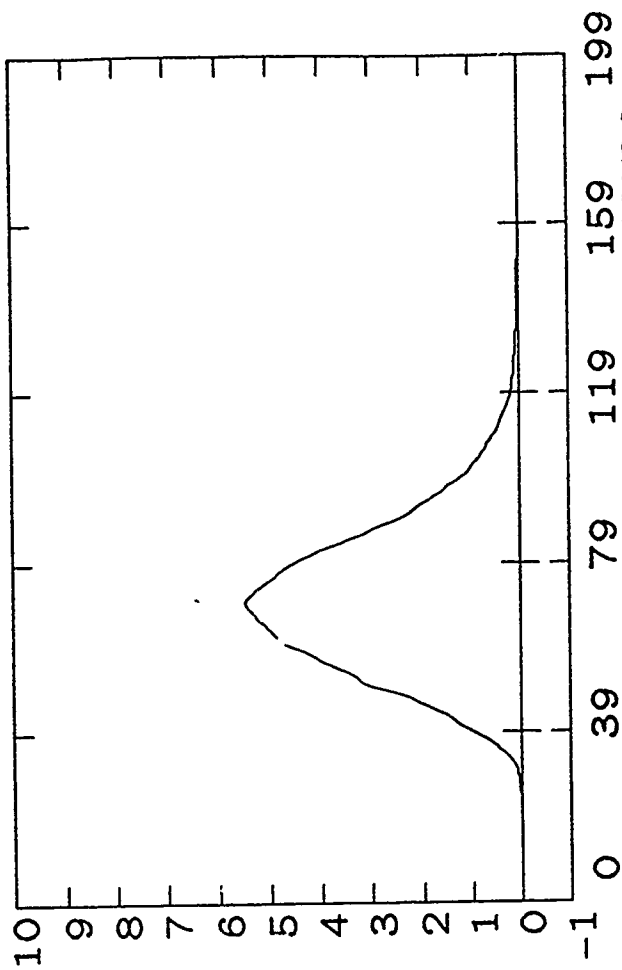
ZL Max:1.00E+01 Units: 1.00E+00



EION Max:2.26E+05 Units: 5.00E+04



PION Max:5.47E+12 Units: 1.00E+12



IEFF Max:3.11E-01 Units: 5.00E-02

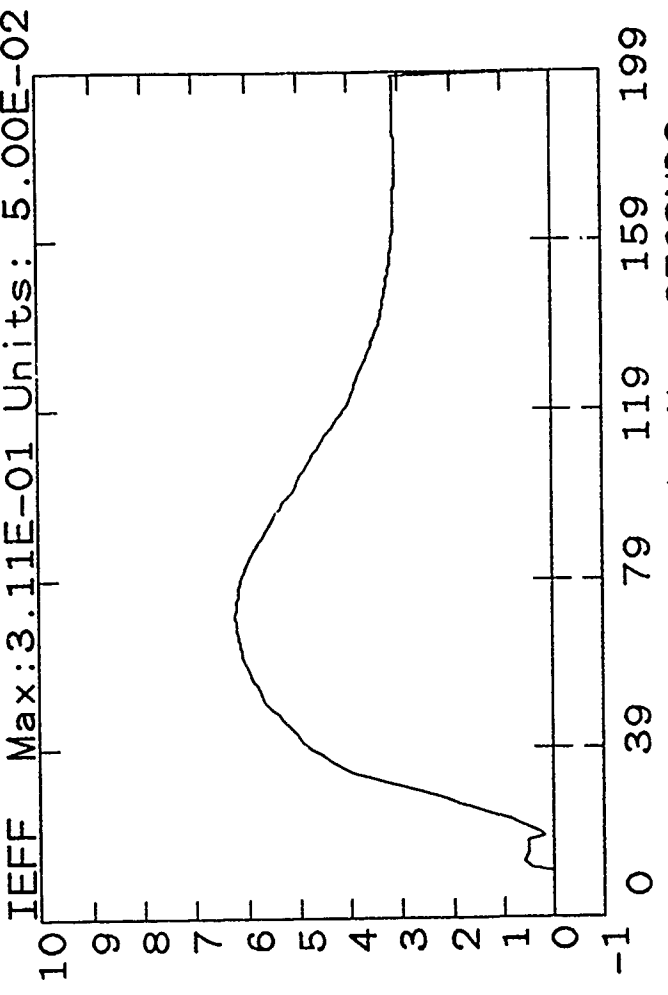
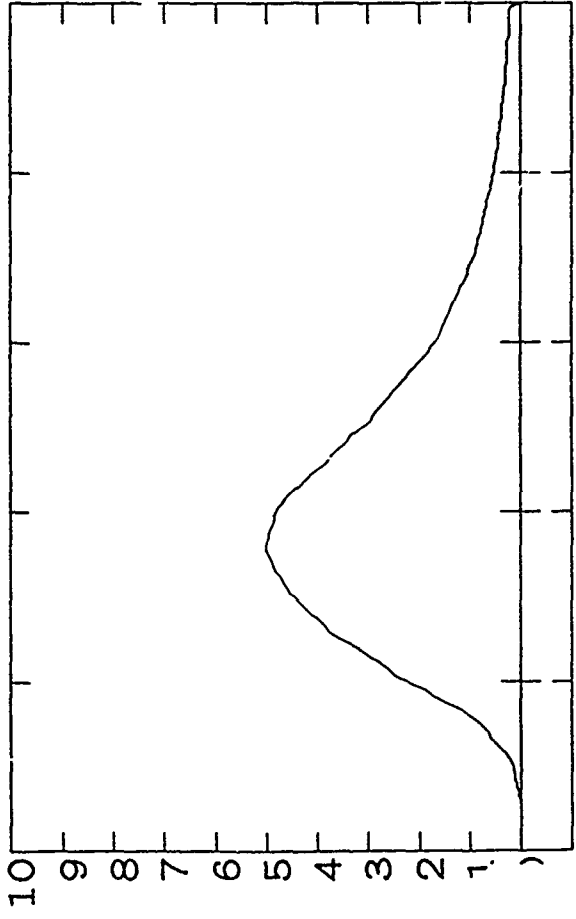


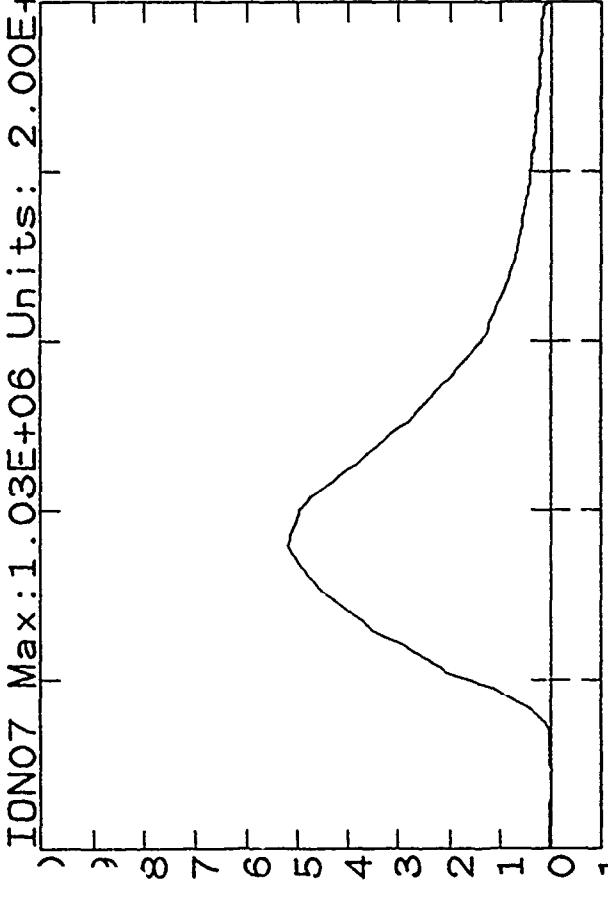
Fig. 5

Shot 1001

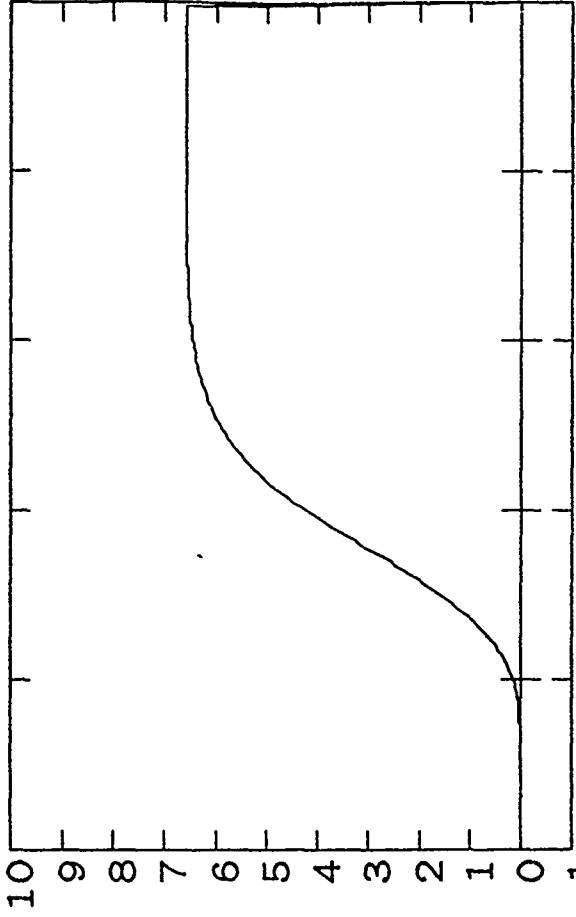
CUR20 Max: 2.49E+06 Units: 5.00E+05



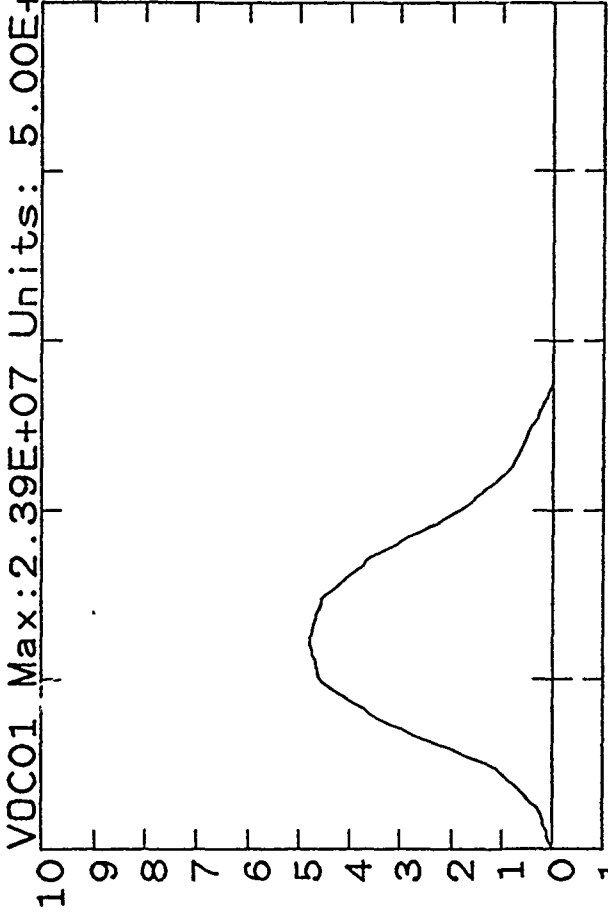
ION07 Max: 1.03E+06 Units: 2.00E+05



ENR20 Max: 6.57E+05 Units: 1.00E+05



VOC01 Max: 2.39E+07 Units: 5.00E+06

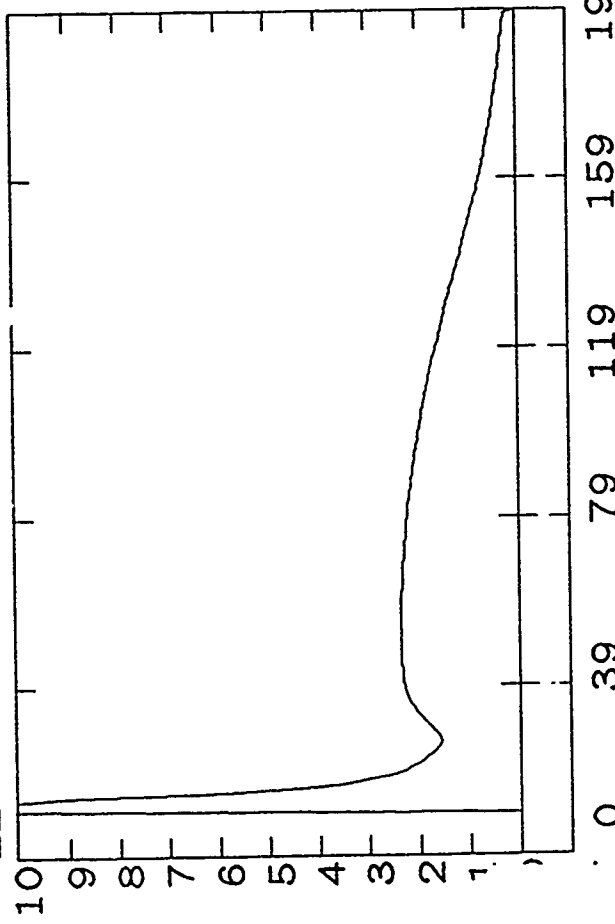


Timescale: NanoSECONDS

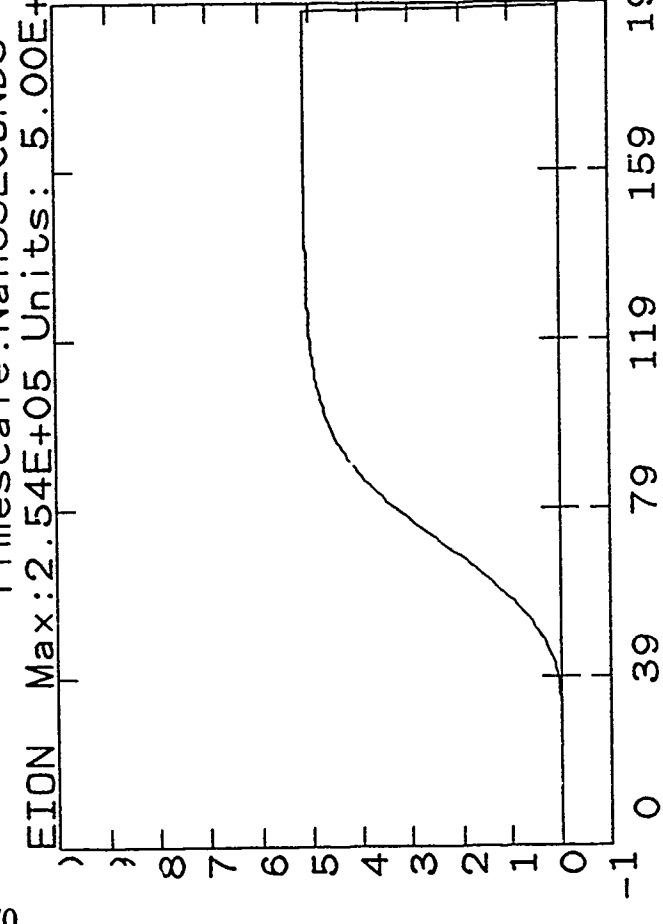
Fig. 7

Shot 1001

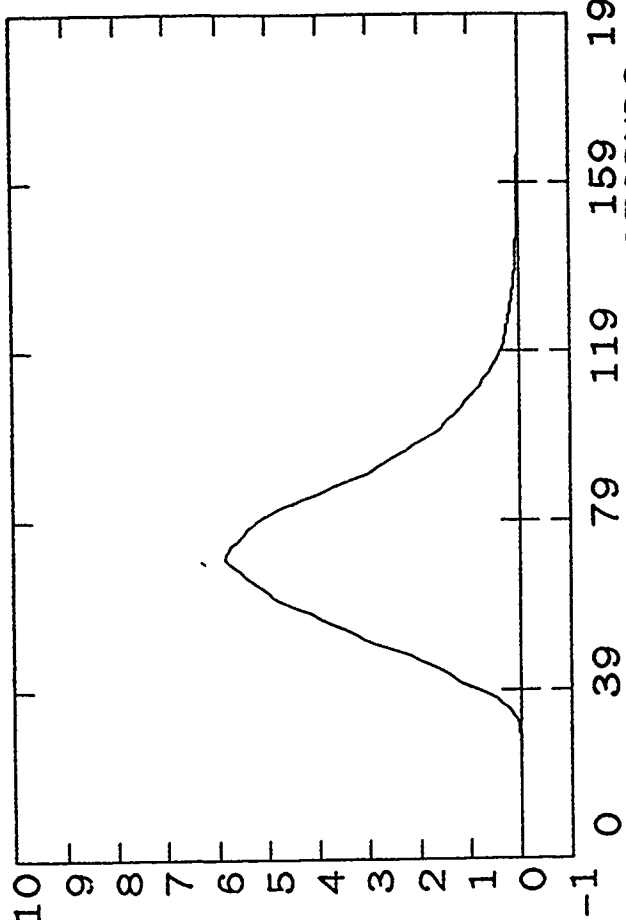
ZL Max:1.00E+01 Units: 1.00E+00



EION Max:2.54E+05 Units: 5.00E+04 Timescale:NanoSECONDS



PION Max:5.83E+12 Units: 1.00E+12



IEFF Max:1.00E+00 Units: 1.00E-01 Timescale:NanoSECONDS

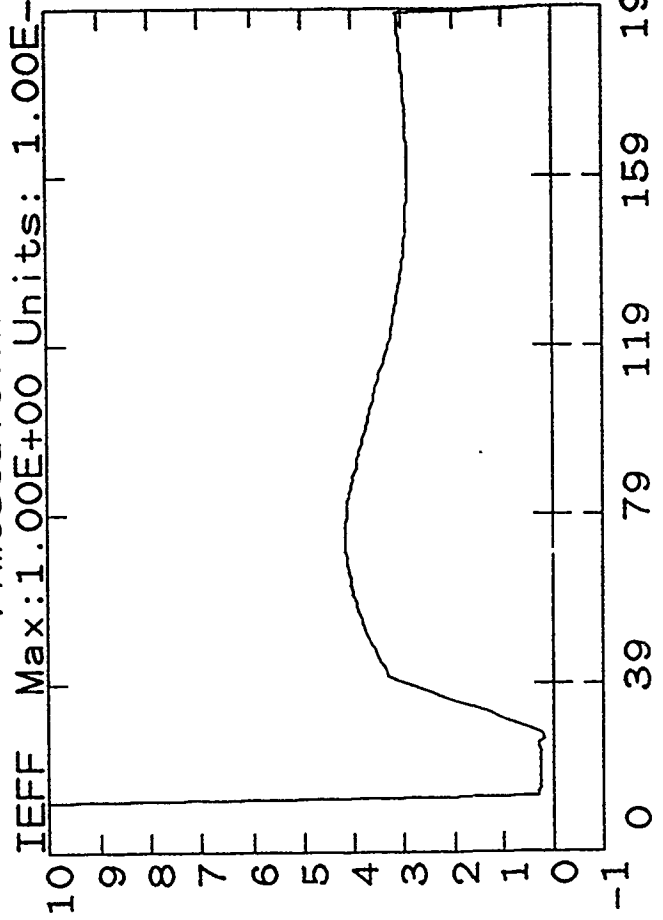
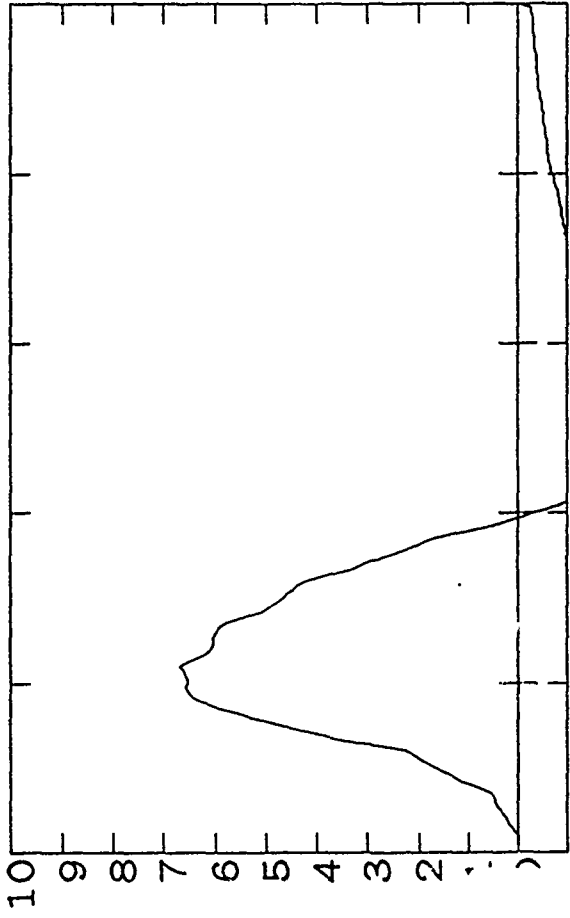


Fig 8

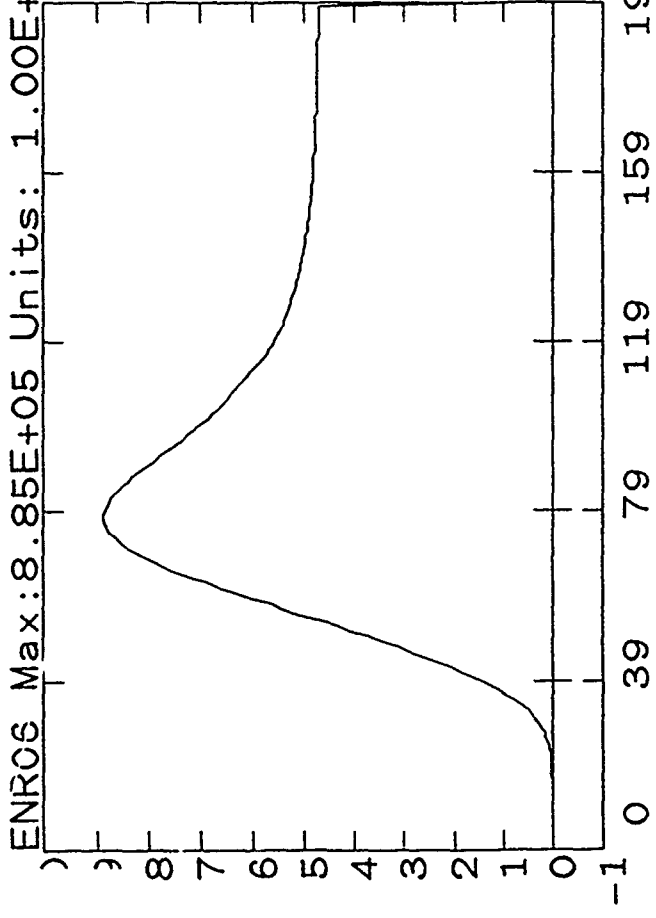
Shot 1002

VOL06 Max:1.33E+07 Units: 2.00E+06

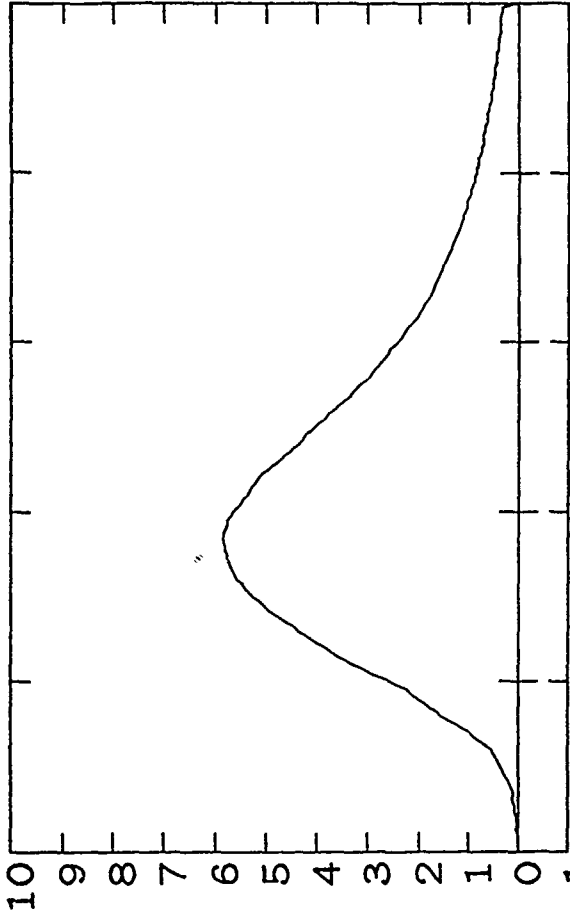


71

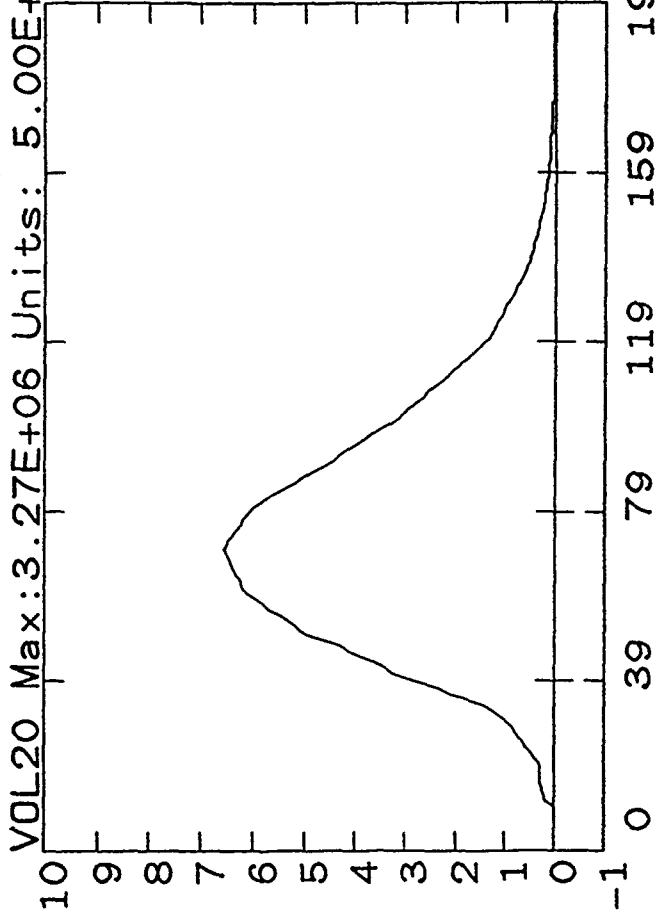
ENR06 Max:8.85E+05 Units: 1.00E+05



CUR06 Max:2.91E+06 Units: 5.00E+05



VOL20 Max:3.27E+06 Units: 5.00E+05

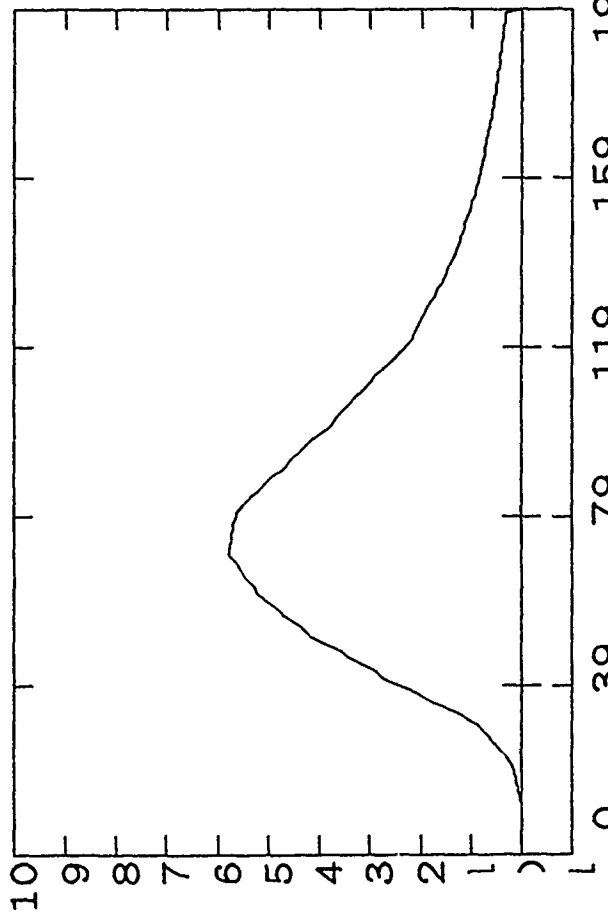


Timescale:NanoSECONDS

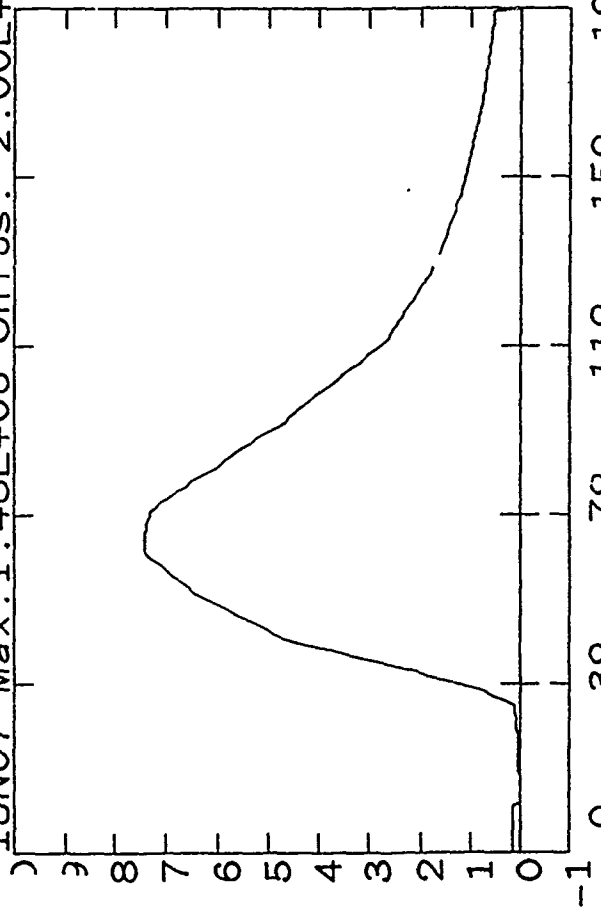
Fig. 9

Shot 1002

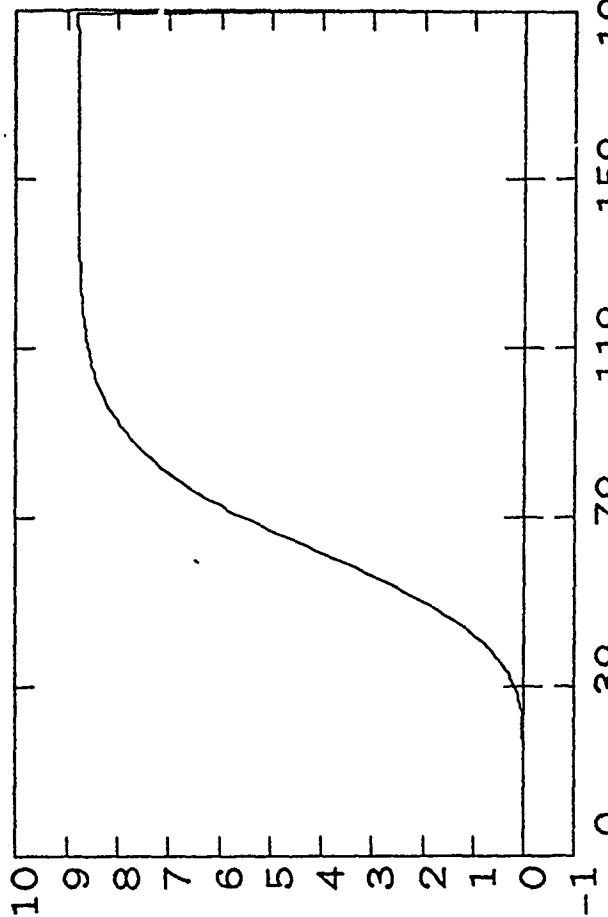
CUR20 Max: 2.87E+06 Units: 5.00E+05



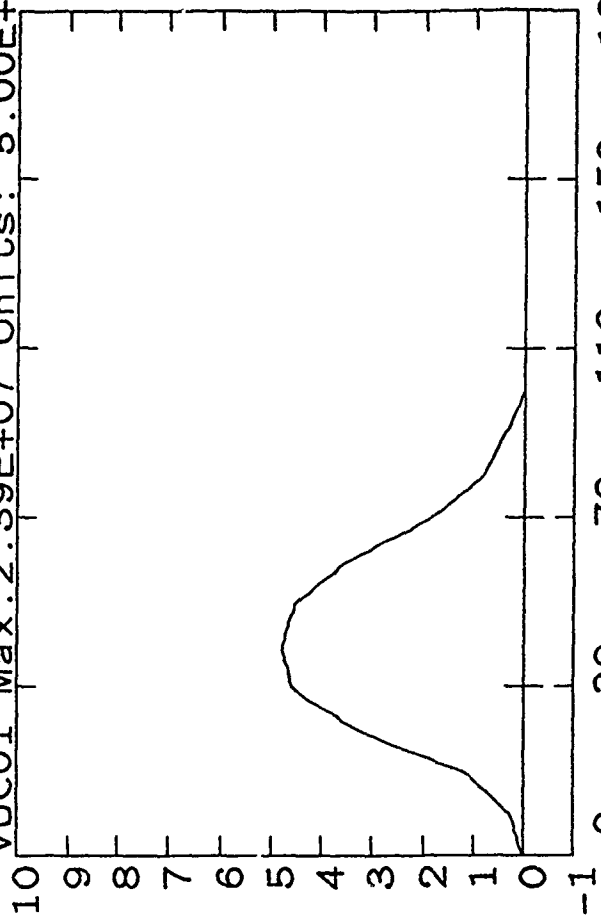
ION07 Max: 1.48E+06 Units: 2.00E+05



ENR20 Max: 4.39E+05 Units: 5.00E+04

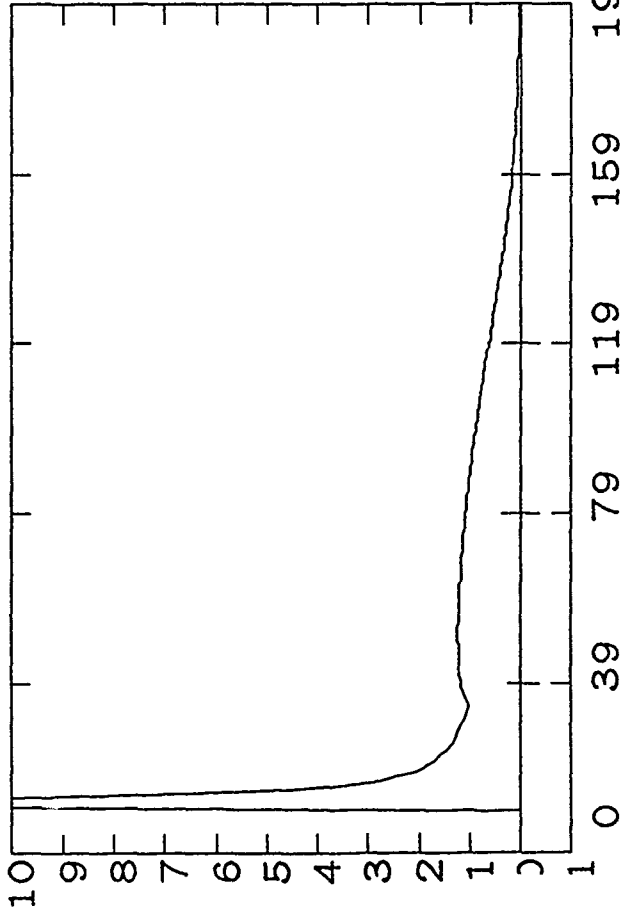


VDC01 Max: 2.39E+07 Units: 5.00E+06



Shot 1002

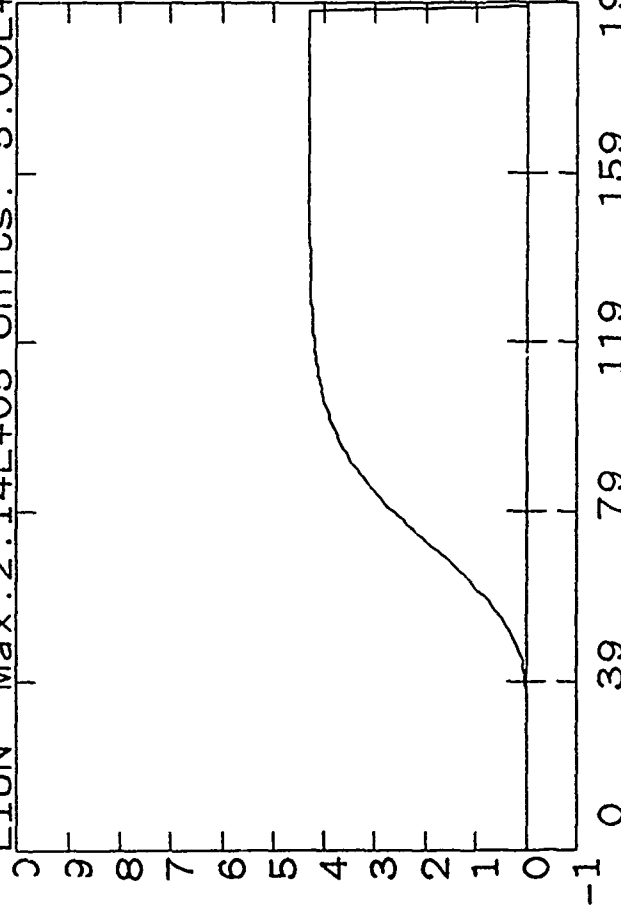
ZL Max:1.00E+01 Units: 1.00E+00



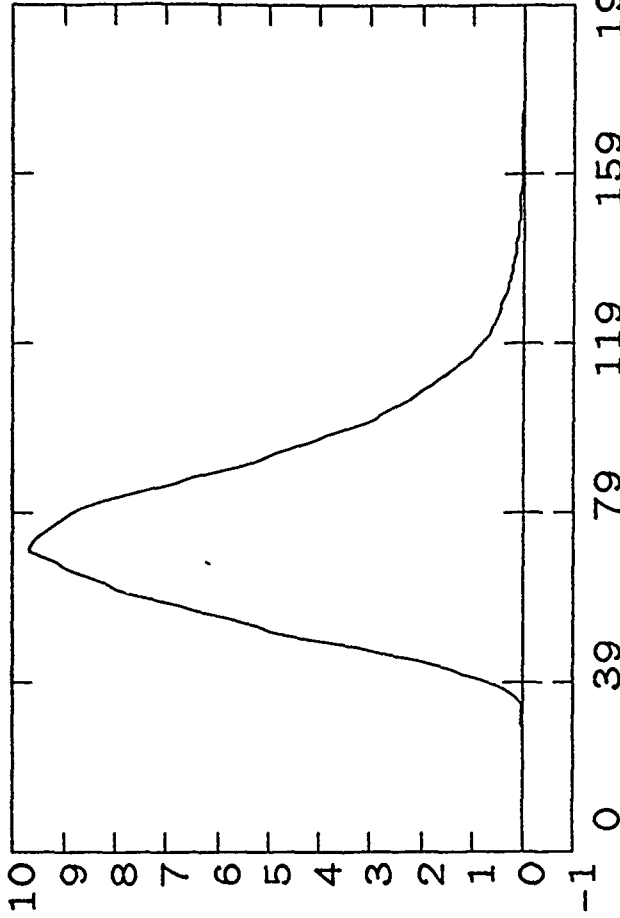
73

EION Timescale:NanoSECONDS

EION Max:2.14E+05 Units: 5.00E+04

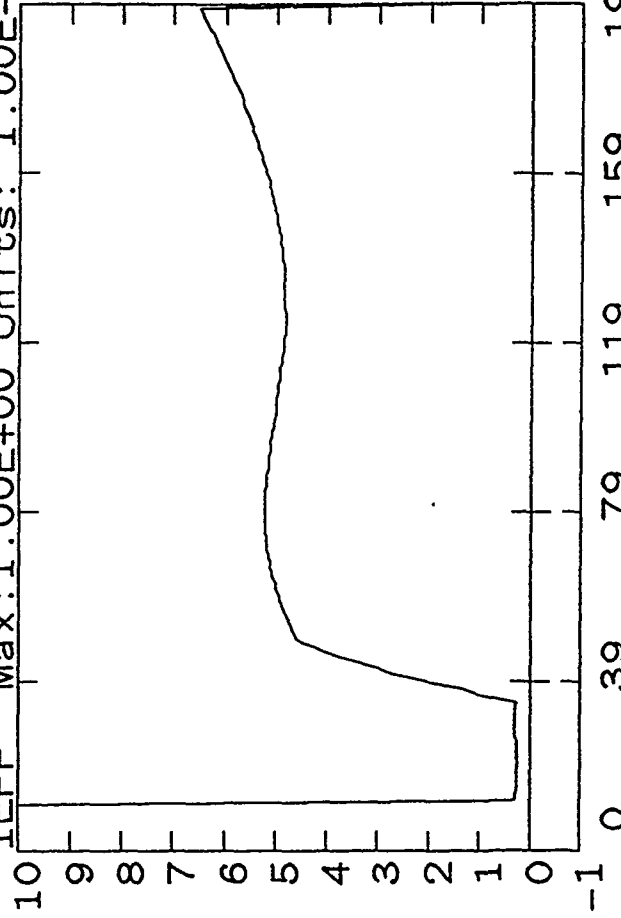


PION Max:4.84E+12 Units: 5.00E+11



IEFF Timescale:NanoSECONDS

IEFF Max:1.00E+00 Units: 1.00E-01



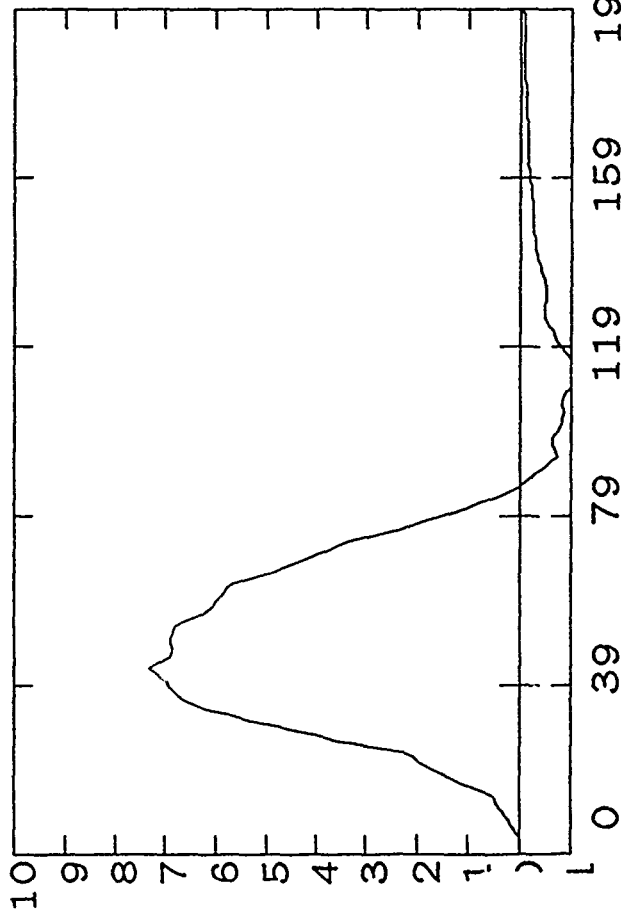
Timescale:NanoSECONDS

Timescale:NanoSECONDS

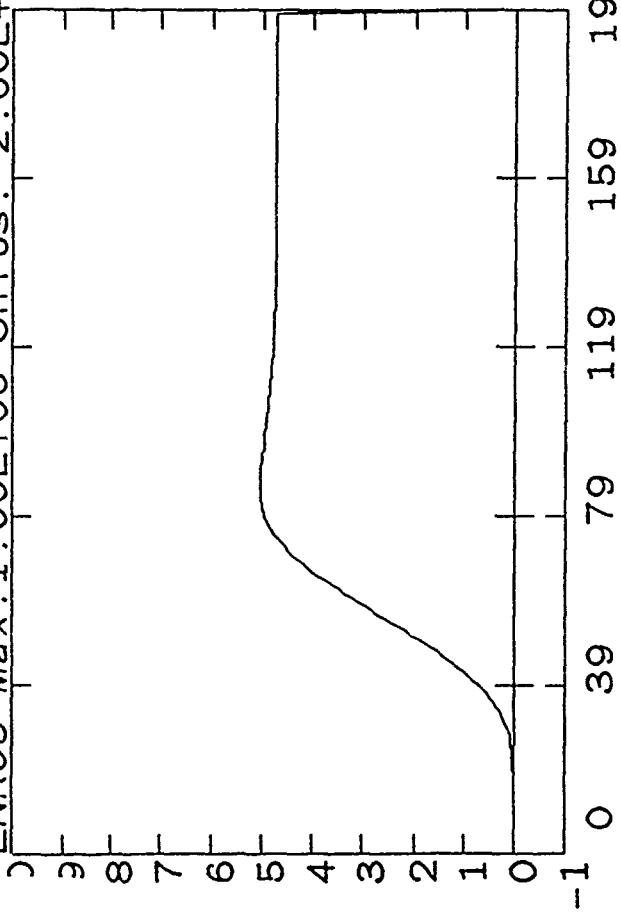
Fig. 11

Shot 1010

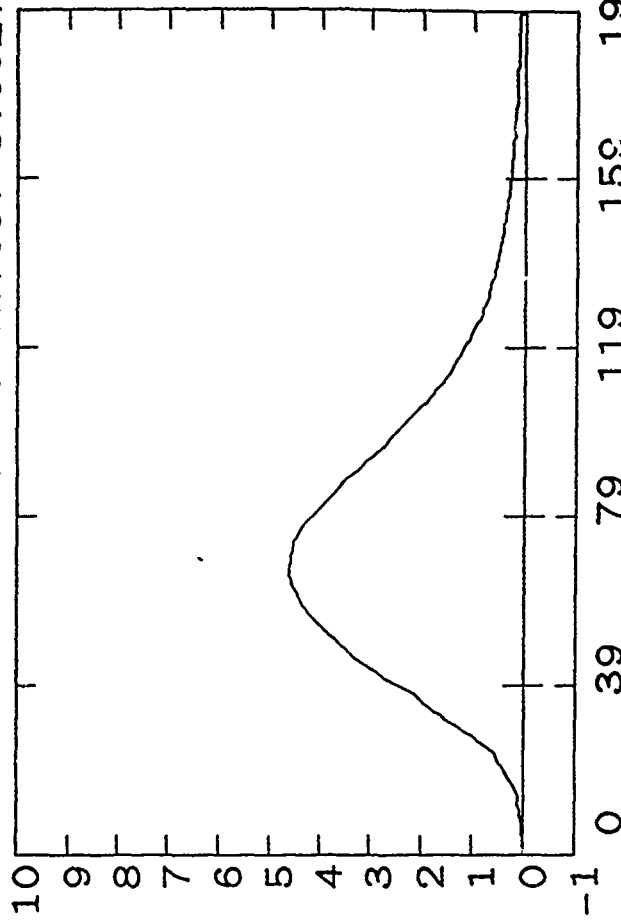
VOL06 Max:1.46E+07 Units: 2.00E+06



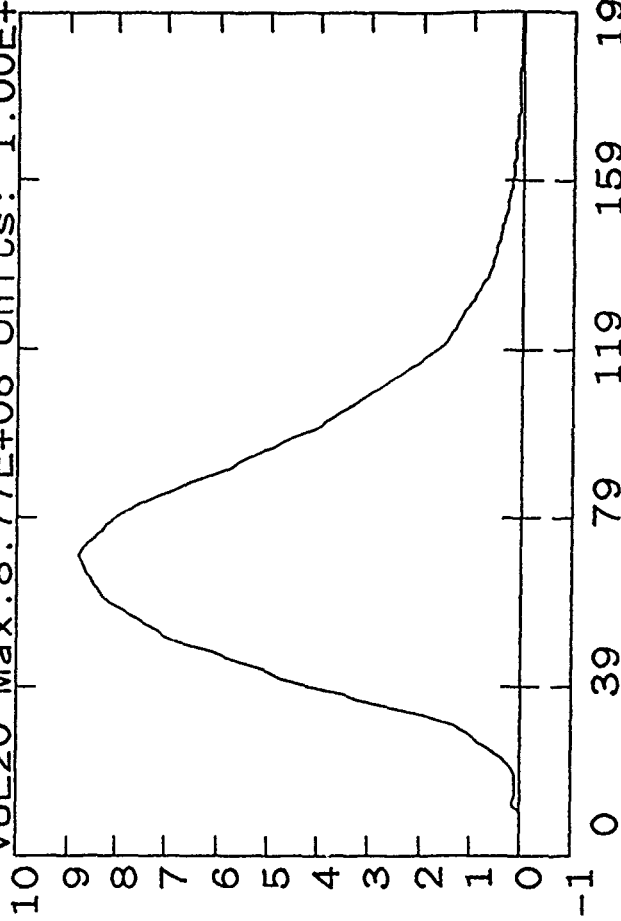
ENR06 Max:1.00E+06 Units: 2.00E+05



CUR06 Max:2.30E+06 Units: 5.00E+05

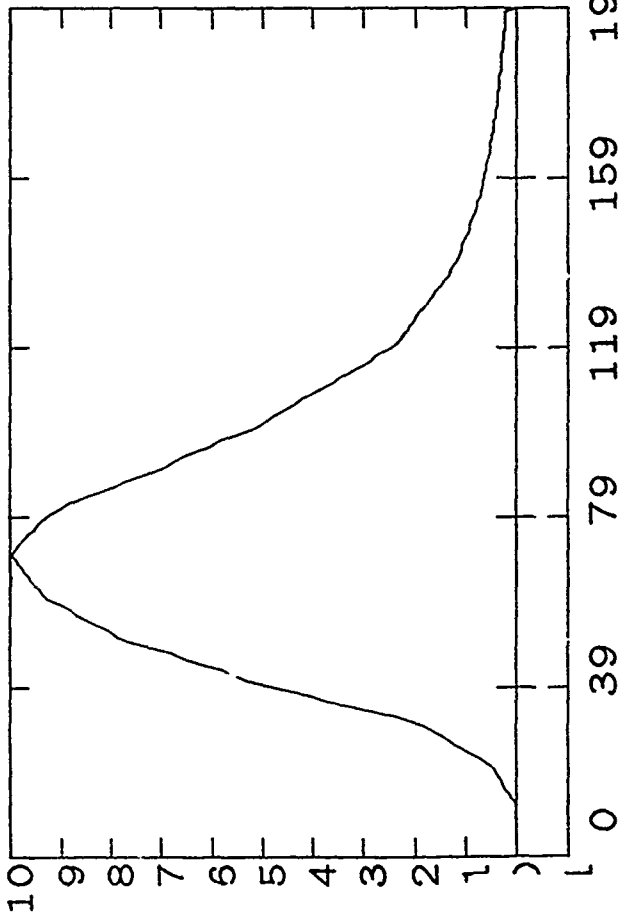


VOL20 Max:8.77E+06 Units: 1.00E+06

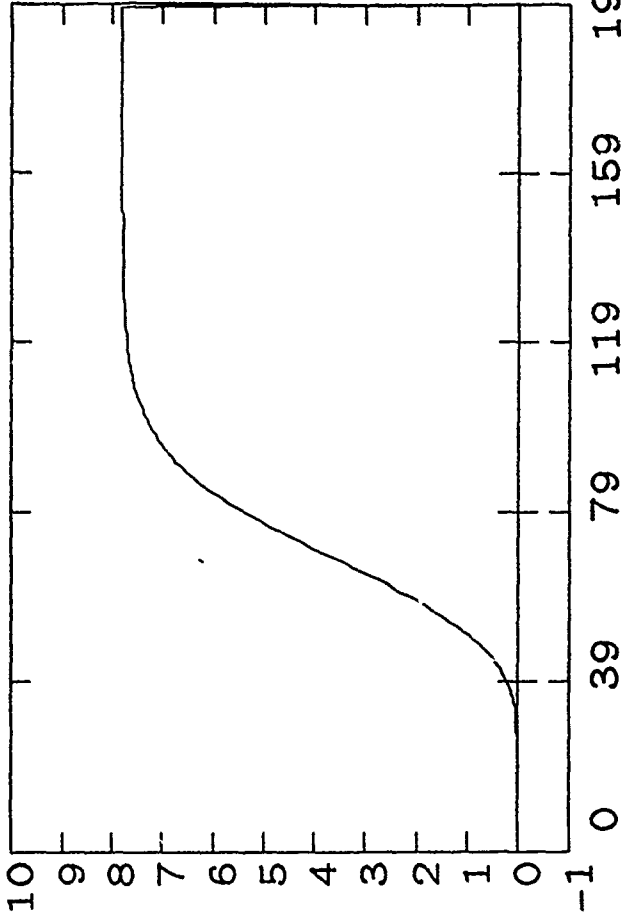


Shot 1010

CUR20 Max: 1.99E+06 Units: 2.00E+05

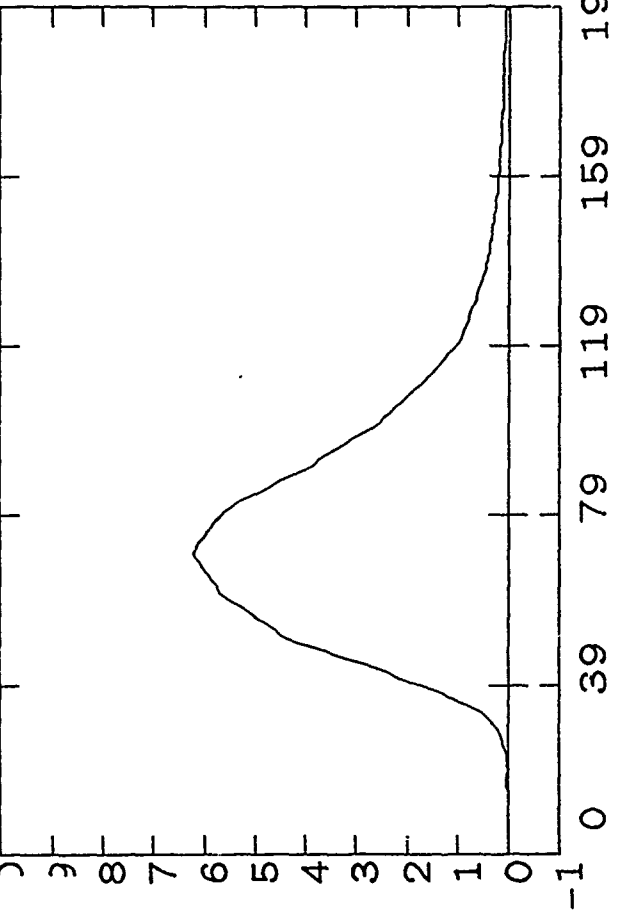


ENR20 Max: 7.79E+05 Units: 1.00E+05



75

ION07 Max: 6.18E+C5 Units: 1.00E+05



VOC01 Max: 2.39E+07 Units: 5.00E+06

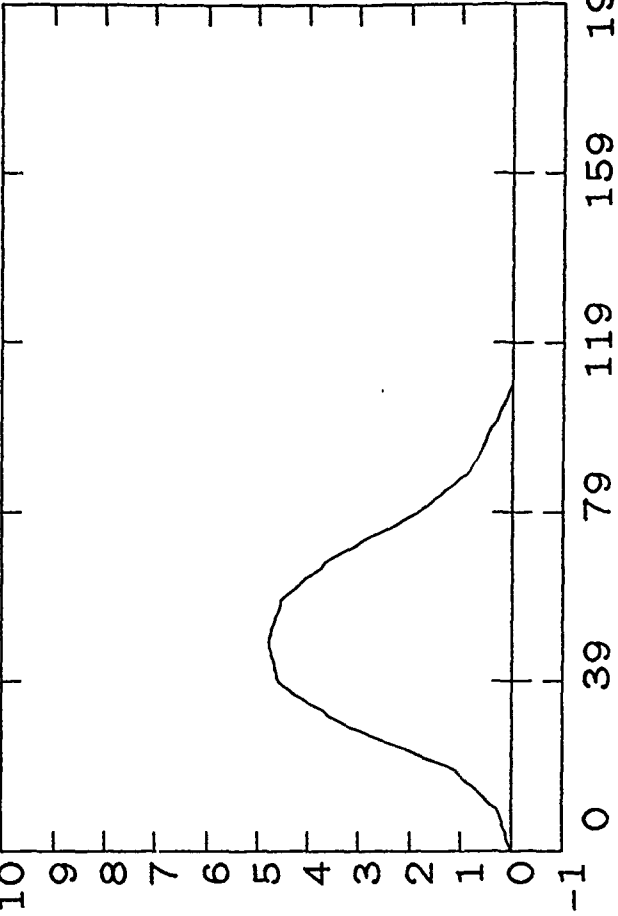
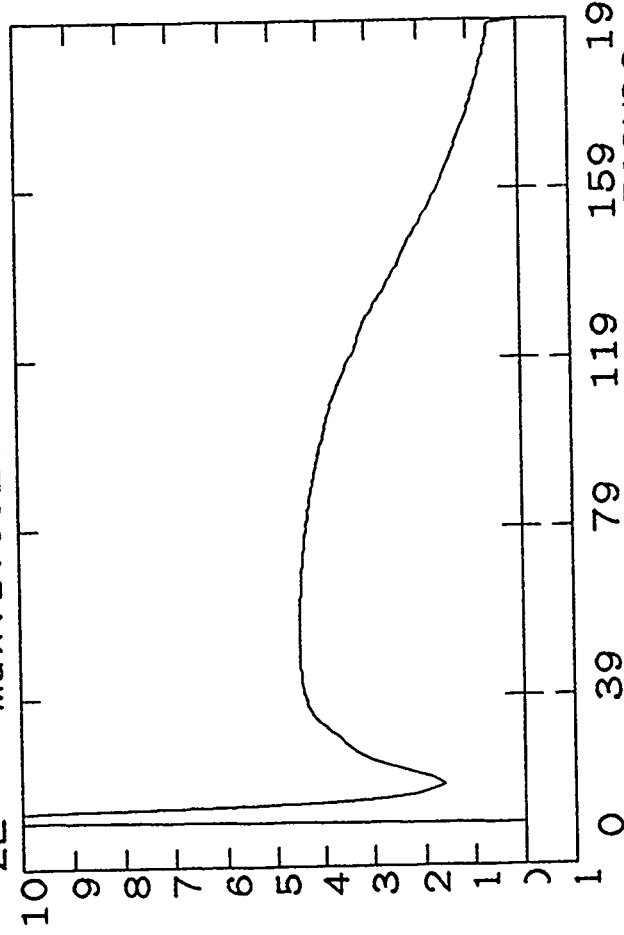


Fig. 13

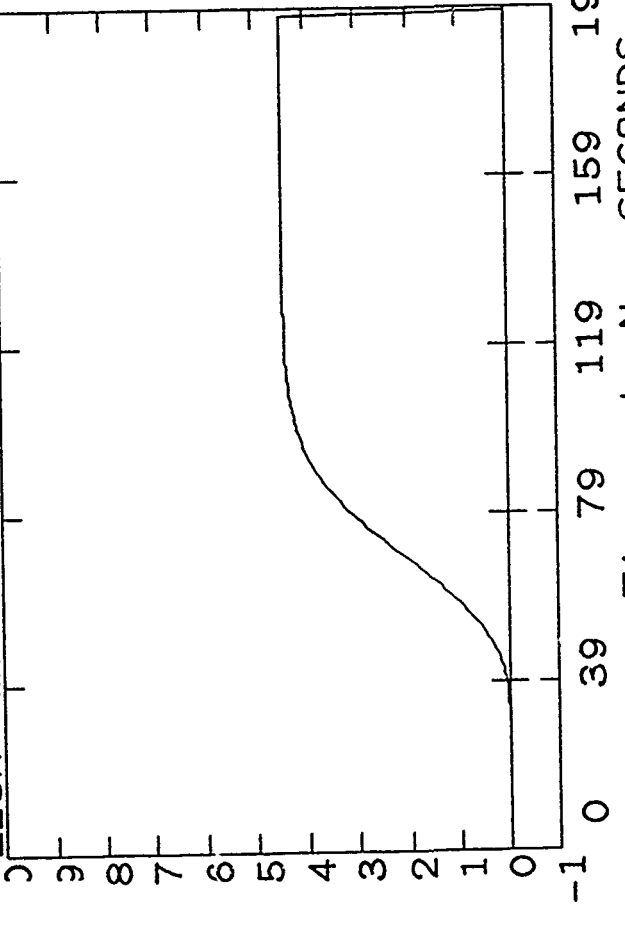
Shot 1010

ZL Max: 1.00E+01 Units: 1.00E+00



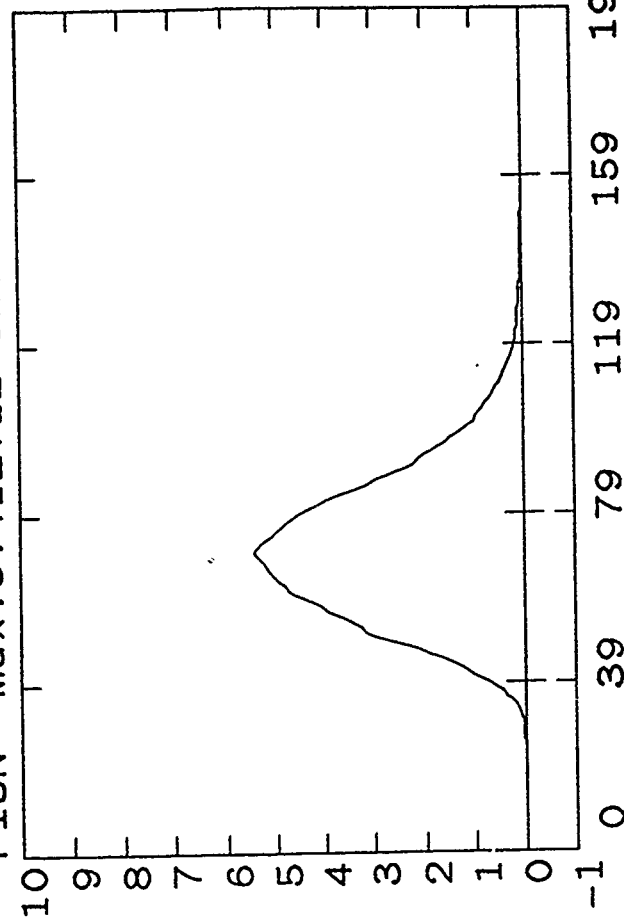
Timescale: NanoSECONDS

EION Max: 2.21E+05 Units: 5.00E+04



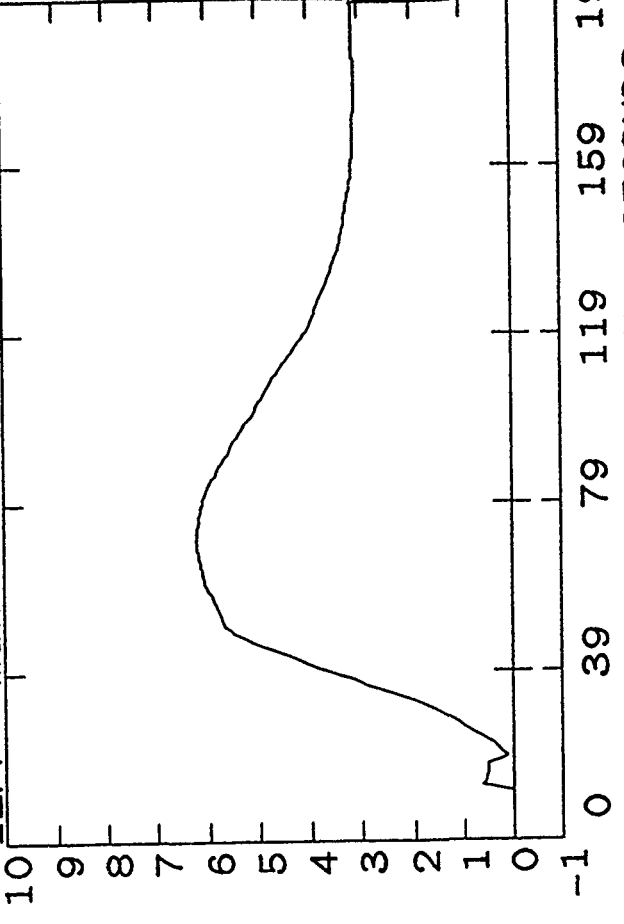
Timescale: NanoSECONDS

PION Max: 5.41E+12 Units: 1.00E+12



Timescale: NanoSECONDS

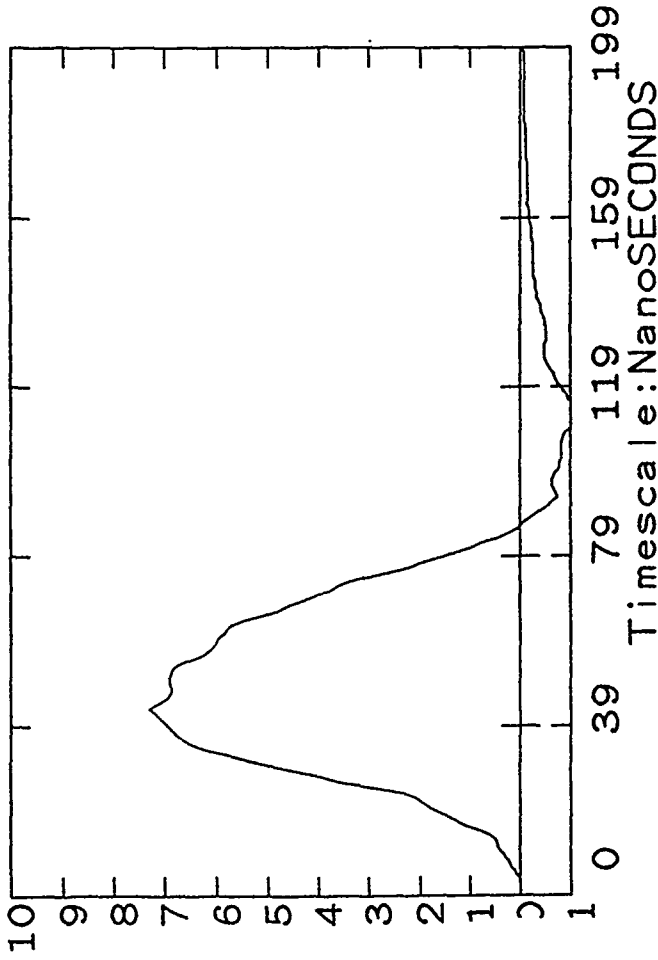
IEFF Max: 3.10E-01 Units: 5.00E-02



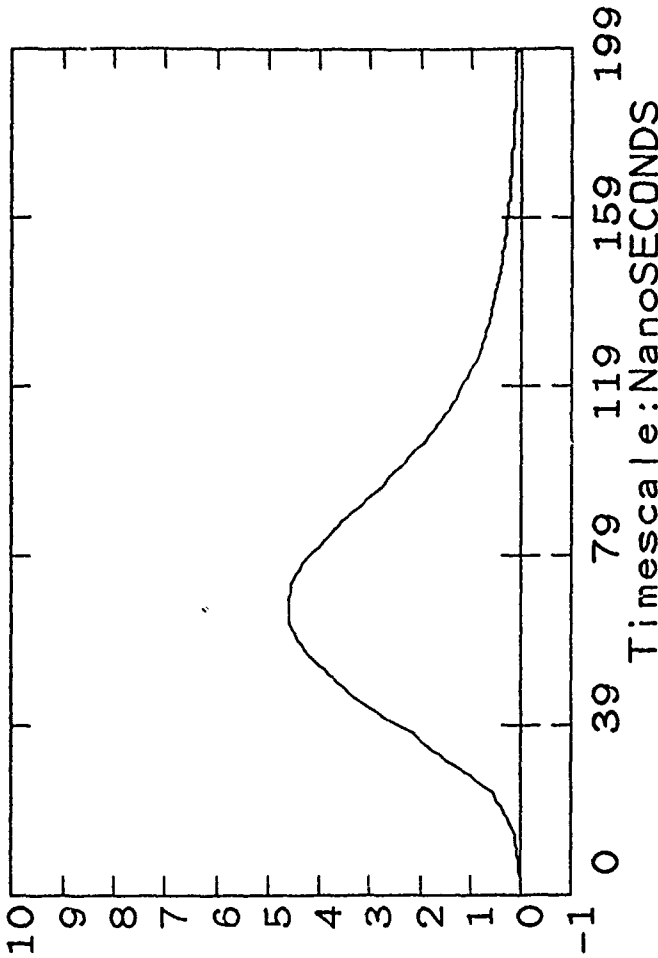
Timescale: NanoSECONDS

Shot 1011

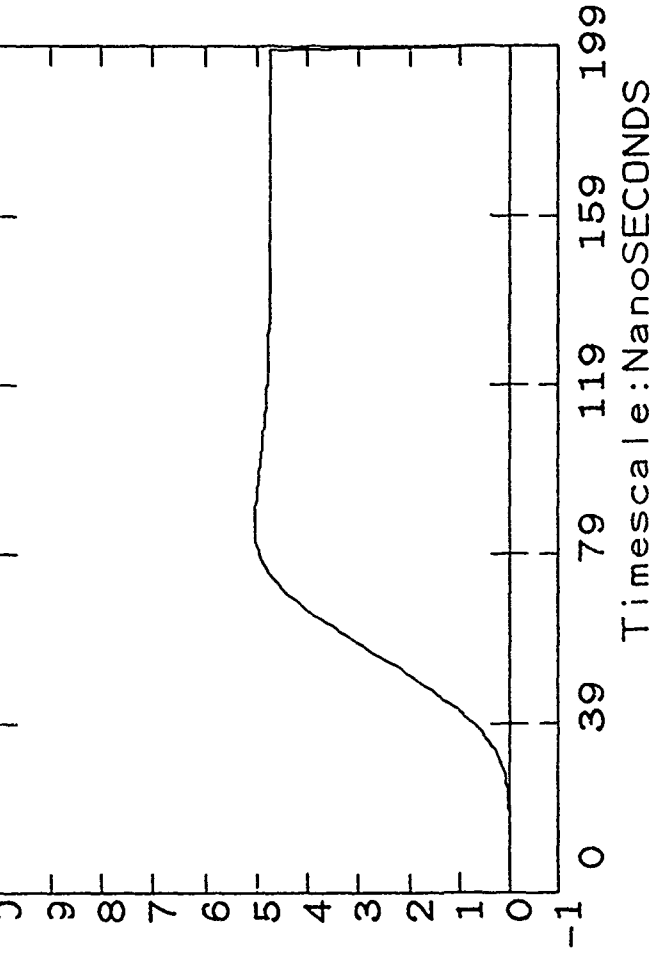
VOL06 Max:1.46E+07 Units: 2.00E+06



CUR06 Max:2.30E+06 Units: 5.00E+05



ENR06 Max:1.00E+06 Units: 2.00E+05



VOL20 Max:8.80E+06 Units: 1.00E+06

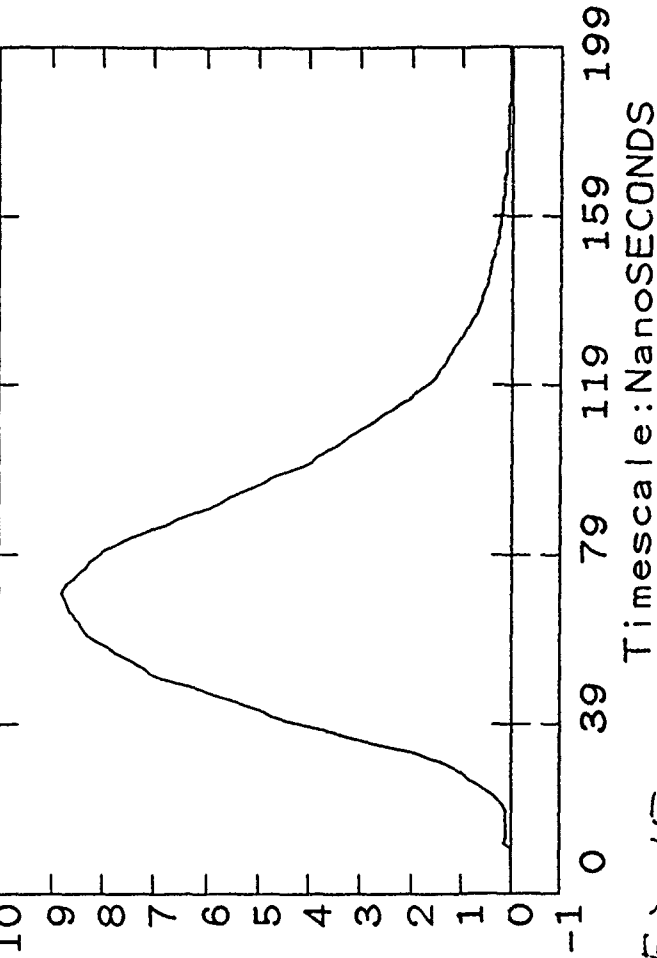
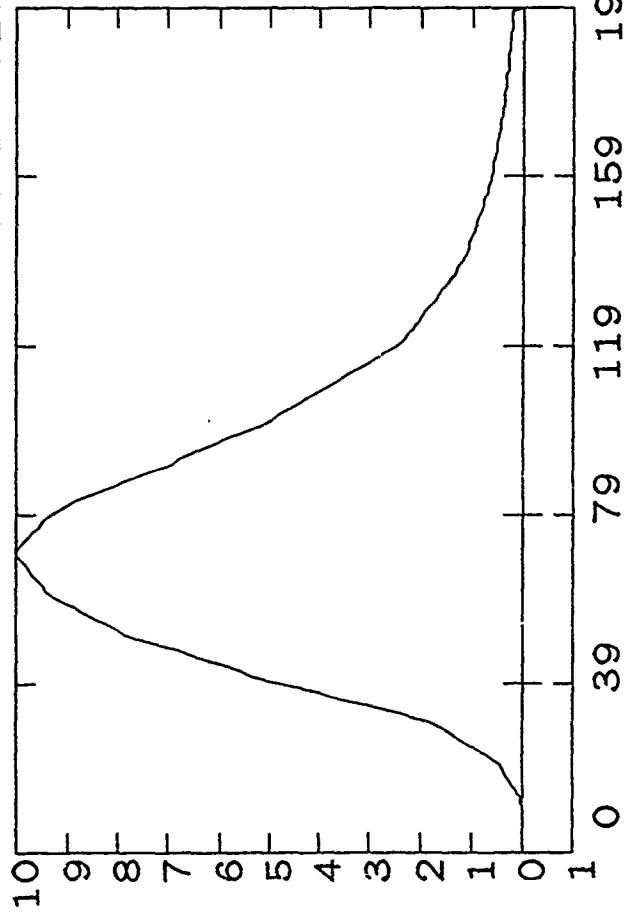


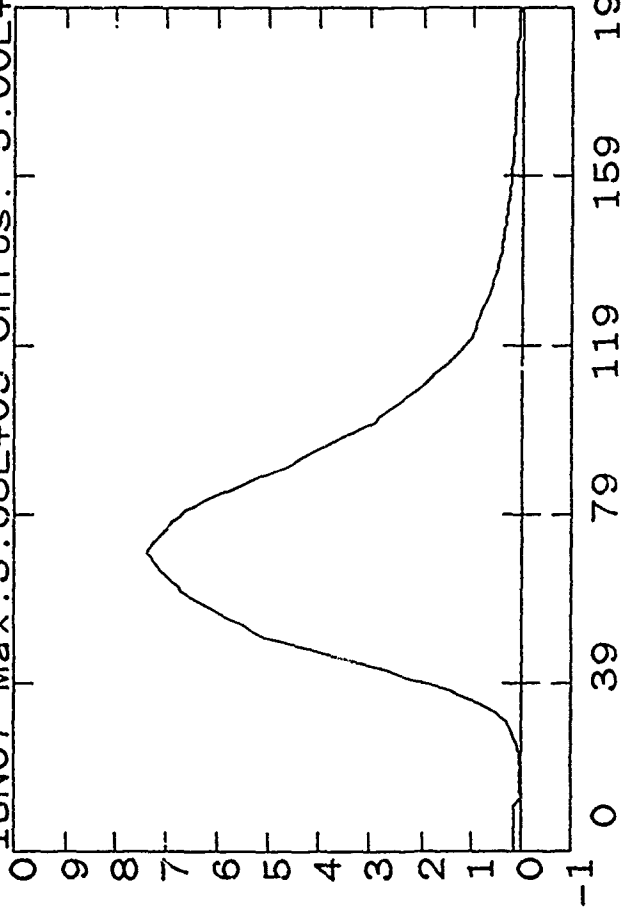
Fig. 15

Shot 1011

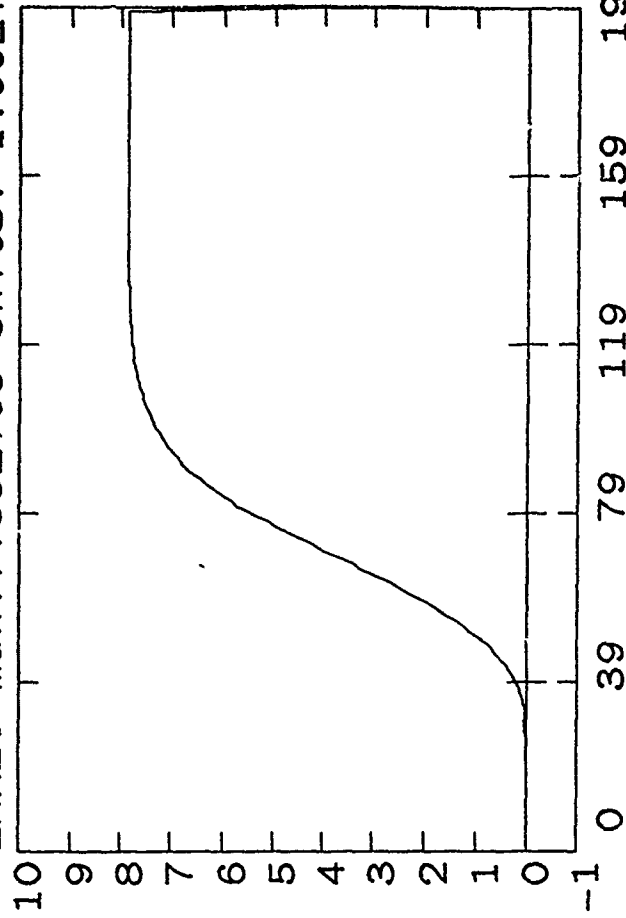
CUR20 Max: 2.00E+06 Units: 2.00E+05



ICN07 Max: 3.68E+05 Units: 5.00E+04



ENR20 Max: 7.85E+05 Units: 1.00E+05



VOCO1 Max: 2.39E+07 Units: 5.00E+06

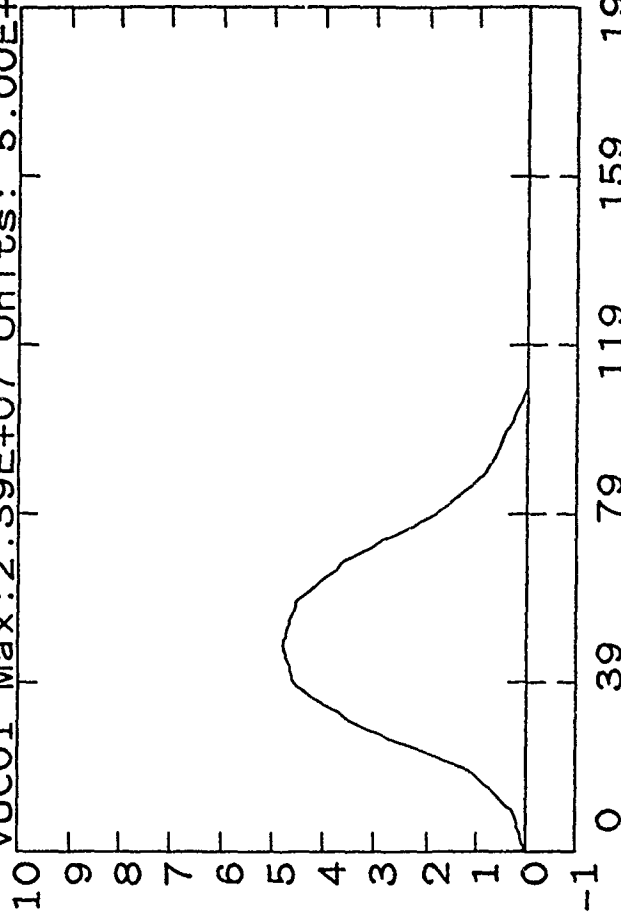
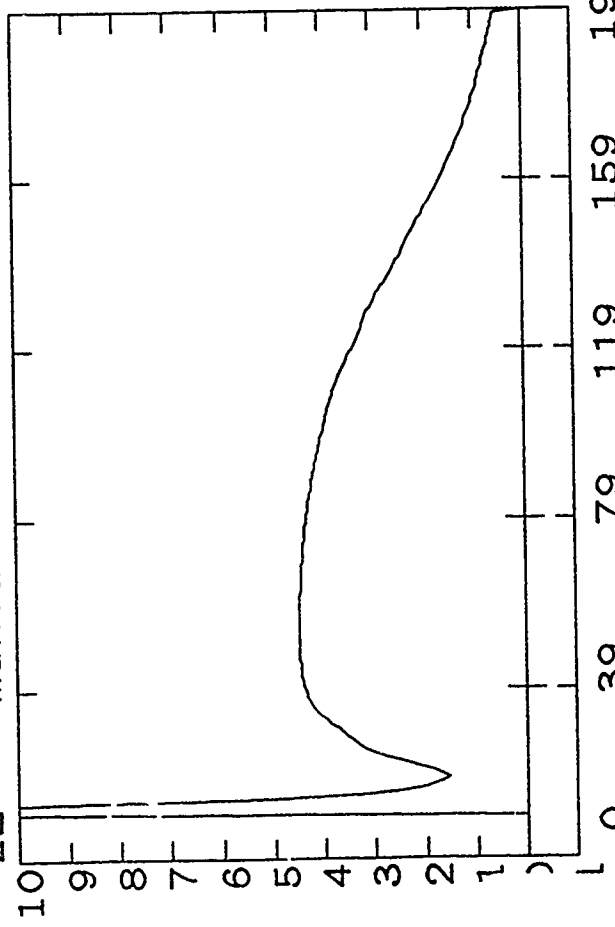


Fig 16

Shot 1011

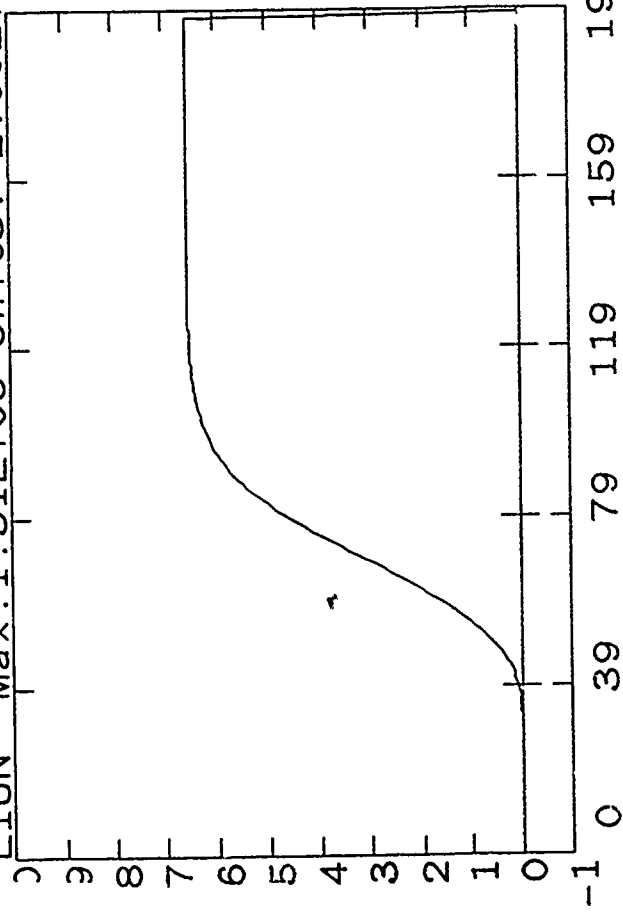
ZL Max:1.00E+01 Units: 1.00E+00



79

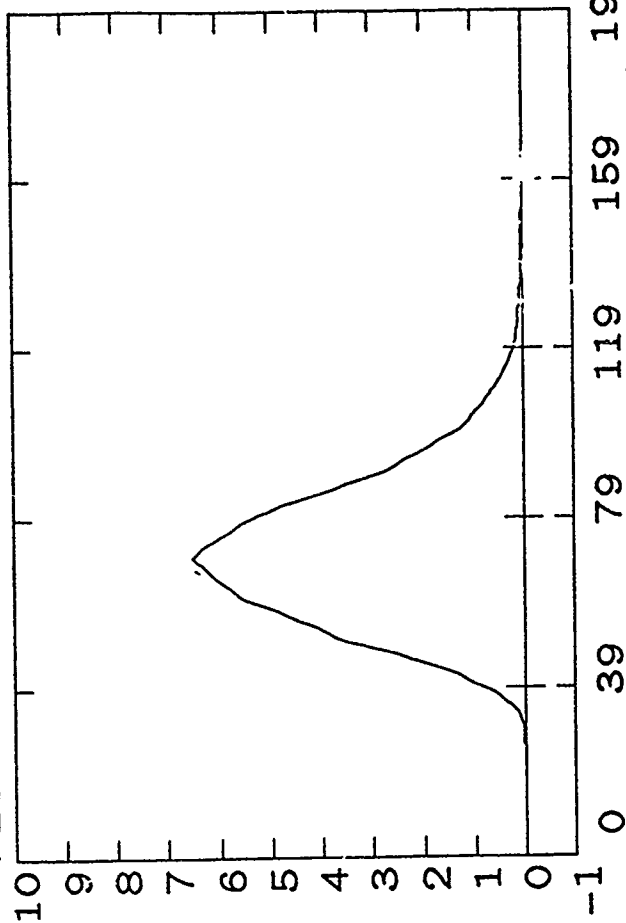
Timescale:NanoSECONDS

EION Max:1.31E+05 Units: 2.00E+04



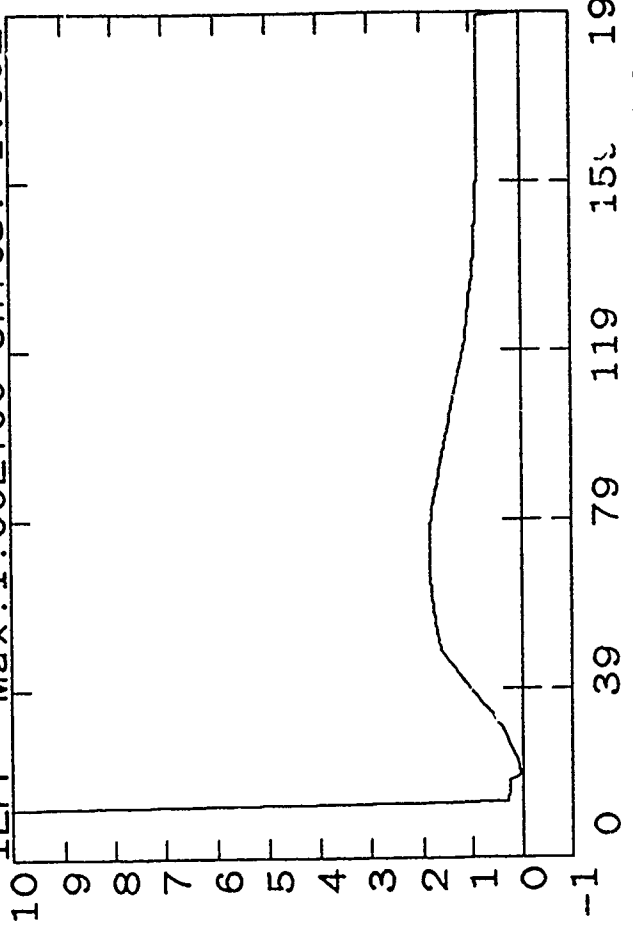
Timescale:NanoSECONDS

PION Max:3.24E+12 Units: 5.00E+11



Timescale:NanoSECONDS

IEFF Max:1.00E+00 Units: 1.00E-01

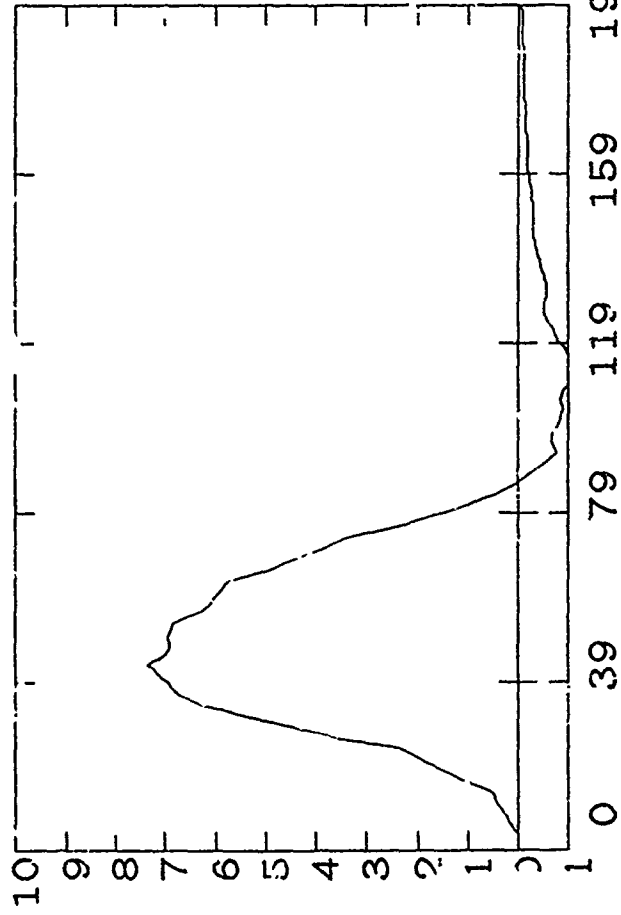


Timescale:NanoSECONDS

Fig. 17

Shot 1012

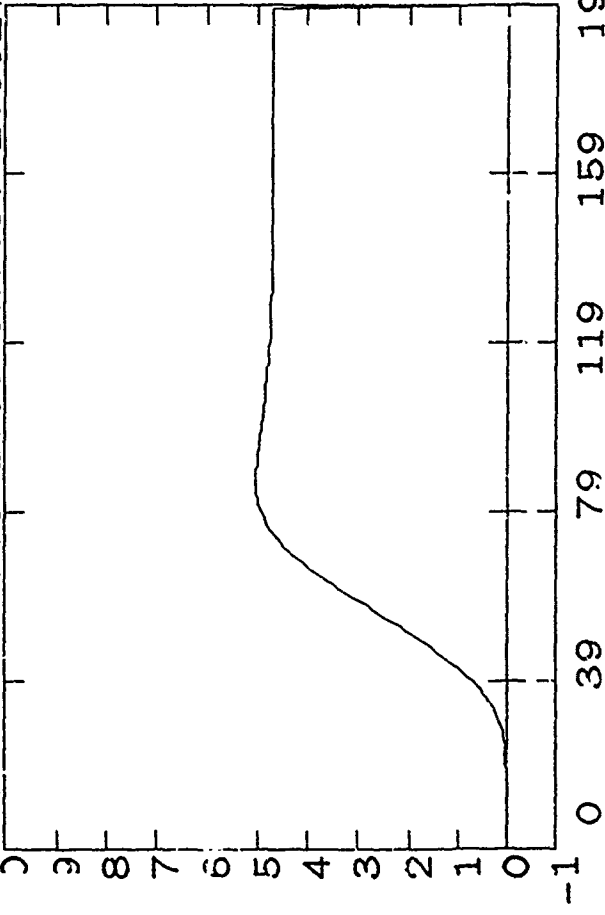
VOL06 Max:1.47E+07 Units: 2.00E+06



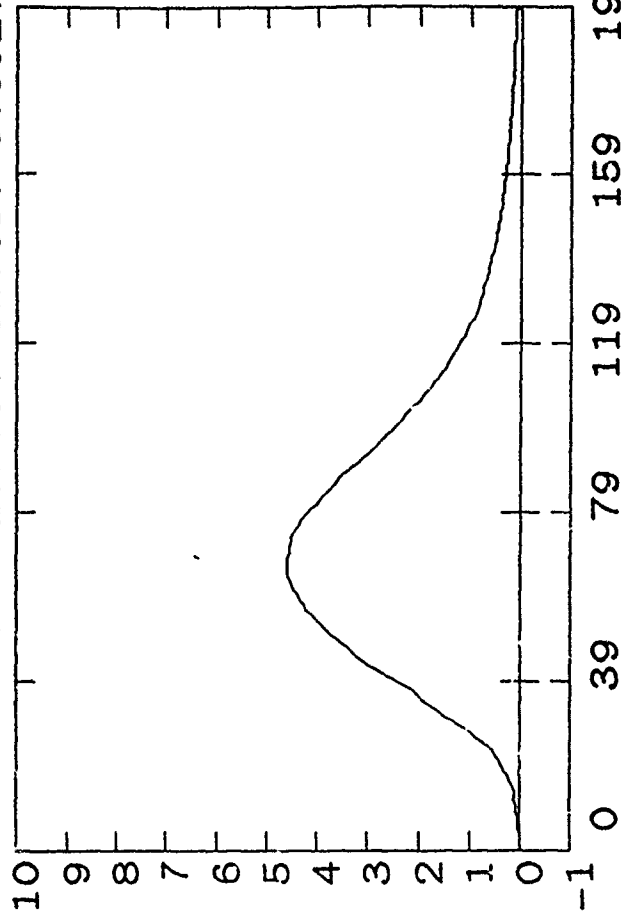
88

ENR06 Max:1.00E+06 Units: 2.00E+05

Timescale:NanoSECONDS

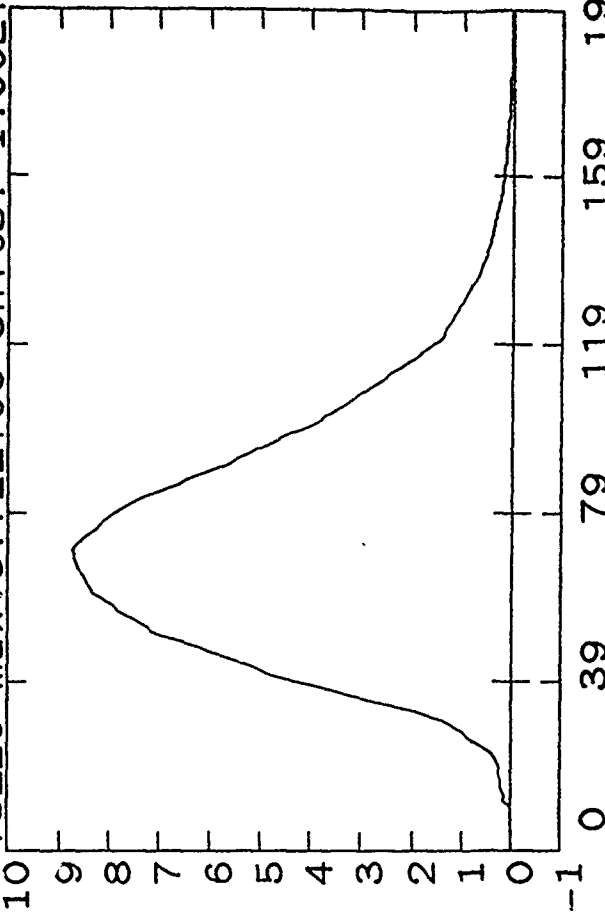


CUR06 Max:2.29E+06 Units: 5.00E+05



Timescale:NanoSECONDS

VOL20 Max:8.72E+06 Units: 1.00E+06



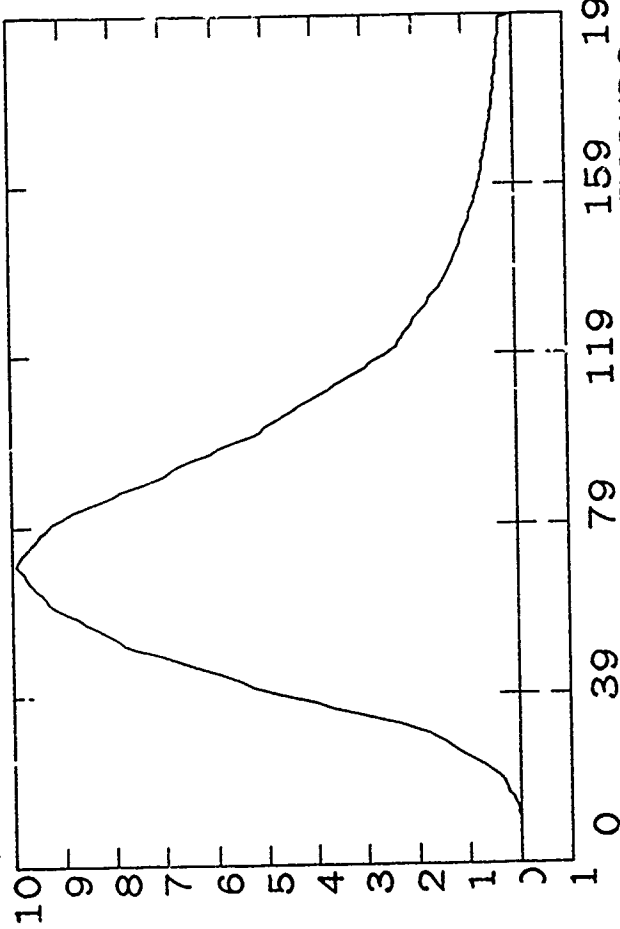
Timescale:NanoSECONDS

Timescale:NanoSECONDS

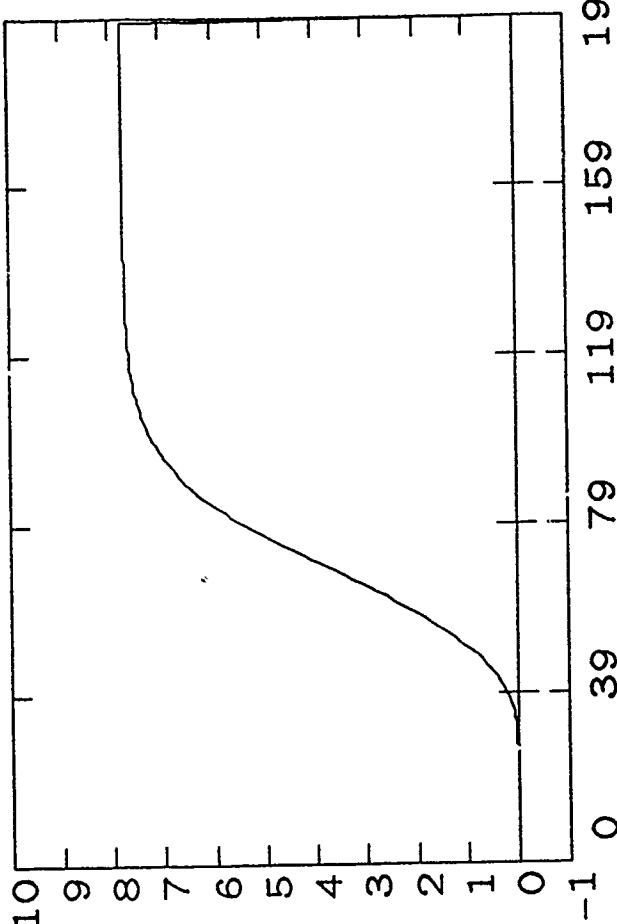
Fig. 18

Shot 1012

CUR20 Max: 1.98E+06 Units: 2.00E+05

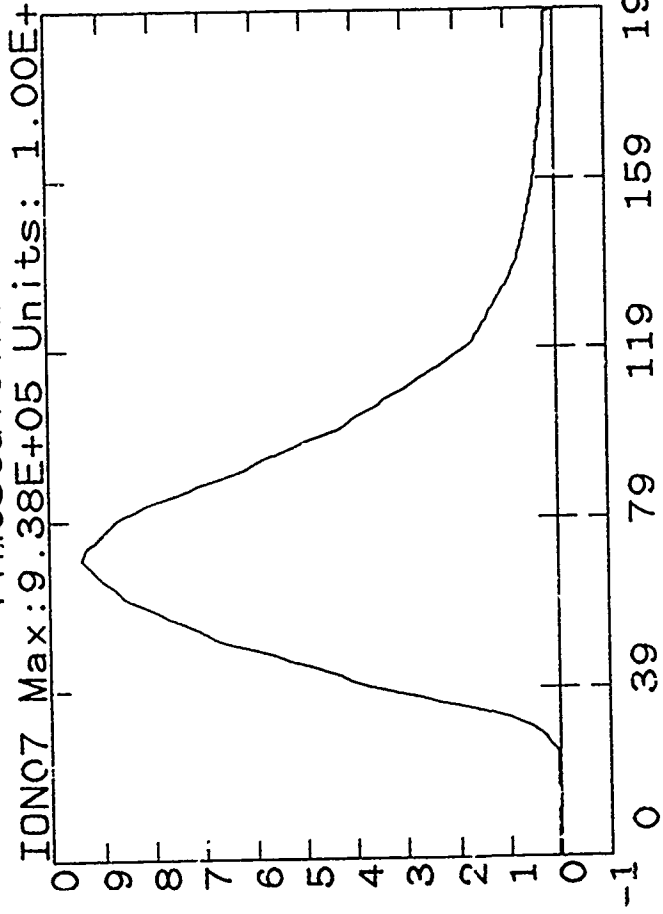


ENR20 Max: 7.72E+05 Units: 1.00E+05



81

IONC7 Max: 9.38E+05 Units: 1.00E+05



VOC01 Max: 2.39E+07 Units: 5.00E+06

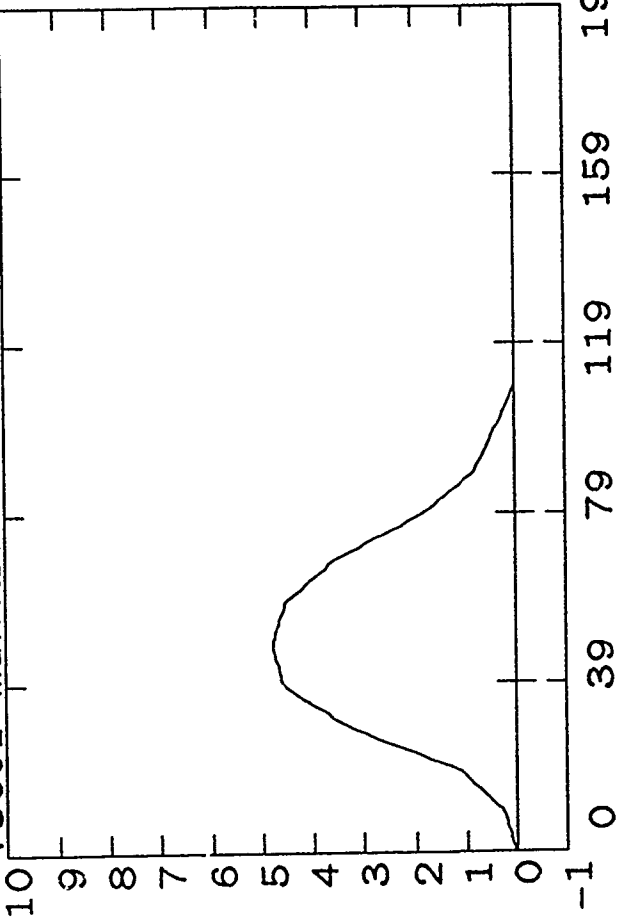
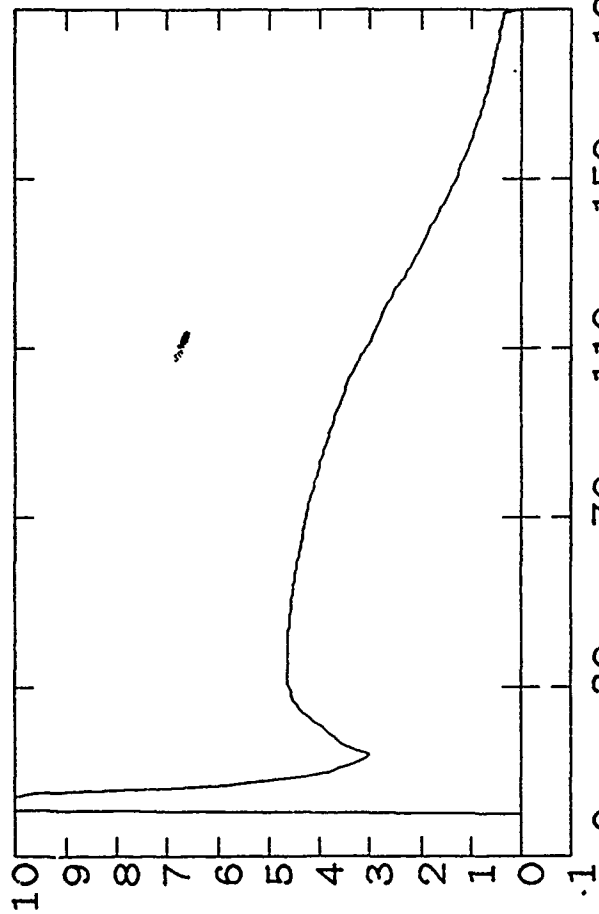


Fig. 17

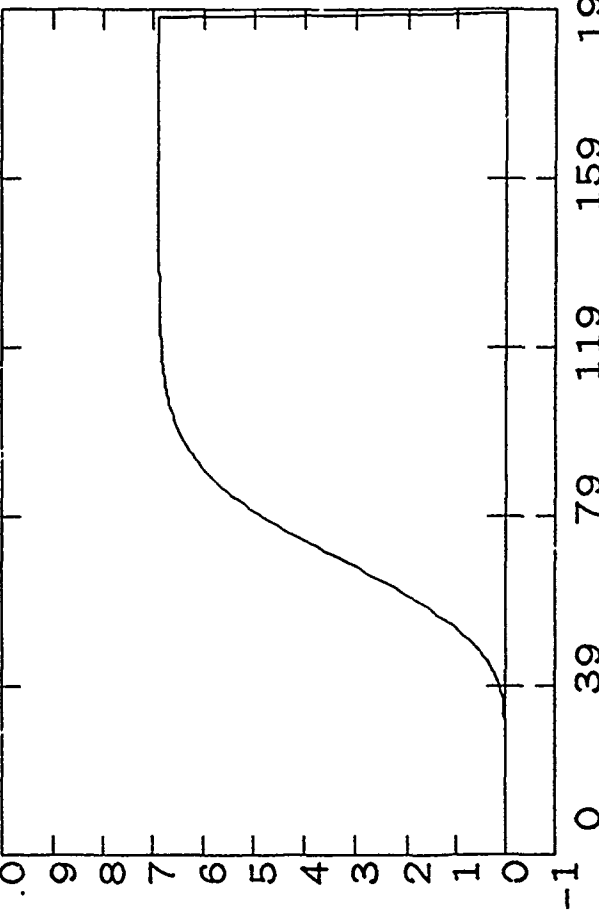
Shot 1012

ZL Max:1.00E+01 Units: 1.00E+00



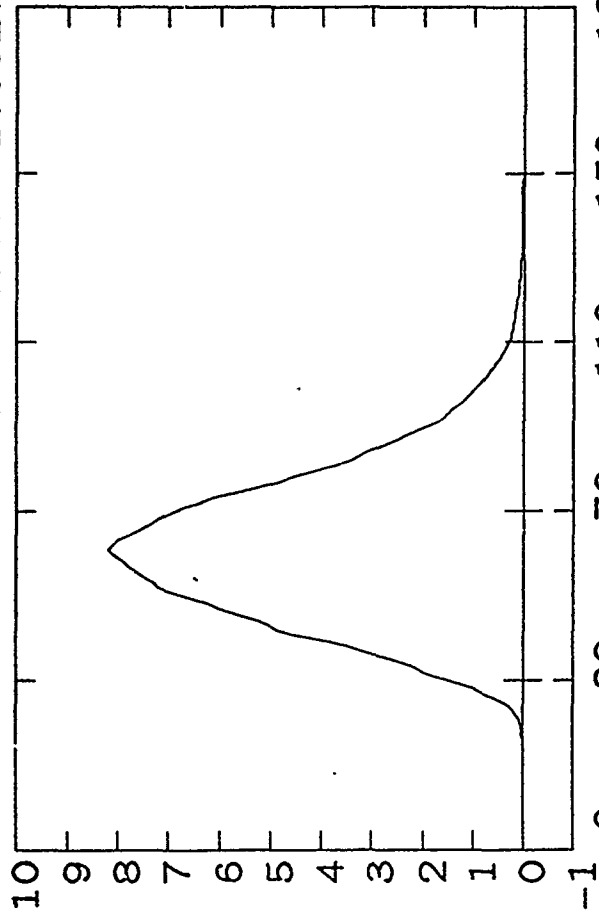
Timescale:NanoSECONDS

EION Max:3.44E+05 Units: 5.00E+04



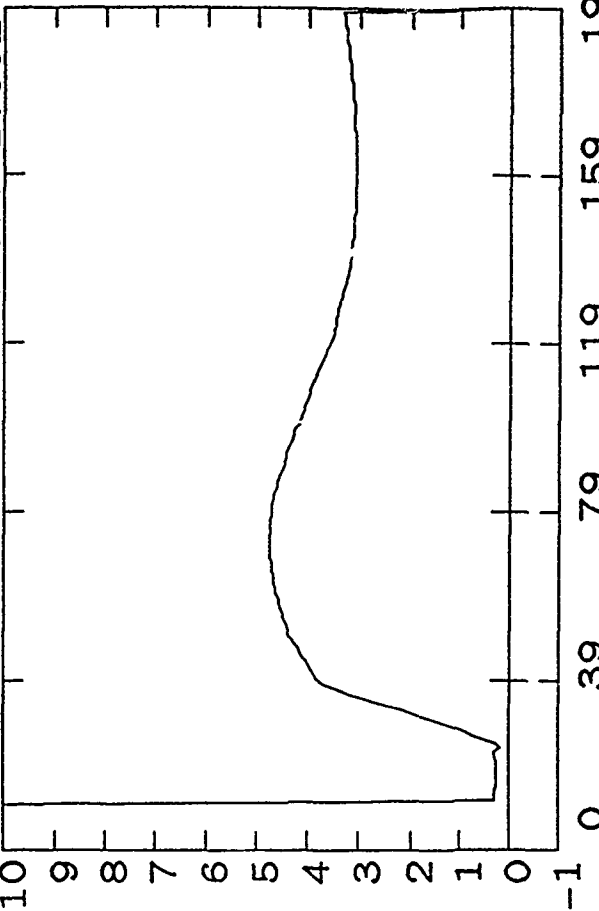
Timescale:NanoSECONDS

PION Max:8.18E+12 Units: 1.00E+12



Timescale:NanoSECONDS

IEFF Max:1.00E+00 Units: 1.00E-01



Timescale:NanoSECONDS

PULSED POWER PHYSICS TECHNOTE 93-03

TITLE: INITIAL RESULTS WITH AN EMFAPS ON GAMBLE II

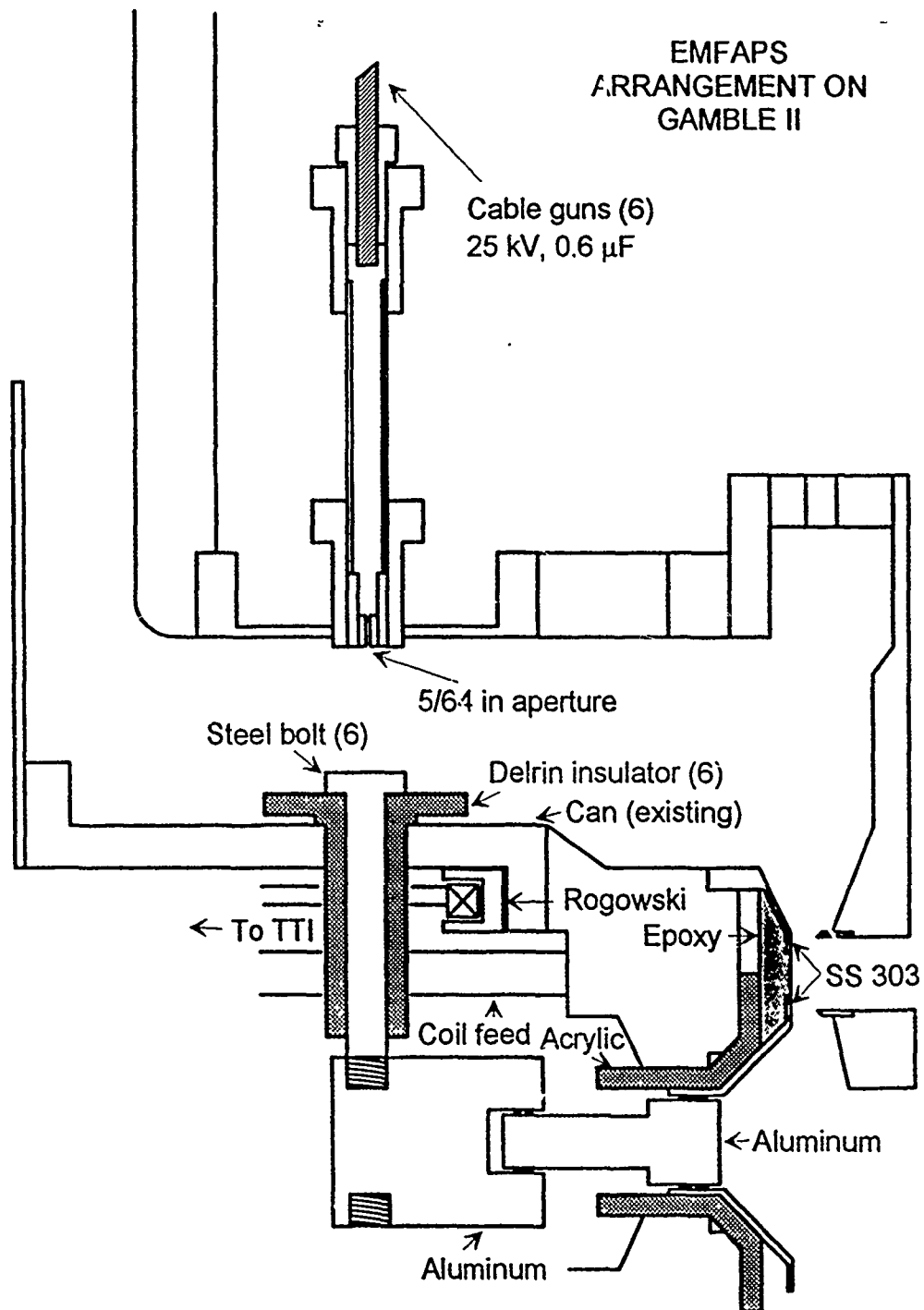
AUTHOR: D. Hinshelwood

DATE: March 23, 1993

ABSTRACT: This note describes the results of our first shots with an EMFAPS (Exploding metallic foil anode plasma source) installed on the Sandia magnetically insulated diode on Gamble II. The main purpose of this run was to relate the POS conditions (plasma delay and injection geometry) to the foil and POS currents, and the metallic foil arrangement used was not expected to produce a very uniform ion source. Nonetheless, on two shots we did obtain significantly improved diode performance. Compared to non-EMFAPS shots, these shots exhibit a faster-rising, higher ion current, a much faster initial impedance drop, a slower subsequent impedance collapse, a reduced peak insulator voltage, and an increased ion beam energy. Plans for future work are also described here.

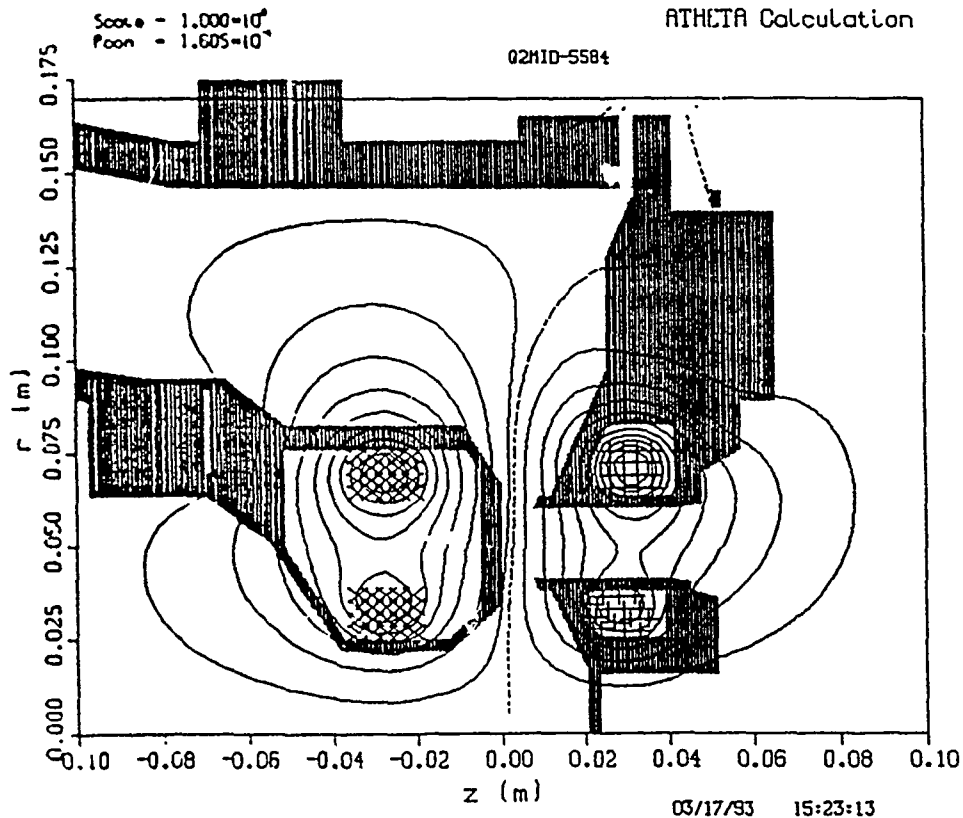
This note describes the results of our first shots with an EMFAPS (Exploding metallic foil anodic plasma source) installed on the Sandia magnetically insulated diode on Gamble II. The main purpose of this run was to relate the POS conditions (plasma delay and injection geometry) to the foil and POS currents, and the metallic foil arrangement used was not expected to produce a very uniform ion source. Nonetheless, on two shots we did obtain significantly improved diode performance.

A drawing of the experiment is shown below:



Six plasma guns inject plasma from the cathode to six steel bolts which are located on the anode, but insulated from it by Delrin bushings. The anode tip comprises two concentric stainless rings connected by Thermoset (600/70) epoxy. A metallic foil on the epoxy surface bridges these rings. The inner ring is connected to the six bolts. When the generator is fired the current flows along the anode, past the bushings, through the foil, out the bolts, and through the plasma across to the cathode. This current heats the metal foil, desorbing adsorbed gases and/or surface contaminants. This material is subsequently ionized by the voltage across the foil, resulting in an anode plasma. Eventually the bushings flash over due to the inductive and resistive voltage drop and because MHD forces push the plasma channels forward from the bolts and off the bushings. At this point the foil current crowbars and subsequent generator current flows in a standard POS arrangement. Finally, the switch opens and energy is transferred to the diode. Performance of this source depends critically on the timings of both the foil current crowbaring and the switch opening.

Because of a bug in the ATHETA program we were not able to calculate the exact applied magnetic field configuration in this experiment. Sandia personnel are fixing this bug; in the mean time, the calculated configuration used immediately prior to this run was used as a starting point. This configuration is shown below:



The EMFAPS anode tip extends 6.4 mm beyond the tip in the configuration above. To compensate for this in the absence of a code calculation, the cathode coil currents were left unchanged while the outer and inner anode coil currents were increased by 25 and 18 percent, respectively. To reduce cost and fabrication time, stainless rather than titanium

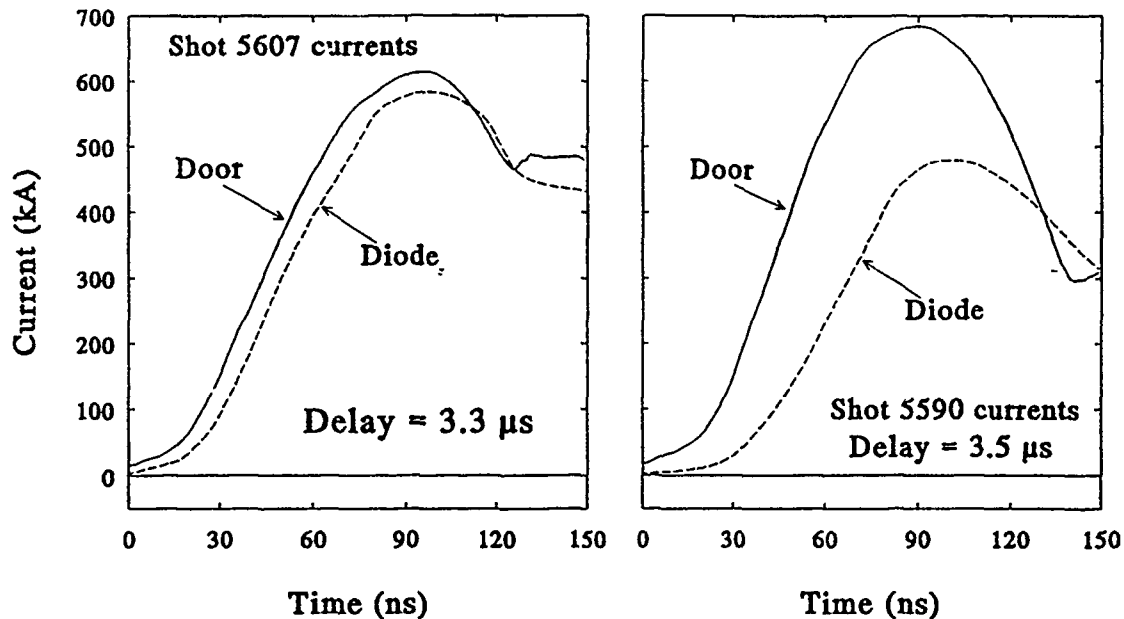
was chosen for the EMFAPS anode tip. Most of the tip is fairly thin, and in particular the inner ring is spun from 0.004-cm sheet. With a coil current rise time of about 100 μ s, the calculated skin depth is about 0.8 cm so that field penetration should not be a problem. The EMFAPS diode gap is 0.4 mm smaller than the 8-mm gap in the configuration above.

Since we do not yet have a coating capability, the vapor-deposited metallic foil was replaced by an aluminized mylar foil which was attached to the stainless anode rings with conducting epoxy. The epoxy was not expected to provide a suitable current contact and indeed the measured resistance was about 1 Ω , much greater than that expected from the foil alone. This may be due in part to a low-voltage contact resistance, but in general, arcing and asymmetrical current flow through the foil would be expected.

The Delrin bushings have steps so that additional insulation can be placed under them if needed. The insulation used at Cornell extends farther from the POS current contact than these bushings do, and premature flashover of the bushings may be a problem here. Because our transit time isolator is not well shielded, we have had trouble in the past extracting signals through it. Since measurement of the foil current is so important, the Rogowski was wound with about 50, 5-mm diam turns and integrated in the screen room. During calibration the time response was observed to be better than 10 ns, sufficient for this experiment.

Cable guns, developed by John Goyer at PI, are used for the plasma source. These have a 60° cone machined in them which greatly increases the resulting plasma density relative to that produced by Mendel guns (we used cable guns because our old Mendel guns are in dubious condition). Therefore, the plasma flow into the POS region must be highly attenuated in order to have a reasonable gun-to-generator timing window for this experiment. A large part of this run comprised short circuit shots to determine POS timing scans for several gun arrangements. For these shots, the Delrin bushings were replaced by metal washers and a short circuit was placed in the diode. Initially, the guns were recessed in the 8-cm tubes shown in the drawing, with 6-mm apertures at the ends. This produced too much plasma. Next, only three guns were used and the doghouse voltage was reduced to 17.5 kV. Our two good shots were obtained with this arrangement although the timing window was narrow. No conduction at all was observed when the 0.6 μ F doghouse capacitors were replaced with 0.02 μ F caps. Finally, the apertures were reduced to 2-mm diam as shown in the drawing, and all six guns were used with a 25 kV doghouse voltage. The timing window is still narrow with this arrangement and even smaller apertures will be used in the future.

Typical short circuit shots are shown below: These shots were taken using different gun configurations so the timings can not be compared directly, but they are representative of all the short circuit data. At small delays (for a given configuration) the load current is simply delayed, at longer delays poor switching is indicated, and risetime sharpening is never observed. Poor switching would be expected in positive polarity at such a large radius, but also note that there are no anode monitors in this experiment and some of the "loss" could be vacuum electron flow.



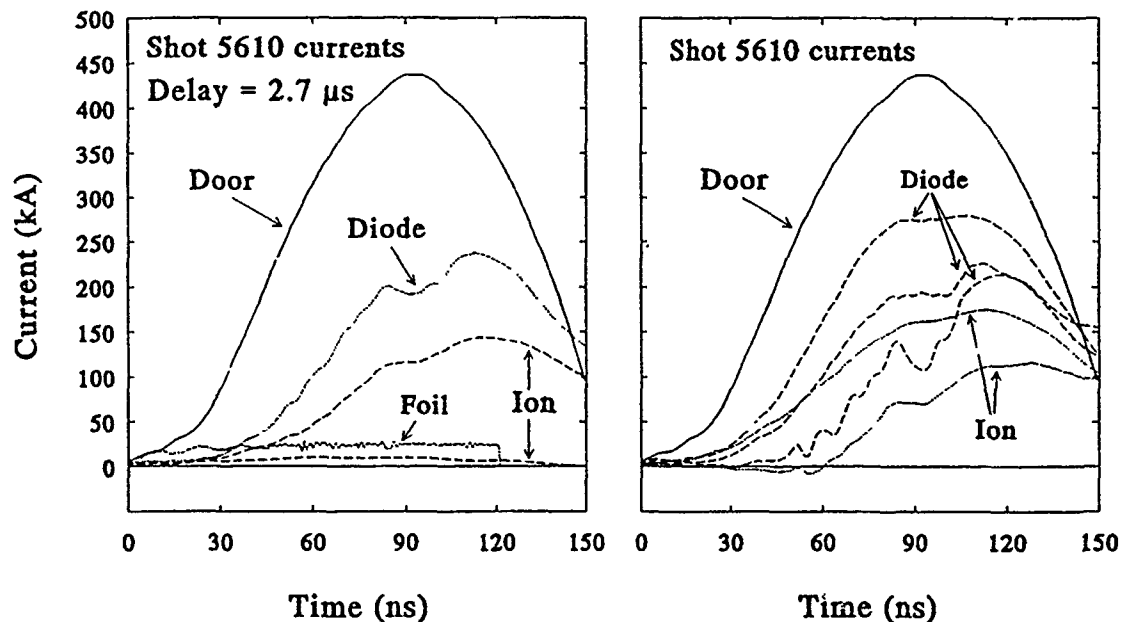
Results from the diode shot below show an interesting feature. Shot 5610 had the same switch configuration as shot 5607 above and a smaller delay. However, the switch appears to conduct more current on shot 5610. Similar behavior was observed on other pairs of shots. John Greenly has observed this feature at Cornell also. In the graphs which follow, the door current is measured by four summed B-dots located in the first part of the vacuum section and upstream of the switch. The diode current is measured by three summed B-dots located just outside the outer cathode. The ion current is obtained by subtracting signals from two sets of three summed B-dots, located just inside the outer cathode and just outside the inner cathode. In practice, the latter signal is almost negligible as seen below, indicating that little electron current is emitted from the inner cathode. (John Greenly has suggested that this is a good operating situation for an MID.) The B-dot signals are integrated and then an ad hoc correction is applied to compensate for the time response degradation resulting from field diffusion around the monitors. This consists of an RC time constant correction using a negative time constant whose value is chosen to give the best waveshape match on short circuit shots.

On the MID shots taken before this run the calibration for the diode current signal appeared to change from shot to shot, as if one of the individual B-dots was not working, and this monitor was basically useless. After the first few shots on this run things seemed to settle down but still the calibration (as determined from periodic short circuit shots without plasma) varied by ten percent or so during the run. With the POS this diagnostic is vital and by the end of this run all three B-dots on both sides of the outer cathode were recorded individually. This will be continued in the future so that if one B-dot is obviously unphysical its signal can be discarded. The anode current monitors were not useable because of our noisy transit time isolator. In the future a high priority should be placed on

installing a better isolator so that at least the total diode anode current can be measured to characterize better the POS.

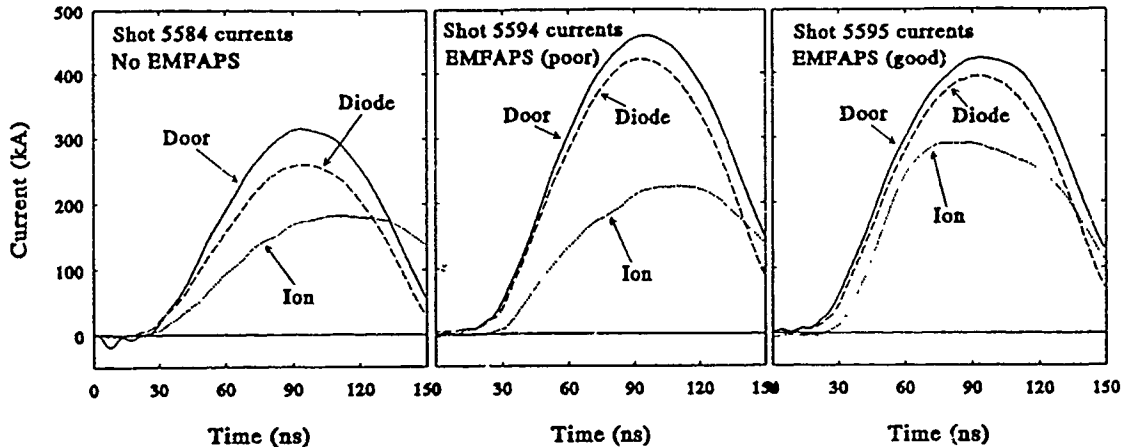
On shot 5610 the foil current reaches about 25 kA before it crowbars. On some shots it reached as high as 50 kA, so that premature flashover of the Delrin bushings may not be a problem

The right hand graph shows signals from individual B-dots, both outside and inside the outer cathode. Note the great asymmetry - one of the ion currents begins well before one of the diode currents. This asymmetry is likely associated with the poor switching and large foil current, and is hopefully not representative of a shot with lower POS conduction.

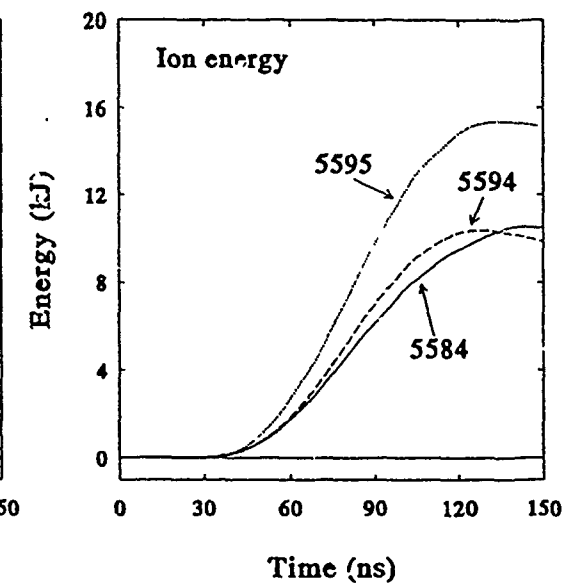
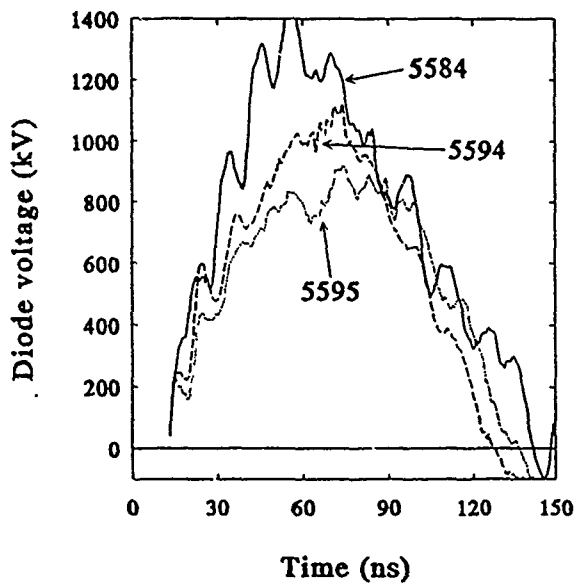
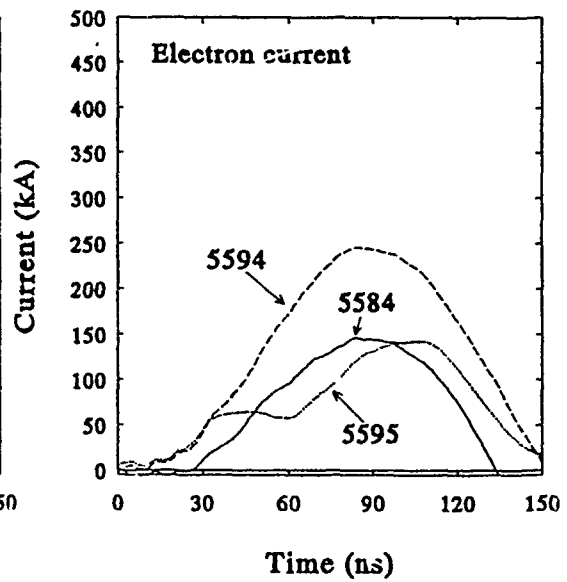
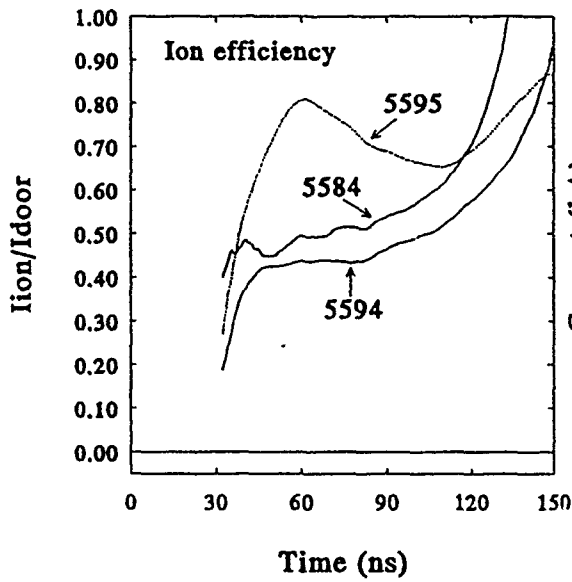
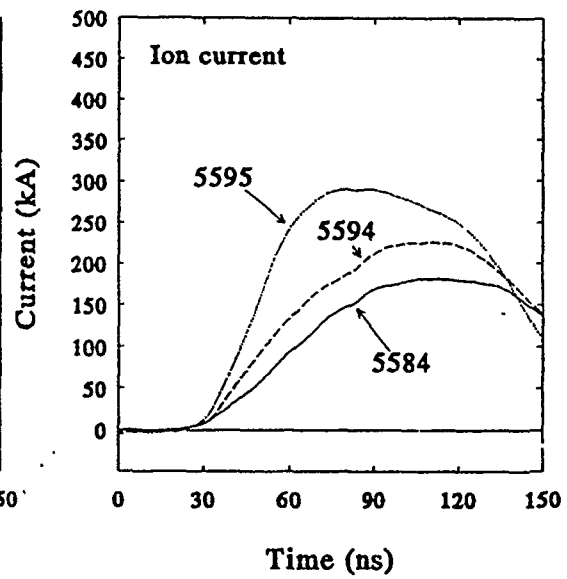
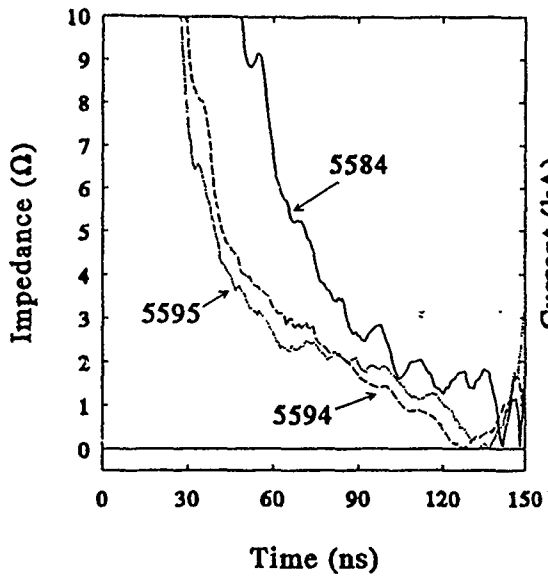


Three shots are compared in more detail in the following graphs. Shot 5584 is the last shot taken before the EMFAPS hardware was installed. The magnetic field contours shown previously were calculated for coil currents used on this shot. Shots 5594 and 5595 were taken during this run. These shots had the same switch configuration and delay time and show no measurable switch conduction (I believe that the discrepancy between the door and diode currents arises from problems with the diode monitor). On both shots a crowbarred foil current of about 5 kA is observed, indicating that some small current conduction through the switch did occur. These two shots differ in that a much higher ion current is observed on shot 5595. Since everything else was the same this difference is attributed to the foil conditions; evidently the foil current on shot 5594 flowed in such a way as to produce a poor anode source. Such a shot to shot variation could be expected for the relatively crude foil arrangement used in this run.

The calculated open circuit voltages for these three shots have the same timing, shape, and amplitude so that waveforms from each shot may be compared directly. Note the much smaller current on the non-EMFAPS shot.



Diode behavior on these three shots is compared further in the next six graphs. The impedance is defined here as the corrected voltage divided by the door current. The electron current is obtained by subtracting the ion current from the door current, and thus includes any vacuum electron flow from the switch. The efficiency is defined as the ion current divided by the door current. The most prominent feature of these graphs is the much faster initial impedance drop on the two EMFAPS shots. These two exhibit relatively similar impedance behavior although shot 5595 shows a slightly faster initial drop and significantly slower subsequent collapse. This similarity is interesting in view of the great difference in ion current between these two shots. While shot 5594 shows a higher ion current than shot 5584, the ion efficiency is actually reduced relative to the non-EMFAPS shot. One possibility is that the difference in impedance behavior between the EMFAPS and non-EMFAPS shots is not due to the improved ion source but is related rather to some subtle difference between the magnetic field contours of the two configurations. This could allow more electron loss on shot 5594. On shot 5595, the additional ion current could conceivably help to insulate the electron loss, maintaining the same total current, analogous to the critical current of a self-insulated diode. Alternatively, the similar impedance behavior on the EMFAPS shots could be fortuitous: On shot 5595 the rapid drop results from the ion current. On shot 5594 the total ion current is presumably reduced because of a poorly formed ion source, and John Greenly has pointed out that any azimuthal asymmetry in the ion current could also cause an increased electron loss.



In any event the results so far are encouraging. Even with the rather crude foil current contacts, on two shots (one other like shot 5595 occurred) we have obtained a much improved impedance behavior (which may not be due completely to the ion source), both in terms of the faster initial drop and slower subsequent collapse, and a much greater ion efficiency. The faster initial impedance drop results in a greatly reduced peak diode voltage. Since the peak ion current occurs earlier, the average ion voltage is not reduced and the ion beam power is increased, as shown in the last two graphs. The ion beam energy has been increased by 50 percent. The reduced peak insulator voltage should allow operation without flashover at an increased machine charge and thus allow higher ion voltages to be achieved. With a proper (i.e., vacuum deposited) foil arrangement, further improvement in the ion current onset and fraction may be expected.

The main thrust of work in the immediate future will be to develop a coating capability here. The deposition so far at both Cornell and KfK has been performed using thermal evaporation. While suitable for aluminum and copper, this technique is generally difficult for titanium and palladium (although Hans Bluhm says that they have had no difficulty). While we were first told that anything other than a thermal evaporation system would be too costly, I now see that a sputter deposition system should be quite affordable and will give much greater capability than a thermal evaporation system. I am in contact with the Sandia technician who will be assisting Mike Cuneo and should have the necessary equipment ordered soon. Also, a local contractor has offered both to coat some anodes in the interim and to help us (as a paid consultant!) get started.

Beyond this, as soon as ATHETA is available we should model the EMFAPS configuration with the goal of optimizing the field configuration. And, as stated before the transit time isolator should be improved to the point where we can monitor the anode currents in the diode.

Finally, Ron and Steve have suggested that we should consider trying to drive the foil with an external pulser. After discussing this idea we have some thoughts on how to do this and may get around to trying them. If successful, this approach would add a large measure of control to the EMFAPS technique.

PULSED POWER PHYSICS TECHNOTE 93-19

TITLE: INITIAL PULSER-DRIVEN EMFAPS RESULTS

Author: D. Hinshelwood, R. Fisher, and J. Neri

Date: November 18, 1993

Abstract: This note describes our work on pulser-driven EMFAPS to date. Anodes have been coated and vaporized, both on the bench and in an experimental run on Gamble II. The results of that run are presented in TN 93-18; this note describes our pulser and coating system status and presents the results of our bench studies. The foils have been diagnosed using electrical measurements, interferometry, spectroscopy, photography, and photometry. We see that the foils vaporize at actions lower than expected, which we attribute to semi-microscopic non-uniformities in the foil. This early vaporization may limit the proton inventory available to the diode. Planned improvements are discussed.

INTRODUCTION

This note is a companion to Jess's TN 93-18: together these describe the current status of our EMFAPS effort. This note focuses on the development of a pulser to drive the foil externally, and bench tests of exploding foils.

Our EMFAPS effort was first suggested by Mike Cuneo as a technique for obtaining a high-quality proton beam from the SABRE diode on Gamble II, in order to facilitate relevant ion beam transport experiments. Later, the goal was expanded to include the study of EMFAPS technology in general with the goal of fielding a source on SABRE. EMFAPS operation requires a current of tens of kA to be driven rapidly through a thin metallic foil on the anode surface. This current can be supplied by a partial diversion of the pulsed power to the diode, by an early diversion of the electron flow in the diode (limiter-EMFAPS), or by an external pulser. All of these approaches have advantages and disadvantages. With only a small fraction of the incoming pulsed power, a high current can be supplied quickly to the foil. In the successful implementations of EMFAPS to date, at Cornell and KfK, a POS in re-entrant geometry is used to divert the early portion of the machine current through the foil. This scheme was also used in our first EMFAPS experiments on Gamble II. The drawback to the POS approach is the difficulty in obtaining reproducible operation. This was particularly true in our first experiment, but even at KfK they are not completely satisfied with this approach and eventually plan to use an external pulser. We have also considered more passive means of diverting the early pulsed power, using inductive, resistive, or capacitive division, and have concluded that it would be very difficult to divert enough current quickly to drive the foil. Limiter-EMFAPS is particularly attractive on Gamble II because of the low generator impedance which gives us plenty of current, and because of the other beneficial effects that result from the use of a limiter. However, this approach may be less attractive on a higher-impedance machine such as SABRE, and serves to constrain diode design. The use of an external pulser offers several advantages: the foil current, and the delay between foil current and machine current, may be varied independently to allow better control of EMFAPS operation; the source may be studied and developed on the bench under the same driving conditions as on machine shots; and in principle the source may be easily transferred to other machines. Pulser-EMFAPS suffers from the difficulty of developing a pulser that can supply the required current, and possible difficulties in synchronizing the pulser to the machine. However, we believe that pulser-EMFAPS has the best long-term potential and have concentrated on this approach.

PULSER DESIGN

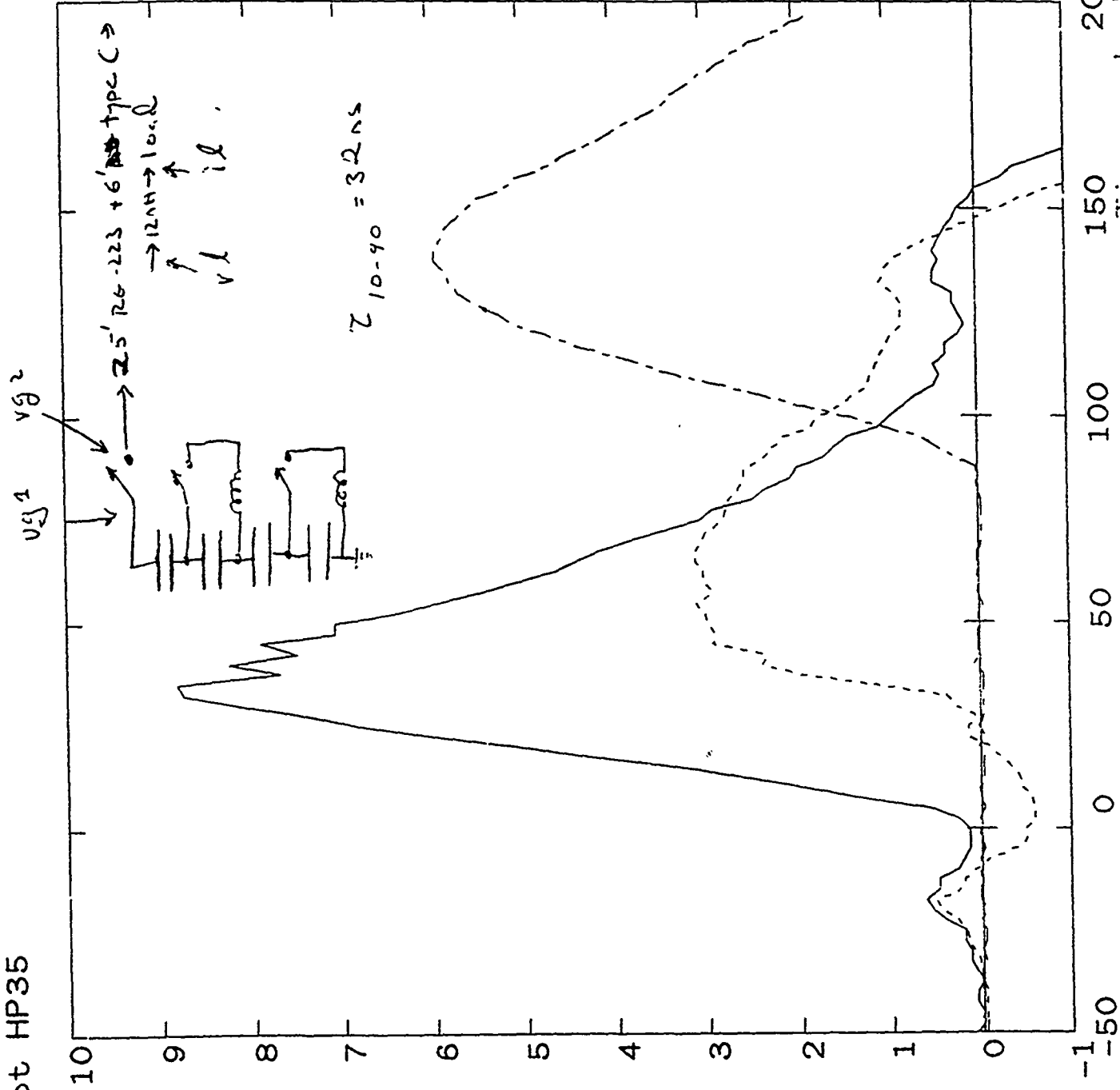
Pulser-EMFAPS can itself be pursued by two approaches. Either a very compact pulser, that can be located close to the foil, can be designed, or a low-impedance cable feed can be used to supply current from outside the machine. For now we have chosen the latter, because the pulser design is simplified (it need not be built for vacuum or water immersion), because access to the pulser (if needed during a run) will not be a problem, and because this scheme will be the easiest to adapt to SABRE.

Our pulser design is still evolving and the gory details will be presented in a later note. Initially, 15, type-C cables were used to provide a 2- Ω feed. However, we had troubles with cable breakdowns during the run and after some testing found that RG-223 has (surprisingly to us) superior breakdown strength. Now we use 30 RG-223 cables to give a 1.6- Ω feed (although we have not yet replaced a 9-ns section of the 2- Ω feed at the load). This is about the maximum number that will fit through the Gamble II transit-time isolator. Our present pulser comprises a four stage LC inversion network, with 8, 2.7-nF, 45 kV doorknob capacitors per stage. A sketch of the circuit, and the waveforms for a roughly 42-kV charge, are shown in Fig. 1. The pulser produces 30 kV across the 1.6- Ω load with a rise time of about 10 ns. This relatively low voltage is the result of energy losses in the spark gaps and an overmatch between the pulser and line impedances. More, lower-inductance capacitors have been ordered to correct the latter problem, and we plan to operate with a 50-kV voltage wave on the cables. Figure 2 compares the calculated forward-going voltage waves at the pulser and at the load. Substantial degradation of the pulse is seen to occur. Reflections at the 2- Ω section near the load probably account for part of this degradation. Most of the degradation, however, appears to be caused by dispersion in the cables. If so, this could be a problem for SABRE where the cables must be even longer. The greater diameter of the SABRE line, however, should allow the use of better (i.e., RG-214), or more, cables. If necessary, a peaking circuit could also be added near the load. For Gamble II, we could always locate the pulser close to the load if necessary. In summary, while this pulser arrangement has allowed a partially successful EMFAPS on Gamble II (see Jess's Technote), further improvement is required. With the new capacitors and a uniform cable feed, we should be able to obtain 50-60 kA through the foil with a rise time of 20-25 ns. If necessary, this rise time could be reduced with a peaking circuit.

Figure 3 shows the current and voltage measured at the load for a short circuit in the foil location. VCOR is the voltage across the foil itself, corrected for the 12 nH between the voltage divider and the foil. The finite corrected voltage calculated for this short circuit results from small errors in the current and voltage measurement and illustrates the uncertainty in determining the foil voltage.

The pulser must be triggered from Gamble II with a minimum of jitter, which we had anticipated to be a potential difficulty. In addition, with the LC circuit used, simultaneous triggering of the two stages is a concern. Gamble II consists of a Marx, intermediate store, water switch, PFL, oil switch, transformer section, and diode. The transformer input is a fast-rising pulse which has no jitter relative to the diode. However, it does not come early enough for the pulser to erect and for the pulser output to reach the diode. The use of a signal derived from the PFL dV/dt provides for a sufficient delay, but this signal has a ~50 ns rise time, and the oil switch jitter now comes into play. In practice, however, we found that the pulser could be triggered quite reliably. An air-gap peaking switch sharpened the trigger pulse, and the use of a 50 Ω trigger cable provided plenty of current so that both of the initial switches on the pulser (see the sketch in Fig. 1) closed together. The output switch was operated in a self-break mode. With this

Shot HP35



Li: V
 Max: 8.80E+04
 Min: 0.00E+00

Vg2: V
 Units: 1.00E+04
 Max: 3.08E+04
 Ts(ns): 0.00E+00

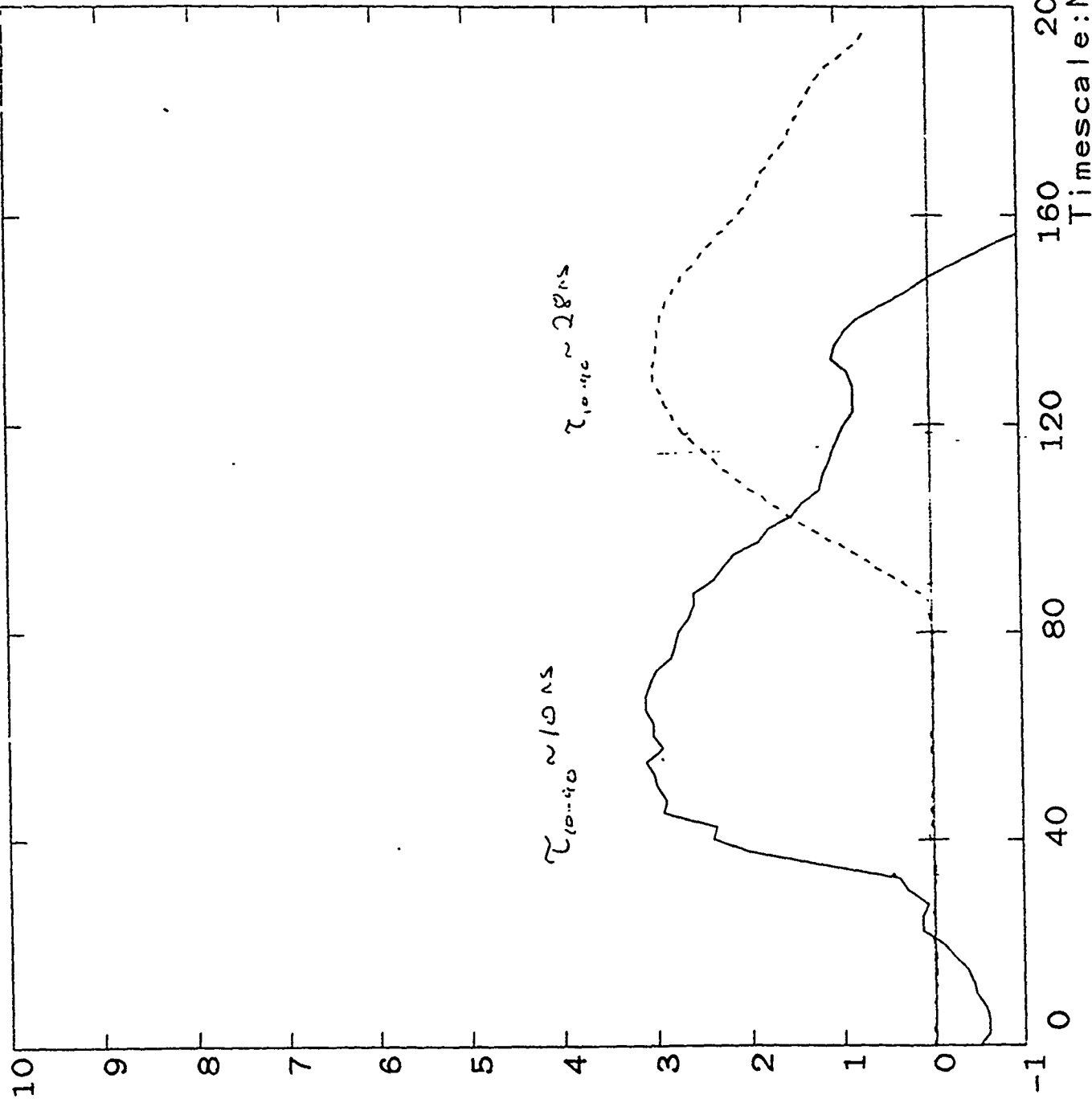
IL: A
 Units: 5.00E+03
 Max: 2.96E+04
 Ts(ns): 0.00E+00

1 - 9 F

FIG 2

AG2 V
Ur: 1.00E+04
Max: 3.08E+04
Ts(ns): 0.00E+00

VFOR V
Units: 1.00E+04
Max: 2.98E+04
Ts(ns): 1.00E+00



6h H1005

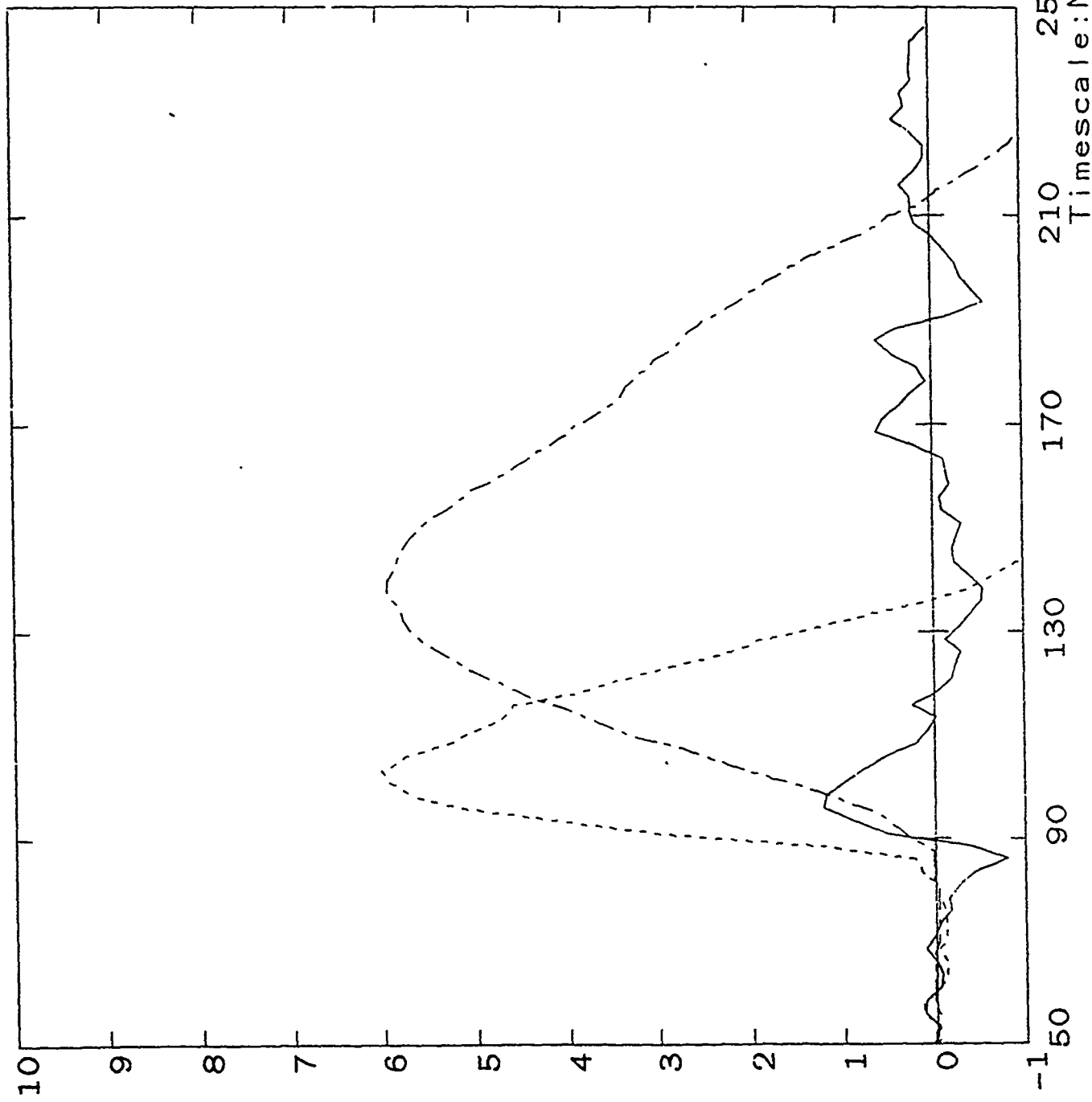
Shot HP35

+195

COR V
 U: 00E+03
 Max: 2.51E+03
 Ts(ns): 1.00E+00

IL V
 Units: 2.00E+03
 Max: 1.20E+04
 Ts(ns): 1.00E+00

A
 Units: 5.00E+03
 Max: 2.96E+04
 Ts(ns): 0.00E+00



arrangement, the combined jitter of the oil switch, two initial pulser switches, and pulser output switch was about 10 ns. If necessary, this could be reduced still further by triggering the pulser output switch from the transformer input signal.

COATING SYSTEM

Our EMFAPS anode design is shown in Figure 4. The anodes consist of two stainless rings held together by low-viscosity epoxy. First, copper contacts are coated at the boundaries of the anode emission area, which extends from about 4.5 to 5.5 cm in radius. Then, aluminum is coated over the emission area and the contacts. Mini-mak sputtering guns, supplied by US Gun, are used to apply the coating (Kerry Lampa from SNL guided us to this manufacturer and has provided invaluable advice in setting up our sputtering system.) The guns are arranged on the emission area circumference and the anode is rotated above them to insure azimuthally uniform deposition. A masking arrangement allows both coatings to be applied without opening up. We had some troubles at first in maintaining a steady discharge. These were resolved after conversations with the manufacturer by reducing the thickness of our targets. The coating system is now working quite well. At present, we coat with copper for 20 minutes at 100 W discharge power and then with aluminum for 4-20 minutes at 50 W. Most of the shots on Gamble II were taken with 4-minute anodes. We will soon calibrate the system using our thin-film monitor. The copper films are estimated to be about 2000 Å thick and the aluminum films estimated to be about 200 Å thick for 4-minute coatings.

Our technology for preparing the anodes for coating is still evolving. The anodes used in the Gamble II shots were prepared by sanding the epoxy and then waxing the surface lightly as was done at Cornell. As at Cornell, this method still results in some visible scratches in the emission surface region and discontinuities at the epoxy-metal boundaries. We are now trying different metal edge profiles, types of epoxy, casting arrangements, and finishing techniques with the goal of reducing these potential problems. Our anodes now are similar to those at Cornell in this regard, but as discussed later, the use of a (longer current rise time) external pulser may place more demands on the foil quality and thus the anode smoothness. One of the goals of our bench tests is to determine just how critical the foil and current-contact smoothness is.

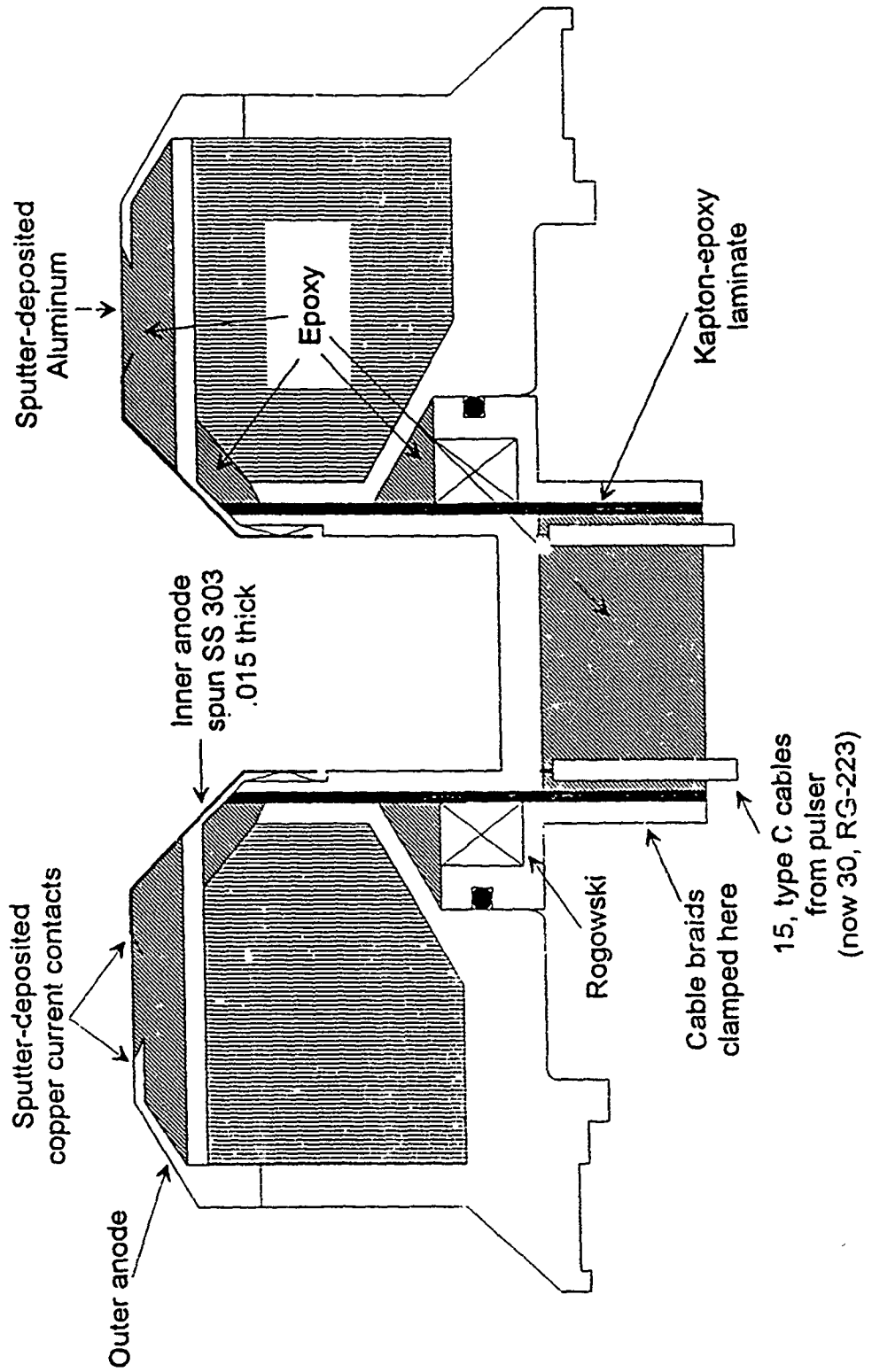
At present, we find that the growth rate of our films is strongly dependent on the anode epoxy surface smoothness, and that slight variations in finishing can lead to variations in the film thickness. This may be due to the relatively low deposition rates used, on the order of 50 Å/minute. We will be discussing this issue with deposition experts at NRL and SNL.

FOIL MEASUREMENTS

The foils were diagnosed using current and voltage measurements, open shutter photography, time-integrated spectroscopy, time resolved measurement of aluminum light emission, streak photography, and interferometry. A typical open shutter picture is shown

EMFAPS arrangement on Gamble II External pulser used to heat foil

1197



in Fig. 5. (The dark ring is the shadow of a quartz viewport.) A reasonably uniform luminosity is seen over the foil region. At the boundaries of this region, where the copper contacts begin, increased luminosity is observed as if arcs are occurring. At the further edges of the copper contacts, particularly at the inner diameter, further spotty light is observed. The degree of uniformity and of apparent arcing varied from shot to shot, in part because of differences in anode preparation, and this picture represents an "average" shot. The degree of arcing seen here is similar to that seen in published data from KfK, and may not be a problem. This shot was taken without an applied field; there is some indication that radial striations in the luminosity are observed when shots are taken with the field coils energized. John Greenly has seen a similar phenomenon at Cornell.

Time-integrated, spatially-resolved spectrograms show only two sets of strong spectral lines: the neutral aluminum resonance lines at 3944 and 3966 Å, which originate mainly from the anode emission area; and neutral copper lines at 3247 and 3274 Å, which originate from the current contacts. One line attributed to Al II was observed, but other lines expected from that species were not. Faint continuum and other line emission is also recorded, and no line emission from hydrogen is observed. The fact that copper light is observed indicates that some form of arcing is occurring at the current contacts since the copper contacts should be much too thick to vaporize under the action applied here.

Electrical characteristics for a shot with a 4-minute aluminum coating are shown in Figure 6. Comparison with Fig. 3 shows that the corrected voltage never rises greatly above the noise level, but the two sets of traces suggest a foil resistance that rises from near zero to a value of about 0.4Ω before dropping to a much lower value.

Optical and interferometric data for this shot is shown in Fig. 7. A large-diameter photodiode (PD) is used to record visible light emission without spatial or spectral resolution. When the photodiode was covered with an interference filter for the Al I line at 3961 Å no signal was observed, indicating that light emission is dominated by the continuum and lines that appear only faintly on the film. A photomultiplier (PMT) is used with a spectrometer to record the Al I line emission. In this case no measurable signal is observed when the spectrometer is detuned. These data are corrected for all optical path lengths and for the photomultiplier tube intrinsic delay. Both broad-band and neutral aluminum light are observed to begin at about the moment of foil voltage collapse.

The electron density is measured using our standard, 40-MHz heterodyne-phase-detection interferometer. The ~3-mm diam beam was aligned to graze the anode. The short (2-cm) path length here leads to a relatively large noise-equivalent average density, and on this shot the electron density barely exceeds that value, rising to $1 \times 10^{15} \text{ cm}^{-3}$ well after the pulse.

Figures 8-10 compare total light, Al I emission, and the calculated electron density for shots using anodes with aluminum coating times of 4, 10, 16, and 30 minutes, giving approximate foil thicknesses of 200, 400, 600, and over 1000 Å. In comparison with the 4-minute anode, the 10-minute anode shows a later onset of both total and aluminum light

FIG 5



SHOW HP49

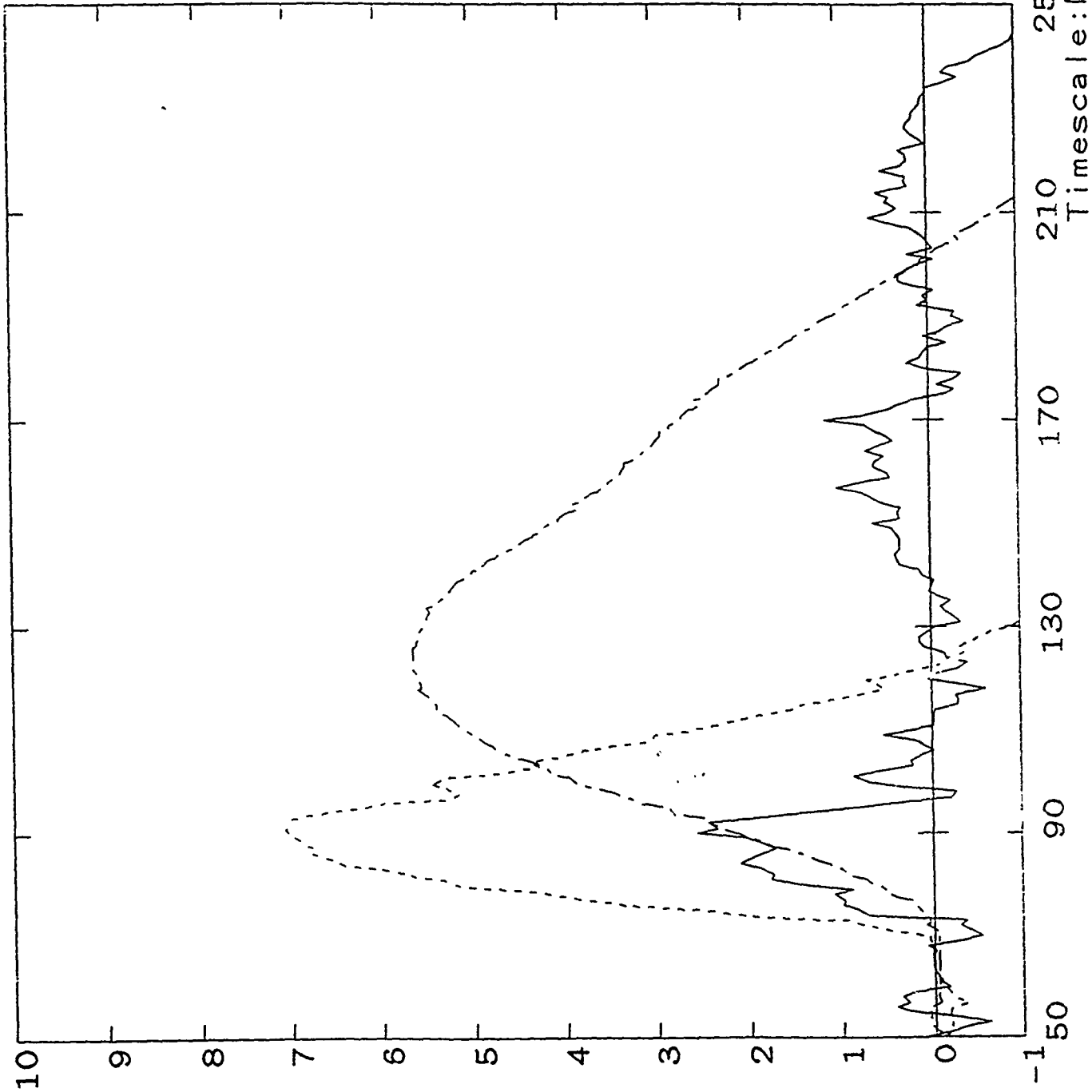
FIR 8

VCOR Volts

Units: 1.00E+03
Max: 5.09E+03
Ts(ns): -8.00E+00

VL Volts
Units: ? 00E+03
Max: 1.41E+04
Ts(ns): -8.00E+00

IL Amps
Units: 5.00E+03
Max: 2.82E+04
Ts(ns): -8.00E+00



Shot HP49

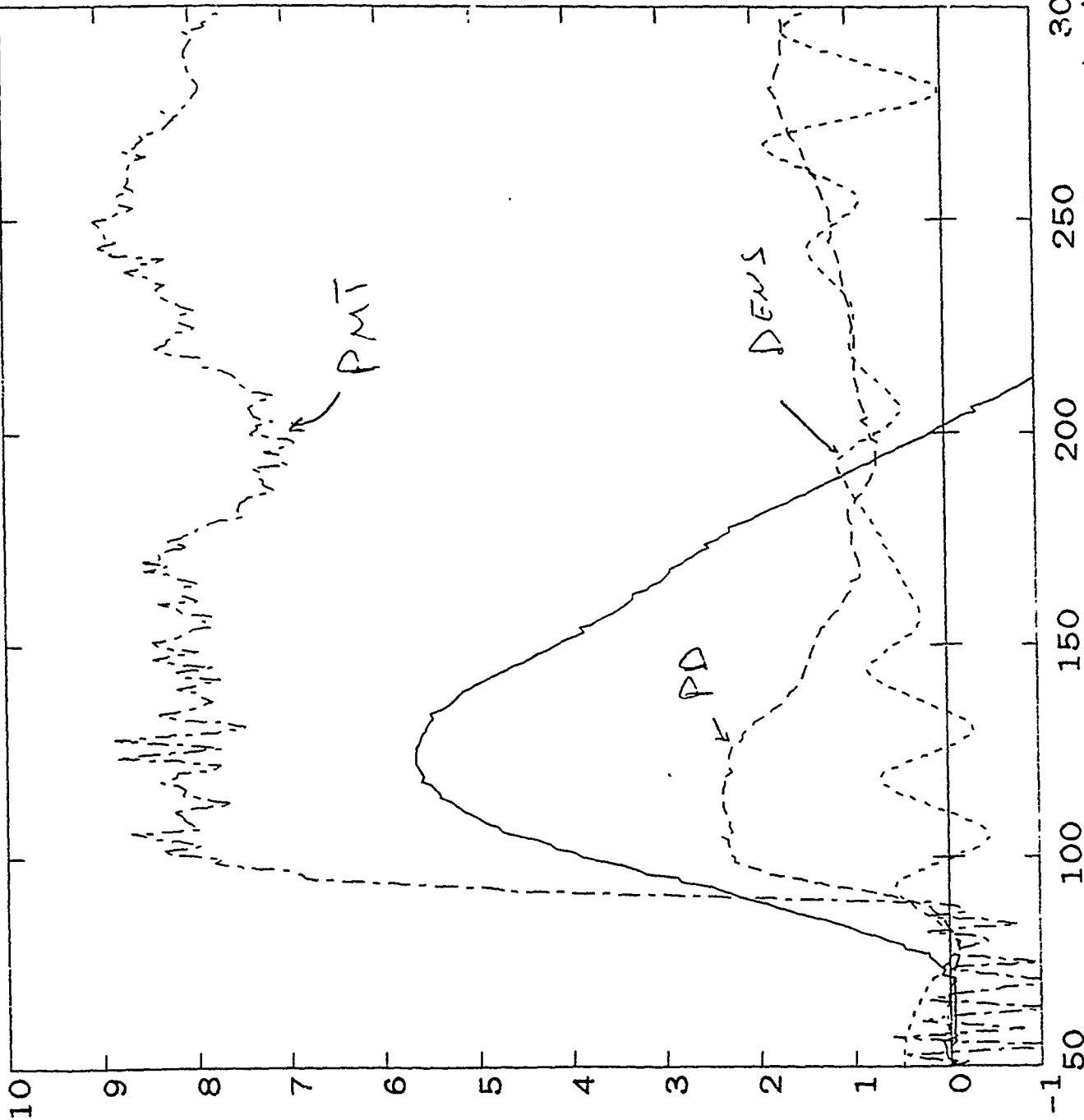
114

IL Amps
Unit: 5.00E+03
Max: 2.82E+04
Ts(ns): -8.00E+00

DENS V
Units: 1.00E+15
Max: 1.87E+15
Ts(ns): -6.00E+00

PMT Volts
Units: 1.00E-01
Max: 9.03E-01
Ts(ns): -3.00E+01

PD Volts
Units: 5.00E+00
Max: 1.19E+01
Ts(ns): -2.00E+00

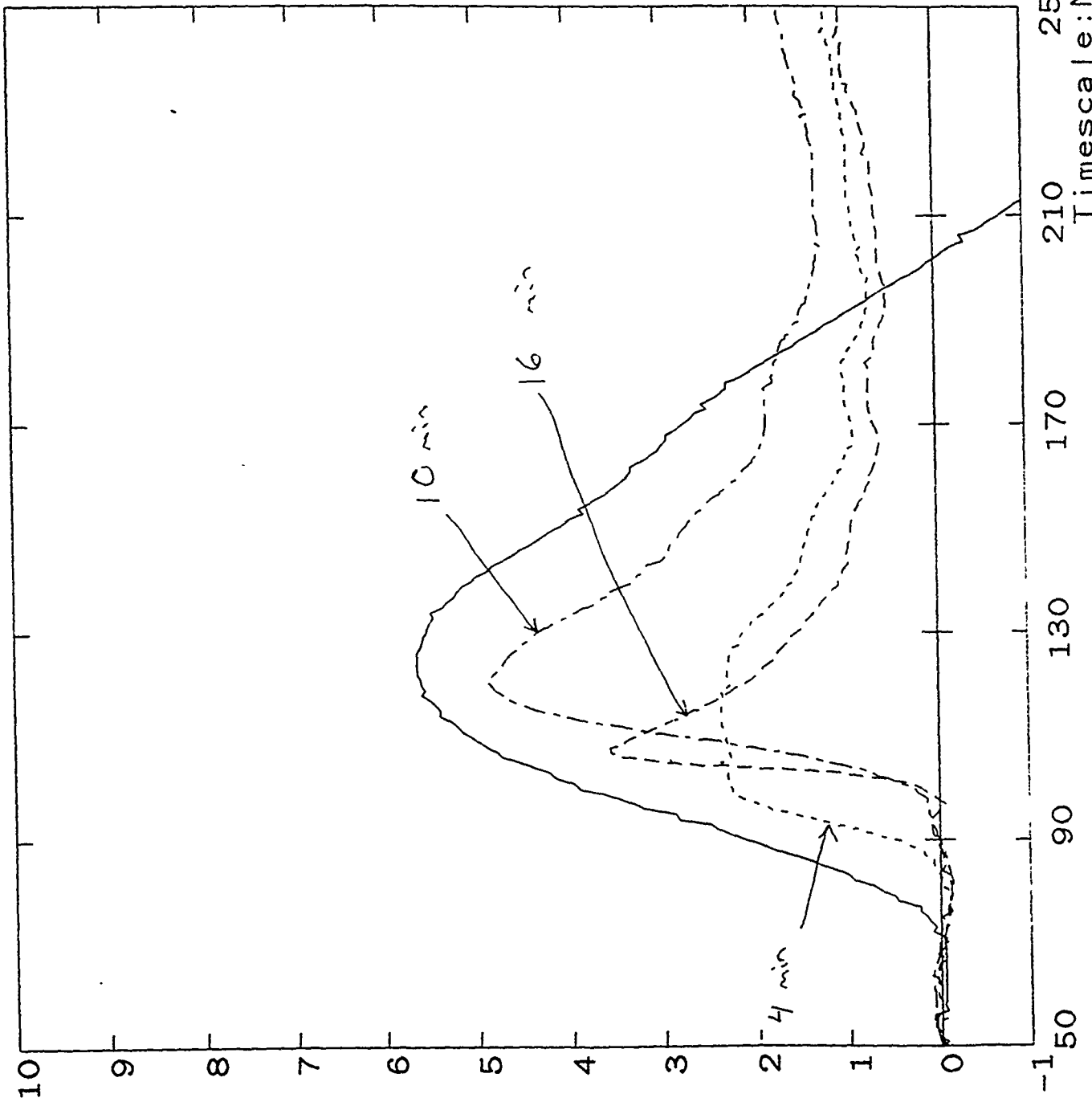


IL Amps
 Uf : 00E+03
 Max: 2.82E+04
 Ts : -8.00E+00

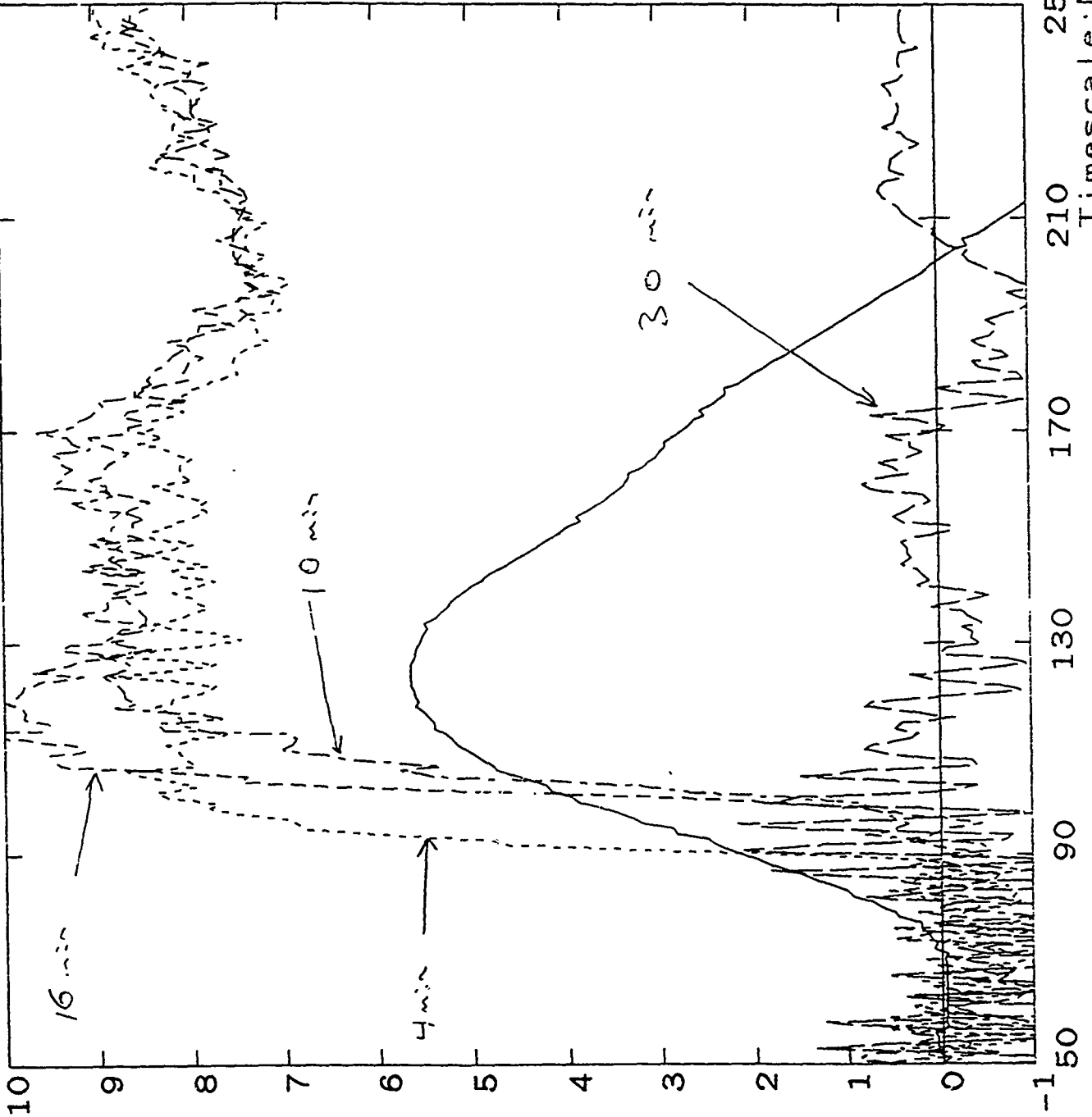
FD Volts
 Units: 5.00E+00
 Max: 1.19E+01
 Ts(ns): -2.00E+00

PDHP50 Volts
 Units: 5.00E+00
 Max: 2.45E+01
 Ts(ns): -2.00E+00

PDHP51 Volts
 Units: 5.00E+00
 Max: 1.79E+01
 Ts(ns): -2.00E+00



Shot HP49



IL
 Units: 00E+03
 Max: 2.82E+04
 Ts(ns): -8.00E+00

FMT
 Units: 1.00E-01
 Max: 9.03E-01
 Ts(ns): -3.00E+01

T/G 1

FMTHF50 Volts
 Units: 1.00E-01
 Max: 9.63E-01
 Ts(ns): -3.00E+01

PMTHP51 Volts
 Units: 1.00E-01
 Max: 1.04E+00
 Ts(ns): -3.00E+01

PMTHP54 Volts
 Units: 1.00E-01
 Max: 3.22E-01
 Ts(ns): -3.00E+01

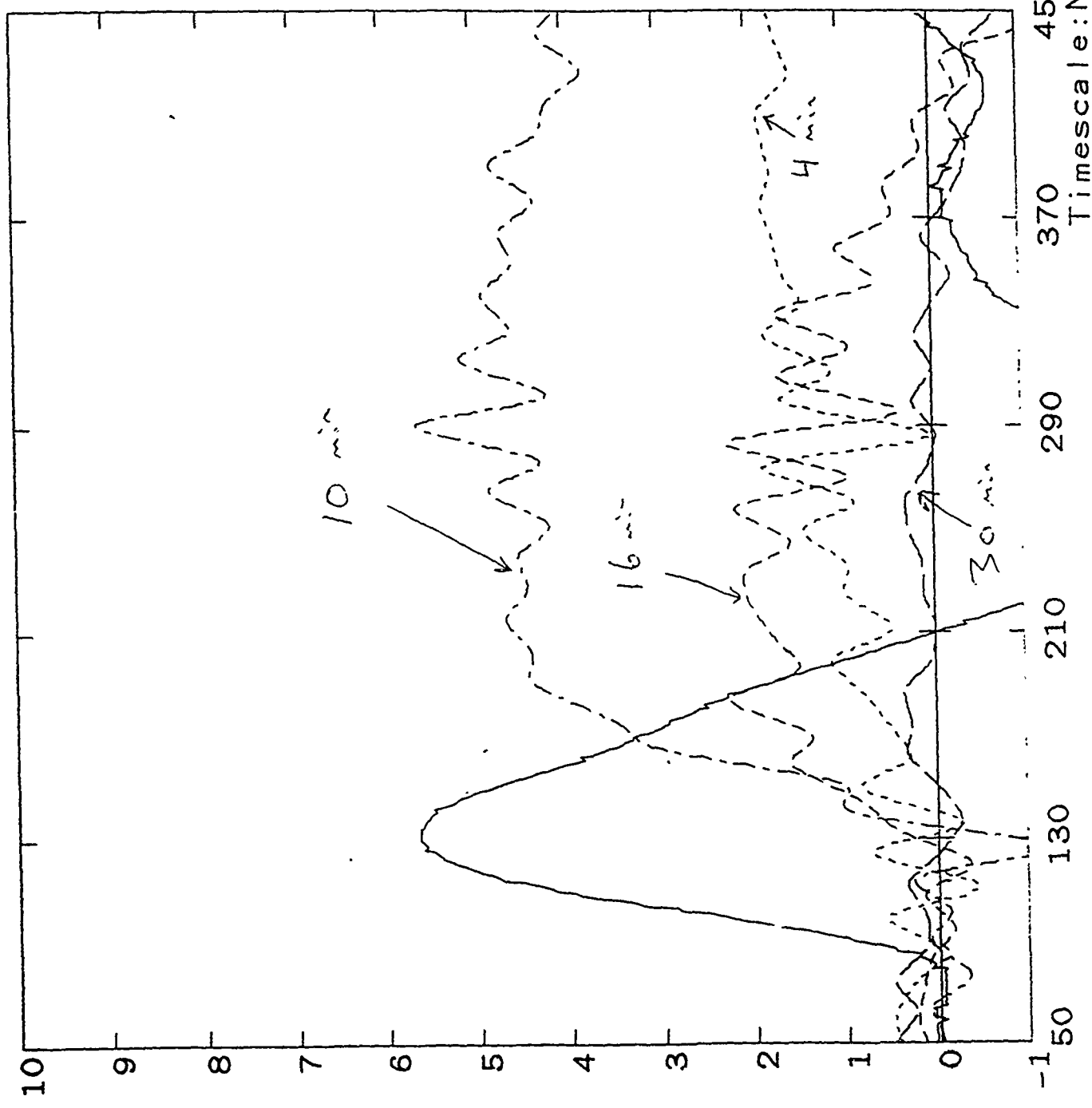
Units: 5.00E+03 Amps
 Max: 2.82E+04
 Ts(ns): 0.00E+00

Units: 1.00E+15 V
 Max: 1.87E+15
 Ts(ns): 0.00E+00

Units: 1.00E+15 denshp50 V
 Max: 5.62E+15
 Ts(ns): 0.00E+00

Units: 1.00E+15 denshp51 V
 Max: 4.05E+15
 Ts(ns): 0.00E+00

Units: 1.00E+15 denshp54 V
 Max: 4.40E+15
 Ts(ns): 0.00E+00



emission and a roughly four-fold higher electron density. With the higher density the S/N ratio improves and the density can be seen to start near the time of peak current, about 30 ns after the onset of light emission. The later apparent vaporization time and higher density seen here would be expected for the thicker coating. With the 16 minute anode, no further increase in time of light emission onset is observed and the electron density is actually lower, relative to the 10 minute anode. For the 30 minute anode, neither aluminum light nor measurable electron density is ever observed. The corrected voltages for these shots are consistent with the light emission traces: for the 10 and 16 minute anodes the corrected voltage drops at the time emission begins, and no noticeable corrected voltage is observed for the 30 minute anode.

INTERPRETATION

Tucker and Toth present resistivity and phase transition occurrences for various metals as functions of specific action ($A^2\text{-s/cm}^4$) and specific energy density in a SNL report (SAND-75-0041). The former is a more useful quantity for comparison with the present experimental results because of the uncertainty in the foil voltage. For aluminum, vaporization begins at a specific action of $4.9 \times 10^8 A^2\text{-s/cm}^4$ and a resistivity of $42 \mu\Omega\text{-cm}$. By the end of vaporization, or burst, these values become 6.6×10^8 and 390, respectively. The calculated actions and resistances corresponding to the beginning of vaporization are compared with those measured at the time of light emission and voltage collapse for the four shots above in the following table (neither occurred on HP54 so the action is that at the end of the current pulse):

Shot	Thickness (Å)	Pred action ($A^2\text{-s}$)	Meas action ($A^2\text{-s}$)	Pred res (Ω)	Meas res (Ω)
HP49	200 +/-100	0.5-4.5	0.2-0.8	.5-1.4	0.2-0.6
HP50	400 +/-150	2.8-14	1-3	.25-.6	0.1-0.4
HP51	600 +/-200	7.2-29	1-3	.17-.35	0.1-0.4
HP54	1000 +/-200	29-65	>40		

At least on two shots, aluminum is vaporized much sooner than predicted. The foil resistance is also lower than expected, especially since the predicted values correspond to the beginning of vaporization; those predicted for burst are almost ten times greater. A likely explanation for the early vaporization is that the foils are not completely uniform. Polishing the anodes prior to waxing leaves a very fine pattern of azimuthal scratches resembling a phonograph record. These persist in the coated films as areas of variable transparency, indicating a non-uniform film thickness, i.e., a radial scan of the film thickness would have a sawtooth profile. The thinner regions would then vaporize at an action much lower than the value predicted for the average foil thickness, and yet these regions may contribute little to the total resistance if they constitute a small fraction of the foil radial extent. The early vaporization may be exacerbated in our experiments because of the relatively slow current rise time.

The collapse of the foil voltage on these shots occurs at values of 5-10 kV, which seems low for a rapid gas breakdown to occur. One possibility is that arcs at the current contacts produce electrons to initiate this breakdown. To examine the breakdown evolution, a few shots have been taken using a streak camera, with the slit aligned in the radial direction. The resolution of this measurement is limited by the low light levels involved, but indications are that light is observed from the foil emission region before the contacts light up. This indicates that arcs at the contacts are not the cause. Another possibility is that if small regions of the foil vaporize first, breakdown may be added by the semi-microscopic field enhancement that would result.

The above data point to two possible factors that may have limited the diode performance on the past Gamble II run: the vaporized foils may not have supplied enough protons, resulting in a source-limited ion current; and, the relatively long delays between foil breakdown and the diode pulse may have allowed plasma and/or neutrals to move out into the diode, possibly causing parallel load losses. Both of these problems should be corrected if the foils could hold off until past the peak of the pulser current pulse, since that would increase the plasma (and thus proton) inventory, and allow a shorter foil-current/diode-current delay to be used. Premature foil vaporization should be impeded by either a faster current rise or a greater foil uniformity, and both of these approaches will be pursued.

FUTURE WORK

Work at present is proceeding in parallel in three areas: (1) A limiter-EMFAPS run will begin on Gamble II next week. In addition to furthering our study of EMFAPS physics, this will allow our programs that require an MID source to proceed. (2) We will continue to investigate the coating process and to study foil explosions on the bench. (3) An improved pulser will be constructed. Progress in these areas should allow us to field a successful pulser-driven EMFAPS source on Gamble II.

SECTION THREE

INTENSE BEAM TRANSPORT

During the contract period, JAYCOR personnel were involved in all aspects of the NRL light-ion beam transport program. This program involved both theoretical and experimental investigation of beam transport in support of the Sandia National Laboratory (SNL)/Department of Energy (DOE) Laboratory Microfusion Facility (LMF). Experimental and theoretical investigations of many transport issues pertinent to the LMF were carried out during the contract period. These investigations included z-discharge transport of light-ion beams, ballistic transport/solenoidal focusing of light-ion beams, wire-guided transport of light-ion beams, time-of-flight (TOF) bunching and focus-sweep effects for light-ion transport, and LMF level, wall-stabilized, discharge channel development. In addition, experiments of conductivity evolution in beam/neutral gas systems were performed. Finally, a study of ion beam-induced radioactivity was performed in support of future ion beam experiments at SNL.

At the direction of the COTR, ion-beam related research was expanded to include the use of ion beams to simulate nuclear weapon effects (NWES), and the use of ion beams to evaporate material for thin-film production.

3.1 Ballistic Transport of Intense Light-Ion Beams

The LMF will employ 10-30 beam generators packed around a centrally located inertial-confinement-fusion target of 1 cm radius. Transport of intense light-ion beams over approximately 4 m from the generator diodes to the target is required for standoff from the explosion, time-of-flight bunching of the beams, and packing of the pulse power generators. The beam produced by applied-B diode designs is annular and is extracted parallel to the axis by appropriate anode shaping. The baseline transport scheme in the Sandia LMF design uses ballistic propagation of a 12-15 cm radius beam to the target chamber wall (of approximately 1.5 m radius), where a solenoidal lens acts to focus the beam on the target. This scheme, referred to as ballistic transport with solenoidal focusing (BTSF), has been analyzed using realistic constraints on diode/generator performance, source microdivergence, and chromatic effects.

Both ideal "thin-lens" approximations and detailed magnetic field maps have been used to evaluate the BTSF scheme for suitability in the LMF design. Energy transport efficiency, the ratio of deliverable energy to total system energy, was determined over a large parameter range appropriate for an LMF. Results indicated that transport efficiencies of 75-100 % are achievable for BTSF in parameter ranges of interest.

3.2 Z-discharge Transport of Intense Light-Ion Beams

Another transport scheme under evaluation for the LMF is z-discharge transport (ZDT). This scheme employs a transport channel of radius approximately equal to the target radius to confine and transport the beam close to the target. A numeric and analytic investigation was carried out to determine transport efficiency under LMF constrained

parameters. In addition, transport in wall-stabilized channels was evaluated experimentally and theoretically with intense proton beams generated by the NRL GAMBLE II accelerator

LMF designs employing z-discharge transport involve geometric focus of an annular beam of 12-15 cm radius over 1.5 m onto the entrance of either a free-standing or wall-stabilized z-discharge channel. Confined by the channel's azimuthal magnetic field profile, beam ions are transported to the end of the channel (approximately 2.5 m) which is placed near the target. Packing of the N discharge channels around the centrally located target determine a final ballistic transport distance from the channel exit to the target. In this standoff region of a few centimeters, the N beams combine to symmetrically drive the target implosion. Similar to the work carried out for BTSF (see Sec. 3.1), a systematic study of the energy transport efficiency under a variety of parameters appropriate for a light-ion LMF was carried out. This study concluded that energy transport efficiencies in the range of 75-100% are obtainable for parameters of interest.

Experiments carried out on the NRL GAMBLE II accelerator employed a wall-stabilized z-discharge transport channel at distances between 20-30 cm from the ion diode. In these experiments, 90% energy transport efficiencies were observed with 2.5 cm diameter, 1.2 m long discharges. Inside the discharge channel, 2 Torr of air was used. Three-dimensional orbits code calculations were performed to analyze shadowbox witness plate images and energy transport efficiencies. These calculations included classical stopping in the discharge gas, variable magnetic field models within the discharge, and actual diode waveforms for voltage and net ion current.

3.3 Effects of Time-of-Flight-Bunching (TOF) on Transport Systems for LMF

Current light-ion LMF designs call for power compression by TOF bunching. TOF bunching is accomplished through suitable ramping of the voltage at the diode. This voltage ramp results in time-dependent focusing of the beam in the diode, which in turn moves the focal spot of the beam in time. Under conditions appropriate for LMF, three transport schemes were examined: BTSF, ZDT, and wire-guided transport (WGT). In this study, energy transport efficiencies were calculated as functions of various system parameters for each transport scheme. The analysis takes into account target requirements and realistic constraints on diode source brightness, packing, beam transport and TOF bunching through voltage ramping. Results indicate that energy transport efficiencies >50% can be obtained for all three transport schemes for parameters of interest.

3.4 Wall-Stabilized Discharge Channel Development

The wall-stabilized z-discharge channel described in Sec. 3.2 was successfully scaled to light-ion LMF design parameters. An investigation of the electrical behavior of discharges with various gas species, pressures, lengths, and currents was performed. From these experiments, the required dielectric strength of the discharge channel wall was determined. A low-mass, low-Z wall construction with sufficient dielectric strength was demonstrated at LMF level parameters. The discharge internal dynamics were studied using interferometry, framing photography, spectroscopy, and magnetic-field

measurements. Measurements showed that the discharge initiates by breakdown along the channel wall, even when the gas is pre-ionized. The discharge was observed to consist of an MHD stable, imploding, thick annulus, whose inner and outer radii both decrease in time. This annular profile contributed to subsequent understanding of proton-beam experiments with z-discharges on GAMBLE II. A zero-dimensional model was developed to model the discharge behavior. This model reproduces approximately both the discharge dynamics and the electrical characteristics over a range of parameters. Calculations indicate that the beam ions will lose only 10% of their energy during transport through the discharge at LMF level parameters. The results of this work confirm that wall-stabilized z-discharge transport is a viable, backup approach to transport in a light-ion LMF.

3.5 Current Neutralization of Intense Ion Beams

Light-ion LMF designs require the stable transport of intense ion beams in background gas densities of approximately 1 Torr. JAYCOR personnel were involved with all aspects of first experiments into ion beam transport in this intermediate pressure regime. LMF designs suggest 1 Torr of helium as the background gas to allow sufficient conductivity grow for stable transport and minimization of collisional energy loss and scattering of the beam. The NRL GAMBLE II accelerator was used to produce 1 MeV proton beams to study ion beam induced gas ionization and subsequent plasma conductivity growth. The proton beams were apertured down to approximately 1kA through a collimator and injected into a transport region. Here, the species and density were systematically varied over a limited parameter range. Net current fractions of 2-8% were measured outside the beam channel. Ionization was observed to be confined mainly to the beam channel with ionization fractions of a few percent. Detailed computational analysis was performed using the IPROP and DYNAPROP simulation codes. This analysis suggested that net currents are 3-5 times larger inside the beam channel than measured net currents and that fast electrons and their secondaries carry a significant fraction of the return current in a halo outside the beam.

3.6 Light-Ion Beam Induced Nuclear Activation

Inherent in the operation of high-power ion diodes is the possible activation of surrounding and support materials in the vicinity of the diode and beam. To examine this issue for the SNL pulsed power devices PBFA II and SABRE, JAYCOR personnel were involved in a survey of radioactivity's produced by these intense beams striking common accelerator materials such as carbon, brass, steel, titanium, and aluminum alloys. Studies were conducted for reactions induced by lithium, proton, and deuteron beams up to 15 MeV for lithium and up to 10 MeV for protons and deuterons. Radioactivity producing reactions were tabulated and data on yield and half life for these reactions was taken from the published literature, when available. For incident lithium ions, the yields for the identified reactions decrease as the atomic number of the target is increased, and these yields increase rapidly with incident lithium energy up to the Coulomb barrier. For incident protons, residual activities with hour-to-day half-lives were observed and yields for these reactions increase rapidly with increasing proton energy. For deuteron beams,

discrepancies for the same reaction cross section measured by different researches was apparent. Deuteron-induced reactions tended to have lower thresholds, and yields increased with increasing incident particle energy.

3.7 Soft X-ray Simulation With Light Ion Beams

JAYCOR personnel were involved with the application of intense ion beams for the simulation of soft x-rays for material-response studies. Proton beams produced by the NRL GAMBLE II accelerator have been demonstrated to simulate the soft x-ray mechanical deposition response in materials. Proton fluences of 50 cal/cm² over target areas of 100 square cm have been measured with a spatial uniformity of ± 10 percent. Ion-orbit codes developed for light-ion transport have been modified to predict fluences for individual GAMBLE II shots utilizing diodes models described in Sec. 2 and were benchmarked against other orbit codes developed during the course of this work. The applicability of the low-debris "backless" diode, described in Sec. 2, was demonstrated in this study.

Also during the course of this and other work with MeV proton beams, JAYCOR personnel were involved with the development of proton-beam fluence diagnostics including carbon-activation arrays and x-ray pinhole imaging of fluence distributions. These diagnostics provided measurements over 100 square cm areas with uncertainties of 20 percent (carbon activation) and spatial resolutions of 3-4 mm (Al K-line x-rays imaged by pinholes).

3.8 Pulsed Ion Beam Evaporation for Thin-Film Deposition

JAYCOR personnel have played an active role in developing new industrial applications for intense ion beam technology. Ion beams have the ability to deposit energy quickly in a highly localized region and so have great promise for materials modification. Pulsed ion beam evaporation is one technique presently under investigation at NRL. The ion beam is used to vaporize and ablate material from a target, and this material is allowed to deposit on a nearby substrate. This technique is a direct analog to the well-established pulsed laser deposition, but has significant potential advantages in that ion beams can be generated much more efficiently than laser beams. In initial experiments, films of several materials have been deposited and characterized, and the expanding plumes of material from the targets have been diagnosed.

3.9 List of Papers

- 3.9.1 "Ballistic transport and solenoidal focusing of intense ion beams for inertial confinement fusion," P.F. Ottinger, D.V. Rose, J.M. Neri, and C.L. Olson, *J. Appl. Phys.* **72**, 395 (1992).
- 3.9.2 "Z-discharge transport of intense ion beams for inertial confinement fusion," P.F. Ottinger, D.V. Rose, D. Mosher, and J.M. Neri, *J. Appl. Phys.* **70**, 5292 (1991).

- 3.9.3 "Transport of Intense Light Ion Beams," P.F. Ottinger, P.J. Goodrich, D.D. Hinshelwood, J.M. Neri, D.V. Rose, S.J. Stephanakis, and F.C. Young, *Proceedings of the IEEE* **80**, 1010 (1992).
- 3.9.4 "Intense Ion-Beam-Transport Experiments Using a Z-Discharge Plasma Channel," J.M. Neri, P.F. Ottinger, D.V. Rose, P.J. Goodrich, D.D. Hinshelwood, D. Mosher, S.J. Stephanakis, and F.C. Young, *Phys. Fluids* **B5**, 176 (1993).
- 3.9.5 "Orbit Calculations For Z-discharge Transport Experiments on Gamble II," D.V. Rose, J.M. Neri, and P.F. Ottinger, *Pulsed Power Physics Technote* 91-07 (1991).
- 3.9.6 "Transport and Focusing Considerations For Light Ion ICF Systems," P.F. Ottinger, D. Mosher, J.M. Neri, D.V. Rose, and C.L. Olson, in the *Proceedings of the Ninth International Conference on High-Power Particle Beams* (Washington, DC, May 1992), p. 60.
- 3.9.7 "Ion Transport For LMF," D. Mosher, D.D. Hinshelwood, J.M. Neri, P.F. Ottinger, J.J. Watrous, C.L. Olson, and T.A. Mehlhorn, in the *Proceedings of the 8th International Conference on High-Power Particle Beams* (Novosibirsk, USSR, July, 1990), p. 26.
- 3.9.8 "Development of Wall-Stabilized Z-Discharges for Intense Ion-Beam Transport in Inertial Confinement Fusion Facilities," D.D. Hinshelwood, *J. Appl. Phys.* **72**, 4581 (1992).
- 3.9.9 "Current Neutralization of Intense MeV Proton Beams Transported in Low-Pressure Gas," F.C. Young, D.D. Hinshelwood, R.F. Hubbard, M. Lampe, J.M. Neri, C.L. Olson, P.F. Ottinger, D.V. Rose, S.P. Slinker, S.J. Stephanakis, and D.R. Welch, *Phys. Rev. Lett.* **70**, 2573 (1993).
- 3.9.10 "Survey of Radioactivities Induced by Lithium Ions," F.C. Young and D.V. Rose, *NRL Memorandum Report* No. 6974 (1992).
- 3.9.11 "Survey of Nuclear Activation's for Intense Proton and Deuteron Beams," F.C. Young and D.V. Rose, *NRL Memorandum Report* No. 7155 (1992).
- 3.9.12 "Light Ion Beams for Material Response Simulation," D. Mosher, S.J. Stephanakis, F.C. Young, G. Cooperstein, R.J. Comisso, P.J. Goodrich, D.D. Hinshelwood, J.M. Neri, B.V. Weber, S.H. Richter, L.M. Lee, and D.V. Keller, in the *Proceedings of the 1990 DNA Advanced Pulsed Power Conference, DASIAC TR-90-006* (Albuquerque, NM, 31 July - 3 August 1990), p.2-24.
- 3.9.13 "High-Fluence Large-Area MeV Proton-Beam diagnostics," F.C. Young, S.J. Stephanakis, V.E. Scherrer, and D. Mosher, *Rev. Sci. Instrum.* **61**, 3122 (1990).

3.9.14 "GAMBLE II Ion Beam Fluence Calculations," D.V. Rose, P.F. Ottinger, D. Mosher, S.J. Stephanakis, and F.C. Young, Pulsed Power Physics Technote 92-16 (1992).

Ballistic transport and solenoidal focusing of intense ion beams for inertial confinement fusion

P. F. Ottinger, D. V. Rose,^{a)} and J. M. Neri
Plasma Physics Division, Naval Research Laboratory, Washington, DC 20375-5000

C. L. Olson
Sandia National Laboratories, Albuquerque, New Mexico 87185

(Received 16 December 1991; accepted for publication 31 March 1992)

Light-ion inertial confinement fusion requires beam transport over distances of a few meters for isolation of the diode hardware from the target explosion and for power compression by time-of-flight bunching. This paper evaluates ballistic transport of light-ion beams focused by a solenoidal lens. The ion beam is produced by an annular magnetically insulated diode and is extracted parallel to the axis by appropriate shaping of the anode surface. The beam propagates from the diode to the solenoidal lens in a field-free drift region. The lens alters the ion trajectories such that the beam ballistically focuses onto a target while propagating in a second field-free region between the lens and the target. Ion orbits are studied to determine the transport efficiency η_t (i.e., the fraction of the beam emitted from the diode which hits the target) under various conditions relevant to light-ion inertial confinement fusion. Analytic results are given for a sharp boundary, finite thickness solenoidal lens configuration, and numerical results are presented for a more realistic lens configuration. From the analytic results, it is found that η_t can be in the range of 75%–100% for parameter values that appear to be achievable. Numerical results show that using a more realistic magnetic-field profile for the lens yields similar values of η_t for small radius diodes but significantly reduced values of η_t for large radius diodes. This reduction results from the radial gradient in the focusing field at larger radius.

I. INTRODUCTION

The Laboratory Microfusion Facility (LMF) has been proposed for the study of high-gain, high-yield inertial confinement fusion (ICF) targets using either lasers or ion beams as a driver. A multimodular light-ion approach, based on Hermes-III accelerator technology,¹ is presently under investigation.^{1,2} Using light-ion beams for the LMF driver will require transport of intense ion beams over distances of a few meters in order to isolate the ion diode hardware from the target explosion and to provide sufficient propagation distance for power compression by time-of-flight (TOF) bunching. Several different transport schemes are being considered for a light-ion LMF.^{1,3,4} The baseline approach involves an achromatic magnetic lens system and ballistic transport.⁵⁻⁷ The achromatic lens system consists of the ion diode itself, through ion orbit bending in the self-magnetic fields in the vacuum region of the diode, and a solenoidal lens. Advantages of this system include its engineering simplicity and the absence of hardware requirements in the target chamber. Alternative approaches^{3,4,7,8} include a wire-guided transport system, a low-mass wall-stabilized z-discharge transport channel, and a laser-initiated free-standing z-discharge transport channel. Advantages of these alternative approaches are that they provide positive beam guidance until the beam is very near the target, and that they allow larger radius target chambers, an important consideration for ICF reactor concepts.^{9,10} Wire-guided transport³ and z-discharge transport⁴ were evaluated for LMF previously. This paper pre-

sents a similar evaluation of ballistic transport with solenoidal lens focusing for LMF.

A schematic of one module of an LMF system using solenoidal lens focusing and ballistic transport is shown in Fig. 1. An extraction applied- B ion diode will be used to generate the Li^{+1} beam.^{11,12} In order to extract the beam parallel to the axis, geometric shaping of the anode is used to compensate for self-magnetic-field focusing of the beam in the vacuum region of the diode. A foil separating the diode vacuum region and the gas-filled ballistic drift region will strip the beam to Li^{+3} . Once through the foil, the gas provides charge and current neutralization of the beam for ballistic transport to the solenoidal lens.¹³ The lens alters the ion trajectories such that the beam focuses as it transports ballistically from the lens to the target.¹⁴ Again, gas in the lens region and in the target chamber provide for beam charge and current neutralization. The gas must also be chosen to avoid beam filamentation, and prevent excessive energy loss due to classical slowing down. Consideration of these and other constraints suggests 1 Torr of helium as a gas background.¹⁵ These constraints are not addressed in this paper.

A multimodular approach will position a number N of such systems around a high-gain fusion target, where N is expected to be in the range of 10–30. With a target radius r_t of about 1 cm, a total energy of about 10 MJ of 30 MeV Li^{+3} ions on target will be required at a total power P_t of about 1000 TW.¹ The total equivalent ion current (flux of Li^{+3} ions) on target I_t is then about 33 MA, while the total electrical current on target is 100 MA because of stripping from Li^{+1} to Li^{+3} when passing through the foil.

^{a)}Permanent address: JAYCOR, Vienna, VA 22182.

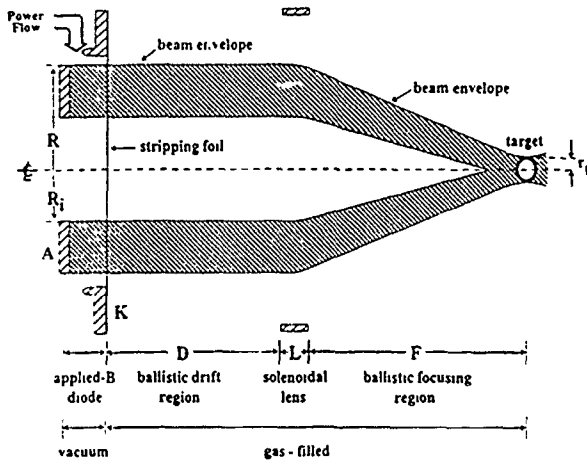


FIG. 1. Schematic of solenoidal focusing and ballistic transport system with an annular beam. Note that the figure is not drawn to scale. Typically, $R \sim 10$ cm, $D \sim 200$ cm, $L \sim 30$ cm, $F \sim 150$ cm, and the diode gap is a few cm.

When an appropriate voltage ramp is applied to the ion diode, beam transport over a distance of a few meters also allows for TOF bunching of the beam so that the original beam pulse duration τ_d is reduced during flight to that appropriate for target implosion τ_r .¹⁶⁻¹⁸ Since the total beam energy remains nearly constant during flight, the beam power increases roughly as τ_d/τ_r ; implosion physics considerations suggest that beam compression factors in the range of 2-4 will be required to achieve pellet driver times of 10-15 ns. Because the tail of the beam may arrive after target implosion, the wave-form efficiency η_w is introduced to account for this wasted portion of the ion power pulse. The wave-form efficiency is defined as the fraction of the ion-beam energy which arrives at the target within the implosion time τ_r . Assuming a power compression factor from bunching of $\alpha = \tau_d/\tau_r$, a total transport efficiency of η_p and a wave-form efficiency of η_w , the diode of each module will need to produce an ion current I_d of

$$I_d = I_r / \alpha \eta_i \eta_w N. \quad (1)$$

For $\alpha = 2$, $\eta_i = 0.8$, $\eta_w = 0.8$, and $N = 20$, I_d is about 1.3 MA.

Because of the voltage ramp required for TOF bunching, the beam is not monoenergetic. Thus, the lens system must be achromatic for good focusing. It has been shown that a diode/solenoidal lens system is achromatic through first order in small voltage variations.⁵ This result was derived for a diode with uniform current density extending to the axis. For an annular diode, the achromatic nature of the diode is somewhat reduced. Aside from allowing for a bunching factor α in Eq. (1), the beam is treated in this study as if it were monoenergetic with a nominal voltage between the end points of the required voltage ramp. The issue of focus sweeping due to chromatic lens effects are not addressed here, but will be addressed in a future paper.

As seen from Fig. 1, the solenoidal lens entrance is positioned a distance D from the diode, and has its axis coincident with the beam centerline. As an axially moving

ion enters the lens, the radial magnetic field acts to impart a small azimuthal velocity. The axial magnetic field inside the solenoid, combined with this azimuthal velocity, focuses the beam. On exiting the lens, the oppositely directed radial magnetic field removes the imparted azimuthal velocity. The lens itself has a length L and the focusing length F (i.e., the distance from the lens to the target) is determined by the field strength of the solenoid. If the lens is positioned in the target chamber wall, F is equal to the target chamber radius R_{tc} . The total distance from the diode to the target, $T = D + L + F$, is associated with the distance required for bunching for a given voltage ramp. Unlike the wire-guided transport and z-discharge transport systems, no packing constraint applies to this problem for presently envisioned target chamber sizes of radius > 150 cm. This results because the packing occurs at large radius in the target chamber walls, where the total cross-sectional area of all N solenoids is expected to a small fraction of the surface area of the target chamber.

For an ideal focusing lens, the beam microdivergence half-width Θ_μ determines r_p , the beam spot size at the target. Here, Θ_μ is expressed in radians, and $r_s = F\Theta_\mu$ for focusing over the distance F . For a target radius of r_p , $r_s < r_t$ is required for optimal transport efficiency. Thus, with $F = R_{tc}$, the target chamber radius specifies the required microdivergence, which can be expressed as $\Theta_\mu < r_t/R_{tc}$. Beam microdivergences as small as about 12.6 mrad have been achieved on applied-B diodes.¹⁹ For LMF, factor of 2 smaller microdivergence values are required for high transport efficiency. For example, with $r_t = 1$ cm and $R_{tc} = 150$ cm, $\Theta_\mu < 6.7$ mrad.

For a nonideal lens, the beam spot size will be larger than $F\Theta_\mu$. Without commensurately reducing Θ_μ , this reduces the transport efficiency. The main purpose of this study is to quantitatively evaluate the transport efficiency for realistically modeled solenoidal lens field profiles.

Although there are many parameters required to describe the solenoidal focusing and ballistic transport system, the above considerations provide an approach for calculating η_r . First, it is assumed that target requirements specify r_p , I_p , the ion speed v_0 , the ion charge state Z , and the ion mass m_r . Next, simple models will be used to describe the characteristics of the diode and the emitted ion current density $j_i(r_d)$, where r_d is the radial position on the anode surface of the diode. Because the diode is expected to be hollow,¹² the active area extends from an inner radius R_i to the outer radius R . Since it is difficult to achieve the correct applied magnetic-field profile for $R_i < R/2$ in an extraction geometry for the applied-B diode,² and since the ion-emitting area increases slowly as R_i is reduced to small values, it will be assumed that $R_i = R/2$.

Finally, complete beam charge and current neutralization by the background plasma will be assumed in the ballistic drift region, in the solenoidal lens section, and in the ballistic focusing region. Then η_i will be calculated. The scaling of η_i with the parameters F , Θ_μ , R , L , and N can then be determined. The variation of η_i with this set of system parameters determines the impact of system re-

quirements on the average ion current density at the diode surface J_i . From Eq. (1), J_i is given by

$$J_i = I_d / \pi (R^2 - R_d^2) = 4I_d / (3\pi\alpha N\eta\eta_w R^2). \quad (2)$$

Using $R = 2R_d = 12$ cm for the same example as that following Eq. (1) where $I_d = 1.3$ MA, Eq. (2) yields $J_i = 3.8$ kA/cm². For $R = 8$ cm, $J_i = 8.6$ kA/cm². Experimental measurements of J_i have demonstrated values as high as 6–10 kA/cm² for the applied- B diode.^{19,20}

Section II of this paper provides an analysis of ion orbits in a solenoid of finite thickness modeled with sharp boundaries so that B_z is uniform inside the solenoid and B_r only exists in a thin boundary layer. Analytic expressions are obtained for ion trajectories which allow for initial conditions including beam microdivergence. The spread in arrival times of transported ions is also considered here in order to evaluate its effect on TOF bunching of the beam. In Sec. III, a diode model is presented and η_i is calculated for specific system parameters using the results of Sec. II. Then, J_i is calculated to illustrate the parameter regimes where reasonable values of the diode current density are obtained. In Sec. IV, a more realistic solenoidal magnetic-field model is presented. Transport efficiency is calculated in this case by numerically integrating the equations of motion to propagate ions from the diode to the target. Results are compared with those of Sec. II to illustrate the effect the more realistic field geometry. Finally, results and conclusions are discussed in Sec. V.

It is found from this work that η_i can be close to 100% for values of diode ion current density that have been achieved and values of microdivergence that are a factor of 2 smaller than those already achieved on applied- B diodes. The analysis suggests that a design for a LMF system with $r_t = 1$ cm and as few as 20 modules could be achievable with $R = 8$ –12 cm, $F \sim 150$ –200 cm, $J_i = 5$ –10 kA/cm², and $\Theta_\mu < 6$ mrad. Such a system would have an η_i of 75%–100%. The higher efficiencies can be obtained by going to the smaller values of F for the same N , r_p , R , and Θ_μ . However, a target chamber radius (with $F = R_{lc}$) of less than about 150 cm may be impractical. Achieving a smaller Θ_μ will relax the requirements on J_i and improve efficiency, while going to larger Θ_μ will require higher values of J_i and decrease efficiency. It was also found that the radius of the solenoidal lens should be about a factor of 3 larger than the diode radius in order to avoid efficiency degradation due to the radial gradient in the focusing field.

II. ORBIT ANALYSIS

In this section, ion propagation through solenoidal lens is analyzed. First, some underlying assumptions are discussed. Then the model for the solenoidal lens is described and ion trajectories through the lens are calculated. The results of this analysis are used in Sec. III to determine beam transport efficiency for specific LMF parameters.

A number of physically reasonable assumptions make the problem tractable. First, it is assumed that the beam front ionizes the background gas as it propagates forward. The resulting plasma density is assumed to be large com-

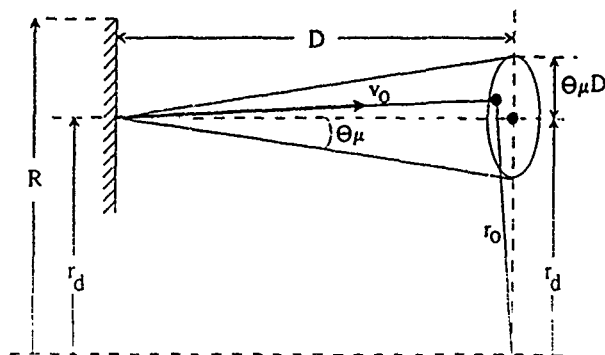


FIG. 2. Schematic of ballistic drift region illustrating geometry of beam injection into the solenoidal lens. As with Fig. 1, this figure is also not drawn to scale. Typically, $R \sim 10$ cm, $D \sim 200$ cm, and $\Theta_\mu D \sim 1.5$ cm.

pared with the beam density and the plasma conductivity is assumed large enough so that complete charge and current neutralization of the beam occurs. In addition, it is assumed that the plasma density is not so high that beam scattering or energy losses become significant for the length scale of beam transport. Beam propagation is also assumed to be stable.¹⁵ Validity of these assumptions is not addressed here, but will be addressed in future work. Under these conditions, ion orbits are determined by their single-particle motion in the magnetic field of the solenoidal lens.

Figure 2 illustrates the injection geometry and parameters employed in the analysis. Ions with speed v_0 are emitted from a hollow extraction diode at radii r_d between R_i and R . The annular beam is extracted parallel to the axis and propagates ballistically a distance D from the plane of the diode to the solenoidal lens. Parallel extraction is accomplished through anode shaping to compensate for ion orbit bending in the vacuum magnetic field of the diode gap. The microdivergence of the diode Θ_μ causes radial beam spreading of order $D\Theta_\mu$. Because the ion orbit is ballistic in this drift region, the velocity components at the entrance to the lens can easily be written in terms of the initial velocity components at the diode. Using conservation of angular momentum and energy yields,

$$r_0 = [(r_d + v_{rd}D/v_{zd})^2 + v_{\theta d}^2 D^2/v_{zd}^2]^{1/2}, \quad (3a)$$

$$v_{z0} = v_{zd} = (v_0^2 - v_{rd}^2 - v_{\theta d}^2)^{1/2}, \quad (3b)$$

$$v_{\theta 0} = r_d v_{\theta d} / r_0, \quad (3c)$$

$$v_{r0} = [v_{rd}^2 + v_{\theta d}^2 (1 - r_d^2/r_0^2)]^{1/2}, \quad (3d)$$

where the subscripts "d" and "0" denote quantities evaluated at the diode and at the entrance to the solenoidal lens, respectively.

In order to formulate an analytically tractable picture for solenoidal focusing, it will be assumed that the magnetic field inside the solenoid of length L is purely axial and uniform in space. The field lines are returned to the outside of the solenoid through a very thin layer where the magnetic field is purely radial. If the center of the lens is positioned at $z = L/2$, the axial magnetic field is given by

$$B_z = \begin{cases} 0, & z < 0, \\ B_{z0}, & 0 < z < L, \\ 0, & z > L. \end{cases} \quad (4)$$

This field can be described by the vector potential

$$A_\theta = \begin{cases} 0, & z < 0, \\ rB_{z0}/2, & 0 < z < L, \\ 0, & z > L. \end{cases} \quad (5)$$

Note that A_θ depends linearly on r inside the solenoid and drops to zero at the sharp boundaries located at $z=0$ and $z=L$.

For any given ion, the velocity components at injection into the solenoidal lens (i.e., v_{r0} , $v_{\theta0}$, and v_{z0}) determine the constants of the motion that govern the orbit. Inside the lens these constants are energy H , and canonical angular momentum P_θ , so that

$$2H/m_i = v_r^2 + v_\theta^2 + v_z^2 = v_0^2 \quad (6)$$

and

$$\frac{P_\theta}{m_i} = r \left(v_\theta + \frac{eZA_\theta}{m_i c} \right) = r_0 v_{\theta0}. \quad (7)$$

The radial equation of motion can be simplified by substituting for B_z and v_θ from Eqs. (4) and (7) yielding

$$\frac{dv_r}{dt} = -\frac{\omega_c^2 r}{4} + \frac{r_0^2 v_{\theta0}^2}{r^3}, \quad (8)$$

where $\omega_c = eZB_{z0}/m_i c$ is the ion cyclotron frequency. The first term on the right-hand side represents the focusing force of the solenoid lens which depends linearly on r . For $R \sim 10$ cm, $B_{z0} \sim 20$ kG, and $\Theta_\mu \sim 10$ mrad, the centrifugal force is comparable to the focusing force for some ions. Thus, the beam microdivergence can have an important effect on focusing.

Equation (8) can be solved for $v_r(r)$ by multiplying both sides by v_r and integrating. Then, this expression for v_r along with v_θ from Eq. (7), can be substituted into Eq. (6) to obtain $v_z(r)$. Collecting the results provides the ion velocity components inside the solenoid,

$$v_r(r) = \pm \left[v_{r0}^2 - \frac{\omega_c^2}{4} (r^2 - r_0^2) - r_0^2 v_{\theta0}^2 \left(\frac{1}{r^2} - \frac{1}{r_0^2} \right) \right]^{1/2}, \quad (9a)$$

$$v_\theta(r) = -\frac{\omega_c r}{2} + \frac{v_{\theta0} r_0}{r}, \quad (9b)$$

and

$$v_z = \left[v_0^2 - v_{r0}^2 - \left(v_{\theta0} - \frac{\omega_c r_0}{2} \right)^2 \right]^{1/2} \equiv v_{zL}. \quad (9c)$$

Since there is no force in the axial direction inside the solenoid, $v_z = v_{zL}$ is a constant. However, note that $v_{zL} \neq v_{z0} = (v_0^2 - v_{r0}^2 - v_{\theta0}^2)^{1/2}$ because of the axial force experienced in passing across the sharp boundary at $z=0$.

The solution for the ion orbit is completed by solving for $r(z)$. Observing that $dr/dz = v_r/v_z$, $r(z)$ is found by integrating to yield

$$r^2(z) = \frac{r_0^2}{2} + \frac{2(v_{r0}^2 + v_{\theta0}^2)}{\omega_c^2} + \left[\frac{r_0^2}{2} - \frac{2(v_{r0}^2 + v_{\theta0}^2)}{\omega_c^2} \right] \cos\left(\frac{\omega_c z}{v_{zL}}\right) + \frac{2r_0 v_{r0}}{\omega_c} \sin\left(\frac{\omega_c z}{v_{zL}}\right). \quad (10)$$

This expression for $r(z)$ can be substituted back into Eq. (9) to provide expression for the velocity components as functions of z . Also, note that $z = v_{zL} t$.

Because the ion trajectory is ballistic between the lens and the target, the ion radial position and velocity at the exit of the lens are all that is needed to project the ion to the target location. Since the magnetic field is purely radial in the sharp boundary layer at $z=L$, the ion experiences no radial force crossing the boundary. Thus, r and v_r at the exit of the lens are found by evaluating Eqs. (10) and (9a) at $z=L$. However, the ion does experience both azimuthal and axial forces in crossing the boundary. The azimuthal velocity at the exit of the lens is given by conservation of canonical angular momentum with $A_\theta=0$ for $z > L$ [see Eq. (4)], and the axial velocity is obtained by applying conservation of energy [i.e., Eq. (6)]. Using the subscript f to denote values at the exit of the lens.

$$r_f = r(L), \quad (11a)$$

$$v_{rf} = v_r(r_f), \quad (11b)$$

$$v_{\theta f} = v_{\theta0} r_0 / r_f, \quad (11c)$$

$$v_{zf} = (v_0^2 - v_{rf}^2 - v_{\theta f}^2)^{1/2}, \quad (11d)$$

where $r(z)$ is given in Eq. (10) and $v_r(r)$ is given in Eq. (9a).

An estimate of the focal length of the solenoidal lens can be obtained by assuming that the microdivergence is negligibly small so that $v_{r0} = v_{\theta0} = 0$. In this case, $v_{\theta f} = 0$ and all ions cross the axis. From geometric considerations, $r_f/F = v_{rf}/v_{zf}$, so that from Eq. (11)

$$F(r_0) = \frac{2v_0}{\omega_c} \frac{\sin(\omega_c L/v_{zL})}{[1 - \cos(\omega_c L/v_{zL})]} \times \left[1 - \frac{\omega_c^2 r_0^2}{8v_0^2} \left[1 - \cos\left(\frac{\omega_c L}{v_{zL}}\right) \right] \right]^{1/2}, \quad (12)$$

where from Eq. (9c) $v_{zL} = v_0(1 - \omega_c^2 r_0^2/4v_0^2)^{1/2}$ in this special case. Assuming $\epsilon \equiv \omega_c r_0/v_0 \ll 1$ and taking the thin lens approximation (i.e., $\omega_c L/v_{zL} \ll 1$) yields the familiar result²¹ that $F = 4v_0^2/\omega_c^2 L$, which is independent of r_0 . However, for LMF parameters used here, $\omega_c L/v_{zL} \sim 0.87$ so that the thin lens approximation is not very accurate. Additionally, although $\epsilon \ll 1$ for LMF, the terms in F and v_{zL} involving ϵ are important because they lead to corrections in F on the order of the target size r_f . Thus, the full expression in Eq. (12) averaged over the beam distribution in r_0 is required to estimate the focal length of the lens. Since F is still only weakly dependent on r_0 , ions from all radii focus to nearly the same spot. For a 30 MeV Li^{+3} beam with $B_{z0} = 20$ kG and $L = 30$ cm, the focal length for individual ions ranges from $F(R) = 150.6$ cm to $F(R_f) = 152$ cm for $R = 2R_f = 10$ cm, where for comparison $r_f \sim 1$ cm. Since the

axis-crossing angle (for ions with zero angular momentum) is on the order of $R/F \sim 0.07$, this small variation in F will not cause these ions to miss the target. However, ions with large values of P_θ (i.e., those that have a distance of closest approach to the axis on the order of r_i) can miss the target as a result of these small variations in F . Including microdivergence and a more realistic solenoidal magnetic-field profile (particularly in terms of the radial gradient in B_z) spreads out the focus even more. These effects will be investigated numerically in the following section.

After exiting the solenoid, the ion again propagates ballistically so that its radial location as a function of z is given by

$$r(z) = [(r_f + v_{rf}z/v_{zf})^2 + v_{\theta f}^2 z^2/v_{zf}^2]^{1/2}, \quad (13)$$

where in Eq. (13) $z=0$ has been redefined to be at the exit of the solenoid. If the target is located a distance F from the exit of the solenoid, then an ion will hit the target if $r(F) < r_t$. This result will be used to calculate the transport efficiency in the following section.

Another quantity of interest for LMF is the spread in arrival times for the ions. This spread determines a limit to ion beam pulse compression by axial bunching produced by a ramped accelerating voltage pulse. For ions simultaneously injected into the system at the same energy, the maximum axial velocity v_{\max} and minimum axial velocity v_{\min} determine the spread in arrival times for a transport distance z through $\Delta t_a = z/v_{\min} - z/v_{\max}$. Using Eqs. (3b), (9c), and (11d) for the axial velocities in each section of the transport system, the spread in arrival times associated with ballistic transport and solenoidal focusing is given by

$$\begin{aligned} \Delta t_a &= \Delta t_D + \Delta t_L + \Delta t_F \\ &= \frac{D\Theta_\mu^2}{2v_0} + \frac{L\Theta_\mu^2}{2v_0} \left(1 + \frac{\omega_c^2 R^2}{2\Theta_\mu^2} \right) + \frac{3R^2}{8v_0 F}, \end{aligned} \quad (14)$$

where Δt_D , Δt_L , and Δt_F are the temporal beam spreading associated with ballistic transport between the diode and the solenoidal lens, the solenoidal lens, and ballistic focusing, respectively. The sum Δt_a must be small compared with the bunched beam pulse length τ_r . For $D=220$ cm, $L=30$ cm, $F=150$ cm, $R=10$ cm, $\Theta_\mu=10$ mrad, and $B_{z0}=20$ kG, $\Delta t_a=0.3$ ns, where the largest contribution comes from Δt_L . Since $\tau_r \sim 10$ ns, spreading in arrival times due to ballistic transport and solenoidal focusing is negligible.

III. TRANSPORT EFFICIENCY

Before proceeding with a description of the calculation of the transport efficiency, the ion diode model will be described. As indicated in Fig. 2 the anode plane of the diode is located a distance D from the entrance to the solenoidal lens and the annular emission surface extends from $R/2$ to R . The ion beam produced by the diode is assumed to be azimuthally uniform, monoenergetic, and extracted parallel to the axis. Ions emitted at each radius r_d are assumed to be uniformly distributed in velocity space within a cone of half-angle Θ_μ about a velocity vector that

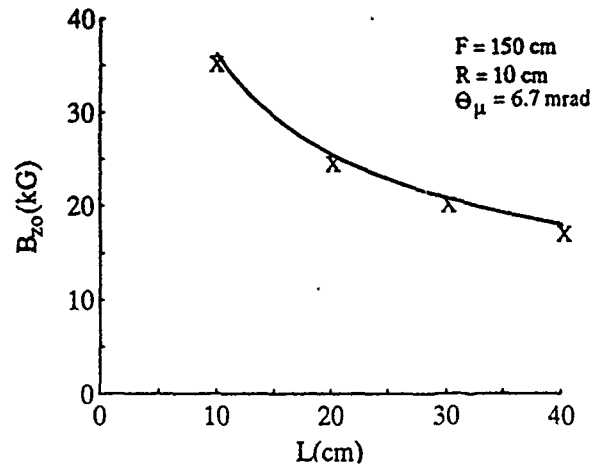


FIG. 3. Plot of required B_{z0} for best focus at F as a function of L . The curve is the thin lens result, $F=4v_0^2/\omega_c^2 L$, and the \times 's indicate code results with $R=10$ cm and $\Theta_\mu=6.7$ mrad.

is parallel to the z axis. It is also assumed that Θ_μ is the same for all r_d . For simplicity, the distribution of ion current density $j_i(r_d)$ over the emission surface will also be taken to be uniform. Although these simplifying assumptions will be used here for the functional forms of both the ion current density and microdivergence at the source, the analysis that follows can easily be extended to treat more complicated functional forms.

A code has been developed to apply this diode model and the results of Sec. II to calculate the transport efficiency for ballistic transport and solenoidal focusing under various conditions. Here, the transport efficiency is defined to be the fraction of the emitted beam that hits the target of radius r_t located a distance F from the end of the solenoid. A distribution of ions is generated by applying the diode model and Eq. (3) is used to project the ions to the solenoidal lens. Equation (11) propagates the beam ions through the lens, and, finally, Eq. (13) provides the radius of the ions in the vicinity of the target. The transport efficiency η_t is calculated by determining whether $r(F) < r_t$ for each ion.

Since the discussion following Eq. (12) has shown that the exact location of the best focus depends on the ion distribution (through r_0) and the beam microdivergence, B_{z0} was varied to find its value that places the best focus at F . This was done in all cases presented here in order to optimize η_t under all conditions. Figure 3 shows results from this procedure for various values of L for the case where $R=10$ cm and $\Theta_\mu=6.7$ mrad. Also shown for comparison is the thin lens result. Although the results are not markedly different, small errors in B_{z0} are important because $F \sim 1/B_{z0}^2$ and $r_t \ll F$. This effect is most important for large R . This is illustrated in Fig. 4 where $\eta_t(z_t)$, the fraction of beam incident on the target, is plotted as a function of axial distance z_t from the exit of the solenoid to the target. (In Fig. 4 the target is placed at z_t rather than F , while in all other cases the target is placed at F , the location of the best focus.) In Fig. 4, $L=30$ cm, $\Theta_\mu=6.7$ mrad

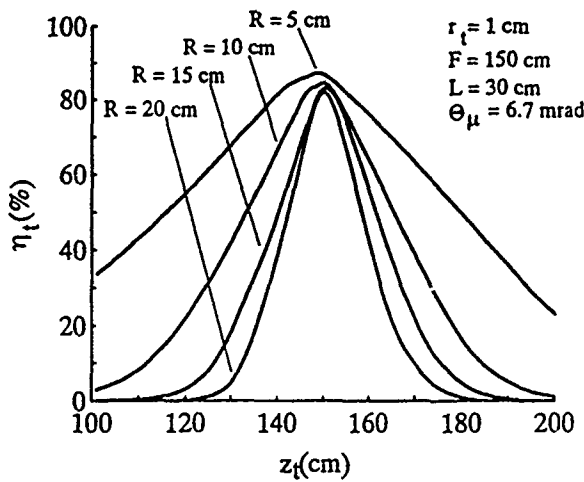


FIG. 4. Plot of the percentage of beam ions on target as a function of axial position with $F=150$ cm, $\Theta_\mu=6.7$ mrad, $L=30$ cm, and $r_t=1$ cm for various values of R .

and B_{z0} is chosen for each R so that $F=150$ cm. Note that the focus is tighter for larger R , and $\eta_t(z_t)$ peaks at F for all R .

In order to design a focusing lens, the length of the solenoid must be chosen. Figure 3 shows that the magnitude of B_{z0} required for a focal length F increases as the solenoid length L decreases. Thus, from an engineering point of view a longer lens may be preferable. The variation of η_t with R for various values of L is illustrated in Fig. 5 for $F=150$ cm, $\Theta_\mu=6.7$ mrad, and $r_t=1$ cm. For $L < 20$ cm, η_t drops significantly for large R , while η_t is uniformly lower over the full range of R as L is increased beyond 20 cm. The value of $L=30$ cm is a physically reasonable length, and shows minimal variation in η_t over the range of R while still providing high transport efficiency. Although any value of L could be used, $L=30$ cm will be used for the remainder of this study.

Figures 6–8 show plots of η_t for various cases. In all

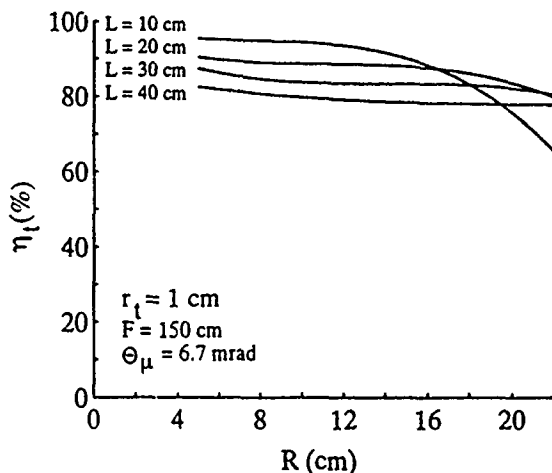


FIG. 5. Plot of transport efficiency as a function of diode radius with $F=150$ cm, $\Theta_\mu=6.7$ mrad, $r_t=1$ cm for various values of L .

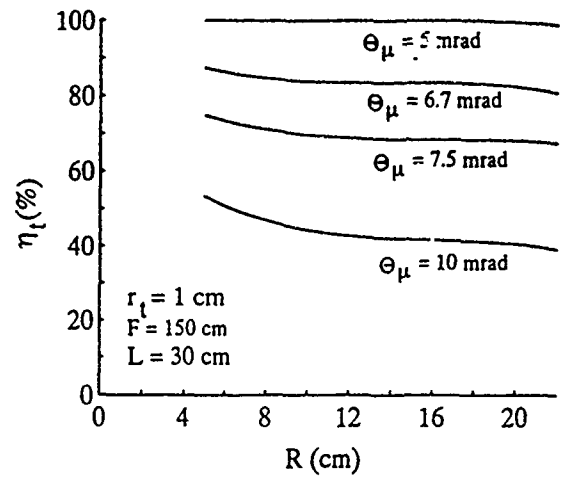


FIG. 6. Plot of transport efficiency as a function of diode radius with $F=150$ cm, $L=30$ cm, and $r_t=1$ cm for various values of Θ_μ .

cases r_t is set equal to 1 cm. As expected from the results of Fig. 5, η_t is nearly independent of R for $L=30$ cm. For typical LMF parameters of $F=150$ cm and $R \sim 10$ cm, $\eta_t > 0.7$ for $\Theta_\mu < 7.5$ mrad. However, η_t decreases roughly linearly with Θ_μ^{-1} . The effect of Θ_μ on the focusing properties of the lens are illustrated in Fig. 6 by the fact that $\eta_t \sim 0.83$ for $\Theta_\mu=6.7$ mrad. If the beam microdivergence had no effect on focusing, the beam spot size at the best focus would be $\Theta_\mu F = 1$ cm. With $r_t=1$ cm, η_t would be 1.0 rather than the reduced value of 0.83. Finally comparing Figs. 6–8, it is seen that η_t decreases rapidly as F is increased. For $\Theta_\mu=7.5$ mrad, η_t decreases by a factor of 2 from ~ 0.7 to ~ 0.35 as F increases from 150 to 200 cm.

Figures 9–11 show plots of J_t from Eq. (2) with $I_t=33$ MA, $\alpha=2$, and $\eta_w=0.8$. Figures 9, 10, and 11 derive their values of η_t from Figs. 6, 7, and 8, respectively. The η_t plots displayed in Figs. 6–8 are independent of the number of modules because, unlike the wire-guided³ and z -discharge transport⁴ systems, there is no packing constraint for this system. Figures 9–11 use $N=20$. Values of

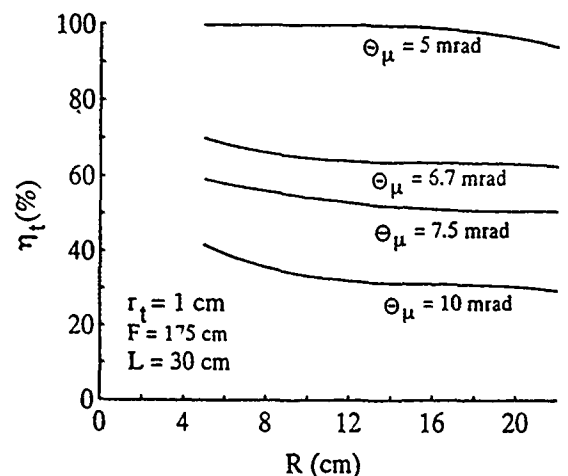


FIG. 7. Plot of transport efficiency as a function of diode radius with $F=175$ cm, $L=30$ cm, and $r_t=1$ cm for various values of Θ_μ .

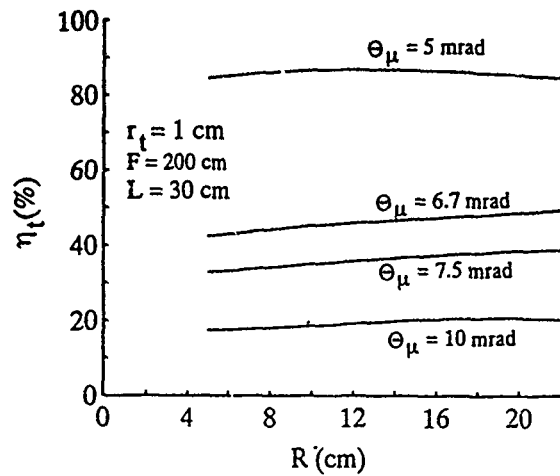


FIG. 8. Plot of transport efficiency as a function of diode radius with $F=200$ cm, $L=30$ cm, and $r_t=1$ cm for various values of Θ_μ .

J_i for different N can be obtained by scaling these results using Eq. (2). Figure 9 shows that, for $F=150$ cm, $\Theta_\mu=6.7$ mrad, $L=30$ cm, $N=20$, and $r_t=1$ cm, an LMF system can be designed with $J_i \sim 7$ kA/cm² at a diode radius of $R \sim 12$ cm. Somewhat lower values of J_i are possible for larger values of R or smaller values of Θ_μ . This value of J_i is comparable to values already achieved with an applied- B diode. From Eq. (2), using fewer modules increases the required ion source current density with all other factors held fixed while using more modules relaxes the required ion source current density. Using more modules, however, increases the cost and complexity of the facility.

To examine the effects of a more realistic solenoidal magnetic-field profile, the magnetic coil design code ATHETA²² was used to produce a magnetic-field map. The radial and axial components of the magnetic field from this map were used in a particle orbit code to calculate η_t for specific cases. The solenoid was modeled by a set of 20 coils of 30 cm radius, equally spaced over a 30 cm length. In

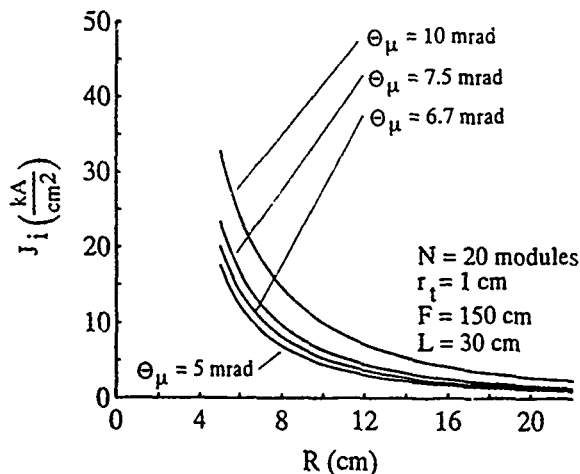


FIG. 9. Plot of required diode ion current density as a function of diode radius with $F=150$ cm, $L=30$ cm, and $r_t=1$ cm for various values of Θ_μ .

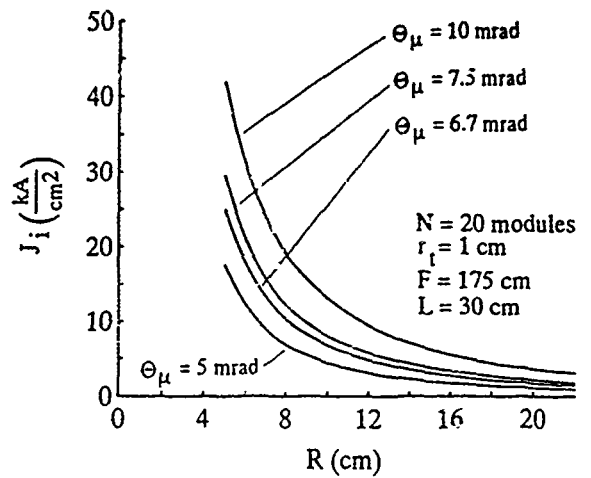


FIG. 10. Plot of required diode ion current density as a function of diode radius with $F=175$ cm, $L=30$ cm, and $r_t=1$ cm for various values of Θ_μ .

order to compress the axial extent of the field, a perfectly conducting annular ring with an inner radius of 25 cm and an outer radius of 50 cm was placed 5 cm beyond each end of the solenoid. The outer radius of these conducting rings may need to be reduced to avoid a packing problem for large N . The resulting magnetic-field map is shown in Fig. 12. From the discussion of Eq. (12) it follows that F scales roughly as $1/B_z^2$. Thus, it is anticipated that the radial gradient in the focusing field B_z will spread out the focus and reduce η_t (compared to the results for the sharp-boundary, finite-length lens model where B_z is uniform). For reference, the normalized axial magnetic field at the center of the lens and its gradient are plotted as a function of radius in Fig. 13.

Figure 14 displays results from simulations of beam focusing in the solenoidal field configuration shown in Fig. 12. All other parameters are the same as used in deriving the results given in Fig. 6. In all simulations the current in solenoidal coils was adjusted so that the best focus occurred at F . For R less than about 12 cm, the results are

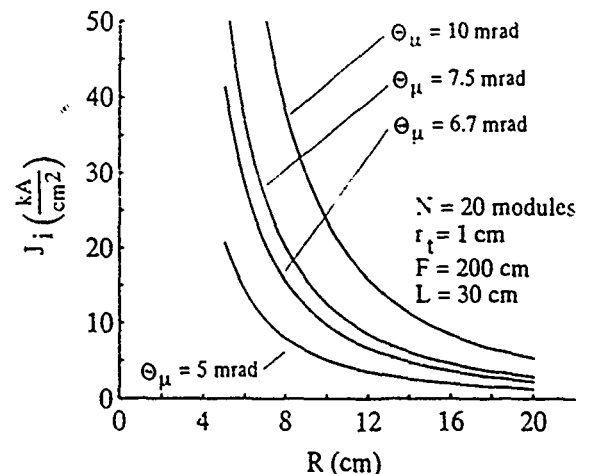


FIG. 11. Plot of required diode ion current density as a function of diode radius with $F=200$ cm, $L=30$ cm, and $r_t=1$ cm for various values of Θ_μ .

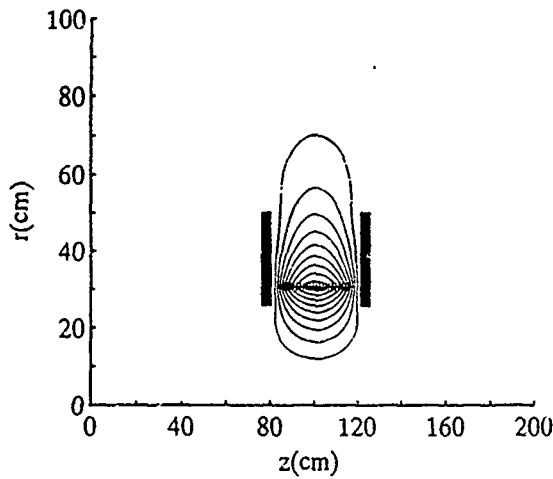


FIG. 12. Magnetic field plot from ATHETA calculation showing position of field coils ($r=30$ cm) and conducting annular rings (solid blocks) for a 30-cm-long solenoid centered at $z=100$ cm.

very similar. For R greater than about 12 cm, η_t begins to drop off sharply because the gradient in B_z is large there (see Fig. 13). Remembering that F scales roughly as $1/B_z^2$, ions at larger radius have significantly shorter focal length than ions from smaller radius. Thus, the focus is spread out. Since the radius of the solenoid is 30 cm, this implies that the diode radius must be about a factor of 3 smaller than the solenoid in order to achieve a sharp focus and optimum η_t . The effect of reduced η_t on the required ion source current density is illustrated in Fig. 15, where here the simulation results displayed in Fig. 14 are used to derive J_i . Compared with Fig. 9, these results show that significantly higher J_i is required at larger R .

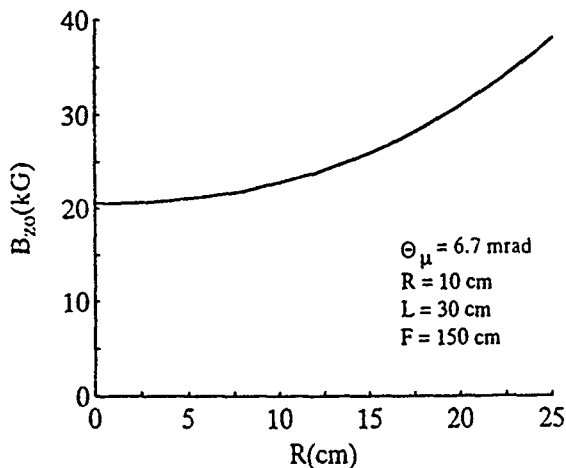


FIG. 13. Plot of axial magnetic field as a function of radius at the center of the lens from the ATHETA field map for 87.5 kA/turn. Case shown has $L=30$ cm and provides the 150 cm focal length lens used for a beam with $R=10$ cm and $\Theta_\mu=6.7$ mrad.

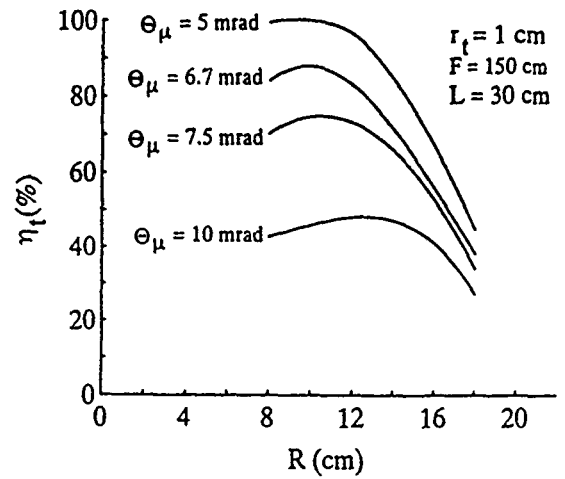


FIG. 14. Plot of transport efficiency as a function of diode radius from numerical simulations using ATHETA field map with $F=150$ cm, $L=30$ cm, and $r_t=1$ cm for various values of Θ_μ .

IV. SUMMARY AND CONCLUSIONS

The LMF has been proposed for the study of high-gain, high-yield ICF targets. A multimodular light-ion approach requires transport of intense ion beams over distances of a few meters in order to isolate the ion diode hardware from the target explosion and to provide sufficient propagation distance for power compression by time-of-flight bunching. This study has investigated the use of ballistic transport and solenoidal focusing for beam propagation. Phenomena important to solenoidal focusing have been studied and the optimum total transport efficiency within a range of achievable system parameters has been determined.

A number of simplifying assumptions were used to reduce the many parameters required to describe transport system. First, it was assumed that target considerations specify the target radius, the power on target, and the ion energy, charge state, and mass. It was also assumed that

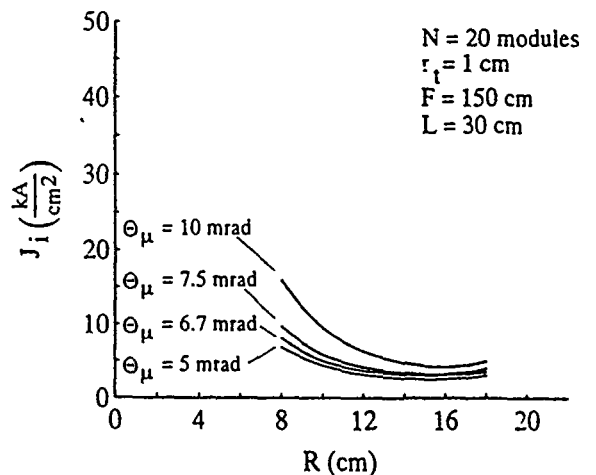


FIG. 15. Plot of required diode ion current density as a function of diode radius from numerical simulations using ATHETA field map with $F=150$ cm, $L=30$ cm, and $r_t=1$ cm for various values of Θ_μ .

the bunching factor is fixed at 2, and that the wave-form efficiency is fixed at 0.8. Next, simple models were used to describe the focusing characteristics of the diode and the emitted ion current density in order to specify the beam distribution at the entrance to the solenoidal lens. It was assumed that ions emitted at radius r_d are aimed parallel to the axis and are uniformly distributed in perpendicular velocity space about this direction within a cone of half-angle Θ_μ . This velocity space distribution was chosen for mathematical simplicity. A more realistic assumption might be a Gaussian distribution which would yield results very similar to those presented here. It is also assumed that Θ_μ and the ion current density are the same for all r_d , and that the beam is monoenergetic (although a bunching factor is included in estimating J_i). Finally, complete charge and current neutralization were assumed.

Section II of this paper provides an analysis of ion orbits. The analysis included beam microdivergence and was done for a sharp-boundary finite-thickness lens. It was shown that the thin lens approximation is not appropriate for LMF parameters and that small correction terms to the focal length which depend on radius can be important. The spread in arrival times of the transported ions was also considered in order to evaluate its effect on time-of-flight bunching of the beam. The spread in arrival times is given in Eq. (14). Results show that beam spreading during transport and focusing will not limit the ability to achieve the required bunching for LMF.

The results of the orbit analysis in Sec. II were used in Sec. III to calculate the transport efficiency and the required ion source current density for LMF. The active area of the diode was assumed to extend from an inner radius $R_i=R/2$ to the outer radius R . It is found from this work that η_i can be close to 100% for values of diode ion current density that have been achieved and values of microdivergence that are a factor of 2 smaller than those already achieved on applied- B diodes. The analysis of the sharp-boundary finite-thickness lens system suggests a point design for a LMF system with $r_i=1$ cm and as few as 20 modules could be achievable with $R=8-12$ cm, $F\sim 150-200$ cm, $J_i=5-10$ kA/cm², and $\Theta_\mu\leq 6$ mrad. Such a system would have an η_i of 75%-100%. The higher efficiencies can be obtained by going to smaller values of F for the same N , r_p , R , and Θ_μ . However, a target chamber radius (with $F=R_{ic}$) of less than about 150 cm may be impractical. Achieving a smaller Θ_μ will relax the requirements on J_i and improve efficiency, while going to larger Θ_μ will require higher values of J_i and decrease efficiency. It was also found from the simulations using the ATHETA field map for the lens that the radius of the solenoid should be about a factor of 3 larger than the diode radius in order to avoid efficiency degradation due to the radial gradient in the focusing field. For a solenoid radius of 30 cm, results show that a diode radius of about 12 cm or less should be used. Results are only presented for $N=20$. Since there is no packing constraint for this system, η_i is independent of N . Thus, J_i results for other values of N are easily obtained from the scaling given in Eq. (2).

The analysis presented here can easily be extended to

treat more complicated models for focusing and emission. Although the diode and solenoid form an approximate achromatic lens system, future work will evaluate higher-order chromatic effects on transport efficiency. The effect of the applied- B diode and solenoidal lens transverse magnetic fields on beam current neutralization will also be investigated in order to more soundly justify this assumption. In addition, future work will consider transport constraints associated with hydrodynamics, possible beam-plasma instabilities, beam energy losses, and beam ion scattering and charge exchange during propagation.

ACKNOWLEDGMENTS

The authors acknowledge Dr. J. Quintenz for making the ATHETA code available for calculating the solenoidal lens magnetic-field profiles used in this work. The authors also acknowledge Dr. J. M. Grossmann and Dr. S. Swanekamp for their assistance with the numerical work. This work was supported by the U.S. Department of Energy under Contract No. DE-AC04-76-DP00789.

- ¹J. J. Ramirez, R. W. Stinnett, D. L. Johnson, C. L. Olson, T. A. Mehlhorn, J. T. Crow, J. P. Quintenz, K. R. Prestwich, M. P. Desjarlais, R. E. Olson, G. O. Allshouse, T. H. Martin, J. P. VanDevender, D. L. Cook, S. A. Slutz, K. B. Coachman, T. R. Lockner, B. N. Turman, S. A. Goldstein, and J. N. Olsen, *Fusion Tech.* **15**, 350 (1989).
- ²D. L. Johnson, J. J. Ramirez, R. W. Stinnett, and K. B. Coachman, in *Proceedings of the 1989 Particle Accelerator Conference*, edited by F. Bennett and J. Kaptan, Chicago, IL, March 20-23, 1989, p. 1017.
- ³J. J. Watrous, D. Mosher, J. M. Neri, P. F. Ottinger, C. L. Olson, J. T. Crow, and R. R. Peterson, *J. Appl. Phys.* **69**, 639 (1991).
- ⁴P. F. Ottinger, D. V. Rose, D. Mosher, and J. M. Neri, *J. Appl. Phys.* **70**, 5292 (1991).
- ⁵C. L. Olson, in *Proceedings of the 1988 Linear Accelerator Conference*, edited by C. Leeman, Newport News, VA, October 3-7, 1988, p. 34.
- ⁶T. A. Mehlhorn and J. P. Quintenz, in *Proceedings of the 1989 Particle Accelerator Conference*, edited by F. Bennett and J. Kaptan, Chicago, IL, March 20-23, 1989, p. 1014.
- ⁷D. Mosher, D. D. Hinshelwood, J. M. Neri, P. F. Ottinger, J. J. Watrous, C. L. Olson, and T. A. Mehlhorn, in *Proceedings of the 8th International Conference on High-Power Particle Beams*, edited by B. N. Breizman and B. A. Knyazev, Novosibirsk, Russia, CIS, July 2-5 1990, p. 26.
- ⁸C. L. Olson, in *Proceedings of the 1989 Particle Accelerator Conference*, edited by F. Bennett and J. Kaptan, Chicago, IL, March 20-23, 1989, p. 1011.
- ⁹G. A. Moses, G. L. Kulcinski, D. Bruggink, R. Engelstad, E. Lovell, J. MacFarlane, Z. Musicki, R. Peterson, M. Sawan, I. Sviatoslavsky, L. Wittenberg, G. Kessler, U. von Mollendorff, E. Stein, D. Cook, R. Olson, I. Smith, P. Corcoran, H. Nishimoto, and J. Fockler, *Fusion Tech.* **15**, 756 (1989).
- ¹⁰R. R. Peterson and G. A. Moses, in *Proceedings of the 7th International Conference on High-Power Particle Beams*, edited by W. Bauer and W. Schmidt, Karlsruhe, Germany, July 4-8, 1988, p. 625.
- ¹¹D. J. Johnson, R. J. Leeper, W. A. Stygar, R. S. Coats, T. A. Mehlhorn, J. P. Quintenz, S. A. Slutz, and M. A. Sweeney, *J. Appl. Phys.* **58**, 12 (1985).
- ¹²S. A. Slutz and D. B. Seidel, *J. Appl. Phys.* **59**, 2685 (1986).
- ¹³D. Hammer and N. Rostoker, *Phys. Fluids* **13**, 1831 (1970).
- ¹⁴J. Maenchen, L. Wiley, S. Humphries, Jr., E. Peleg, R. N. Sudan, and D. A. Hammer, *Phys. Fluids* **22**, 555 (1979).
- ¹⁵C. L. Olson, in *IEEE Conference Record—Abstracts, the 1991 IEEE International Conference on Plasma Science*, edited by K. Schoenbach, Williamsburg, VA, June 3-5, 1991, p. 165.
- ¹⁶F. Winterberg, *Plasma Phys.* **17**, 69 (1975).
- ¹⁷S. A. Goldstein, G. Cooperstein, R. Lee, D. Mosher, and P. F. Ottinger, in *IEEE Conference Record—Abstracts, the 1978 IEEE International*

Conference on Plasma Science, edited by F. Schwirzke, Monterey, CA, May 15-17, 1978, p. 112.

¹⁸G. Cooperstein, S. A. Goldstein, D. Mosher, R. J. Barker, J. R. Boller, D. G. Colombant, A. Drobot, R. A. Meger, W. F. Oliphant, P. F. Ottinger, F. L. Sandel, S. J. Stephanakis, and F. C. Young, in *Laser Interaction and Related Plasma Phenomena*, Vol. 5, edited by J. J. Schwartz, H. Hora, M. Lubin, and B. Yaakobi (Plenum, New York, 1981), p. 105.

¹⁹J. P. VanDevender, J. A. Swegle, D. J. Johnson, K. W. Bieg, E. J. T.

Burns, J. W. Poukey, P. A. Miller, J. N. Olsen, and G. Yonas, *Laser and Particle Beams* 3, 93 (1985).

²⁰P. L. Dreike, E. J. T. Burns, S. A. Slutz, J. T. Crow, D. J. Johnson, P. R. Johnson, R. J. Leeper, P. A. Miller, L. P. Mix, D. B. Seidel, and D. F. Wenger, *J. Appl. Phys.* 60, 878 (1986).

²¹See, for example, S. Humphries, Jr., *Principles of Charged Particle Acceleration* (Wiley, New York, 1986), p. 127.

²²J. P. Quintenz and D. B. Seidel, in *Particle Beam Fusion Progress Report*, January-June 1984, SAND84-1336 (unpublished).

Z-discharge transport of intense ion beams for inertial confinement fusion

P. F. Ottinger, D.V. Rose,^{a)} D. Mosher, and J. M. Neri
Plasma Physics Division, Naval Research Laboratory, Washington, DC 20375-5000

(Received 30 May 1991; accepted for publication 6 August 1991)

Ion inertial confinement fusion requires beam transport over distances of a few meters for isolation of the diode hardware from the target explosion and for power compression by time-of-flight bunching. This paper evaluates light ion beam transport in a wall-stabilized z-discharge channel, where the discharge azimuthal magnetic field radially confines the ion beam. The ion beam is focused onto the entrance aperture of the transport channel by shaping the diode to achieve beam convergence in a field-free drift region separating the diode from the transport section. Ion orbits are studied to determine the injection efficiency (i.e., the fraction of the beam emitted from the diode which is transported) under various conditions. Ions that are focused onto the channel entrance at too large of an angle for confinement hit the wall and are lost. For a multimodular scheme (10–30 beams), individual transport channels are packed around the target with the exit apertures at some standoff distance from it. The fraction of the beam that is lost in this field-free standoff region is also evaluated under various conditions. The standoff efficiency is then combined with the injection efficiency to give the dependence of the total transport efficiency η_t on diode, focusing, transport and standoff parameters. It is found that η_t can be in the range of 75%–100% for parameter values that appear to be achievable.

I. INTRODUCTION

The Laboratory Microfusion Facility (LMF) has been proposed for the study of high-gain, high-yield inertial confinement fusion (ICF) targets using either lasers or ion beams as a driver. A multimodular light-ion approach, based on Hermes-III accelerator technology, is presently under investigation.^{1,2} Using light ion beams for the LMF driver will require transport of intense ion beams over distances of a few meters in order to isolate the ion diode hardware from the target explosion and to provide sufficient propagation distance for power compression by time-of-flight bunching. Several different transport schemes are being considered for a light-ion LMF.^{1,3} The baseline approach involves an achromatic magnetic lens system and ballistic transport.^{4–6} Alternative approaches^{3,6,7} include a wire-guided transport system, a low-mass wall-stabilized z-discharge transport channel, and a laser-initiated free-standing z-discharge transport channel. Advantages of these alternative approaches are that they provide positive beam guidance until it is very near the target, and that they allow larger radius target chambers, an important consideration for ICF reactor concepts.^{8,9} Wire-guided transport for LMF was evaluated previously.³ This paper presents a similar evaluation of wall-stabilized z-discharge transport for LMF. Because the discharge is wall confined, this approach has the added advantage of having the option of using different gases in the transport channel and the target chamber.

Wall-stabilized z-discharge transport has been studied extensively both theoretically^{10–14} and experimentally.^{15,16} Experiments have demonstrated efficient ion-beam transport over distances of up to 5 m using a ceramic insulating liner within a brass current-return tube. For LMF, the

mass of the transport hardware placed in the target chamber should be minimized in order to minimize debris and activation in the target chamber. Because of this, a low-mass version of the wall-stabilized transport channel is under development.¹⁷ Free-standing (i.e., without a stabilizing wall) z-discharge transport channels have also been studied previously.^{18–20}

A schematic of one module of an LMF system using a wall-stabilized z-discharge channel is shown in Fig. 1. An extraction applied-B ion diode is used to focus a Li^{-1} beam onto the entrance of the transport system.^{21,22} Focusing is achieved by a combination of geometric focusing from anode shaping and magnetic focusing from ion orbit bending in the self-field of the beam. A foil separating the diode vacuum region and the gas-filled ballistic focusing region strips the beam to Li^{+3} . Once through the foil, the gas provides charge and current neutralization of the beam for ballistic propagation and focusing onto the entrance of the transport channel. The multimodular approach positions a number N of such systems around a high-gain fusion target, where N is expected to be in the range of 10–30. With a target radius r_t of about 1 cm, a total energy of about 10 MJ of 30-MeV Li^{+3} ions on target is required at a total power P_t of about 1000 TW.¹ The total equivalent ion current (flux of Li^{+3} ions) on target I_t is then about 33 MA, while the total electrical current on target is 100 MA because of stripping from Li^{+1} to Li^{+3} when passing through the foil.

When an appropriate voltage ramp is applied to the ion diode, beam transport over a distance of a few meters also allows for time-of-flight bunching of the beam so that the original beam pulse duration τ_d is reduced during flight to that appropriate for target implosion τ_i .^{23,24} Since the total beam energy remains nearly constant during flight, the beam power increases roughly as τ_d/τ_i ; implosion physics

^{a)}Permanent address: JAYCOR, Vienna, VA 22182.

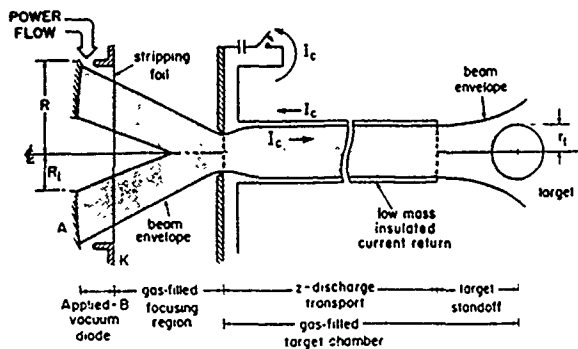


FIG. 1. Schematic of z-discharge transport system.

considerations suggest that beam compression factors in the range of 2–4 will be required to achieve pellet driver times of 10–15 ns. Because the tail of the beam may arrive after target implosion, the wave form efficiency η_w is introduced to account for this wasted portion of the ion power pulse. The wave form efficiency is defined as the fraction of the ion-beam energy that arrives at the target within the implosion time τ_r . Assuming a power compression factor from bunching of $\alpha = \tau_d/\tau_r$, a total transport efficiency of η_n and a wave form efficiency of η_w , the diode of each module will need to produce an ion current I_d of

$$I_d = I_t / \alpha \eta_i \eta_w N. \quad (1)$$

For $\alpha = 2$, $\eta_i = 0.8$, $\eta_w = 0.8$, and $N = 20$, I_d is about 1.3 MA.

The basic components of the z-discharge transport channel are illustrated in Fig. 1. The azimuthal magnetic field produced by the discharge current I_c confines some fraction of the ion beam within the channel radius r_c . Ions which hit the channel wall are lost. The current returns to ground through a conducting layer on the outside of the insulating tube that confines the discharge plasma. The discharge is established on a microsecond time scale before ion-beam injection and creates a highly ionized few-eV temperature plasma. The resulting channel plasma density is much greater than the beam density so that when the beam arrives complete beam charge and current neutralization²⁵ is assumed. The discharge gas density is chosen to achieve an acceptable combination of weak pinching during the discharge time, low beam energy loss and scattering during transport,¹⁴ and weak return-current-driven hydrodynamic expansion of the plasma.¹⁴ For a 1.5-MA (particle flux), 30-MV Li^{+3} beam with a radius of 1 cm and an initial pulse duration of 40 ns, these constraints require a plasma mass density in the $\mu\text{g}/\text{cm}^3$ range for a discharge current of 80 kA. This translates into a plasma density of about $10^{18}/A_p \text{ cm}^{-3}$, where A_p is the atomic weight of the plasma ion. At this density and few-eV temperatures, the plasma is highly collisional so that magnetic field penetrates the plasma rapidly on the microsecond timescale of the discharge. Therefore, current is uniformly distributed throughout the discharge when the beam enters the channel. Higher density will increase beam energy losses due to collisions with the plasma and decel-

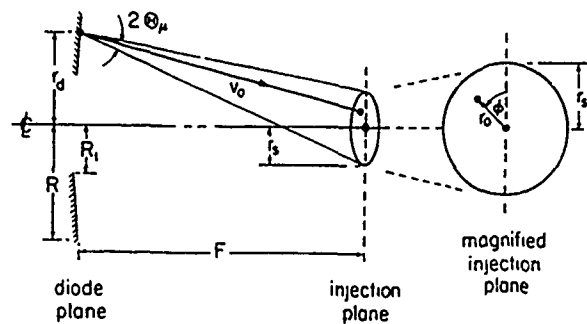


FIG. 2. Schematic of ballistic focusing region illustrating geometry of beam injection into the transport channel.

eration in the axial electric field that drives the return current. Lower densities will result in excessive pinching of the discharge plasma from the stabilizing wall and the growth of magnetohydrodynamic (MHD) instabilities. After beam injection, lower densities will also allow excessive beam-driven channel expansion. For LMF, a density range of a factor of 2 or 3 separates these high- and low-density limits.

Figure 2 shows a schematic representation of the injection geometry. Ions of speed v_0 enter the transport system through an aperture located at the best focus of a focusing ion diode. The diode radius R and focal length F determine the maximum injection angle. Since $R/F \ll 1$ for all cases of interest, this maximum injection angle is given by R/F to first order. The beam microdivergence Θ_μ determines the beam spot size r_s through

$$r_s = F\Theta_\mu. \quad (2)$$

Here, Θ_μ is expressed in radians and must be much smaller than R/F so that $r_s \ll R$. Beam microdivergences as small as about 0.0126 rad have been achieved on applied-B diodes.²⁶

Once in the transport system, ions propagate axially while rotating azimuthally and oscillating radially in the confining magnetic field. The beam radius will ripple at first since the radial oscillations of most ions are initially in phase, and then settle down after phase mixing to a radius r_b (see Fig. 2, Ref. 10). The ion beam rotates in phase space within an envelope defined by the beam and channel parameters. Phase mixing occurs because ions with different initial conditions have slightly different betatron wavelengths, thus leading to a spreading of the region of phase space within the envelope occupied by the beam as it propagates down the transport channel. Complete phase mixing occurs when the beam phase-space distribution fills the entire envelope and no longer changes as a function of propagation distance. This will require many betatron wavelengths, so that phase mixing is, in general, not complete for the finite length LMF systems. The beam radius r_b is larger than r_s because ions injected at r_s can have radial velocities as high as $(R/F)v_0$. In Sec. II, it will be shown that r_b can be written in terms of $r_s = F\Theta_\mu$, R/F , and I_c . Thus, given values of the system parameters F , Θ_μ , R , and I_c fix the value of r_b . When $r_b^2 = r_c^2 = 2r_s^2$, the loss of beam brightness due to phase mixing is minimized.¹³ Since loss

of beam brightness impacts the ability to deliver a beam on target, it will be assumed here that $r_c^2 = 2r_s^2$. If $r_b < r_c$ the entire beam is confined. If $r_b > r_c$, then part of the beam will be lost to the channel wall. The injection efficiency η_i is calculated by determining the fraction of beam ions which hits the wall.

Once the beam exits the channel it propagates ballistically to the target. The standoff distance D required for packing N transport systems around the target is given by

$$D = (Nr_c^2/4f)^{1/2}, \quad (3)$$

where f is the packing fraction (i.e., the fraction of the spherical surface of radius D which is covered by the exit apertures of the transport systems). The calculated phase-space distribution of the beam at the exit of the transport section is used to determine the fraction of the beam that strikes the target at this standoff distance. This standoff efficiency η_s is combined with the injection efficiency to give a total transport efficiency $\eta_t = \eta_i \eta_s$.

Since beam expansion in the standoff region scales with R/F (i.e., the maximum injection angle into the transport system),¹⁴ F should be made as large as possible for a given R . In addition, in order to insure that most of the beam strikes the target, it will be assumed that $r_c \leq r_t$. Since $r_c^2 = 2r_s^2$, this requirement and Eq. (2) imply that $F < r_t/2^{1/2}\Theta_\mu$. For typical values of $r_t = 1$ cm and $\Theta_\mu = 7$ mrad, the diode focal length F must be less than about 100 cm.

Although there are many parameters required to describe the z-discharge transport system, the above considerations provide an approach for calculating η_t . First, it is assumed that target requirements specify r_t, I_t , the ion velocity v_0 , the ion charge state Z and the ion mass m_i . Unless explicitly stated otherwise, it will be assumed for simplicity in this paper that f is fixed at 0.5, and that $r_c^2 = 2r_s^2$. Although f and r_c could be varied, fixing them is reasonable since the range of values for both parameters is limited.

Next, simple models will be used to describe the focusing characteristics of the diode and the emitted ion current density $j_i(r_d)$, where r_d is the radial position on the anode surface of the diode. Complete beam charge and current neutralization by the background plasma will be assumed in the ballistic focusing region, in the transport section, and in the target standoff region. Then, the local injection efficiency $\sigma_i(r_d)$ is calculated for given values of F, Θ_μ , and I_c with r_s determined from Eq. (2). Here $\sigma_i(r_d)$ is the fraction of ions emitted in an annulus centered at radius r_d which are confined in the transport section. Using $j_i(r_d)$ to integrate $\sigma_i(r_d)$ over the active area of the diode yields η_i . Since the diode is expected to be hollow,²² the active area extends from an inner radius R_i to the outer radius R . Since it is difficult to achieve the correct applied magnetic-field profile for $R_i < R/2$ in a extraction geometry for the applied-B diode,² and since the ion emitting area increases slowly as R_i is reduced to small values, it will be assumed that $R_i = R/2$. The scaling of η_i with the parameters F, Θ_μ, R , and I_c can then be determined.

Finally, η_t is calculated from the phase-space distribution of the transported beam for a given value of N with D

determined by r_c from Eq. (3). The product of η_i and η_s yields η_t , the total efficiency of current transfer from the diode to the target. The variation of η_t with the set of system parameters (F, Θ_μ, R, I_c , and N) illustrates the impact of system requirements on the average ion current density at the diode surface J_i . From Eq. (1), J_i is given by

$$J_i = I_d/\pi(R^2 - R_i^2) = 4I_d/(3\pi\alpha N\eta_t R^2). \quad (4)$$

Using $R = 2R_i = 12$ cm for the same example as that following Eq. (1) where $N=20$ and $I_d = 1.3$ MA, Eq. (4) yields $J_i = 3.8$ kA/cm². For $R=8$ cm, $J_i = 8.6$ kA/cm². Experimental measurements of J_i have demonstrated values as high as 6–10 kA/cm² for the applied-B diode.^{26,27}

Section II of this paper provides an analysis of ion orbits in a z-discharge transport channel. This analysis specifies the inner and outer turning points of the ion orbit, so that radial confinement in the transport system can be determined and provides the understanding required to determine losses to the wall. The spread in time-averaged axial velocity of transport ions is also considered here in order to evaluate its effect on time-of-flight bunching of the beam. In Sec. III, a diode model is presented and η_t is calculated for specific system parameters using the results of Sec. II. In Sec. IV, beam spreading in the standoff region is estimated so that η_s can be calculated for a given target size. Finally, results and conclusions are discussed in Sec. V.

It is found from this work that η_t can be close to 100% for values of diode ion current density which have been achieved and values of microdivergence which are less than a factor of 2 smaller than those already achieved on applied-B diode. The analysis suggests that a design for an LMF system with $r_t = 1$ cm and as few as 20 modules could be achievable with $R=8-12$ cm, $F \sim 100$ cm, $J_i = 5-10$ kA/cm², $\theta_\mu \sim 7.5$ mrad, and $I_c = 20-60$ kA. Such a system would have an η_t of 75–100%. The higher efficiencies can be obtained by going to the smaller values of R and/or higher values of I_c for the same N, r_t, F , and Θ_μ . However, a diode radius of less than about 8 cm may be impractical. In addition, it may be technically difficult to establish a z-discharge in a low-mass channel for LMF at currents above about 75 kA.¹⁷ Achieving a smaller Θ_μ will relax the requirements on J_i and improve efficiency, while going to larger θ_μ will require higher values of J_i and decrease efficiency.

II. ORBIT ANALYSIS

In this section, the dynamics of ion propagation in a z-discharge transport channel are analyzed. First, some underlying assumptions are discussed and the constants of the motion are used to derive an expression for the radial turning points. This expression is required to determine the beam envelope radius and the fraction of the injected ions lost to the wall. Next, some characteristic orbits are displayed and some important properties of the orbits are determined. The results of this analysis are used in Sec. III to determine injection efficiency for specific LMF parameters.

A number of physically reasonable assumptions make the problem tractable. First, it is assumed that the discharge current is distributed uniformly in radius at the time of beam injection. In this case,

$$B_\theta(r) = \frac{2I_c r}{r_c c} \quad (5)$$

for $r < r_c$. The plasma density in the channel is assumed to be large compared with the beam density and the plasma conductivity is assumed large enough so that complete charge and current neutralization of the beam occurs. In addition, it is assumed that the plasma density is high enough so that plasma hydromotion is negligible on the time scale of the beam pulse duration, but not so high that beam scattering or energy losses become significant for the length scale of the transport system. Beam propagation is also assumed to be stable. A window in parameter space has been shown to exist where such conditions exist, however these considerations place constraints on the beam power which can be transported in each module.¹⁴ These considerations are not addressed here. Under the conditions discussed above, ion orbits are determined by their single-particle motion in the field of the discharge current given by Eq. (5).

For any given ion, the velocity components at injection into the transport system (i.e., v_{r0} , $v_{\theta0}$, v_{z0}) determine the constants of the motion that govern the orbit. These constants are energy H , angular momentum P_θ , and canonical axial momentum P_z , so that

$$2H/m_i = v_r^2 + v_\theta^2 + v_z^2 = v_0^2 \quad (6)$$

$$P_\theta/m_i = r v_\theta = r_0 v_{\theta0} \quad (7)$$

$$P_z/m_i = v_z - v_c r^2/2r_c^2 = v_{z0} - v_c r_0^2/2r_c^2 \quad (8)$$

where

$$v_c = 2ZeI_c/m_i c^2 \quad (9)$$

The radial equation of motion can be obtained by substituting for v_θ and v_z from Eqs. (7) and (8) into Eq. (6) and solving for v_r . The azimuthal and axial equations of motion can be obtained directly from Eqs. (7) and (8).

Figure 2 illustrates the injection geometry and parameters employed in the analysis. Ions with speed v_0 are emitted from a hollow extraction diode at radii r_d between R_1 and R_2 and are focused onto the entrance of the transport section an axial distance F downstream from the plane of the diode. Ion focusing is accomplished through a combination of electrode shaping and bending in the vacuum magnetic field of the diode gap. The centimeter-sized variations of axial position at different points in the diode are ignored in comparison with the much larger value of F . In accordance with Eq. (2), the microdivergence of the diode θ_μ limits the focused beam to a spot of radius r_s at the injection plane. Consider an ion emitted from the diode in the plane of the page and entering the focal spot at a radius r_o between 0 and r_s , and at an angle ϕ with respect to the plane of the page. (For ions emitted at any azimuth of the diode, ϕ is a velocity-space angle that defines the azimuthal velocity component at emission.) Because the ion orbit is

ballistic in the focusing drift region, the velocity components at the focal spot can be written in cylindrical coordinates as

$$v_{r0} \approx -v_0 r_d \cos \phi / F, \quad (10a)$$

$$v_{\theta0} \approx v_0 r_d \sin \phi / F, \quad (10b)$$

$$v_{z0} = (v_0^2 - v_{r0}^2 - v_{\theta0}^2)^{1/2} \approx v_0 [1 - (r_d/F)^2/2]. \quad (10c)$$

The right-hand sides follow for the hollow-diode, small-injection-angle geometry of LMF for which the scaling $F \gg r_d \gg r_s$ always holds. LMF parameters satisfy

$$r_d/F \sim r_s/r_d \sim v_r/v_0 \sim v_\theta/v_0 \sim O(\epsilon),$$

with $\epsilon \sim 0.1$. This convenient scaling will be applied in the analysis that follows.

Since the transport efficiency is determined only by the number of ions confined within r_c , a complete analytic solution of the equations of motion is unnecessary. The radial turning points of an ion provide all the necessary information. Substituting for v_θ and v_z from Eqs. (7) and (8) into Eq. (6) yields

$$\frac{v_r}{v_0} = \left(\frac{v_{r0}^2 + v_{\theta0}^2}{v_0^2} - \frac{r_0^2 v_{\theta0}^2}{r^2 v_0^2} + \frac{v_c}{v_0} \frac{1 - r^2/r_c^2}{2r_c^2/r_0^2} \right)^{1/2} + O(\epsilon^3), \quad (11)$$

where $v_c/v_0 \sim O(\epsilon^2)$ has been used to eliminate higher-order terms. Setting $v_r = 0$ and using Eq. (10) for v_{r0} and $v_{\theta0}$ provides the turning point equation. To lowest order in ϵ ,

$$(r_o/r_*)^2 \sin^2 \phi - A_c (r_o^2 - r_*^2)/r_c^2 = 1, \quad (12)$$

where

$$A_c = (v_c/v_0) (F/r_d)^2 \quad (13)$$

is of order unity. In Eq. (12), r_* represents either the inner or outer turning point. Solving for r_* yields

$$\frac{r_*^2}{r_o^2} = \frac{r_c^2}{2A_c r_o^2} + \frac{1}{2} \pm \left[\left(\frac{r_c^2}{2A_c r_o^2} + \frac{1}{2} \right)^2 - \frac{r_c^2}{A_c r_o^2} \sin^2 \phi \right]^{1/2}, \quad (14)$$

where the choice of the plus sign corresponds to the outer turning point r_{out} , and the minus sign corresponds to the inner turning point r_{in} . The general solution of Eq. (14) is shown in Fig. 3 for a range of interesting A_c values. For the special case of $\sin \phi = 0$ (i.e., when $v_{\theta0} = 0$ and the ion has zero angular momentum), $r_{in} = 0$ and ions follow betatron orbits. This special case was treated previously.¹⁰ Another special case occurs when both $A_c = (r_c/r_o)^2$ and $v_{r0} = 0$ ($\sin \phi = 1$). In that case, $r_o = r_{in} = r_{out}$ and there is no radial excursion. When $v_{r0} = 0$ ($\sin \phi = 1$), $r_o = r_{out}$ for $A_c > (r_c/r_o)^2$ and $r_o = r_{in}$ when $A_c < (r_c/r_o)^2$. When $v_{r0} \neq 0$ ($|\sin \phi| < 1$), $r_{in} < r_o < r_{out}$ for all A_c .

Figure 3 shows that for fixed $A_c (r_o/r_c)^2$ the largest outer turning occurs when $\phi = 0$. From Eq. (14) this maximum r_{out} is equal to $(r_c^2/A_c + r_o^2)^{1/2}$. The beam envelope radius r_b results when r_o is set equal to its maximum value r_s and A_c is minimized by setting $r_d = R$. The entire beam is confined within the channel when $r_b \leq r_c$. Combining Eqs. (9), (13), and (14) yields

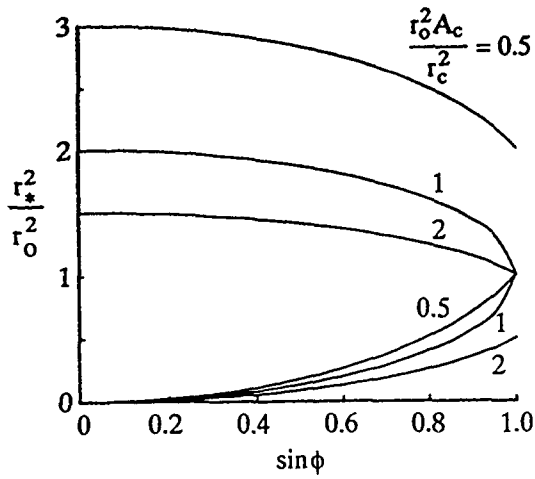


FIG. 3. Plot of radial turning points as a function of $\sin \phi$ for several values of the parameter $r_o^2 A_c / r_c^2$.

$$I_{cm} = \frac{v_o R^2 m c^2}{2ZeF^2 [1 - (r_s^2 / r_c^2)]} = \frac{v_o R^2 m c^2}{ZeF^2}, \quad (15)$$

where I_{cm} defines the channel current required to match the beam radius r_b to the channel radius r_c . The condition $r_s^2 = r_c^2/2$ is applied in the right-hand side of Eq. (15) to minimize beam emittance growth during transport.¹³

Figure 4 illustrates some sample orbits for system parameters in the regime of interest for LMF: 30-MeV Li^{+3} ($v_o = 2.9 \times 10^9$ cm/s) with $r_s = 0.75$ cm, $I_c = 80$ kA, and $r_d/F = 0.1$. From Eqs. (9) and (13), $A_c = 2.29$. Figures 4(a)–4(c) display orbits for ions injected at $r_o = 0.6r_s$ with $\phi = 0^\circ, 30^\circ,$ and 90° . With all other parameters equal, the orbits illustrated in Fig. 4 are self-similar in the radial scale, i.e., they are invariant in r/r_o . This self-similar property follows from the dependence of v_r on only r/r_o in Eq. (11). Figure 4 exhibits orbits that are nearly closed, where closed means that after a finite number of excursions be-

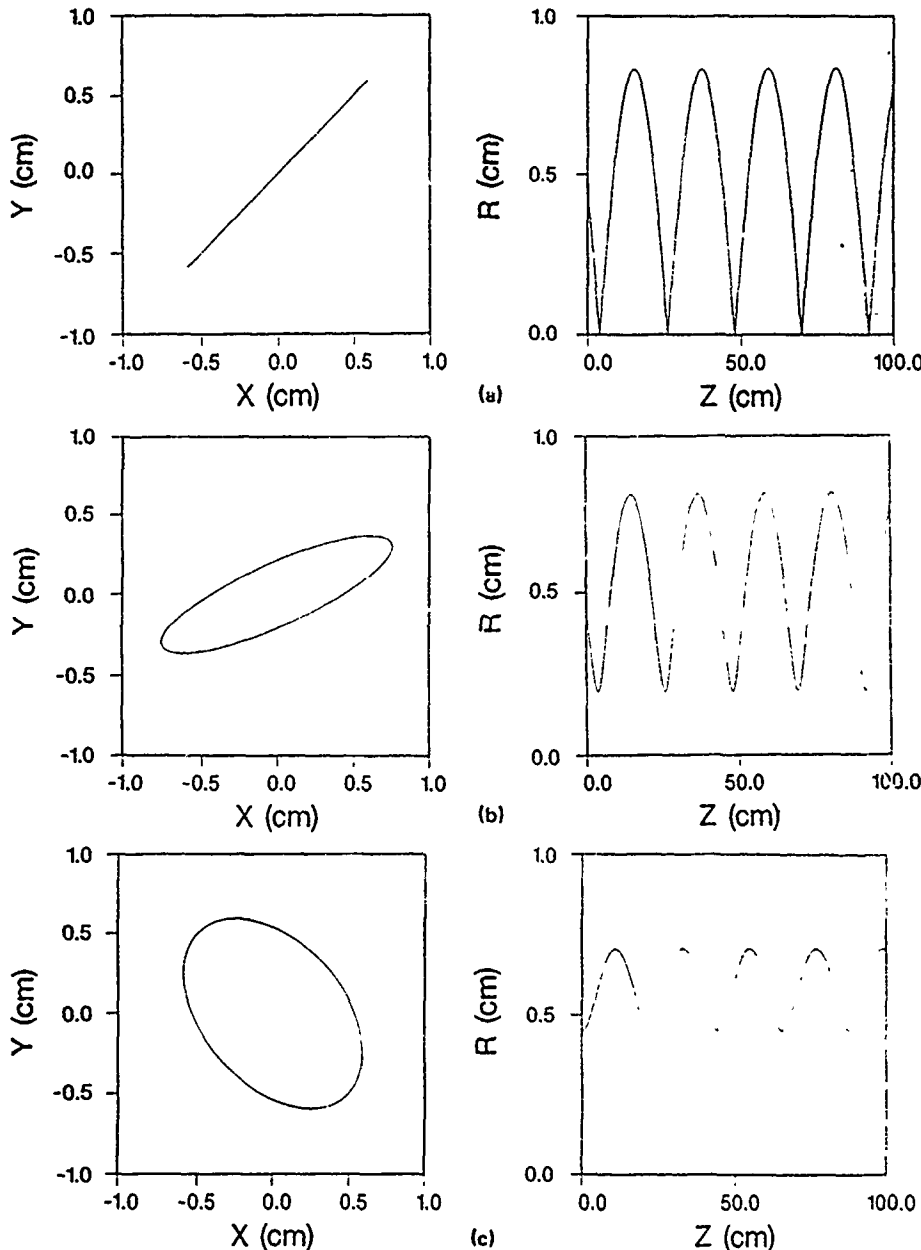


FIG. 4 (a) Typical ion orbit with $I = 80$ kA, $r_s = 0.75$ cm, $r_d/F = 0.1$, and with $r_o = 0.6r_s$ and $\phi = 0^\circ$. (b) Typical ion orbit with $I = 80$ kA, $r_s = 0.75$ cm, $r_d/F = 0.1$, and with $r_o = 0.6r_s$ and $\phi = 30^\circ$. (c) Typical ion orbit with $I = 80$ kA, $r_s = 0.75$ cm, $r_d/F = 0.1$, and with $r_o = 0.6r_s$ and $\phi = 90^\circ$.

tween r_{in} and r_{out} the ion motion exactly repeats itself. This closure property can be shown to be a general property of the ion orbits. The rotation number, defined as the change in azimuth experienced by an ion executing one complete radial oscillation, is

$$\Delta\theta = 4 \int_{\theta(r_{in})}^{\theta(r_{out})} d\theta = 4 \int_{r_{in}}^{r_{out}} \frac{v_{\theta} dr}{rv_r} \quad (16)$$

Using Eqs. (7) for $v_{\theta}(r)$ and Eq. (11) for $v_r(r)$, Eq. (16) can be integrated by expanding the integrand in powers of ϵ yielding $\Delta\theta = 2\pi + O(\epsilon^2)$. Thus, within terms of $O(\epsilon^2)$, all ions close their orbits by making one complete azimuthal rotation for each radial betatron oscillation. Similarly, using Eq. (8) for $v_z(r)$, Eq. (10c) for v_{z0} , and Eq. (11) for $v_r(r)$, the betatron wavelength is found to be

$$\lambda_{\beta} = 4 \int_{z(r_{in})}^{z(r_{out})} dz = 4 \int_{r_{in}}^{r_{out}} \frac{v_z dr}{v_r} = 2\pi r_c \left(\frac{v_0}{v_c} \right)^{1/2} [1 + O(\epsilon^2)]. \quad (17)$$

Here, λ_{β} is the axial distance an ion travels in completing one full radial betatron oscillation. This result is identical to that calculated previously for the case with zero angular momentum.¹⁰

Another quantity of interest for LMF is the spread in time-averaged axial velocity of transported ions in the z-discharge channel. This spread determines a limit to ion-beam pulse compression by axial bunching produced by a ramped accelerating voltage pulse. The time-averaged axial velocity is given by

$$\frac{\langle v_z \rangle}{v_0} = \frac{\int_0^T v_z dt}{v_0 \int_0^T dt} = \frac{\int_{r_{in}}^{r_{out}} v_z dr / v_r}{\int_{r_{in}}^{r_{out}} dr / v_r} = 1 - \frac{v_c r_o^2}{4v_0 r_c^2} - \frac{v_{r0}^2 + v_{\theta 0}^2}{4v_0^2} + O(\epsilon^4). \quad (18)$$

Here again Eq. (8) was used for $v_z(r)$, and Eq. (11) was used for $v_r(r)$. In addition, Eq. (10c) was used for v_{z0} . Using Eqs. (10a) and (10b) for v_{r0} and $v_{\theta 0}$, reduces Eq. (18) to

$$\frac{\langle v_z \rangle}{v_0} = 1 - \frac{v_c r_o^2}{4v_0 r_c^2} - \frac{r_d^2}{4F^2} + O(\epsilon^4). \quad (19)$$

The minimum value of $\langle v_z \rangle / v_0$ occurs when $r_o = r_s$ and $r_d = R$, and the maximum value occurs when $r_o = 0$ and $r_d = R/2$. Thus, the spread in arrival times associated with channel transport $(\Delta t)_c$ for ions simultaneously injected into the channel at a given energy will be

$$(\Delta t)_c = \frac{L}{v_0} \left(\frac{v_c}{8v_0} + \frac{3R^2}{16F^2} \right), \quad (20)$$

where L is the axial length of the channel. When $r_b = r_c$, $v_c = 2v_0 R^2 / F^2$, so that

$$(\Delta t)_c = (7R^2 / 16F^2) (L / v_0) \equiv (\Delta t)_{cb}.$$

When $r_b < r_c$, $(\Delta t)_c > (\Delta t)_{cb}$, and when $r_b > r_c$, so that some ions hit the channel wall, $(\Delta t)_c < (\Delta t)_{cb}$. For z-discharge transport, $(\Delta t)_c$ is comparable with the spread in arrival times associated with the ballistic focusing of the beam, which is given by $(\Delta t)_f = (3R^2 / 8F^2) (F / v_0)$. The sum of $(\Delta t)_c$ and $(\Delta t)_f$ must be small compared with the bunched beam pulse length τ_r . For $R/F = 0.1$, $F = 100$ cm, $L = 300$ cm, and $v_0 = 2.9 \times 10^9$ cm/s, $(\Delta t)_{cb} + (\Delta t)_f = 0.6$ ns, whereas $\tau_r \sim 10$ ns. Thus, spreading in arrival times is negligible.

III. INJECTION EFFICIENCY

Before proceeding with a description of the calculation of the local injection efficiency, the ion diode model will be described. As indicated in Fig. 2 the anode plane of the diode is located a distance F from the entrance of the transport channel and the annular emission surface extends from $R/2$ to R . The ion beam produced by the diode is assumed to be azimuthally uniform and monoenergetic at any given instant in time. Focusing is achieved by a combination of geometric focusing from anode shaping and magnetic focusing from ion orbit bending in the self-field of the beam. Ions emitted at radius r_d are aimed at the center of the entrance aperture with an average angle of r_d / F and are assumed to be uniformly distributed in velocity about this average angle within a cone of half angle Θ_{μ} . It is also assumed that Θ_{μ} is the same for all r_d . As illustrated in Fig. 2, this provides the beam spot size $F\Theta_{\mu}$ given in Eq. (2). For simplicity, the distribution of ion current density $j_i(r_d)$ over the emission surface will also be taken to be uniform. Although these simplifying assumptions will be used here for the functional forms of both the ion current density and microdivergence at the source, the analysis that follows can easily be extended to treat more complicated functional forms.

The local injection efficiency $\sigma_i(r_d)$ is the fraction of ions emitted from the diode at radius r_d which are confined within the channel. Ions that have an outer turning point that is larger than r_c are lost to the wall [i.e., $\sigma_i(r_d)$ is calculated by determining the fraction of the beam ions that have $r_{out} \leq r_c$]. As discussed in Sec. I, the free parameters that need to be set are F, Θ_{μ}, R , and I_c . Using $j_i(r_d)$ to weight the integral of $\sigma_i(r_d)$ over the area of the diode yields the injection efficiency, η_i , which can be written as

$$\eta_i = \frac{2\pi \int_{R/2}^R j_i(r_d) \sigma_i(r_d) r_d dr_d}{2\pi \int_{R/2}^R j_i(r_d) r_d dr_d} = \frac{8}{3R^2} \int_{R/2}^R \sigma_i(r_d) r_d dr_d. \quad (21)$$

The expression on the right-hand side is obtained by applying the assumptions $R_i = R/2$ and $j_i(r_d) = J_i = \text{const}$.

Since $\sigma_i(r_d)$ is the ratio of the number of ions that are transported without hitting the wall to the total number of ions injected into the transport channel, the required information for the calculation is contained in the equation for the outer turning point of the ion orbits. The outer turning

point depends on the ion position and velocity at the entrance to the transport system. However, because the beam is generated in the diode, the most physically meaningful approach for calculating $\sigma_i(r_d)$ is to express this turning point in terms of the initial conditions at the diode. Thus, the first step in calculating $\sigma_i(r_d)$ will be to relate the initial conditions of an ion at the entrance aperture to the transport system to those at the diode source plane. Note this is one step back from the approach in the previous section, where details of the ion orbits were related to the position and velocity at injection.

Here the subscript d will indicate that a variable is evaluated at the source plane. Using conservation of angular momentum to substitute for v_θ , and using $z = v_{zd}t$, the radial equation of motion in the ballistic drift focusing region can be written as

$$\frac{d^2r}{dz^2} - \left(\frac{r_d v_{\theta d}}{v_{zd}}\right)^2 \frac{1}{r^3} = 0. \quad (22)$$

The solution to this equation is

$$r^2(z) = r_d^2 + 2 \frac{v_{rd}}{v_{zd}} r_d z + [(v_{rd}^2 + v_{\theta d}^2)/v_{zd}^2] z^2. \quad (23)$$

To lowest order in ϵ , $v_{zd} = v_0$, so that evaluation at the channel entrance plane (i.e., at $r = r_0$ and $z = F$) yields

$$\left(\frac{r_d}{F} + \frac{v_{rd}}{v_0}\right)^2 + \left(\frac{v_{\theta d}}{v_0}\right)^2 = \left(\frac{r_0}{F}\right)^2. \quad (24)$$

Equation (24) is an equation for a circle of radius r_0/F centered at $v_{rd}/v_0 = -r_d/F$ and $v_{\theta d}/v_0 = 0$ in the $v_{rd}/v_0, v_{\theta d}/v_0$ plane. Ions generated at the source plane at radius r_d within the circular region of velocity space defined by Eq. (24) will arrive at the entrance plane within a circular region of configuration space of radius r_0 . For $r_0 = r_s$, the radius of the circular region in $v_{rd}, v_{\theta d}$ space is defined to be the beam microdivergence Θ_μ , through Eq. (2).

The radial and azimuthal velocity components at the entrance plane can be put into a simple form after defining a polar coordinate system centered on the circle defined by Eq. (24). Let ρ and ψ be the coordinates of that polar system defined by

$$\rho^2 = \left(\frac{r_d}{F} + \frac{v_{rd}}{v_0}\right)^2 + \left(\frac{v_{\theta d}}{v_0}\right)^2 \quad (25a)$$

and

$$\psi = \tan^{-1} \left(\frac{v_{\theta d}/v_0}{(r_d/F) + (v_{rd}/v_0)} \right). \quad (25b)$$

Taking advantage of the conservation of angular momentum and kinetic energy, the velocity components at the entrance plane can be written as

$$v_{r_0} = v_0[\rho - (r_d/F) \cos \psi] \approx -v_{rd} \cos \psi / F \quad (26a)$$

and

$$v_{\theta_0} = v_{rd} \sin \psi / F. \quad (26b)$$

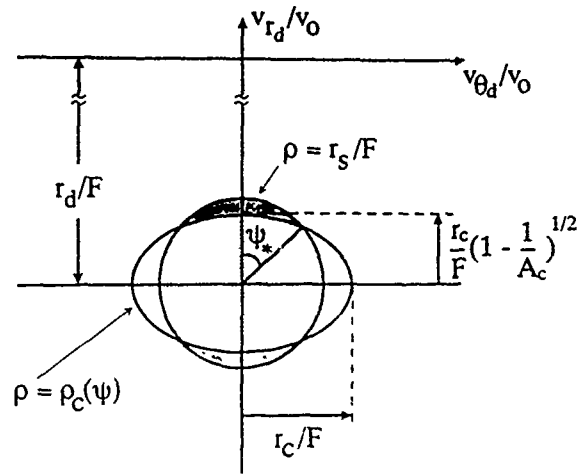


FIG. 5. Plot of outer turning point curve (oval) and beam distribution (circle) in velocity space at diode surface. Lightly shaded region contains ions that are transported, while ions in darkly shaded region hit the channel wall.

Comparing Eqs. (10) and (26) shows the equivalence of the configuration space angle ϕ at the entrance of the transport system with the velocity space angle ψ at the source plane. As in the previous section, Eqs. (6)–(8) can now be used with Eq. (26) to derive an expression for determining the ion turning points but now in terms of ρ and ψ . This procedure yields through lowest order in ϵ

$$(\rho/\rho_*)^2 \sin^2 \psi - (A_c F^2/r_c^2)(\rho^2 - \rho_*^2) = 1, \quad (27)$$

where A_c is defined in Eq. (13) and $\rho_* = r_*/F$, so that Eq. (12) is recovered. For $r_{out} = r_c$, $\rho_* = r_c/F$ and Eq. (27) generates a curve that corresponds to initial conditions in $v_{rd}, v_{\theta d}$ space for ions with an outer turning point of r_c . Equation (27) can be solved for $\rho(\rho_*, \psi)$, which, as noted, will be a function of ρ_* and ψ . Defining $\rho_c \equiv \rho(r_c/F, \psi)$, this curve can be written as

$$\rho_c^2 = \frac{r_c^2}{F^2} \left(\frac{1 - (1/A_c)}{1 - (\sin^2 \psi / A_c)} \right). \quad (28)$$

Figure 5 illustrates this curve. Ions with initial conditions that lie outside the outer turning point curve ρ_c will have $r_{out} > r_c$ and will hit the channel wall.

The object then is to compare the area of $v_{rd}, v_{\theta d}$ space occupied by the beam with that bounded by this outer turning point curve. Referring to Fig. 5, beam ions leaving the diode at r_d occupy an area in $v_{rd}, v_{\theta d}$ space defined by a disk of radius $\rho = r_s/F = \Theta_\mu$ and centered at $r_d = r_d/F$ and $v_{\theta d} = 0$ (shaded regions in Fig. 5). Ions that lie inside ρ_c are confined (lightly shaded region in Fig. 5). Ions that lie outside ρ_c hit the wall and are lost (heavily shaded region in Fig. 5). Because A_c is a function of r_d [see Eq. (13)] and the center of the beam phase-space disk varies with r_d , there is a different phase-space picture similar to Fig. 5 for each value of r_d . In order for all ions to be confined within r_c , the circle of radius $\rho = \Theta_\mu$ enclosing the ion distribution must lie within ρ_c for all r_d .

Since the beam is uniformly distributed in phase space, the local injection efficiency $\sigma_l(r_d)$ can be determined by calculating the areas of the appropriate regions of phase space for each r_d between R and $R/2$. Remembering that $r_c^2 = 2r_s^2$ is assumed, note first that for $A_c > 2$, the beam phase space lies entirely within ρ_c so that $\sigma_l(r_d) = 1$. Then note that as A_c is decreased from 2 to 1, the area enclosed by the ρ_c curve approaches zero, so that $\sigma_l(r_d) = 0$ for $A_c < 1$. For $1 < A_c < 2$,

$$\sigma_l(r_d) = 1 - \frac{4 \int_0^{\psi_*} \int_{\rho_c}^{r_c/F} \rho d\rho d\psi}{4 \int_0^{\pi/2} \int_{\rho_c}^{r_c/F} \rho d\rho d\psi} \quad (29)$$

where

$$\psi_*(r_d) = \sin^{-1}\{[2 - A_c(r_d)]^{1/2}\} \quad (30)$$

defines the angle at which the ρ_c curve and the $\rho = \Theta_\mu$ curve intersect (see Fig. 5). In obtaining Eq. (30), Eq. (2) and $r_c^2 = 2r_s^2$ were used. Combining these results and doing the required integrations yields

$$\sigma_l(r_d) = \begin{cases} 1, & A_c > 2, \\ 1 - \frac{2\psi_*}{\pi} + \frac{4}{\pi} \left(1 - \frac{1}{A_c}\right)^{1/2} \tan^{-1} \left[\left(1 - \frac{1}{A_c}\right)^{1/2} \tan \psi_* \right], & 2 > A_c > 1, \\ 0, & A_c < 1, \end{cases} \quad (31)$$

where A_c and ψ_* are functions of r_d through Eqs. (13) and (30), respectively. The injection efficiency η_i is calculated from Eq. (21) using Eq. (31) for $\sigma_l(r_d)$.

Since σ_l and ψ_* only depend on the system parameters through the combination in A_c , a universal injection efficiency curve can be derived. Defining A_{cm} as

$$A_{cm} = A_c(r_d=R) = (v_c/v_0)(F/R)^2, \quad (32)$$

η_i is plotted as a function of $1/A_{cm}$ in Fig. 6. The three system parameters, F , R , and I_c are contained in A_{cm} which defines η_i . The fourth system parameter Θ_μ is used through Eq. (2) to define the channel size, which will be required for determining the standoff efficiency.

IV. STANDOFF EFFICIENCY

An efficient multimodular approach requires N beams with r_c comparable with r_t which overlap at the target location. Each transport system must be terminated at a standoff distance D from the target in order to pack the N systems around the target. An expression for this standoff distance is given in Eq. (3). Considerations outside the scope of this paper are required to determine an appropriate value for the packing fraction f . Here, in most cases it will be assumed that $f = 0.5$. The purpose of this section is to calculate the standoff efficiency η_s and the total transport efficiency $\eta_t = \eta_i \eta_s$ as functions of N , r_s and the four system parameters, F , Θ_μ , R , and I_c . This result will then be used to calculate J_i in terms of these six system parameters. Each of the N diodes must generate an ion-beam current of J_d , which corresponds to an ion source current density given by Eq. (4). Here, a bunching factor $\alpha = 2$ and a wave form efficiency $\eta_w = 0.8$ will be assumed. The values of J_i that are calculated in this manner can then be compared with presently achievable values of the ion source current density to determine the practicality of the specific system.

The standoff efficiency η_s is defined as the fraction of the beam that strikes a target of radius r_t located at a distance D from the exit of the transport channel. In principle, η_s could be calculated analytically by using the velocity space distribution at the exit of the transport channel to ballistically project the beam forward to the target. Integrating over velocity space at the target location would then provide the density profile required for calculating η_s . In practice, this is a formidable problem because of the complexity of the transported beam distribution function and the difficulty in performing the inversion required to project the distribution forward. However, an analysis of the asymptotic behavior of the beam expansion, augmented by numerical simulations, provides an adequate description of the standoff efficiency.

The asymptotic behavior of beam expansion can be determined by examining the ballistic trajectory of ions at

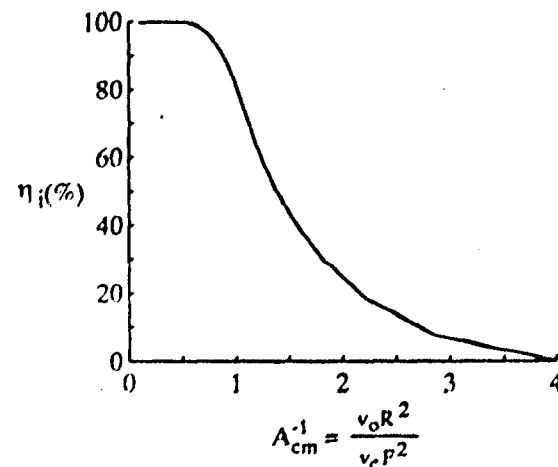


FIG. 6. Universal plot of injection efficiency as a function of the parameter $1/A_{cm}$.

large distances from the exit of the transport channel. the ballistic trajectory is given by

$$r^2(z) = \{r(0) + [zv_r(0)/v_0]\}^2 + z^2[v_\theta(0)/v_0]^2, \quad (33)$$

which, for large z , becomes

$$r^2(z) = \{[v_r^2(0) + v_\theta^2(0)]/v_0^2\}z^2. \quad (34)$$

Here, $z=0$ is defined as the exit of the transport system. The asymptotic behavior of the beam envelope is determined by evaluating Eq. (34) for an ion with the largest transverse energy on exiting the transport system.

The transverse energy can be found from Eq. (6) after using Eq. (8) to substitute for v_r . Maximizing this expression yields to lowest order in ϵ

$$(v_1^2)_{\max} = [v_r^2(0) + v_\theta^2(0)]_{\max} = v_0 v_c r_b^2 / r_c^2, \quad (35)$$

where $r_b = r_c$ for $I_c < I_{cm}$ and $r_b = r_c[(I_{cm} + I_c)/2I_c]^{1/2}$ for $I_c > I_{cm}$ with I_{cm} defined in Eq. (15) and with $r_s^2 = r_c^2/2$. Combining Eqs. (34) and (35) provides an expression for the radius of the asymptotic envelope, $r_a(z)$, given by

$$r_a(z) = z(v_c r_b^2 / v_0 r_c^2)^{1/2}. \quad (36)$$

Numerical simulations also show that for $z \geq z_a$, where $r_a(z_a) \equiv r_c$, Eq. (36) approximates the beam envelope closely. Normalizing z to $(v_0 r_b^2 / v_0 r_c^2)^{1/2} r_c$ is then a natural scaling.

With this scaling in mind, a systematic series of numerical simulations with system parameters in the range of interest were run to find an analytic fit for η_s . In these simulations a collection of ions are propagated ballistically from the diode through the focusing region, and then ion trajectories in the transport channel are calculated from the equations of motion to propagate the beam to the channel exit. Ions were randomly distributed in phase space at the diode according to the diode model described in Sec. III, and ions that hit the channel wall during transport are removed from the beam. The injection efficiency calculated from these simulation results closely matched (within $\sim 1\%$) the analytic result presented in Fig. 6. The ion-beam distribution in phase space at the channel exit is used to ballistically project the beam forward to the target. The standoff efficiency is then calculated by counting the number of ions that hit the target compared with the number of ions that exited the channel. Figures 7, 8, and 9 show plots of the standoff efficiency as a function of the scaled standoff distance $\xi \equiv (z/r_c)(r_b^2 v_c^2 / r_c^2 v_0^2)^{1/2}$ for $r_c/r_t = 0.7, 0.85$, and 1.0, respectively. This procedure yields the fit

$$\eta_s = \begin{cases} 1, & \xi < 2.76 - 2.19r_c/r_t \\ \left(2.26 - \frac{r_c}{r_t}\right) - 0.456\xi, & \xi > 2.76 - 2.19r_c/r_t \end{cases} \quad (37)$$

The fit given in Eq. (37) is shown as the dashed lines in Figs. 7-9 and agrees within about $\pm 10\%$ or better for these simulations in the $\eta_s > 0.5$ region of interest. Other simulations have shown deviations as large as $\pm 20\%$ from the fit for η_s . These occasional larger deviations result from the details of the beam location in phase space at the exit from the channel because of incomplete phase mixing.

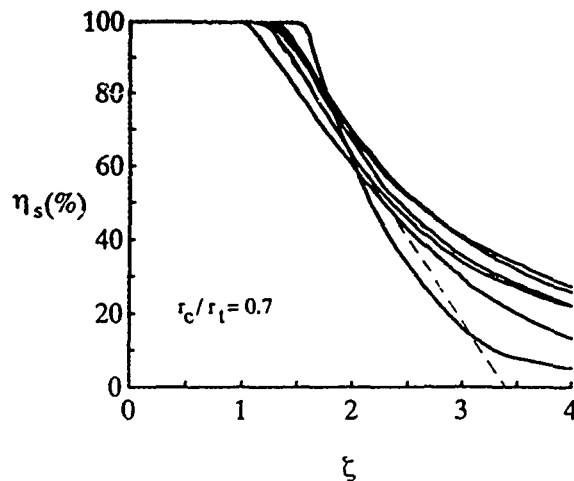


FIG. 7. Standoff efficiency as a function of normalized standoff distance from six sample simulations with $r_c = 0.7r_t$. Dashed line shows linear fit given in Eq. (37).

Generally, the channel length must be tens of betatron wavelengths long for complete phase mixing to occur, while here L is only on the order of $10\lambda_\beta$. This problem can be dealt with by simulating individual cases of interest; however, for the purposes of presenting an overview, the fit for η_s provides a reasonable average value for the standoff efficiency when $\eta_s > 0.5$. For $\eta_s < 0.5$, the numerical data fall more slowly than the linear fit, so that the fit underestimates η_s ; however, this region of low η_s values is not of great interest.

By setting $z=D$, where D is defined in Eq. (3), the normalized standoff distance becomes

$$\xi_D = (Nv_c r_b^2 / 4fv_0 r_c^2)^{1/2}. \quad (38)$$

Combining the results presented in Fig. 6 for η_i and the fit given in Eq. (37) for η_s (evaluated at $\xi = \xi_D$) provides the desired expression for $\eta_t = \eta_i \eta_s$ in terms of the six system

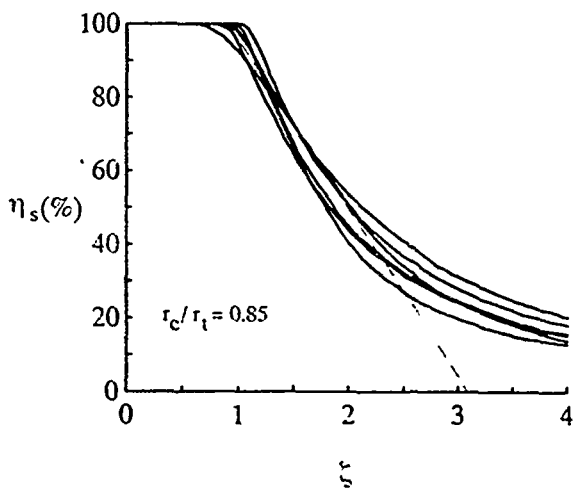


FIG. 8. Standoff efficiency as a function of normalized standoff distance from six sample simulations with $r_c = 0.85r_t$. Dashed line shows linear fit given in Eq. (37).

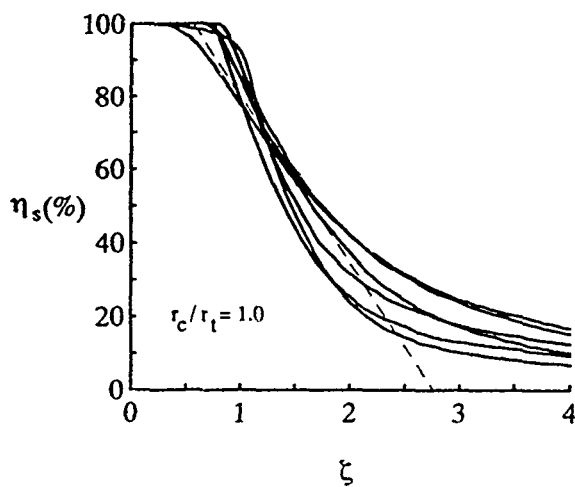


FIG. 9. Standoff efficiency as a function of normalized standoff distance from six sample simulations with $r_c = r_t$. Dashed line shows linear fit given in Eq. (37).

parameters N , r_b , F , Θ_μ , R , and I_c . Figures 10–17 show plots of η_t for various cases. In all cases r_t is set equal to 1.06 cm and $r_c < r_r$. A typical value of v_c is 6.6×10^7 cm/s for $I_c = 80$ kA. The four points marked with an \times on each of Figs. 11, 15, and 17 are derived from specific simulation results for $I_c = 80$ kA and illustrate the uncertainty of the fit to η_s . The points marked on Fig. 17 show the largest deviations observed.

In general, lower η_t is obtained as R is increased at fixed I_c and higher η_t is obtained as I_c is increased at fixed R . Figures 10, 11, and 12 illustrate cases where the product of F and Θ_μ is fixed so that $r_c = r_t$ but Θ_μ has decreasing values of 10, 7.5, and 5 mrad, respectively. For a fixed R , results show that, as Θ_μ is increased (or F is decreased), higher I_c is required to maintain the same high η_t . This stems from Eq. (15), which shows that a higher I_c is required to confine a beam with larger R/F . Figures 13 and

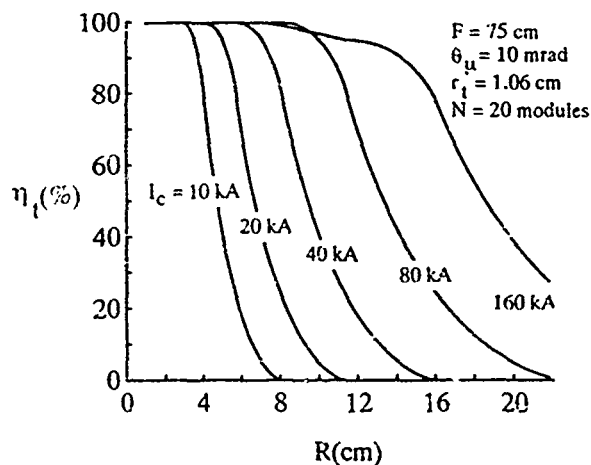


FIG. 10. Plot of transport efficiency as a function of diode radius with $F = 75$ cm, $\Theta_\mu = 10$ mrad, $r_t = 1.06$ cm, and $N = 20$ for various values of I_c . Also $r_s = F\Theta_\mu = 0.75$ cm and $f = 0.5$.

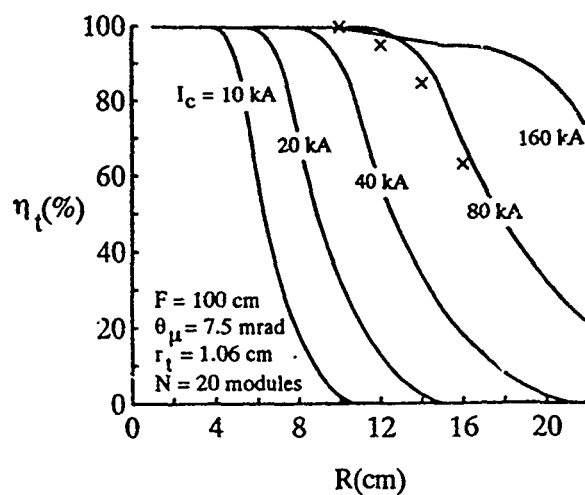


FIG. 11. Plot of transport efficiency as a function of diode radius with $F = 100$ cm, $\Theta_\mu = 7.5$ mrad, $r_t = 1.06$ cm, and $N = 20$ for various values of I_c . Also $r_s = F\Theta_\mu = 0.75$ cm and $f = 0.5$. The points marked with \times are from numerical simulations.

14 show results for smaller radius channels. Figure 13 should be compared with Fig. 11 and Fig. 14 with Fig. 12. In both comparisons, in order to obtain the same η_t at fixed R , higher I_c is required for the smaller radius channels. Again this stems from Eq. (15) because smaller F was used to obtain the smaller beam size at fixed Θ_μ .

Equations (37) and (38) show that the standoff efficiency only depends weakly on R through r_b when $I_c > I_{cm}$. In general, the standoff efficiency only plays a minor role in the parameter regimes shown, with the $\eta_s < 1$ only at large I_c (i.e., only for some of the $I_c = 80$ and 160 kA curves). The packing fraction f can have an important effect on the η_s . For most of the cases shown here, it was assumed that $f = 0.5$. Figure 15 shows a case where f was decreased by a factor of 2 to 0.25, allowing for more space between channels but increasing the standoff distance D by

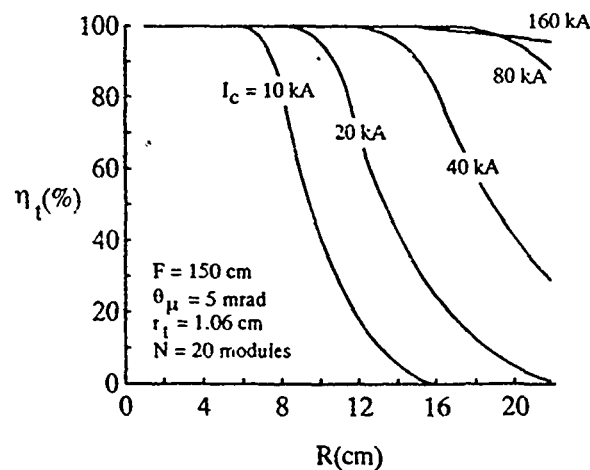


FIG. 12. Plot of transport efficiency as a function of diode radius with $F = 150$ cm, $\Theta_\mu = 5$ mrad, $r_t = 1.06$ cm, and $N = 20$ for various values of I_c . Also $r_s = F\Theta_\mu = 0.75$ cm and $f = 0.5$.

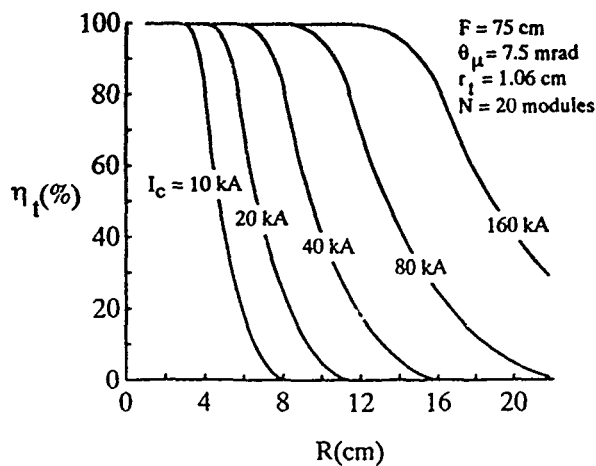


FIG. 13. Plot of transport efficiency as a function of diode radius with $F=75$ cm, $\Theta_\mu = 7.5$ mrad, $r_t = 1.06$ cm, and $N=20$ for various values of I_c . Also $r_s = F\Theta_\mu = 0.5625$ cm and $f = 0.5$.

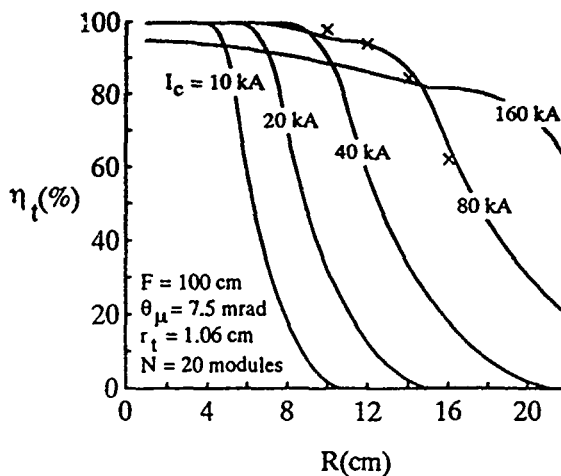


FIG. 15. Plot of transport efficiency as a function of diode radius with $F=100$ cm, $\Theta_\mu = 7.5$ mrad, $r_t = 1.06$ cm, and $N=20$ for various values of I_c . Also $r_s = F\Theta_\mu = 0.75$ cm and $f = 0.25$. The points marked with \times are from numerical simulations.

$\sqrt{2}$. Comparing Figs. 11 and 15 shows the effect on η_t of decreasing f .

The η_t plots displayed so far apply to 20-module systems (i.e., $N=20$). Figures 16 and 17 show results for systems with $N=10$ and 30, respectively. These two figures should be compared with Fig. 11. Since N only affects η_t through η_s because of the dependence of D on N , the results only differ at large I_c . As N is increased from 10 to 30, the η_t curve for $I_c = 160$ kA drops by $\sim 12\%$.

Figures 18–20 show plots of J_i from Eq. (4) with $I_t = 33$ MA, $\alpha = 2$, and $\eta_w = 0.8$. Figures 18, 19, and 20 derive their values of η_t from Figs. 16, 11, and 17, respectively. Figure 19 shows that, for $F=100$ cm, $\Theta_\mu = 7.5$ mrad, $N=20$, and $r_t = 1.06$ cm, an LMF system can be designed with $J_i \sim 5$ kA/cm² at a diode radius of $R=10$ cm and a channel current of $I_c = 80$ kA. Somewhat lower values of J_i are possible for larger values of I_c and R . This

value of J_i is less than values already achieved with an applied-B diode. As would be expected, Fig. 18 shows that using fewer modules increases the required ion source current density with all other factors held fixed, while Fig. 20 shows that using more modules relaxes the required ion source current density. Using more modules, however, increases the cost and complexity of the facility. Although not displayed, it is also found that going to smaller Θ_μ will relax the requirements on J_i while going to larger Θ_μ will require even higher values of J_i .

V. SUMMARY AND CONCLUSIONS

The LMF has been proposed for the study of high-gain, high-yield ICF targets. A multimodular light-ion approach requires transport of intense ion beams over distances of a few meters in order to isolate the ion diode hardware from the target explosion and to provide suffi-

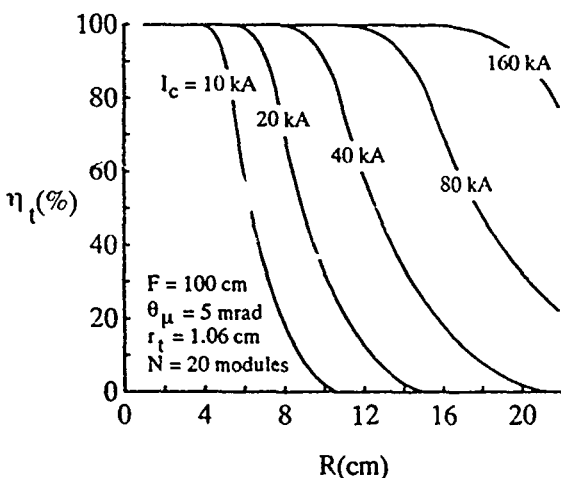


FIG. 14. Plot of transport efficiency as a function of diode radius with $F=100$ cm, $\Theta_\mu = 5$ mrad, $r_t = 1.06$ cm, and $N=20$ for various values of I_c . Also $r_s = F\Theta_\mu = 0.5$ cm and $f = 0.5$.

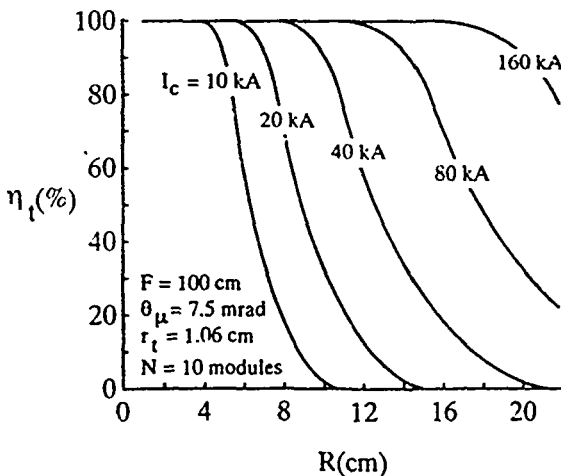


FIG. 16. Plot of transport efficiency as a function of diode radius with $F=100$ cm, $\Theta_\mu = 7.5$ mrad, $r_t = 1.06$ cm, and $N=10$ for various values of I_c . Also $r_s = F\Theta_\mu = 0.75$ cm and $f = 0.5$.

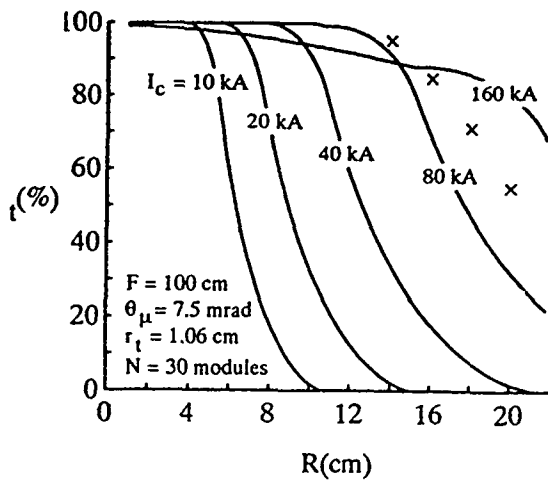


FIG. 17. Plot of transport efficiency as a function of diode radius with $F=100$ cm, $\Theta_\mu = 7.5$ mrad, $r_t = 1.06$ cm, and $N=30$ for various values of I_c . Also $r_s = F\Theta_\mu = 0.75$ cm and $f = 0.5$. The points marked with \times are from numerical simulations.

cient propagation distance for power compression by time-of-flight bunching. This study has investigated the use of a z-discharge transport channel for beam propagation. Phenomena important to z-discharge ion-beam transport have been studied and the optimum total transport efficiency within a range of achievable system parameters has been determined.

A number of simplifying assumptions were used to reduce the many parameters required to describe the z-discharge transport system. First, it was assumed that target considerations specify the target radius, the power on target, and the ion energy, charge state, and mass. It was also assumed that the bunching factor is fixed at 2, that the packing fraction is fixed at 0.5, and that the wave form efficiency is fixed at 0.8. Next, simple models were used to describe the focusing characteristics of the diode and the emitted ion current density in order to specify the beam

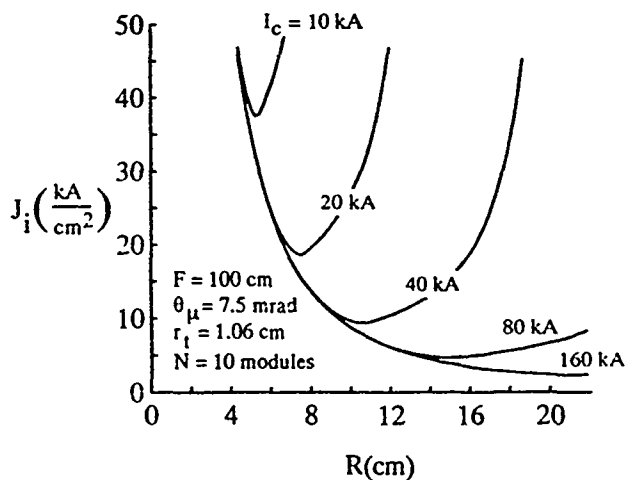


FIG. 18. Plot of required diode ion current density as a function of diode radius with $F=100$ cm, $\Theta_\mu = 7.5$ mrad, $r_t = 1.06$ cm, and $N=10$ for various values of I_c . Also $r_s = F\Theta_\mu = 0.75$ cm and $f = 0.5$.

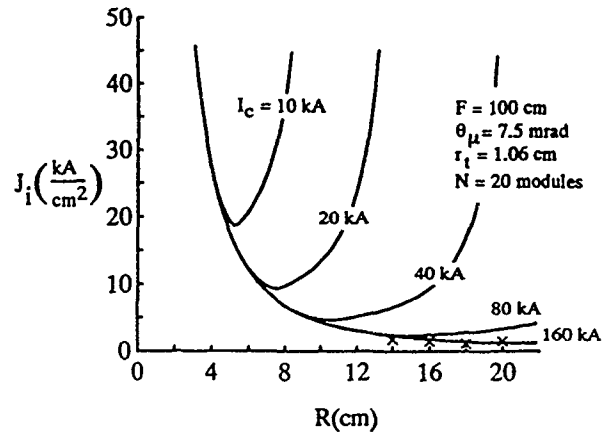


FIG. 19. Plot of required diode ion current density as a function of diode radius with $F=100$ cm, $\Theta_\mu = 7.5$ mrad, $r_t = 1.06$ cm, and $N=20$ for various values of I_c . Also $r_s = F\Theta_\mu = 0.75$ cm and $f = 0.5$. The points marked with \times are from numerical simulations.

distribution at the entrance of the transport system. It was assumed that ions emitted at radius r_d are aimed at the center of the entrance aperture a distance F from the diode with an average angle $r_d/F \ll 1$ and are uniformly distributed in perpendicular velocity space about this average angle within a cone of half-angle $\Theta_\mu \ll R/F$. This velocity space distribution was chosen for mathematical simplicity. A more realistic assumption might be a Gaussian distribution which would yield results very similar to those presented here. Because $\Theta_\mu \ll R/F \ll 1$, additional losses would be minimal, being restricted to a very small number of ions in the extreme wings of the Gaussian distribution. It is also assumed that Θ_μ and the ion current density are the same for all r_d , and that the focal distance F does not change in time. Finally, complete charge and current neutralization were assumed in the ballistic focusing region, in the z-discharge transport section, and in the target standoff region.

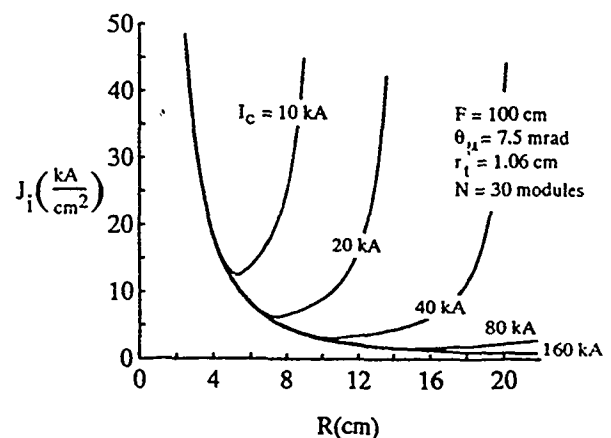


FIG. 20. Plot of required diode ion current density as a function of diode radius with $F=100$ cm, $\Theta_\mu = 7.5$ mrad, $r_t = 1.06$ cm, and $N=30$ for various values of I_c . Also $r_s = F\Theta_\mu = 0.75$ cm and $f = 0.5$.

Section II of this paper provides an analysis of ion orbits in a z-discharge transport channel. This analysis specifies the inner and outer turning points of the ion orbit, so that radial confinement in the transport system can be determined and provides the understanding required to determine losses to the channel wall. In order to confine the entire beam, the channel current must be large enough so that all ions have outer turning points less than r_c . This current is given by I_{cm} in Eq. (15).

Other important properties of the ion orbits were also identified. All ions have nearly closed orbits and exhibit betatronlike radial oscillations with an axial wavelength given by λ_β in Eq. (17). The spread in time-averaged axial velocity of the transported ions was also considered in order to evaluate its effect on time-of-flight bunching of the beam. The spread in arrival times is given in Eq. (20). Results show that beam spreading during transport is comparable with the spreading during focusing and will not limit the ability to achieve the required bunching for LMF.

The results of the orbit analysis in Sec. II were used in Sec. III to calculate the injection efficiency. The injection efficiency η_i is calculated by determining the fraction of beam ions that hit the channel wall because of too large transverse energy. First, the local injection efficiency σ_i was calculated for given values of F , Θ_μ , and I_c , and then integrated over the diode surface with $j_i(r_d)$ to find η_i . The active area of the diode was assumed to extend from an inner radius, $R_i = R/2$, to the outer radius R . Because σ_i depends only on the combination of system parameters found in A_c , a generalized plot of injection efficiency (Fig. 6) could be generated. Each point along the curve in Fig. 6 corresponds to a given system defined by choosing the three system parameters F , R , and I_c to specify A_{cm} [Eq. (32)] and the fourth system parameter Θ_μ to specify the channel radius ($r_c^2 = 2r_s^2 = 2F^2\Theta_\mu^2$).

Finally, in Sec. IV the standoff efficiency was calculated for a given N and r_t from estimates of beam expansion in the field-free standoff region. The expression used for η_s was derived from fitting data from simulations and using scaling arguments from analysis of the asymptotic beam envelope radius. The product of η_i and η_s yields η_p , the total efficiency of current transfer from the diode to the target. The variation of η_i with N then illustrates the impact of system requirements on the average ion current density at the diode surface J_i . It is found from this work that η_i can be close to 100% for values of diode ion current density that have been achieved and values of microdivergence which are less than a factor of 2 smaller than those already achieved on applied-B diodes. The analysis suggests a point design for an LMF system with $r_t = 1$ cm and as few as 20 modules could be achievable with $R = 8-12$ cm, $F \sim 100$ cm, $J_i = 5-10$ kA/cm², $\Theta_\mu \sim 7.5$ mrad, and I_c as low as 20-60 kA. Such a system would have an η_i of 75%-100%. The higher efficiencies can be obtained by going to smaller values of R and/or higher values of I_c for the same N , r_t , F , and Θ_μ . However, a diode radius of less than about 8 cm may be impractical. In addition, it may be technically difficult to establish a z-discharge in a low-mass channel for LMF at currents above about 75 kA.¹⁷ Achiev-

ing a smaller Θ_μ will relax the requirements on J_i and improve efficiency, while going to larger Θ_μ will require higher values of J_i and decrease efficiency.

The analysis presented here can easily be extended to treat more complicated models for focusing and emission. Future work will consider transport constraints associated with hydrodynamics, possible beam-plasma instabilities, beam energy losses, and beam ion scattering and charge exchange during propagation.

ACKNOWLEDGMENTS

The authors would like to acknowledge useful discussions with Dr. J. J. Watrous during the early stages of this work. This work was supported by the U.S. Department of Energy under contract No. DE-AC04-76-DP00789.

- ¹J. J. Ramirez, R. W. Stinnett, D. L. Johnson, C. L. Olson, T. A. Mehlhorn, J. T. Crow, J. P. Quintenz, K. R. Prestwich, M. P. Desjarlais, R. E. Olson, G. O. Allshouse, T. H. Martin, J. P. VanDevender, D. L. Cook, S. A. Slutz, K. B. Coachman, T. R. Lockner, B. N. Turman, S. A. Goldstein, and J. N. Olsen, *Fusion Tech.* **15**, 350 (1989).
- ²D. L. Johnson, J. J. Ramirez, R. W. Stinnett, and K. B. Coachman, in *Proceedings of the 1989 Particle Accelerator Conference*, edited by F. Bennett and J. Kapt, Chicago, IL, March 20-23, 1989, p. 1017.
- ³J. J. Watrous, D. Mosher, J. M. Neri, P. F. Ottinger, C. L. Olson, J. T. Crow, and R. R. Peterson, *J. Appl. Phys.* **69**, 639 (1991).
- ⁴C. L. Olson, in *Proceedings of the 1988 Linear Accelerator Conference*, edited by C. Leemann, Newport News, VA, October 3-7, 1988, p. 34.
- ⁵T. A. Mehlhorn and J. P. Quintenz, in *Proceedings of the 1989 Particle Accelerator Conference*, edited by F. Bennett and J. Kapt, Chicago, IL, March 20-23, 1989, p. 1014.
- ⁶D. Mosher, D. D. Hinshelwood, J. M. Neri, P. F. Ottinger, J. J. Watrous, C. L. Olson, and T. A. Mehlhorn, in *Proceedings of the 5th International Conference on High-Power Particle Beams*, edited by B. N. Breizman and B. A. Knyazev, Novosibirsk, U.S.S.R., July 2-5, 1990, p. 26.
- ⁷C. L. Olson, in *Proceedings of the 1989 Particle Accelerator Conference*, edited by F. Bennett and J. Kapt, Chicago, IL, March 20-23, 1989, p. 1011.
- ⁸G. A. Moses, G. L. Kulcinski, D. Bruggink, R. Engelstad, E. Lovell, J. MacFarlane, Z. Musicki, R. Peterson, M. Sawan, I. Sviatoslavsky, L. Wittenberg, G. Kessler, U. von Mollendorff, E. Stein, D. Cook, R. Olson, I. Smith, P. Corcoran, H. Nishimoto, and J. Fockler, *Fusion Tech.* **15**, 756 (1989).
- ⁹R. R. Peterson and G. A. Moses, in *Proceedings of the 7th International Conference on High-Power Particle Beams*, edited by W. Bauer and W. Schmidt, Karlsruhe, Germany, July 4-8, 1988, p. 625.
- ¹⁰P. F. Ottinger, D. Mosher, and S. A. Goldstein, *Phys. Fluids* **23**, 999 (1980).
- ¹¹P. F. Ottinger, D. Mosher, and S. A. Goldstein, *Phys. Fluids* **22**, 332 (1979).
- ¹²P. F. Ottinger, D. Mosher, and S. A. Goldstein, *Phys. Fluids* **24**, 104 (1981).
- ¹³P. F. Ottinger, S. A. Goldstein, D. Mosher, and D. G. Colombant, in *Proceedings of the 5th International Conference on High-Power Particle Beams*, edited by R. J. Briggs and A. J. Toepfer, San Francisco, CA, September 12-14, 1983, p. 97.
- ¹⁴D. Mosher, D. G. Colombant, S. A. Goldstein, and P. F. Ottinger, in *Proceedings of the 4th International Topical Conference on High Power Electron and Ion Beam Research and Technology*, edited by H. J. Doucet and J. M. Buzzi, Palaiseau, France, June 29-July 3, 1981, p. 19. For more details, see National Technical Information Service Document No. ADA121472 (P. F. Ottinger, S. A. Goldstein, and D. Mosher, NRL Memorandum Report No. 4948, Nov. 12, 1982). Copies may be ordered from the National Technical Information Service, Springfield, VA 22161. The price is \$5.00 plus a \$3.00 handling fee. All orders must be prepaid.
- ¹⁵F. L. Sandel, S. J. Stephanakis, F. C. Young, and W. L. Oliphant, in

- Proceedings of the 4th International Topical Conference on High Power Electron and Ion Beam Research and Technology, edited by H. J. Doucet and J. M. Buzzi, Palaiseau, France, June 29–July 3, 1981 p. 129.
- ¹⁶J. M. Neri, J. R. Boller, G. Cooperstein, D. Mosher, P. F. Ottinger, V. E. Scherrer, S. J. Stephanakis, and F. C. Young, in Proceedings of the 7th International Conference on High-Power Particle Beams, edited by W. Bauer and W. Schmidt, Karlsruhe, Germany, July 4–8, 1988, p. 165.
- ¹⁷D. D. Hinshelwood, P. J. Goodrich, J. M. Neri, W. F. Oliphant, S. J. Stephanakis, J. J. Watrous, and F. C. Young, in IEEE Conference Record Abstracts, the 1990 IEEE International Conference on Plasma Science, edited by J. Benford, Oakland, CA, May 21–23, 1990, p. 143.
- ¹⁸J. N. Olsen and R. J. Leeper, *J. Appl. Phys.* **53**, 3397 (1982).
- ¹⁹S. Nakai, K. Imasaki, S. Miyamoto, S. Higaki, T. Ozaki, A. Yoshinouchi, H. Fujita, K. Mima, K. Nishihara, T. Yabe, S. Ido, Y. Ohgaki, and C. Yamanaka, *Laser and Particle Beams* **1**, 29 (1983).
- ²⁰J. R. Freeman, L. Baker, and D. L. Cook, *Nucl. Fusion* **22**, 383 (1982).
- ²¹D. J. Johnson, R. J. Leeper, W. A. Stygar, R. S. Coats, T. A. Mehlhorn, J. P. Quintenz, S. A. Slutz, and M. A. Sweeney, *J. Appl. Phys.* **58**, 12 (1985).
- ²²S. A. Slutz and D. B. Seidel, *J. Appl. Phys.* **59**, 2685 (1986).
- ²³F. Winterberg, *Plasma Phys.* **17**, 69 (1975).
- ²⁴S. A. Goldstein, G. Cooperstein, R. Lee, D. Mosher, and P. F. Ottinger, in IEEE Conference Record-Abstracts, the 1978 IEEE International Conference on Plasma Science, edited by F. Schwirzke, Monterey, CA, May 15–17, 1978, p. 112.
- ²⁵D. Hammer and N. Rostoker, *Phys. Fluids* **13**, 1831 (1970).
- ²⁶J. P. VanDevender, J. A. Swegle, D. J. Johnson, K. W. Bieg, E. J. T. Burns, J. W. Poukey, P. A. Miller, J. N. Olsen, and G. Yonas, *Laser and Particle Beams* **3**, 93 (1985).
- ²⁷P. L. Dreike, E. J. T. Burns, S. A. Slutz, J. T. Crow, D. J. Johnson, P. R. Johnson, R. J. Leeper, P. A. Miller, L. P. Mix, D. B. Seidel, and D. F. Wenger, *J. Appl. Phys.* **60**, 878 (1986).

Transport of Intense Light Ion Beams

PAUL F. OTTINGER, MEMBER, IEEE, PHILLIP J. GOODRICH, DAVID D. HINSELWOOD, DAVID MOSHER, JESSE M. NERI, DAVID V. ROSE, STAVROS J. STEPHANAKIS, AND FRANK C. YOUNG, SENIOR MEMBER, IEEE

Invited Paper

Theoretical and experimental research concerning two techniques for transporting intense light ion beams is described. The first technique uses the magnetic field associated with a wall-stabilized z-discharge to radially confine and guide the beam, and the second technique uses the magnetic field from a central current-carrying wire. The ion beam for the experiments is generated and weakly focused onto the aperture of the transport system using a pinch-reflex ion diode on the Naval Research Laboratory Gamble II generator. Typically, 1.2-MeV, 100-kA proton beams are transported within radii as small as 1 cm. High efficiency transport of beams has been demonstrated for both techniques over distances of a few meters. Beam charge and current neutralization were also confirmed. In z-discharge channels, beams were transported up to 5 m, and beam currents up to 400 kA have been transported in 2-cm radius channels. Nuclear diagnostics and shadowboxes were used to measure beam transport efficiency and phase space information for comparison with theoretical predictions. Particle transport efficiencies as high as 100% for the z-discharge technique and 80% for the wire-guided technique were observed. Energy losses for transported ions were less than 10% for both techniques.

I. INTRODUCTION

Using light ion beams as an inertial confinement fusion (ICF) driver will require transport of intense ion beams over distances of a few meters in order to isolate the ion-diode hardware from the target explosion [1] and to provide sufficient propagation distance for power compression by time-of-flight bunching [2], [3]. Several different transport techniques have been proposed [4], [5]. These include a wire-guided transport system [5]–[8], a wall-stabilized z-discharge transport channel [5], [9]–[15], an achromatic lens system with ballistic transport [16]–[17], a laser-initiated freestanding z-discharge transport channel [18]–[20], and self-pinched transport [21]. Wall-stabilized z-discharge transport and wire-guided transport have been

studied extensively at the Naval Research Laboratory (NRL). Experimental and theoretical results of this research are summarized in this paper.

The components of the z-discharge transport channel are illustrated in Fig. 1. The azimuthal magnetic field produced by the discharge current, I_c , confines some fraction of the ion beam within the channel radius r_c . Ions which hit the channel wall are lost. The discharge current returns to ground through a conducting layer on the outside of the insulating tube which confines the discharge plasma. The discharge is established on a microsecond time scale before ion-beam injection and creates a fully ionized, few-eV temperature plasma. The plasma density is much greater than the beam density so that complete beam charge and current neutralization results [22]. The discharge gas density is chosen to achieve an acceptable combination of weak pinching of the discharge, low-beam energy loss and scattering during transport, and weak-return current-driven hydrodynamic expansion of the plasma [23], [24]. These constraints require a plasma mass density in the $\mu\text{g}/\text{cm}^3$ range or a plasma density of about $10^{18}/A_p \text{ cm}^{-3}$, where A_p is the atomic weight of the plasma ion. For this density and few-eV temperature, the plasma is highly collisional so that the magnetic field penetrates the plasma rapidly on the microsecond timescale of the discharge. For higher density, beam-energy losses are increased by collisions with the plasma and by deceleration in the larger axial electric field of the more resistive plasma. Lower densities will result in excessive plasma pinching and in the growth of MHD instabilities. After beam injection, lower densities also allow excessive beam-driven channel expansion.

Figure 2 shows a schematic representation of the injection geometry appropriate for both transport techniques discussed here. A pinch-reflex ion-diode [25]–[27] of radius R is used to produce a proton beam on the Gamble II generator at NRL [28]. Ions are weakly focused by self magnetic bending of the ion orbits in vacuum over the distance Δ between the anode and the cathode foil. Since the ion current density varies as r^{-1} in this type diode, the

Final manuscript received November 25, 1991. This work was supported by the U.S. Department of Energy through Sandia National Laboratories, Albuquerque, NM.

P. F. Ottinger, D. Mosher, J. M. Neri, S. J. Stephanakis, and F. C. Young are with the Plasma Physics Division, Naval Research Laboratory, Washington, DC 20375-5000.

P. J. Goodrich, D. D. Hinshelwood, and D. V. Rose are with JAYCOR, Inc., Vienna, VA 22182.

IEEE Log Number 9201881.

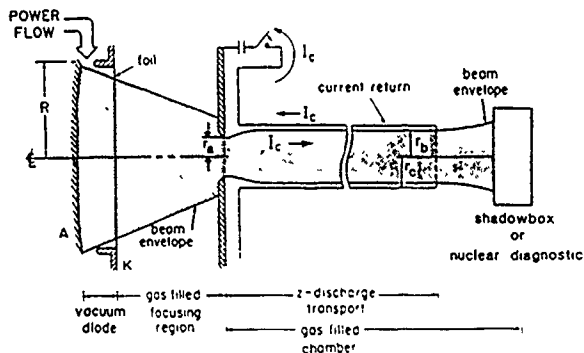


Fig. 1. Schematic of z-discharge transport system.

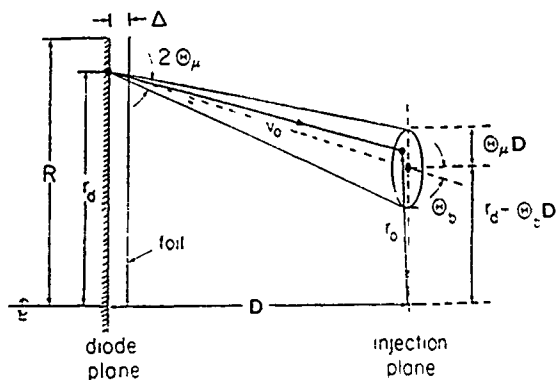


Fig. 2. Schematic of ballistic focusing region illustrating geometry of beam injection into the transport channel.

bending angle is independent of radius and is given by $\theta_b = \omega_c \Delta / v_0 \sim I_i(t) / [V(t)]^{1/2}$, where $\omega_c = 2eZI_i / m_i c^2 R$ and c is the speed of light. Here, v_0 is the ion speed exiting the diode. $I_i(t)$, and $V(t)$ are the ion beam current and the diode voltage, and eZ and m_i are the ion charge and mass. Ions emitted at radius r_d are assumed to be uniformly distributed in velocity about this bending angle within a microdivergence cone of half angle θ_μ . It is assumed that θ_μ is the same for all r_d and all time. Ions follow ballistic trajectories in the gas-filled region between the foil and the entrance aperture of the transport system. Ions of speed v_0 enter the transport system through an aperture of radius r_a located a distance, D , from the anode surface. Ions with $r_0 > r_a$ hit the channel entrance plate and are lost. The diode radius, R , and the distance, D , specify the maximum injection angle into the transport section to be about R/D where, in general, $R/D \ll 1$.

Once in the transport system, ions propagate axially while rotating azimuthally and oscillating radially in the confining magnetic field. The beam radius in the channel, r_b , is larger than the entrance aperture, r_a , because ions injected at r_a can have radial velocities as high as $(R/D)v_0$. For a channel wall radius of r_c , the entire beam is confined if $r_b \leq r_c$. If $r_b > r_c$, then part of the beam will be lost to the wall. The injection efficiency, η_i , for z-discharge transport is calculated by determining the fraction of beam

ions which hit the wall. Once the beam exits the channel, it again propagates ballistically. The standoff efficiency, η_s , is calculated by determining the fraction of the beam exiting the channel which would hit a target of specified radius and distance from the channel exit. The product of these two efficiencies is defined as the transport efficiency $\eta_t = \eta_i \eta_s$. Note that these efficiencies are defined in terms of particle losses and not energy losses.

The wire-guided transport technique is similar to the z-discharge technique and is illustrated in Fig. 3. The transported ion beam is confined by the azimuthal magnetic field produced by an axial current flowing in a gas-embedded guide wire. The wire current is returned through a small number N_w of wires outside the beam envelope. Once the beam is injected, the beam head quickly ionizes the gas surrounding the wire, and beam charge and current neutralization is established [22]. The same constraints on beam-energy loss and scattering and channel expansion apply for wire-guided transport as for z-discharge transport, so that the required gas density is similar. However, since ions injected into the channel with low angular momentum intersect the wire, the injection efficiency for wire-guided transport is calculated by determining the fraction of beam ions which hit the wire. There is no outer wall in this case, but ions can be lost to large radius if the return-current wires are too close to the beam envelope.

Diagnostics of the ion beam include shadowboxes and prompt- γ radiation from lithium-fluoride targets. The shadowbox consists of a pinhole array and witness plate mounted just outside the channel exit and is used to sample the transverse velocity distribution of the transported beam [7], [8], [13], [14]. Prompt γ rays from $^{19}\text{F}(p, \alpha \gamma)$ reaction are used to obtain timing information and qualitative information about transport efficiency [29]. These prompt- γ measurements of transport efficiency are imprecise because the cross section for this reaction is sensitive to the proton energy. A second technique with much weaker energy sensitivity uses 16-MeV prompt γ rays from the $^7\text{Li}(p, \gamma)$ reaction to activate an adjacent copper target via the $^{63}\text{Cu}(\gamma, n)^{62}\text{Cu}$ reaction [30]. After a shot, the 10-min half-life ^{62}Cu β^+ -decay is measured to determine the time-integrated proton flux. Results of these measurements are compared with theoretical predictions to evaluate beam transport. Results demonstrate that beam-energy transport is highly efficient; the only significant energy loss is classical stopping in the gas. The experimental beam injection efficiency and the beam phase-space distribution at the channel exit (from shadowbox measurements) are consistent with theoretical predictions for both transport techniques, thus confirming beam charge and current neutralization during transport.

Z-discharge transport is discussed in detail in Section II. Both experimental and theoretical results are presented. A similar discussion of wire-guided transport is given in Section III. Section IV provides a brief outline of system considerations for multimodule ICF systems using these transport techniques. Results and conclusions are presented in Section V.

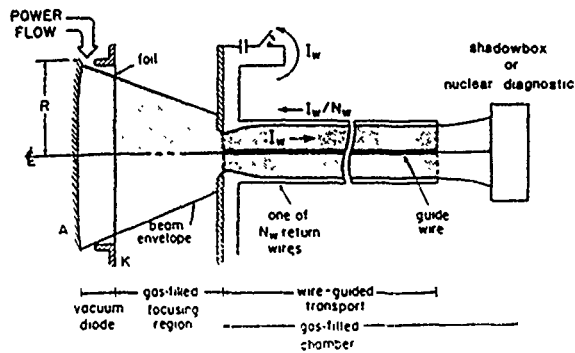


Fig. 3. Schematic of wire-guided transport system.

II. Z-DISCHARGE TRANSPORT

The z-discharge carries a current, I_c , which is distributed radially across the channel out to the wall at radius r_c . For any given ion, the radial position r_o and velocity components at injection into the transport system (v_{ro} , $v_{\theta o}$, and v_{zo}) determine the constants of the motion that govern the orbit. These constants are energy, H , angular momentum, P_θ , and canonical axial momentum, P_z . Using the constants of the motion to solve for v_r yields

$$\frac{v_r}{v_o} = \left(\frac{v_{ro}^2 + v_{\theta o}^2}{v_o^2} - \frac{r_o^2 v_{\theta o}^2}{r^2 v_o^2} + \frac{v_c}{v_o} \frac{r_o^{N+1} - r^{N+1}}{(N+1)r_c^{N+1}} \right)^{1/2} + O(\epsilon^3) \quad (1)$$

where the model $B_\theta \sim r^N$ has been applied, $v_c/v_o \equiv 2eZI_c/m_i v_o c^2$ and the small parameter $\epsilon \sim R/D \sim 0.1$ has been used to eliminate higher order terms. By setting $v_r = 0$ in (1), the radial turning points for the ion orbit are obtained. Ions with outer turning points larger than r_c , hit the wall and are lost. Using the diode model discussed in Section I to model the injected beam, (1) can be utilized to calculate the injection efficiency. Results of this calculation will be compared with experimental measurements.

The minimum channel current I_{cm} required to confine all injected ions within the channel radius r_c is determined by setting $v_r = 0$ at $r = r_c$ for an ion with maximum transverse energy, i.e., an ion entering the channel at the entrance aperture radius r_a from the edge of the anode at radius R . This minimum current is given by

$$I_{cm} = \frac{(N+1)v_o m_i c^2}{4Ze(1 - (r_a^{N+1}/r_c^{N+1}))} \left(\frac{R}{D} \right)^2 \quad (2)$$

For $I_c < I_{cm}$, ions with larger transverse energies will be lost to the wall.

Integrating (1) yields the ion trajectory. Sample orbits for the $N = 1$ case, that of a uniform discharge current density, are shown in Fig. 4 for different injection conditions. The orbits are closed, with the motion repeating itself after the ion propagates axially one betatron wavelength, $\lambda_\theta = 2\pi r_c (v_c/v_o)^{1/2}$. The ion orbits which pass through the aperture and do not hit the wall can be followed

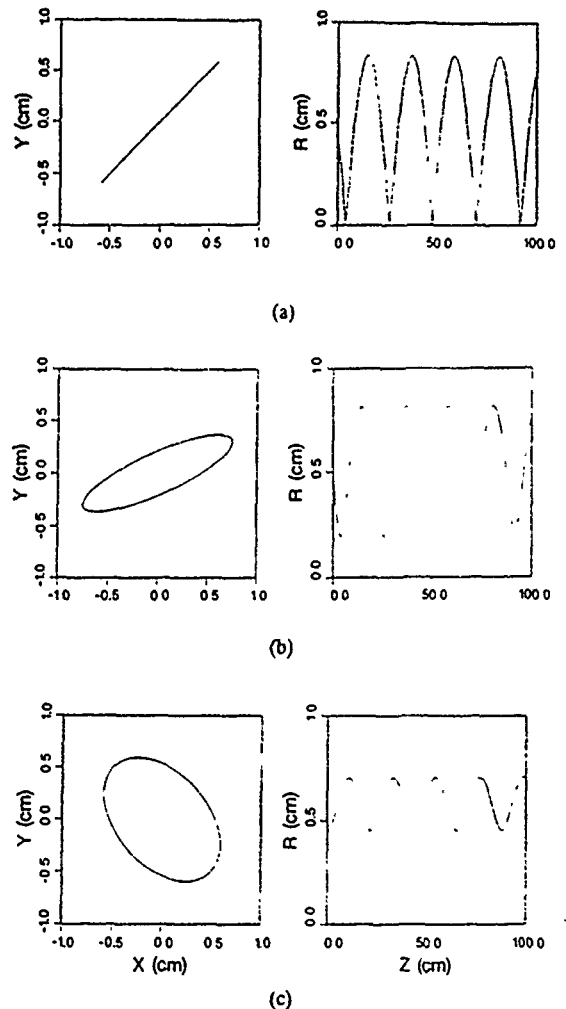


Fig. 4. Z-discharge ion orbits with $I_c = 80$ kA and $r_c = 0.45$ cm for (a) $v_{ro}/v_o = 0.1$ and $v_{\theta o}/v_o = 0$, (b) $v_{ro}/v_o = 0.08661$, and $v_{\theta o}/v_o = 0.05$, and (c) $v_{ro}/v_o = 0$, and $v_{\theta o}/v_o = 0.1$.

to the channel exit. The resulting ion-beam phase-space distribution can be used to calculate a shadowbox image for comparison with experimental images. After accounting for beam-energy loss in the foil and gas due to classical slowing down, the calculated beam distribution at the channel exit can also be used to predict prompt- γ yields for the nuclear diagnostics.

In recent NRL experiments [31], [32], 1.2-MeV proton beams were transported with $R = 5$ cm, $D = 20$ –30 cm, $r_a = 0.85$ cm, and $r_c = 1.25$ cm. For the experimental parameter set with $D = 30$ cm, (2) yields $I_{cm} = 45$ kA for $N = 1$, a typical value used in the experiments. The diode vacuum is separated from the gas (typically 2 torr air) in the focusing region and transport channel by a 1.8- μ m thick polycarbonate foil. An insulating inner liner defines r_c and separates the discharge from a conducting outer tube that returns the current in a low inductance path that helps to stabilize the plasma against MHD modes. The insulator also provides a breakdown surface that permits the discharge to be struck in a several-meter long column of gas with a low-voltage (40 kV) capacitor bank. Magnetic probe and interferometric measurements [33] suggest that the current

has not quite penetrated to the axis of the discharge and that the plasma is just beginning to pinch when the ion beam is injected into the channel. Timing beam injection in this manner (about $1 \mu\text{s}$ into the discharge current rise for the NRL experiments) also avoids the development of the sausage and kink instabilities. Typically, the best agreement between theory and experiment is obtained with N between two and three for the magnetic field modeled by $B_\theta \sim r^N$.

Z-discharge transport experiments have been carried out using 1.6-, 2.5-, and 4-cm diameter channels with lengths of $i-5 \text{ m}$. The transport efficiency is determined by comparing measured prompt- γ signals with computed signals derived from beam current and voltage traces. The computed signals take into account energy losses in the transmission foil and gas and the energy dependence of the thick-target γ -ray yield. These measurements demonstrate that transport efficiencies approach 100% for all geometries with up to 400 kA transported in the 4-cm diameter channel [13].

A comparison of measured and calculated nuclear-activation yields was used to infer ion transport efficiency as a function of D for shots with $I_c \sim 40 \text{ kA}$, $r_c = 1.25 \text{ cm}$, and $R = 5 \text{ cm}$ [31], [32]. Nuclear diagnostic targets were placed either at the entrance or exit of the transport channel, and Li prompt- γ yields from front and rear targets were compared after adjustments were made to compensate for small shot-to-shot variations in the diode-voltage and ion-current histories. Experimental yields are plotted versus the theoretically calculated yields in Fig. 5 for targets at the channel input. Calculated yields were normalized using a shot with a large area target designed to intercept the total ion current and a best fit was obtained by adjusting the assumed value for the microdivergence θ_μ . Figure 6 compares yields obtained with targets at the channel exit with calculated yields for $N = 3$. If the injection efficiency η_i is defined as the number of ions transported divided by the number of ions which pass through the aperture, these results imply that $\eta_i = 0.69$ for $D = 20 \text{ cm}$, 0.84 for 25 cm, and 0.96 for 30 cm. The scatter of the data in Fig. 6 from the line is a measure of the uncertainty in these values. This analysis indicates that the transport efficiency is reduced, as expected from (2), for anode-to-channel-aperture separations less than 30 cm due to loss of confinement of ions with higher transverse energy. Higher I_c would trap these ions and increase η_i . Only about 8% of the beam energy was lost during transport which is consistent with classical slowing down in the gas.

Experimental and calculated shadowbox images are shown in Fig. 7 for $D = 20, 25,$ and 30 cm . The calculated images reproduce the trends in spot size and location of the measured images. The size of the damage spots associated with each pinhole is a direct measure of the radial velocity spread at the pinhole radius. The maximum velocity spread can be defined as $\theta_{\max} = \delta/\zeta = \Delta v_r/v$, where δ is the spot radius and ζ is the distance from the pinhole to the witness plate. Figure 8 compares measurements of θ_{\max} on a single shot (circles) with orbit theory. From conservation of axial canonical momentum for an ion with $v_\theta = 0$ that

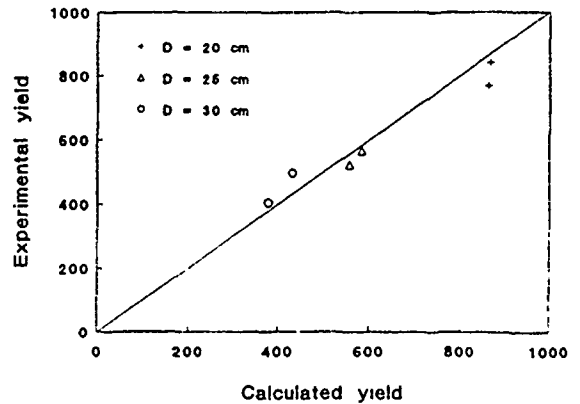


Fig. 5. Experimental yield versus calculated yield for lithium-activation targets at the input of the z-discharge transport channel.

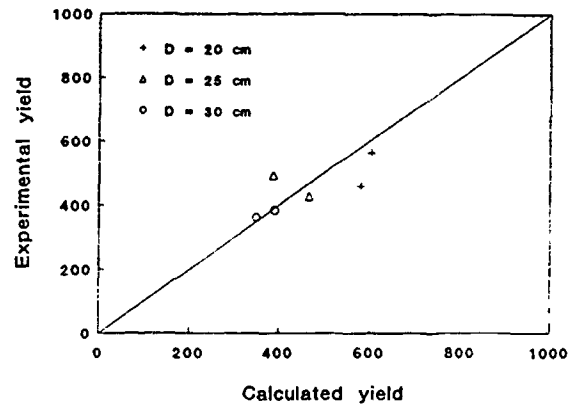


Fig. 6. Experimental yield versus calculated yield for lithium-activation targets at the exit of the z-discharge transport channel.

grazes the channel wall and $\Delta v_r/v \ll 1$,

$$\theta_{\max}^2 = \frac{2v_c}{(N+1)v_o} \left(1 - \frac{r^{N+1}}{r_c^{N+1}} \right). \quad (3)$$

Measurements of θ_{\max} are compared with (3) for different values of N in Fig. 8. A best-fit to the measurements is achieved for N between 2 and 3; this result agrees with both the magnetic-field measurements and the analysis of the nuclear-activation measurements. Taken together, results from all the measurements confirm beam charge and current neutralization during transport.

III. WIRE-GUIDED TRANSPORT

Wire-guided transport employs a current-carrying wire rather than a z-discharge to provide the azimuthal magnetic field that confines the ion beam. The equivalent of (1) for wire-guided transport is

$$\frac{v_r}{v_o} = \left[\frac{v_{r_o}^2 + v_{\theta_o}^2}{v_o^2} - \frac{r_o^2 v_{\theta_o}^2}{r^2 v_o^2} - \frac{v_w}{v_o} \ln \left(\frac{r^2}{r_o^2} \right) \right]^{1/2} + O(\epsilon^3) \quad (4)$$

where $B_\theta \sim 1/r$, and $v_w/v_o \equiv 2eZI_w/m_i v_o c^2$. Again, by setting $v_r = 0$ in (4), the radial turning points for the ion orbit are obtained. Ions with inner turning points smaller

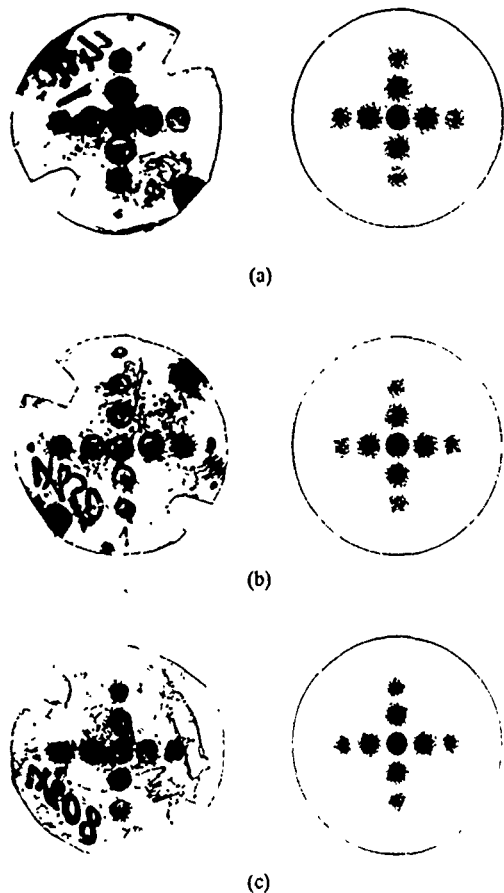


Fig. 7. Experimental and calculated z-discharge shadowbox images for (a) shot # 4810 with $D = 20$ cm, (b) shot # 4850 with $D = 25$ cm, and (c) shot # 4808 with $D = 30$ cm.

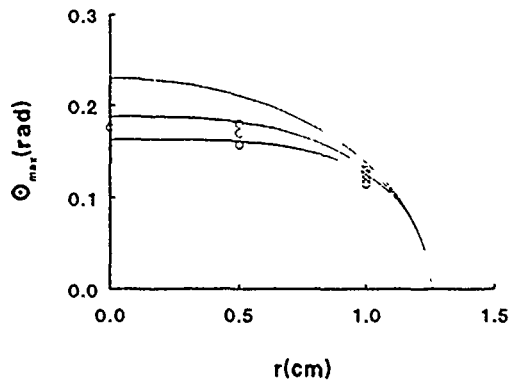


Fig. 8. Experimental values and calculated curves of θ_{\max} versus pinhole radius from z-discharge shadowbox images for shot # 4810 with $D = 20$ cm. The curves correspond to (3) with $N = 1$ (top), $N = 2$ (middle), and $N = 3$ (bottom).

than the wire radius r_w , hit the wire and are lost. Equation (4) can be utilized to calculate the injection efficiency for wire-guided transport [6]. Trajectories for ion orbits in the magnetic field of the guide wire can be obtained by integrating (4). Sample orbits are shown in Fig. 9, where it can be seen that, in general, the wire-guided orbits are not closed. The wire current I_{wm} is defined to be that current which confines the ions (that do not impact the wire) within

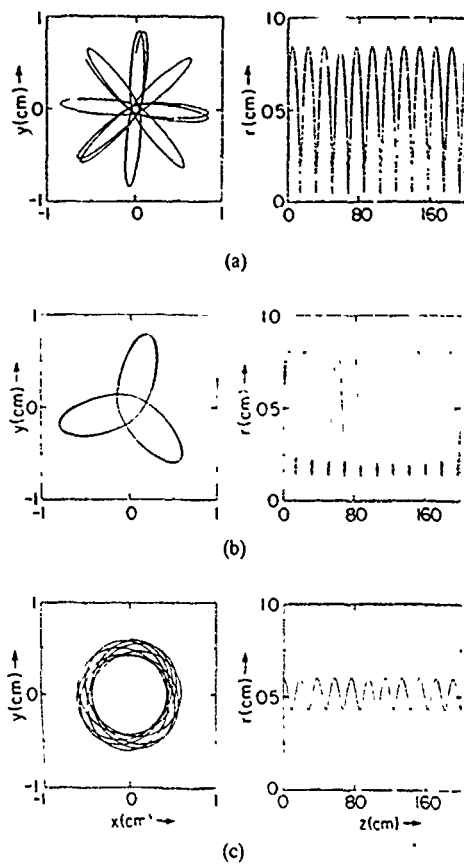


Fig. 9. Wire-guided ion orbits with $I_w = 50$ kA, $r_w = 0.04$ cm, and $r_o = 0.6$ cm for (a) $v_{r0}/v_o = 0.098$ and $v_{\theta0}/v_o = 0.021$, (b) $v_{r0}/v_o = 0.087$, and $v_{\theta0}/v_o = 0.05$, and (c) $v_{r0}/v_o = 0$, and $v_{\theta0}/v_o = 0.1$.

a specified radius r_c . For $R/D \ll 1$, I_{wm} is given by

$$I_{wm} = \frac{v_o m_i c^2}{2Ze \ln(r_a^2/r_c^2)} \left(\frac{R}{D}\right)^2 \quad (5)$$

In NRL experiments with 1.2-MeV protons [7], [8], $R = 5$ cm, $D = 20$ –30 cm, $r_a = 1.25$ cm, $r_w = 0.05$ cm, and $I_w = 20$ –30 kA. For $D = 30$ cm, all ions not lost to the wire are confined within $r_c = 2$ cm during transport for $I_w = 25$ kA. For the same injection conditions, a larger wire current would confine the beam within a smaller r_c , but would result in more losses to the wire. Larger r_w would also result in more losses to the wire.

Measurements of particle transport efficiency with prompt- γ nuclear activation for 1- and 1.5-m long wires of radius $r_w = 0.05$ cm gave $\eta_t = 0.75$ –0.8. These results are consistent with calculations based on (4). Orbit analysis has also been used to predict the shapes of shadowbox images. Calculated and experimental images are compared for a radial array of pinholes in Fig. 10 for two shots with different experimental conditions. The absence of damage on the axis reflects the loss of low-angular-momentum ions to the wire. Similarities in size and shape of the calculated and measured images indicate that the transverse phase-space distribution of transported ions is determined primarily by orbital motion in the applied B_θ field without major perturbations from beam-background interactions,

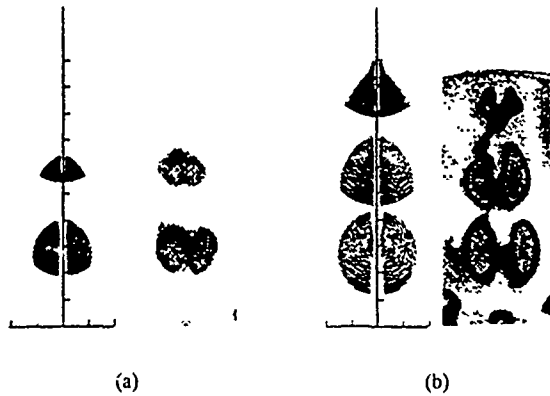


Fig. 10. Experimental and calculated shadowbox images for wire-guided transport (a) for shot # 4727 with $D = 10$ cm, $I_w = 15$ kA, and $r_a = 0.78$ cm and (b) for shot # 4470 with $D = 10$ cm, $I_w = 27$ kA, and $r_a = 1.27$ cm.

instabilities, or asymmetries.

Initial experiments employed a large-radius cylindrical current return. More recent experiments have used a small number N_w of current-return wires mounted at small radius R_w . The return wires break cylindrical symmetry so that the loss of angular-momentum conservation leads to irregular motion and additional losses to the central guide wire. This is particularly serious for $N_w = 3$ because many ions have orbits similar to that illustrated in Fig. 9(b) and will interact strongly with the return wires. A large number of orbit calculations in the magnetic-field distribution of the central guide wire and return-current wires have determined the minimum values of R_w and N_w that do not enhance losses beyond those in the cylindrically symmetric case [6]. Results show that $N_w = 4$ and $R_w = 1.4r_c$ can provide 95% of the ideal transport efficiency.

IV. SYSTEM CONSIDERATIONS

In order to apply these transport techniques to ICF scenarios, other system considerations must be addressed. For example, the Laboratory Microfusion Facility (LMF) requires a minimum amount of hardware in the target chamber [34]. To this end, a low-mass version of the z-discharge transport channel hardware is being investigated. A 2-cm diameter Kapton tube with a metal-foil outer conductor has been fabricated. Analysis shows that such tubes should meet LMF debris requirements [35]. The tubes are rigid over several-meter lengths so that they need be supported only at the containment-vessel wall. Experiments with 1- and 2-m lengths have been carried out with channel currents up to 75 kA [33], [36]. Containing the discharge in a tube has the potential advantage of separating the discharge gas from the target-chamber gas, which allows for different gases and pressures to satisfy different requirements.

A variety of theoretical calculations have been carried out to determine limits on transportable ion power associated with instabilities [10], [11], the MHD response of the channel to beam transit [24], energy loss during transport, channel packing, and standoff around the pellet

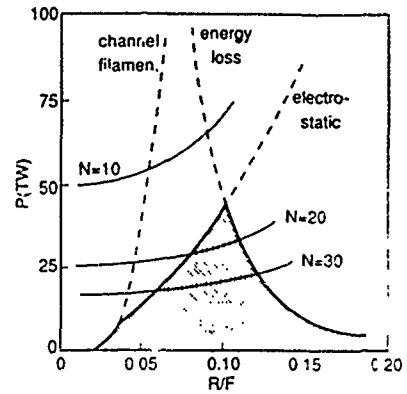


Fig. 11. Operational window for ion beam transport showing ion beam power P versus R/F with various system constraints for a Li^{+3} beam with a 23–37 MeV ramp in injected energy for bunching. The required LMF ion power per beam for 10, 20, or 30 beams is also indicated.

[23]. Power-limiting constraints for LMF parameters are summarized in Fig. 11 for a Li^{+3} beam with an injection energy ramped from 23–37 MeV to achieve bunching of a 40-ns extracted beam to 10 ns over a 3.3-m long z-discharge channel. Here F is used instead of D , where F denotes the focal length of a diode which focuses the ion beam to a spot of radius $F\theta_\mu$ at the channel aperture. The channel radius is taken to be 1 cm and a microdivergence of 7 mrad is assumed. Acceptable transported powers are in the shaded region below limits associated with the channel-filamentation and electrostatic instabilities, and a 25% energy loss due to collisional stopping and deceleration in return-current-driven and induced electric fields. These limits are compared with the required extracted power per beam for 10, 20, and 30 modules delivering a total of 1000 TW to the pellet with 50% on-target efficiency. These considerations indicate that 20 or more modules with R/F of about 0.1 can satisfy LMF requirements in a z-discharge transport configuration. Similar results can be derived for wire-guided and other transport techniques.

System studies have also been carried out to determine the total particle transport efficiency (i.e., $\eta_t \eta_s$, where η_s is the standoff efficiency) for LMF using either z-discharge or wire-guided transport [6], [15]. Here, η_s is the ratio of the number of ions which hit the target to the number of ions which exit the transport channel as a function of the standoff distance between the channel exit and the target. In these studies, the channel aperture was set equal to the beam radius at best focus, which is equal to $F\theta_\mu$ for a focusing diode. For z-discharge transport, the channel radius r_c was set equal to $2^{1/2}r_a$ and r_a was used to determine the pellet stand off distance. For wire-guided transport, the wire radius was chosen so that melting did not occur for a wire current rising to I_w in 10 μs . The diode radius R then determined the transporting beam envelope radius r_c and return-wire radius R_w , which, in turn, were used to determine the stand off distance from the pellet. Orbit analysis provided the total transport efficiency from the diode to the pellet for each technique. Examples of these

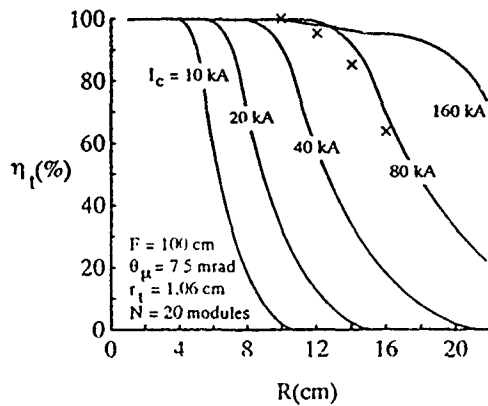


Fig. 12. Plot of z-discharge transport efficiency as a function of diode radius with $F = 100$ cm, $\theta_{\mu} = 7.5$ mrad, $r_t = 1.06$ cm, and $N = 20$ for various values of I_c . The points (x) are from numerical simulations.

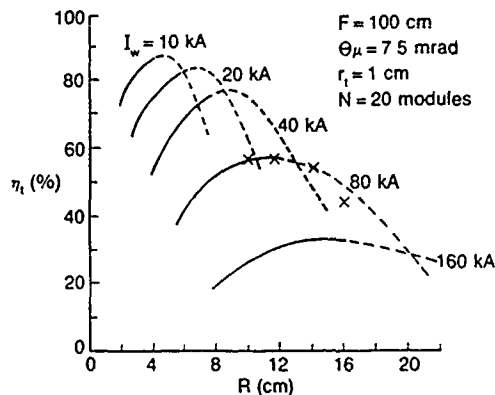


Fig. 13. Plot of wire-guided transport efficiency as a function of diode radius with $F = 100$ cm, $\theta_{\mu} = 7.5$ mrad, $r_t = 1$ cm, and $N = 20$ for various values of I_w . The points (r) are from numerical simulations.

calculations are shown in Fig. 12 for z-discharge transport [15] and Fig. 13 for wire-guided transport [6] for a 1-cm radius pellet fed by 20, 30-MeV Li-beam modules. The figures show total transport efficiencies of 60%–100% for z-discharge transport and 55%–75% for wire-guided transport for diode radii in the 8- to 12-cm range for confining currents of 40–80 kA.

V. CONCLUSIONS

Two promising transport options for light-ion ICF scenarios have been presented. Z-discharge transport is the most studied concept both theoretically and experimentally. Experiments with proton beams demonstrate efficient z-discharge transport of focused beams for discharge currents, channel radii, and lengths comparable to those required for ICF. Beam-channel-interaction studies indicate that LMF ignition requirements can be satisfied with 20 or more accelerators and transport modules, but the need for discharge hardware in the reaction chamber makes this option more difficult to extend to a reactor. Similar experimental results and conclusions have been obtained for wire-guided transport and the negligible mass of the wire arrays makes

this technique attractive for LMF. However, the background gas must satisfy wall-buffer and beam-interaction requirements, and not break down during the current rise in the wire; these conditions may be difficult to meet simultaneously. Although system studies show that both techniques will provide greater than 50% particle transport efficiency from the diode to the target for LMF, experimental tests with MA-level Li beams are required to accurately evaluate beam-channel-interaction limitations under LMF conditions. Transport for an ICF reactor will require this transport work to be extended to other techniques, such as ballistic transport, freestanding z-discharge transport, and self-pinch transport.

ACKNOWLEDGMENT

The authors acknowledge the early pioneering experiments of Dr. F. Sandel and the theoretical efforts of Dr. J. J. Watrous while at NRL. The authors also acknowledge the many useful discussions and encouragement of Dr. C. Olson concerning this work.

REFERENCES

- [1] J. J. Ramirez, R. W. Stinnett, D. L. Johnson, C. L. Olson, T. A. Mehlhorn, J. T. Crow, J. P. Quintenz, K. R. Prestwich, M. P. Desjarlais, R. E. Olson, G. O. Allshouse, T. H. Martin, J. P. VanDevender, D. L. Cook, S. A. Slutz, K. B. Coachman, T. R. Lockner, B. N. Turman, S. A. Goldstein, and J. N. Olsen. "Design issues for a light ion beam LMF driver." *Fusion Tech.*, vol. 15, pp. 350–356, 1989.
- [2] F. Winterberg, "Production of dense thermonuclear plasmas by intense ion beams." *Plasma Phys.*, vol. 17, pp. 69–77, 1975.
- [3] S. A. Goldstein, G. Cooperstein, R. Lee, D. Mosher, and P. F. Ottinger, "Pulse shaping and power multiplication of intense light ion beams." in *IEEE Conf Record-Abstracts, the 1978 IEEE Int. Conf. Plasma Sci.*, F. Schwirzke, Ed., Monterey, CA, 1978, p. 112.
- [4] C. L. Olson, "Phase space acceptance of LMF transport schemes." in *Proc 1989 Particle Accelerator Conf.*, F. Benner and J. Kaptan, Chicago, IL, Mar. 20–23, 1989, pp. 1011–1013.
- [5] D. Mosher, D. D. Hinshelwood, J. M. Neri, P. F. Ottinger, J. J. Watrous, C. L. Olson, and T. A. Mehlhorn, "Ion transport for LMF." in *Proc 8th Int. Conf. High-Power Particle Beams*, B. N. Breizman and B. A. Knyazev, Eds., Novosibirsk, USSR, July 2–5, 1990, pp. 26–38.
- [6] J. J. Watrous, D. Mosher, J. M. Neri, P. F. Ottinger, C. L. Olson, J. T. Crow, and R. R. Peterson, "Wire-guided transport of intense ion beams." *J. Appl. Phys.*, vol. 69, pp. 639–655, 1991.
- [7] J. J. Watrous, P. J. Goodrich, D. Mosher, J. M. Neri, P. F. Ottinger, V. C. Scherrer, S. J. Stephanakis, and F. C. Young, "Analysis of NRL wire-guided ion beam transport experiments." in *IEEE Conf Record-Abstracts, the 1990 IEEE Int. Conf. Plasma Sci.*, Oakland, CA, May 1990, p. 145.
- [8] J. M. Neri, P. J. Goodrich, D. Mosher, W. F. Oliphant, P. F. Ottinger, S. J. Stephanakis, J. J. Watrous, and F. C. Young, "Experimental investigations of wire-guided transport for light-ion-beam ICF." in *IEEE Conf Record-Abstracts, the 1990 IEEE Int. Conf. Plasma Sci.*, Oakland, CA, May 1990, p. 144.
- [9] P. F. Ottinger, D. Mosher, and S. A. Goldstein, "Propagation of intense ion beams in straight and tapered Z-discharge plasma channels." *Phys. Fluids*, vol. 23, pp. 909–920, 1980.
- [10] P. F. Ottinger, D. Mosher, and S. A. Goldstein, "Microstability of focused ion beam propagating through a Z-pinch plasma." *Phys. Fluids*, vol. 22, pp. 332–337, 1979.
- [11] P. F. Ottinger, D. Mosher, and S. A. Goldstein, "Electromagnetic instabilities in a focused ion beam propagating through a Z-discharge plasma." *Phys. Fluids*, vol. 24, pp. 164–170, 1981.
- [12] P. F. Ottinger, S. A. Goldstein, D. Mosher, and D. G. Colombant, "Transport and focusing considerations for light ion ICF"

- in *Proc. 5th Int. Conf. High-Power Particle Beams*, R. J. Briggs and A. J. Foepfer, Eds., San Francisco, CA: Sept. 1983, pp. 97-100.
- [13] F. L. Sandel, S. J. Stephanakis, F. C. Young, and W. L. Oliphant, "Experimental studies of intense light-ion beam transport," in *Proc. 4th Int. Topical Conf. High Power Electron and Ion Beam Research and Technology*, H. J. Doucet and J. M. Buzzi, Eds., Palaiseau, France, 1981, pp. 129-136.
 - [14] J. M. Neri, J. R. Boller, G. Cooperstein, D. Mosher, P. F. Ottinger, V. E. Scherrer, S. J. Stephanakis, and F. C. Young, "Transport and focusing of intense ion beams for ICF with Z-discharge plasma channels," in *Proc. 7th Int. Conf. High Power Particle Beams*, W. Bauer and W. Schmidt, Eds., Karlsruhe, Germany: 1988, pp. 165-170.
 - [15] P. F. Ottinger, D. V. Rose, D. Mosher, and J. M. Neri, "Z-discharge transport of intense ion beams for inertial confinement fusion," *J. Appl. Phys.*, vol. 70, pp. 5292-5305, 1991.
 - [16] C. L. Olson, "Achromatic magnetic lens systems for high current ion beams," in *Proc. 1988 Linear Accelerator Conf.*, C. Leemann, Ed., Newport News, VA: Oct. 3-7, 1988, pp. 34-37.
 - [17] T. A. Mehlhorn and J. P. Quintenz, "PIC simulations of an achromatic solenoidal focusing system for LMF," in *Proc. 1989 Particle Accelerator Conf.*, F. Bennett and J. Kapt, Eds., Chicago, IL: Mar. 20-23, 1989, pp. 1014-1016.
 - [18] J. N. Olsen and R. J. Leeper, "Ion beam transport in laser-initiated discharge channels," *J. Appl. Phys.* 53, pp. 3397-3404, 1982.
 - [19] S. Nakai, K. Imasaki, S. Miyamoto, S. Higaki, T. Ozaki, A. Yoshinouchi, H. Fujita, K. Mima, K. Nishihara, T. Yabe, S. Ido, Y. Ohgaki, and C. Yamanaka, "Inertial confinement fusion research by particle beams at ILE Osaka," *Laser and Particle Beams*, vol. 1, pp. 29-65, 1983.
 - [20] J. R. Freeman, L. Baker, and D. L. Cook, "Plasma channels for intense-light-ion-beam reactors," *Nucl. Fusion*, vol. 22, pp. 383-393, 1982.
 - [21] R. F. Hubbard, M. Lampe, G. Joyce, S. P. Slinker, I. Haber, and R. F. Fernsler, "Target chamber propagation of heavy ion beams in the pressure regime above 10-3 Torr," in *Proc. Int. Symp. Heavy Ion Fusion*, Monterey, CA, Dec. 1990, to be published.
 - [22] D. Hammer and N. Rostoker, "Propagation of high current relativistic electron beams," *Phys. Fluids*, vol. 13, pp. 1831-1850, 1970.
 - [23] D. Mosher, D. G. Colombant, S. A. Goldstein, and P. F. Ottinger, "System requirements for light-ion ICF," in *Proc. 4th Int. Topical Conf. High Power Electron and Ion Beam Research and Technology*, H. J. Doucet and J. M. Buzzi, Eds., Palaiseau, France, 1981, pp. 19-26, for more details see National Technical Information Service Document ADA121472 (P. F. Ottinger, S. A. Goldstein, and D. Mosher, "Constraints on transportable ion beam power," NRL Memorandum Rep. 4948, Nov. 12, 1982). Copies may be ordered from the National Technical Information Service, Springfield, VA, 22161. The price is \$5.00 plus a \$3.00 handling fee. All orders must be prepaid.
 - [24] D. G. Colombant, S. A. Goldstein, and D. Mosher, "Hydrodynamic response of plasma channels to propagating ion beams," *Phys. Rev. Lett.*, vol. 45, pp. 1252-1256, 1980.
 - [25] S. J. Stephanakis, D. Mosher, G. Cooperstein, J. R. Boller, J. Golden, and S. A. Goldstein, "Production of intense proton beams in pinched-electron-beam diodes," *Phys. Rev. Lett.*, vol. 37, pp. 1543-1546, 1976.
 - [26] S. A. Goldstein, G. Cooperstein, R. Lee, D. Mosher, and S. J. Stephanakis, "Focusing of intense ion beams from pinched-beam diodes," *Phys. Rev. Lett.*, vol. 40, pp. 1504-1507, 1978.
 - [27] G. Cooperstein, S. A. Goldstein, D. Mosher, R. J. Barker, J. R. Boller, D. G. Colombant, A. Drobot, R. A. Mejer, W. F. Oliphant, P. F. Ottinger, F. L. Sandel, S. J. Stephanakis, and F. C. Young, "NRL light ion beam research for inertial confinement fusion," in *Laser Interaction and Related Plasma Phenomena*, J. J. Schwartz, H. Hora, M. Lubin, and B. Yaakobi, Eds., New York: Plenum, 1981, pp. 105-134, vol. 5.
 - [28] L. S. Levine and I. M. Vitkovitsky, "Pulsed power technology for controlled thermonuclear fusion," *IEEE Trans. Nucl. Sci.*, vol. 18, pp. 255-264, 1971.
 - [29] F. C. Young, W. F. Oliphant, S. J. Stephanakis and A. R. Knudson, "Absolute calibration of a prompt gamma-ray detector for intense bursts of protons," *IEEE Trans. Plasma Sci.*, vol. PS-9, pp. 24-29, 1981.
 - [30] R. J. Leeper, E. J. T. Burns, D. J. Johnson, and W. M. McMurtry, "Proton current measurement using the prompt gamma ray diagnostic technique," in *Proc. Workshop on Measurements of Electrical Quantities in Pulsed Power Systems*, National Bureau of Standards Special Publication 628, 1982, pp. 267-276.
 - [31] J. M. Neri, D. Mosher, P. F. Ottinger, D. V. Rose, S. J. Stephanakis, and F. C. Young, "Transport of intense ion beams with Z-discharge plasma channels," in *IEEE Conf. Record-Abstracts, the 1991 IEEE Int. Conf. Plasma Sci.*, Williamsburg, VA, June 1991, p. 164.
 - [32] P. F. Ottinger, D. Mosher, J. M. Neri, D. V. Rose, and F. C. Young, "Analysis of Z-discharge ion-beam transport experiments," in *IEEE Conf. Record-Abstracts, the 1991 IEEE Int. Conf. Plasma Sci.*, Williamsburg, VA, June 1991, p. 165.
 - [33] D. D. Hinshelwood, P. J. Goodrich, P. F. Ottinger, and D. V. Rose, "LMF Z-discharge transport channel development," in *IEEE Conf. Record-Abstracts, the 1991 IEEE Int. Conf. Plasma Sci.*, Williamsburg, VA, June 1991, p. 165.
 - [34] K. R. Prestwich, J. J. Ramirez, R. W. Stinnett, D. L. Johnson, C. L. Olson, M. J. Clauser, T. A. Mehlhorn, M. P. Desjarlais, G. O. Allshouse, J. P. Corley, D. L. Hanson, M. E. Cuneo, P. F. McKay, J. W. Poukey, S. E. Rosenthal, S. A. Slutz, J. P. Quintenz, D. L. Cook, J. P. VanDevender, R. Peterson, R. Engelstad, and J. W. Powers, "Design of a light-ion-beam driver for the laboratory microfusion facility," in *Proc. 8th Int. Conf. High-Power Particle Beams*, B. N. Breizman and B. A. Knyazev, Eds., Novosibirsk, USSR, July 2-5, 1990, pp. 143-151.
 - [35] R. R. Peterson, R. L. Engelstad, J. W. Powers, H. Y. Khater, M. E. Sawan, E. G. Lovell, G. A. Moses, and J. S. Lipschultz, "An overview of target chamber design and analysis for the light ion beam microfusion facility," Univ. Wisconsin Fusion Technology Inst. Rep. UWFD-819, Feb. 1990.
 - [36] D. D. Hinshelwood, P. J. Goodrich, J. M. Neri, W. F. Oliphant, S. J. Stephanakis, J. J. Watrous, and F. C. Young, "Low mass wall-confined discharge for light ion beam transport," in *IEEE Conf. Record-Abstracts, the 1990 IEEE Int. Conf. Plasma Sci.*, J. Benford, Ed., Oakland, CA, 1990, p. 143.



Paul F. Ottinger (Member, IEEE) was born in Philadelphia, PA. He received the B.A. degree in physics from the University of Pennsylvania in 1970 and the M.S. and Ph.D. degree in theoretical plasma physics from the University of Maryland, College Park, in 1974 and 1977, respectively.

Since 1986 he has been with the Naval Research Laboratory (NRL) as the Head of the Theory and Analysis Section in the Pulsed Power Physics Branch. Before joining the NRL, he was a National Research Council Associate at the NRL and worked as a Senior Research Scientist in private industry for JAYCOR. During his career he has developed expertise in the specialized areas of intense particle beams, fast opening plasma switches, and plasma radiation sources. In particular, his research has concentrated on the areas of ion beam transport and stability in z-discharge channels, wire-guided transport systems, and ion beam final focusing. He has also been involved in the development of theoretical models for the plasma erosion opening switch.



Phillip J. Goodrich was born in San Francisco, CA. He received the B.S. degree in engineering physics from the University of California, Berkeley, in 1982, and the M.S. degree in nuclear engineering from the Massachusetts Institute of Technology, Cambridge, in 1986, where he studied plasma physics.

Since 1986 he has been with JAYCOR, Vienna, VA, where his research interests include pulsed power development, plasma opening switches, and ion beam transport.

David D. Hinshelwood was born in Washington, DC. He received the B.S. degrees in physics and mathematics in 1978 and the Ph.D. degree in physics in 1984 from the Massachusetts Institute of Technology, Cambridge.

From 1984 to the present he has worked for JAYCOR, Vienna, VA, as a Research Physicist at the Naval Research Laboratory. His research has included plasma opening switches, plasma radiation sources, and ion beam transport.



David Musher received the Ph.D. degree in plasma physics from Princeton University, NJ, in 1968.

Following a post-doctoral appointment at the Los Alamos Scientific Laboratory and a faculty position at Ohio State University, he joined the Naval Research Laboratory, Plasma Physics Division in 1972. Since that time he has carried out pulsed-power based experimental and theoretical research on the creation and manipulation of intense ion and electron beams, their interactions

with matter, high-energy density plasmas, and x-radiation produced by these sources to meet a variety of DoE and DoD objectives.



Jesse M. Neri was born in Ames, IA. He received the B.S. degree in physics and mathematics from the University of Denver, CO, in 1976 and the M.S. and Ph.D. degrees in applied physics from Cornell University, Ithaca, in 1979 and 1982, respectively, where he studied intense ion beam sources.

Since 1982 he has been with the Naval Research Laboratory (NRL), first with JAYCOR and then as an NRL employee. He is currently a Research Physicist in the Theory and Analysis

Section of the Pulsed Power Physics Branch. His research includes intense electron and ion beam sources, ion beam transport for inertial confinement fusion, and data acquisition and analysis systems for pulsed power experiments.



David V. Rose was born in Harrisburg, PA. He received the B.A. in physics in 1986 from Temple University, Philadelphia, PA, and the M.S. degree in applied physics in 1991 from Johns Hopkins University, Baltimore, MD.

From 1987 to the present he has worked for JAYCOR, Vienna, VA, as a Computer Scientist and Research Physicist. His research has included ion beam transport/focusing and high power diode physics.



Stavros J. Stephanakis was born in Salonica, Greece. He received the B.S. degree in electrical engineering in 1963 and the Ph.D. degree in electrical engineering and physics in 1969 from North Carolina State University, Raleigh, where he studied gas focusing of e-beams in a high-Z plasma background.

He joined the Naval Research Laboratory in 1968 and since that time he has performed experimental research on rocket exhaust plume plasmas, z-pinches, e-beams, ion beams, plasma

filled diodes, plasma opening switches and advanced pulsed power development.



Frank C. Young (Senior Member, IEEE) was born in Roanoke, VA. He received the B.A. degree in physics from Johns Hopkins University, Baltimore, MD, in 1957 and the Ph.D. degree in nuclear physics from the University of Maryland in 1962.

From 1962 to 1963 he held a postdoctoral Research Associateship in the Nuclear Science Division at the Naval Research Laboratory (NRL). Then, from 1963 to 1972 he served on the faculty of the Department of Physics and Astronomy at the University of Maryland. While at the University of Maryland, he participated in an experimental nuclear physics research program studying the structure of the light nuclei and nuclear reaction mechanisms. In 1972 he returned to NRL, where he is presently. He has applied his nuclear physics expertise to studies of intense pulsed plasma sources. This has included, for example, laser-matter interactions, intense light ion beams for inertial confinement fusion, imploding Z-pinch plasma sources, and the development of short wavelength lasers.

Intense ion-beam-transport experiments using a z-discharge plasma channel

J. M. Neri, P. F. Ottinger, D. V. Rose,^{a)} P. J. Goodrich,^{a)} D. D. Hinshelwood,^{a)} D. Mosher, S. J. Stephanakis, and F. C. Young

Pulsed Power Physics Branch, Plasma Physics Division, Naval Research Laboratory, Washington, D.C. 20375

(Received 20 April 1992; accepted 14 September 1992)

A z-discharge plasma channel is used to confine and transport an intense proton beam. A pinch-reflex ion diode on the NRL Gamble II accelerator focuses a proton beam onto the entrance aperture of a 2.5 cm diam, 1.2 m long z-discharge transport system. The beam ions are charge and current neutralized in the discharge plasma, and execute betatronlike orbits in the magnetic field of the discharge. Ion beam diagnostics include shadowbox imaging and prompt- γ radiation measurements from LiF targets. Under appropriate conditions, 95% particle transport and 90% energy transport are observed, with the only energy loss attributed to classical stopping in the channel gas. The transverse phase-space distribution of the beam measured by the shadowbox is consistent with full charge and current neutralization of the transported beam.

I. INTRODUCTION

Light ion beams are a promising driver for inertial confinement fusion (ICF).¹ Beam transport of several meters² is required to isolate the accelerator and ion source from the blast and radiation of an ICF target explosion. An additional benefit of the transport distance is that time-of-flight bunching, using a programmed accelerator voltage pulse, can be used to increase the ion-beam power and decrease the pulse duration at the target.³ The z-discharge transport of intense ion beams over distances of up to several meters⁴⁻⁸ has been demonstrated. For this technique, the plasma density and electrical conductivity of the discharge are sufficiently high to provide charge and current neutralization of the ion beam, so that the discharge magnetic field alone guides the ions along the channel path.⁹ Thus, for nearly paraxial ion beams, ion-beam-pulse energies far greater than the energy invested in channel formation can be efficiently transported to a target. The limits to the peak power and energy that can be carried by a channel of a given diameter are associated with beam-plasma interactions.¹⁰⁻¹² The transportable power per channel then determines the minimum number of system modules required to meet ICF target requirements.

A conceptual drawing of z-discharge transport in an ICF module is shown in Fig. 1. The complete ICF system will pack 10-30 such modules around the target. At present, an ICF module is expected to transport a few megampere, 30 MeV Li^{+3} beam. The ion diode focuses the ion pulse onto the entrance of the z-discharge channel over a distance of approximately 1 m. The diode radius is about 10 cm and the beam is transported within a radius comparable to the ICF target radius which is about 1 cm. The beam is transported 2 to 3 m in the discharge channel, through the target chamber to the vicinity of the ICF target. The ion beam then expands ballistically over the few

centimeter distance from the channel exit to the target. In this standoff region, beams from other channels combine to symmetrically drive the target implosion.

In order to evaluate this scheme as an ICF driver, the coupling efficiency of the ion source to the transport channel, the transport efficiency of ion-beam energy through the channel, and the pellet coupling efficiency associated with expansion and overlap of the ion beams after exiting the channel must be determined. Because the pulsed power and ion source for an ICF level test do not yet exist, experiments and analyses at currently achievable levels must first be carried out to provide understanding of key physics issues before scaling to an ICF level demonstration.

The experiments presented here measure for the first time the ion-source coupling to the channel from the diode through the entrance aperture for various injection conditions and the ion-trapping efficiency of the channel for these injection conditions. These will be defined more carefully in Sec. IV as the aperture efficiency and the injection efficiency. Previous experiments^{4,8} generally concentrated upon diagnosing that portion of the ion beam confined in the channel by making the first ion-beam-intensity measurement well back from the entrance aperture. This measurement, referred to as the energy transport efficiency, is also made here. A new nuclear activation diagnostic employed in the present experiments provides more accurate measurements of energy transport efficiency than previous work.

For the present work, the discharge parameters were held nominally constant for all shots. The aperture efficiency, the injection efficiency, the energy transport efficiency, and post-transport expansion were measured for various injected beam conditions. The phase-space distribution of the ion beam delivered to the channel entrance aperture was varied by placing the channel entrance at distances of 20, 25, and 30 cm from the ion diode. The ion-beam intensity at the diode exit plane, at the channel entrance, and at the channel exit were measured with a

^{a)}Permanent address: JAYCOR, Vienna, Virginia 22182.

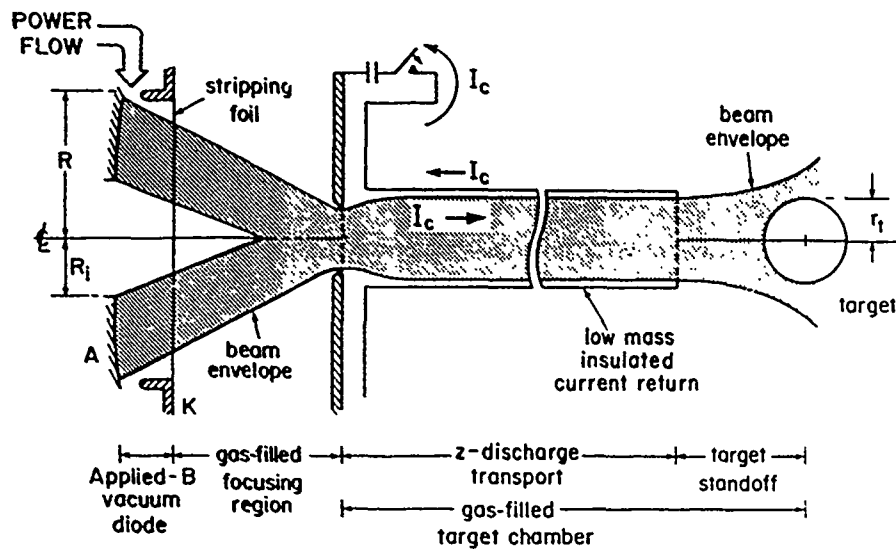


FIG. 1. Schematic drawing of a z-discharge transport system for ICF.

prompt- γ diagnostic that is immune to ablation effects. These beam intensity measurements were used to evaluate the three efficiencies. The beam intensity data was analyzed with a three-dimensional (3-D) particle-transport code, using the measured diode voltage and ion current waveforms to correct for shot-to-shot variations in the injected ion beam. The transported ion-beam phase-space distribution was sampled at the channel exit with a shadowbox to evaluate post-transport expansion. The transport code was also used to simulate shadowbox measurements for various assumed magnetic field distributions in the channel.

In the work presented here, efficient transport of MV level proton beams through a 1.2 m long z-discharge plasma channel is demonstrated. A 1.2 MeV, 500 kA proton beam produced on the Gamble II generator¹³ with a pinch-reflex ion diode¹⁴⁻¹⁶ is weakly focused onto the 1.7 cm diam entrance aperture of a 2.5 cm diam, wall-stabilized, z-discharge transport channel.^{4,8,17} The discharge current is provided by a 60 kV, 1.8 μ F capacitor bank producing a 45 kA peak discharge current through a 2 Torr air fill. A combination of time-resolved and time-integrated prompt- γ measurements demonstrate that, as expected, classical collisional slowing in the channel gas results in 90% efficient energy transport. The shadowbox measurements of post-transport beam expansion indicate that the confined ion-beam distribution is consistent with ion trajectories for a fully charge- and current-neutralized ion beam in a cylindrically symmetric channel. At the 30 cm diode-to-channel spacing, where the injected ion distribution is predicted to be well confined by the discharge current, the particle transport efficiency of the system is measured to be greater than 95%. For the 25 and 20 cm spacings, analysis of particle losses to the walls of the discharge channel indicate that the radial magnetic field profile in the channel is hollow.

In Sec. II we describe the experimental hardware used to generate the intense proton beam, the plasma channel used to transport the beam, and the diagnostic techniques

used to assess the beam transport characteristics. In Sec. III we present a brief review of the theory of z-discharge transport, and discuss the numerical modeling used to analyze the characteristics of the ion source and the transport system. In Sec. IV we present the results of the ion-beam-transport experiments and analyses. Discussion and conclusions are given in Sec. V.

II. EXPERIMENTAL SETUP

The components of the experiments are described in the following section; the ion source, the transport channel, and the ion-beam diagnostics.

A. Ion beam source

The proton beam is produced with a modified pinch-reflex diode (PRD).¹⁴⁻¹⁶ In these experiments, a fiat anode foil is used to provide a weakly focused ion beam for injection into the z-discharge channel. The beam is focused by self-pinching forces of the ion beam in the diode vacuum gap. With the resulting weak focus, a variety of ion-beam input conditions are obtained simply by locating the channel entrance aperture at different distances from the ion diode.

The geometry of the ion diode is shown in Fig. 2. A 6 cm radius annular cathode of 2 mm width is used. An anode, consisting of a 12.7 μ m thick polyethylene foil mounted on a 0.18 mm thick, 5.5 cm inner radius aluminum ring, is positioned opposite the cathode tip with an anode-cathode spacing of 5 mm. The diode and the region behind the anode foil are evacuated to less than 1×10^{-4} Torr. The diode region is separated from the air-filled focusing and transport region by a 2 μ m thick, 5.4 cm radius polycarbonate foil (Kimfol¹⁸), located 8 mm behind the cathode tip. Ion current incident on this foil is measured with a Rogowski coil, as shown in Fig. 2. Charge and current neutralization required for ballistic propagation² is provided when the 2 Torr gas fill behind the Kimfol is ionized by the beam front. Full current neutralization im-

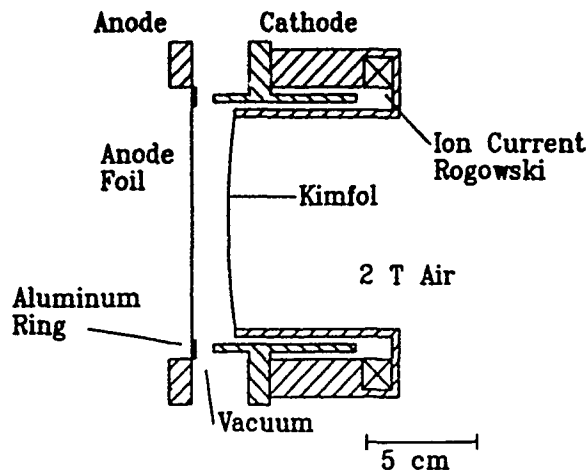


FIG. 2. Schematic of the modified pinch-reflex ion diode.

plies that the current measured by the Rogowski coil is the incident ion-beam current.

Electrical quantities of interest for the ion diode are the voltage, the total current, and the ion current. The diode voltage is obtained by correcting the voltage measured at the water-vacuum interface of the generator by the inductive voltage drop to the diode gap. The total diode current is measured with a resistive shunt located behind the water-vacuum interface and with magnetic loops located in vacuum between the insulator and the diode. The ion current is measured with the Rogowski coil, as discussed above. Typical waveforms for these electrical quantities are shown in Fig. 3. The diode voltage and the ion current are used to calculate ion trajectories and to evaluate nuclear reaction yields. A detailed description of the diode model used for analysis of the transport experiments is presented in Sec. III A.

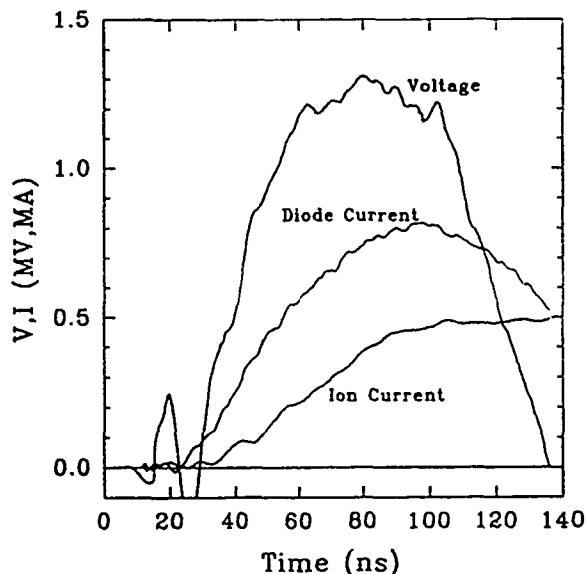


FIG. 3. Typical ion-diode waveforms.

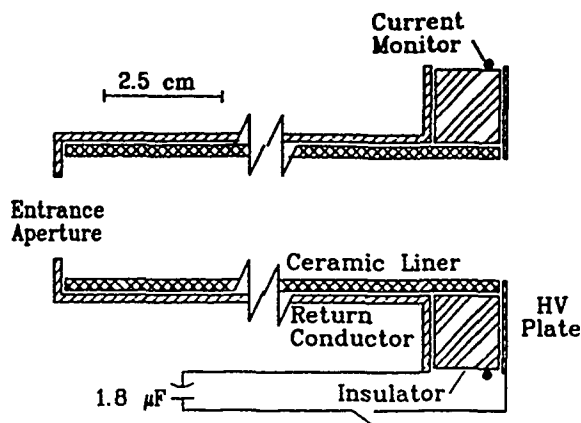


FIG. 4. Schematic of the z-discharge channel used in the experiment.

B. Transport channel

The plasma channel is generated by a wall-stabilized z-discharge,^{4,8,17} as shown in Fig. 4. The discharge is initiated on the inside surface of a ceramic liner at the high-voltage connection and travels the full length of the liner to connect to the outer return conductor. An entrance aperture, $r_a=0.85$ cm, is used at the low-voltage end of the channel to define the input ion-beam radius. A 1.2 m long, 2.54 cm diam liner is used, and the discharge is driven by a 60 kV, 1.8 μ F capacitor bank. The discharge current is measured with a Rogowski coil placed around the insulator. The brass return conductor suppresses kink instabilities, while the gas density is sufficiently high and the 800 nsec rise time to peak current is sufficiently short so that pinching and magnetohydrodynamic (MHD) instabilities do not occur. A capacitor bank voltage of 40 kV and a gas fill of 2 Torr air result in a peak discharge current of 45 kA. The discharge plasma is nearly fully ionized when the beam is injected just prior to peak current.

Magnetic probes have been used to measure the magnetic field profiles in the discharge channel.¹⁰ Results indicate a nearly uniform current distribution across the entire channel cross section during the current rise. However, the finite size (≈ 0.2 cm across) of the probe may result in an overestimate of the magnetic field near the axis of the channel. Laser interferometric measurements¹² of the plasma density indicate a lower density near the axis, perhaps implying a hollow current profile. An effort is underway to investigate this issue in more detail using one-dimensional simulations.

This plasma channel meets all the requirements for a transport channel. As discussed in more detail in Sec. III B, the peak discharge current of 45 kA is expected to result in efficient trapping of the ion beam for a diode-to-channel spacing of 30 cm. The 2 Torr fill pressure gives an initial molecular density of 7×10^{16} cm^{-3} , while a proton beam current of 50 kA at 1.2 MeV delivered to the channel entrance aperture (a generous estimate of the experimental conditions) gives a beam density n_b of 9×10^{13} cm^{-3} . Thus, the condition of $n_b \ll n_c$ for charge and current

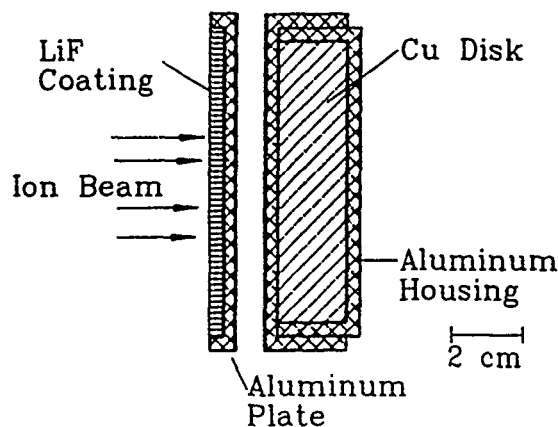


FIG. 5. Schematic of the LiF nuclear activation diagnostic.

neutralization² is easily satisfied, where n_e is the plasma electron density.

C. Ion-transport diagnostics

The characteristics of the ion-beam transport are measured with two different techniques. A dual prompt- γ diagnostic is used to determine the aperture efficiency, the injection efficiency, and energy-transport efficiency, while a shadowbox is used to sample the ion-beam phase-space distribution after transport.

The dual prompt- γ activation technique uses proton bombardment of a LiF target to generate a flux of 6–7 MeV prompt γ rays from the $^{19}\text{F}(p,\alpha\gamma)$ reaction²⁰ and a flux of 15–18 MeV prompt γ rays from the $^7\text{Li}(p,\gamma)$ reaction.^{21,22} The target is located 7–8 cm behind the entrance aperture or channel exit so that the ion beam is deposited on the central 4–5 cm diameter of the 7.5 cm diam target in all cases. This distance maintains a consistent geometry between the γ -ray source and the copper detector (Fig. 5). The γ -ray yields from these reactions are measured simultaneously using two different techniques. The $^{19}\text{F}(p,\alpha\gamma)$ reaction yield is measured with a scintillator/photomultiplier detector mounted in a lead shield and located behind a 30 cm thick concrete wall, 3.5 m from the target. The concrete differentially shields lower energy bremsstrahlung produced in the ion diode from the higher energy prompt- γ rays. Also, this detector is positioned to provide equal time-of-flight and approximately equal shielding for γ rays from targets located at either the entrance or the exit of the transport channel. The γ -ray yield from the $^7\text{Li}(p,\gamma)$ reaction is measured using secondary activation. The 15–18 MeV γ rays from the reaction activate a nearby copper sample via the $^{63}\text{Cu}(\gamma,n)^{62}\text{Cu}$ reaction (Fig. 5). After a shot, the copper sample is removed and the 9.76 min ^{62}Cu positron activity is measured using NaI coincidence counting. Multichannel scaling is used to record the ^{62}Cu decay for more than 20 half-lives. The initial ^{62}Cu activity is determined by a least-squares fit to the measured decay curve. Also, a correction is made for the delay from the shot to the start of counting. Activity from the competing $^{65}\text{Cu}(\gamma,n)^{64}\text{Cu}$ reaction is also ob-

served, but the strength of the 12.7 h ^{64}Cu decay is only a small fraction of the measured activity. The ^{64}Cu activity and the background counting rate are included in the least-squares-fitting process. The coincidence counting system is calibrated between shots with a ^{22}Na source to provide consistent measurements. Uncertainties in the relative activities are about 1%, based on the statistical uncertainty in the least-squares fits, and the uncertainties in the time delay correction and the counting system calibration.

Simultaneous prompt- γ measurements for the proton-induced reactions on ^{19}F and ^7Li are independent. The 6–7 MeV γ rays from the ^{19}F reaction and bremsstrahlung x rays are too low in energy to activate copper, because the threshold for $^{63}\text{Cu}(\gamma,n)^{62}\text{Cu}$ reaction is 10.9 MeV. On the other hand, the scintillation detector measures γ rays primarily from fluorine because the $^{19}\text{F}(p,\alpha\gamma)$ yield is 30–60 times that of the $^7\text{Li}(p,\gamma)$ yield for 0.9–1.2 MeV protons.^{20,21} The relative contribution of these two reactions to the scintillation detector was determined by replacing the LiF target with a LiCl target to produce only ^7Li γ rays. Gamma rays from nuclear reactions on chlorine are assumed to be negligible at these proton energies. This measurement indicates that the ^7Li yield contributes less than 10% to the scintillation detector signal. Finally, replacing the LiF target with a brass target gave no activation of the copper sample, and a bremsstrahlung signal only about 20% of the prompt- γ signal.

The signal from the ^{19}F reaction is used only as a qualitative measure of ion-beam transport. Quantitative data reduction is complicated by the strong proton energy dependence of this reaction, by the necessity of maintaining equal shielding between the target and detector for all target locations, and by contributions from bremsstrahlung and the ^7Li reaction. In previous experiments nuclear techniques were also used, but either the $^{19}\text{F}(p,\alpha\gamma)$ reaction,^{4,8} or reactions subject to ablation effects^{5–7} were used. The ^7Li reaction with secondary Cu activation combines an insensitivity to ablation with a relatively smooth energy dependence similar to that of the $^{12}\text{C}(p,\gamma)^{13}\text{N}$ reaction^{5,7} or the $^{10}\text{B}(p,\gamma)^{11}\text{C}^*(\beta^+)^{11}\text{B}$ and $^{14}\text{N}(p,\gamma)^{15}\text{O}^*(\beta^+)^{15}\text{N}$ reactions.⁶ Copper activation is used to obtain a quantitative measure of ion-beam transport. Analysis of the nuclear reaction measurements is described in detail in Sec. III C.

A shadowbox is used to sample the local ion distribution by recording ion-beam damage on a witness plate located behind an array of pinholes. This technique is shown in Fig. 6. The witness plate material is a thermoplastic with a thin emulsion layer that is stripped from the witness plate after the shot to remove damage caused by low-energy ions or the discharge plasma. High-energy ions penetrate this emulsion layer, and damage the plastic substrate. Damage is observed if both the ion beam and the discharge are fired and properly timed. No damage is observed if the discharge is not fired or if the discharge is fired without an ion beam. The damage patterns consistently show symmetry in the θ direction as expected from the cylindrical symmetric geometry of the experiment. The shadowbox damage patterns provide a measure of the angular distribution of

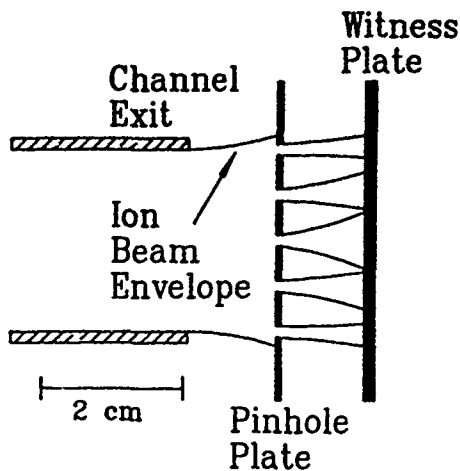


FIG. 6. Schematic of the shadowbox diagnostic.

the ion beam imaged through the various shadowbox pinholes, but do not provide a quantitative measure of the ion intensity. The shadowbox results are compared with predictions based on Monte Carlo simulation of ion-beam propagation through the channel and the shadowbox pinholes. Although the calculations provide intensity information within the shadowbox damage spots, only the boundaries for the damage patterns are used to compare with the measurements. Details of the calculations are given in Sec. III D.

III. THEORY AND FRAMEWORK FOR DATA ANALYSIS

The theory of ion-beam transport in a z-discharge channel has been treated previously in some detail. Axisymmetry is assumed in all analyses. Early work⁹ treated the main features of beam propagation by assuming that all ions possessed negligibly small angular momentum. More recent analysis²³ has included the effects of ion angular momentum. Here, angular momentum must be included in the analysis in order to quantitatively interpret transport efficiency measurements and properly compare calculated and measured shadowbox damage patterns. In this analysis the magnetic-field distribution in the channel is allowed to vary as $(r/r_c)^N$ where r_c is the channel radius. The $N=1$ case corresponds to a discharge with uniform discharge current density. By using the experimentally measured voltage and current waveforms, the shot-to-shot variations in the focusing properties of the ion source are accounted for and the energy-dependent nuclear reaction yields are properly treated. For the shadowbox analysis, the ions from the diode model are transported through the channel using a fully 3-D, nonrelativistic orbit code, and projected onto the shadowbox structure to obtain shadowbox damage patterns. For the nuclear reaction calculations, a turning point equation is used to determine which ions are trapped by the channel and which ions are lost to the channel wall. Then, analytic techniques are used to project the trapped ions through the channel, incorporating time-of-flight effects and energy loss in the channel gas. The

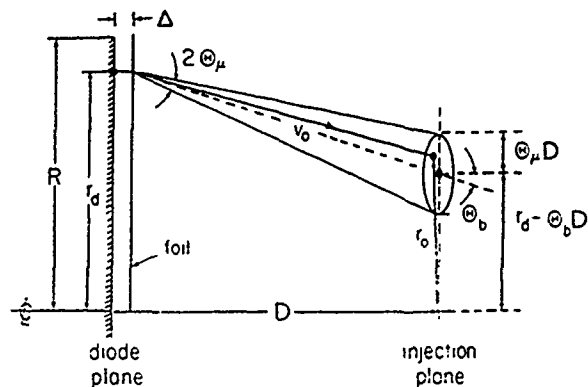


FIG. 7. Geometry for ion injection into the transport channel.

only free parameters in this analysis are the microdivergence of the ion beam at the source, and the radial structure assigned to the magnetic field in the channel. The microdivergence is determined by fitting the ion source calculations to the results of the copper activation measurements at the channel entrance. The radial structure of the magnetic field is determined by fitting the shadowbox results and the nuclear reaction measurements of the transported beam. In Sec. III A we present the model for the ion source, and Sec. III B is a presentation of the model for z-discharge transport of the ion beam. Based on these models, in Secs. III C and III D we present the numerical techniques used to analyze and interpret the experimental nuclear activation and shadowbox measurements.

A. Ion source model

The model of the ion source follows the physical description given in Sec. II A and in Fig. 2. The corrected voltage and ion-current time histories measured for a shot are divided into 20 bins, of 4.5 nsec duration. The timing of the first bin is selected so that the initial ion energy is approximately 400 keV. Protons below that energy are stopped by the Kimfol and channel gas, and do not contribute to the nuclear reactions. Equally weighted ion "particles," typically 50 000 per calculation, are distributed among the 20 bins, according to the measured ion current. Each particle in a bin is then given a random launch time within the time frame of that bin and is assigned a voltage determined by a linear interpolation of the voltage between neighboring bins for that launch time.

The geometry for ions launched from the diode and injected into the transport channel is illustrated in Fig. 7. The particles are distributed uniformly in azimuth and are launched from the plane of the Kimfol with a $1/r_d$ radial distribution²⁴ of current density. Since the orbits of the ions are bent toward the axis in the vacuum gap Δ of the diode by their self-magnetic field, ions are launched at an angle

$$\Theta_b(t) = \frac{\omega_c(t)\Delta}{v_{zd}(t)}, \quad (1)$$

where

$$\omega_c = \frac{2Z_d e I_i(t)}{m_i c^2 R},$$

Z_d is the ion charge state in the diode, v_{zd} is the axial component of the ion velocity in the diode, I_i is the total ion current, m_i is the ion mass, e is the electron charge, c is the speed of light, R is diode radius, $\Theta_b \ll 1$ is assumed, and all parameters are expressed in cgs units unless explicitly stated. Because the ion current density in the diode varies as $1/r_d$, the self-magnetic field is uniform and ions at all radii have the same bending angle. The magnetic field associated with the electron current in the diode contributes insignificantly to ion orbit bending because the electrons pinch to the axis in a thin layer δ at the anode, where $\delta \ll \Delta$. For these proton beam experiments, $Z_d = 1$, $m_i = m_p$, $R = 6$ cm, and $\Delta = 1.4$ cm so that

$$\Theta_b(t) = 0.32 \frac{I_i(t)}{V^{1/2}(t)}, \quad (2)$$

for Θ_b expressed in radians, current in MA, and voltage in MV.

A beam microdivergence Θ_μ is introduced in order to model nonuniformities in the electron and ion emission, electromagnetic-field fluctuations in the diode, and scattering in the foil. As illustrated in Fig. 7, ions are distributed in velocity space uniformly within a cone of half-angle Θ_μ centered about Θ_b while keeping the total ion energy constant. The value for the microdivergence is chosen by matching calculations for the ${}^7\text{Li}$ nuclear activation at the entrance of the channel with the experimental results for the various diode-to-channel spacings (see Sec. IV A for details).

The particles are propagated ballistically from the Kimfol to the plane of the channel entrance with their energy corrected for collisional losses in the Kimfol and gas.²⁵ The air is treated as 80% N_2 and 20% O_2 . Particles that have a radius r_0 at the injection plane less than the entrance aperture radius r_a are used as the input for either the shadowbox or the nuclear reaction yield calculations. The calculations predict aperture efficiencies of from 2.4% to 6%, where the aperture efficiency is defined as the efficiency of delivering ions from the ion source to the channel entrance aperture (see Sec. IV for further discussion). The lower number results when the diode-to-channel spacing is 30 cm, and the higher number results for the 20 cm diode-to-channel spacing. For a typical ion current of 500 kA from the diode, these results correspond to 12 kA injected into the channel for the 30 cm diode-to-channel spacing and 30 kA for the 20 cm diode-to-channel spacing.

B. Basic theory of z-discharge transport

The transport channel is assumed to be a high-density z-discharge in which $n_e \gg n_b$. For modeling the experiments, the discharge current is distributed in a prescribed profile across the discharge radius. Once in the transport channel, ions are confined radially by the magnetic field associated with the z-discharge current. The charge and current of the

ion beam are assumed to be fully neutralized by the discharge plasma. The magnetic field in the discharge is modeled by

$$B_\theta = \frac{2I_c}{cr_c} \left(\frac{r}{r_c} \right)^N, \quad (3)$$

where I_c is the discharge current. Since complete charge and current neutralization of the beam is assumed and beam/plasma scattering collisions are negligible, beam propagation can be described in terms of single-particle orbits in the magnetic field given by Eq. (3). For any given ion, the velocity components and the radial position at injection into the transport system, v_{r0} , $v_{\theta0}$, v_{z0} , and $r_0 < r_c$ (see Fig. 7) determine the constants of the motion that govern the orbit. These constants are energy, H , angular momentum, P_θ , and canonical axial momentum, P_z . The ions are nonrelativistic, so that

$$\frac{2H}{m_i} = v_r^2 + v_\theta^2 + v_z^2 = v_0^2, \quad (4)$$

$$\frac{P_\theta}{m_i} = r v_\theta = r_0 v_{\theta0}, \quad (5)$$

and

$$\frac{P_z}{m_i} = v_z - \frac{v_c}{N+1} \frac{r^{N+1}}{r_c^{N+1}} = v_{z0} - \frac{v_c}{N+1} \frac{r_0^{N+1}}{r_c^{N+1}}, \quad (6)$$

where $v_0^2 = v_{z0}^2 + v_{\theta0}^2 + v_{r0}^2$,

$$v_c = \frac{2ZeI_c}{m_i c^2}, \quad (7)$$

and Z is the ion charge state in the transport channel. The radial equation of motion can be obtained by substituting for v_θ and v_z from Eqs. (5) and (6) into Eq. (4) and solving for v_r . The azimuthal and axial equations of motion can be obtained directly from Eqs. (5) and (6).

By setting $v_r = 0$ in the radial equation of motion, an equation for the radial turning points r_{ip} is obtained:

$$1 = \frac{r_0^2 v_{\theta0}^2}{r_{ip}^2 v_0^2} + \left(\frac{v_{z0}}{v_0} - \frac{v_c (r_0^{N+1} - r_{ip}^{N+1})}{(N+1) v_0 r_c^{N+1}} \right)^2. \quad (8)$$

This equation defines the inner, $r_{ip} \equiv r_*$, and outer, $r_{ip} \equiv r^*$, turning points for any given ion entering the channel with specified initial conditions. In the special case of $N=1$ and $P_\theta=0$, $r_* = 0$ and the ions follow nearly sinusoidal betatron orbits⁹ with betatron wavelength, λ_b , given by

$$\lambda_b = 2\pi r_c \left(\frac{v_0}{2v_c \cos \alpha} \right)^{1/2}, \quad (9)$$

where $\tan \alpha = v_{r0}/v_{z0}$. Typically, $\tan \alpha \sim R/D \ll 1$, where D is the diode-to-channel spacing. When $P_\theta=0$, λ_b still provides a good measure of the axial wavelength of radial oscillations for $N=1$. A typical ion orbit for $P_\theta \neq 0$ and $N=1$ is shown in Fig. 8.

Ions with $r^* < r_c$ will be transported and ions with $r^* > r_c$ are lost to the wall within the first betatronlike oscillation. The aperture radius $r_a < r_c$ placed at the entrance of the channel defines the input spot size, and allows some

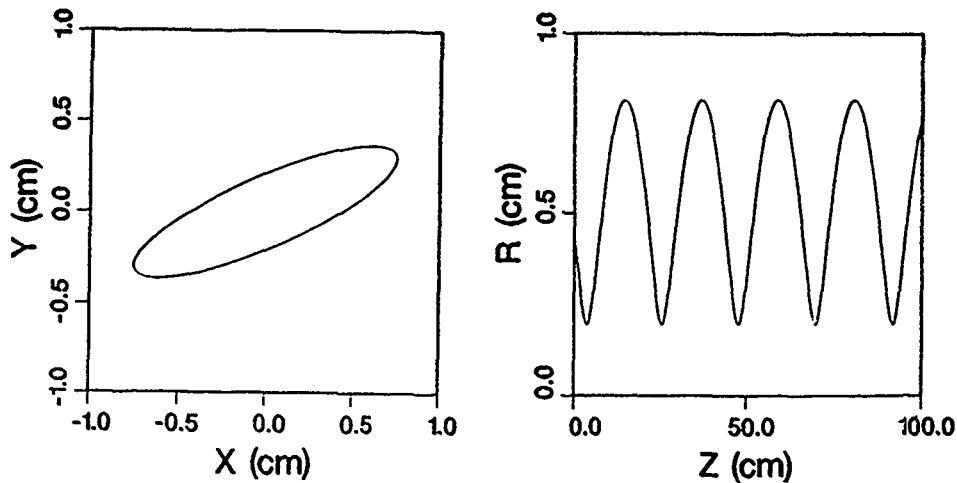


FIG. 8. Sample orbit for an ion with $P_{\theta} \neq 0$ and $N=1$.

radial distance for the ions to turn in the magnetic field without striking the channel wall. Thus, the ions confined in the channel have $r^* < r_c$, as defined by Eq. (8), and $r_* < r_a$, as determined by the entrance aperture. The turning point equation [Eq. (8)] can be reformulated to identify the minimum discharge current required to confine all ions that pass through the aperture:

$$I_{cm} = \frac{v_0 m_e c^2 (N+1)}{4Ze[1 - (r_a/r_c)^{N+1}]} \frac{(R+r_a)^2}{D^2}. \quad (10)$$

This result is obtained by setting $r^* = r_c$ for an ion entering the channel at the largest possible angle [$\tan \alpha = (R+r_a)/D$] and at the largest possible radius ($r_0 = r_a$). Note that I_{cm} decreases as the diode-to-channel spacing increases, because the ion injection angles decrease. With a more hollow magnetic field profile (i.e., higher N), higher magnetic field is required at the outer edge of the discharge to turn the ions and prevent them from striking the channel wall. Thus, a larger I_{cm} is required to confine the beam for higher N .

Equation (10) was derived by considering the confinement of ions with the maximum perpendicular energy. It contains no information about the distribution of ions in phase space. Thus, considerably less current may be required to confine the majority of the injected ions. Figure 9 shows a plot of injection efficiency, η_i , as a function of R/D . The injection efficiency is the fraction of the beam ions that pass through the aperture ($r_0 < r_a$) that are confined and transported ($r^* < r_c$). Here R/D is the ratio of the radius of the ion source to the source-to-channel spacing and serves as a measure of the maximum perpendicular velocity of the ion beam. The results in Fig. 9 were derived using the experimental geometry, the diode model described in Sec. III A, and the typical voltage and ion-current waveforms illustrated in Fig. 3. Curves are shown for the typical discharge current of 45 kA used in the experiments and for $N=1, 2$, and 3 which show the effect of different magnetic-field profiles on confinement. Higher injection efficiency is obtained with smaller R/D and lower N . For a 20 cm diode-to-channel spacing ($R/D \sim 0.25$), η_i falls within the range of about 0.65–0.9, while for a 30 cm

diode-to-channel spacing ($R/D \sim 0.17$) higher efficiency is expected with η_i falling within the range of about 0.9–1.0. For typical Gamble II experimental parameters ($R=5.1$ cm, $r_a=0.85$ cm, $r_c=1.25$ cm, $D=30$ cm, and $V=1.3$ MV) and $N=1$, $I_{cm} \sim 60$ kA, while Fig. 9 shows that 45 kA is sufficient to confine nearly all of the injected ions. For $N=3$, I_{cm} increases to about 80 kA, while Fig. 9 shows that 45 kA still confines more than 95% of the injected ions.

C. Nuclear diagnostic calculations

Nuclear diagnostic calculations are performed for LiF targets at the entrance aperture locations and at the output of the transport channel. Calculations for the entrance aperture locations use the output of the ion source model, where particles that have $r_0 < r_a$ at the aperture location are used to calculate a time-integrated yield for the ${}^7\text{Li}$ diagnostic or a time-dependent yield for the ${}^{19}\text{F}$ diagnostic.

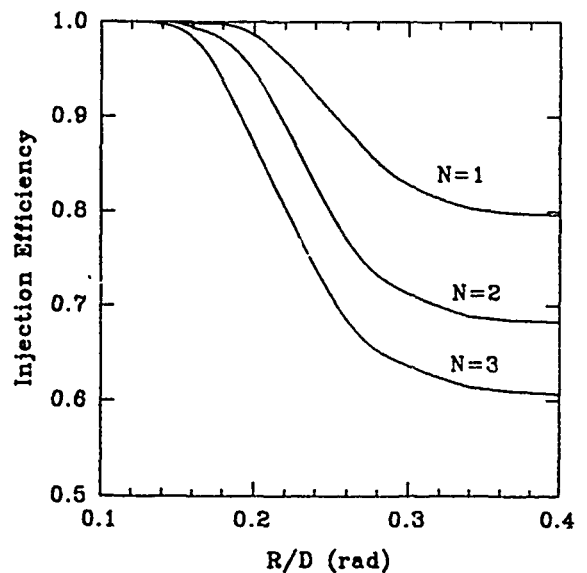


FIG. 9. Injection efficiency as a function of R/D for magnetic-field profiles with $N=1, 2$, and 3 . Efficiencies are for $I_c=45$ kA, $r_c=1.25$ cm, $r_a=0.85$ cm, and a proton beam produced from the waveforms in Fig. 3 with $\Theta_{\mu}=0.175$ rad.

using the energy-dependent yield curves.^{20,21} These results are used to determine the microdivergence of the source model (see Sec. IV A).

Calculations for transported beams use an analytic approximation of the ion orbits to transport the particles rather than the explicit orbit code used for the shadowbox analysis (Sec. III D). Since the nuclear reaction yields only depend on the ion energy and ion current on target, details of the phase space distribution of the beam are not required for this calculation. The diode source model again provides the input particle distribution. For each particle injected into the transport section, Eq. (8) is solved to determine if the particle is trapped, i.e., $r^* < r_c$, so that the injection efficiency is calculated by determining what fraction of the particles are confined by the magnetic field of the channel. The trapped particles are propagated to the end of the channel by using their average axial velocity to determine the time-of-flight.²³ To calculate collisional slowing of the ions in the channel gas, a total path length along the beta-tronlike trajectory of the ions is calculated.²³ The input energy of each ion is then corrected for collisional slowing along this total path length to yield the final energy at the end of the channel. These transported particles are then used to calculate a time-integrated yield for the ${}^7\text{Li}$ diagnostic or a time-dependent yield for the ${}^{19}\text{F}$ diagnostic, using the energy-dependent yield curves.^{20,21}

The energy-dependent shape of the yield curve for the ${}^7\text{Li}$ reaction is taken from Leeper *et al.*²¹ Integrating the ${}^7\text{Li}(p,\gamma)$ cross section²⁶ over a thick target gives a nearly isotropic yield for activating a copper sample located in the forward hemisphere. Therefore the shape of the yield curve is insensitive to geometric differences between the detector in Fig. 5 and that used in Ref. 21. The natural abundance of deuterium in the beam induces ${}^{63}\text{Cu}(n,2n){}^{62}\text{Cu}$ activation from the ${}^7\text{Li}(d,n)$ reaction, leading to a 20% correction factor for 1.2 MeV ion energies.²¹ Integrating the ${}^7\text{Li}(d,n)$ cross section²⁷ over a thick target gives nearly isotropic neutron emission. Therefore, any deuteron correction is insensitive to the detector geometry, and a similar deuteron correction should be expected for our detector (Fig. 5). Nevertheless, this correction is not made in our experiments, for two reasons. First, the deuteron correction in Ref. 21 is for deuterons with the same energy as the protons. That is not the case in our experiment. In passing through the Kimfol and the 25–35 cm of 2 Torr air separating the ion-source vacuum and the beam transport region 1.2 MeV protons lose 72 keV, while 1.2 MeV deuterons lose 150 keV.²⁵ In propagating an additional 1.2 m in the transport channel, the protons lose another 85 keV, while the deuterons lose another 300 keV. Thus the correction factor is less than 20% at the entrance aperture and less than 5% at the transport channel exit, because the correction factor decreases with decreasing ion energy. Second, deuterons are less effectively trapped by the transport channel than are protons. This is most clearly seen in Eq. (10), where the current required to trap equivalent energy deuterons is 1.4 times greater than that required for protons. The net effect of greater dE/dx energy loss for deuterons and less effective trapping of deuterons by the

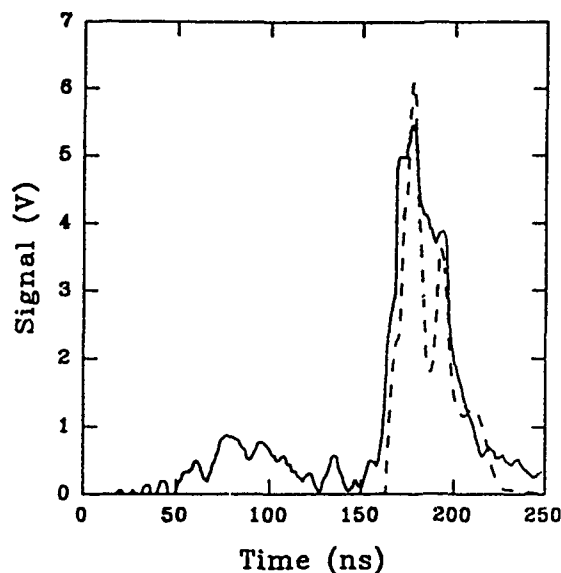


FIG. 10. Comparison of experimental (solid line) and calculated (dashed line) ${}^{19}\text{F}$ prompt- γ signals for $D=25$ cm. The LiF target is located at the end of the transport channel.

transport channel is to make the deuteron correction negligible for the Cu activation measurement at the transport channel exit, while it is perhaps 15% at the transport channel entrance. Thus, the measured transport efficiencies should be considered lower limits, because any deuteron correction would decrease the activity at the entrance aperture, while not altering the activity at the transport channel exit.

Analysis of the nuclear reaction yield data concentrates on the ${}^7\text{Li}$ results. The uncertainty in the calculated ${}^7\text{Li}$ signal (neglecting the deuteron correction discussed above) is $\pm 5\%$, derived from uncertainties of $\pm 3\%$ in measurements of the voltage and ion current and a statistical variation of $\pm 2\%$ in the computation, based on the number of ions used in the simulation. Details of the analysis are presented along with the experimental results in Sec. IV. The calculation for the ${}^{19}\text{F}$ diagnostic is complicated by the strong proton energy dependence of this reaction. However, the measurements confirm earlier analysis of z-discharge transport of ion beams⁴ and demonstrate by timing that there are no unexpected ion energy losses during transport. Calculated and measured yields for the ${}^{19}\text{F}$ diagnostic are compared in Fig. 10, for a target after the transport channel and a diode-to-channel spacing of 25 cm. The agreement in timing between the calculation and the measurement is quite reasonable, which indicates the corrected voltage measured in the experiment accurately represents the proton energy. The disparity in wave shapes is due to small variations in the corrected voltage amplified by the strong energy dependence of the ${}^{19}\text{F}$ reaction yield.

D. Shadowbox analysis

The shadowbox analysis uses a 3-D, nonrelativistic orbit code to explicitly propagate computational particles from the channel entrance to the shadowbox. The radial distribution of the magnetic field in the channel is modeled

by $B_\theta \propto r^N$ with $N=1, 2,$ and 3 . Particles that hit the channel wall ($r^* > r_c$) are removed from the system. Particles that have $r^* < r_c$ are propagated to the end of the channel, accounting for collisional energy losses in the channel gas²⁵ by reducing the particle speed as it propagates. At the end of the transport channel, the particles that pass through the shadowbox pinholes are projected ballistically onto the shadowbox witness plate. Statistics are improved by using the assumed axisymmetry of the problem to rotate the particle distribution in the θ direction and thus increase the number of particles projected onto the witness plate. The calculations provide the geometric pattern of damage, and can also provide intensity information. However, the witness targets in the experiment only provide the pattern of the spots and no quantitative intensity information. Thus, comparisons between the calculations and the measurements are only based on the size of the damage spots.

IV. EXPERIMENTAL RESULTS

This section presents the results of the measurements and the accompanying analysis. The experimental arrangement is described in Sec. II. The ion source and the transport channel are operated with nominally the same settings for all shots. The firing of the ion beam is usually timed to be at, or slightly before, the peak of the discharge current, so the discharge current is 45 kA. Shots are taken with diode-to-channel spacings of 20, 25, and 30 cm. The change in this spacing alters the phase space of the ions presented to the entrance of the channel, and allows comparison of the experimental results and theoretical expectations for a range of input conditions. In particular, the maximum injection angle of ions into the channel decreases as the spacing increases. Because of the uncertainty in the magnetic-field profile, the analysis models the magnetic field as varying as r^N . The best fit to the data determines N .

Three different efficiencies are considered in analyzing an ion transport system. The first efficiency is the aperture efficiency, and is defined as the fraction of diode protons which pass through the transport channel aperture. The aperture efficiency is measured by comparing the yield from the ${}^7\text{Li}$ reaction at the various input locations behind the $r_a=0.85$ cm entrance aperture with the yield obtained from full-target ${}^7\text{Li}$ shots, where the entire ion beam is deposited on the LiF. The aperture efficiency is expected to be small for these experiments, due to the mismatch between the large spot size from the weak-focusing flat-geometry diode and the small entrance aperture diameter. High aperture efficiency could be achieved with diodes with smaller microdivergence and by shaping the diode for a tight focus at a specific location. The experimental diode geometry was not chosen to optimize the aperture efficiency, but rather to provide a number of different ion-beam conditions to test the ion transport physics without changing the ion source.

The injection efficiency is the fraction of the proton beam passing through the aperture ($r_0 \leq r_a$) that is confined and transported ($r^* \leq r_c$). It is determined by applying the channel trapping conditions expressed by Eq. (8) to the phase space of the ion beam delivered to the channel en-

trance. The different diode-to-channel spacings used in the experiment vary the ion beam phase space, and hence this efficiency. The injection efficiency is measured by comparison of ${}^7\text{Li}$ yields behind the entrance aperture to that at the transport channel output.

The third efficiency is the energy transport efficiency. This efficiency has two components; one is the efficiency with which initially trapped protons remain trapped, and the other is the efficiency with which the energy of the protons is retained during transport. Ions undergoing transport lose energy because of collisional slowing in the channel gas. These losses are minor in the present experiment. For 1.2 MeV protons in air, the stopping power is 33 keV/m/Torr,²⁵ so that the total energy loss in the channel is 80 keV, or about 7%. Other energy losses from induced electric fields in the plasma^{9,12} are also small for these experimental conditions, but can be quite important in an ICF system. The energy transport efficiency is also measured by comparison of ${}^7\text{Li}$ yields behind the entrance aperture to that at the transport channel output. The distinction between injection losses and energy transport losses is made on the basis of numerical analysis of the nuclear yield measurements.

A. Aperture efficiency measurements

Measurements of the ${}^7\text{Li}$ reaction yields at the three input distances are used to assess the fraction of the ion beam that is delivered to the channel entrance at each location. They are also used to determine the microdivergence to be used in subsequent calculations. The measured quantity is the initial activity of the copper disk activated by the ${}^7\text{Li}(p,\gamma)$ reaction. A calculated activity is obtained from the calculations described in Sec. III C. A similar calculation is performed for shots where the entire proton beam is intercepted by the LiF target (and are hence independent of the microdivergence), to determine the scale factor between the calculated and experimental nuclear reaction yields. The results of fitting the calculated ${}^7\text{Li}$ yields to the experimental yields are shown in Fig. 11, for an assumed microdivergence of 0.175 rad. For perfect agreement between the calculations and the measurements, the points would fall on the line. Several neglected aspects in the ion source model can lead to such discrepancies between the calculations and the measurements, despite the small uncertainties in both. The electron-beam pinch can be slightly off-center, and the ion source is known to have some azimuthal asymmetry.¹⁶ Figure 11 represents the degree to which these effects can be included in the ion source model through the microdivergence. Calculated activities for several values of Θ_μ are given in Table I. Smaller microdivergences (e.g., 0.150 rad) give calculated activities that are too large, especially for the 20 and 25 cm spacings. Larger microdivergences (e.g., 0.2 rad) give activities that are too low. A microdivergence of 0.175 rad is used for all of the following results.

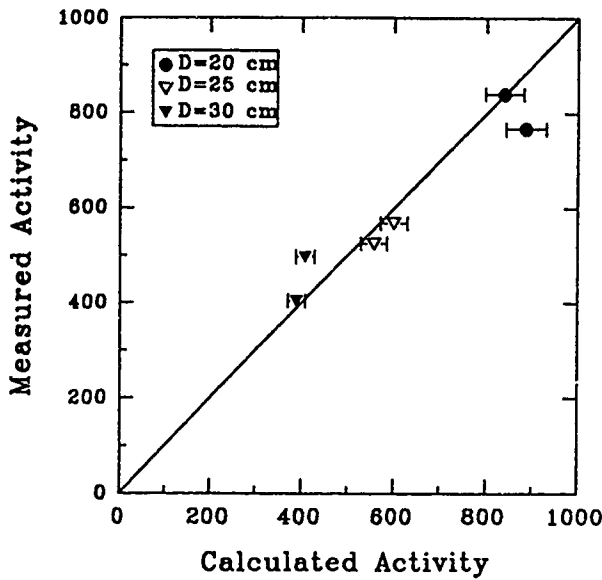


FIG. 11. Comparison of measured and calculated copper activities at the transport channel entrance for $\Theta_\mu=0.175$ rad.

B. Injection and energy transport efficiency measurements

The ^7Li activation data are used to determine the injection and energy transport efficiencies following the analysis procedure described in Sec. II C. The injection efficiency is determined by calculating the fraction of the injected ion beam that is confined by the magnetic field. The confined portion of the ion beam is then numerically propagated through the channel with classical slowing in the channel gas, to calculate an activation yield at the end of the channel. The profile of the magnetic field is varied to obtain agreement between the calculated and measured activities for the various diode-to-channel spacings.

Calculations of the ^7Li activation for magnetic field profiles with $N=3$ and $N=1$ are compared with the measured activities in Fig. 12. The error bars on the measured activities are the size of the symbols, while the error bars on the calculations are shown. The numerical values of these activities are listed in Table II. For the $D=30$ cm case, there is good agreement between the calculations and the measurements for both magnetic field geometries. In this case, the ion-beam distribution is well trapped, and

TABLE I. The Li activation results for input shots where Θ_μ is the beam microdivergence.

Shot No.	D (cm)	Measured activity	Calculated activity		
			$\Theta_\mu=0.175$ rad	$\Theta_\mu=0.150$ rad	$\Theta_\mu=0.200$ rad
4846	30	404	372	525	304
4849	30	497	421	550	317
4841	25	568	591	779	443
4842	25	525	563	769	431
4843	20	768	891	1129	704
4844	20	841	859	1083	657

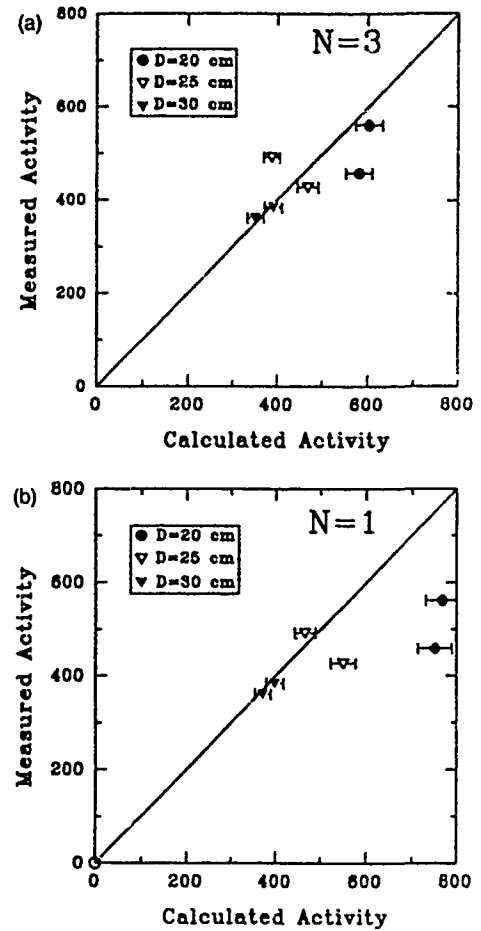


FIG. 12. Comparison of measured and calculated copper activities at transport channel exit, for $\Theta_\mu=0.175$ rad, and (a) $N=3$ and (b) $N=1$.

thus the calculated activity is insensitive to the details of the magnetic field distribution. For $D=25$ cm, both the $N=1$ and $N=3$ calculations are consistent with the measurements. For $D=20$ cm, the $N=3$ calculation gives much better agreement with the measurements.

To understand the effects of varying the magnetic field geometry and the diode-to-channel spacing, an accounting of the ion energy is examined in detail. An energy accounting for $D=30$ cm is given in Table III. The total transported energy for the $N=3$ and $N=1$ cases is not substantially different. Approximately 10% of the ion-beam energy is lost to classical slowing in the channel gas, and

TABLE II. The Li activation results for output shots where $B \propto r^N$.

Shot No.	D (cm)	Measured activity	Calculated activity	
			$N=3$	$N=1$
4845	30	361	350	370
4847	30	384	391	398
4839	25	492	387	465
4840	25	427	468	549
4824	20	562	603	768
4829	20	459	581	751

TABLE III. Energy accounting for $D=30$ cm ion transport calculations where $B \propto r^N$.

Shot No.	N	Energy loss to wall (%)	Energy loss to gas (%)	Total energy transported (%)
4845	3	4.8	9.3	85.9
4847	3	3.8	8.9	87.3
4845	1	0.3	9.6	91.1
4847	1	0.5	9.2	90.3

less than 5% of the ion-beam energy is lost to the channel wall due to untrapped ions. A similar analysis of the measurements for $D=25$ cm and $D=20$ cm indicates that the total transported energy is decreased due to decreased injection efficiency, and not due to increased losses from classical slowing in the channel gas. An energy accounting for $D=20$ cm is presented in Table IV. In this case, the portion of the ion beam confined by the channel is less for $N=3$ and this improves the agreement with the experimental data (see Fig. 12). Again, the portion of the ion beam that is confined and transported loses approximately 10% of its energy to classical slowing in the channel gas.

C. Shadowbox measurements

The shadowbox diagnostic is used to sample the ion trajectories after transport, and compare them with the expectations of the theory presented in Sec. II B. Damage patterns from the shadowboxes are presented in Fig. 13 for the 20 and 30 cm diode-to-channel spacings. Also shown are the corresponding results of the shadowbox calculations for $N=3$. Qualitatively, larger damage spots (i.e., ions exiting the channel at larger angles) are obtained for smaller diode-to-channel spacing because ions are available to enter the channel at larger transverse angles as the channel entrance is located closer to the ion source. Since the confinement characteristics of the channel are fixed for given values of r_w , r_c , and I_c , the injection efficiency is expected to increase as the diode-to-channel spacing increases. Simple geometric considerations of the ion source and the channel confinement characteristics predict nearly 100% injection efficiency for $D=25$ and 30 cm (see Fig. 9). However, the damage spot sizes should be limited by the channel confinement characteristics for $D=20$ cm. This is in qualitative agreement with the results shown in Fig. 13.

TABLE IV. Energy accounting for $D=20$ cm ion transport calculations where $B \propto r^N$.

Shot No.	N	Energy loss to wall (%)	Energy loss to gas (%)	Total energy transported (%)
4824	3	22	7	61
4829	3	32	6	62
4824	1	12	9	79
4829	1	12	8	80

A quantitative analysis of the shadowbox results is obtained by using the equation for the radial velocity as a function of radius for trapped ions. The ion with the maximum radial velocity at any radius has zero angular momentum and an outer turning point of r_c . The radial velocity of this ion, $v_{rm}(r)$, defines the maximum radial angle, $\Theta_{\max}(r) = v_{rm}(r)/v_0$, and is given by

$$\Theta_{\max}(r) = \left(\frac{2v_c}{(N+1)v_0} \right)^{1/2} \left[1 - \left(\frac{r}{r_c} \right)^{N+1} \right]^{1/2}. \quad (11)$$

This angle is calculated for $N=1, 2,$ and 3 , and compared with the experimental data, as shown in Fig. 14. The data points are derived from regions of intense damage on the shadowbox targets (Fig. 12), where material has been ablated by the ion beam. Four data points each at $r=0.5$ cm and $r=1.0$ cm are derived from the four individual damage patterns at those radii. Corrections are made for the finite size of the shadowbox pinhole. The discharge current is 45 kA for $D=20$ cm and 35 kA for $D=30$ cm. The lower channel current for the $D=30$ cm case (obtained by injecting the ion beam during the rise of the channel current) reduces the confinement properties of the channel, so that the channel confinement characteristics dominate the shadowbox results, rather than the ion source characteristics. The experimental points for both $D=20$ cm and $D=30$ cm fall between the $N=2$ and $N=3$ values. This analysis indicates that the radial distribution of ions exiting the channel is more consistent with a hollow magnetic field profile, than a linear magnetic field profile.

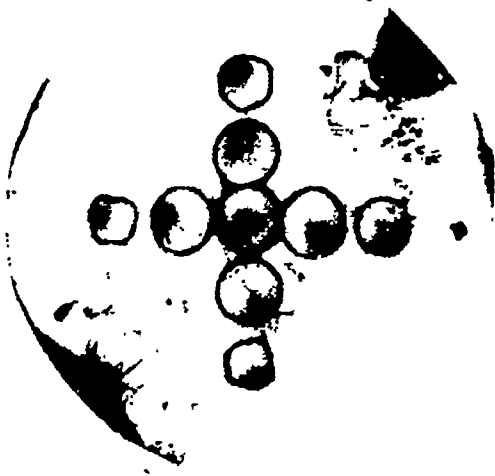
A similar conclusion is obtained from the calculated shadowbox patterns. The calculated shadowbox patterns include the effects of angular momentum that are neglected in the analysis in Fig. 14. The calculated patterns for $N=3$ in Fig. 13 are a better match to the experimental data than the patterns calculated for $N=1$. The effect of the less effective confinement by the hollow magnetic field is reduced size of the damage patterns at all radii.

The agreement between the calculated and measured shadowbox patterns supports the assumptions that the ion beam is fully charge and current neutralized in the gas fill and channel plasma. In addition, the current monitor placed around the z-discharge channel shows no change when the ion beam is injected, which indicates greater than 95% current neutralization (limit of the monitor sensitivity).

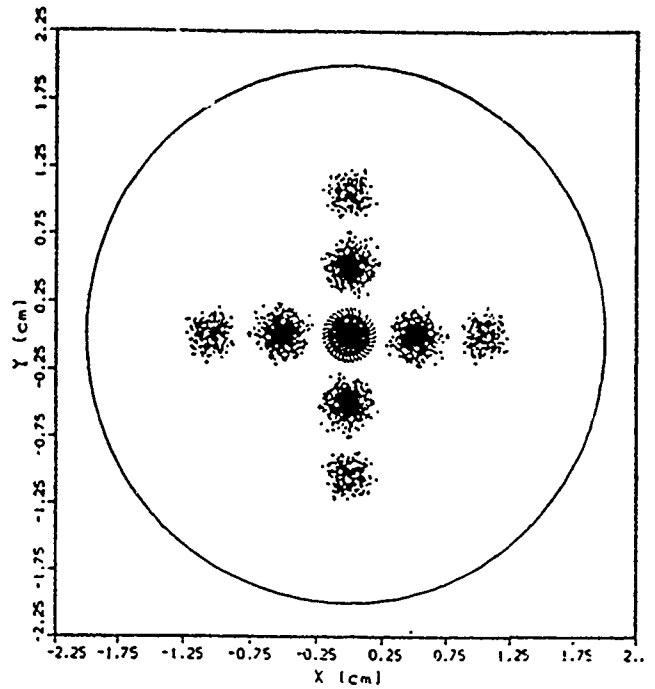
V. DISCUSSION

The z-discharge plasma channel has the essential properties required for a light-ion ICF transport scheme. The channel provides full charge and current neutralization of the ion beam, and efficiently transports the ion-beam pulse in experiment, with 1.2 MeV protons, greater than 95% of the ion beam delivered to the channel entrance is transported for a $D=30$ cm diode-to-channel spacing. Less than 10% of the transported ion beam energy is lost to classical stopping in the channel gas, for a total energy transport efficiency of greater than 85%. These results are obtained from 3-D, axisymmetric, time-dependent numerical analy-

(a)



(b)



(c)



(d)

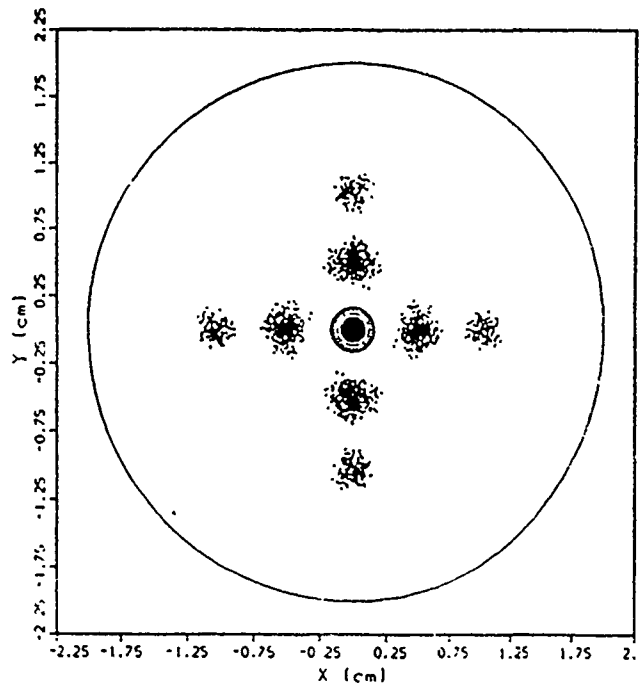


FIG. 13 Shadowbox damage patterns for $D=20$ cm from (a) experiment and (b) calculation, and for $D=30$ cm from (c) experiment and (d) calculation

sis of measured ${}^7\text{Li}(\rho,\gamma)$ nuclear reaction yields. Ion trajectories after transport, sampled with a shadowbox diagnostic, are consistent with this analysis, adding confidence to the analysis procedure. The results obtained for $D=30$

cm are insensitive to the structure of the magnetic field in the transport channel, as a consequence of strong trapping of the beam. For diode-to-channel spacings of $D=20$ and 25 cm, where trapping is not as strong, analysis of nuclear

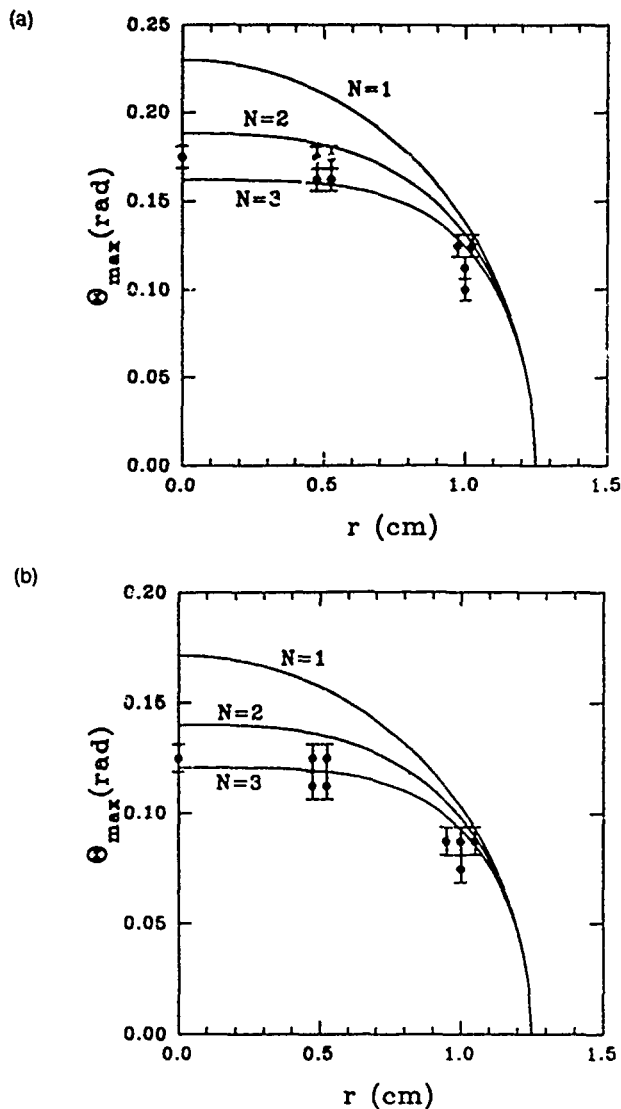


FIG. 14 Maximum angle of beam ions vs channel radius for magnetic-field profiles with $N=1$, $N=2$, and $N=3$. (a) for the shot in Fig. 13(b) with $D=20$ cm and (b) for the shot in Fig. 13(c) with $D=30$ cm

yield and shadowbox data indicates that the magnetic-field structure of plasma channel is hollow. The total energy transported is reduced to 60% for diode-to-channel spacing of 20 cm, due to a decreased injection efficiency as a consequence of the hollow channel magnetic field profile. Analysis of the ion trajectories from shadowbox data for $D=20$ cm is also consistent with a hollow channel magnetic-field profile.

Several variations of the experimental conditions, investigated with analysis of the ${}^7\text{Li}$ nuclear reaction diagnostic, were found to be insufficient to otherwise account for the low injection efficiency measured at small diode-to-channel spacings. The channel pressure was increased by 10%, to increase energy losses to the channel gas, the channel current was decreased by 20%, to decrease channel confinement properties; and the channel was misaligned with the ion beam by 5° , to decrease trapping of the ion beam by the channel. Although all of these changes are

substantially larger than the experimental uncertainties, none of these effects can account for the reduced total energy transport efficiency for the smaller diode-to-channel spacings.

To extend these results to the level required for an ICF system²³ requires significant scaling. The baseline ion beam for ICF is a 30 MeV, 1 MA, singly ionized lithium beam, in contrast to the 1.2 MeV, 30 kA proton beam used in the present experiment. The lithium beam will be fully ionized before entering the channel, and thus have a 3 MA current. The channel diameter required for an ICF system is approximately the same as in the present experiment, but a longer channel (2.5 m) and possibly larger discharge current (40–80 kA) are required. Only a modest increase in discharge current is required, despite the large increase in ion energy, because the microdivergence of the ion source is reduced and the R/D is reduced to about 0.1. The stopping power of the channel gas is reduced for 30 MeV lithium, but this is offset by a requirement to increase the channel gas pressure to mitigate the MHD response of the channel to the larger ion beam current.¹² Suitable discharge channels have been tested,¹⁹ but ICF level ion sources and pulsed power¹ and still under development.

In summary, a z-discharge plasma channel for 1.2 MeV protons is operated with a transport efficiency approaching 100%. The ion beam is charge and current neutralized in the channel. Analysis of ion trajectories indicates that the beam is confined by a hollow magnetic-field profile. Once confined in the channel, the beam propagates with classical slowing in the channel gas as the only energy loss.

ACKNOWLEDGMENTS

The authors acknowledge the pioneering work done by Fred Sandel in the field of z-discharge ion beam transport.⁴ He performed the first intense ion beam transport experiments, using wall-stabilized z-discharges, and demonstrated efficient beam transport at distances of up to 5 m. The authors also acknowledge the support of the Gamble II operating crew, Walt Snider, Frank Hollis, and Bruce Roberts

This work was sponsored by the U.S. Department of Energy, through Sandia National Laboratories

¹J. P. VanDevender and D. L. Cook, *Science* 232, 831 (1986); J. Ramirez, R. W. Stunnett, D. L. Johnson, C. L. Olson, T. A. Melcher, J. T. Crow, J. P. Quitenz, K. R. Prestwich, M. P. Desjarlais, R. E. Casner, G. O. Allshouse, T. H. Martin, J. P. VanDevender, D. L. Cook, S. A. Slutz, K. B. Coachman, T. R. Lockner, B. N. Turman, S. A. Goldstein, and J. N. Olsen, *Fusion Technol.* 15, 350 (1989)

²C. L. Olson, *J. Fusion Energy* 1, 309 (1982) and references therein; F. Winterberg, *Plasma Phys.* 17, 69 (1975)

⁴F. L. Sandel, S. J. Stephanakis, F. C. Young, and W. F. Oliggett, *Proceedings of the 4th International Topical Conference on High-Frequency Electron and Ion Beam Research and Technology*, edited by H. J. D. Uffink and J. M. Buzzi (Ecole Polytechnique, Palaiseau, France, 1987), p. 129.

⁵T. Yamada, K. Masugata, K. Yatsui, and M. Matsui, *Jpn. J. Appl. Phys.* 21, L699 (1982)

⁶T. Ozaki, S. Miyamoto, K. Imasaki, S. Nakai, and C. Yamamoto, *J. Appl. Phys.* 58, 2145 (1985)

- ⁷J. N. Olson, D. J. Johnson, and R. J. Leeper, *Appl. Phys. Lett.* **36**, 808 (1980).
- ⁸J. M. Neri, J. R. Boller, G. Cooperstein, D. Mosher, P. F. Ottinger, V. E. Scherrer, S. J. Stephanakis, F. C. Young, P. J. Goodrich, D. D. Hinshelwood, and J. J. Watrous, in *Proceedings of the 7th International Conference on High-Power Particle Beams*, edited by W. Bauer and W. Schmidt (Kernforschungszentrum Karlsruhe GmbH, Karlsruhe, Germany, 1988), p. 165.
- ⁹P. F. Ottinger, D. Mosher, and S. A. Goldstein, *Phys. Fluids* **23**, 909 (1980).
- ¹⁰P. F. Ottinger, D. Mosher, and S. A. Goldstein, *Phys. Fluids* **22**, 332 (1979).
- ¹¹P. F. Ottinger, D. Mosher, and S. A. Goldstein, *Phys. Fluids* **24**, 164 (1981).
- ¹²See National Technical Information Service Document No. ADA121471 (P. F. Ottinger, S. A. Goldstein, and D. Mosher, NRL Memorandum Report 4948, 12 November 1982). Copies may be ordered from the National Technical Information Service, Springfield, Virginia 22161.
- ¹³J. D. Shipman, *IEEE Trans. Nucl. Sci. PS-18*, 243 (1971).
- ¹⁴S. J. Stephanakis, D. Mosher, G. Cooperstein, J. R. Boller, J. Golden, and S. A. Goldstein, *Phys. Rev. Lett.* **37**, 1543 (1976).
- ¹⁵S. A. Goldstein, G. Cooperstein, R. Lee, D. Mosher, and S. J. Stephanakis, *Phys. Rev. Lett.* **40**, 1504 (1978).
- ¹⁶G. Cooperstein, S. A. Goldstein, D. Mosher, R. J. Barker, J. R. Boller, D. G. Colombant, A. Drobot, R. A. Meger, W. F. Oliphant, P. F. Ottinger, F. L. Sandel, S. J. Stephanakis, and F. C. Young, in *Laser Interaction and Related Plasma Phenomena*, edited by J. J. Schwartz, H. Hora, M. Lubin, and B. Yaakobi (Plenum, New York, 1981), Vol. 5, p. 105.
- ¹⁷D. Mosher, D. D. Hinshelwood, J. M. Neri, P. F. Ottinger, J. J. Watrous, C. L. Olson, and T. A. Melhorn, in *Proceedings of the 8th International Conference on High-Power Particle Beams*, edited by B. N. Breizman and B. A. Knyazev (World Scientific, Singapore, 1991), p. 26.
- ¹⁸Available from Kimberly-Clark Corporation, Lee, MA 01238.
- ¹⁹D. D. Hinshelwood, *J. Appl. Phys.* **72**, 4581 (1992).
- ²⁰J. Golden, R. A. Mahaffey, J. A. Pasour, F. C. Young, and C. A. Kapetanakis, *Rev. Sci. Instrum.* **49**, 1384 (1978); F. C. Young, W. F. Oliphant, S. J. Stephanakis, and A. R. Knudson, *IEEE Trans. Plasma Sci. PS-9*, 24 (1981).
- ²¹R. J. Leeper, E. J. T. Burns, D. J. Johnson, and W. M. McMurtry, *Proceedings of the Workshop on Measurements of Electrical Quantities in Pulsed Power Systems*, National Bureau of Standards Special Publication 628 (National Bureau of Standards, Gaithersburg, 1982), p. 267; and R. J. Leeper (private communication, 1982).
- ²²P. L. Dreike, E. J. T. Burns, S. A. Slutz, J. T. Crow, D. J. Johnson, P. R. Johnson, R. J. Leeper, P. A. Miller, L. P. Mix, D. B. Seidel, and D. F. Wenger, *J. Appl. Phys.* **60**, 878 (1986).
- ²³P. F. Ottinger, D. V. Rose, D. Mosher, and J. M. Neri, *J. Appl. Phys.* **70**, 5292 (1991).
- ²⁴S. A. Goldstein and R. Lee, *Phys. Rev. Lett.* **35**, 1079 (1975).
- ²⁵H. H. Andersen and J. F. Zeigler, *The Stopping Powers and Ranges of Ions in Matter* (Pergamon, New York, 1977), Vol. 3.
- ²⁶B. Mainsbridge, *Nucl. Phys.* **21**, 1 (1960).
- ²⁷W. Whaling, J. E. Evans, and T. W. Bonner, *Phys. Rev.* **75**, 688 (1949); C. Nussbaum, *Helv. Phys. Acta* **42**, 361 (1969).

PULSED POWER PHYSICS TECHNOTE NO. 91-07

TITLE: ORBIT CALCULATIONS FOR Z-DISCHARGE TRANSPORT EXPERIMENTS ON GAMBLE II

AUTHORS: D.V. Rose, J.M. Neri, and P.F. Ottinger

DATE: 8 March 1991

ABSTRACT: In support of recent z-discharge transport experiments performed on Gamble II, a set of computer codes was developed to model experimentally measured prompt- γ yields and witness plate damage patterns. These computations are described in detail, including assumptions used in modeling the Gamble II experiments.

THIS REPORT REPRESENTS
UNPUBLISHED INTERNAL
WORKING DOCUMENTS AND
SHOULD NOT BE REFERENCED
OR DISTRIBUTED

3/1/91

cc to:

Rose

Neri

Ottinger

Mosher

Stephanakis

Hinshelwood

Young

Orbit Calculations For Z-Discharge Transport Experiments On GAMBLE II

D. V. Rose, J. M. Neri, and P. F. Ottinger

March 8, 1991

Abstract

In support of recent z-discharge transport experiments performed on GAMBLE II, a set of computer codes was developed to model experimentally measured prompt- γ yields and witness plate damage patterns. These computations are described in detail, including assumptions used in modeling the GAMBLE II experiments.

Contents

1	Introduction	2
2	Experimental Model	2
3	Analytic Calculations	5
4	Sample Output	7
A	Diode Loading	9
B	Activation, Energy Loss, and RTP Subroutines	27
C	Channel Propagation	42
D	Channel Exit to Target Projection	50
E	Plotting of Phase Space Quantities From Output Files	55

1 Introduction

This report documents computer calculations carried out in support of recent z-discharge channel transport experiments performed at NRL on the GAMBLE II accelerator [1]. Although the results of this work are reported in Ref. [1], this paper details the calculations more fully than they can be covered in a journal article.

Section 2 of this report reviews the key features of the experimental configurations used and the elements modeled by the simulations. The analytic calculations used in the coding are discussed in Section 3, and Section 4 gives sample results and conclusions. Included as Appendices A-E is the complete set of codes used in this work. The source codes contain a large number of comments and have a relatively simple structure.

2 Experimental Model

The experimental configuration is fully documented in Ref.[1] and the key elements pertaining to the simulation model are reviewed here. Experimental runs consisted of essentially 3 general hardware configurations, each of which was used with 3 different diode to channel distances, F . The first configuration, the shadowbox diagnostic, is illustrated in Fig. 1 in (R, Z) coordinates. Highlighted are the anode and Kimfol planes of the diode, the channel entrance aperture and the location of the shadowbox hardware (witness plate and plastic target). The second hardware configuration consisted of an aperture at $Z = F$ and LiF yield targets 8cm downstream of the aperture. No channel hardware was present for these input shots. The last configuration consists of the discharge channel, but instead of the shadowbox hardware, the LiF yield targets are placed 8cm downstream of the channel exit. In modeling the output yield shots, the LiF targets are assumed to be placed directly at the channel exit. However, the input yield shots were time-of-flight corrected for the extra aperture-to-target distance. In each hardware configuration, F was varied between 20, 25, and 30cm.

The computational model for the z-discharge transport experiments treats the ion diode as being fully decoupled from the transport channel and shadowbox assembly. The diode model is described below and is used to provide a full 3D phase space distribution of ions at the aperture/channel entrance. In the case of the shadowbox targets (Fig. 1), this phase space distribution is transported to the channel exit with a fully 3D non-relativistic orbit code

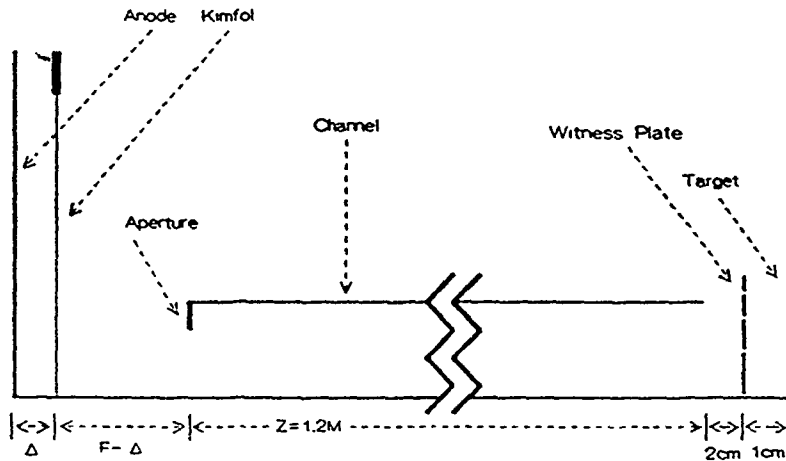


Figure 1: Schematic in (R, Z) coordinates showing essential experimental components.

(Appendix C). For input and output yield calculations, the ion phase space distribution is projected through the channel using purely analytic techniques to determine confinement, time of flight, average path length and energy loss. All of these analytic calculations will be discussed in Section 3.

All shots examined were divided in time by current and voltage into 20 bins of 4.5ns each. The start time of the first bin is adjusted so that the average voltage in bin 1 is approximately 400kV. A predetermined number of weighted ions are distributed among the 20 bins according to the average experimental ion current value in that bin. A random spread in voltage is then determined by linear interpolation between neighboring bins.

The ions are then launched at randomly determined positions at the Kimfol plane with a $1/r$ weighting out to the maximum Kimfol radius of 5.1cm. Ions are assumed to have been launched at the diode surface which has a radius $R = 6.0cm$ and are deflected toward the axis according to the bending angle formula

$$\Theta_{b0} = \frac{\omega_c \Delta}{v_{zd}}, \quad (1)$$

where

$$\omega_c = \frac{\mu_0 e I_d Z_d}{2\pi m_i R}, \quad (2)$$

Z_d is the ion charge state in the diode gap, v_{zd} is the z -velocity of the ion at the diode, I_d is the ion current at the time the ion is launched, and m_i is the ion mass (protons are used throughout this work). SI units are used throughout except where explicitly noted. The diode plane is parallel to the (X, Y) plane and chosen to be at $Z = 0.0\text{cm}$ and the Kimfol plane is at $Z = \Delta$, with $\Delta = 1.4\text{cm}$ throughout.

The option to model a pimple[3] at the Kimfol surface on axis to get ions launched near the axis into the channel is also included. The model holds for the smaller 2.7cm radius pinch reflex diode and was derived from shadowbox analysis. The relation used is

$$\Theta_b = \Theta_{b0} + \Theta_M, \quad (3)$$

where Θ_{b0} is given by Eq. 1 and

$$\Theta_M = \frac{r\delta}{r_m^2} \exp\left(-\frac{r^2}{2r_m^2}\right). \quad (4)$$

The radius of the pimple is r_m and is given to be 4mm and δ , the pimple height (i.e. distance out from the Kimfol plane), is time-dependent and was modeled as

$$\delta = \delta_0 \frac{t}{60}, \quad (5)$$

where δ_0 is 1mm and t is in nanoseconds. Runs were made with this pimple model and with $\delta_0 = 2\text{mm}$ but no significant effects were observed. All data presented here and in Ref.[1] was calculated with no pimple on the Kimfol ($\delta_0 = 0$).

Once the bending angle is determined, the microdivergence, Θ_μ , is applied to defocus the ion. Through careful analysis of 'full target' diagnostic shots, Θ_μ was determined to be $\approx 175\text{milliradians}$. Previous shadowbox analysis of 'backed' pinch reflex diodes yielded $\Theta_\mu \approx 125\text{milliradians}$ [4].

3 Analytic Calculations

Yield data for these experiments was simulated by using the beam phase space at the channel entrance and determining ion confinement from the

radial turning point equation (Rtp) Ref. [2]

$$0 = v_o^2 - \frac{r_o^2 v_{\theta o}^2}{r_*^2} - \left(v_{zo} - v_{cn} \frac{r_o^{n+1} - r_*^{n+1}}{r_c^{n+1}} \right)^2 \quad (6)$$

Here r_* is the radial turning point in an azimuthal magnetic field of the form

$$B(r) \approx B_o \left(\frac{r}{r_c} \right)^n, \quad (7)$$

where

$$B_o = \frac{\mu_o I_c}{2\pi r_c} \quad (8)$$

where I_c is the discharge channel current (typically 40–45kA for these experiments) and r_c is the discharge channel radius with $r_c = 1.2\text{cm}$ throughout. Complete charge and current neutralization is assumed for all runs. The 'o' subscript on phase space variables signifies parameters evaluated at the channel entrance. Equation (6) can be rearranged to give a polynomial of order $2n + 4$

$$\begin{aligned} 0 = & r_*^{2n+4} \\ & + \left(\frac{2v_{zo}r_c^{n+1}}{v_{cn}} - 2r_o^{n+1} \right) r_*^{n+3} \\ & + \left(r_o^{2n+2} - \frac{2v_{zo}r_o^{n+1}r_c^{n+1}}{v_{cn}} - \frac{r_c^{2n+2}(v_{ro}^2 + v_{\theta o}^2)}{v_{cn}^2} \right) r_*^2 \\ & + \frac{r_o^2 v_{\theta o}^2 r_o^{2n+2}}{v_{cn}^2} \end{aligned} \quad (9)$$

where

$$v_{cn} = \frac{\mu_o I_c r_c Z e}{(n+1)2\pi m_i} \quad (10)$$

For the $n = 1$ case, the roots of eq. (9) are easily determined and can be written

$$r_* = \left(\frac{B \pm (B^2 - 4AC)^{1/2}}{2A} \right)^{1/2} \quad (11)$$

where A , B , and C are

$$A = \frac{2v_{zo}v_{c1}}{v_o^2 r_c^2}, \quad (12)$$

$$B = 1 - \frac{v_{zo}^2}{v_o^2} + \frac{2v_{zo}v_{c1}r_o^2}{v_o^2r_c^2} \quad (13)$$

$$C = \frac{r_o^2v_{\theta o}^2}{v_o^2} \quad (14)$$

and r_c is the channel radius. The (+) version of the linear ($n = 1$) B-field Rtp equation gives the outer turning point of an individual orbit. Eq. (6) is derived from the equations of conservation of energy, axial momentum, and angular momentum. Terms of the order v_c^2/v_o^2 are ignored in eq. (11)-(14). After the confinement of a particular ion is determined, the average z-velocity is then computed for the confined ion from

$$\langle V_z \rangle = v_o - \frac{v_c r_o^2}{2r_c} - \frac{v_{ro}^2 + v_{\theta o}^2}{4v_o} + \dots \quad (15)$$

This is then used to determine a single ions time-of-flight to the channel exit. To get the energy loss due to classical stopping in the channel gas, the path length of an ion in the discharge channel is required and is computed from

$$R_{total} = L \left(1 + \frac{\Delta S}{\lambda_\beta} \right), \quad (16)$$

where L is the channel length ($= 1.2m$) and the ratio $\Delta S/\lambda_\beta$ is given as

$$\frac{\Delta S}{\lambda_\beta} = \left(\frac{v_{c1}}{2v_o} \right) \left(\frac{r_o^2}{r_c^2} + \frac{v_{ro}^2 + v_{\theta o}^2}{2v_o v_{c1}} \right). \quad (17)$$

The notation used in the last equation is consistent with Ref. [2]. Eqs. (15)-(17) are used only in determining output yields.

To examine the effects of higher order B-fields in the discharge channel for each n considered, a separate subroutine was written to isolate and return the correct root of Eq. (9). A Laguerre root solver technique [6] was employed, but convergence to the real roots of the polynomial was difficult to achieve. Instead, a first order correction technique was employed in the neighborhood of the correct root. By interpolating between two values of r that caused the polynomial to change sign, a first guess to the correct solution was obtained. Iterating until a reasonable degree of precision was achieved gives the desired radial turning point.

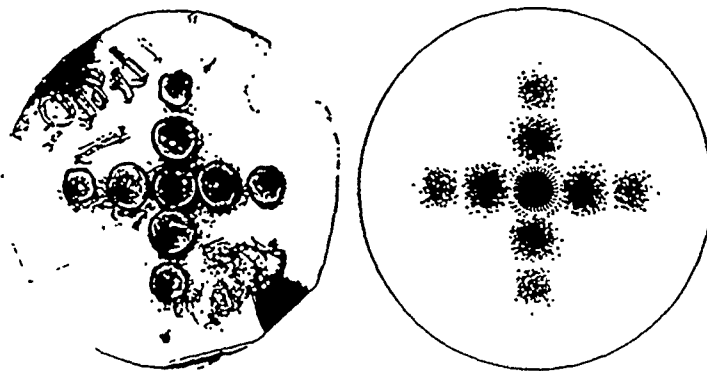


Figure 2: Reproduction of actual target with calculated result (Shot 4810).

4 Sample Output

The model described in this paper provided reasonable agreement with experimental results and the codes described herein could be used as a starting place for calculations on future experiments. We conclude this note with some figures illustrating some sample output of the computer codes described in the Appendices. Figure (2) compares a shadowbox calculation with an actual target. Figure (3) is a 3D plot of a single (typical) ion trajectory. This figure highlights the small number of betatron wavelengths an ion can execute over the channel distance and the significance of angular momentum. Figure (4) shows the results of a time dependent (Fluorine) calculation.

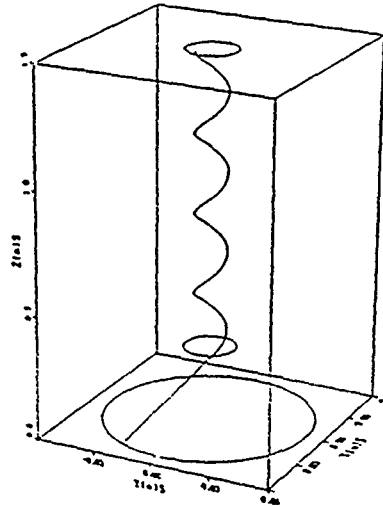


Figure 3: Typical ion orbit path in 3D. The large circle at the $Z = 0$ plane represents the Kimfol surface of the diode where the ion is launched and the smaller circles denote the channel entrance and exit planes.

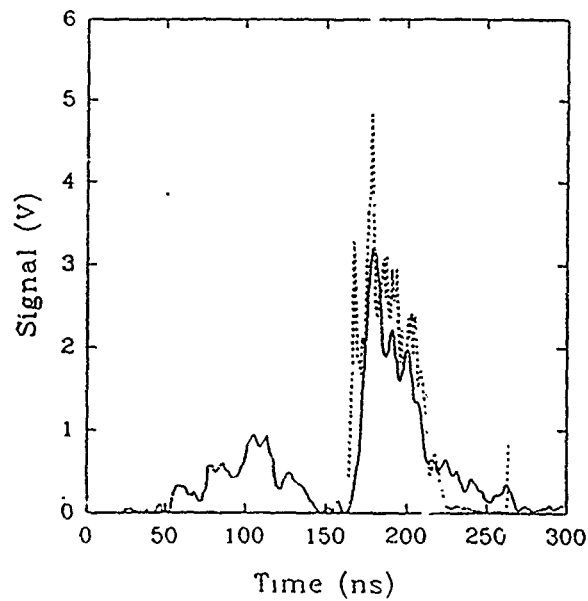


Figure 4: Sample yield curve showing both experimental (solid) and calculated (dash) data. (Shot 4324)

A Diode Load

This is the first and most complex program in the SHD suite of codes. Its primary function is to randomly fill the diode with properly focused ions. It stores ions that get into the channel aperture in files DIODE. and CHANIN. which represent the ion phase space distributions at the Kimfol plane and channel entrance respectively. Additionally, this code performs the yield calculations at either/both channel entrance and exit. Time-dependent (Fluorine) yield calculations are stored in the file YIELD. and time-independent (Lithium) calculations are reported to the user via the terminal screen.

```
program SHDLOAD
```

```

C
C The SHADowbox suite of programs is a direct rip-off of the LMF
C suite. These programs are used to get witness plate pictures
C for Jess's transport experiments.
C
C This program gets all input variables used by the SHD programs.
C These programs include:
C
C     SHDLOAD -- This program.
C     SHDCHAN -- Take ions at channel entrance and move 'em
C               to end of channel.
C     SHDTARG -- Take ions at end of channel and project them
C               onto the target.
C     SHDPLOT -- Plot any of the dump files left behind by the
C               above programs.
C
C SHDLOAD creates a randomly distributed 'plane' of test
C mono-energetic ions with microdivergence mu (in radians).
C The SHD diode is planar
C and produces a soft-focus beam of ions over the entire radius.
C A small 'scatter' or dispersion of the perfect focus is
C created by randomly defocusing each ion within the limits of
C the microdivergence.
C
C Program structure is:
C   1. Get user input.
C   2. Generate X,Y positions and Vx,Vy velocities at diode.
C   3. Add microdivergence to velocity and write out 'diode.'
C   4. Project ions from diode to channel entrance.
C   5. Write this out in 'chanin.' file.
C
C Variables in LMFLOAD:
C   a,b,c,e,g -- Random variables needed per ion.
```

```

C   radius      -- user supplied outer diode radius for Wc calc.
C   uradius     -- user supplied outer diode radius for propogation.
C   Vx,Vy       -- Velocity arrays.
C   X,Y         -- Position arrays.
C   mu          -- user supplied microdivergence.
C   F           -- User supplied diode to channel distance.
C   Energy      -- User supplied ion energy.
C   Vo          -- Ion velocity Energy = (1/2)*m(Vo)**2
C   jseed       -- Random number generator seed.
C   nions       -- User supplied number of ions.
C   asize       -- Max number of ions (array sizes).
C   nq          -- number of removed electrons in ion.
C   nmass       -- ion mass in number of proton masses.
C   Rc          -- Channel radius.
C   nilcin      -- number of ions lost at channel entrance.
C   nilc        -- number of ions lost in channel.
C   nihtar      -- number of ions that hit the target.
C   nilRtp      -- number of ions lost using the Radial Turning
C               point equation.
C   Tradius     -- Radius of target.
C   Tpos        -- Target position.
C   CLEN        -- Channel length.
C   aper        -- Channel entrance aperature radius.
C   curr()      -- Net ion current.
C   volt()      -- corrected diode voltage.
C   bend()      -- bending angle library.
C   DELTA       --" distance separating anode surface and the foil
C               separating the diode vacuum region and the
C               gas filled focusing region..."
C   Pressure    -- channel and focusing region background gas
C               pressure in Torr.
C   LiF_yield   -- Logical to do activation calculations.
C   Zyield      -- Zposition of activation target (beginning or
C               end of channel).
C   Time()      -- time storage array.
C   Tyield      -- Total yield for Li reaction.
C   qm          -- charge/mass for ion.
C   mq          -- mass/charge for ion.
C
C
C   INTEGER     asize,nmass,nq,jseed,nilcin,nilc,nihtar,I,K,nions
C   INTEGER     uid,ionbin,bin,totion,bnum,M,icount,Zyield,nilRtp
C   INTEGER     iring,Ni,No,Nw,pimple,Rtpnum,badroot
C   PARAMETER   (asize=30000)
C   REAL*4      a,b,R,radius,rscaler,a2,x,y,phi,F,theta,c,d,Energy
C   REAL*4      e,g,Vx,Vy,Vrnu,Vxmu,"ymu,Vo,mu,time,Vz,Rc,quad
C   REAL*4      current,clen,Rtarget,Tpos,aper,bend,volt,curr,pi2

```

```

REAL*4   Wc,DELTA,Xc,Yc,Tvx,Tvy,Zcross,Ri,Tbend,totcur,pi
REAL*4   Yprime,Zprime,Xprime,Rmicro,Rtotal,uradius,alpha
REAL*4   xfocus,yfocus,Pressure,Voi,MVnew,KIMFOL,MV,clair
REAL*4   kVpMpT,yield,ylif,MVold,iyield,Rstar,Vf,Vthetao,Vro
REAL*4   Rstar1,VzAvg,Ro,Vc,ring,Vxc,Vyc,VcTotal,VcAvg,AvgRo
REAL*4   AvgVth,AvgVr,Tiyield,TIMED,MVi,dt,voltb,vob,dslb,mq
REAL*4   Zavg,pradius,ptheta,T2yield,Rm,Tbend0,delo,Ic,q,qm
REAL*4   Ew,Eo,Ei,Etin,Etout,Etwall,volto,volti,voltw,mass
REAL*4   percent,hold,y1b,y2b,bigQ,Qratio,Qrq
CHARACTER*100 info
CHARACTER*4  shot
CHARACTER*2  ans
LOGICAL  LiF_yield
DIMENSION x(ASIZE),y(ASIZE),bnum(ASIZE),Vo(20),Voi(ASIZE)
DIMENSION Vx(ASIZE),Vy(ASIZE),volt(21),curr(21),bend(20)
DIMENSION Xc(ASIZE),Yc(ASIZE),ionbin(20),icount(20)
DIMENSION time(ASIZE),iyield(ASIZE),ring(21),iring(20)
DIMENSION Vxc(ASIZE),Vyc(ASIZE),AvgRo(20),AvgVth(20),AvgVr(20)
DIMENSION Ew(20),Eo(20),Ei(20),volto(20),volti(20),voltw(20)
DIMENSION Ni(20),No(20),Nw(20),percent(20),y1b(20),y2b(20)
C
C Get input from user.
C
pimple = 0
LiF_yield = .false.

WRITE(6,*) ' SHDLOAD -- '
WRITE(6,*) ' Enter shot number (4 char.) '
READ(5, '(A)') shot
10 WRITE(6,*) ' Enter number of ions to emit '
READ(5,*) nions
WRITE(6,*) ' Enter random number between 500 & 999 '
READ(5,*) jseed
WRITE(6,*) ' Enter microdivergence (radians) '
READ(5,*) mu
WRITE(6,*) ' Do you want activation calculation (y/n)? '
READ(5, '(A)') ans
IF ((ans(1:1).eq.'Y').or.(ans(1:1).eq.'y')) THEN
  ans=' '
  WRITE(6,*) ' Enter activation target position (1 or 2) '
  WRITE(6,*) ' (or 3 for both, with no yield file.) '
  READ(5,*) Zyield
  LiF_yield=.true.
  IF ((Zyield.eq.3).or.(Zyield.eq.2)) THEN
    WRITE(6,*) ' Enter 1: norm Rtp eq., 2: quad Rtp eq., 3: cubic '
    READ(5,*) Rtpnum
  ENDIF

```

```

ENDIF
WRITE(6,*) ' Enter some run info (1 line) '
READ(5, '(A)') info
WRITE(6,*) ' Enter 0:no pimple, 1:normal, 2:double size pimple '
READ(5,*) pimple

K=1
bnum(1) = 1
pi = 3.1459265
pi2 = 3.1459265*0.5
nid = 0 ! # ions launched at diode.
nilcin=0 ! # ions lost @ chan. entrance.
Pressure = 2.0 ! 2 Torr for all of Jess's experiments.

IF (pimple.eq.1) del0 = 1.e-3 ! bending angle correction const. for
IF (pimple.eq.2) del0 = 2.e-3 !
IF (pimple.eq.0) del0 = 0.0 !
Rm = 4.e-3 ! pimple.

radius = 6.0e-2 ! radius of anode (m)
uradius = 5.1e-2 ! radius of kimfol (m)
DELTA = 1.4e-2 ! dist. between anode & kimfol (m)
nq = 1 ! ion charge state
nmass = 1 ! # of nucleons of ion
Rc = 1.27e-2 ! channel radius (m)
aper = 0.85e-2 ! aperature radius (m)
Clen = 1.2 ! channel length (m)

q = 1.6022e-19*FLOAT(nq)
mass = 1.6726e-27*FLOAT(nmass)
mq = mass/q
qm = q/mass

C
C Fill volt(),cu r(),bend() arrays.
C

DO 72 I=1,20
  Ei(I) = 0.0
  volti(I) = 0.0
  Ni(I) = 0
  Eo(I) = 0.0
  volto(I) = 0.0
  No(I) = 0
  Ew(I) = 0.0

```

```

      vltw(I) = 0.0
      Nw(I)   = 0
72  CONTINUE

      totcur = 0.0

      INCLUDE 'shotinfo.for'      ! tables of shot data

      Qratio = bigQ/FLOAT(nions)
      Qrq    = Qratio/q

      DO 2 I=1,20
        M=20-I+1
        vlt(M+1)=vlt(M)
        curr(M+1)=curr(M)
2     CONTINUE
      vlt(1) = vlt(2)-50.e3
      curr(1)= curr(2)/2.

      DO 3 bin=2,21
        totcur = curr(bin) + totcur
3     CONTINUE

      DO 4 bin=1,20
        ionbin(bin) = INT((curr(bin+1)/totcur) * nions)
4     CONTINUE

5     CONTINUE

      totion = 0

      DO 6 bin=1,20
        totion = totion + ionbin(bin)
6     CONTINUE

      WRITE(6,*) ' total ions = ',totion,'ions in 21',ionbin(20)

      I=22
      IF (totion.lt.nions) THEN
38     continue .
        I=I-1
        IF (vlt(I).eq.0.) GOTO 38
        ionbin(I-1) = ionbin(I-1) + 1
        GOTO 5
      ENDIF
C

```

```

C Fill ring() for diagnostics.
C
  DO 37 I=1,21
37 ring(I) = FLOAT(I-1)*0.1*Rc
C
C Begin LOOP over ions.
C
  DO 50 bin=1,20

      DO 120 M=1,ionbin(bin)

100      CONTINUE

      a=ran(jseed)
      b=ran(jseed)
      pradius=a*uradius           ! scale over diode region
      ptheta=b*2.0*pi            !

      nid = nid+1
      K=K+1
      IF (K.ge. asize) STOP 666

      X(K) = pradius*COS(ptheta)
      Y(K) = pradius*SIN(ptheta)

      IF ((X(K).ge. 0.0).and.(Y(K).ge. 0.0)) THEN
          c = 0.15
      ENDIF
      IF ((X(K).lt. 0.0).and.(Y(K).ge. 0.0)) THEN
          c = 0.35
      ENDIF
      IF ((X(K).lt. 0.0).and.(Y(K).lt. 0.0)) THEN
          c = 0.65
      ENDIF
      IF ((X(K).ge. 0.0).and.(Y(K).lt. 0.0)) THEN
          c = 0.85
      ENDIF
      bnum(K) = bin

C
C      Get a randomly selected voltage between bins and do
C      KIMFOL correction.
C

```

```

a=ran(jseed)
dt = a*4.5e-9
voltb=(volt(bin+1)-volt(bin))*dt/4.5e-9 + volt(bin)
Vob = SQRT(2.0*voltb*qm)
MV = 1.0e-6*voltb
MVold=MV
MVnew = KIMFOL(MV)
IF (MVnew.ge.MVold) THEN
  WRITE(6,*) ' Hey!! KIMFOL error!'
  STOP 687
ENDIF
IF (MVnew.le. 0.0) THEN
c   MVnew = 0.0
c   WRITE(6,*) ' Ion',K,'dead at KIMFOL'
  Xc(K)=13.13
  nilcin=nilcin+1
  K=K-1
  GOTO 120
ENDIF
voltb=1.e6*MVnew
Voi(K) = SQRT(2.0*voltb*qm)

C
C   End of KIMFOL correction.
C
  time(K) = FLOAT(BIN-1)*4.5E-9 + dt

C
C   Now do velocity space and microdivergence
C

  rscale = SQRT(X(K)*X(K) + Y(K)*Y(K))

  IF (volt(bin+1) .eq. 0.) THEN
    Tband = 0.0
  ELSE
    Ic = (curr(bin+1)-curr(bin))*dt/4.5e-9 + curr(bin)
    Wc = 2.0e-7*qm*Ic/radius
    Tband = Wc*DELTA/Vob
    Tband0 = del0*time(K)*rscale/(60.e-9*Rm*Rm)
    Tband0 = Tband0*EXP(-0.5*rscale*rscale/(Rm*Rm))
    Tband = Tband - Tband0
cccc  Tband = Tband*1.15          !!! Enhanced bending.
  ENDIF

  iyield(K)=Tband          !!! diagnostic use only.

```

```

      Zcross=rscale*TAN(pi2-Tbend)
      Ri = SQRT(rscale**2. + Zcross**2.)
      Rmicro=Ri*TAN(mu)
102  d = ran(jseed)
      e = ran(jseed)
      Xprime =Rmicro * d
      Yprime =Rmicro * e
      quad =ran(jseed)

      rscale=SQRT(Xprime**2. + Yprime**2.)
      IF (rscale.gt.Rmicro) GOTO 102

      IF (quad.lt. 0.25) THEN
        Xprime=Xprime
        Yprime=Yprime
      ELSEIF (quad.lt. 0.50) THEN
        Xprime=-Xprime
        Yprime=Yprime
      ELSEIF (quad.lt. 0.75) THEN
        Xprime=-Xprime
        Yprime=-Yprime
      ELSE
        Xprime=Xprime
        Yprime=-Yprime
      ENDIF

      Zprime = Zcross + Yprime*COS(pi2-Tbend)

      Yprime=Yprime*COS(Tbend) ! put Yprime in correct coor. system

C
C      Now by orthogonal transformation, get 'focus' plane aligned
C      with diode plane.
C
      xfocus = Xprime*COS(alpha) - Yprime*SIN(alpha)
      yfocus = Xprime*SIN(alpha) + Yprime*COS(alpha)
      Xprime = xfocus
      Yprime = yfocus

      Rtotal = SQRT( (X(K)+Xprime)**2. + (Y(K)+Yprime)**2. +
                    (Zprime)**2. )
      Tvy=ACOS( ABS(Y(K)+Yprime)/Rtotal )
      Tvx=ACOS( ABS(X(K)+Xprime)/Rtotal )

      xfocus = X(K)+Xprime
      yfocus = Y(K)+Yprime

```

```

IF ((xfocus.ge. 0.0).and.(yfocus.ge. 0.0)) THEN
  Vx(K)=-Voi(K)*COS(Tvx)
  Vy(K)=-Voi(K)*COS(Tvy)
ENDIF
IF ((xfocus.lt. 0.0).and.(yfocus.ge. 0.0)) THEN
  Vx(K)=Voi(K)*COS(Tvx)
  Vy(K)=-Voi(K)*COS(Tvy)
ENDIF
IF ((xfocus.lt. 0.0).AND.(yfocus.lt. 0.0)) THEN
  Vx(K)=Voi(K)*COS(Tvx)
  Vy(K)=Voi(K)*COS(Tvy)
ENDIF
IF ((xfocus.ge. 0.0).AND.(yfocus.lt. 0.0)) THEN
  Vx(K)=-Voi(K)*COS(Tvx)
  Vy(K)=Voi(K)*COS(Tvy)
ENDIF

```

C
C
C

Move ions to channel entrance.

```

IF ( (Vx(K)**2.+Vy(K)**2.) .gt. Voi(K)**2. ) THEN
  WRITE(6,*) ' X(K),Y(K) = ',X(K),Y(K)
  WRITE(6,*) ' xfocus,yfocus =',xfocus,yfocus
  WRITE(6,*) ' Xprime,Yprime =',Xprime,Yprime
  WRITE(6,*) ' bin, K, c=',bin,K,c
  WRITE(6,*) ' Tvx, Tvy =',Tvx,Tvy
  WRITE(6,*) ' Vo,Vx,Vy=',Voi(K),Vx(K),Vy(K)
ENDIF

```

```

Vz = SQRT(Voi(K)**2. - Vx(K)*Vx(K) - Vy(K)*Vy(K) )
IF (Vz.le . 1.0) THEN
  Xc(K)=13.13
  nilcin=nilcin+1
  K=K-1
  GOTO 120
ENDIF
timeD = (F-DELTA)/Vz
Xc(K)= X(K)+Vx(K)*timeD
Yc(K)= Y(K)+Vy(K)*timeD
TIME(K)=TIME(K)+TIMED

```

C
C
C

Figure out how many ions are lost. If X(K) = 13.13, no ion.

```

rscale = SQRT( Xc(K)**2. + Yc(K)**2. )
IF (rscale.gt.aper) THEN
  Xc(K)=13.13

```

```

        nilcin=nilcin+1
        K=K-1
        GOTO 120
    ENDIF

C
C      Since ion has made it to channel (and inside aperature)
C      attenuate its velocity in air at pressure to find Voi().
C      This velocity will be used for channel work.
C

    Rtotal = SQRT( (X(K)-Xc(K))**2. + (Y(K)-Yc(K))**2. +
                  (F-DELTA)**2. )
    MV = 1.e-6*voltb
    MVold = MV
    kVpMpT = ELAIR(MV)
    MVnew = 1.e-6*voltb - Rtotal*Pressure*kVpMpT*1.e-3
    IF (MVnew.ge.MVold) THEN
        WRITE(6,*) ' Hey!!! ELAIR error!'
        STOP 551
    ENDIF
    IF (MVnew.le. 0.0) THEN
        WRITE(6,*) ' ion',k,' out of energy.'
        X(K)=13.13
        K=K-1
        GOTO 120
    ENDIF
    Voi(K) = SQRT( 2.0*MVnew*1.e6*qm)
    IF (Voi(K) .lt. 100.0 ) THEN
        WRITE(6,*) ' Voi,K =',Voi(K),K
        STOP 124
    ENDIF

    Ei(bin)=Ei(bin) + Qrq*0.5*mass*Voi(K)*Voi(K)
    volti(bin) = volti(bin) + MVnew*1.e6 ! for energy check.
    Ni(bin) = Ni(bin) + 1

    IF ((xfocus.ge. 0.0).and.(yfocus.ge. 0.0)) THEN
        Vxc(K)=-Voi(K)*COS(Tvx)
        Vyc(K)=-Voi(K)*COS(Tvy)
    ENDIF
    IF ((xfocus.lt. 0.0).and.(yfocus.ge. 0.0)) THEN
        Vxc(K)=Voi(K)*COS(Tvx)
        Vyc(K)=-Voi(K)*COS(Tvy)
    ENDIF
    IF ((xfocus.lt. 0.0).AND.(yfocus.lt. 0.0)) THEN
        Vxc(K)=Voi(K)*COS(Tvx)

```

```

        Vyc(K)=Voi(K)*COS(Tvy)
    ENDIF
    IF ((xfocus.ge. 0.0).AND.(yfocus.lt. 0.0)) THEN
        Vxc(K)=-Voi(K)*COS(Tvx)
        Vyc(K)=Voi(K)*COS(Tvy)
    ENDIF

120    CONTINUE                                ! End of ion loop.

121    CONTINUE

50    CONTINUE                                ! End of BIN loop.

    IF (K.gt.asize) STOP 123
    nions = K-1

    Vxc(1)=FLOAT(nions)
    Vyc(1)=FLOAT(nions)
    Voi(1)=FLOAT(nions)
    Vx(1)=FLOAT(nions)
    Vy(1)=FLOAT(nions)
    x(1)=FLOAT(nions)
    y(1)=FLOAT(nions)
    xc(1)=FLOAT(nions)
    yc(1)=FLOAT(nions)
    time(1)=FLOAT(nions)

    WRITE(6,*) ' Writing out Diode file.'
    WRITE(6,*) ' # of ions generated at diode =',nid
    WRITE(6,*) ' # of ions in channel = ',nions

C
C Write out diode. file.
C
    IF (Zyield.ne. 3) THEN
    OPEN(1,FILE='diode.',form='unformatted',access='sequential',
        STATUS='NEW')
    WRITE(1)nions,F,uradius,Rc,current,Clen,Rtarget,Tpos,Energy,
        nmass,nq,nilcin,nilc,nihtar,info
    DO 368 I=1,20
368  WRITE(1)volt(I),curr(I),ionbin(I),bend(I),Vo(I)
    DO 304 I=1,nions+1
304  WRITE(1)X(I),Y(I),Vx(I),Vy(I),bnum(I),Vo(bnum(I)),time(I),
        iyield(I)

```

```

        CLGSE(1)

C
C Write out chanin. file.
C
        OPEN(1,FILE='chanin.',form='unformatted',access='sequential',
             STATUS='NEW')
        WRITE(1)nions,F,uradius,Rc,current,Clen,Rtarget,Tpos,Energy,
             nmass,nq,nilcin,nilc,nihtar,info
        DO 367 I=1,20
367 WRITE(1)volt(I),curr(I),ionbin(I),bend(I),Vo(I)
        DO 305 I=1,nions+1
305 WRITE(1)Xc(I),Yc(I),Vxc(I),Vyc(I),bnum(I),Voi(I),time(I),
             iyield(I)
        CLOSE(1)
        ENDIF

        WRITE(6,*)' # ions lost at chan. entrance = ',nilcin

C
C Check efficiency per bin.
C
        DO 5001 I=2,nions+1
             icount(bnum(I)) = icount(bnum(I)) + 1
5001 CONTINUE
        WRITE(6,*)'          --bin, emitted,   captured,   percent'
        DO 5002 I=1,20
             IF (ionbin(I).eq.0) THEN
                WRITE(6,*)' ',I,ionbin(I),icount(I),'   na'
             ELSE
                WRITE(6,*)' ',I,ionbin(I),icount(I),FLOAT(icount(I))/
                     FLOAT(ionbin(I))
             ENDIF
5002 CONTINUE

C
C ACTIVATION section.
C
C Zyield = 1 means that activation target is at channel entrance.
C Zyield = 2 means that activation target is at channel exit.
C Zyield = 3 means that activation target is at both locations.
C
C For targets at end of channel, the following calculations are
C performed:
C -- Radial turning point: To see if ion is confined in
C channel.
C -- Energy loss in air: Using same routine for diode to
C channel propogation above.
C

```

```

C      -- Yield for either LiF or F. The Li reaction is
C      time integrated, so no yield file is written out.
C      The F reaction is time-dependent and so the yield
C      per particle is saved.
C      -- Average Vz: To determine time of flight information.
C

```

```

DO 5999 I=1,20
  Vo(I) = 0.0
  AvgVth(I)=0.0
  AvgVr(I)=0.0
  AvgRo(I)=0.0
5999 CONTINUE

```

```

nilRtp = 0          ! set counter
badroot = 0

```

```

IF (LiF_yield) THEN

```

```

  WRITE(6,*) ' Starting activation calculations.'

```

```

DO 6001 I=2,nions+1
  IF ((Xc(I).ne. 13.13).and.(Xc(I).ne. 13.14)) THEN
    IF ((Zyield.eq.2).or.(Zyield.eq.3)) THEN
      IF (Rtpnum.eq.1) THEN
        CALL Rtp(current,Vxc(I),Vyc(I),Voi(I),Rc,Xc(I),
          Yc(I),Rstar,Vthetao,Vro,Rstar1,Ro,Vc)
      ENDIF
      IF (Rtpnum.eq.2) THEN
        CALL Rtp2(current,Vxc(I),Vyc(I),Voi(I),Rc,Xc(I),
          Yc(I),Rstar,Vthetao,Vro,Rstar1,Ro,Vc)
      IF ((Rstar1.lt. Ro).or.(Rstar1.eq. 13.13)) THEN
        badroot = badroot +1
        GOTO 6001
      ENDIF
      ENDIF
      IF (Rtpnum.eq.3) THEN
        CALL Rtp3(current,Vxc(I),Vyc(I),Voi(I),Rc,Xc(I),
          Yc(I),Rstar,Vthetao,Vro,Rstar1,Ro,Vc)
      IF ((Rstar1.lt. Ro).or.(Rstar1.eq. 13.13)) THEN
        badroot = badroot +1
        GOTO 6001
      ENDIF
      ENDIF
    DO 6040 K=1,20

```

```

IF ((Rstar1.ge.ring(K)).and.
    (Rstar1.lt.ring(K+1))) THEN
    iring(K)=iring(K)+1
    Vo(K) = Vo(K) + Voi(I)
    AvgVth(K) = AvgVth(K) + Vthetao
    AvgVr(K) = AvgVr(K) + Vro
    AvgRo(K) = AvgRo(K) + Ro
    GOTO 6041
ENDIF
6040 CONTINUE
6041 CONTINUE
c WRITE(6,*) ' I,Rstar,Rstar1=',I,Rstar,Rstar1

IF (Rstar1.le.Rc) THEN

    MV = 1.e-6*0.5*mq*Voi(I)*Voi(I)
    MVi=MV
    hold = ylif(MV)
    hold = hold*Qratio
    IF (hold.lt.0.0) hold=0.0
    tlyield=tlyield+hold
    y1b(bnum(I)) = y1b(bnum(I)) + hold
    dslb = ( 0.5*Vc/Voi(I) )*( Ro*Ro/(Rc*Rc) +
        (Vro*Vro+Vthetao*Vthetao)/(2.0*Voi(i)*Vc) )
    Rtotal = Clen*(1.0+dslb)
    IF (Rtotal.lt. CLEN) STOP 333
    kVpMpT = ELAIR(MVi)
    MVnew =
        1.e-6*0.5*mq*Voi(I)*Voi(I)
        - Rtotal*Pressure*kVpMpT*1.e-3
    IF (MVnew.ge.MV) THEN
        WRITE(6,*) ' Hey!!! ELAIR error!'
        STOP 552
    ENDIF
    IF (MVnew.le. 0.0) MVnew = 0.0
    Vf = SQRT( 2.0*MVnew*1.e6*qm )
    IF (Zyield.ne.3) THEN
        iyield(I)=yiela(MVnew)*Qratio
        IF (iyield(I).lt. 0.0) iyield(I) = 0.0
    ENDIF
    hold = ylif(MVnew)
    hold = hold*Qratio
    IF (hold.lt. 0.0) hold = 0.0
    t2yield=t2yield+hold
    y2b(bnum(I)) = y2b(bnum(I)) + hold
    VzAvg = Voi(I)
        *(1.0 - ((Voi(I)**4.-Vf**4.)/(8.*Voi(I)**4.)))

```

```

      *(1.0 - Vc*Ro*Ro/(2.*Voi(I)*Rc*Rc) -
        (Vro**2.+Vthetao**2.)/(4.*Voi(I)**2.) )
      IF ((VzAvg.lt. 0.0).or.(VzAvg.gt. 3.0e8)) STOP 623
      Time(I) = Clen/VzAvg + Time(I)
      Voi(I) = Vf
      IF (Zyield.eq.3) THEN
        Eo(bnum(I))=Eo(bnum(I))
          +Qrq*0.5*mass*Voi(I)*Voi(I)
      ENDIF
      VcTotal = VcTotal + Vc
      No(bnum(I)) = No(bnum(I)) + 1
      volto(bnum(I)) = volto(bnum(I)) + MVnew*1.e6

```

```

ELSE
  MV = 1.e-6*0.5*mq*Voi(I)*Voi(I)
  hold = ylif(MV)
  hold = hold*Qratio
  IF (hold.lt.0.0) hold=0.0
  tlyield=tlyield+hold
  y1b(bnum(I)) = y1b(bnum(I)) + hold
  Nw(bnum(I)) = Nw(bnum(I)) + 1
  voltw(bnum(I)) = voltw(bnum(I)) +
    0.5*mq*Voi(I)*Voi(I)
  Ew(bnum(I))=Ew(bnum(I)) +
    Qrq*0.5*mass*Voi(I)*Voi(I)
  nilRtp = nilRtp + 1
  Xc(I)=13.14
  Yc(I)=F+Clen-DELTA
ENDIF

```

```

ENDIF

```

```

IF (Zyield.eq.1) THEN
  MV = 1.e-6*0.5*mq*Voi(I)*Voi(I)
  MVi= MV

```

```

C

```

```

C Propagate ions over the 8cm distance to the yield target.

```

```

C

```

```

  Vz = SQRT(Voi(I)**2. - Vx(I)*Vx(I) - Vy(I)*Vy(I) )
  IF (Vz le . 1.0) THEN
    GOTO 1208
  ENDIF
  timeD = 0.08/Vz
  Xprime= Xc(I)+Vxc(I)*timeD
  Yprime= Yc(I)+Vyc(I)*timeD
  TIME(I)=TIME(I)+TIMED
  Rtotal = SQRT( (Xc(I)-Xprime)**2.

```

```

      + (Yc(I)-Yprime)**2. + (0.08)**2. )
kVpMpT = ELAIR(MVi)
MVnew =
  1.e-6*0.5*nq*Voi(I)*Voi(I)
  - Rtotal*Pressure*kVpMpT*1.e-3
IF (MVnew.ge.MV) THEN
  WRITE(6,*) ' Hey!!! ELAIR error!'
  STOP 552
ENDIF
IF (MVnew.le. 0.0) MVnew = 0.0
Vf = SQRT( 2.0*MVnew*1.e6*qm )
MV = MVnew
iyield(I)=yield(MV)*Qratio
IF (iyield(I).lt. 0.0) iyield(I)=0.0
hold=yIif(MV)
hold = hold*Qratio
IF (hold.lt. 0.0) hold=0.0
tIyield=tIyield+hold
yIb(bnum(I)) = yIb(bnum(I)) + hold
1208 CONTINUE
      ENDIF
    ENDIF
6001 CONTINUE
C
C Write out YIELD. file.
C
  IF (Zyield.ne.3) THEN
    OPEN(1,FILE='yield.',form='unformatted',access='sequential',
      STATUS='NEW')
    WRITE(1) nions, F, uradius, Rc, current, Clen, Rtarget, Tpos, Energy,
      nmass, nq, nilcin, nilc, nihtar, info
    DO 381 I=1,20
381 WRITE(1) volt(I), curr(I), ionbin(I), bend(I), Vo(I)
    DO 382 I=1, nions+1
382 WRITE(1) Xc(I), Yc(I), Vx(I), Vy(I), bnum(I), Voi(I), time(I), iyield(I)
    CLOSE(1)
    ENDIF

    IF (zyield.eq.2) THEN
      WRITE(6,*) ' ION TURNING POINT RANGES'
      DO 6045 I=1,20
        IF (iring(I).gt. 0) THEN
          Vo(I)=Vo(I)/iring(I)
          AvgVth(I)=AvgVth(I)/iring(I)
          AvgVr(I)=AvgVr(I)/iring(I)
          AvgRo(I)=AvgRo(I)/iring(I)
        ENDIF
      ENDIF
    ENDIF
  ENDIF

```

```

        WRITE(6,6046)'ring',I,' has',iring(I),' ions of Radius '
            ,ring(I),' to ',ring(I+1),' Avg Vo=',Vo(I)
6045  CONTINUE
6046  FORMAT(1X,A,I3,1p,A,I4,A,G9.2e1,A,G9.2e1,A,G10.2E2)
      DO 6055 I=1,20
        WRITE(6,6056)'ring',I,' Avg Vtheta=',AvgVth(I),
            ' Avg Vr=',AvgVr(I),' Avg Ro=',AvgRo(I)
6055  CONTINUE
6056  FORMAT(1X,A,I3,1p,A,G10.2e2,A,G10.2E2,A,G10.2E2)

      VcAvg = VcTotal/FLOAT(nions-nilRtp)
      WRITE(6,*)' Average Vc for confined ions = ',VcAvg

ENDIF

WRITE(6,*)' # ions lost in chan. (radial tp eq.) = ',nilRtp

WRITE(6,*)' total yield for Li reaction (back)=' ,t2yield

WRITE(6,*)' total yield for Li reaction (front)=' ,t1yield

WRITE(6,*)' time resolved data for F reaction in "YIELD."'

      DO 887 M=1,20

c      IF (No(M).gt. 0) THEN
c          Eo(bin)=0.5*mass*Voi(K)*Voi(K)
c          Eo(M) = curr(M)*volto(M)*4.5e-9
c          Eo(M) = curr(M)*volto(M)*4.5e-9/(No(M)*No(M))
c      ELSE
c          Eo(M) = 0.0
c      ENDIF
c      IF (Nw(M).gt. 0) THEN
c          Ew(M) = curr(M)*voltw(M)*4.5e-9/(Nw(M)*Nw(M))
c          Ew(M) = curr(M)*voltw(M)*4.5e-9
c      ELSE
c          Ew(M) = 0.0
c      ENDIF

      Etin = Etin + Ei(M)
      Etout = Etout + Eo(M)
      Etwall = Etwall + Ew(M)

      IF (Ei(M).gt. 0.0) percent(M)=(Ei(M)-Eo(M)-Ew(M))/Ei(M)

      WRITE(6,7112)M,Ei(M),Eo(M),Ew(M),percent(M),y1b(M),y2b(M)

```

887 CONTINUE

7112 FORMAT(1X,I2,1X,1p,6(G11.2e2,1X))

```

WRITE(6,*)' # ions lost at chan. entrance = ',nilcin
WRITE(6,*)' # of ions in channel = ',nions
WRITE(6,*)' # ions lost in chan. (radial tp eq.) = ',nilRtp
WRITE(6,*)' total yield for Li reaction (back)=' ,t2yield
WRITE(6,*)' total yield for Li reaction (front)=' ,t1yield
WRITE(6,*)' pimple delta = ',del0,pimple
WRITE(6,*)' Energy in chan      = ',Etin
Write(6,*)' Energy out chan     = ',Etout
Write(6,*)' Energy to chan walls = ',Etwall

```

ENDIF

WRITE(6,*)' bad root count =',badroot

```

C
C All done.
C

```

END

B Activation, Energy Loss, and RTP Subroutines

This appendix lists the subroutines required by SHDLOAD and SHDCHAN. Included are FUNCTION calls for calculating prompt- γ yields from the $Li(p, \gamma)$ reaction (YLIF) and the $F(p, \alpha\gamma)$ reaction (YIELD), and energy loss due to classical dE/dx stopping in the Kimfol (KIMFOL) and air (ELAIR). Subroutines for calculating outer radial turning points for linear (RTP), quadratic (RTP2), and cubic (RTP3) B-field profiles are also included. The KIMFOL, ELAIR, YLIF, and YIELD routines are taken from VAX-ANALYSIS [5].

```

CCCCCCCCCCCCCCCCCCCCCCCCCCCCCCCCCCCCCCCCCCCCCCCCCCCCCCCCCCCC
C
C Function KIMFOL -- calculates energy loss in KIMFOL.
C
C This was lifted from VAX-ANALYSIS routine 'LIF'.
C
C To be used in SHDLOAD for KIMFOL loss at diode.
C e0 is in MV and is returned as the NEW corrected MegaVoltage.
C

```

```

REAL*4    FUNCTION KIMFOL(e0)
C
C
C
INTEGER   J
REAL*4    e0,akim,etemp,eloss
DIMENSION akim(2,6)

DATA akim / -3.0, -2.44, 5.0, 2.22, 506.0, 1045.0,
           226.0, 464.0, -9.57, -14.46, 2.04, 6.39 /

J=1
etemp = e0
IF (etemp .GT. 1.0 ) J=2
etemp = etemp*akim(J,2)+akim(J,1)
eloss = akim(J,3) + akim(J,4)*etemp + akim(J,5)*etemp*etemp +
        akim(J,6)*etemp*etemp*etemp
e0 = eloss*0.001
IF (e0.le. 0.0) e0=0.0
KIMFOL = e0

RETURN
END
CCCCCCCCCCCCCCCCCCCCCCCCCCCCCCCCCCCCCCCCCCCCCCCCCCCCCCCCCCCCCCCC
C
C
real*4 function elair(e)
*
* energy loss in kev/m/torr in air, from Andersen and Zeigler,
* with 80% N2 and 20% O2.  e in MeV
*
real*4 e,sl,sh,sn,so,etemp,ietemp
etemp = 1.0E3*e
ietemp = 1.0/etemp
sl = 3.35*(etemp**0.45)
sh = (1683.*ietemp)*alog(1.0+(1900.0*ietemp)+0.02513*etemp)
sn = 7.07*(sl*sh)/(sl+sh)
sl = 3.0*(etemp**0.45)
sh = (1920.*ietemp)*alog(1.0+(2000.0*ietemp)+0.0223*etemp)
so = 7.07*(sl*sh)/(sl+sh)
elair = 0.8*sn + 0.2*so
return
end

real*4 function yield(e)
c

```

```
c
real*4  pg,e
dimension pg(2,11)

c
data pg / 0., 0., 31.2, 143.6, -1318., 2490., -524., 1330.,
>         -81217., 95160., -6637., 10890., -93560., 76000.,
>         -13200., 20000., -81216., 61600., -325135., 191000.,
>         -620900., 340000. /

c
if ( e .le. 0.34) then
  y: ld = 0.
  return
endif
if (e .le. 0.575) then
  yield = pg(1,2) + pg(2,2)*e
  return
endif
if (e .le. 0.685) then
  yield = pg(1,3) + pg(2,3)*e
  return
endif
if (e .le. 0.86) then
  yield = pg(1,4) + pg(2,4)*e
  return
endif
if (e .le. 0.885) then
  yield = pg(1,5) + pg(2,5)*e
  return
endif
if (e .le. 1.335) then
  yield = pg(1,6) + pg(2,6)*e
  return
endif
if (e .le. 1.435) then
  yield = pg(1,7) + pg(2,7)*e
  return
endif
if (e .le. 1.635) then
  yield = pg(1,8) + pg(2,8)*e
  return
endif
if (e .le. 1.885) then
  yield = pg(1,9) + pg(2,9)*e
  return
endif
if (e .le. 1.985) then
  yield = pg(1,10) + pg(2,10)*e
```

```

      return
    endif
    yield = pg(1,11) + pg(2,11)*e
    return
  end

```

```

      real*4 function ylif(e)

```

```

*
* calculates thick target yield of Li reaction
*
* fitted from data of Leeper et al. e in MeV
*
      real*4 e1,e,y
      e1 = e*1.0e3
      if (e1 .lt. 400 ) then
        ylif = 0.0
        return
      end if
      if (e1 .lt. 500 ) then
        ylif = 7.3897E-9*(atan((e1-441.)/12.1) + 1.28382)
        return
      endif
      e1 = e1-500.
      y = 1.96 + e1*1.3E-3 + e1*e1*8.163E-7
      ylif = y*1E-8
      return
    end
CCCCCCCCCCCCCCCCCCCCCCCCCCCCCCCCCCCCCCCCCCCCCCCCCCCCCCCCCCCCCCCC
C
C
C
      SUBROUTINE Rtp(Ic,Vx,Vy,Vo,Rc,Xc,Yc,Rstar,Vtheta,Vr,Rstar1,Ro,Vc)
C
C
C This subroutine calculates the outer radial turning point of the
C ion in the discharge field.
C
C Xc,Yc Channel entrance plane coordinates of ion.
C Vx,Vy Channel entrance velocity components of ion.
C Vo Velocity of particle at channel entrance.
C Ic Discharge current.
C Rc Chann ` radius.
C Rstar Outer radial turning point to be calculated and returned.
C Rstar1 Alternate calculation of radial turning point.
C

```

```

C
REAL*4 X,Y,Ic,Vx,Vy,Vo,Rc,Xc,Yc,A,B,C,inner,middle,Rstar
REAL*4 Ro,Vc,Mu_o,mass,q,pi,Vz,Vtheta,Theta,pi2,epsilon
REAL*4 Yabs,Xabs,Rtpi,Vr,Rstar1,D,Rprime

C
C Ion = proton. Ze = 1
C
epsilon = 1.0e-31
pi = 3.14159
mass = 1.6726e-27
q = 1.6022e-19
Mu_o = 4.0e-7*pi

C
C
C
Vz = SQRT(Vo**2. - Vx**2. - Vy**2.)
Ro = SQRT(Xc**2. + Yc**2.)
C
Vc = (Mu_o*Ic*q*Ro)/(4.0*pi*mass*Rc)
Vc = (Mu_o*Ic*q)/(4.0*pi*mass)
Xabs=ABS(Xc)
Yabs=ABS(Yc)
IF ((Xabs.lt.epsilon).AND.(Yabs.lt.epsilon)) THEN
WRITE(6,*)' ==FLAG 1'
Theta=0.
ELSEIF(Xabs.lt.epsilon) THEN
WRITE(6,*)' ==FLAG 2'
IF (Yc.gt. 0.0) THEN
Theta = pi/2.
ELSE
Theta = 3.0*pi/2.
ENDIF
ELSEIF(Yabs.lt.epsilon) THEN
WRITE(6,*)' ==FLAG 3'
IF (Xc.gt. 0.0) THEN
Theta = 0.
ELSE
Theta = pi
ENDIF
ELSE
C
WRITE(6,*)' ==FLAG 4'
IF (Xabs.gt.Yabs) THEN
Theta = ACOS( Xabs/Ro )
ELSE
Theta = ASIN( Yabs/Ro )
ENDIF
IF ((Yc.lt. 0.0).AND.(Xc.lt. 0.0)) THEN
Theta = Theta + pi

```

```

      ELSEIF ((Yc.lt. 0.0).AND.(Xc.gt. 0.0)) THEN
        Theta = 2.0*pi - Theta
      ELSEIF ((Yc.gt. 0.0).AND.(Xc.lt. 0.0)) THEN
        Theta = pi - Theta
      ELSE
        Theta = Theta
      ENDIF
    ENDIF
    pi2 = 2.0*pi
    Theta = MOD(Theta,pi2)
    Vtheta= Vy*COS(Theta) - Vx*SIN(Theta)
    Vr     = Vx*COS(Theta) + Vy*SIN(Theta)
  C
  C Now calculate the A,B,C constants to get Rstar.
  C
    A = 2.0*Vz*Vc/((Vo*Rc)**2.)
    B = 1.0 - (Vz/Vo)**2. + 2.0*Vz*Vc*Ro*Ro/((Vo*Rc)**2.)
    C = (Ro*Vtheta/Vo)**2.

    inner = B*B - 4.0*A*C

    IF (inner.lt. 0.0) STOP 661

    middle = ( B + SQRT(inner) ) / (2.0*A)

    IF (middle.lt. 0.0) STOP 662

    Rstar = SQRT(middle)
  C
  C Do alternate calculation for comparison.
  C
    A = Ro*Ro/2.
    B = (Vr**2.+Vtheta**2.)*Rc*Rc/(4.*Vo*Vc)
    C = ( B*2. + Ro*Ro )**2.
    D = 2.*Ro*Ro*Rc*Rc*Vtheta*Vtheta/(Vo*Vc)

    IF ( C-D .le. 0.0 ) THEN
      Rstar1 = 0.0
      Return
    ELSE
      inner = 0.5*SQRT(C-D)
    ENDIF

    middle = A+B+inner
    IF (middle.le. 0.0) THEN
      Rstar1 = 0.0
      WRITE(6,*)'   imaginary root!'

```

```

      Return
    ELSE
      ~Rstar1 = SQRT(middle)
    ENDIF

C
C Do Paul's first order correction.
C

      Rprime = Vc*Vc*((Ro*Ro - Rstar1*Rstar1)**2.)
      Rprime = Rprime/(Rc**4.)
      C = 2.0*Vtheta*Vtheta*Ro*ro/(Rstar1**3.)
      D = 4.0*Vz*Vc*Rstar1/(Rc*Rc)
      Rprime = Rprime/( C - D )

      Rs1 = Rstar1+Rprime

      RETURN
    END

CCCCCCCCCCCCCCCCCCCCCCCCCCCCCCCCCCCCCCCCCCCCCCCCCCCCCCCCCCCC
C
C
C
C      SUBROUTINE Rtp2(Ic,Vx,Vy,Vo,Rc,Xc,Yc,Rstar,Vtheta,Vr,Rs1,Ro,Vc)
C
C
C This subroutine calculates the outer radial turning point of the
C ion in the discharge field. The discharge field in this case is
C quadratic. The roots of an 8th order polynomial are required in
C order to find the ion's outer turning point.
C
C   Ic,Yc Channel entrance plane coordinates of ion.
C   Vx,Vy Channel entrance velocity components of ion.
C   Vo Velocity of particle at channel entrance.
C   Ic Discharge current.
C   Rc Channel radius.
C   Rstar Outer radial turning point to be calculated and returned.
C   Rs1 Alternate calculation of radial turning point.
C
C This routine will return the desired turning point as Rs1.
  INTEGER M,I,RR,J
  LOGICAL lessthan
  REAL*4 X,Y,Ic,Vx,Vy,Vo,Rc,Xc,Yc,A,B,C,Rstar,F,Rosave
  REAL*4 Ro,Vc,Mu_o,Vz,Vtheta,pi2,R(51),del_R(51),rfall
  REAL*4 Rtpi,Vr,Rs1,D,Rprime,dummy,middle,diff

```

```

REAL*4 Rc3,Rc6,Ro3,epsilon,Voc,Vtc,Vzc,Rnew,Rstart
REAL*4 Yabs,Xabs,pi,Theta,q,mass,Vr_inspec,top,bottom

```

```

lessthan = .false.

```

```

C
C Ion = proton, Z = 1
C
epsilon = 1.0e-31
pi = 3.14159
mass = 1.6726e-27
q = 1.6022e-19
Mu_o = 4.0e-7*pi
C
C Calc. phase space coordinates.
C
Vz = SQRT(Vo**2. - Vx**2. - Vy**2.)
Ro = SQRT(Xc**2. + Yc**2.)
Rosave = Ro
Vc = (Mu_o*Ic*q)/(4.0*pi*mass)*(2./3.)
Xabs=ABS(Xc)
Yabs=ABS(Yc)
IF ((Xabs.lt.epsilon).AND.(Yabs.lt.epsilon)) THEN
  WRITE(6,*)' ==FLAG 1'
  Theta=0.
ELSEIF(Xabs.lt.epsilon) THEN
  WRITE(6,*)' ==FLAG 2'
  IF (Yc.gt. 0.0) THEN
    Theta = pi/2.
  ELSE
    Theta = 3.0*pi/2.
  ENDIF
ELSEIF(Yabs.lt.epsilon) THEN
  WRITE(6,*)' ==FLAG 3'
  IF (Xc.gt. 0.0) THEN
    Theta = 0.
  ELSE
    Theta = pi
  ENDIF
ELSE
  WRITE(6,*)' ==FLAG 4'
  IF (Xabs.gt.Yabs) THEN
    Theta = ACOS( Xabs/Ro )
  ELSE
    Theta = ASIN( Yabs/Ro )
  ENDIF

```

```

      IF ((Yc.lt. 0.0).AND.(Xc.lt. 0.0)) THEN
        Theta = Theta + pi
      ELSEIF ((Yc.lt. 0.0).AND.(Xc.gt. 0.0)) THEN
        Theta = 2.0*pi - Theta
      ELSEIF ((Yc.gt. 0.0).AND.(Xc.lt. 0.0)) THEN
        Theta = pi - Theta
      ELSE
        Theta = Theta
      ENDIF
    ENDIF
    pi2 = 2.0*pi
    Theta = MOD(Theta,pi2)
    Vtheta= Vy*COS(Theta) - Vx*SIN(Theta)
    Vr     = Vx*COS(Theta) + Vy*SIN(Theta)

    Voc = Vo/Vc
    Vzc = Vz/Vc
    Vtc = Vtheta/Vc
    Rc6 = Rc**6.
    Rc3 = Rc**3.
    Ro3 = Ro**3.

C
C do polynomial coeff.
C
      A = 2.0*Vz*Rc3/Vc - 2.0*Ro3

      B = Vzc*Vzc*Rc6 - Voc*Voc*Rc6 - 2.0*Vzc*Ro3*Rc3 + Ro3*Ro3

      C = Vtc*Vtc*Ro*Ro*Rc6

C
C find an 'r' that goes positive on the (Vr,r) curve.
C
      Rnew = Ro*1.1
      Vr_inspec = Rnew**8. + A*(Rnew**5.) + B*(Rnew**2.) + C
      IF (Vr_inspec.gt. 0.0) GOTO 12
      DO 10 I=1,10000
        Rnew = Rnew+ Ro*0.1
        Vr_inspec = Rnew**8. + A*(Rnew**5.) + B*(Rnew**2.) + C
        IF (Vr_inspec.gt. 0.0) THEN
          Diff = 0.1*Ro
          Rstart = Rnew - Ro*0.1
          DO 20 J=1,98
            Rnew = FLOAT(J)*0.01*Diff + Rstart

```

```

      Vr_inspec = Rnew**8.+A*(Rnew**5.)+B*(Rnew**2.)+C
      IF (Vr_inspec.gt. 0.0) THEN
        R(1) = Rnew
        Rfall = Rnew
        GOTO 12
      ENDIF
20     CONTINUE
      GOTO 11
    ENDIF
10  CONTINUE
    WRITE(6,*)' %%%%%%%%% failed to make Vr positive. %%%%%%%%%'
11  CONTINUE

c     R(1) = Rnew - Ro*0.1
      R(1) = Rnew

12  CONTINUE

C
C Now loop over, doing correction, testing, and then R's again.
C

      DO 5001 I=1, 50

        IF (R(I).lt. 0.0) THEN
          WRITE(6,*)' Rtp2 -- Converging to wrong root.',I
          R(1) = R(1)*1.1
          GOTO 12
        ENDIF

        top    = (R(I)**8.) + A*(R(I)**5.) + B*(R(I)**2.) + C
        bottom = 8.0*(R(I)**7.) + 5.0*A*(R(I)**4.) + 2.0*B*R(I)

        IF (ABS(bottom) .gt. 1.e-36) THEN
          del_R(I) = -1.0*top/bottom
        ELSE
          WRITE(6,*)' Rtp2 -- Demoninator too small.',I
          Rs1 = 13.13
          Ro = Rosave
          RETURN
        ENDIF

        R(I+1) = R(I) + del_R(I)

        IF (I .gt. 3) THEN
          diff = ABS(R(I+1)-R(I))+ABS(R(I)-R(I-1)) +

```



```

C
C This subroutine calculates the outer radial turning point of the
C ion in the discharge field. The discharge field in this case is
C quadratic. The roots of an 8th order polynomial are required in
C order to find the ion's outer turning point.
C
C   Xc,Yc Channel entrance plane coordinates of ion.
C   Vx,Vy Channel entrance velocity components of ion.
C   Vo Velocity of particle at channel entrance.
C   Ic Discharge current.
C   Rc Channel radius.
C   Rstar Outer radial turning point to be calculated and returned.
C   Rsl Alternate calculation of radial turning point.
C
C This routine will return the desired turning point as Rsl.
C   INTEGER M,I,RR,J
C   LOGICAL lessthan
C   REAL*4 X,Y,Ic,Vx,Vy,Vo,Rc,Xc,Yc,A,B,C,Rstar,F,Rosave
C   REAL*4 Ro,Vc,Mu_o,Vz,Vtheta,pi2,R(S1),del_R(S1),rfall
C   REAL*4 Rtpi,Vr,Rsl,D,Rprime,dummy,middle,diff,Ro8,Vrc
C   REAL*4 Rc4,Rc8,Ro4,epsilon,Voc,Vtc,Vzc,Rnew,Rstart
C   REAL*4 Yabs,Xabs,pi,Theta,q,mass,Vr_inspec,top,bottom

      lessthan = .false.

C
C Ion = proton, Z = 1
C
      epsilon = 1.0e-31
      pi = 3.14159
      mass = 1.6726e-27
      q = 1.6022e-19
      Mu_o = 4.0e-7*pi
C
C Calc. phase space coordinates.
C
      Vz = SQRT(Vo**2. - Vx**2. - Vy**2.)
      Ro = SQRT(Xc**2. + Yc**2.)
      Rosave = Ro
      Vc = (Mu_o*Ic*q)/(4.0*pi*mass)*(2./4.)
      Xabs=ABS(Xc)
      Yabs=ABS(Yc)
      IF ((Xabs.lt.epsilon).AND.(Yabs.lt.epsilon)) THEN
        WRITE(6,*) ' ===FLAG 1'
        Theta=0.
      ELSEIF(Xabs.lt.epsilon) THEN

```

```

WRITE(6,*)'      ==FLAG 2'
IF (Yc.gt. 0.0) THEN
  Theta = pi/2.
ELSE
  Theta = 3.0*pi/2.
ENDIF
ELSEIF(Yabs.lt.epsilon) THEN
WRITE(6,*)'      ==FLAG 3'
IF (Xc.gt. 0.0) THEN
  Theta = 0.
ELSE
  Theta = pi
ENDIF
ELSE
c WRITE(6,*)'      ==FLAG 4'
IF (Xabs.gt.Yabs) THEN
  Theta = ACOS( Xabs/Ro )
ELSE
  Theta = ASIN( Yabs/Ro )
ENDIF
IF ((Yc.lt. 0.0).AND.(Xc.lt. 0.0)) THEN
  Theta = Theta + pi
ELSEIF ((Yc.lt. 0.0).AND.(Xc.gt. 0.0)) THEN
  Theta = 2.0*pi - Theta
ELSEIF ((Yc.gt. 0.0).AND.(Xc.lt. 0.0)) THEN
  Theta = pi - Theta
ELSE
  Theta = Theta
ENDIF
ENDIF
pi2 = 2.0*pi
Theta = MOD(Theta,pi2)
Vtheta= Vy*COS(Theta) - Vx*SIN(Theta)
Vr     = Vx*COS(Theta) + Vy*SIN(Theta)

Voc = Vo/Vc
Vrc = Vr/Vc
Vzc = Vz/Vc
Vtc = Vtheta/Vc
Rc4 = Rc**4.
Ro4 = Ro**4.
Ro8 = Ro4*Ro4
Rc8 = Rc4*Rc4

c
c do polynomial coeff.
c

```

A = 1.0

B = 2.0*Vzc*Rc4 - 2.0*Ro4

C = Ro8 - Vtc*Vtc*Rc8 - Vrc*Vrc*Rc8 - 2.0*Vzc*Ro4*Rc4

D = Ro*Ro*Vtc*Vtc*Rc8

C

C find an 'r' that goes positive on the (Vr,r) curve.

C

Rnew = Ro*1.1

Vr_inspec = A*(Rnew**10.) + B*(Rnew**6.) + C*(Rnew**2.) + D

IF (Vr_inspec.gt. 0.0) GOTO 12

DO 10 I=1,10000

Rnew = Rnew+ Ro*0.1

Vr_inspec = A*(Rnew**10.) + B*(Rnew**6.) + C*(Rnew**2.) + D

IF (Vr_inspec.gt. 0.0) THEN

Diff = 0.1*Ro

Rstart = Rnew - Ro*0.1

DO 20 J=1,98

Rnew = FLOAT(J)*0.01*Diff + Rstart

Vr_inspec = A*(Rnew**10.)+B*(Rnew**6.)+C*(Rnew**2.)+D

IF (Vr_inspec.gt. 0.0) THEN

R(1) = Rnew

Rfall = Rnew

GOTO 12

ENDIF

20 CONTINUE

GOTO 11

ENDIF

10 CONTINUE

WRITE(6,*) ' %%%%%%%%% failed to make Vr positive. %%%%%%%%%'

11 CONTINUE

C R(1) = Rnew - Ro*0.1

R(1) = Rnew

12 CONTINUE

C

C Now loop over, doing correction, testing, and then R's again.

C

DO 5001 I=1, 50

```

IF (R(I).lt. 0.0) THEN
  WRITE(6,*)' Rtp3 -- Converging to wrong root.',I
  R(I) = R(I)*1.1
  GOTO 12
ENDIF

top    = A*(R(I)**10.) + B*(R(I)**6.) + C*(R(I)**2.) + D
bottom = 10.*A*(R(I)**9.) + 6.0*B*(R(I)**5.) + 2.0*C*R(I)

IF (ABS(bottom) .gt. 1.e-36) THEN
  del_R(I) = -1.0*top/bottom
ELSE
  WRITE(6,*)' Rtp3 -- Demoninator too small.',I
  Rs1 = 13.13
  Ro = Rosave
  RETURN
ENDIF

R(I+1) = R(I) + del_R(I)

IF (I .gt. 3) THEN
  diff = ABS(R(I+1)-R(I))+ABS(R(I)-R(I-1))
  IF (diff .lt. 3.e-6) THEN

    Rs1 = R(I+1)
    IF (Rs1 .lt. Rosave) THEN
      diff = (ABS(Rs1-Rosave))/Rosave
      IF (diff .lt. 0.001) THEN
        WRITE(6,*)' Rtp3 -- correction made.'
        Rs1 = Rosave
      ELSE
        IF (.not. lessthan) THEN
          R(I) = rfall*4.0
          WRITE(6,*)' repeat.'
          lessthan = .true.
          GOTO 12
        ENDIF
        Rs1 = rfall
        WRITE(6,*)' failed.'
      ENDIF
    ENDIF
    Ro = Rosave
    RETURN

  ENDIF
ENDIF
ENDIF

```

```
5001 CONTINUE
```

```

C
C Didn't converge.
C
      WRITE(6,*) ' No convergence.'
      Rsl = 13.13
      Ro = Rosave
C
C Done.
C
      RETURN
      END
CCCCCCCCCCCCCCCCCCCCCCCCCCCCCCCCCCCCCCCCCCCCCCCCCCCCCCCCCCCC

```

C Channel Propagation

The program SHDCHAN performs orbit calculations for ions injected into the discharge channel. The equation of motion integrator is the common leap-frog method. The time step size is determined by an individual ions energy and can decrease for a single ions flight as energy loss due to classical stopping is calculated at integral number of time steps. The equations of motion are fully 3D, non-relativistic and energy loss is performed by the ELAIR function (see Appendix B). Note, that for ion energies below $\approx 1.2MV$, a simple variable timestep scheme is used to help optimize the calculations. The code included here uses a linear rising B-field. This can easily be modified to the quadratic B-field case by examining the variables Bo and Vc.

```
program SHDCHAN
```

```

C
C This program does the real work in the LMF/SHD suite. Ions
C are moved through a ideal wall-stabilized discharge channel
C of constant radius and current. 100% current and charge
C neutralization is assumed, no self-field effects are treated.
C
C Conervation of energy, angular momentum, and axial momentum
C is reported in the LOG file (when run in batch mode) or
C terminal screen (when in interactive mode).
C
C Note: Arrays are stored such that the number of data
C points appears as the first element. This is

```

```

C      done to make plotting the data in the PLOT10 AGII
C      package easier.
C
C      This program differs from the LMF version mostly in reading and
C      writing of data files.
C
C      For ions that hit the channel wall, the X() coordinate is labeled
C      with the value '13.14' and the Y() coordinate is used to hold the
C      ions last Z() position. An option in the plotting package with
C      enable the user to see where ions stop in the channel.
C
C      Variables:
C      radius      -- user supplied out radius at diode.
C      Vx,Vy       -- Velocity arrays.
C      X,Y         -- Position arrays.
C      F           -- User supplied diode to channel distance.
C      Energy      -- User supplied ion energy.
C      Vo          -- Ion velocity Energy = (1/2)m(Vo)**2
C      nions       -- User supplied number of ions.
C      asize       -- Max number of ions (array sizes).
C      nq          -- number of removed electrons in ion.
C      nmass       -- ion mass in number of proton masses.
C      Rc          -- Channel radius.
C      nilcin      -- number of ions lost at channel entrance.
C      nilc        -- number of ions lost in channel.
C      nihtar      -- number of ions that hit the target.
C      Tradius     -- Radius of target.
C      Tpos        -- Target position.
C      CLEN        -- Channel length.
C
C      Variables specific to SHDCHAN:
C      isteps      -- # of time steps
C      dt          -- time step size in sec.
C      adist       -- average particle distance for ions that
C                  clear channel exit.
C      tdist       -- total single particle distance
C      rdist       -- 1000 step distance for ELAIR calc.
C      sdist       -- single time step distance.
C      maxdist     -- max. particle travel distance.
C      mindist     -- min. particle travel distance.
C      ismod       -- modulus for energy loss calc.
C      MV          -- used in ELAIR calc. (MegaVolts)
C      MVnew       -- " " " " "
C      MVi         -- " " " " "
C      kVpMpT      -- kiloVolts per Meter per Torr
C      nilqrtr     -- # of ions lost after a quarter of the
C                  channel length

```

```

C
C
INTEGER  asize,nmass,nq,nilcin,nilc,nihtar,I,K,nions
INTEGER  isteps,L,offset,bnum,ionbin,iring,M,ismod
INTEGER  nilqrtr,nillow
LOGICAL  conserv
PARAMETER (asize=30000)
REAL     R,rscale,Vo,Vz,Bo,tmpmax,tmpmin,kVpMpt,rdist
REAL     q,qm,mass,Vxo,Vyo,Vzo,time,Xchan,Ychan,adist
REAL     Zo,Xo,Yo,X1,Y1,Z1,Vx1,Vy1,Vz1,dt,Rth,tdist,sdist
REAL     Vxs,Vys,Vf,Vt,Vfmax,Vfmin,Ro,Rf,volt,curr,Voi
REAL     Pphimax,Pphimin,Pphio,Pphif,Pphid,Pphit,Vd,Rc2
REAL     Pzt,Pzmax,Pzmin,Pzf,Pzo,Vzi,Pzdiff,MV,MVi,MVnew
REAL     X,Y,Vx,Vy,F,radius,Rc,current,Clen,Rtarget,qrtr
REAL     Tpos,Energy,bend,Voi,iy,timei,ring,ringmax
REAL     ratio,mindist,maxdist,Voi_old,Pressure,clair
CHARACTER*100 info
DIMENSION X(asize),Y(asize),bnum(asize),Vo(20),curr(20)
DIMENSION Vx(asize),Vy(asize),bend(20),Voi(asize)
DIMENSION iy(asize),timei(asize),iring(10),ring(11)
DIMENSION Vxs(asize),Vys(asize),volt(20),ionbin(20)

conserv = .false.

C
C Read in the chanin. file.
C
OPEN(1,FILE='chanin.',form='unformatted',access='sequential',
     STATUS='OLD')
READ(1)nions,F,radius,Rc,current,Clen,Rtarget,Tpos,Energy,
     nmass,nq,nilcin,nilc,nihtar,info
DO 303 I=1,20
303 READ(1)volt(I),curr(I),ionbin(I),bend(I),Vo(I)
DO 304 I=1,nions+1
304 READ(1)X(I),Y(I),Vx(I),Vy(I),bnum(I),Voi(I),timei(I),iy(I)
CLOSE(1)

C
C Set defaults.
C
maxdist = 0.0
mindist = 1000.
nillow = 0
nilqrtr = 0
qrtr = 0.25*Clen + F
dt = 2.0e-12
q = nq*1.6022e-19
mass=nmass*1.6726e-27

```

```

      qa =q/mass
      Rc2 = Rc*Rc
      nrlc = 0
      offset = 1
      Pressure = 2.0          ! 2.0 Torr for all Jess's runs.
      Bo = 2.0e-7*current/(Rc*Rc)

      DO 57 I=1,11
57  ring(I)=FLOAT(I-1)*0.1*Rc

C
C  Begin particle loop.
C
      WRITE(6,*) ' # of ions to loop over = ',nions

      DO 100 I=1,nions

C
C      Is this particle available for moving?
C
      IF (X(I+offset).eq. 13.13) GOTO 100
      IF (Voi(I+offset) .lt. 6.92e6) THEN
          nilow = nilow+1
          X(I+offset) = 13.13
          GOTO 100
      ENDIF

C
C      Set up particle for propogation.
C
      dt = 2.0e-12
      tdist = 0.0
      rdist = 0.0

      Voi = Voi(I+offset)
      IF (Voi.lt.1.52e7) THEN
          dt = 3.04e-5/Voi
      ENDIF

      Vxo = Vx(I+offset)
      Vyo = Vy(I+offset)
      Vz0 = SQRT(Voi*Voi - Vxo*Vxo - Vyo*Vyo )
      Xo = X(I+offset)
      Yo = Y(I+offset)
      Zo = F
      isteps=0

```

```

Vfmin=3.e10
Vfmax=0.
Vt=0.
Pphit = 0.
Pphimax=0.
Pphimin=1.e20
Pzt=0.
Pzmax=0.
Pzmin=1.e20
Ringmax=0.0

50  CONTINUE

isteps = isteps+1
rscale = Xo*Xo+Yo*Yo
IF (rscale.gt.Rc2) THEN
  X(I+offset) = 13.14
  Y(I+offset) = Zo
  nilc = nilc+1
  IF (Zo.ge.qrtr) nilqrtr = nilqrtr+1
  GOTO 100
ENDIF

Vx1 = Vxc - dt*qm*Vzo*Bo*Xo

X1 = Xo + dt*Vxo

Vy1 = Vyo - dt*qm*Vzo*Bo*Yo

Y1 = Yo + dt*Vyo

Vz1 = Vzo + dt*qm*(Vxo*Xo + Vyo*Yo)*Bo

Z1 = Zo + dt*Vzo

sdist = Z1-Zo
rdist = rdist + sdist
tdist = tdist + sdist

IF (Z1.gt. Clen+F) THEN
C
C   Get p's and q's at channel exit plane.
C
time = (Clen+F-Zo)/Vzo
Vx1 = Vxo - time*qm*Vzo*Bo*Xo
X1 = Xo + time*Vxo

```

```

Vyi = Vyo - time*qm*Vzo*Bo*Yo
Y1 = Yo + time*Vyo
Vzi = Vzo + time*qm*(Vxo*Xo + Vyo*Yo)*Bo
C
C      Check Energy conversation for this ion.
C
      IF (conserv) THEN

Vf = SQRT(Vzi**2 + Vxi**2 + Vy1**2)      ! final vel.
Vd = ABS(Vf-Voi)
Vfmax = MAX(Vfmax,Vd)                    ! Max Vd
Vfmin = MIN(Vfmin,Vd)                    ! Min Vd
Vt = Vt+Vd                               ! Total Vd
C
C      Check Angular Momentum conservation for this ion.
C
Vzi=SQRT(Voi**2. - Vx(I+offset)**2.- Vy(I+offset)**2.)
Ro=SQRT( X(I+offset)**2. + Y(I+offset)**2. )
Rf=SQRT(X1*X1 + Y1*Y1)                   ! final R
Pphio=Vy(I+offset)*X(I+offset)-Vx(I+offset)*Y(I+offset)
Pphif=Vy1*X1-Vx1*Y1
Pphio=mass*Pphio                          ! init momentum
Pphif=mass*Pphif                          ! final momentum
Pphid=ABS(Pphif-Pphio)                    ! (+) diff.
Pphit=Pphif+Pphid                         ! total diff.
Pphimax=MAX(Pphif,Pphid)                  ! momentum max.
Pphimin=MIN(Pphif,Pphid)                 ! momentum min.
C
C      Check Axial Momentum consevation for this ion.
C
Pzo = mass*(Vzi - (qm*Bo/2.)*Ro*Ro)
Pzf = mass*(Vzi - (qm*Bo/2.)*Rf*Rf)
Pzdif=ABS(Pzo-Pzf)
Pzt=Pzo+Pzdif
Pzmax=MAX(Pzmax,Pzdif)
Pzmin=MIN(Pzmin,Pzdif)
C
C      Find the max. turning point radius of ion.
C
DO 686 M=1,10
  IF ((Ringmax.ge.ring(M)).and.
      (Ringmax.lt.ring(M+1))) THEN
    iring(M) = iring(M)+1
    GOTO 689
  ENDIF
686 CONTINUE
689 CONTINUE

```

```

      ENDIF
C
C   Store final phase space coordinates for this ion.
C
      Vx(I+offset)=Vx1
      Vy(I+offset)=Vy1
      X(I+offset)=X1
      Y(I+offset)=Y1
C
C   Do ion travel distance statistics.
C
      IF (conserve) THEN
      MAXDIST = MAX(MAXDIST,tdist)
      MINDIST = MIN(MINDIST,tdist)
      adist  = adist + tdist
      ENDIF

      GOTO 100
ENDIF

C
C Section to do energy loss in air.
C
      ismod = MOD(isteps,2000)
      IF ((ismod.eq.1).AND.(isteps.gt.3)) THEN

      Voi_old      = Voi
      MV           = 1.e-6*0.5*mass*Voi*Voi/q
      MVi         = MV
      kVpMpT      = ELAIR(MV)
      MVnew       = MVi - rdist*Pressure*kVpMpT*1.e-3
      IF (MVnew .lt. 0.0) THEN
      nilow = nilow+1
      X(I+offset) = 13.13
      GOTO 100
      ENDIF
      Voi         = SQRT( 2.0*qn*1.e6*MVnew )
      Voi(I+offset) = Voi

      ratio       = Voi/Voi_old
      Vx1        = Vx1*ratio
      Vy1        = Vy1*ratio
      Vz1        = SQRT(Voi*Voi-Vx1*Vx1-Vy1*Vy1)

      IF (Voi.lt.1.52e7) THEN

```

```

      dt = 3.04e-5/Voi
    ENDIF

      rdist = 0.0

    ENDIF

C
C End Section for energy loss.
C
      Vxo = Vx1
      Vyo = Vy1
      Vzo = Vz1
      Xo = X1
      Yo = Y1
      Zo = Z1

      GOTO 50

C
C
C End particle loop.
C

100 CONTINUE

WRITE(6,*)' # of ions lost before channel = ',nilcin
WRITE(6,*)' # of ions lost in channel = ',nilc
WRITE(6,*)' # of ions lost after 1/4 chan.= ',nilqrtr
WRITE(6,*)' # of low vel. ions removed = ',nillo
WRITE(6,*)' Check conservation of energy (T/F) = ',conserv
IF (conserv) THEN
WRITE(6,*)' ----- Conservation of Energy -----'
Vf = Vt/(nions-nilc)
WRITE(6,*)' Average diff. in Vo from front to back= ',Vf
WRITE(6,*)' Max Velocity at channel end = ',Vfmax
WRITE(6,*)' Min Velocity at channel end = ',Vfmin

WRITE(6,*)' ----- Conservation of Angular Momentum -----'
Pphit = Pphit/(nions-nilc)
WRITE(6,*)' Avg. diff. in Pphi from front to back = ',Pphit
WRITE(6,*)' Max phi Momentum diff. at channel end = ',Pphimax
WRITE(6,*)' Min phi Momentum diff. at channel end = ',Pphimin

WRITE(6,*)' ----- Conservation of Axial Momentum -----'
Pzt = Pzt/(nions-nilc)

```

```

WRITE(6,*)' Avg. diff. in Pz from front to back = ',Pzt
WRITE(6,*)' Max Z Momentum diff. at channel end = ',Pzmax
WRITE(6,*)' Min Z Momentum diff. at channel end = ',Pzmin
WRITE(6,*)' ----- Conservation of Axial Momentum -----'
adist = adist/(nions-nilc)
WRITE(6,*)' Avg. ion travel dist. at channel exit = ',adist
WRITE(6,*)' Max. ion travel dist. at channel exit = ',maxdist
WRITE(6,*)' Min. ion travel dist. at channel exit = ',mindist
ENDIF

C
C Write out chanex. file.
C
OPEN(1,FILE='chanex.',form='unformatted',access='sequential',
STATUS='NEW')
WRITE(1)nions,F,radius,Rc,current,Clen,Rtarget,Tpos,Energy,
nmass,nq,nilcin,nilc,nihtar,info
DO 306 I=1,20
306 WRITE(1)volt(I),curr(I),ionbin(I),bend(I),Vo(I)
DO 307 I=1,nions+1
307 WRITE(1)X(I),Y(I),Vx(I),Vy(I),bnum(I),Voi(I),timei(I),iy(I)
CLOSE(1)

WRITE(6,*)' F = ',F
WRITE(6,*)' Rc = ',Rc
WRITE(6,*)' current = ',current
WRITE(6,*)' Clen = ',Clen
WRITE(6,*)' Rtarget,Tpos ',Rtarget,Tpos
WRITE(6,*)' info = ',info

IF (conserv) THEN
WRITE(6,*)' ION TURNING POINT RANGES'
DO 6045 I=1,10
WRITE(6,6046)'ring',I,' has',iring(I),' ions of Radius '
,ring(I),' to ',ring(I+1)
6045 CONTINUE
6046 FORMAT(1X,A,I3,2P,A,I4,A,F6.2,A,F6.2)
ENDIF

END

```

D Channel Exit to Target Projection

Several small codes were written to project the ion phase space distribution from the channel exit the witness plate/target assembly. In all of these codes

no classical stopping was considered. Included here is SHDTARG2 which was used to generate the phase space distributions at the target presented in Ref. [1].

```

      program SHDTARG2
C
C This program takes the ions from the channel exit plane and
C projects them onto the witness plate and target.
C The user inputs channel to witness plate distance and
C target distance. The 'target' is a flat
C disk in the (X,Y) plane(the blue plastic).
C The witness plate is the aluminum plate with radial pin hole
C rays.
C The number of ions that hit the
C target is stored along with their phase space coordinates.
C
C Programs in this set include:
C
C   SHDLOAD  -- Initial ions distribution at diode and
C              projection to channel entrance.
C   SHDCHAN  -- Take ions at channel entrance and move 'em
C              to end of channel.
C   SHDTARG  -- Take ions at end of channel and project them
C              onto the target (through witness plate).
C   SHDPLOT  -- Plot any of the dump files left behind by the
C              above programs.
C
C Program structure is:
C   1. Get user input.
C   2. Read channel exit phase space coordinates.
C   3. Project ions from channel exit to target.
C   4. Write this out in 'target.'
C
C Variables in SHDTARG:
C   radius   -- user supplied out radius at diode.
C   Vx,Vy    -- Velocity arrays.
C   X,Y      -- Position arrays.
C   mu       -- user supplied microdivergence.
C   F        -- User supplied diode to channel distance.
C   Energy   -- User supplied ion energy.
C   Vo       -- Ion velocity Energy = (1/2)m(Vo)**2
C   jseed    -- Random number generator seed.
C   nions    -- User supplied number of ions.
C   asize    -- Max number of ions (array sizes).
C   nq       -- number of removed electrons in ion.

```

```

C      nmass      -- ion mass in number of proton masses.
C      Rc         -- Channel radius.
C      nilcin     -- number of ions lost at channel entrance.
C      nilc       -- number of ions lost in channel.
C      nihtar     -- number of ions that hit the target.
C      Tradius    -- Radius of target.
C      Tpos       -- Target position.
C      CLEN       -- Channel length.
C
C
C      INTEGER   asize,nmass,nq,nilcin,nilc,nihtar,I,K,nions
C      INTEGER   offset,M,npass,nhitwit,ionbin,bnum,retry,J
C      PARAMETER (asize=30000)
C      REAL      a,b,R,radius,rscale,x,y,F,c,d,Energy,bend,curr
C      REAL      e,g,Vx,Vy,Vo,mu,time,Vz,Rc,xpass,ypass,Rion,volt
C      REAL      current,clen,Tpos,Wpos,xh,yh,Rtarget,delh,rh,Voi
C      REAL      iy,timei,Voii,tpass,Xprime,Yprime,VXprime,VYprime
C      REAL      Cangle,Sangle
C      CHARACTER*100 info
C      DIMENSION x(asize),y(asize),xpass(asize),ypass(asize)
C      DIMENSION Vx(asize),Vy(asize),xh(7),yh(7),bnum(asize)
C      DIMENSION bend(20),curr(20),volt(20),ionbin(20),Vo(20)
C      DIMENSION timei(asize),Voii(asize),iy(asize),tpass(asize)
C      DIMENSION Sangle(9),Cangle(9)

      DO 10 I=1,9
          Sangle(I) = SIN(FLOAT(I-1)*0.174533)
          Cangle(I) = COS(FLOAT(I-1)*0.174533)
10     CONTINUE

C
C      Read in chanex. file
C
      OPEN(1,FILE='chanex.',form='unformatted',access='sequential',
          .   STATUS='OLD')
      READ(1)nions,F,radius,Rc,current,Clen,Rtarget,Tpos,Energy,
          .   nmass,nq,nilcin,nilc,nihtar,info
      DO 302 I=1,20
302    READ(1)volt(I),curr(I),ionbin(I),bend(I),Vo(I)
      DO 303 I=1,nions+1
303    READ(1)X(I),Y(I),Vx(I),Vy(I),bnum(I),Voii(I),timei(I),iy(I)
      CLOSE(1)

C
C      Get input from user.
C
      WRITE(6,*)' SHDTARG -- '

```

```

WRITE(6,*) ' Enter channel exit to witness plate distance(m). '
READ(5,*)Wpos
WRITE(6,*) ' Enter witness plate to target distance(m). '
READ(5,*)Tpos

C
C Constants
C

rh = 0.5e-3                ! radius of pin holes
delh = 5.e-3              ! center to center dist. between holes.
DO 45 I=1,4
  xh(I) = delh*FLOAT(I-1)
  yh(I) = 0.0
45 CONTINUE
DO 46 I=1,3
  xh(I+4) = 0.0
  yh(I+4) = delh*FLOAT(I)
46 CONTINUE

C
C Move ions to witness plate.
C

offset = 1
npass = 0
nhitwit = 0

DO 700 I=2,nions+1

  IF ((X(K).ne.13.13).and.(X(K).ne.13.14)) THEN

    Voi = Voi(I)
    A = Voi*Voi - Vx(I)*Vx(I) - Vy(I)*Vy(I)
    IF (A.lt. 0.0) THEN
      WRITE(6,*) ' Error --'
      WRITE(6,*) ' Voi = ',Voi
      WRITE(6,*) ' Vx = ',Vx(I)
      WRITE(6,*) ' Vy = ',Vy(I)
      WRITE(6,*) ' I = ',I
      STOP 123
    ENDIF
    Vz = SQRT(A)
    time = Wpos/Vz
    X(I)= X(I)+Vx(I)*time
    Y(I)= Y(I)+Vy(I)*time
    timei(I) = time+timei(I)

  DO 674 J= 1,9

```

```

Xprime = X(I)*Cangle(J) + Y(I)*Sangle(J)
Yprime = Y(I)*Cangle(J) - X(I)*Sangle(J)
VXprime = Vx(I)*Cangle(J) + Vy(I)*Sangle(J)
VYprime = Vy(I)*Cangle(J) - Vx(I)*Sangle(J)

C      Check to see if ion goes through a hole.

      DO 671 M = 1,7
      Rion = SQRT( ( ABS(Xprime)-xh(M) )**2. +
                  ( ABS(Yprime)-yh(M) )**2. )
      IF (Rion.le. rh) THEN
      time = Tpos/Vz
      npass = npass+1
      Xpass(npass+1)= Xprime+Vxprime*time
      Ypass(npass+1)= Yprime+Vyprime*time
      Tpass(npass+1)= timei(I) + time
      ENDIF
671      CONTINUE

674      CONTINUE

      ENDIF

700 CONTINUE

      Ypass(1)=FLOAT(npass)
      Xpass(1)=FLOAT(npass)
      tpass(1)=FLOAT(npass)

      nihtar=npass

      OPEN(1,FILE='target.',form='unformatted',access='sequential',
      .      STATUS='NEW')
      WRITE(1)inions,F,radius,Rc,current,Clen,Rtarget,Tpos,Energy,
      .      nmass,nq,nilcin,nilc,nihtar,info
      DO 315 I=1,20
315  WRITE(1)volt(I),curr(I),ionbin(I),bend(I),Vo(I)
      DO 305 I=1,npass+1
305  WRITE(1)Xpass(I),Ypass(I),Vx(I),Vy(I),bnum(I),Voii(I),
      .      tpass(I),iy(I)
      CLOSE(1)

C
C Give the user some info.
C
      WRITE(6,*)' -----'

```

```

WRITE(6,*) '# ions that hit at the target = ',nihtar
WRITE(6,*) '# ions that hit witness plate = ',nhitwit
WRITE(6,*) '-----'
WRITE(6,*) info(1:80)
WRITE(6,*) Diode radius           = ',radius
WRITE(6,*) Diode the channel distance = ',F
WRITE(6,*) Channel radius         = ',Rc
WRITE(6,*) Channel current        = ',current
WRITE(6,*) Channel length         = ',Clen
WRITE(6,*) Channel to witness distance = ',Wpos
WRITE(6,*) Witness to target distance = ',Tpos
WRITE(6,*) '-----'
WRITE(6,*) '# of ions at diode           = ',nions
WRITE(6,*) '# of ions lost at channel entrance = ',nilcin
WRITE(6,*) '# of ions lost in channel    = ',nilc

```

end

E Plotting of Phase Space Quantities From Output Files

The phase space quantities can be obtained by reading the different output files. For this work, both *PLOT-10* and *DISSPLA* graphics packages were used. Sample plotting codes using either of these packages can be found in the following locations:

- VMD::D70A:[ROSE.ZDISCHARGE.SHD] — *DISSPLA* routines.
- FERMI::DISK1:[ROSE.ZDISCHARGE.SHD] — *PLOT-10* routines.

References

- [1] J. M. Neri, et. al., Transport of Intense Ion Beams with Z-Discharge Plasma Channels, *To be published*.
- [2] P. F. Ottinger, et. al., Z-Discharge Transport of Intense Ion Beams, *To be published, JAP*.
- [3] D. Mosher, et. al., *Bull. Am. Phys. Soc.*, 33, p.1864, 1988.
- [4] D. Mosher, *private communication*.

- [5] J. M. Neri, D. V. Rose, *VAX-ANALYSIS Users Manual*, unpublished.
- [6] W. H. Press, et. al., *NUMERICAL RECIPES*, 1988.

TRANSPORT AND FOCUSING CONSIDERATIONS FOR LIGHT ION ICF SYSTEMS*

P.F. Ottinger, D. Mosher, J.M. Neri, and D.V. Rose
Plasma Physics Division, Naval Research Laboratory
Washington, DC USA 20375

C.L. Olson
Sandia National Laboratories, Albuquerque, NM USA 87185

Abstract

The Laboratory Microfusion Facility (LMF) has been proposed for the study of high-gain, high-yield ICF targets. A number of transport and focusing schemes are being considered for LMF. The schemes which have been studied most extensively include ballistic transport with solenoidal lens focusing, z-discharge channel transport and wire-guided transport. Transport efficiency η_t has been calculated as a function of various system parameters so that point designs can be developed for each scheme. The analysis takes into account target requirements and realistic constraints on diode source brightness, packing, and beam transport. The effect on η_t of voltage ramping for time-of-flight bunching has also been considered. Results show that transport efficiencies of $> 50\%$ can be obtained for all three systems with diode-microdivergence (5-10 mrad), diode-radius (10-15 cm), and diode-ion-current-density (2-10 kA/cm²) values which seem achievable.

I. Introduction

A multimodular light-ion inertial-confinement-fusion (ICF) system directs energy from about 10 to 30 intense ion beams onto a target for implosion. Each beam is focused and transported over a distance of a few meters from the ion diode to the target. This standoff allows for packing the pulsed power generators around the target chamber. It also provides for isolation of the diode hardware from the target explosion and for power compression by time-of-flight (TOF) bunching.

The Laboratory Microfusion Facility (LMF) has been proposed for the study of high-gain, high-yield ICF targets.¹ A number of transport and focusing schemes are being considered for LMF.² The baseline approach is ballistic transport with solenoidal lens focusing^{3,4} (BTSF), and alternate approaches include z-discharge channel transport⁵ (ZDT), wire-guided transport⁶ (WGT), and self-pinched transport⁷. Because they have been most extensively studied, this paper will concentrate on BTSF, ZDT, and WGT.

Transport efficiency is defined to be the ratio of ion energy which is delivered to the target to the total ion energy produced in the diode. Transport efficiency has been calculated as a function of various system parameters for each scheme so that LMF point designs can be de-

veloped. The analyses take into account target requirements and realistic constraints on diode source brightness, packing, and beam transport. Results show that transport efficiencies of $> 50\%$ can be obtained for all three systems with diode-microdivergence (5-10 mrad), diode-radius (10-15 cm), and diode-ion-current-density ($2\text{-}10 \text{ kA/cm}^2$) values which seem achievable. Not included in the analysis is waveform efficiency and beam energy losses. The waveform efficiency accounts for energy in the head and tail of the power pulse which is not usable. Beam energy losses, which are typically on the order of 10%, are due to beam ion deceleration in the self-consistent electric fields and the collisional stopping power of the background gas.

II. Ion Source Model

For LMF, lithium ions will be extracted from an applied-B diode.⁸ It is assumed that the ion current density is uniform across the annular anode surface which extends from a radius of $R/2$ to R . Ions orbits are bent toward the axis in the diode vacuum region by the self-magnetic field of the beam. For small bending angles, $\Theta_b(r,t) = \omega_c \Delta/v$, where ω_c is the beam ion cyclotron frequency associated with the self-magnetic field in the diode region, v is the ion speed, and Δ is the distance from the anode to a transmission foil which separates the diode vacuum region and the gas-filled, charge- and current-neutralized transport region. There is no bending at the inner edge of the annular beam, where the self-magnetic field is zero. Anode shaping is used to compensate for the magnetic bending in the diode to provide a forward directed, parallel beam for BTSF or a focused beam for ZDT and WGT. Beam ions are stripped from Li^{+1} to Li^{+3} as they pass through the transmission foil. Ions are assumed to leave the diode region distributed uniformly in a cone of half angle Θ_μ about the average angle $\Theta_d = \Theta_b(r,t) + \Theta_s(r)$, where Θ_μ is the source microdivergence and $\Theta_s(r)$ results from the anode surface shaping. Since Θ_b varies in time as $I/V^{1/2}$, where I is the beam current and V is the accelerating voltage, Θ_s can only compensate for Θ_b at one point in time. This time is chosen to be when the average voltage, V_0 , is reached. Assuming here that the diode current scales⁹ as $I(t) = I_0 [V(t)/V_0]^2$ and that V increases in time for TOF bunching, it is seen that Θ_s over-compensates for Θ_b early in time and under-compensates late in time. This will lead to an inward sweeping of Θ_d as a function of time. This model assumes changes in Θ_s in time due to anode plasma motion are negligible.

The bunching factor is defined as $\beta = \tau_0/\tau_t$, where τ_0 is the beam pulse duration at the diode, and τ_t is the beam pulse duration at the target. If D is the total path length for the beam from the diode to the target, then the ideal voltage ramp for TOF bunching¹⁰ is given by

$$v(t) = \frac{v(0)}{\left(1 - \frac{t}{T} \frac{\beta - 1}{\beta}\right)^2} \quad (1)$$

where $T = D/v(0)$. For these calculations, $V_0 \equiv [V(0)+V(\tau_0)]/2 = 30$ MeV, $D = 400$ cm, and $\tau_t = 15$ ns is set by pellet design requirements for a 10 MJ total beam energy. Setting the total beam energy per module,

$$E_T = \int_0^{\tau_0} IV dt = \frac{I_0}{v_0^2} \int_0^{\tau_0} [v(t)]^3 dt \quad (2)$$

to $(10/N)$ MJ specifies I_0 for given values of $\tau_0 = \beta\tau_t$ and N , where N is the number of modules. For LMF, bunching factors of $\beta = 2 - 4$ will be required for ion pulse durations of 30 - 60 ns at the diode. The required diode ion current density is derived from $J_0 = 4I_0/3\pi R^2$ with R on the order of 10 cm.

III. Ballistic Transport With Solenoidal Lens Focusing

For BTSF, the beam is extracted from the diode parallel to the z -axis and is propagated about 250 cm at large radius. The solenoidal lens then focuses the beam over a distance $F = 150$ cm onto a target of radius $r_t = 1$ cm. Since $F = r_t/\Theta_\mu$, it is chosen as the smallest practical target chamber radius in order to maximize allowable Θ_μ values. Beam-induced breakdown of the background gas provides beam charge and current neutralization¹¹, which is assumed to be complete. This system is illustrated in Fig. 1. A 30-cm long (L_S), 30-cm radius (R_S) solenoid is used with 25-cm radius flux excluding shields on either side to confine the field to the vicinity of the lens. The solenoid radius is limited by packing constraints in the target chamber wall. The magnetic field strength of the lens is adjusted to provide a 150-cm focal length at V_0 and is typically about 20 kG on axis at the center of the solenoid. The code ATHETA¹² is used to create the solenoidal magnetic field map used for the transport efficiency calculations. The diode region is protected from the target blast by a center plug in the solenoid (not shown in Fig. 1). The outer radius of this plug is determined by the line-of-sight from the center of the target chamber to the outer edge of the diode. Ions at small radius are removed from the beam if they strike this plug.

The diode and solenoidal lens parameters can be matched to minimize chromatic effects due to the TOF voltage ramp. For the BTSF system discussed here, this results in the

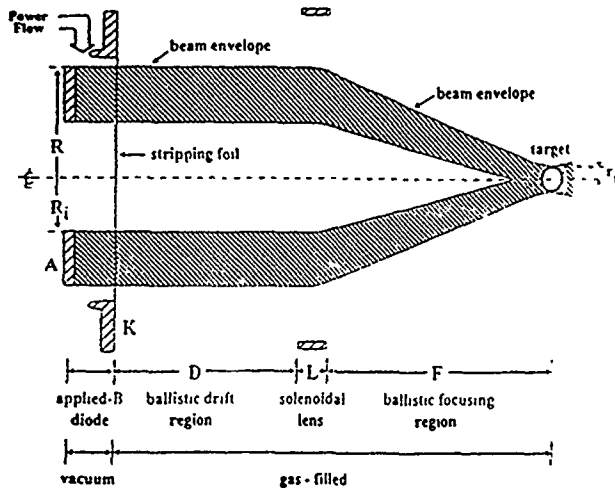


Figure 1. Schematic of BTSF system.

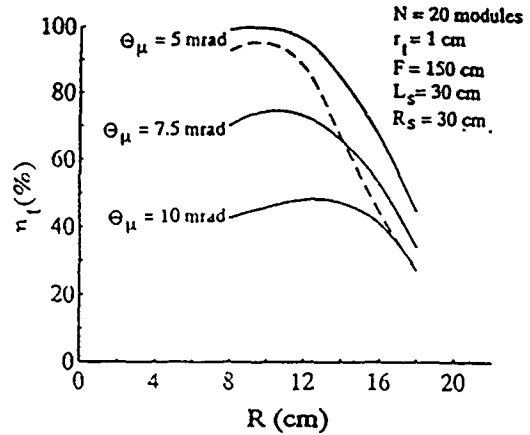


Figure 2. Plot of η_t vs. R for BTSF without focus sweeping (solid curves) and with focus sweeping (dashed curve).

condition $\Delta = 0.047R^2/I_0$ (MA), where I_0 changes with the choices of β and N [see Eq. (2)]. For ZDT and WGT, Δ is fixed independently of R or I_0 . Because the BTSF system is nearly achromatic, the reduction in η_t due to focus sweeping should be less for BTSF than for either ZDT or WGT. Constraints on the stripping foil placement due to beam ion angular momentum considerations in an extraction diode¹³ are not considered here, but will be investigated in the future.

The solid curves in Fig. 2 show the calculated transport efficiency η_t as a function of diode radius R for BTSF without including focus sweeping due to the TOF voltage ramp. Results are shown for $N = 20$ and show a decrease in η_t at $R = 10$ cm from about 100% to about 50% as Θ_μ increases from 5 mrad to 10 mrad. The fall off in η_t for large R is caused by the increasing gradient in the magnetic field away from the center of the solenoid.⁴ This gradi-

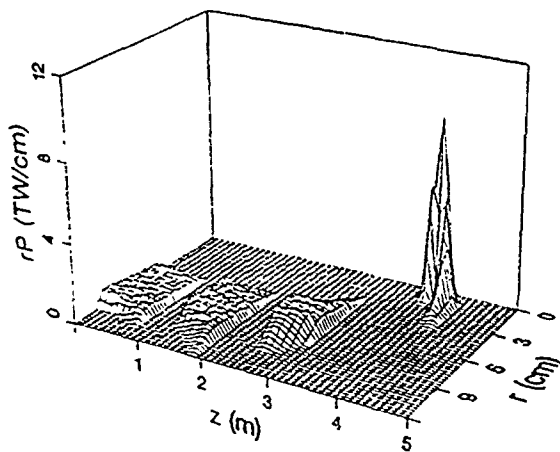


Figure 3. Plot of $rP(r,z)$ at four points in time during transport for BTSF.

ent causes ions at different radii to focus at different axial locations. The dashed curve shows η_t for $\Theta_\mu = 5$ mrad including focus sweeping with $\beta = 2$. The TOF voltage ramp reduces η_t at $R = 10$ cm from about 100% to about 95%. At larger R , the increasing gradient in the solenoidal magnetic field (i.e., non-ideal lens effects) causes a larger reduction in η_t . Within the constraints of packing, high efficiency could be extended to larger R by increasing the radius of the solenoid. For all three transport

schemes discussed here, larger values of β further reduce η_t . Figure 3 shows $rP(r,z)$ (i.e., the beam power density multiplied by r) at four times during transport for the case with $N = 20$, $\Delta = 8$ cm, $R = 10$ cm, $\Theta_\mu = 5$ mrad and $\beta = 2$. For BTSF, P increases rapidly near the target where the beam both bunches and focuses.

IV. Ballistic Focusing With Z-Discharge Transport

For ZDT, the anode is shaped to ballistically focus the beam onto the aperture of the transport channel located a distance F from the diode. Inside the channel, the magnetic field associated with the discharge current radially confines the ions. Once focused, the beam then propagates down the channel with a small radius on the order of the target size. At the exit, the beam expands slightly over the pellet standoff distance d . The ZDT system is illustrated in Fig. 4. The low-mass current return wall provides stability for the discharge and results in a small but tolerable amount of debris for LMF.¹⁴ The aperture radius is chosen to be $r_a = F\Theta_\mu$ so that at V_0 the full beam enters the channel. Because of the time dependance of Θ_d , the focus sweeps inward in time so that early and late in the pulse some ions will strike the aperture and be lost. To allow for trapping of the expanding portion of the beam⁵, the channel radius is chosen so that $r_c^2 = 2r_a^2$. Unlike the BTSF case where F is restricted by the target chamber size, F is allowed to decrease for ZDT as Θ_μ increases to maintain a channel size on the order of the target size. Consequently, $F = r_t/2^{1/2}\Theta_\mu$ with $r_c = r_t$. Finally, a typical channel current of $I_c = 40$ kA is chosen. For these calculations, the discharge current density is assumed to be uniform and complete beam charge and current neutralization is assumed in both the gas-filled ballistic focusing region and in the transport channel. Packing considerations determine a

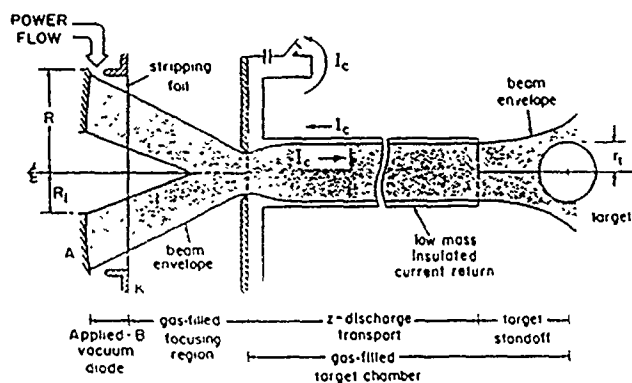


Figure 4. Schematic of ZDT system.

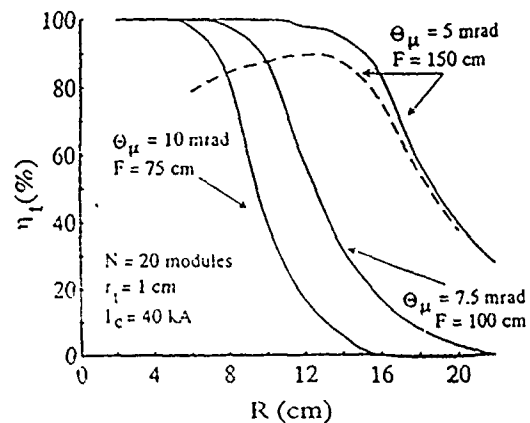


Figure 5. Plot of η_t vs. R for ZDT without focus sweeping (solid curves) and with focus sweeping (dashed curve).

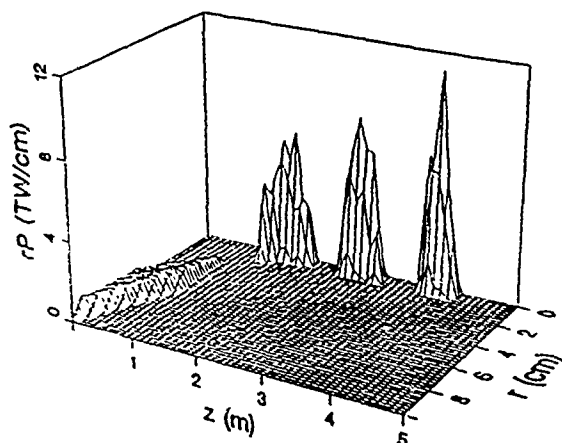


Figure 6. Plot of $rP(r,z)$ at four points in time during transport for ZDT.

(at fixed I_c) is caused by increased ion losses to the channel wall as ions enter the channel at larger angles. This ion entrance angle scales roughly as R/F . High efficiency can be extended to larger R by increasing I_c (to reduce losses to the wall), however, more rapid beam expansion in the stand-off region eventually limits this.⁵ The dashed curve in Fig. 5 shows η_t for $\Theta_\mu = 5$ mrad ($F = 150$ cm) including focus sweeping with $\beta = 2$. The TOF voltage ramp reduces η_t at $R = 10$ cm from about 100% to about 87%. Because Θ_b scales as R^{-1} for fixed Δ , the reduction in η_t due to focus sweeping decreases as R increases. Figure 6 shows $rP(r,z)$ at four times during transport for ZDT with $N = 20$, $\Delta = 8$ cm, $R = 10$ cm, $\Theta_\mu = 5$ mrad and $\beta = 2$. Unlike the BTSF case, here P increases first near the channel aperture where the beam focuses and continues to increase as the beam bunches approaching the target.

V. Ballistic Focusing With Wire-Guided Transport

The WGT system is illustrated in Fig. 7. Here, the magnetic field associated with the current flowing in the gas-embedded central guide wire provides the radial confinement of the ions. The focal distance and aperture size are chosen for a given Θ_μ in the same way as for ZDT so that $r_a = F\Theta_\mu = r_t/2^{1/2}$. The wire radius is set at $r_w = 0.035$ cm and a wire current of $I_w = 40$ kA is chosen.⁶ For WGT, there is no confining wall and the transported beam radius⁶ is given by $r_b = F\Theta_\mu \exp(vR^2/2v_w F^2)$ where $v_w = 2ZeI_w/m_i c^2$, Ze and m_i are the ion charge and mass, and c is the speed of light. Beam-induced breakdown of the gas in the ballistic focusing region and in the gas surrounding the guide wire again results in beam charge and current neutralization during transport. Return-current wires are placed around the central guide wire at a radius of about $1.4r_b$ in order to minimize losses due to chaotic orbit effects while maintaining

standoff distance of $d = r_t(N/2)^{1/2}$ between the channel exit and the target.⁵ The length of the transport channel is given by $D - F - d$ and is on the order of about 250 cm.

The solid curves in Fig. 5 show η_t versus R for ZDT without including focus sweeping. Results are shown for $N = 20$ and $\Delta = 4$ cm, and show a decrease in η_t at $R = 10$ cm from about 100% to about 40% as Θ_μ increases from 5 mrad ($F = 150$ cm) to 10 mrad ($F = 75$ cm). For ZDT, the fall off in η_t for large R

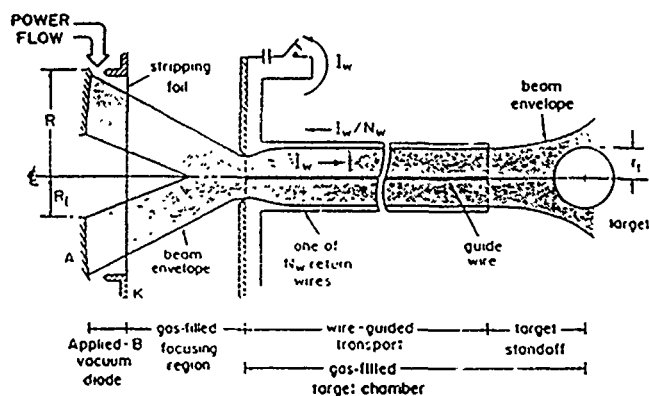


Figure 7. Schematic of WGT system

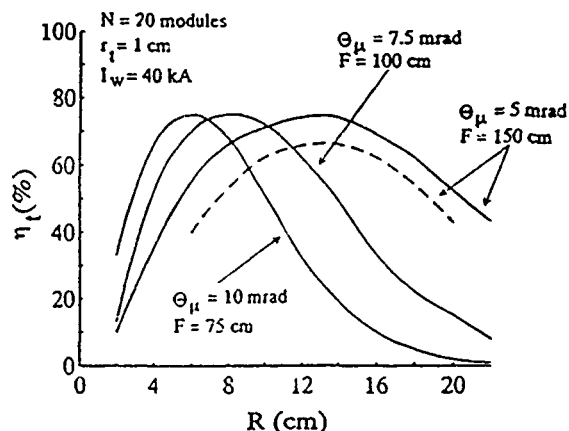


Figure 8. Plot of η_t vs. R for WGT without focus sweeping (solid curves) and with focus sweeping (dashed curve).

as compact as possible WGT system radius for packing.⁶ Because the return wires are placed at $1.4r_D$, the standoff distance becomes $d = r_D N^{1/2}$ for WGT.

The solid curves in Fig. 8 show η_t versus R for WGT without including focus sweeping. Results are shown for $N = 20$ and $\Delta = 4$ cm, and show a range in η_t at $R = 10$ cm from about 55% to about 75% for Θ_μ between 5 mrad ($F = 150$ cm) and 10 mrad ($F = 75$ cm). For WGT, the fall off in η_t for small R is caused by ions with small angular momentum hitting the central guide wire. The fall off in η_t for large R (at fixed I_w) is caused by an increase in the beam radius (beyond the target size) as ions enter the channel at larger angles. Here again, this ion entrance angle scales roughly as R/F . Losses are bigger for WGT than for ZDT because of the larger standoff distance and more rapid beam expansion in the standoff region. The more rapid expansion is a result of larger average transverse ion energies because of the larger average magnetic field with the centrally located current in WGT than with the distributed current in ZDT. Because of this more rapid expansion in the standoff region, increasing I_w for WGT is not as effective as increasing I_c for ZDT in extending high efficiency to larger R .⁶ The dashed curve in Fig. 8 shows η_t for $\Theta_\mu = 5$ mrad ($F = 150$ cm) including focus sweeping with $\beta = 2$. The TOF voltage ramp reduces η_t at $R = 10$ cm from about 70% to about 60%. Aside from accounting for somewhat lower η_t and showing more rapid beam expansion in the target standoff region, the beam power density $P(r, z)$ for WGT is similar to that shown for ZDT in Fig. 6.

VI. Summary

Transport efficiency has been calculated as a function of various system parameters so that LMF point designs can be developed for BTSF, ZDT, and WGT schemes. The analysis

takes into account target requirements and realistic constraints on diode source brightness, packing, and beam transport. Focus sweeping due to voltage ramping for TOF bunching has been considered. Because the BTSF system is nearly achromatic, the focus sweep effect reduces η_t the least for BTSF (when $R \leq R_S/3$). Results show that reasonably high transport efficiency ($> 50\%$) can be obtained for all three systems with diode-microdivergence (5-10 mrad), diode-radius (10-15 cm), and diode-ion-current-density (2-10 kA/cm²) values which seem achievable. Initial point design values are $\Theta_\mu = 5$ mrad, $R = 15$ cm, and $J_i = 2$ kA/cm². High η_t can be extended to larger R than displayed in Figs. 2, 5 and 8 by increasing R_S for BTSF,⁶ I_c for ZDT⁵ and I_w for WGT⁴. Eventually this is limited by packing constraints for BTSF and more rapid beam expansion in the target standoff region for ZDT and WGT. For the ZDT and WGT analyses presented here, the beam was focused onto the aperture at F near the midpoint of the voltage pulse (at the time of average voltage). Future work will investigate optimizing η_t by adjusting the aperture size r_a and focal length F to minimize the focus sweep effect for ZDT and WGT. Minor adjustments of the solenoidal lens field strength will be studied to optimize η_t for BTSF with focus sweeping. Waveform efficiency and beam energy losses during transport have not been considered and will reduce the overall efficiency. The sensitivity of the transport efficiency on the beam microdivergence model also needs to be studied.

References

*Work supported by US DOE through Sandia National Laboratories.

JAYCOR, Vienna, VA 22182.

1. J.J. Ramirez, et al., *Fusion Tech.* **15**, 350 (1989).
2. D. Mosher, et al., *Proc. of the 8th Inter. Conf. on High-Power Particle Beams*, (Novosibirsk, USSR, July 1990), p. 26.
3. C.L. Olson, *Proc. of the 1988 Linear Accel. Conf.*, (Newport News, VA, Oct. 1988), p. 34.
4. P.F. Ottinger, et al., to be published in *J. Appl. Phys.* (July, 1992).
5. P.F. Ottinger, et al., *J. Appl. Phys.* **70**, 5292 (1991).
6. J.J. Watrous, et al., *J. Appl. Phys.* **69**, 639 (1991).
7. R.F. Hubbard, et al., *Part. Accel.* **37-38**, 161 (1992).
8. D.L. Hanson, et al., *IEEE Trans. Plasma Sci.* **19**, 831 (1991).
9. D.L. Johnson, et al., *Proc. of the 1989 Part. Accel. Conf.* (Chicago, IL, March 1989), p. 1017.
10. F. Winterberg, *Plasma Phys.* **17**, 69 (1975).
11. C.L. Olson, *Proc. of the 1990 Linear Accel. Conf.* (Albuquerque, NM, September 1990), LANL Report LA12004-C, p. 396.
12. J.P. Quintenz and D.B. Seidel, Sandia Nat. Lab. Report SAND84-1336 (June 1984).
13. S.A. Slutz and D.B. Seidel, *J. Appl. Phys.* **59**, 2685 (1986).
14. D.D. Hinshelwood, et al., 1990 IEEE Inter. Conf. on Plasma Sci. (Oakland, CA, May 1990), p. 143.

D. Mosher, D. D. Hinshelwood*, J. M. Neri,
P. F. Ottinger, and J. J. Watrous*

Plasma Physics Division

Naval Research Laboratory, Washington, DC 20375-5000

C. L. Olson and T. A. Mehlhorn

Sandia National Laboratories, Albuquerque, NM 87185

Abstract Theoretical and experimental research concerning three ion transport techniques designed to meet the requirements of the Laboratory Microfusion Facility are described. The three are solenoidal focusing of a drifted Li^{+3} beam onto the fusion target, z-discharge channel transport of a prefocused beam, and a wire-guided channel technique.

I. INTRODUCTION

The light-ion Laboratory Microfusion Facility (LMF) is based on the focusing and transport of 20 or more, megampere, 30-MeV lithium beams onto a 1-cm-radius fusion pellet.¹ Beam transport over a 3- to 4-m distance separating the extraction diode from the pellet is required for time-of-flight bunching of the 40-ns extracted beam to the 10- or 15-ns pellet-drive duration, and for protection of the diode hardware. Three transport techniques have been researched to meet this accelerator stand-off requirement: ballistic transport with solenoidal focusing onto the pellet², low-mass, wall-confined z-discharge transport of a prefocused beam³⁻⁵, and wire-guided channel transport⁶.

The three transport techniques are illustrated in Fig. 1 (not to scale). In the solenoidal focusing scheme, the extracted beam ballistically drifts several meters in the charge- and current-neutralizing plasma formed by beam heating of the gas background. The beam is then focused over a distance F onto the pellet by a solenoidal magnet located behind the containment vessel wall. The

*JAYCOR, Vienna, VA 22180

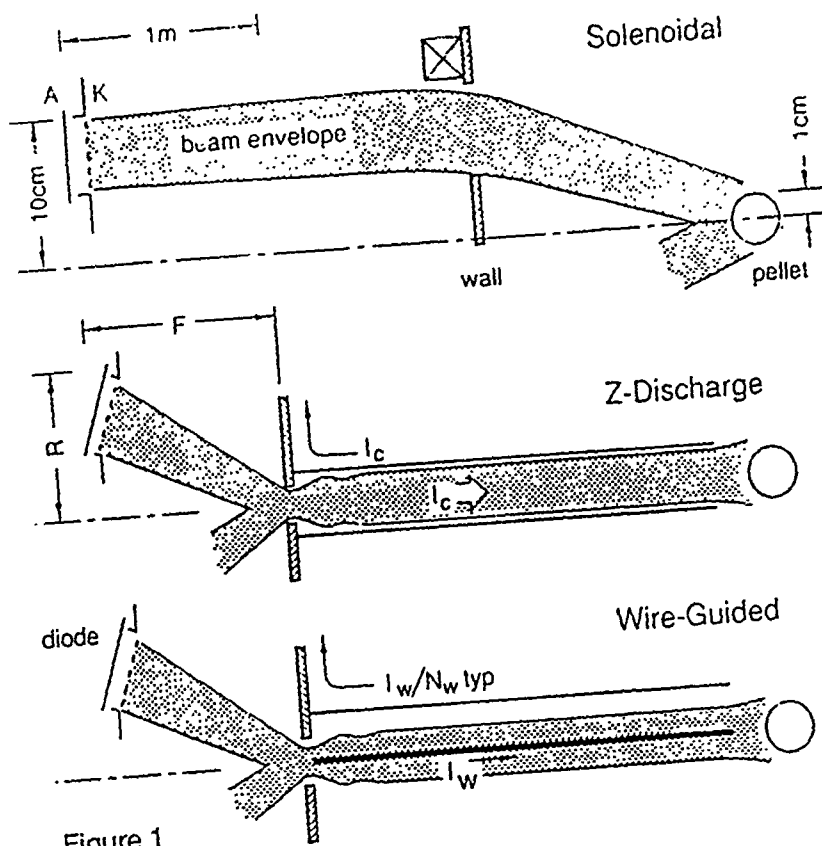


Figure 1

focal spot size r_s
 $\geq \Theta_\mu F$ so that the
microdivergence
 Θ_μ determines
the maximum
radius of the
containment
vessel. For $\Theta_\mu =$
6 mrad and a
pellet radius $r_t =$
 $r_s = 1$ cm, the
chamber radius
cannot exceed
about 1.5 m for
efficient focusing
of the beam onto
the target. A
main advantage

of the solenoidal-focusing technique is that no hardware or externally-driven discharges are required within the containment vessel. Thus, no shot-to-shot replacement of material is required, and the explosion debris and inventory of induced-radioactive mass are minimal. These advantages make the solenoidal-focusing technique most easily extendable to a reactor configuration. Primary concerns are the small containment vessel, sensitivity to beam-background interactions that can disrupt transport and focusing, and the need for proof-of-principle experiments.

The z-discharge transport technique employs a preformed, wall-stabilized z-discharge of radius r_c (comparable to r_t) to confine and transport a focused beam several meters to the pellet. The exit of the discharge must be within about 10 cm of the target to avoid excessive post-transport expansion with the resulting poor pellet coupling. Close packing around the pellet then provides an upper limit to the number of modules that can be employed in LMF. Since the channel entrance aperture r_s must be less than r_c , the achievable microdivergence limits the diode focusing length F to about 1 m. To date, the

z-discharge technique has been the most widely studied.³⁻⁵ Z-discharge experiments with MeV proton beams at the 100 kA level have demonstrated efficient particle transport of few-cm diameter beams over several meters. Advantages of this technique are that transport over several meters allows for larger containment vessels, and that separate, optimized gas compositions can be employed for the discharge and containment vessel. A major concern is the need for hardware within the containment vessel to establish the discharge. Work has begun on low mass versions of the discharge hardware to meet LMF debris requirements.

The wire-guided transport technique is similar to the z-discharge technique and shares many of its advantages and limitations. The transported ion beam is confined by the azimuthal magnetic field produced by a preestablished axial current flow in a gas-embedded wire rather than a uniform z-discharge. In order to minimize both the hardware mass within the LMF containment vessel and the wire-circuit inductance, the wire current can be returned through a small number N_w of wires outside the beam envelope rather than through a cylindrical annulus. Unlike the z-discharge case, wire-guided transport efficiency cannot be 100% since the lowest angular momentum ions injected into the transport channel must be lost to the wire. However, both orbit theory applied to LMF and MeV proton experiments achieve about 80% particle transport efficiency.⁶

II. BALLISTIC TRANSPORT WITH SOLENOIDAL FOCUSING

A major feature of the solenoidal focusing concept is that the combined effects of magnetic bending in the diode and bending in the solenoid can lead to nearly-achromatic focusing of the beam onto the target: the focus location is close to stationary even though the accelerating voltage V increases in time to produce bunching during transport. For a uniform, solid ion beam extracted from the diode ions are bent by their self magnetic field in the vacuum diode according to

$$\theta_d(r,t) = 2Z_d e I_i(t) r d / m_i v(t) R^2, \quad (1)$$

where $Z_d = 1$ is the Li charge state in the diode, e is the electronic charge, I_i is the ion current, d is the distance from the anode to the boundary of the

neutralizing background, r is the radius, m_i and v are the ion mass and speed, and R is the diode radius. Since v scales like $V^{1/2}$ and I_i varies nearly like V^2 from diode theory⁷, θ_D increases in time. Additional bending in the solenoid follows from²

$$\theta_S(r,t) = Z_S^2 e^2 B_z^2 r / 4 m_i^2 v^2(t) \quad (2)$$

where $Z_S = 3$ is the Li charge state in background gas, B_z is the solenoidal field strength, and l is the length of the magnet. For a voltage ramped for bunching, θ_S decreases in time so that proper choices of B_z , d , and l lead to a total bending angle $\theta_D + \theta_S$ that is nearly constant in time and proportional to radius at the exit of the solenoid. The beam is then focused at the target location within a radius Δr given by the small time variation in $\theta_D + \theta_S$, and microdivergence²

$$\Delta r = R(\Delta V/V)^2(L/F) + \Theta_\mu F \quad (3)$$

where $\Delta V/V$ is the fractional change in voltage during the voltage ramp, L is the drift length between the diode and solenoid and F is the containment vessel radius. For $\Delta V/V$ below about 0.2, and $R = 10 - 15$ cm, time variations contribute less to Δr than microdivergence.

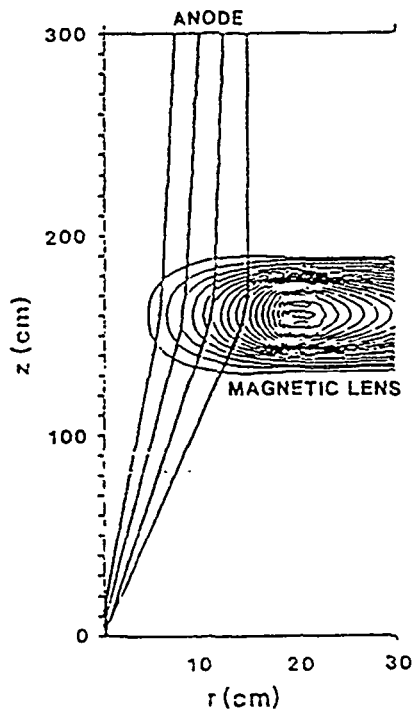


Figure 2

were calculated from the generalization of Eq. (1) for the self-field distribution in a hollow diode. Full charge and current neutralization were assumed over total

Ion orbit simulations of focusing performance of the solenoidal system have been carried out with the accurate field distribution of a 20-kG, 30-cm-long focusing magnet.⁸ A snapshot in time from these computations is shown in Fig. 2. Lithium ions were emitted from a hollow 15-cm-radius extraction diode with accelerating voltage ramped from 30 to 33 MV. Beam currents of 1 to 1.2 MA were determined from circuit and diode modeling, and diode bending angles

transport lengths of 3 and 4 m. Results show that with zero microdivergence, 92% of the 1.57 MJ beam energy was delivered to within a 1-cm radius at the pellet location. Additional calculations are in progress to determine the effects of steeper voltage ramps, nonzero microdivergence, net-current in the drifting beam, and applied - B diode magnetic fields.

A variety of instabilities associated with the beam-background interaction have been examined. Plasma two-stream and ion acoustic modes are found to be stable since the return-current electron drift velocity is much less than the electron thermal velocity and sound speed. The beam two-stream is collisionally quenched in the drift region prior to focusing for a parallel ion velocity dispersion $\Delta v_z/v_z \geq 0.002$ and this quantity is about 0.01 for LMF. This threshold is exceeded when the beam is focused to small radius, but the axial dependence of unstable modes washes out instability growth.⁹ The filamentation instability is stabilized for a plasma conductivity σ in excess of

$$\sigma^* = 1.4 \times 10^{13} Z^2 \tau (\text{ns}) J (\text{kA/cm}^2) / A \beta_i \Theta_\mu^2 (\text{mrad}) \quad , \quad (4)$$

where Z and A are the ion charge state and atomic number, τ is the beam duration, J is its current density, and β_i is its relativistic factor. For a 30 ns beam of 30 MeV Li^{+3} , $J = 2 \text{ kA/cm}^2$, and $\Theta_\mu = 6 \text{ mrad}$, Eq. (4) yields $\sigma^* = 3.2 \times 10^{14} \text{ s}^{-1}$.

An additional constraint on the plasma conductivity is provided by the need for nearly perfect current neutralization since appreciable self-magnetic fields in the drifting beam can disrupt transport and focusing. A simple magnetic diffusion argument indicates that greater than 99% current neutralization requires that σ rise to 10^{10} s^{-1} within 1 ns of passage of the beam front. The combined effects of ion impact ionization, electron avalanching, and ohmic heating have been studied to determine the growth of conductivity due to beam passage through the background gas. These calculations show that ion impact ionization alone produces $\sigma > 5 \times 10^{10} \text{ s}^{-1}$ in under 1 ns and that the three processes produce $\sigma > 10^{14} \text{ s}^{-1}$ in a 10-eV, 1-Torr He plasma at peak current. Note that this degree of plasma heating is achieved with less than 50 kJ of deposited energy so that energy losses in the transported beam are small.

III. Z-DISCHARGE TRANSPORT

An idealized z-discharge transport channel carries a uniformly distributed current (B_θ proportional to r) out to an insulating annulus at radius r_c . The channel current I_c required to confine all injected ions within the channel radius r_c is determined from conservation of axial canonical momentum and energy for an ion with maximum transverse energy: one entering the channel at the entrance aperture radius r_s from the edge of the anode at radius R . For $R/F \ll 1$, the required current is given by⁴

$$ZeI_c/m_i v = (R/F)^2/2[1 - (r_s/r_c)^2] \quad (5)$$

For LMF, 30 MeV Li^{+3} is chosen with $R = 10$ cm and $F = 1$ m. Assuming $\Theta_\mu = 7$ mrad leads to a focal spot size $r_s = 0.7$ cm. Choosing the channel radius equal to the pellet radius $r_c = r_t = 1$ cm, then leads to $I_c = 67$ kA. In comparison, the most recent NRL transport experiments employ 1.2 MeV protons with $R = 5$ cm, $F = 20$ to 30 cm, $r_s = 0.85$ cm, and $r_c = 1.25$ cm. For the experimental parameter set with $F = 30$ cm, Eq. (5) yields $I_c = 45$ kA, a typical value in NRL experiments. Although the ion species and energy are

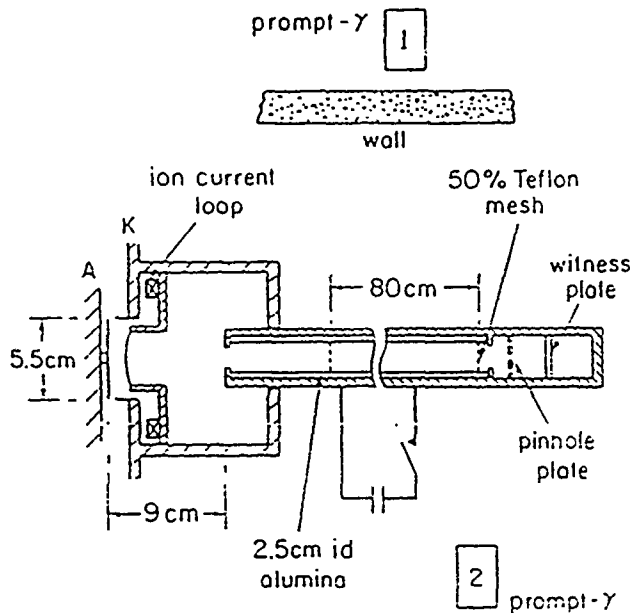


Figure 3

very different for LMF and the NRL experiments, the transport geometries and discharge current are similar.

Figure 3 illustrates the set-up for a series of z-discharge transport experiments employing smaller diode radii and focal lengths that preserve small R/F .³ The proton beam is focused onto the entrance aperture of the transport channel by self-magnetic-field bending in the vacuum diode. The diode vacuum is separated from the gas in the focusing drift region and transport channel (typically 1 Torr air) by a 1.8- μm -thick polycarbonate foil. The alumina insulator defines r_c and separates the

discharge from a conducting tube that returns the current in a low inductance path that helps to stabilize the plasma against MHD modes. The insulator also provides a breakdown surface that permits the discharge to be struck in a several-meter-long column of gas with a low-voltage (20 kV) capacitor bank. Magnetic probe measurements demonstrate the current distribution is uniform within the discharge if the beam is injected into the channel before the discharge begins to pinch. Timing beam injection in this manner (about 1 μ s into the discharge current rise for the NRL experiments) also avoids the development of the sausage and kink instabilities.

Z-discharge transport experiments have been carried out in channels of 1.6-, 2.5-, and 4-cm diameter with lengths of 1 to 5 m. Transport efficiency has been measured using 6 MeV prompt γ rays from the interaction of beam protons with the fluorine in Teflon targets.¹⁰ Two time-of-flight-separated γ -ray pulses are recorded by a photodiode equidistant between fifty-percent-transmitting Teflon screens near the transport channel entrance and exit. The transport efficiency is determined by comparing the observed prompt- γ signals with computed signals derived from beam current and voltage traces, energy losses in the transmission foil and gas, and the proton-energy-dependent cross-section for γ production. These measurements demonstrate transport efficiencies approaching 100% for all geometries with up to 400 kA transported in the 4-cm-dia. channel.³

The prompt- γ measurements of transport efficiency are imprecise because of the sensitivity of cross-section on proton energy and the indirect determination of energy losses suffered during transport. For this reason, a second measurement technique with weaker energy dependence has recently been implemented to confirm the prompt- γ measurements. Prompt-gamma rays created in some LiF targets by the ${}^7\text{Li}(p,\gamma)$ reaction activate an adjacent Cu target via the ${}^{63}\text{Cu}(\gamma,n){}^{62}\text{Cu}(\beta^+)$ reaction.¹¹ After the shot, the 10-minute half-life beta decay is counted to determine the time-integrated proton flux on the target. Targets were placed either at the transport entrance or exit aperture. Yields from front and rear targets were compared once adjustments were made to compensate for small shot-to-shot variations in the diode voltage and ion current histories. For $I_c = 45$ kA and $r_c = 1.25$ cm in the $R = 5$ cm geometry, the transport efficiency was determined as a function of focal

distance F : $\eta_t = 0.59 \pm 0.02$ for $F = 20$ cm, 0.83 ± 0.02 for 25 cm, and 0.88 ± 0.05 for 30 cm. These figures demonstrate the reduction in transport efficiency expected from Eq. (5) at focal lengths below 30 cm due to loss of confinement of ions with higher transverse energy.

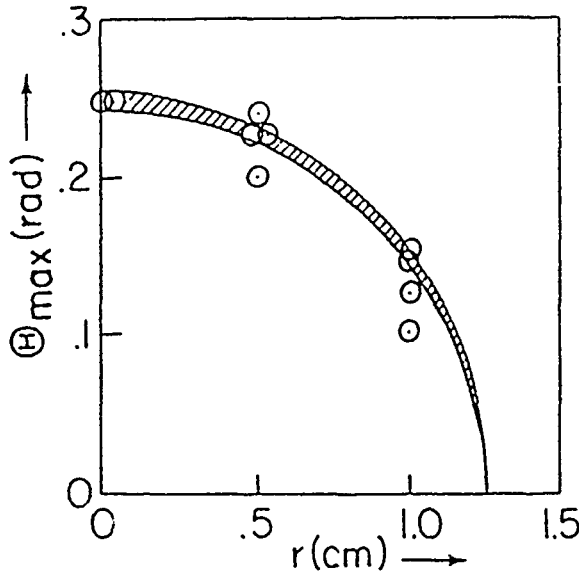


Figure 4

In a number of transport experiments, pinhole arrays and witness plates were mounted just outside the channel exit to sample the transverse velocity distribution of the transported beam.^{3,12} The radial extent of damage spots associated with each pinhole is a direct measurement of the radial velocity spread at the pinhole radius: $\Theta_{\max} = \delta/\zeta = \Delta v_r/v$, where δ is the spot radius and ζ is the distance separating the pinhole and

witness plate. Figure 4 compares Θ_{\max} measurements on a single shot (circles) with orbit theory. From conservation of axial canonical momentum for an ion with $v_\theta = 0$ that grazes the channel wall and $\Delta v_r/v \ll 1$,

$$\Theta_{\max}^2 = (2ZeI_c/m_i v)(1 - r^2/r_c^2) \quad (6)$$

The hatched region is a plot of Eq. (6) for the same shot including uncertainties in ion energy and channel current. Good agreement between transverse phase-space measurements and analysis indicates that there are no unknown sources of emittance growth during beam transport so that orbit-theory extrapolations to LMF conditions can be made with confidence.

A low-mass version of the transport channel hardware is needed to meet LMF debris requirements.¹³ To this end, 2.5-cm-dia. spiral-wound Kapton tubes with a metal foil outer conductor have been fabricated. The tubes are droop free over several-meter lengths so that they can be supported only at the containment-vessel wall. Preliminary experiments¹⁴ with 1- and 2-m lengths have been carried out with channel currents limited to 25 kA by the power supply. These experiments show 60 - 70% transport efficiency (with higher

efficiency expected at higher channel current), uniform and stable current profiles, and phase-space measurements that agree well with analysis.

A variety of theoretical calculations have been carried out for inertial-confinement-fusion scenarios to determine limits to transportable ion power associated with instabilities,¹⁵ the MHD response of the channel to beam transit¹⁶, energy loss during transport, channel packing and standoff around the pellet.⁵ Power limiting constraints for LMF parameters are summarized in Fig. 5 for a Li^{+3} beam with accelerating voltage ramped from 23 to 37 MV

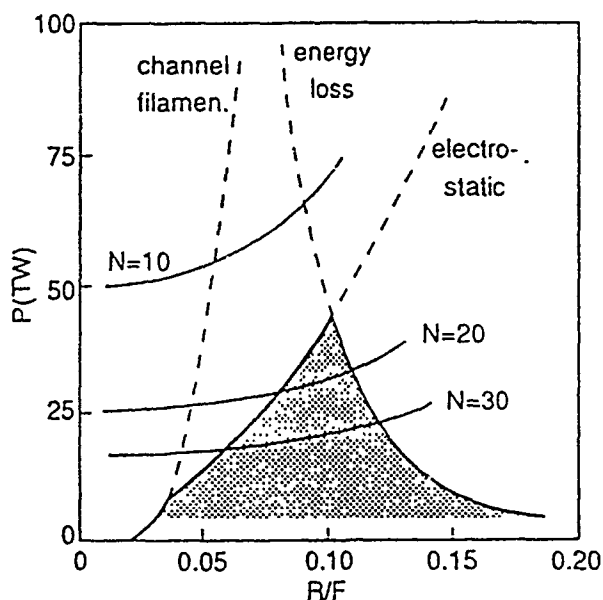


Figure 5

to achieve bunching of a 40-ns extracted beam to 10 ns over a 3.3-m-long z-discharge channel. The channel radius is taken to be 1 cm and a microdivergence of 7 mrad is assumed. Acceptable transported powers are in the shaded region below limits associated with the channel-filamentation and electrostatic instabilities, and a 25% energy loss due to collisional stopping, and return-current and induced electric fields. These limits are

compared to the required extracted power per beam for 10, 20, and 30 modules delivering a total of 1000 TW to the pellet with 50 % on-target efficiency. These considerations indicate that 20 or more modules with R/F of about 0.1 can satisfy LMF requirements in a z-discharge transport configuration.

IV. WIRE-GUIDED TRANSPORT

Wire-guided transport employs a current-carrying wire rather than a z-discharge to provide the B_θ that confines the focused ion beam. The wire current I_w is chosen so that ions in the transport channel that do not impact the wire must be confined within a specified r_c . For $R/F \ll 1$, this current is given by⁶

$$Zel_w/m_i v = (R/F)^2 / 4 \ln(r_c/r_s) \quad (7)$$

For the LMF conditions following Eq. (5), $I_w = 50$ kA. In the NRL experiments with 1.2 MeV protons¹⁷, $R = 5$ cm, $F = 20 - 30$ cm, $r_s = 0.75 - 1.25$ cm, and $I_w = 20 - 30$ kA. For $F = 30$ kA and $r_s = 1.25$ cm, all ions are confined within $r_c = 2$ cm during transport when $I_w = 25$ kA.

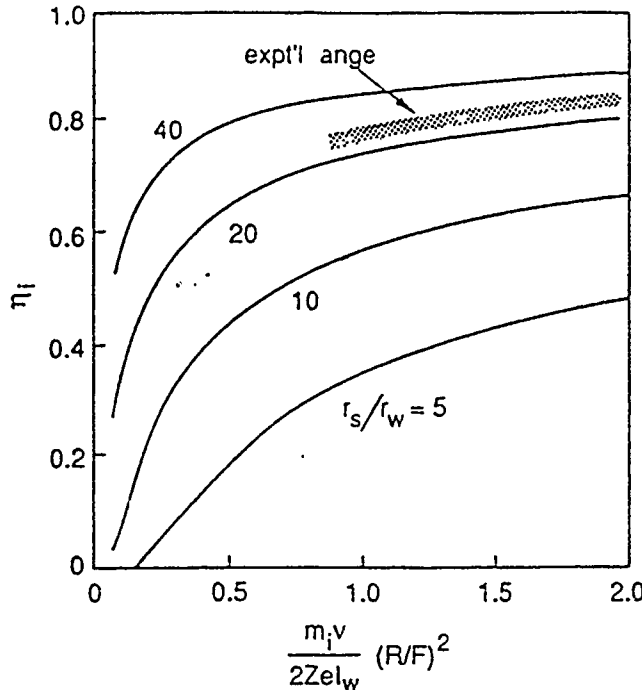


Figure 6

Prompt- γ measurements carried out for 1- and 1.5-m-long wires of radius $r_w = 0.05$ cm showed $\eta_i = 75 - 80\%$ efficient particle transport. These experimental results are compared to orbit theory calculations of losses to the wire in Fig. 6, for which ions from a solid anode uniformly fill the entrance aperture.⁶ The experimental range determined from the above parameters is indicated by the shaded region and the predicted range of η_i agrees well with the experimental efficiencies.



Figure 7

The orbit analysis has also been used to predict the shape of damage patterns from pinhole arrays and witness plates mounted at the exit of the wire channel. Theory (top) and witness-plate measurements (bottom) are compared in Fig. 7 for $I_w = 27$ kA and $r_s = 1.25$ cm for pinholes at three different radii.

The absence of damage on the axis reflects loss of low-angular-momentum ions to the wire. Comparisons using other I_w and r_s values show similar agreement. The similarities in size and shape indicate that the transverse phase-space distribution of transported ions is

determined primarily by orbital motion in the applied B_θ field without major perturbations caused by beam-background interactions, instabilities, or asymmetries.

NRL experiments employ a large-radius cylindrical current return. For LMF, a small number N_W of current-return wires (to minimize the debris mass) mounted at small radius R_W (to permit close packing of transport channels near the pellet) is being considered. The return wires break cylindrical symmetry so that the loss of angular momentum conservation leads to irregular motion and additional losses to the central guide wire. A large number of orbit calculations in the magnetic-field distribution of the central guide wire and return-current wires have determined the minimum values of R_W and N_W that do not enhance losses beyond those occurring in the cylindrically-symmetric case⁶: $N_W = 4$ and $R_W = 1.4r_C$ can provide 95% of the ideal transport efficiency. These values were used in LMF system studies to determine optimal diode, focusing, and wire-transport parameters.⁶

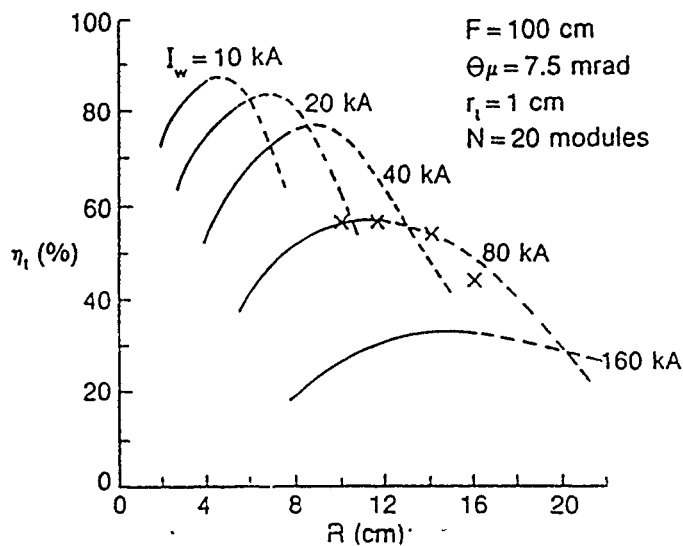


Figure 8
return-wire radius R_W which, in turn, were used to determine the stand-off distance from the pellet. Orbit analysis then provided the total transport efficiency from the diode to the pellet. An example of these calculations is shown in Fig. 8 for a 1-cm-radius pellet fed by 20, 30-MeV Li-beam modules. The figure shows 55 - 75% total transfer efficiency for diode radii in the 8- to 12-cm range when wire currents of 40 to 80 kA are chosen. As with the z-discharge channels, a variety of beam-background interactions will further limit

In the system studies, the injection spot diameter was determined from the focusing length F and microdivergence Θ_μ , and the wire radius was chosen so that melting did not occur for a wire current rising to I_W in $10 \mu s$. Choice of diode radius R then determined the transporting beam envelope radius r_C and

choices of system parameters. These calculations are in progress for wire-guided systems.

V. CONCLUSIONS

Three promising transport options for the light-ion Laboratory Microfusion Facility have been presented. Ballistic transport with solenoidal focusing has the advantage of a hardware-free containment vessel and is therefore most easily extendable to a reactor configuration. However, beam microdivergence limits the vessel diameter to 3 m or less. Calculations indicate that beam ionization and heating of the neutralizing background are sufficient to avoid disruptive induced fields and instabilities, but additional calculations and proof-of-principle experiments are required. Z-discharge transport has been the most studied concept both theoretically and experimentally. Proton-beam experiments demonstrate efficient z-discharge transport of focused beams at discharge currents, channel radii, and lengths comparable to those required for LMF. Beam-background studies indicate that LMF ignition requirements can be satisfied with 20 or more accelerators and transport modules, but the need for discharge hardware in the reaction chamber makes this option more difficult to extend to a reactor. Similar experimental results and LMF conclusions have been obtained for wire-guided transport and the required wire arrays may be easier to implement than the z-discharge hardware. However, the background gas must satisfy wall-buffer and beam-interaction requirements, and not break down during the current rise in the wire: conditions that may be difficult to meet simultaneously. All three techniques require experimental tests with MA-level Li beams to accurately evaluate beam-background limitations under LMF conditions.

VI. REFERENCES

1. Prestwich, K. R., et al., these proceedings.
2. Olson, C. L., Proc. 1988 Linear Accel. Conf., Newport News, CEBAF Rep. 89-001, June 1989, p34.

3. Sandel, F. L., et al., Proc. 4th International Topical Conf. on High Power Electron and Ion Beam Research and Technology, BEAMS 81 Palaiseau, June 1981, p129.
4. Ottinger, P. F., Mosher, D., and Goldstein, S. A., Phys. Fluids 23, 909(1980).
5. Mosher, D., et al., BEAMS 81, p19.
6. Watrous, J. J., et al., submitted to J. Appl. Phys.
7. Quintenz, J. P., et al., these proceedings.
8. Mehlhorn, T. A. and Quintenz, J. P., Proc. 1989 IEEE Part. Accel. Conf., IEEE 89CH2669-0, p1014.
9. Stroud, P., Laser and Part. Beams 4, 261(1986).
10. Young, F. C., et al., IEEE Trans. on Plasma Sci. PS-9, 24(1981).
11. Leeper, R. J., Proc. NATO Advanced Study Inst. on Fast Electrical and Optical Diagnostic Principles and Techniques, vol. 1, J. E. Thompson and L. H. Luessen, eds., Martinus Nijhoff, The Netherlands, 1986, pp263-315.
12. Neri J. M., et al., Proc 7th International Conf. on High Power Part. Beams, Karlsruhe, July 1988, p165.
13. Peterson R. R., et al., Univ. Wisconsin Fusion Technology Inst. Rep. UWFD-819, Feb. 1990.
14. Hinshelwood, D. D., et al., Proc. 1990 IEEE International Conf. on Plasma Sci., IEEE 90, Oakland, May 1990.
15. Ottinger, P. F.; Mosher D., and Goldstein, S. A., Phys. Fluids 22, 332(1979), and Phys. Fluids 24, 164(1981).
16. Colombant, D. G., Goldstein, S. A., and Mosher D., Phys. Rev. Lett. 45, 1252(1980).
17. Watrous J. J., et al., and Neri J. M., et al., IEEE 90.

Development of wall-stabilized z discharges for intense ion-beam transport in inertial confinement fusion facilities

David Hinshelwood¹⁾

Plasma Physics Division, Naval Research Laboratory, Washington, DC 20375-5000

(Received 27 April 1992; accepted for publication 23 July 1992)

The wall-stabilized z discharge has been scaled successfully to the parameters required for a light-ion-beam-driven inertial confinement fusion facility. The electrical behavior of discharges with various gas species, pressures, lengths, and currents has been investigated. These investigations identify the required dielectric strength of the discharge channel wall. A low-mass, low-Z wall construction with sufficient dielectric strength is demonstrated. The discharge internal dynamics have been studied using temporal and imaging interferometry, framing photography, magnetic-field measurement, and spectroscopy. The discharge current radial profile, and its dependence on discharge parameters, has been diagnosed. The discharge consists of a magnetohydrodynamically stable, imploding thick annulus. The observed radial profile explains data from previous transport experiments. Contamination of the discharge by wall material is found to be negligible during the times of interest. These observations motivate a zero-dimensional model of discharge behavior. This model reproduces approximately both the discharge dynamics and the electrical characteristics over a range of parameters. Calculations indicate that the beam ions will lose only 10% of their energy during transport through the discharge in a fusion facility. A conceptual design for a z-discharge transport system is presented. The results of this work confirm that wall-stabilized z-discharge transport is a viable, backup approach to transport in a light-ion-beam-driven inertial confinement fusion facility.

I. INTRODUCTION

A laboratory microfusion facility (LMF), to allow the study of high-gain, high-yield inertial confinement fusion (ICF) target implosions, has been proposed. A shot rate of ~ 2 shots per day and an operating lifetime of many years is envisioned.¹ Light-ion beams produced by pulsed power generators are a possible driver for the LMF.² Beam transport over several meters from the generator to the target is required in order to compress, by time-of-flight bunching,³ the ~ 40 ns extracted-ion-beam power pulse to the 10–15 ns pulse dictated by target implosion physics. Transport is also required to isolate the ion source and to buffer the target-chamber first wall from the target explosion, allowing the LMF shot rate and lifetime requirements to be achieved. In addition, the ion beam must be focused from the source radius down to the ~ 1 cm target radius. A multimodule, light-ion-beam LMF, based on an extension of the Hermes III accelerator technology developed at Sandia National Laboratories, has been proposed.^{1,2,4} Each module uses a roughly 10-cm-radius extraction applied-B diode to produce 30-MeV lithium ions with a peak current on the order of 1 MA. 20–36 modules are used to deliver about 10 MJ of ions, at 1000 TW, to the target with good deposition uniformity.

Several transport schemes are being investigated.^{2,5} The most attractive approaches at present do not require hardware or externally driven discharges inside the target chamber. One such system uses ballistic transport and a solenoidal magnetic lens. The solenoid combines with the diode self-magnetic-field to produce an achromatic lens

pair for focusing the beam.^{6–8} Another uses anode surface shaping to focus the beam ballistically, followed by pinched-beam propagation along a preionized channel.⁹ Although solenoidal focusing of intense ion beams has been studied,^{10,11} to date neither technique has been extensively tested experimentally for a LMF. Beam microdivergence, imperfect focusing, and beam/background-gas interactions will place an upper limit on the focal length and thus limit the obtainable target-chamber radius.

Wall-stabilized z-discharge transport is an attractive backup approach. A schematic of this technique is shown in Fig. 1. A thin foil separates the diode vacuum from the transport system. The Li^+ ions produced in the diode are stripped to Li^{+3} by this foil. The ions are ballistically focused over ~ 100 cm onto the entrance of the channel. The channel has a length of several meters, a radius nominally equal to the target radius, and initially comprises a few Torr of gas enclosed by an insulating wall. An auxiliary circuit drives a tens-of-kA z-discharge through the channel gas. A conducting surface on the outside of the insulating wall provides the current return. The conducting wall helps to stabilize the discharge against magnetohydrodynamic (MHD) modes. Surface breakdown along the wall mitigates the current and allows a long discharge to be created with a modest voltage. The initial surface discharge leads to ionization and breakdown of the channel gas. Ideally, a uniform discharge is established with a constant current density across the channel cross section, at which time the beam is injected. The channel plasma has sufficient density to charge and current neutralize the ion beam, and the ions execute betatronlike orbits in the discharge magnetic field. The channel-exit-to-target distance

¹⁾Also with Jaycor, Vienna, VA 22182-2270

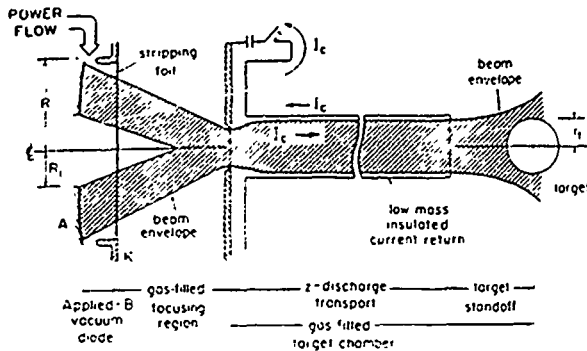


FIG 1 Schematic of z-discharge transport approach

is only a few cm and under optimum conditions, essentially all of the ions exiting the channel hit the target.

This approach has several attractive features. The 250–350-cm-long channel allows for a comparably large target-chamber radius. The gas and pressure in the channel can be chosen independently of those in the target chamber (and, if needed, those in the ballistic focusing region). Using a higher chamber pressure (~ 100 Torr) and larger wall radius significantly reduces the wall loading.¹ Experiments^{12,13} have demonstrated efficient ion-beam transport over distances of several meters. Analysis of the ion distribution at the channel exit indicates full charge and current neutralization of the transported beam. Several theoretical studies^{14–18} have also been carried out. Limits to transportable beam power arising from microinstabilities and energy loss in the channel have been identified, and a system study of z-discharge transport for LMF has been performed. Analysis of ion orbits has been used to determine the transport efficiencies for various sets of system parameters. A total particle transport efficiency (diode to target) of 75%–100% is predicted for reasonable LMF parameter values.

The obvious drawback to this approach is that it requires hardware in the target chamber. Transport experiments to date have used channels with ceramic walls and brass current returns. Such an arrangement is unacceptable for a LMF because of the shrapnel and activation that would result from the target explosion. In principle, the channel mass can be reduced greatly, but the wall must have sufficient dielectric strength to withstand the discharge voltage. The insulating wall can be fabricated from a low-mass, low-Z material with a high dielectric strength, such as Kapton. Replacing the current return with a thin layer of vapor-deposited aluminum would be straightforward.

In addition to reducing the channel mass, the discharge parameters must be adjusted for LMF. As discussed in the next section, LMF requires a higher channel current, smaller channel radius, and longer channel length than in most previous experiments. These changes place increased demands on the channel-wall dielectric strength.

This paper describes the successful scaling of wall-stabilized discharge parameters to values required for a LMF. The electrical behavior of discharges in various sizes at various pressures, lengths, and currents has been

investigated, including discharges with Kapton walls and at LMF parameters. These investigations identify the required wall dielectric strength and a wall construction with sufficient dielectric strength is demonstrated. The discharge internal dynamics have been studied using temporal and imaging interferometry, framing photography, magnetic-field measurement, and spectroscopy. The discharge current radial profile, and its dependence on discharge parameters, has been diagnosed and is invoked to explain data from previous transport experiments. Contamination of the discharge by wall material is evaluated and found to be negligible during the times of interest. Based on these observations a zero-dimensional model of discharge behavior has been developed. This model reproduces approximately both the discharge dynamics and the electrical characteristics over a range of parameters. The model results are used to help interpret the data, and afford some predictive capability for LMF system optimization. Initial calculations of ion energy propagation through the channel, including beam bunching and the channel response, indicate that ion energy losses are acceptable ($\sim 10\%$).

This work addresses the engineering and discharge physics issues related to z-discharge transport for a LMF. Other alternate approaches, involving wire-guided^{19,20} and free-standing z-discharge (no stabilizing wall)^{21,22} transport have been studied previously. Transport has been demonstrated in both cases, but there are significant engineering concerns with both approaches that have not been addressed to date.

The general discharge requirements for a LMF are discussed in Sec. II. Since the requirements are not precisely determined at this time, the predictive capability afforded by the discharge model will be useful in extrapolating the results of this work to possible different choices of discharge parameters. Electrical behavior of different discharges is described in Sec. III. Section IV describes the internal measurements under a variety of conditions. Discharge modeling is detailed in Sec. V. Beam propagation calculations and a conceptual design of a LMF z-discharge transport system are presented in Sec. VI. Finally, a summary and conclusions are given in Sec. VII.

An analogous study of z discharges, but at tenfold greater initial radii and several times larger currents, is reported in Refs. 23 and 24. That work was directed toward the final, imploded phase of the discharge, which is used for focusing heavy-ion beams.²⁵

II. LMF REQUIREMENTS

The exact, optimum set of transport system parameters is not established at present. For example, the system study in Ref. 18 did not include energy loss in the channel or a possible radial nonuniformity in the channel current density. A complete optimization will depend in part on the results of the present work. However, a fairly narrow acceptable range can be assigned to each parameter. The channel radius will be equal to, or slightly less than, the target radius; a target radius of 1 cm is assumed here. Beam bunching and pulsed-power geometric packing con-

cerns dictate a total transport length of about 400 cm. Beam microdivergence will limit the ballistic focusing length to <150 cm, resulting in a >250 -cm-long channel. The channel current required to confine the injected ions depends on the diode radius, the focal length, the channel radius, and the beam radius at the channel entrance. In Ref. 18 channel currents of 40–80 kA were found appropriate for LMF.

Several considerations will determine the channel gas and pressure. Most important, the channel density n_0 must be large enough (i.e., $n_0 \gg Z_b n_b$) to charge and current neutralize the beam. The 30 MeV, 3 MA (after stripping) ion beam in a 1-cm-radius channel has a density $Z_b n_b$ of about 2×10^{15} cm $^{-3}$. Next, the ion energy loss must be acceptably small. Ions lose energy in the channel by three processes.¹⁵ First, an axial electric field E_{res} , which is necessary to drive the return current through the channel plasma, decelerates the beam. Second, this return current flowing across the discharge magnetic field causes the channel to expand, which results, through the generalized Ohm's law, in an additional inductive, axial electric field E_{ind} . This field also decelerates the beam ions. The inductive field scales as¹⁵ $E_{ind} \propto I_c^2 Z_b I_b / (A_p n_0 r_c^2)$, where I_c is the discharge current, $Z_b I_b$ is the beam current in the channel, A_p is the atomic weight of the channel gas, and r_c is the channel radius. Third, the ions lose energy in collisions with the channel plasma. For a given gas, collisional losses scale directly with n_0 . Since collisional losses scale with n_0 , and inductive losses scale with $1/n_0$, consideration of only inductive and collisional losses leads to an optimum density for a given set of conditions. Resistive losses are more difficult to calculate. In general they will be lower at lower channel densities because the beam will supply more eV/particle to the channel plasma, thereby increasing the conductivity.

Calculated collisional and inductive kinetic energy losses for 30 MeV Li^{+3} ions in a 275-cm-long, 1-cm-radius, channel are shown in Fig. 2. This calculation assumes a channel current of 60 kA and a beam current $Z_b I_b$ of 3 MA. Figure 2 shows that the energy loss is minimized for Ar, N_2 , and Ne at pressures of a few Torr. The minima are broad—a factor of 2 change in background pressure changes increases the loss by only 25%—and the difference between gases is rather small. With a different set of system parameters or the inclusion of resistive losses the optimum pressures will change, but not by more than a factor of a few. Including resistive losses will increase the minimum loss (see Sec. VI) and shift the optimum pressure to a lower value. At these pressures, the condition for charge and current neutrality is also easily satisfied.

Another factor influencing the choice of channel gas and pressure is that the current density should be as uniform as possible over the channel cross section, because incomplete current penetration into the discharge interior will increase the current required to confine the beam. As Sec. IV will show, this uniformity varies for different gases.

Finally, all other things being equal, the channel gas and pressure would be chosen to facilitate driving the channel current and to minimize the discharge voltage.

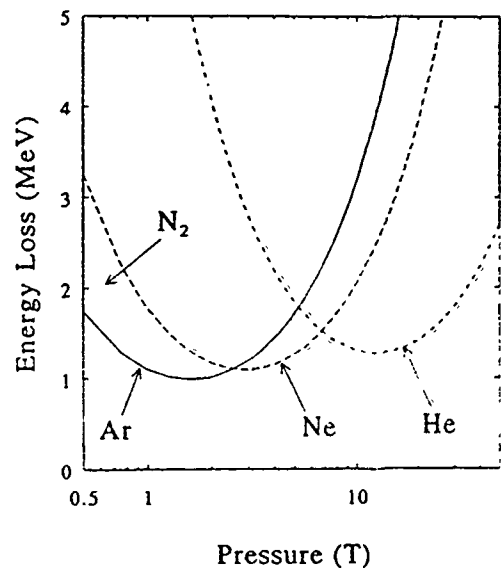


FIG. 2. Calculated collisional plus inductive energy loss for 30 MeV Li^{+3} ions in a 275-cm-long, 1-cm-radius channel with a discharge current of 60 kA. A beam current $Z_b I_b$ of 3 MA is assumed.

III. DISCHARGE ELECTRICAL BEHAVIOR

Earlier ion-beam transport experiments¹³ on the Gamble II generator at NRL used a 120-cm-long, 2 Torr air-filled channel, with a peak current of 45 kA. As a first step in scaling to a LMF, the electrical characteristics of 120-cm-long channels were examined for a range of discharge currents, gas species, and gas pressures. The first attempts at Kapton-walled channels used spiral wound, 2.5-cm-diam, 0.025-cm-thick, Kapton tubing.²⁶ This tubing, with a helical spiral construction in the form of a drinking straw, had only sufficient dielectric strength to support 35 kA currents in 200-cm-long channels, with breakdown occurring through the spiral seams. Therefore, thick (~ 0.3 cm) ceramic- or acrylic-wall channels, with or without Kapton liners, were used for most of the shots described in this section. A subsequently developed Kapton wall construction with sufficient dielectric strength is described at the end of this section. In all of this work, care is taken to insure uniform static pressure inside the channel.

A 45 kV, 1.9 μ F capacitor drove the discharge current through an inductance external to the discharge of about 200 nH. Typical voltage and current wave forms are shown in Fig. 3. The voltages are corrected for all inductance outside of the initial discharge radius. For a given charging voltage, each gas is seen to have a pressure which results in a maximum current. At lower pressures the current rises quickly but plateaus, while at higher pressures the current rises more slowly. The maximum currents are about 55 kA for He and N_2 and 65 kA for Ar and Ne. The discharge voltage at peak current ranges from 20 to 35 kV. Other data show that the effect of capacitor voltage is similar to that of pressure. At low charging voltages the current rises more slowly; as the voltage is raised the current rises more rapidly but plateaus earlier, resulting in a slightly less than linear dependence of peak current on charging voltage.

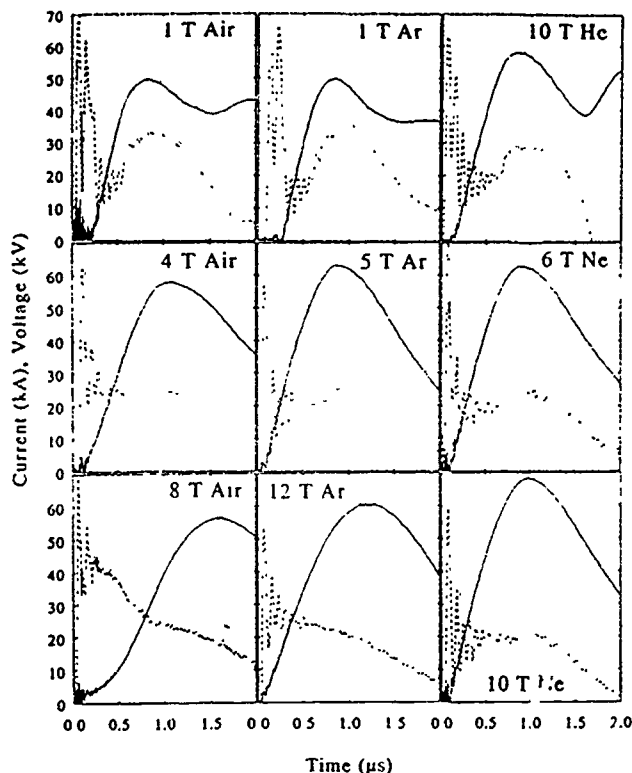


FIG. 3. Currents (solid lines) and voltages (dashed lines) for discharges in 120-cm-long, 1.27-cm-radius channels with different gases and pressures.

A dB/dt loop was used to measure the radial magnetic field profile. As in previous experiments,^{12,13} the probe was located in a 0.64-cm-diam tube, resulting in a rather poor resolution of 0.6–0.7 cm. Qualitatively, the measurements show that field penetration occurs more rapidly at higher voltages and lower pressures.

The inductive voltage drop between the channel edge and center, estimated from the magnetic-field measurements, is much less than the discharge voltage. This means that the discharge voltage is mostly resistive and that an axial electric field exists at the channel center well before current flows there. Therefore, current penetration into the channel is limited by energy diffusion rather than by magnetic-field diffusion. Initially the conductivity, and thus the current density, is much higher at the edge. With time, inward radial energy transport raises the conductivity of the channel interior and resistive division partitions the current among different radii.

This picture explains the dB/dt measurements and the general features of the wave forms in Fig. 3. The average energy/particle is higher at higher voltage and lower pressure. This results in higher conductivity and an initially larger cross section because of faster current penetration. Both of these reduce the discharge resistance. With time, however, magnetic compression reduces the cross section and increases the resistance [in addition to any $d(LI)/dt$ effects]. If the pressure is too low, the reduction in cross section due to compression offsets the increased conductivity and reduces the peak current.

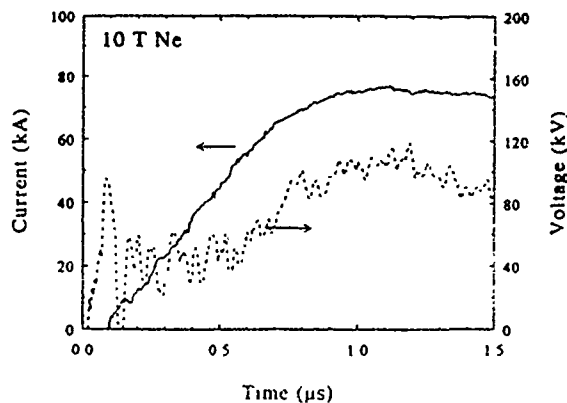


FIG. 4. Current (solid line) and voltage (dashed line) for a 250-cm-long, 1-cm-radius discharge at LMF level discharge current.

Except at the lowest pressures, the breakdown delay time is insignificant. Formation of the initial surface discharge might be expected to be affected by the driver polarity or the wall thickness, but no obvious difference is observed between polarities, or when comparing discharges in ceramic and thin Kapton (only) channels.

Next, LMF-level discharges in N_2 and Ne were diagnosed. The increased current, increased length, and reduced radius require a more energetic driving circuit. The circuit comprises a 1.1 μF , 160 kV capacitor bank with 870 nH outside of the initial discharge radius. Wave forms for a 1-cm-radius, 250-cm-long, 10 Torr Ne discharge are shown in Fig. 4. At peak current the discharge voltage reaches 110 kV. Even with the longer channel, the initial breakdown delay is negligible. Discharges in N_2 at 4–6 Torr show a higher initial discharge impedance, with a 15% slower current rise, than those in 10 Torr Ne. Impedances at peak current are similar for the two gases.

These data show that Ne is the most attractive gas from the standpoint of driving the discharge current, although the differences between gases are not great. Slightly higher currents were also obtained in the first series with Ar than with N_2 (see Fig. 3).

For both series of shots no significant difference in electrical behavior was observed when Kapton liners were present.

The application of a 3 kA, $\sim 0.6 \mu s$ prepulse, using an additional capacitor and current limiting resistor, does not reduce the voltage necessary to drive the discharge.

Finally, a Kapton wall construction with sufficient dielectric strength was fabricated. To avoid breakdown through the helical seams, the seams were eliminated by rolling the Kapton lengthwise. A thicker wall was also used, with a 40 cm width of 0.013-cm-thick Kapton rolled to give 6.5 turns at 1 cm inner radius. The turns were laminated with epoxy. This is a rather primitive technique; Kapton is available with a heat and pressure sensitive adhesive backing,²⁷ and fabrication of 250-cm-long channels with a heated rolling press should pose no problem for industry. Kapton composed 75% of the final 0.1 cm wall thickness. A 20-cm-long section of this tube was joined to the generator end of a 230-cm-long acrylic channel. Several

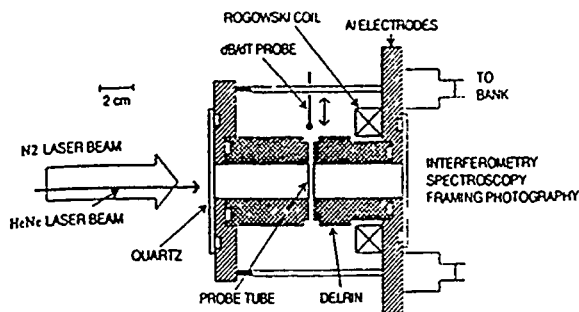


FIG 5. Schematic of the short-channel experimental arrangement.

shots were taken with peak voltages across the Kapton of about 110 kV, after which no damage to the Kapton was observed. This wall construction is 16 times less massive than the ceramic wall used in previous experiments. The brass current return will also be replaced by a thin layer of aluminum on the outside of the Kapton tube. A 250-cm-long channel would be rigid, self-supporting, and have a mass of less than 120 g. A thinner construction may be possible for these discharge currents, and will certainly be possible if discharge currents lower than 75 kA are required.

IV. DISCHARGE PLASMA MEASUREMENTS

A series of experiments with discharges in short (10 cm long) channels have been performed. The short length allows interferometric measurements along the discharge and facilitates other optical diagnostics. These experiments have been performed to study the effect of wall impurities on the discharge and to diagnose the discharge radial structure. A schematic of the arrangement is shown in Fig. 5. Diagnostics comprise magnetic-field measurement, N_2 - and HeNe-laser interferometry, framing photography, and spectroscopy. A $1.9 \mu\text{F}$ capacitor charged to 27 kV drives peak currents of 75 kA through the 1-cm-radius channel. On some shots lower currents are used to match the conditions on Gamble II shots. The current rise time is comparable to that of the LMF-level shots in the previous section. Because of the small impedance of the short channel, the current rise time is not affected by the channel gas, pressure, or driving voltage. Air, N_2 , Ne, He, Ar, and CO_2 channel gases are used. No significant difference is observed between discharges in air, N_2 , or CO_2 . Delrin is the channel wall material for most shots. No change to the inner wall is visible after hundreds of discharges. Kapton inserts have been used on some shots, with no significant effect on the measurements. Two aluminum end flanges serve as electrodes and quartz optical flats provide optical access. Nine cables at 5 cm radius form the current return.

There are three obvious concerns regarding the relevance of these experiments to long channels: (i) the short-channel discharges might be influenced by end effects; (ii) the large current return radius might decrease MHD stability, (iii) both the short-channel and the large return

radius might alter the initial, surface breakdown mechanism. The data will show that these concerns are not borne out.

The voltages and energy densities in these discharges require that any probe inserted in the plasma be well insulated. To improve on the resolution of previous magnetic-field measurements, a <1 -mm-diam probe is used, surrounded by a 0.2-cm-o.d., 0.15-cm-i.d. quartz capillary, which survives the discharge intact. The capillary bridges the channel along a diameter. The two-turn dB/dt loop is connected to coax by a long, tightly twisted pair. The resolution was checked by replacing the discharge with an axial, 1-cm-diam plastic rod covered with copper tape which provided a radial δ -function current distribution. The resolution is about 0.2 cm as would be expected. Even this resolution is sufficiently coarse that optical diagnostics are required to characterize fully the discharge radial profile.

Nitrogen-laser (imaging) interferometry provides a measurement of the line-averaged electron density radial profile over a few ns exposure time. Details of the N_2 laser and interferometry are given in Ref. 28. The present experiment requires a larger field of view, probes higher densities with much larger gradients, and has a much greater plasma light background, than that in Ref. 28. A beam expander is used to increase the field and improve the beam uniformity. A 25-cm-focal-length achromatic doublet is used to conjugate the discharge with the film plane. The lens recaptures refracted rays and grazing incidence reflections from the channel walls. An achromat is necessary because spherical aberration in a normal lens will degrade the image. Residual uncertainties result from the finite, 10 cm depth of field. At the locations of maximum density gradient, where the problem is most acute, the resulting uncertainties in spatial location and phase shift are less than 0.05 cm and one full fringe, respectively. Plasma light is preferentially attenuated by spatial filtering, using a 0.5-cm-diam pinhole placed at the focal plane of the lens. This passes rays that are paraxial within 10 mrad, including the <3 mrad refracted light, while rejecting most of the plasma light. A spectral line filter further attenuates plasma light. The interferograms are recorded on Polaroid type 55 film. The direction of fringe shift is calibrated by observing the pattern produced by a convex drop of alcohol on one of the windows.

The N_2 -laser interferometer is complemented by a HeNe-laser (temporal) interferometer which provides the line-averaged electron density at a given location as a function of time. The beam is directed through the channel at various radii with an uncertainty of about 0.1 cm. Detection is complicated by the large spatial and temporal density gradients involved, which have almost twice the effect for the 6328 Å HeNe as for the 3371 Å N_2 laser. To record fringes with high contrast ratio the imaged beam size at the channel must be small enough to have a constant phase shift over its area. A pinhole at the detector images a 0.005-cm-diam section of the discharge. Even over this small area, the phase shift at maximum gradient varies by about one full fringe. The low beam power density further limits

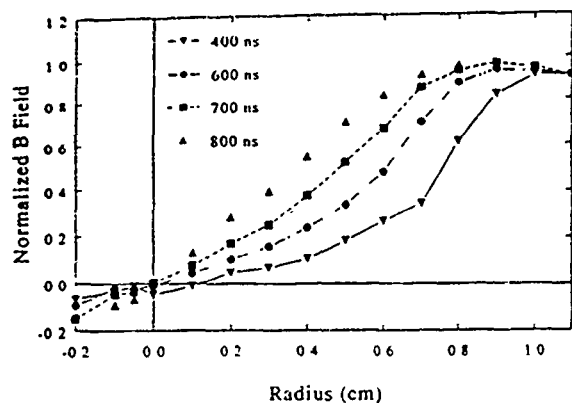


FIG. 6. Magnetic-field profiles for 75 kA, 5 Torr N_2 discharges. (The corresponding current trace is shown in Fig. 9.)

fringe detection; it is not possible to accept all refracted light while rejecting enough plasma light to observe the signal at later times during the discharge. Limitations resulting from finite beam size, refraction, and plasma light effectively restrict HeNe-laser interferometry to measurement of roughly the first five fringes. For 5 Torr N_2 discharges this corresponds to about 50% ionization.

The discharge is viewed end on with an Imacon 790 camera producing 40 ns frames every 200 ns. Spectroscopic measurements are obtained with a 0.5 m visible spectrograph. A large-diameter, gated image intensifier is used to provide a coarse timing window of ~ 300 ns. On most shots the discharge is viewed end on; on a few shots a fiber optic inserted in the channel wall has been used to view the discharge side on, halfway along its length.

Inferred magnetic-field profiles for 5 Torr N_2 discharges are shown in Fig. 6. The probe location, with an uncertainty of less than 0.05 cm, is varied randomly shot to shot to avoid systematic errors. The smooth curves obtained indicate good shot-to-shot reproducibility. The field is normalized to the nominal value at the 1-cm-radius outer edge. The profiles indicate a radially nonuniform current density distribution. By peak current (700 ns), current does not appear to have completely penetrated to the axis while there is evidence of compression at the edge.

A sequence of N_2 -laser interferograms is shown in Fig. 7. Timings are indicated on the current wave form in the figure. The interferometer is aligned to give horizontal reference fringes. The channel gas was air at 2 Torr with a peak current of 40 kA. Interferograms taken with higher pressures and peak currents exhibit the same features as those in Fig. 7, but with correspondingly larger fringe shifts. Free electrons will cause an upward fringe shift in the figure. For a 10 cm path length, one full fringe corresponds to an electron density of $6.5 \times 10^{16} \text{ cm}^{-3}$, or about 45% ionization.

Results of HeNe-laser interferometry are used to calibrate absolutely these profiles. For example, signals from shots with the HeNe beam on the channel axis show no density at the times of the first two frames and 10% ionization at the time of the third frame. By following each

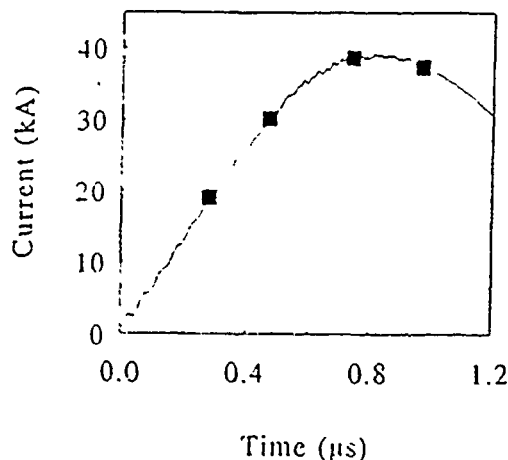
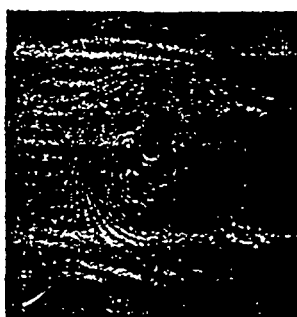


FIG. 7. Nitrogen-laser interferograms taken at four times during 40 kA, 2 Torr air discharges. Timing is indicated on the graph.

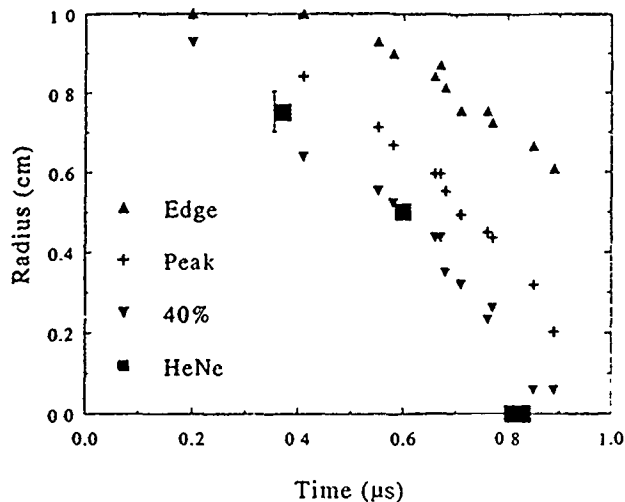


FIG. 8. A summary of interferometric data for 75 kA, 5 Torr N_2 discharges. The outer edge, peak density, and inner edge (40% ionization) locations are obtained from N_2 laser interferograms. The times at which the ionization reaches 40%, obtained from HeNe-laser interferometry, are shown at three radii for comparison.

fringe, the density is determined absolutely over the channel cross section.

At 280 ns, plasma is only observed at the outer edge of the channel. By 470 ns the radius of maximum density has increased and moved into the channel. Observable ionization is still restricted to the outer 0.4 cm radius. By 740 ns, at about peak current, the peak electron density is about three times the initial particle density. The inner boundary of the ionized region has moved in, but the inner 0.3-cm-radius region is still un-ionized. The outer boundary has been compressed to 8 mm radius. There is a hint of fringe reversal at the outer edge, indicating the presence of high-density neutral material. The density calibration for neutrals depends on the material, but for C and H the density/fringe is about ten times higher at this wavelength than that for free electrons. At 970 ns the channel has been compressed to 0.6 cm radius and ionization has reached the center. The outer neutral cloud has moved in 0.1 cm. The most striking feature here is the annular density profile; at no time is the density uniform across the entire channel cross section. The implosion is also seen to proceed with good azimuthal symmetry.

The data in Figs. 8–11 below were obtained from shots with 5 Torr N_2 at 75 kA peak current. Interferometric data are summarized in Fig. 8. Three radii are plotted for each shot, corresponding to the outer edge, the density maximum, and the inner edge of the density profile, as measured by the N_2 interferometer. The last is defined as the radius at which the ionization fraction has dropped to 40% (two fringes at 5 Torr initial pressure). The large squares represent HeNe interferometric data from shots with different laser beam radii. Each square indicates the time when the ionization fraction reaches 40% at the laser beam radius; data from both interferometers are seen to be in good agreement. The data also indicate good shot-to-shot reproducibility.

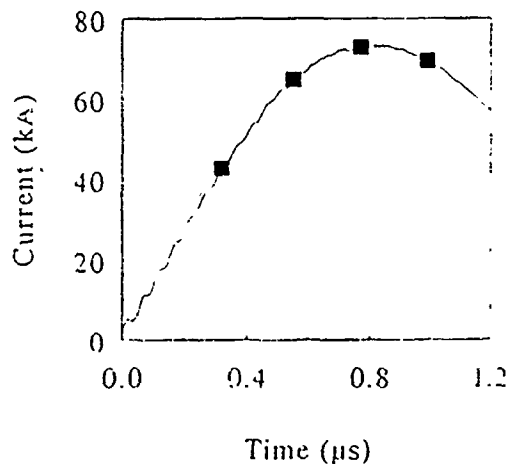
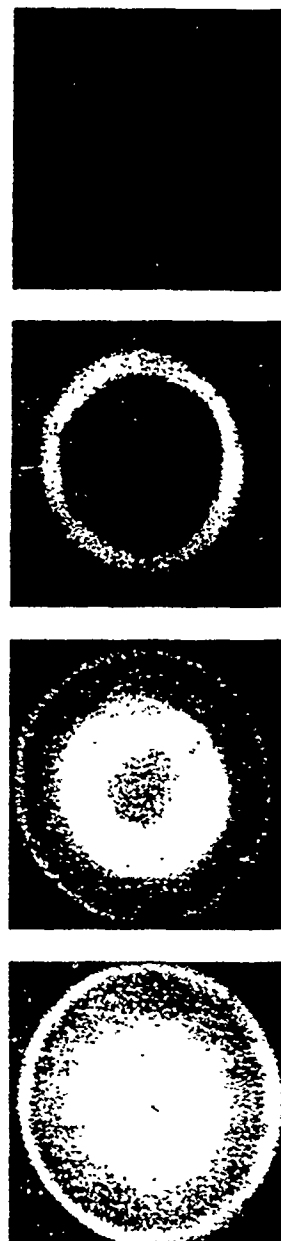


FIG. 9. A sequence of end-view framing photographs taken during 75 kA, 5 Torr N_2 discharges. Timing is indicated on the graph.

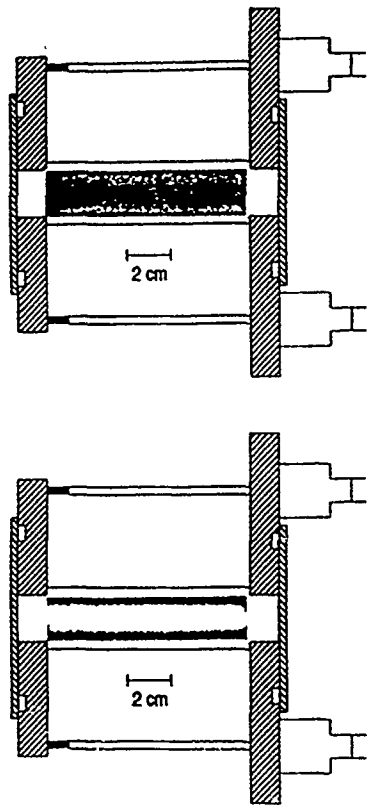


FIG. 10. Two side-view framing photographs taken during 75 kA, 5 Torr N_2 discharges. The first frame was taken with greater luminous gain. The times correspond roughly to the first and third frames in Fig. 9.

Typical end-view framing photographs are shown in Fig. 9. These are entirely consistent with the interferograms, showing luminosity first at the edge, and then in an imploding annulus. Like the interferograms, these show azimuthally symmetric implosions.

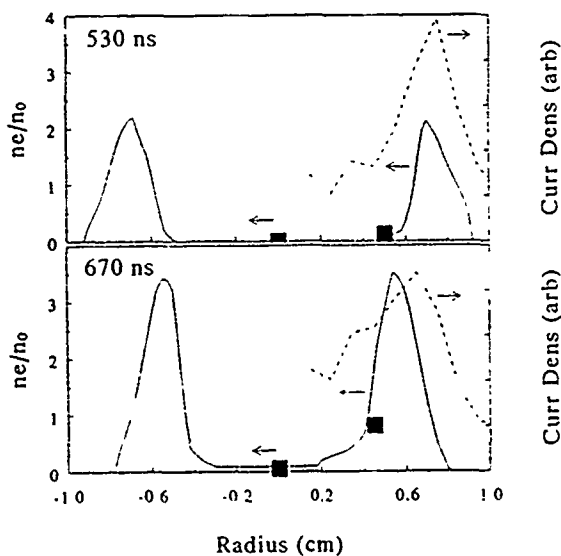


FIG. 11 The electron density profile obtained from N_2 (solid lines) and HeNe-laser interferometry (squares), compared with the current density profile derived from the dB/dt probe signals (dashed lines), at two times.

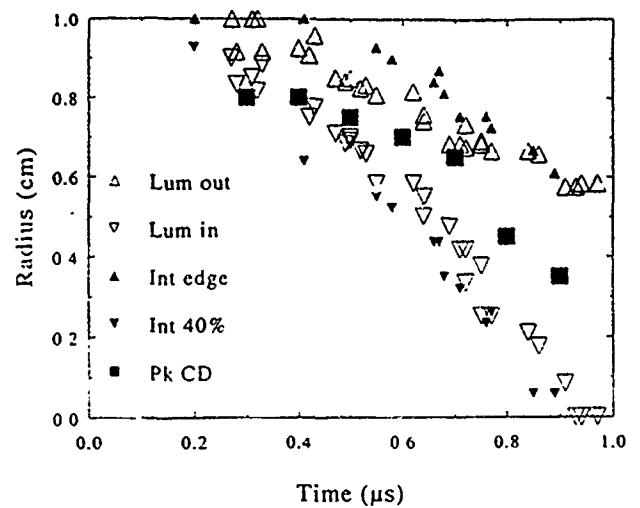


FIG. 12. The luminosity outer and inner edges, obtained from framing photography, compared with the interferometric data in Fig. 8. The locations of peak current density derived from dB/dt probe signals are also shown.

A few shots were taken using a 1-cm-inner-radius acrylic channel, permitting a side view of the entire discharge, except for the regions inside the electrodes. Framing photographs from 5 Torr air, 75 kA discharges are shown in Fig. 10. The highly axially uniform luminosity shows that MHD instabilities are absent. End effects are also unimportant; evidently the discharge connects to the electrodes inside the electrodes themselves, which make up 20% of the total channel length. Finally, the photographic and interferometric data show that breakdown initiates along the surface as it does in the long channels. These results remove the concerns stated at the beginning of this section.

Electron and current density profiles are compared for two times in Fig. 11. The electron density profiles are obtained from analysis of individual interferograms. The current density profiles are calculated from the magnetic field data in Fig. 6. The two are in general agreement. An unphysically finite current density is inferred at inner radii where the electron density is negligible. Since the heavy particle density inside the annulus must be comparable to the initial density, the ionization fraction and conductivity in this region must be very low. The discrepancy is attributed to the limited probe resolution and illustrates the importance of the interferometric measurements. The apparent current density near the channel edge may be real. The sensitivity limit of the interferometer is about $1-2 \times 10^{16} \text{ cm}^{-3}$, so that there may be plasma with a low absolute density, but a high degree of ionization, outside the compressed annulus.

Interferometric, magnetic-field, and photographic data are summarized and compared in Fig. 12. The inner and outer radii of observed luminosity are compared with the interferometric measurements of the inner and outer edges in Fig. 8, and with the radii of peak current density inferred from dB/dt probe data. All the data are in reasonable agreement.

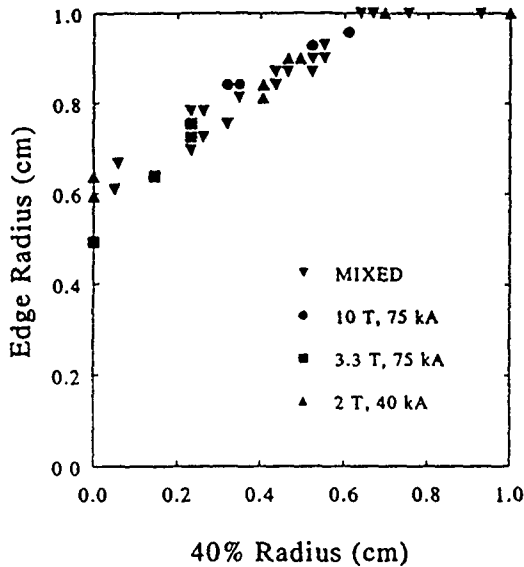


FIG. 13. A summary of interferometric data for N_2 discharges with various currents and pressures. The electron density outer edge is plotted against the inner edge (40% ionization). Most of the "mixed" category were 5 Torr, 75 kA discharges.

Changes in pressure and/or driving current which increase the rate of discharge compression (i.e., lower pressure or higher current) are also observed to increase the rate of inward penetration of the discharge in air/ N_2 discharges, as was also inferred from the dB/dt measurements in the previous section. Therefore, it is not possible to optimize the radial uniformity by varying these parameters. This is illustrated in Fig. 13. Each point on the graph is obtained from an interferogram taken during an individual shot. For each interferogram, the outer edge radius is plotted against the inner edge (40% ionization) radius. These data represent shots with peak currents ranging from 40 to 87 kA and pressures ranging from 2 to 10 Torr of N_2 . Points with a given inner radius correspond to different times, depending on the current and pressure. Within the experimental scatter the points lie on a universal curve. In order to obtain current penetration in to 4 mm radius, for example, one must accept compression to about 8 mm radius.

Subject to packing constraints, it may be possible in a LMF to start the discharges in slightly larger channels in the hope of achieving a more uniform profile by the time at which channel compression to the target radius occurs. Figure 14 compares luminosity data from the shots in Fig. 12 with those from shots with a larger wall radius but a similar gas inventory. Given outer radii are associated with about the same inner radii in both cases, so that using a slightly larger wall radius provides little advantage. Packing constraints will preclude the use of channels with much larger wall radii.

These data explain results of previous transport experiments on Gamble II.¹³ In those experiments, analysis of the transport efficiency and of the ion trajectories at the channel exit indicates a relatively hollow magnetic field profile. For analytical simplicity a power-law profile $B \propto r^N$

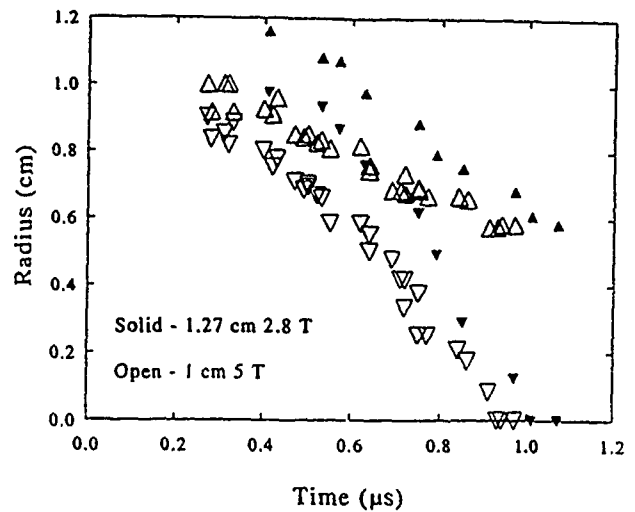


FIG. 14. A comparison of luminosity inner and outer edges for 1.27-cm-radius, 2.8 Torr N_2 , and 1.0-cm-radius, 5 Torr N_2 discharges.

was assumed in Ref. 13. In this case the current I_{ch} necessary to confine the beam scales as

$$I_{ch} \propto \frac{N+1}{2[1-(r_a/r_c)^{N+1}]}, \quad (1)$$

where r_a is the aperture radius at the channel entrance and r_c is the channel radius. A best fit to the data is obtained with N about equal to 3. In the Gamble II experiments $r_a=0.85$ cm and $r_c=1.27$ cm. With $N=3$, I_{ch} is about 1.4 times that required for $N=1$. The results of this work suggest that a better description of the field would be that produced by an annulus of constant current density. By a similar analysis to that in Ref. 13, using conservation of canonical axial momentum, the required channel current is calculated to vary as

$$I_{ch} \propto \frac{1-r_i^2/r_0^2}{1-r_a^2/r_0^2-(2r_i^2/r_0^2)\ln(r_0/r_a)}, \quad (2)$$

where r_o and r_i are the discharge outer and inner radii. The 45 kA, 2 Torr air, 1.27-cm-channel-radius discharge in Ref. 13 had a similar risetime to those studied here. Data from corresponding discharges in the present experiments indicate that the annulus in the Gamble II experiments had inner and outer radii of about 1.2 and 0.7 cm at the time of beam injection. For these radii, Eq. (2) also predicts a required current about 1.4 times greater than that for a linear profile, in reasonable agreement with the experimental results.

No effect on the discharge is observed when a 0.0025-cm-diam tungsten wire is installed on the channel axis, or when the shot is taken during a dc discharge established with a Tesla coil. Nor is uniformity improved by the use of a 3 kA prepulse. Driving the prepulse for 1 μ s before the main discharge has no effect other than accelerating both the compression and penetration by about 100 ns. Driving the prepulse for 3 μ s results in a pronounced azimuthal nonuniformity, as shown in Fig. 15. Preionization techniques such as a dc discharge, wire initiation,²⁹ or laser



FIG. 15. Framing photograph taken near peak current during a 5 Torr N_2 , 75 kA discharge with a 3 kA, 3 μ s prepulse.

initiation^{21,22} enhance breakdown but do not by themselves create a highly conducting current path. It is likely here that the enhancement associated with streamer propagation along the channel wall is greater than that provided by the above methods, so that the discharge will continue to initiate along the wall.

The scaling of penetration with compression is not surprising. Penetration results from inward energy transport which increases the inner conductivity. Inward energy flow will increase at higher discharge current, and specific heating of the channel interior will be greater at lower particle density. Compression will scale roughly with I_{ch}^2/M where M is the mass density. Therefore, for a given gas species, compression and penetration will exhibit the same qualitative scaling with discharge current and initial gas pressure. Since compression scales inversely with mass density and heating scales approximately inversely with particle density, current-density uniformity should be increased (i.e., a broader annulus should result) by using a higher atomic weight gas. This indeed is observed, as shown in Fig. 16. Electron density profiles from shots with four gases are compared at two times. A wider ionized region is observed for Ar, and a narrower region for He, than for N_2 discharges.

The ionization fraction can be estimated from the interferograms. The measured density profile (see Fig. 16) is used to determine the discharge inner edge. It is assumed that the initial gas is undisturbed inside the inner edge radius. Then, the density profile is integrated from the inner edge to the channel wall, and the resulting electron inventory is divided by the original gas inventory in that region. This calculation happens to be rather insensitive to the assumed location of the inner edge. Estimated average ionization fractions at peak current are roughly 1.1 for N_2 , 0.75 for Ne, 1.6 for Ar, and 0.3 for He.

Magnetic-field profiles for Ar and N_2 discharges are

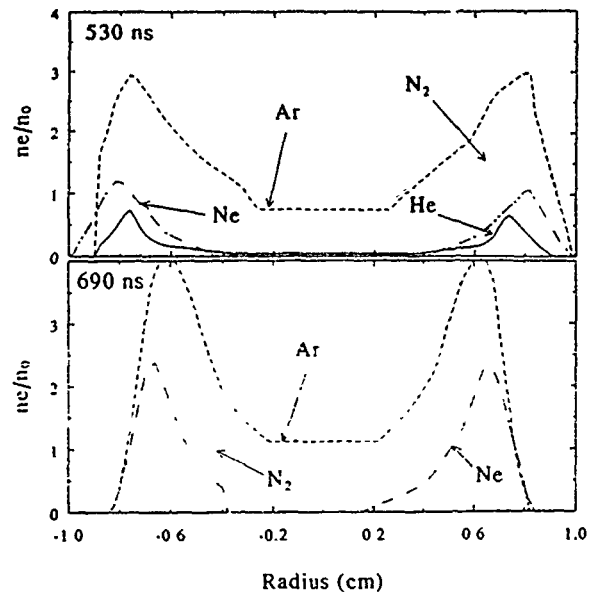


FIG. 16. Electron density profiles obtained from N_2 -laser interferometry for different gases at two times.

compared in Fig. 17. These data also show a more rapid current penetration with Ar.

Side-view spectra obtained with a fiber optic at the channel midpoint are identical with those viewed end on. All significant spectral line emission from the first ~ 900 ns originates from the fill gases. A spectrum taken very late, at 2 μ s, shows significant carbon emission, presumably from wall material, only at the outer few mm of the channel. Identical spectra were obtained from shots with Delrin-, Kapton-, and ceramic-wall channels. These data, together with the interferograms which show only a thin layer of material at the channel wall during the first 700–800 ns, indicate that significant contamination of the discharge with wall material does not occur during this time.

The spectroscopic data here do not permit quantitative, time resolved measurements of line intensity ratios. Qualitatively, analysis of the spectra suggests that the ion-

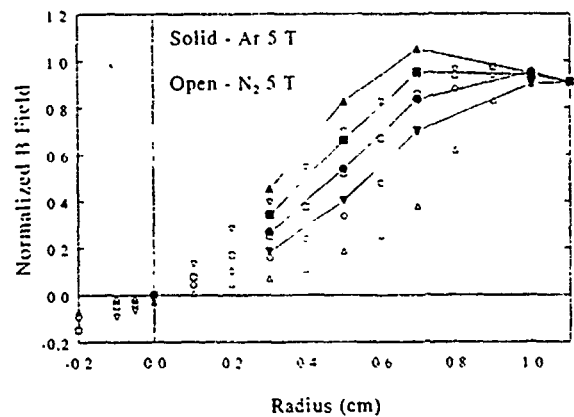


FIG. 17. A comparison of magnetic-field profiles for 5 Torr N_2 and 5 Torr Ar discharges, both at 75 kA. The times are the same as those in Fig. 6.

ization fraction is higher with N_2 than with Ne, which is in agreement with the interferometric data. Around peak current the ratio of N III/N II ions is estimated to be >1 , giving $Z \approx 1.5$, which is somewhat more than that estimated from the interferograms.

If compression of the discharge outer radius can be tolerated, the problem of incomplete current penetration can be alleviated simply by using a sufficiently long rise time for a given channel pressure and peak current. One effect of the compressed discharge radius is to alter the magnetic-field profile. As the discharge inner radius reaches the axis and the outer radius compresses to a fraction of the channel radius, the field profile approaches that of a wire on axis. Transport in this profile requires a lower current to confine the beam but results in increased ion radial velocity at $r=0$, leading to a more rapid beam expansion between the channel exit and the target.¹⁹ This assumes, however, that ions whose orbits pass between the discharge outer radius and the channel wall remain confined. Confinement requires that the ions be charge and current neutralized in this region. Only a small fraction of the initial density n_0 need remain outside the compressed annulus in order to charge neutralize the beam, and the ions could also drag electrons out from the discharge, so that charge neutralization is reasonable to assume. Current neutralization may be more difficult. There are several issues associated with passage of the return current through the rarified region outside the compressed discharge, such as instabilities and anomalous resistivity, that would need to be investigated.

At present, argon appears to be the optimum channel gas for a LMF because it allows the most radially uniform discharges and because it is associated with slightly lower ion energy loss than the other gases considered (see Fig. 2). Ion energy loss due to the resistive electric field associated with the return current is a possible concern with argon since it will be more resistive during the ion beam pulse than the other, lower-Z gases.

V. DISCHARGE MODELING

Efforts are presently directed toward modeling the discharges, and their response to the injected ion beam, with the 1D radiative transport MHD code Z-PINCH.³⁰ One-dimensional modeling may provide an estimate of the density of material left behind the collapsing annulus, give a better idea of the exact radial magnetic-field profile, and predict the resistive ion energy loss. In the interim, calculations with two simple models have been carried out: (i) A zero-dimensional discharge model of the discharge alone has been developed, with the goal of reproducing both the long channel impedance behavior and aspects of the short-channel experiments; and (ii) ion-beam propagation through the channel has been calculated, including beam bunching, channel heating, channel expansion, and channel resistivity evolution. The first model is described in this section and the second in Sec. VI.

Breakdown is assumed to occur in a thin layer adjacent to the channel outer radius R . Subsequent current flow is assumed to occur within an annulus, henceforth referred to

as the shell, ranging from the compressed outer radius r_o to an inner radius r_i . Within the shell the current density, particle density, and temperature are assumed to be constant. The electron and ion temperatures are assumed to be equal. (Since most of the internal energy goes into ionization, and since kinetic pressure effects are seen to be fairly small, the results are relatively insensitive to the equipartition between T_e and T_i .) Inside r_i the material is assumed to be undisturbed and cold. The channel resistance/length is given by the plasma resistivity divided by the cross section. Compression of the outer radius is determined by magnetic pressure, kinetic pressure, and inertia. The resistivity is determined by a simple Saha model and ohmic heating. Rather than attempt a similaritylike model for inward penetration of the current, the inner radius is just assumed to move from $r_i=0.95R$ to the center at a constant velocity from $t=0$. This velocity is estimated based on the interferometric data; the results did not depend strongly on this velocity. Note that this "velocity" is not necessarily connected with radial particle motion.

This model differs from other zero-dimensional Z-pinch models^{31,32} in that the shell width varies with time and can be a significant fraction of the shell radius.

All gases are assumed to be initially monatomic with a specific internal energy of 3 eV/heavy particle (the results are fairly insensitive to this parameter). A Saha-like calculation is used to derive the ionization balance: The first excited level is assumed to be in local thermodynamic equilibrium (LTE) with respect to the next stage, and that level is coupled to the ground state by both collisional and radiative processes, using standard rate formulas. This formalism results in Saha-like equations relating ground states; for the conditions here the results are not too different from those for pure LTE. Two excited states are included in the partition function calculations although these have negligible effect on the results. The calculated ionization distributions are used to derive the charge state Z , internal energy ϵ_i , and resistivity η , as functions of the electron temperature T_e . Spitzer parallel resistivity is assumed because of the high collisionality under the present conditions. In calculating the electron-neutral resistivity, the cross sections for electron-neutral collisions are estimated from data in Ref. 33. The calculations are then inverted to express Z , T_e , and η as functions of ϵ_i . Calculated resistivities are shown in Fig. 18. Another reason for the rapid relative current penetration in argon is seen here: The resistivity decrease with ϵ_i is weakest for this gas, which facilitates resistive penetration of the current.

The discharge model is incorporated in a transmission-line circuit code.³⁴ The assumed current density profile is used to calculate the time-varying magnetic flux in the channel, this appears as an inductive term in the code.

Radiative loss and compressional heating were not included in most runs. Spectroscopy indicates that the discharge is optically thin away from resonance lines. Adding a loss term equal to 10% of the blackbody value, which should be an upper limit, has only a small effect on the results. Adding an average compressional heating term has a negligible effect on the results for the first μs , and a small

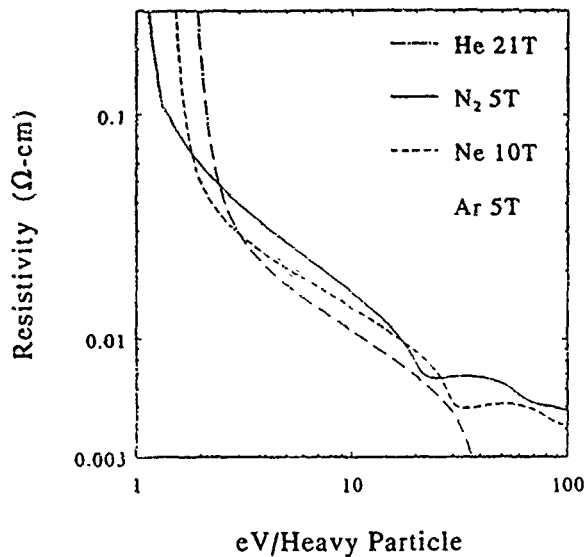


FIG. 18. Results of equation-of-state calculations used in code modeling

effect after that. Nonequilibrium effects are also not included in the atomic physics model. Ionization equilibria may not be completely established on the timescale here, particularly for He and Ne. Incomplete ionization will result in a lower resistivity for a given ϵ_n , as more energy will go into T_e . Errors from neglect of all of the above effects will be within the inherent inaccuracy of a zero-dimensional code.

Figures 19–22 show results from modeling the short-channel experiments for different gases. The dots on each graph display the interferometrically measured inner and outer edge locations. The inner edge locations are used to determine the inner edge penetration velocity assumed by the code; this assumed penetration is indicated by the lower line on each graph. (Again, the code results are not strongly affected by the choice of penetration velocity.)

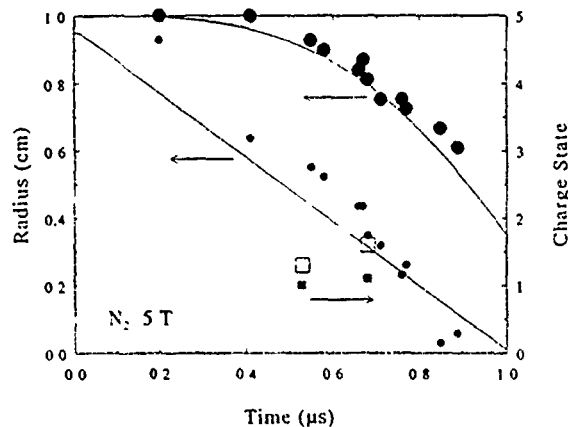


FIG. 19. Code predictions for a 5 Torr N_2 , 75 kA discharge. The dots indicate the outer and inner (40% ionization) edges of the interferometrically measured density profile. The lines display the inner edge motion input to the code and the outer edge motion predicted by the code. The squares indicate the average charge state derived from interferograms (solid) and predicted by the code (open).

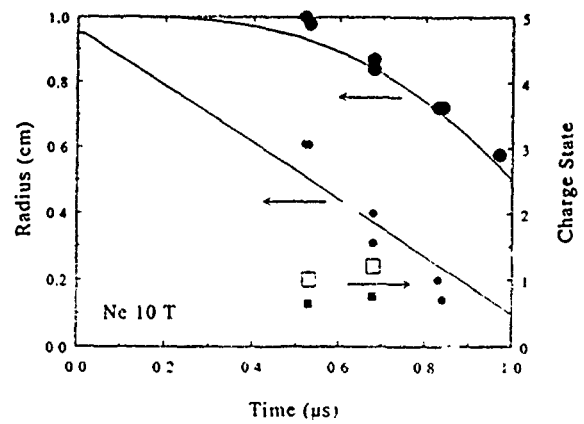


FIG. 20. Corresponding code predictions for a 10 Torr Ne, 75 kA discharge.

The upper line indicates the calculated outer edge motion. Good agreement with data is observed. Changing the mass by $\pm 30\%$ in the code results in an obvious disagreement with the data. This confirms that a significant quantity of wall material does not enter the discharge, and that most of the initial mass is contained in the compressed shell. The dark squares represent the average charge state in the shell obtained from the observed electron density profiles. The light squares represent the corresponding code predictions. Good relative agreement is observed although the code generally overpredicts the ionization derived from the interferograms by about 40%. The code predictions for N_2 are consistent with the spectroscopic results, however.

Long-channel impedance behavior is modeled in Figs. 23 and 24. Calculated and observed currents, for the shots in Fig. 3, are compared in Fig. 23. The inner edge penetration velocities are estimated based on extrapolations of the short-channel data; thus no free parameters are adjusted to optimize the fit to the data. Good qualitative and quantitative agreement is observed, at least until just past peak current. The LMF level discharge in Fig. 4 is modeled in Fig. 24. Again, good agreement is observed until peak current. The discrepancy at later times could not be ac-

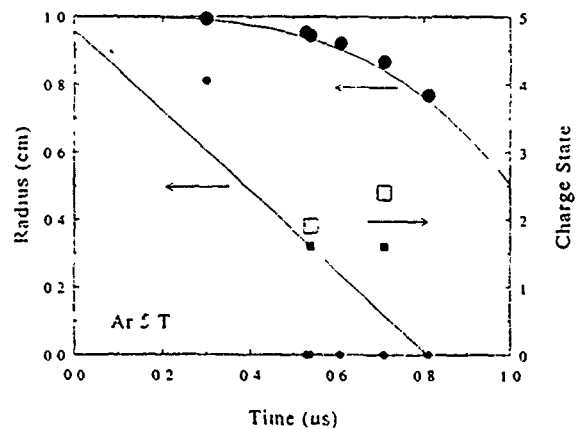


FIG. 21. Corresponding code predictions for a 5 Torr Ar, 75 kA discharge.

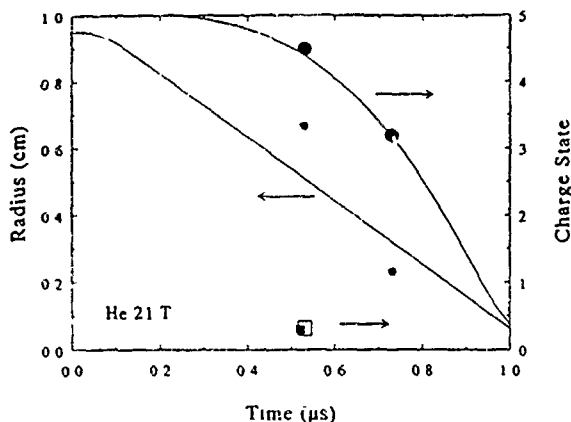


FIG. 22. Corresponding code predictions for a 21 Torr He, 75 kA discharge.

counted for by modeling thermalization of the implosion; it could be indicative of current flow outside the shell, perhaps along the channel wall. In any case, channel behavior past peak current is not relevant for LMF applications.

VI. BEAM PROPAGATION CALCULATIONS

An axially resolved calculation of ion-beam propagation and channel response has been carried out to estimate resistive energy losses in an argon channel. The ion-beam parameters at the channel input are based on projected LMF wave forms.³⁵ These comprise a ramped (27–33

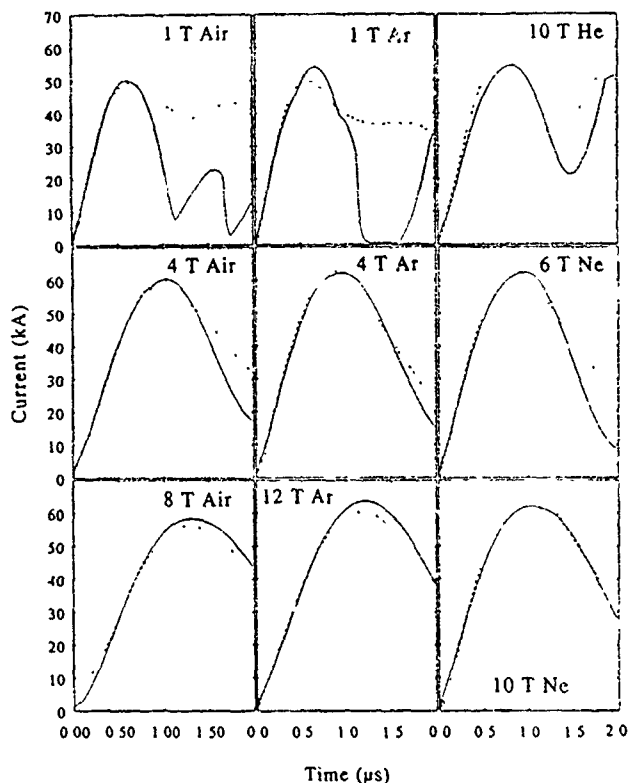


FIG. 23. Predicted (solid lines) and observed (dashed lines) discharge currents for the shots in Fig. 3.

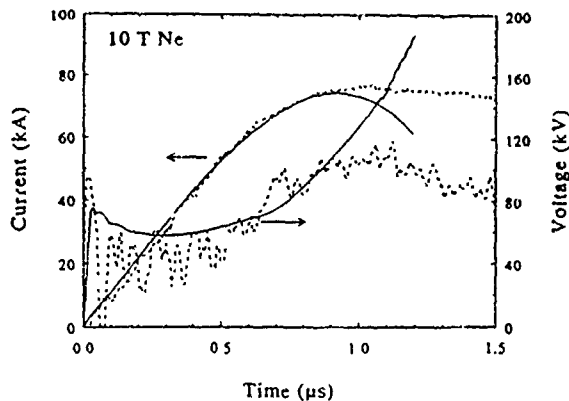


FIG. 24. Predicted (solid lines) and observed (dashed lines) currents and voltages for the shot in Fig. 4.

MV) voltage pulse and a 1.2-MA-peak current pulse. To account for losses in the diode and at the channel aperture an ion current of 1 MA at the channel input is assumed. The ion beam is time-of-flight bunched over the distance between the diode and the channel, and over the channel length. The local channel expansion is determined by the ion current and the kinetic pressure. Transverse Spitzer resistivity is assumed; heating during the ion-beam pulse will reduce the plasma collision frequency to a value much less than the cyclotron frequency. The resulting collisional, inductive, and resistive losses are used to calculate the rate of energy deposition in the plasma. Channel resistivity evolution is determined by the balance between heating and radiation.

Since LTE would not be expected at the higher temperatures here, the ionization balance is taken from results of a collisional-radiative equilibrium (CRE) calculation.³⁶ (Inverting this calculation yields a resistivity as a function of internal energy that differs from the LTE prediction by less than 20% over the region of interest here. A purely coronal calculation³⁷ would yield a lower resistivity as a function of internal energy, as less energy would go into ionization.)

An accurate prediction of the radiative loss requires detailed CRE modeling including opacity effects and is beyond the scope of this work. CRE calculations of radiation from argon plasmas have been performed,^{36,38} but only for temperatures above 100 eV, so that *M*-shell radiation was not considered. The only predictions including *M*-shell radiation known to this author result from optically thin, coronal equilibrium calculations,³⁹ and so these are used in this modeling. Extrapolating these to the densities in the present work will lead to an overestimation of the radiative loss. Comparisons of the predictions from Refs. 36–39 suggest that the coronal calculations overestimate the *L*-shell radiation by a factor of a few, and the *M*-shell radiation by more than that.

Results from one calculation are shown in Figs. 25–27. The system parameters for this case are: 100 cm focal length; 300 cm channel length; 60 kA channel current; 2 Torr Ar channel gas; 0.9 cm initial channel diameter. The reduced diameter is used to compensate for return-current-

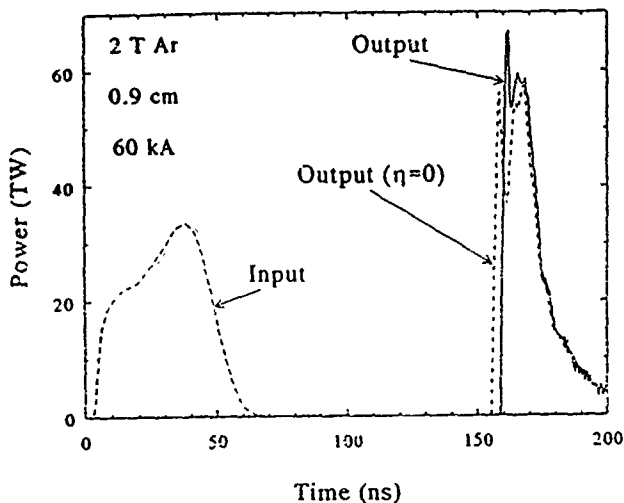


FIG. 25. Calculated ion-beam powers, with and without resistive energy loss, after propagating for 100 cm in the ballistic focusing region and then through a 2 Torr Ar, 300-cm-long, 60 kA discharge. The assumed input power is also shown.

driven expansion; the pressure is chosen to restrict expansion to 0.1 cm during the times of interest. This pressure is close to that for minimum collisional and inductive energy loss. Ion-beam powers at the diode and at the channel output are shown in Fig. 25. Output energies of 0.55 MJ in the first 10 ns and 0.75 MJ in the first 15 ns are calculated, at an average ion kinetic energy of 27.5 MeV. The 2.5 MeV average energy loss represents 6% of the initial energy. Cold collisional-stopping cross sections from Ref. 40 were used; enhanced stopping was not considered here. Estimates based on Ref. 41 suggest that the enhancement will be less than a factor of 2, increasing the energy loss by <0.6 MeV. Also, stopping in the 100-cm-long ballistic focusing region is not included; with 2 Torr Ar this will add another 0.3 MeV to the energy loss.

The third curve in Fig. 25 shows the results of a calculation with the resistivity artificially set to zero. While resistive energy loss accounts for about 60% of the total loss, it actually increases the calculated output power. This increase occurs because the resistive loss is greatest at the

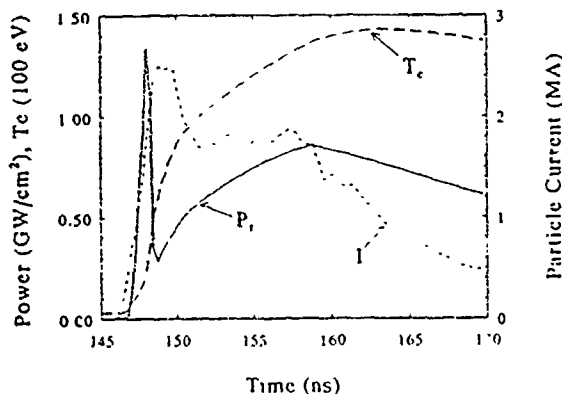


FIG. 26. Calculated bunched beam (particle) current, electron temperature, and radiated power at 30 cm before the channel output, for the conditions of Fig. 25.

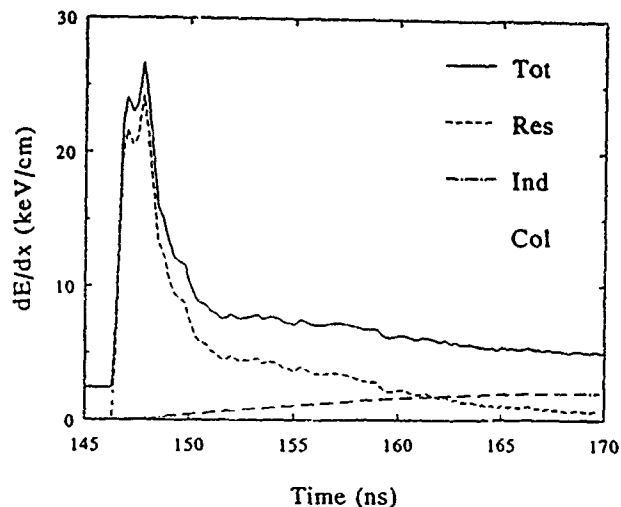


FIG. 27. Calculated resistive, inductive, collisional, and total dE/dx at 30 cm before the channel output, for the conditions of Fig. 25.

beam front, where the plasma is coldest. Slowing the ions at the beam front enhances the time-of-flight bunching, which more than offsets the 1.5 MeV resistive energy loss.

Figure 26 shows the calculated bunched beam (particle) current, electron temperature, and radiated power at 30 cm before the channel output. The first peak in radiated power corresponds to M -shell radiation which is burned through in a few ns, as the electron temperature quickly reaches 100 eV. At this time the argon is ionized to $Z_p \approx 10$.

The calculated resistive, inductive, collisional, and total dE/dx at 30 cm from the channel output are shown in Fig. 27. If a slightly larger increase in channel diameter could be tolerated, a somewhat lower gas density could be used which would reduce the total energy loss.

To check the sensitivity of these calculations to the assumed radiative rate, calculations were performed with the rate arbitrarily doubled, and with the rate set to zero. The results from both differed negligibly from those in Figs. 25–27. The time dependence of the atomic physics is not treated here; the effect of time-dependent ionization will be to allow more of the internal energy to go into the electron temperature, further reducing the resistivity. Thus, the simple modeling here indicates that resistive energy loss is not expected to preclude the use of argon as the channel gas.

The discharge model in Sec. VI is used to define the necessary driving circuit. An initial channel-wall diameter of 1.1 cm is used, in order to isolate the discharge from the thin, <1 mm layer of cold material at the channel wall. A circuit, comprising a 140 kV, 1 μ F capacitor and 600 nH inductance external to the 300-cm-long channel, is predicted to drive the required 60 kA by 700 ns. At 700 ns the discharge radius has compressed to the value of 0.9 cm used in the above calculation, and the voltage has reached 100 kV, below the value at which Kapton walls have already been tested.

Figure 28 shows a conceptual design of a z-discharge transport system based on the above calculations. Two

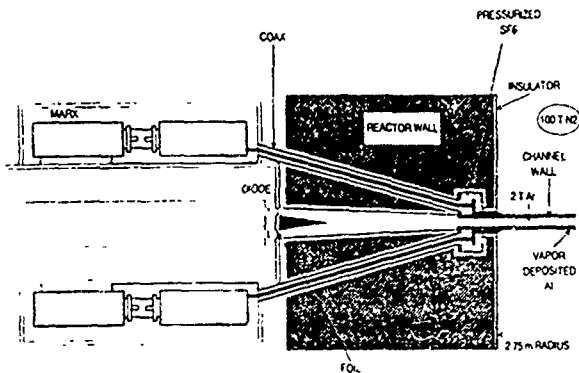


FIG. 28 Conceptual design of a z-discharge transport system for a LMF

Marxes operating in parallel drive the discharge current. Each consists of two, $1 \mu\text{F}$, 70 kV capacitors and is about $150 \times 40 \times 50 \text{ cm}^3$ in size. Each Marx is connected to the channel by a section of high-voltage (rigid, if necessary) coax. The two coaxes join the channel in a pressurized SF_6 housing. Sliding vacuum seals and current contacts in this housing allow the channels to be replaced quickly. The total inductance can easily be kept within the 600 nH assumed in the circuit calculation. In fact, with minor design effort a single Marx of the same size, with higher-energy-density capacitors, could be used instead.

The z-discharge approach has the advantage of allowing different gases and pressures to be used in the channel, target chamber, and (if desired) the ballistic focusing region. If needed, the output ends of the channels could be held together by a low-mass spherical holder. This holder would assure proper alignment between the channel ends and the pellet, and could, if necessary, isolate the channel and reactor gases. With the channels thus connected, a single pumping system could regulate the channel gas pressure. The z-discharge approach also allows a relatively large target-chamber radius of 2.75 m. The large radius and relatively high pressure, $\sim 100 \text{ T}$, target-chamber gas help to buffer the chamber wall from the target explosion.¹

VII. CONCLUSIONS

The wall-stabilized z discharge has been scaled successfully to parameters appropriate for a light-ion-beam-driven LMF. The electrical behavior of discharges under various conditions has been investigated, and the discharge internal dynamics have been studied using a variety of diagnostics. These measurements show that discharge initiation occurs by breakdown along the channel wall, even when the gas is preionized or a thin wire is installed along the axis.

Current is subsequently carried in a radial annulus. The inner and outer radii of the annulus both decrease with time. Magnetic compression reduces the outer radius. Inward penetration of the discharge current is determined in part by conductivity development in the channel interior. Since both compression and penetration scale in the same direction with discharge current, radius, and pressure, the annular profile is unavoidable. This annular profile can

explain data from previous Gamble II experiments. Radial uniformity is increased with a higher-atomic-number gas, e.g., argon.

The discharge continues to remain MHD stable during the time of interest. Except for a thin layer at the channel outer radius, wall material does not contaminate the discharge during the time of interest.

A zero-dimensional model of the channel behavior has been developed. The model reproduces approximately both the discharge dynamics and the electrical characteristics over a range of parameters. The model has adequate predictive capability to be used as a tool in an ultimate LMF transport system design study.

Argon is associated with maximum radial uniformity and minimum (collisional plus inductive) energy loss. Calculations indicate that the higher resistivity of an argon discharge, compared to lower-Z gases, will not result in an unacceptable additional energy loss. The calculated total ion energy loss in a 2 Torr Ar z-discharge transport system is about 10% of the initial ion energy.

Engineering concerns about driving the discharge in a LMF have been addressed: The required wall dielectric strength has been identified and a lightweight channel wall with sufficient dielectric strength has been demonstrated. The discharge driver requirements are modest.

Based on these results a conceptual design for a z-discharge transport system for a LMF is presented. This system allows a large, 275 cm target-chamber radius and a high-pressure fill gas, both of which reduce damage to the chamber wall.

The results here, along with those from the system study in Ref. 18 and the transport experiments in Refs. 12 and 13, demonstrate that wall-stabilized z-discharge transport is a practicable backup approach for beam transport in a light-ion-beam-driven LMF.

ACKNOWLEDGMENTS

This work was supported by the U.S. Department of Energy through Sandia National Laboratories. This work profited greatly from the support of Paul Ottinger, David Mosher, Jess Neri, and Craig Olson. It is also a pleasure to acknowledge useful discussions with John Apruzese, Ron Boller, Bob Commisso, Dave Rose, Steve Stephanakis, Bob Terry, and Jack Watrous. Portions of this work were performed with the expert technical assistance of Rick Fisher and Bruce Roberts. The author is also indebted to Paul Ottinger and Dave Rose for reviewing this manuscript.

¹ K. R. Prestwich, J. J. Ramirez, R. W. Stinnett, D. L. Johnson, C. L. Olson, M. J. Clauser, T. A. McHorn, M. P. Desjarlais, G. O. Allshouse, J. P. Corley, D. L. Hanson, M. E. Cuneo, P. F. McKay, J. W. Poukey, S. E. Rosenthal, S. A. Slutz, J. P. Quintenz, D. L. Cook, J. P. Vandevender, R. Peterson, R. Engelstad, and J. W. Powers, in Proceedings of the 8th International Conference on High-Power Particle Beams, Vol. 1, edited by B. N. Breizman and B. A. Knyazev, Novosibirsk, U.S.S.R. July 2-5, 1990, p. 143.

² J. J. Ramirez, R. W. Stinnett, D. L. Johnson, C. L. Olson, T. A. McHorn, J. T. Crow, J. P. Quintenz, K. R. Prestwich, M. P. Desjarlais, R. E. Olson, G. O. Allshouse, T. H. Martin, J. P. Vandevender, D. L. Cook, S. A. Slutz, K. B. Coachman, T. R. Lockner, B. N. Turman, S. A. Goldstein, and J. N. Olsen, Fusion Tech. 15, 350 (1989).

- ³F. Winterberg, *Plasma Phys.* 17, 69 (1975).
- ⁴D. L. Johnson, J. J. Ramirez, R. W. Stinnett, and K. B. Coachman, in *Proceedings of the 1989 Particle Accelerator Conference*, edited by F. Bennett and J. Kaptan, Chicago, IL, March 20-23, 1989, p. 1017.
- ⁵D. Mosher, D. D. Hinshelwood, J. M. Neri, P. F. Ottinger, J. J. Watrous, C. L. Olson, and T. A. Melhorn, in *Proceedings of the 8th International Conference on High-Power Particle Beams Vol. 1*, edited by B. N. Breizman and B. A. Knyazev, Novosibirsk, U.S.S.R., July 2-5, 1990, p. 26.
- ⁶C. L. Olson, in *Proceedings of the 1989 Linear Accelerator Conference*, edited by C. Leemann, Newport News, VA, October 3-7, 1988, p. 34.
- ⁷T. A. Melhorn and J. P. Quintenz, in *Proceedings of the 1989 Particle Accelerator Conference*, edited by F. Bennett and J. Kaptan, Chicago, IL, March 20-23, 1989, p. 1014.
- ⁸P. F. Ottinger, D. V. Rose, J. M. Neri, and C. L. Olson, *J. Appl. Phys.* 72, 395 (1992).
- ⁹R. F. Hubbard, M. Lampe, G. Joyce, S. P. Shinker, I. Haber, and R. F. Fensler, *Part. Accel.* 37-38, 161 (1992).
- ¹⁰J. Maenchen, L. Wiley, S. Humphries, Jr., E. Peleg, R. N. Sudan, and D. A. Hammer, *Phys. Fluids* 22, 555 (1979).
- ¹¹J. Olson, Cornell University (unpublished).
- ¹²F. L. Sandel, S. J. Stephanakis, F. C. Young, and W. L. Oliphant, in *Proceedings of the 4th International Topical Conference on High Power Electron and Ion Beam Research and Technology*, edited by H. J. Doucet and J. M. Buzzi, Palaiseau, France, June 29-July 3, 1981, p. 129.
- ¹³J. M. Neri, P. F. Ottinger, D. V. Rose, P. J. Goodrich, D. D. Hinshelwood, D. Mosher, S. J. Stephanakis, and F. C. Young, *Phys. Fluids B* (to be published).
- ¹⁴P. F. Ottinger, D. Mosher, and S. A. Goldstein, *Phys. Fluids* 23, 909 (1980).
- ¹⁵P. F. Ottinger, S. A. Goldstein, and D. Mosher, *NRL Memorandum Rep.* 4618, 1982.
- ¹⁶P. F. Ottinger, D. Mosher, and S. A. Goldstein, *Phys. Fluids* 22, 332 (1979).
- ¹⁷P. F. Ottinger, D. Mosher, and S. A. Goldstein, *Phys. Fluids* 24, 164 (1981).
- ¹⁸P. F. Ottinger, D. V. Rose, D. Mosher, and J. M. Neri, *J. Appl. Phys.* 70, 5292 (1991).
- ¹⁹J. J. Watrous, D. Mosher, J. M. Neri, P. F. Ottinger, C. L. Olson, J. T. Crow, and R. R. Peterson, *J. Appl. Phys.* 69, 639 (1991).
- ²⁰J. M. Neri, P. J. Goodrich, D. D. Hinshelwood, D. Mosher, P. F. Ottinger, S. J. Stephanakis, and J. J. Watrous, *Bull. Am. Phys. Soc.* 34, 2142 (1989).
- ²¹J. N. Olsen and L. Baker, *J. Appl. Phys.* 52, 3286 (1981).
- ²²J. N. Olsen and R. J. Leeper, *J. Appl. Phys.* 53, 3397 (1982).
- ²³B. Autin, H. Riege, E. Boggasch, K. Frank, L. De Menna, and G. Miano, *IEEE Trans. Plasma Sci.* PS-15, 226 (1987).
- ²⁴F. Dothan, H. Riege, E. Boggasch, and K. Frank, *J. Appl. Phys.* 62, 3585 (1987).
- ²⁵E. Boggasch, J. Jacoby, H. Wahl, K.-G. Dietrich, D. H. H. Hoffmann, W. Laux, M. Elfers, C. R. Haas, V. P. Dubenkov, and A. A. Golubev, *Phys. Rev. Lett.* 66, 1705 (1991).
- ²⁶Electrolock, Inc., Chagrin Falls, OH 44022.
- ²⁷Du Pont E I De Nemours and Co., Wilmington, DE 19803.
- ²⁸D. D. Hinshelwood, *NRL Memorandum Rep.* 5492, 1985.
- ²⁹P. A. Miller, L. Baker, J. R. Freeman, L. P. Mix, J. W. Poukey, and T. P. Wright, in *Proceedings of the Second International Topical Conference on High Power Electron and Ion Beam Research and Technology*, Cornell University, Ithaca, NY, Vol. 1, p. 393.
- ³⁰J. J. Watrous, G. A. Moses, and R. R. Peterson, *University of Wisconsin Fusion Tech. Inst. Rep.* UWFD-584.
- ³¹S. W. McDonald and P. F. Ottinger, *NRL Memorandum Rep.* 5785, 1986.
- ³²T. Miyamoto, *Nucl. Fusion* 24, 337 (1984).
- ³³S. C. Brown, *Basic Data of Plasma Physics* (MIT Press, Cambridge, MA, 1967).
- ³⁴D. D. Hinshelwood, *NRL Memorandum Rep.* 5185, 1983.
- ³⁵D. L. Johnson, Sandia National Laboratories (personal communication).
- ³⁶R. E. Terry, Naval Research Laboratory (personal communication).
- ³⁷D. E. Post, R. V. Jensen, C. B. Tarter, W. H. Grasberger, and W. A. Lokke, *At. Data Nucl. Data Tables* 20, 397 (1977).
- ³⁸D. Duston and J. Davis, *J. Quant. Spectrosc. Radiat. Transfer* 27, 267 (1982).
- ³⁹H. P. Summers and R. P. McWhirter, *J. Phys. B* 12, 2387 (1979).
- ⁴⁰L. C. Northcliffe and R. F. Schilling, *Nucl. Data Tables A* 7, 233 (1970).
- ⁴¹T. A. Melhorn, *J. Appl. Phys.* 52, 6522 (1981).

Current Neutralization of Intense MeV Proton Beams Transported in Low-Pressure Gas

F. C. Young,⁽¹⁾ D. D. Hinshelwood,⁽²⁾ R. F. Hubbard,⁽¹⁾ M. Lampe,⁽¹⁾ J. M. Neri,⁽¹⁾ C. L. Olson,⁽³⁾
P. F. Ottinger,⁽¹⁾ D. V. Rose,⁽²⁾ S. P. Slinker,⁽¹⁾ S. J. Stephanakis,⁽¹⁾ and D. R. Welch⁽⁴⁾

⁽¹⁾Plasma Physics Division, Naval Research Laboratory, Washington, D.C. 20375

⁽²⁾JAYCOR, Incorporated, Vienna, Virginia 22182

⁽³⁾Sandia National Laboratories, Albuquerque, New Mexico 87185

⁽⁴⁾Mission Research Corporation, Albuquerque, New Mexico 87106

(Received 4 February 1993)

This paper reports on the first experiments designed to study ion-beam-induced gas ionization and subsequent conductivity growth using intense proton beams transported through various gases in the 1-Torr pressure regime. Net-current fractions of 2% to 8% are measured outside the beam channel. Ionization is confined predominantly to the beam channel with ionization fractions of a few percent. Analysis suggests that net currents are larger inside the beam channel and that fast electrons and their secondaries carry a significant fraction of the return current in a halo outside the beam.

PACS numbers: 52.40.Mj, 41.85.Ja, 52.25.Jm, 52.65.+z

In ion-driven inertial confinement fusion (ICF), it is necessary to transport intense ion beams over several meters to isolate the ion source from the target explosion and to allow for focusing and time-of-flight bunching. Several light-ion ICF schemes [1], as well as some heavy-ion ICF schemes [2,3], envision ballistic (i.e., field-free) transport and focusing of the beam in neutral gas. This is possible if rapid beam-induced gas ionization leads to formation of a plasma with conductivity sufficient to charge and current neutralize the beam during the pulse duration [4]. Complete charge neutrality is expected; however, large net currents could arise which would shift, and possibly degrade, the beam focal spot [5,6]. The conductivity must also be sufficient to avoid beam filamentation instabilities [7,8] which could disrupt the beam tail. The required conductivity growth results from ion impact ionization, secondary electron impact ionization, electron avalanche breakdown, and late-time Ohmic heating.

The primary light-ion scheme for the proposed Laboratory Microfusion Facility uses ballistic transport with solenoidal lens focusing of 1-MA, 30-MeV, 40-ns lithium beams [9]. A typical beam current density before focusing is of order 1 kA/cm². Helium at 1-Torr pressure is suggested for the background gas to satisfy the above requirements while minimizing collisional energy loss and scattering of the beam. Transport in this 1-Torr regime is not well understood. This paper reports on the first experiments designed to study ion-beam-induced gas ionization and subsequent plasma conductivity growth in this regime.

This pressure range falls between the high-density regime treated by resistive models, and the low-density regime treated by collisionless models. To understand this intermediate regime, additional physics must be considered. Fast electrons created by beam-ion impact ionization (i.e., knockon electrons [10] or delta rays), which act to neutralize beam current for ion beams, could be important for intense beams. Also, runaway electrons

can result from high electric fields at the beam front. Fast electrons created by these processes can have mean free paths on the order of the beam radius, leading to nonlocal secondary ionization. A significant nonthermal electron population, which persists for the beam pulse duration, can also alter the plasma conductivity. Thus, collisional processes involving both thermal and fast electrons are important in this intermediate regime, and resistive models, which do not treat fast electron effects, are inadequate. Results of theoretical modeling of these experiments using the DYNAPROP [11] and IPROP [12] codes are presented to evaluate the importance of these effects. These codes are described when the modeling results are presented.

The experimental arrangement is shown in Fig. 1. A 1-MeV proton beam, generated in vacuum with a pinch-reflex diode [13] on the Gamble II generator is injected through a 2- μ m-thick polycarbonate foil into a collimator consisting of two 3-cm-diam apertures separated by 40 cm. The collimator region is maintained at 1-Torr air to provide reproducible injection into the transport region. A 1-kA/cm² beam exits the collimator through another 2- μ m-thick polycarbonate foil, and the interaction of this

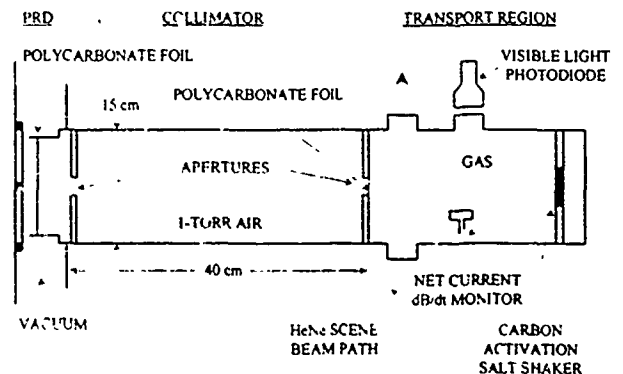


FIG. 1. Experimental arrangement of the pinch-reflex diode (PRD), the collimator, and the transport region.

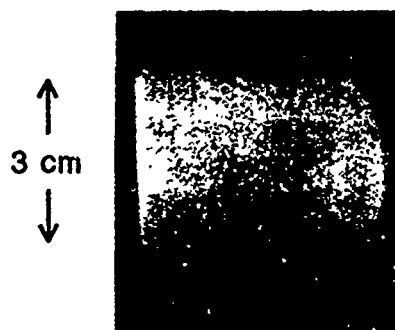


FIG. 2. Visible-light image of the ion-beam excitation of helium at 5 cm into the transport region. The beam is incident from the left.

beam with different gases in the transport region is studied.

The beam itself is characterized using several diagnostics at various distances from the collimator exit. The number of protons in the beam is measured by carbon activation [14]. A "salt shaker" detector located 26 cm beyond the collimator exit is used to minimize blowoff loss of radioactivity [15]. The beam size and uniformity in the transport region are determined from ion-induced $K\alpha$ x-ray images of aluminum targets, and from damage patterns on plastic witness plates. The beam profile is also recorded after transport over 170 cm in gas using chlorostyrene radiachromic film shielded by a $6.4\text{-}\mu\text{m}$ thickness of aluminum. These measurements indicate a uniform beam of 50-mrad divergence with a penumbra extending to 75 mrad, consistent with the collimator geometry. The energy distribution of ions in the beam is measured using a stacked-foil diagnostic as described below.

Interaction of the beam with the gas is diagnosed using photometry, magnetic-field measurements, and interferometry. Visible light emitted from the gas is monitored with a photodiode and a framing camera. A visible-light image, recorded 5 cm beyond the collimator exit with a 400-ns gated camera, is shown in Fig. 2. This image is uniform with no apparent structure. Net currents are recorded with a dB/dt monitor located 13 cm downstream of the collimator exit and outside the beam envelope at 4 cm radius. A HeNe interferometer using heterodyne phase detection is used to determine the electron density [16]. This technique provides high sensitivity and signal-to-noise ratio at the expense of time resolution. The sensitivity for this setup is limited by the noise-equivalent-average density of $5 \times 10^{14} \text{ cm}^{-3}$, with a time resolution of 25 ns. The path of the interferometer scene beam is 5 cm from the collimator exit as shown in Fig. 1.

Data from a typical shot are shown in Fig. 3. Current and voltage traces in the diode [Fig. 3(a)] indicate that a 50-ns-duration, $> 400\text{-kA}$ ion pulse is generated with most of the ions in the range of 1.0 to 1.2 MV. Adjusting

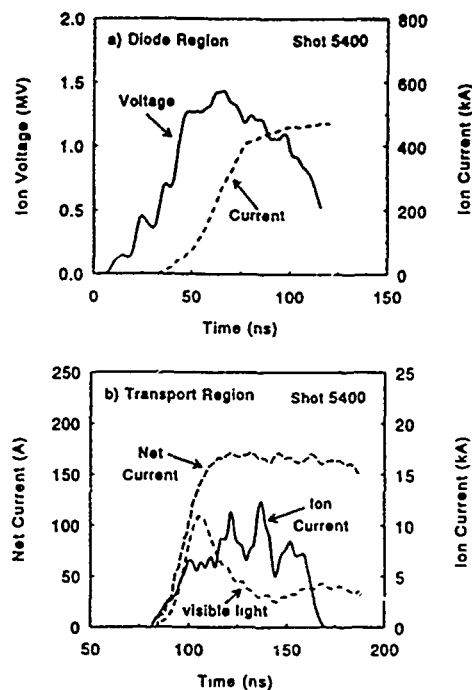


FIG. 3. (a) Ion-voltage and ion-current traces in the diode and (b) time-of-flight shifted ion current compared with measured net-current and visible-light traces.

this pulse for proton time of flight results in the ion-current pulse in Fig. 3(b) in the transport region. This pulse includes only protons above the 460-keV thick-target carbon-activation threshold and is normalized to the number of protons determined from this activation. This pulse duration is evaluated for each shot to determine the average proton current in the transport region. The net-current trace and the visible-light emission begin when the ion beam reaches the transport region.

The energy spectrum of the proton beam is measured in 1-Torr air with a carbon-activation foil stack located at 170 cm from the collimator exit. At this distance, a stack of ten $2\text{-}\mu\text{m}$ -thick polycarbonate foils with a $1.8\text{-}\mu\text{m}$ -thick aluminum cover survives, and the ^{13}N activity in each foil can be measured after the shot. A foil area of 124 cm^2 is used to provide measurable activity. The activity in each foil, produced by the 37-keV FWHM $^{12}\text{C}(p,\gamma)^{13}\text{N}$ resonance at 460 keV, is unfolded using the range-energy relation for protons in polycarbonate ($\text{C}_{16}\text{H}_{14}\text{O}_3$) to give the solid histogram in Fig. 4. The width of each step in this histogram corresponds to the energy interval over which protons activate that foil in the stack. This spectrum has been shifted up in energy to correct for energy loss in the aluminum cover on the stack. The dashed histogram is the spectrum determined from the diode current and voltage for this shot. It has been shifted down in energy to correct for energy loss in the two polycarbonate foils and air in the collimator and transport regions. Note the $400\times$ difference in these two scales. The spectral intensity in the transport region is

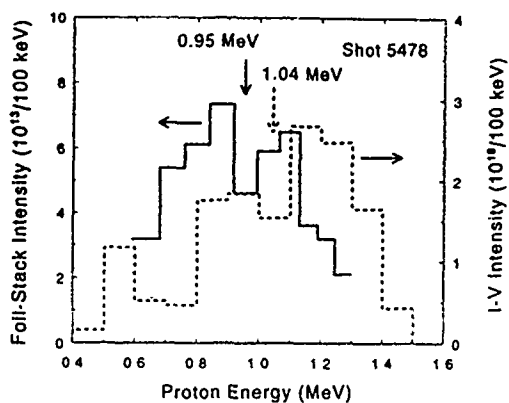


FIG. 4. Histograms of proton number vs proton energy in the transport region deduced from stacked-foil activations (solid) and from the diode current and voltage (dashed). Average energies for these histograms are indicated.

only a small fraction of that in the diode and corresponds to somewhat lower-energy protons. Average energies for these two spectra differ by about 100 keV. Since most of the protons have energies less than 1 MeV and the deuteron fraction in the beam is unknown, no correction is made for carbon activation by deuterons [14].

Simulations using a ray-trace code and a diode model [17] for the pinch-reflex diode have been carried out to calculate beam transport through the collimator and into the transport section. Experimental diode voltage and current wave forms and a beam microdivergence of 125 mrad at the anode were used to generate the time-dependent ion distribution function. Complete charge and current neutralization of the beam are assumed and ion energies are corrected for losses in the foils and gas. Ions which hit aperture plates or walls are removed from the simulation. Results predict beam currents, radial density profiles, and divergences which agree with those observed in the transport region. The predicted energy spectrum, however, agrees with the dashed curve in Fig. 4 rather than the measured spectrum (solid curve). An electric field induced at the beam front by a rising net current could explain the lower energy of the measured spectrum. Higher-energy ions, which reside at the beam head, would be slowed by this induced field. Because complete current neutralization is assumed, this energy loss is precluded in the simulations. If this is the correct explanation for the observed energy spectrum, the downshift would be considerably less at the collimator exit than at 170 cm downstream where the measurement was made.

Net currents and electron densities were measured for helium, neon, and air at pressures ranging from 0.25 to 4 Torr. Peak values of these measurements are given in Table I. From shot to shot the average current of the incident proton beam ranged from about 5 to 7 kA corresponding to current densities of about 0.7 to 1 kA/cm² at

TABLE I. Net current and electron density measurements.

Gas	Pressure (Torr)	Proton current (kA)	Peak net current (kA)	Electron density (10 ¹⁵ cm ⁻³)
Ne	0.34	4.5	0.11	...
	1.0	6.3	0.20	1.6
	1.25	6.4	0.22	...
Air	4.0	4.6	0.17	2.6
	0.25	4.8	0.18	...
	1.0	6.9	0.21	0.9
He	4.0	5.5	0.28	1.8
	0.25	6.2	0.31	...
	1.0	6.8	0.32	0.7
	4.0	5.9	0.47	1.5

the collimator exit. Net current wave forms from the dB/dt monitor have current rise times of 15 to 50 ns and decay times of several hundred ns. The uncertainty in the peak net currents is estimated to be $\pm 10\%$. Net-current fractions range from 2.3% to 8.0%. The local electron density is obtained by dividing the interferometrically measured line density by the 3-cm beam diameter. Peak electron densities are of order 10^{15} cm⁻³ and correspond to ionization fractions of 0.6% to 4.6%. For 0.25-Torr gas pressure, electron densities are too small to be measured. Negligible line density (less than the instrument sensitivity) was observed when the scene beam was located about 1.5 cm off center, indicating that ionization is largely confined to the beam diameter.

DYNAPROP and IPROP simulations were carried out to evaluate beam-induced net currents and electron densities in helium. DYNAPROP is a 1D code which uses a resistive model to treat plasmas created by beam interaction with high-density collisional gases. Beam dynamics is described by envelope and emittance equations; the plasma density, temperature, and conductivity are determined by rate equations; and the net current is calculated with a circuit equation. IPROP is a 3D hybrid code which treats beam ions and fast electrons (above 100 eV) as particles. The remaining electrons are treated as a resistive medium, while plasma ions are represented as a stationary background. Rate equations are used to create electron-ion pairs and Maxwell's equations are used to solve for the fields. Because azimuthal symmetry is assumed, IPROP was used in $2\frac{1}{2}$ D mode.

Results are compared with the measurements in Table II. For all three pressures, IPROP predicts a net current inside the dB/dt probe ($r=4$ cm) that is within 30% of the measured value. However, IPROP predicts a net current within the 1.5-cm beam radius that is a factor of 3 larger than the measured values. DYNAPROP calculates the effective net current (a radially averaged current weighted by the beam current density), which is predicted to be somewhat larger than the IPROP current within

TABLE II. Comparisons with theory for helium.

Pressure (Torr)	Measured ($r=4$ cm)	Net currents (kA)			Electron densities (10^{15} cm $^{-3}$)			
		IPROP ($r=4$ cm)	IPROP ($r=1.5$ cm)	DYNAPROP ($r \approx 1.5$ cm)	Measured (line average)	IPROP ($r=0$)	IPROP ($r=1.5$ cm)	DYNAPROP ($r=0$)
0.25	0.31	0.31	0.9	1.3	...	0.2	0.2	0.2
1.0	0.32	0.39	1.0	1.5	0.7	1.0	0.6	0.7
4.0	0.47	0.63	1.6	2.1	1.5	3.2	1.8	1.9

the beam radius. The small net current at the probe location observed in IPROP is a consequence of fast electrons carrying a significant fraction of the return current in a halo outside the beam. These electrons create additional ionization at large radius which contributes to the return current. These comparisons suggest that fast electrons play an important role in return-current conduction, and that the magnetic field within the beam channel is larger than that measured outside the beam envelope. An effective net-current fraction of about 25% in the ray-trace calculations mentioned earlier would be required to down-shift the high energy edge of the calculated spectrum to match the solid histogram in Fig. 4. This fraction is consistent with IPROP and DYNAPROP predictions within the beam. Both IPROP and DYNAPROP predict electron densities that are in reasonable agreement with the measured values.

In summary, 1-MeV, 1-kA/cm 2 proton beams have been transported through helium, neon, and air at pressures of 0.25 to 4 Torr. Small net current fractions of 2% to 8%, are measured outside the beam channel. Ionization is confined predominantly to the beam channel where ionization fractions are only a few percent. Analysis of the beam energy spectrum after transport suggests that larger effective net currents exist inside the beam channel. Similarly, IPROP and DYNAPROP calculations predict net currents in the beam channel 3 to 5 times larger than measured net currents. Outside the beam channel, IPROP predicts small net currents in agreement with measurements. Fast electrons and their secondaries carry a significant fraction of the return current outside the beam (although their density is low compared with the plasma electron density within the beam channel). More extensive experiments and modeling are required to develop sufficient understanding of beam-induced gas ionization and conductivity growth in this pressure regime to confidently scale results to ICF scenarios.

The expert assistance of J. R. Boller and B. Roberts in supporting these experiments is appreciated. This work was supported by the U.S. Department of Energy through Sandia National Laboratories.

- [1] D. Mosher *et al.*, in *Proceedings of the Eighth International Conference on High-Power Particle Beams*, edited by B. N. Breizman and B. A. Knyazev (World Scientific, Singapore, 1991), p. 26.
- [2] C. L. Olson, *J. Fusion Energy* **1**, 309 (1982).
- [3] *Proceedings of the Conference on Heavy Ion Inertial Fusion, Washington, DC, 1986*, AIP Conf. Proc. No. 152 (American Institute of Physics, New York, 1986).
- [4] C. L. Olson, in *Proceedings of the 1990 Linear Accelerator Conference, Albuquerque, New Mexico, September 1990* (LANL Report No. LA-12004-C), p. 396.
- [5] J. A. Swegle and S. A. Slutz, *J. Appl. Phys.* **60**, 3444 (1986).
- [6] D. J. Johnson *et al.*, *J. Appl. Phys.* **58**, 12 (1985).
- [7] C. L. Olson, in *Proceedings of the 1991 IEEE Conference on Plasma Science, Williamsburg, Virginia, June 1991*, *IEEE Conference Records-Abstracts*, edited by K. Schoenbach (IEEE, New York, 1992), p. 165.
- [8] E. P. Lee *et al.*, *Phys. Fluids* **23**, 2095 (1980).
- [9] P. F. Ottinger, D. V. Rose, J. M. Neri, and C. L. Olson, *J. Appl. Phys.* **72**, 395 (1992).
- [10] R. F. Hubbard, S. A. Goldstein, and D. Tidman, in *Proceedings of the Heavy Ion Beam Fusion Workshop, Berkeley, California, 1979*, edited by W. B. Hermannsfeldt (Lawrence Berkeley Laboratory Report No. LBL-10301, 1980), p. 488.
- [11] See R. F. Hubbard *et al.*, NRL Memorandum Report No. 7112, 1992 (National Technical Information Service Document No. ADA256070). Copies may be ordered from the National Technical Information Service, Springfield, VA 22161. The price is \$17.50 plus a \$3.00 handling fee. All orders must be prepaid.
- [12] B. B. Goufey and D. R. Welch, in *Proceedings of the Twelfth Conference on Numerical Simulations of Plasmas* (Lawrence Livermore National Laboratory, San Francisco, CA, 1987), Paper CMI.
- [13] S. J. Stephanakis *et al.*, *Phys. Rev. Lett.* **37**, 1543 (1976).
- [14] F. C. Young, J. Golden, and C. A. Kapetanakis, *Rev. Sci. Instrum.* **48**, 432 (1977).
- [15] A. E. Blaugrund and S. J. Stephanakis, *Rev. Sci. Instrum.* **49**, 866 (1978).
- [16] B. V. Weber and D. D. Hinshelwood, *Rev. Sci. Instrum.* **63**, 5199 (1992).
- [17] J. M. Neri *et al.*, *Phys. Fluids B* **5**, 176 (1993).

Naval Research Laboratory

Washington, DC 20375-5000



NRL/MR/4770-92-6974

Survey of Radioactivities Induced by Lithium Ions

FRANK C. YOUNG AND DAVID V. ROSE*

*Pulsed Power Physics Branch
Plasma Physics Division*

**JAYCOR
Vienna, VA 22180-2270*

June 15, 1992

Contents

Introduction..... 2
Survey of Nuclear Reactions..... 2
Nuclear Reaction Yields..... 3
References.....16

SURVEY OF RADIOACTIVITIES INDUCED BY LITHIUM IONS

I. Introduction

Nuclear reactions produced by lithium ions which lead to radioactive products are surveyed for application to experiments with intense pulsed lithium beams. Experiments using lithium beams have been carried out at Sandia National Laboratories on the PBFA II generator and are planned for the Sabre generator. In this survey, radioactivities induced in the commonly used materials, carbon, aluminum, steel and brass, are identified. In addition, radioactivities induced in the alloy, titanium 6-4, are identified because this alloy is used in the ion-diode region of the Sabre generator. Experiments on the PBFA II generator indicate that the lithium beam is primarily singly-ionized ${}^7\text{Li}$. This beam is produced from natural-abundance lithium which is primarily ${}^7\text{Li}$ (i.e., 92.5% ${}^7\text{Li}$ and 7.5% ${}^6\text{Li}$). Therefore, reactions induced by ${}^6\text{Li}$ nuclei are not included in this survey. The diode voltage on the Sabre generator may be as high as 10 MV, and experiments on PBFA II have achieved voltages of up to 15 MV. Therefore, lithium beams with energies of up to 15 MeV are considered in this survey.

In Sec. II, the nuclear reactions on these targets which produce radioactivity are listed, and the decay properties of the radioactive nuclei are identified. In a survey of the published literature, measured yields have been reported only for one of these reactions, but measurements for other lithium-induced reactions indicate that the reaction yields are dominated by the Coulomb barrier in this energy range. Yield estimates based on Coulomb-barrier penetration are presented in Sec. III.

II. Survey of Nuclear Reactions

Nuclear reactions with positive Q-values which lead to radioactive residual nuclei are identified in this survey. Lithium-induced reactions leading to the following products are considered: n, p, d, t, ${}^3\text{He}$, α , ${}^6\text{Li}$ and ${}^6\text{He}$. The tabulation of Q-values by Keller et al.¹ is used as a guide to identify

positive Q-value reactions. Since the Q-values in Ref. 1 are listed with only two-significant-figure precision, the Q-values in this survey are calculated to four-significant-figure precision using atomic masses from Ref. 2. The reactions and their Q-values are listed in Table I for carbon and aluminum, in Table II for titanium 6-4 alloy, in Table III for steel, and in Table IV for brass. The natural abundance of each isotope is also listed.

For the alloy targets, this survey only includes target isotopes for which the product of the isotopic abundance and the alloy proportion exceeds 1%. The titanium 6-4 alloy consists of 90% titanium, 6% aluminum, and 4% vanadium. The steel target is assumed to be #304 stainless with a 70%-iron, 20%-chromium, and 10%-nickel composition. For brass, a 67%-copper and 33%-zinc composition is assumed. Each of these elements consists of several stable isotopes with significant fractional abundances. The target isotopes for which the product of the isotopic abundance and the alloy proportion exceeds 1% are expected to be the primary sources of radioactivity. In addition, reactions which produce the long-lived isotopes ^{53}Mn ($T_{1/2} = 3.7 \times 10^6$ yr), ^{59}Ni ($T_{1/2} = 8 \times 10^4$ yr), and ^{63}Ni ($T_{1/2} = 10^2$ yr) are not included in this survey. Unrealistically large ion-beam fluences would be required to produce significant activities of these long-lived isotopes. The decay mode of each residual nucleus is identified as β^- for electron decay, β^+ for positron decay, and ϵ for electron capture. For β -decay, E_{β} is the end-point energy of the β -spectrum, and E_{γ} is the energy of the most intense γ -ray(s) associated with the decay. The symbol ^{52m}Mn in Table II refers to a metastable state where ^{52}Mn is the ground state. The decay modes, half-lives, end-point energies and γ -ray energies are taken from Ref. 2. The most intense γ -decays are identified from Ref. 3.

III. Nuclear Reaction Yields

For each target isotope, at least one reaction with a positive Q-value of several MeV is listed. Reactions with positive Q-values are allowed by kinematics for any bombarding

Table I

Radioactivities Induced by ${}^7\text{Li}$ Ions on Carbon and Aluminum

Target		Nuclear Reaction		Residual Nucleus			
Iso- tope	Abun- dance	Reaction	Q-Value (MeV)	Decay Mode	Half Life	E_{β} (MeV)	E_{γ} (MeV)
${}^{12}\text{C}$	98.9%	${}^{12}\text{C}({}^7\text{Li},n){}^{18}\text{F}$	5.96	β^+	110 min	0.63	0.51
${}^{13}\text{C}$	1.1%	${}^{13}\text{C}({}^7\text{Li},p){}^{19}\text{O}$	7.41	β^-	27 s	4.60	0.20 1.36
		${}^{13}\text{C}({}^7\text{Li},\alpha){}^{16}\text{N}$	9.92	β^-	7.1 s	4.3	6.13
		${}^{13}\text{C}({}^7\text{Li},2n){}^{18}\text{F}$	1.02	β^+	110 min	0.63	0.51
${}^{27}\text{Al}$	100%	${}^{27}\text{Al}({}^7\text{Li},p){}^{33}\text{P}$	16.76	β^-	25 da	0.25	-
		${}^{27}\text{Al}({}^7\text{Li},d){}^{32}\text{P}$	8.89	β^-	14 da	1.71	-
		${}^{27}\text{Al}({}^7\text{Li},{}^3\text{He}){}^{31}\text{Si}$	5.74	β^-	2.6 hr	1.49	-
		${}^{27}\text{Al}({}^7\text{Li},{}^6\text{Li}){}^{28}\text{Al}$	0.48	β^-	2.2 min	2.86	1.78

Table II

Radioactivities Induced by ${}^7\text{Li}$ Ions on Titanium and Vanadium

Target		Nuclear Reaction		Residual Nucleus			
Iso- tope	Abun- dance	Reaction	Q-Value (MeV)	Decay Mode	Half Life	E_{β} (MeV)	E_{γ} (MeV)
${}^{46}\text{Ti}$	8.0%	${}^{46}\text{Ti}({}^7\text{Li},n){}^{52}\text{Mn}$	13.42	β^+	5.7 da	0.57	1.43
		${}^{46}\text{Ti}({}^7\text{Li},n){}^{52\text{m}}\text{Mn}$	13.04	β^+	21 min	2.63	1.43
		${}^{46}\text{Ti}({}^7\text{Li},d){}^{51}\text{Cr}$	9.10	ϵ	28 da	-	0.32
		${}^{46}\text{Ti}({}^7\text{Li},\alpha){}^{49}\text{V}$	16.31	ϵ	331 da	-	-
		${}^{46}\text{Ti}({}^7\text{Li},2n){}^{51}\text{Mn}$	2.90	β^+	46 min	2.2	0.51
		${}^{46}\text{Ti}({}^7\text{Li},\alpha n){}^{48}\text{V}$	4.76	β^+	16.0 da	0.70	1.31
${}^{47}\text{Ti}$	7.5%	${}^{47}\text{Ti}({}^7\text{Li},t){}^{51}\text{Cr}$	6.48	ϵ	27.7 da	-	0.32
		${}^{47}\text{Ti}({}^7\text{Li},2n){}^{52}\text{Mn}$	4.54	β^+	5.7 da	0.57	1.43
		${}^{47}\text{Ti}({}^7\text{Li},2n){}^{52\text{m}}\text{Mn}$	4.16	β^+	21 min	2.63	1.43
		${}^{47}\text{Ti}({}^7\text{Li},2p){}^{52}\text{V}$	6.84	β^-	3.8 min	2.5	1.43
		${}^{47}\text{Ti}({}^7\text{Li},\alpha n){}^{49}\text{V}$	7.44	ϵ	331 da	-	-
${}^{48}\text{Ti}$	73.7%	${}^{48}\text{Ti}({}^7\text{Li},n){}^{54}\text{Mn}$	13.91	ϵ	312 da	-	0.835
		${}^{48}\text{Ti}({}^7\text{Li},{}^3\text{He}){}^{52}\text{V}$	2.93	β^-	3.8 min	2.5	1.43
		${}^{48}\text{Ti}({}^7\text{Li},2p){}^{53}\text{V}$	4.03	β^-	1.6 min	2.4	1.00
${}^{49}\text{Ti}$	5.5%	${}^{49}\text{Ti}({}^7\text{Li},p){}^{55}\text{Cr}$	14.17	β^-	3.6 min	2.59	-
		${}^{49}\text{Ti}({}^7\text{Li},{}^3\text{He}){}^{53}\text{V}$	3.60	β^-	1.6 min	2.4	1.00
		${}^{49}\text{Ti}({}^7\text{Li},\alpha){}^{52}\text{V}$	15.36	β^-	3.8 min	2.5	1.43
		${}^{49}\text{Ti}({}^7\text{Li},2n){}^{54}\text{Mn}$	5.76	ϵ	312 da	-	0.835
		${}^{49}\text{Ti}({}^7\text{Li},2p){}^{54}\text{V}$	1.40	β^-	43 s	3.0	2.21

continued

Table II Continued

Radioactivities Induced by ${}^7\text{Li}$ Ions on Titanium and Vanadium

Target		Nuclear Reaction		Residual Nucleus			
Iso- tope	Abun- dance	Reaction	Q-Value (MeV)	Decay Mode	Half Life	E_{β} (MeV)	E_{γ} (MeV)
${}^{50}\text{Ti}$	5.2%	${}^{50}\text{Ti}({}^7\text{Li},n){}^{56}\text{Mn}$	12.31	β^-	2.6 hr	2.85	0.847
		${}^{50}\text{Ti}({}^7\text{Li},p){}^{56}\text{Cr}$	11.48	β^-	5.9 min	1.5	0.083
		${}^{50}\text{Ti}({}^7\text{Li},d){}^{55}\text{Cr}$	5.45	β^-	3.6 min	2.59	-
		${}^{50}\text{Ti}({}^7\text{Li},\alpha){}^{53}\text{V}$	13.23	β^-	1.6 min	2.4	1.00
		${}^{50}\text{Ti}({}^7\text{Li},\alpha n){}^{52}\text{V}$	4.42	β^-	3.8 min	2.5	1.43
${}^{51}\text{V}$	99.8%	${}^{51}\text{V}({}^7\text{Li},p){}^{57}\text{Mn}$	12.90	β^-	1.6 min	2.56	0.122
		${}^{51}\text{V}({}^7\text{Li},d){}^{56}\text{Mn}$	6.48	β^-	2.58 hr	2.85	0.847
		${}^{51}\text{V}({}^7\text{Li},{}^3\text{He}){}^{55}\text{Cr}$	2.89	β^-	3.6 min	2.59	-
		${}^{51}\text{V}({}^7\text{Li},2p){}^{56}\text{Cr}$	3.42	β^-	5.9 min	1.5	0.083
		${}^{51}\text{V}({}^7\text{Li},{}^6\text{Li}){}^{52}\text{V}$	0.06	β^-	3.8 min	2.5	1.43

Table III

Radioactivities Induced by ${}^7\text{Li}$ Ions on Chromium, Iron and Nickel

Target		Nuclear Reaction		Residual Nucleus			
Iso- tope	Abun- dance	Reaction	Q-Value (MeV)	Decay Mode	Half Life	E_{β} (MeV)	E_{γ} (MeV)
${}^{52}\text{Cr}$	83.8%	${}^{52}\text{Cr}({}^7\text{Li},n){}^{58}\text{Co}$	11.26	ϵ, β^+	71 da	0.47	0.81
		${}^{52}\text{Cr}({}^7\text{Li},{}^3\text{He}){}^{56}\text{Mn}$	1.47	β^-	2.6 hr	2.85	0.847
		${}^{52}\text{Cr}({}^7\text{Li},2n){}^{57}\text{Co}$	2.69	ϵ	271 da	-	0.122
		${}^{52}\text{Cr}({}^7\text{Li},2p){}^{57}\text{Mn}$	2.40	β^-	1.6 min	2.56	0.122
		${}^{52}\text{Cr}({}^7\text{Li},\alpha n){}^{54}\text{Mn}$	4.55	ϵ	312 da	-	0.835
${}^{54}\text{Fe}$	5.8%	${}^{54}\text{Fe}({}^7\text{Li},n){}^{60}\text{Cu}$	8.94	β^+	23 min	3.77	1.76 1.33
		${}^{54}\text{Fe}({}^7\text{Li},{}^3\text{He}){}^{58}\text{Co}$	3.57	ϵ, β^+	71 da	0.47	0.81
		${}^{54}\text{Fe}({}^7\text{Li},\alpha){}^{57}\text{Co}$	15.58	ϵ	271 da	-	0.122
		${}^{54}\text{Fe}({}^7\text{Li},\alpha n){}^{56}\text{Co}$	4.20	β^+	77 da	1.46	0.847
		${}^{54}\text{Fe}({}^7\text{Li},{}^6\text{Li}){}^{55}\text{Fe}$	2.05	ϵ	2.7 yr	-	-
${}^{56}\text{Fe}$	91.7%	${}^{56}\text{Fe}({}^7\text{Li},n){}^{62}\text{Cu}$	9.04	β^+	9.8 min	2.93	0.51
		${}^{56}\text{Fe}({}^7\text{Li},{}^3\text{He}){}^{60}\text{Co}$	1.02	β^-	5.3 yr	0.321	1.17 1.33
		${}^{56}\text{Fe}({}^7\text{Li},2n){}^{61}\text{Cu}$	0.14	β^+	3.4 hr	1.22	0.51
		${}^{56}\text{Fe}({}^7\text{Li},2p){}^{62}\text{Co}$	2.65	β^-	1.65 hr	1.24	0.068
		${}^{56}\text{Fe}({}^7\text{Li},\alpha n){}^{58}\text{Co}$	3.64	ϵ, β^+	71 da	0.47	0.81

continued

Table III Continued

Radioactivities Induced by ${}^7\text{Li}$ Ions on Chromium, Iron and Nickel

Target		Nuclear Reaction		Residual Nucleus			
Iso- tope	Abun- dance	Reaction	Q-Value (MeV)	Decay Mode	Half Life	E_{β} (MeV)	E_{γ} (MeV)
${}^{57}\text{Fe}$	2.1%	${}^{57}\text{Fe}({}^7\text{Li}, {}^3\text{He}){}^{61}\text{Co}$	2.73	β^-	1.65 hr	1.24	0.068
		${}^{57}\text{Fe}({}^7\text{Li}, \alpha){}^{60}\text{Co}$	13.96	β^-	5.27 yr	0.321	1.17 1.33
		${}^{57}\text{Fe}({}^7\text{Li}, 2n){}^{62}\text{Cu}$	1.40	β^+	9.8 min	2.93	0.51
		${}^{57}\text{Fe}({}^7\text{Li}, 2p){}^{62}\text{Co}$	1.68	β^-	14 min	2.88	1.17
		${}^{57}\text{Fe}({}^7\text{Li}, 2p){}^{62m}\text{Co}$	1.30	β^-	1.5 min	4.1	1.17
${}^{58}\text{Ni}$	68.3%	${}^{58}\text{Ni}({}^7\text{Li}, n){}^{64}\text{Ga}$	5.54	β^+	2.6 min	6.05	0.51
		${}^{58}\text{Ni}({}^7\text{Li}, d){}^{63}\text{Zn}$	3.76	β^+	38 min	2.34	0.51
		${}^{58}\text{Ni}({}^7\text{Li}, t){}^{62}\text{Zn}$	0.85	ϵ, β^+	9.3 hr	0.67	0.51
		${}^{58}\text{Ni}({}^7\text{Li}, {}^3\text{He}){}^{62}\text{Cu}$	2.56	β^+	9.8 min	2.93	0.51
		${}^{58}\text{Ni}({}^7\text{Li}, \alpha){}^{61}\text{Cu}$	14.24	β^+	3.4 hr	1.22	0.51
		${}^{58}\text{Ni}({}^7\text{Li}, \alpha n){}^{60}\text{Cu}$	2.56	β^+	23 min	3.77	1.76 1.33
${}^{60}\text{Ni}$	26.1%	${}^{60}\text{Ni}({}^7\text{Li}, n){}^{66}\text{Ga}$	6.07	β^+	9.5 hr	4.15	0.51
		${}^{60}\text{Ni}({}^7\text{Li}, d){}^{65}\text{Zn}$	3.22	ϵ	245 da	-	1.115
		${}^{60}\text{Ni}({}^7\text{Li}, {}^3\text{He}){}^{64}\text{Cu}$	0.93	β^-	12.8 hr	0.575	-
				β^+	12.8 hr	0.656	0.51
${}^{60}\text{Ni}({}^7\text{Li}, \alpha n){}^{62}\text{Cu}$	2.75	β^+	9.8 min	2.93	0.51		

Table IV

Radioactivities Induced by ${}^7\text{Li}$ Ions on Copper and Zinc

Target		Nuclear Reaction		Residual Nucleus			
Iso- tope	Abun- dance	Reaction	Q-Value (MeV)	Decay Mode	Half Life	E_{β} (MeV)	E_{γ} (MeV)
${}^{63}\text{Cu}$	69.1%	${}^{63}\text{Cu}({}^7\text{Li},n){}^{69}\text{Ge}$	8.35	ϵ, β^+	39 hr	1.20	0.51
		${}^{63}\text{Cu}({}^7\text{Li},d){}^{68}\text{Ga}$	3.26	β^+	68 min	1.90	0.51
		${}^{63}\text{Cu}({}^7\text{Li},t){}^{67}\text{Ga}$	1.24	ϵ	78 hr	-	0.093
		${}^{63}\text{Cu}({}^7\text{Li},\alpha n){}^{65}\text{Zn}$	4.75	ϵ	245 da	-	1.115
		${}^{63}\text{Cu}({}^7\text{Li},{}^6\text{Li}){}^{64}\text{Cu}$	0.66	β^- β^+	12.8 hr 12.8 hr	0.575 0.656	- 0.51
${}^{65}\text{Cu}$	30.9%	${}^{65}\text{Cu}({}^7\text{Li},n){}^{71}\text{Ge}$	9.47	ϵ	11 da	-	-
		${}^{65}\text{Cu}({}^7\text{Li},d){}^{70}\text{Ga}$	3.40	β^-	21 min	1.65	-
		${}^{65}\text{Cu}({}^7\text{Li},{}^3\text{He}){}^{69}\text{Zn}$	1.14	β^-	57 min	0.91	-
${}^{64}\text{Zn}$	48.9%	${}^{64}\text{Zn}({}^7\text{Li},n){}^{70}\text{As}$	5.16	β^+	50 min	2.1	1.04
		${}^{64}\text{Zn}({}^7\text{Li},d){}^{69}\text{Ge}$	2.27	ϵ, β^+	39 hr	1.20	0.51
		${}^{64}\text{Zn}({}^7\text{Li},t){}^{68}\text{Ge}$	0.53	ϵ	287 da	-	-
		${}^{64}\text{Zn}({}^7\text{Li},{}^3\text{He}){}^{68}\text{Ga}$	1.05	β^+	68 min	1.90	0.51
		${}^{64}\text{Zn}({}^7\text{Li},\alpha){}^{67}\text{Ga}$	13.35	ϵ	78 hr	-	0.093
		${}^{64}\text{Zn}({}^7\text{Li},\alpha n){}^{66}\text{Ga}$	2.12	β^+	9.5 hr	4.15	0.51
		${}^{64}\text{Zn}({}^7\text{Li},{}^6\text{Li}){}^{65}\text{Zn}$	0.74	ϵ	245 da	-	1.115

continued

Table IV Continued

Radioactivities Induced by ${}^7\text{Li}$ Ions on Copper and Zinc

Target		Nuclear Reaction		Residual Nucleus			
Iso- tope	Abun- dance	Reaction	Q-Value (MeV)	Decay Mode	Half Life	E_{β} (MeV)	E_{γ} (MeV)
${}^{66}\text{Zn}$	27.8%	${}^{66}\text{Zn}({}^7\text{Li},n){}^{72}\text{As}$	6.17	β^+	26 hr	2.50	0.835
		${}^{66}\text{Zn}({}^7\text{Li},d){}^{71}\text{Ge}$	2.79	ϵ	11 da	-	-
		${}^{66}\text{Zn}({}^7\text{Li},{}^3\text{He}){}^{70}\text{Ga}$	-0.01	β^-	21 min	1.65	-
		${}^{66}\text{Zn}({}^7\text{Li},\alpha n){}^{68}\text{Ga}$	2.60	β^+	68 min	1.90	0.51
${}^{68}\text{Zn}$	18.6%	${}^{68}\text{Zn}({}^7\text{Li},n){}^{74}\text{As}$	7.70	ϵ, β^+ β^-	18 da 18 da	1.53 1.35	0.60 0.64
		${}^{68}\text{Zn}({}^7\text{Li},2p){}^{73}\text{Ga}$	0.08	β^-	4.9 hr	1.19	0.29
		${}^{68}\text{Zn}({}^7\text{Li},\alpha n){}^{70}\text{Ga}$	3.31	β^-	21 min	1.65	-

energy. On the other hand, lithium-induced reactions are inhibited by a repulsive Coulomb barrier between the incident lithium nucleus and the target nucleus. For a nucleus of atomic number Z_1 and mass number A_1 incident on a target of atomic number Z_2 and mass number A_2 , the energy of this barrier is E_b (MeV) = $1.44Z_1Z_2/R$ where R is expressed in fermis and is given by $R = 1.2(A_1^{1/3} + A_2^{1/3})$. The value of this barrier is listed in Table V for each target element. For elements consisting of several stable isotopes, the most abundant isotope is used. For incident energies below the barrier, the lithium must tunnel quantum-mechanically through the barrier to initiate a nuclear reaction. The probability for tunneling increases rapidly with increasing energy below the barrier. Therefore, for medium-weight targets (Ti to Zn) where E_b is comparable to or larger than 15 MeV, cross sections for lithium-induced reactions below 15 MeV are expected to be small and to increase rapidly as the incident lithium energy increases. For carbon and aluminum targets, the Coulomb barrier is exceeded for incident energies greater than 5.1 and 9.5 MeV, respectively. If the ${}^7\text{Li}$ energy approaches or exceeds these barrier heights, appreciable radioactivity may be produced by reactions on these targets.

In a survey of the published literature, measured cross sections or thick-target yields in the energy range of interest were found only for the ${}^{12}\text{C}({}^7\text{Li},n){}^{18}\text{F}$ reaction.^{5,6} No cross sections or thick-target yields were found for the other reactions listed in Tables I through IV. Thick-target yields or cross sections have been measured for lithium-induced reactions on other low-atomic-number targets (i.e., ${}^6\text{Li}$, ${}^7\text{Li}$, ${}^9\text{Be}$, ${}^{10}\text{B}$, ${}^{14}\text{N}$, ${}^{16}\text{O}$, ${}^{19}\text{F}$ and ${}^{23}\text{Na}$) in the energy range below 15 MeV.⁵⁻⁷ Invariably, these results indicate that the reaction yields increase rapidly with increasing lithium energy until the incident energy becomes comparable with the Coulomb barrier. This behavior suggests that the reactions in this survey are dominated by Coulomb-barrier effects in the energy range of interest.

To estimate the magnitude of Coulomb-barrier inhibition, the barrier penetrability for ${}^7\text{Li}$ is evaluated for the different

Table V

Coulomb Barrier Energies for ${}^7\text{Li}$
on Different Target Nuclei

Target	Z_2	A_2	E_b (MeV)
C	6	12	5.14
Al	13	27	9.52
Ti	22	48	14.3
V	23	51	14.7
Cr	24	52	15.3
Fe	26	56	16.3
Ni	28	58	17.4
Cu	29	63	17.7
Zn	30	64	18.3

targets in this survey. In general, the barrier penetration factor is expressed in terms of tabulated Coulomb functions.⁸ However, an analytic expression can be obtained for s-waves in the WKB approximation.⁹ In this approximation it is assumed that the wave function of the incoming lithium is slowly varying in the region under the barrier. In this region, the wave function is not sinusoidal, but exponentially decaying. The WKB approximation is good if the lithium energy is close to the barrier potential, E_b , and deteriorates as the lithium energy decreases. We use the analytic WKB expression for the barrier penetration factor to compare reaction yields for different targets with lithium energies near E_b . If the incoming lithium is not described by an s-wave, an additional angular momentum barrier should be included. Neglecting this barrier results in larger penetrations and larger yield estimates.

In the WKB approximation, the s-wave Coulomb-barrier penetration factor⁹ is given by $P = \exp(-\gamma)$ where

$$\gamma = 8\pi Z_1 Z_2 e^2 / (hv) \{ \cos^{-1}(T/E_b)^{1/2} - (T/E_b)^{1/2} (1 - T/E_b)^{1/2} \}. \quad (1)$$

In this expression, $T = \frac{1}{2}\mu v^2$ is the incident ${}^7\text{Li}$ energy, and $\mu = A_1 A_2 / (A_1 + A_2)$ is the reduced mass. This penetration factor is presented in Figs. 1 and 2 as a function of the ${}^7\text{Li}$ energy for the targets in this survey. The values of Z_2 and A_2 listed in Table V are used for these calculations. The penetration factors are expressed in yield units by normalizing the carbon-target penetration factor to measured thick-target yields⁶ for the ${}^{12}\text{C}({}^7\text{Li}, n){}^{18}\text{F}$ reaction on a carbon target in the range from 2.5 to 3.5 MeV. For the targets in Fig. 1, the penetration factors extend up to the Coulomb barrier. As the atomic number of the target is increased, these curves shift to higher ${}^7\text{Li}$ energy. For the targets in Fig. 2, the Coulomb barriers are larger than 15 MeV (see Table V). Again, the penetration factors shift to higher ${}^7\text{Li}$ energy as the atomic number of the target is increased.

The curves in Figs. 1 and 2 are intended to show the trend in reaction yield due to the Coulomb barrier. Thick-target

yields of up to 10^{-5} reactions/ ${}^7\text{Li}$ can be expected for carbon and aluminum. Somewhat lower yields are estimated for the higher atomic number targets. Actual yields may be larger or smaller than these estimates due to different nuclear reaction mechanisms and due to different internal structures of the target and final nuclei in the reactions.^{10,11} For example, a reaction such as (${}^7\text{Li},n$) requires that all of the charged particles in the ${}^7\text{Li}$ be transferred to the target to form the final nucleus. Such a reaction may be expected to proceed through the formation of a compound nucleus. In this case, the reaction is inhibited by the Coulomb barrier as previously described. On the other hand, a reaction such as (${}^7\text{Li},{}^6\text{Li}$) may proceed by simply transferring a neutron; the charged particles in the ${}^7\text{Li}$ need not penetrate the Coulomb barrier but only get sufficiently close to the target for neutron transfer to occur. Coulomb-barrier inhibition is less in this case. In the present survey, the largest Q-values tend to occur for (${}^7\text{Li},n$) and (${}^7\text{Li},p$) reactions which have the largest barrier inhibitions. The less inhibited (${}^7\text{Li},{}^6\text{Li}$) reactions tend to have small positive Q-values, and the (${}^7\text{Li},{}^6\text{He}$) reactions have negative Q-values. These kinematic trends suggest that effects due to different nuclear reaction mechanisms are not likely to overwhelm the trends due to Coulomb-barrier inhibition.

The (${}^7\text{Li},\alpha$) and (${}^7\text{Li},t$) reactions are favored by the internal structure of ${}^7\text{Li}$. The ${}^7\text{Li}$ nucleus has a significant ($\alpha+t$) cluster structure so that these reactions may proceed by the transfer of either an α -particle or a triton from the ${}^7\text{Li}$ to the target.^{10,11} These cluster-transfer reactions resemble stripping reactions which proceed selectively to ground and excited states of the final nucleus which have the appropriate cluster structure. To evaluate the probability of such reactions requires detailed knowledge of the nuclear structure of the target and of the final nucleus and is beyond the scope of this survey.

In conclusion, nuclear reactions, which are induced by up to 15-MeV ${}^7\text{Li}$ ions and which produce radioactivity, are surveyed for several commonly used target materials: carbon, aluminum, steel, brass, and a titanium alloy. Positive Q-value reactions

are identified along with the decay properties of the radioactive nuclei. Yields for these reactions are dominated by penetration of the Coulomb barrier in the entrance channel. Barrier-penetration calculations indicate the reaction yields decrease as the atomic number is increased and increase rapidly with ${}^7\text{Li}$ energy up to the Coulomb barrier.

Acknowledgements

The encouragement of John Maenchen of Sandia National Laboratories to carry out this survey is appreciated. This work was supported by the Department of Energy through Sandia National Laboratories.

REFERENCES

1. K.A. Keller, J. Lange and H. Münsel, in Landolt-Bornstein Numerical Data and Functional Relationships in Science and Technology Vol. 5, Part a, Q-Values, edited by H. Schopper (Springer-Verlag, New York, 1973).
2. Chart of the Nuclides, Knolls Atomic Power Laboratory, 11th Edition, April, 1972.
3. C.M. Lederer, J.M. Hollander and I. Perlman, Table of Isotopes, 6th Edition (John Wiley, New York, 1967).
4. J.B. Marion and F.C. Young, Nuclear Reaction Analysis (North-Holland, Amsterdam, 1968), p. 157.
5. E. Norbeck, Jr. and C.S. Littlejohn, *Phys. Rev.* 108, 754 (1957).
6. E. Norbeck, *Phys. Rev.* 121, 824 (1961).
7. R.R. Carlson and H.W. Wyborny, *Phys. Rev.* 178, 1529 (1969); D.J. Johnson and M.A. Waggoner, *Phys. Rev. C* 2, 41 (1970); H.W. Wyborny and R.R. Carlson, *Phys. Rev. C* 3, 2185 (1971).
8. J.M. Blatt and V.F. Weisskopf, Theoretical Nuclear Physics (John Wiley, New York, 1952), Chapt. 8.
9. R.D. Evans, The Atomic Nucleus (McGraw Hill, New York, 1955) pp. 874-6.
10. R.R. Carlson, "Lithium Induced Reactions," in Nuclear Research with Low Energy Accelerators, J.B. Marion and D.M. Van Patter, Eds. (Academic Press, New York, 1967), pp. 475-496.
11. A.A. Ogloblin, "The Study of Lithium-Induced Reactions at the Kurchatov Atomic Energy Institute," in Nuclear Reactions Induced by Heavy Ions, R. Bock and W.R. Hering, Eds. (North Holland, Amsterdam, 1970), pp. 231-262.

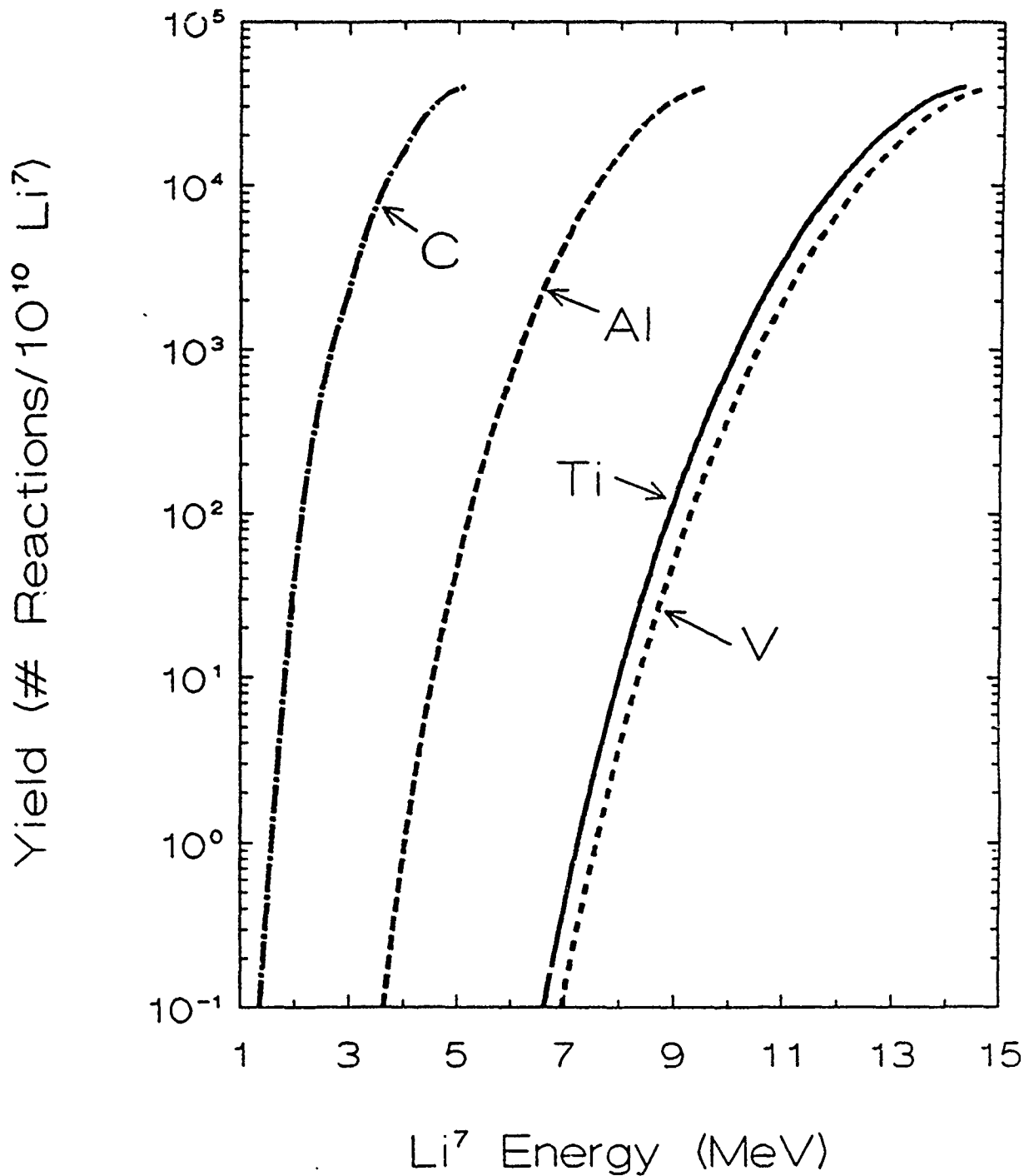


Fig. 1. Coulomb barrier penetration factors for ⁷Li nuclei incident on carbon, aluminum, titanium and vanadium targets. The penetration factor is expressed in yield by normalizing to measured thick-target yields for the ¹²C(⁷Li,n)¹⁸F reaction.

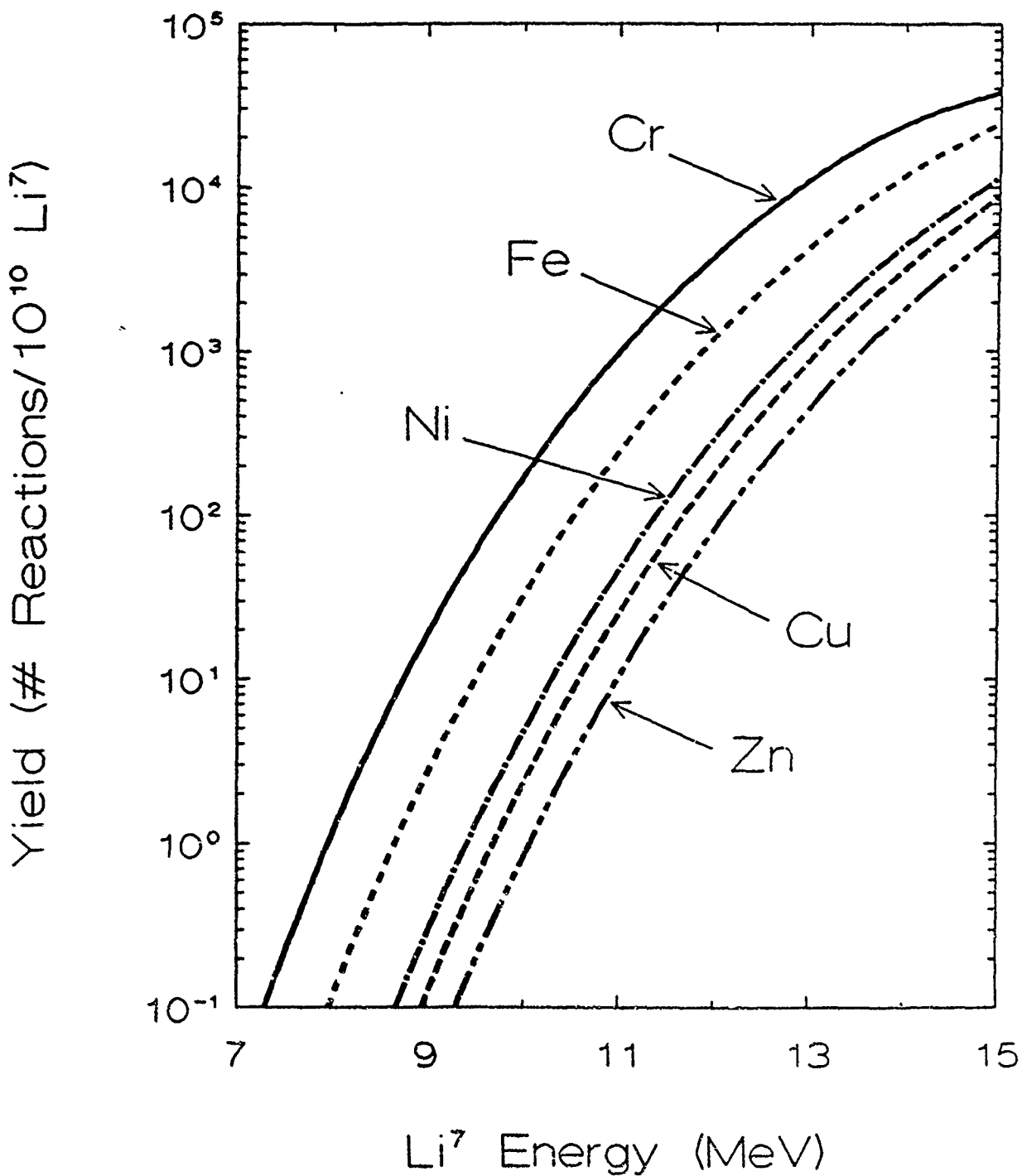


Fig. 2. Coulomb barrier penetration factors for ${}^7\text{Li}$ nuclei incident on chromium, iron, nickel, copper and zinc targets. The penetration factor is expressed in yield by normalizing to measured thick-target yields for the ${}^{12}\text{C}({}^7\text{Li},n){}^{18}\text{F}$ reaction.



NRL/MR/6770-92-7155

**Survey of Nuclear Activations for Intense Proton
and Deuteron Beams**

FRANK C. YOUNG

*Pulsed Power Physics Branch
Plasma Physics Division*

AND

DAVID V. ROSE

*JAYCOR
Vienna, VA 22180-2270*

December 24, 1992

REPORT DOCUMENTATION PAGE

Form Approved
OMB No. 0704-0188

Public reporting burden for this collection of information is estimated to average 1 hour per response, including the time for reviewing instructions, searching existing data sources, gathering and maintaining the data needed, and completing and reviewing the collection of information. Send comments regarding this burden estimate or any other aspect of this collection of information, including suggestions for reducing this burden, to Washington Headquarters Services, Directorate for Information Operations and Reports, 1215 Jefferson Davis Highway, Suite 1204, Arlington, VA 22202-4302, and to the Office of Management and Budget, Paperwork Reduction Project (0704-0188), Washington, DC 20503.

1. AGENCY USE ONLY (Leave Blank)	2. REPORT DATE December 24, 1992	3. REPORT TYPE AND DATES COVERED Interim	
4. TITLE AND SUBTITLE Survey of Nuclear Activations for Intense Proton and Deuteron Beams			5. FUNDING NUMBERS SNL F.A.O. No. AA-9158 under DOE Contract No. DE-04-76-DP00789
6. AUTHOR(S) Frank C. Young and David V. Rose*			8. PERFORMING ORGANIZATION REPORT NUMBER NRL/MR/6670-92-7155
7. PERFORMING ORGANIZATION NAME(S) and ADDRESS(ES) Naval Research Laboratory Washington, DC 20375-5320			
9. SPONSORING/MONITORING AGENCY NAME(S) AND ADDRESS(ES) Sandia National Laboratories Albuquerque, NM 87185			10. SPONSORING/MONITORING AGENCY REPORT NUMBER
11. SUPPLEMENTARY NOTES *JAYCOR, Vienna, VA 22180-2270			
12a. DISTRIBUTION/AVAILABILITY STATEMENT Approved for public release; distribution unlimited.			12b. DISTRIBUTION CODE
13. ABSTRACT (<i>Maximum 200 words</i>) Proton- and deuteron-induced nuclear reactions which produce radioactivities are surveyed for application to experiments with intense ion beams from pulsed power generators. Positive Q-value reactions with up to 10-MeV protons or deuterons on carbon, aluminum, titanium-alloy, steel, and brass targets are identified. For each radioactivity, the half-life and decay products are tabulated. Measured cross sections from the published literature are used to identify reaction yields. For protons, thick-target yields are evaluated for (p,n) reactions on these targets. For deuterons, thick-target yields are evaluated for several (d,n), (d,p) and (d,α) reactions on these targets.			
14. SUBJECT TERMS Proton-induced nuclear reactions; Deuteron-induced nuclear reactions; Intense proton beam; Intense deuteron beam; Radioactive products			15. NUMBER OF PAGES 48
17. SECURITY CLASSIFICATION OF REPORT UNCLASSIFIED			16. PRICE CODE
18. SECURITY CLASSIFICATION OF THIS PAGE UNCLASSIFIED		19. SECURITY CLASSIFICATION OF ABSTRACT UNCLASSIFIED	20. LIMITATION OF ABSTRACT UL

CONTENTS

INTRODUCTION	1
CARBON TARGET	2
ALUMINUM TARGET	5
PROTON-INDUCED RADIOACTIVITIES IN THE ALLOY TARGETS	6
DEUTERON-INDUCED RADIOACTIVITIES IN THE ALLOY TARGETS	12
SUMMARY	23
ACKNOWLEDGMENTS	25
REFERENCES	26

SURVEY OF NUCLEAR ACTIVATIONS FOR INTENSE PROTON AND DEUTERON BEAMS

I. Introduction

Nuclear reactions induced by light-ion beams which lead to radioactive products are of interest to pulsed-power experiments on the Sabre generator at Sandia National Laboratories. Light-ion beams (proton, deuteron or lithium) may be accelerated through 0 to 10 MV on this generator. Radioactivities induced in the commonly used materials, carbon, aluminum, steel, and brass may pose a radiological hazard. Because a titanium alloy is used in the ion-diode region of the Sabre generator, radioactivity induced by reactions in this alloy are also considered. Radioactivities induced by lithium ions in these targets have already been surveyed.¹ In this report, radioactive products from proton and deuteron beams incident on carbon, aluminum, titanium-alloy, steel, and brass targets are identified. For these singly-charged ion beams, incident energies of up to 10 MeV are considered.

Nuclear reactions on these targets which lead to radioactive nuclei are identified. Proton- and deuteron-induced reactions leading to the following products are considered: n, p, d, t, ³He, and α . Both positive and negative Q-value reactions are included. The tabulation of Keller et al.² is used as a guide to identify the more energetically favorable reactions. Tabulated Q-values are based on mass excesses from Ref. 3. Positive Q-value reactions are allowed by kinematics for any bombarding energy. Negative Q-value reactions have a threshold energy given by $(M_1 + M_2)(-Q)/M_2$ where M_1 is the incident projectile mass and M_2 is the target mass.

For each reaction, the residual nucleus and its decay properties are tabulated. Reactions which produce the long-lived isotopes ⁵³Mn ($T_{1/2} = 3.7 \times 10^6$ yr), ⁵⁹Ni ($T_{1/2} = 8 \times 10^4$ yr), and ⁶³Ni ($T_{1/2} = 10^2$ yr) are not included in this survey. Unrealistically large ion-beam fluences would be required to produce significant activities of these long-lived isotopes. The decay modes are

identified as β^- for electron decay, β^+ for positron decay, and ϵ for electron capture. Both β^+ and ϵ are listed when these decay modes are of comparable intensity. For β -decay, E_β is the end-point energy of the β -spectrum, and E_γ is the energy of the most intense γ -ray(s) associated with the decay. The decay modes, half-lives, end-point energies and γ -ray energies are taken from Ref. 4. The most intense γ -decays are identified from Ref. 5.

Measured cross sections for some of these reactions were found in the published literature. Compilations in Ref. 6 were used to locate published sources prior to 1976. Compilations in Ref. 7 were used to locate additional sources. The computerized catalog DIALOG⁸ was used for the period from 1976 to 1992. Since DIALOG does not include all the journals of interest in this time period, Physics Abstracts was used to supplement this survey. No attempt was made to incorporate cross sections from unpublished technical reports. Cross sections determined from residual activities, rather than prompt particle emissions, are the desired quantities. In many cases, excitation functions (cross sections as a function of incident proton energy) are determined by measuring delayed radioactivities induced in stacked foils. For reactions where sufficient excitation functions are available, the cross sections are combined with known stopping cross sections⁹ to determine thick-target yields. Graphs of thick-target yield versus incident ion energy are included in this report.

Reactions on carbon are discussed in Sec. II. Reactions on aluminum are discussed in Sec. III. Proton-induced reactions on titanium alloy, steel, and brass are discussed in Sec. IV. Deuteron-induced reactions on these alloy targets are discussed in Sec. V. For the alloy targets, only isotopes for which the product of the isotopic abundance and the alloy proportion exceeds 1% are included because these isotopes are expected to be the primary sources of radioactivity.

II. Carbon Target

Nuclear reactions on carbon leading to radioactive products

are listed in Table I. A natural carbon target consists of two isotopes, ^{12}C and ^{13}C , with the abundances given in Table I. For thick-target calculations, the target is assumed to be natural-abundance carbon. A brief discussion of each reaction listed in Table I follows.

$^{12}\text{C}(p,\gamma)^{13}\text{N}$: The thick-target yield for this reaction below 3 MeV is determined by resonances at 457 keV and 1.70 MeV.¹⁰ A graph of the thick-target yield is given in Fig. 1. Above 3 MeV, the ^{13}N activity from the $^{13}\text{C}(p,n)$ reaction exceeds the $^{12}\text{C}(p,\gamma)$ activity even though the isotopic abundance of ^{13}C in natural carbon is only 1.1%. For a plasma source with a natural deuterium abundance (0.015%) operating in the space-charge-limited regime, the ^{13}N activity from the $^{12}\text{C}(d,n)$ reaction for deuterons above 1.3 MeV exceeds the (p,γ) reaction yield.¹⁰

$^{13}\text{C}(p,n)^{13}\text{N}$: The threshold for this reaction is 3.25 MeV. The thick-target yield in Figs. 1 and 2 is based on measured cross sections.¹¹ It should be noted that the ^{13}N activity can also be produced by the $^{16}\text{O}(p,\alpha)^{13}\text{N}$ reaction with comparable cross sections¹² for proton energies above 7 MeV.

$^{12}\text{C}(d,n)^{13}\text{N}$: The threshold for this reaction is 0.33 MeV.¹³ The thick-target yield from 2 to 5 MeV has been reported for a natural carbon target,¹⁴ and this yield has been extended to lower energies using measured relative cross sections.¹⁰ The measured cross sections of Wilkinson¹⁵ were used to extend the thick-target yield to 10 MeV. The thick-target yield for this reaction is given in Figs. 1 and 2. This reaction is the most prolific source of radioactivity for a carbon target over the energy range of interest.

$^{13}\text{C}(d,p)^{14}\text{C}$: This reaction was not seriously considered in this survey for three reasons. First, the small natural abundance of ^{13}C reduces the radioactivity from this reaction by two orders of magnitude for a natural carbon target. Second, the activity will be small because the ^{14}C half-life is long, e.g., it takes more radioactive nuclei to produce a given activity for a longer half-life. Third, the ^{14}C decay produces only a low energy β -particle which is easily shielded.

Table I

Radioactivities Induced by Protons or Deuterons
on Carbon and Aluminum

Target		Nuclear Reaction		Residual Nucleus			
Iso- tope	Abun- dance	Reaction	Q-Value (MeV)	Decay Mode	Half Life	E_{β} (MeV)	E_{γ} (MeV)
C	98.9%	$^{12}\text{C}(\text{p}, \gamma)^{13}\text{N}$	+1.94	β^+	10 min	1.20	0.51
		$^{12}\text{C}(\text{d}, \text{n})^{13}\text{N}$	-0.28	β^+	10 min	1.20	0.51
C	1.1%	$^{13}\text{C}(\text{p}, \text{n})^{13}\text{N}$	-3.00	β^+	10 min	1.20	0.51
		$^{13}\text{C}(\text{d}, \text{p})^{14}\text{C}$	+5.95	β^-	5.7 yr	0.16	-
^{27}Al	100%	$^{27}\text{Al}(\text{p}, \text{n})^{27}\text{Si}$	-5.59	β^+	4.2 s	3.8	0.51
		$^{27}\text{Al}(\text{p}, \text{d})^{26}\text{Al}$	-10.8	β^+, ϵ	6.4 s	3.21	0.51
		$^{27}\text{Al}(\text{d}, \text{p})^{28}\text{Al}$	+5.51	β^-	2.24 min	2.86	1.78
		$^{27}\text{Al}(\text{d}, \alpha\text{p})^{24}\text{Na}$	-5.36	β^-	15.0 hr	1.39	2.75 1.37
		$^{27}\text{Al}(\text{d}, 2\text{p})^{27}\text{Mg}$	-4.06	β^-	9.45 min	1.77	0.844

III. Aluminum Target

Nuclear reactions on aluminum leading to radioactive products are also listed in Table I. Aluminum consists of a single isotope, ^{27}Al . The target is assumed to be 100% aluminum for thick-target calculations. A brief discussion of each reaction in Table I follows.

$^{27}\text{Al}(p,n)^{27}\text{Si}$: The reaction threshold is 5.8 MeV. The thick-target yield in Fig. 3 is based on measured cross sections.¹⁶

$^{27}\text{Al}(p,d)^{26}\text{Al}$: The threshold for this reaction is 11.6 MeV. No activity is possible for proton energies below 10 MeV.

$^{27}\text{Al}(d,p)^{28}\text{Al}$: The cross section for this reaction is not well known. A best fit to cross sections measured in three different experiments (Refs. 17, 18 and 19) was used to generate a thick-target yield to 5 MeV for this reaction.²⁰ This best-fit cross section curve is shown in Fig. 4, and the thick-target yield is given in Fig. 3. Cross sections from Ref. 19 were used to extend this yield curve to 10 MeV. Two more recent cross section measurements^{21,22} are much larger than the best fit from Ref. 20, as shown in Fig. 4. The reason for the large differences ($\times 160$ at 3 MeV and $\times 4$ at 6.8 MeV) is not known. The values in Ref. 21 (0.6 to 3.2 MeV) are based on thick-target measurements and are much larger than (d,p) cross sections on other nuclei in this mass range.⁷ In a thick target, additional ^{28}Al activity may be produced by the $^{27}\text{Al}(n,\gamma)^{28}\text{Al}$ reaction induced by neutrons from the $^{27}\text{Al}(d,n)^{28}\text{Si}$ reaction in the same target. This process may account for the large cross sections in Refs. 21 and 22. This process was shown to be negligible for the measurements in Ref. 19.

$^{27}\text{Al}(d,\alpha p)^{24}\text{Na}$: The kinematic threshold for this reaction is 5.8 MeV, but measured excitation functions^{22,23} for this reaction indicate that the cross section is small below 10 MeV. Therefore no significant activity is expected from this reaction.

$^{27}\text{Al}(d,2p)^{27}\text{Mg}$: The kinematic threshold for this reaction is 4.4 MeV, but measured cross sections^{22,24} indicate that the yield is small below 10 MeV. Therefore, no thick-target yield was evaluated for this reaction.

IV. Proton-Induced Radioactivities in the Alloy Targets

For the medium-weight nuclei in titanium-alloy, steel, and brass targets, radioactivities are produced typically by either (p,n) or (p, α) reactions. Radioactivities produced by these reactions are identified, and reaction yields are briefly discussed for constituent elements of these alloys. Thick-target yields for these targets are not reduced by the alloy composition since these may change from one material to another.

A. Titanium-Alloy Target

The titanium 6-4 alloy used in the ion-diode region of the Sabre generator consists of 90%-titanium, 6%-aluminum and 4%-vanadium. Titanium consists of five stable isotopes with abundances ranging from 5% to 74%, while vanadium is 99.8% ^{51}V . Radioactivity produced by irradiation of the aluminum in this alloy was discussed in Sec. III. Proton-induced reactions on titanium and vanadium leading to radioactive products are listed in Table II. A brief discussion of the (p,n) and (p, α) reactions in Table II follows.

(p,n) Reactions: The threshold for the (p,n) reaction on ^{46}Ti is 8.0 MeV. Immediately above threshold, ^{46}V activity has been measured,²⁵ but the cross section was not reported. The (p,n) reactions on ^{47}Ti and ^{48}Ti have lower thresholds of 3.78 and 4.90 MeV, respectively, and their cross sections have been measured.²⁶ Smooth fits were made to these cross sections, and thick-target yields based on these cross sections are presented in Fig. 5 for a natural-abundance titanium target. These reactions are primary sources of radioactivity from the proton bombardment of titanium. To produce significant activation of the long-lived ^{49}V isotope by the $^{49}\text{Ti}(p,n)$ reaction, extremely large proton fluences would be required. Furthermore, ^{49}V decays only by electron capture so its radiation hazard is minimal. For vanadium, the threshold for the (p,n) reaction is 1.56 MeV, and cross sections for this reaction have been determined from 3.1 to 10.4 MeV by measuring ^{51}Cr activity²⁷ and from 1.6 to 4.5 MeV by measuring neutron emission.²⁸ Independent measurements with

Table II

Radioactivities Induced by Protons on Titanium and Vanadium

Target		Nuclear Reaction		Residual Nucleus			
Iso- tope	Abun- dance	Reaction	Q-Value (MeV)	Decay Mode	Half Life	E_{β} (MeV)	E_{γ} (MeV)
^{46}Ti	8.0%	$^{46}\text{Ti}(p,n)^{46}\text{V}$	-7.85	β^+	0.43 s	6.04	0.51
		$^{46}\text{Ti}(p,\alpha)^{43}\text{Sc}$	-3.09	β^+	3.89 hr	1.20	0.51
^{47}Ti	7.5%	$^{47}\text{Ti}(p,n)^{47}\text{V}$	-3.70	β^+	31 min	1.90	0.51
		$^{47}\text{Ti}(p,\alpha)^{44}\text{Sc}$	-2.25	β^+	3.93 hr	1.47	1.16
^{48}Ti	73.7%	$^{48}\text{Ti}(p,n)^{48}\text{V}$	-4.80	β^+, ϵ	16.0 da	0.70	1.31 0.98
^{49}Ti	5.5%	$^{49}\text{Ti}(p,n)^{49}\text{V}$	-1.39	ϵ	331 da	-	-
		$^{49}\text{Ti}(p,\alpha)^{46}\text{Sc}$	-1.94	β^-	83.8 da	0.36	1.12 0.89
^{50}Ti	5.3%	$^{50}\text{Ti}(p,\alpha)^{47}\text{Sc}$	-2.24	β^-	3.41 da	0.44	0.16
^{51}V	99.8%	$^{51}\text{V}(p,n)^{51}\text{Cr}$	-1.53	ϵ	27.7 da	-	0.32

these two techniques²⁹ are consistent and are in agreement with the measurements in Ref. 28. Therefore, the cross sections from Ref. 27 are scaled to values in Ref. 28 to provide cross sections from 1.6 to 10.5 MeV. A smooth fit to these cross sections was used to calculate the thick-target yield presented in Fig. 6.

(p,α) Reactions: Thresholds for the (p,α) reactions on ⁴⁶Ti, ⁴⁷Ti, ⁴⁹Ti and ⁵⁰Ti range from 2.0 to 3.2 MeV. The (p,α) reaction on ⁴⁸Ti, the most abundant isotope, produces no radioactivity. These reactions tend to have small cross sections as described in Sec. IVB. The reactions on ⁴⁶Ti and ⁵⁰Ti have been measured by detecting α-emission, and ground-state differential cross-sections of only 0.03 to 0.4 mb/sr for 9- to 10-MeV protons have been reported.³⁰ For 14-MeV protons, total cross sections of 30 mb for ⁴⁸Ti and 25 mb for ⁵¹V have been measured.³¹ Because cross sections below 10 MeV are expected to be small and measured excitation functions are not available in the literature, no thick-target yields were evaluated for these reactions.

B. Steel and Brass Targets

These alloy targets contain several elements in different proportions. For this survey, a 70%-iron, 20%-chromium, 10%-nickel composition is assumed for #304 stainless steel, and a 67%-copper, 33%-zinc composition is assumed for brass. Each of these elements consists of several stable isotopes with significant fractional abundances. Proton-induced reactions leading to radioactive products are listed in Table III for a steel target and in Table IV for a brass target. A brief discussion of the reactions listed in these Tables follows.

(p,n) Reactions: Thresholds for the (p,n) reactions range from 1.65 MeV for ⁵⁷Fe to 9.51 MeV for ⁵⁸Ni. These reactions have been studied extensively and their cross sections increase rapidly from zero at threshold to relatively large values (10²-10³ mb) a few MeV above threshold. For chromium, two activities are produced: the 5.6-da ground state and a 21-min isomer. The symbol ^{52m}Mn in Tables III and VI refers to an isomeric state where ⁵²Mn is the ground state. Thick-target yields for the (p,n) reaction on ⁵²Cr, calculated using cross sections from

Table III

Radioactivities Induced by Protons on Chromium, Iron and Nickel

Target		Nuclear Reaction		Residual Nucleus			
Iso- tope	Abun- dance	Reaction	Q-Value (MeV)	Decay Mode	Half Life	E_{β} (MeV)	E_{γ} (MeV)
^{52}Cr	83.8%	$^{52}\text{Cr}(p,n)^{52}\text{Mn}$	-5.49	ϵ, β^+	5.6 da	0.57	1.434 0.94 0.74
		$^{52}\text{Cr}(p,n)^{52m}\text{Mn}$	-5.87	β^+	21 min	2.63	1.434
		$^{52}\text{Cr}(p,\alpha)^{49}\text{V}$	-2.60	ϵ	331 da	-	-
^{54}Fe	5.8%	$^{54}\text{Fe}(p,n)^{54}\text{Co}$	-9.03	β^+	1.5 min	4.3	0.51
		$^{54}\text{Fe}(p,\alpha)^{51}\text{Mn}$	-3.12	β^+	46 min	2.2	0.51
^{56}Fe	91.7%	$^{56}\text{Fe}(p,n)^{56}\text{Co}$	-5.36	ϵ, β^+	78 da	1.46	0.847
^{57}Fe	2.1%	$^{57}\text{Fe}(p,n)^{57}\text{Co}$	-1.62	ϵ	271 da	-	0.122
		$^{57}\text{Fe}(p,\alpha)^{54}\text{Mn}$	+0.24	ϵ	312 da	-	0.835
^{58}Ni	68.3%	$^{58}\text{Ni}(p,n)^{58}\text{Cu}$	-9.35	β^+	3.2 s	7.5	1.45
		$^{58}\text{Ni}(p,\alpha)^{55}\text{Co}$	-1.35	β^+, ϵ	17 9 hr	1.5	0.51
^{60}Ni	26.1%	$^{60}\text{Ni}(p,n)^{60}\text{Cu}$	-6.91	β^+	23 min	3.77	1.76 1.33
		$^{60}\text{Ni}(p,\alpha)^{57}\text{Co}$	-0.27	ϵ	271 da	-	0.122

Table IV

Radioactivities Induced by Protons on Copper and Zinc

Target		Nuclear Reaction		Residual Nucleus			
Iso- tope	Abun- dance	Reaction	Q-Value (MeV)	Decay Mode	Half Life	E_{β} (MeV)	E_{γ} (MeV)
^{63}Cu	69.1%	$^{63}\text{Cu}(p,n)^{63}\text{Zn}$	-4.15	β^+	38 min	2.34	0.51
		$^{63}\text{Cu}(p,d)^{62}\text{Cu}$	-8.62	β^+	9.8 min	2.93	0.51
^{65}Cu	30.9%	$^{65}\text{Cu}(p,n)^{65}\text{Zn}$	-2.13	ϵ	244 da	-	1.115
		$^{65}\text{Cu}(p,d)^{64}\text{Cu}$	-7.69	β^-	12.8 hr	0.575	-
				ϵ, β^+	12.8 hr	0.656	0.51
		$^{65}\text{Cu}(p,\alpha d)^{61}\text{Co}$	-6.76	β^-	1.65 hr	1.24	0.068
		$^{65}\text{Cu}(p,\alpha\alpha)^{57}\text{Mn}$	-7.35	β^-	1.6 min	2.56	0.122
^{64}Zn	48.9%	$^{64}\text{Zn}(p,n)^{64}\text{Ga}$	-7.85	β^+	2.6 min	6.05	0.51
		$^{64}\text{Zn}(p,\alpha)^{61}\text{Cu}$	+0.85	β^+, ϵ	3.4 hr	1.22	0.51
^{66}Zn	27.8%	$^{66}\text{Zn}(p,n)^{66}\text{Ga}$	-5.96	β^+, ϵ	9.5 hr	4.15	0.51
		$^{66}\text{Zn}(p,d)^{65}\text{Zn}$	-8.81	ϵ	244 da	-	1.115
^{68}Zn	18.6%	$^{68}\text{Zn}(p,n)^{68}\text{Ga}$	-3.70	β^+	68 min	1.90	0.51

Refs. 27, 32, and 33, is presented in Fig. 7. For iron, (p,n) cross sections are taken from Ref. 26 for ^{57}Fe and from Ref. 34 for ^{56}Fe . The cross sections from Ref. 34 below 10 MeV fit smoothly onto the cross sections from Ref. 35 above 10 MeV. A precise threshold measurement has been reported for the (p,n) reaction on ^{54}Fe , (Ref. 36) but no cross sections were found in the literature. The 9.20-MeV threshold for this reaction suggests that little activity can be expected below 10 MeV. Thick-target yields for the $^{56}\text{Fe}(p,n)$ and $^{57}\text{Fe}(p,n)$ reactions are given in Fig. 8. For nickel, little activation is expected below 10 MeV. Activity from the (p,n) reaction on Ni^{58} is limited by the 9.51-MeV threshold. The thick-target yield for the (p,n) reaction on ^{60}Ni , calculated from cross sections in Ref. 37, is presented in Fig. 9. For copper, a seminal study of the (p,n) cross sections for ^{63}Cu and ^{65}Cu may be found in Ref. 38, and thick-target yields based on these cross sections are given in Fig. 10. For zinc, (p,n) cross sections were taken from Ref. 39 for ^{64}Zn , and from Refs. 39-41 for ^{66}Zn and ^{68}Zn . Smooth fits were made to these cross sections, and thick-target yields based on these cross sections are presented in Fig. 11.

(p, α) reactions: No excitation functions were found in the literature for chromium, iron, or copper targets for proton energies below 9 MeV. Above 9 MeV, excitation functions have been determined for a variety of targets by measuring emitted α -particles,⁴²⁻⁴⁴ rather than residual radioactivities. These (p, α) studies indicate that this reaction proceeds by a compound-nucleus process where the incident proton penetrates the Coulomb barrier of the target nucleus and excites the target. The density of nuclear excited states is large for these medium weight nuclei so that a statistical treatment of the compound nucleus is appropriate. The α -particle emission is described by an α -particle preformation coefficient in the nucleus and by Coulomb barrier transmission to exit the nucleus. Since the Coulomb barrier in this mass range is about 6.5 MeV for protons and about 13 MeV for α -particles, (p, α) cross sections should be small below 10 MeV. At 10 MeV, modest cross sections (31 mb for copper, 29 mb for zinc, 9 mb for iron, and 5 mb for chromium)

have been reported.^{42,43} The $^{64}\text{Zn}(p,\alpha)$ cross section has been determined from 8 to 22 MeV by measuring residual radioactivity.⁴⁵ Despite the positive Q-value of this reaction, the cross section is only 17 mb at 8 MeV and increases to a maximum of 80 mb at 15 MeV. For nickel, thick-target yields to produce ^{55}Co and ^{57}Co activities, calculated using cross sections from Ref. 46, are presented in Fig. 9. For all these (p,α) reactions, the excitation functions decrease rapidly with decreasing energy as expected from Coulomb-barrier-penetration considerations. A similar argument applies to the $^{65}\text{Cu}(p,\alpha\alpha)$ and $^{65}\text{Cu}(p,\alpha d)$ reactions.

(p,d) reactions: These reactions on copper and zinc have large negative Q-values. Experiments indicate that these reactions are not common for medium-weight elements.⁴⁷ On the other hand, (p,pn) reactions are commonly observed. These reactions require an additional 2.22 MeV which corresponds to thresholds greater than 10 MeV for the (p,pn) reactions on ^{65}Cu and ^{66}Zn .

V. Deuteron-Induced Radioactivities in the Alloy Targets

For the medium-weight elements in the titanium-alloy, steel, and brass targets, a specific radioactivity may be produced by several different deuteron-induced reactions. Therefore, it is difficult to associate a measured radioactivity with one nuclear reaction. Consequently, only a limited number of excitation functions for deuteron-induced reactions have been measured for these elements. Furthermore, the (d,n) , (d,p) and (d,α) reactions all have positive Q-values and cross sections on the order of 100 mb above the Coulomb barrier. For deuterons in the few MeV range (below the Coulomb barrier), the (d,α) reactions have appreciably smaller cross sections than the (d,n) and (d,α) reactions.⁴⁸ Substantial radioactivities can be expected from these reactions, and the following discussion will focus on these reactions. Deuteron-induced reactions leading to radioactivities are identified, and activation yields are briefly discussed for these alloy targets.

A. Titanium-Alloy Target

Deuteron-induced reactions on titanium and vanadium in the titanium alloy target which lead to radioactive products are listed in Table V. For titanium, there are four isotopes with abundances of 5% to 8%, while ^{48}Ti is 74% abundant. Cross sections for the $^{47}\text{Ti}(d,n)$ reaction and for the (d,α) reactions on ^{46}Ti , ^{48}Ti and ^{49}Ti have been determined in the range from 5.5 to 10 MeV,⁴⁹ but these measurements are insufficient to evaluate thick-target yields. These cross sections increase monotonically up to 10 MeV with values at 10 MeV of 130 mb for the (d,n) reaction and 40 to 80 mb for the (d,α) reactions. For the bombardment of a natural titanium target with 6.5-MeV deuterons, a thick-target yield of 8.3×10^{-5} ^{48}V /deuteron has been reported for producing ^{48}V activity.⁵⁰ This activity includes both the $^{47}\text{Ti}(d,n)^{48}\text{V}$ and $^{48}\text{Ti}(d,2n)^{48}\text{V}$ reactions. Cross sections for several of the negative Q-value reactions on titanium are negligible below 5 MeV and increase rapidly with energy from 5 and 10 MeV. For example, the $^{47}\text{Ti}(d,2n)^{47}\text{V}$ reaction cross section is negligible at 5.5 MeV, but approaches 200 mb at 10 MeV.⁴⁹ A similar behavior is observed for the $^{48}\text{Ti}(d,2n)^{48}\text{V}$ reaction.⁵¹ The (d,n) and (d,α) reactions on the most abundant ^{46}Ti isotope lead to rather long-lived isotopes so large activities are not expected for these reactions. Shorter half-life activities are produced by these reactions on the other isotopes, however these activities are reduced by the smaller isotopic abundances. Consequently, the activation of titanium by deuterons is not as large as for some other target materials.

For vanadium, the most likely source of radioactivity is the positive Q-value $^{51}\text{V}(d,p)^{52}\text{V}$ reaction. Cross sections for this reaction, based on proton measurements, are 11 mb at 3.8 MeV and 17 mb at 4.5 MeV.⁵² Even larger cross sections can be expected for the activation of ^{52}V because these proton measurements include only higher-energy emitted protons. Thick-target yields for producing ^{51}Cr by deuteron bombardment of vanadium has been reported.⁵³ This yield is nearly zero at 5 MeV and increases monotonically to 2.3×10^{-4} ^{51}Cr /deuteron at 10 MeV. This activity is attributed to the $^{51}\text{V}(d,2n)^{51}\text{Cr}$ reaction. No other

Table V

Radioactivities Induced by Deuterons on Titanium and Vanadium

Target		Nuclear Reaction		Residual Nucleus			
Iso- tope	Abun- dance	Reaction	Q-Value (MeV)	Decay Mode	Half Life	E_{β} (MeV)	E_{γ} (MeV)
^{46}Ti	8.0%	$^{46}\text{Ti}(d,n)^{47}\text{V}$	+2.95	β^+	31 min	1.90	0.51
		$^{46}\text{Ti}(d,t)^{45}\text{Ti}$	-6.94	β^+	3.08 hr	1.04	0.51
		$^{46}\text{Ti}(d,\alpha)^{44}\text{Sc}$	+4.40	β^+	3.93 hr	1.47	1.16
		$^{46}\text{Ti}(d,2p)^{46}\text{Sc}$	-3.81	β^-	83.8 da	0.36	1.12 0.89
		$^{46}\text{Ti}(d,\alpha n)^{43}\text{Sc}$	-5.31	β^+	3.89 hr	1.20	0.51
^{47}Ti	7.5%	$^{47}\text{Ti}(d,n)^{48}\text{V}$	+4.61	β^+, ϵ	16.0 da	0.70	1.31 0.98
		$^{47}\text{Ti}(d,^3\text{He})^{46}\text{Sc}$	-4.97	β^-	83.8 da	0.36	1.12 0.89
		$^{47}\text{Ti}(d,2p)^{47}\text{Sc}$	-2.04	β^-	3.41 da	0.44	0.16
		$^{47}\text{Ti}(d,2n)^{47}\text{V}$	-5.92	β^+	31 min	1.90	0.51
		$^{47}\text{Ti}(d,\alpha n)^{44}\text{Sc}$	-4.47	β^+	3.93 hr	1.47	1.16
^{48}Ti	73.7%	$^{48}\text{Ti}(d,n)^{49}\text{V}$	+4.52	ϵ	331 da	-	-
		$^{48}\text{Ti}(d,^3\text{He})^{47}\text{Sc}$	-5.95	β^-	3.41 da	0.44	0.16
		$^{48}\text{Ti}(d,\alpha)^{46}\text{Sc}$	+3.98	β^-	83.8 da	0.36	1.12 0.89
		$^{48}\text{Ti}(d,2p)^{48}\text{Sc}$	-5.42	β^-	43.7 hr	0.65	1.31 1.04 0.98
		$^{48}\text{Ti}(d,2n)^{48}\text{V}$	-7.02	β^+, ϵ	16.0 da	0.70	1.31 0.98
		$^{48}\text{Ti}(d,\alpha p)^{45}\text{Ca}$	-4.25	β^-	163 da	0.26	-
		$^{48}\text{Ti}(d,2\alpha)^{42}\text{K}$	-5.18	β^-	12.4 hr	3.52	1.53

Continued on next page.

Table V Continued

Radioactivities Induced by Deuterons on Titanium and Vanadium

Target		Nuclear Reaction		Residual Nucleus			
Iso- tope	Abun- dance	Reaction	Q-Value (MeV)	Decay Mode	Half Life	E_{β} (MeV)	E_{γ} (MeV)
^{49}Ti	5.5%	$^{49}\text{Ti}(d, ^3\text{He})^{48}\text{Sc}$	-5.85	β^-	43.7 hr	0.65	1.31 1.04 0.98
		$^{49}\text{Ti}(d, \alpha)^{47}\text{Sc}$	+6.48	β^-	3.41 da	0.44	0.16
		$^{49}\text{Ti}(d, 2p)^{49}\text{Sc}$	-3.45	β^-	57 min	2.00	-
		$^{49}\text{Ti}(d, \alpha n)^{46}\text{Sc}$	-4.16	β^-	83.8 da	0.36	1.12 0.89
		$^{49}\text{Ti}(d, 2\alpha)^{43}\text{K}$	-3.69	β^-	22.2 hr	0.83	0.62 0.37
^{50}Ti	5.3%	$^{50}\text{Ti}(d, p)^{51}\text{Ti}$	+4.16	β^-	5.8 min	2.14	0.32
		$^{50}\text{Ti}(d, ^3\text{He})^{49}\text{Sc}$	-6.68	β^-	57 min	2.00	-
		$^{50}\text{Ti}(d, \alpha)^{48}\text{Sc}$	+3.79	β^-	43.7 hr	0.65	1.31 1.04 0.98
		$^{50}\text{Ti}(d, 2p)^{50}\text{Sc}$	-7.91	β^-	1.7 min	3.7	1.55
		$^{50}\text{Ti}(d, \alpha n)^{47}\text{Sc}$	-4.47	β^-	3.41 da	0.44	0.16
		$^{50}\text{Ti}(d, \alpha p)^{47}\text{Ca}$	-5.66	β^-	4.54 da	0.69	1.30
		$^{50}\text{Ti}(d, 2\alpha)^{44}\text{K}$	-7.79	β^-	22 min	5.66	1.16
^{51}V	99.8%	$^{51}\text{V}(d, p)^{52}\text{V}$	+5.08	β^-	3.8 min	2.5	1.43
		$^{51}\text{V}(d, 2p)^{51}\text{Ti}$	-3.90	β^-	5.8 min	2.14	0.32
		$^{51}\text{V}(d, 2n)^{51}\text{Cr}$	-3.76	ϵ	27.7 da	-	0.32
		$^{51}\text{V}(d, \alpha p)^{48}\text{Sc}$	-4.27	β^-	43.7 hr	0.65	1.31 1.04 0.98
		$^{51}\text{V}(d, 2\alpha)^{45}\text{Ca}$	-3.10	β^-	163 da	0.26	-

activation cross sections have been published for deuterons on vanadium.

B. Steel Target

Deuteron-induced reactions leading to radioactive products are listed in Table VI for a steel target. For the 20%-chromium component of this target, only ^{52}Cr and ^{53}Cr have significant abundances. For natural-abundance chromium, the thick-target yield (reactions/deuteron) at 8 MeV for activating ^{52}Mn by the $^{52}\text{Cr}(d,2n)^{52}\text{Mn}$ reaction is 7x less than the thick-target yield for activating ^{51}Cr by the $^{50}\text{Cr}(d,n)^{51}\text{Mn}(\beta^-)^{51}\text{Cr}$ and $^{50}\text{Cr}(d,p)^{51}\text{Cr}$ reactions.⁵⁴ The isotopic abundance of ^{50}Cr is only 4.4%. Reactions on ^{50}Cr are not included in Table VI because the abundance of this isotope in a steel target is less than 1%, and ^{51}Cr is not expected to be a primary source of radioactivity. Above 8 MeV, the activation of ^{52}Mn increases rapidly with energy, and calculated thick-target yields for Mn^{52} and the isomer Mn^{52m} , evaluated using cross sections from Ref. 55, are presented in Fig. 12. The thick-target yield for producing ^{54}Mn by deuteron bombardment of chromium has been determined.⁵⁴ This yield increases monotonically from nearly zero at 1 MeV to 5.8×10^{-5} ^{54}Mn /deuteron at 10 MeV.

Radioactivities produced by deuteron-induced reactions on natural iron have been identified and excitation functions have been measured for deuterons above 5 MeV.⁵⁶ In the range from 5 to 10 MeV, the largest activation cross sections are for ^{55}Co , ^{57}Co , and ^{54}Mn . The cobalt activities are induced principally by the $^{54}\text{Fe}(d,n)^{55}\text{Co}$ and $^{56}\text{Fe}(d,n)^{57}\text{Co}$ reactions. Below 5 MeV, ^{55}Co activation cross sections,⁵⁷ measured over the energy range from 2.44 to 5.5 MeV, are a factor-of-two smaller than the cross sections in Ref. 56. The cross sections in Ref. 57 were used to evaluate thick-target yields because the initial deuteron energy for the stacked-foil measurements in this experiment is 5.5 MeV, compared with 40 MeV in Ref. 56. The excitation function for ^{55}Co in Ref. 56 is scaled to cross sections in Ref. 57 to give activation cross sections for ^{55}Co and ^{57}Co up to 10 MeV. The ^{54}Mn activity is produced principally by the $^{56}\text{Fe}(d,\alpha)^{54}\text{Mn}$ and

Table VI

Radioactivities Induced by Deuterons on Chromium,
Iron and Nickel

Target		Nuclear Reaction		Residual Nucleus			
Iso- tope	Abun- dance	Reaction	Q-Value (MeV)	Decay Mode	Half Life	E_{β} (MeV)	E_{γ} (MeV)
^{52}Cr	83.8%	$^{52}\text{Cr}(d,t)^{51}\text{Cr}$	-5.78	ϵ	27.7 da	-	-
		$^{52}\text{Cr}(d,2n)^{52}\text{Mn}$	-7.78	ϵ, β^+	5.6 da	0.57	1.434 0.94 0.74
		$^{52}\text{Cr}(d,2n)^{52m}\text{Mn}$	-8.10	β^+	21 min	2.63	1.43
		$^{52}\text{Cr}(d,2p)^{52}\text{V}$	-3.98	β^-	3.8 min	2.5	1.43
^{53}Cr	9.5%	$^{53}\text{Cr}(d,n)^{54}\text{Mn}$	5.34	ϵ	312 da	-	0.835
		$^{53}\text{Cr}(d,^3\text{He})^{52}\text{V}$	-5.64	β^-	3.8 min	2.5	1.43
		$^{53}\text{Cr}(d,2p)^{53}\text{V}$	-4.5	β^-	1.6 min	2.4	1.00
^{54}Fe	5.8%	$^{54}\text{Fe}(d,n)^{55}\text{Co}$	2.83	β^+, ϵ	17.9 hr	1.5	0.51
		$^{54}\text{Fe}(d,p)^{55}\text{Fe}$	7.08	ϵ	2.7 yr	-	-
		$^{54}\text{Fe}(d,t)^{53}\text{Fe}$	-7.36	β^+	8.5 min	2.8	0.51
		$^{54}\text{Fe}(d,\alpha)^{52}\text{Mn}$	5.17	ϵ, β^+	5.6 da	0.57	1.434 0.94 0.74
		$^{54}\text{Fe}(d,\alpha)^{52m}\text{Mn}$	4.79	β^+	21 min	2.63	1.43
		$^{54}\text{Fe}(d,2p)^{54}\text{Mn}$	-2.14	ϵ	312 da	-	0.835
		^{56}Fe	91.7%	$^{56}\text{Fe}(d,n)^{57}\text{Co}$	3.80	ϵ	271 da
		$^{56}\text{Fe}(d,t)^{55}\text{Fe}$	-4.95	ϵ	2.7 yr	-	-
		$^{56}\text{Fe}(d,\alpha)^{54}\text{Mn}$	5.66	ϵ	312 da	-	0.835
		$^{56}\text{Fe}(d,2n)^{56}\text{Co}$	-7.58	ϵ, β^+	78 da	1.46	0.847
		$^{56}\text{Fe}(d,2p)^{56}\text{Mn}$	-5.14	β^-	2.58 hr	2.85	0.847

Continued on next page

Table VI Continued

Radioactivities Induced by Deuterons on Chromium,
Iron and Nickel

Target		Nuclear Reaction		Residual Nucleus			
Iso- tope	Abun- dance	Reaction	Q-Value (MeV)	Decay Mode	Half Life	E_{β} (MeV)	E_{γ} (MeV)
^{57}Fe	2.1%	$^{57}\text{Fe}(d,n)^{58}\text{Co}$	4.73	ϵ, β^+	71 da	0.47	0.81
		$^{57}\text{Fe}(d,^3\text{He})^{56}\text{Mn}$	-5.07	β^-	2.58 hr	2.85	0.847
		$^{57}\text{Fe}(d,2n)^{57}\text{Co}$	-3.84	ϵ	271 da	-	0.122
		$^{57}\text{Fe}(d,2p)^{57}\text{Mn}$	-4.14	β^-	1.6 min	2.56	0.122
^{58}Ni	68.3%	$^{58}\text{Ni}(d,n)^{59}\text{Cu}$	1.20	β^+	82 s	3.78	0.51
		$^{58}\text{Ni}(d,\alpha)^{56}\text{Co}$	6.51	ϵ, β^+	78 da	1.46	0.847
		$^{58}\text{Ni}(d,t)^{57}\text{Ni}$	-5.94	ϵ, β^+	36 hr	0.84	1.37
		$^{58}\text{Ni}(d,^3\text{He})^{57}\text{Co}$	-2.68	ϵ	271 da	-	0.122
		$^{58}\text{Ni}(d,2p)^{58}\text{Co}$	-1.83	ϵ, β^+	71 da	0.47	0.81
		$^{58}\text{Ni}(d,\alpha n)^{55}\text{Co}$	-3.57	β^+, ϵ	17.9 hr	1.5	0.51
		$^{58}\text{Ni}(d,\alpha p)^{55}\text{Fe}$	0.67	ϵ	2.7 yr	-	-
		$^{58}\text{Ni}(d,2\alpha)^{54}\text{Mn}$	3.61	ϵ	312 da	-	0.835
^{60}Ni	26.1%	$^{60}\text{Ni}(d,n)^{61}\text{Cu}$	2.58	β^+, ϵ	3.4 hr	1.22	0.51
		$^{60}\text{Ni}(d,\alpha)^{58}\text{Co}$	6.08	ϵ, β^+	71 da	0.47	0.61
		$^{60}\text{Ni}(d,2n)^{60}\text{Cu}$	-9.13	β^+	23 min	3.77	1.33
		$^{60}\text{Ni}(d,2p)^{60}\text{Co}$	-4.26	β^-	5.27 yr	0.32	1.17 1.33
		$^{60}\text{Ni}(d,\alpha n)^{57}\text{Co}$	-2.49	ϵ	271 da	-	0.122

$^{54}\text{Fe}(d,2p)^{54}\text{Mn}$ reactions, and cross sections for ^{54}Mn are taken from Ref. 56. Thick-target yields for a natural iron target, calculated using these cross sections, are presented in Fig. 13.

For the 10%-nickel component in the steel target, only ^{58}Ni and ^{60}Ni have significant abundances. Excitation functions⁵⁸ for (d,n) reactions on these nuclei have been measured over the energy range from 2 to 12 MeV. These cross sections increase rapidly with energy up to peaks of 200 mb at 8 MeV for ^{58}Ni and 470 mb at 8 MeV for ^{60}Ni . Above these peaks, the cross sections decrease slowly with increasing energy. These activation cross sections are smaller than the cross sections for ^{58}Ni at 3.0, 3.5 and 4.0 MeV in Ref. 59 and larger than the cross sections for ^{60}Ni at 7.2 and 9.4 MeV in Ref. 60. Thick-target yields were evaluated using the cross sections in Ref. 58 because they encompass a broad energy range. These yields are presented in Fig. 14. Activation cross sections for the (d, α) reactions on ^{58}Ni and ^{60}Ni are smaller than the (d,n) cross sections.^{60,61} The (d, α) cross sections increase monotonically with increasing deuteron energy from 5 to 10 MeV. The thick-target yield for the reaction $^{58}\text{Ni}(d,\alpha)^{56}\text{Co}$, calculated using cross sections in Refs. 60 and 61, is displayed in Fig. 14. For a natural nickel target, ^{58}Co activation may be produced by both the $^{60}\text{Ni}(d,\alpha)^{58}\text{Co}$ and $^{58}\text{Ni}(d,2p)^{58}\text{Co}$ reactions. The ^{58}Co activation in Fig. 2 of Ref. 62 is presumably due to both reactions rather than just the $^{58}\text{Ni}(d,2p)^{58}\text{Co}$ reaction. The thick-target yield for ^{58}Co activation, calculated from cross sections in Refs. 60 and 62 is presented in Fig. 14. Cross sections for the (d,t), (d, ^3He), (d, αn), (d, αp) and (d,2 α) reactions on ^{58}Ni and the (d,2n) and (d, αn) reactions on ^{60}Ni have been measured,⁶⁰⁻⁶³ and activities induced by these reactions are negligible below 10 MeV.

C. Brass Target

Deuteron-induced reactions leading to radioactive products are listed in Table VII for the 67%-copper component in this target. The (d,p) and (d,2n) reactions on ^{63}Cu and ^{65}Cu are prolific sources of radioactivity for deuterons below 10 MeV. A seminal study of activations for these reactions may be found in

Table VII

Radioactivities Induced by Deuterons on Copper

Target		Nuclear Reaction		Residual Nucleus			
Iso- tope	Abun- dance	Reaction	Q-Value (MeV)	Decay Mode	Half Life	E_{β} (MeV)	E_{γ} (MeV)
^{63}Cu	69.1%	$^{63}\text{Cu}(d,p)^{64}\text{Cu}$	5.69	β^-	12.8 hr	0.575	-
				ϵ, β^+	12.8 hr	0.656	0.51
		$^{63}\text{Cu}(d,t)^{62}\text{Cu}$	-4.58	β^+	9.8 min	2.93	0.51
		$^{63}\text{Cu}(d,2n)^{63}\text{Zn}$	-6.37	β^+	38 min	2.34	0.51
^{65}Cu	30.9%	$^{65}\text{Cu}(d,p)^{66}\text{Cu}$	4.84	β^-	5.1 min	2.63	1.04
				ϵ, β^+	12.8 hr	0.575	-
		$^{65}\text{Cu}(d,t)^{64}\text{Cu}$	-3.65	β^-	12.8 hr	0.656	0.51
		$^{65}\text{Cu}(d,2n)^{65}\text{Zn}$	-4.36	ϵ	244 da	-	1.115
		$^{65}\text{Cu}(d,2p)^{65}\text{Ni}$	-3.57	β^-	2.52 hr	2.13	1.48
		$^{65}\text{Cu}(d,\alpha p)^{62}\text{Co}$	-2.32	β^-	14 min	2.88	1.17

Ref. 64. For the (d,p) reactions, significant disagreements in the magnitude and shape of the excitation functions are observed between three independent cross-section measurements. For the (d,2n) reactions, there is good agreement between the same three experiments. Thick-target yields, based on cross sections from Ref. 64, are presented in Fig. 15. Measurements of the $^{63}\text{Cu}(d,t)^{62}\text{Cu}$ and $^{65}\text{Cu}(d,2p)^{65}\text{Ni}$ reactions^{65,66} indicate that the activation cross sections for these reactions are much less than for the (d,p) and (d,2n) reactions.

For the zinc in this target, deuteron-induced reactions leading to radioactive products are listed in Table VIII. The ^{64}Zn , ^{66}Zn , and ^{68}Zn isotopes have significant abundances for the 33%-zinc component of the target. Excitation functions have been measured for the (d,p) and (d,n) reactions in Table VIII. Activation cross sections for the $^{64}\text{Zn}(d,p)^{65}\text{Zn}$ reaction include the $^{64}\text{Zn}(d,n)^{65}\text{Ga}$ reaction because the 15-min ^{65}Ga isotope decays to the 244-da ^{65}Zn isotope.^{67,68} This short-lived precursor is included in delayed activation measurements of ^{65}Zn . For ^{66}Zn , cross sections⁶⁹ for the $^{66}\text{Zn}(d,n)^{67}\text{Ga}$ reaction include a small contribution from the $^{67}\text{Zn}(d,2n)^{67}\text{Ga}$ reaction at higher deuteron energy. The natural abundance of ^{67}Zn is only 4.1%. For ^{68}Zn , the (d,p) reaction produces either ^{69}Zn or the isomer, ^{69m}Zn . The isomer decays by an isomeric transition (IT) with the emission of a 0.44-MeV γ -ray to ^{69}Zn . Separate cross sections have been measured for these two activities.⁷⁰ Thick-target yields, based on cross sections from Refs. 67-70, are presented in Fig. 16.

For the (d, α) reactions in Table VIII, only the cross section for activating ^{64}Cu has been published.⁷¹ Isotopically enriched targets were required to extract the excitation function for this activity. The more intense (d,p) and (d,n) reactions which induce competing short-lived activities make measurements of the smaller (d, α) cross sections difficult. No excitation functions have been reported for the 10-min ^{62}Cu or 5-min ^{66}Cu activities. The thick-target yield for ^{64}Cu activity, based on the cross sections in Ref. 71, is presented in Fig. 16.

Table VIII

Radioactivities Induced by Deuterons on Zinc

Target		Nuclear Reaction		Residual Nucleus			
Iso- tope	Abun- dance	Reaction	Q-Value (MeV)	Decay Mode	Half Life	E_{β} (MeV)	E_{γ} (MeV)
^{64}Zn	48.9%	$^{64}\text{Zn}(d,n)^{65}\text{Ga}$	1.72	β^+	15 min	2.24	0.51
		$^{64}\text{Zn}(d,p)^{65}\text{Zn}$	5.76	ϵ	244 da	-	1.115
		$^{64}\text{Zn}(d,t)^{63}\text{Zn}$	-5.60	β^+	38 min	2.34	0.51
		$^{64}\text{Zn}(d,\alpha)^{62}\text{Cu}$	7.52	β^+	9.8 min	2.93	0.51
		$^{64}\text{Zn}(d,2p)^{64}\text{Cu}$	-2.01	β^- ϵ, β^+	12.8 hr 12.8 hr	0.575 0.656	- 0.51
^{66}Zn	27.8%	$^{66}\text{Zn}(d,n)^{67}\text{Ga}$	3.05	ϵ	78 hr	-	0.093
		$^{66}\text{Zn}(d,t)^{65}\text{Zn}$	-4.78	ϵ	244 da	-	1.115
		$^{66}\text{Zn}(d,\alpha)^{64}\text{Cu}$	7.26	β^- ϵ, β^+	12.8 hr 12.8 hr	0.575 0.656	- 0.51
		$^{66}\text{Zn}(d,2p)^{66}\text{Cu}$	-4.07	β^-	5.1 min	2.63	1.04
		$^{66}\text{Zn}(d,2n)^{66}\text{Ga}$	-8.18	β^+, ϵ	9.5 hr	4.15	0.51
^{68}Zn	18.6%	$^{68}\text{Zn}(d,p)^{69}\text{Zn}$	4.28	β^-	57 min	0.91	-
		$^{68}\text{Zn}(d,p)^{69}\text{Zn}$	3.84	IT	13.9 hr	-	0.44
		$^{68}\text{Zn}(d,^3\text{He})^{67}\text{Cu}$	-4.50	β^-	62 hr	0.57	0.185
		$^{68}\text{Zn}(d,\alpha)^{66}\text{Cu}$	6.97	β^-	5.1 min	2.63	1.04
		$^{68}\text{Zn}(d,2n)^{68}\text{Ga}$	-5.93	β^+	68 min	1.90	0.51
		$^{68}\text{Zn}(d,2p)^{68}\text{Cu}$	-6.03	β^-	31 sec	3.51	1.08

Excitation functions have been measured for several of the negative Q-value reactions in Table VIII. For the $^{64}\text{Zn}(d,2p)$ reaction, the cross section is small (5 mb) at 10 MeV and negligible below 8 MeV.⁷¹ For the $^{66}\text{Zn}(d,2n)^{66}\text{Ga}$ reaction, the cross section increases from zero at the 8.4-MeV threshold to 150 mb at 10 MeV.⁷⁰ For the $^{68}\text{Zn}(d,2n)^{68}\text{Ga}$ reaction the threshold is 6.1 MeV, but some ^{68}Ga activity is produced at lower energy from the $^{67}\text{Zn}(d,n)^{68}\text{Ga}$ reaction. The thick-target yield for ^{68}Ga activity, based on the cross sections in Ref. 70, is presented in Fig. 16.

VI. Summary

For the proton-induced reactions in this survey, radioactivities are produced primarily by (p,n) reactions. Yields for these reactions increase rapidly from threshold. Thresholds are less than 4 MeV for the carbon, titanium-alloy, steel, and brass targets and 5.8 MeV for an aluminum target. At 10 MeV, the $^{51}\text{V}(p,n)$ and $^{65}\text{Cu}(p,n)$ reactions have the largest thick-target yields ($\sim 10^{-3}$ reactions/proton); these two reactions also have the smallest thresholds. Residual activities with hour-to-day halflives resulting from the proton bombardment of aluminum, titanium, steel and brass have been measured and specific radioisotopes were identified.⁷² The observed activities are consistent with the expectations from this survey.

For the deuteron-induced reactions, radioactivities are produced primarily by the (d,n), (d,p), and (d, α) reactions. The (d, α) yields are smaller than the (d,n) or (d,p) yields. Thick-target yields for the (d,n) and (d,p) reactions increase rapidly at low energy and approach 5×10^{-4} reactions/deuteron at 10 MeV. At low energy, the (d,n) yield for carbon is larger than for the other targets presumably due to the smaller Coulomb barrier. In the energy range from 8 to 10 MeV, thick-target yields for the (d,n) and (d,p) reactions are similar so differences in the yields for different targets are due primarily to the different target abundances. For some of these reactions, significant differences are found in the literature for the same reaction

cross section measured in different experiments by different researchers. In some cases, additional measurements have been reported in order to sort out these differences. However, large differences remain for the $^{27}\text{Al}(d,p)^{28}\text{Al}$ reaction, as indicated in Fig. 4. Additional measurements are needed to provide reliable cross sections for this reaction from zero to 10 MeV.

The radioactivity produced by a single intense pulse of ions can be evaluated from the thick-target yield. For a 100-kA, 100-ns duration pulse of protons or deuterons, the initial activity in Curies is given by $1.2 \times 10^6 f Y(E) / T_{1/2}$, where f is the fractional abundance of the target element in the alloy target; $Y(E)$ is the thick-target yield at energy E ; and $T_{1/2}$ is the half-life of the induced radioactivity in seconds. To illustrate this evaluation, activities are determined for two reactions which have large yields. For 10-MeV protons on brass, the ^{65}Zn activity from the $^{65}\text{Cu}(p,n)$ reaction is 34 μCurie , while the ^{63}Zn activity from the $^{63}\text{Cu}(p,n)$ reaction is 0.16 Curie. The large difference in these activities is due to the shorter ^{63}Zn half-life (38 min) compared with the ^{65}Zn half-life (244 da). For 10-MeV deuterons on carbon, the ^{13}N activity from the $^{12}\text{C}(d,n)$ reaction is 0.96 Curie. These examples indicate that relatively large radioactivities can be produced by intense proton or deuteron beams under some conditions. Much smaller activities are obtained for targets which have smaller yields and produce longer half-life activities. For example, for 10-MeV protons on the titanium-alloy target, the ^{47}V and ^{48}V activities from the $^{47}\text{Ti}(p,n)$ and $^{48}\text{Ti}(p,n)$ reactions are only 13 mCurie and 0.31 mCurie, respectively. These activities are even less for lower energy protons.

In addition to radioactivity induced in the target by proton or deuteron beams, radioactivity may be induced in the target or in surrounding materials by neutrons from (p,n) or (d,n) reactions. These activities, however, are expected to be small because neutron intensities from these reactions are much less than the ion-beam intensities.

Nuclear activations provide an attractive technique for determining the properties of intense ion beams in pulsed power

experiments. Ion-beam intensities and energies can be determined by measuring delayed activations.¹⁰ A variety of techniques have been employed including: thick-target yields from resonance reactions,¹⁰ stacked-foil activations,^{20,73,74} simultaneous activations of different target materials,^{20,74} (p,n) threshold reactions,^{74,75} and secondary-reaction activation.⁷⁶ For this purpose, reactions with large yields which produce short-lived activities (minute-to-hour) are usually preferred. Activations produced by the nuclear reactions on carbon and aluminum in this survey have been used to diagnose proton and deutron beams with energies below 5 MeV. In the future, it is expected that nuclear activation techniques will be used to diagnose ion beams at higher energies where a larger choice of nuclear reactions on a variety of targets is available.

Acknowledgements

Appreciation is expressed to Dr. Richard Peacock and Ms. Harriet Oxley of the NRL Library Staff for their assistance with the DIALOG literature search. The encouragement of John Maenchen to carry out this work is appreciated. This work was supported by the Department of Energy through Sandia National Laboratories.

REFERENCES

1. F.C. Young and D.V. Rose, Survey of Radioactivities Induced by Lithium Ions, NRL Memorandum Report No. 6974, 1992.
2. K.A. Keller, J. Lange and H. Münzel, in Landolt-Bornstein Numerical Data and Functional Relationships in Science and Technology Vol. 5, Part a, Q-Values, edited by H. Schopper (Springer-Verlag, New York, 1973).
3. J.B. Marion and F.C. Young, Nuclear Reaction Analysis (North-Holland, Amsterdam, 1968) p. 157.
4. Chart of the Nuclides, Knolls Atomic Power Laboratory, 11th Edition, April, 1972.
5. C.M. Lederer, J.M. Hollander and I. Perlman, Table of Isotopes, 6th Edition (John Wiley, New York, 1967).
6. F.K. McGowan, W.T. Milner, H.J. Kim and Wanda Hyatt, Nuclear Data Tables A6, 353 (1969); A7, 1 (1969); F.K. McGowan and W.T. Milner, Nuclear Data Tables A8, 199 (1970); 9, 469 (1971); 11, 1 (1972); Atomic Data and Nuclear Data Tables 12, 499 (1973); 15, 189 (1975); 18, 1 (1976).
7. K.A. Keller, J. Lange, H. Münzel and G. Pfennig, in Landolt-Bornstein Numerical Data and Functional Relationships in Science and Technology Vol. 5, Part b, Excitation Functions for Charged-Particle Induced Nuclear Reactions, edited by H. Schopper (Springer-Verlag, New York, 1973).
8. DIALOG Information Services, Inc., 3460 Hillview Ave., Palo Alto, CA 94304.
9. H.H. Andersen and J.F. Ziegler, The Stopping and Ranges of Ions in Matter, Vol. 3, Hydrogen (Pergamon Press, New York, 1977).
10. F.C. Young, J. Golden and C.A. Kapetanacos, Rev. Sci. Instrum. 48, 432 (1977).
11. P. Dagley, W. Haerberli and J.X. Saladin, Nucl. Phys. 24, 353 (1961).
12. A.B. Whitehead and J.S. Foster, Can. J. Phys. 36, 1276 (1958).
13. T.W. Bonner, J.E. Evans and J.E. Hill, Phys. Rev. 75, 1398 (1949).
14. R.J. Jaszczak, R.L. Macklin and J.H. Gibbons, Phys. Rev. 181, 1428 (1969).
15. D.H. Wilkinson, Phys. Rev. 100, 32 (1955).

16. I.F. Bubb, J.M. Poate and R.H. Spear, Nucl. Phys. 65, 655 (1965).
17. E. McMillan and E.O. Lawrence, Phys. Rev. 47, 343 (1935).
18. C.S. Lin and E.K. Lin, Nuovo Cimento A 66, 336 (1970).
19. J.M. Flores, Phys. Rev. 127, 1246 (1962).
20. F.C. Young and M. Friedman, J. Appl. Phys. 46, 2001 (1975).
21. E. Schuster and K. Wohlleben, J. Appl. Rad. Isotopes 19, 471 (1968).
22. R.L. Wilson, D.J. Frantsvog and A.R. Kunselman, C. Détraz and C.S. Zaidins, Phys. Rev. C 13, 976 (1976).
23. H.F. Röhm, C.J. Verwey, J. Steyn and W.L. Rautenbach, J. Inorg. Nucl. Chem. 31, 3345 (1969).
24. R. Radicella, J. Rodriguez, G.B. Baró and O. Hittmair, Z. Physik 150, 653 (1958).
25. J. Jänecke, Phys. Lett. 6, 69 (1963).
26. S. Tanaka and M. Furukawa, J. Phys. Soc. Japan 14, 1269 (1959).
27. J. Wing and J.R. Huizenga, Phys. Rev. 128, 280 (1962).
28. J.L. Zyskind, C.A. Barnes, J.M. Davidson, W.A. Fowler, R.E. Marrs and M.H. Shapiro, Nucl. Phys. A343, 295 (1980).
29. S. Kailas, S.K. Gupta, S.S. Kerekatte and C.V. Fernandes, Pramana 24, 629 (1985).
30. H.S. Plendl, L.J. Defelice and R.K. Sheline, Nucl. Phys. 73, 131 (1965).
31. N.T. Porile, C.R. Lux, J.C. Pacer and J. Wiley, Nucl. Phys. A240, 77 (1975).
32. F. Boehm, P. Marmier and P. Preiswerk, Helv. Phys. Acta 25, 599 (1952).
33. H. Taketani and W. Parker Alford, Phys. Rev. 125, 291 (1962).
34. I.L. Jenkins and A.G. Wain, J. Inorg. Nucl. Chem. 32, 1419 (1970).
35. E. Gadioli, A.M. Grassi Strini, G. Lo Bianco, G. Strini and G. Tagliaferri, Nuovo Cimento 22A, 547 (1974).
36. S.D. Hoath, R.J. Petty, J.M. Freeman, G.T.A. Squier and W.E. Burcham, Phys. Lett. 51B, 345 (1974).

37. S. Tanaka, M. Furukawa and M. Chiba, J. Inorg. Nucl. Chem. 34, 2419 (1972).
38. R. Collé, R. Kishore and J.B. Cumming, Phys. Rev. C 9, 1819 (1974).
39. H.A. Howe, Phys. Rev. 109, 2083 (1958).
40. J.-P. Blaser, F. Boehm, P. Marmier and D.C. Peaslee, Helv. Phys. Acta 24, 3 (1951).
41. M. Hille, P. Hille, M. Uhl and W. Weisz, Nucl. Phys. A198, 625 (1972).
42. C.B. Fulmer and C.D. Goodman, Phys. Rev. 117, 1339 (1960).
43. I. Kumabe, C.L. Wang, M. Kawashima, M. Yada and H. Ogata, J. Phys. Soc. Japan 14, 713 (1959).
44. L. Milazzo Colli, G.M. Braga Marcazzan, R. Bonetti, M. Milazzo and J.W. Smits, Nuovo Cimento 39, 171 (1977).
45. B.L. Cohen, E. Newman, R.A. Charpie and T.H. Handley, Phys. Rev. 94, 620 (1954).
46. F. Tárkányi, F. Szelecsényi and P. Kopecky, Appl. Radiat. Isot. 42, 513 (1991).
47. B.L. Cohen and E. Newman, Phys. Rev. 99, 718 (1955).
48. J.H. Bjerregaard, P.F. Dahl, O. Hansen and G. Sidenius, Nucl. Phys. 51, 641 (1964).
49. K.L. Chen and J.M. Miller, Phys. Rev. 134, B1269 (1964).
50. P.P. Dmitriev, I.O. Konstantinov and N.N. Krasnov, Soviet Atomic Energy, 29, 916 (1970).
51. W.H. Burgess, G.A. Cowan, J.W. Hadley, W. Hess, T. Shull, M.L. Stevenson and H.F. York, Phys. Rev. 95, 750 (1954).
52. J.P. Schiffer and L.L. Lee, Jr., Phys. Rev. 115, 1705 (1959).
53. C.P. Dmitriev, I.O. Konstantinov and N.N. Krasnov, Soviet Atomic Energy, 29, 917 (1970).
54. P. Kafalas and J.W. Irvine, Jr., Phys. Rev. 104, 703 (1956).
55. H.I. West, Jr., R.G. Lanier and M.G. Mustafa, Phys. Rev. C 35, 2067 (1987).
56. J.W. Clark, C.B. Fulmer and I.R. Williams, Phys. Rev. 179, 1104 (1969).
57. P.P. Coetzee and M. Peisach, Radiochim. Acta 17, 1 (1972).

58. M. Cogneau, L.J. Lilly and J Cara, Nucl. Phys. A99, 686 (1967).
59. J.H. Carver and G.A. Jones, Nucl. Phys. 24, 607 (1961).
60. J. Zweit, A.M. Smith, S. Downey and H.L. Sharma, Appl. Radiat. Isot. 42, 193 (1991).
61. M. Blann and G. Merkel, Phys. Rev. 131, 764 (1963).
62. C.K. Cline, Nucl. Phys. A174, 73 (1971).
63. R. Radicella, J. Rodriguez, G.B. Baró and O. Hittmair, Z. Physik 153, 314 (1958).
64. H. Okamura and S. Tamagawa, Nucl. Phys. A169, 401 (1971).
65. C.B. Fulmer and I.R. Williams, Nucl. Phys. A155, 40 (1970).
66. J.W. Irvine, Jr., J. Chem. Soc. (London) Suppl. S356 (1949).
67. S.J. Nassiff and H. Münzel, Radiochem. Radioanal. Lett. 12, 353 (1972).
68. J.H. Carver and G.A. Jones, Nucl. Phys. 11, 400 (1959).
69. S.J. Nassiff and H. Münzel, Radiochim. Acta 19, 97 (1973).
70. L.J. Gilly, G.A. Henriet, M. Preciosa Alves and P.C. Capron, Phys. Rev. 131, 1727 (1963).
71. D.C. Williams and J.W. Irvine, Jr., Phys. Rev. 130, 265 (1963).
72. C.L. Ruiz and G.W. Cooper, in Particle Beam Fusion Progress Report 1988, Sandia Report SAND91-0225, p. 90, April, 1992.
73. J.M. Neri, J.R. Boller, P.F. Ottinger, B.V. Weber and F.C. Young, Appl. Phys. Lett. 50, 1331 (1987).
74. F.C. Young, S.J. Stephanakis and D. Mosher, J. Appl. Phys. 48, 3642 (1977).
75. F.C. Young, J.M. Neri, B.V. Weber, R.J. Commisso, S.J. Stephanakis and T.J. Renk, Ion Energy Diagnostics for Voltage Determinations in Plasma-Erosion-Opening-Switch Experiments, NRL Memorandum Report 6059, December, 1987.
76. R.J. Leeper, K.H. Kim, D.E. Hebron and N.D. Wing, Nucl. Instrum. Meth. Phys. Res. B24/25, 695 (1987).

THICK-TARGET YIELDS

Carbon Target

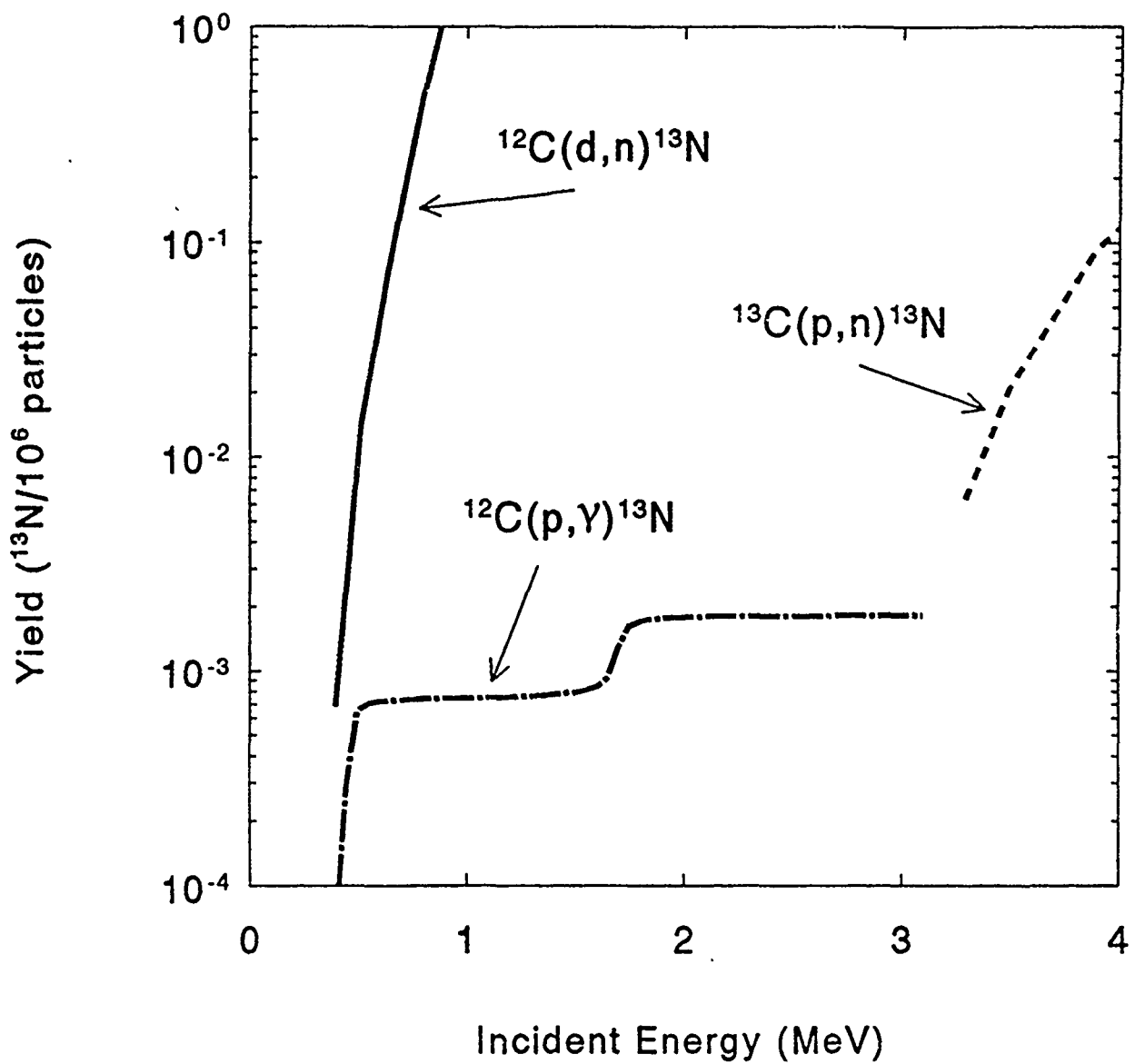


Fig. 1. Thick-target yields for the $^{12}\text{C}(p,\gamma)^{13}\text{N}$, $^{13}\text{C}(p,n)^{13}\text{N}$ and $^{12}\text{C}(d,n)^{13}\text{N}$ reactions below 4 MeV in a natural carbon target.

THICK-TARGET YIELDS

Carbon Target

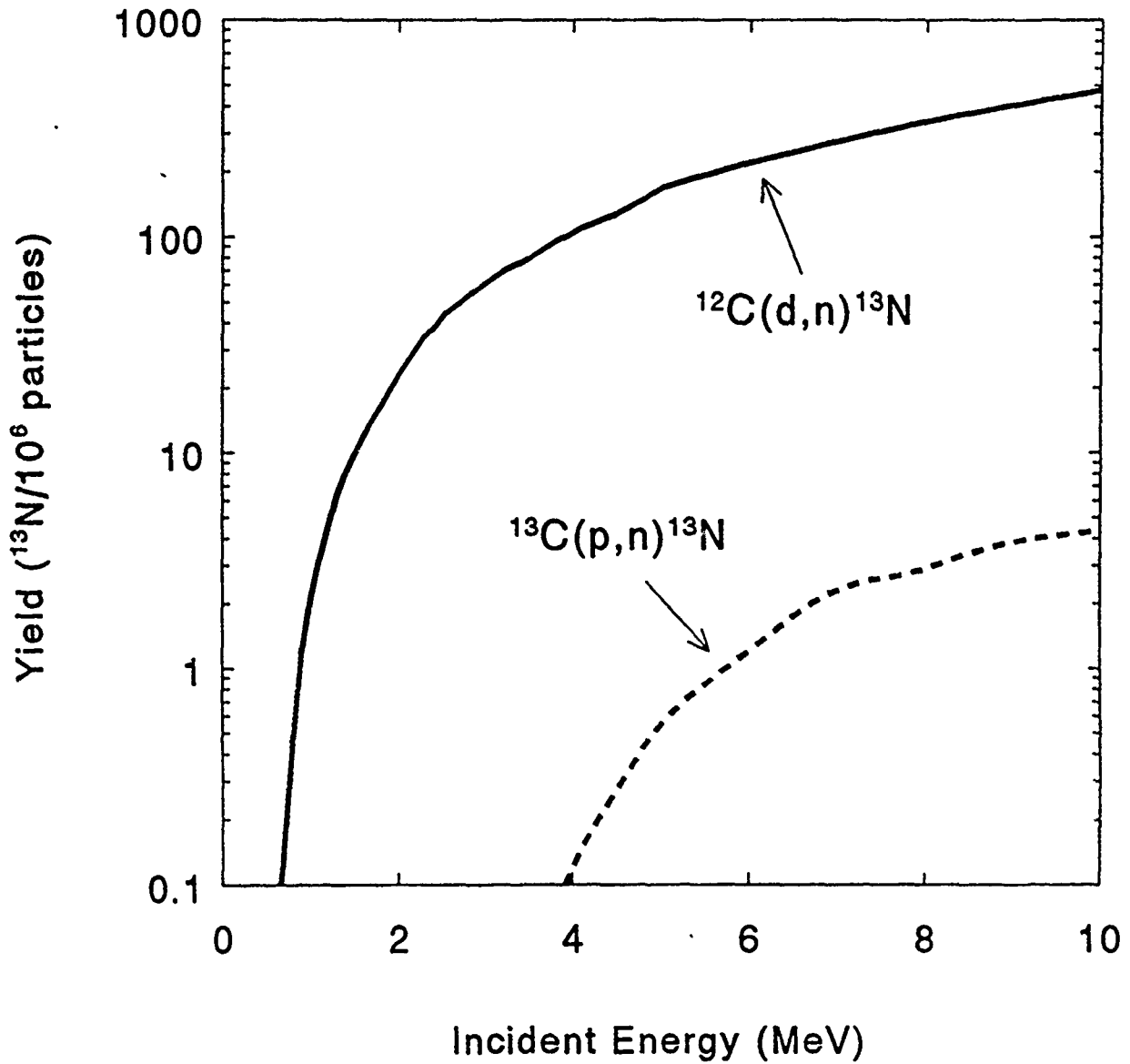


Fig. 2. Thick-target yields for the $^{13}\text{C}(p,n)^{13}\text{N}$ and $^{12}\text{C}(d,n)^{13}\text{N}$ reactions up to 10 MeV in a natural carbon target.

THICK-TARGET YIELDS

Aluminum Target

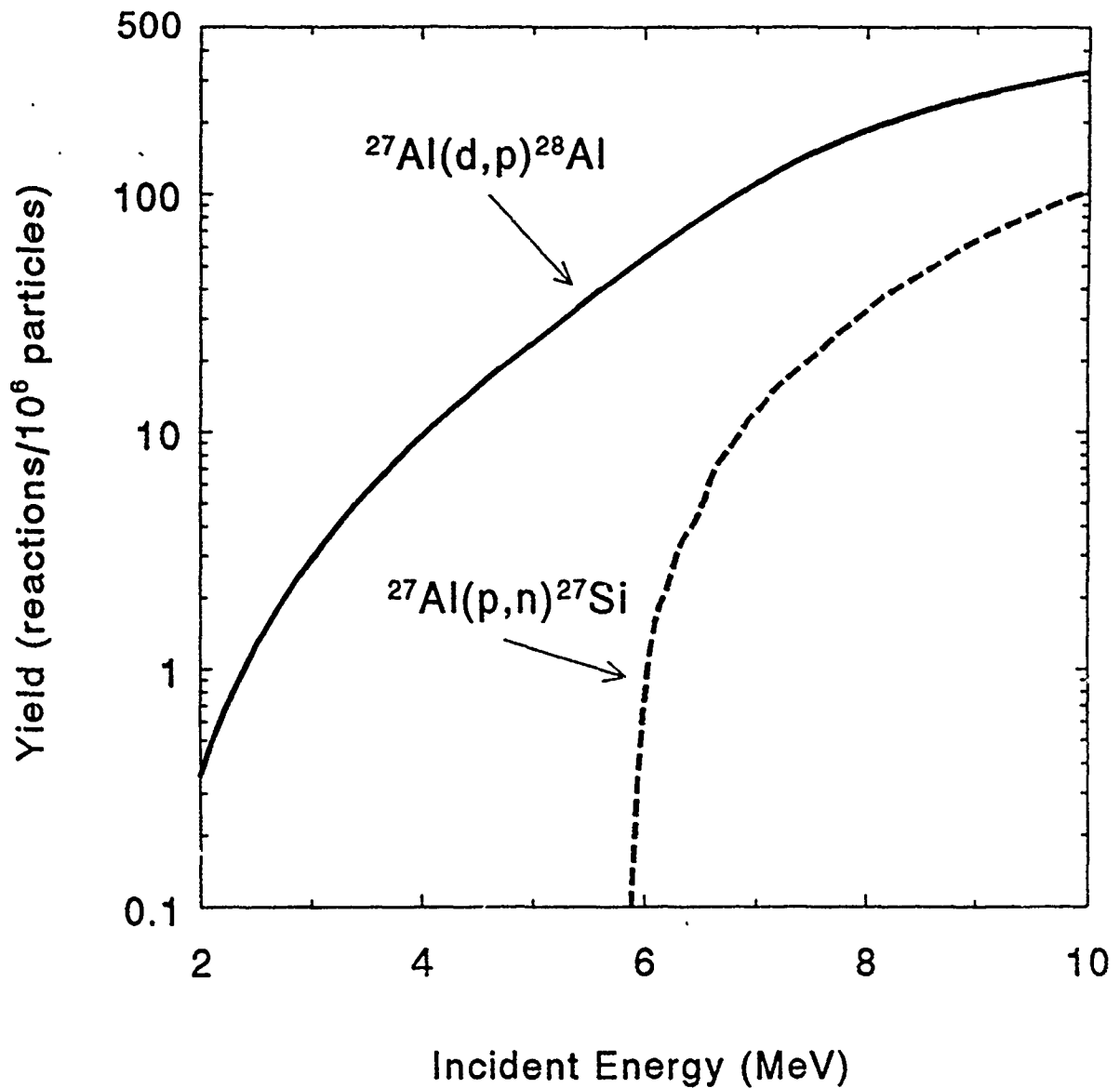


Fig. 3. Thick-target yields for the $^{27}\text{Al}(p,n)^{27}\text{Si}$ and $^{27}\text{Al}(d,p)^{28}\text{Al}$ reactions in an aluminum target.

CROSS SECTIONS

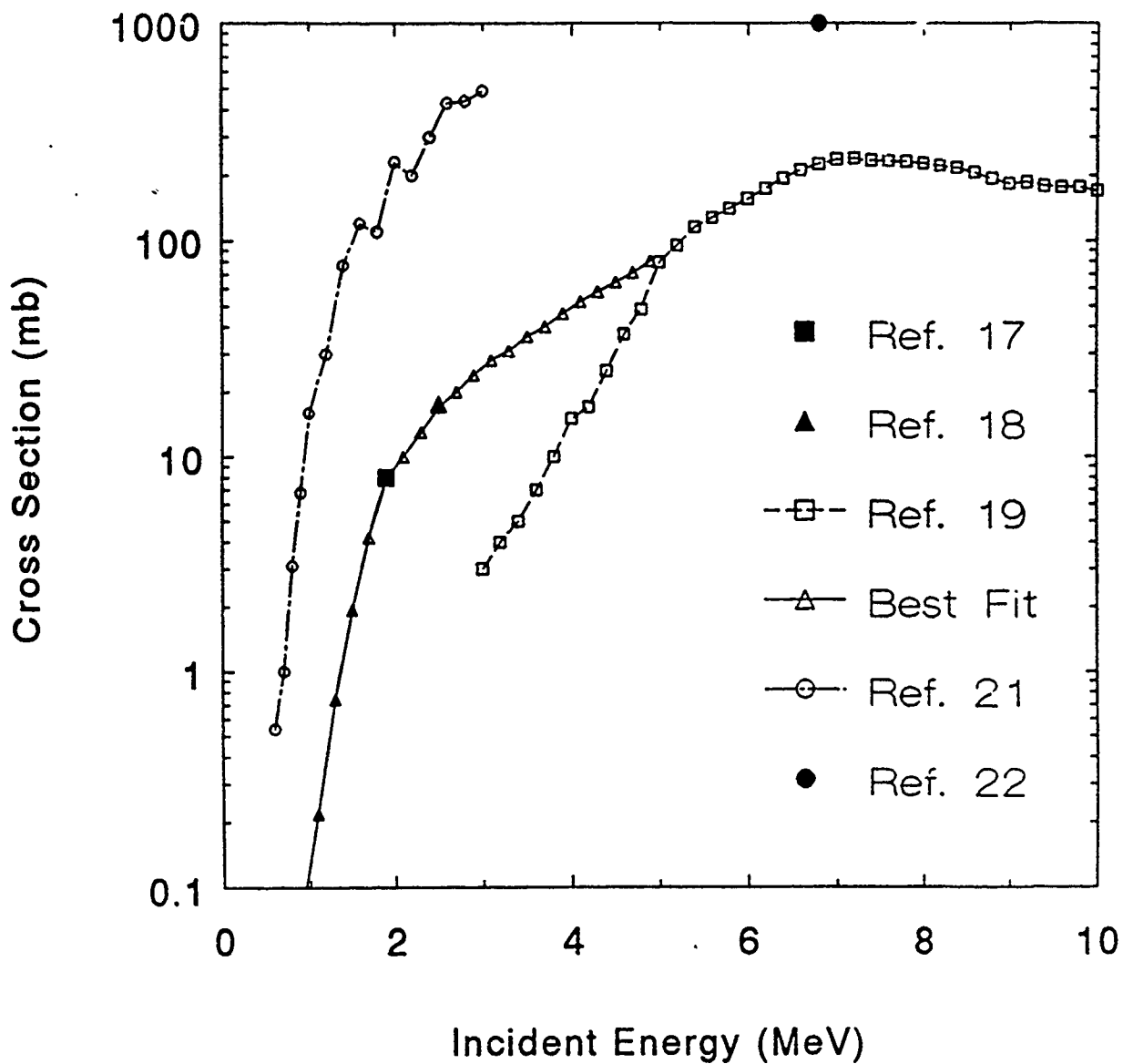
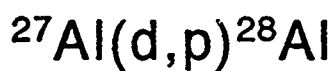


Fig. 4. Measured cross sections for the $^{27}\text{Al}(d,p)^{28}\text{Al}$ reaction. The References are identified in the text. The best fit is for cross sections from References 17, 18 and 19.

THICK-TARGET YIELDS

Titanium Target

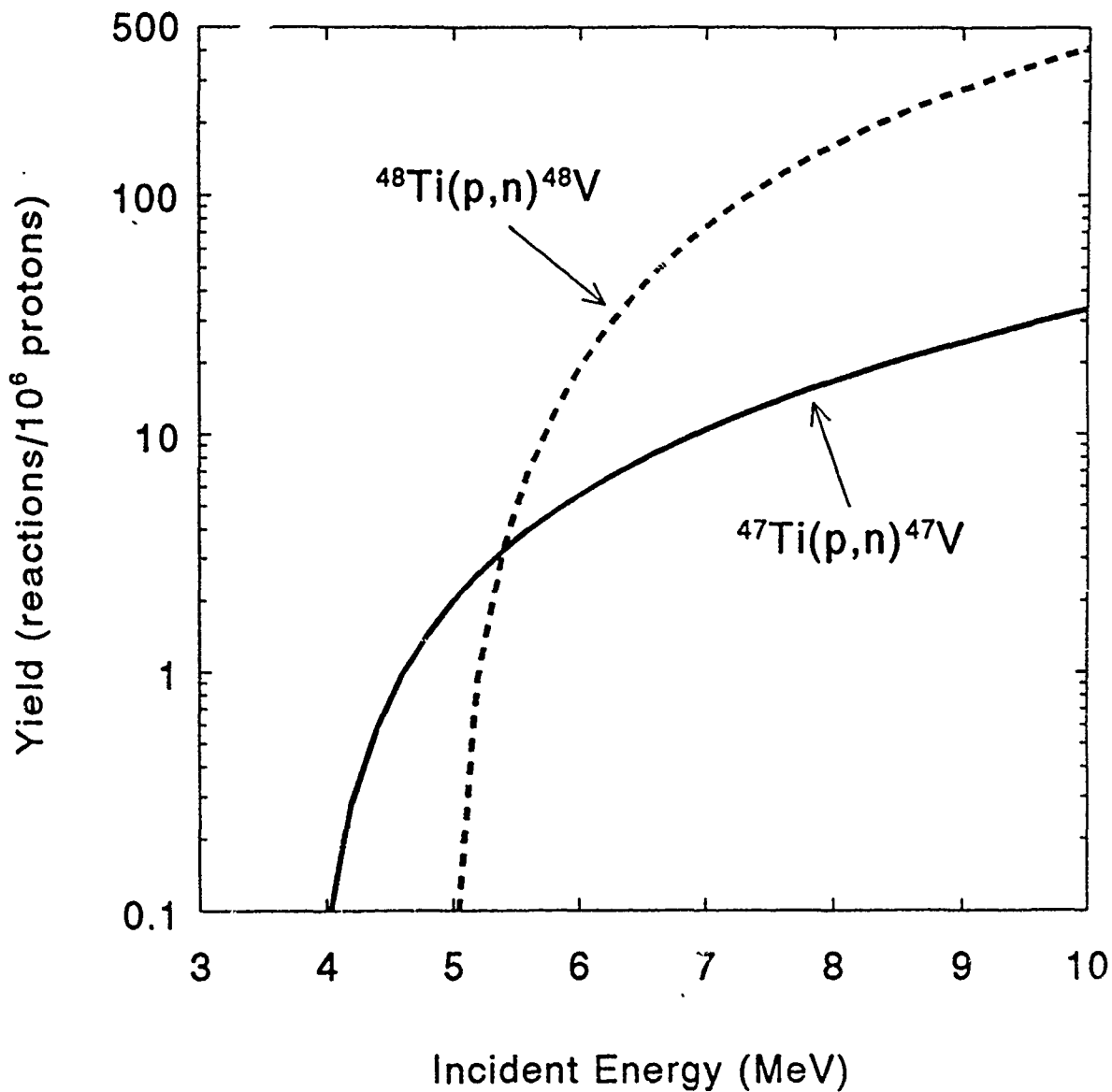


Fig. 5. Thick-target yields for the $^{47}\text{Ti}(p,n)^{47}\text{V}$ and $^{48}\text{Ti}(p,n)^{48}\text{V}$ reactions in a natural titanium target.

THICK-TARGET YIELD

Vanadium Target

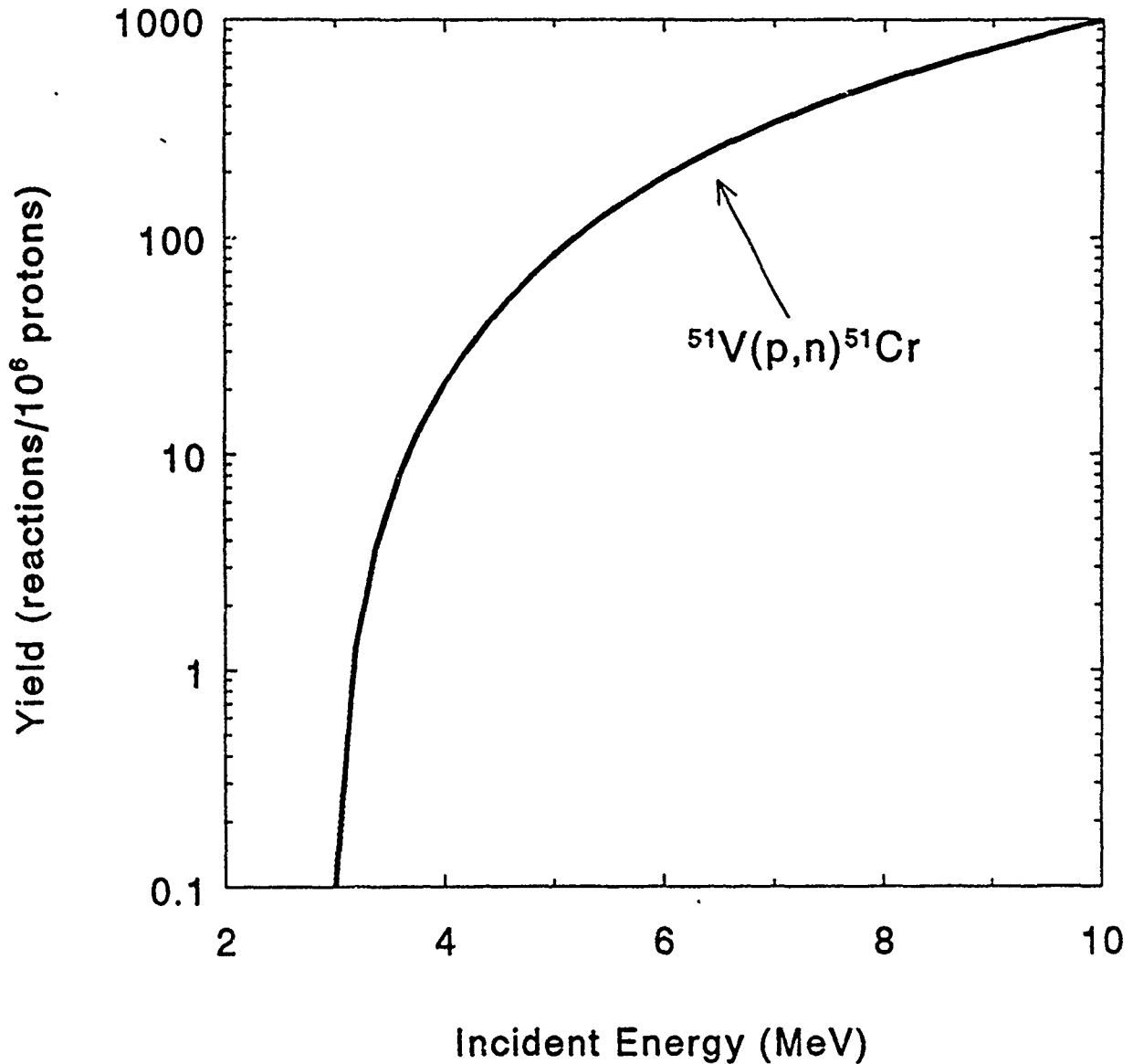


Fig. 6. Thick-target yield for the $^{51}\text{V}(p,n)^{51}\text{Cr}$ reaction in a natural vanadium target.

THICK-TARGET YIELDS

Chromium target

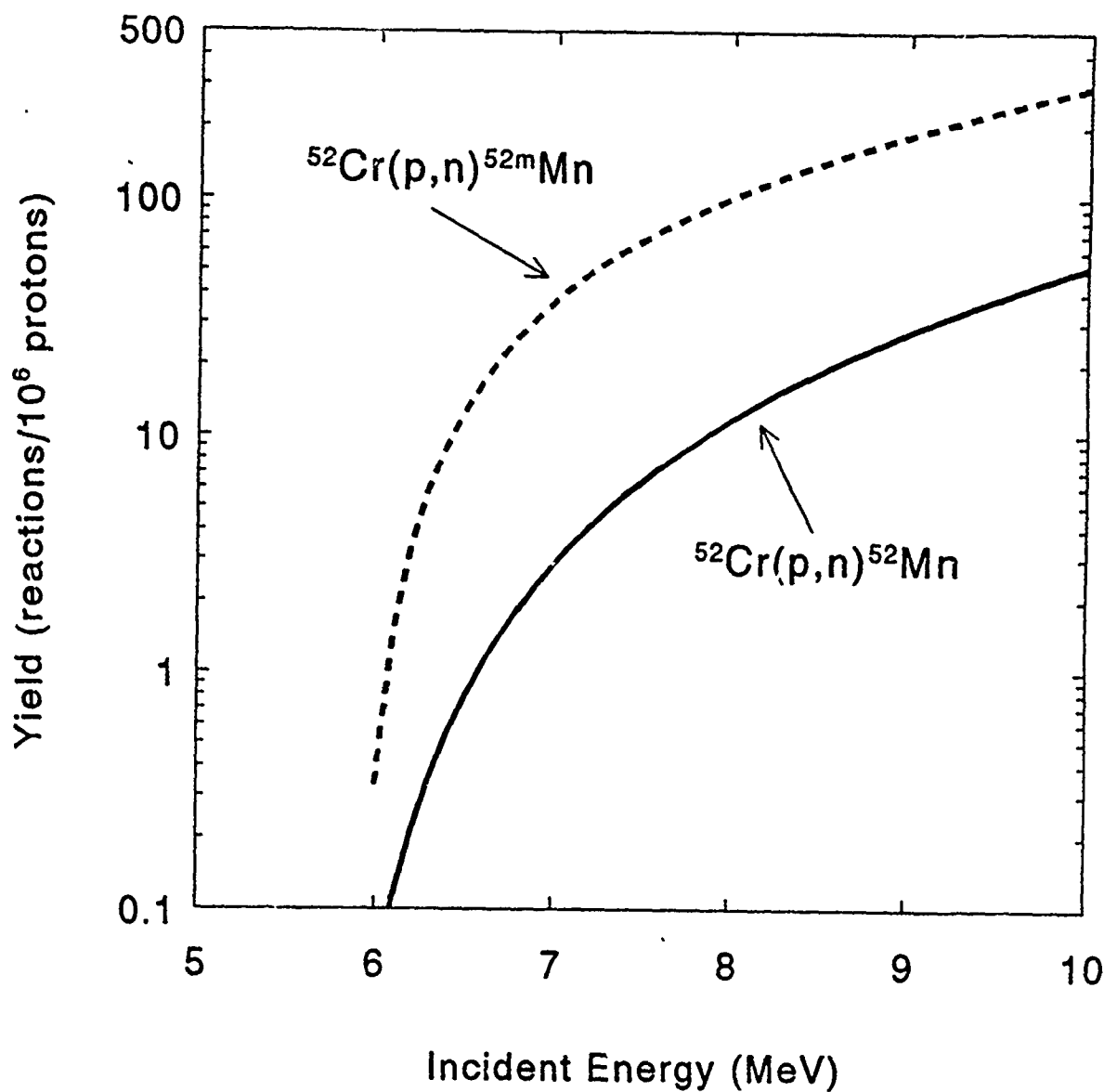


Fig. 7. Thick-target yields for the $^{52}\text{Cr}(p,n)^{52}\text{Mn}$ and $^{52}\text{Cr}(p,n)^{52m}\text{Mn}$ reactions in a natural chromium target.

THICK-TARGET YIELDS

Iron Target

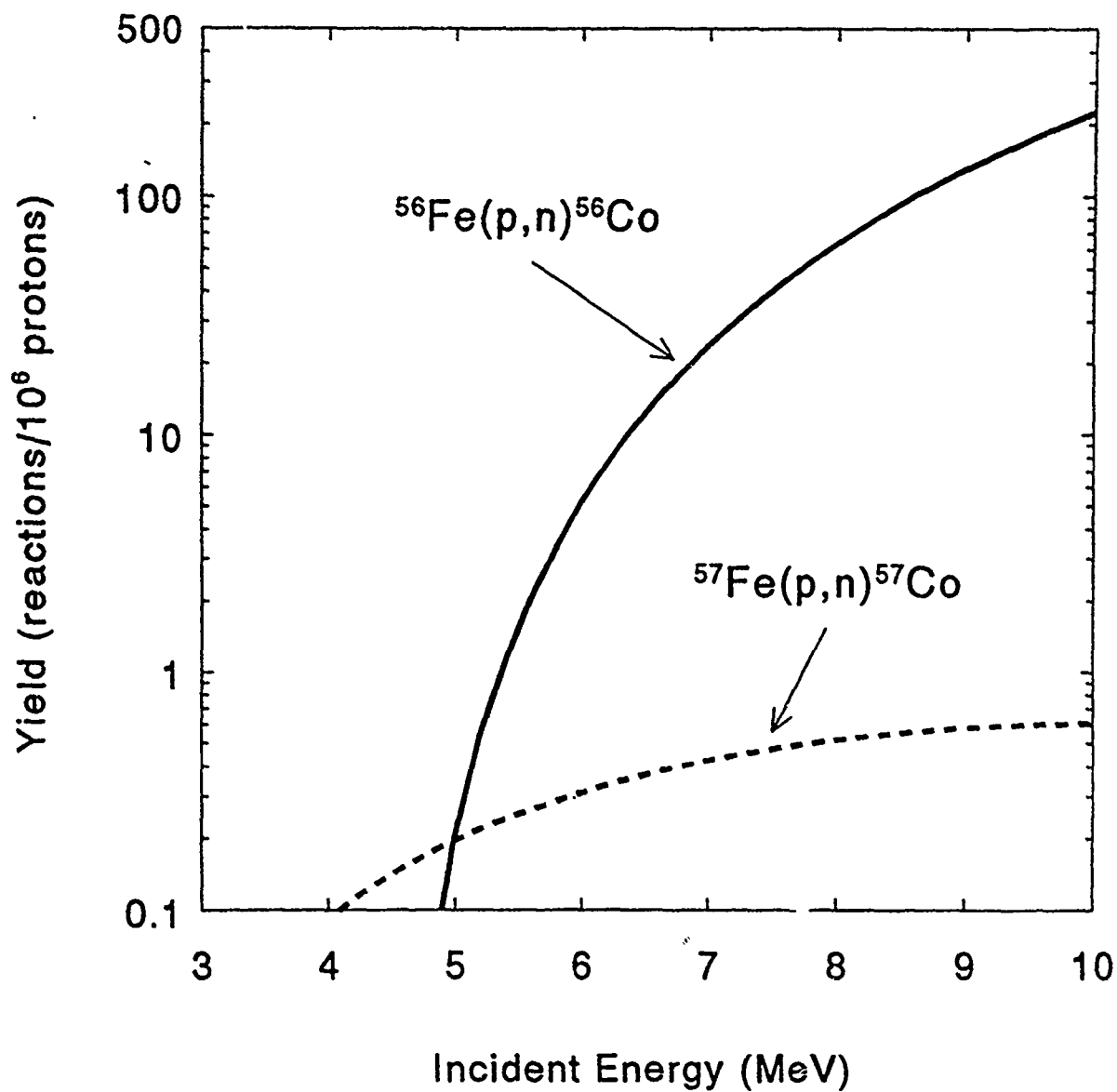


Fig. 8. Thick-target yields for the $^{56}\text{Fe}(p,n)^{56}\text{Co}$ and $^{57}\text{Fe}(p,n)^{57}\text{Co}$ reactions in a natural iron target.

THICK-TARGET YIELDS

Nickel Target

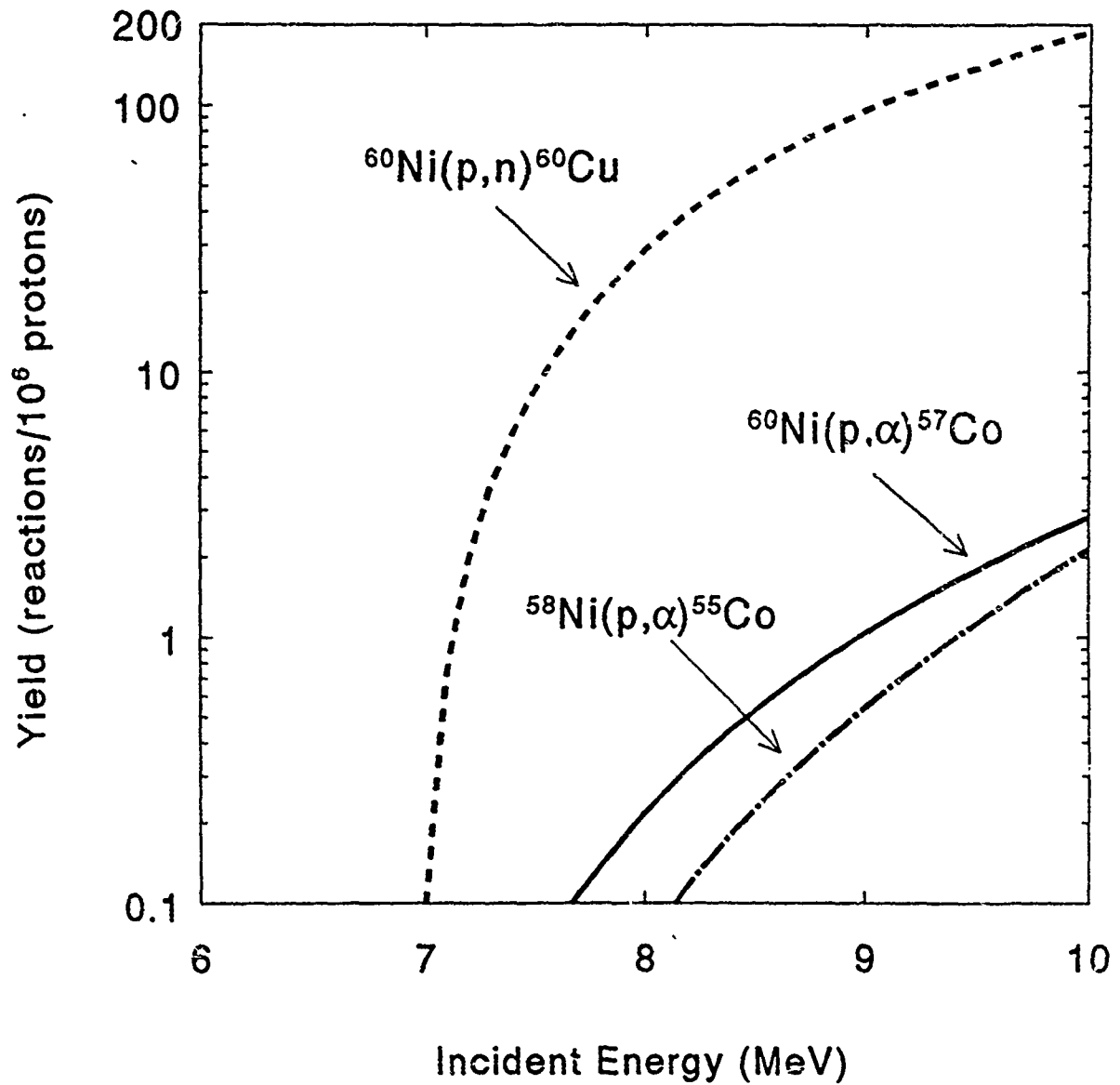


Fig. 9. Thick-target yields for the $^{60}\text{Ni}(p,n)^{60}\text{Cu}$, $^{60}\text{Ni}(p,\alpha)^{57}\text{Co}$, and $^{58}\text{Ni}(p,\alpha)^{55}\text{Co}$ reactions in a natural nickel target.

THICK-TARGET YIELDS

Copper target

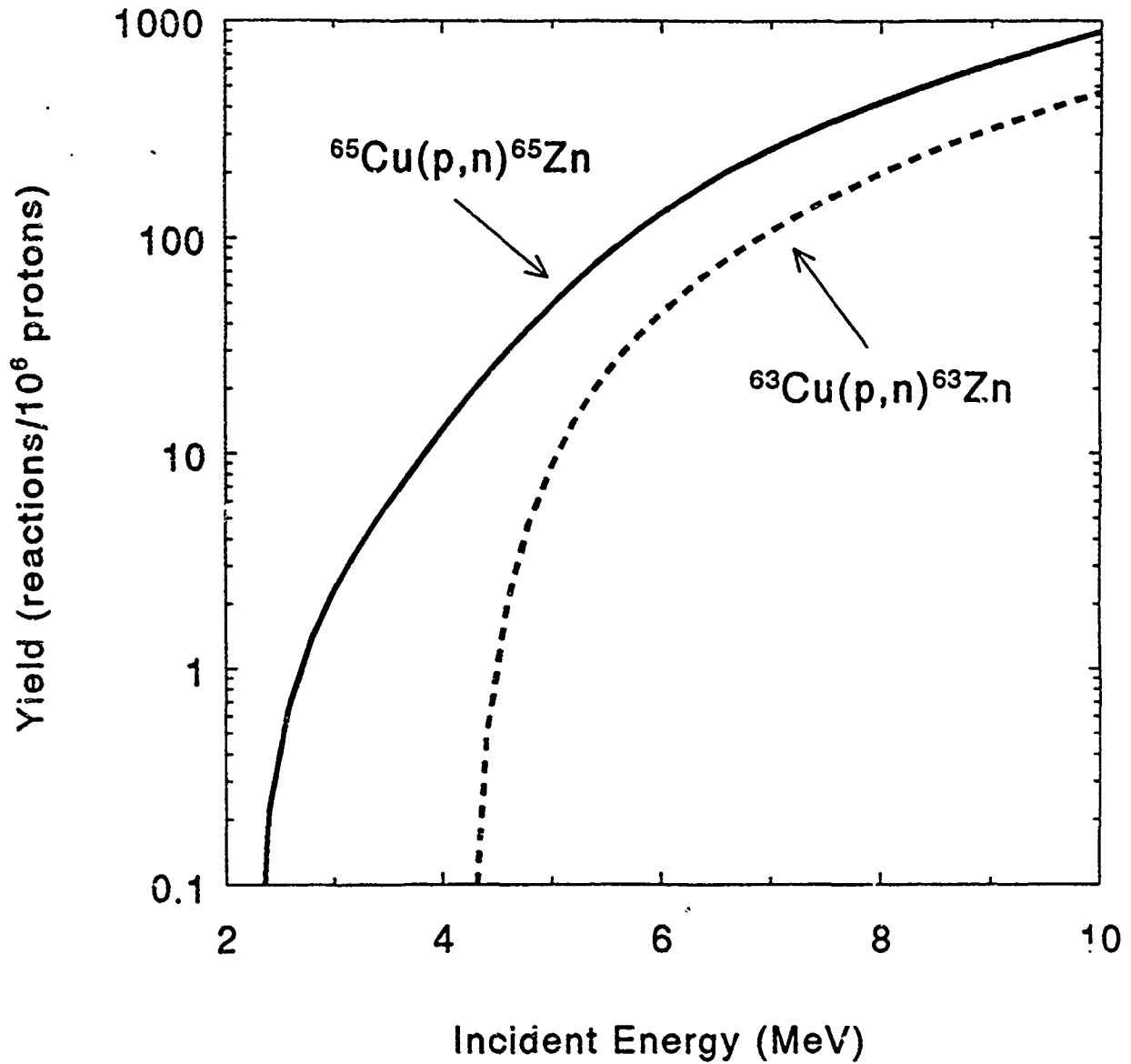


Fig. 10. Thick-target yields for the $^{65}\text{Cu}(p,n)^{65}\text{Zn}$ and $^{63}\text{Cu}(p,n)^{63}\text{Zn}$ reactions in a natural copper target.

THICK-TARGET YIELDS

Zinc Target

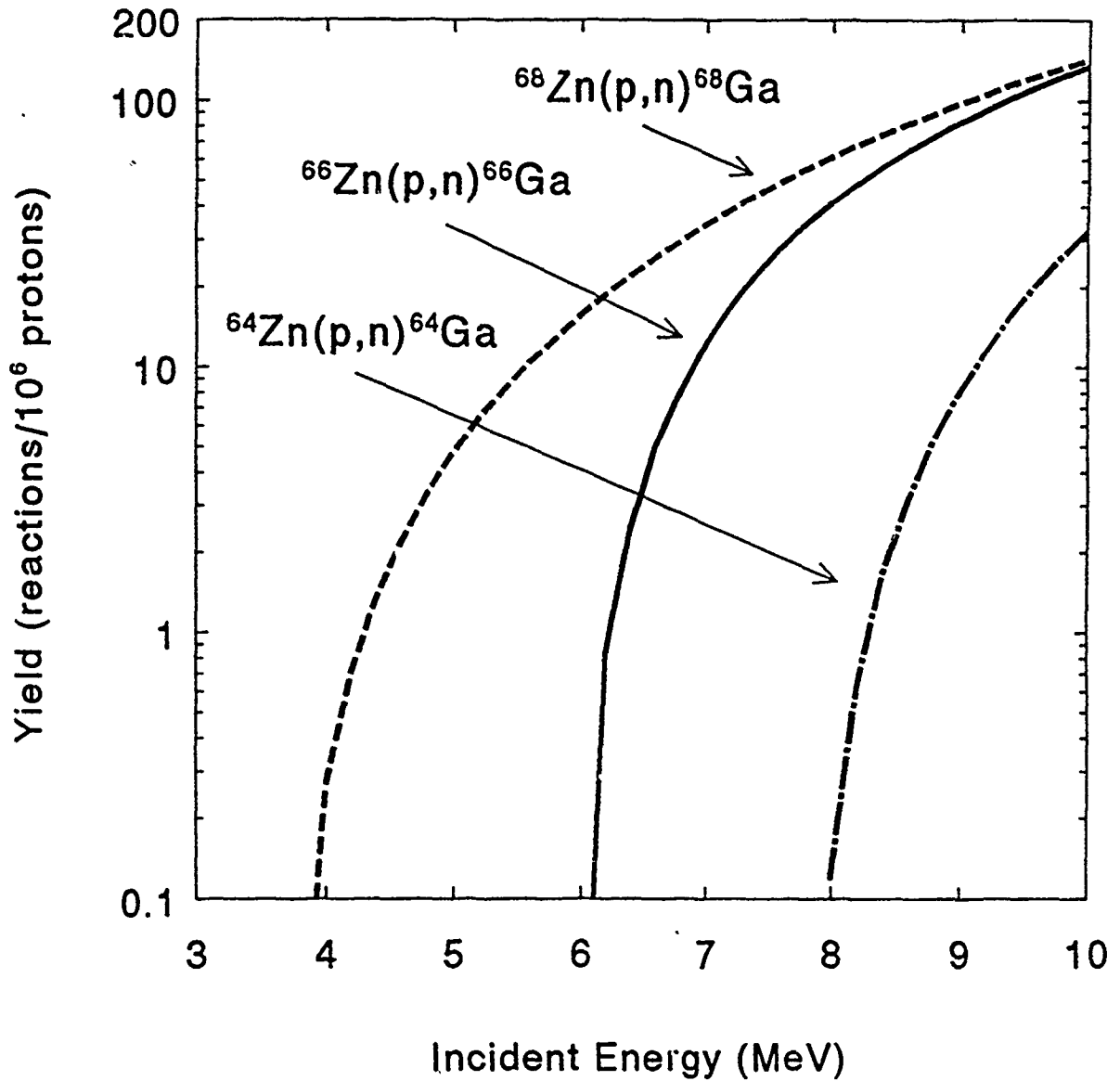


Fig. 11. Thick-target yields for the $^{64}\text{Zn}(p,n)^{64}\text{Ga}$, $^{66}\text{Zn}(p,n)^{66}\text{Ga}$, and $^{68}\text{Zn}(p,n)^{68}\text{Ga}$ reactions in a natural zinc target.

THICK-TARGET YIELDS

Chromium Target

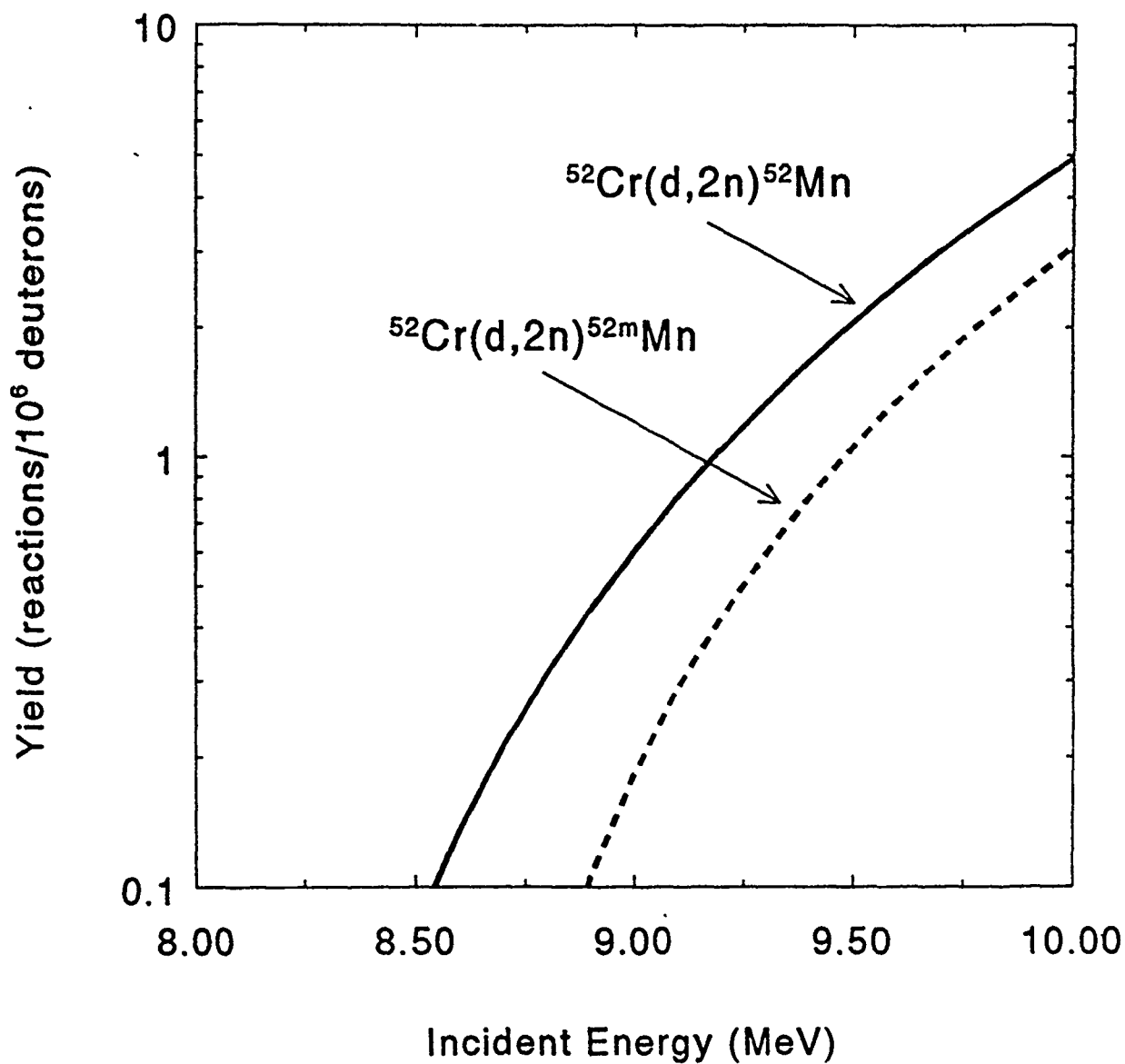


Fig. 12. Thick-target yields for the $^{52}\text{Cr}(d,2n)^{52}\text{Mn}$ and $^{52}\text{Cr}(d,2n)^{52m}\text{Mn}$ reactions in a natural chromium target.

THICK-TARGET YIELDS

Iron Target

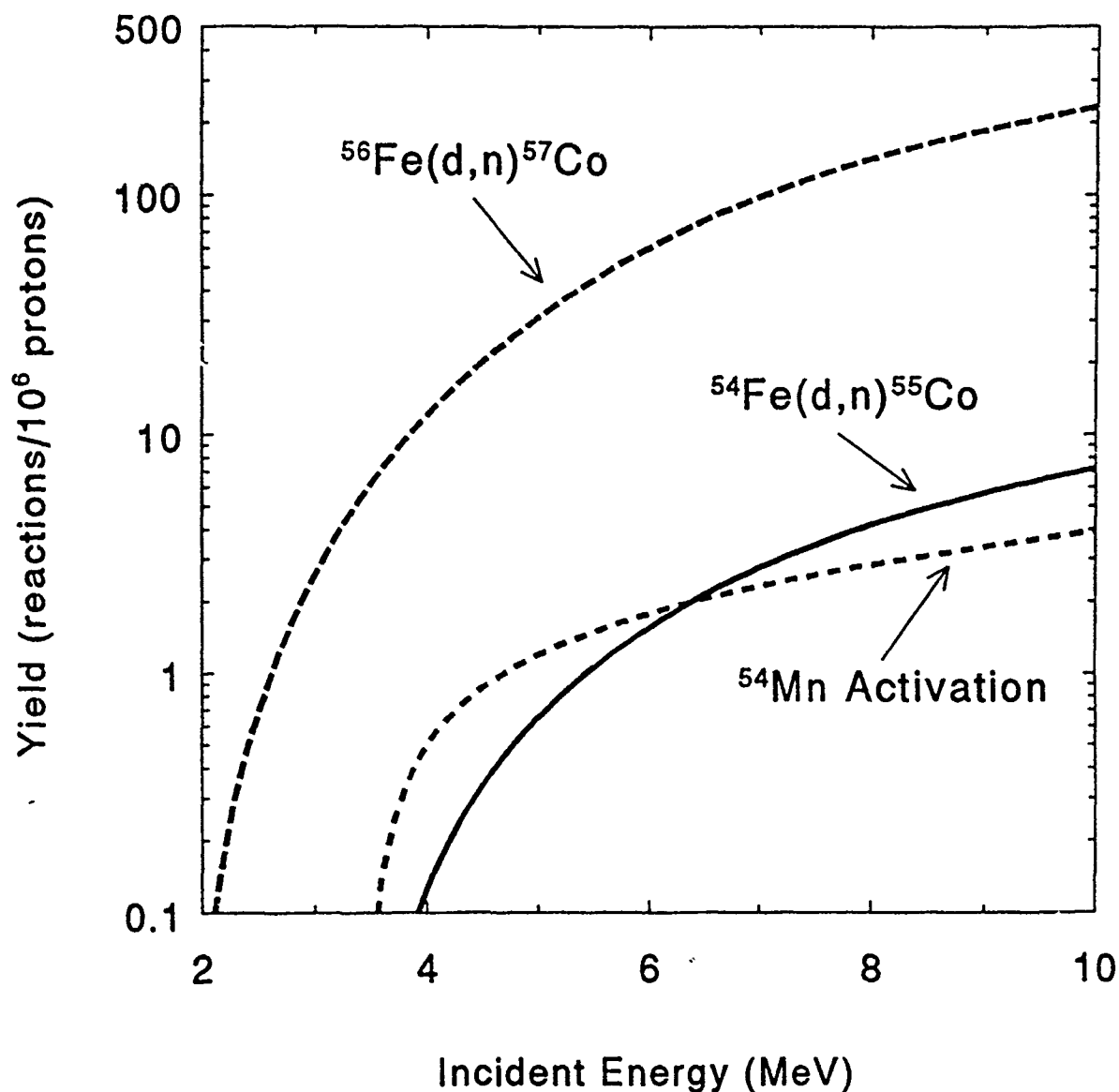


Fig. 13. Thick-target yields for the $^{56}\text{Fe}(d,n)^{57}\text{Co}$ and $^{54}\text{Fe}(d,n)^{55}\text{Co}$ reactions and for the activation of ^{54}Mn by deuterons on a natural iron target.

THICK-TARGET YIELDS

Nickel Target

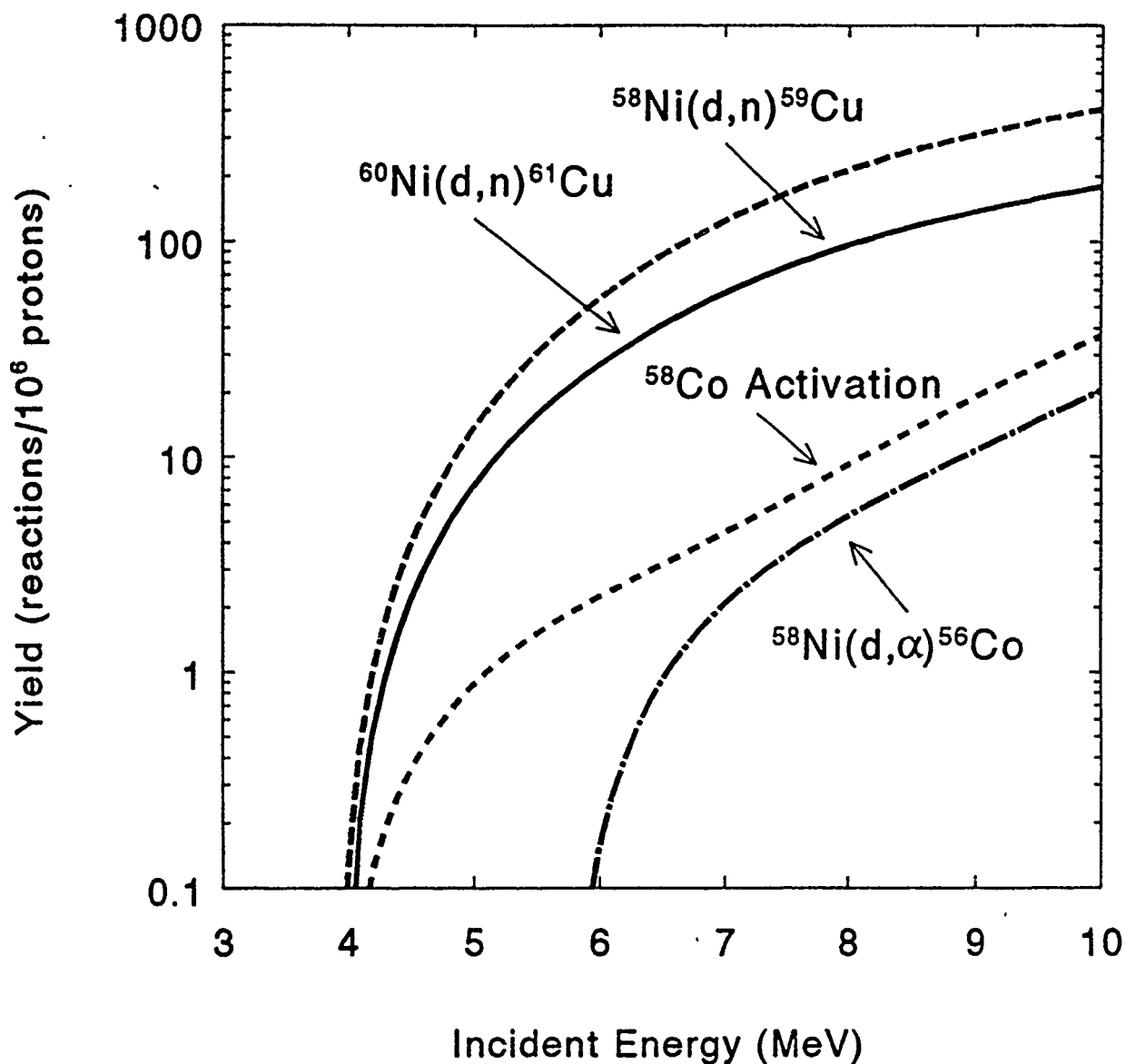


Fig. 14. Thick-target yields for the $^{58}\text{Ni}(d,n)^{59}\text{Cu}$, $^{60}\text{Ni}(d,n)^{61}\text{Cu}$, and $^{58}\text{Ni}(d,\alpha)^{56}\text{Co}$ reactions and for the activation of ^{58}Co by deuterons on a natural nickel target.

THICK-TARGET YIELDS

Copper Target

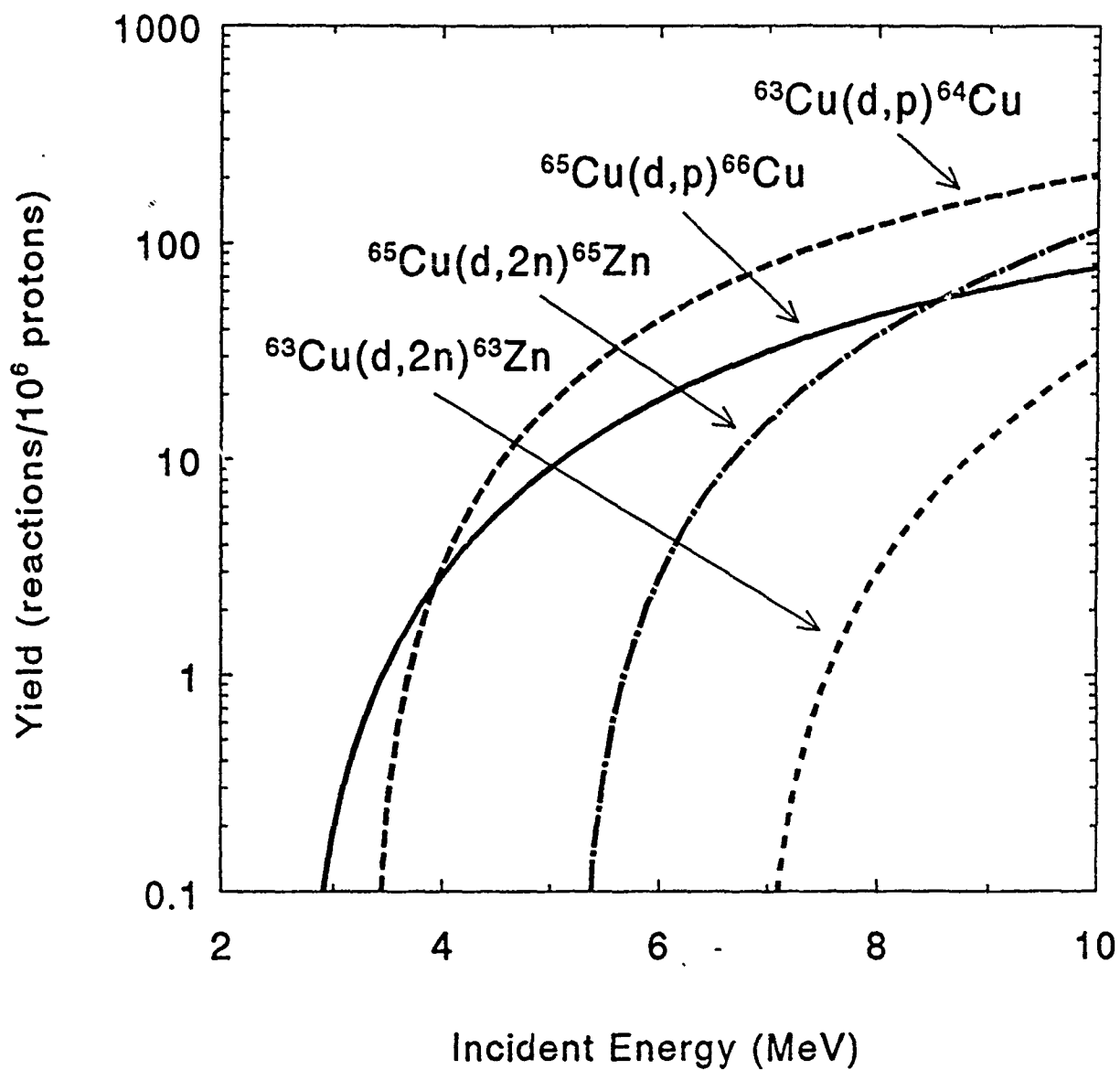


Fig. 15. Thick-target yields for the $^{63}\text{Cu}(d,p)^{64}\text{Cu}$, $^{65}\text{Cu}(d,p)^{66}\text{Cu}$, $^{63}\text{Cu}(d,2n)^{63}\text{Zn}$, and $^{65}\text{Cu}(d,2n)^{65}\text{Zn}$ reactions in a natural copper target.

THICK-TARGET YIELDS

Zinc Target

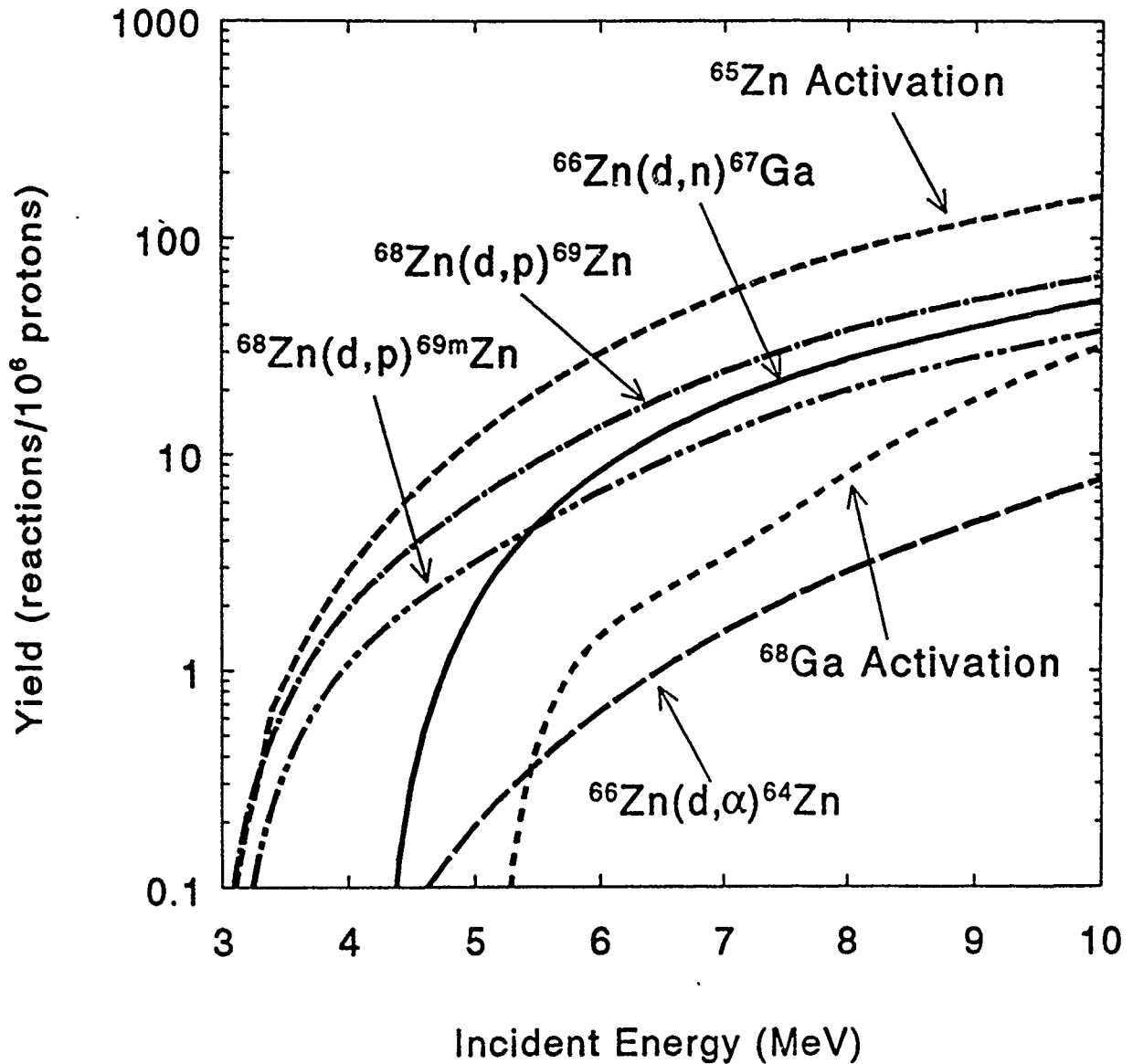


Fig. 16. Thick-target yields for the activation of ^{65}Zn by deuterons and for the $^{66}\text{Zn}(d,n)^{67}\text{Ga}$, $^{68}\text{Zn}(d,p)^{69}\text{Zn}$, $^{68}\text{Zn}(d,p)^{69m}\text{Zn}$, $^{66}\text{Zn}(d,\alpha)^{64}\text{Cu}$, and $^{68}\text{Zn}(d,2n)^{68}\text{Ga}$ reactions in a natural zinc target.

Light Ion Beams for Material Response Simulation

**D. Mosher, S.J. Stephanakis, F.C. Young, G. Cooperstein,
R.J. Commisso, P.J. Goodrich, D.D. Hinshelwood, J.M. Neri,
and B.V. Weber**

**Plasma Physics Division
Naval Research Laboratory
Washington, D.C. 20375-5000
(202)767-6775**

S. H. Richter, L. M. Lee, and D. V. Keller

**Ktech Corporation
Albuquerque, N.M. 87110-7491**

Work supported by the Defense Nuclear Agency under DNA MIPR Nos. 90-582M and 90-614

Distribution authorized to U.S. Government agencies and their contractors; Critical Technology, 3 Aug. 90. Other requests for this document shall be referred to Defense Nuclear Agency, 6801 Telegraph Rd., Alexandria, VA 22310-3398.

WARNING - This document contains technical data whose export is restricted by the Arms Export Control Act (Title 22, U.S.C. Sec 2751, et seq.) or the Export Administration Act of 1979, as amended, Title 50, U.S.C., App 2401 et seq. Violations of these export laws are subject to severe criminal penalties. Disseminate in accordance with provisions of DoD Directive 5230.25.

Abstract

The positive-polarity Gamble II generator has been used to produce megavolt-level proton beams to simulate soft x-rays for material-response studies. Mean ion energies can be varied within the 1- to 2-MeV regime with $\pm 5\%$ voltage reproducibility and $\pm 10\%$ ion power and energy reproducibility. The plasma erosion opening switch has been used to vary the ion power half width from about 20 to 50 ns. Ion-fluences in the 5- to 100-cal/cm² range have been measured over target areas approaching 100 cm² with a spatial uniformity of $\pm 10\%$ at the 50-cal/cm² level. These fluence-area products are about three orders-of-magnitude higher than available from plasma radiation sources driven from comparable pulsed power. Comparison of stress-wave measurements in strategic materials with hydrocode calculations employing the measured beam characteristics show good general agreement. Small differences between experiment and computation suggest that refinements to equation-of-state modeling may be required. Other computations comparing the stress-wave responses of these materials to ion and x-ray deposition demonstrate the equivalence of Gamble II ions to 3- to 10-keV photons. Impulse measurements show that a low-mass version of the pinch-reflex ion diode combined with a large-diameter baffled drift chamber produces an immeasurable debris impulse (under 50 taps). These results demonstrate that light-ion beams represent an alternative to soft x-rays for material- and structural-response studies requiring high fluence and large area in cases where results are not sensitive to the details of the depth-dose profile.

I. Introduction

The mechanical response of materials and structures to high fluences of soft (several keV) x-radiation is an area of continuing interest to the simulation community. In the above-ground environment, material response has been studied using the soft x-rays emitted from the plasma radiation source (PRS), a high-current z-discharge created in a variety of high-atomic number gases and fibers.¹⁻⁴ Although PRS facilities that provide the spectrum, fluence, and exposure area to meet advanced simulation objectives are in the planning stage, the fluences and irradiation areas available with existing facilities are frequently limited (by the inverse-square fall off of fluence with distance) to values below those required for testing.

In cases where higher fluences and larger areas are required and the material response under study is not sensitive to the details of the depth-dose profile, light ion beams represent an attractive alternative to soft x-rays. Techniques to efficiently produce and manipulate intense light ion beams⁵⁻⁸ using low-impedance water-line generators were developed in the period 1975-

1980 to meet DoD and DoE inertial-confinement-fusion objectives.⁹ Major accomplishments of this effort were the extraction of MeV-level proton and deuteron beams containing greater than 50% of the diode electrical energy, and the ability to efficiently deposit these beams onto target areas ranging from a few to several-hundred cm^2 . The ability to deliver the beam to a given target area without inverse-square losses, coupled with the high beam production efficiency, leads to dose-area products about three orders-of-magnitude higher than available from a PRS driven by comparable electrical power. Moreover, the one- to several-MeV ion energies attainable with TW-level pulsed power correspond to absorption depths of 3- to 10-keV photons in materials of interest, a spectral region in which the PRS radiation efficiency is strongly reduced. Electron beams created with water-line generators have absorption depths two to three orders-of-magnitude greater than ion and soft x-ray values. In addition, the 50-ns ion-beam-power half width is appropriate for simulation and can be shortened to about 10 ns using a combination of energy filtering and pulse-sharpening techniques.

A few years ago, comprehensive material-response calculations and preliminary experiments conducted on the HydraMITE-II accelerator at Sandia National Laboratories demonstrated the utility of ion beams for nuclear weapons effects simulation of soft x-rays in applications where peak stress generation is of primary interest.¹⁰ In the present work, we report on experiments conducted at the Naval Research Laboratory that extend the SNL results to order-of-magnitude higher beam energies and exposure areas and demonstrate the ability of proton beams to simulate the stress-profile response of materials to soft x-rays.¹¹⁻¹² The positive-polarity Gamble II generator has been used to produce 1- to 2-MeV mean energy proton beams with $\pm 5\%$ voltage reproducibility and $\pm 10\%$ ion power and energy reproducibility. The plasma erosion opening switch has been used to vary the ion power half width from about 20 to 50 ns. Ion-fluences in the 5- to 100-cal/ cm^2 range have been measured over target areas approaching 100 cm^2 with a spatial uniformity of $\pm 10\%$ at the 50-cal/ cm^2 level. These fluence-area products are about three orders-of-magnitude higher than available from plasma radiation sources driven from comparable pulsed power.

During the past few years, this ion source has been used to test strategic materials and structures at dose-area products not previously available above ground. Comparison of stress-wave measurements in Teflon, tape-wrapped carbon phenolic, and aluminum with hydrocode calculations employing the measured beam characteristics show good general agreement, while small differences between experiment and computation suggest that refinements to the equation-of-state modeling of Teflon may be required. Other computations comparing the stress-wave responses of these materials to ion and x-ray deposition demonstrate the equivalence of Gamble II ions to 3- to 10-keV

photons. Impulse measurements show that a low-mass version of the pinch-reflex ion diode combined with a baffled drift chamber produces an immeasurable debris impulse (under 50 taps). These results demonstrate that light-ion beams represent an alternative to soft x-rays for material- and structural-response studies requiring high fluence and large area in cases where results are not sensitive to the details of the depth-dose profile.

The presentation of the work is divided into two main subject areas: development and documentation of the proton source, and measurements of material response to proton deposition and debris. In Sec. II, the experimental arrangement is presented, beam production and delivery techniques are described, and beam diagnosis is discussed. In Sec. III, ion-induced stress-profile measurements are presented and compared to material-response calculations employing the measured Gamble II beam conditions. Other code calculations are then used to compare the material response to ion deposition with that produced by soft x-rays. Diode-debris measurements at the target location are then discussed. In Sec. IV, the results are summarized, ion-simulation-fidelity issues are discussed, and future plans in this research area are presented.

II. Proton Source Development

The experimental arrangement for ion simulation experiments on Gamble II is shown in Fig. 1. Protons are extracted from a 12-cm diameter polyethylene-foil anode and are accelerated across a 1.3 cm vacuum gap by the applied voltage. The MeV-level, 500-kA beam then passes through a thin cathode transmission foil (a 1.8- μm thick "KIMFOL" polycarbonate foil manufactured by Kimberly-Clark Corp.) separating the vacuum diode from a gas-filled drift region. The drift region contains about 1 Torr of air in which the ion beam propagates in a charge- and current-neutralized state. The neutralized beam drifts 30-100 cm to a target structure that contains ion-fluence and material-response diagnostics, and test samples.

The electrical diagnostics employed in the ion simulation experiments are also shown in Fig. 1. The proton energy is determined from the voltage drop between the ring cathode and the foil anode. A capacitive voltage divider, located in the water behind the polyurethane insulator, measures the voltage V_d across the insulator. The total current (ion + electron) flowing in the diode is measured at four sites by a resistive shunt in the water (I_{sh}^t) and four B-dot loops (I_{out}) located in the vacuum feed. When averaged in azimuth, the two current measurements agree within 10% as long as flashover does not occur along the surface of the insulator. The voltage drop V across the anode-cathode gap is determined by subtracting the inductive component LdI_{sh}^t/dt from V_d . The inductance L between the voltmeter location and the ion diode load is determined

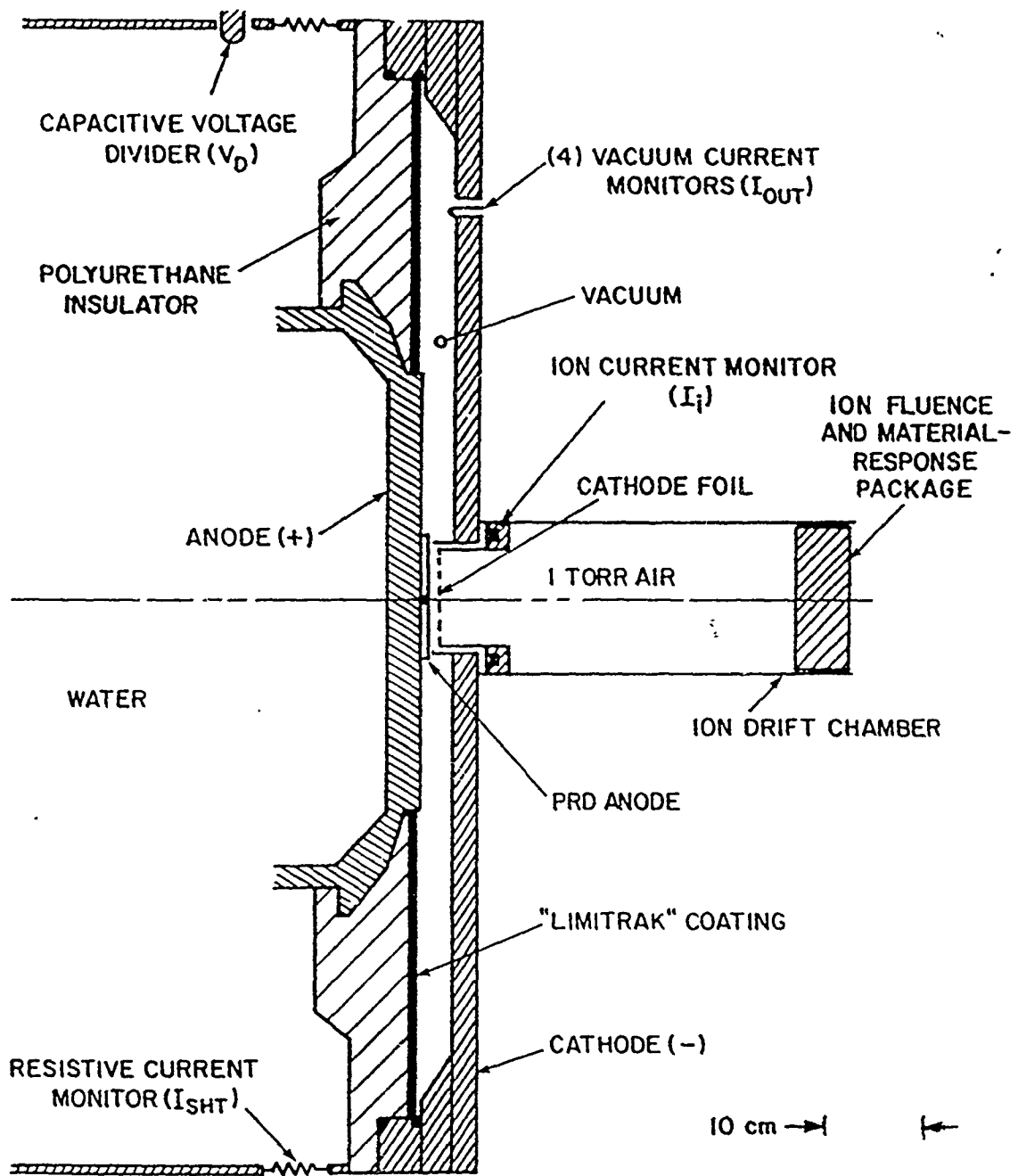


Fig. 1. Experimental arrangement showing electrical diagnostics.

experimentally on short-circuit shots in which the anode and cathode are physically connected. The ion current I_i is measured by a Rogowski coil that monitors ions that cross the polycarbonate transmission foil. Given the above measurements, the instantaneous ion power emitted by the diode $P_i = I_i V$ and total ion beam energy $E_i = \int P_i dt$ can be determined.

Figure 2 illustrates the operating principles of the Pinch Reflex Diode (PRD) used in the experiments. Electrons that are drawn off the thin ring cathode and accelerated across the gap d are constrained to reflex through the thin plastic anode foil by magnetic forces behind the foil and electric forces in the diode gap. Electron reflexing produces the anode plasma (from which beam protons are extracted) by surface-flashover and collisional heating. Electric-field enhancement near the anode produced by the space-charge cloud of reflexing electrons causes the ion current density extracted from the PRD to greatly exceed the Child-Langmuir space-charge limit for one-dimensional flow. Theory and experiment¹³ demonstrate that the extracted ion current for the PRD can be approximated by

$$I_i/I_e = .05RV^{1/2}/d, \quad (1)$$

where the measured diode current I_d is the sum of the ion current I_i and electron current I_e and V is the accelerating voltage expressed in MV. For most Gamble II simulation experiments, $R = 5.7$ cm and d is set at 0.5 cm but gets smaller in time during the power pulse because of plasma closure. For this set of parameters, $I_i/I_e \geq 1$ is predicted and observed. Values of this ratio as high as two have been achieved in higher-power ion experiments conducted on the PITHON generator.¹⁴ Note that the ion efficiency and diode impedance are determined by d and not the gap Δ between the anode foil and cathode transmission foil.

Figure 3 shows a typical set of electrical characteristics for ion beams extracted from the Gamble II diode during simulation experiments. These measurements demonstrate a 40- to 50-ns FWHM ion-power pulse. Integration of ion power over time leads to 30-35 kJ of ion-beam energy with an rms shot-to-shot variation of about $\pm 10\%$ in either ion power or energy. The energy determined from the electrical data is consistent with the radial integral of ion fluence determined from the carbon-activation measurements.^{11,15,16} Reproducibility is demonstrated in Fig. 4 where ion power and diode voltage are overlaid in eight consecutive shots. Positive-polarity plasma-erosion-opening-switch (PEOS) experiments¹⁷ on Gamble II have demonstrated both a reduction in ion pulse duration and a modest increase in accelerating voltage (Fig. 5). The reduction in ion power FWHM to about 20 ns may provide a more realistic simulation of the x-ray threat. Increases in accelerating voltage achievable with the PEOS will provide ions that can simulate higher-energy x-ray spectra than

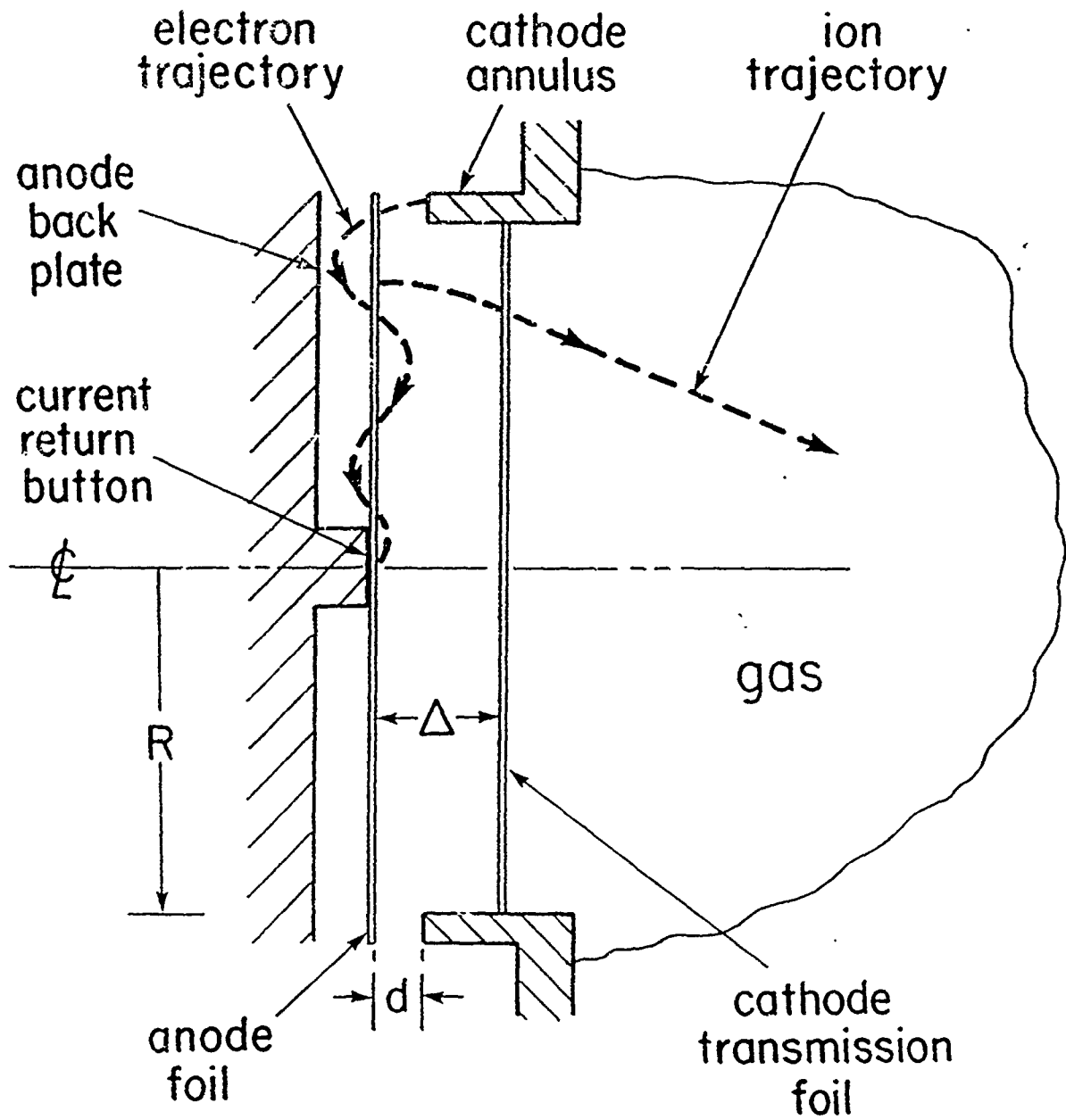


Fig. 2. Simplified drawing of the pinch-reflex ion diode.

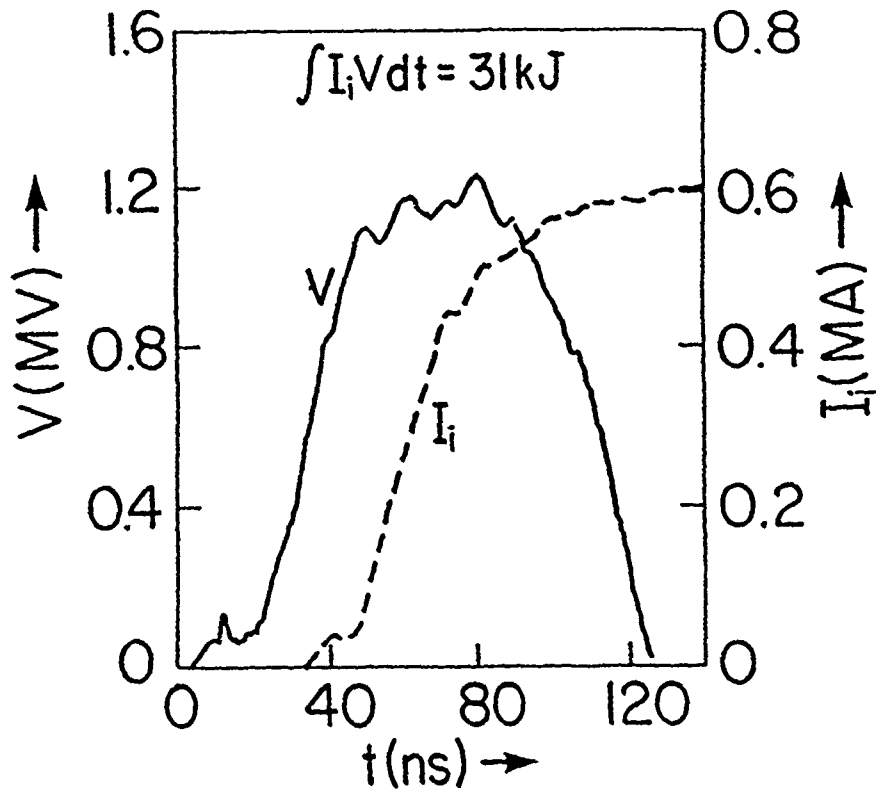


Fig. 3. Ion current and accelerating voltage vs. time for shot 4556.

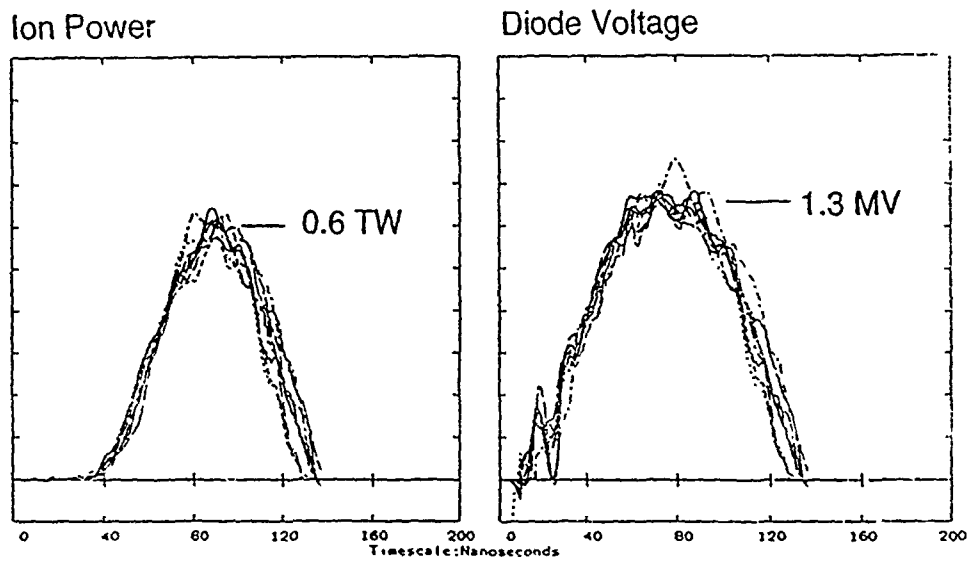


Fig. 4. Overlaid ion power and diode voltage histories for 8 consecutive shots (shots 4786 - 4793).

would otherwise be possible on Gamble II. The fast-rising voltage may also promote more uniform anode plasma formation, thereby reducing beam nonuniformities and asymmetries on the target.

The ion deposition profile is strongly dependent on the time-integrated distribution of proton energies determined from the variation of accelerating voltage with time. Lacking particle detectors that measure the ion-energy spectrum directly, time-integrated energy histograms are derived from the electrical data for each shot. The ion power pulse is divided into small time intervals dt . Each beam-energy increment $dE_i = P_i dt$ is added to the energy contained in the accelerating-voltage bin associated with the voltage at the time of the increment. Energy histograms calculated in this manner are shown in Fig. 6 for standard and high impedance diode operation. These histograms are used to calculate time-integrated depth-dose profiles and the resulting material response for comparison with experimental measurements. The range of ion spectra attainable with Gamble II is equivalent to photon deposition in the 3- to 10-keV range, a region of prime simulation interest with insufficient above-ground x-ray fluence capability.

As ions are accelerated across the vacuum gap Δ , they are bent radially inward by their azimuthal self magnetic field. For a PRD, the ion current density in the vacuum gap has been shown to vary inversely with radius.¹⁸ The azimuthal magnetic field produced by ion flow in the vacuum gap is then nearly constant in radius so that nearly all ions are bent through an angle

$$\theta_M = 1.4 I_i \Delta / (RV^{1/2}) , \quad (2)$$

with I_i in MA and V in MV. During the high-ion-power portion of the beam pulse, θ_M varies from about 0.1 to about 0.15 rad for most ions. However, ions emitted near the axis of symmetry, where anode-plasma motion distorts the accelerating field structure and magnetic forces are reduced, can have positive radial velocity. In addition to this systematic deflection, ions experience random deflections θ_p of about 0.1 rad associated with plasma irregularities and field fluctuations in the diode. After passing through the cathode transmission foil, the ions drift ballistically to the target through the gas-filled, field-free drift region. Megavolt-energy protons lose about 10% of their kinetic energy due to collisional slowing-down in the transmission foil and low-pressure gas but, unlike high-energy electrons, are not significantly scattered by the collisions.

The theoretical ion-flux and bending-angle distributions in the diode are coupled with straight-line ion orbits in the field-free drift region to calculate the radial profiles of ion fluence at different distances from the diode. Figure 7 illustrates fluence profiles using typical ion-current and accelerating-voltage waveforms and $\theta_p = 0.1$ rad. Close to the diode, the radial fluence distribution

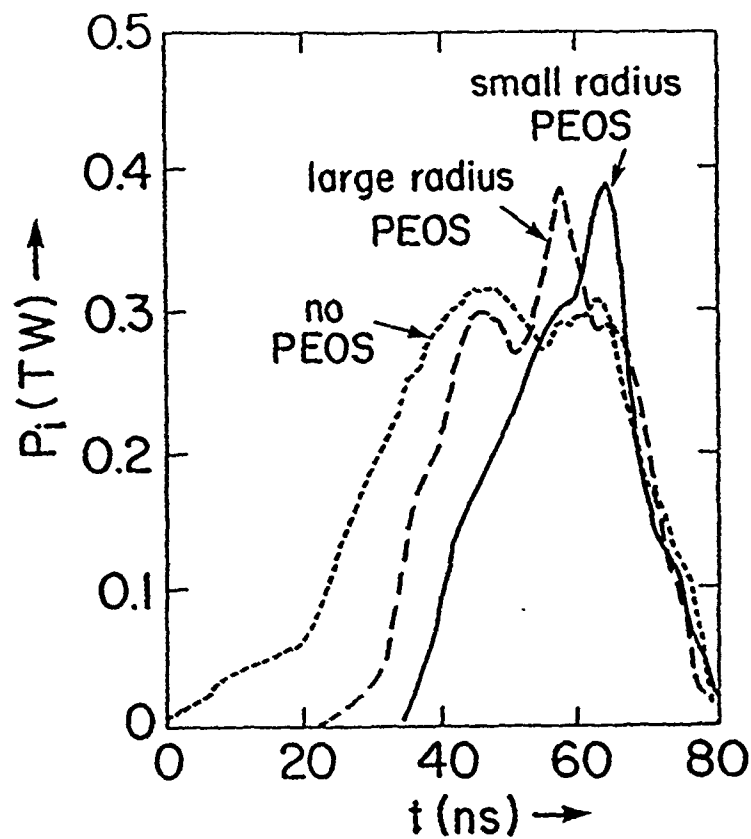


Fig. 5 Ion power histories without the PEOS and with two positive-polarity PEOS configurations.

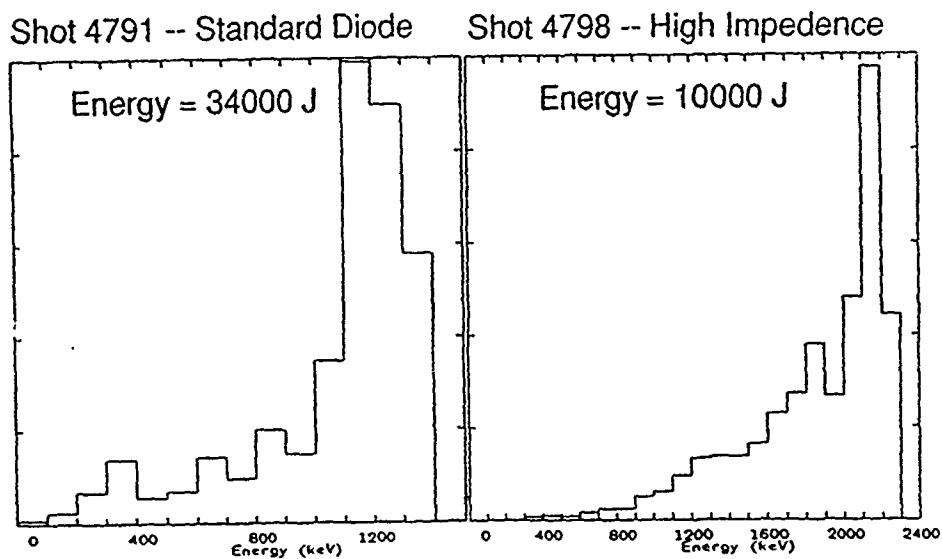


Fig. 6. Ion energy histograms for shot 4791 (standard diode impedance) and shot 4798 (high impedance). Note different energy scales.

follows the $1/r$ variation of emitted ion current density predicted for the PRD. As one moves away from the diode, the inner portion of the beam spreads while the outer portion contracts. Mixing of ions from different regions of the diode due to orbit crossing and beam divergence (θ_p) produces more uniform radial distributions. Uniformity over diode-sized areas is expected beyond the point $z = F$ where an ion emitted from $r = R$ crosses the axis of symmetry.

$$F = R/\theta_M = V^{1/2}R^2/(1.4I_i\Delta) . \quad (3)$$

For the parameters of simulation experiments, F is in the range of 40 to 60 cm where 30- to 60-cal/cm² fluences are calculated. Further from the diode, lower fluences uniform over larger areas are expected: Fig. 7 shows 10 cal/cm² uniform over about 300 cm² at about 1 m from the diode.

The experimental proton-fluence distribution was determined at the target plane by carbon-activation measurements.^{11,15,16} The ¹³N radioactivity produced by the ¹²C(p, γ)¹³N(β^+)¹³C reaction was measured to determine the number of protons incident on a carbon sample. Coincidence counting of the 10-min half-life β^+ decay with NaI scintillation detectors was used to measure weak activities. An aerial distribution of small-area, carbon-activation devices (CADS) activated on a single shot provided the proton-fluence distribution.

Four azimuthally-separated CAD measurements at each radius are averaged to give the radial distribution of the proton fluence. Experimental radial fluence profiles are shown for various axial separations from the diode in Fig. 8. Close to the diode, the distribution follows the sharply-peaked variation of emitted ion current density with radius predicted for the PRD with peak fluences in excess of 100 cal/cm². In agreement with Eqn. (3) and the associated discussion, a nearly uniform beam profile over a 5-cm radius is observed between $z = 50$ and 60 cm with fluences of 40-60 cal/cm². Figure 9 shows a contour map of fluence for $z = 62$ cm demonstrating a peak-to-peak variation of $\pm 20\%$ and an rms variation of $\pm 5\%$ over the area. Such maps are used to estimate the ion fluence at the locations of material-response measurements. When combined with the counting statistics, errors in carbon-activation measurements associated with ablating-plasma closure of the 2-mm holes and loss of vaporized activated material lead to fluence uncertainties of about $\pm 20\%$.

The fluence data shown in Figs. 8 and 9 were obtained when power flow problems limited the ion beam energy to 10-20 kJ. Recent increases in ion beam energy (Figs. 3,4, and 6) and improved diode designs should increase the fluence-area capability of Gamble II by a factor of two.

Improvements in ion diagnostics are required for more precise fluence measurements. The carbon-activation diagnostic has limited spatial resolution, and may be inaccurate at high fluences where ablation of carbon leads to loss of

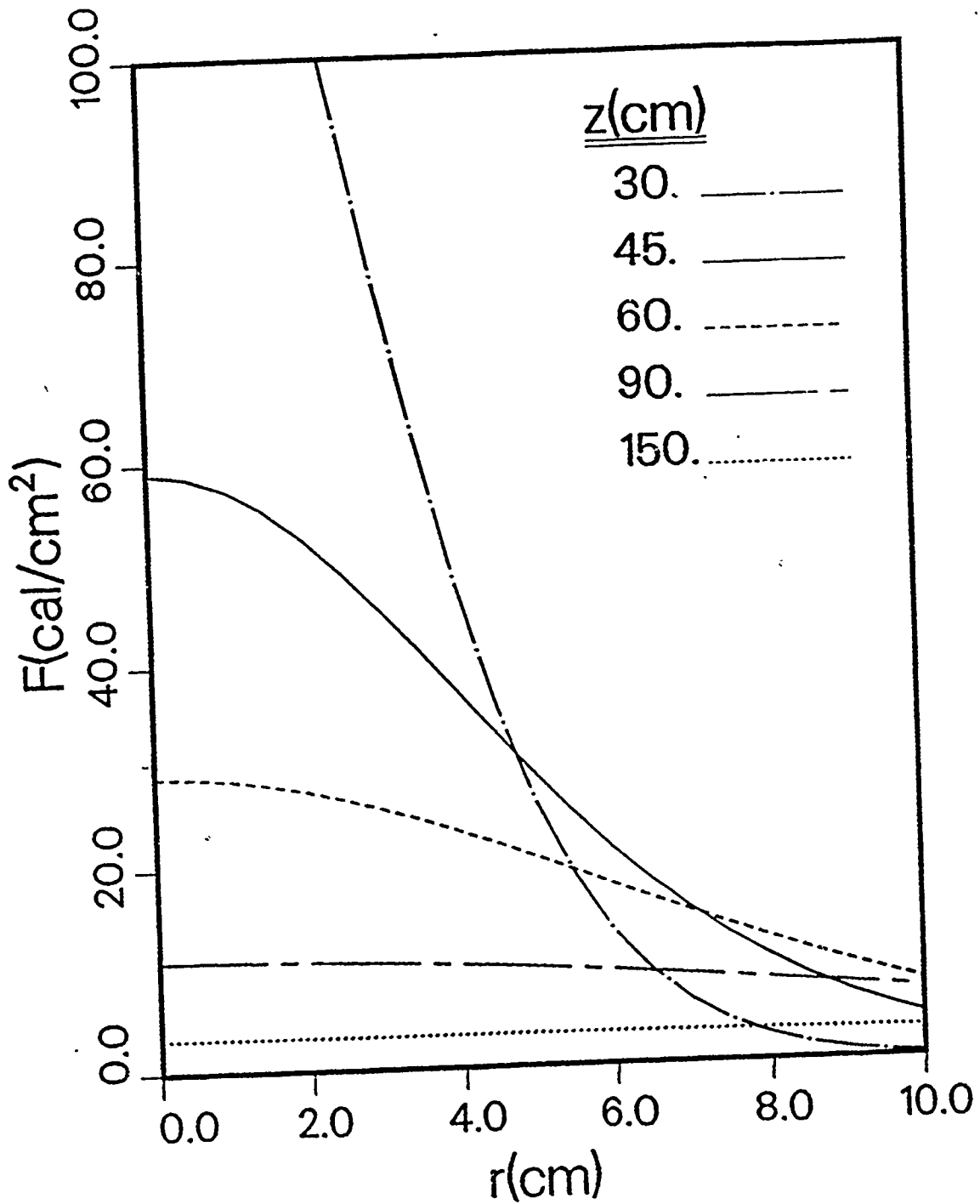


Fig. 7. Orbit code calculation of fluence vs. radius at different distances from the diode for typical ion-current and accelerating-voltage histories and $\theta_p = 0.1$ rad.

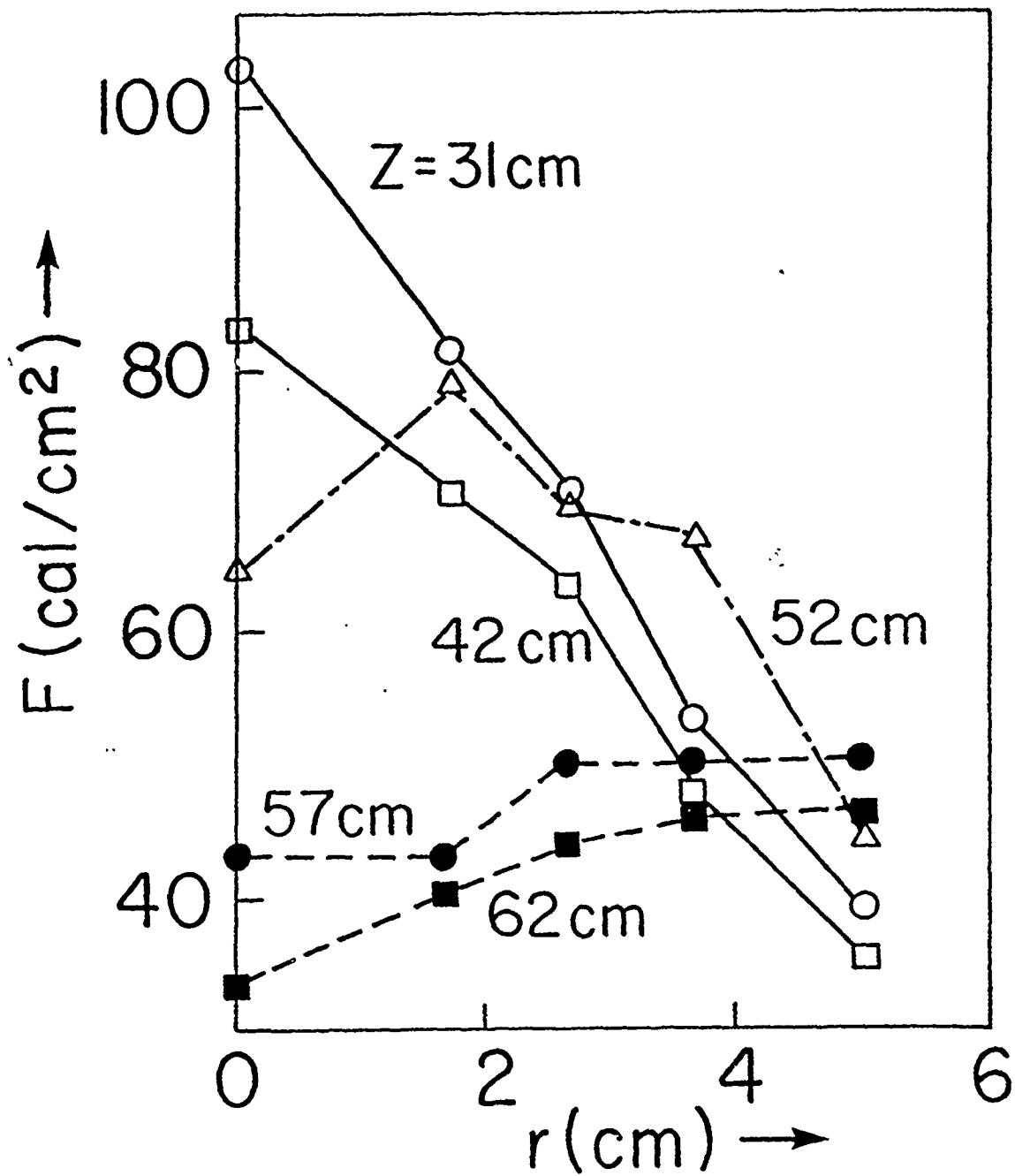


Fig. 8. Experimental radial ion fluence profiles for various separations from the diode.

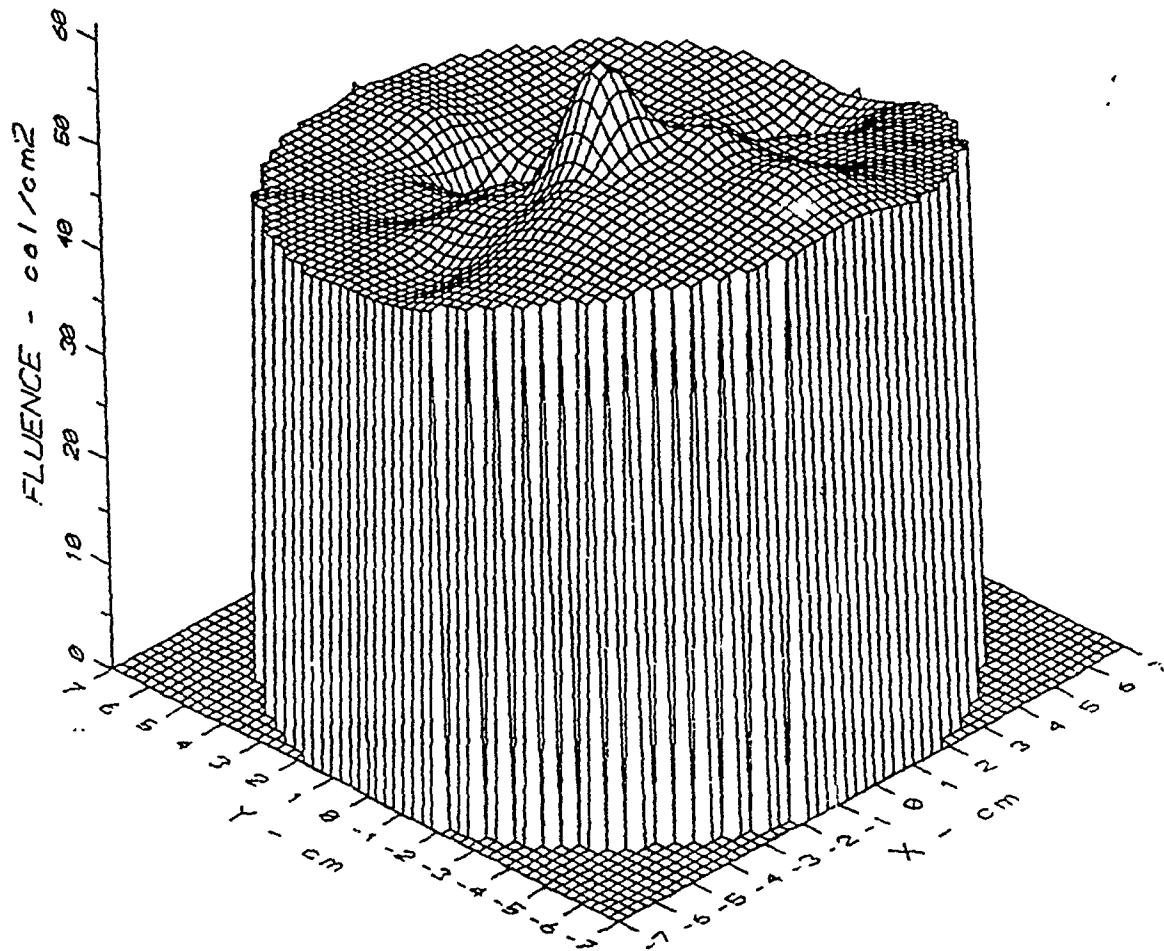


Fig. 9. Fluence map at $z = 62$ cm for shot 4252.

the entrained nitrogen. Higher accuracy and improved (few-millimeter) spatial resolution can be attained by imaging proton-induced, K-line x-ray emission from an aluminum target on photographic film.¹⁹ Measurement of this K-line emission with a gated microchannel-plate detector may provide time-resolved imaging of the ion-beam flux distribution at the test location. Aluminum K- α images were obtained with the x-ray pinhole arrangement shown in Fig. 10. Two cameras with different pinhole sizes were used to image the front surface of an aluminum foil target at the test location. The cameras face away from the diode to minimize diode-bremsstrahlung fogging of the film. Images for two shot are shown in Fig. 11. The shadowed regions correspond to areas of the CAD array not covered in aluminum. Sophisticated data-reduction algorithms are required to unfold the fluence distribution from the imaged film density in the complex exposure geometry. However, the observed exposure is consistent with the known fluence distribution and the results demonstrate that high resolution mapping with the technique can be carried out.

III. Material-Response Measurements and Analyses

The NRL ion source has been used in a comprehensive simulation program to evaluate the simulation fidelity of proton beams, perform material- and structural-response measurements previously relegated to an underground environment, and carry out associated analyses.^{11,12} In one portion of the program, detailed stress-wave profiles generated by well-characterized ion beams were measured in materials of strategic interest and compared to theoretical ion- and x-ray-induced stress profiles in the same materials. In addition to demonstrating the ability of ions to simulate soft x-ray effects, these measurements have been used to benchmark material-response codes in an AGT environment. A few of the stress measurements and calculations are presented here to highlight ion simulation fidelity issues

Stress-profile measurements were made by replacing selected CADs with targets of Teflon, tape-wrapped carbon phenolic (TWCP), and aluminum 1100-0 backed with PVF₂ stress gauges.^{11,12,20} Measurements with neighboring CADs were used to determine fluences on the targets. Target thicknesses for the Teflon and aluminum samples (55.9 μm and 25.4 μm respectively) were chosen to be slightly in excess of the the peak ion range so that measurements could be made with a minimum of stress-wave degradation, and differences between ion and (code-generated) photon responses would be most apparent. Stress-response and impulse-response measurements in these materials were made with ion fluences in the 4- to 80-cal/cm² range. Impulse-response measurements were made with a Linear Velocity Transducer (LVT) momentum gauge.²¹ This gauge had a characteristic response time of 30 to 100 μs so that the signal

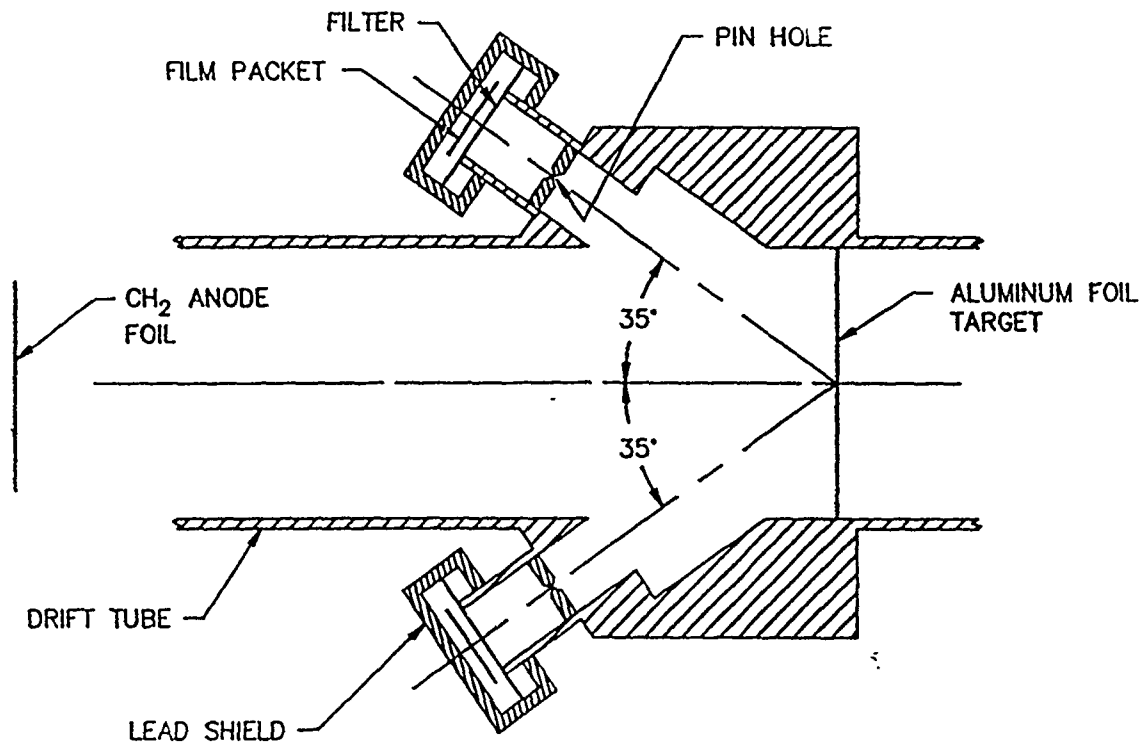


Fig. 10. Aluminum K- α pinhole camera arrangement in Gamble II experiments.

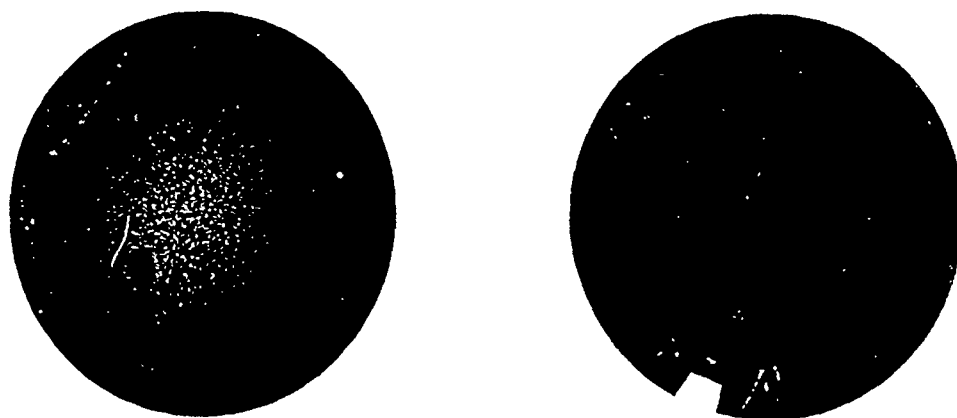


Fig. 11. Aluminum K- α pinhole images of ion deposition on two shots with different pinhole sizes. The shadowed regions are portions of the CAD assembly not covered in aluminum.

associated with slow-moving debris originating at the diode could be separated in time from the prompt ion-beam signal.

Energy deposition profiles for the ion beams were calculated using the Linhard, Scharff, and Schiott (LSS) model for ion stopping power²². In the PROTRAN code developed for this purpose, the target material is specified by the mix of elements, each characterized by atomic number, atomic weight, mean ionization potential, and density. For the hydrodynamic calculations of stress shown here, time-integrated spectra (exemplified by Fig. 6) were employed to determine the ion-energy deposition profiles. In a few cases, time-dependent spectra derived from ion-current and accelerating-voltage histories, and the associated time-of-flight mixing, were used to determine time-varying deposition profiles. Predicted stress-wave profiles using the time-varying profiles were within 10% of those based on time-averaged profiles.

The calculated deposition profiles were combined with hydrodynamic calculations in a 1-dimensional Lagrangian code²³ called PUFF-74 to predict stress profiles. Material equation-of-state data were taken from libraries compiled by Rice²⁴, Rosen²⁵, and Childs²⁶. One major function of the code was to determine differences in stress response to ion and x-ray deposition in order to assess the value of ion beams for material-response simulation. Figure 12 compares the calculated deposition profiles in Teflon for monoenergetic 3-keV photons and a typical Gamble II proton beam. The ion-deposition profile corresponds to a 10^0 range of incidence angles about the normal (typical of the irradiation geometry employed). The multiple peaks in the ion-deposition profile of Fig. 12 are a result of the coarse energy resolution of the ion-energy spectrum. A small, unknown fraction of ionized carbon in the beam has been ignored in the ion deposition profile. Hydrodynamic stress calculations which include a 5% carbon fraction in the beam do not show significantly altered material response. Since carbon ions deposit their energy in a very thin layer (about 10^{-4} mg/cm²) at the material surface, the associated low-mass blow-off produces negligible recoil. (Note that the ion-response measurements presented in this paper are for beam energies in the 10- to 20-kJ range. Subsequent pulsed-power improvements resulted in the 30-kJ beams described in Sec. II.)

Figure 13 compares the experimental and calculated stress-profile responses of Teflon to the ion-deposition profile of Fig. 12 delivered in a 40 ns FWHM beam pulse in accordance with the calculated $P_i(t)$. The PUFF-74 code utilized an elastic-plastic equation of state with a yield strength of 1.2×10^8 dyne/cm² for Teflon. The Teflon equation-of-state parameters were developed from data accumulated in underground events.^{11,12} The 10-ns risetime observed experimentally but not predicted suggests that a strain-rate-dependent equation of state, such as an elasto-viscoplastic model, may be required to more realistically predict the material response to soft x-rays. The need for such an

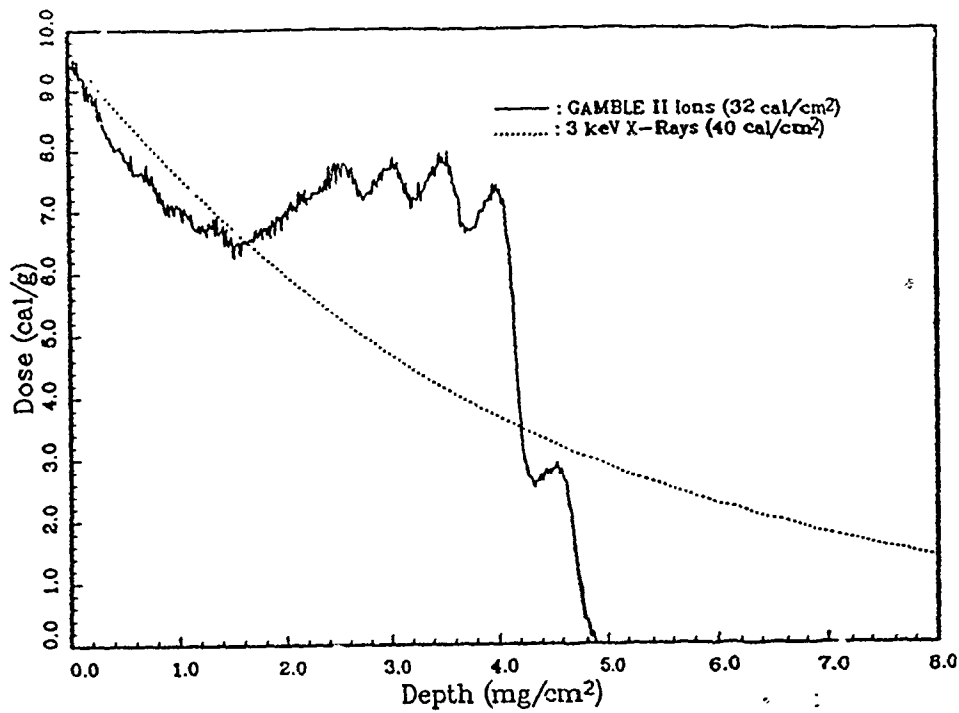


Fig. 12. Energy deposition profiles in Teflon for 3-keV x-rays and the Gamble II ion beam on shot 4248.

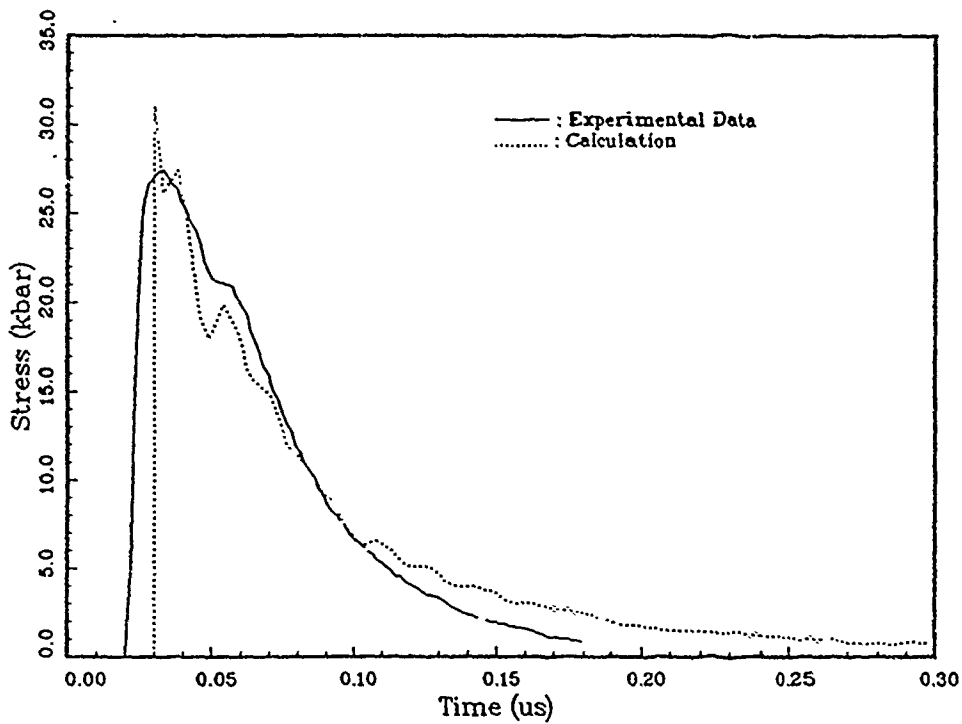


Fig. 13. Experimental and calculated stress in Teflon due to ion beam deposition at 30 cal/cm² for shot 4248.

improvement in modeling may not have been apparent without ion-response measurements since: a) UGTs have employed more highly-penetrating radiation for which the elastic-plastic models were developed, and b) soft x-ray fluences with realistic spectra from AGTs have fluences orders-of-magnitude below that required to test the equation-of-state models.

Figure 14 compares the calculated stress responses in Teflon to 3-keV x-rays and the Gamble II ion beam at fluences of 20 and 30 cal/cm² respectively at a point about 80 μm (17 mg/cm²) from the front surface. A theoretical, rather than experimental, comparison of x-ray and ion responses is made because no high-fluence x-ray sources exist above ground. Referring to Fig. 12, a small portion of the x-ray fluence is deposited at and beyond 80 μm so that stresses at the monitor location are created instantaneously. This deep penetration produces the early-time foot in the calculated stress response to x-rays. The exponential fall-off of x-ray intensity with penetration distance means that a melt region will be produced between vaporized and solid regions. The stress-wave rise time is lengthened as it propagates through the melt region. Ion deposition, on the other hand, is strong throughout the range with a sharp cut-off at the end of the range. Material is therefore vaporized throughout the ion deposition region with the vapor expanding onto an effectively solid surface. This interaction generates a steeply-rising wave front propagating into the material in a manner similar to a cold impact response.

Figure 14 demonstrates that, although differences in rise time can be expected near the deposition region, similar peak stresses and stress-wave histories can be expected from the two types of radiation when the ion range is comparable to the 1/e attenuation length of the photon deposition, and similar fluences are employed. The higher accelerating voltage available from high-impedance Gamble-II operation can simulate the stress-wave profiles produced by several-keV black-body x-ray spectra (10-keV photons).

Early time-resolved impulse measurements made with the LVT demonstrated that the late-arriving debris impulse from the original ion diode could be larger than the ion-generated impulse from target ablation. At the 25-cal/cm² fluence level, the ion-generated impulses varied from 1 to 2 ktaps, while the debris-generated impulses can be more than twice these values.¹¹ Although the LVT can resolve these two components in time, effects such as damage response that depend on total impulse will be distorted by the unrealistic debris component. Most of the debris impulse is due to vaporization of the polyethylene anode foil, carbon anode button, and backplate by the reflexing electron beam (see Fig. 2). Measurements with a new anode design have demonstrated dramatic reductions in the debris-generated impulse. Results for the two types of diodes are shown in Fig. 15. Variations in the ion fluence and target material on the two shots lead to different early ion-impulse responses.

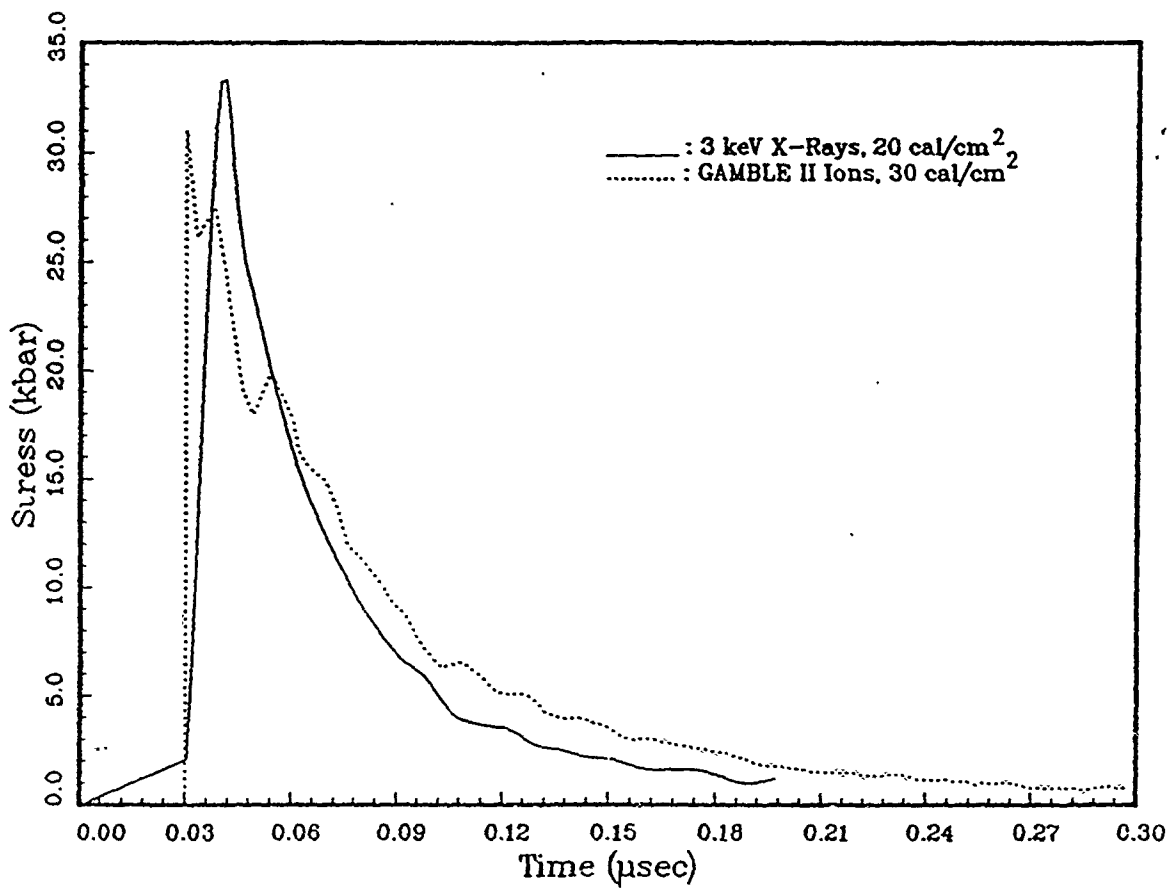


Fig. 14. Calculated responses in Teflon to 3 keV x-rays at 20 cal/cm² and the ion beam of shot 4248 at 30 cal/cm².

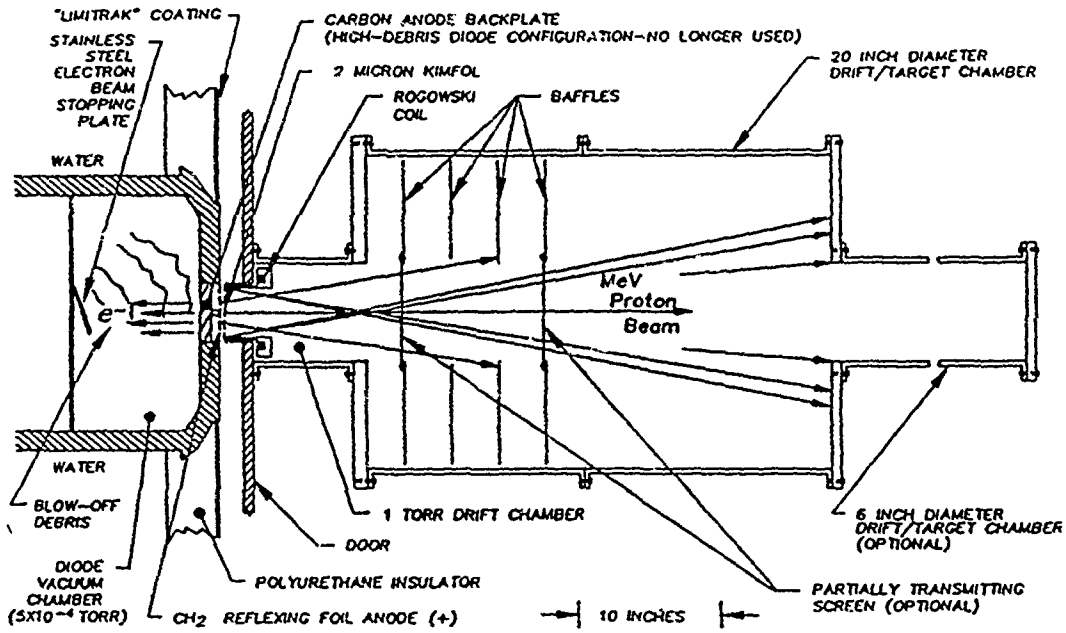


Fig. 15. Debris impulse measurements for standard and low-mass backless diodes at the target location.

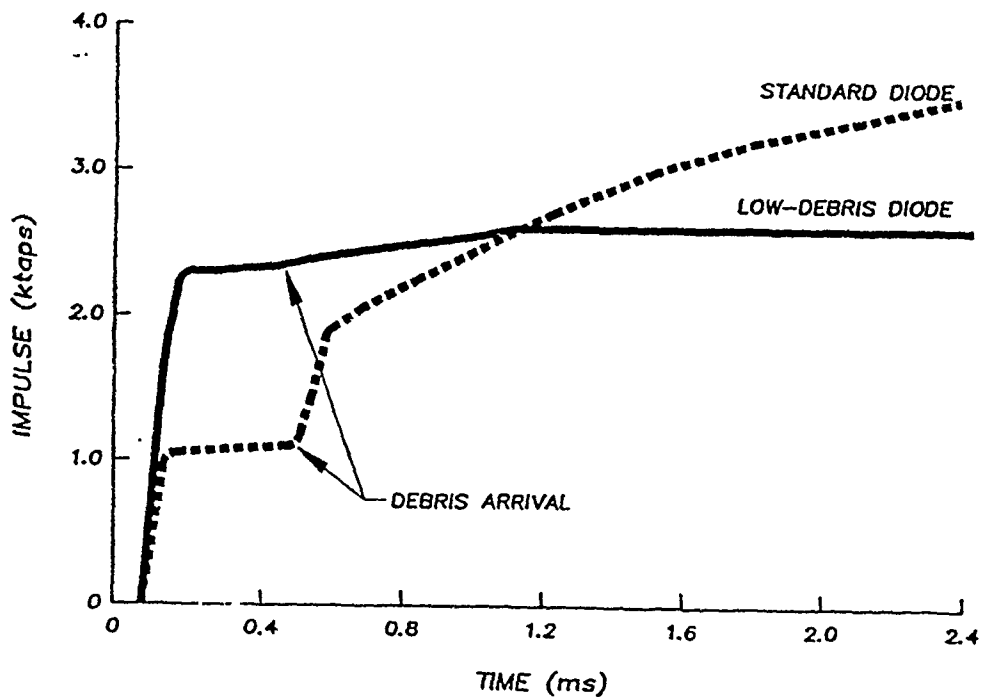


Fig. 16. Large-diameter drift chamber mounted on the Gamble II ion diode showing debris-reducing baffles.

The new design combines an order-of-magnitude reduction in anode-foil thickness with elimination of the carbon button and backplate to reduce the mass available for debris formation. Measurements show an order-of-magnitude reduction in the late-time debris impulse with the new backless diode to levels below 300 taps, i.e. about 10% of the ion-generated impulse.

Debris from the backless diode has been further reduced at the target location by employing the large-radius drift chamber and debris-baffle arrangement shown in Fig. 16. With this target chamber, debris impulse at the target has been reduced to immeasurable levels (≤ 50 taps).

IV. Summary of Results and Future Research

Light-ion beams represent an alternative to soft x-rays for material and structural-response studies requiring high fluence and large area in cases where results are not sensitive to the details of the depth-dose profile. Ongoing research and development are aimed at improving the validity of light-ion simulation on the positive-polarity Gamble II facility and extending the capability to other tests. Results achieved to date in this program and plans for future development are described below.

A. Ion Beams for Simulation

The pinch reflex diode operating on the positive-polarity Gamble II generator produces large-area, megavolt-level proton beams suitable for simulating the response of materials and structures to high fluences of soft x-rays. Mean ion energies can be varied within the 1- to 2-MeV regime with $\pm 5\%$ voltage reproducibility and $\pm 10\%$ ion power and energy reproducibility. Beam energies of 30 - 35 kJ are available for 1-MeV mean-energy ions. The plasma erosion opening switch has been used to vary the ion power half width from about 20 to 50 ns. Ion-fluences in the 5- to 100-cal/cm² range have been measured over target areas approaching 100 cm² with a spatial uniformity of $\pm 10\%$ at the 50-cal/cm² level. These fluence-area products are about three orders-of-magnitude higher than available from plasma radiation sources driven from comparable pulsed power and simulate photon deposition in the 3- to 10-keV regime. Electron beams created with waterline pulsed power have absorption depths two to three orders-of-magnitude greater than the ion and soft x-ray values. The demonstrated ion-beam capability is appropriate for realistic pre-UGT simulation studies of materials, and structural-response simulation of nose-tips, antenna and button windows, satellite and other space-based components.

Modifications to pinch reflex diodes are being considered to improve their utility for x-ray simulation. Existing pinch reflex diodes are designed to tightly focus ion beams rather than distribute the beam uniformly over large areas. Of

particular concern is the intrinsic $1/r$ fluence distribution of the beam emitted by the diode. The reported experiments show that a nearly uniform fluence distribution is achieved by ion-orbit mixing at particular distances from the diode with a narrow range of fluence values. New diode designs are required to achieve uniformity over a broad range of fluence values and target areas. One possible approach is to degrade the beam brightness by roughening the anode surface so as to cause ions to be emitted over a range of angles. More uniform fluence distributions may then result over a range of distances from the diode with corresponding broad fluence variations. In particular, a uniform distribution of fluence over areas large compared to the achieved 100 cm^2 is desired to extend testing to large components, such as satellite sub-assemblies, full-scale nose-tips, exhaust nozzles, motor cases and frusta. Even without such modifications, ion orbit analysis indicates that uniformity over about 300 cm^2 can be achieved at the 10 cal/cm^2 level at 1-m distances from the existing diode.

B. Opening Switch Research for Ion Simulation

Positive-polarity plasma-erosion-opening-switch (PEOS) experiments will continue on Gamble II to provide additional pulse-width control and voltage multiplication for ion simulation experiments. The ion power FWHM can be reduced to below 10 ns by a combination of improved positive-polarity PEOS performance, energy filtering, or time-of-flight bunching. (Because of the strong dependance of ion range on energy, lower-energy ions can be filtered through thin plastic transmission foils to provide pulse narrowing without strongly degrading the transmitted high-energy fraction of the beam. MeV proton beams can be bunched to higher power over 1-m drift distances by ramping the accelerating voltage in time.) The higher accelerating voltages achievable with improved PEOS performance will provide ions that can simulate higher-energy x-ray spectra than would otherwise be possible on Gamble II. The fast-rising voltage due to the PEOS may also promote more uniform anode plasma formation, thereby reducing asymmetries and nonuniformities on the target.

C. Diagnostic Development

Improvements in ion diagnostics are required for more precise fluence measurements. The carbon-activation diagnostic has limited spatial resolution, and may be inaccurate at high fluences where ablation of carbon leads to loss of the entrained nitrogen. Higher accuracy and improved (few-millimeter) spatial resolution can be attained by imaging proton-induced, K-line x-ray emission from an aluminum target on photographic film. Measurement of this K-line emission with a gated microchannel-plate detector may provide time-resolved imaging of the ion-beam flux distribution at the test location. Aluminum K- α images were obtained to demonstrate the utility of the diagnostic. The observed exposures

are consistent with the known fluence distribution and the results demonstrate that high resolution mapping with the technique can be carried out.

Diagnostics must be developed to determine the beam constituents other than protons and their spectral distributions. In Gamble II experiments, carbon is likely to be the primary beam contaminant. Singly-ionized carbon is not sufficiently energetic to pass through the polycarbonate transmission foil separating the diode vacuum from the gas-filled target chamber. However, higher ionization states can be accelerated to a multiple of the diode voltage and can reach the test structure. Such higher-atomic-number constituents strongly increase energy deposition near the front surface of targets. Their measurement can represent a first step towards developing a capability to more closely approximate x-ray spectra by controlling the abundances of various atomic species in the beam. This beam-content-control capability has not yet been developed for the pinch-reflex ion diode and represents a long-term objective of the ion simulation program.

D. Stress Measurements

Hydrodynamic calculations that determine the responses of materials to both the Gamble II ion beam and soft x-rays demonstrate similar stress-wave histories in homogeneous materials despite differences in the energy deposition characteristics of the two radiations. A best match of deposition characteristics is made when the ion range is close to the $1/e$ attenuation length of the x-radiation to be simulated. One- to 2-MeV protons produce stress-wave profiles similar to those created by 3- to 10-keV photons. Simulation of more energetic x-ray spectra is achieved by raising the accelerating voltage. Differences between the theoretical ion- and x-ray-generated responses can be attributed to a small fraction of the x-ray energy penetrating more deeply than the ion range. A theoretical comparison of ion and x-ray responses was necessary because high-fluence above-ground x-ray sources do not exist. Comparison of ion-generated stress-wave measurements with code calculations employing the measured beam characteristics show good general agreement. However, differences between the experimental and calculated stress-wave rise times in Teflon suggest a need for improved equation-of-state modeling. It is interesting that this need was not made apparent in UGTs that employed more highly-penetrating radiation.

E. Debris Measurements

Early time-resolved impulse measurements made with the LVT demonstrated that the late-arriving debris impulse from the original ion diode could be larger than the ion-generated impulse from target ablation. Although the LVT can resolve these two components in time, effects such as damage

response that depend on total impulse will be distorted by the unrealistic debris component. Measurements with a new anode design have demonstrated dramatic reductions in the debris-generated impulse. The new design combines an order-of-magnitude reduction in anode-foil thickness with elimination of the carbon button and backplate to reduce the mass available for debris formation. Measurements show an order-of-magnitude reduction in the late-time debris impulse with this new backless diode to levels below 300 taps, i.e. about 10% of the ion-generated impulse. Debris from the backless diode has been further reduced at the target location by employing a large-radius drift chamber and debris-baffle arrangement. With this target chamber, debris impulse at the target has been reduced to immeasurable levels (≤ 50 taps). At these low debris levels, ion simulation studies can be extended to pre-UGT impulse simulation, impulse-gauge-correlation and design-organization studies, and optical-component testing.

With debris reduced to such low levels, it becomes possible to design transmission foils that separate the drift gas from an evacuated region containing test samples. Depending on the ion spectrum, ion fluences as high as 10 cal/cm^2 may be available for testing in optically clean environments with such an arrangement. Complete isolation of the test structure from anode debris may also be accomplished through spatial filtering. For this technique, the ion beam is focussed onto a small (few cm^2) hole in a plate separating the two portions of the chamber containing the diode and test structure. On passing through the hole, the ion beam expands to cover the test structure. A fast valve then closes over the hole before debris reaches the plate.

F. Simulation Fidelity

Even if accurate x-ray deposition profiles can be synthesized for homogeneous materials by combining various ion species, a poor simulation of photon deposition occurs when the test structure consists of composites or very-thin (less than an ion range) laminates composed of materials with widely-different atomic numbers. This problem arises because the ion range (expressed in terms of mass/unit area) is nearly independent of atomic number, while photon attenuation is a strong function of it. Differential heating effects can then be very different for photons and ions in composite materials. Additional research is required to assess the utility of ion-beams to simulate soft x-ray effects in these materials.

V. Acknowledgement

The authors would like to acknowledge the valuable assistance of R. Boller and V. Scherrer of NRL as well as T. Meluso, R. Hallett, C. De La Cruz, and E. Smith of Ktech Corporation during the Gamble II experiments. In addition, the

Gamble II technician crew consisting of F. Hollis, K. Britton, and J. Negri is commended for a job well done.

VI. References

1. D. Mosher, et al., Appl. Phys. Lett. 23, 429(1973).
2. R. Dukart, et al., Proc. 5th International Conf. on High Power Particle Beams, (San Francisco, CA, Sept. 12-14, 1983).
3. W. Clark, et al., ibid.
4. R. B. Spielman, et al., J. Appl. Phys. 57, 830(1985).
5. S. J. Stephanakis, et al., Phys. Rev. Lett. 37, 1543(1976).
6. S. A. Goldstein, et al., Phys. Rev. Lett. 40, 1504(1978).
7. D. Mosher, et al., Proc. 4th International Topical Conf. on High Power Electron and Ion Beam Research and Technology, (Palaiseau, France, June 29 - July 3, 1981).
8. P. F. Ottinger, D. Mosher, and S. A. Goldstein, Phys. Fluids 23, 909(1980).
9. J. P. VanDevender and D. L. Cook, Science 232, 831(1986).
10. D. L. Hanson, M. K. Matzen, and J. P. Quintenz, J. of Radiation Effects Research and Engineering 6, 98(1988).
11. S. H. Richter and L. M. Lee, "Ion Beam Simulation Technique Validation: 1988 Results," Air Force Weapons Lab. Report AFWL-TR-89/97, Kirtland AFB, NM, March 1990.
12. S. Richter, et al., Proc. Simulation Fidelity Workshop III, (Colorado Springs, Sept. 19 - 21, 1989), in publication.
13. G. Cooperstein, et al., in "Laser Interactions and Related Plasma Phenomena, Vol. 5," J. J. Schwartz, et al., eds.,(Plenum, NY, 1981) p105.
14. J. Maenchen, et al., J. Appl. Phys. 54, 89(1983).

15. F. C. Young, et al., Rev. Sci. Instrum. 48, 432(1977).
16. A. E. Blaugrund and S. J. Stephanakis, Rev. Sci. Instrum. 49, 866(1978).
17. B. V. Weber, et al., IEEE Trans. on Plasma Sci. PS-15, 635(1987).
18. A. T. Drobot, et al., Proc. 4th International Topical Conf. on High Power Electron and Ion Beam Research and Technology, (Palaiseau, France, June 29 - July 3, 1981).
19. R. D. Bleach, D. J. Nagel, D. Mosher, and S. J. Stephanakis, J. Appl. Phys. 52, 3064(1981).
20. F. Bauer, "Piezoelectric and Pyroelectric Polymers," Proc. Polymers as Synthetic Metals Conf., (London, U. K., May 17 - 18, 1983).
21. C. W. Cook and E. S. Ames, "The Linear Velocity Transducer Momentum Gauge," Sandia National Labs. Report SC-DR-69-531, Albuquerque, NM, Aug. 1969.
22. T. A. Melhorn, J. Appl. Phys. 52, 6522(1981).
23. R. A. Cecil, C. D. Newlander, and R. J. Scammon, "PUFF74-- A Material Response Computer Code, Vols. I and II," Air Force Weapons Lab. Report AFWL-TR-76-43, Kirtland AFB, NM, Aug. 1980.
24. H. H. Rice, "PUFF74 EOS Compilation," Air Force Weapons Lab. Report AFWL-TR-80-21, Kirtland AFB, NM, Aug. 1980.
25. J. J. Rosen and R. Globus, "TWCP Correlation Study Program," Air Force Weapons Lab. Report AFWL-TR-80-132, Kirtland AFB, NM, Apr. 1981.
26. W. H. Childs, "Thermophysical Properties of Selected Space-Related Materials," Aerospace Corp. Report TOR-008(6435-02)-1, Feb. 1981.

High-fluence large-area MeV proton-beam diagnostics

F. C. Young, S. J. Stephanakis, V. E. Scherrer,^{a)} and D. Mosher
Plasma Physics Division, Naval Research Laboratory, Washington, DC 20375-5000

S. H. Richter
Ktech Corporation, Albuquerque, New Mexico 87110

(Presented on 9 May 1990)

The spatial distribution of intense MeV pulsed proton beams over 100 cm² area is measured with two techniques. An array of carbon-activation samples gives fluences of 100–400 J/cm² with 1–2 cm resolution. Continuous distributions with 3–4 mm resolution are obtained by imaging proton-induced Al *K*-line x rays.

I. INTRODUCTION

Intense light-ion beams are being developed to provide large-area irradiations using the Gamble II pulsed power generator at the Naval Research Laboratory. Proton beams from a pinch-reflex diode¹ produce fluences of about 200 J/cm² over 100 cm² and fluences approaching 400 J/cm² over smaller areas. By operating the generator in positive polarity, the ion beam is directed away from the generator and can be used for target irradiations. To determine the proton fluence, both the distribution in kinetic energy of the beam and the spatial distribution of the beam intensity at various distances from the ion source must be determined. Electrical measurements are used to determine the energy distribution of the beam. Proton-fluence distribution measurements are made with two diagnostics: a carbon-activation technique described in Sec. II and spatial imaging of proton-induced *K*-shell x rays described in Sec. III. This paper addresses the application of these diagnostics to large-area irradiations.

Electrical measurements of ion current and voltage provide the ion-energy distribution. The ion current is measured by a Rogowski coil that monitors all ions from the pinch-reflex diode that pass through a hollow annular cathode. The voltage drop across the anode-cathode gap of the diode is determined by correcting the voltage measured across the insulator of the generator for the inductive voltage drop between the voltmeter location and the ion-diode load. A time-integrated energy distribution of the 40-ns FWHM beam pulse is derived from these electrical measurements. A typical energy histogram for the ion beam from Gamble II is shown in Fig. 1. The total ion energy determined from the electrical data is consistent with the spatial integral of ion fluence determined from carbon-activation measurements described in Sec. II.

II. CARBON-ACTIVATION ARRAY

The proton-fluence distribution at various distances from the ion source is determined by carbon-activation measurements. This technique has been used extensively to diagnose proton beams from pulsed plasma sources and has been described in detail elsewhere.² The ¹³N activity produced by the ¹²C(*p*,*γ*)¹³N(*β*⁺)¹³C reaction is measured to determine the number of protons incident on a carbon sample. Coincidence counting of the 10-min half-life

β⁺ decay with NaI detectors is used to measure weak activities with high signal-to-background ratio. For protons with energies of 0.5–1.6 MeV, the thick-target yield for this reaction is nearly independent of proton energy, and this is just the energy range of interest for proton beams from Gamble II.

An array of small-area samples, activated on a single shot, provides the proton-fluence distribution. For fluences below the carbon-vaporization threshold, the ¹³N is entrained in the carbon sample and the induced activity measures the proton fluence. For higher fluences, a pillbox activation technique³ is employed to minimize the loss of ¹³N activity. The carbon sample is encapsulated in a brass can with one or more 2-mm-diam holes to allow direct irradiation of the carbon by the proton beam. The brass can is shielded from diode debris to minimize deposition of radioactivity from the diode onto the carbon activation device (CAD). The size of each CAD is limited by counting statistics, and the number of CADs in the array is limited by the ability to count all of the CADs before the activity decays. Two different CAD geometries are used. For lower proton fluences, the ¹³N activity is increased by increasing the number of holes in the CAD lid. Devices with three holes and one hole are shown in Fig. 2(a). To measure the proton-fluence distribution, an array of 17 CADs is used on a single shot as shown in Fig. 2(b). After exposure the CADs are removed and counted individually. To achieve 10% counting statistics (a few hundred counts), each CAD is counted for 1 min. Seventeen

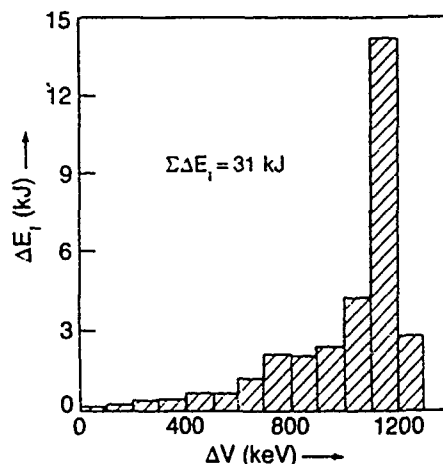


FIG. 1 Ion-energy distribution for Shot 4556 on Gamble II.

^{a)}Present address: JAYCOR, Vienna, VA 22180.

(a) CAD devices



(b) CAD array

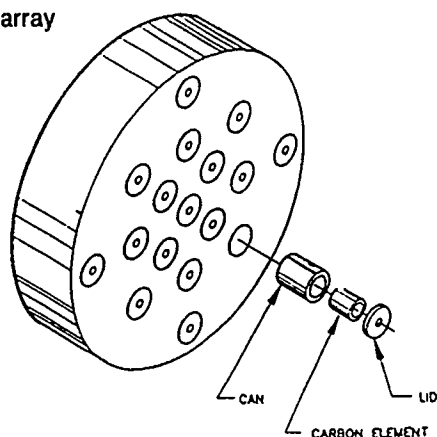


FIG. 2 (a) Photograph of two CAD devices before assembly and (b) schematic of an array of 17 CADs for spatial fluence mapping

CADs could be counted with one coincidence counting system before the activity decayed below statistically meaningful levels.

The spatial resolution of the CAD array is limited to a few cm due to the physical size and packing constraints on the CADs. The 1.5- and 0.76-cm-diam CADs in Fig. 2(a) represent a compromise between higher ^{13}N activity with larger devices and higher spatial resolution with smaller devices. For the array in Fig. 2(b), one CAD is located in the center and 16 CADs are distributed at radii of 1.75, 2.80, 3.75, and 5.00 cm.

Radial-distribution measurements of the proton fluence at five different distances from the diode are shown in Fig. 3. The four CAD measurements at each radius are averaged to give the radial distribution. Close to the diode the distribution follows the sharply peaked variation of emitted ion-current density associated with the pinch-relax diode.⁴ At 50–60 cm from the diode, a nearly uniform beam profile is observed, and a central hole forms at larger distances. In the uniform region, a fluence of 160–200 J/cm^2 is measured over an area of about 100 cm^2 with a peak-to-peak variation of $\pm 20\%$ and a rms variation of $\pm 5\%$. Counting statistics, ablating-plasma closure of the 2-mm-diam holes on the CADs, and loss of activated material lead to uncertainties of about $\pm 20\%$. Errors may be larger at the highest fluences due to enhanced vaporization.

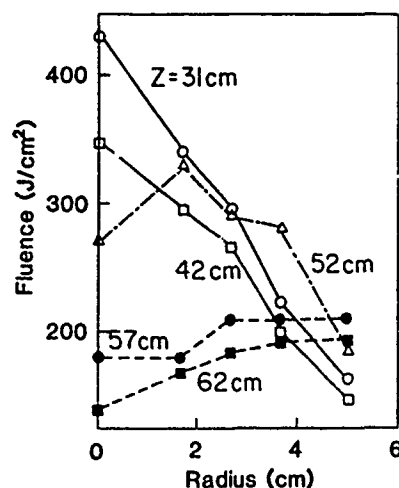


FIG. 3. Radial proton fluence distributions for several distances from the diode.

III. SPATIAL IMAGING OF PROTON-INDUCED X RAYS

X-ray imaging provides a "picture" of the proton-fluence distribution at the target plane on a single shot. Protons with MeV energies incident on a target create *K*-shell vacancies by collisional ionization. The vacancies may be filled by radiative de-excitation resulting in x-ray line emission. Images of *K*-line radiation emitted from an Al target are used to determine the fluence and spatial distribution. This technique was initially developed for intense focused proton beams⁵ and has been applied extensively to intense beams generated for inertial-confinement-fusion applications.⁶ This diagnostic provides a continuous profile of the proton fluence with a resolution of a few mm. Hot spots or localized intensity variations not resolved by the CAD may be observed with x-ray imaging.

The x-ray fluence I_x is related to the incident proton fluence n_p according to

$$I_x \sim n_p N_t \int_0^t \exp[-\mu d(x)] \sigma(x) dx, \quad (1)$$

where $\sigma(x)$ is the proton-induced *K*-line x-ray cross section at a depth x into the target; $\exp[-\mu d(x)]$ is the absorption fraction for x rays traversing a path d in a target of thickness t ; and N_t is the atomic density of target atoms. As protons travel through the target, their energy is degraded and the *K*-line cross section decreases. Because this cross section⁷ is rapidly increasing in the vicinity of 1 MeV, the *K*-line x-ray image is representative of more energetic protons in the beam. X rays generated at different depths in the target pass through target thicknesses $d(x)$ before emerging from the target. The absorption of these x rays depends on the depth in the target and on the angle of emission of the x rays. The integral over target thickness in Eq. (1) is evaluated for different incident proton energies, Al target thicknesses, and angles of x-ray emission. The results of these calculations are used to optimize pinhole-camera designs.

In the present experiments, the proton current density is a few kA/cm^2 over 100 cm^2 area. To record Al *K*-line x

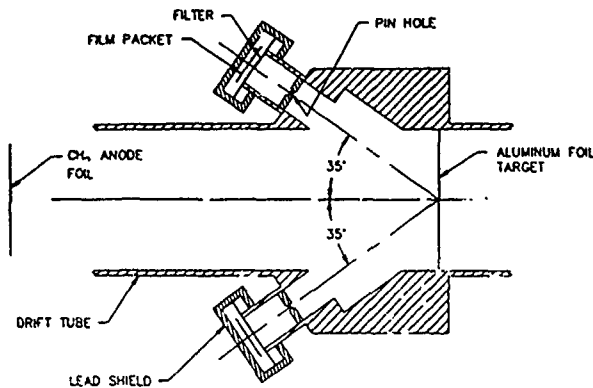


FIG. 4. Pinhole-camera geometry for imaging from the front of the target.

rays (1.5 keV) with adequate sensitivity (6×10^7 photons/cm² for unity specular density), the source is imaged onto Kodak DEF film located about 20 cm from the target with a $0.3 \times$ magnification. The target is oriented perpendicular to the beam, and x rays are imaged at an angle to the beam, either from the back or front of the target. Pinhole cameras were tested using both geometries. Imaging x rays from the back of the target was unsuccessful due to intense keV x-ray emission in the vicinity of the diode. Images were measured from the front of the target and compared with CAD measurements.

X rays are detected from the front of the target with two pinhole cameras located at 145° to the beam direction as shown in Fig. 4. For this angle, the variation in x-ray emission across a $25\text{-}\mu\text{m}$ -thick target is calculated to be less than $\pm 5\%$ for 1 MeV protons. X rays are imaged through 1- and 0.7-mm-diam pinholes from a 100-cm^2 area target located at least 40 cm from the diode. The film is shielded from diode bremsstrahlung by 6.4-mm-thick Pb. To prevent exposing the film to visible light or hot gases from the diode, a filter consisting of two layers of Al-coated $6.4\text{-}\mu\text{m}$ mylar and one layer of $1.8\text{-}\mu\text{m}$ Al-coated polycarbonate is used.

Two images obtained with this camera are presented in Fig. 5. For Shot 4643, a 0.7-mm-diam pinhole was used and the target was 43 cm from the diode. For Shot 4649, a 1-mm-diam pinhole was used and the target was 63 cm from the diode. For Shot 4643, an array of three CAD devices was mounted behind the target and exposed to the proton beam through 1.1-cm-diam holes in the target to provide simultaneous carbon-activation measurements. The top hole is at a radius of 4.4 cm, while the bottom holes are at a radius of 3.17 cm. For Shot 4649, an Al-target impulse gauge was mounted 1.2 cm behind a circular on-axis hole in the 100-cm^2 Al target. A nonirradiated crescent-shaped region is observed due to viewing the target and impulse gauge at 55° to the target plane. X rays

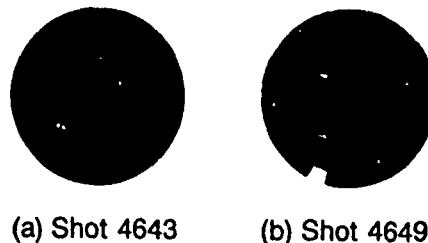


FIG. 5. Proton-induced Al K-line x ray images for (a) Shot 4643 and (b) Shot 4649.

from the Al face of the impulse gauge contribute to this image. The maximum width of the crescent shape at the target is 0.7 mm, and this shape is discernible even for widths of only 3–4 mm. Time-varying current and energy distributions of the proton pulse are required to extract absolute fluences so only relative measurements are presented here. The K-line emission in Fig. 5(a) is more strongly peaked on axis than for Fig. 5(b). This difference is consistent with the variation in the proton-fluence distribution with target distance reported in Fig. 3. There is no evidence for hot spots or localized intensity variations of the proton beam in these images.

Two techniques have been applied to measure the spatial distribution of intense MeV pulsed proton beams over 100 cm^2 area. For absolute measurements, an array of carbon activation samples gives fluences of $100\text{--}400\text{ J/cm}^2$ with 20% uncertainty and with spatial resolution limited to 1–2 cm by physical size and packing constraints on the activation devices. Continuous fluence distributions with 3–4 mm resolution are obtained by imaging proton-induced Al K-line x rays. Both techniques give similar variations in the proton-fluence distribution with axial distance from the diode.

ACKNOWLEDGMENT

This work was supported by the Defense Nuclear Agency.

¹G Cooperstein *et al.*, in *Layer Interactions and Related Plasma Phenomena*, Vol. 5, edited by J J Schwartz (Plenum, New York, 1981), p. 105

²F. C. Young, J. Golden, and C. A. Kapetanakis, *Rev. Sci. Instrum.* **48**, 432 (1977)

³A. E. Blaugrund and S. J. Stephanakis, *Rev. Sci. Instrum.* **49**, 866 (1978).

⁴A. T. Drobot *et al.*, *Proc. 4th Inter. Topical Conf. on High Power, Electron and Ion Beam Research and Technology* (Palaiseau, France), June 29–July 3, 1981

⁵D. J. Johnson *et al.*, *J. Appl. Phys.* **50**, 4524 (1979), and R. D. Bleach, D. J. Nagel, D. Mosher, and S. J. Stephanakis, *J. Appl. Phys.* **54**, 3064 (1981).

⁶J. Maenchen *et al.*, *Rev. Sci. Instrum.* **59**, 1706 (1988).

⁷G. Baybas, W. Brandt, and R. Laubert, *Phys. Rev. A* **7**, 983 (1973), and H. Tawara, Y. Hachiya, K. Ishii, and S. Morita, *Phys. Rev. A* **13**, 572 (1976)

PULSED POWER PHYSICS TECHNOTE NO. 92-16

TITLE: GAMBLE II ION BEAM FLUENCE CALCULATIONS

AUTHORS: D.V. Rose, P.F. Ottinger, D. Mosher, S.J. Stephanakis,
and F.C. Young

DATE: 22 September 1992

ABSTRACT: As a result of systematic differences in calorimetric and carbon activation fluence measurements, calculations of the expected fluences are performed for selected GAMBLE II shots. These calculations use the diode model and microdivergence value from previous work. Good agreement is found between simulations and the calorimetric measurements. The carbon activation measurements, which are consistently a factor of 2 larger, are as yet unexplained.

THIS REPORT REPRESENTS
UNPUBLISHED INTERNAL
WORKING DOCUMENTS AND
SHOULD NOT BE REFERENCED
OR DISTRIBUTED

GAMBLE II Ion Beam Fluence Calculation

D. V. Rose, P. F. Ottinger, D. Mosher, S. J. Stephanakis, and F. C. Young

9/22/92

As a result of systematic differences in calorimetric and carbon activation fluence measurements, calculations of the expected fluence are performed for selected GAMBLE II shots. These calculations use the diode model and microdivergence value from previous work. Good agreement is found between simulations and the calorimetric measurements. The carbon activation measurements, which are consistently a factor of 2 larger, are as yet unexplained.

In support of the 'hockey puck' experiment on GAMBLE II, an accurate knowledge of the fluence over a 20 cm radius target area, 2.2 m downstream of the diode, is required. Bolometer and calorimeter data indicate fluence levels of $\sim 0.1 \text{ cal/cm}^2$ for apertured shots (see below) and $\sim 1.0 \text{ cal/cm}^2$ for unapertured shots. For the same shots, carbon activation results are consistently a factor of 2 higher. The motivation of these calculations is then to determine which of the 2 sets of measurements is giving the more accurate result, based on previously determined microdivergence values.

The simulated experimental configuration consists of an ion diode (6 cm radius anode, 5.1 cm radius Kimfol mounted on the Inet monitor), producing a proton beam with bending angle Θ_b which is proportional to

$$\Theta_b \propto \frac{I_d \Delta}{\sqrt{V}}$$

Since the microdivergence, Θ_μ , is $\sim 175 \text{ mrad}$ [1], the maximum bending angle is typically on the order of the microdivergence. This indicates that some ions are launched nearly parallel to the beam axis over most of the pulse. This in turn, indicates that the energy spectrum at 2.2m downstream should be comprised of the full energy range of ions but may be weighted somewhat towards lower-energy, early-time ions with smaller Θ_b . The ions are ballistically projected through the aperture (if one is present) at $z = 15 \text{ cm}$. Energy loss due to the beam passing through the Kimfol and the $\sim 1 \text{ Torr}$ of air is accounted for. The beam is then projected onto the 20 cm radius target area at $z = 2.2 \text{ m}$. Again, energy losses between the aperture and target position are accounted for.

In order to more accurately represent the energy spectrum by the ion energy associated with the diode voltage pulse, several high impedance diode shots were taken. This reduces Θ_b , allowing Θ_μ to dominate the beam dynamics. Here, the Marx charge on GAMBLE II was reduced and the diode gap spacing was increased. Similarly, the spacing between the anode and Kimfol, Δ , was increased from 1.4 cm to 2.7 cm. This resulted in a lower ion current by a

factor of 8 but similar diode voltage. The desired effect to reduce the bending in the diode is achieved with Θ_b reduced by a factor of 4. Note that for all shots reported here, no transmission screen was used.

The diode loader code from the z-discharge transport work[1] was modified to allow ballistic propagation over the full 2.2 m transport length. The code was run with 25,000 ions, which yielded rather noisy fluence calculations across the 20 cm target radius. All values taken from these code results are average values. Some tapering off of the fluence levels as a function of radius is observed for all runs, with the fluence at $r=20$ cm about 70-90% of the value at $r=0$. For the full current (low impedance) shots described above, shot 5436 was selected as having typical diode voltage and ion current waveforms. This run was repeated with and without a 1.5 cm radius aperture at $z = 15$ cm. For the apertured shot, calorimeters and bolometers reported fluences of ~ 0.096 - 0.12 cal/cm². Code results indicate a fluence of ~ 0.3 cal/cm². Therefore, the apertured runs would seem to agree more with the carbon activation data than the calorimetric data.

For the unapertured shots, good agreement is found between the calorimetric data and code results. For the full current/voltage (low impedance) shot with no aperture (shot 5464), the typical experimental results for bolometers and calorimeters is ~ 1.0 -- 1.3 cal/cm². The code results indicated fluences of ~ 1.0 - 1.2 cal/cm². For the high impedance, unapertured shot, experimental results indicated fluence levels of 0.22 - 0.28 cal/cm², while code results give ~ 0.25 cal/cm².

In conclusion, for the unapertured shots (both high and low impedance), good agreement between the calorimetric data and the code is evident. But, for the apertured (low impedance) shot, calculated fluences are higher than calorimetric data and are in close agreement with carbon activation results. For the high impedance shot, this work is in agreement with calculations of D. Mosher. Additional work, such as a pimple model, varying the microdivergence, and modelling the effect of the measured net current can be carried out to further explore this problem.

References:

- [1] J. M. Neri, et. al., to be published Phys. Fluids B, Jan. 1993.

SECTION FOUR

PLASMA OPENING SWITCHES

A plasma opening switch (POS) consists of a plasma injected in vacuum across the output of a pulsed power generator between the generator and its load. Initially the plasma forms a short circuit which conducts current from the generator, resulting in an accumulation of inductive energy behind the switch. At some time which depends on the plasma and generator parameters, the switch opens, transferring power to the load. Inductive energy storage with POS's results in a very efficient class of pulsed power generators. The generator efficiency increases with the length of time the switch can conduct while still achieving a rapid opening. Understanding of the mechanisms that control current conduction, and of the switch opening dynamics, is essential to the advancement of this technology. During the previous contract period, experiments at NRL, performed with strong JAYCOR participation, were instrumental in establishing the feasibility of microsecond-conduction-time plasma opening switches. As a result of this work and of similar successful experiments in the (then) Soviet Union, microsecond-conduction-time POS development became a major priority of the NRL program. At the direction of the COTR, JAYCOR efforts in this area during the period of performance of this contract were expanded, at the expense of other tasks. A critical element in this effort was the construction of the Hawk generator, which permitted microsecond POS experiments at relevant (600 kA) current levels. Experiments on this generator have led to great advances in the worldwide understanding of microsecond POS operation. This work in part influenced the decision by DNA to construct the Decade nuclear weapon effects simulator using inductive storage with POS's. By the end of the period of performance, JAYCOR personnel were tasked by the COTR to assist in modifying the ZFX facility at NRL to allow POS experiments at still higher (~1.5 MA) current levels and slightly shorter (300-500 ns) conduction times more relevant to Decade. Work performed for this contract is described in the sub-sections below and in more detail in the enclosed publications and reports. Hawk and ZFX are described in Section 4.1; conduction phase studies, including the development of an interferometric density diagnostic, are described in Section 4.2; the development of a model of switch opening is discussed in Section 4.3; studies of the effect of switch geometry are discussed in Section 4.4; and plasma source studies are described in Section 4.5.

4.1 Facility Development

With JAYCOR assistance, a new pulsed power generator called Hawk was assembled and successfully operated. This generator consists of a fast, oil-insulated Marx bank, a vacuum inductive store, a POS, and either a diode or short-circuit load. The generator provides a rapid turn-around, high shot rate test bed for microsecond POS experiments. At the maximum Marx energy of 277 kJ, up to 800 kA can be transferred to a short circuit load. During the period of performance, several modifications were

performed to improve the generator operation. Early on, a problem with current contacts in the Marx was identified. A new contact was designed, tested, and implemented, solving the problem. Subsequently, an improved current contact for the main vacuum interface was tested and installed. As a result of these and other improvements, this facility has become very reliable and robust.

Data from experiments at NRL and elsewhere indicate that while successful operation of microsecond POS's is possible, the optimum POS conduction time may be about 300-500 ns. The DNA Decade facility is being designed to operate in this regime. In order to permit Decade-relevant experiments to be performed at NRL, a new facility is being developed. JAYCOR personnel are also assisting in an ongoing effort to complete construction of the NRL ZFX facility and to modify it for POS operation. This generator resembles Hawk with the addition of a water capacitor and closing switch between the Marx and the POS. By using an intermediate capacitor, energy transfer to the POS becomes more rapid, allowing higher currents and shorter rise times to be obtained. To date, many of the sub-systems have been completed and full operation of the generator is planned for December, 1993.

4.2 Conduction Phase Studies

Experiments performed during the previous contract period indicated that for tens-of-ns conduction times, the POS opens by an erosion mechanism in which ions are extracted from the switch plasma to the cathode faster than they can be supplied by the incoming plasma. During this period of performance, these studies were extended to microsecond-conduction times. Conduction phase experiments comprise both scaling studies which relate the POS peak conduction current to the switch parameters, and investigations of the switch plasma using various diagnostics.

Scaling experiments were performed in which the rise time of the generator current and the number of switch plasma sources were varied. At microsecond conduction times, a much greater number of plasma sources is required to conduct the same peak current. At these higher plasma densities, erosion alone would not be expected to interrupt the current. The results of the scaling experiments suggest that hydrodynamic motion of the switch plasma during the conduction phase plays a role in limiting conduction.

The POS plasma was diagnosed in a series of experiments on Hawk using short-circuit loads. These experiments were directed toward obtaining axial resolution of processes in the switch. Diagnostics included dB/dt loops, collimated fiber optic light probes, and Faraday cups. A new Faraday cup construction was developed which yielded information on the trajectories of the incoming ions. The results of this work provide important information about the axial dependence of switch phenomena: a current channel is seen to propagate through the switch, and this channel is associated with a locally enhanced ion current to the cathode, formation of a plasma on the cathode, and increased light emission from the switch plasma. Switch opening is correlated with the time when this channel reaches the end of the switch region. Once the channel has passed, the ion current to the cathode decreases, suggesting a local opening of the upstream regions of the switch during the conduction phase.

A powerful new diagnostic for probing the POS plasma was developed during the period of performance. An optical interferometer using heterodyne phase detection was used to measure the electron density in the switch. This diagnostic is quantitative, non-perturbing, and easy to use. The use of heterodyne phase detection results in high sensitivity and signal-to-noise ratio. With this technique, the first measurements of the line-integrated electron density in a POS during switch operation were obtained. Current conduction is observed to cause a radial redistribution of the switch plasma, with a large increase in axial line density over most of the radial extent of the switch. A local reduction in line density of more than an order of magnitude occurs by the time opening begins. Data obtained using a chordal line-of-sight show that the density at a given axial location first increases and then decreases as the current front reaches that location. These data indicate that hydrodynamic forces snowplow the plasma in the axial direction. Because of the radial gradients of these forces, this axial motion is accompanied by a radial redistribution leading to the observed line density decrease in between the electrodes. It is now believed that this density decrease allows the switch to open by an erosion mechanism.

The results obtained from interferometry help to explain many of the data obtained with the other diagnostics above and the results of scaling studies. The scaling of conduction current with measured density is consistent with a hydrodynamic limit on conduction at microsecond conduction times and an erosion mechanism at nanosecond times. At intermediate (few hundred ns) conduction times the data are suggestive of yet another mechanism. A simple model of hydrodynamically-limited current conduction has shown a very high degree of predictive capability at microsecond conduction times.

4.3 Switch Opening Model

Experiments with diode loads were performed in which the switch center conductor radius and the diode load impedance were varied. For a given switch geometry, a general behavior is seen as the diode impedance increases from zero in that "load-limited" and "switch-limited" regimes are observed. In the load-limited regime, the load impedance determines the voltage. In the switch-limited regime, the voltage is independent of the impedance, for a given conduction current. In this case, the voltage is limited by the switch, and the load current is less than the generator current, as current is lost in the switch region or between the switch and the load. Maximum load power occurs at the intersection of these two regimes. This behavior points to a simple picture of the opened POS as a magnetically-insulated vacuum gap. In the load-limited case the electron flow in the gap does not extend across the gap and no current is lost. In the switch-limited case the electron flow extends across the gap and some current is lost. In this case the gap acts to determine the voltage. The criterion for magnetic insulation relates the voltage to the generator current times the gap divided by the cathode radius. In order to increase the voltage, and thus the power to the load, either the gap must be increased or the radius must be decreased. Experiments have been performed with reduced cathode radii which have shown and increase in the load voltage. Peak load voltages of 0.8 MV were obtained with a 5-cm-radius cathode, 1.7 MV with a 2.5-cm

radius cathode, and over 2 MV with a 1.3-cm radius cathode. (In the latter case the conduction current was limited by hydrodynamics to a lower value.)

4.4 Switch Variations

The effects of switch geometry were examined in further experiments on Hawk. While the switch voltage increases as the cathode radius decreases, the conduction time and current also decrease because of the greater hydrodynamic forces that result. Tapering the cathode in the switch region was investigated as a possible compromise. Shots taken with a cathode that tapered from 5-cm radius at the upstream end of the switch region to 1.3-cm radius at the downstream end showed the highest load powers yet produced: 0.7 TW with 55 kJ, a 20 percent energy efficiency. A helical center conductor in the switch region was tested as a means to increase the insulating magnetic field. This resulted in dramatically degraded switch performance.

Coupling of the switch to a plasma-filled diode load was studied. The use of a plasma fill in the diode resulted in a diode impedance that increased with time in contrast to the usual case of a falling impedance. With a plasma-filled diode the load power increased relative to that obtained with a standard diode load by 30 percent.

Operation of the POS in positive polarity was also studied. For given conditions the conduction current appears to be slightly greater in positive polarity. It is speculated that this apparent, longer conduction time may be related to a greater delay in establishing magnetic insulation between the switch and the load.

4.5 Plasma Source Studies

In most of the Hawk experiments the switch plasma was supplied by flashboards: arrays of carbon coated surface gaps across which current is driven to create and propel a carbon plasma into the switch region. These flashboards were developed during the previous contract with JAYCOR assistance. These sources were also fielded by NRL personnel with JAYCOR participation on a POS experiment at Physics International during the present period. Use of the NRL/JAYCOR flashboards was seen to result in an increase of the possible conduction current.

Coaxial gas guns were investigated as POS plasma sources. In these sources, gas is injected between coaxial conductors. Current is driven through this gas, again creating a plasma and propelling it toward the switch region. The attractive feature of these sources is that the plasma composition may easily be varied. Performance of these sources however, was found to be poor. In other experiments, gas was injected into the switch region directly and then ionized by the switch current. In this case the switch performance was even worse.

Finally, cable guns, developed at Physics International, were constructed and fielded on Hawk. These were seen to provide switch performance similar to that obtained using flashboards, but to be simpler in practice to use.

4.6 List of Papers

- 4.6.1 "Design and Performance of HAWK, A Versatile Pulsed Power Generator," NRL Memorandum Report 6748 (1991).
- 4.6.2 "Current Contacts in the HAWK Marx," D.D. Hinshelwood, J.R. Boller, P.J. Goodrich, R.J. Fisher, and G. Longrie, Plasma Technology Technote 90-08 (1990).
- 4.6.3 "ZFX - A Pulsed Power Driver Using a Parallel Plate Water Capacitor," J.D. Sethian, J.R. Boller, R.J. Commisso, J.C. Kellogg, B.V. Weber, P.J. Goodrich, and D.D. Hinshelwood, Pulsed Power Physics Technote 93-13 (1993).
- 4.6.4 "Investigation of Plasma Opening Switch Conduction and Opening Mechanisms," B.V. Weber, R.J. Commisso, P.J. Goodrich, J.M. Grossmann, D.D. Hinshelwood, J.C. Kellogg, and P.F. Ottinger, IEEE Trans. on Plasma Sci. PS-19, 757 (1991).
- 4.6.5 "POS Conduction Dependence on Current Rise Rate," B.V. Weber, R.J. Commisso, P.J. Goodrich, J.M. Grossmann, D.D. Hinshelwood, J.C. Kellogg, P.F. Ottinger, S.J. Stephanakis, and J.R. Goyer, Pulsed Power Physics Technote 93-04 (1993).
- 4.6.6 "Recessed B-dot Probes," D.D. Hinshelwood, J.R. Boller, and G. Longrie, Plasma Technology Technote 90-09 (1990).
- 4.6.7 "Faraday Cup Measurements on HAWK," D.D. Hinshelwood, Pulsed Power Physics Technote 91-25 (1991).
- 4.6.8 "Axially Resolved PEOS Measurements at Microsecond Conduction Times," D.D. Hinshelwood, R.J. Commisso, P.J. Goodrich, J.M. Grossmann, J.C. Kellogg, P.F. Ottinger, and B.V. Weber, in the Proceedings of the 8th International Conference on High-Power Particle Beams (Novosibirsk, USSR, July 1990), p. 1034.
- 4.6.9 "Plasma Erosion Opening Switch Operation in the 50 ns - 1 μ s Conduction Time Range," B.V. Weber, R.J. Commisso, G. Cooperstein, P.J. Goodrich, J.M. Grossmann, D.D. Hinshelwood, J.C. Kellogg, D. Mosher, J.M. Neri, and P.F. Ottinger, in the Proceedings of the 8th International Conference on High-Power Particle Beams (Novosibirsk, USSR, July 1990), p. 1034.
- 4.6.10 "Microsecond-Conduction-Time POS Experiments," B.V. Weber, J.R. Boller, R.J. Commisso, P.J. Goodrich, J.M. Grossmann, D.D. Hinshelwood, J.C. Kellogg, P.F. Ottinger, and G. Cooperstein, in the Proceedings of the Ninth International Conference on High-Power Particle Beams (Washington, DC, May 1992), p. 375.

- 4.6.11 "He-Ne Interferometer for Density Measurements in Plasma Opening Switch Experiments," B.V. Weber, and D.D. Hinshelwood, *Rev. Sci. Instruments* **63**, 5199 (1992).
- 4.6.12 "Density Redistribution in a Microsecond-Conduction-time Plasma Opening Switch," D.D. Hinshelwood, B.V. Weber, J.M. Grossmann, and R.J. Commisso, *Phys. Rev. Lett.* **68**, 3567 (1992).
- 4.6.13 "Density Measurements of Microsecond-Conduction-Time POS Plasmas," D.D. Hinshelwood, B.V. Weber, R.J. Commisso, P.J. Goodrich, J.M. Grossmann, and J.C. Kellogg, in the Proceedings of the Ninth International Conference on High-Power Particle Beams (Washington, DC, May 1992), p. 603.
- 4.6.14 "Plasma Opening Switch Experiments on HAWK with an E-beam Diode Load," P.J. Goodrich, J.R. Boller, R.J. Commisso, D.D. Hinshelwood, J.C. Kellogg, and B.V. Weber, 8th IEEE Pulsed Power Conference (San Diego, CA, 17 June - 19 June 1991), p. 515.
- 4.6.15 "Characterization of a Microsecond-Conduction-Time Plasma Opening Switch," R.J. Commisso, P.J. Goodrich, J.M. Grossmann, D.D. Hinshelwood, P.F. Ottinger, and B.V. Weber, *Phys. Fluids B* **4**, 2368 (1992).
- 4.6.16 "Microsecond Plasma Opening Switch Experiments on HAWK with an E-beam Diode Load," P.J. Goodrich, R.C. Fisher, D.D. Hinshelwood, J.R. Boller, R.J. Commisso, and B.V. Weber, in the Proceedings of the Ninth International Conference on High-Power Particle Beams (Washington, DC, May 1992), p. 609.
- 4.6.17 "High Power Opening Switch Experiments on HAWK," P.J. Goodrich, D.D. Hinshelwood, R.J. Commisso, J.C. Kellogg, and B.V. Weber, Ninth IEEE Pulsed Power Conference (Albuquerque, NM, June 1993).
- 4.6.18 "Positive Polarity POS Operation on HAWK," D.D. Hinshelwood, and R.J. Fisher, *Pulsed Power Physics Technote* 93-10 (1993).
- 4.6.19 "EYESS PEOS Experiment with NRL Flashboards," B.V. Weber, P.J. Goodrich, and R.J. Fisher, *Pulsed Power Physics Technote* 90-31 (1990).
- 4.6.20 "Gas Puff PEOS Source on HAWK," D.D. Hinshelwood, and R.J. Fisher, *Pulsed Power Physics Technote* 91-30 (1991).
- 4.6.21 "Initial Cable Gun Experiments on HAWK," B.V. Weber, D.D. Hinshelwood, and R.J. Commisso, *Pulsed Power Physics Technote* 93-06 (1993).
- 4.6.22 "Interferometric Studies of Gas Gun Plasmas," D.D. Hinshelwood, *Pulsed Power Physics Technote* 93-09 (1993).



Design and Performance of Hawk, A Versatile Pulsed Power Generator

J. R. BOLLER, R. J. COMMISSO, P. J. GOODRICH,* D. D. HINSHELWOOD,*
J.C. KELLOGG, J. D. SHIPMAN JR.,† B. V. WEBER AND F. C. YOUNG

*Pulsed Power Physics Branch
Plasma Physics Division*

**JAYCOR
Vienna, VA 22180-2270*

*†SFA, Inc.
Landover, MD 20785*

January 25, 1991

REPORT DOCUMENTATION PAGE			Form Approved OMB No 0704-0188	
Public reporting burden for this collection of information is estimated to average 1 hour per response, including the time for reviewing instructions, searching existing data sources, gathering and maintaining the data needed, and completing and reviewing the collection of information. Send comments regarding this burden estimate or any other aspect of this collection of information, including suggestions for reducing this burden, to Washington Headquarters Services, Directorate for Information Operations and Reports, 1215 Jefferson Davis Highway, Suite 1204, Arlington, VA 22202-4302, and to the Office of Management and Budget, Paperwork Reduction Project (0704-0188), Washington, DC 20503.				
1. AGENCY USE ONLY (Leave blank)	2. REPORT DATE 1991 January 25	3. REPORT TYPE AND DATES COVERED Interim		
4. TITLE AND SUBTITLE DESIGN AND PERFORMANCE OF HAWK, A VERSATILE PULSED POWER GENERATOR			5. FUNDING NUMBERS NRL Problem No. 47-0881-0-0	
6. AUTHOR(S) J.R. Boller, R.J. Comisso, P.J. Coodrich*, D.D. Hinshelwood*, J.C. Kellogg, J.D. Shipman, Jr.†, B.V. Weber, and F.C. Young				
7. PERFORMING ORGANIZATION NAME(S) AND ADDRESS(ES) Code 4770 Naval Research Laboratory Washington, D.C. 20375-5000			8. PERFORMING ORGANIZATION REPORT NUMBER NRL Memorandum Report No. 6748	
9. SPONSORING/MONITORING AGENCY NAME(S) AND ADDRESS(ES) Defense Nuclear Agency 6801 Telegraph Road Alexandria, VA 22310-3398			10. SPONSORING/MONITORING AGENCY REPORT NUMBER DNA Task No. T99QAXLB-00023	
11. SUPPLEMENTARY NOTES *JAYCOR, Vienna, VA 22180-2270 †SFA, Inc., Landover, MD 20785				
12a. DISTRIBUTION / AVAILABILITY STATEMENT Distribution authorized to U.S. government agencies and their contractors; critical technology; January 1991. Other requests shall be referred to the Commanding Officer, Naval Research Laboratory, Washington, DC 20375-5000.			12b. DISTRIBUTION CODE	
13. ABSTRACT (Maximum 200 words) A new pulsed power generator called Hawk has been assembled and successfully operated as part of the DNA/NRL facility upgrade in the Pulsed Power Physics Branch. This generator consists of a fast, oil-insulated Marx bank, a vacuum inductive store, a plasma opening switch (POS), and a diode load. Hawk provides a rapid turn-around, high shot rate test bed for POS experiments at long ($\approx 1 \mu s$) conduction times. During initial testing at ± 72 kV charge on the Marx (178 kJ stored), the POS transferred 640 kA to a short circuit load in < 90 ns after conducting for 900 ns. This output current level scales to 800 kA for ± 90 kV charge (277 kJ stored).				
14. SUBJECT TERMS Pulsed Power Inductive Store Opening Switches			15. NUMBER OF PAGES 36	
			16. PRICE CODE	
17. SECURITY CLASSIFICATION OF REPORT UNCLASSIFIED	18. SECURITY CLASSIFICATION OF THIS PAGE UNCLASSIFIED	19. SECURITY CLASSIFICATION OF ABSTRACT UNCLASSIFIED	20. LIMITATION OF ABSTRACT SAR	

CONTENTS

I. INTRODUCTION	1
II. ELECTRICAL DESCRIPTION	1
III. INSULATOR TESTS AND DESIGN	10
IV. PHYSICAL DESCRIPTION	11
A. Marx Room Modifications	11
B. Marx Components	15
C. Marx Modifications	15
D. Radiation Shielding	18
E. Interlocks and Audible/Visual Warnings	22
V. INITIAL PERFORMANCE	24
VI. ACKNOWLEDGEMENTS	27
VII. REFERENCES	27
DISTRIBUTION LIST	29

DESIGN AND PERFORMANCE OF HAWK, A VERSATILE PULSED POWER GENERATOR

I. INTRODUCTION

A new pulsed power generator called Hawk has been developed as part of the DNA/NRL facility upgrade in the Pulsed Power Physics Branch.¹ This generator replaced the Gamble I generator which was built in 1968. Rather than using water dielectric energy storage as part of the pulse compression stages, Hawk uses the newer inductive storage/opening switch technology.² This results in more energy being delivered to a diode load at slightly higher voltage than the Gamble I generator while physically being much more compact. Hawk consists of a fast, oil insulated Marx generator, a vacuum inductive store, a plasma opening switch (POS), and a diode load.

Hawk provides a rapid-turn-around, high-shot-rate test bed for POS experiments at long ($\approx 1 \mu\text{s}$) conduction times. These experiments will use both short circuit and diode loads.

II. ELECTRICAL DESCRIPTION

The Hawk Marx generator, designed and built by Physics International Co. (PI) under DNA auspices, is an NRL-modified version of the original Eyess Marx³. The original Marx consisted of four sub-modules operating in parallel, each using nine 2.2- μF , 100-kV capacitors and five switches. Modifications to use only eight capacitors and four switches will be described. A mini-Marx generator was purchased from Maxwell Laboratories, Inc. for triggering the four sub-modules of Hawk. The six-stage mini-Marx has a maximum output voltage of 600 kV and 2.4 kJ of stored energy. A power supply with $\pm 100\text{-kV}$, 120-mA outputs was purchased for charging the Marx generator. This 24-kW power supply can charge Hawk in about 30 seconds, as recommended by PI to avoid electrical breakdowns in oil.

Manuscript approved November 8, 1990.

The equivalent circuit diagram of the original Eyess generator as used by PI is shown in Fig. 1. The NRL Bertha transmission line program⁴ was used to predict the generator performance in order to evaluate the effects of the planned modifications. The total inductance of the Hawk generator was estimated to be similar to the inductance of the PI circuit, thus this equivalent circuit was used for the preliminary calculations. Figure 2 shows the output current waveform that would be delivered to an opening switch with a ± 90 -kV charge (810 kV on the capacitor shown in Fig. 1). The current peaks at 866 kA in slightly less than $1.2 \mu\text{s}$. This is somewhat less than the expected 1 MA at this charging voltage, mostly as a result of the protection resistors included in the 0.18Ω of Fig. 1.

The voltage across the vacuum insulator was also calculated for a charging voltage of ± 90 kV and is shown in Fig. 3. Because most of the inductance for this system is in the oil, flashover at the vacuum insulator could limit the energy available to drive a load. As shown in Fig. 3, the insulator voltage initially rises to 265 kV due to inductive division and then decays to zero as the current reaches its peak. This waveform has been smoothed to eliminate the ringing caused by reflections in the discrete transmission line elements used in the model. Although transient ringing is observed in actual measurements on Hawk, the equivalent circuit used here was not intended to accurately model these high frequency transients. Also not shown here is the effect of an opening switch which would produce a voltage that is much higher, but of shorter duration, than that shown in Fig. 3.

The Hawk output current was also calculated for the case where each Marx module has eight capacitors instead of nine. This reduced number has several advantages. Most importantly, eight capacitors present a balanced capacitive load to the charging power supply. The schematic diagram in Fig. 4 is a simplified version of a Marx module showing only the capacitors and switches. It is evident that with nine capacitors, five will be charged negatively and four positively. It is also apparent that if the last capacitor, C_9 , is removed, the switch S_5 is also not needed, and the output can be taken directly from the case of C_8 .

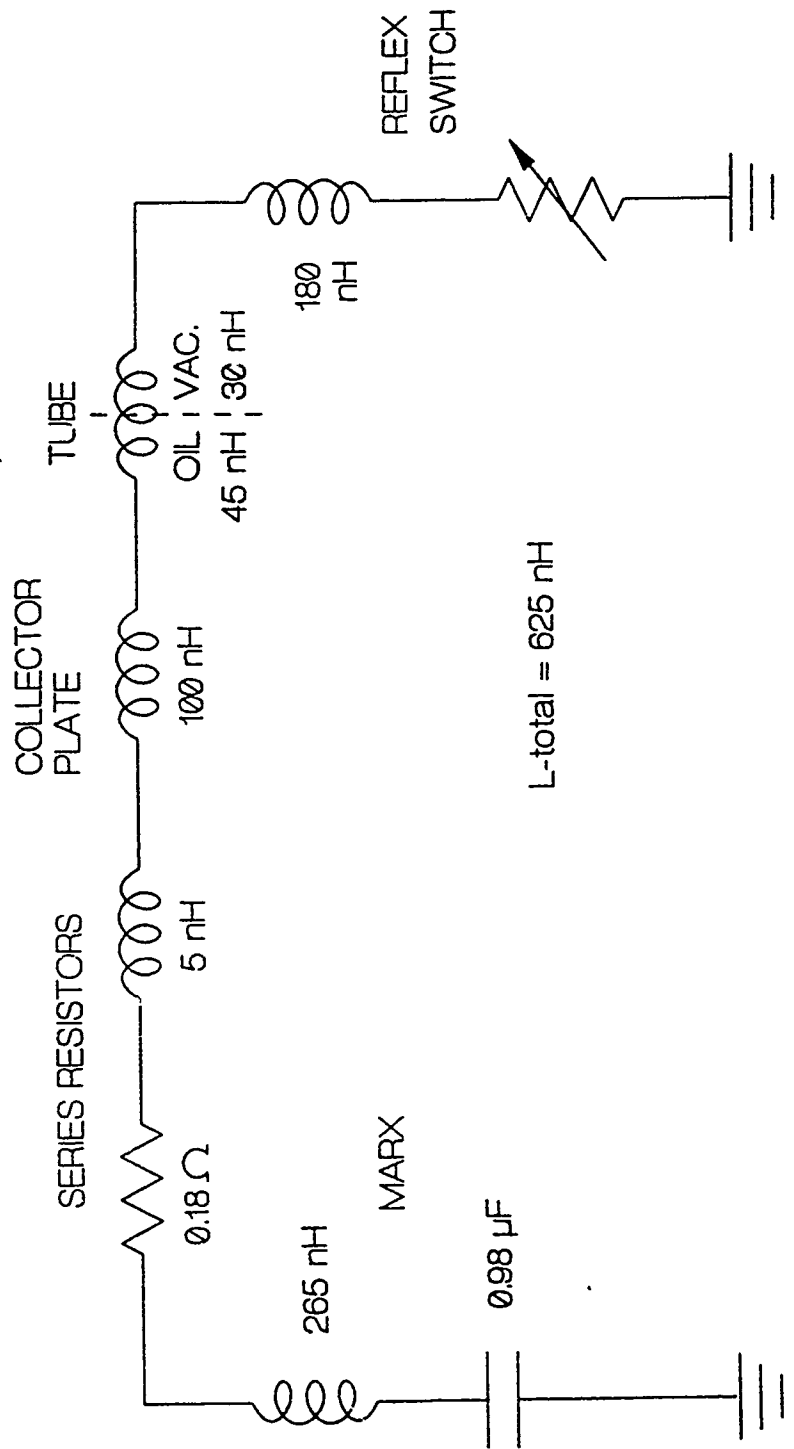


Figure 1. Original PI Eyess Circuit Diagram

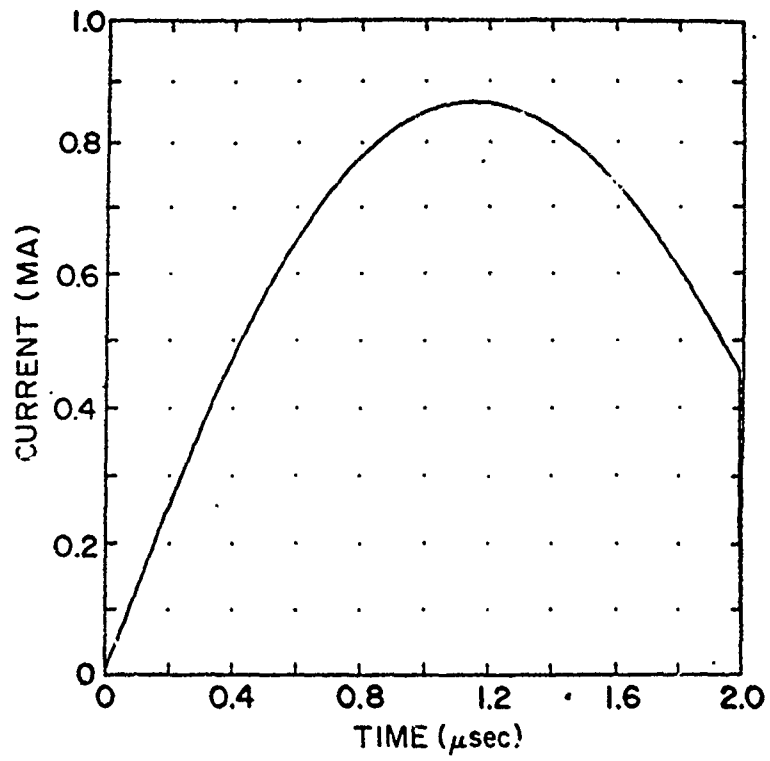


Figure 2. Calculated Current into Opening Switch

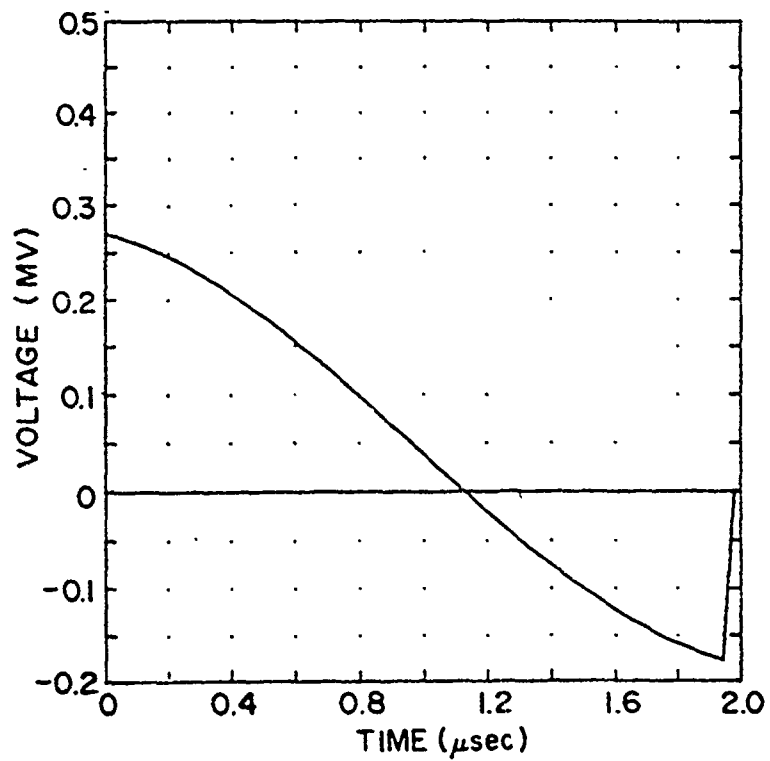


Figure 3. Calculated Insulator Voltage

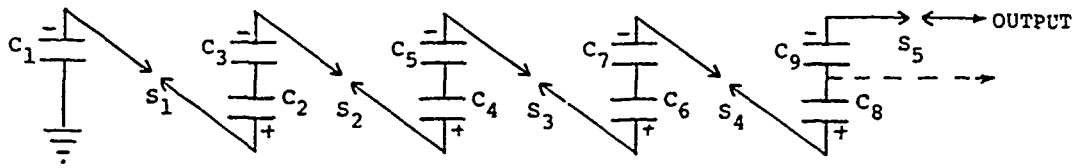


Figure 4. Simplified Marx Circuit

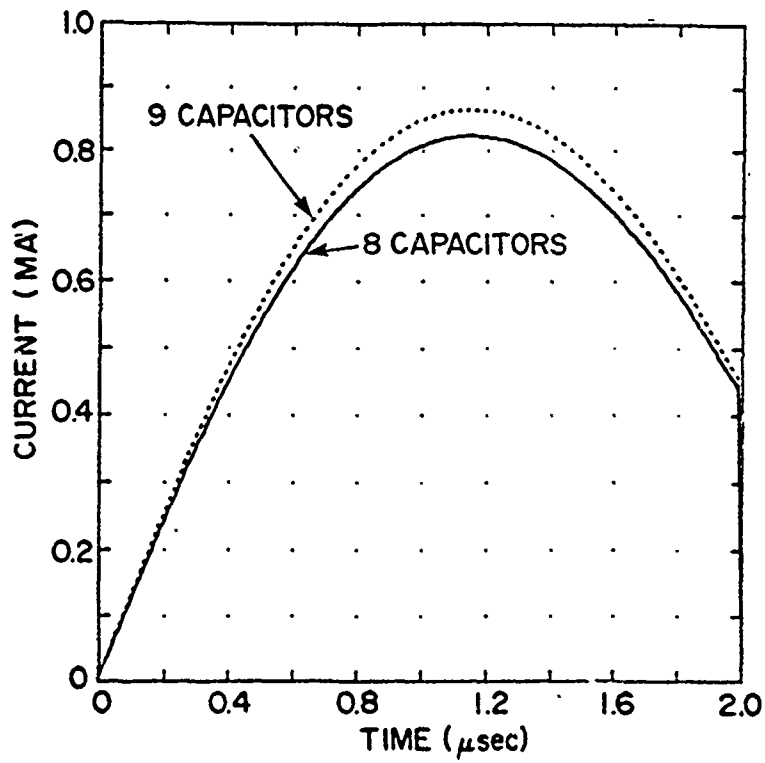


Figure 5. A Comparison of Output Currents for 8 and 9 Capacitors per Module

Another advantage in reducing the number of capacitors resulted from the lack of spares during the installation and initial operation. Two of the four free capacitors were used as filters to protect the power supply from transients while the other two served as the only available spares until additional capacitors were procured.

The penalty for this choice is not severe, as illustrated in Fig. 5. Here, the calculated output current for the eight-capacitor modules is compared to the original output current for nine capacitors per module. The peak current decreases by 5% to 824 kA. This calculation assumes that the total Marx inductance is reduced by 45 nH due to the smaller number of capacitors and switches.

The circuit modeling was extended to include an opening switch and realistic diode loads as shown in Fig. 6. Estimates of diode load parameters were necessary for the design of radiation shielding. To obtain a conservative estimate of the required shielding, the calculations were based on the equivalent circuit using nine capacitors per module. The circuitry up to the opening switch in Fig. 6 is identical to that shown in Fig. 1 except that the inductances in the oil are lumped together (415 nH) and likewise those in the vacuum (210 nH). The opening switch was modeled as a linearly increasing resistance, conducting for 1 μ s to a current level of 838 kA, then opening from 0 to 20 Ω at several different rates. The pinched-beam-diode parameters were 6-cm radius, 5-mm gap, and two different gap closure velocities. Results are given in Table I.

Table I. Tabulation of Calculated Output Parameters

Run No.	Opening Rate (Ω/ns)	Diode Closure ($\text{cm}/\mu\text{s}$)	Peak Voltage (MV)	Total Energy (kJ)	Peak Power (TW)	Power FWHM (ns)
452A	0.05	3.6	0.84	28	0.4	77
452B	0.2	3.6	1.54	61	0.8	76
452C	0.2	2.0	1.75	104	0.9	107
452D	0.05	2.0	1.09	67	0.5	138

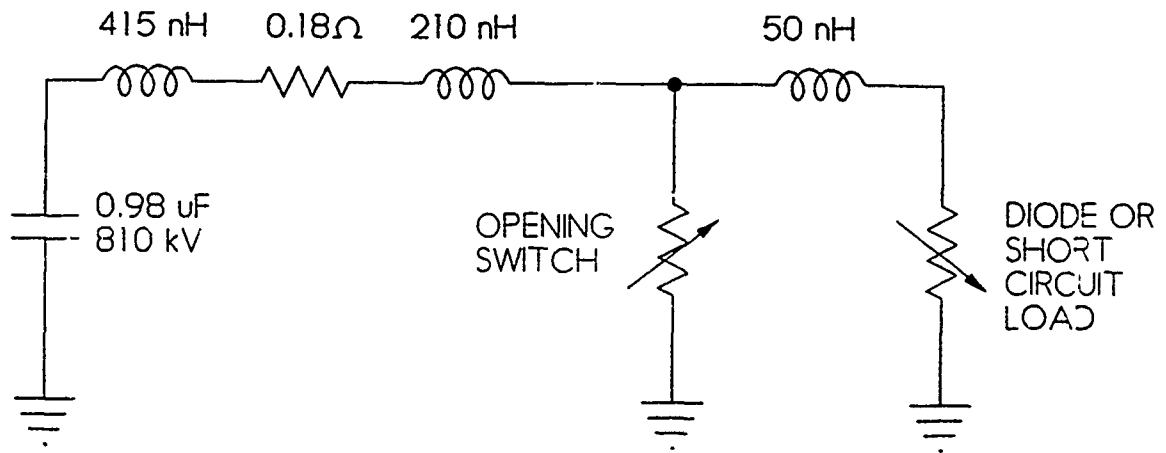


Figure 6. Equivalent Circuit Used for Estimating Output Parameters with an Opening Switch

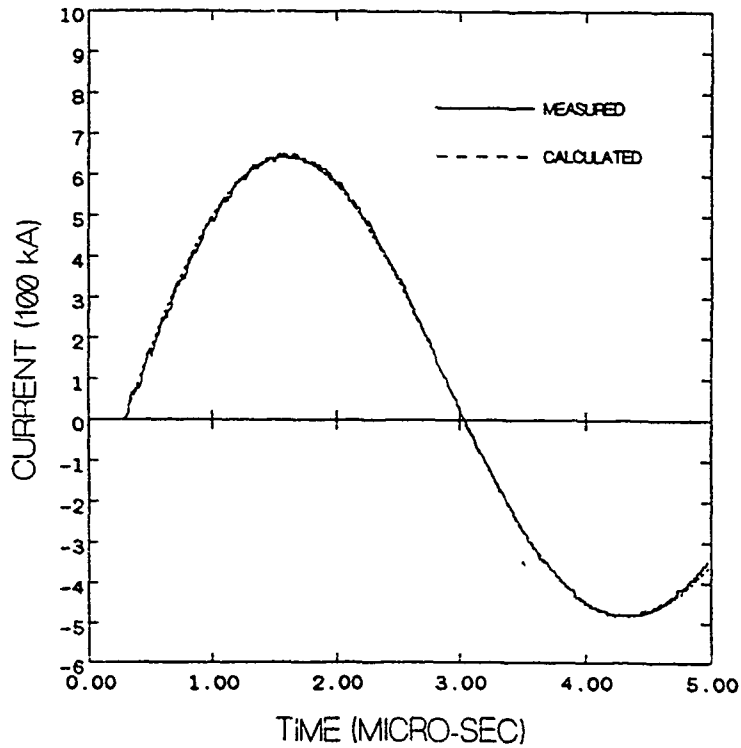


Figure 7. Comparison of Measured Output Current and Best Fit from RLC Program

The opening rate of $0.05 \Omega/\text{ns}$ is close to the POS performance initially obtained on the Marx generator for similar currents and conduction times, and the value of $0.2 \Omega/\text{ns}$ is closer to the desired properties of a POS for the Hawk generator. The $3.6 \text{ cm}/\mu\text{s}$ diode-gap closure velocity is approximately the same as observed on the Gamble machines while the slower value of $2.0 \text{ cm}/\mu\text{s}$ would either require an improvement in diode performance or would be representative of a diode with a larger gap and the faster closure rate. The calculated parameters for run 452B were considered as the most reasonable output parameters for the purpose of designing radiation shielding. These were also similar to the best results from Eyess experiments at PI.

Actual circuit values of the final Hawk design were determined experimentally using the NRL RLC computer program⁵ to analyze the initial test shots. This program uses an experimentally measured, un-calibrated output current waveform, the known capacitance, and the known charge voltage to calculate the calibration factor of the current monitor and the effective circuit resistance and inductance that gives the best fit to the measured waveform. Figure 7 shows the extremely good agreement between calculated and measured currents. The results of this analysis were combined with other calculations and measurements to produce the Hawk equivalent circuit shown in Fig. 8. The total circuit inductance is segmented in this figure to show the distribution of the inductance within generator. The total inductance up to the opening switch of 683 nH is higher than that used in the original circuit analysis presented above due to the removal of the aluminum Marx module side panels during the early generator checkout phase. These panels were removed to improve oil circulation in the Marx tank and to aid in visual inspection of the Marx circuitry. The Marx inductance was about 70 nH smaller before the panels were removed. This total inductance ($683 - 70 = 613 \text{ nH}$) is slightly higher than the value (580 nH) used in the preliminary performance calculations for 8 capacitors per module shown in Fig. 5. The experimentally determined series resistance (0.15Ω) is slightly less than originally assumed. The major contribution to this resistance is from 16 parallel protection resistors ($\sim 2\text{-}\Omega$ each, 4 per module) that are inserted between the modules and the center conductor buswork to limit

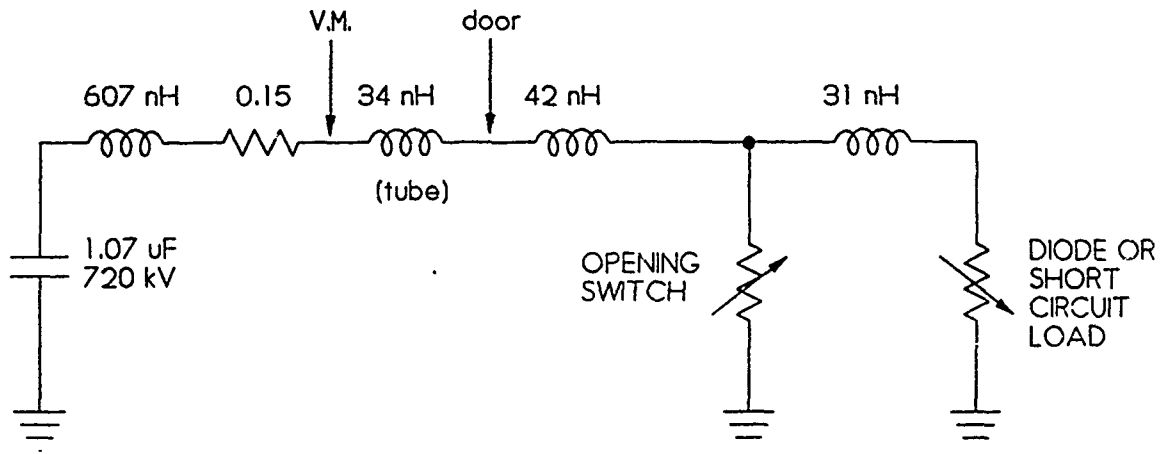


Figure 8. Hawk Equivalent Circuit Based on Measured Parameters

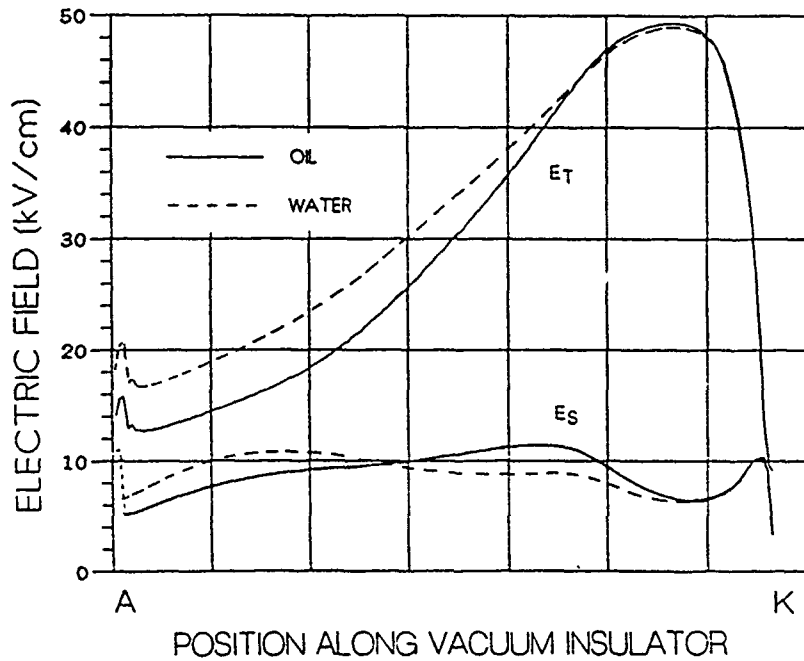


Figure 9. Comparisons of the Effect of Using Water instead of Oil on the Electric Field at the Vacuum Insulator

voltage reversals on the capacitors to ~70%. The value of the Marx capacitance is based on actual measurements of individual capacitors.

III. INSULATOR TESTS AND DESIGN

Early in the Hawk design it was recognized that it would be advantageous to use the existing Gamble I G5 vacuum insulator for Hawk. In addition to substantial cost savings by using existing hardware, this insulator is easier to service and maintain than the stacked ring insulator used by PI. The major concern was whether this insulator could withstand the longer voltage pulse associated with Hawk. Gamble II was used to test the G5 insulator for longer duration pulses.⁶ The intermediate-store output water switch and the pulse-forming-line output oil switch on Gamble II were shorted to produce a MV level, μs duration output pulse. Circuit modeling of this Gamble II configuration predicted that an open circuit output voltage of ≈ 1 MV and a full width at half maximum of $1.5 \mu\text{s}$ could be produced for a Marx charging voltage of 26 kV. Experimental tests of the G5 insulator on Gamble II in this configuration indicated that voltages of 556 to 843 kV are required to initiate flashover. Total times from the beginning of the pulse to flashover ranged from 0.8 to $2.25 \mu\text{s}$, corresponding to a t_{eff} (time that the voltage exceeds 89% of the maximum value) of 0.17 to $0.55 \mu\text{s}$. The t_{eff} of the Hawk insulator voltage from Fig. 3 is $0.3 \mu\text{s}$. The G5 tests on Gamble II indicated a flashover level of at least 675 kV (843 kV on one shot) for $t_{\text{eff}} \approx 0.3 \mu\text{s}$. Thus the G5 insulator should easily meet the longer duration voltage pulse requirements of Hawk, assuming arcs from current joints and/or UV from the plasma sources do not degrade the observed Gamble II performance.

Since Hawk uses oil instead of water up to the vacuum insulator, potential plots near the insulator were calculated for both cases to determine if any modifications should be made in the feed to the diode to properly grade the electric field along the insulator. The results of those calculations are shown in Fig. 9. Here E_T and E_S , the total electric field vector magnitude and the component parallel to the surface of the vacuum insulator, respectively, are plotted with respect to position along the surface between the anode (A) and the cathode (K).

The magnitude of the fields in this figure corresponds to an applied voltage of 265 kV. Although the potential distributions are altered somewhat by changing from water to oil, the effects are too small to warrant fabricating new wave directing hardware at this time.

A cross-sectional view of the front end of Hawk with the G5 diode and additional adaptor parts is shown in Fig. 10. The G5 diode, current shunt, and voltmeter section are standard parts that have been used on both Gamble generators. They are supported by an adaptor plate which mounts on the existing 72-inch diameter opening of the Marx tank. A new feature of this diode design is the use of a urethane safety diaphragm to limit the amount of oil that would be lost in the event of a failure of the G5 acrylic vacuum insulator. Less than 35 gallons of oil from the total Marx content of 10,000 gallons could potentially leak into the experimental area if this insulator breaks. This figure also shows the collector plate which provides electrical connections to the Marx output resistors, and the connection point for an inductive isolator to bring signal cables from the "hot" center conductor to ground potential for diagnostic purposes.

IV. PHYSICAL DESCRIPTION

A. Marx Room Modifications

In addition to the formidable task involving the demolition and removal of Gamble I, extensive modifications to other existing facilities were necessary to install Hawk. The Gamble I Marx tank was lengthened by 60 in. as shown in Fig. 11 to accommodate the Hawk Marx modules and required peripheral equipment. This was accomplished by cutting the tank approximately in half and adding a prefabricated mid-section to increase the length. A modified catwalk and railing were also installed on both sides of the tank as shown in Fig. 11. A new 2-ton bridge crane was installed over the tank and servicing area in the Marx room to lift the modules in and out of the Marx tank for servicing. An end view of this crane structure is shown in Fig. 12. The crane design was complicated by the low roof which severely limited the height of the crane. A hoist which required less than normal head room was procured and the height of the rear wall of the Marx tank was reduced, thus lowering the

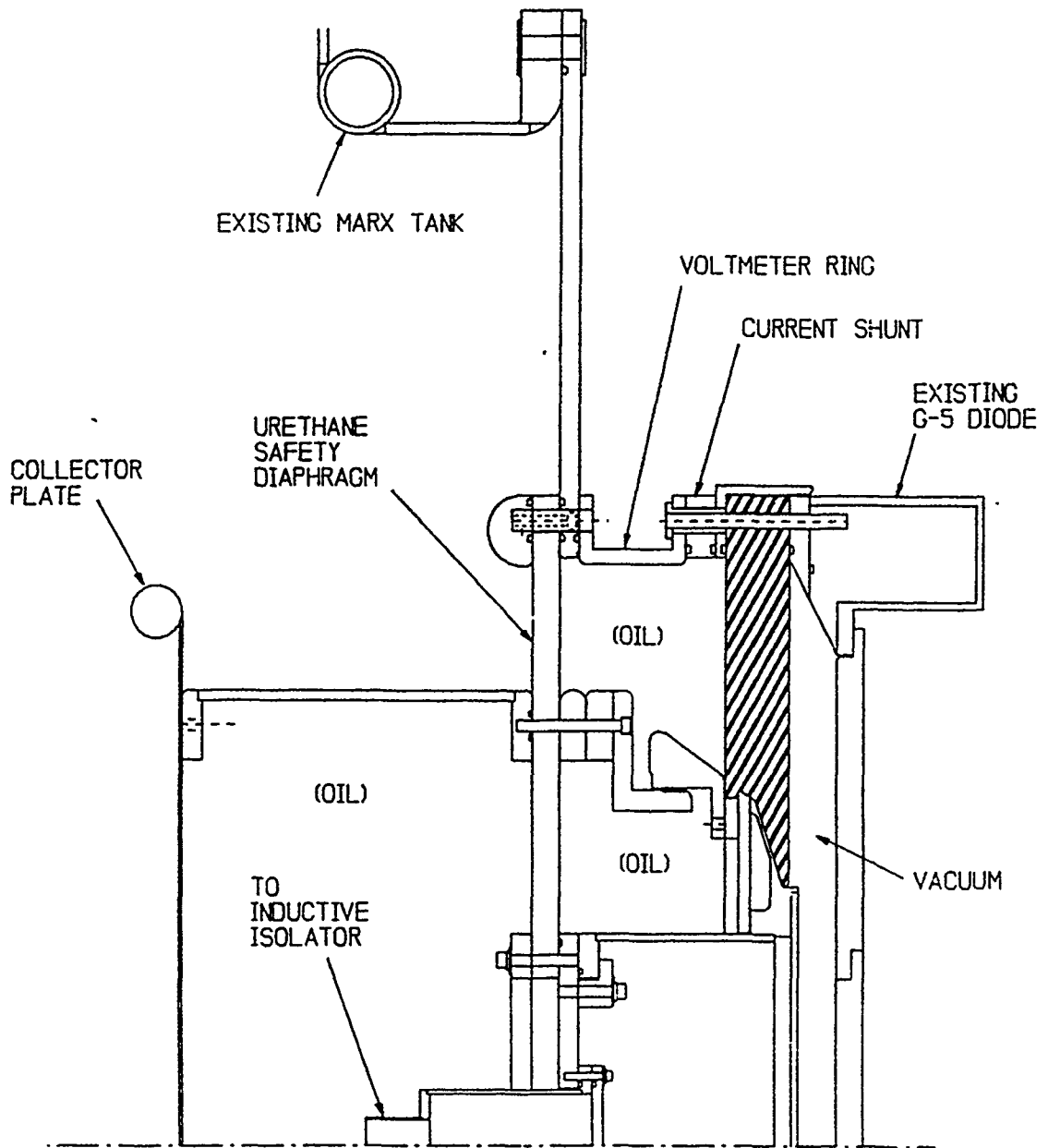


Figure 10. Cross-Sectional View of Hawk Front End

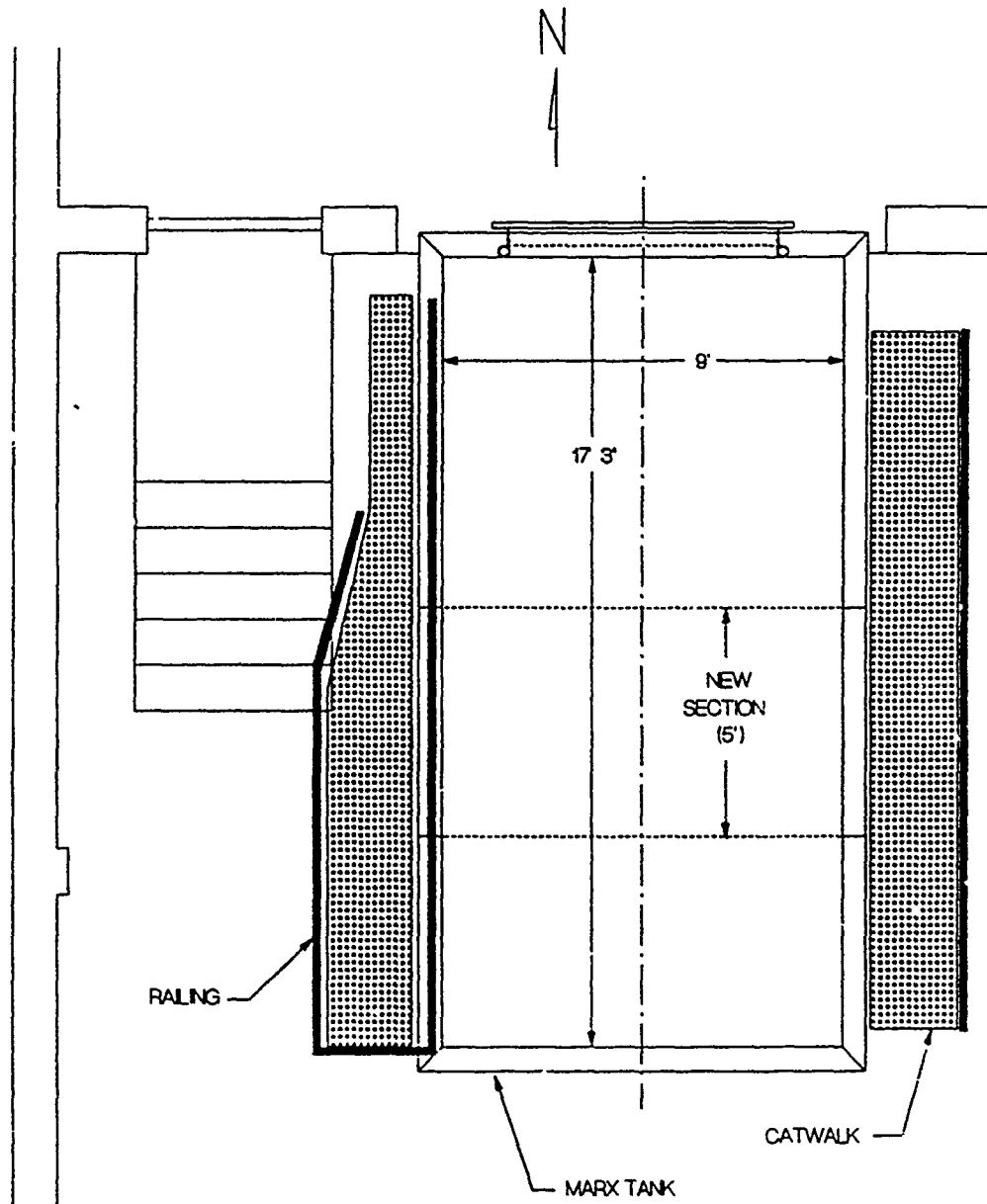


Figure 11. Modified Marx Tank

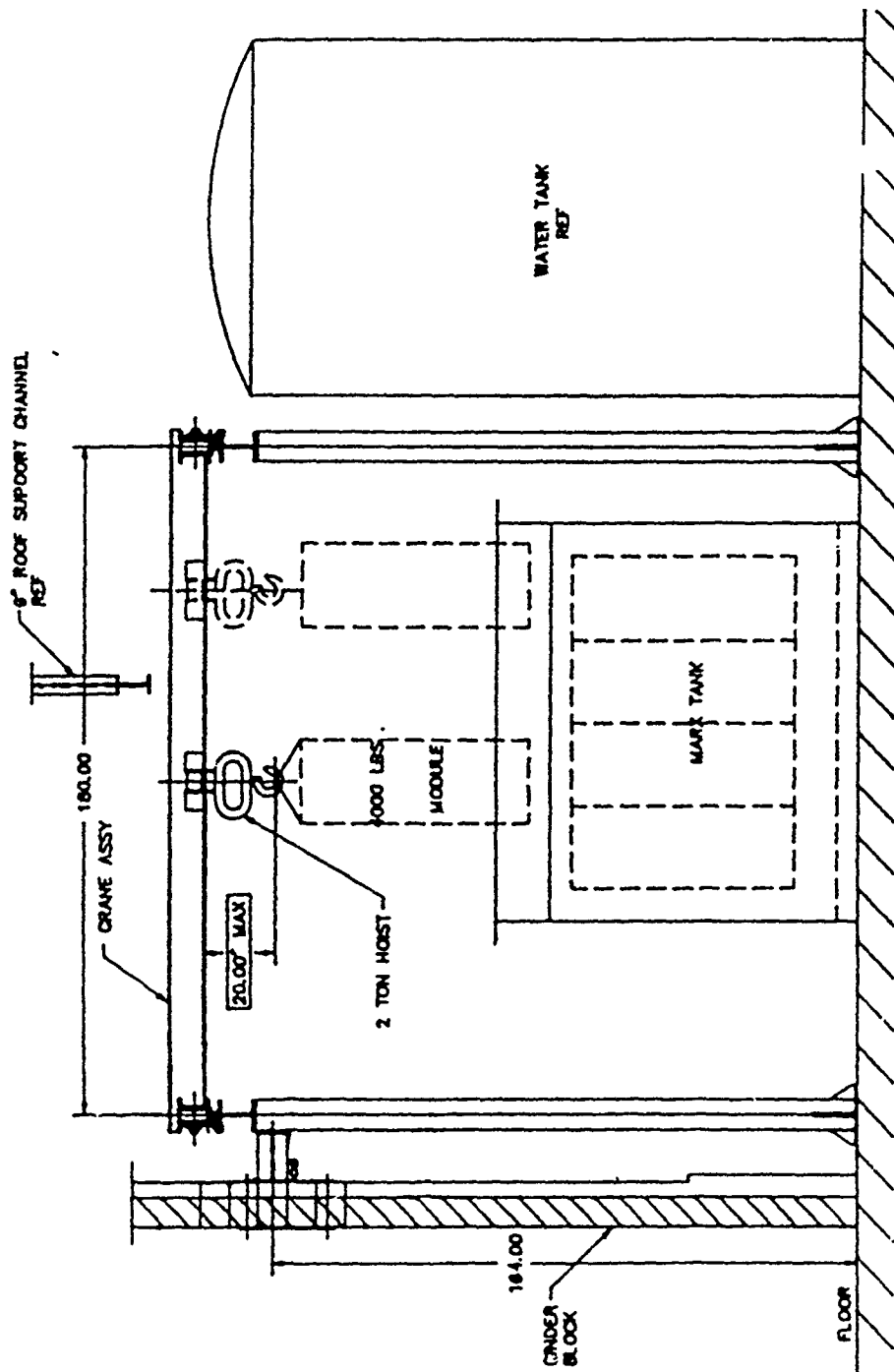


Figure 12. 2-Ton Bridge Crane for Marx Servicing

height that the Marx modules have to be raised to clear the tank. This tank wall modification was possible because the 96-in. height of the original Marx tank was higher than needed for the new Marx modules.

B. Marx Components

Two views of the layout of the components in the Marx tank are shown in Fig. 13. The Marx modules rest on support beams 11" above the tank floor to provide proper alignment with the output collector plate. The modules are positioned to one side of the tank to leave a 12-in. clearance at the other tank wall for maintenance access. This space can also be used to rout a pipe from the center conductor of the diode to an inductive isolator coil located at the back of the Marx tank for diagnostic cables. The increased length of the tank was used to provide space for the trigger marx, filter capacitors, charge/dump relays (not shown), and access to electrical connections at the rear of the modules.

C. Marx Modifications

During the initial checkout of Hawk, several electrical breakdowns occurred in the Marx modules in the vicinity of the capacitor headers. After close inspection and consultation with PI, it was determined that arcing joints at the capacitors were causing carbon build-up which contaminated the oil and led to the breakdowns. Because the capacitors are mounted vertically, carbon build-up can settle into the header area rather than descend harmlessly to the bottom of the Marx tank. The original PI design used wire screening as current gaskets between various spacers and connections to the capacitor headers, and mechanical limitations on the capacitors restrict the torque on the 3/4-inch bolt through these pieces to no more than 25 ft-lbs. Increasing the torque to minimize arcing was not possible. To overcome this problem, these contact points were redesigned using both RG-223 cable center conductor with braid and braided o-rings as current gaskets. A diagram of the new current contacts is shown in Fig. 14. This design was evaluated on a test stand⁷ and installed on Hawk. The major constraint on this design was to complete the modifications and get Hawk back into operation as soon as possible. Several new designs which would eliminate nearly all

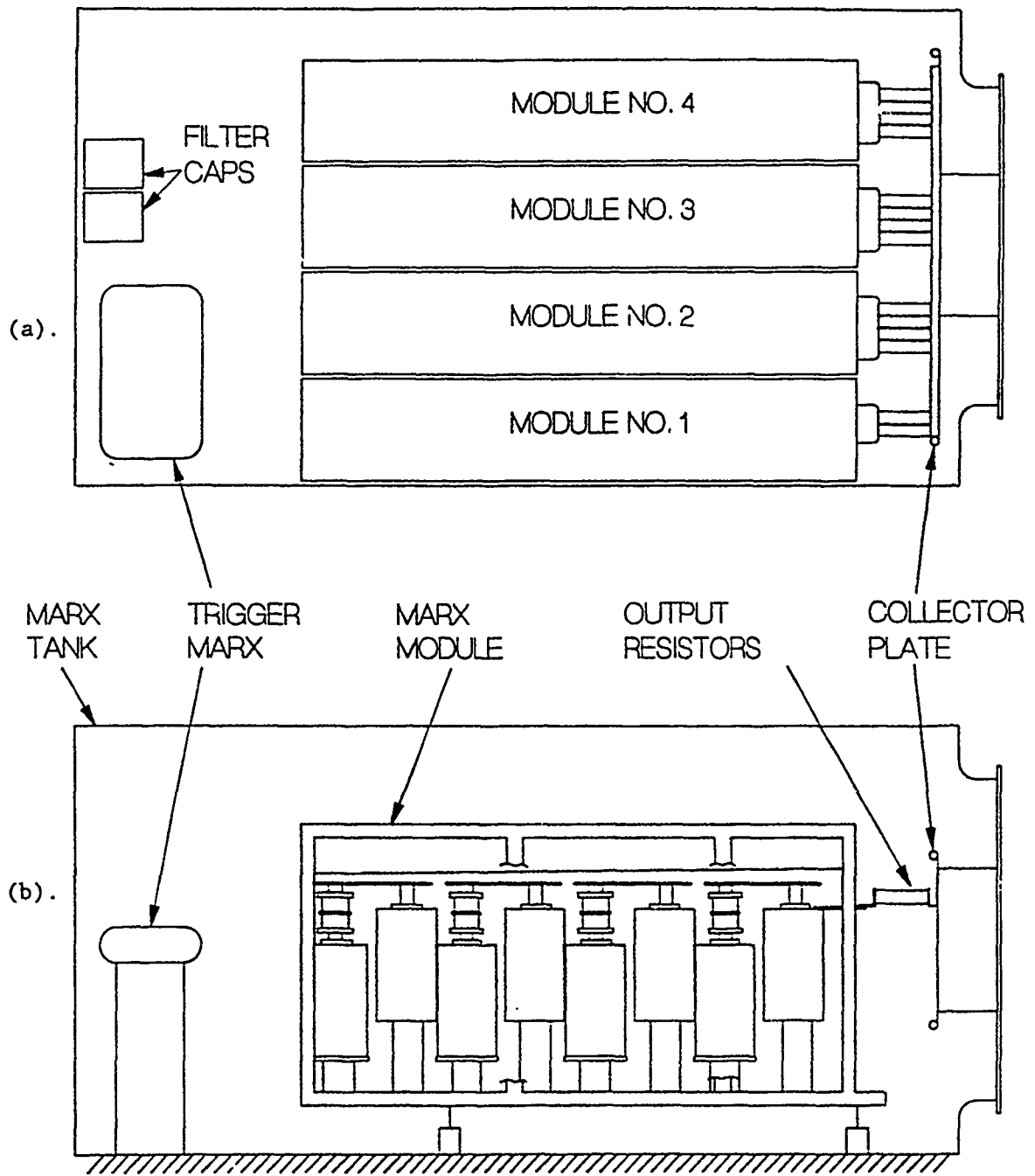


Figure 13. Marx Tank Layout, (a) top view, (b) side view

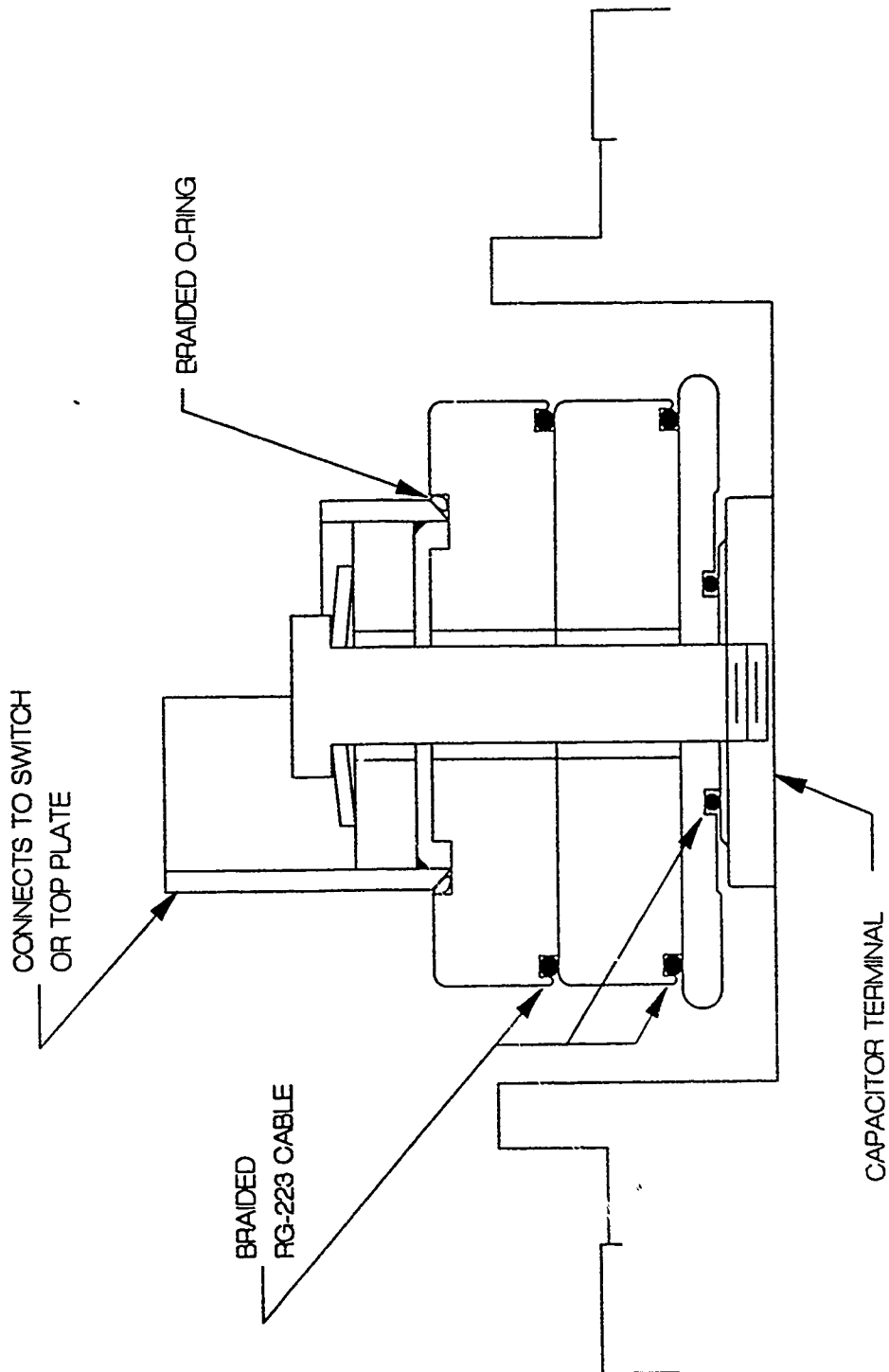


Figure 14. Modified Capacitor Header Current Contacts

of the contacts have been considered, but the present modification has worked so well that there are no plans to implement a new design.

D. Radiation Shielding

The location of the Hawk generator relative to nearby offices and laboratories in Building 71 is shown in Fig. 15. The shielding around the diode, located about 67 in. above the floor of Room 1117, was upgraded significantly compared with the shielding provided for Gamble I. The modifications were designed to confine the radiation to the test cell area. Improvements were based on calculations of shielding requirements using the peak voltage (1.5 MeV) and total energy (61 kJ) from run No. 452B in Table 1.

An analytic model for bremsstrahlung radiation was used to estimate the shielding required for Hawk. Thick-target bremsstrahlung from an electron-beam diode was used for the radiation source. For monoenergetic electrons of kinetic energy T , the bremsstrahlung energy spectrum is $S(E) = C(T-E)$ where C is a constant, E is the photon energy, and the total bremsstrahlung energy is proportional to T^2 (Ref. 8). Therefore, $S(E) = (2E_s/T^2)(T-E)$ represents the bremsstrahlung energy spectrum for electrons of energy T and total radiated energy E_s . This spectrum is attenuated by shielding. For the Hawk generator, lead and concrete shielding materials were considered. In addition, a 1-cm thick layer of iron was used to represent the vacuum chamber on the diode. The attenuation factor for the spectrum is given by

$$F(E) = \exp(-\mu_{Fe}x_{Fe})\exp(-\mu_{Pb}x_{Pb})\exp(-\mu_c x_c) \quad (1)$$

where x_{Fe} is 1 cm and μ_{Fe} , μ_{Pb} , and μ_c are attenuation coefficients for iron, lead, and concrete respectively. Values of these coefficients are taken from Ref. 9 for E above 1 MeV and Ref. 10 for E below 1 MeV for iron and lead and from Ref. 11 for concrete. The lead and concrete thicknesses, x_{Pb} and x_c , are varied to determine the thicknesses of shielding required. The total photon energy E_s is scaled inversely as the square of the distance and is converted to dose using water to represent the absorber.¹² Then the dose at a distance R in meters from

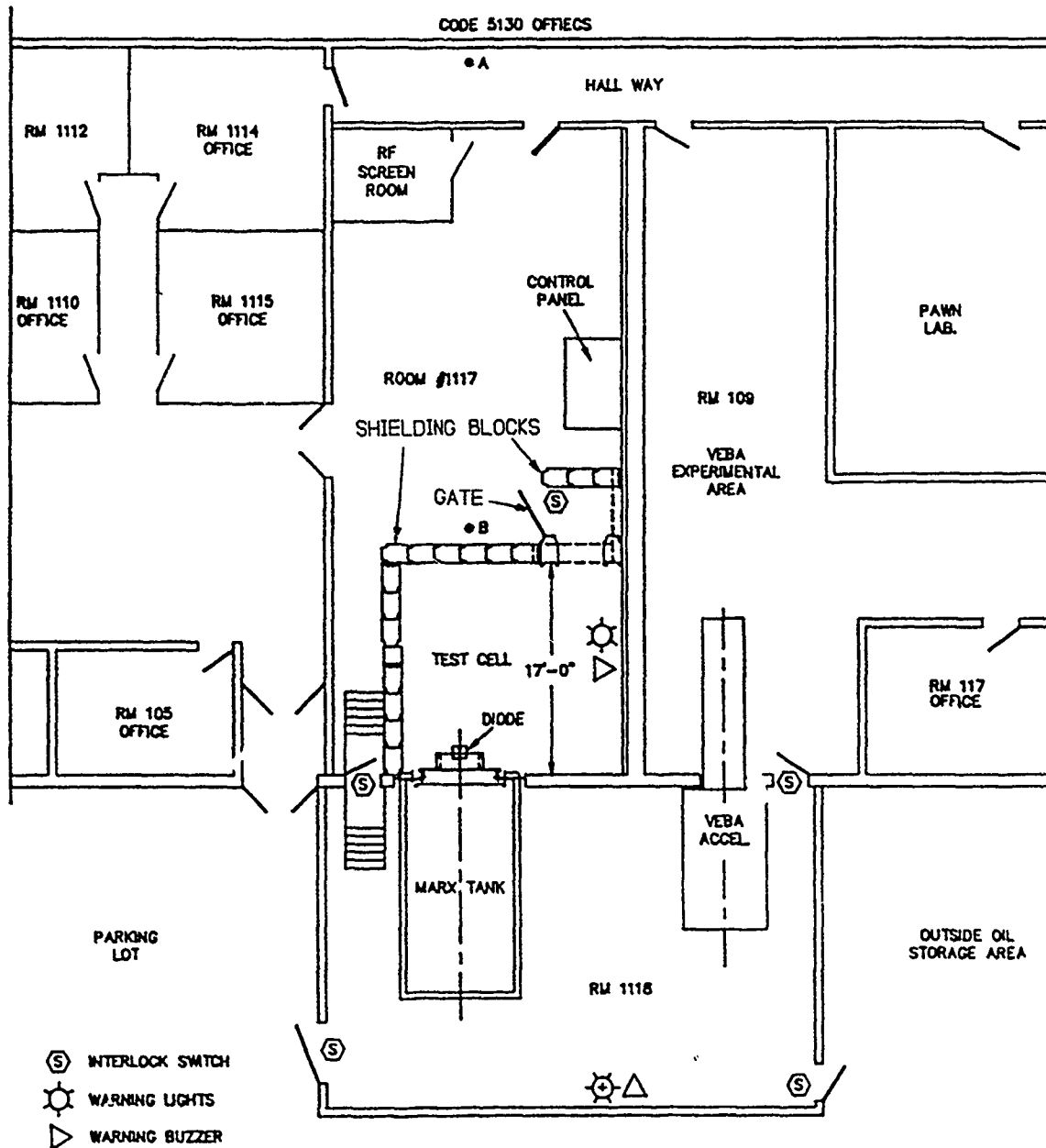


Figure 15. First Floor Radiation Shielding, Area Warning, and Interlocks

the source is given by:

$$\text{Dose (Rem)} = \frac{10^4}{4\pi R^2} \int_0^T \mu_w F(E) S(E) dE \quad , \quad (2)$$

where the total radiated energy E_s is in kJ and the absorption coefficient for water μ_w is in cm^2/gm . The value of μ_w is nearly constant at $0.03 \text{ cm}^2/\text{gm}$ over the range of interest for Hawk, 100-keV to 1.5-MeV photons.¹³ Then the dose as a fraction of the total radiated energy is given by:

$$\frac{\text{Dose (Rem)}}{E_s \text{ (kJ)}} = \frac{50}{R^2 \text{ (m)}} \int_0^T F(E) \left(1 - \frac{E}{T} \right) \frac{dE}{T} \quad . \quad (3)$$

For thick target bremsstrahlung, the conversion efficiency from electron beam energy E_e to total radiated energy is given by:¹⁴

$$\frac{E_s}{E_e} = 5 \times 10^{-4} ZT \quad , \quad (4)$$

where Z is the atomic number of the target and T is in MeV. For Hawk shielding estimates, $Z=80$ was used, representative of a tantalum ($Z=73$) or lead ($Z=82$) target. By combining Eqs. 3 and 4, the dose is determined for an electron beam of kinetic energy T and total energy E_e . Dose estimates at one meter from the source for several thicknesses of lead or concrete are given in Table II. These estimates do not include additional radiation from scattering or from dose buildup in the shielding. However, actual doses are expected to be less than these estimates because it was assumed for these calculations that all the radiation is produced by 1.5-MeV electrons rather than a more realistic sinusoidal voltage waveform. Also it was assumed that the source is isotropic rather than having the usual forward distribution typical of e-beam diode loads.

Table II

Dose* per Shot at 1 Meter
for Various Thicknesses of Lead or Concrete

<u>Lead</u>		<u>Concrete</u>	
Thickness (in.)	Dose (Rem)	Thickness (in.)	Dose (Rem)
1/8	22	10	0.46
1/4	14	12	0.22
1/2	7.5	18	0.020

* Based on $T = 1.5$ MeV, $E_e = 61$ kJ and 1-cm iron thickness.

Radiation shielding around the test cell (see Fig. 15) was improved in several ways based on these shielding calculations. Shielding blocks 18-in. thick and 96-in. high were extended along the west side of the test cell up to the south wall. Similar shielding blocks were added at the entry to the test cell to protect against radiation exiting through the entry way. All the 96-in. high shielding blocks were topped with new 19-in. thick poured concrete blocks to extend the shielding to within 1-in. of the ceiling. Previously, lower density blocks were used which extended only part way to the ceiling. The ceiling above the test cell was shielded by installing 1/4-in. thick lead which extended down to the concrete block walls. The existing wall on the east side (next to the Veba Laboratory) is 18-in. solid concrete to a height of 96 in. with hollow core block above this height. Lead of 1/4-in. thickness was added to the block portion of this wall to reduce the scattered radiation in this direction. No personnel are located at a level where they could receive direct exposure to radiation from the source passing through this portion of the wall. No additional shielding was added to the south wall (backward direction from the source). The Hawk oil-filled Marx tank is directly behind the source providing more than adequate shielding over a large solid angle in this direction.

With these shielding improvements, radiation doses at various locations have been calculated by scaling the dose at 1 meter (Table II) according to Eq. 2. The dose at points A and B in Fig. 15, where personnel may be routinely located, are 0.06 mRem/shot and 0.64 mRem/shot,

respectively. Point A is in an uncontrolled access hallway, and point B is in a controlled access area where personnel wear radiation dosimeters. It should be stressed that these are maximum doses expected, and no more than five of these shots per week would be fired. The maximum allowable whole body exposure to the general public is not to exceed 0.5 Rem/year¹⁵ which is 8000 times larger than the dose/shot at point A and 800 times larger than the dose/shot at point B. The maximum allowable radiation dose for personnel in controlled areas (Point B) is 1.25 Rem per calendar quarter.¹⁵ Therefore, the calculated doses at points A and B are substantially less than the allowable exposure, even for 5 shots/wk for one year at the maximum diode voltage.

The roof above Hawk is potentially a more hazardous area. The second floor area immediately above Hawk is a high radiation area and is safety interlocked as described in the next section. The roof of Building 71 is 32 feet above Hawk, and the calculated dose beneath this roof is 150 mRem/shot. It is expected that the roofing material will lower the dose above the roof to an acceptable level for controlled areas. Signs are posted at the access points to this roof warning against entry without proper authorization. If in the future the roof shielding is inadequate, an additional 1/8 in. of lead could be safely added to the ceiling above Hawk to reduce the dose. The NRL Health Physics Staff is continuously monitoring the radiation levels as the operating power level of Hawk is gradually increased.

E. Interlocks and Audible/Visual Warnings

Interlocked doors or gates are used to prevent firing of Hawk if personnel have entered either the test cell, Marx room, or second floor high radiation area. The locations of interlocked doors for the first floor area are shown in Fig. 15. The entrance gate to the test cell has an interlocked switch to prevent charging and firing of the generator if entry is attempted. The four entrances to Room 1118 (Marx room) also have interlocked switches for the same purpose. The three interlocked gates on the second level are shown in Fig. 16. These also prevent firing of the generator if a person enters the high radiation area on the second floor level above the test cell. All of these interlocks

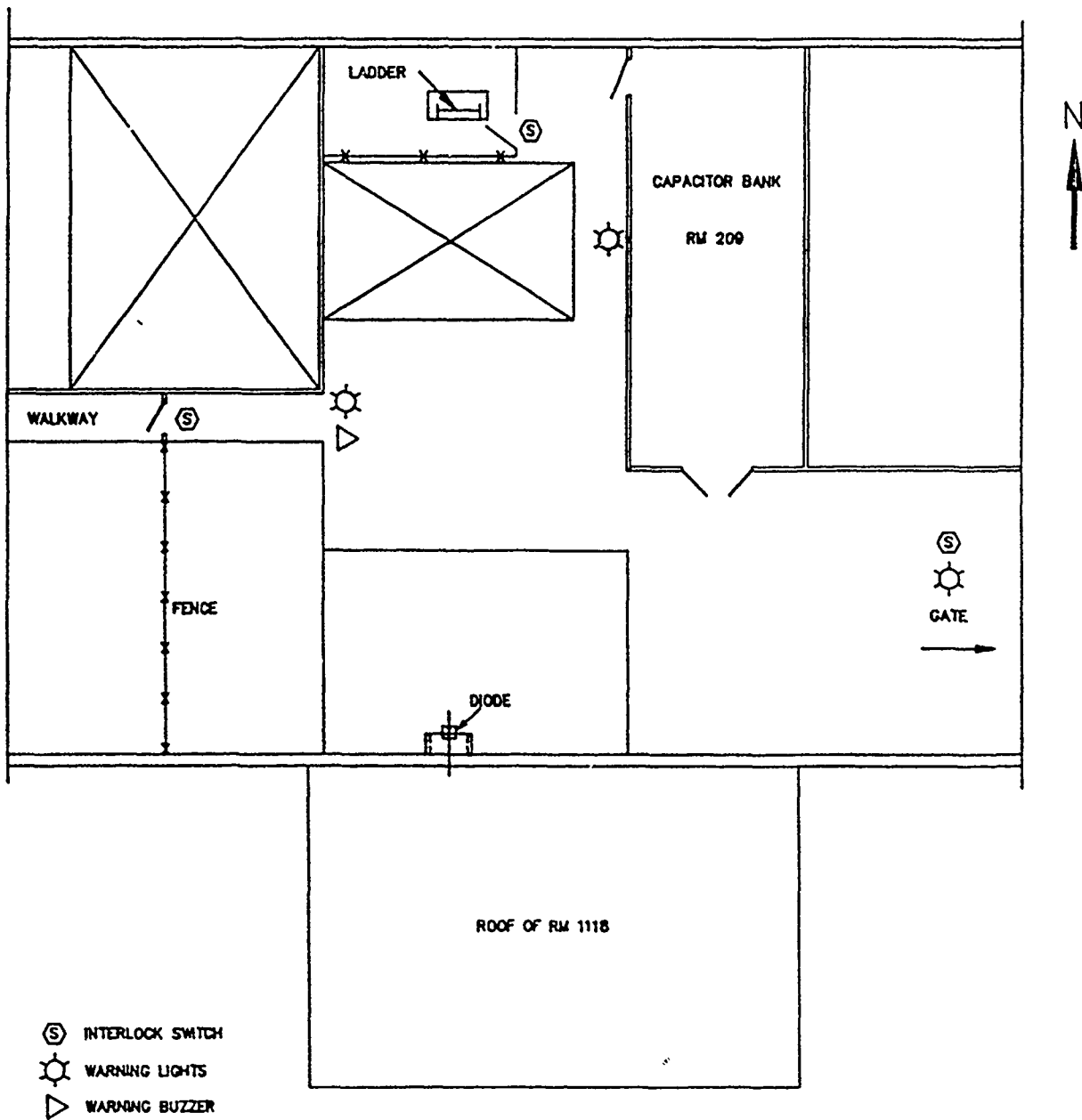


Figure 16. Second Floor Area Warnings and Interlocks

have the feature that they will not automatically reset if someone simply closes the gate behind them after passing through. Fencing is also installed on the second floor where needed to prevent people from entering the high radiation area without triggering the interlock system.

Emergency disabling of the generator is possible with "Scram" or panic switches which are located in the test cell and the second floor areas. These switches have the feature that they must be reset manually before firing procedures can be resumed. Also audible/visual warnings are installed in the test cell, Marx Room (1118), and second floor areas as shown in Figs. 15 and 16. These devices are activated during the charging and firing sequence of the generator.

V. INITIAL PERFORMANCE

After the initial checkout shots with a short circuit located at the door of the G-5 diode, POS hardware was added with a short circuit load as shown in Fig. 17. The figure shows the electrical diagnostics, consisting of a capacitive voltmeter in the oil section, V_0 ; a current shunt between V_0 and the insulator, I_{SHT} ; four B-dot loops which are added together to provide an average current in the vacuum region at the insulator, I_{OUT} ; a Rogowski coil upstream of the POS, I_{SU} ; and two B-dot loops at the load, I_{LU} and I_{LL} . Eighteen flashboards provided the plasma source for the POS. The opening switch hardware was taken directly from Pawn.^{16,17} Figure 18 shows the upstream and downstream currents as measured by I_{OUT} and an average of the load B-dots for a typical shot with a short circuit load. After conducting for 900 ns the POS opened, transferring a peak current of 640 kA to the load in less than 90 ns (10 to 90% points) with a ± 72 kV charge on the Marx. This current is at the level expected for this charge voltage and scales to 800 kA for a charging voltage of ± 90 kV.

A comparison of the output currents of Hawk and the present upgraded Eyess generator at PI is shown in Fig. 19 for a ± 80 kV charge voltage. The upgraded Eyess has eight capacitors per Marx module as in Hawk, but the modules have been repackaged into much smaller units which

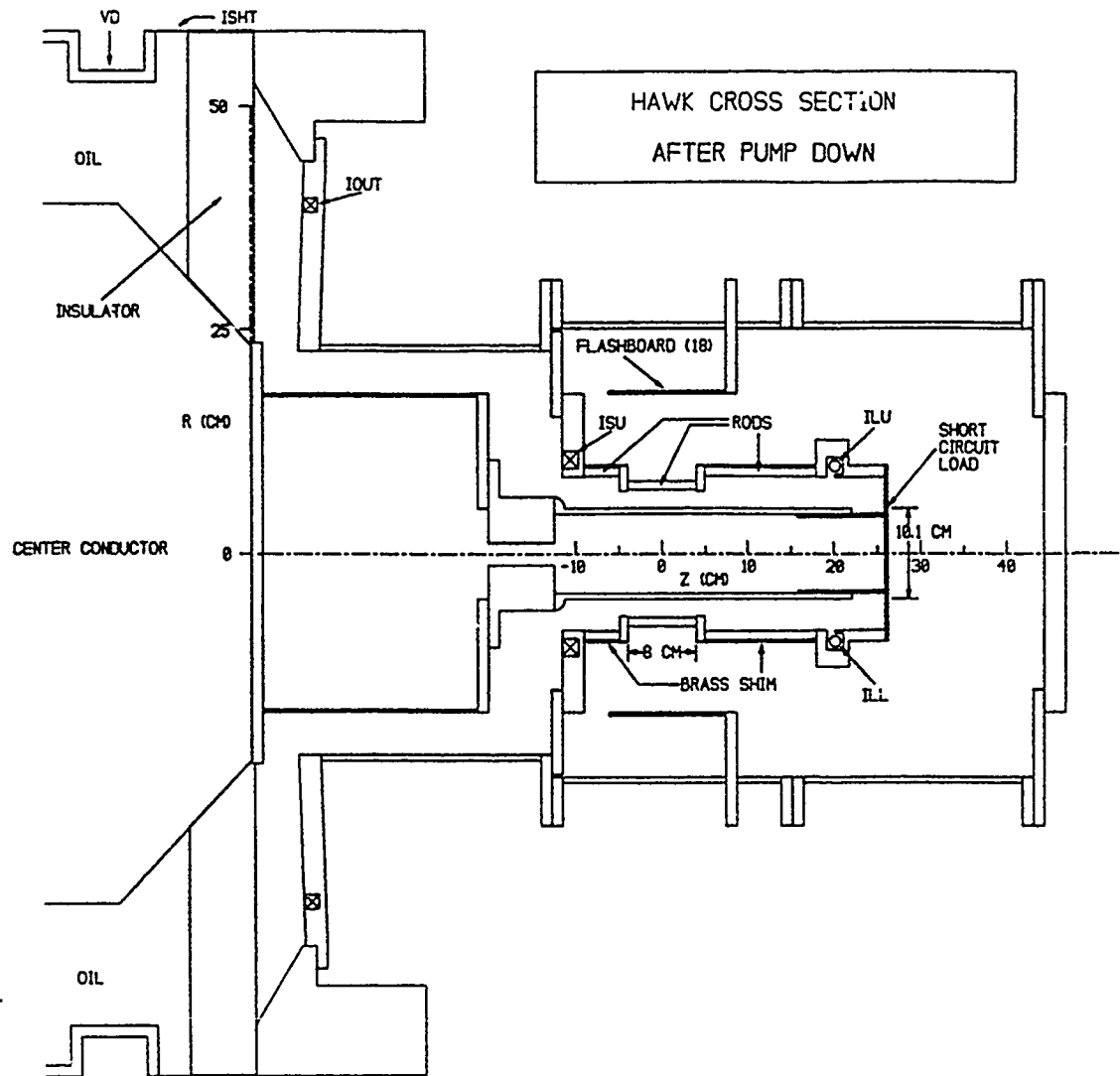


Figure 17. POS Configuration for Initial Opening Switch Experiments

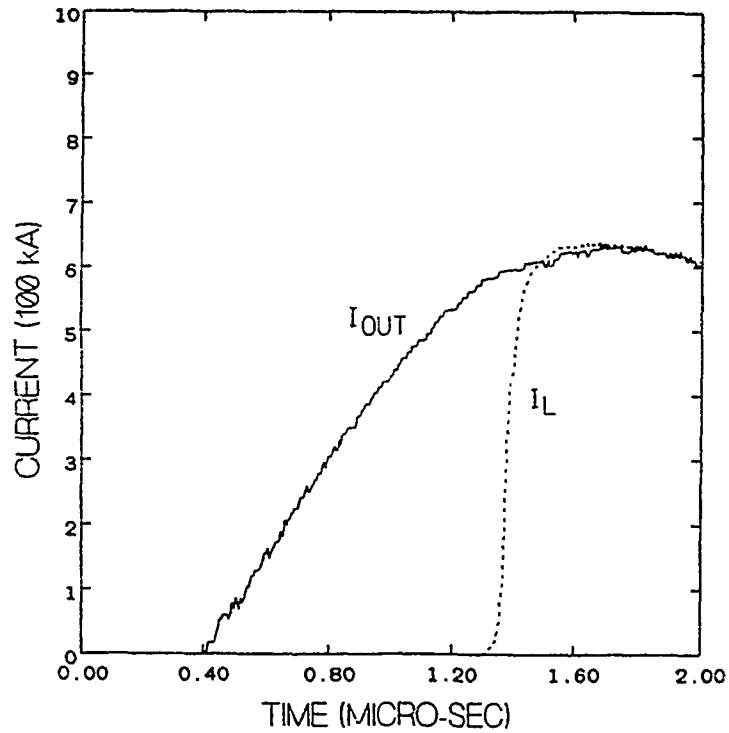


Figure 18. Upstream and Load Currents with POS and Short Circuit Load

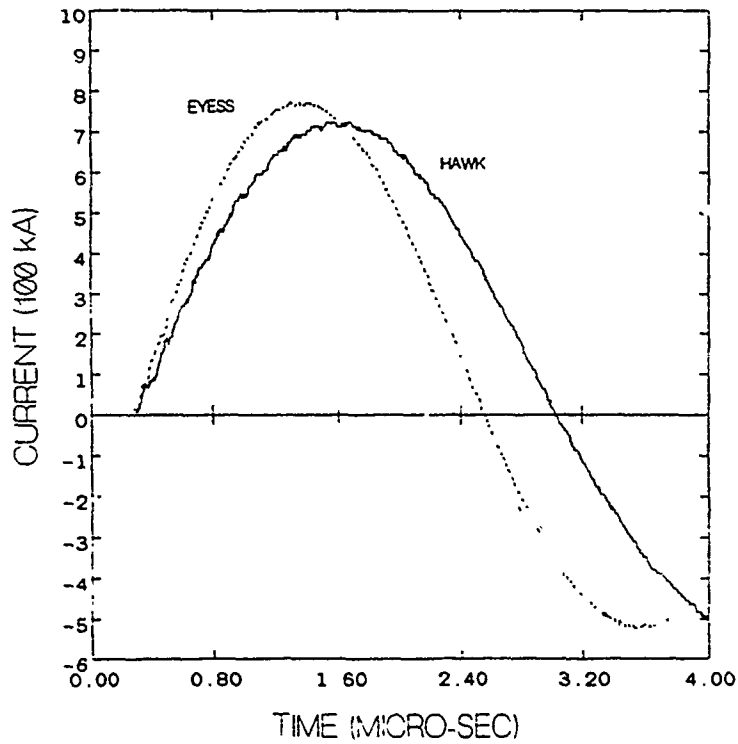


Figure 19. A Comparison of the Output Currents of Hawk and the Upgraded Eyess Generator at PI

has significantly reduced the Marx inductance. This accounts for the faster rising, higher peak current of Eyess shown in the figure.

The Hawk generator is now operational, with investigations of long-conduction-time POS currently in progress. Hawk has proved to be a very reliable, high-shot-rate generator for opening switch research in the 800-kA, 1- μ s regime.

VI. ACKNOWLEDGEMENTS

The authors wish to acknowledge useful technical discussions with members of the Pulsed Power Physics Branch, the guidance and encouragement of Dr. G. Cooperstein, and the critical assistance of the Plasma Physics Division (Code 4700) and the Director of Research (Code 1001) at NRL. This work would not have been possible without the guidance of J. Burton for site modification and preparation and without the expert technical assistance of J. Fields, R. Fisher, G. Longrie, and B. Roberts. Personnel from PI were extremely helpful during the design and installation of Hawk, especially Dr. P. Sincerny and T. Tucker. This work was supported in part by the Defense Nuclear Agency.

VII. REFERENCES

1. "Proposal for Joint DNA/NRL Facilities Upgrade", Plasma Technology Branch Tech Note No. 88-47, Proposal No. 47-023-88/89-90, unpublished.
2. G. Cooperstein and P.F. Ottinger, "Fast Opening Vacuum Switches for High-Power Inductive Energy Storage," IEEE Trans. Plasma Science, PS-15, Guest Editorial, 1987, p. 629.
3. P. Sincerny, D. Drury, J. Goyer, G. James, M. Krishnan, J. Levine, C. McDonald, and I. Roth, "A Microsecond Marx Bank for Driving High Current Electron Beams," 7th IEEE Pulsed Power Conference, Monterey, CA 1989, IEEE Cat. No. 89CH2678-2, p. 275.
4. D.D. Hinshelwood, "BERTHA - A Versatile Transmission Line and Circuit Code," NRL Memorandum Report 5185, Nov. 1983.
5. H. Nguyen and B.V. Weber, "Technote for RLC Program," Plasma Technology Branch Tech Note No. 85-25, unpublished.

6. J.D. Shipman Jr., J.R. Boller, P.J. Goodrich, and S.J. Stephanakis, "Results of G5 Diode Insulator Flashover Tests at Longer Than the Original Design Times Utilizing Gamble II in a Special Long Time Output Mode of Operation," Plasma Technology Branch Tech Note No. 89-12, unpublished.
7. D. Hinshelwood, R. Boller, P. Goodrich, R. Fisher, and G. Longrie, "Current Contacts in the Hawk Marx," Plasma Technology Branch Tech Note No. 90-08, unpublished.
8. R.D. Evans, The Atomic Nucleus (McGraw Hill, New York, 1955) p. 615.
9. "Shielding for High-Energy Electron Accelerator Installations," National Bureau of Standards Handbook 97, 1964, p. 48.
10. Wm. J. Veigele et al., "X-Ray Cross Section Compilation from 0.1 keV to 1 MeV", Defense Nuclear Agency No. DNA 2433F, Kaman Sciences Corp., Colorado Springs Colorado, July 31, 1971.
11. J.B. Marion and F.C. Young, Nuclear Reaction Analysis (North-Holland, Amsterdam, 1968) p. 100.
12. Op. cit., ref. 9, p. 35.
13. Op. cit., ref. 8, p. 714.
14. Op. cit., ref. 9, p. 10.
15. Radiation Protection Manual, NRLINST 5100.11D, Feb. 1982.
16. R.J. Comisso, J.R. Boller, G. Cooperstein, R.D. Ford, D.D. Hinshelwood, D.J. Jenkins, J.C. Kellogg, W.H. Lupton, J.D. Shipman, Jr., and B.V. Weber, "Pawn, an Inductive Storage Pulsed Power Generator for High Power Operation," Seventh IEEE Pulsed Power Conference, Monterey, CA, June 1989, IEEE Cat. No. 89CH2678-2, p. 272.
17. B.V. Weber, R.J. Comisso, P.J. Goodrich, J.M. Grossmann, D.D. Hinshelwood, J.C. Kellogg, and P.F. Ottinger, "Experimental PEOS Research at NRL," DNA Opening Switch Workshop, Alexandria, VA, Jan. 1990, unpublished.

PLASMA TECHNOLOGY BRANCH TECH-NOTE NO. 90-08

TITLE: "CURRENT CONTACTS IN THE HAWK MARX"

DATE: 27 March 1990

AUTHORS: D. Hinshelwood, R. Boller, P. Goodrich, R. Fisher, and G. Longrie.

ABSTRACT: This note describes our modifications to the current contacts in the Hawk Marx. A test assembly allowed us to evaluate and compare several contact techniques under realistic conditions. The new contacts are a significant improvement over the old design.

** THIS REPORT REPRESENTS
UNPUBLISHED INTERNAL WORKING
DOCUMENTS AND SHOULD NOT BE
REFERENCED OR DISTRIBUTED

** THIS REPORT CONTAINS REALLY
BORING ENGINEERING DETAILS

Background

During the initial testing of Hawk, breakdowns in the Marx occurred, especially above 80 kV charging voltage. Carbon build-up from sparking current contacts was determined to be the culprit, based on visual inspection and conversations with Terry Tucker at PI. The sparking seemed to occur only at connections related to the capacitor high voltage terminals; those involving the ground rings, which have lower linear current densities, appeared fine. We have now significantly improved these contacts.

Old arrangement

The original arrangement is best described with reference to Fig. 1. The capacitor terminal was connected to a 5/16 in plate and two, 1 in plates, all of mild steel. The connections were made by disk-shaped sections of brass screen. The top plate made a butt contact with 3 in OD x 3/16 wall aluminum tube. All of these were held together by a 3/4-10 bolt torqued to 25 ft-lbs and a spring washer. Half of the top of the aluminum tube was cut away and the remaining half was connected to a section of 2-5/8 OD aluminum tube with a hose clamp. The OD of this tube was a few mils over the ID of the half-tube. This tube was either connected to a top plate, or to a switch which was connected to the top plate. The top plate was connected to the thigh bone. All of these connections were of the tube/half-tube type. This type of connection allowed the switches to be removed easily, and did not seem to be the source of much sparking. The screen and butt contacts seemed to be bigger problems.

Initial testing

In the first modification the screen connections were replaced by sections of RG-223 center conductor with both braids on. These were forced into grooves with the dimensions indicated in Fig. 1. The ends were dressed with solder in attempt to eliminate frayed edges. They were lightly coated with flux, dipped in hot solder, and then sanded down. This turned out to be a fairly time-consuming procedure.

A variation of the "Capitals" pulser was used to test different contact techniques. The first set-up, shown in Fig. 1, tested all of the contacts used in the original and modified arrangements. In addition, an extra plate was added where the RG-223 was replaced by one of our standard braided O-rings. This consisted of 1/8 in O-ring material covered with one of the RG-223 braids. (The use of both braids was previously shown to reduce compressibility and degrade performance.) After gluing the O-ring the braid ends were pushed together and smoothed out but were not soldered, so that some fraying remained. The top

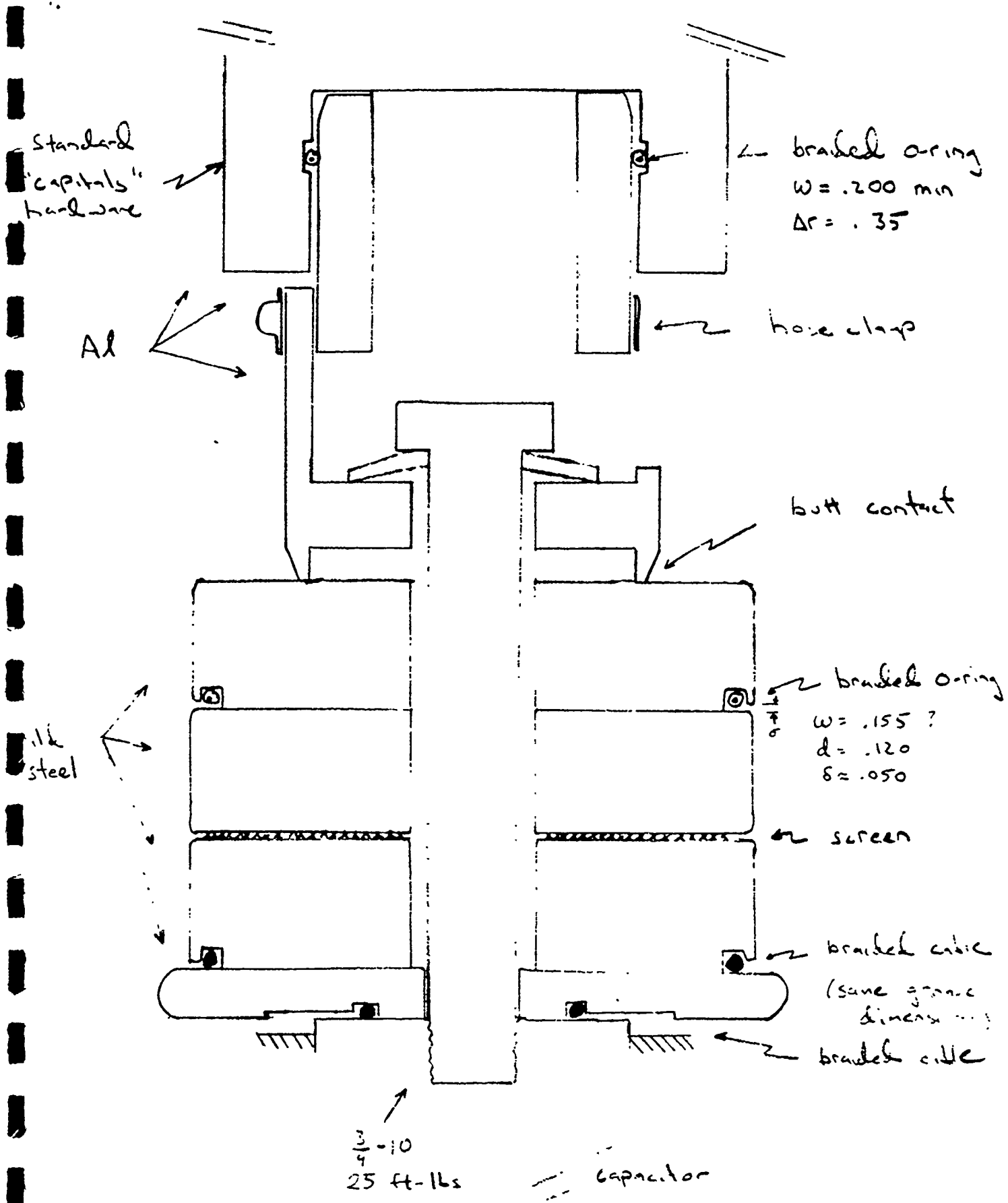


Fig. 1: Test assembly set-up.

2-5/8 tube slid into the standard capitals hardware. Thus, this arrangement also tested other contacts: a braided O-ring sliding seal, with the groove dimensions shown, and two other braided O-ring flat seals (not shown) with grooves that were .100 in deep but $>.200$ wide, so that no pressure was exerted by the side walls. The pulser was terminated by 21, 2 ft. long type C cables with shorted ends. These cables were connected by banana plugs and type N connectors. The sliding seal in the "Capitals" hardware was new, but the other connections had many shots on them.

The $2.1 \mu\text{F}$ capacitor was charged at 2 mA to 49 kV and discharged about every two minutes for 200 shots. The current had a $2.8 \mu\text{s}$ period and roughly $10 \mu\text{s}$ time constant, indicating 230 kA peak current, 90 nH, and about $.01\Omega$. The calculated inductance outside of the switch and capacitor was 40 nH and 20–25 nH is a reasonable number for the switch, so the capacitor inductance is much less than the 100 nH specified maximum. By comparison, the 82 kV charge, single module Hawk parameters are about 190 kA peak current and $7.5 \mu\text{s}$ time constant. Thus, each test shot had the $\int I^2 dt$ of about 2 Hawk shots.

The connections were examined after testing. As expected, the screen connection showed carbon build-up and signs of arcing. The sliding and flat braided O-ring connections were completely unaffected, except for slight marks on the electrodes corresponding to the braid joint. No burning was evidenced at the braid ends, either. The cable braids also looked fine, although the larger diameter braid showed some faint signs of burning (the silver color was beginning to look coppery). There were no signs of trouble at the soldered braid ends. The butt joint showed the worst damage, with a lot of carbon and significant arc damage on the aluminum. The hose clamp connection seemed to work surprisingly well; there were some faint signs of arcing, but nothing like we would have expected.

Second design

We felt that the hose clamp connection was adequate for now, but the butt joint had to be improved. It was replaced by a braided O-ring connection, as shown in Fig. 2. The groove dimensions and bevel angle used allowed the aluminum piece to seat against the steel, preventing it from being cocked, and gave a fairly uniform compression of the O-ring. These dimensions were chosen after several cut-and-fit attempts.

The test set-up was reassembled with the new contact, and with the screen replaced by another cable braid connection. The cable braids were new but the braided O-rings were re-used, and no attempt was made to clean the oil off of them or their grooves. After 150 shots the connections were examined and everything looked good. The new contact had absolutely no sign of damage

3-26-90

HAWK
CAPACITOR HEADER TOP SPACER
MODIFICATION

ALUM. COUPLING
MODIFIED WITH
45° BEVEL TO
SHARP POINT

BRAID COVERED
O-RING

3.070 O.D.
2 1/4 ±0
-1/8 ID
.150 DEEP
Sand outer edge

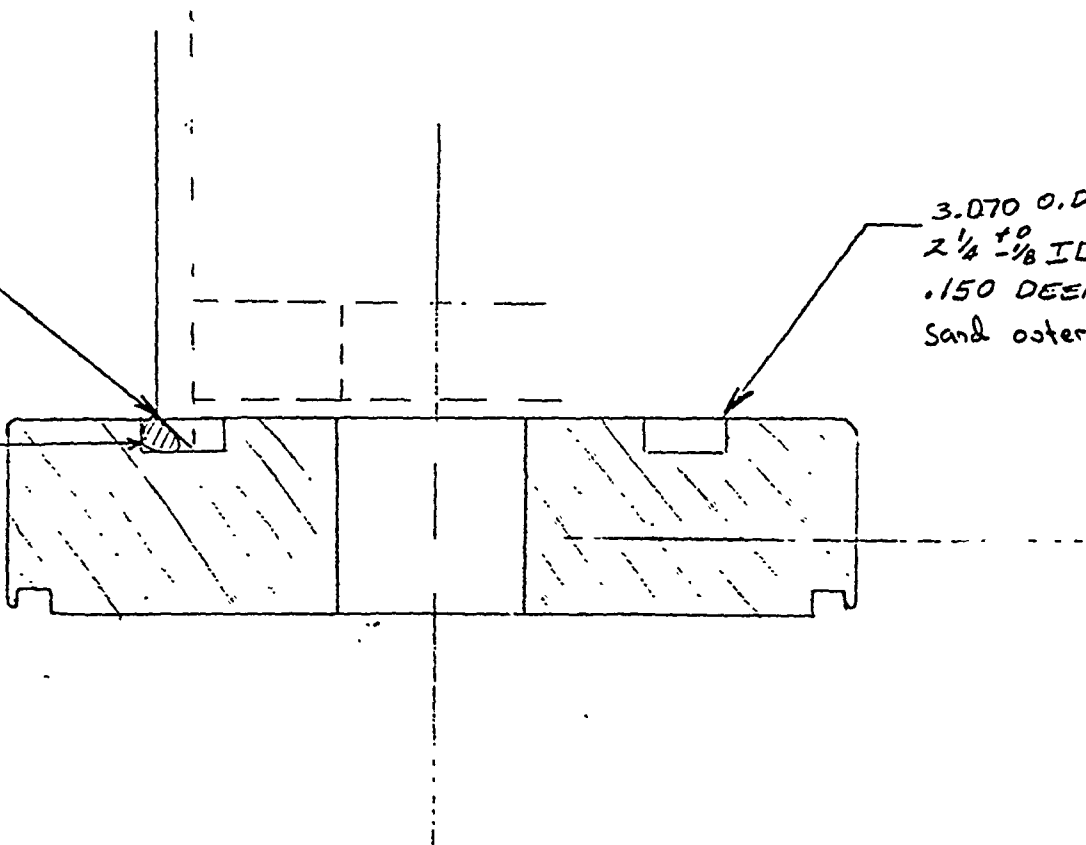


Fig. 2: Improved connection.

except for a tiny dot of carbon at the braid joint. The cable braids showed no sign of burning, either.

Examination of the oil showed some small (<0.5 mm) pieces of metal and one (few mm) fragment of braid. This gives some cause for concern, but the metal may well have come from other connections on the "Capitals" hardware, for example washers on the type N connectors at the top. Some arcing was observed at these locations, and between connections on the outer can, although it may have occurred before the testing.

Summary

We now have a set of current contacts on the Hawk Marx that should work quite well. We might want to improve the hose clamp connections at some point in the future but right now that does not seem to be a high priority. After 50-100 shots it will probably be a good idea to drop the oil and examine one capacitor for the presence of metal particles. Braided O-rings seem to make the best current contacts although fraying the the ends might be a problem. The test assembly was useful, since several of the contacts worked differently than expected.

(Note: for the PI confined discharge experiment, similar currents were carried by a 1/2 in ID braided O-ring seal, with a Δr of 0.132 in. This also showed no sign of damage, although the rod was re-inserted every shot, which may have helped by scraping a clean surface each time.)

PULSED POWER PHYSICS TECHNOTE NO. 93-13

TITLE: ZFX--A PULSED POWER DRIVER USING A PARALLEL PLATE WATER CAPACITOR (Summary of the oral presentation at the 9th Pulsed Power Conference, 21-23 June 1993, Albuquerque, NM)

AUTHOR(S): J.D. Sethian, J.R. Boller, R.J. Comisso, J.C. Kellogg, B.V. Weber, P.J. Goodrich, and D.D. Hinshelwood

DATE: 21 July 1993

ABSTRACT: A new pulsed power generator that uses a thin parallel plate water capacitor as the intermediate store is nearing completion at the Naval Research Laboratory. The plates are made of relatively thin (2.54 cm thick) aluminum sheets and rely on "plastic field attractors" to reduce the field enhancement at the plate edge.

The water capacitor is pulse charged by a conventional 340 kJ Marx, and then discharged by a self-break rimfire-type switch into the load. Because the plates are thin, over 70% of the stored water is used to store energy, and thus the system is very compact. Other potential advantages of this system might be cost and ease of fabrication and maintenance.

The first experiments on ZFX, will be to drive current through a plasma opening switch. It is anticipated that ZFX should be able to deliver a current of 1 MA with a risetime of 300 nsec to the switch. Peak current would be 1.4 MA at 625 nsec.

THIS REPORT REPRESENTS
UNPUBLISHED INTERNAL
WORKING DOCUMENTS AND
SHOULD NOT BE REFERENCED
OR DISTRIBUTED

- Figure 1: Title
- Figure 2: Schematic layout of the system showing the system architecture, the electrical parameter range, and the power conditioning times scales appropriate for the ZFX water capacitor.
- Figure 3: Comparison of two approaches for storing electrical energy using water capacitors; In the coaxial system (left) a large fraction of the water, namely that inside the inner conductor, does not store energy and hence a significant volume wasted. In contrast, a parallel plate water capacitor (right) can be much smaller because a greater fraction of the water is used to store energy. The problem with the coaxial construction can be ameliorated somewhat by using multiple parallel coaxes, as described below. The problem with a parallel plate arrangement is what to do about the field enhancement at the edges. By using the techniques described below, we show that the parallel plate construction results in more efficient use of the water compared with an optimized multiple coax system.
- Figure 4: The enhancement at the edges is shown in graphic detail in this plot. This is an equipotential plot of the circled area shown in Figure 3, for a parallel plate capacitor charged to 950 kV and an interplate spacing of 12.5 cm. Note that while the field between the plates is uniform at 75 kV/cm, that at the edges is 360 kV/cm, which will exceed the breakdown strength in water.
- Figure 5: If however, one places a plastic block at the edge of the plate, the lower dielectric constant of the plastic (2.2 vs 81 in the water) causes the equipotential lines to be pulled away from the plate edges. In a sense the plastic is "attracting" field lines into it, and hence can be thought of as a "Plastic Field Attractor" (PFA). Note that in this example the field between the plates is uniform at 75 kV/cm, except at the transition to the curved edge of the plate where it increases to 108 kV/cm. This is still below breakdown. The field in the bulk plastic is 184 kV/cm and should also be well below breakdown, provided the plastic is free of voids and impurities. This technique using shaped plastic to locally reduce field stresses in water is not new, however, this is the first time that it has been proposed as the basis for an entire system. Note that these plastic pieces are essential for the parallel plate capacitor to be a viable concept. Otherwise the plates would have

to be so thick (in order to have a large enough radius to reduce the field enhancement) that the volumetric efficiency would be dismal.

Figure 6: Experimental apparatus used to test the PFA concept on a small scale. This tests the PFA concept for both positive and negative high voltage plates (see the ground aperture at the feed), and it tests the more severe conditions where the corners of the plates must be rounded.

Figure 7: Data from the test apparatus show the concept should be viable; According to these results it should be possible to operate a full scale water capacitor at 14% above its design value of 1000 kV. Autopsies indicated the system was as likely to break along the plastic as in the water gap itself, implying the plastic/water interface was no weaker than the rest of the system. During these tests a number of "construction faults" were deliberately introduced in order to determine the robustness of the system. These included gaps in the plastic (perpendicular to the plate edge), gaps between the plastic and the edge of the plate, holes drilled into the plastic to simulate voids, and trapped air in the water. Only the latter two caused a problem, which was taken as a clear warning of the importance of removing all trapped air.

Figure 8: Line drawing of the ZFX water capacitor. The water capacitor is housed in two boxes, each 8 feet wide x 10 feet long x 5 feet high, situated on either side of the switch load region. The latter is mounted on a "raft" that bridges the two water capacitors. The plates are oriented so they behave as several parallel plate transmission lines feeding into a common collector.

Figure 9: Photo of a model of the ZFX water capacitor.

Figure 10: Photo of the ZFX water capacitor under construction

Figure 11: Photo of the ZFX water capacitor under construction

Figure 12: Performance of ZFX as modelled with a simple transmission line code. Maximum predicted current is 1.5 MA @ 600 nsec.

- Figure 13: Calculations show that ZFY should operate well below the limits of electrical breakdown in water, provided a divertor switch is incorporated in the system. These breakdown strengths were calculated using rather pessimistic assumptions: It was assumed that the $A^{.058}$ dependence holds for large areas, and that the breakdown is a cumulative process; i.e. once a streamer is launched, it will continue independent of the polarity of the surface.
- Figure 14: Using available data, the surface of the plastic should also be operating well below breakdown.
- Figure 15: Equivalent circuit of ZFX as it was configured for the first, low voltage power tests. The switch inductance in this circuit is about a factor of 2.4 higher than in the circuit used to compute the maximum performance shown in Figure 12. This reflects the reluctance of the switch to multichannel at lower voltages.
- Figure 16: Comparison of calculated and measured water capacitor waveforms.
- Figure 17: Comparison of calculated and measured output current waveforms. Load is a 1" diameter bolt.
- Figure 18: A comparison between a multiple coaxial tube water capacitor (based on the PI Decade design) and a parallel plate arrangement. The parallel plate arrangement can store the same amount of energy but in 75% of the volume.
- Figure 19: Summary

**ZFX -- A PULSED POWER DRIVER USING
A PARALLEL PLATE WATER CAPACITOR**

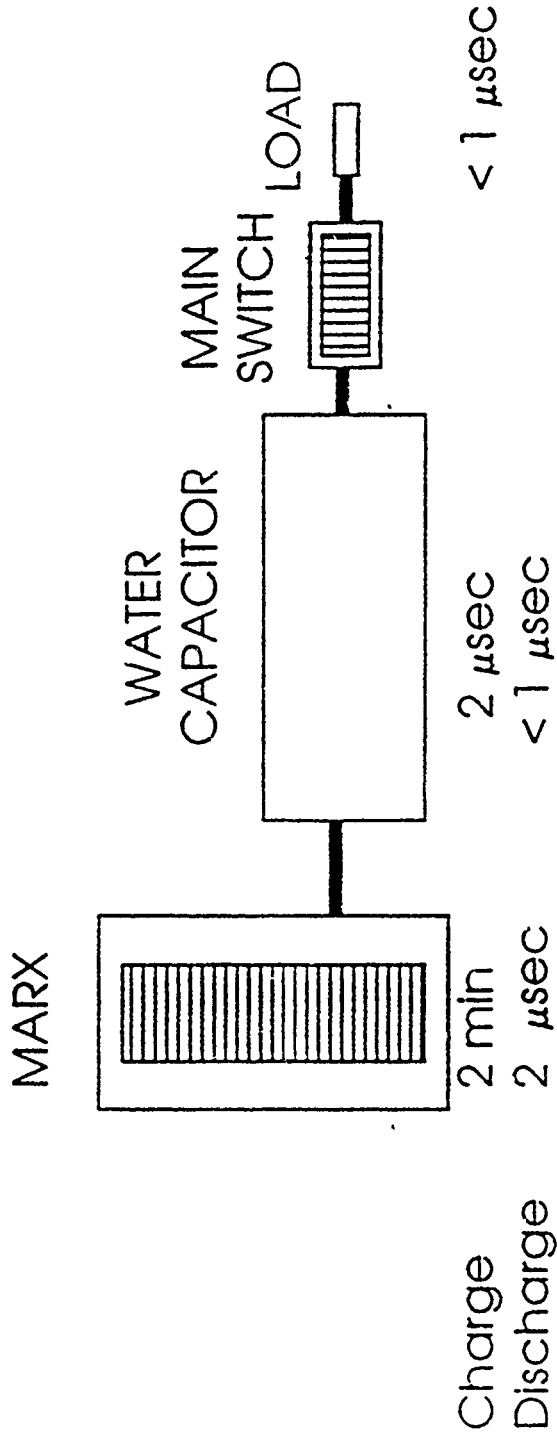
J.D. Sethian, J.R. Boller, R.J. Commisso, J.C. Kellogg and B.V. Weber
Naval Research Laboratory
Plasma Physics Division
Washington, D.C. 20375-5346

P.J. Goodrich and D.D. Hinselwood
JAYCOR, Inc
Vienna, VA 22180-2270

(2)

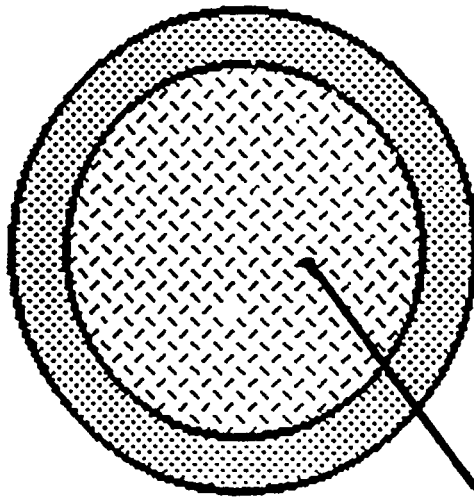
Water Capacitor is used as an Intermediate Store between Marx and Load

System Energy: ~ 300 kJ, Voltage ~ 500 - 1000 kV, Current 1 - 2 MA



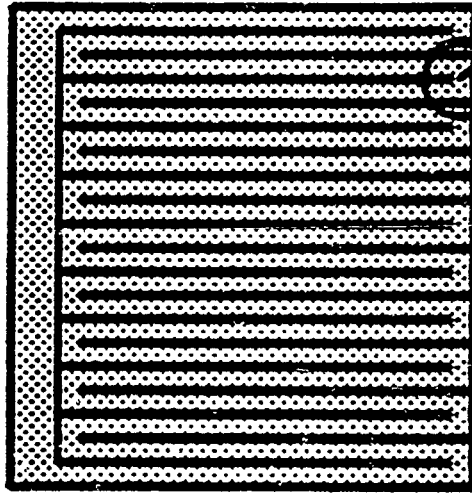
A Parallel Plate Water Capacitor can have a Very High Volumetric Efficiency

Coaxial Line
(Inefficient)



Wasted
Space

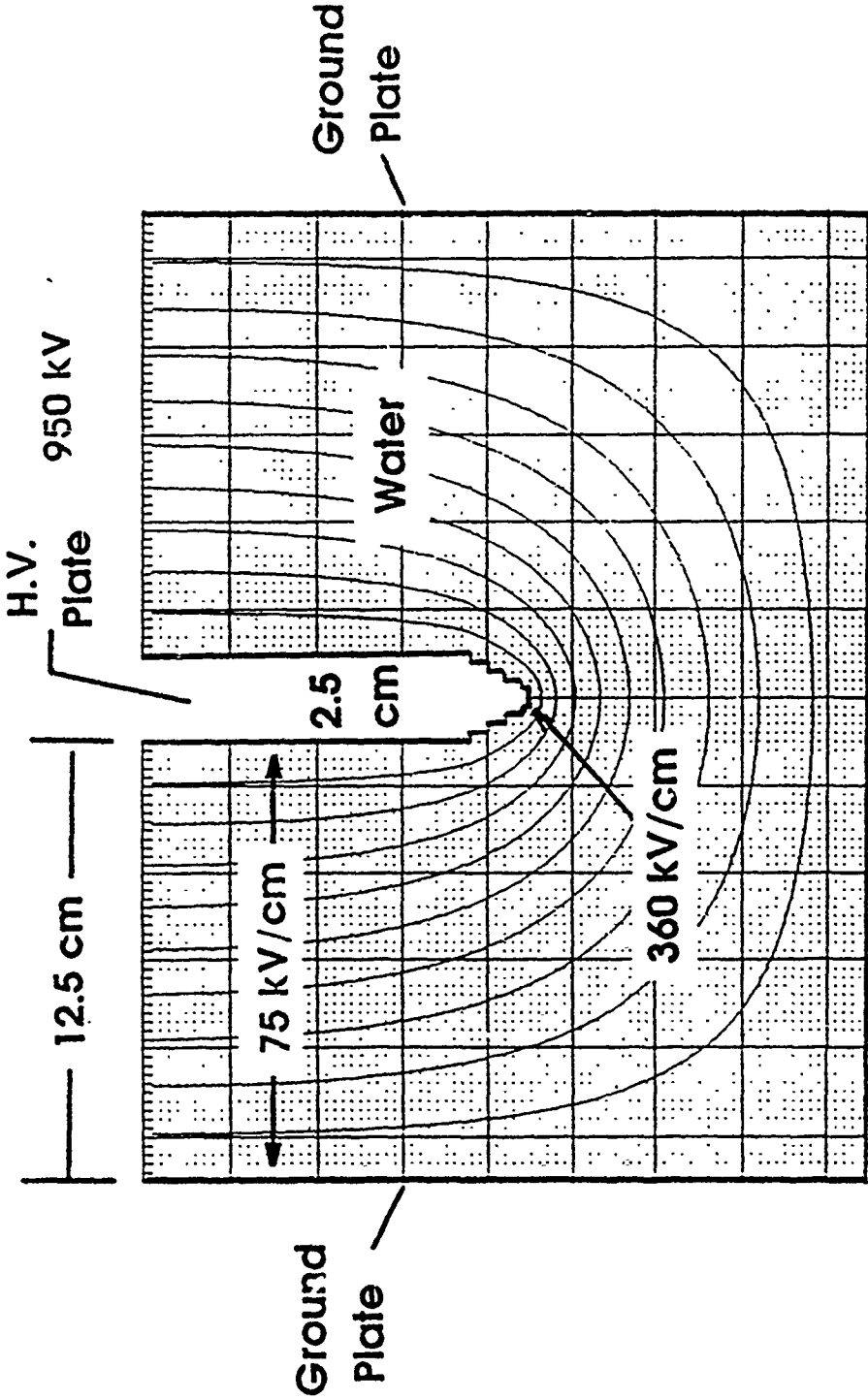
Parallel plate capacitor
(Efficient)



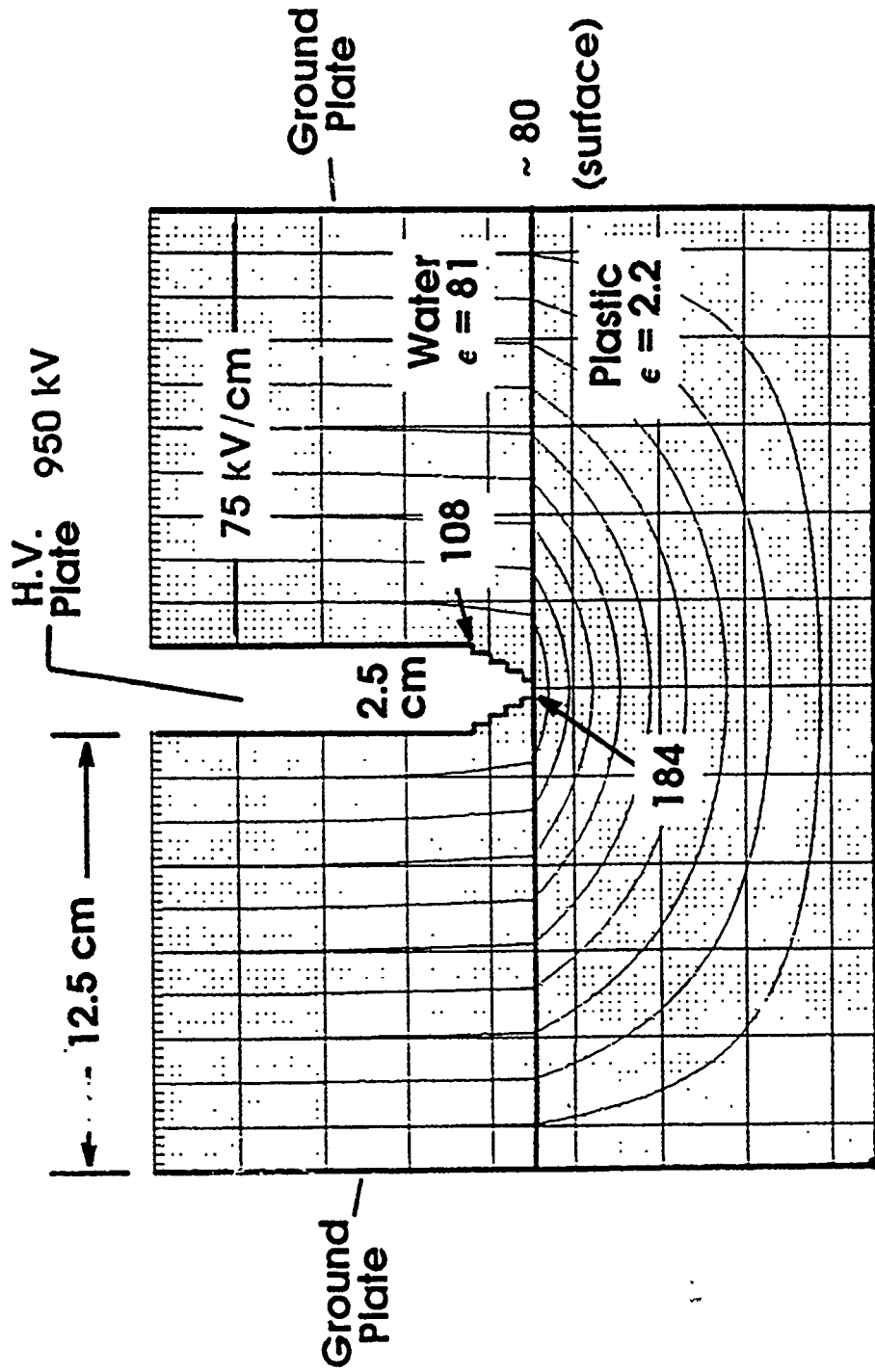
**BIG PROBLEM:
WHAT ABOUT THE EDGES?**

(4)

Fundamental problem is field enhancement at the edges of the plates

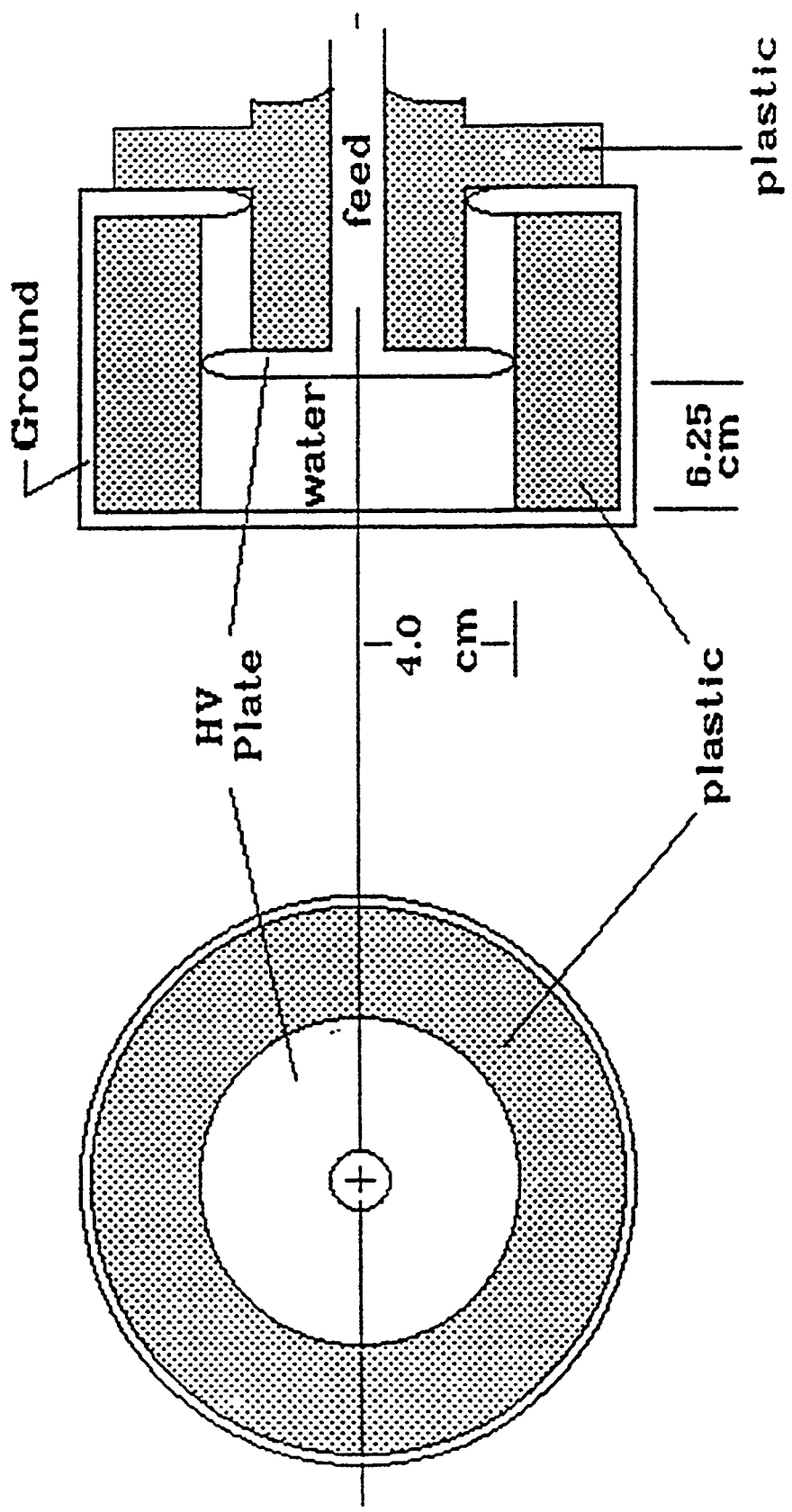


Plastic Field Attractor (PFA) reduces field enhancement in water

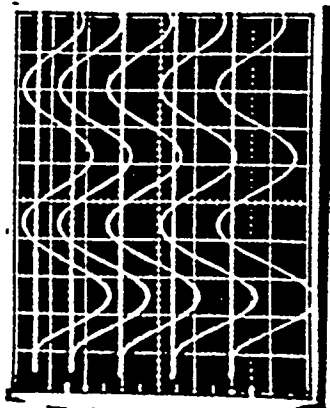


(6)

PFA Concept has been tested with a half-scale module



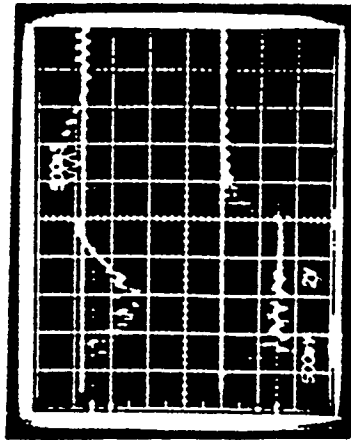
Module results predict good electrical performance



635 kV
 ~ 100 shots
 No breakdown

All data:
 $\tau_{\text{eff}} = 1.2 \mu\text{sec}$

1 $\mu\text{sec/div}$



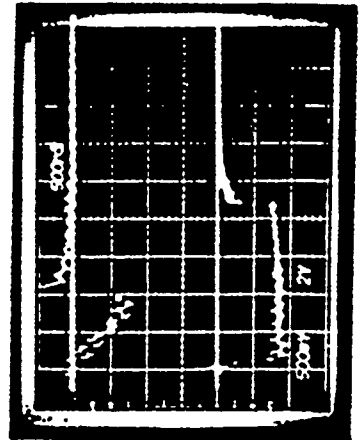
892 kV
 No breakdown

Predicted performance:

$$V = 892 \times (648/10^6)^{.058} \times 2 = 1165 \text{ kV}$$

└─ module voltage
└─ area scaling
└─ half scale

.5 $\mu\text{sec/div}$



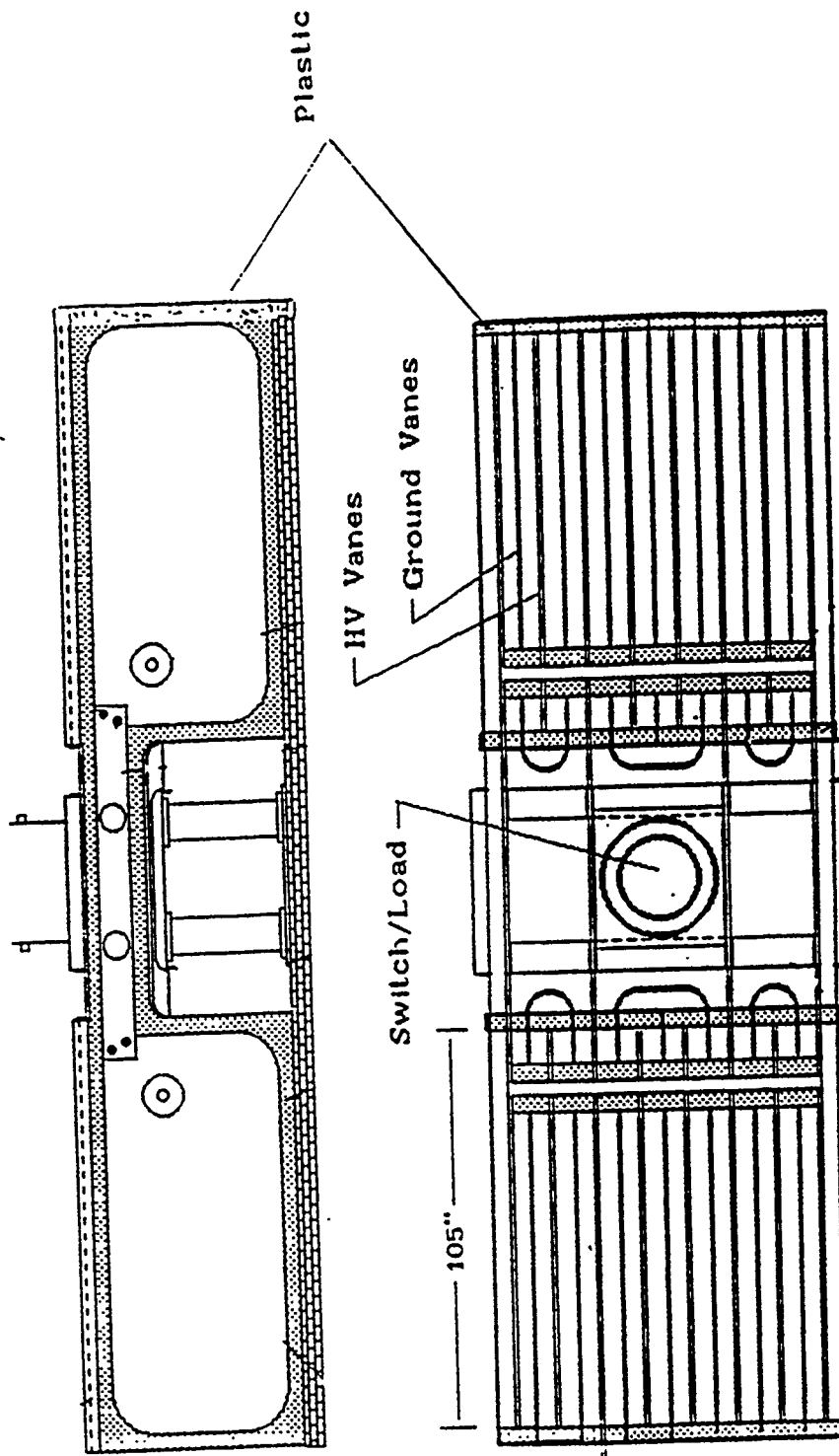
1040 kV
 50% breakdown

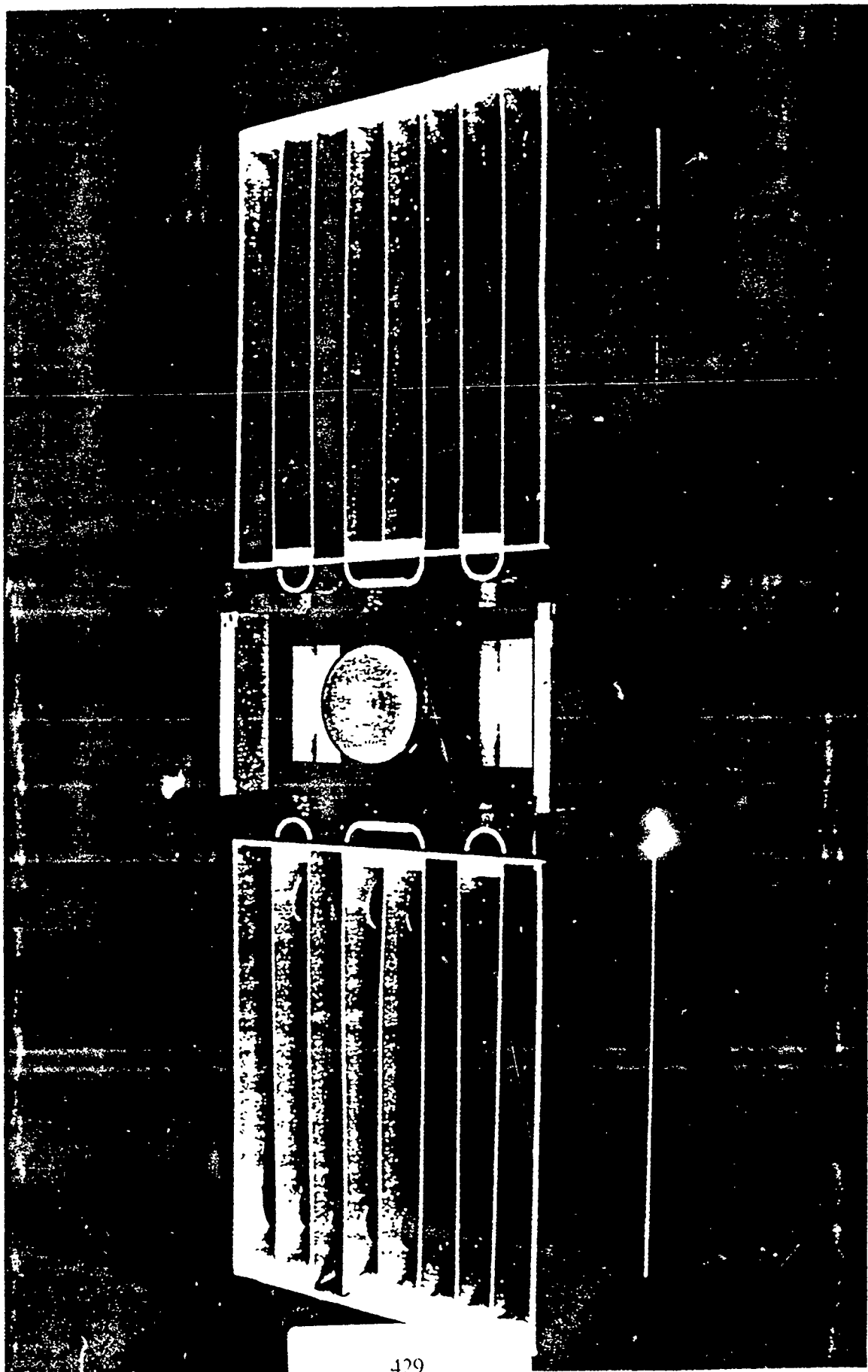
Require 1000 kV (86% of max)

.5 $\mu\text{sec/div}$

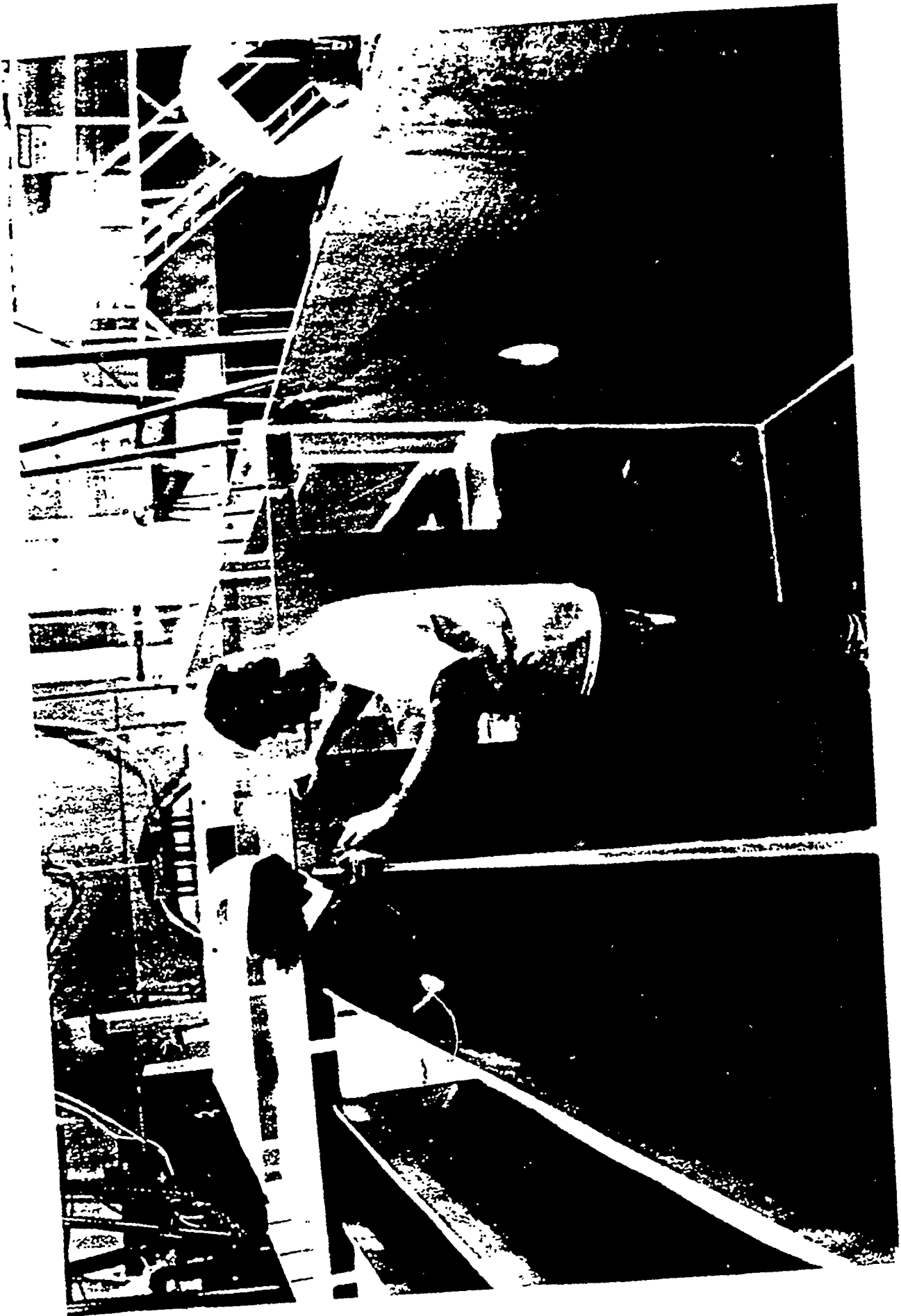
(2)

ZFX, A 1 MV, .58 μ F PARALLEL PLATE WATER CAPACITOR





(9)

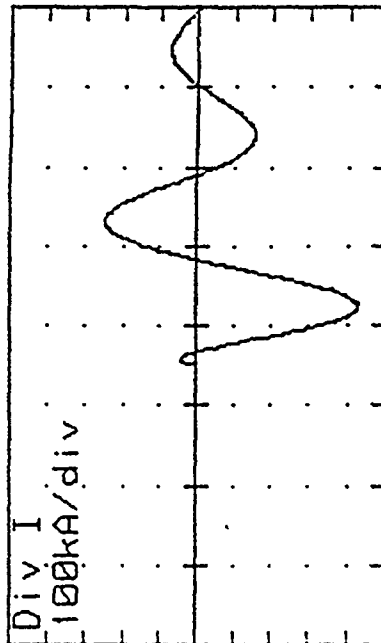
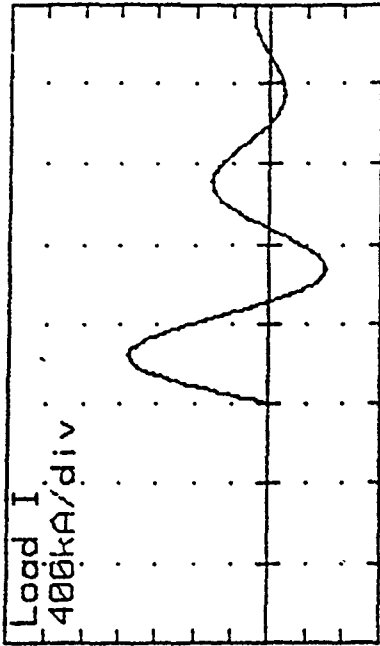
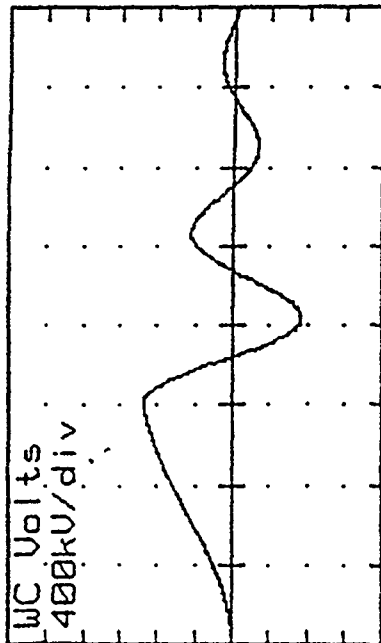


11



(16)

PERFORMANCE OF ZFX shows 1.5 MA at 600 nsec



PULSE RISE - 3500 NS
 MAIN SW - 3000 NS

TIME: 1000 ns/div

WC Volts	:	Max V	=	946.31	kV	at	T =	3030	ns
(at Node 6)	:	Min V	=	-740.02	kV	at	T =	4090	ns
Load I	:	Max I	=	1.51	MA	at	T =	3600	ns
(at Node 12)	:	Min I	=	-605.39	KA	at	T =	4660	ns
Div I	:	Max I	=	251.97	KA	at	T =	5290	ns
(at Node 14)	:	Min I	=	-426.41	KA	at	T =	4230	ns

Calculations show ZFX should operate well within the limits of electrical breakdown

$$E_{ave} = 75 \text{ kV/cm}$$

$$E_{+br} = 230 / \tau_{eff}^{1/3} A^{.058} \text{ [kV/cm]}$$

$$= 100 / \tau_{eff}^{1/3} \text{ [kV/cm]} @ 10^6 \text{ cm}^2$$

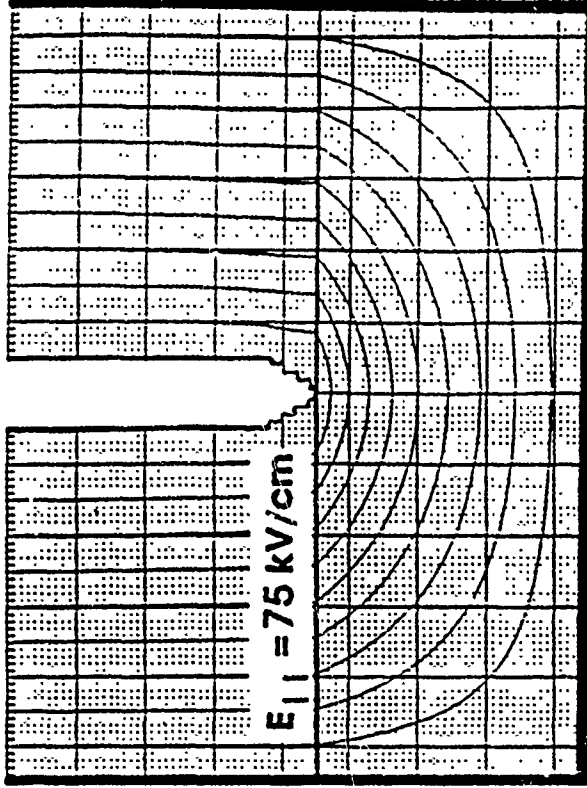
CASE	τ_{eff}	E_{+br}	$75/E_{+}$
Normal Switch & Diverfor	$1.45 + (.75 \times .2) = 1.60$	87 kV/cm	86%
Diverfor only	2.02	79 kV/cm	95%
Switch only	$2.03 + (.75 \times 1.00) = 2.780$	71.3 kV/cm	105%
Nothing fires	5.90 (two cycles)	55 kV/cm	135%

Stress on water/plastic interface also below breakdown

From I.D. Smith, MBS device ran successfully with

$$E_{II} = 165 \text{ kV/cm @ } \tau = 0.3 \text{ } \mu\text{sec}$$

I.D. Smith also suggests $\tau^{.33}$ scaling

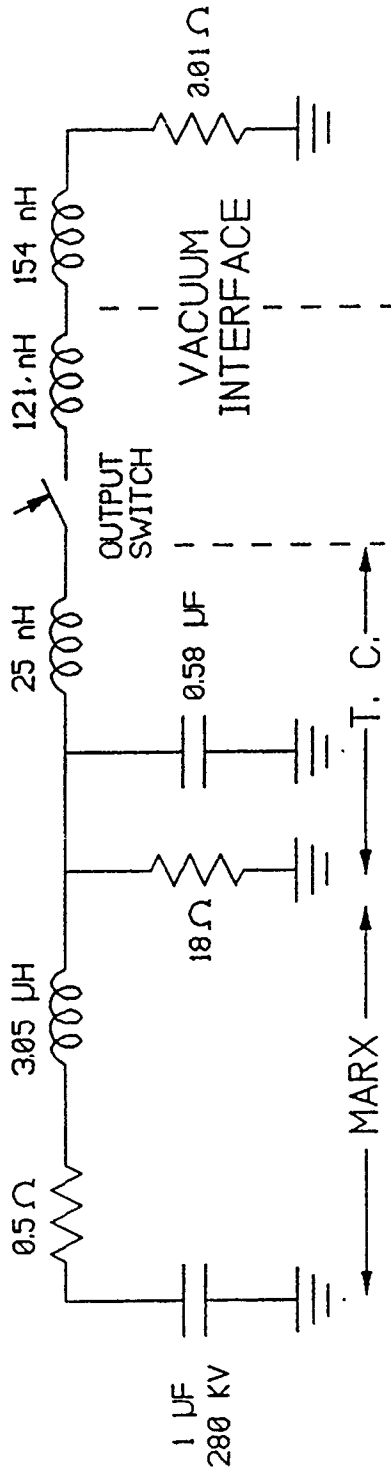


I	Normal switch and diverter	$\tau = 1.6 \text{ } \mu\text{sec}$	80%
II	Diverter, no switch:	$\tau = 2 \text{ } \mu\text{sec}$	85%
III	Switch, no diverter	$\tau = 2.8 \text{ } \mu\text{sec}$	96%
IV	No switch or diverter	$\tau = 5.9 \text{ } \mu\text{sec}$	122%

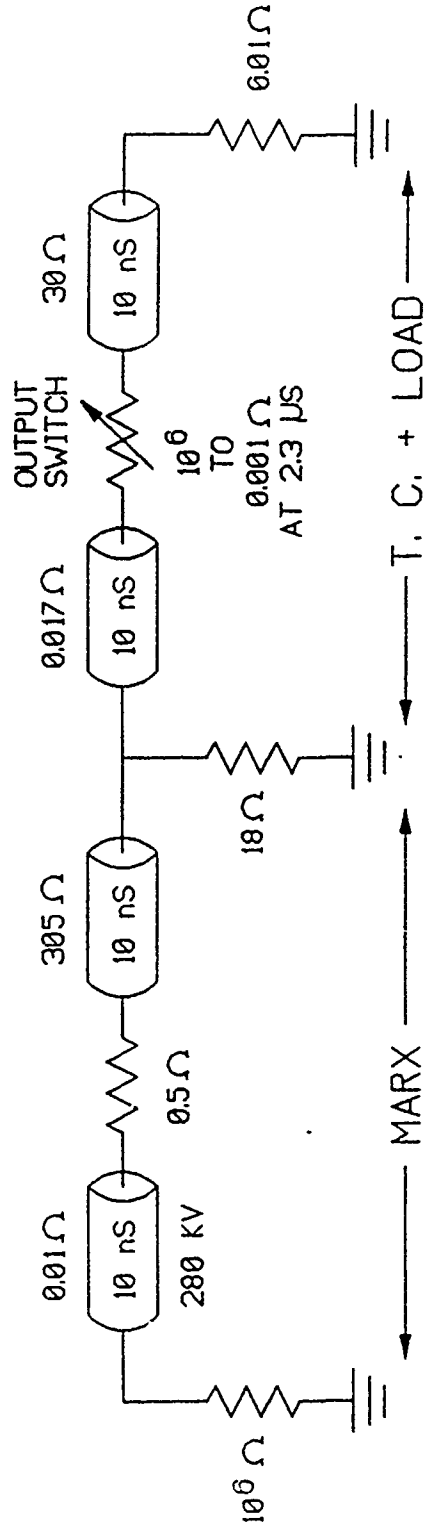
Since the MBS device worked successfully, it is safe to assume that we are well below breakdown

ZFX EQUIVALENT CIRCUIT

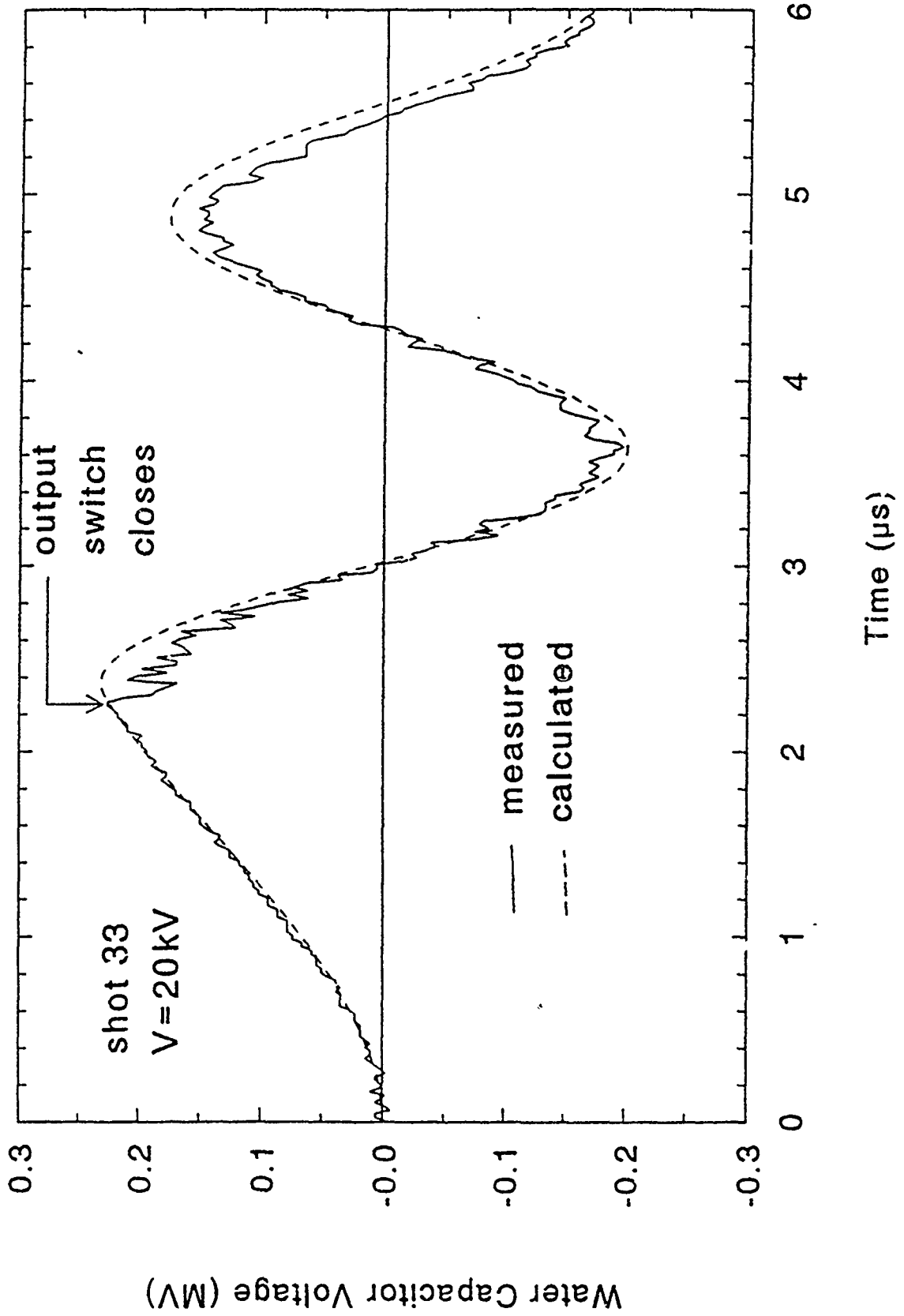
FOR S.C. SHOT 33



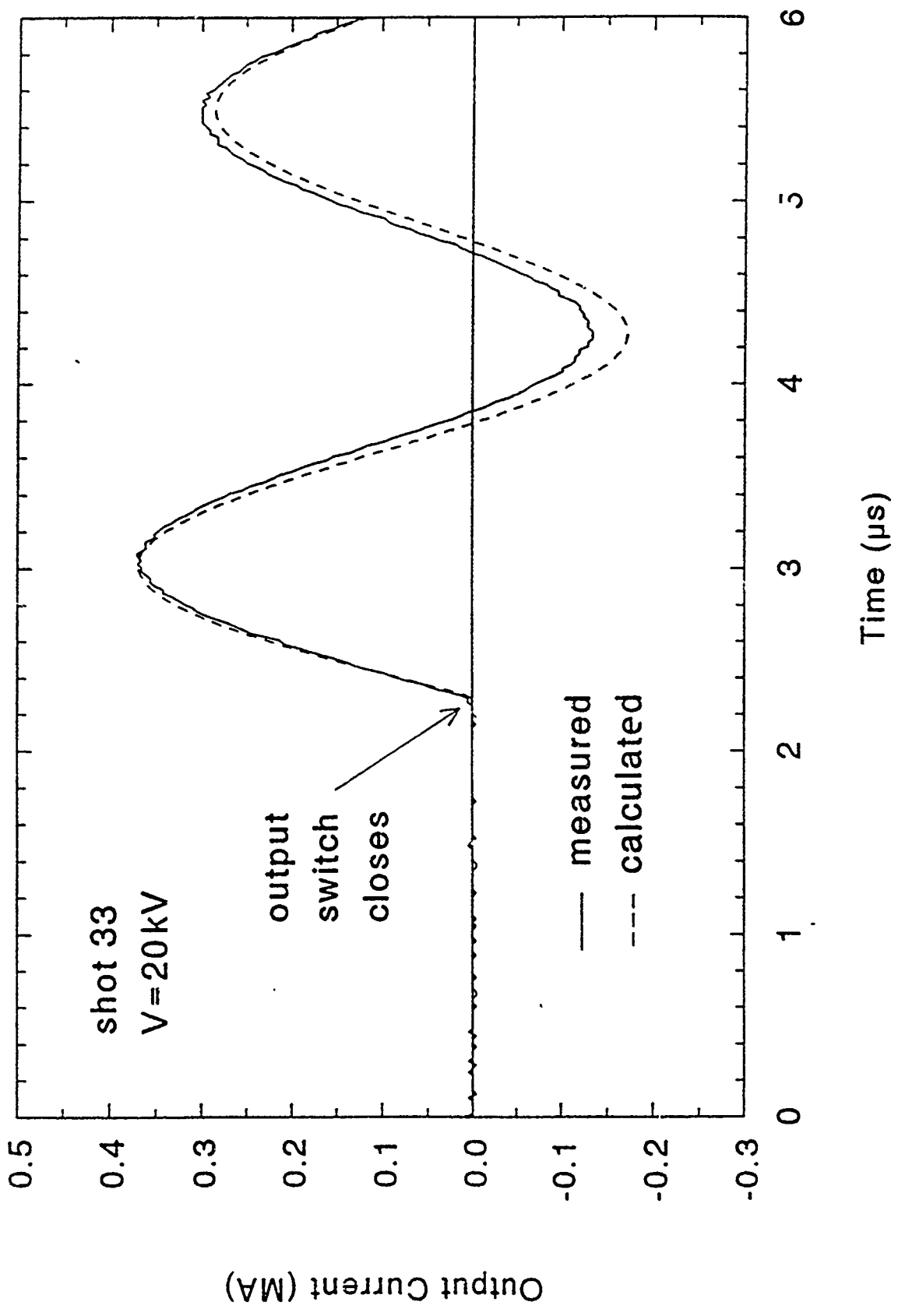
EQUIVALENT TRANSMISSION LINE CIRCUIT



CALCULATED AND MEASURED ZFX WATER CAPACITOR VOLTAGE AGREE

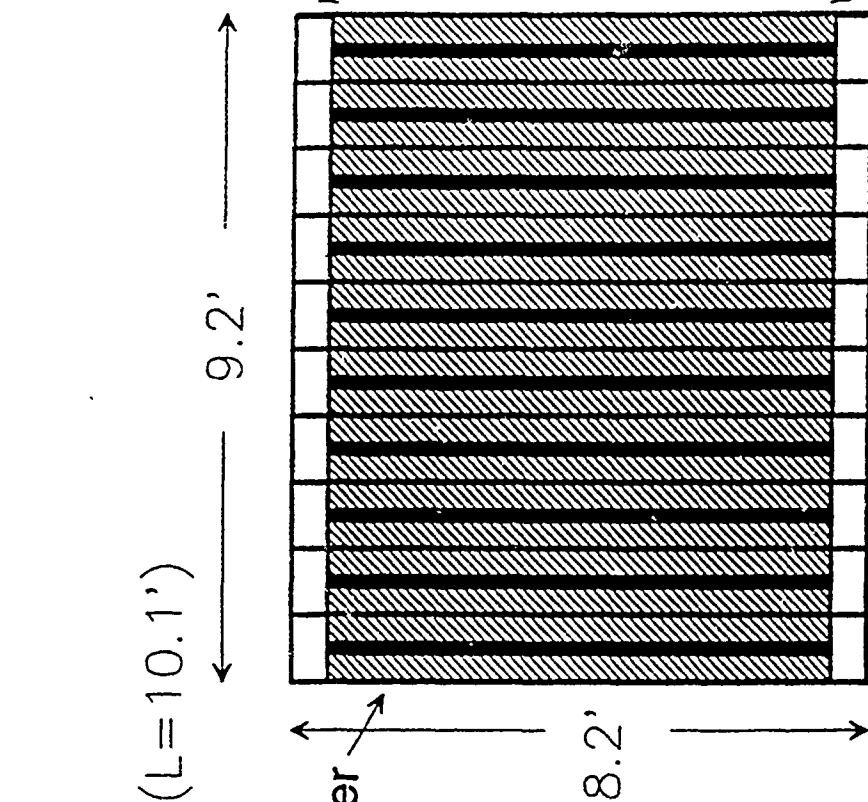
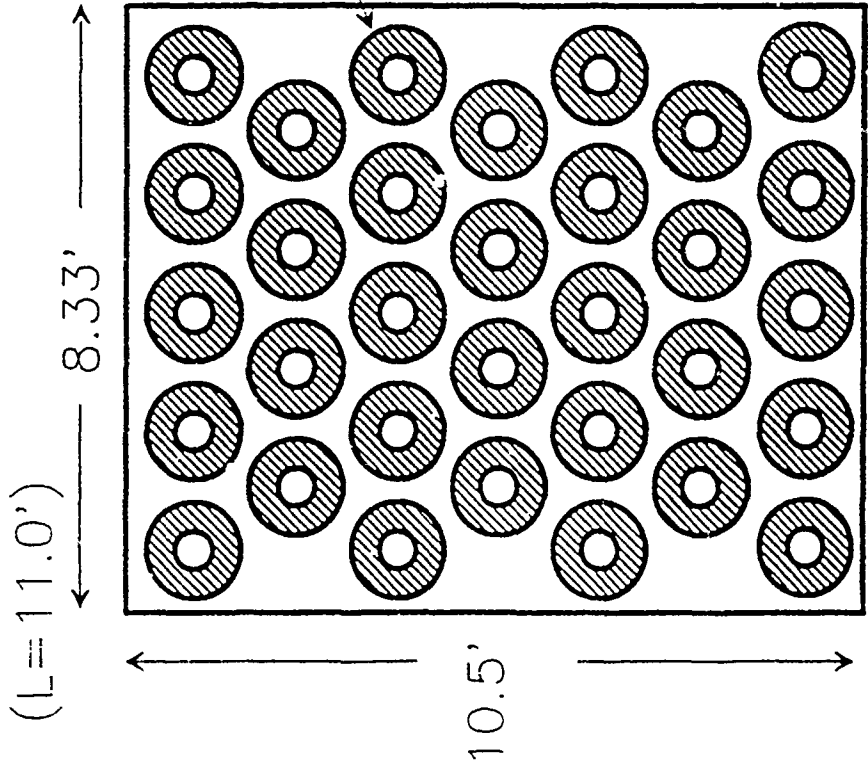


CALCULATED AND MEASURED ZFX
OUTPUT CURRENT AGREE



(18)

MULTIPLE COAX LINES and PARALLEL PLATES - TWO DESIGN OPTIONS for WATER CAPACITORS



Vol=962 ft³

Vol=761 ft³

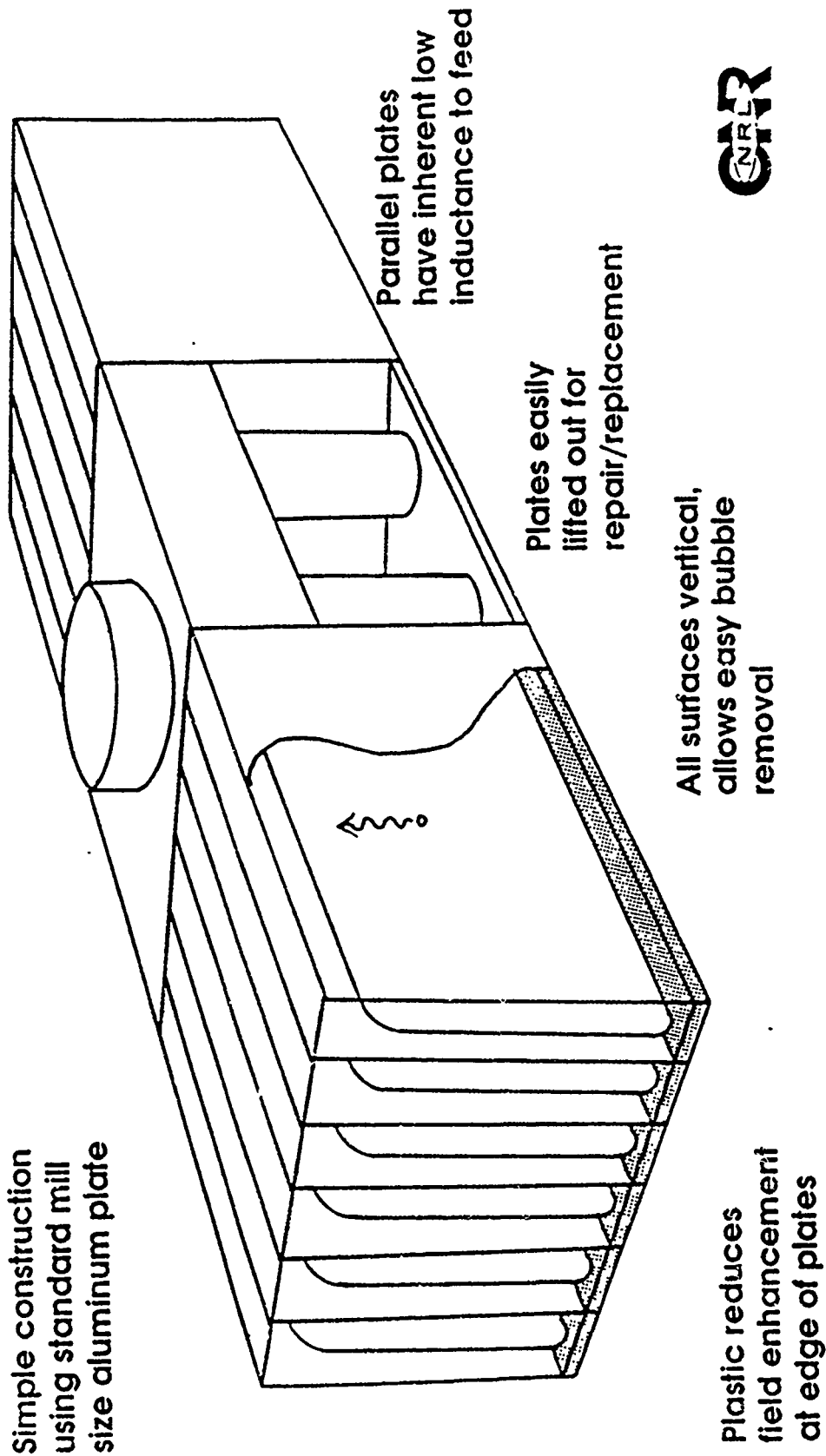
Teff=0.55 μs

C=0.375 μF

V=1.2 MV

E=270 kJ

The ZFX Parallel Plate Water Capacitor could be a compact, relatively inexpensive, easy to operate/maintain alternative for an intermediate store



INVESTIGATION OF PLASMA OPENING SWITCH CONDUCTION AND OPENING MECHANISMS

B.V. Weber, R.J. Commisso, P.J. Goodrich,* J.M. Grossmann,
D.D. Hinshelwood,* J.C. Kellogg, and P.F. Ottinger

Plasma Physics Division, Naval Research Laboratory, Washington, DC 20375-5000 USA

Abstract: Plasma opening switch techniques have been developed for pulsed power applications to exploit the advantages of electrical energy storage in a vacuum inductor compared to conventional, capacitive-based energy storage. Experiments are described that demonstrate the successful application of these techniques in conduction time ranges from 50 ns to over 1 μ s. Physics understanding of the conduction and opening mechanisms is far from complete; however, many insights have been gained from experiments and theory. Measurements of current distribution, plasma density and ion emission indicate that conduction and opening mechanisms differ for 50 ns and 1 μ s conduction times. For the 50 ns conduction time case, switching begins at the bipolar emission limit and opening is by erosion. In the 1 μ s conduction time case, limited hydrodynamic plasma displacement implies far higher plasma density than is required by the bipolar emission limit. Magnetic pressure is required to augment erosion to generate the switch gap inferred from experiments.

applications require ever-increasing power levels from the generators, which eventually may be limited by size, cost, and physics constraints.[1] New approaches are being sought that will enable power levels in excess of that possible from present generators, which are based on capacitive energy storage and water-filled transmission lines. One technique that might overcome these constraints is the use of a plasma opening switch (POS) to exploit the advantages of inductive energy storage (higher energy density in vacuum compared with the electrical energy density stored in a liquid-dielectric capacitor).

The POS technique has been successfully used at many laboratories.[2] Two different objectives can be identified: 1) to compress the power pulse of a conventional generator, and 2) use the POS as the primary switch in an inductive generator. An important example of the use of a POS on a conventional generator for pulse compression is PBFA II at Sandia National Laboratories, where an injected plasma conducts the generator current as it rises to 5 MA in 50 ns, then opens, delivering an 11 MV, 30 TW pulse to a diode load.[3] This technique will allow the production of a higher power, faster pulse than could be achieved without the POS. Newer, "inductive" generators use a POS to conduct current during the time required to transfer energy from a high current Marx bank to an inductor, usually about 1 μ s. This allows the use of lower voltage capacitor banks and eliminates the need for large, water filled transmission lines. If the opening switch performance is ideal, generators could be developed with output powers exceeding capacitive systems. At present, results are promising but far from ideal. An impressive

Inductive Pulsed Power Using Plasma Opening Switches

Pulsed power generators are used to produce intense electron and ion beams, and to drive high current through plasmas for several applications, including: inertial confinement fusion research, magnetic fusion research, and high-power radiation production, from microwaves to gamma rays. These

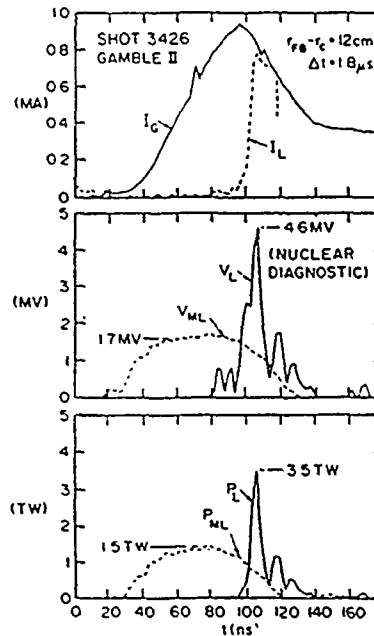
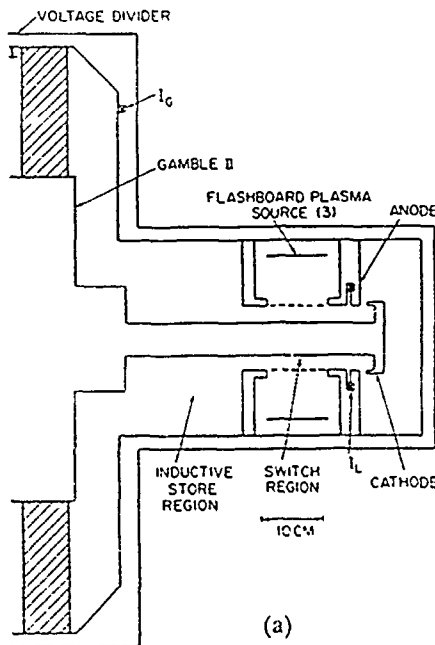


Fig. 1 (a) Gamble 2 POS experiment (b) measured load current, voltage and power (I_L , V_L , P_L), and ideal matched load voltage and power (V_{ML} , P_{ML})

example of the application of the $1 \mu\text{s}$ conduction time POS is the GIT-4 generator at the Institute of High Current Electronics. Power pulses over 3 TW have been generated after conducting up to 2 MA in $1 \mu\text{s}$. [4]

Experiments have been performed at the Naval Research Laboratory (NRL) on smaller generators in both the 50 ns and $1 \mu\text{s}$ conduction time ranges. These NRL experiments will be used to illustrate several properties of the POS. One example [5] of the 50 ns conduction time POS on a high power conventional generator is shown in Fig. 1. A POS configuration using three flashboards [6] on Gamble 2 at NRL is diagrammed in Fig. 1a. Experimental results are shown in Fig. 1b. On this shot, the PEOS conducts the generator current, I_G , for 60 ns as it rises to 900 kA. Rapid switching then occurs, resulting in a peak load voltage of $V_L = 4.6 \text{ MV}$. The peak load power, $P_L = 3.5 \text{ TW}$, is higher than the ideal matched load value, $P_{ML} = 1.5 \text{ TW}$, by a factor of 2.3. This power amplification is the result of the voltage multiplication over the matched load value, $V_{ML} = 1.7 \text{ MV}$, and the relatively high load current, $I_L = 750 \text{ kA}$, compared to the matched load value, $I_{ML} = V_{ML}/2\Omega = 850 \text{ kA}$.

An example [7] of the $1 \mu\text{s}$ conduction time POS is shown in Fig. 2. The "Hawk" generator at NRL uses a fast, high-current Marx bank to drive a POS. The POS configuration using 18 flashboards is shown in Fig. 2a. Data from a high power shot are shown in Fig. 2b. The generator current is conducted by the injected plasma during its rise to 650 kA in $1 \mu\text{s}$. Most of this current is rapidly switched into the diode load, generating a load voltage of 750 kV and 0.37 TW peak power.

The examples in Figs. 1 and 2 illustrate a fundamental difference between 50-ns and $1 \mu\text{s}$ conduction time POS results. The energy stored in the Marx bank (200 kJ) and the energy dissipated in the load (40 kJ) are about the same for both cases. The power obtained in the short conduction time case is about 10 times higher, and the pulse width ten times smaller, than for the long conduction time case. This is equivalent to the notion that the switch opening time is proportional to the conduction time, and that the switch resistance after opening is correspond-

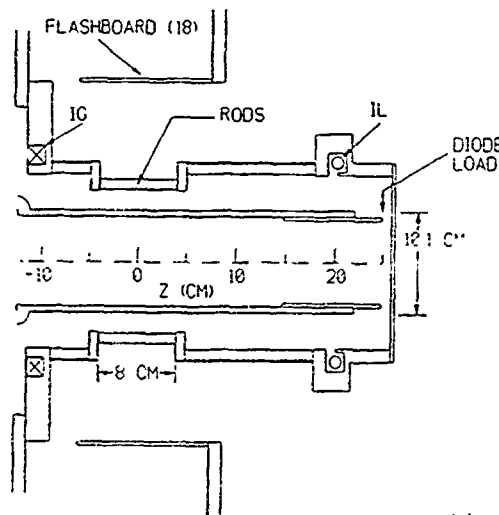
ingly higher in the short conduction time case. It may be possible to understand the difference in basic physics in these different conduction time ranges. This is especially important in order to exploit the POS for higher power generation in the $1 \mu\text{s}$ conduction time range.

Descriptions of Conduction and Opening Mechanisms

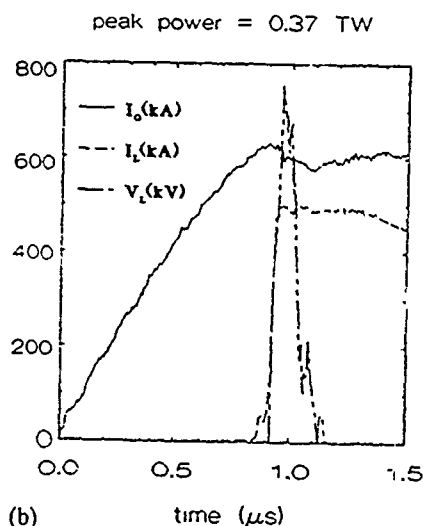
In this section, conduction and opening mechanisms are described in an intuitive way for later interpretation of experimental results. The initial plasma conditions are not well known for most POS experiments, but a reasonable starting point is shown schematically in Fig. 3. The plasma is injected into the switch region from outside of the outer conductor. The plasma flows with supersonic velocity ($\sim 10 \text{ cm}/\mu\text{s}$) through apertures in the outer conductor (anode) toward the center conductor (cathode), bridging the gap before the generator is fired. The ion species is primarily C^{++} . The plasma will conduct current as a short circuit and then "open" (i.e., current will suddenly increase into a downstream load). In the high power experiments under consideration, it is assumed that the cathode (or cathode plasma) becomes a space-charge-limited emitter and the anode becomes an electron collector. Plasma ions are collected at the cathode and ions can be injected into the switch region through the anode.

Conduction is primarily by emitted electrons passing through the background plasma. The electron orbits can be influenced by electric and magnetic fields in the plasma and by plasma turbulence (anomalous collisions). (The problem of detailed interactions between conduction electrons and the plasma is beyond the scope of this paper, but is an active area of research with fluid and PIC codes. [8]) Assuming bipolar conduction across a stable gap, the emitted electron current density is orders-of-magnitude higher than the ion current density,

$$\frac{J_e}{J_i} = \sqrt{\frac{M_i}{Z m_e}} \approx 105 \text{ for } \text{C}^{++} \quad (1)$$



(a)



(b)

Fig. 2 (a) Hawk POS experiment (b) generator (I_G) and load (I_L) current and voltage (V_L)

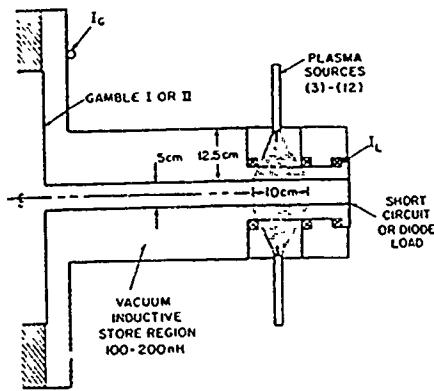


Fig. 3 Coaxial POS geometry and plasma injection region

where J_i (J_e) is the ion (electron) current density, M_i (m_e) is the ion (electron) mass, and Z is the ion charge state. The maximum current density that can be conducted in this way is limited by the maximum ion current density, $J_i \leq n_i Z e v$, where n_i is the ion density and v is the maximum ion collection rate at the cathode. This bipolar current density limit is

$$J_{BP} = J_e = \sqrt{\frac{M_i}{Z m_e}} n_e e v \gg J_i \quad (2)$$

where n_e is the electron density, and quasineutrality is assumed. Bipolar conduction is illustrated in Fig. 4a.

Magnetic forces may displace or distort the plasma during conduction, as shown in Fig. 4b. The azimuthal field on the generator side of the POS is unbalanced on the load side during conduction (the load current is zero). This results in an axial displacement of the plasma toward the load. The plasma center-of-mass displacement in the axial direction of a thin cylinder at radius r and length l_0 is independent of the actual current and mass distributions in the plasma and is given by

$$\Delta z = \frac{\mu_0 Z}{8 \pi^2 r^2 l_0 M_i n_e} \iint I^2 dt^2 \quad (3)$$

where $\mu_0 = 4\pi \times 10^{-7}$ H/m. This bulk plasma displacement is useful for estimation purposes, but does not indicate the plasma distribution after displacement. This axial plasma motion is associated with radial current in the plasma. Radial motion can occur if the plasma conducts current in the axial direction. Estimating the radial displacement requires knowledge of the current and plasma mass distributions. In POS experiments, switching could be induced by these magnetic forces at current levels far less than the bipolar value in Eq. (2). The competition between hydrodynamic processes and emission processes will be discussed in the following section.

The POS is "open" when the current flows in a downstream load, or when the switch resistance increases to a high value compared with the resistance during conduction (essentially zero). For the high power levels involved here, it is imagined that a magnetically insulated gap forms near the cathode, preventing electron conduction between the switch electrodes, as shown in Fig. 5. This occurs when the gap size is roughly equal to the electron gyroradius. This condition leads to

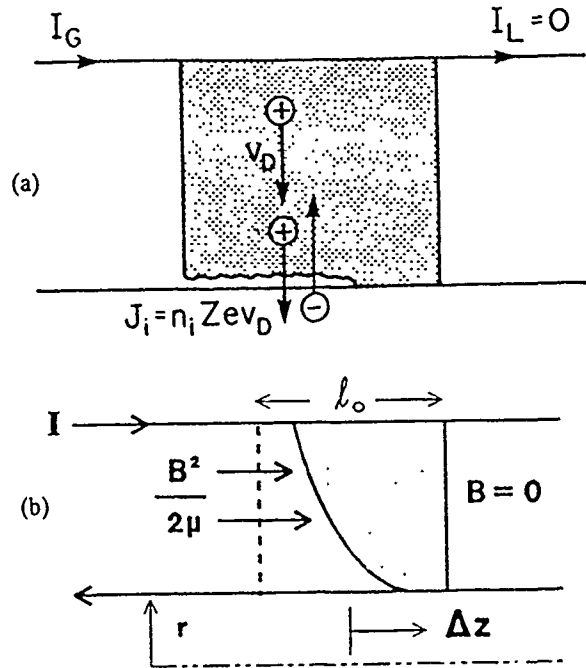


Fig. 4 Conduction physics: (a) bipolar, space-charge-limited emission, (b) axial plasma displacement by magnetic pressure

the familiar "critical current" formula,

$$I_c = \frac{2\pi m_e c}{e \mu_0} (\gamma^2 - 1)^{1/2} \frac{r}{D} = 8500 (\gamma^2 - 1)^{1/2} \frac{r}{D} \text{ Amps} \quad (4)$$

where r is the cathode radius, D is the gap size, and the relativistic factor, γ , is related to the voltage across the gap, V , by

$$\gamma = 1 + 2 V(\text{MV}) \quad (5)$$

The ability of the switch to open effectively is equivalent to its ability to generate a large enough gap. This is the critical issue of POS physics. Understanding the gap opening mechanism and how conduction and opening are related are subjects of research. Here, two possible opening mechanisms, erosion and magnetic pressure, will be discussed.

Erosion opening begins when the influx of ion current is insufficient to maintain a steady gap. The bipolar current

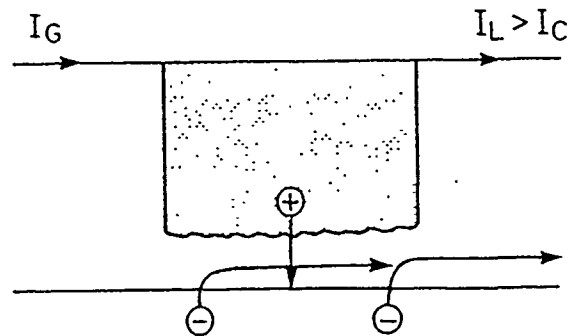


Fig. 5 Magnetic insulation gap near the cathode

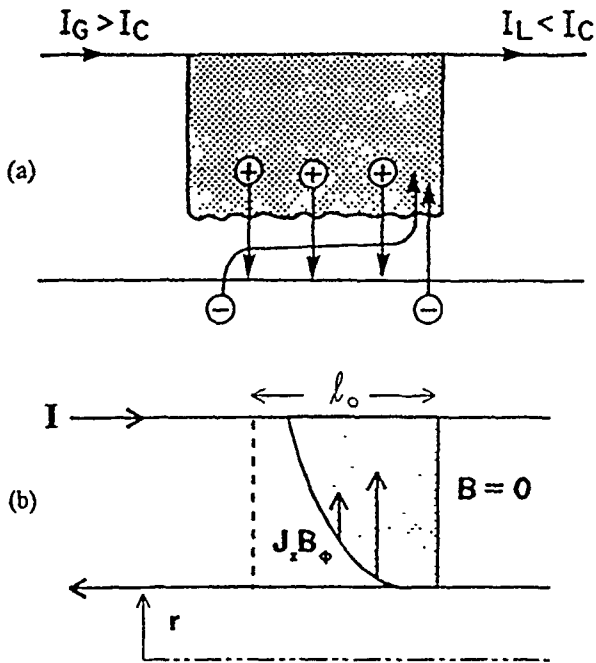


Fig. 6 Opening mechanisms: (a) erosion (b) magnetic pressure

density limit [Eq. (2)], multiplied by the emission area gives this conduction current limit:

$$I_{BP} = 2 \pi r l J_{BP} \quad (6)$$

where $l \leq l_0$ is the length of the emitting area on the cathode. If the current exceeds this value, the gap may grow by the erosion mechanism illustrated in Fig. 6a, where ions are removed from the plasma surface faster than they are replaced. The gap opening rate is

$$\frac{dD}{dt} = \frac{J_i}{n_i Z e} = v \quad (7)$$

"Enhanced erosion" occurs when the magnetic field increases the electron life time in the gap, greatly increasing the ion current fraction as in an ion diode. The opening rate in Eq. 7 can be very fast in this case.[9] Another opening mechanism candidate is magnetic pressure pushing the switch gap open. Radial displacement of the plasma is related to axial plasma current

$$\frac{d}{dt} \left(\rho \frac{dD}{dt} \right) = J_z B_\phi \quad (8)$$

where ρ is the mass density and B_ϕ is the azimuthal magnetic field. This opening mechanism is illustrated in Fig. 6b.

For a given switch configuration, the size of the gap generated in the POS limits the power that can be delivered to a load, assuming the magnetic insulation requirement of Eq. (4). The maximum load current, I_{max} , is determined by the generator (and storage inductance). This maximum current, and the gap size, determine the maximum voltage, V_{max} [Eqs. (4) and (5)], possible to maintain insulation. This maximum voltage is obtained when the load impedance is V_{max}/I_{max} . For the usual case of a pinch beam diode load at critical current, this impedance corresponds to equal D/l ratios for the load and

POS. For higher load impedance, the insulation requirement is violated, and current loss in the switch occurs. (The load may also have an effect on the gap obtained through feedback between switch and load.) These basic POS concepts will be used in the interpretation of experimental results of the following section.

Experimental Measurements and Comparison With Theory

Several experimental results are presented in this section that characterize POS operation. Magnetic field probe measurements in the plasma during shots show the evolution of the current distribution and can be used to estimate plasma motion. Plasma density is measured using the plasma sources only, without firing the generator, to determine the dependence of POS operation on the initial density. Biased charge collectors inside the center conductor are used to measure the ion current density distribution to evaluate opening processes. Measurements are presented for short and long conduction times to demonstrate the relative importance of the conduction and opening mechanisms described above.

Current Distribution Measurements

The azimuthal magnetic field is measured in the plasma cross section by inserting small pickup loops into the switch region. The integral of the signal is proportional to the current flowing through the circle with radius equal to the probe radial location, assuming axisymmetry. The probes are calibrated on shots with no plasma injection, normalizing the probe signals to the measured current.

An example of a current distribution measurement in Gamble 1 is shown in Fig. 7. The plasma injection region is 10 cm in axial length ($z = 2-12$ cm in Fig. 7). The center conductor radius is 2.5 cm, the outer conductor radius is 5 cm. The Gamble 1 current rises to 200 kA in 50 ns, as indicated by the current at $z = 0$. The (short circuit) load current ($z = 21$ cm) is zero for $t \leq 40$ ns, and rises quickly at about $t = 50$ ns. The probes in the plasma, ≈ 1 cm from the center conductor, indicate the current distribution evolving with time. The current flows in a wide channel, about 6 cm at $t = 40$ ns, which is 30 times wider than the collisionless skin depth ($c/\omega_{pe} = 0.1$ cm for

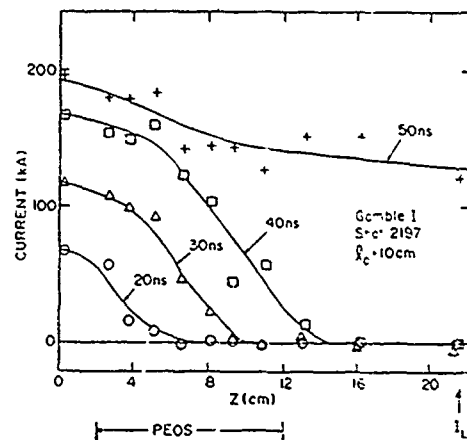


Fig. 7 Current distribution in Gamble 1 POS experiment

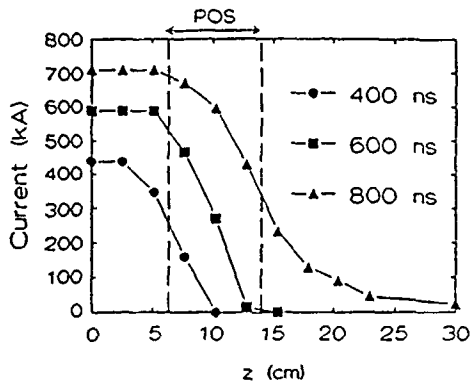
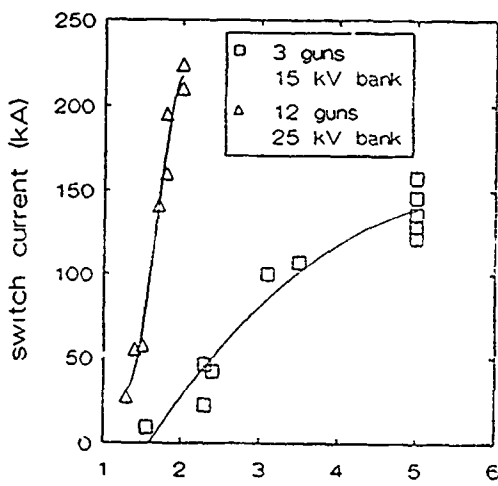


Fig. 8 Current distribution in Hawk POS experiment

$n_e = 2.5 \times 10^{13} \text{ cm}^{-3}$). Opening occurs by current interruption in the plasma injection region instead of by current convection to the load. This can be interpreted to mean that the axial plasma displacement is small. Other measurements[10] at different radial locations indicate that the plasma current is predominately radial and that the current is interrupted in the vicinity of the cathode (center conductor).

Similar measurements[11] are shown in Fig. 8 for a long ($1 \mu\text{s}$) conduction time experiment on Hawk. In this case, the center conductor radius is 5.5 cm, the outer conductor radius is 9 cm, the injection region is 8 cm long and the short circuit load is located at $z = 3^{\circ}$ cm. The Hawk current rises to 700 kA in 800 ns, as indicated by the current at $z = 0$. Switching begins at 800 ns. These data are qualitatively similar to the Gamble 1 case, except on a far longer time scale. Current is conducted through a wide channel that penetrates the plasma length during the conduction period. When switching begins, the current is still located in the plasma injection region with little displacement toward the load, implying that the plasma is localized in this region also. (The small current levels indicated between the injection region and the load are probably the result of low density plasma injected into this region by the plasma sources instead of current convection from the injection region toward the load.) These two examples illustrate a basic similarity between short and long conduction POS operation:



(a) time delay (μs)

the current penetrates the plasma, the current channel is broad, opening begins when the current reaches the load end of the injection region, and the plasma center-of-mass translation is limited to about half the injection length.

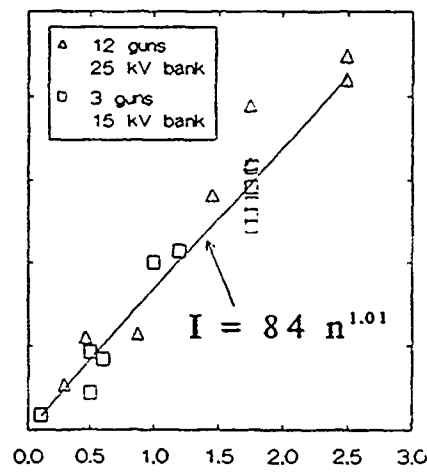
Plasma Density Measurements

In Gamble 1 POS experiments the conduction current is proportional to the initial density. The plasma density is varied by changing the number of sources, the voltage on the capacitor bank driving the sources, and the time delay before the start of the generator current. Peak switch current is plotted vs. time delay in Fig. 9a for two different plasma sources, 3 guns at 15 kV and 12 guns at 25 kV. The conduction current is higher for the high density plasma source (12 guns). The average electron density was measured for these sources in the actual experimental configuration, but without firing the generator, using a 140 GHz microwave interferometer. The switch current is plotted against the initial electron density in Fig. 9b. The switch current is directly proportional to the initial density, with data from both sources collapsing to the same fitting curve. Measurements[12] of the initial density in the Magnetically Injected Plasma (MIP) configuration[13] used on PBFA II indicate a similar trend, as shown in Figs. 10a and 10b. In this experiment, the switch current depends on the timing and on the magnetic field strength used to direct the plasma into the switch region. When plotted against density, (Fig. 10b), the data points fall on a straight line that intercepts the y-axis near the origin.

The Gamble 1 and PBFA II experiments differ in current magnitude, plasma injection scheme and conduction area, however, the average current density, $J = I/(2\pi r_0^2)$, at switching is proportional to the density, with about the same proportionality constant. These results may be generalized for all short conduction time experiments by [7]

$$J \text{ (kA/cm}^2\text{)} \approx 0.6 \times n_e \text{ (} 10^{13} \text{ cm}^{-3}\text{)} \quad (9)$$

This proportional dependence of J on n_e agrees with emission-limited conduction, Eq. (2), but is smaller by about a factor of 3,



(b) density (10^{13} cm^{-3})

Fig. 9 Gamble 1 conduction current vs. (a) time delay and (b) density, for different plasma sources

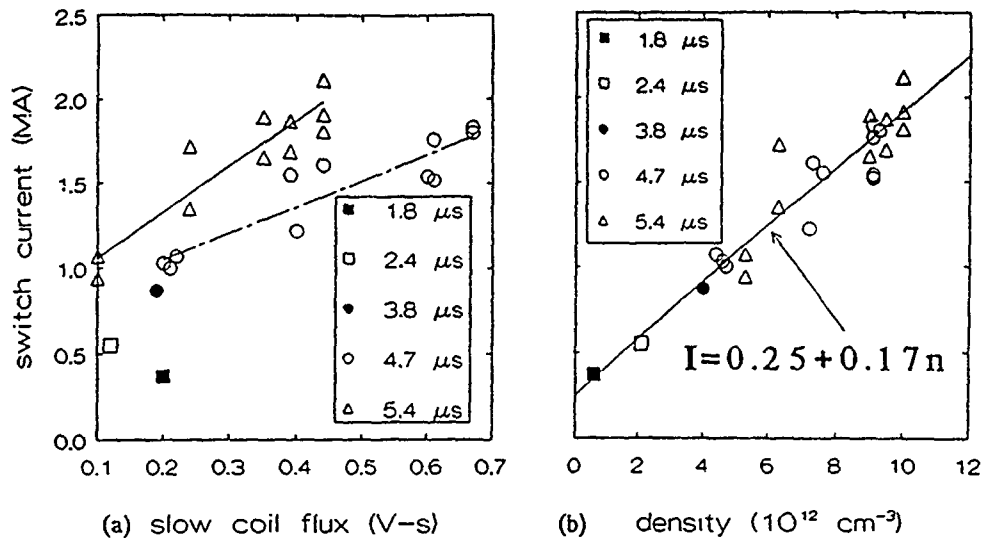


Fig. 10 MIP switch current for different plasma timings plotted against (a) slow field and (b) density

assuming C^{++} , $v = 10 \text{ cm}/\mu\text{s}$, and $l_0 = 10 \text{ cm}$. The limited emission length inferred from the current distribution measurements ($l \approx l_0/2$, Fig. 7) bring the bipolar limit and the empirical relation into closer agreement. This quantitative result supports the basic physics idea of emission-limited conduction.

The limited hydrodynamic displacement of the switch plasma during conduction makes the empirical scaling of Eq. (9) invalid for the $1 \mu\text{s}$ conduction time case. The center-of-mass displacement of Eq. (3) can be used to estimate the importance of hydrodynamics for these different conduction time regimes. For Gamble 1 and PBFA II, using measured densities, the plasma displacement during conduction is negligible, $\Delta z < 1 \text{ cm} \ll l_0$. Assuming Eq. (9) is also valid for Hawk, a density of $5 \times 10^{13} \text{ cm}^{-3}$ is predicted. Using this density in Eq. (3), the plasma displacement would be 400 cm, far higher than the estimated displacement based on magnetic probe measurements, that imply switching before the plasma displacement exceeds half of the switch length (about 4 cm from Fig 8). The limited plasma displacement during conduction indicates that the plasma density in Hawk is at least 100 times higher than predicted by Eq. (9), or $n_e \geq 5 \times 10^{15} \text{ cm}^{-3}$. Observations supporting this include the larger number of flashboards (18) required to conduct the Hawk current, compared to the number (3) used in Gamble 2 for similar conduction current, and density measurements with the microwave interferometer that indicate the density is $> 1 \times 10^{14} \text{ cm}^{-3}$ (the limit of the measurement). This argues that Eq. (9) does not apply to the $1 \mu\text{s}$ conduction time case, or to any situation where hydrodynamic displacement would be greater than half the switch length before reaching the bipolar limit. Setting $\Delta z = l_0/2$ in Eq. (3) defines a "hydro-limit" for conduction

$$J_{\text{hydro}}^2 \tau^2 = \frac{12 M_i n_e}{\mu_0 Z} \quad (10)$$

where τ is the conduction time and a linear current rise is assumed for simplicity. The conduction limits of Eqs. (9) and

(10) are compared in Fig. 11, for a given plasma density. The generator current density rises from the origin in this plot and intersects either J_{BP} or J_{hydro} , depending on the slope of $J(t)$.

Hydro-limited conduction, as described by Eq. (10), predicts scaling with density that is less than linear. For the case of $J(t) \propto t$, $J^2 t^2 \sim J^4 \Rightarrow J \propto n^{1/4}$. In the absence of a direct density measurement, this scaling is tested on Hawk by varying the average plasma density by changing the number of plasma sources. The density at opening is related to the time delay between the flashboard driver current and the load current. The average density is then proportional to the number of flashboards at a given time delay. Results of this experiment[7] are shown in Fig. 12, where peak switch current is plotted vs. time delay for shots using 3, 6, 9 or 18 flashboards. It is immediately evident that the scaling is less than linear. The data points in Fig. 12 are fit by quadratic polynomials. The ratios of these polynomials are plotted in Fig. 13. For comparison, the square root and fourth root of the flashboard number ratio (density ratio) are shown on the right side. The measured switch current ratio is close to the fourth root of the density, as predicted by the "hydro-limit" of Eq. (10). The ratio obtained for 18 and 3 flashboards is higher for small delay times. This may be the result of the small conduction times in these cases where, eventually, scaling proportional to density is expected.

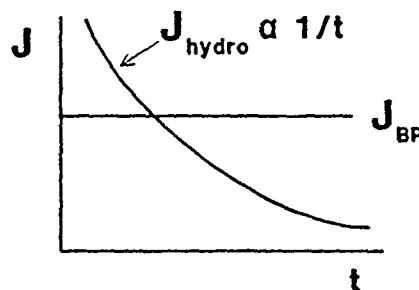


Fig. 11 Switching thresholds for emission- and hydro- limits

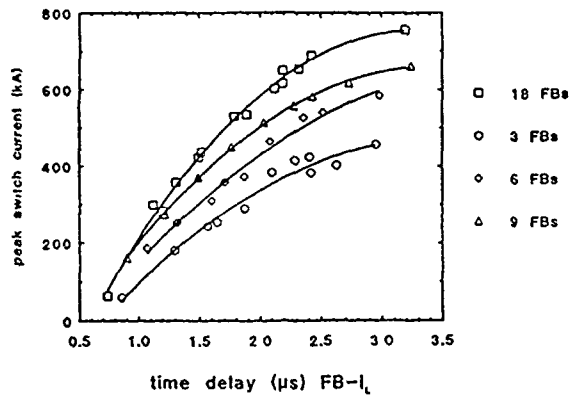


Fig. 12 Hawk conduction current as a function of time delay for different numbers of flashboards

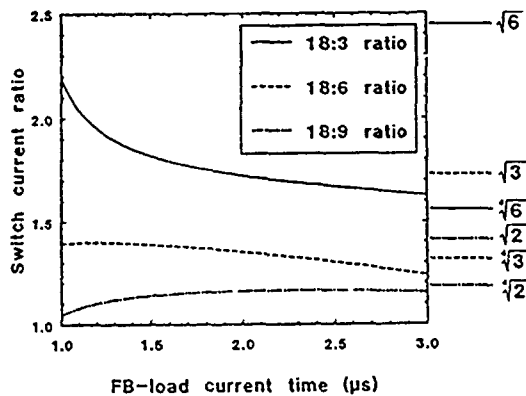


Fig. 13 Hawk conduction current ratios as functions of time delay for different numbers of flashboards

The experimental measurements of the current distribution and initial plasma density lead to a physical picture of the conduction phase of the POS. The current distribution measurements indicate that the plasma remains localized in the original plasma injection region. The required density depends on the lower of the switching thresholds in Eq. (9) (emission limited) and Eq. (10) (hydro limited). The minimum required

density can be orders-of-magnitude higher in the $1 \mu\text{s}$ conduction time case compared with the 50 ns conduction time case. This affects the gap opening rate for both erosion opening, Eq. (7), and for magnetic pressure opening, Eq. (8).

Ion Current Measurements

Biased charge collectors inside the center conductor measure the ion current density during POS conduction and opening. An example[14] of this measurement using two collectors on Gamble 1 is shown in Fig. 14a. Signals proportional to the ion current density are compared to the timing of the generator and load currents in Fig. 14b. During conduction, the ion current increases after the current channel reaches the measurement location. At opening, the ion current increases drastically at both locations. The total ion current estimated from these localized collectors is $> 15\%$ of the switch current during opening. This is a lower limit because of the collimating apertures used to measure the ion current.

The same technique used on Hawk[11] shows somewhat different results. At a given ion collector location, the signal peaks and decreases during the conduction phase. The total ion current is compared with the generator and load currents in Fig. 15. The ion current is a large fraction, $\sim 50\%$, of the switch current with most of the ion current density distributed over an 8 cm length, centered at the load end of the plasma injection region. (In this case, non-collimating apertures were used to obtain better quantitative measurements.)

Both short and long conduction time POS experiments indicate large ion currents to the cathode that could be the cause of gap opening according to Eq. (7). The ion current detected during conduction may indicate local gap opening that progresses along the switch length. The ion current signals increase when the current front in the plasma passes the probe location. In long conduction time experiments, the ion current is concentrated in a small axial region that moves along the cathode during conduction. The gap behind this ion current channel could continue to open by magnetic pressure, as described by Eq. (8).

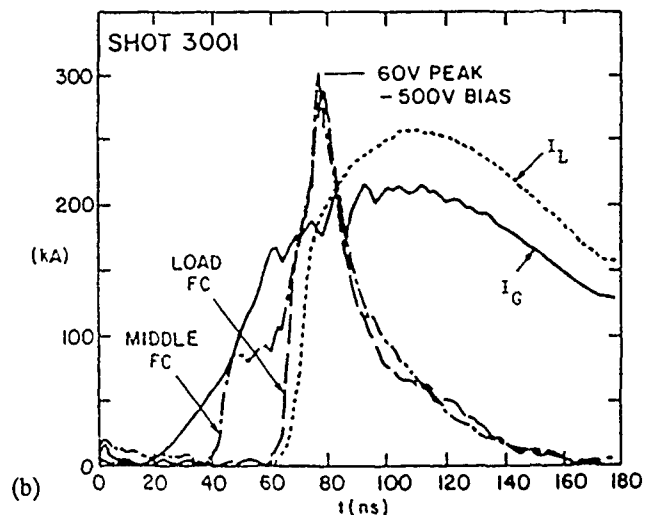
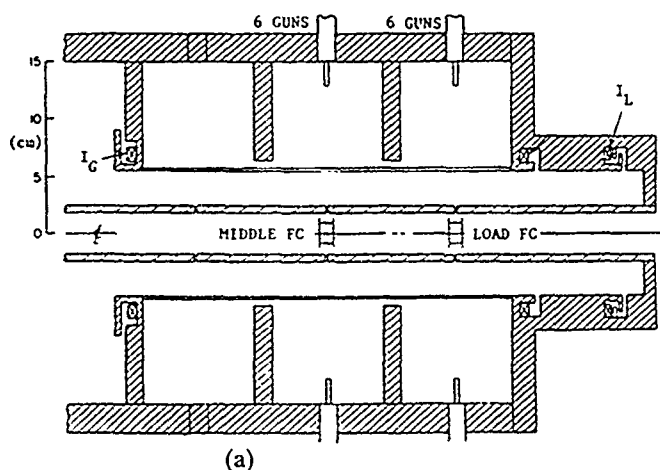


Fig 14 (a) Gamble 1 experimental setup with two ion current monitors (b) signals proportional to local ion current density and I_G , I_L signals

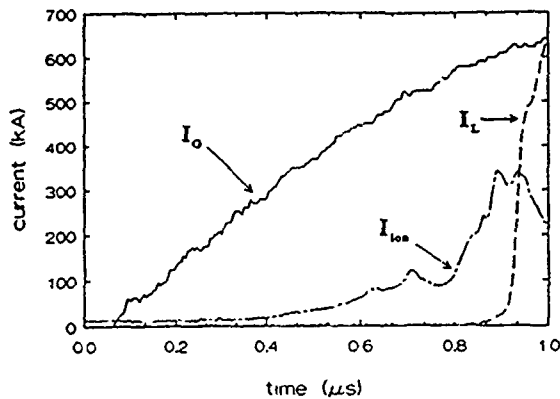


Fig. 15 Total ion current compared to generator and load currents on Hawk

Discussion of Opening Mechanisms

The measurements described above allow an estimation of the gap generated by the erosion opening mechanism, Eq. (7). The examples in Figs. 1 and 2 will be used to evaluate erosion opening for 50 ns and 1 μs conduction time POS experiments. In Gamble 2, the gap required to insulate 4.6 MV with 0.75 MA load current at a radius of 2.5 cm is, according to Eq. (4), $D = 0.3$ cm. Assuming this gap is formed in 10 ns, the opening time, results in an average gap opening rate of $dD/dt = 30$ cm/μs. The density can be estimated using $l_0 = 10$ cm and $I = 900$ kA in Eq. (9) (emission limited) yielding $n_e = 9.5 \times 10^{13}$ cm⁻³. The hydro displacement for this density is estimated from Eq. (3) to be 4.5 cm, about half the switch length. (In this case, the hydro limit, Eq. (10), and the emission limit imply similar densities.) The ion current density required to erode the gap open at the estimated rate is

$$J_i = n_e e \left(\frac{dD}{dt} + v \right) \approx 12 \quad (11)$$

$$\approx 12 \left[30 \frac{\text{cm}}{\mu\text{s}} + v \frac{\text{cm}}{\mu\text{s}} \right] \frac{\text{A}}{\text{cm}^2}$$

Using the estimated value of $v = 10$ cm/μs, the required ion current density is $J_i = 0.5$ kA/cm². This is only a small fraction of the switch current density of $I/(2\pi r l_0) = 6$ kA/cm², indicating that only about a 10% ion current fraction is required to open an insulated gap by the erosion process. This ion current is exceeded in other short-conduction-time POS experiments, as evidenced by results for Gamble 1 shown in Fig. 14. Opening by hydrodynamic displacement, Eq. (8), cannot be ruled out in the Gamble 2 case, because of the high magnetic field. Other short conduction time experiments (Gamble 1 and PBFA II, for example) have far smaller B fields and probably open entirely by erosion.

For the 1 μs conduction time example (Hawk, Fig. 2) the density must be at least 5×10^{15} cm⁻³ to limit the plasma displacement as inferred from magnetic probe measurements. The gap required to insulate 0.75 MV with 0.5 MA at a radius of 5 cm is $D = 0.2$ cm. The opening time is about 50 ns, resulting in an average gap opening rate $dD/dt = 4$ cm/μs. The ion current density required to open the gap by erosion is:

$$J_i = 800 \left(4 \frac{\text{cm}}{\mu\text{s}} + v \frac{\text{cm}}{\mu\text{s}} \right) \quad (12)$$

$$\approx 3 \frac{\text{kA}}{\text{cm}^2} < J_i < 11 \frac{\text{kA}}{\text{cm}^2}$$

where the lower limit corresponds to $v = 0$ (the ion flux is impeded by magnetic or electric fields) and the upper limit corresponds to $v = 10$ cm/μs. The measured ion current density in Hawk has a peak value of ≈ 1 kA/cm², less than the lower limit in Eq. (12). This argues that erosion is not the only opening mechanism acting in this case. One possibility is a combination of magnetic pressure opening and subsequent erosion, the magnetic pressure clearing the high density from the region near the cathode during the conduction phase followed by erosion of the remaining low density to disconnect the plasma from the cathode. Investigations of this possibility and methods to improve switching under these circumstances are subjects of future research.

Summary and Conclusions

POS applications for pulsed power include power multiplication for conventional generators and primary switching for newer, inductive generators. Short conduction time (50 ns) POS operation may be understood as emission-limited conduction followed by erosion opening. In many of these cases, magnetic displacement of the switch plasma during conduction is negligible. At longer conduction times (1 μs), the effects of magnetic forces are more apparent, and may dominate conduction and opening processes. Simple estimates of plasma displacement, combined with measurements of the current distribution in POS plasmas impose a lower limit on the plasma mass, and therefore, on the plasma density. This density can be orders-of-magnitude higher in the μs conduction time range than that required for emission limited conduction in the 50 ns conduction time case. The rate of gap opening is decreased in this case because of the increased density. Erosion opening is probably not the dominant mechanism in the 1 μs conduction time case. A combination of hydrodynamic displacement with erosion as a final step is hypothesized. Theoretical analyses and improved experimental measurements are required to more fully examine this case. Improved opening could be achieved in the μs case if the opening mechanism is understood and exploited. Increased gap size of a few times is needed to improve pulsed power generators based on inductive energy storage to levels comparable to conventional technologies.

• JAYCOR, Vienna, VA

REFERENCES

- [1] G. Cooperstein and P. Ottinger, "Guest editorial: fast opening vacuum switches for high-power inductive energy storage," IEEE Trans Plasma Sci., vol. PS-15, no. 6, pp. 629-634, Dec. 1987.
- [2] see IEEE Trans. Plasma Sci., vol. PS-15, no 6, Dec. 1987
- [3] G. E. Rochau, D. H. McDaniel, C. W. Mendel, Jr., M. A. Sweetney, W. B. S. Moore, G. R. Mowrer, W. W. Simpson, and D. M. Zagar, "Performance of magnetically-injected-plasma opening switches for the particle beam fusion accelerator II (PBFA II)," to be published in Proc. 8th Int. Conf. High-Power Particle Beams (Novosibirsk, USSR), 1990.

- [4] B. M. Koval'chuk and G. A. Mesyats, "Superpower pulsed systems with plasma opening switches," to be published in Proc. 8th Int. Conf. High-Power Particle Beams (Novosibirsk, USSR), 1990.
- [5] J. M. Neri, J. R. Boller, P. F. Ottinger, B. V. Weber, and F. C. Young, "High-voltage, high power operation of the plasma erosion opening switch," Appl. Phys. Lett., vol. 50, pp. 1331-1333, 1987.
- [6] D. G. Colombant and B. V. Weber, "A simple model for flashboard plasma expansion," IEEE Trans. Plasma Sci., vol. PS-15, no. 6, pp. 741-746, Dec. 1987.
- [7] B. V. Weber, R. J. Commisso, G. Cooperstein, P. J. Goodrich, J. M. Grossmann, D. D. Hinshelwood, J. C. Kellogg, D. Mosher, J. M. Neri, and P. F. Ottinger, "Plasma erosion opening switch operation in the 50 ns - 1 μ s conduction time range," to be published in Proc. 8th Int. Conf. High-Power Particle Beams (Novosibirsk, USSR), 1990.
- [8] J. M. Grossmann, P. F. Ottinger, and R. J. Mason, "Current channel migration and magnetic field penetration in a perfectly conducting plasma with emitting, conducting boundaries," J. Appl. Phys., vol. 66, pp. 2307-2314, 1989, and references therein.
- [9] P. F. Ottinger, S. A. Goldstein, and R. A. Meger, "Theoretical modeling of the plasma erosion opening switch for inductive storage applications," J. Appl. Phys., vol. 56, pp. 774-784, 1984.
- [10] B. V. Weber, R. J. Commisso, R. A. Meger, J. M. Neri, W. F. Oliphant, and P. F. Ottinger, "Current distribution in a plasma erosion opening switch," Appl. Phys. Lett., vol. 45, pp. 1043-1045, 1984.
- [11] D. D. Hinshelwood, R. J. Commisso, P. J. Goodrich, J. M. Grossmann, J. C. Kellogg, P. F. Ottinger, and B. V. Weber, "Axially resolved PEOS measurements at microsecond conduction times," to be published in Proc. 8th Int. Conf. High-Power Particle Beams (Novosibirsk, USSR), 1990.
- [12] B. V. Weber, D. H. McDaniel, and G. E. Rochau, "Plasma density measurements in PBFA II opening switch configurations," in Proc. IEEE Int. Conf. Plasma Science (Oakland, CA), 1990, p.187.
- [13] G. E. Rochau, D. H. McDaniel, C. W. Mendel, M. A. Sweeney, W. B. S. Moore, G. R. Mowrer, and D. M. Zagar, "Performance of magnetically-injected-plasma opening switches on the particle beam fusion accelerator II (PBFA II)," in Proc. IEEE Int. Conf. Plasma Science (Oakland, CA), 1990, p.187.
- [14] B. V. Weber, R. J. Commisso, P. J. Goodrich, D. D. Hinshelwood, W. F. Oliphant, P. F. Ottinger, and F. C. Young, "Ion emission from PEOS plasmas," Proc. 7th Int. Conf. High-Power Particle Beams (Karlsruhe, W. Germany), pp. 1131-1136, 1988.

TN file

PULSED POWER PHYSICS TECHNOTE NO. 93-04

TITLE: POS CONDUCTION DEPENDENCE ON CURRENT RISE RATE

AUTHORS: B.V. Weber, R.J. Comisso, F.J. Goodrich, J.M. Grossmann,
D.D. Hinshelwood, J.C. Kellogg, P.F. Ottinger, S.J. Stephanakis, and
J.R. Goyer (Physics International Co.)

DATE: 19 November 1992

ABSTRACT: This talk was presented at the APS/DPP meeting in Seattle, Washington. Experimental evidence for different POS conduction regimes is presented based on density measurements during shots on Hawk using various POS parameters: density, length, radius, and the generator current rise rate, and *in situ* density measurements on Gamble II (prior to shots) where density and plasma length were varied. The conduction scaling observed on Hawk follows the dependencies predicted by simple MHD and EMH conduction limit derivations. Gamble II POS experiments (ten times greater dI/dt than Hawk) show scaling more like the modified bipolar (MBP) prediction, where conduction current is independent of plasma length and proportional to the square root of the density. The square root of length dependence predicted by EMH, expected to apply in the Gamble II case, was not evident. Diagnostic limitations and the small range of parameter variations so far limit the conclusiveness of the non-MHD scaling experiments, but the contrast with the MHD-limited conduction on Hawk is evident. Experiments with density measurements during shots on Gamble II with more parameter variations (radius and dI/dt in addition to n and l) are needed to adequately diagnose the conduction scaling in this important case.

THIS REPORT REPRESENTS
UNPUBLISHED INTERNAL
WORKING DOCUMENTS AND
SHOULD NOT BE REFERENCED
OR DISTRIBUTED

Plasma Opening Switch Conduction* Dependence on Current Rise Rate

B.V. Weber, R.J. Commisso, P.J. Goodrich,** J.M. Grossmann,
D.D. Hinshelwood,** J.C. Kellogg, P.F. Ottinger, S.J. Stephanakis

Plasma Physics Division
Naval Research Laboratory
Washington, DC

J.R. Goyer
Physics International Co.
San Leandro, CA

Paper 7E4 APS/DPP
19 November 1992

* Work Supported by DNA
** JAYCOR, Vienna, VA

Motivation: Physics of POS Conduction

NRL

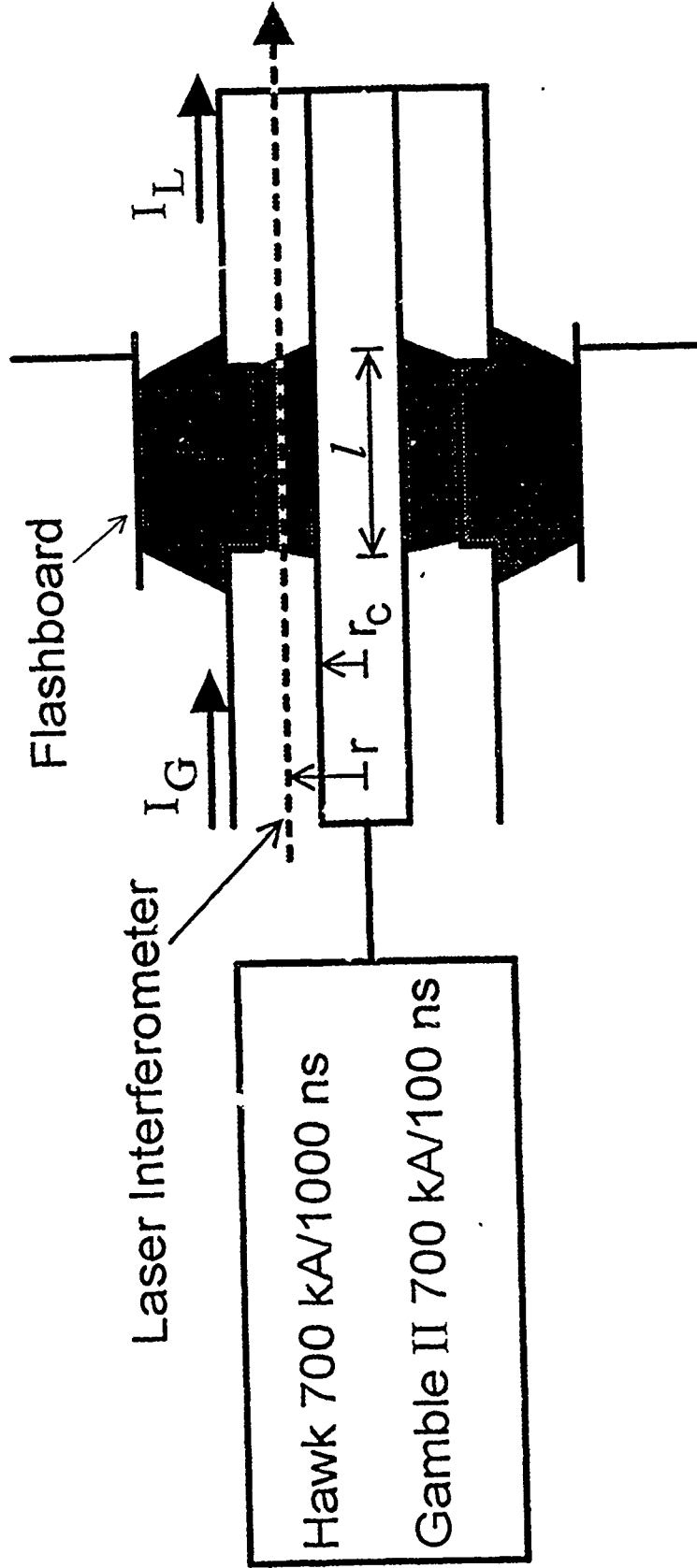
- Introduction: POS experiments on Hawk and Gamble II
 - ◆ Hawk: 700 kA, 1000 ns
 - ◆ Gamble II: 700 kA, 100 ns

$I(n) \Rightarrow$ different scaling

- Hypothetical conduction models
 - ◆ Bipolar (BP), Modified BP (MBP), EMH, MHD
 - ◆ Experimental regime determined by POS parameters
- Hawk scaling experiments $I(n, r, l, dI/dt) \Rightarrow$ MHD, (EMH?)
- Gamble II scaling experiments $I(n, l) \Rightarrow$ MBP? (EMH)
- Conclusions and Future Work

POS Experiment on Hawk and Gamble II

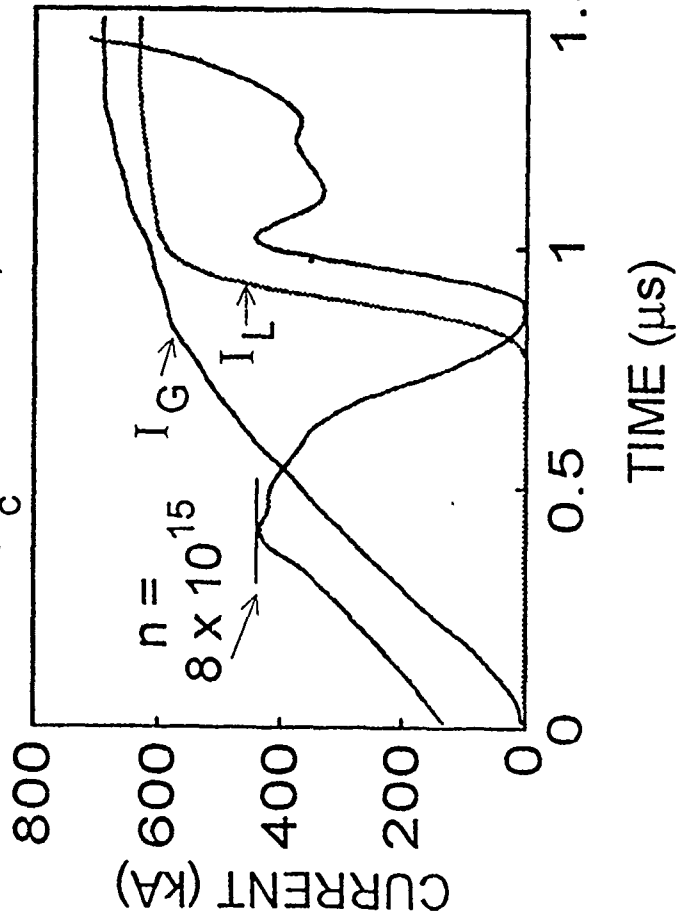
NRL



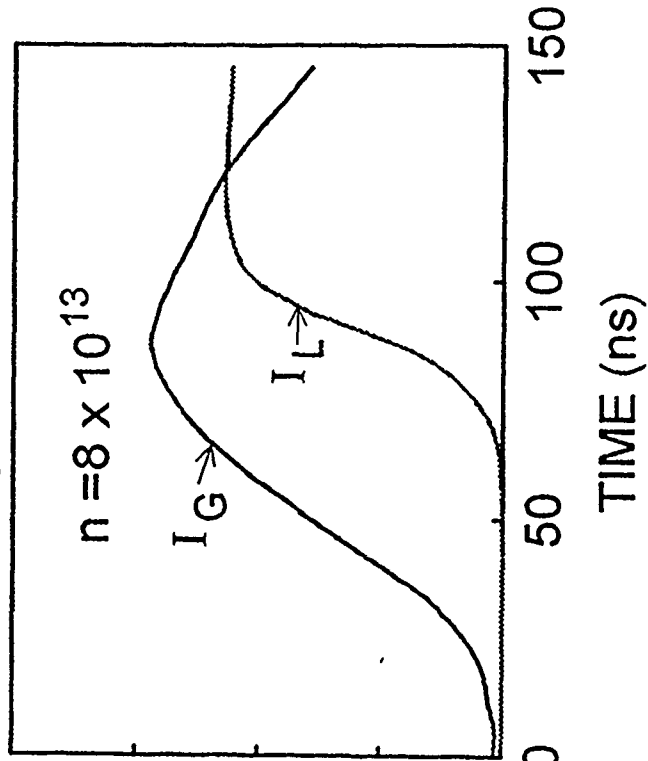
Higher n required to conduct longer time

NRL

Hawk, $r_c = 2.5 \text{ cm}$, $l = 8 \text{ cm}$



Gamble II: $r_c = 2.5 \text{ cm}$, $l = 8 \text{ cm}$

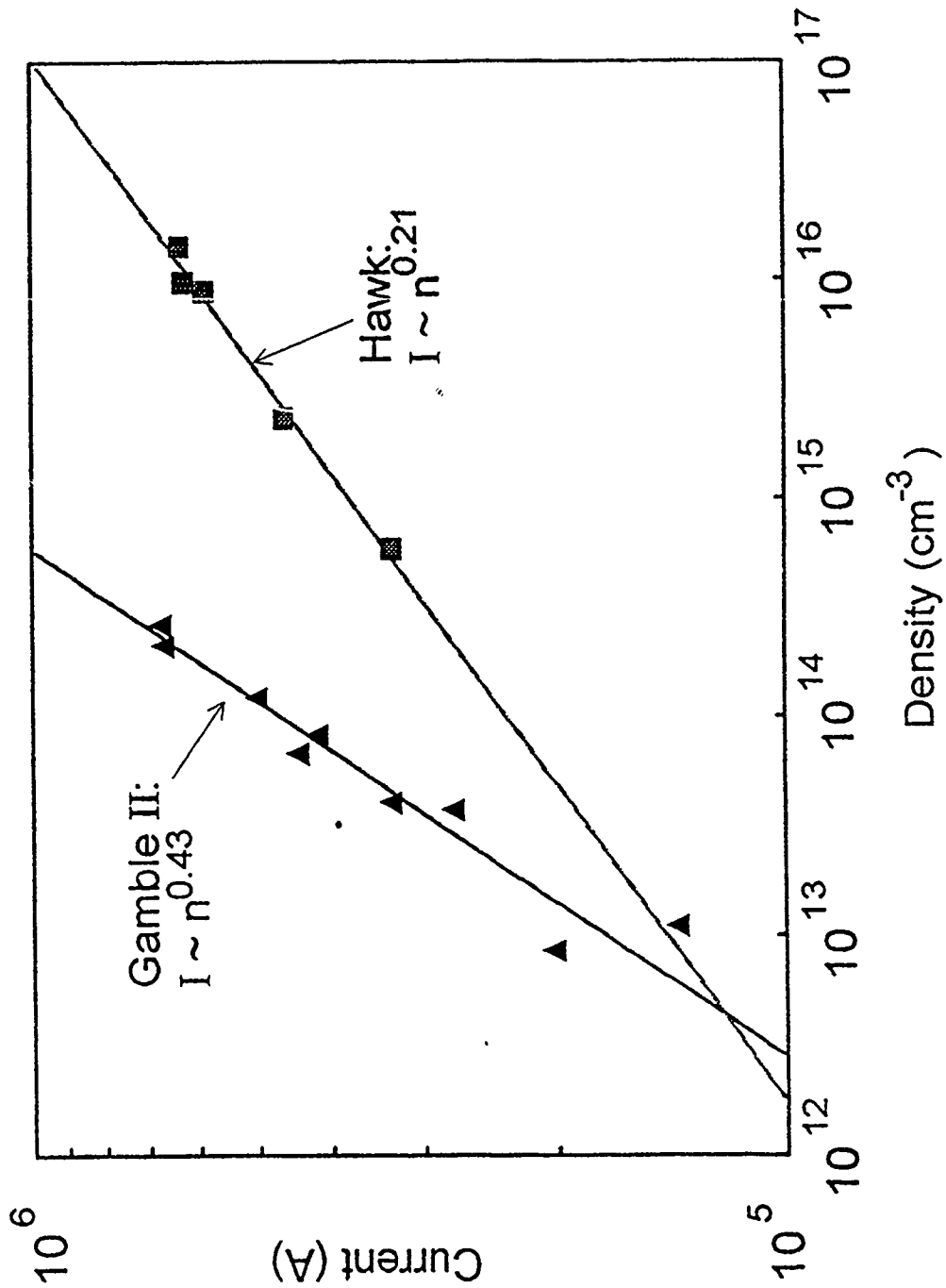


Hawk:	600 kA,	800 ns	$8 \times 10^{15} \text{ cm}^{-3}$
Gamble II:	500 kA,	50 ns	$8 \times 10^{13} \text{ cm}^{-3}$

I(n) scaling different for Hawk, Gamble II

NRL

POS I(n) scaling: $r_c = 2.5$ cm, $l = 8$ cm



Four scaling laws predict different I(n, r, l, dI/dt) scaling

NRL

1. Bipolar: conduction limit: onset of erosion (P.F. Ottinger, et al., JAP 56, 1984)

$$I = \sqrt{M/Zm}(2\pi r l)nev \quad I_{BP} = 3.77 \times 10^{-10} r l n$$

2. Modified Bipolar: onset of magnetic insulation (J. Goyer, IEEE Trans. Plasma Sci., Oct. 1991)

$$I = 1.02 \times 10^{-2} r \sqrt{n} \quad I_{MBP} = 1.0 \times 10^{-2} r n^{1/2}$$

3. EMH: field penetrates plasma (A.S. Kingsep, et al., Fizika Plazmy 8, 1982)

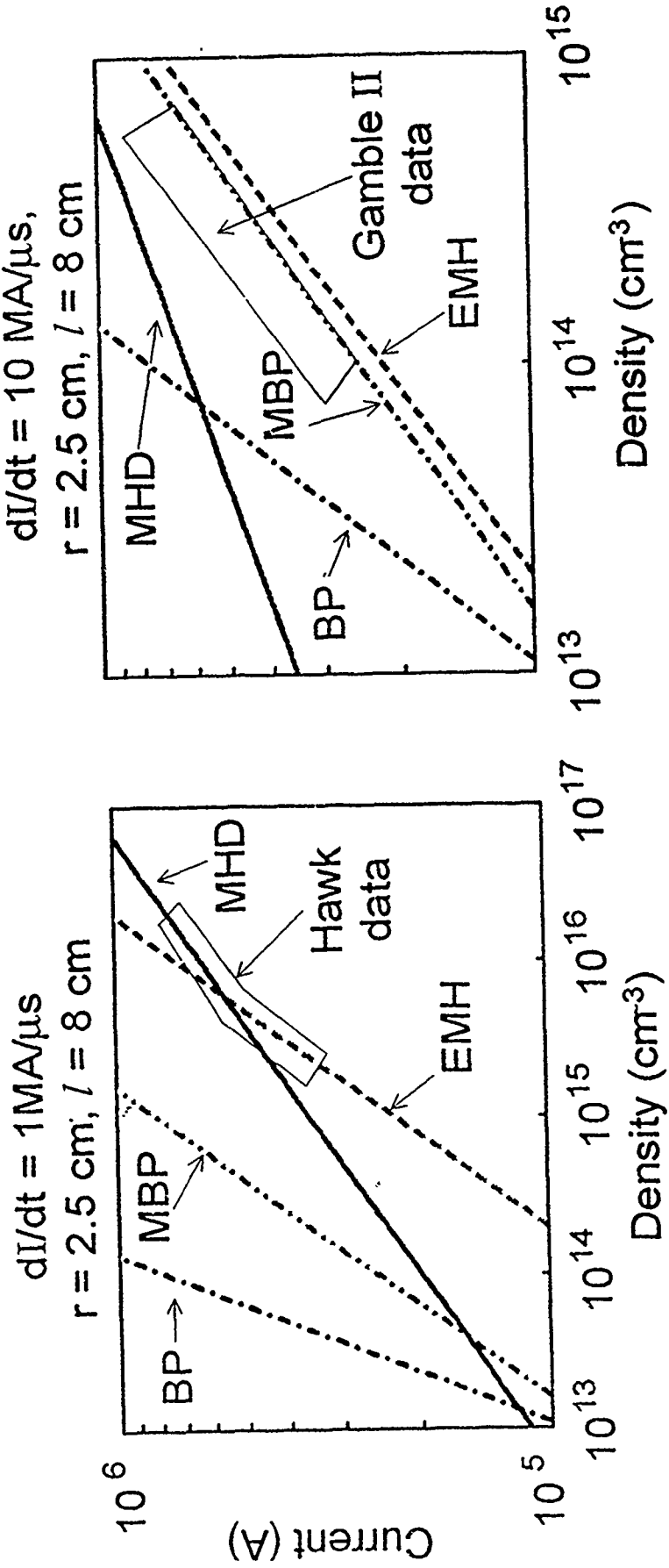
$$\int I dt = \pi e r^2 l n \quad I_{EMH} = 1.0 \times 10^{-9} r (l \dot{I} n)^{1/2}$$

4. MHD: plasma displaced/distorted (W. Rix, et al., IEEE Trans. Plasma Sci., 19, 1991)

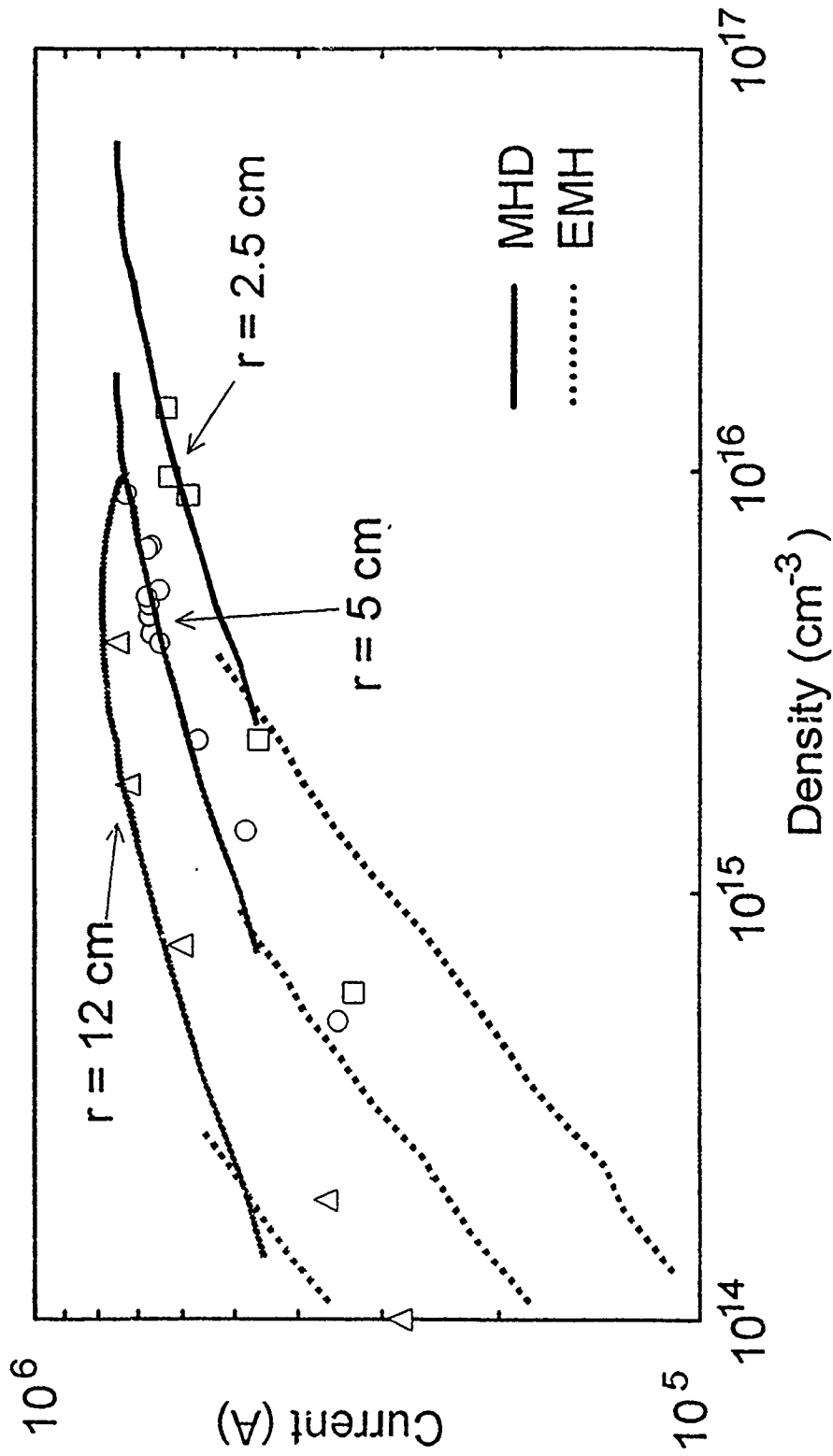
$$\iint I^2 dt^2 = \frac{100\pi^2 r^2 l^2 M n}{Z} \quad I_{MHD} = 1.4 \times 10^{-5} (r^2 l^2 \dot{I}^2 n)^{1/4}$$

Different conduction limits apply for Hawk and Gamble II (linear current ramp approx.)

NRL

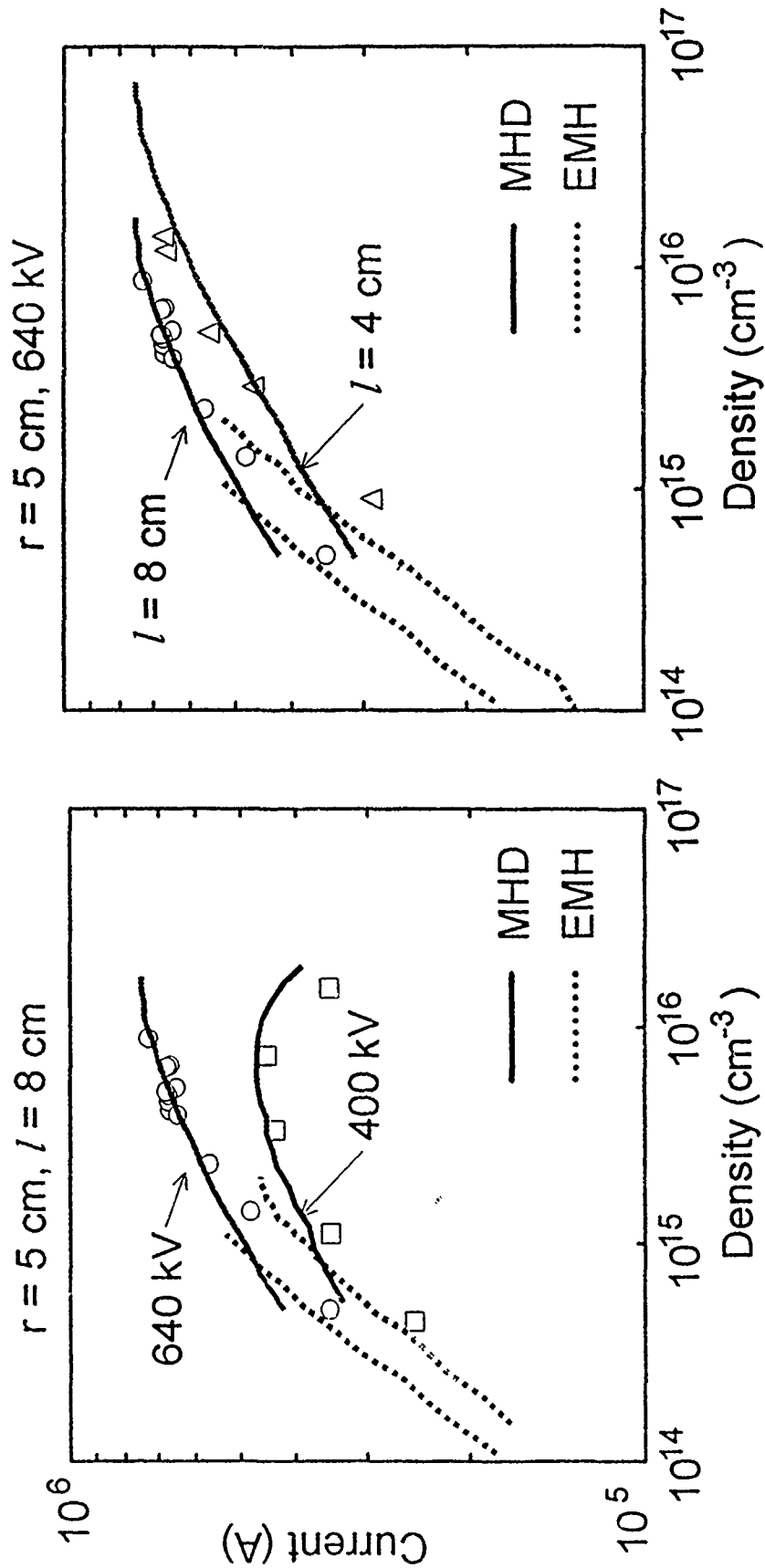


Hawk I(n) scaling follows MHD for $I > 450$ kA (vary $r = 2.5, 5, 12$ cm)



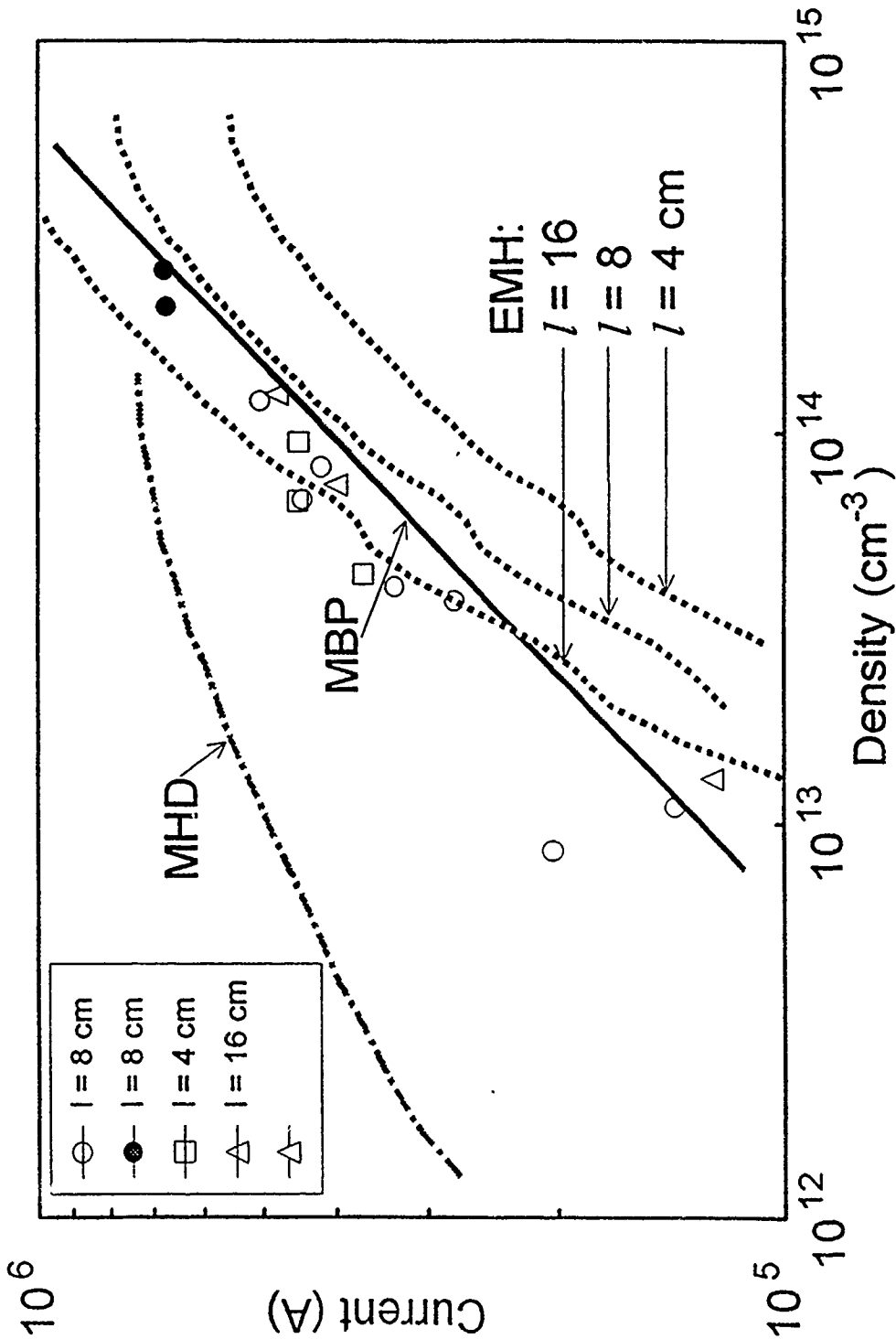
Hawk I(n) scaling follows MHD for $I > 450$ kA (vary l , dI/dt factor of 2)

NRL



Gamble II I(n) scaling (vary $l = 4, 8, 16$ cm)

NRL



Conclusions: POS conduction regime depends on n , r , l , and dI/dt

NRL

POS on Hawk and Gamble II operate in different regimes
different $I(n)$ scaling

Scaling expts on Hawk \Rightarrow MHD for $I > 450$ kA
non-MHD (EMH?) for $I < 450$ kA

Scaling expts on Gamble II $\Rightarrow I \propto n^{1/2}$, independent of l
(MBP?, contrary to EMH)

caveat: non-MHD regimes not adequately diagnosed

Future work: More scaling experiments!

NRL

Determine scaling in non-MHD regime:
measure $n(r,t)$ while varying dI/dt and r
scaling expts on other generators (*ie*, DPM1)

Improved density measurements:
multi-chord He-Ne on Hawk
CO₂ during shots on Gamble II
high resolution interferometer (SRL)

Vary plasma sources:
gas gun sources tested on Hawk
"slow" plasma guns used at PI

PLASMA TECHNOLOGY BRANCH TECH-NOTE NO. 90-09

TITLE: "RECESSED B-DOT PROBES"

DATE: 18 April 1990

AUTHORS: D. Hinshelwood, R. Boller, and G. Longrie.

ABSTRACT: This note describes calibrations of recessed B-dot loops in the geometry to be used on Hawk. The sensitivity and frequency response of the final design are sufficient for Hawk experiments. The first design, involving a 20 turn loop, had an inadequate frequency response. The measured risetimes are consistent with those calculated from an inductance formula.

** THIS REPORT REPRESENTS
UNPUBLISHED INTERNAL WORKING
DOCUMENTS AND SHOULD NOT BE
REFERENCED OR DISTRIBUTED

** THIS REPORT CONTAINS REALLY
BORING ENGINEERING DETAILS

Background

The POP experiment used B-dot loops in the cathode to measure the cathode current and thus compare current penetration at the cathode with that in the plasma. The probes seemed to work well as long as they were electrically isolated from the cathode. We are designing a similar array for Hawk. We do not want to perturb the cathode surface by any protrusions and since the probes must be insulated, the loops will have to be recessed at least a mm or so. In addition, the hole in the cathode should be as small as possible to minimize its perturbation on the current flow. These two requirements raise questions about possible frequency response limitations arising from penetration of field into the hole. The POP probes were only calibrated at the μs timescale of aplanatic shots and not at the tens of ns timescale of PEOS shots. We would also like as large a signal as possible to reduce noise problems. This can be done by using a multi-turn loop, but then loop inductance can limit frequency response. To study B-dot response and sensitivity in the Hawk geometry we performed the test described here.

Arrangement

A top view of the test rig is shown in Fig. 1. A Pulspak 10-A fed a coax system comprising the 4.25 in OD \times 1/8 in wall aluminum center conductor and 12 return rods at 6 in diam, giving a gap of 2 cm which will be typical of Hawk experiments. The peak current was estimated to be about 650 kA. The loop was about 1/4 in high by 1/8 in Δr and was positioned at different radii with a translation stage. Both 20 and 5-turn loops of .25 mm diam wire were checked. A 3/8 in diam hole was used first. For comparison, the POP arrangement comprised a 2 in OD \times 1/8 wall brass cathode with 3/8 diam holes, 5.5 in diam return rods, and a 5-turn, 5 mm square loop.

Results

First we looked at inherent loop frequency response. Waveforms from 20 and 5-turn loops are compared with that from a small single turn reference loop in Fig. 2 (the baselines have been offset for clarity). Here the b-dots were located in the cathode-return rod gap. The 20-turn loop is seen to have a poor frequency response. The 5-turn loop is seen to have adequate response for Hawk. Afterwards, the inductance was calculated using a formula from the PDR:

$$L = .0126 R n^2 \left(\ln \left(\frac{8R}{a n^{1/2}} \right) - 1.75 \right)$$

where L is in μH , R is the loop radius, a is the wire radius (both in cm), and n the number of turns. This implied a response time of about 45 ns for the 20-turn loop, 4 ns for the 5-turn loop, and a fraction of a ns for the small reference loop as well as the Hawk door B-dots. The calculated response times are consistent with those measured for both the 20 and 5-turn loops. (The calculated response time of the loops used in the low-mass experiment is about 8 ns).

Next, the frequency response of a recessed loop was examined. The waveform from the 5-turn loop located outside the cathode is compared in Fig. 3 with that from a location .050 in farther in than the location planned for Hawk (the signals are normalized to one another). No difference in frequency response is observed, indicating that field penetration into the hole is not a problem in our case.

The solid line in Fig. 4 shows the (5-turn) probe signal as a function of radius. Significant fields are measured both beyond the return rods and inside the hole. The presence of the hole reduces the field just beyond the cathode radius. Comparison with the signal from a shorted loop shows that the twisted leads gave no appreciable pickup. The planned loop center location for Hawk experiments is indicated. Next, a 1/2 in diam hole was used as shown by the dotted line. The larger hole caused somewhat greater field penetration but reduced fields closer to the surface, as would be expected. The signal at the eventual Hawk location is about the same for either hole so a 3/8 in hole will be large enough. The signals on Hawk shots will be at a good level, needing attenuation for CAMAC recording.

In summary, recessed 5-turn b-dots will have sufficient signal levels and frequency response for the Hawk experiments. B-dot signals are not necessarily increased by using a larger hole. The inductance formula is useful for calculating b-dot risetimes.

Fig 1
Top view of
Set-up

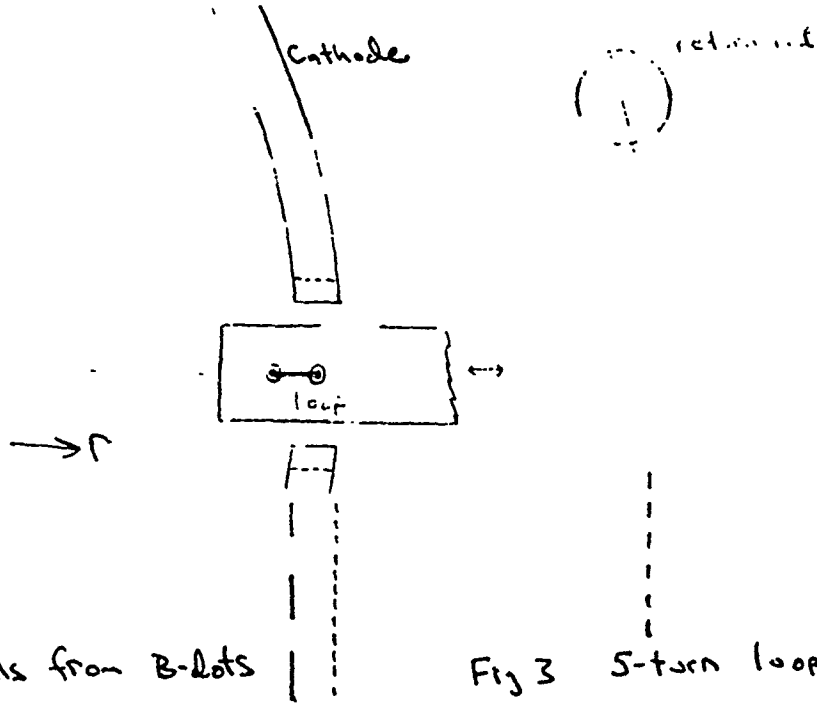


Fig 2 signals from B-dots

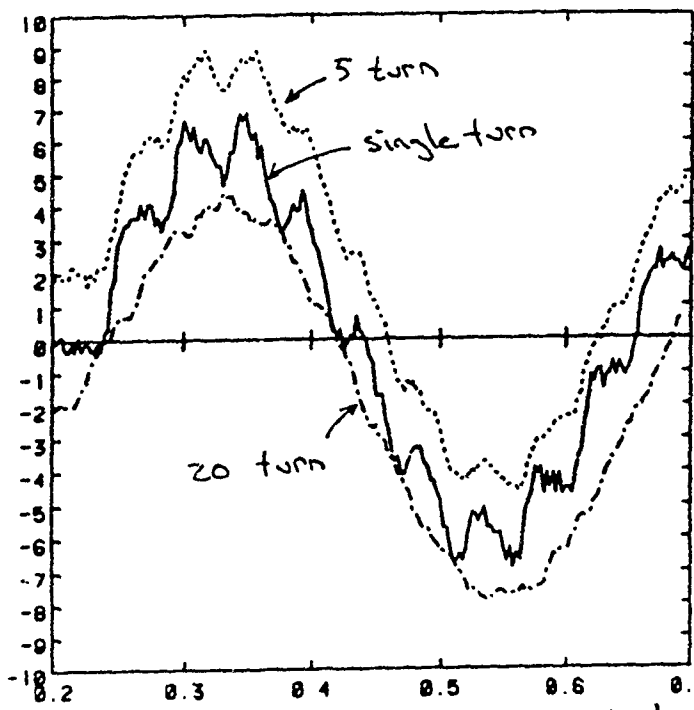


Fig 3 5-turn loop at different
locations

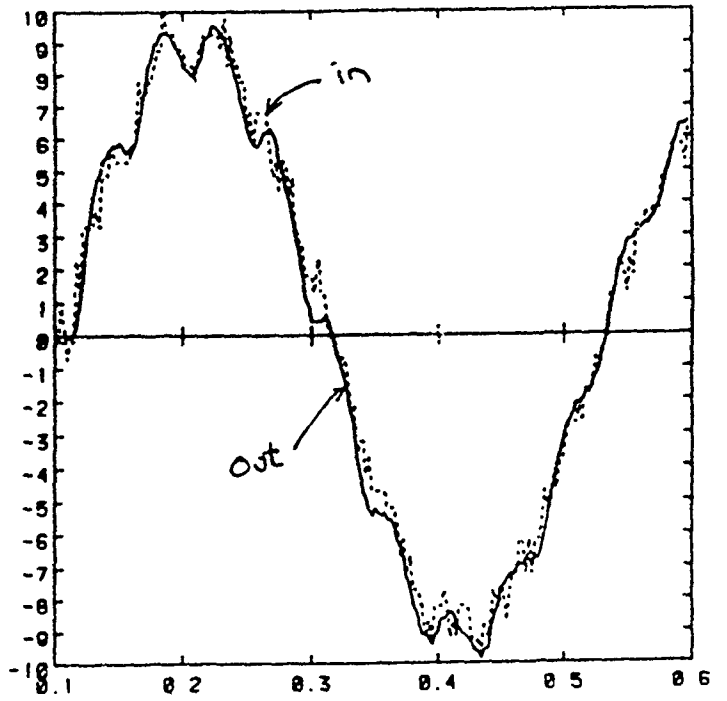
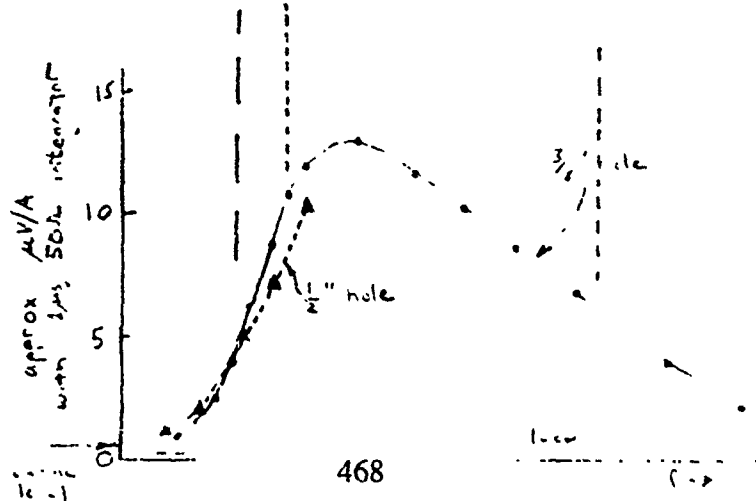


Fig 4
Signal vs radius
Axis lines up
with Fig 2



BW 8/12/91

TITLE: "Faraday Cup Measurements on Hawk"

DATE: 4 Aug 1991

AUTHOR: D. Hinshelwood

ABSTRACT: Faraday cup data from Hawk is described here. The cup arrangement comprised apertures at different axial locations. Many apertures had multiple collectors, allowing measurement of the ion azimuthal and axial velocity distributions. The results are similar to those in previous POP experiments: the ion signals peak and then decline during the conduction phase. Apertures closer to the load show successively later ion current pulses. The angular velocity distributions are fairly wide. The total ion current during the conduction phase is much greater than the bipolar value.

** THIS REPORT REPRESENTS
UNPUBLISHED INTERNAL WORKING
DOCUMENTS AND SHOULD NOT BE
REFERENCED OR DISTRIBUTED

Introduction

Three series of shots were taken last year on Hawk, comprising a wide array of diagnostics including dB/dt loops, Faraday cups, and optical measurements. This work was an extension of a similar experiment on POP which was described in TN 90-06. The Hawk results, which were presented at Beams '90, are described in more detail here. Faraday cup results are presented in this note, with the rest to be discussed in a later note. In general the results on Hawk were quite similar to those on POP.

The set-up on Hawk is shown in Fig. 1. The Hawk Marx was operated at 80 kV charge, driving about 700 kA through the switch. Plasma was supplied by 18 flashboards located 13 cm from the cathode. The anode rods were masked off outside of the 8 cm switch region, which was located about 15 cm before the short circuit load. The cathode and anode diameters were 11 and 18 cm, respectively. The generator current (IOUTC) was measured by a Rogowski located upstream of the switch. The load current (ILAVG) was measured by averaging two dB/dt loops located just before the load. The signals obtained from these were often suspect, and the apparent low current transfer on some longer conduction time shots may not be real. Diagnostics included dB/dt loops, Faraday cups, and collimated fiber optic light probes.

Faraday cup diagnostics

The Faraday cup assemblies used here are shown in Fig. 2. The basic arrangement was developed during the POP experiments. The apertures consisted of ~ 0.4 mm holes in 0.08 mm thick copper tape, as shown in Fig. 2, and thus offered no collimation to the incoming ions. The collectors consisted of sections of copper tape on a plastic tube inside the cathode. A novel feature was the use of multiple collectors for given apertures, which allowed measurement of the ion angular distributions. The simple construction made it easy to alter the arrangement of collectors. In the Hawk experiments the inner tube was 7.5 cm diam, giving an aperture-to-collector gap of 1.3 cm. Seven apertures were used, separated axially by 2.5 cm. They were located alternately in two rows, separated azimuthally by 90 degrees. The bias was -300 V. Two shots were taken at -400 V and the signals were not noticeably different. No signals were observed when the apertures were covered with copper tape.

Eight shots were taken with the collector arrangement pictured at the top of Fig. 2. FC4 was located in the center of the switch region. This hole had six collectors which diagnosed both the azimuthal and axial distributions. FC6 and 8 had two collectors each while FC3, 5, 7, and 9 had one each.

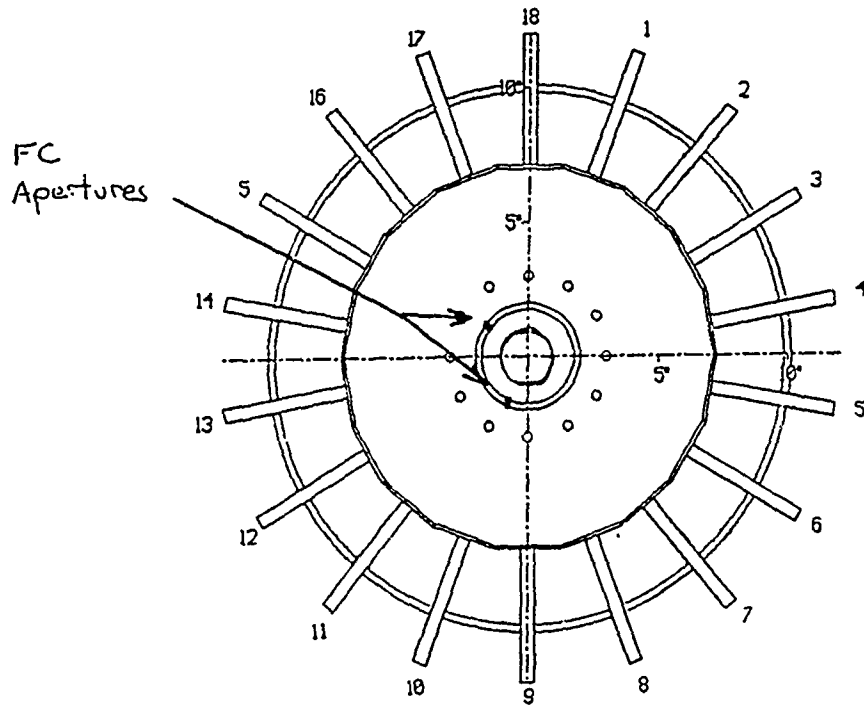
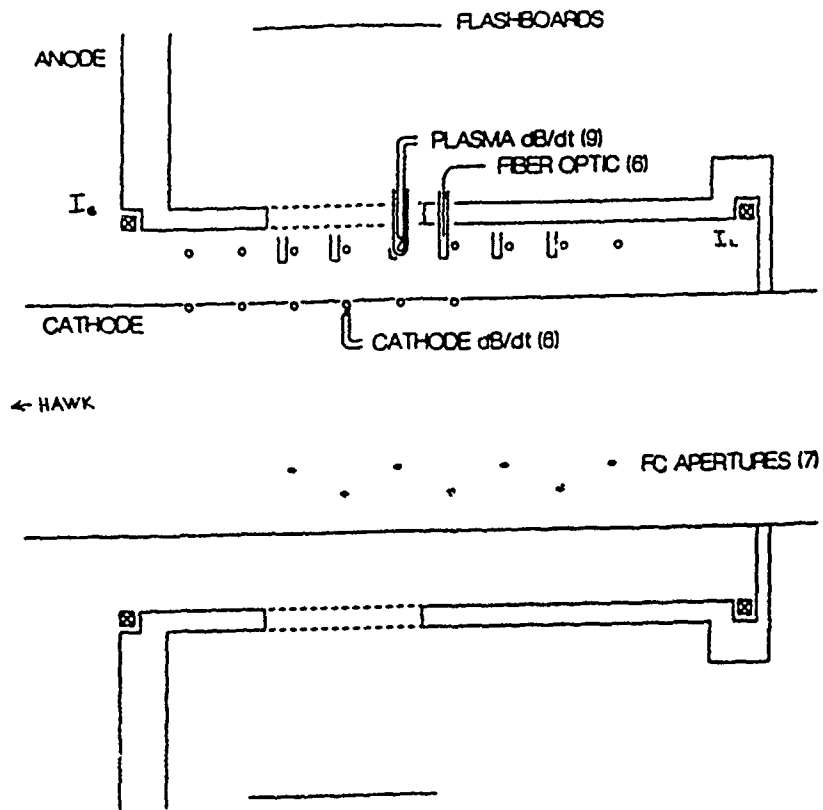


Fig. 1: (top) Hawk experimental arrangement. (bottom) Azimuthal orientation.

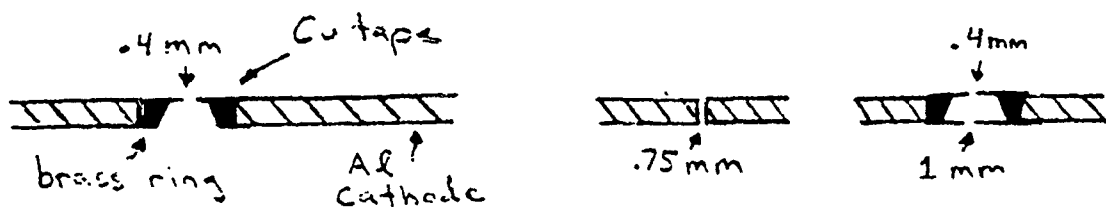
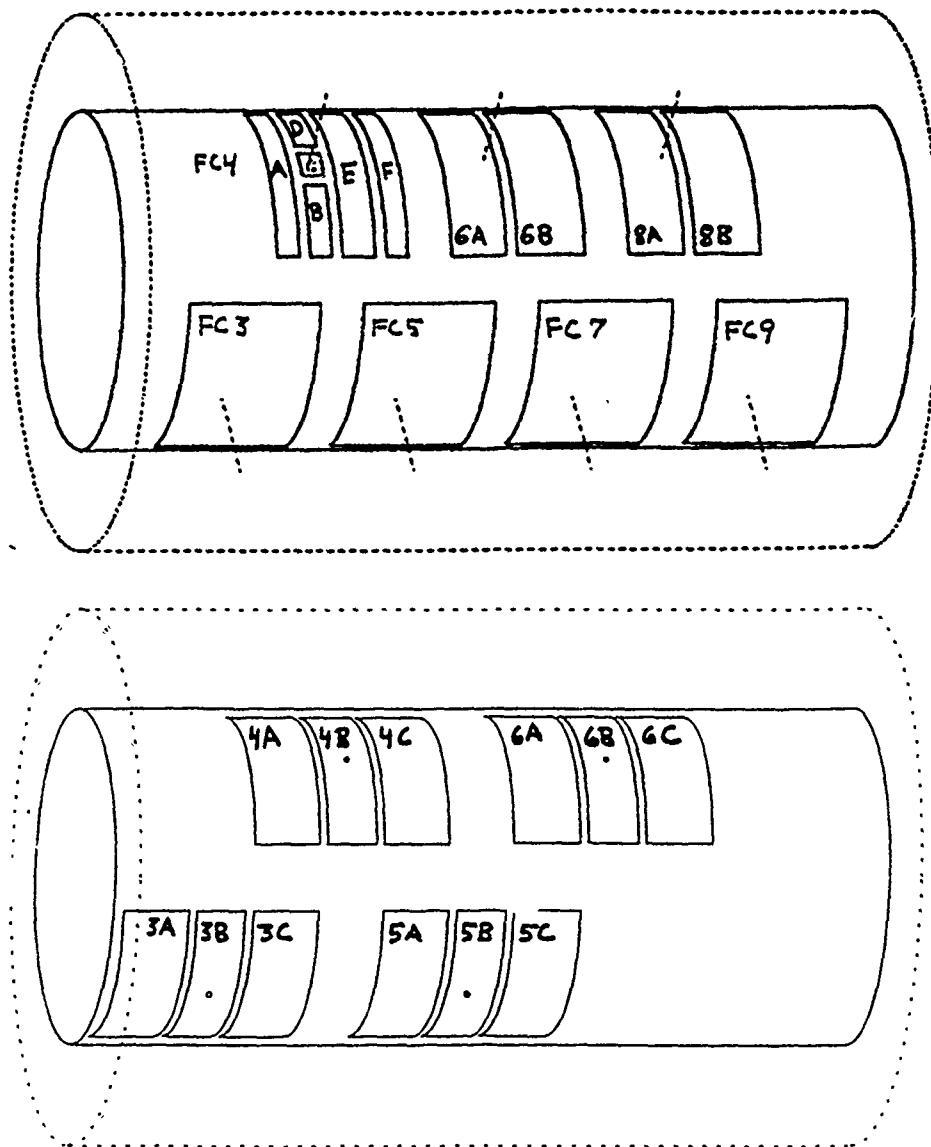


Fig. 2: First (top) and second (bottom) Faraday cup collector arrangements. Details of the three apertures used are shown at the bottom. Most of the data was taken with the first type.

Eighteen shots were taken with the second arrangement in Fig. 2. Here only four holes were used, FC3-6, but each had three collectors arranged axially.

The azimuthal orientation is shown at the bottom of Fig. 1. For some shots, flashboards 10 and 15, which were located directly opposite the cups, were disconnected. This had no significant effect on signals during shots but reduced the signals from flashboards alone. The locations of FC4B-C in the first arrangement are shown also.

The signals were calibrated by projecting the aperture sizes to 2.5 cm-long, 84 cm² area, axial sections of the cathode. They are expressed in amps/2.5 cm. The holes were measured with a magnifying glass, giving an areal uncertainty of about 15%.

In summing signals from multiple collectors, an attempt was made to account for the uncovered areas. On the first arrangement:

$$FC4MS \equiv 1.3 \times (FC4B + FC4C + FC4D)$$

$$FC4S \equiv 1.3 \times (FC4A + FC4MS + FC4E + FC4F)$$

$$FC6,8S \equiv 1.1 \times (FC6,8A + FC6,8B)$$

$$FCS \equiv FC3 + FC4S + FC5 + FC6S + FC7 + FC8S + FC9,$$

and on the second arrangement:

$$FC3,4,5,6S \equiv 1.1 \times (FC3 - -6A + FC3 - -6B + FC3 - -6C)$$

$$FCS \equiv FC3 + FC4 + FC5 + FC6.$$

Several shots were also taken with different constructions to study shorting of the cups. Those results are presented at the end.

Flashboard shots

Ten flashboard-only shots were taken with the first arrangement, the last four with flashboards 10 and 15 disconnected. With all flashboards connected, FC4B and C had similar amplitudes while FC4D was quite small. This may be indicative of flashboard-to-flashboard variation. FC4A and E were small, as were FC7-9. Thus there are few incoming ions with axial angles greater than 30 degrees. Typical signals from FC3-6 are shown at the top of Fig. 3. The signals have a double peak at about 1 μ s after the boards are fired. A third peak is observed about 1 μ s later, followed by a fourth peak about 2 μ s after that. At this time some of the collectors would sometimes go off scale. Of course, the cups are not quantitatively accurate at late times with flashboards alone (if indeed they ever are). The signals from FC3-5 were comparable

What is
T = 0 for FBS?

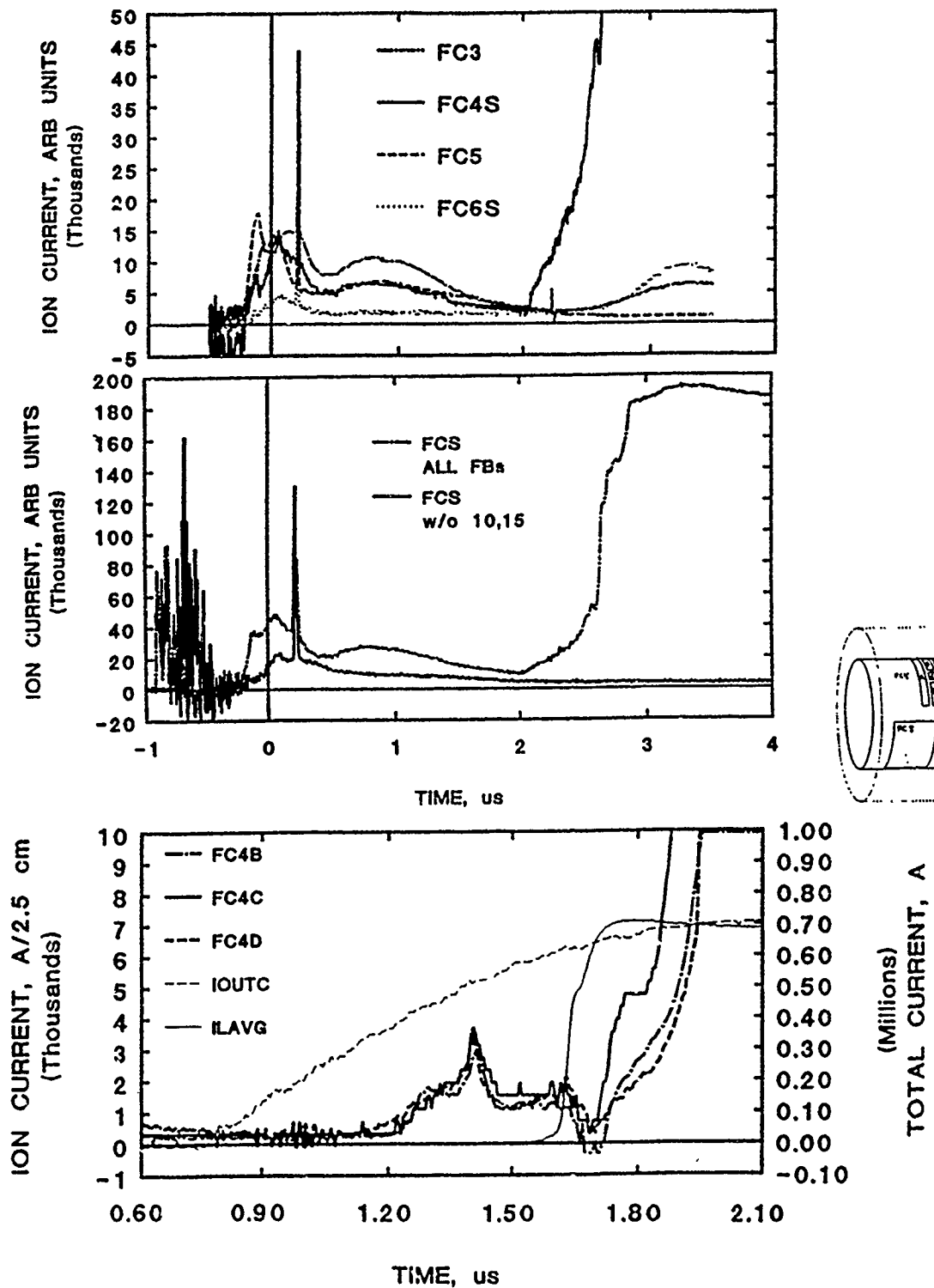


Fig. 3: (top) Summed signals from three apertures, and (middle) total summed signals for flashboard-only shots. The middle graph compares the signals with and without connecting the two boards directly opposite the apertures. (bottom) Typical data from azimuthally separated collectors. The generator (IOUTC) and load (ILAVG) current are shown for comparison, and are described by the right hand axis in Figs. 3-6.

while those from FC6 were smaller. The signals showed rather large variations, on the order of 100-150% for FC4B-D, 50-100% for FC4MS, 50% for FC3,4S,5, and 25% for FCS. With the two flashboards disconnected, the signals dropped by 2-3 \times and the later peaks went away. FC4B also went away, as might be expected (see Fig. 1). Typical waveforms of FCS, with and without the two flashboards, are shown in the second graph in Fig. 3.

In the second arrangement with all boards connected the results were similar. FC3-5B were several times larger than FC3-5A,C. FC6C was small and FC6A,B were negligible. FC3-5S were comparable, and the values of FCS were comparable to their values in the first arrangement. On two shots, boards 9, 10, and 11 were disconnected. In this case the first peaks from FC3 and 5 disappeared.

Azimuthal velocity distribution

On full shots with the first arrangement, the signals from FC4B, C, and D were quite similar in both shape and amplitude. Signals from a typical shot are shown in the last graph in Fig. 3. This implies an azimuthal ion velocity distribution of roughly ± 30 degrees. These signals were then summed, as stated above, as FC4MS.

Axial velocity distributions

Typical signals from the first arrangement of FC4 collectors are shown in Fig. 4. Again, the FC4 aperture was located in the center of the switch region. The signal from FC4A begins after the others. This occurred on all shots. Typically FC4MS and FC4E began at the same time, but on some shots FC4E came slightly earlier as seen on this shot. This is suggestive of a wave of ion current passing over the aperture toward the load. The signals peak at the same time. In general, except for the onsets, signals from each collector had the same waveshape. The relative amplitudes of signals from different collectors had a shot-to-shot variation of about 30%. The average values for both collector arrangements are used in the graph at the bottom of Fig. 4. This shows the angular distributions of ions in the plasma inferred from the relative collector signals. The width of each bar is given by the angular extent of the collector. The height h is given by the average relative peak amplitude divided by the angular extent and divided further by the average foreshortened area of the aperture: $h = I_p / \Delta\theta / \cos\theta_{av}$ where θ is the angle from the radial direction. Note that, as with POP, the ions have a broad distribution of axial velocities. On POP,

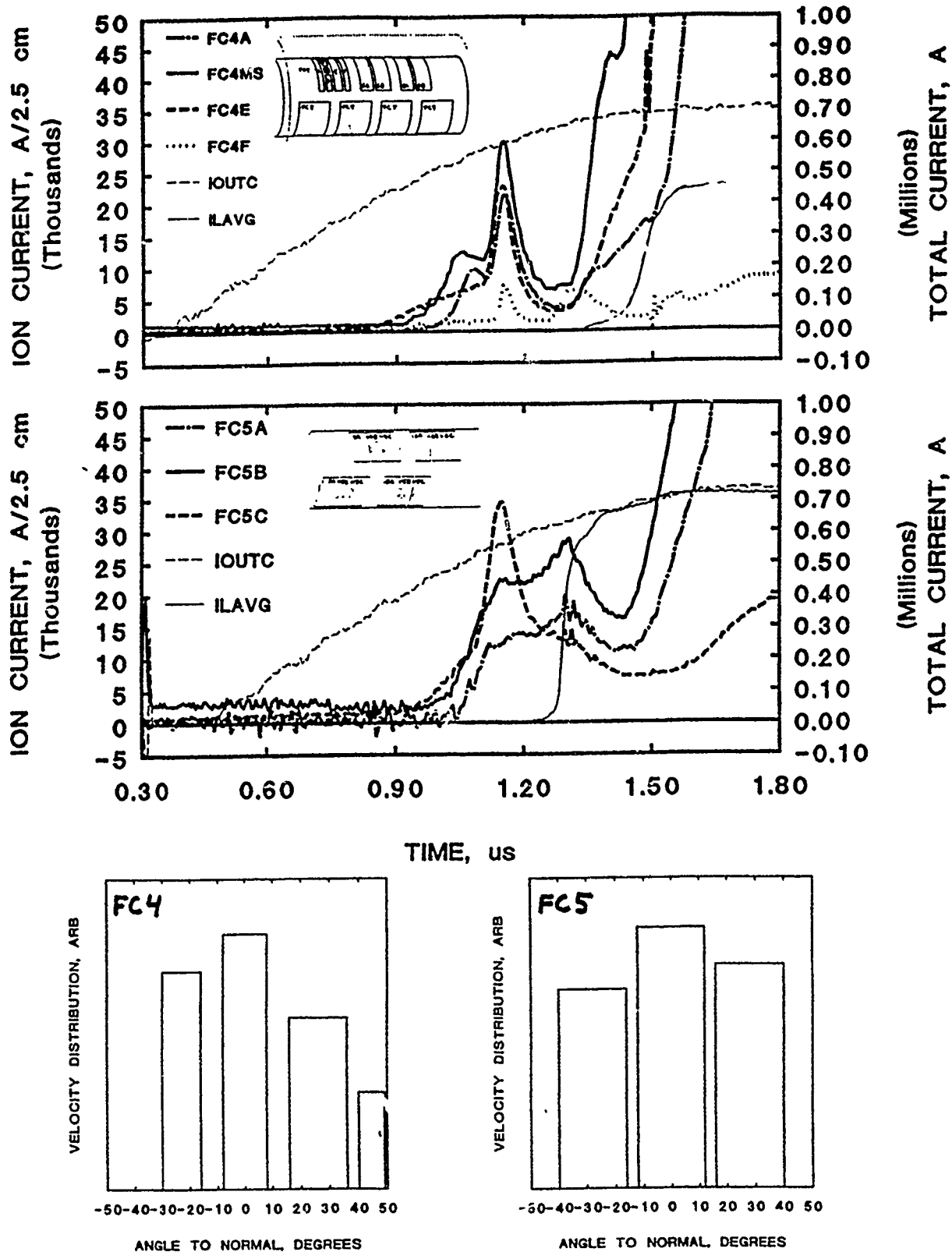


Fig. 4: Typical signals from axially separated collectors at aperture 4 (top) and 5 (middle). The inferred ion velocity angular distributions for both apertures are shown at the bottom. These are averages of all shots in the run for which data was available.

however, the distribution was biased toward the load whereas on Hawk the distribution at this location appears relatively symmetric.

Signals from FC3 in the second arrangement exhibited the same features and had the same average relative amplitudes, and thus the same inferred angular distributions, as those from FC4.

Typical signals from the FC5 collectors in the second arrangement are shown in the middle graph in Fig. 5. These signals had a peak toward the end of the conduction phase, often followed by a second peak at opening. For this aperture the relative signal amplitudes had a large (>100%) shot-to-shot variation and more variation in shape than at apertures 3 and 4. In general, at the first peak the inferred ion velocity distribution is biased in the forward direction, while later in time the distribution is biased toward the generator. Distribution plots for each peak are shown for this shot at the bottom of Fig. 5.

The relative signals from FC6 were similar to those from FC5. At first the inferred angular distribution is biased forward, while after opening it is biased toward the rear.

Signals from FC8 in the first arrangement consisted of a sharp spike at opening, followed by a later shorting. Typically the signal from FC8B was about twice as large as that from FC8A, indicating a strong bias in the forward direction.

Total aperture signals

By summing the collector signals as described above, the total current at each aperture location can be estimated. Sums for apertures 3, 4, and 5 are shown in Fig. 5. The most important features of these data are also seen in data from POP and all other Faraday cup studies: signals from each aperture peak and then decrease during the conduction phase, and the peaks occur successively beginning at the generator and moving to the load end of the switch. The exact shapes of these signals varied from shot to shot. An interesting feature, that is difficult to quantify, is that the waveshapes at different apertures were fairly well correlated. This is seen in comparing the first two shots in Fig. 5: on the first, the signals show a single peak with a "front porch," while on the second shot all signals show a double peak structure.

For shots with the same conduction time, signal timings were reproducible. Among shots with similar conduction times, the signal amplitudes had about a 30% variation, with a maximum difference of a factor of two. The average relative values of currents at apertures 3, 4, and 5 were about 5:8:9.

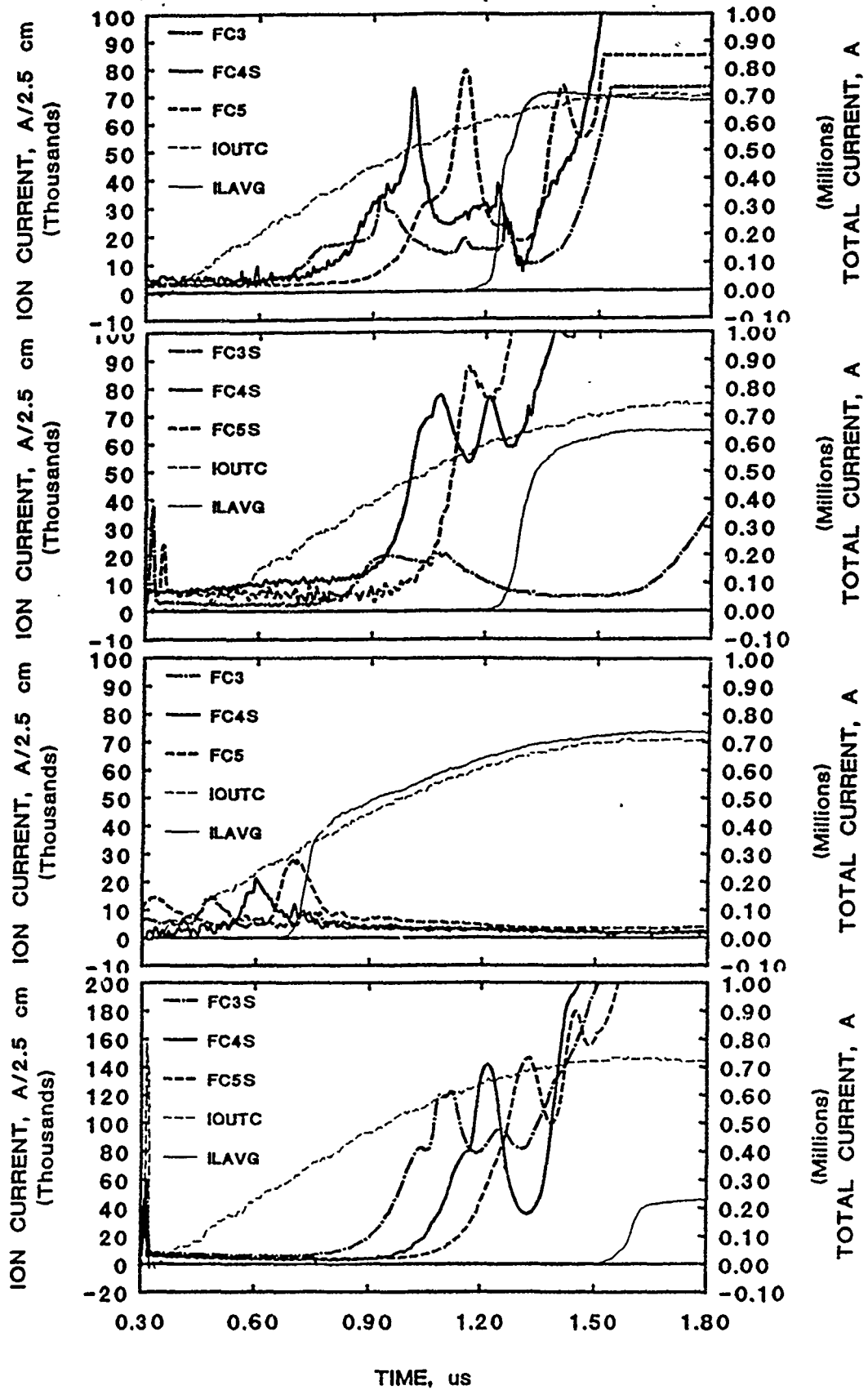


Fig. 5: Typical summed signals from apertures 3, 4, and 5. The bottom two represent extremes of conduction time in this work. Note the different units on the bottom graph.

The signals go off scale after or as the switch opens. The maximum absolute signal here was 50 V, but based on other shots the signals most likely went up to the 300 V bias. They remain off scale for over 10 μ s. In general, this shorting out happened more rapidly when the ~~when the~~ initial peaks were larger. On some shots it occurred during the conduction phase. This phenomena^{ON ?} complicates quantitative interpretation of the signals.

Signals from two more shots, at relatively short and long conduction times of 300 and 1150 ns, are also shown in Fig. 5. The data are qualitatively the same over the range of conduction times studied here.

Typical sums from aperture 6, located just beyond the initial switch region, are shown in Fig. 6. Signals from this aperture were about twice as large as those from aperture 5, and showed a larger shot to shot variation. They began toward the end of the conduction phase and often had subsequent peaks after the switch opened. At longer conduction times the signals peaked earlier relative to opening, as shown in the figure.

Signals from apertures 7-9 in the first arrangement consisted of spikes just before or during opening. At the longest conduction times the signals peaked during the conduction phase. Signals from the three apertures were closely spaced, with 10-40 ns delays. The amplitudes tended to increase with increasing conduction time. Typical data for two conduction times are shown in Fig. 6.

Total ion currents

By summing all the signals the total ion current can be estimated. The top graph in Fig. 7 compares the calculated total ion currents for an early conduction time shot and the previous flashboard test. The ion current does not exceed the injected flux until about halfway into the conduction phase. By the time of opening the ion current ^{composes} 5-10% of the total current, and during opening the ion current increases sharply to about half of the total. The second graph shows data from a typical conduction time. The ion current rises above the injected flux about halfway through the conduction phase. It increases with time to roughly a third of the total current just before opening. During opening there is a further increase to more than half of the total. The third graph shows data from a long conduction time shot. Here the total current rises to an unphysically large value during the shot as some of the collectors short out. Except at the shortest conduction times the ion current seems to persist

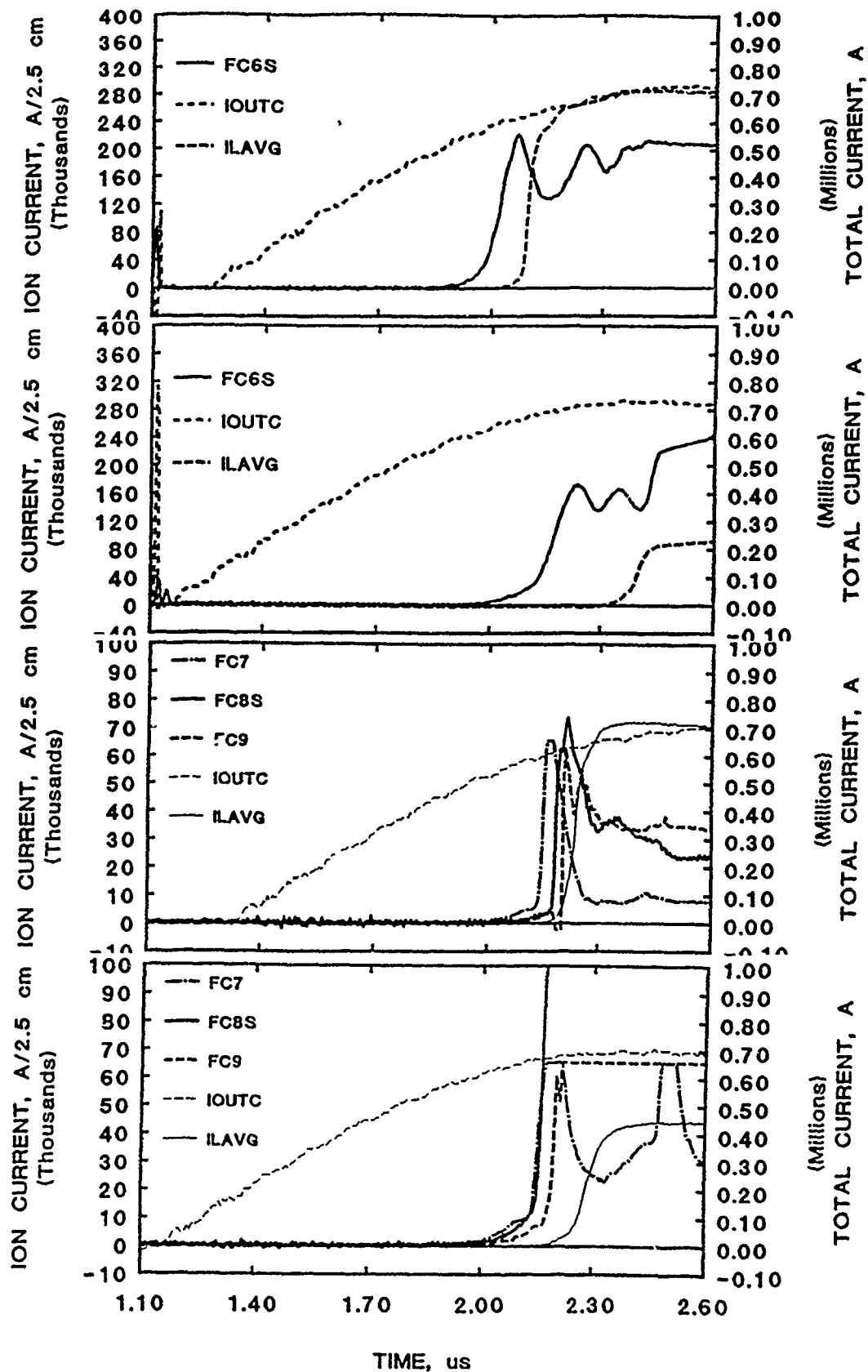


Fig. 6: Typical signals from apertures 6 (top graphs) and 7-9 (bottom graphs) for medium and long conduction times. Note the different units. At short conduction times, signals from apertures 6-9 occurred at the time of opening.

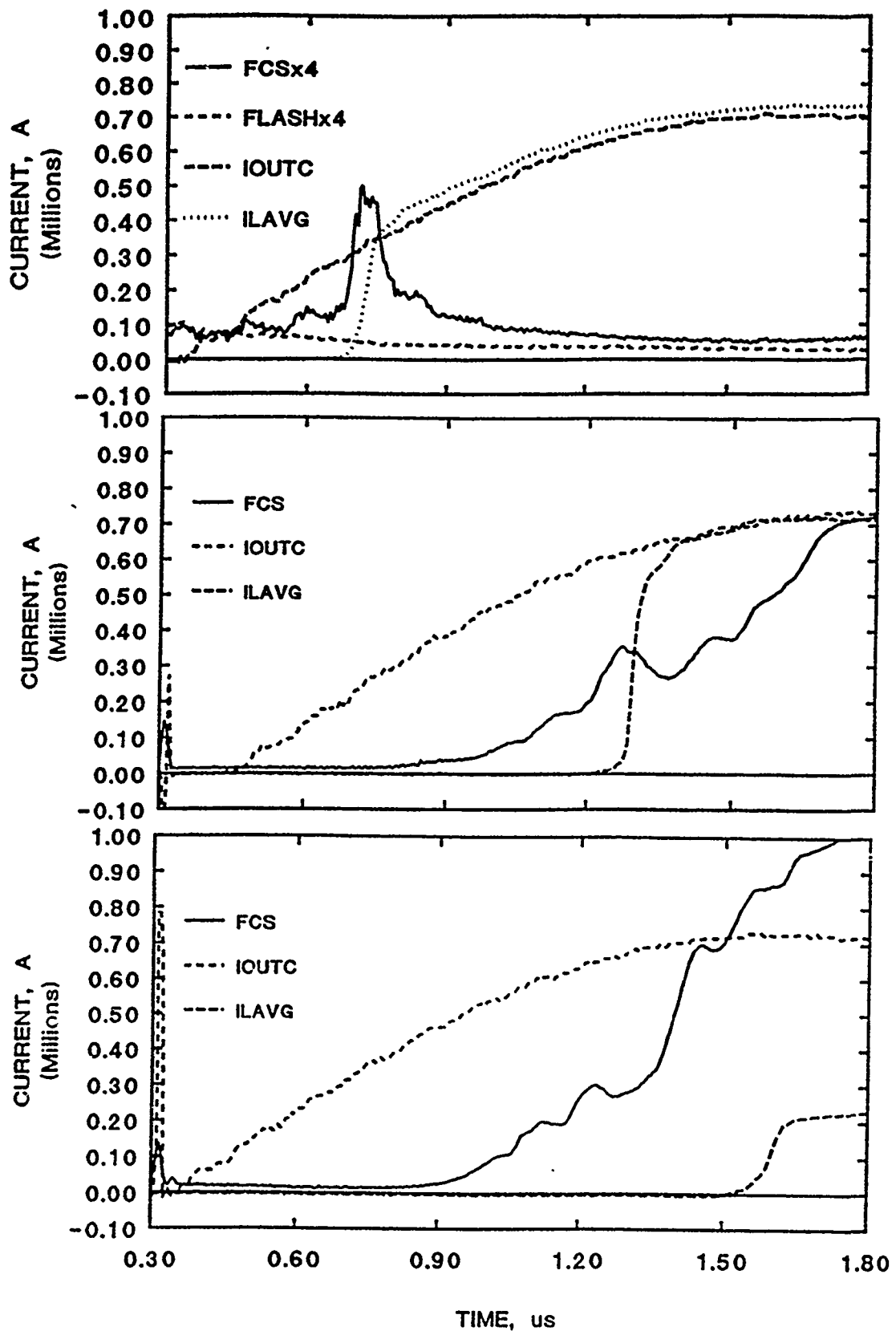


Fig. 7: Calculated total ion currents for shots at different conduction times. On the first graph the ion current from a corresponding flashboard-only shot is also shown, and the ion currents are shown magnified four times.

after opening, even though there is no net current through the switch, which is also unphysical.

Faraday cup variations

Several alternate constructions were tried in an effort to prevent the collectors from shorting out. Three shots were taken with a cathode having collimated apertures. These were 0.75 mm diam and 3.2 mm deep, as pictured at the bottom of Fig. 2. Shorting still occurred, even for collectors out of the direct line of sight which had very small signals, as shown in Fig. 8a. With other apertures the collectors out of the line of sight had small but finite signals.

On one of these shots the bias was left off. Fairly clean positive signals were observed at or after opening, as shown in Fig. 8b. This is interesting and may not be related to the apertures, as no other shots without bias were taken for comparison. Roughly equal signals were seen on the A, B, and C collectors for this shot, even though only the B collector was in the line of sight.

A few shots were taken with another collimating arrangement, also shown at the bottom of Fig. 2. Shorting out still occurred, but negligible signals were observed on the A and C collectors. This is compared with the small but finite signals observed from collectors out of the line of sight with the thicker holes. This indicates that some "bouncing" off the walls of the thicker holes may be occurring.

In another test, using the standard apertures, the cylinder upon which the collectors were mounted was reduced in diameter from 7.5 to 5 cm, doubling the collector-to-ground gap from 1.3 to 2.5 cm. Shorting out still occurred, but at least on one shot it was delayed, as shown in Fig. 8c. Reducing the bias to -100 V had no effect.

Summary

The incoming ions have a relatively large distribution, both axially and azimuthally, of incoming angles. This is larger than the distribution of ions when the flashboards alone are fired. The Faraday cup data show a wave of enhanced ion current propagating down the switch region toward the load. This is seen both in the timing of signals from different apertures and in the shift in angular distribution with time for given apertures. Signals from successive apertures peak and then decline at successively later times during the conduction phase. With time the distribution becomes biased toward the generator as if the region of enhanced current had passed beyond the aperture.

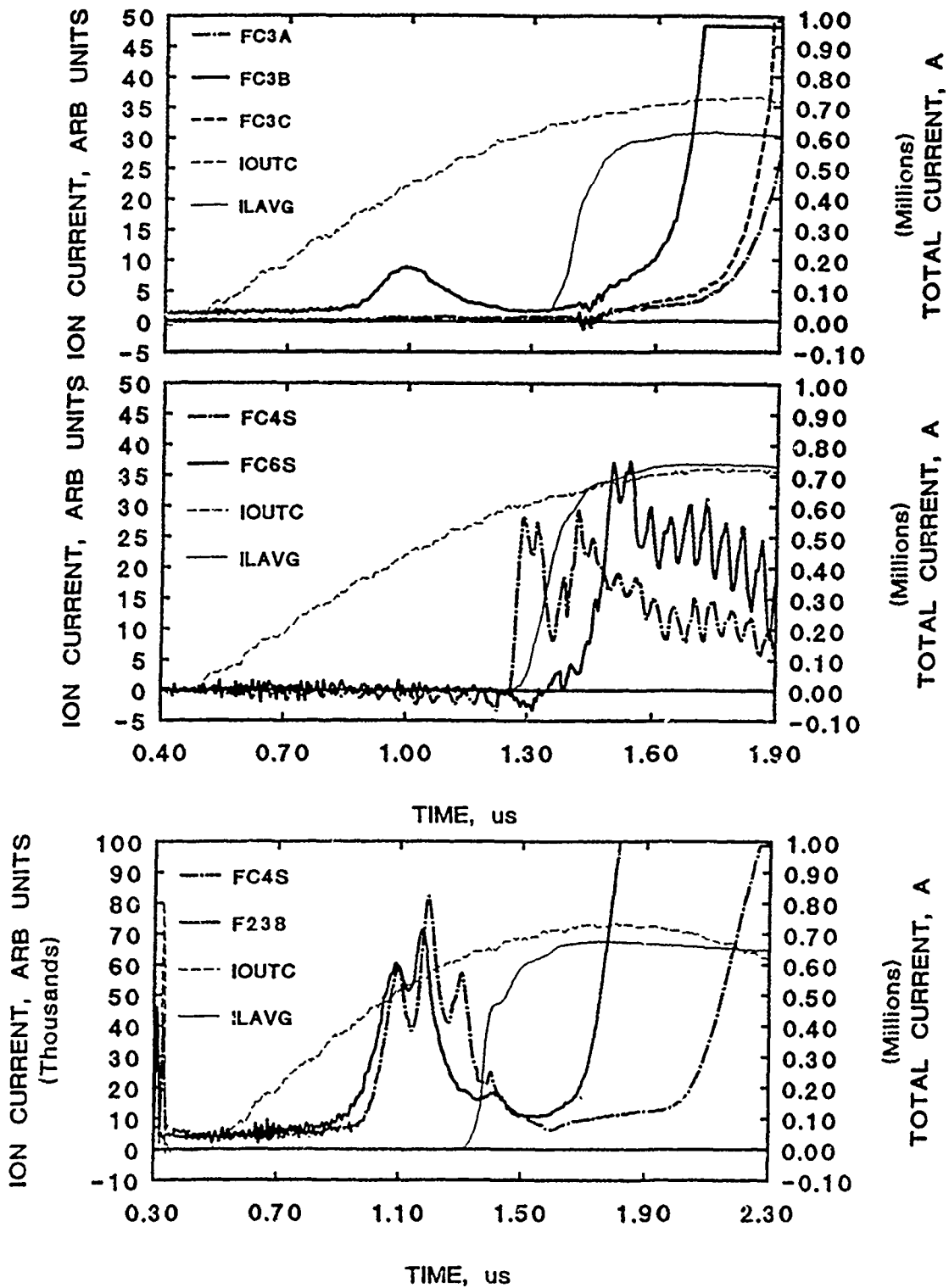


Fig. 8: Faraday cup variations. (top) Signals with collimated holes. (middle) Collimated holes with no bias. (bottom) Larger collector-to-ground distance. The signal here is compared with a standard shot.

Ion current flows to the cathode in the region between the initial switch region and the load at or just before the time of opening, depending on the conduction time. The signal timings indicate a fast penetration in this region, which could be explained by a creep/ejecta plasma less dense than the initial plasma.

The ion current is evidently a much larger fraction of the switch current than that given by the bipolar formula. The peak ion current densities measured here exceed 1 kA/cm^2 . This level of current density could be supplied by a drifting plasma with parameters of $5 \times 10^{15} / \text{cm}^3$ and $1-2 \text{ cm/m} \text{ s}$. Thus, the large ion currents are not necessarily indicative of local opening during the conduction phase.

All of the above was also observed in earlier experiments on POP.

Late time shorting of the cups prevents measurement of ion current after opening. Several attempts to prevent this were unsuccessful. Applied magnetic fields might help. An improved Faraday cup, coupled with interferometric density measurements, would be very useful in probing microsecond PEOS dynamics.

What about secondaries?

AXIALLY RESOLVED PEOS MEASUREMENTS AT MICROSECOND CONDUCTION TIMES

D. D. Hinshelwood,* R. J. Comisso, P. J. Goodrich,*
J. M. Grossmann, J. C. Kellogg, P. F. Ottinger, and B. V. Weber.

Plasma Physics Division
Naval Research Laboratory, Washington, DC 20375-5000

* Jaycor

Abstract Plasma erosion opening switch conduction phase studies, at microsecond conduction times and both 200 and 800 kA current levels, are reported here. Similar data were obtained from both experiments. A current channel is seen to propagate toward the load, and this channel is associated with an increased ion current and cathode and switch plasma luminosity. There is evidence of local opening during the conduction phase, which may be related to hydrodynamic effects.

INTRODUCTION

The conduction phase of the plasma erosion opening switch (PEOS) is of particular interest at microsecond conduction times because of the observed reduction in conduction current (relative to that under the same conditions at shorter conduction times) and the predicted large hydrodynamic effects. The work here consists of PEOS conduction phase studies with particular emphasis on the variations of measured quantities along the switch length.

The experiments were performed on two generators: POP and Hawk, with short circuit loads on each. Hawk is based on a fast Marx developed by Physics International. Typically operated at 640 kV, it drives 700 kA through the switch via a roughly 700 nH upstream inductance. The Hawk experimental arrangement, which is representative of both experiments, is shown in Fig. 1. Plasma is supplied by 18 flashboards, with delays of 1–2 μ s. The cathode and anode diameters are 11 and 18 cm, respectively. The anode rods are masked off outside of the 8 cm long switch region, which is located about 15 cm before the short-circuit load. Diagnostics include dB/dt loops, Faraday cups, and collimated fiber optic light probes.

POP is a small, 50 kV capacitor bank which drives about 200 kA through the switch in 800 ns. The cathode and anode diameters are 5 and 14 cm, and plasma is supplied by two flashboards. Diagnostics include dB/dt loops, Faraday cups, framing photography, and spectroscopy. Some of these results were reported at the 1989 Opening Switch Workshop in Novosibirsk.

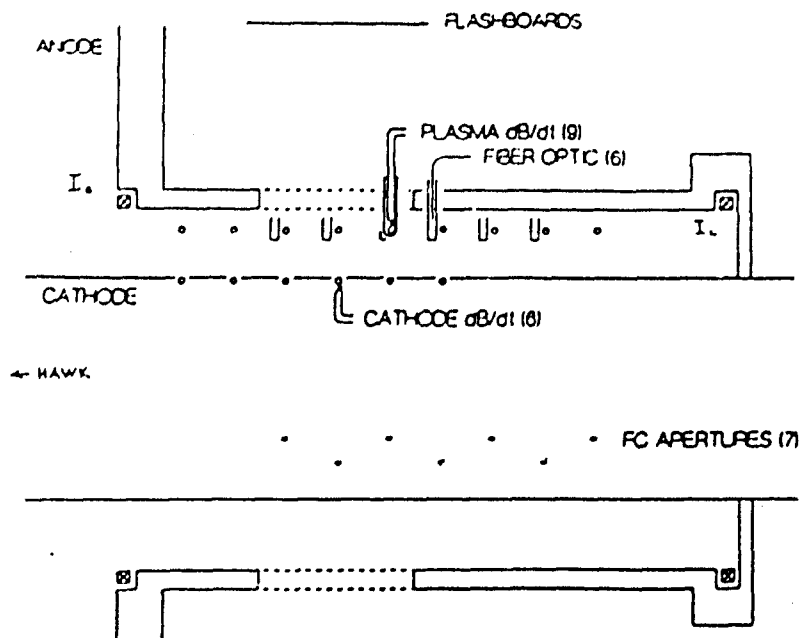


Figure 1: Hawk experimental arrangement.

dB/dt PROBE RESULTS

Arrays of dB/dt probes were used on both experiments to diagnose current flow in the switch. The probes were located both in the plasma and in the cathode surface. In the latter case it is assumed that the field penetrates the explosive emission cathode plasma. While simple estimates suggest that this is reasonable, it remains an open question. Probe data from both experiments are quite similar, and current profiles inferred from Hawk data are shown for three times in Fig. 2a. The "plasma" data was taken with the loops about 1 cm in from the anode, and opening began at 800 ns on this shot. Penetration occurs faster in the plasma than on the cathode. POP signals from probes at different radii in the plasma begin simultaneously, indicating that the current front is primarily radial. Until opening, current is still localized in and just beyond the switch region; i. e., the switch does not open by axial convection. After opening begins diamagnetic plasma currents are seen between the switch and the load. The probe results point to a general picture of current flow, which is shown in Fig. 2b for the time just before opening. This picture differs from the results of experiments on the Double generator at the Tomsk Institute of Nuclear Physics (Ananjin, et al, this conference) in that the axial segments of the current streamlines are much closer (<1 cm) to the cathode in our experiments. One possible reason for the discrepancy is that the Double experiments had a larger radial gap.

The probe measurements resemble those at short conduction times. However, the plasma density is estimated, based on microwave measurements and $\vec{j} \times \vec{B}$ calculations, to be in the 10^{14} – 10^{15} range, which would predict a conduction current 1–2 orders of magnitude greater than that observed.

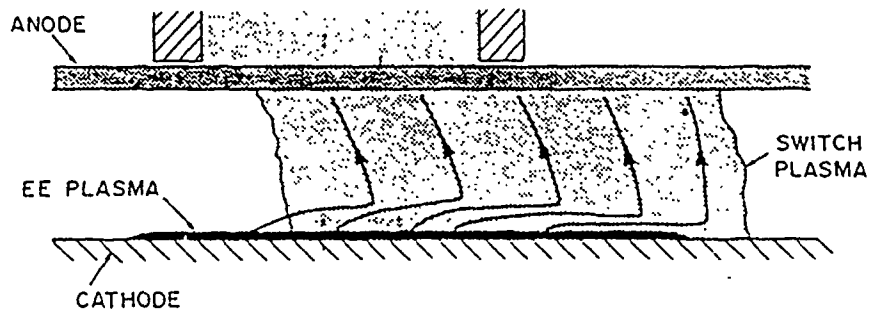
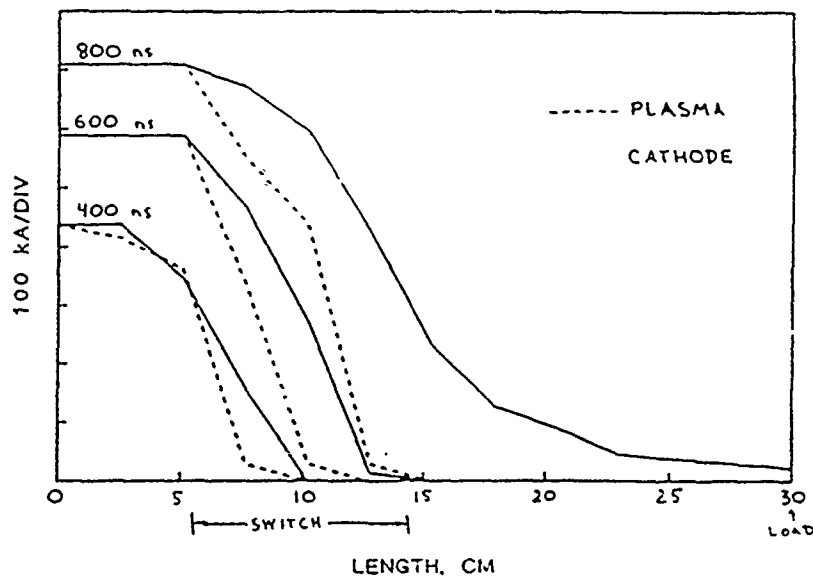


Figure 2: (a) Current penetration on Hawk. (b) General picture of current flow, at the time just before opening.

FARADAY CUP MEASUREMENTS

Two Faraday cup arrays were used on POP: five axially spaced cups, and a single hole with five axially spaced collectors to diagnose the angular distribution of the incoming ions. The Hawk arrangement employed seven holes, and three of these had multiple collectors. In this case information about the ion azimuthal as well as axial distributions was obtained. The cups were operated at a -300 V bias; the signals showed little change from -100 to -400 V.

Signals from a Faraday cup and cathode and plasma dB/dt probes, all located in the center of the switch region on Hawk, are shown in Fig. 3a. A large increase in ion current is associated with current penetration; the ion current later decreases. Signals from other axial locations in the switch region show the same behavior with correspondingly different timings. No ion current is registered downstream of the switch until opening begins. All of these results were also seen on POP.

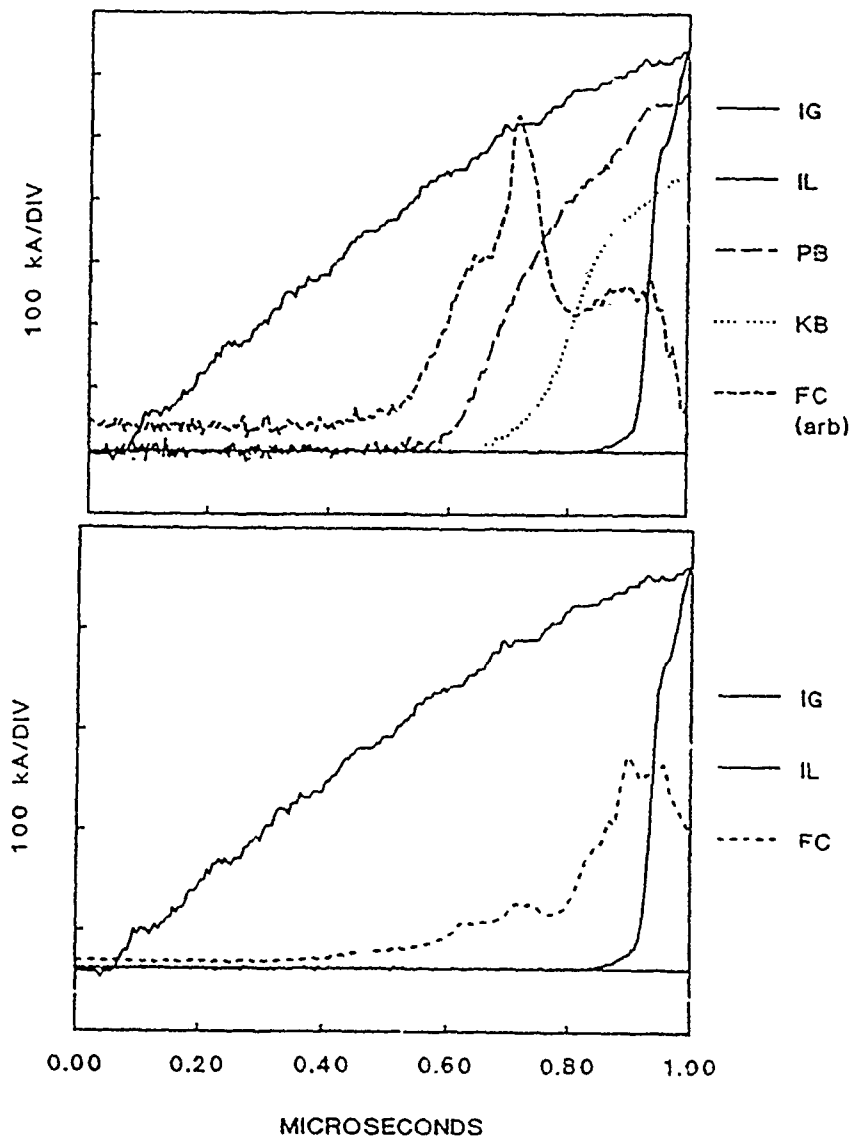


Figure 3: (a) Signals from a Faraday cup (FC, in relative units), and plasma (PB) and cathode (KB) probes, in the center of the switch region on Hawk. Generator (IG) and load (IL) currents are also shown. (b) The total calculated ion current (absolute units).

These measurements show a propagating channel of enhanced ion current, which may be indicative of local enhanced erosion and opening during the conduction phase.

Signals from multi-collector apertures on Hawk indicate an azimuthal velocity distribution of roughly $\pm 30^\circ$. The axial distribution on POP has a similar width and is strongly biased toward the load, as would be expected for magnetically deflected ions. In the center of the switch region on Hawk, the distribution is biased slightly toward the generator. The current density and magnetic field are twice as large on Hawk, and one might expect even more bending toward the load. Perhaps the "reverse" bending is due to an axial electric field or an altered ion density distribution caused by the greater hydrodynamic forces. At downstream locations the ion velocity distributions are biased toward the load on both experiments. In all cases the distributions do not change appreciably with time.

On both generators the calculated total ion current is a large fraction of the total switch current, as shown for Hawk in Fig. 3b. The implied ion current ratio is significantly greater than the bipolar value. Many of the cups tend to short out after the switch opens, which raises questions about their quantitative accuracy. Further measurements with less sensitive cups are planned.

VISIBLE LIGHT MEASUREMENTS

Six collimated fiber optic cables viewed the cathode and part of the switch plasma at different axial locations on Hawk. The signals resembled those from Faraday cups, showing successive sharp peaks associated with current penetration. Light and plasma dB/dt signals from the center of the switch are shown in Fig. 4. An Imacon 790 framing camera imaged the switch region on POP. A luminous channel, consisting of spokes between the cathode and the anode rods, is observed. This channel propagates along the switch region, approximately correlated with current penetration. At opening, light emission begins simultaneously from a 10–20 cm length of the cathode beyond the switch region.

SPECTROSCOPY

Time integrated measurements on POP showed the existence of H, Cl-IV, and (aluminum) cathode and (brass) anode constituents. Time resolved measurements of the Al III line at 3610 Å, indicative of cathode plasma formation, were taken on POP. Light is observed to begin later at locations further down the switch region. Light is not seen beyond the switch region until

opening. This is consistent with the total visible light framing photography. A sharp burst in emission from a highly excited state of CIV is seen in the plasma during the conduction phase, at about the time of current penetration. This emission could be caused by plasma heating or by electrons emitted from the cathode. Future measurements will spectrally resolve the fiber optic signals in an attempt to correlate cathode plasma formation and plasma heating with the other probe measurements.

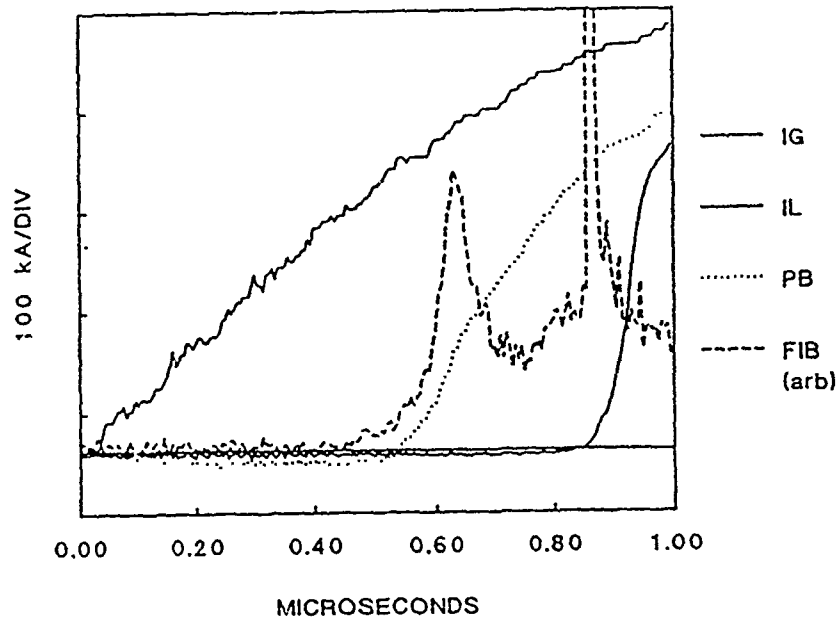


Figure 4: Signals from the fiber optic (FIB, relative units) and plasma probe (PB), in the center of the switch region on Hawk.

CONCLUSIONS

The data provide important information about the axial dependence of switch phenomena: a current channel propagates through the switch, and this channel is associated with locally enhanced ion current, cathode plasma formation, and switch plasma luminosity. Opening is correlated with this channel reaching the end (or somewhat beyond) the initial switch region. The pattern of current flow is similar to that at short conduction times although the estimated plasma density is very much greater. The apparent local opening of the switch during the conduction phase may be caused by radial hydrodynamic motion and may be one limitation on conduction current. The data also show the presence of plasma between the switch region and the load. With sufficient plasma density, shunt current through this plasma could reduce the effective opening rate and may be a factor limiting switch performance.

B90

PLASMA EROSION OPENING SWITCH OPERATION IN THE 50 ns - 1 μs CONDUCTION TIME RANGE

B.V. Weber, R.J. Comisso, G. Cooperstein, P.J. Goodrich,*
J.M. Grossmann, D.D. Hinshelwood,* J.C. Kellogg,
D. Mosher, J.M. Neri, and P.F. Ottinger

Plasma Physics Division, Naval Research Laboratory
Washington, DC 20375-5000 USA

Abstract. Results of PEOS experiments are examined where the conduction time varies from 50 ns to 1 μs. Conduction current scaling is proportional to plasma density in the 50 ns conduction time range, based on interferometry. Far higher density is required to conduct for 1 μs, and the scaling is less than linear in this regime. The difference between the two cases may be explained by different physical mechanisms that determine the conduction limit: in the 50 ns range, conduction ends when an emission limit is reached; in the 1 μs range, plasma distortion and displacement by hydrodynamic forces is proposed to limit conduction. These "emission-limited" and "hydro-limited" conduction regimes can be described by a simple plot applicable to all PEOS experiments.

INTRODUCTION

Plasma Erosion Opening Switch (PEOS) experiments have been performed in many laboratories, with various generators as drivers. The required conduction time depends on the generator, and generally is about 50 ns for "conventional" water-line generators, and about 1 μs for newer "inductive" generators. Successful switching results have been obtained in both cases.

One example¹⁾ of the 50 ns conduction time PEOS on a high power conventional generator is shown in Fig. 1. A PEOS configuration using three flashboards on Gamble II at NRL is diagrammed

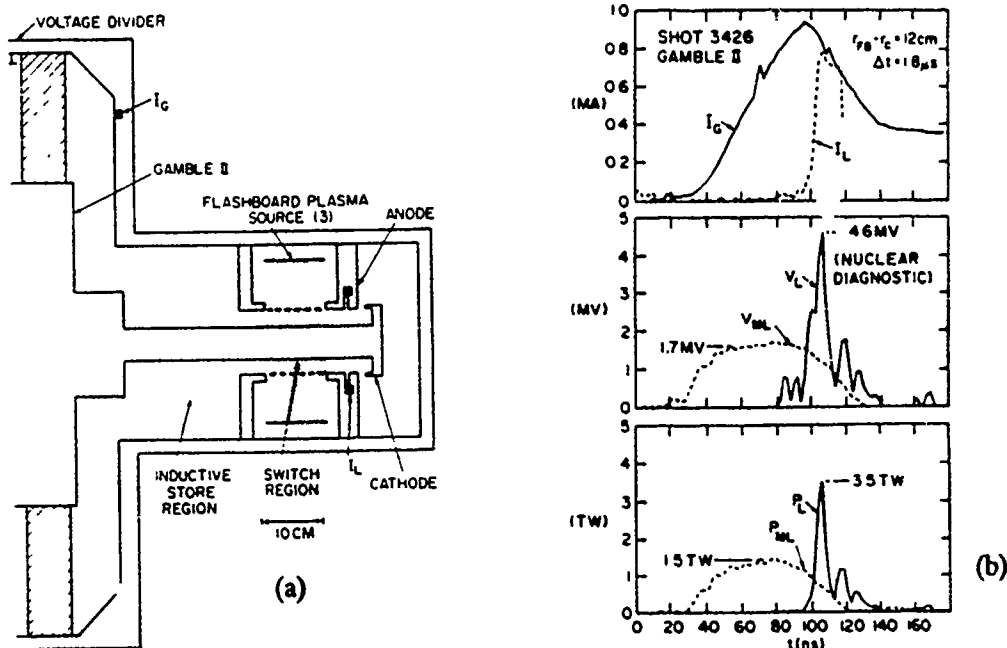


Fig. 1 Gamble II PEOS experiment (a) Setup (b) Measured load (I_L , V_L , P_L) and ideal matched load (V_{ML} , P_{ML}) data.

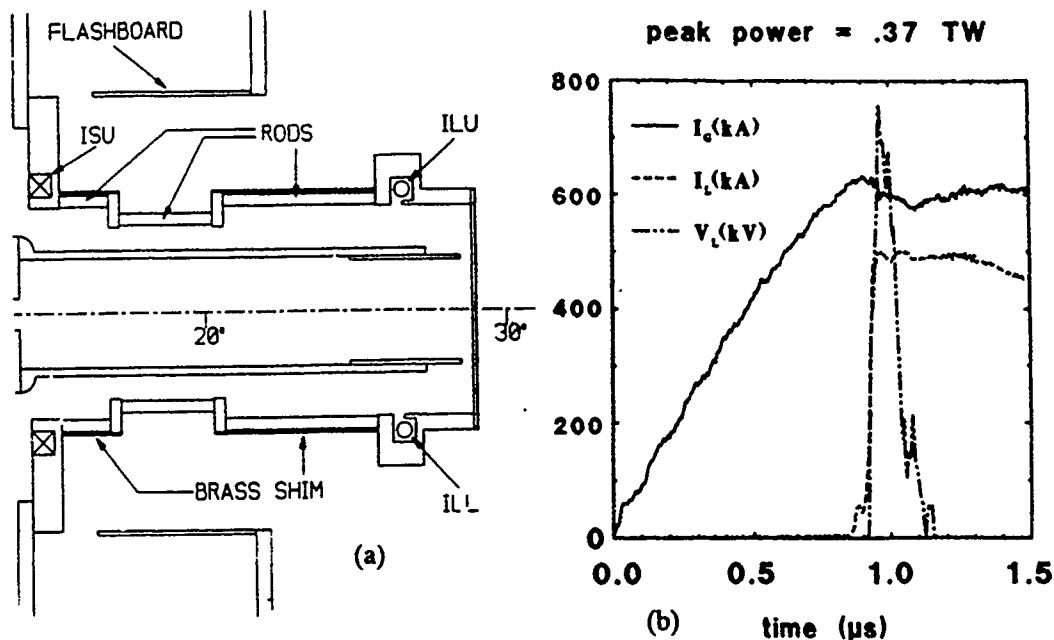


Fig. 2 Hawk PEOS experiment (a) Setup (b) Generator (I_G) and load current (I_L) and voltage (V_L).

in Fig. 1a, and experimental results are shown in Fig. 1b. On this shot, the PEOS conducts the current for 60 ns as it rises to 900 kA. Rapid switching then occurs, resulting in a peak load voltage of 4.6 MV. The peak load power, 3.5 TW, is higher than the ideal matched load value, 1.5 TW, by a factor of 2.3.

An example of the 1 μs conduction time PEOS is shown in Fig. 2. The "Hawk" generator at NRL uses a fast, high current Marx bank to drive a PEOS. The PEOS configuration using 18 flashboards is shown in Fig. 2a. Data from a high power shot are shown in Fig. 2b. The generator current is conducted by the injected plasma during its rise to 650 kA in 1 μs . Most of this current is rapidly switched into the diode load, generating a load voltage of 750 kV and 0.37 TW peak power.

The examples in Figs. 1 and 2 may be compared; the stored energy (200 kJ) and generator current are about the same in both cases. The energy dissipated in the load is about the same (40 kJ). The difference is the peak power and pulse width, which differ by a factor of ten -- ten times higher power and ten times smaller pulse width for the case of 50 ns conduction time. It is important to understand the difference in basic physics in these different conduction time ranges, especially to exploit the PEOS for higher power generation in the 1 μs conduction time range. The remainder of this paper will examine part of this difference in physics, the dependence of conduction current on plasma density in the 50 ns and 1 μs conduction time ranges.

50 ns CONDUCTION TIME RANGE

Two PEOS experiments in the 50 ns conduction time range will be used to illustrate scaling with plasma density. The first example is Gamble I at NRL. In this case, the generator current rises to 250 kA in 70 ns. The plasma density is varied by changing the number of guns, the voltage on the capacitor bank driving the guns, and the time delay before the start of the generator current. Peak switch current is plotted vs. time delay in Fig. 3a for two different plasma sources, 3 guns at 15 kV and 12 guns at 25 kV. The conduction current is higher for the high density plasma source (12 guns). The average electron density was measured for these sources in the actual experimental

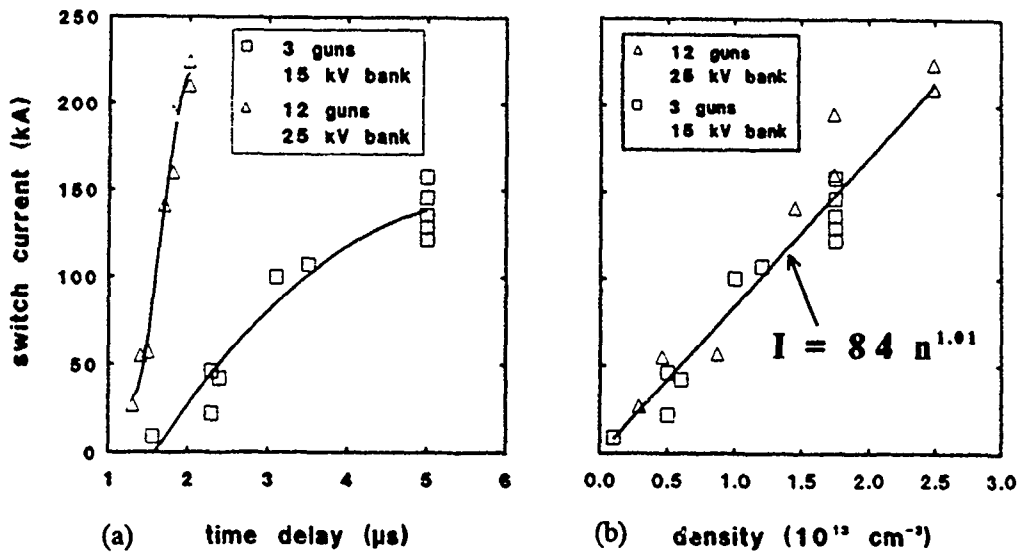


Fig. 3 Gamble I conduction current vs. (a) time delay and (b) density, for different plasma sources.

configuration, but without firing the generator, using a 140 GHz microwave interferometer. The switch current is plotted vs. the initial electron density in Fig. 3b. The switch current is directly proportional to the initial density, with data from both sources collapsing to the same fitting curve.

The second example in the 50 ns conduction time range is the MIP² (Magnetically Injected Plasma) configuration used on PBFA II at Sandia. In this configuration, plasma is injected by flashboards, using a slow magnetic field to direct the plasma into the transmission line gap. The conduction current depends on the strength of the magnetic field and on the time delay. This is plotted in Fig. 4a, where the horizontal axis, slow coil flux, is proportional to the slow magnetic field strength. The plasma density was measured in the experimental configuration in a separate vacuum chamber. The conduction current is plotted vs. density in Fig. 4b. The data points fall on a straight line that intercepts the y-axis near the origin. This suggests that the conduction current depends only on the initial density, where the density is the result of time delay and magnetic field strength.

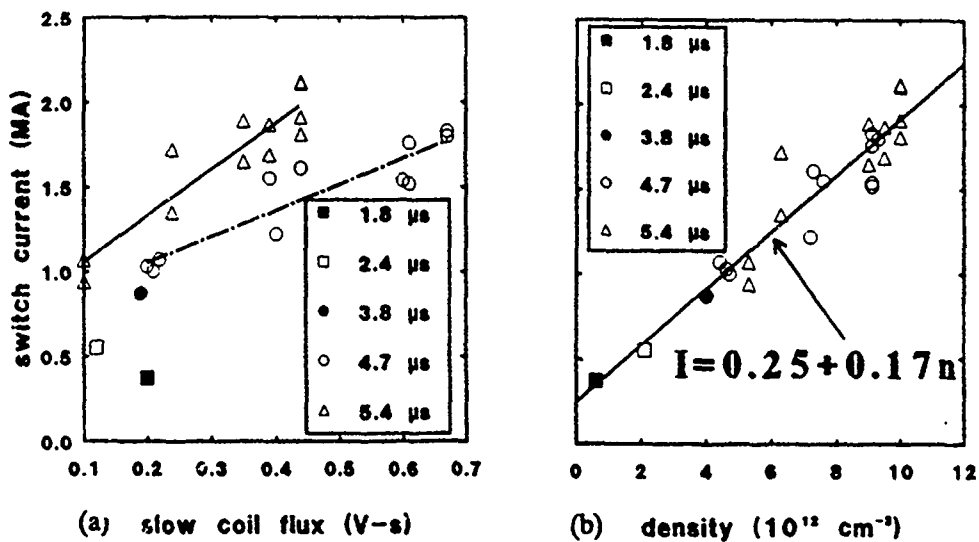


Fig. 4 MIP switch current vs. (a) timing and slow field and (b) density.

Expt.	r	l _o	I/n	J/n
Gamble I	2.5	10	84	.54
PBFA II	20	20	1700	.68

Table I. Short conduction time scaling: cathode radius r(cm), plasma length l_o(cm), conduction current I(kA), plasma density n(10¹³ cm⁻³) and average current density J(kA/cm²)=I/(2π r l_o).

The Gamble I and PBFA II experiments differ in current magnitude, plasma injection scheme and conduction area, however, the average current density, $J = I/(2\pi r l_o)$, at switching is proportional to the density with about the same proportionality constant. This is illustrated in Table I. These results may be generalized for all short conduction time experiments as:

$$J \text{ (kA/cm}^2\text{)} \approx 0.6 \times n \text{ (10}^{13} \text{ cm}^{-3}\text{)} \quad (1)$$

A possible explanation for this scaling has been given before,³⁾ that is, the current is limited by bipolar emission from the cathode, directly proportional to the plasma density. The bipolar limit can be expressed as a limit on the average current density, $I/(2\pi r l_o)$,

$$J_{BP} = (M_i/Zm_e)^{1/2} n_e e v \quad (2)$$

where M_i (m_e) is the ion (electron) mass, Z is the ion charge state, n_e is the electron density, e is the electronic charge, and v is the ion collection speed at the cathode. Assuming the plasma is predominately composed of C^{++} ions, the empirical relation, Eq. 1, is reproduced by Eq. 2 if $v = 3.5$ cm/ μ s. This velocity is about $3 \times$ smaller than the measured plasma velocity (10 cm/ μ s), but is higher than the ion sound speed (about 1 cm/ μ s), therefore the ion collection speed is in the correct range for these plasma sources.

1 μ s CONDUCTION TIME RANGE

Hydrodynamic displacement of the switch plasma during conduction makes the simple scaling of Eq. 1 impossible at μ s conduction time. The simplest measure of plasma motion is the center-of-mass displacement in the axial direction that results from the magnetic pressure difference when no current is flowing on the load side of the plasma. This is illustrated in Fig. 5a. The displacement is greatest at the center conductor, and is given by:

$$\Delta z = \frac{\mu_o Z}{8 \pi^2 r^2 l_o M_i n_e} \iint I^2 dt^2 \quad (3)$$

For Gamble I and PBFA II, the plasma displacement during conduction is negligible, $\Delta z < 1\text{cm} \ll l_o$. For the Hawk experiment (Fig. 2), the current rises to about 700 kA in 800 ns. Assuming Eq. 1 is also valid for this case, a density of 5×10^{13} cm⁻³ is predicted. Using this density in Eq. 3, the plasma displacement would be 400 cm, far higher than the estimated displacement based on magnetic probe

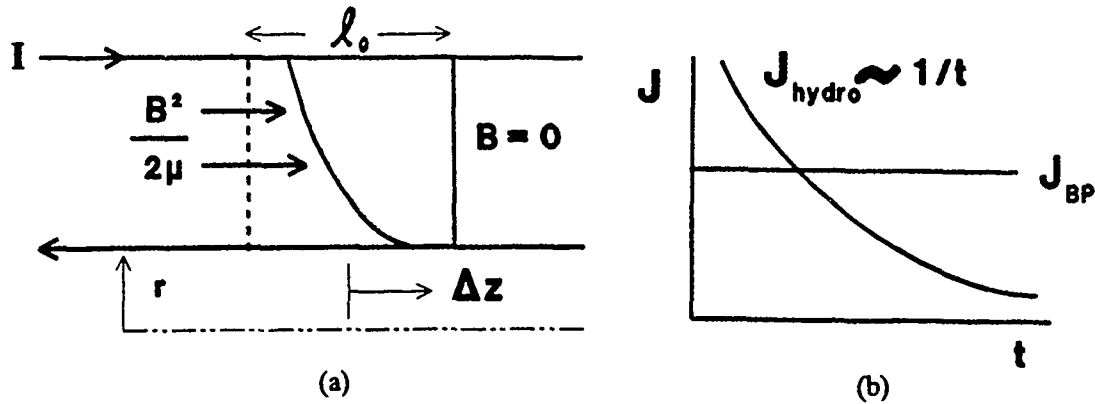


Fig. 5 (a) Axial displacement of plasma by magnetic pressure. (b) Switching thresholds for emission- and hydro- limits.

measurements⁴) that imply switching before the plasma displacement exceeds half of the switch length, about 4 cm.

The limited plasma displacement during conduction indicates that the plasma density in Hawk is at least $100\times$ higher than predicted by Eq. 1, or $n_e \geq 5 \times 10^{15} \text{ cm}^{-3}$. Several observations support this. First, a larger number of flashboards (18) are required to conduct the Hawk current, compared to the number (3) used in Gamble II for similar conduction current. Second, density measurements with the microwave interferometer indicate that the density is $\gg 1 \times 10^{14} \text{ cm}^{-3}$, the limit of the measurement.

Setting $\Delta z = l_0/2$ in Eq. 3 defines a "hydro-limit" for conduction:

$$J_{hydro}^2 \tau^2 = \frac{12 M_i n_e}{\mu_o Z} \quad (4)$$

where τ is the conduction time, $\mu_o = 4\pi \times 10^{-7} \text{ H/m}$, and a linear current rise is assumed for simplicity. The conduction limits of Eqs. 2 and 4 are compared in Fig. 5b, for a given plasma density. The generator current rises from the origin in this plot and intersects J_{BP} or J_{hydro} , depending on the slope of $J(t)$.

Hydro-limited conduction, as described by Eq. 4, predicts scaling with density that is less than linear. For the case of $J(t) \propto t$, $J^2 t^2 \sim J^4 \Rightarrow J \propto n^{1/4}$. In the absence of a direct density measurement, this scaling is tested on Hawk by varying the average plasma density by changing the number of plasma sources, shown in Fig. 6a. The density at opening is related to the time delay between the flashboard driver current, I_{FB} , and the load current, I_L , shown in Fig. 6b. The average density is then proportional to the number of flashboards at a given time delay. Results of this experiment are shown in Fig. 7a, where peak switch current is plotted vs. time delay for shots using 3, 6, 9 or 18 flashboards. It is immediately evident that the scaling is less than linear. The data points in Fig. 7a are fit by quadratic polynomials. The ratios of these polynomials are plotted in Fig. 7b. For comparison, the square root and fourth root of the density ratio is shown on the right side. The measured switch current ratio is close to the fourth root of the density, as predicted by the "hydro-limit" of Eq. 4. The ratio obtained for 18 and 3 flashboards increases as the delay time decreases. This may be the result of the small conduction times in these cases where, eventually, scaling proportional to density is expected.

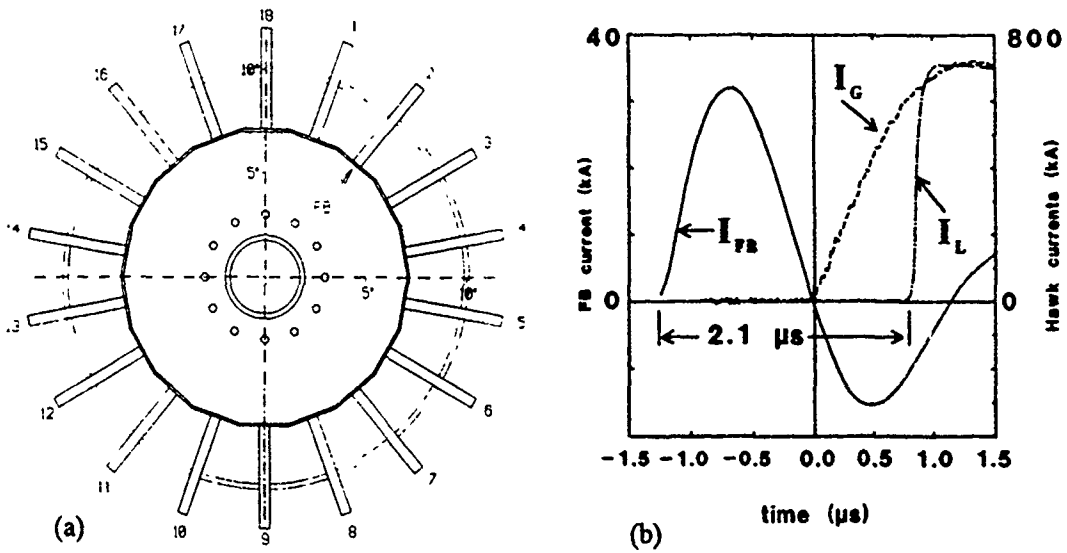


Fig. 6 (a) Hawk flashboard configuration and (b) timing for density scaling experiment.

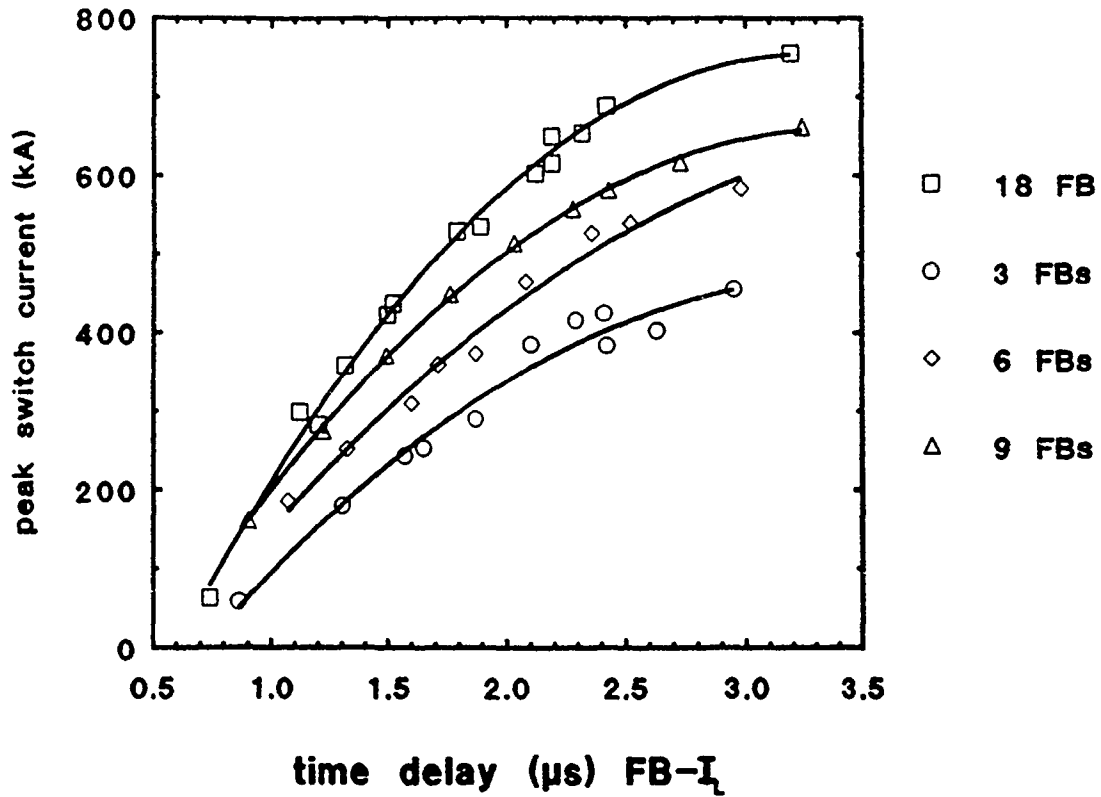


Fig. 7 (a) Conduction current vs. time delay for different number of flashboards.

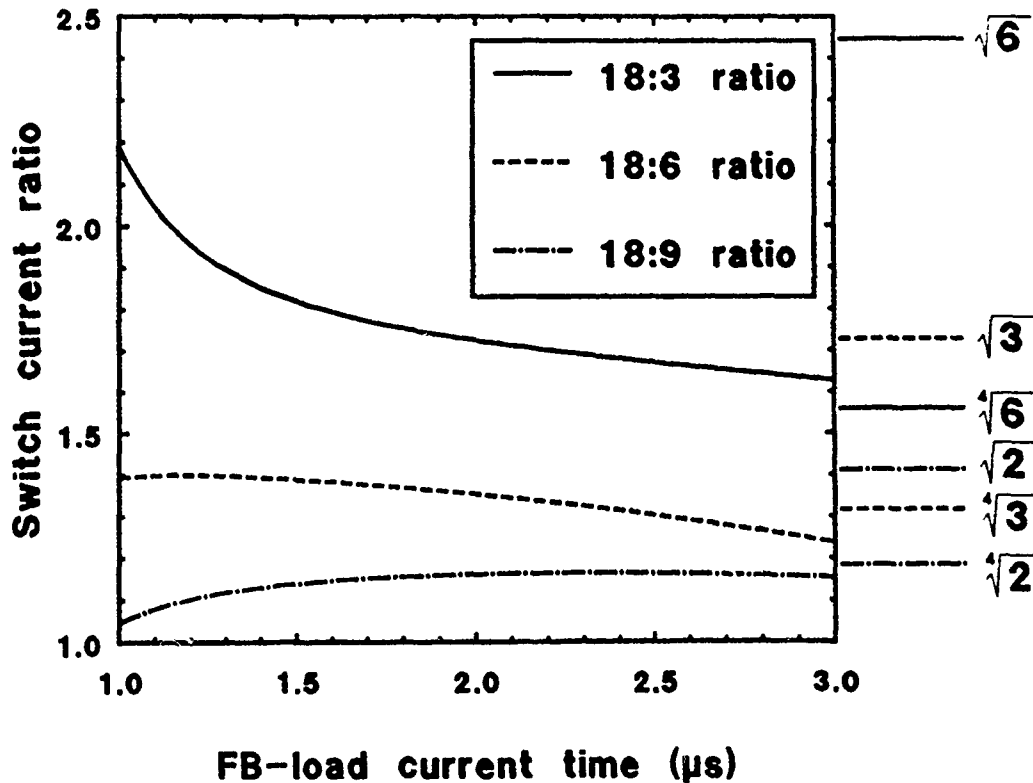


Fig. 7 (b) Conduction current ratios vs. time delay for different number of flashboards.

The emission limit and hydro limit intersect in (J,t) space as shown in Fig. 5b. The equation for the intersection point is given by combining Eqs. 1 and 4:

$$J \tau^2 = 20 \frac{M_1}{\mu_0 Z}$$

$$\begin{aligned} m_0 &= 12 \\ Z &= 2 \\ M_0 &= 4 \times 10^{-7} \\ &(5) \end{aligned}$$

$$9.6 \times 10^{-7}$$

This relation depends only on the ion specie. Eq. 5 is plotted in Fig. 8a and b, assuming C⁺⁺, for comparison with the PEOS experiments described in this paper. In Fig. 8a, the hydro limit is plotted with current density waveforms for Gamble I, Gamble II and MIP (PBFA II). In Fig 8b, the same hydro limit is plotted over a longer time domain with waveforms for Hawk and Pawn. The "hydro limit" curve divides the space into two regions: switching on the origin-side of this curve occurs when $\Delta z < l_0/2$, where conduction current is proportional to density (emission limited). To the right of the hydro limit, switching occurs when $\Delta z \approx l_0/2$, the density is higher than for the same J with short conduction time, and scaling is like $n^{1/4}$. Fig. 8 shows the point where some experiments (Gamble II, Hawk, Pawn) cross the hydro-limit curve, beyond which conduction is not proportional to density.

for shot 239

$$A \approx 10 \times 2 \times \pi \times 10$$

$$Z = 3.5 \times 10^{-7}$$

$$\text{if } J = \frac{1}{2}$$

$$1 \text{ kA} \sim 480 \text{ A/cm}^2$$

$$\rightarrow 6 \times 10^{-7}$$

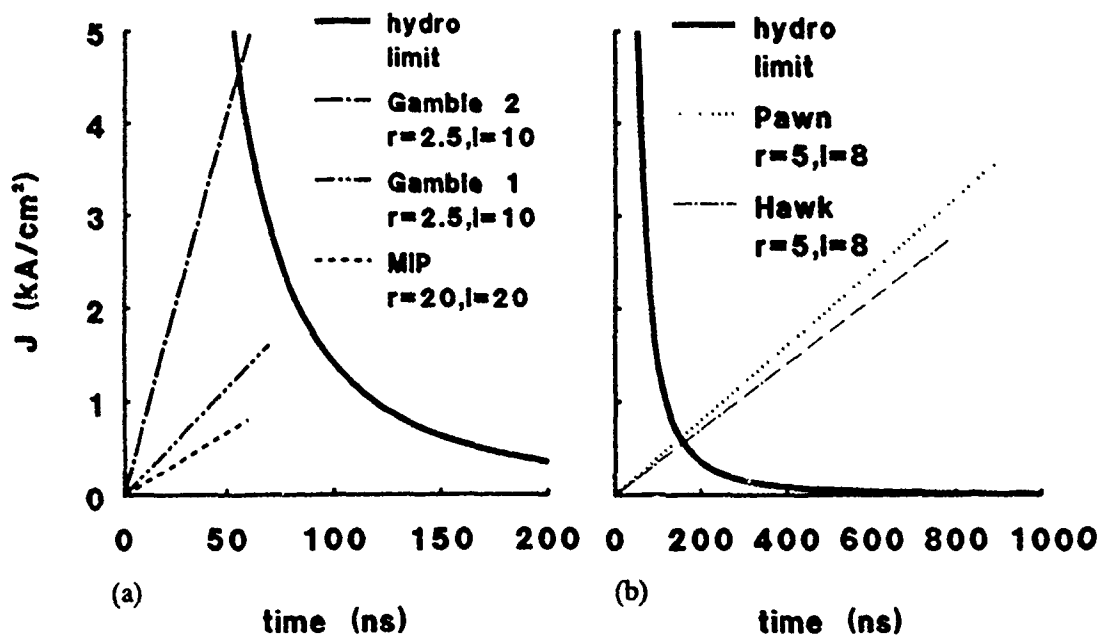


Fig. 8 Hydro limit of Eq. 5 plotted with current waveforms for (a) 50 ns conduction time experiments and (b) 1 μ s conduction time experiments.

SUMMARY AND CONCLUSIONS

PEOS switching occurs at a current level that depends on the plasma density, geometry and conduction time. Two different cases are examined in this paper: 50 ns and 1 μ s conduction time. In the 50 ns case, conduction current is proportional to the initial density. The experimental results agree with bipolar (emission-limited) conduction if the plasma specie is C^{++} and the ion collection speed is 3-4 cm/ μ s. In the 1 μ s conduction time range, initial scaling experiments indicate a weaker dependence on initial density, where the current scales like n^x , with $1/4 < x < 1/2$. Plasma distortion and displacement by hydrodynamic forces may be the physical mechanism limiting conduction in this case. This hydro-limit requires higher density to conduct a given current than the emission-limit at short conduction time. Higher density results in a slower opening rate, which is probably the fundamental reason opening is slower for the 1 μ s conduction time PEOS than for the 50 ns conduction time PEOS (compare Gamble II and Hawk, Figs. 1 and 2).

Of fundamental importance for improved understanding of 1 μ s PEOS physics are measurements of plasma density. A CO_2 laser interferometer is being constructed for this purpose. Improved switching requires new techniques to overcome the "excess" density required for conduction. Among these new (and old) ideas are: staged switches, changing plasma specie, geometry changes, and pulsed B fields.

REFERENCES

- * JAYCOR, Vienna, VA
- 1) Neri, J.M., et al., APL 50, 1331 (1987).
- 2) Rochau, G.E., et al., "Performance of Magnetically-Injected-Plasma Opening Switches for the Particle Beam Fusion Accelerator II (PBFA II)," these Proceedings.
- 3) Ottinger, P.F., et al., JAP 56, 774 (1984).
- 4) Hinshelwood, D.D., et al., "Axially Resolved PEOS Measurements at Microsecond Conduction Times," these Proceedings.

MICROSECOND-CONDUCTION-TIME POS EXPERIMENTS

B. V. Weber, J. R. Boller, R. J. Commisso, P. J. Goodrich,* J. M. Grossmann,
D. D. Hinshelwood,* J. C. Kellogg, P. F. Ottinger and G. Cooperstein

Plasma Physics Division
Naval Research Laboratory, Washington, DC 20375-5000
*Jaycor, Vienna, VA 22182-2270

Abstract Experiments have been performed to improve the understanding of the μ s-conduction-time plasma opening switch (POS). Measurements with a He-Ne laser interferometer show that the line-integrated plasma density reaches a peak value during conduction, then decreases to a relatively small value before opening begins. During opening, the density is low over a large fraction of the electrode gap, but is relatively high at both electrodes, indicating that opening actually occurs in the middle of the electrode gap. The dependence of conduction current and conduction time on density and other POS parameters (radius, length, and current waveform) indicate that conduction is controlled by hydrodynamic displacement and distortion of the plasma, resulting in a low density region where opening occurs, possibly by erosion. Experiments with electron-beam diode loads have been performed for a variety of load and POS configurations. Assuming the POS gap at peak power equals the radial extent of the electron orbits, the calculated switch gap is about 2-3 mm over a wide range of load impedances, conduction currents, and center conductor radii. Increased load power requires increasing the (effective) gap size. Fluid and PIC codes may be suitable to simulate the conduction and opening phases, respectively, and a combined fluid/particle model could indicate promising methods for increasing the output power using a POS.

I. Introduction

Inductive-store pulsed power generators require a fast opening switch to transfer current from an energy-storage inductor to a load. One approach[1] is to use a plasma opening switch (POS) to conduct current during the discharge of a Marx generator into an inductor, which generally takes about 1 μ s. After this conduction phase, the POS opens and transfers most of the current to a load. This approach to inductive-store pulsed power generators is attractive compared with conventional (capacitive water-line) generators because of decreased size and cost, and the potential to scale up to higher energy.[2]

POS experiments have been performed on the Hawk inductive-store pulsed power generator at the Naval Research Laboratory (NRL). Hawk consists of a high-current, 1- μ F Marx bank[3] with a typical output voltage of 640 kV and stored energy of 0.23 MJ at 80-kV charging voltage. The discharge of the Marx into the circuit inductance, shorted by a POS, results in a sinusoidal current with peak amplitude 720 kA and quarter period 1.2 μ s. When the POS opens, current is transferred to an electron-beam diode load, resulting in load power as high as 0.7 TW (450 kA, 1.6 MV).[4] The overall energy efficiency of the Hawk generator is about 20%, about two times smaller than for conventional water-line generators. (For example, the Gamble II generator at NRL is about 40% efficient and generates 1-2 TW into a load for similar stored energy.) The volume of Hawk (50 m³) is far smaller than its conventional counterpart, (Gamble

II: 2000 m³), making it an attractive alternative for many applications, especially if the efficiency and power could be increased.

The output power of Hawk, and of similar generators, is limited by the POS. Research on Hawk has concentrated on identifying the physical mechanisms that determine conduction and opening for the μ s-conduction-time POS. This paper gives an overview of this research work. Interferometry is used to measure the distribution and evolution of the plasma density during POS operation, and to determine the dependence of conduction current and time on density and other POS parameters. Experiments with electron-beam diode loads demonstrate that the size of the vacuum gap generated in the plasma during opening is limited to about 3 mm. Understanding the gap opening mechanism and increasing its size, perhaps with the aid of computer simulations, could lead to significant improvement in output power and efficiency.

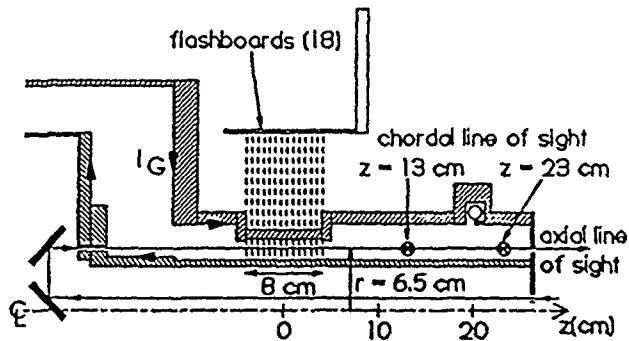


Fig. 1. Hawk POS arrangement showing axial and chordal He-Ne laser lines-of-sight for interferometry.

II. Physics of conduction based on interferometry

Measurements of plasma dynamics and conduction scaling on Hawk have been made using a He-Ne interferometer[5,6]. Details of the interferometer are given in Ref. [7]. A sketch of the POS on Hawk and sample laser lines-of-sight used for density measurements are shown in Fig. 1. The POS plasma is injected between the coaxial conductors using 18 flashboards, each driven by a capacitor circuit generating about 35 kA in 0.6 μ s. Currents are measured on the generator (I_G) and load (I_L) sides of the POS. A short circuit load is used to minimize debris and prevent high voltages that could adversely affect the density measurement. The axial line-of-sight measures the line integrated electron density in the plasma injection region at a selected radial location. The length of the plasma injection aperture, $l = 8$ cm in Fig. 1, is used to convert the line-integrated density to more convenient density units (cm^{-3}). The precision of the density measurement using the axial line-of-sight is about $1 \times 10^{14} \text{ cm}^{-3}$.

Fig. 2 shows data taken on Hawk using an $r = 5$ cm center conductor using the axial line-of-sight located at $r = 6.5$ cm, 1.5 cm from the center conductor and 0.5 cm from the outer conductor in the POS region (as shown in Fig. 1). The average density measured by firing the flashboards alone, n_{FB} , increases from about $2 \times 10^{15} \text{ cm}^{-3}$ at the time the Hawk current would begin ($t = 0$), to over $8 \times 10^{15} \text{ cm}^{-3}$ at the time the load current would begin ($t = 0.9 \mu\text{s}$). The density measured during the Hawk shot, n_e , follows n_{FB} for the first 0.4 μs and then decreases, becoming relatively small at the time opening begins. The decrease in density during conduc-

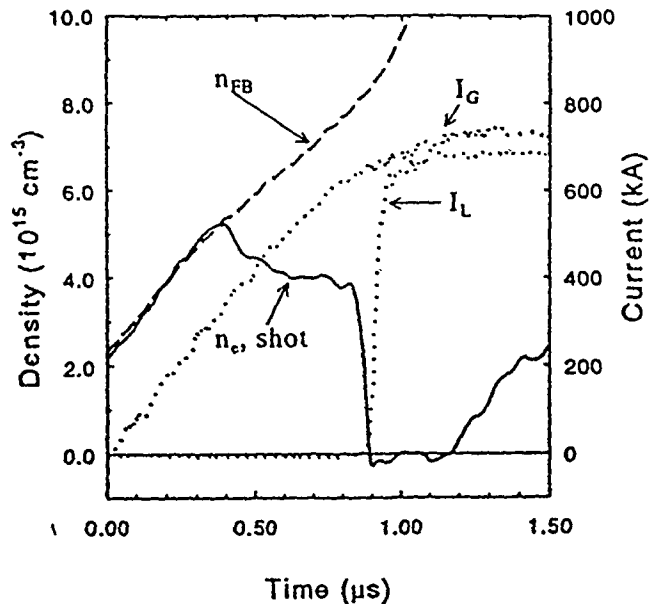


Fig. 2. Density measured in Hawk, 1.5 cm from the $r = 5$ cm center conductor.

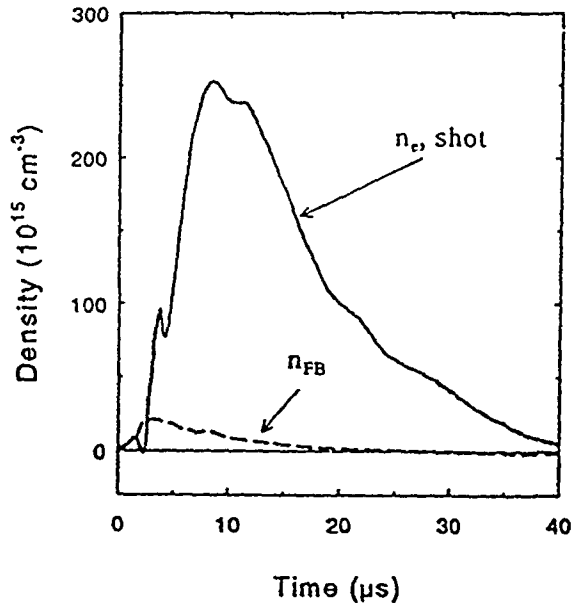


Fig. 3. Density measured on a long time scale, 1.0 cm from the $r = 5$ cm center conductor.

tion is typical for Hawk experiments, although the rapid decrease shown in Fig. 2 is not necessarily typical. After opening, the density is lower than the measurement limit for $0.3 \mu\text{s}$ before increasing. The density eventually exceeds 10^{17}cm^{-3} , an order of magnitude higher than the peak flashboard density, as shown in Fig. 3. The high density after switching is attributed to plasmas generated at the electrodes after bombardment by the energetic particles generated during the opening phase.

The radial dependence of the density is measured by changing the radial location of the laser line-of-sight for shots with the same nominal POS parameters. The measured density distributions at the start of conduction and during opening are shown in Fig. 4. The density distributions measured by firing the flashboards alone are indicated by dashed lines. The distribution at the start of conduction for the Hawk shots matches the flashboard-only data. The density distribution at the start of conduction shows a drastic density increase near the center conductor resulting from a plasma-surface interaction. The density is relatively constant between $r = 6$ and 7 cm. At a time during opening, $t = 900 \text{ ns}$ in Fig. 4, the density measured on Hawk shots has a minimum at $r = 6.5$ cm, and increases toward both conductors. Presumably, opening occurs in this region. For comparison, the density distribu-

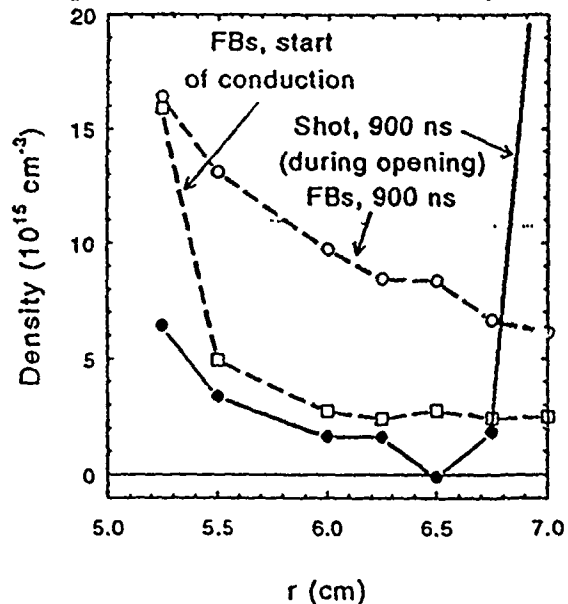


Fig. 4. Radial distribution of density at the start of conduction and during opening.

tion measured at the corresponding time but without firing Hawk is shown. The consequence of current conduction is that this additional plasma does not completely enter the switch region, and the density is redistributed by $\mathbf{J} \times \mathbf{B}$ forces during conduction, resulting in a rarefied region where fast opening can occur.

Measurements[8] made using other electrode radii (2.5-13 cm) and inner-outer conductor spacings (2-4.5 cm) indicate that the minimum density region during opening extends over a larger region (1-2 cm) of the gap between the conductors. In all cases, opening probably occurs between the conductors where the density is low, instead of near the cathode or anode surfaces, where the density is relatively high.

Measurements[8] using the chordal lines-of-sight shown in Fig. 1 indicate that opening occurs before plasma is displaced to these locations (9 cm and 19 cm from the edge of the plasma injection aperture). The reduction in density occurs in the switch region, without significant translation of the switch plasma toward the load.

An illustration of the physical process that could explain the density reduction is shown in Fig. 5. Here, the POS is simulated using the Anthem code[9] to model the plasma as two fluids (electrons and ions). The experimentally measured radial density distribution 300 ns after conduction begins is used in the simulation. During conduction, the plasma is compressed, and a thick "snowplow" effect is seen. The current streamlines follow the electron contours in the compressed density region, resulting in primarily radial current with a slight bow in the middle where the plasma has been displaced the farthest. At the end of conduction, the plasma has accumulated near the load end of the switch region. The axial components of the current density cause a radial displacement of plasma toward both electrodes. This forms a valley in the plasma distribution at about $r = 6.7$ cm, close to the location of the minimum density in the corresponding Hawk experiment (Fig. 4). The line-integrated density decreases rapidly at this location at

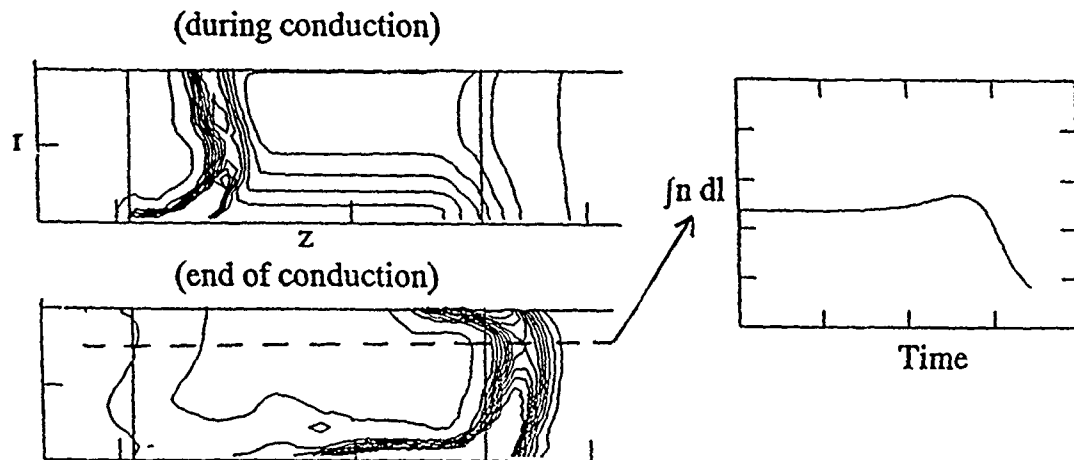


Fig. 5. Anthem simulation of Hawk POS. Electron contours are plotted during conduction (above left) and at the end of conduction (below left). Line-integrated electron density at $r = 6.7$ cm is plotted vs. time (right).

the end of conduction. The fluid version of the code is probably inadequate to simulate the opening phase, when it is believed particle effects (magnetically insulated electrons and enhanced erosion) dominate the physics. However, a fluid code could be sufficient to model the conduction phase and provide the input to a particle code to model the opening phase.

Interferometry was used to test the scaling of the POS conduction current (and time) with simplified predictions from theory. At least four conduction limits have been proposed: bipolar [10], modified bipolar, [11] electro-magnetohydrodynamics (EMH), [12] and magnetohydrodynamics (MHD) [13,14]. For the long conduction times considered here, only the EMH and MHD cases are expected to apply. A simple EMH limit can be derived assuming ion motion is negligible and that radial current is conducted by electrons executing $E \times B$ drifts. It can then be shown [15] that the azimuthal magnetic field penetrates through the plasma with an axial velocity, u , given by:

$$u = \frac{I}{2\pi enr} \left[\frac{1}{n} \frac{dn}{dr} + \frac{2}{r} \right], \quad (1)$$

where e is the electron charge, r is the radius where opening occurs and n is the density. For Hawk, penetration ($u > 0$) could occur in the region where $dn/dr \sim 0$ ($r = 6-7$ cm in Fig. 4). Opening is assumed to begin when the field penetrates the length of the plasma, $\int u dt = l$, resulting in the conduction limit:

$$\int I_{EMH} dt = \pi er^2/n. \quad (2)$$

For a linearly rising current, $I(t) \propto t$, the conduction current $I_{EMH} \propto n^{1/2}$.

The MHD limit occurs when ion motion is not negligible and the plasma is displaced or distorted by $J \times B$ forces. Based on empirical evidence [16,17] and the simulation results presented earlier, conduction is assumed to end when the plasma center-of-mass is displaced to the load end of the POS. This results in an MHD conduction limit:

$$\iint I_{MHD}^2 dt^2 = \frac{100\pi^2 r^2 l^2 M_i}{Z} n, \quad (3)$$

where M_i and Z are the ion mass and charge state, respectively, and cgs units are used except for I (Amps). For a linearly rising current, $I_{MHD} \propto n^{1/4}$.

These simplified scaling laws are in general agreement with Hawk experiments. Fig. 6 shows data and scaling predictions from Eqs. 2 and 3. The horizontal axis is the peak density measured during conduction, about 1.5 cm from the center conductor. In both graphs in Fig. 6, a standard case is shown, where $r = 5$ cm, the Marx capacitors are charged to 80 kV, and the plasma length is 8 cm. The data (circles) match the MHD limit, both in the density scaling and magnitude. For currents less than 450 kA, the EMH limit should be reached before the MHD limit. The trend in the data suggests this may occur in the Hawk experiments. The graph on the left in Fig. 6 shows the effect of changing dI/dt by lowering the Marx voltage to 50 kV. The

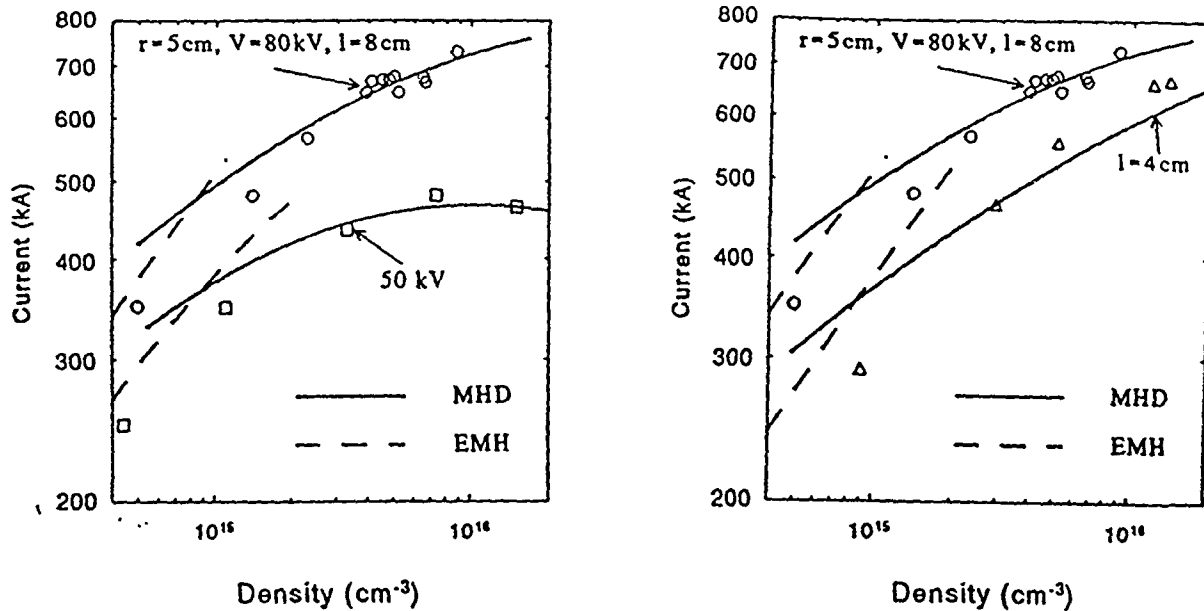


Fig. 6. Hawk conduction current scaling and comparisons with MHD and EMH scaling laws.

graph on the right in Fig. 6 shows the effect of decreasing the length to 4 cm. For both changes, the data match the MHD/EMH prediction. Similar agreement occurs for radii of 2.5, 5, and 12 cm.[8]

A striking difference between the MHD and EMH regimes is shown in Fig. 7. In the top graph in Fig. 7, load currents are shown for different plasma densities. The conduction current varies from 200 kA (#1) to 700 kA (#6). The bottom graph in Fig. 7 shows the density measured 9 cm from the load edge of the plasma aperture using a chordal line-of-sight ($z = 13$ cm in Fig. 1). A large plasma density, comparable to the density in the POS region, appears at this location *after* opening for cases 3-6, that is, for currents greater than 450 kA. For currents less than 450 kA, the measured densities at this location are negligible (much less than the density in the POS region during conduction). This phenomenon is consistent with the difference between the MHD and EMH limits. In the EMH case, switching occurs before the plasma is translated. Evidently, plasma motion in the axial direction is negligible compared with radial motion. In the MHD case, the plasma center-of-mass is translated a fixed distance during conduction. The measured downstream density begins later for longer conduction times.

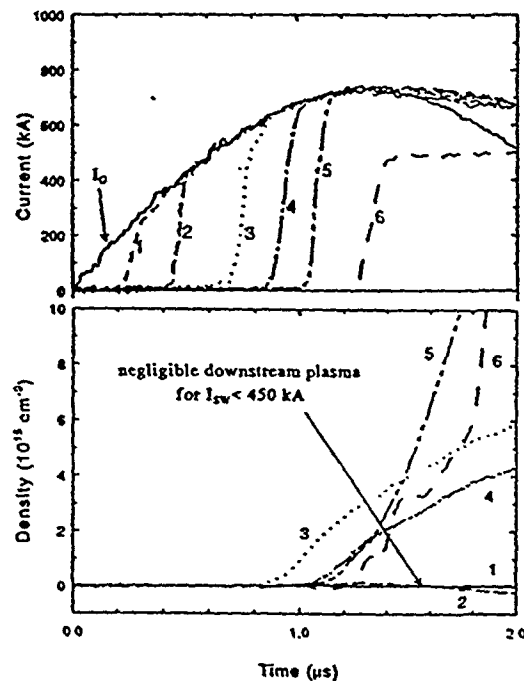


Fig. 7. Density measured using a chordal line-of-sight 9 cm from the edge of the POS (bottom) and corresponding load currents (top).

III. Physics of opening based on electrical measurements with diode loads

Experiments have been performed on Hawk using various POS configurations and electron-beam diode loads.[18,4] Results from experiments using an $r = 5$ cm center conductor are summarized in Fig. 8, which is a plot of peak switch voltage (essentially the same as the load voltage) as a function of the load impedance at the time of peak load power. Different symbols in this plot correspond to different conduction current ranges. The two dashed lines define "load-limited" and "switch-limited" regimes. In the load-limited regime, the load impedance determines the voltage. In the switch-limited regime, the voltage is independent of the impedance, for a given conduction current. In this case, the voltage is limited by the switch to about 900 kV, and the load current is less than the generator current (current is lost in the switch region or between the switch and load). Maximum load power occurs at the intersection of these two lines, about 0.4 TW in this case.

The data in Fig. 8 suggest a simple picture of the opened POS, illustrated in Fig. 9. At peak power, a vacuum gap is assumed to have formed in the POS plasma. Electron orbits are illustrated in Fig. 9 for the load-limited and switch-limited cases (see, for example, [19]). The electron flow extends a distance D from the cathode side of the POS gap. Within a numerical factor, D can be calculated from a critical current formula:

$$D = 1.6 \times 8500 \beta \gamma \frac{r}{I}, \quad (4)$$

where the factor 1.6 is a correction factor from PIC simulations, β and γ are the standard relativistic factors and I is the generator current (in Amps) at the time of peak power. The load-limited case corresponds to low load impedance, so that the electron flow extent D is less than (or equal to) the vacuum gap. The switch-limited case corresponds to high load impedance where the electron flow extends across the plasma, and current is lost across the POS. In this case, the calculated value of D using Eq. 4 will be approximately equal to the physical gap in the plasma, assuming the electron flow is in equilibrium.

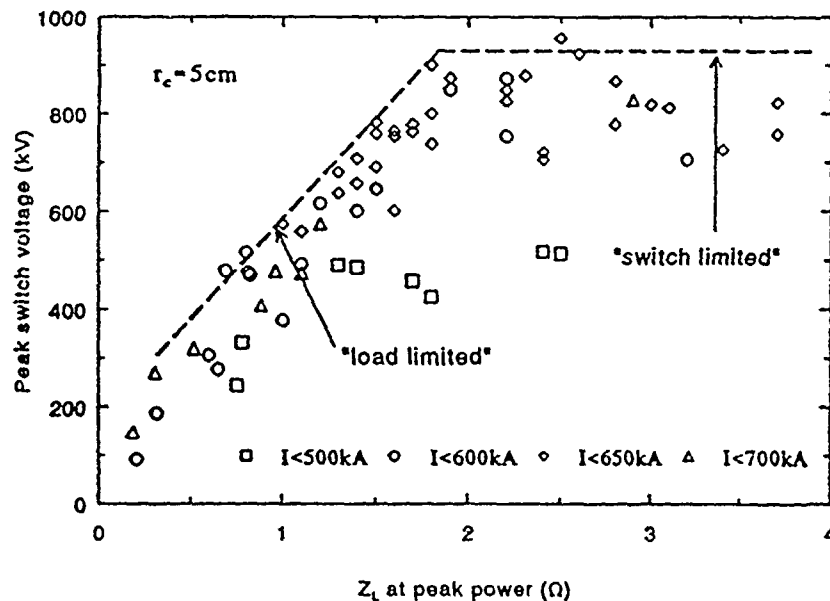


Fig. 8. Peak voltage vs. load impedance for Hawk shots using an $r = 5$ cm center conductor. Symbols correspond to different ranges of conduction current.

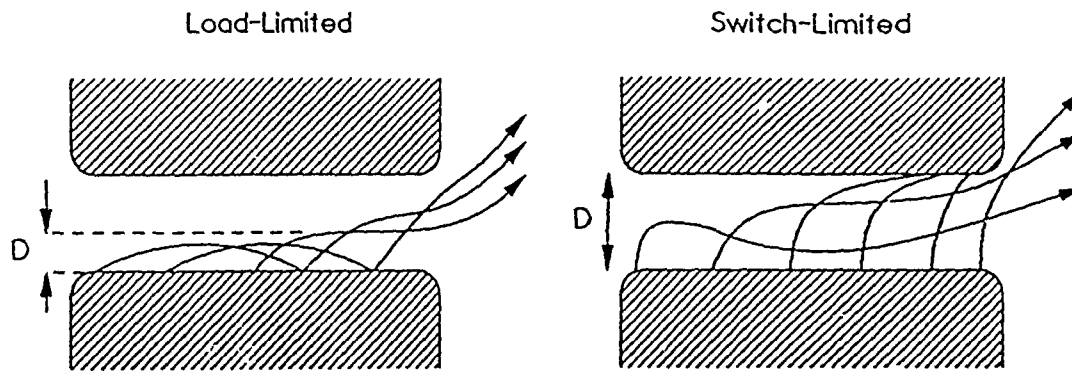


Fig. 9. Electron flow patterns across a vacuum gap in a POS for "load-limited" and "switch-limited" cases.

The calculated values of D are shown in Fig. 10 for the same shots corresponding to the data in Fig. 8. In the switch-limited regime, the calculated gap, D , is in the 2.5-3 mm range, independent of load impedance and conduction current. (For comparison, the radial distance between the POS conductors is 20 mm.) In the load-limited regime, D is independent of conduction current and an increasing function of load impedance. It is not clear whether the gap in this case is larger than D , as illustrated in Fig. 9, or if the gap generated in the plasma stops growing when the electron flow is insulated. In either case, the simple picture of a 2.5-3 mm gap forming in the plasma explains all the data in Fig. 8.

The limited gap size results in a limited load power, and determines the "matched load" impedance to maximize the load power ($1.5-2 \Omega$ in Fig. 8). If the gap size or magnetic field could be increased, the matched load impedance would be higher resulting in higher load voltage and power. Empirically, reducing the center conductor radius on Hawk results in higher voltage and a fixed gap size. Experiments[4] using an $r = 2.5$ cm center conductor are limited to a voltage of 1.5 MV, and the calculated gap is ≤ 3 mm. Further reduction of the center conductor radius to 1.3 cm results in the highest voltage to date on Hawk, about 2 MV, and a similar calculated switch gap. An example of data from a Hawk shot with an $r = 1.3$ cm center conductor is shown in Fig. 11. The conduction current is

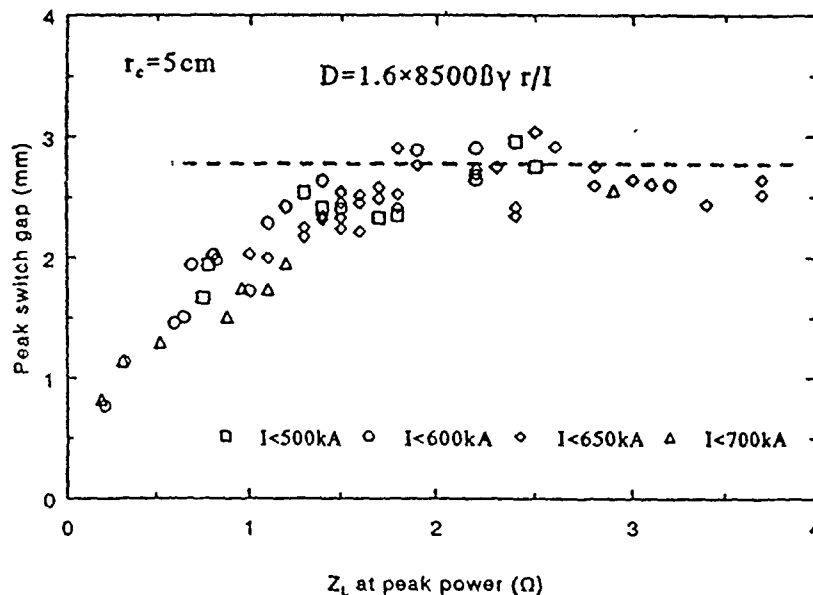


Fig. 10. Gap size, D , for the data in Fig. 8., as a function of load impedance. The gap is limited to ≤ 3 mm.

limited to lower values in this case (500 kA with $r = 1.3$ cm compared with 700 kA with $r = 5$ cm) because of the MHD scaling (Eq 3) and the limited plasma density available from the flashboards. The maximum load power obtained on Hawk, 0.7 TW, used a tapered center conductor

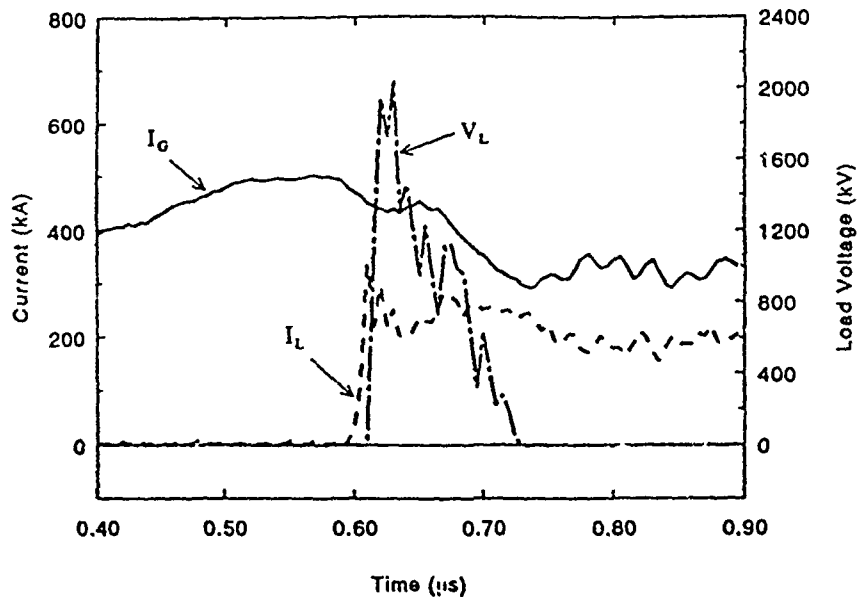


Fig. 11. Highest load voltage (2 MV) obtained on Hawk using an $r = 1.3$ cm center conductor.

($r = 5$ cm at the generator end of the switch region to $r = 1.3$ cm at the load end) in an attempt to extend the conduction phase and increase the magnetic field in the region where opening occurs.[4]

One possible explanation of the limited gap has been deduced from PIC code simulations[20] of a low density ($< 10^{13} \text{ cm}^{-3}$) shorter time scale (< 100 ns) POS. As mentioned before, these simulations may be applicable to the μs POS after the density has been reduced during the conduction phase. The PIC simulations show a region of net positive charge (potential hill) resulting from electron depletion. This potential hill migrates axially through the rarefied plasma, leaving behind a vacuum gap where electrons are magnetically insulated. When the ion-rich region reaches the load end of the plasma, the ions erode and the preformed gap exists along the extent of the plasma, independent of the load impedance. In simulations, the size of the gap increases by increasing the magnetic field and by decreasing the density. These results could be applied to Hawk using a density distribution determined by a fluid code. In the future, a combined fluid/particle treatment could provide a reliable modeling tool for the μs POS.

IV. Summary and conclusions

POS experiments on Hawk are leading to improved understanding of μs -conduction-time POS physics. Density measurements during Hawk shots have been the most revealing new technique. These measurements show that the density decreases during conduction, that opening occurs in the middle of the electrode gap instead of near the cathode or anode electrodes, and that the conduction current scaling can be understood from simple limits: MHD for high currents, where opening begins when the axial plasma displacement is about half the switch length, and EMH for low currents, where axial field penetration occurs before plasma displacement is significant. Experiments with diode loads indicate that the POS operates as if a ~ 3 -mm vacuum

gap forms in the plasma, independent of conduction current, load impedance, and center conductor radius. Consistent with this limited gap, higher voltage is obtained when the center conductor radius is reduced. Optimizing the POS parameters to maximize the output power is a trade-off between higher voltage generated using a small radius center conductor, and the corresponding reduction of conduction current because of the MHD limit. Fluid and particle codes may be able to simulate the conduction and opening phases, respectively, and to indicate promising methods to increase the output power, making this technique even more attractive for pulsed power applications.

It is a pleasure to acknowledge Rick Fisher for his expert technical assistance on Hawk experiments. We also benefited from many discussions of POS physics with J. Thompson and E. Waisman of Maxwell Labs and J. Goyer of Physics International Co.

References

1. G.A. Mesyats and B.M. Koval'chuk, *Sov. Phys. -- Dokl.* **30**, 879 (1987).
2. G. Cooperstein and P.F. Ottinger, *Guest Editorial, IEEE Trans. Plasma Sci.* **PS-15**, 629 (1987).
3. P. Sincerny, D. Drury, J. Goyer, G. James, M. Krishnan, J. Levine, C. McDonald, I. Roth, in *Proc. Seventh IEEE Pulsed Power Conf.*, B.H. Bernstein and J.P. Shannon, eds., Monterey, CA (IEEE, New York, 1989), IEEE Cat. No. 89CH2678, p. 275.
4. P.J. Goodrich, J.R. Boller, R.J. Commisso, D.D. Hinshelwood, J.C. Kellogg, B.V. Weber, these proceedings.
5. David Hinshelwood, Bruce Weber, J.M. Grossmann and R.J. Commisso, to be published in *Phys. Rev. Lett.*, June 1992.
6. R.J. Commisso, P.J. Goodrich, J.M. Grossmann, D.D. Hinshelwood, P.F. Ottinger and B.V. Weber, to be published in *Phys. Fluids B*, July 1992.
7. B.V. Weber and D.D. Hinshelwood, to be published in *Rev. Sci. Instrum.*, Oct., 1992.
8. D.D. Hinshelwood, R.J. Commisso, F.J. Goodrich, J.M. Grossmann, J.C. Kellogg and B.V. Weber, these proceedings.
9. R.J. Mason, M.E. Jones, J.M. Grossmann, and P.F. Ottinger, *Phys. Rev. Lett.* **61**, 1835 (1983).
10. P.F. Ottinger, Shyke A. Goldstein and R.A. Meger, *J. Appl. Phys.* **56**, 774 (1984).
11. J.R. Goyer, *IEEE Trans. Plasma Sci.* **19**, 920 (1991).
12. K.V. Chukbar and V.V. Yan'kov, *Sov. Phys. Tech. Phys.* **33**, 1293 (1988).
13. B.V. Weber, R.J. Commisso, G. Cooperstein, P.J. Goodrich, J.M. Grossmann, D.D. Hinshelwood, J.C. Kellogg, D. Mosher, J.M. Neri, and P.F. Ottinger, in *Proc. Eighth Int'l. Conf. on High-Power Particle Beams Vol. 1*, B.N. Breizman and B.A. Knyazev, eds., Novosibirsk, USSR (World Scientific, New York, 1991), p. 406.
14. W. Rix, D. Parks, J. Shannon, J. Thompson, and E. Waisman, *IEEE Trans. Plasma Sci.* **19**, 400 (1991).
15. A. Fruchtman, *Phys. Fluids B* **3**, 1908 (1991).
16. D.D. Hinshelwood, R.J. Commisso, P.J. Goodrich, J.M. Grossmann, J.C. Kellogg, P.F. Ottinger and B.V. Weber, in *Proc. Eighth Int'l. Conf. on High-Power Particle Beams Vol. 1*, B.N. Breizman and B.A. Knyazev, eds., Novosibirsk, USSR (World Scientific, New York, 1991), p. 1034.
17. B.V. Weber, R.J. Commisso, P.J. Goodrich, J.M. Grossmann, D.D. Hinshelwood, J.C. Kellogg and P.F. Ottinger, *IEEE Trans. Plasma Sci.* **19**, 757 (1991).
18. P.J. Goodrich, J.R. Boller, R.J. Commisso, D.D. Hinshelwood, J.C. Kellogg, B.V. Weber, in *Proc. Eighth IEEE Pulsed Power Conf.*, R White and K. Prestwich, eds., San Diego, CA (IEEE, New York, 1991), IEEE Cat. No. 91CH3052-8 p. 515.
19. C.-K. Ng and R.N. Sudan, *J. Appl. Phys.* **69**, 137 (1991).
20. J.M. Grossmann, P.F. Ottinger, and R.J. Mason, *J. Appl. Phys.* **66**, 2307 (1989).

Density Redistribution in a Microsecond-Conduction-Time Plasma Opening Switch

David Hinshelwood,^(*) Bruce Weber, J. M. Grossmann, and R. J. Comisso
Plasma Physics Division, Naval Research Laboratory, Washington, D.C. 20375-5000
 (Received 6 January 1992)

The first measurements of the line-integrated electron density in a coaxial microsecond-conduction-time plasma opening switch during switch operation are presented. Current conduction is observed to cause a radial redistribution of the switch plasma, with a large decrease in axial line density over most of the radial extent of the switch. A local reduction in line density of more than an order of magnitude occurs by the time opening begins. It is hypothesized that this density reduction allows the switch to open by an erosion mechanism. Initial numerical modeling efforts have reproduced the principal observed results.

PACS numbers: 52.75.Kq, 52.40.Hf, 52.65.+z, 52.70.Kz

Pulsed power generators that use inductive energy storage techniques offer potential benefits for producing TW and higher electrical power pulses [1]. Applications for such generators include inertial confinement fusion and the production of intense x-ray pulses. A plasma opening switch [1] (POS) allows the use of vacuum inductive storage for the generation of such high power pulses. A POS consists of plasma injected between two conductors in vacuum, through which current flows, storing magnetic energy in the circuit. At some point, depending on the details of the POS and the driving current, this conduction phase ends and the switch opens, transferring energy to a load. Over the past decade much attention has been directed toward microsecond-conduction-time POS development [2-7]. This technology has promise for the development of compact, multi-TW, multi-MA generators. In experiments to date switches have conducted MA-level peak currents for $\sim 1 \mu\text{s}$ before opening in tens of ns [4-6]. Magnetic probe measurements (discussed below) show that large-scale translation of the current-carrying plasma toward the load does not occur, indicating a relatively high ($\sim 10^{15}$ - 10^{16} cm^{-3}) plasma density. This high density makes the observed, rapid opening of the switch difficult to explain. We report here the first quantitative, nonperturbing, *in situ* measurements of the plasma electron density during POS operation. The electron density is measured using heterodyne-phase-detection HeNe interferometry. These measurements indicate that the plasma mass is rarified during the conduction phase. Based on these observations, we propose a mechanism by which current conduction is limited and opening occurs.

A schematic of the experiment, on the Hawk generator [8], is shown in Fig. 1. The coaxial switch geometry comprises a 5-cm-radius center-conductor cathode and an array of twelve axial anode rods at a radius of 7.5 cm. A short-circuit load is located 25 cm beyond the switch. Plasma is injected by eighteen flashboards positioned at an 18-cm radius. Each flashboard consists of an array of surface discharges across a carbon-coated insulator. A mask outside the anode rods shields all but the 8-cm-long switch region from the injected plasma. The flashboards

are typically pulsed 1 to 2 μs before the generator is fired. Electrical diagnostics include sets of dB/dt loops at the generator and at the load. In the absence of opening, the generator drives 720 kA through the switch in 1.2 μs .

The details of the interferometer will be presented in the future [9] and are only summarized here. An acousto-optic modulator splits a 10-mW cw HeNe laser beam into two beams with a 40-MHz relative frequency shift. A scene beam is directed through the switch region in the axial direction, parallel to the cathode (see Fig. 1). A reference beam traverses an equal path length outside of the vacuum system before combining with the scene beam at the beam splitter. The intensity of the combined beam exhibits a 40-MHz beat signal whose phase depends on the relative phase shift between the two beams. The zero-crossing times of the beat signal are used to determine the time-varying phase shift of the scene beam, from which the line-integrated density $\int n_e dz$ is calculated. Several null tests were performed to verify that the measured phase shift is caused by material in the switch region [9]. These tests showed a small spurious phase shift leading to an apparent negative density when the switch opens. This effect gives a measurement limit of less than $2 \times 10^{15} \text{ cm}^{-2}$, or 2° of phase shift. Neutrals are not expected to affect significantly the phase shift be-

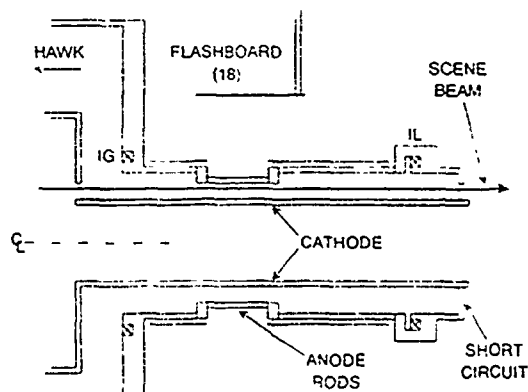


FIG. 1. The Hawk POS geometry, showing the scene beam path and the generator (IG) and load (IL) current monitors.

cause the densities required are too high: The phase shifts from neutral C and H are 27 and 80 times lower, respectively, than those from free electrons at the HeNe wavelength. Before each shot the flashboards alone are fired and the density is evaluated for comparison with shots where the POS plasma conducts current.

Typical data are shown in Fig. 2. On this shot the switch current rises to 660 kA in 900 ns before the switch opens, i.e., before current is delivered to the load. The detected portion of the scene beam was located radially 1.5 ± 0.05 cm from the cathode surface, and azimuthally between two anode rods. At about 350 ns into the conduction phase on this shot, the line density departs abruptly from the flashboard-only behavior. Rather than increasing, the line density decreases somewhat until just before the switch opens. At that time it decreases sharply. During opening, the line density is less than the measurement limit of 2×10^{15} cm⁻². This represents a decrease of over an order of magnitude relative to the value of 350 ns. Later, the line density increases again, eventually rising to a level exceeding 10^{18} cm⁻² for tens of μ s. When the switch opens, an inductive voltage appears across the switch gap. We believe that the late-time density increase reflects enhanced electrode plasma formation due to bombardment by energetic particles accelerated by the switch voltage.

Measurements at other radii, except those within a few mm of either electrode, are qualitatively similar to those in Fig. 2; the line density departs from the flashboard-only value early in the conduction phase and decreases until opening occurs. At 0.25 cm from the cathode the line density increases relative to the flashboard-only case during the first few hundred ns. It then decreases, but remains finite at opening. At 0.1 cm from the anode the

line density increases sharply toward the end of the conduction phase. The results are similar at different azimuthal locations relative to the anode rods.

Line densities as a function of radius are summarized in Fig. 3 for a series of shots similar to the one in Fig. 2. Line densities are shown for two times, early (300 ns) in the pulse and just before opening (900 ns), and compared with data from flashboard-only shots at the same times. At the beginning of the generator pulse (\sim ns, not shown) the line density is higher at the cathode because of stagnation of the injected plasma and/or secondary plasma formation due to bombardment of the surface by the injected plasma. At 300 ns there is little effect of current conduction other than a further increase in line density at the cathode. This may be indicative of the explosive-emission cathode plasma. By the time of opening, current conduction through the plasma has greatly altered the line density profile. Conduction causes an approximately fourfold line density reduction over most of the radial extent, relative to that at the same time on flashboard-only shots, and a twofold reduction relative to that at 300 ns. The latter comparison confirms that the initial plasma has been redistributed. Since the interferometer integrates along the axis, and the same results are observed at different azimuths, this redistribution must be associated with radial displacement of the plasma. These measurements indicate that plasma is pushed out to the anode radius. Plasma may also be pushed into the cathode, accumulating closer than the minimum observed distance of 0.25 cm. The lowest line density immediately prior to opening occurs most frequently at 1.5 ± 0.1 cm from the cathode; opening presumably occurs at this location. We believe that the minimum occurs here, rather than at the cathode, because of the much higher initial line density at

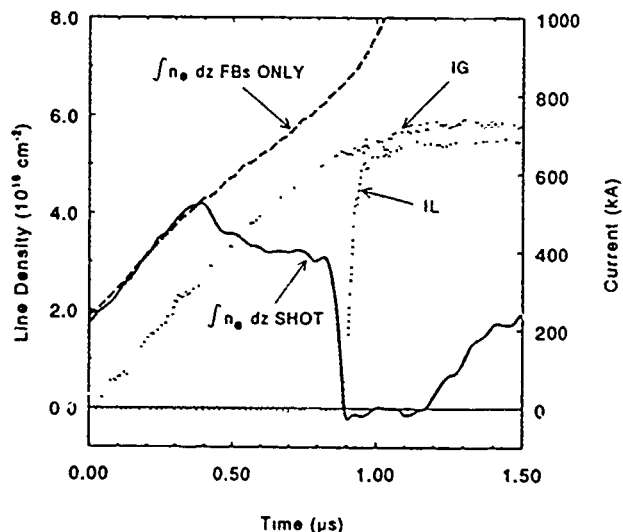


FIG. 2. The electron line density at 1.5 cm from the cathode during a shot on Hawk. The line density ($\int n_e dz$, FBs) when the flashboards alone are fired is shown for comparison. The generator (IG) and load (IL) currents are also shown.

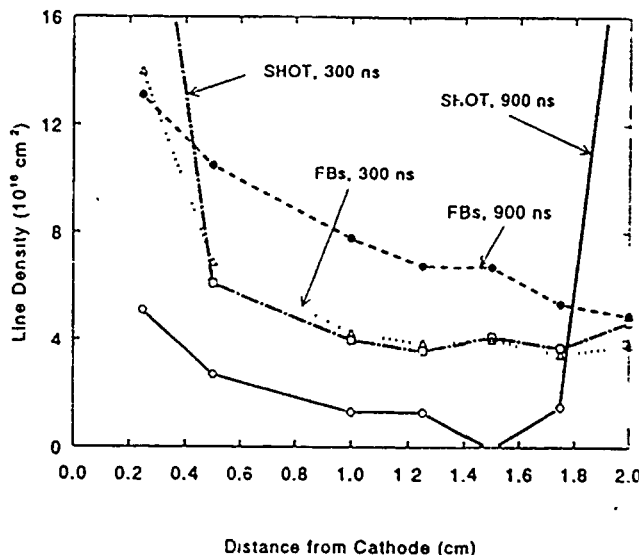


FIG. 3. Electron line density as a function of radial position, early in the conduction phase and just before opening. Flashboard-only data are shown for comparison.

the cathode (Fig. 3). Fast framing photography of POS plasmas has shown a decrease in visible light emission near the center of the switch gap at the end of the conduction phase [10,11].

In previous experiments, current flow in the switch region was diagnosed with arrays of dB/dt loops immersed in the switch plasma [12]. These measurements indicate that current is conducted across the switch in a broad (4 to 8 cm wide), predominantly radial channel that propagates toward the load as the conduction phase progresses. At opening, the center of the current channel is located near the load end of the 8-cm-long switch aperture. This translation is consistent with calculations of the center-of-mass hydrodynamic translation of a C^{++} switch plasma, using the current wave form and measured electron line density. The observed radial plasma displacement toward the anode and cathode can be explained by a relatively small axial ($j_z/j_r \sim 10\%$) tilt or bend in the current streamlines, which would not be resolved by the magnetic probe measurements. We believe that the axial component of the current streamlines arises from a combination of the radial dependence of the magnetic field and the radial variation of the initial plasma line density. A radial variation of B^2/n will result in a radial variation of the axial displacement, and thus a bend in the current streamlines.

Hydrodynamic motion of the switch plasma was modeled with the ANTHEM two-fluid code [13]. The measured electron line density profile at 300 ns was divided by 8 cm to get an average local density. To reduce computation time, the plasma mass and length and the current rise time were reduced. A 4-cm-long, H^+ plasma was assumed, with a current rise time of 200 ns. This rise time was chosen to provide the same calculated center-of-mass translation as the experimental parameters. Results are shown in Fig. 4. Figure 4(a) shows electron density contours at 210 ns, corresponding to the time of switch opening in the experiment. The current streamlines follow these contours—mostly radial, but bowed. The plasma has been displaced toward the load end of the switch region, albeit in a narrower channel than indicated by the magnetic field measurements. We believe that the observed current channel width could be reproduced by incorporating anomalously enhanced resistivity in the modeling [14]. More importantly, the slight bending of current streamlines has led to a radial density redistribution, with a density minimum at 1.7 cm from the cathode. This compares well with the results in Fig. 3. Figure 4(b) shows the calculated time history of the axial line density at this radius. (Note that because of the reduced length of the switch aperture in the computation the initial line density is a factor of 2 less than the experimental value.) A sharp decrease is seen at the end of the conduction phase, which compares well with the results in Fig. 2.

The ultimate opening of the switch, causing voltage

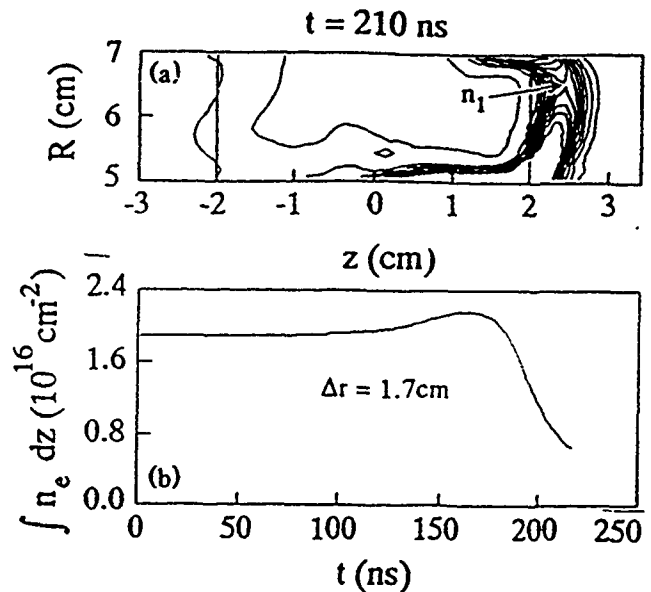


FIG. 4. ANTHEM code predictions: (a) Electron density contours at the end of the conduction phase. The vertical lines indicate plasma location. The electron density at n_1 is $1.3 \times 10^{16} \text{ cm}^{-3}$. The density rises to over $4 \times 10^{16} \text{ cm}^{-3}$ near the cathode. (b) Axial line density at 1.7 cm from the cathode.

generation and current transfer to the load, occurs in a (relatively short) few tens of ns. Similar results were obtained in Refs. [2-7]. The observed reduction in the line density by more than an order of magnitude at 1.5 cm from the cathode may allow the switch to open by enhanced erosion [15] of the switch plasma. Erosion occurs when the ion current drawn from the switch plasma exceeds the saturation value. A vacuum gap D forms at a rate given by $dD/dt = j_i/en_e - v_D$, where v_D is the ion injection velocity perpendicular to the cathode and j_i and n_e are the line-integrated ion current density and electron density. Effective switch gap opening rates are inferred from similar shots with diode loads [6]. Based on magnetic insulation arguments and electrical data from these experiments, gap opening rates of $\sim 5 \text{ cm}/\mu\text{s}$ and switch gaps at opening of a few mm are inferred. Faraday-cup measurements [12] indicate that the ion current is on the order of 20% of the total current at the time of opening. At the line density of $4 \times 10^{16} \text{ cm}^{-2}$ measured at 300 ns (Fig. 3), j_i/en_e is about $0.4 \text{ cm}/\mu\text{s}$, which is far too small to explain the observed opening rate. However, at the reduced electron line density at the end of the conduction phase of $2 \times 10^{15} \text{ cm}^{-2}$ (the interferometer measurement uncertainty), j_i/en_e exceeds $10 \text{ cm}/\mu\text{s}$. This rate may well exceed the ion injection velocity and can explain the observed rapid opening.

In conclusion, line-integrated electron density measurements during POS experiments have shown new features of plasma dynamics relating to the conduction and opening mechanisms in a POS. Current conduction causes a reduction in line density during most of the conduction

phase and over most of the plasma radial extent. The global density reduction during the conduction phase indicates that current conduction in this experiment is limited by hydrodynamic motion, as suggested in Ref. [5]. Even though the magnetic force is primarily in the axial direction, it is the radial redistribution of the switch plasma that controls conduction. This is supported by fluid code computation. We hypothesize that opening occurs in a two-stage process: a slow line density reduction by radial $\mathbf{j} \times \mathbf{B}$ forces followed by rapid gap formation by erosion of the rarified plasma.

It is a pleasure to acknowledge valuable contributions to this work from Richard Fisher, Phillip Goodrich, and James Kellogg.

^(a)Permanent address: Jaycor, Vienna, VA 22182-2270.

- [1] G. Cooperstein and P. F. Ottinger, Guest Editorial, *IEEE Trans. Plasma Sci.* **15**, 629 (1987).
- [2] B. M. Koval'chuk and G. A. Mesyats, *Dokl. Akad. Nauk SSSR* **284**, 857 (1985) [*Sov. Phys. Dokl.* **30**, 879 (1985)].
- [3] D. D. Hinshelwood, J. R. Boller, R. J. Commisso, G. Cooperstein, R. A. Meger, J. M. Neri, P. F. Ottinger, and B. V. Weber, *Appl. Phys. Lett.* **49**, 1635 (1986).
- [4] B. M. Koval'chuk and G. A. Mesyats, in *Proceedings of the Eighth International Conference on High-Power Particle Beams*, edited by B. N. Breizman and B. A. Knyazev (World Scientific, New York, 1991), Vol. 1, p. 92.
- [5] W. Rix, D. Parks, J. Shannon, J. Thompson, and E. Waisman, *IEEE Trans. Plasma Sci.* **19**, 400 (1991).
- [6] B. V. Weber, R. J. Commisso, P. J. Goodrich, J. M. Grossmann, D. D. Hinshelwood, J. C. Kellogg, and P. F. Ottinger, *IEEE Trans. Plasma Sci.* **19**, 757 (1991).
- [7] M. E. Savage, G. W. Cooper, W. W. Simpson, and M. A. Usher, in Program Abstracts, Proceedings of the Ninth International Conference on High-Power Particle Beams, 1992 (unpublished), p. 473.
- [8] J. R. Boller, R. J. Commisso, P. J. Goodrich, D. D. Hinshelwood, J. C. Kellogg, J. D. Shipman, Jr., B. V. Weber, and F. C. Young, NRL Memorandum Report No. 6748, 1991 (unpublished).
- [9] B. V. Weber and D. D. Hinshelwood, *Rev. Sci. Instrum.* (to be published).
- [10] Yu. P. Golvanov, G. I. Dolgachev, L. P. Zakatov, E. V. Noskin, D. Yu. Ramzaev, and V. A. Skoryupin, in *Proceedings of the Thirteenth International Symposium on Discharges and Electrical Insulation in Vacuum*, edited by J. M. Buzzi and A. Septier (Les Editions de Physique, Paris, 1988), Vol. 2, p. 418.
- [11] L. K. Adler, A. Ben-Amar Baranga, J. B. Greenly, D. A. Hammer, and N. Qi, in *Proceedings of the Eighth International Conference on High-Power Particle Beams* (Ref. [4]), Vol. 2, p. 371.
- [12] D. D. Hinshelwood, R. J. Commisso, P. J. Goodrich, J. M. Grossmann, J. C. Kellogg, P. F. Ottinger, and B. V. Weber, in *Proceedings of the Eighth International Conference on High-Power Particle Beams* (Ref. [4]), Vol. 2, p. 1034.
- [13] R. J. Mason, M. E. Jones, J. M. Grossmann, and P. F. Ottinger, *Phys. Rev. Lett.* **61**, 1835 (1988).
- [14] J. M. Grossmann, R. Kulsrud, J. M. Neri, and P. F. Ottinger, *J. Appl. Phys.* **64**, 6648 (1988).
- [15] P. F. Ottinger, S. A. Goldstein, and R. A. Meger, *J. Appl. Phys.* **56**, 774 (1984).

He-Ne interferometer for density measurements in plasma opening switch experiments

B. V. Weber and D. D. Hinshelwood¹⁾

Plasma Physics Division, Naval Research Laboratory, Washington, D.C. 20375-5000

(Presented on 19 March 1992)

A He-Ne interferometer is used to measure the line-integrated electron density in the plasma of an operating plasma opening switch (POS). A heterodyne technique is used, where an acousto-optic modulator generates a 40-MHz frequency shift between the reference and scene beams. The phase shift is calculated numerically from the zero-crossing times of the beat signal. The precision of the phase measurement is $\pm 0.5^\circ$, however, several nonplasma sources of phase shift are present just after the current through the POS is interrupted. In particular, charged particle flow into the vacuum window results in a negative phase shift. This anomalous phase shift is effectively eliminated by using magnets to deflect the particles away from the window. Measurements during POS shots show a localized decrease in line density prior to current interruption.

I. INTRODUCTION

A plasma opening switch (POS) is essentially a plasma injected between the output conductors of a pulsed power generator.¹ The plasma short circuits the conductors as current is delivered from the generator. After a conduction-current or conduction-time limit is reached, the plasma current is interrupted quickly, resulting in a fast-rising, high-power pulse into a downstream load, for example, an *e*-beam diode.

One application of a POS is on the Hawk generator² at the Naval Research Laboratory. Hawk consists of an oil-filled Marx bank with a typical output voltage of 640 kV. The output of the Marx is connected to a coaxial vacuum section where a POS and load are located, as illustrated in Fig. 1. The current into a short-circuit load without the POS plasma is a sine wave, with a peak amplitude of 720 kA and 1.2- μ s quarter period. Plasma is injected into a localized region of the coaxial vacuum section with an azimuthal array of 18 flashboard sources. Each flashboard consists of an array of flashover gaps on a circuit board with a return-current plane to eject plasma by $\mathbf{J} \times \mathbf{B}$ forces.³ The current sources for the flashboards are fired before the Hawk generator in order to inject a suitable plasma density in the switch region. These plasma sources produce a high velocity (10–20 cm/ μ s), mostly C^{++} plasma.

POS experiments on Hawk with an *e*-beam diode load demonstrate 0.4-TW load power (0.8 MV, 500 kA) with a 20 ns rise time after conducting 600 kA in 0.9 μ s.⁴ This POS technology is being studied internationally in an effort to develop high-power, compact, inexpensive, inductive-store generators.¹ To understand the physics of POS operation, time- and space-resolved measurements of the plasma density during conduction and opening are required. The interferometer technique reported here provides the first measurements of the line-integrated electron density in the plasma during POS operation. The interfer-

ometer setup and phase-shift calculation are described in Sec. II. Nonplasma sources of phase shift are discussed in Sec. III. Finally, an example of a line-integrated density measurement during POS operation is presented in Sec. IV.

II. INTERFEROMETER SETUP

A diagram of the interferometer, as used to diagnose the Hawk POS plasma, is shown in Fig. 1. An acousto-optic modulator (AOM) is used to split the 10-mW He-Ne laser beam (633 nm) into reference and scene beams with a 40 MHz frequency difference for heterodyne phase detection.⁵ The beams are recombined at a beam splitter (BS) and monitored with a photodiode (PD). This signal is amplified by 55 dB and bandpass filtered (typically using a 10 MHz bandwidth) before being recorded by a digitizer, typically at 5 ns/point for 5–50 μ s. This interferometer technique has been used before, with a He-Ne interferometer as part of a two-color interferometer.⁶

The phase shift is determined by numerical analysis of the digitized beat signal. This technique is chosen over more conventional techniques using digital⁶ or analog⁷ electronics for simplicity and because the beat signal itself

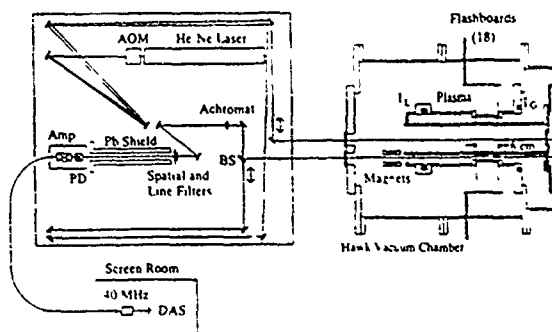


FIG. 1. Schematic of the Hawk generator with a POS. The arrangement of the He-Ne interferometer to measure the POS plasma density is shown. The Marx generator for Hawk is located to the right of the figure

¹⁾Present address: JAYCOR, Vienna, VA 22180.

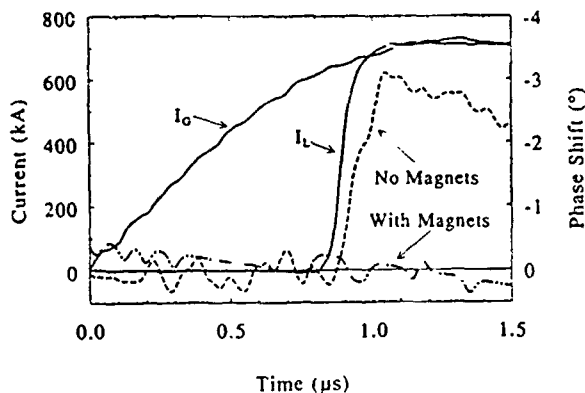


FIG. 2. Phase shifts measured in a null test where the laser beam is isolated inside a metal tube. Currents measured on the generator (I_G) and load (I_L) sides of the switch during a POS shot are shown. Phase shifts are shown for shots with and without magnets.

short time after the load current. The amplitude of this phase shift is 3° , and the negative sign indicates that the phase is opposite to the phase from plasma electrons. With the magnets, the phase is zero within the $\pm 0.5^\circ$ uncertainty during the 1.5- μ s interval of the measurement.

IV. DENSITY MEASUREMENTS DURING POS OPERATION

An example of a plasma-density measurement during POS operation is shown in Fig. 3.⁹ For this measurement, the line-of-sight of the laser beam is located 1.5 cm from the surface of the center conductor. The flashboard plasma density n_{FB} (averaged over the 8-cm plasma length) is measured if only the flashboards are fired. The flashboard density rises from $2.5 \times 10^{15} \text{ cm}^{-3}$ at the time conduction would begin to more than $8 \times 10^{15} \text{ cm}^{-3}$ at the time opening would begin. During a Hawk POS shot, the density n_e follows n_{FB} for about 0.3 μ s, but then slowly decreases from the flashboard density. Prior to opening, the density decreases abruptly. During and after opening, the density is zero within the measurement uncertainty. A small neg-

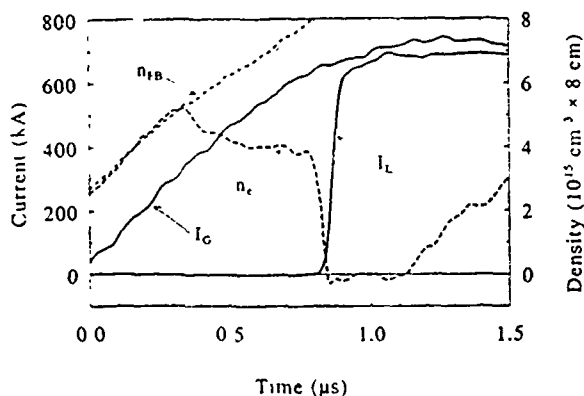


FIG. 3. Density measurements during POS operation on Hawk. The density measured during the shot n_e departs from the flashboards only density n_{FB} during the conduction phase and decreases abruptly prior to opening.

ative density, corresponding to about -2° , is evident in Fig. 3 just after opening begins. It is unclear whether this small negative phase shift is caused by x rays, charged particles, or other sources. About 0.3 μ s after opening begins, the density increases, and eventually (at a time beyond the range shown in Fig. 3) reaches a maximum value greater than 10^{17} cm^{-3} , more than ten times larger than the maximum flashboard density. This large density probably arises from electrode plasmas expanding into the line-of-sight.

Measurements⁹ at other radial locations indicate that the density decreases prior to opening throughout most of the 2-cm radial gap of the switch, although the minimum density occurs at the 1.5-cm location in this case. Other interferometry measurements indicate the plasma is not displaced significantly toward the load. Therefore, switch opening occurs in the rarefied plasma-density region in the vicinity of 1.5 cm from the center conductor for the conditions in Fig. 3. Plasma densities have been measured for a variety of switch configurations using various initial densities, conductor radii, injection aperture lengths, and generator current rise times. Also, other lines-of-sight (radial and chordal) have been used to measure axial dependencies.

Multichord He-Ne interferometry is being considered to allow measurement of spatial dependencies without relying on shot-to-shot reproducibility. Finally, the He-Ne interferometer can be used in conjunction with a CO₂ laser interferometer as a kind of two-color interferometer where the CO₂ interferometer can improve the resolution of small densities in the POS switch gap.

ACKNOWLEDGMENTS

The authors are indebted to their colleagues in the Pulsed Power Physics Branch for enthusiastic support of this work, especially R. Boller, R. Commisso, P. Goodrich, and J. Kellogg. The Hawk experiments were performed with the expert assistance of R. Fisher. One of the authors (B.V.W.) would like to acknowledge many useful discussions on interferometry with J. Irby of the Massachusetts Institute of Technology. This work was supported by the Defense Nuclear Agency.

¹ IEEE Trans. Plasma Sci. Special Issue on Fast Opening Vacuum Switches, PS 15, No. 6, (1987), and references therein.

² J. R. Boller, R. J. Commisso, P. J. Goodrich, D. D. Hinshelwood, J. C. Kellogg, J. D. Shipman Jr., B. V. Weber, and F. C. Young, NRL Memorandum Report No. 6748, Washington, DC, January 25, 1991.

³ D. G. Colombant and B. V. Weber, IEEE Trans. Plasma Sci. PS 15, 741 (1987).

⁴ B. V. Weber, R. J. Commisso, P. J. Goodrich, J. M. Grossmann, D. D. Hinshelwood, J. C. Kellogg, and P. F. Ottinger, IEEE Trans. Plasma Sci. 19, 757 (1991).

⁵ A. R. Jacobson, Rev. Sci. Instrum. 49, 673 (1978).

⁶ J. H. Irby, E. S. Marmor, E. Sevillano, and S. M. Wolfe, Rev. Sci. Instrum. 59, 1568 (1988).

⁷ P. Innocente and S. Martini, Rev. Sci. Instrum. 59, 1571 (1988).

⁸ P. Marchand and L. Marmet, Rev. Sci. Instrum. 54, 1034 (1983).

⁹ David Hinshelwood, Bruce Weber, J. M. Grossmann, and R. J. Commisso, Phys. Rev. Lett. 68, 3567 (1992).

is an important monitor of the interferometer. The zero-crossing times of the beat signal are calculated by linear interpolation using a simple computer program, and the corresponding phase shift ϕ is calculated using

$$\phi(t_n) = n\pi - \omega t_n,$$

where t_n is the n th zero-crossing time, and ω is the angular-frequency difference between the reference and scene beams. The numerical accuracy of this calculation depends on the digitizing rate; at 5 ns/point, the maximum numerical error in t_n for an ideal 40 MHz sine wave is ± 0.14 ns, or about 2° maximum phase error. This numerical phase error oscillates at 40 MHz and thus appears as high frequency noise on the phase signal, so it can be numerically filtered. For a frequency response of ± 5 MHz, a 20-pass binomial smoothing filter⁸ is appropriate. This reduces the numerical phase noise to about $\pm 0.5^\circ$ using the actual beat signal. In principle, a faster digitizing rate would result in higher precision, but other sources of phase noise in the present experiments make this change unnecessary.

The scene beam passes through a quartz window into the Hawk vacuum chamber and reflects off two mirrors inside the center conductor to direct the beam along an axial line-of-sight through the 8-cm-long POS plasma region (Fig. 1). The beam passes through a hole in the annular short-circuit-load plate, and exits the vacuum chamber through a quartz window. The plasma region is imaged onto the detector by an achromatic doublet lens of focal length f which is located a distance $2f$ from the plasma and $2f$ from the PD detector, resulting in unity magnification. The lens serves two other functions: to redirect laser rays refracted by electron-density gradients onto the detector (without additional phase shift) and to focus the laser beam through a spatial filter (typically 0.04-cm diam) to block much of the plasma light that otherwise would reach the detector. The PD detector samples a 1-mm-diam portion of the beam in the plasma, where the full beam is about 5 mm in diameter.

III. NONPLASMA SOURCES OF PHASE SHIFT

Several null tests were performed to determine sources of phase shift from causes other than plasma electron density. Tests for vibrational phase shifts were made by firing Hawk without injecting any plasma. Over the time range of interest (a few μ s), no significant vibrational phase shift was observed. Other sources of nonplasma phase shift investigated include: plasma light and x rays, refraction, and charged-particle flow into the vacuum window. Phase shifts from these sources were observed, and methods were developed to minimize these unwanted phase shifts so that accurate plasma-density measurements could be made during POS operation.

To measure signals resulting from plasma light and x rays, POS discharges were made without the He-Ne laser. Plasma light was attenuated before reaching the detector by the lens-aperture spatial filter and by a spectral line filter, as shown in Fig. 1. Even so, a signal was observed during the time current is rapidly switched into the short-

circuit load. This signal is attributed to bremsstrahlung generated by the stopping of high-energy electrons from the POS region in the metal walls. The inductive voltage generated at the switch during opening is typically 200 to 400 kV, with a pulse duration of about 50 ns. This x-ray pulse produces a detector signal with frequency components near 40 MHz that add to the beat signal and change the phase. The stray radiation reaching the detector was reduced by introducing lead shielding around the detector, as shown in Fig. 1. This technique may not be sufficient if higher voltage is generated, for example, by using a diode load. In this case, a fiber optic may be used to transmit the laser light to a remote detector.

Density gradients perpendicular to the line-of-sight refractively bend the scene beam by an angle $\alpha = -(l_0 \nabla n) / 2n_c$, where l_0 is the axial length of the plasma, ∇n is the density gradient (for example, in the radial direction), and n_c is the critical density. For the Hawk plasma l_0 is 8 cm, and the refractive bending angle is 1 mrad for $\nabla n = 7 \times 10^{17} \text{ cm}^{-4}$. This deflection angle would be sufficient to move the scene beam off the detector if the lens were not used. Density gradients of this magnitude probably do not exist in the Hawk plasma, but even smaller deflections can alter the amplitude of the beat signal and introduce phase errors. Test shots were taken with and without the lens to check for refraction. On many shots, the beat signal decreases significantly during conduction if the lens is not used. The lens corrects for refractive bending in all but a few cases (for example, when the beam is located very close to a conductor where higher density gradients are observed), resulting in a relatively constant beat-signal amplitude throughout the conduction and opening phases of the POS.

An unexpected source of nonplasma phase shift was discovered by isolating the scene beam from the POS plasma with a metal tube. The tube is attached to the center conductor and extends from the short-circuit plate to a location far upstream of the plasma injection region. The tube diameter is smaller than the gap between the inner and outer conductors in the switch region, allowing normal POS operation. The laser beam was directed through this tube. During POS shots, a phase shift beginning just after opening was observed. This anomalous phase shift is opposite in sign to the phase shift from plasma electrons. This phase shift is attributed to a transient increase in the index of refraction of the vacuum window which results from an electro-optic effect when charged particle flows (most likely fast electrons from the switch region) impinge on the quartz vacuum window. This phase shift was reduced by using permanent magnets located beyond the short-circuit plate (see Fig. 1) to deflect charged particles away from the window. The decrease of this anomalous phase shift, measured by using the tube to isolate the beam from the plasma, is shown in Fig. 2. For these shots, the generator current I_G increases to more than 600 kA in 0.8 μ s, while the load current I_L remains zero (the current is conducted through the POS plasma). After this 0.8 μ s conduction phase, the POS "opens," and the load current rises rapidly. Without the magnets, an anomalous phase shift is detected, beginning a

DENSITY MEASUREMENTS OF MICROSECOND-CONDUCTION-TIME POS PLASMAS

David Hinshelwood,* B. V. Weber, R. J. Commisso,
P. J. Goodrich,* J. M. Grossmann, and J. C. Kellogg.

Plasma Physics Division
Naval Research Laboratory, Washington, DC 20375-5000
*Jaycor, Vienna VA 22182-2270

Abstract: Measurements of the electron density in a coaxial microsecond conduction time plasma opening switch during switch operation are described. Current conduction is observed to cause a radial redistribution of the switch plasma. A local reduction in axial line density of more than an order of magnitude occurs by the time opening begins. This reduction, and the scaling of conduction current with plasma density, indicate that current conduction in this experiment is limited by hydrodynamic effects. It is hypothesized that the density reduction allows the switch to open by an erosion mechanism. Initial numerical modeling efforts have reproduced the principal observed results. A model that predicts accurately the conduction current is presented.

Plasma density measurements are critical to the understanding of plasma opening switch (POS) operation. HeNe interferometry is a relatively simple, quantitative, non-perturbing technique for *in situ* electron density measurement during POS operation. The first such measurements were reported recently.¹ A schematic of the arrangement, on the Hawk generator at the Naval Research Laboratory, is shown in Fig. 1. Measurements have been obtained on shots with various cathode and anode radii. A short-circuit load is located 25 cm beyond the switch. A mask outside the anode rods shields all but the (usually) 8-cm-long switch region from the plasma injected by 18 flashboards. The flashboards are typically pulsed 1 to 2 μ s before the generator is fired. In the absence of opening, the generator drives 720 kA through the switch in 1.2 μ s.

Details of the interferometer are given in Ref. 2 and are only summarized here. An acousto-optic modulator splits a 10-mW cw HeNe laser beam into two beams with a 40-MHz relative frequency shift. A scene beam is directed through the switch region in the axial direction, parallel to the cathode (see Fig. 1). A reference beam traverses an equal path length outside of the vacuum system before combining with the scene beam at a beamsplitter. The intensity of the combined beam exhibits a 40-MHz beat signal whose phase depends on the relative phase shift between the two beams. The zero-crossing times of the beat signal are used to determine the time-varying phase shift of the scene beam, from which the line-integrated density $\int n_e dz$ is calculated. Several null tests were performed to verify that the measured phase shift is caused by electrons in the switch region.² Several sources of spurious phase shift have been identified. After taking corrective measures,² a measurement limit during shots of less than $2 \times 10^{15} \text{ cm}^{-2}$, or 2° of phase shift, has been achieved. Before each shot the flashboards alone are fired and the density is evaluated for comparison with shots where the POS plasma conducts current.

of the injected plasma and/or secondary plasma formation. At 300 ns there is little effect of current conduction other than a further increase in line density at the cathode. This may be indicative of the explosive-emission cathode plasma. By the time of opening, current conduction through the plasma has greatly altered the density profile. Since the interferometer integrates along the axis, and the same results are observed at different azimuths, this alteration must be associated with radial displacement of the plasma. These measurements indicate that plasma is pushed out to the anode radius, and perhaps in to the cathode. The lowest average density immediately prior to opening occurs most frequently at 1.5 ± 0.1 cm from the cathode; opening presumably occurs at this location. Data taken during shots with 2.5-cm-radius and 12-cm-radius cathodes show a strong density decrease over most of the switch gap and the radial location of opening is not as obvious.

The observed radial plasma displacement toward the anode and cathode can be explained by a relatively small axial ($j_z/j_r \sim 10\%$) tilt or bend in the current streamlines. We believe that this axial component arises from a combination of the radial dependence of the magnetic field and the radial variation of the initial plasma line density. A radial variation of B^2/n will result in a radial variation of the axial displacement, and thus a bend in the current streamlines. The different radial density profiles at opening observed with different cathode diameters may result from different initial density and magnetic field profiles.

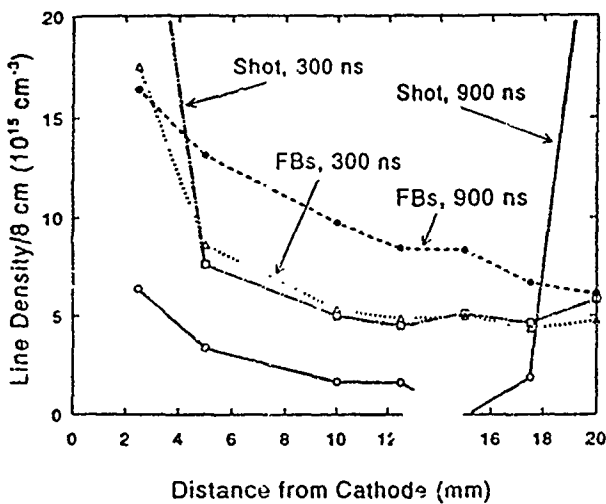


Figure 3: Electron density as a function of radial position early in the conduction phase and just before opening. Flashboard-only data are shown for comparison.

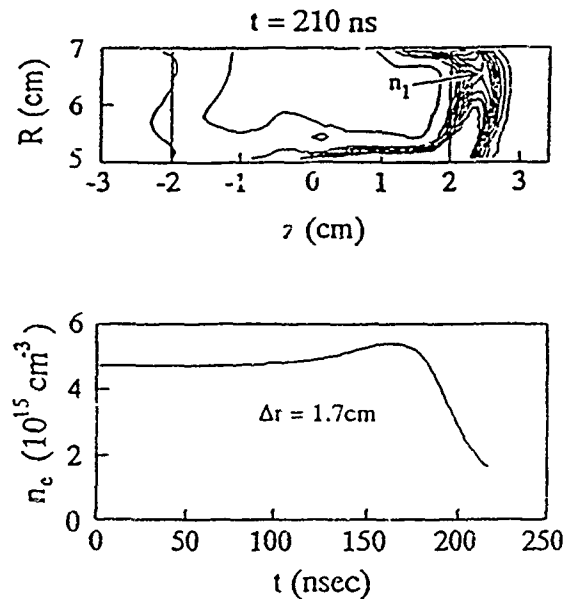


Figure 4: ANTHEM code predictions: (top) Electron density at the end of the conduction phase. The vertical lines indicate the initial plasma location. (bottom) Average density at 17 mm from the cathode.

Hydrodynamic motion of the switch plasma has been modeled with the ANTHEM two-fluid code,⁴ using the measured, average electron density profile at 300 ns. To reduce computation time, the plasma mass and length and the current risetime were reduced. A 4-cm-long, H^+ plasma was assumed, with a current risetime of 200 ns.

This risetime was chosen to provide the same calculated center-of-mass translation as the experimental parameters. Results are shown in Fig. 4. Figure 4a shows electron density contours at 210 ns, corresponding to the time of switch opening in the experiment. The current streamlines follow these contours — mostly radial, but bowed. Plasma has been displaced toward the load end of the switch region, albeit in a narrower channel than indicated by previous magnetic field measurements.⁵ We believe that the wider current channel indicated by the field measurements could be reproduced by incorporating anomalous resistivity in the modeling.⁶ More importantly, the slight bending of current streamlines has led to a radial density redistribution, with a density minimum at 1.7 cm from the cathode. This compares well with the results in Fig. 3. Fig. 4b shows the calculated time history of the average density at this radius. A sharp decrease is seen at the end of the conduction phase, which compares well with the results in Fig. 2.

The ultimate opening of the switch occurs in a (relatively short) few tens of ns. The observed reduction in the average density by more than an order of magnitude at 1.5 cm from the cathode may allow the switch to open by enhanced erosion of the switch plasma. Effective switch gap opening rates are inferred from similar shots with diode loads.⁷ Based on magnetic insulation arguments and electrical data from these experiments, gap opening rates of ~ 5 cm/ μ s and switch gaps at opening of a few mm are inferred. Faraday cup measurements⁵ indicate that the ion current is on the order of 20% of the total current at the time of opening. At the reduced average electron density measured at the end of the conduction phase in these experiments, the value of j_i/en_e exceeds 10 cm/ μ s. This rate may well exceed the ion injection velocity and can explain the observed, rapid opening.

Data have also been obtained using the chordal lines of sight shown in Fig. 1. Measurements at four locations in the switch region were taken during shots with 2.5-cm-radius cathodes. Tubes shielded the scene beam from plasma outside the switch region. Typical data, from a shot with the line-of-sight located 3 cm from the generator end of the switch region, are shown in Fig. 5. The average density at each location first increases, and then decreases. The density increase is larger toward the load end, as would be expected from axial displacement of the switch plasma. The density decrease at each location is correlated with the arrival of the current front, as determined by dB/dt probe data taken during similar shots, as seen in Fig. 5.

Measurements beyond the switch region were taken during shots with 5-cm-radius cathodes. Typical data are shown in Fig. 6. No significant electron density is observed beyond the switch region until well after opening. This confirms that opening does not arise from a large-scale translation of the switch plasma as it does in a plasma flow switch. An interesting phenomena is observed (see Ref. 3): For conduction currents below 450 kA, no significant plasma is observed beyond the switch, even after opening, while at larger currents plasma is observed. This is suggestive of two different regimes of switch operation.

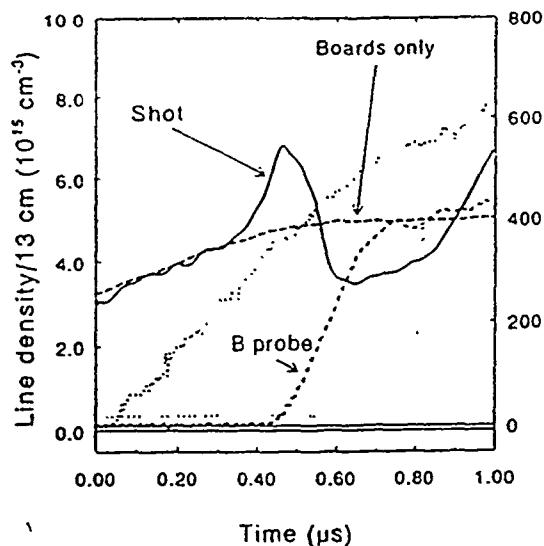


Figure 5: Average density along a chordal line of sight located in the switch region. The signal from a magnetic probe, at the same location on a similar shot, is shown for comparison.

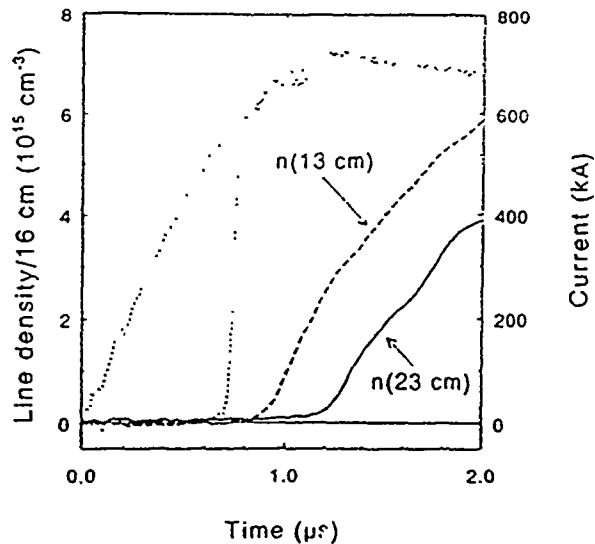


Figure 6: Average densities along lines of sight beyond the initial switch region.

Several models have been proposed to explain the limitations on current conduction in plasma opening switches. Field penetration by the Hall term (EMH)⁸ and $\vec{j} \times \vec{B}$ hydrodynamic displacement (MHD)⁹ are relevant to the parameters of this experiment. Peak conduction current scaling with density has been studied by taking timing scans using different cathode radii, switch lengths, and current risetimes. Data from timing scans using three cathode radii are compared with predictions in Fig. 7. The peak density at 1.5 cm from the cathode is used in the predictions. In calculating the MHD limit it is assumed that opening occurs when the plasma center-of-mass is displaced by half of the initial switch length. This is consistent with previous magnetic field measurements.⁵ Good agreement between the data and the MHD predictions are observed for most shots. Data from a few shots at lower switch currents are suggestive of an EMH mechanism. Data from shots with different switch lengths and current risetimes (see Ref. 3) show agreement with prediction similar to that in Fig. 7.

The MHD calculation has been refined to account for the time-varying density by using a snowplow model.¹⁰ In front of the snowplow, the density is given by data from flashboard-only shots. Behind the snowplow, the self-magnetic field is assumed to prevent further plasma from entering the switch gap. Conduction is assumed to cease when the snowplow reaches the end of the initial switch region. The underlying assumption is that this level of axial displacement is associated with the level of radial displacement necessary to allow opening. Predicted and observed peak conduction currents are shown in Fig. 8 for shots with different cathode radii, switch lengths, and current risetimes. This simple model is seen to have very good predictive capability.

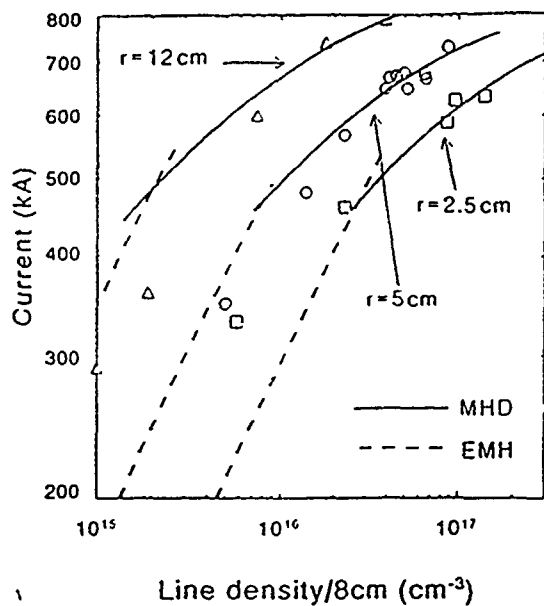


Figure 7: Conduction current as a function of peak density for three cathode radii, compared to that calculated from the MHD and EMH models.

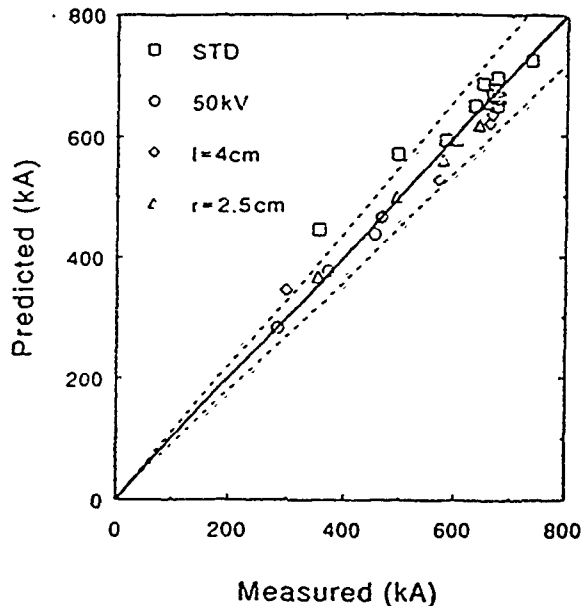


Figure 8: Conduction current versus predictions of the snowplow model, for a range of switch parameters.

In conclusion, electron density measurements during POS experiments have shown new features relating to the conduction and opening mechanisms in a POS. Current conduction causes a density reduction over most of the plasma radial extent, indicating that current conduction in this experiment is limited by hydrodynamic effects. Opening occurs without a large-scale axial displacement. We suggest that a radially-nonuniform axial snowplow gives rise to a radial redistribution of the switch plasma, and that opening occurs by erosion of the rarified region. This picture is supported by axial and chordal line of sight data, fluid code calculations, and the scaling of conduction current with switch parameters. The density measured during flashback shots can be used to predict accurately the conduction current over a range of switch parameters.

It is a pleasure to acknowledge valuable contributions to this work from Rick Fisher.

References

1. David Hinshelwood, Bruce Weber, R. J. Comisso and J. M. Grossmann, to be published in Phys. Rev. Lett., June 1992.
2. B. V. Weber and D. D. Hinshelwood, to be published in Rev. Sci. Inst., Oct., 1992.
3. B. V. Weber, J. R. Boller, R. J. Comisso, P. J. Goodrich, J. M. Grossmann, D. D. Hinshelwood, J. C. Kellogg, P. F. Ottinger, and G. Cooperstein, these proceedings.
4. R. J. Mason, M. E. Jones, M. Grossmann, and P. F. Ottinger, Phys. Rev. Lett. **61**, 1835 (1988).
5. D. D. Hinshelwood, R. Comisso, P. J. Goodrich, J. M. Grossmann, J. C. Kellogg, P. F. Ottinger, and B. V. Weber, in Proc. 8th Int. Conf. on High-Power Particle Beams Vol. 2, ed. by B. N. Breizman and B. A. Knyazev (World Scientific, New York, 1991), p. 1034.
6. J. M. Grossmann, R. Kulsrud, J. M. Neri, and P. F. Ottinger, J. Appl. Phys. **64**, 6648 (1988).
7. B. V. Weber, R. J. Comisso, P. J. Goodrich, J. M. Grossmann, D. D. Hinshelwood, J. C. Kellogg, and P. F. Ottinger, IEEE Trans. Plasma Sci. **19**, 757 (1991).
8. K. V. Chukbar and V. V. Yan'kov, Sov. Phys. Tech. Phys. **33**, 1293 (1988).
9. W. Rix, D. Parks, J. Shannon, J. Thompson, and E. Waisman, IEEE Trans. Plasma Sci. **19**, 400 (1991).
10. Eduardo Waisman, Maxwell Laboratories, personal communication.

PLASMA OPENING SWITCH EXPERIMENTS ON HAWK
WITH AN E-BEAM DIODE LOAD

P.J. Goodrich,* J.R. Boller, R.J. Comisso,
D.D. Hinshelwood,* J.C. Kellogg, B.V. Weber

Pulsed Power Physics Branch, Plasma Physics Division
Naval Research Laboratory, Washington, DC 20375

Abstract

Successful application of inductive energy storage depends critically on the performance of the opening switch. The new Hawk generator at NRL¹ is used in plasma opening switch (POS) experiments in the 1- μ s conduction time regime to study long conduction time POS physics. In this experiment, different POS configurations were used, including various switch to load distances and different cathode center conductor radii. The load was an e-beam diode. Peak load powers of 0.5 TW, with load current risetimes of 20 ns and current transfer efficiencies of 80%, were achieved with a POS conduction time of 0.75 μ s using a 5 cm diam cathode. Typically, 40 kJ were coupled into the diode, which is 20% of the energy stored in the Hawk capacitance. The data indicate that above a critical load impedance the final switch gap, as determined from magnetic insulation arguments, is fixed to 2.5-3 mm, independent of conduction current and center conductor radius. Above this critical load impedance, current is shunted into the transition section between the switch and the load such that the voltage remains constant. At lower impedance values, the load voltage decreases in proportion to the load impedance. This critical load impedance is then the optimum impedance for maximum load power. Increasing the cathode magnetic field by conducting more current (up to a limit) or by decreasing the cathode center conductor radius at a given current level allows the switch to remain insulated at a higher voltage. Peak load voltages up to 1.7 MV were achieved using a 5 cm diam center conductor, a factor of 2 higher than that obtained with a 10 cm diam center conductor and 2.7 times higher than the predicted Marx voltage (640 kV).

Introduction

Pulsed power generators traditionally use water line and vacuum transmission line technology for power conditioning--power gain and pulse compression--of the microsecond output pulses from Marx banks. The emergence of inductive store technology² allows the development of more compact pulsed power generators. An opening switch such as a POS is used for power conditioning of the output pulse from the Marx. Hawk uses a 607 nH Marx, designed by Physics International Co.,³ with 225 kJ stored at 80-kV charge to deliver up to 700 kA in 1.2 μ s to a POS. By varying the switch plasma density, the switch can be made to conduct from 0 to 1.2 μ s. The goals of these experiments were to study the physics of the switch for these long conduction times and optimize the switch/e-beam diode performance to generate high power short duration (<100 ns FWHM) power pulses.

Hawk Experimental Configuration

The switch/load vacuum section of one experimental configuration is shown in Fig. 1. Different center conductor (cathode) diameters were used, notably a 10 cm diam

cathode (pictured here) and a 5 cm diam cathode. The current monitors shown here consist of a Rogowski loop, ISU, on the generator side of the POS (upstream) and two B-dot monitors, ILU and ILL, on the load side of the POS (downstream) at the e-beam diode. The plasma was produced by 18 carbon-coated flashboards in the POS region. The banks driving the flashboards were typically fired 1-2 μ s before current was conducted in the switch.

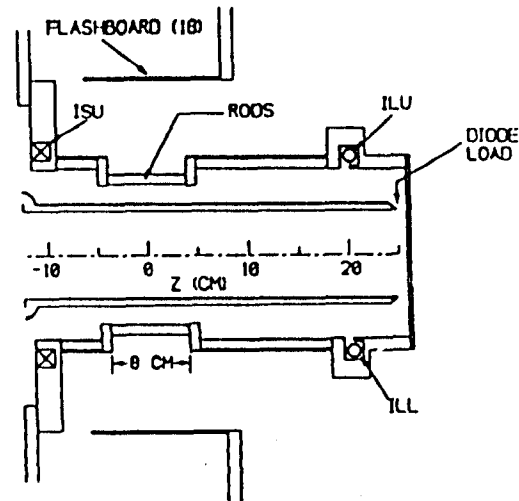


Fig. 1. Hawk switch/load vacuum section in the standard configuration.

The set-up in Fig. 1 with a switch to load length of 26 cm is called the standard configuration. In this configuration, for conduction times greater than 0.6 μ s, plasma reaches the diode before switch opening. This is plasma directly from the flashboards and plasma accelerated to the load by JxB forces during conduction (confirmed by Faraday cups in the load). The bulk of the plasma does not reach the load--independent magnetic probe measurements indicate the center of mass motion of the plasma is only about 4 cm downstream--but enough plasma reaches the load for it to act like a plasma-filled diode with a rising load impedance. This uncontrolled load plasma ultimately limits the impedance to a relatively low value, independent of the actual diode gap spacing and well below the vacuum value (for large enough gaps).

To obtain higher load impedances and control the impedance with the gap spacing, plasma must be kept out of the load. This was accomplished by extending the conductors downstream of the switch so that the switch to load length is 40 cm or more. The two (originally load) B-dot current monitors were left in place to measure current in the transition section, about halfway between the switch and the load, and two B-dot monitors were added at the load. In this configuration, called the extended

configuration, the load looks like a vacuum diode with a falling load impedance and the impedance can be controlled by changing the gap spacing.

Results with a 10 cm Diam Cathode

Fig. 2 shows representative data from a Hawk shot with a 10 cm diam cathode in the standard configuration. The plasma delay is 1.5 μ s and the switch conducts for 0.9 μ s before opening. The 10-90% load current risetime is 40 ns with an 80% current transfer efficiency and 500 kA delivered to the load. There is about 100 kA of residual current in the switch. Peak load voltage is 770 kV, peak load power is 0.4 TW, and almost 40 kJ is delivered to the load. Best opening (highest voltage and power and fastest risetimes) on shots with a 10 cm diam cathode occurs for conduction times of \sim 1 μ s, near peak current.

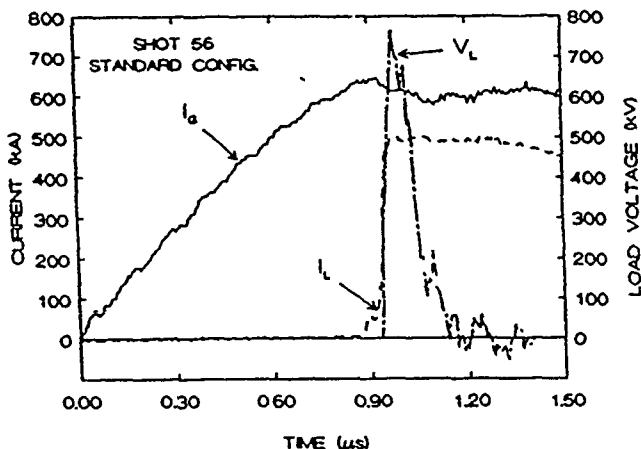


Fig. 2. Current and voltage data for a 0.9 μ s conduction time POS shot with a 10 cm diam cathode in the standard configuration.

Load data for this shot are shown in Fig. 3. The load acts like a plasma-filled diode with an impedance rising from 0 Ω to 1.5 Ω at peak load power. The diode gap spacing is 1 cm which represents a vacuum impedance, assuming critical current, of 8 Ω . An impedance of 1.5-2 Ω was the highest that could be obtained in this configuration, regardless of the gap spacing (including removal of the anode plate) for conduction times over 0.6 μ s.

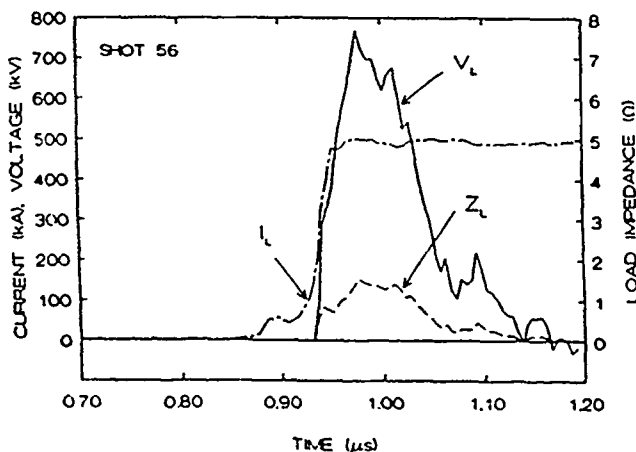


Fig. 3. Load data for the shot in Fig. 2.

Fig. 4 shows data from two shots in the extended configuration. Here the load looks like a vacuum diode with a falling load impedance. By increasing the diode gap spacing from 0.5 cm to 1.0 cm the load impedance at peak power increases from 2 Ω to about 4 Ω . However, the voltage generated on these shots is the same, \sim 800 kV, so the impedance "mismatch" with the larger gap spacing resulted in greater current loss.

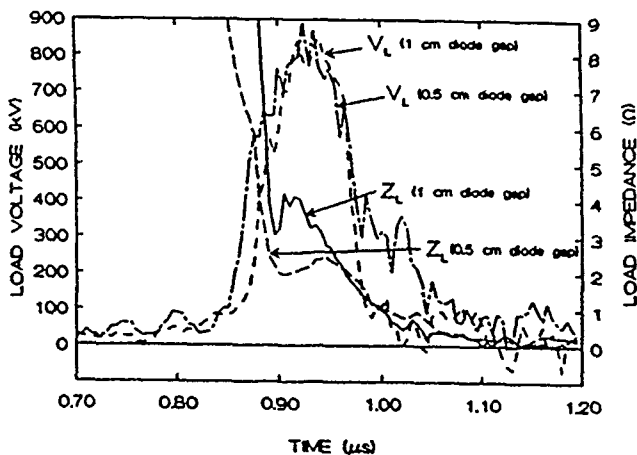


Fig. 4. Load data for two shots in the extended configuration.

The dependence of voltage on load impedance is shown in Fig. 5 for numerous shots with a 10 cm diam cathode. Below a critical load impedance, \sim 1.7 Ω , the voltage decreases in proportion to the load impedance. This is termed the load limited regime. Above the critical impedance, the voltage is constant for a given conducted current. This is called the switch limited regime. As the load impedance is increased above 1.7 Ω , current is lost between the switch and the load, although well downstream of the switch, where the plasma density is zero. Also, the maximum voltage increases with conducted current. For example, with conducted currents of 500 kA the maximum voltage is \sim 500 kV, for 650 kA it is \sim 900 kV.

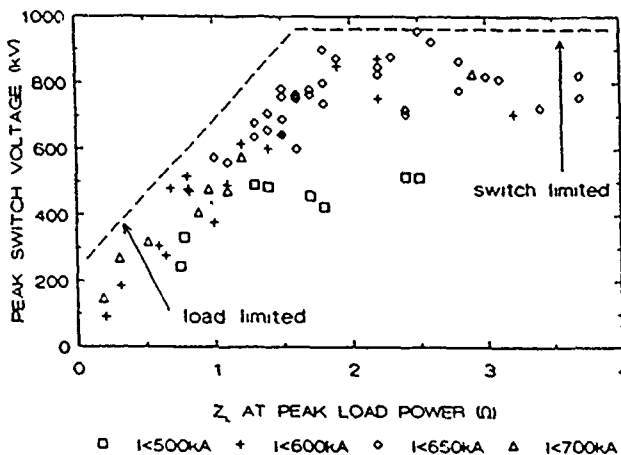


Fig. 5. Peak voltage as a function of load impedance with the 10 cm diam cathode. Above a critical impedance, \sim 1.7 Ω , the voltage is constant for a given conduction current.

Maximum power is delivered to a load operating at the critical impedance, as shown in Fig. 6. Furthermore, the peak load power increases with conduction time up to 1 μ s. Thus, the highest power generated, 0.4 TW, occurs for 1 μ s conduction at a load impedance of 1.7 Ω .

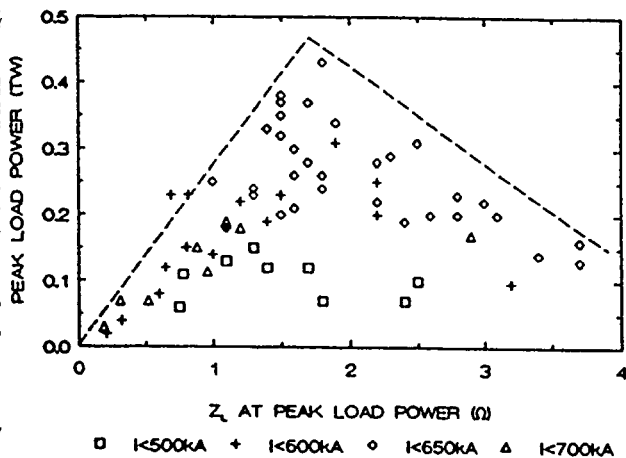


Fig. 6. Peak load power versus load impedance with the 10 cm diam cathode. Maximum power is delivered to a load operating at the critical impedance with $\sim 1 \mu$ s conduction times.

The switch gap at peak power is calculated assuming the switch operates at the critical current for magnetic insulation, $I_C = 1.6 \times 85000 \beta r / D$, where I_C is the generator current, r is the cathode radius, D is the gap between the plasma and the cathode (or cathode plasma), and 1.6 is an empirical factor. The switch gap at peak power is plotted versus load impedance, Z_L , at peak power in Fig. 7. At a given load impedance, the gap is independent of conduction current. The voltage increases with conduction current such that the gap size, at a given load impedance, is the same for different conduction currents. The gap is 2.5-3 mm, independent of Z_L , for $Z_L > 1.7 \Omega$. For $Z_L < 1.7 \Omega$, the calculated gap decreases as Z_L decreases to zero. The calculation may be misleading in this case, because the switch voltage is limited by the load; the switch gap could still be 2.5-3 mm. This data analysis gives a physical picture of the Hawk POS: at peak power the switch acts like a magnetically insulated transmission line (MITL) operating at critical current with an effective electrode gap of 2.5-3 mm. Important implications of this fixed gap size model include a voltage limit as the load impedance is increased and a load impedance for maximum load power (data shown above). The current that is lost operating above the 1.7 Ω critical impedance appears to be mainly electron loss. It occurs in regions where the plasma density is zero and from x-ray pinhole pictures as well as observation of physical damage the loss is at the outer conductor (anode). Higher power would be possible if the gap size could be increased (the electrode gap in the POS is 2 cm), or if the magnetic field could be increased at the same gap size. The latter approach was investigated by decreasing the center conductor radius.

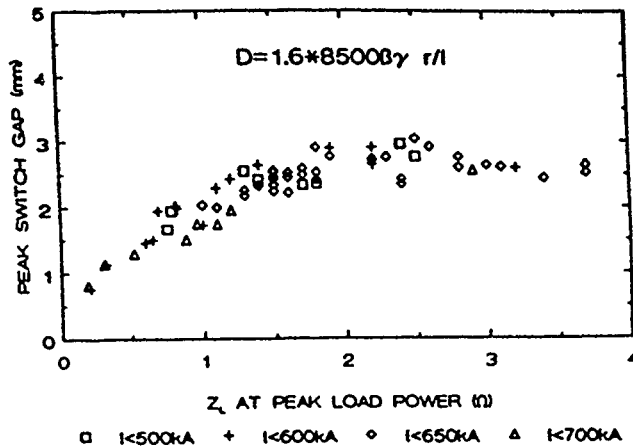


Fig. 7. Switch gap calculated at peak power, assuming the switch is at critical current, as a function of load impedance with the 10 cm diam cathode. The gap is independent of conduction current and, above the critical impedance, is fixed to 2.5-3 mm.

Results with a 5 cm Diam Cathode

Data from a Hawk shot with the 5 cm cathode in the standard configuration are shown in Fig. 8. The switch conducts for 0.7 μ s and opens in 20 ns, delivering 80% of the current, 400 kA, to the load. There is about 100 kA of residual switch current. The voltage generated on this shot is 1.2 MV, well above the -900 kV voltage limit of the 10 cm cathode. The peak load power is 0.5 TW and 40 kJ is coupled into the load. Optimum switch opening with a 5 cm cathode occurs for $\sim 0.75 \mu$ s conduction with a $\sim 1.6 \mu$ s plasma delay, also the delay for best opening with the 10 cm cathode. To conduct longer than this requires a large increase in plasma delay. (A similarly large increase is necessary to conduct beyond 1 μ s with the 10 cm cathode.) The poorer switch opening observed with these much longer plasma delays could be due to a small gap in the higher density switch and not a consequence of load-limited operation.

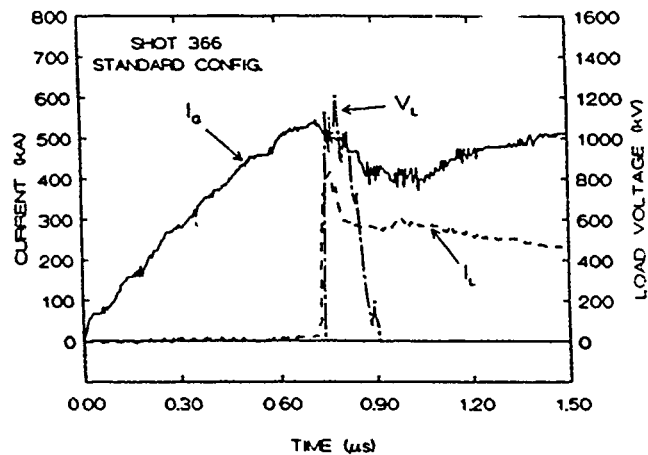


Fig. 8. Current and voltage data for a 0.7 μ s conduction time POS shot with a 5 cm diam cathode in the standard configuration.

Load voltages as high as 1.7 MV have been generated with the 5 cm cathode, a factor of 2 higher than the best 10 cm cathode shots and 2.7 times higher than the erected Marx voltage. The data indicate gap opening rates up to $dD/dt = 10^7$ cm/sec.

The relationship between voltage and load impedance for numerous shots with the 5 cm cathode is shown in Fig. 9. Similar to the results using the 10 cm cathode, there is a critical or optimum impedance, here 3.5 Ω . Below this value the voltage depends on impedance; above it the voltage is limited for a given conducted current. For $-0.75 \mu\text{s}$ conduction, this limit is 1.5-1.7 MV.

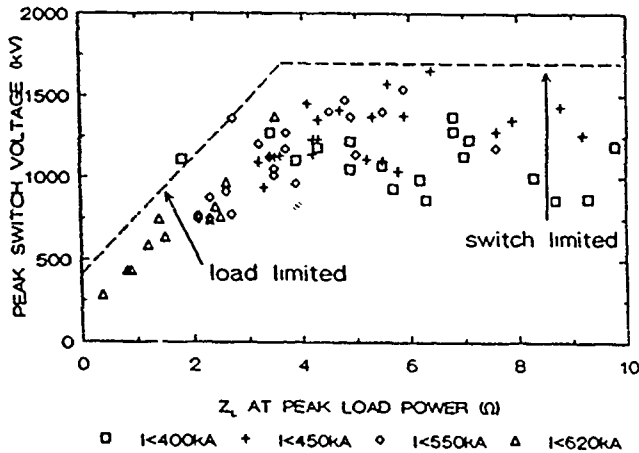


Fig. 9. Peak voltage as a function of load impedance with the 5 cm diam cathode. Above a critical impedance, $\sim 3.5 \Omega$, the voltage is constant for a given conduction current.

In Fig. 10 the calculated switch gap is shown as a function of load impedance for the 5 cm cathode shots. The switch gap is 2.5-3 mm, for $Z_L > 3.5 \Omega$, the same gap size as the 10 cm cathode shots. The larger magnetic field associated with the smaller radius cathode allows a larger voltage to exist across the gap at peak power (critical current). Above the 3.5 Ω critical impedance, current is shunted into the transition section, the losses occurring well downstream of the switch, where the plasma density is zero.

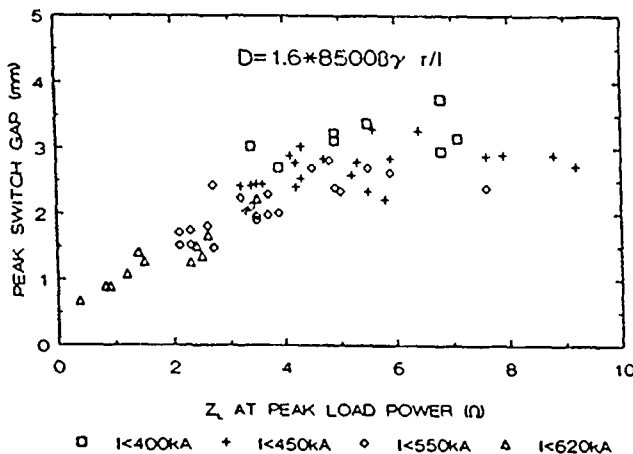


Fig. 10. Calculated switch gap at peak power versus load impedance with the 5 cm diam cathode. The gap is fixed to 2.5-3 mm above the critical impedance.

In Fig. 11 voltage generated with four different cathode diameters is plotted vs. cathode magnetic field. Lines of constant switch gap, D , calculated from the critical current formula are also shown. The data show the voltage increase possible as the magnetic field increases, with the switch gap remaining constant at 2.5-3 mm. This happens as the conducted current is increased, up to a $1 \mu\text{s}$ conduction time with the 10 cm cathode and $0.75 \mu\text{s}$ conduction time with the 5 cm cathode, or as the cathode radius is decreased. Moving vertically down on this graph is in the direction of decreasing load impedance. Data points below the $D=2.5$ mm curve are in the load limited regime. The five shots with the 2.5 cm diam cathode were in the standard configuration with enough JxB plasma accelerated to the load to consistently be in the load limited regime.

Higher voltage and power could be achieved if the gap size can be increased, preferably with the 10 cm or larger diam cathode which can readily conduct the full $1\text{-}\mu\text{s}$ current pulse.

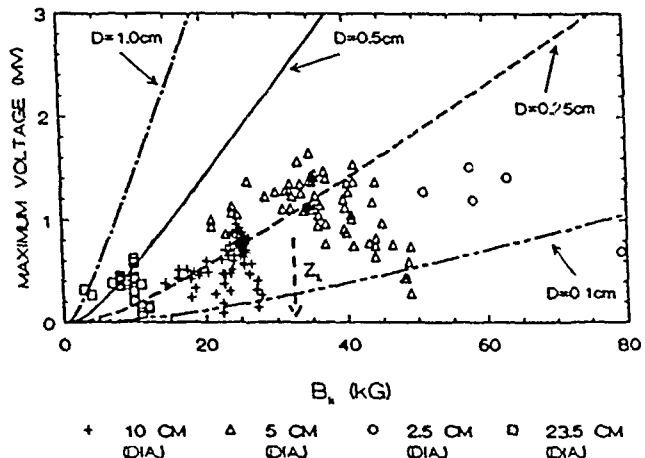


Fig. 11. Maximum voltage generated as a function of cathode magnetic field for different cathode diameters. Here the critical current model indicates ways to increase switch voltage.

Summary and Future Work

High power pulses have been generated on the Hawk generator at NRL using a $0.75\text{-}1 \mu\text{s}$ conduction time POS. Peak load powers of 0.5 TW with 20 ns risetimes were achieved with $0.75 \mu\text{s}$ conduction times using a 5 cm diam cathode. Typically, 40 kJ was coupled into the γ -beam diode, which represents an energy efficiency of 20%.

The data indicate that an effective gap of 2.5-3 mm was produced in the switch. This ultimately limits the voltage and determines an optimum load impedance for maximum load power. The gap is independent of conducted current, center conductor radius, and the load impedance, at least above the critical impedance. Increasing the conducted current (up to a limit) or decreasing the cathode radius increases the voltage consistent with a fixed gap. In particular, the voltage increases from 0.9 MV to 1.7 MV when the cathode diameter was decreased from 10 cm to 5 cm.

Higher power could be achieved if the switch gap size can be increased. One possibility is to use a controlled plasma-filled diode (PFD) decoupled from the switch.⁴ Preliminary results on Hawk with the 5 cm diam cathode suggest peak load powers up to 1.7 times higher using such a PFD in conjunction with a POS for short conduction times of 0.4 μ s. A second possibility is to use a hydrogen plasma source in place of the carbon flashboard sources for the POS. Experiments⁵ have shown higher voltages and powers (presumably larger switch gaps) are generated with a hydrogen POS.

References

- [1] J.R. Boller, et. al., NRL Memorandum Report 6748, January 1991.
- [2] G. Cooperstein and P.F. Ottinger, Guest Editorial, IEEE Trans. Plasma Science, PS-15, Dec. 1987.
- [3] P. Sincerny, et. al., 7th IEEE Pulsed Power Conference, Monterey, CA, 1989, IEEE Cat. No. 89CH2678-2, p. 275.
- [4] J.M. Grossmann, et. al., Bull. A.P.S., 34, p. 2076, 1989.
- [5] P.S. Ananjin, et. al., 14th Inter. Symposium on Discharges and Electrical Insulation in Vacuum, Santa Fe, NM, Sept. 1990, p. 417.

*Jaycor, Vienna, VA 22182

Characterization of a microsecond-conduction-time plasma opening switch*

R. J. Commisso,[†] P. J. Goodrich,[‡] J. M. Grossmann, D. D. Hinshelwood,[‡] P. F. Ottinger, and B. V. Weber

Pulsed Power Physics Branch, Plasma Physics Division, Naval Research Laboratory, Washington, D.C. 20375

(Received 10 December 1991; accepted 27 February 1992)

This paper presents data and analyses from which emerges a physical picture of microsecond-conduction-time plasma opening switch operation. During conduction, a broad current channel penetrates axially through the plasma, moving it toward the load. Opening occurs when the current channel reaches the load end of the plasma, far from the load. During conduction, the axial line density in the interelectrode region is reduced from its value with no current conduction as a result of radial hydrodynamic forces associated with the current channel. A factor of 20 reduction is observed at opening in a small, localized region between the electrodes. When open, the switch plasma behaves like a section of magnetically insulated transmission line with an effective gap of 2 to 3 mm. Increasing the magnetic field in this gap by 50% results in an improvement of 50% in the peak load voltage and load current rise time, to 1.2 MV and 20 nsec, respectively. An erosion opening mechanism explains the inferred gap growth rate using the reduced line density at opening. Improved switch performance results when the maximum gap size is increased by using a rising load impedance.

I. INTRODUCTION

Pulsed-power generators produce electrical power pulses of 10^{12} to 10^{14} W with < 100 nsec duration. These pulses are generally used to drive loads, such as intense electron- and ion-beam diodes (for inertial confinement fusion, flash radiography, and matter interaction studies), and high-density Z pinches (for fusion and high-energy-density plasma research). The power conditioning required to produce such high-power pulses can be accomplished through several approaches.¹ Typically, electric field energy is stored in a capacitor and switched to the load through a closing switch. An alternative, developmental approach employs magnetic field energy stored in an inductor. The stored energy is transferred to the load using an opening switch. The inductive approach has the potential for smaller, less complex systems¹ because the stored energy density for inductive systems, where energy density is limited by mechanical strength, can be much higher than for capacitive systems, where energy density is limited by dielectric strength. Inductive systems, however, require a vacuum opening switch that can conduct current long enough to energize an inductor and then divert the current to the load in a time short compared with the required pulse width, while withstanding the ensuing high voltage with little or no residual current flowing in the opening switch. A plasma opening switch (POS) uses a plasma injected in vacuum between the electrodes of a pulsed-power generator to conduct current while an inductor is energized. At the end of the conduction phase the current

flow is interrupted, i.e., the switch opens, and the current is transferred to the load.

The first POS studies were done at relatively short conduction times of < 100 nsec. In this application, a POS was used on a conventional, capacitive pulsed-power generator, retrofitted with a small inductive-storage section, to reduce the current rise time and to increase the power above the generator matched-load output power.¹⁻¹⁹ The POS proved successful in this application, with reported increases of 2.7 in voltage (to 4.6 MV) and 2.4 in power (to 3.6 TW) above the ideal matched-load values.^{20,21} Shortly thereafter, experiments in Russia²² and the United States²³ demonstrated the potential for a POS to operate at conduction times of $1 \mu\text{sec}$. Voltage increases^{22,24} of three to five times the initial voltage on the capacitor bank and pulse compressions^{24,25} of 20 to 30 (also see the results in Fig. 8) have been reported. As is well known,¹ the inherent advantages of inductive storage can be more fully exploited if the conduction time can be increased while maintaining the same opening behavior. Results and analyses of microsecond-conduction-time POS (hereafter denoted $1 \mu\text{sec}$ POS) experiments continue to be reported.^{1,10,24-36} This paper will review past experiments and present new data and analyses aimed at characterizing and understanding the behavior of a $1 \mu\text{sec}$ POS plasma.

Measurements to characterize the conduction and opening phases of a $1 \mu\text{sec}$ POS in coaxial geometry have been carried out at the 0.5 MA, 1 MV level. Analysis of these measurements suggest a physical picture of the POS plasma behavior. During conduction, a current channel penetrates axially through the plasma, moving the POS plasma toward the load. This channel is azimuthally symmetric, predominately radial, and broad relative to the collisionless skin depth. Opening occurs when the current

*Paper 914, Bull. Am. Phys. Soc. 36, 2482 (1991).

[†]Invited speaker.

[‡]Permanent address: Jaycor, Inc., Vienna, Virginia 22182.

channel reaches a position near the load end of the POS, in contrast to the current being convected to the load. Almost identical observations have been made for a POS operating at < 100 nsec conduction times.^{10,37} The $1 \mu\text{sec}$ POS plasma density integrated along an axial line of sight (the line density) between the electrodes is reduced during conduction from the measured value with no current conduction. A factor of 20 reduction is observed at opening in a small (relative to the electrode separation) portion of the interelectrode region. These observations suggest that hydrodynamic forces associated with the conducted current act to reduce the line density by displacing the plasma in the radial direction. The current conducted by the plasma scales less than linearly with plasma density. This contrasts with results from < 100 nsec conduction-time experiments where hydrodynamic forces are not expected to be significant and the conducted current scales linearly with density.^{25,30}

When the POS is open, the data suggest that the switch plasma behaves like a section of magnetically insulated transmission line with a maximum effective gap limited to 2 to 3 mm over a wide range of load impedances, currents, POS cathode radii, and electrode separations. The size of this gap determines the value of the load impedance that maximizes the load power. Experiments performed with a reduced radius for the POS center conductor resulted in a 50% increase in the peak load voltage, to 1.2 MV and a 50% decrease in the load current rise time, to 20 nsec. The larger magnetic field associated with the smaller radius allowed insulation at higher voltage. Assuming plasma erosion^{2,4,6,9,10,21,25,38} (dynamic sheath expansion resulting from space-charge effects) controls the gap growth, the inferred gap growth rate is explained using the reduced line density observed at opening. Preliminary results at low power suggest that an electron-beam (e -beam) load whose impedance initially rises with time, as opposed to the usual falling impedance, can result in a larger gap and up to a factor of 1.5 increase in load power.

The experimental setup and diagnostics are described in Sec. II. The experiments were performed on the Hawk generator. Diagnostics include magnetic field probes and HeNe laser interferometry. The results of measurements and analyses of the conduction phase and the opened state are presented in Sec. III. In Sec. IV, the opening process is discussed and the gap growth rate is estimated assuming an erosion model and using the reduced line density obtained from interferometry. The results are summarized in Sec. V.

II. EXPERIMENTAL SETUP AND DIAGNOSTICS

The Hawk pulsed-power generator comprises a 600 nH Marx bank³⁹ and a POS. At the normal output voltage of 640 kV, the Marx stores 225 kJ. It delivers a sinusoidal current pulse of 720 kA peak amplitude and $1.2 \mu\text{sec}$ quarter period to the POS. Figure 1 is an illustration of the vacuum section of Hawk, showing the POS coaxial geometry and the diagnostics used to characterize the POS plasma. The axial midplane of the POS defines $z=0$. Application of negative high voltage from the Marx at the POS cathode (center conductor) results in current flow

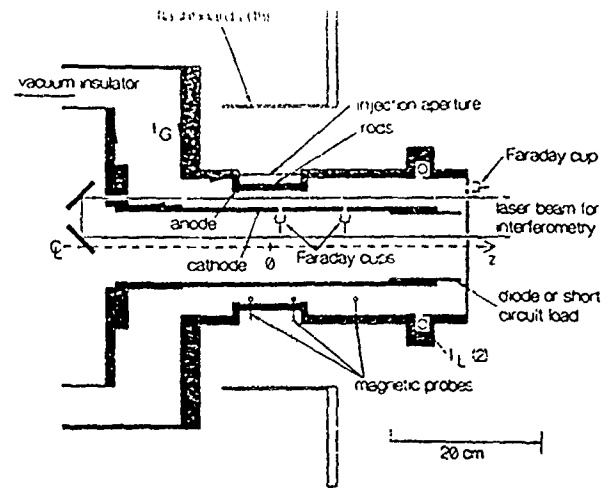


FIG. 1. Drawing of the Hawk vacuum section illustrating the POS geometry and indicating the location of diagnostics. The diagnostics include generator and load current monitors, I_G and I_L magnetic probes, Faraday cups, and HeNe laser interferometry; $z=0$ defines the axial midplane of the POS. The arrows in the conductors indicate the direction of the current flow.

from the POS anode (outer conductor) to the cathode and magnetic energy storage in the system inductances. When the POS opens, current is diverted from the POS to an e -beam or short-circuit (inductive) load. Cathode radii, R_C of 5 cm and 2.5 cm have been used. Unless otherwise noted, the anode radius is 7 cm in the POS region and 9 cm in the region between the POS and e -beam diode load. Thus for $R_C = 5$ cm ($R_C = 2.5$ cm), the vacuum transmission line impedance is 20Ω (62Ω) in the POS region, and is 35Ω (77Ω) in the region between the POS and the load. Voltage, V_D , is measured with a capacitive voltage divider on the oil side of the vacuum insulator (not shown). The current, I_G , on the generator (upstream) side of the POS is measured by averaging four magnetic probes located near the vacuum insulator and separated in azimuth by 90° . Two shielded magnetic probes located on the load (downstream) side of the POS and separated in azimuth by 180° are averaged to measure the load current I_L . From the axial midplane of the POS, the inductance to the capacitive voltage monitor is $L_V \approx 75$ nH and the inductance to the load is $L_L \approx 30$ nH (55 nH) for $R_C = 5$ cm (2.5 cm). From these measured parameters, other useful quantities are calculated to analyze the switch performance including switch current $I_{SW} = I_G - I_L$, switch voltage $V_{SW} = V_D - L_V dI_G/dt$, load voltage $V_L = V_{SW} - L_L dI_L/dt$, load power $P_L = V_L I_L$, and load impedance $Z_L = V_L/I_L$.

The source for the POS plasma is an array of 18 flashboards,^{10,29,40} each having six parallel rows of 20 gaps. Each flashboard is connected to a $0.6 \mu\text{F}$ capacitor charged to 25 kV. The current driving the flashboard reaches 30 kA in $0.5 \mu\text{sec}$, producing a predominantly doubly ionized carbon plasma^{10,29} that is injected into the POS interelectrode region. The flashboards are located 12.5 cm (15 cm) from the POS cathode for $R_C = 5$ cm (2.5 cm).

Shown in Fig. 1 are typical locations of magnetic

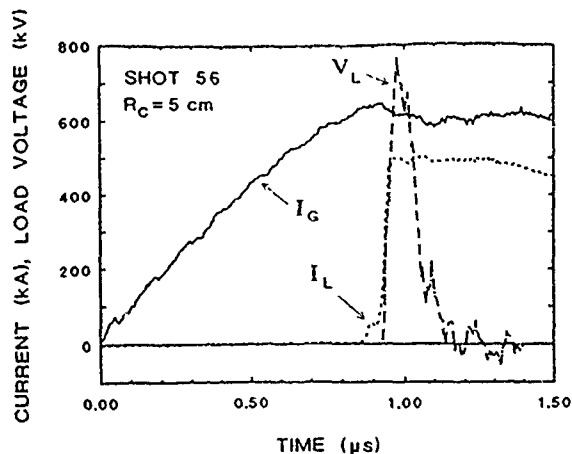


FIG. 2. Time history of the generator current I_G , load current I_L , and load voltage V_L for Hawk shot 56 with a 5 cm radius center conductor. Peak power for this shot is 0.4 TW.

probes to characterize the current evolution in the POS plasma. Both axial and radial arrays have been fielded. The probe loops are ≈ 3 mm in diameter, have an estimated subnanosecond response time, and have been calibrated *in situ* on a shot with no POS plasma. The line of sight for the HeNe laser interferometer is also depicted in Fig. 1. This measurement⁴¹ gives the electron line density in the axial direction, $\int n dz$, during a Hawk shot. The radial spatial resolution is 1 mm. The phase associated with plasma density is measured to a precision of $\pm 0.5^\circ$ using a heterodyne technique. However, various noise sources during opening result in a maximum phase error (at that time) of $\pm 3^\circ$, or less than $\pm 3 \times 10^{15} \text{ cm}^{-2}$ of line density. Negatively biased charge collectors (Faraday cups) are placed behind small apertures in the center conductor and in the load anode plate (see Fig. 1) to detect ions moving radially or axially, respectively, from the POS plasma. A small fraction of the POS plasma density ($\sim 1\%$, as detected by the axially viewing Faraday cup) can reach the load as a result of the initial plasma injection and axial $\mathbf{J} \times \mathbf{B}$ forces. In some cases, the distance between the POS and load has been extended from 25 to 40 cm to reduce this density.

Typical data traces for $I_G(t)$, $I_L(t)$, and $V_L(t)$ with $R_C = 5$ cm are shown in Fig. 2. The flashboard sources are fired 1.5 μsec before the initiation of current flow in the POS plasma. The switch conducts for 0.9 μsec before opening. The 10%–90% load current rise time is 40 nsec with 80% of I_G (500 kA) flowing in the load at the time of peak V_L . Peak V_L is 770 kV and occurs at the same time as peak load power, which is 0.4 TW for the shot in Fig. 2. The load power pulse has a full width at half-maximum of 85 nsec. About 35 kJ is delivered to the load in 100 nsec. For this configuration, typical values for the peak load voltage vary between 750 and 900 kV.

III. RESULTS OF MEASUREMENTS AND ANALYSES

In this section, data and analyses are presented for times during the conduction phase and at the time of peak load power. The opening process is discussed in Sec. IV.

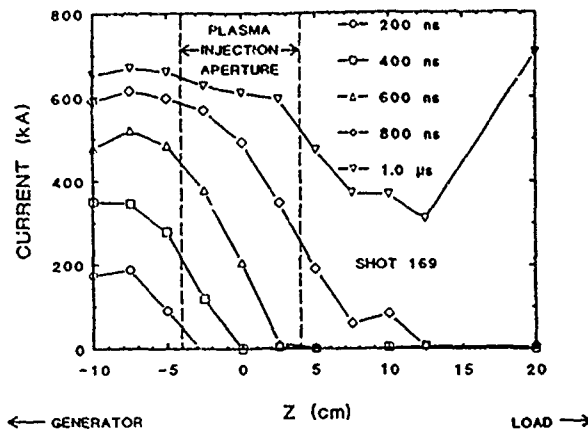


FIG. 3. Axial distribution of current for various times on a Hawk shot. The plasma injection aperture is 8 cm wide; $z=0$ defines the axial midplane of the POS. The radius of the center conductor is 5 cm.

A. Conduction phase

The axial distribution of current at different times during the operation of the POS on Hawk is shown in Fig. 3. These data were obtained with an array of magnetic probes located at ten axial positions, radially midway between the POS cathode and anode.³¹ The axial location of the POS plasma injection aperture is noted on Fig. 3, with $z=0$ the axial midplane of the POS. The data in Fig. 3 suggest that injected plasma extends upstream and downstream of this aperture. The probe signals are integrated to give the azimuthal component of the magnetic field, B_θ , directly. Other measurements demonstrate that B_θ is azimuthally symmetric, so the current flowing under any probe is proportional to the product of B_θ and the measurement radius.

Several observations can be made from the data in Fig. 3. The current channel width is comparable with the injection aperture size of 8 cm. This width is very large relative to the classical collisionless skin depth, c/ω_{pe} , where c is the speed of light and ω_{pe} is the electron plasma frequency. A typical plasma density obtained from HeNe laser interferometry (see below) of $5 \times 10^{15} \text{ cm}^{-3}$ results in an upper bound for c/ω_{pe} of about 10^{-2} cm. Current flow through the plasma is interrupted, and current is diverted to the load, i.e., opening occurs, when the current channel reaches a position near the load end of the initial location of the plasma. That is, the current flow is interrupted locally, in the region of the POS. This is in sharp contrast to the plasma flow switch,⁴² where the current channel is connected past the load by an axially moving plasma. At the time of opening, one can infer that the POS plasma center of mass has been displaced toward the load a distance equal to about half the injection aperture size, or about 4 cm, assuming the position of the center of the current channel is approximately the same as the POS plasma center of mass. Other measurements have shown that during conduction, the current in the POS plasma flows predominantly in the radial direction. Almost identical observations have been made for a PCS operating at < 100 nsec conduction times.^{10,37} Various mechanisms, for both short and long conduction times, have been proposed to explain

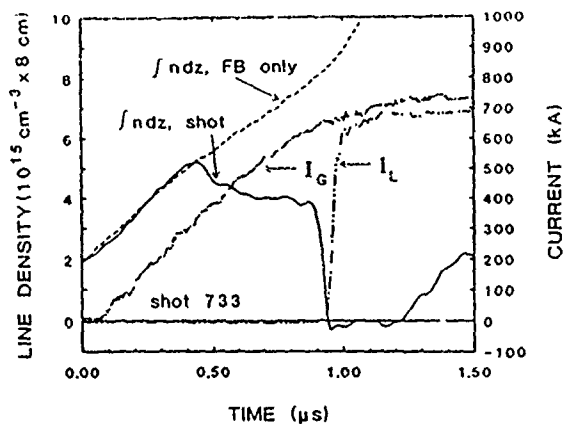


FIG. 4. Measured line densities for a Hawk shot with $R_C = 5$ cm, where the POS conducted current, and for a test case, where the flashboards were fired with no current conduction. Also shown are the generator current I_G and load current I_L as functions of time for the Hawk shot.

the rate of axial penetration and width of the current channel. 7-10,16,18,28,37,43-53 A discussion of these processes is beyond the scope of this paper.

The electron line density, $\int n dz$, measured 1.5 cm from the 5 cm radius cathode on Hawk, is shown as a function of time in Fig. 4 for two cases:³⁴ (1) a Hawk shot where the POS plasma conducted the Hawk current, and (2) a test case where the flashboard sources were fired without the POS plasma conducting any current. Also shown are the generator and load current waveforms for the case where the POS conducted current. The line densities for the two cases agree until 0.45 μsec , at which time the line density for the Hawk shot begins to decrease while the line density for the flashboard only case continues to increase. Assuming an 8 cm plasma length (the injection aperture size), the average density over the line of sight at 0.45 μsec is $5 \times 10^{15} \text{ cm}^{-3}$. The line density on the Hawk shot decreases rapidly prior to the time of opening, and during opening it is below the minimum detectable level of about $3 \times 10^{15} \text{ cm}^{-2}$. This is over a factor of 10 lower than the peak value during conduction, $4 \times 10^{16} \text{ cm}^{-2}$, and at least a factor of 20 lower than the line density for the flashboard only case at the equivalent time, $6 \times 10^{15} \text{ cm}^{-2}$. Data obtained at other radial locations show similar behavior to those shown in Fig. 4, but with a higher minimum line density. At the time of opening, the average line density over the central 1.2 cm radial region of the 2 cm electrode separation is about $1.5 \times 10^{16} \text{ cm}^{-2}$.³⁴

These data, along with the current distribution data in Fig. 3, suggest a physical picture for the conducting plasma. A broad current channel penetrates the POS plasma in the axial direction and moves the bulk of the POS plasma axially toward the load. The POS opens when the center of the current channel reaches a position near the lead end of the POS region. The B_θ field associated with the current channel apparently inhibits plasma from the flashboard source from flowing into the POS interelectrode region. During this time, the POS plasma line density is reduced because of plasma displacement in the radial

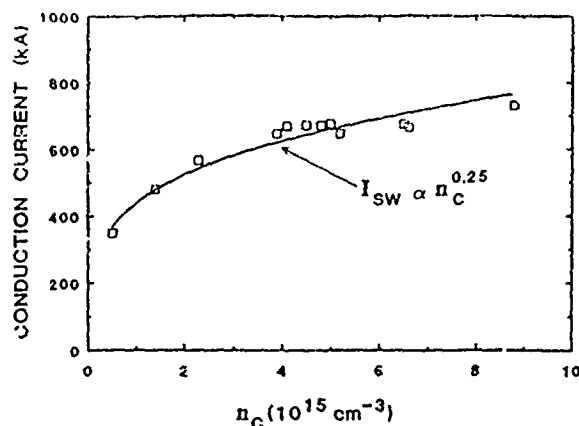


FIG. 5. Conducted current at the time of opening, $I_{SW}(\tau_C)$, as a function of the effective density during conduction, n_C . The curve is a power-law fit. The plasma injection aperture is 8 cm wide.

direction, toward the POS anode and cathode, as a result of hydrodynamic forces associated with the penetrating current channel. A small departure from purely radial current flow, on the order of $J_z/J_r \sim \Delta r/2l_0 \approx 10\%$, could provide a radial $\mathbf{J} \times \mathbf{B}$ force sufficient to explain these results. Here, J_z (J_r) is the axial (radial) component of the conducted current density, Δr is the distance between the POS anode and cathode, and l_0 is the initial POS plasma length (approximately equal to the injection aperture size). The magnetic probe array does not have the resolution to detect such a variation from purely radial flow. A lower density plasma is presumably left behind the leading edge of the penetrating current to support the observed broad channel.

To observe trends and make comparisons with < 100 nsec conduction time data, we identify a density that characterizes the conducting plasma. A reasonable choice for this effective density, n_C during conduction on Hawk is the peak line density near the midpoint between the POS electrodes divided by $l_0 = 8$ cm, e.g., $n_C = 5.2 \times 10^{15} \text{ cm}^{-3}$ at 0.45 μsec in Fig. 4. The conducted current at the time of opening, $I_{SW}(\tau_C)$, where τ_C is the conduction time, is plotted as a function of n_C in Fig. 5. The best fit power law to the data is $I_{SW}(\tau_C) \propto n_C^{1/4}$. This behavior contrasts short-conduction time results from experiments performed on the Gamble I³⁴ capacitive generator at a 50 nsec conduction time,^{25,30} collisional particle-in-cell (PIC) code calculations,¹⁸ and the bipolar conduction model,^{6,9,10,37} which all indicate that the conducted current scales linearly with the density.

This difference can be reconciled by considering the displacement during conduction of the center of mass of a radially thin annulus of switch plasma near the POS cathode.^{25,30} This displacement depends on the plasma mass and magnetic pressure, is independent of the current distribution and the plasma density distribution, and can be approximated by

$$\Delta z(t) \approx \frac{Z\mu_0}{8\pi^2 R_C^2 l_0 M n_C} \int_0^t dt' \int_0^r I_C^2(r') dr', \quad (1)$$

where Z is the ion charge state, μ_0 is the permeability of free space, and M_i is the ion mass. It has been assumed that the time dependence of the density can be accounted for by using n_C outside the integral. We assume that hydrodynamics is important in understanding the conduction phase physics if Δz approaches $l_0/2$ for times $< \tau_C$. That is, under these conditions the plasma center of mass moves to the downstream edge of the POS and hydrodynamic forces have a chance to alter the plasma distribution during the conduction phase. For the Hawk shot of Fig. 4, $\Delta z \approx 4$ cm $= l_0/2$. A similar calculation for the short-conduction-time POS Gamble I experiments^{25,30} results in $\Delta z \approx l_0/50$. Accordingly, one could expect hydrodynamics to change the conduction current scaling with density in the 1 μ sec POS Hawk experiments compared with the short-conduction-time POS experiments on Gamble I.

A simple relationship that may be useful for scaling purposes can be derived by setting $\Delta z = l_0/2$, $t = \tau_C$ and by assuming the current increases linearly with time, $I_G(t) = kt$ (where k is a constant), in Eq. (1). This results in the following expression for $I_{SW}(\tau_C)$:

$$I_{SW}(\tau_C) \sim (48\pi^2 M_i n_C / Z \mu_0)^{1/4} (R_C \rho_0 k)^{1/2}. \quad (2)$$

The scaling of $I_{SW}(\tau_C)$ with n_C in Eq. (2) is in agreement with the results of Fig. 5. Physically, this implies that for the Hawk data, hydrodynamics can determine the rate of penetration of the current channel and, thus, the switching point.^{25,30,33} While this may well be the case, a strict interpretation of Eq. (2) does not elucidate the complicated processes involved. The interferometer and magnetic probe data presented in this section, as well as other observations and analyses, suggest that a more complete understanding of the detailed mechanisms controlling the conduction phase may require two-dimensional (2-D), time-dependent theoretical studies that correctly account for electron emission, magnetically insulated electron flow, the spatial distribution of plasma density in the presence of electrodes, axial and radial ion motion, and resistivity.

B. Opened state

Data and analyses are now presented for the time at which peak power is delivered to the load. The load voltage, V_L and load current, I_L , are plotted in Fig. 6 as a function of the load impedance, Z_L , all at the time of peak load power P_L . The time of peak P_L is always very near the time of peak V_L , and at that time $dI_L/dt \approx 0$ (see Fig. 2), so $V_L \approx V_{SW}$. For these data, the conducted current, $I_{SW}(\tau_C)$, is 635 kA with a standard deviation of 25 kA. The curves in Fig. 6 are linear fits to the data; except for the I_L data to the right of the vertical dashed line, which is a power law fit. The data can be grouped into two regimes. To the left of the dashed vertical line, which serves as a guide to separate these regimes, increasing Z_L results in proportionately higher V_L , while I_L is approximately constant. This is called the load limited regime because $V_L \propto Z_L$. To the right of this line, the load voltage remains relatively constant, independent of Z_L , and as Z_L increases beyond about 1.5 Ω , I_L decreases. To a good approxima-

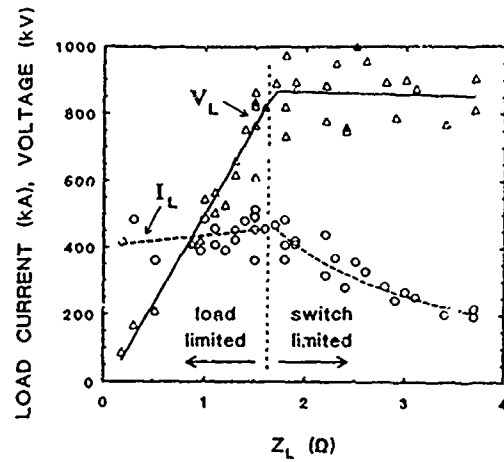


FIG. 6. Plot of peak load voltage, V_L ($\approx V_{SW}$), and peak load current I_L , as a function of load impedance, Z_L , at the time of peak load power. The vertical dashed line is a guide to separate the load limited from the switch limited regime. The critical impedance is $Z_L^* = 1.5 \Omega$ and $I_{SW}(\tau_C)$ is 635 kA \pm 25 kA.

tion, $I_L \propto Z_L^{-1}$. The remaining load current is observed to flow in the POS and between the POS and the load. This is called the switch limited regime because $V_L \approx V_{SW}$ is independent of Z_L . Maximum load power is observed when Z_L is near 1.5 Ω . Qualitatively similar behavior was obtained for experiments performed at conduction times of < 100 nsec.¹⁰

The behavior illustrated in Fig. 6 can be understood from a simple physical picture. Assume a sheath region of radial thickness D forms in the plasma. In this sheath, large space-charge electric fields can exist, and the region can serve as an effective gap for magnetic insulation⁵⁵⁻⁵⁷ of electrons emitted from the cathode (or cathode plasma). Further assume that at peak power, this gap is always about equal to the average electron gyroradius of an emitted electron in the magnetic field associated with I_G , i.e., the POS runs at the critical current for insulation, I_{CR} .^{6,58,59} So at peak power, I_G , V_L ($\approx V_{SW}$), and D are related by

$$I_G = I_{CR} \approx 1.6(2\pi m_e c / \mu_0 e)(\gamma^2 - 1)^{1/2}(R_C/D), \quad (3)$$

where m_e is the electron rest mass, e is the electron charge, and $\gamma = 1 + eV_L/m_e c^2$ is the ratio of the electron energy to its rest energy. The factor of 1.6 is used to obtain agreement with PIC code computations and approximately accounts for geometric and ion space-charge effects.⁶⁰ We have assumed that the electrons are emitted near the POS cathode and that D is small relative to R_C . In general, the gap may be located anywhere in the POS interelectrode region.

The effective gap, D , obtained from Eq. (3), is plotted against Z_L in Fig. 7 at the time of peak load power, for a range of I_G at peak load power (including the data in Fig. 6). In the load limited regime— Z_L less than about 1.5 Ω — D varies nearly linearly with Z_L and is large enough to be magnetically insulated. Thus, $I_L \approx I_G$ and $V_L \propto Z_L$ as in the left-hand portion of Fig. 6. In this load limited case,

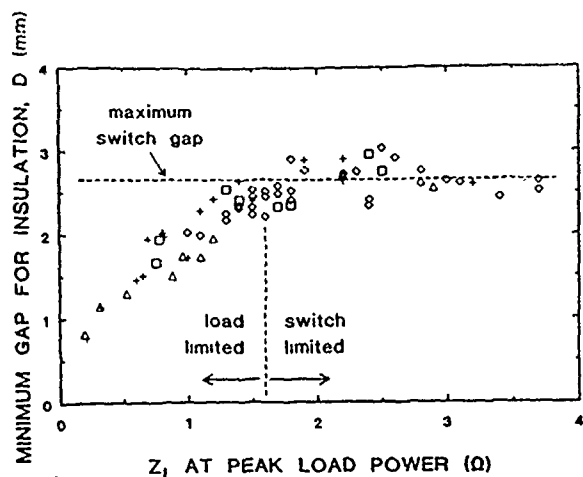


FIG. 7. The effective gap for magnetic insulation, D , as a function of load impedance, Z_L , at the time of peak load power. Data are shown for various values of the generator current, I_G , at the time of peak load power: \square , $I_G < 500$ kA; $+$, 500 kA $< I_G < 600$ kA; \diamond , 600 kA $< I_G < 650$ kA; \triangle , 650 kA $< I_G < 700$ kA. The vertical dashed line is a guide to separate the load limited from the switch limited regimes. The critical impedance is $Z_L^* \approx 1.5 \Omega$.

D , calculated from Eq. (3) and displayed in Fig. 7, is a lower bound because the data in Fig. 6 would display the same trend if D were larger. On the other hand, the data in Fig. 6 indicate that less than 100% of the conducted current reaches the load, which suggests that D is not larger than that shown in Fig. 7. In the switch limited regime— Z_L greater than about 1.5Ω — D is independent of Z_L and limited to about 2.5 mm, with remarkably little variation. In this regime, D is limited to a maximum size and the effective gap is no longer fully insulated. According to Eq. (3), the voltage is limited by this maximum D . Thus, the voltage is clamped by the maximum D and the load current is reduced as Z_L^{-1} , as seen in Fig. 6. This maximum D also determines the value of Z_L for which P_L is maximum. Maximum load power results when $Z_L = Z_L^*$, the largest value of Z_L for which the maximum D is insulated. From the data in Figs. 6 and 7, $Z_L^* \approx 1.5 \Omega$. For both switch and load limited regimes, the value of D at a given Z_L appears to be independent of conduction current, as can be seen from the data plotted in Fig. 7 for different values of I_G at peak load power. The data in Figs. 6 and 7 suggest that higher voltages will be attained if the transition to the switch limited regime can be extended to larger D . The trends illustrated in Fig. 6 were also observed on short-conduction-time experiments,¹⁰ where inferred effective gaps of 5 to 8 mm were reported.⁶

To explore the effect of a higher magnetic field on the POS operation, the POS cathode radius was reduced. Improved performance was obtained on Hawk with $R_C = 2.5$ cm and an e -beam diode load, as seen in Fig. 8. The POS plasma conducts current for $0.7 \mu\text{sec}$ and opens in 20 nsec, delivering 80% of the current (400 kA) to the load. The opening time is a factor of 2 less than that observed with the 5 cm radius cathode. The peak voltage generated on this shot is 1.2 MV, a factor of 1.5 increase over the

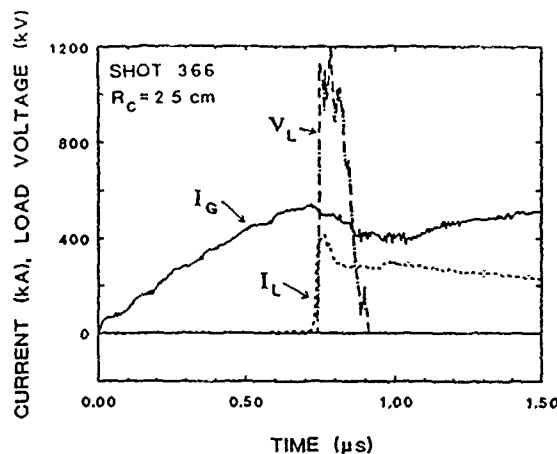


FIG. 8. Time history of the generator current I_G , load current I_L , and load voltage V_L for Hawk shot 366 with a 2.5 cm radius cathode. The peak load voltage amplitude and load current rise time are improved by $\approx 50\%$ over the shot illustrated in Fig. 2, where $R_C = 5$ cm. The peak power for this shot is 0.5 TW.

voltage in Fig. 2, and well above the 900 kV voltage limit for the 5 cm radius cathode. Measurements of bremsstrahlung from the load using filtered scintillator-photodiode detectors are consistent with higher voltage in the 2.5 cm radius case. The conducted current at optimum performance is reduced from 650 kA (with the $R_C = 5$ cm) to 500 kA, so only a 25% increase in peak power is obtained, up to 0.5 TW. In this case, I_G/R_C increased about a factor of 1.5 but the limiting value of D remained the same, 2 to 3 mm, compared with the $R_C = 5$ cm case. The higher magnetic field provided insulation at the higher voltage. Note that the calculated D for $R_C = 2.5$ cm exhibits the same behavior as shown in Fig. 7 for $R_C = 5$ cm, except that Z_L^* increases to 3Ω .

For the data in Fig. 8, the anode radii in the POS region and downstream of the POS remained the same as the $R_C = 5$ cm case (7 and 9 cm, respectively), thus increasing the electrode separation in the two regions an additional 2.5 cm. Experiments in which both anode radii were reduced to give the same electrode separations as the $R_C = 5$ cm case yielded similar results to those shown in Fig. 8, with the same inferred gap.

Characterizing and understanding the mechanisms responsible for the 2 to 3 mm limited gap size in these experiments, independent of the load impedance at peak power, conducted current, cathode radius, and POS electrode separation requires further experimental and theoretical study.

The magnetic insulation picture can be summarized by using Eq. (3) to obtain the maximum voltage at which insulation can occur for a given gap. This voltage is shown in Fig. 9 as a function of I_G/R_C for several values of D . The shaded areas indicate the range of typical load voltage data from Hawk with 5 and 2.5 cm radius cathodes. At a given I_G/R_C , the lower voltage data are from shots where $Z_L < Z_L^*$ (load limited regime), while the higher voltages are from shots where $Z_L > Z_L^*$ (maximum power or switch lim-

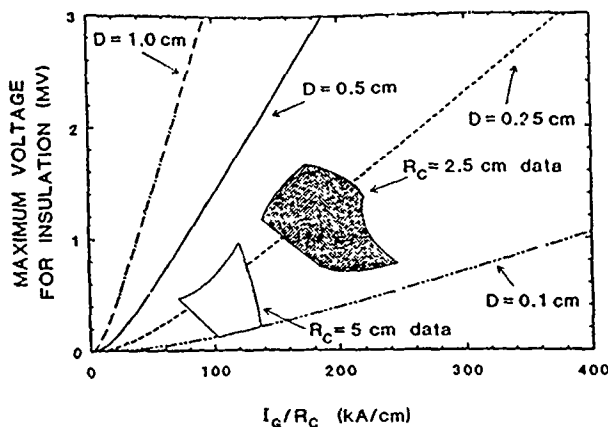


FIG. 9. Plot of maximum voltage for which magnetic insulation can occur, from Eq. (3), as a function of the ratio of generator current at peak load power, I_G , to cathode radius, R_C , for various values of the effective gap, D . Also shown are regions representing load voltage data from Hawk with both 5 and 2.5 cm radius cathodes.

ited regime). Increasing I_G/R_C at fixed D extends the POS performance to higher voltage. Hydrodynamic displacement and practical inductance constraints will eventually limit the minimum value of R_C . Increasing I_G will require a higher POS plasma density (see Fig. 5), as well as the compensating line density reduction illustrated in Fig. 4 to recover rapid opening. Clearly, increasing D at the same I_G/R_C will also result in higher voltage. Identifying methods to increase D is a subject for future investigation (see below).

IV. DISCUSSION OF POS OPENING PROCESS

The transition between the conduction phase and the state at the time of peak load power is the least well understood aspect of POS physics. We propose a model for this process where at the end of the conduction phase, current is conducted in a space-charge-limited bipolar fashion⁶¹ across a relatively small gap or sheath. The gap grows when the ion current collected at the cathode exceeds the radially directed ion flux associated with the injected POS plasma. This is the so-called erosion^{2,4,6,9,10,21,25,38} process. The rate at which the gap grows determines the opening time, and its final size determines Z_L^* , the optimum load impedance for maximum load power.

The rate for erosion-driven gap growth is approximately given by^{6,9,10,25,38}

$$\frac{dD}{dt} \approx \frac{I_i}{2\pi R_C \epsilon f n dz} - v_i \quad (4)$$

where I_i is the total ion current collected at the POS cathode and v_i is the radially directed component of the ion velocity entering the gap. An average value for dD/dt of 6 cm/ μ sec is inferred from the calculated effective gap size of 2.5 mm (see Fig. 8) divided by the measured opening time of 40 nsec (see Fig. 2). Estimating the gap growth rate from Eq. (4) requires knowledge of the line density, $f n dz$.

From Fig. 4, an upper bound for the line density during opening is $3 \times 10^{15} \text{ cm}^{-2}$, based on measurement accuracy (see Sec. II). Using this value for the line density in Eq. (4) with $R_C = 5 \text{ cm}$ and assuming $v_i = 0$ yields $dD/dt > 6 \text{ cm}/\mu\text{sec}$ if $I_i > 0.15 I_G$. Measurements of I_i , using negatively biased Faraday cups inside the POS cathode³¹ and nuclear activation⁶² suggest that I_i ranges from $0.3 I_G$ to $0.5 I_G$ during opening. If the line density for the flashboard only case at the equivalent time of opening ($6 \times 10^{16} \text{ cm}^{-2}$ in Fig. 4) is used in Eq. (4), $I_i > 3 I_G$ for $dD/dt > 6 \text{ cm}/\mu\text{sec}$. Thus, the reduction in line density resulting from hydrodynamic forces during conduction allows for rapid gap growth from erosion,³⁴ as suggested in Ref. 25. While this model is useful for developing an intuitive understanding of the opening process, a more complete understanding should result from time-dependent, 2-D studies that correctly account for electron and ion space charge in the gap. References 33 and 63 develop an alternate treatment for gap evolution that assumes a magnetic pushing model.

The final magnitude of D limits the ultimate load power. Recent Russian work suggests that higher voltage, presumably because of a larger D , results when a hydrogen (instead of a carbon) plasma is used for the POS.⁶⁴ Another effect that may limit D is the time history of the load impedance. PIC code simulations of the POS suggests that a larger D may result if the electron flow can be more easily insulated during the initial stages of the opening process. This may occur, for example, if the initial impedance of the e -beam diode load is small, as in a plasma-filled diode (PFD).⁶⁵⁻⁶⁷ Preliminary experiments to investigate this hypothesis were carried out on Hawk at low power. For these experiments, $R_C = 2.5 \text{ cm}$, the POS to load distance has been extended from 25 cm (see Fig. 1) to 40 cm to prevent POS plasma from reaching the load (see Sec. II), and the PFD plasma is injected from the e -beam anode to the e -beam cathode along the axis. The results are given in Fig. 10. In Fig. 10(a), the load impedance time history for the usual e -beam diode is compared with that of a PFD case. The impedance for the PFD case increases from zero and then decreases, overlaying the non-PFD impedance. This PFD impedance behavior is presumed to be a result of the same erosion process postulated to occur in the POS plasma.⁶⁵ The load power for these two cases is plotted in Fig. 10(b). The load power for the PFD case is up to a factor of 1.5 higher as a result of nearly equal increases in V_L and I_L . In this case, D calculated using Eq. (3) is 4.8 mm, compared with 3.4 mm for the non-PFD case. While these results are preliminary, they suggest that a load impedance that increases from zero can result in a larger gap, leading to improved POS performance.

V. SUMMARY AND CONCLUSION

The POS has demonstrated both the ability to enhance the power output of conventional pulsed-power generators at conduction times $< 100 \text{ nsec}$ and the performance required to make it a key element in inductive pulsed-power generators where the conduction time approaches 1 μsec . Diagnostic measurements and analyses of a 1 μsec POS suggest a physical picture for the POS operation. During

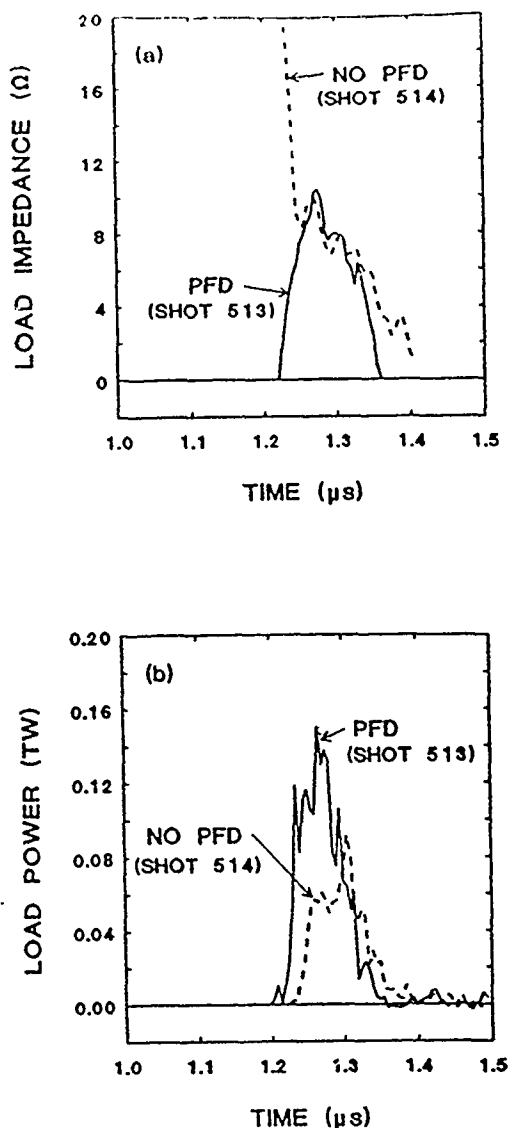


FIG. 10. (a) Comparison of the load impedance as a function of time for a case where plasma was independently injected into the e -beam load (PFD) with a case where no plasma was injected into the e -beam load (NO PFD). (b) Comparison of the load power as a function of time for a case where plasma was independently injected into the e -beam load (PFD) with a case where no plasma was injected into the e -beam load (NO PFD).

conduction, a broad current channel penetrates the POS plasma, moving the POS plasma axially toward the load. Radial hydrodynamic forces associated with this channel reduce the axial line density through a large portion of the interelectrode region compared with the value the line density would have if the POS does not carry current. A factor of 20 reduction in line density at opening is observed in a small (relative to the electrode separation) portion of this region. A simple analysis of conduction current scaling suggest that, for the Hawk data, hydrodynamics determines the rate of penetration of the magnetic field and, thus, the switching point.

After conduction, a magnetic insulation model implies that an effective gap in the plasma determines the load impedance that results in maximum load power. At load

impedance values greater than this critical value, the effective gap is limited to 2 to 3 mm over a wide range of load impedances, currents, POS cathode radii, and electrode spacings. A 50% increase in load voltage is observed when the magnetic field in this gap is increased by 50%, while maintaining the same effective gap size. Estimates show that erosion can explain the gap opening rate because of the reduced line density at the end of conduction. Results from preliminary experiments indicate that the load impedance time history influences the final gap size and resultant power delivery to the load. A 4.8 mm inferred gap results from using a PFD, which allows the load impedance to rise with time from zero, compared with 3.4 mm inferred gap obtained by using a conventional e -beam diode, where the load impedance falls with time from a high value. The load power is up to a factor 1.5 higher with the PFD compared with the non-PFD case. Understanding the evolution of the opening process and the detailed coupling to the load is an important area for further investigation.

More detailed analyses are needed to more fully understand the physical mechanisms that govern the POS conduction and opening processes. These analyses should be time dependent and two dimensional, and should correctly account for electron emission, magnetically insulated electron flow, POS plasma density spatial distribution in the presence of electrodes, axial and radial ion motion, resistivity, and electron and ion space charge.

ACKNOWLEDGMENTS

This work would not have been possible without the expert assistance of J. R. Boller and J. C. Kellogg. The authors are indebted to J. Fields, R. Fisher, G. Longrie, and B. Roberts for their outstanding technical expertise. The authors also acknowledge the continuing support of Dr. G. Cooperstein and useful discussions with the members of the Pulsed Power Physics Branch at the Naval Research Laboratory.

- ¹G. Cooperstein and P. F. Ottinger, Guest Editorial, *IEEE Trans. Plasma Sci.* PS-15, 629 (1987). Note, this "Special Issue on Fast Opening Vacuum Switches," and the references therein, provides an excellent compilation of (mostly short conduction time) experimental and theoretical opening switch work.
- ²C. W. Mendel, Jr. and S. A. Goldstein, *J. Appl. Phys.* 48, 1004 (1977).
- ³R. Stringfield, R. Schneider, R. D. Genuario, I. Roth, K. Childers, C. Stallings, and D. Dakin, *J. Appl. Phys.* 52, 1278 (1981); R. Stringfield, P. Sincerny, S.-L. Wong, G. James, T. Peters, and C. Gilman, *IEEE Trans. Plasma Sci.* PS-11, 200 (1983).
- ⁴R. A. Meger, R. J. Commisso, G. Cooperstein, and S. A. Goldstein, *Appl. Phys. Lett.* 42, 943 (1983).
- ⁵S. Miyamoto, A. Yoshinouchi, N. Yugami, K. Imasaki, S. Nakai, and C. Yamanaka, *Jpn. J. Appl. Phys.* 23, L109 (1984).
- ⁶P. F. Ottinger, S. A. Goldstein, and R. A. Meger, *J. Appl. Phys.* 56, 774 (1984).
- ⁷E. M. Waisman, P. G. Steen, D. E. Parks, and A. Wilson, *Appl. Phys. Lett.* 46, 1045 (1985).
- ⁸J. M. Grossmann, P. F. Ottinger, J. M. Neri, and A. Drobot, *Phys. Fluids* 29, 2724 (1986).
- ⁹R. J. Commisso, G. Cooperstein, R. A. Meger, J. M. Neri, and P. F. Ottinger, in *Opening Switches*, edited by A. Guenther, M. Kristiansen, and T. Martin (Plenum, New York, 1987), p. 149.
- ¹⁰B. V. Weber, R. J. Commisso, G. Cooperstein, J. M. Grossmann, D. D. Hinselwood, D. Mosher, J. M. Neri, P. F. Ottinger, and S. J. Stephanakis, *IEEE Trans. Plasma Sci.* PS-15, 635 (1987) and references therein.

- ¹¹H. Bluhm, K. Bohnel, P. Hoppe, H. U. Karow, and D. Rusch, IEEE Trans. Plasma Sci. PS-15, 654 (1987) and references therein.
- ¹²C. Bruno, J. Delvaux, A. Nicolas, and M. Roche, IEEE Trans. Plasma Sci. PS-15, 686 (1987) and references therein.
- ¹³S. Miyamoto, N. Yugami, K. Imasaki, S. Nakai, and C. Yamanaka, IEEE Trans. Plasma Sci. PS-15, 667 (1987) and references therein.
- ¹⁴A. I. Arbozov, A. M. Bystritskii, Ya. E. Krasik, and A. A. Sinebryukhov, IEEE Trans. Plasma Sci. PS-15, 674 (1987) and references therein.
- ¹⁵V. M. Bystritskii, Ya. E. Krasik, and A. A. Sinebryukhov, IEEE Trans. Plasma Sci. PS-15, 678 (1987).
- ¹⁶R. J. Mason, J. M. Wallace, J. M. Grossmann, and P. F. Ottinger, IEEE Trans. Plasma Sci. PS-15, 715 (1987).
- ¹⁷R. W. Stinnett, D. H. McDaniel, G. E. Rochau, W. B. Moore, E. W. Grey, T. J. Renk, H. N. Woodall, T. W. Hussey, S. S. Payne, R. J. Commisso, J. M. Grossmann, D. D. Hinshelwood, R. A. Meger, J. M. Neri, W. F. Oliphant, P. F. Ottinger, and B. V. Weber, IEEE Trans. Plasma Sci. PS-15, 557 (1987).
- ¹⁸J. M. Grossmann, R. M. Kulsrud, J. M. Neri, and P. F. Ottinger, J. Appl. Phys. 64, 6646 (1988).
- ¹⁹G. E. Rochau, D. H. McDaniel, C. W. Mendel, Jr., M. A. Sweeney, W. B. S. Moore, G. R. Mower, W. W. Simpson, and D. M. Zagar, in *Proceedings of the 8th International Conference on High-Power Particle Beams*, Novosibirsk, edited by B. N. Breizman and B. A. Knyazev (World Scientific, New York, 1991), Vol. 1, p. 386.
- ²⁰J. M. Neri, J. R. Boller, P. F. Ottinger, B. V. Weber, and F. C. Young, Appl. Phys. Lett. 50, 1331 (1987).
- ²¹B. V. Weber, J. R. Boller, D. G. Colombant, R. J. Commisso, G. Cooperstein, J. M. Grossmann, D. D. Hinshelwood, R. A. Meger, D. Mosher, J. M. Neri, W. F. Oliphant, P. F. Ottinger, V. E. Scherrer, S. J. Stephanakis, F. C. Young, R. W. Stinnett, E. W. Grey, D. H. McDaniel, T. J. Renk, and G. Rochau, Laser Part. Beams 5, Part 3, 537 (1987).
- ²²B. M. Koval'chuk and G. A. Mesyats, Sov. Phys. Dokl. 30, 879 (1985).
- ²³D. D. Hinshelwood, J. R. Boller, R. J. Commisso, G. Cooperstein, R. A. Meger, J. M. Neri, P. F. Ottinger, and B. V. Weber, Appl. Phys. Lett. 49, 1635 (1986); IEEE Trans. Plasma Sci. PS-15, 564 (1987).
- ²⁴B. M. Koval'chuk and G. A. Mesyats, in Ref. 19, p. 92.
- ²⁵B. V. Weber, R. J. Commisso, P. J. Goodrich, J. M. Grossmann, D. D. Hinshelwood, J. C. Kellogg, and P. F. Ottinger, IEEE Trans. Plasma Sci. PS-19, 757 (1991).
- ²⁶G. A. Mesyats, S. P. Bugaev, A. A. Kim, B. M. Koval'chuk, and V. A. Kokshenev, IEEE Trans. Plasma Sci. PS-15, 649 (1987).
- ²⁷H. Akiyama, T. Majima, K. Fujita, and S. Maeda, Jpn. J. Appl. Phys. 26, L1743 (1987).
- ²⁸R. J. Mason, M. A. Jones, and C. Bergman, in *Proceedings of 7th IEEE Pulsed Power Conference*, Monterey, CA, edited by B. H. Bernstein and J. P. Shannon (IEEE, New York, 1989), IEEE Catalog No. 89CH2678, p. 255.
- ²⁹L. K. Adler, A. B.-A. Baranga, J. B. Greenly, D. A. Hammer, and N. Qi, in Ref. 19, p. 371.
- ³⁰B. V. Weber, R. J. Commisso, G. Cooperstein, P. J. Goodrich, J. M. Grossmann, D. D. Hinshelwood, J. C. Kellogg, and P. F. Ottinger, in Ref. 19, p. 406.
- ³¹D. D. Hinshelwood, R. J. Commisso, P. J. Goodrich, J. M. Grossmann, J. C. Kellogg, P. F. Ottinger, and B. V. Weber, in Ref. 19, Vol. 2, p. 1034.
- ³²V. M. Bystritskii, Ya. E. Krasik, I. V. Lisitsyn, and A. A. Sinebryukhov, IEEE Trans. Plasma Sci. PS-19, 607 (1991).
- ³³W. Rix, D. Parks, J. Shannon, J. Thompson, and E. Waisman, IEEE Trans. Plasma Sci. PS-19, 400 (1991).
- ³⁴D. D. Hinshelwood, B. V. Weber, J. M. Grossmann, and R. J. Commisso, to appear in Phys. Rev. Lett.
- ³⁵J. Goyer, IEEE Trans. Plasma Sci. PS-19, 920 (1991).
- ³⁶D. Parks, E. Waisman, and I. Katz, Appl. Phys. Lett. 59, 2808 (1991).
- ³⁷B. V. Weber, R. J. Commisso, R. A. Meger, J. M. Neri, W. F. Oliphant, and P. F. Ottinger, Appl. Phys. Lett. 45, 1043 (1984).
- ³⁸J. M. Grossmann, S. B. Swanekamp, and P. F. Ottinger, Phys. Fluids B 4, 44 (1992).
- ³⁹P. Sincerny, D. Drury, J. Goyer, G. James, M. Krishnan, J. Levine, C. McDonald, and I. Roth, in Ref. 28, p. 275.
- ⁴⁰D. G. Colombant and B. V. Weber, IEEE Trans. Plasma Sci. PS-15, 741 (1987).
- ⁴¹B. V. Weber and D. D. Hinshelwood, to appear in Rev. Sci. Instrum.
- ⁴²P. J. Turchi, M. L. Alme, G. Bird, C. N. Boyer, S. K. Coffey, D. Conte, J. F. Davis III, and S. W. Seiler, IEEE Trans. Plasma Sci. PS-15, 747 (1987).
- ⁴³A. S. Kingsep, Yu. V. Mokhov, and K. V. Chukbar, Sov. J. Plasma Phys. 10, 495 (1984).
- ⁴⁴D. Mosher, J. M. Grossmann, P. F. Ottinger, and D. G. Colombant, IEEE Trans. Plasma Sci. PS-15, 695 (1987).
- ⁴⁵J. M. Grossmann, D. Mosher, and P. F. Ottinger, IEEE Trans. Plasma Sci. PS-15, 704 (1987).
- ⁴⁶S. S. Payne, T. W. Hussey, R. W. Stinnett, and N. F. Roderick, IEEE Trans. Plasma Sci. PS-15, 725 (1987).
- ⁴⁷R. M. Kulsrud, P. F. Ottinger, and J. M. Grossmann, Phys. Fluids 31, 1741 (1988).
- ⁴⁸R. J. Mason, M. E. Jones, J. M. Grossmann, and P. F. Ottinger, Phys. Rev. Lett. 61, 1835 (1988).
- ⁴⁹J. M. Grossmann, P. F. Ottinger, and R. J. Mason, J. Appl. Phys. 66, 2307 (1989).
- ⁵⁰L. I. Rudakov, C. E. Seyler, and R. N. Sudan, Comments Plasma Phys. Controlled Fusion 14, 171 (1991).
- ⁵¹A. Fruchtman, Phys. Fluids B 3, 1908 (1991); A. Fruchtman and Y. Maron, *ibid.* 3, 1546 (1991).
- ⁵²R. J. Mason, M. E. Jones, D. C. Wilson, C. Bergman, and K. Thiem, in Ref. 19, Vol. 2, p. 1058.
- ⁵³B. Oliver, L. I. Rudakov, R. J. Mason, and P. Auer, Phys. Fluids B 4, 294 (1992).
- ⁵⁴G. Cooperstein, J. J. Condon, and J. R. Boller, J. Vac. Sci. Technol. 10, 961 (1973).
- ⁵⁵C. W. Mendel, Jr., D. B. Seidel, and S. E. Rosenthal, Laser Part. Beams 1, Part 3, 311 (1983).
- ⁵⁶C. W. Mendel, Jr., D. B. Seidel, and S. A. Slutz, Phys. Fluids 26, 3628 (1983).
- ⁵⁷M. DiCapua, IEEE Trans. Plasma Sci. PS-11, 205 (1987).
- ⁵⁸S. A. Goldstein and R. Lee, Phys. Rev. Lett. 35, 1079 (1975).
- ⁵⁹C.-K. Ng and R. N. Sudan, J. Appl. Phys. 69, 137 (1991).
- ⁶⁰R. J. Barker and S. A. Goldstein, Bull. Am. Phys. Soc. 26, 921 (1981).
- ⁶¹I. Langmuir and K. B. Blodgett, Phys. Rev. 22, 347 (1923); I. Langmuir, Phys. Rev. 2, 450 (1913).
- ⁶²A. N. Bostrikov, S. P. Bugaev, V. M. Bystritskii, S. V. Grigoriev, V. Fursov, B. M. Koval'chuk, A. A. Kim, V. A. Kokshenev, G. Mesyats, Ya. E. Krasik, and V. P. Yakovlev, in Ref. 19, Vol. 1, p. 152.
- ⁶³C. W. Mendel, J. P. Quintenz, S. E. Rosenthal, D. B. Seidel, M. P. Desjarlais, R. S. Coats, and M. E. Savage, in *Proceedings of the 7th International Conference on High-Power Particle Beams*, edited by W. Bauer and W. Schmidt (Kernforschungszenrum, Karlsruhe GmbH, Karlsruhe, 1989), Vol. 1, p. 83.
- ⁶⁴I. V. Lisitsyn (private communication).
- ⁶⁵R. A. Miller, J. W. Poukey, and T. P. Wright, Phys. Rev. Lett. 35, 940 (1975).
- ⁶⁶E. N. Abdullin, G. P. Bazhenov, A. N. Bostrikov, S. P. Bugaev, A. A. Kim, B. M. Koval'chuk, V. A. Kokshenev, O. B. Ladyzhenskii, G. A. Mesyats, and K. N. Sukhushin, Sov. J. Plasma Phys. 11, 66 (1985).
- ⁶⁷A. E. Blazgrund, G. Cooperstein, W. F. Oliphant, S. J. Stephanakis, and B. V. Weber, in Ref. 19, Vol. 1, p. 463.

B92

MICROSECOND PLASMA OPENING SWITCH EXPERIMENTS ON HAWK WITH AN E-BEAM DIODE LOAD

P.J. Goodrich, R.C. Fisher, D.D. Hinshelwood
Jaycor, Vienna, VA 22182

J.R. Boller, R.J. Comisso, B.V. Weber
Pulsed Power Physics Branch, Plasma Physics Division
Naval Research Laboratory, Washington, DC 20375

Abstract

The Hawk generator is used in plasma opening switch (POS) experiments in the 1- μ s conduction time regime to study long conduction time switch physics. Peak load powers of 0.7 TW with 55 kJ delivered to the diode--20% energy efficiency--were achieved with a POS. The data indicate that above a critical load impedance the final switch gap size is limited to about 3 mm. This limits the voltage. Maximum load power is obtained at this critical impedance. Increasing the cathode magnetic field--by conducting more current or by decreasing the cathode radius--allows the fixed-gap POS to remain insulated at a higher voltage. Peak load voltages up to 2 MV were achieved with a 2.5 cm diam cathode, a factor of 2.8 higher than the Marx voltage. Load powers were up to 70% higher with a plasma-filled diode (PFD) used in conjunction with the POS for short POS conduction times. The switch gap may be larger (> 3 mm) on these short conduction PFD shots.

I. Introduction

Pulsed power generators have traditionally used waterline and vacuum transmission line technology for power conditioning of the microsecond output pulses from Marx banks. The emergence of inductive store technology¹ allows the development of more compact pulsed power generators. An opening switch, such as a plasma opening switch (POS), is used for power multiplication and pulse compression of the microsecond Marx output pulse. Hawk² uses a 600 nH Marx,³ with 225 kJ stored and an erected voltage of 640 kV at 80-kV charge to deliver up to 720 kA in 1.2 μ s to a POS. By varying the switch plasma density, the switch can be made to conduct from 0 to 1.2 μ s. The goal of these experiments was to study the physics of the switch and optimize the switch/e-beam diode performance to generate high power short duration (< 100 ns FWHM) power pulses.

II. Experimental Configuration

The front end coaxial vacuum section of the basic configuration is shown in Fig. 1. Different configurations of POS hardware were used, including different switch to load lengths, different cathode center conductor diameters (10 cm diam pictured here), and various cathode tapers--both gradual and abrupt--in the switch and outside the switch. An independent plasma-filled diode (PFD) was also used in some experiments.

The diagnostics consist of a capacitive voltage monitor behind the insulator in oil and several current monitors including a shunt monitor behind the insulator, four B-dot monitors on the vacuum side of the insulator which are added together, a Rogowski monitor just upstream of the switch and two anode B-dot current monitors at the load. A carbon switch plasma was produced by 18 aerodagged flashboards arranged azimuthally around the 8 cm length switch region. The flashboards were 17.75 cm from the axis. This plasma was injected radially through anode rods to the cathode center conductor. The flashboards were driven by 25-kV capacitor banks fired 1-2 μ s before current

was conducted in the switch. The current in the flashboards rises to 35 kA in 0.6 μ s. Typically, the peak switch current density is 2-4 kA/cm².

The set up in Fig. 1 with a switch-to-load length of 26 cm is called the standard configuration. In this configuration, for conduction times greater than about 0.6 μ s, switch plasma reaches the diode. Some plasma comes directly from the flashboards but most is accelerated to the load by JxB forces during conduction (confirmed by Faraday cups in the load region). The bulk of the plasma does not reach the load--the center of mass motion of the plasma is only about 4 cm downstream^{4,5,6}--however, enough plasma ($n_e \leq 10^{12}$ cm⁻³) does reach the load for the load to act like a plasma-filled diode with a rising impedance. Also, more plasma (although still low density) reaches the load with smaller radii cathodes due to the larger JxB force associated with the smaller cathodes. Extending the conductors downstream of the switch to a length of 40 cm or more generally prevented plasma from reaching the load. Two B-dot current monitors were added in this transition section, about halfway between the switch and the load. In this configuration, called the extended configuration, the load looks like a vacuum diode with a falling impedance and the impedance at peak power can be controlled by changing the gap spacing.

III. Experimental Results with a 10 cm Diam Cathode

Fig. 2 shows Hawk shot 56 with a 10 cm diam cathode in the standard configuration. The plasma delay is 1.5 μ s and the switch conducts for 0.9 μ s before opening. The 10-90% load current risetime is 40 ns with an 80% current transfer efficiency and 500 kA delivered to the load. Peak load voltage is 770 kV, peak load power is 0.4 TW. Best switch performance (highest voltage and power and fastest risetimes) for shots with a 10 cm diam cathode occurs for conduction times of \sim 1 μ s, almost the time of peak current.

In this configuration, for conduction times over 0.6 μ s, the load acts like a plasma-filled diode. On shot 56 the load impedance rose from 0 Ω to 1.5 Ω at peak power, although with a diode gap of 1 cm the vacuum impedance is 8 Ω . Load impedances of 1.5-2 Ω were the highest possible in this configuration regardless of the gap spacing, limited by significant switch plasma in the load (for conduction times over 0.6 μ s).

Fig. 3 shows two shots in the extended configuration with 0.95 μ s conduction times. Here the load behaves as a vacuum diode with a falling load impedance. Opening the diode gap from 0.5 cm to 1.0 cm increased the impedance at peak power from 2 Ω to over 3 Ω . Note that the voltage generated on these shots was the same, about 800 kV, resulting in more current loss on the overmatched 3- Ω load impedance shot.

The voltage as a function of the load impedance at peak power is shown in Fig. 4 for numerous shots with a 10 cm diam cathode. Below a critical load impedance, \sim 1.7 Ω , the voltage increases linearly with impedance. This is called the "load-limited" regime^{6,7}. Above the critical impedance, however, the voltage is constant for a given conduction current. This is called the "switch-limited" regime^{6,7}. The voltage limit increases with conduction current.

The current transfer efficiency at peak power for 1 μ s conduction is constant at 80% for load impedances less than or equal to the critical impedance, but falls as $(Z_L)^{-1}$ in the switch limited regime. Maximum power is delivered to a load operating at the critical impedance (Fig. 5). Furthermore, the peak load power increases with conduction time up to 1 μ s. Thus, the highest power generated, 0.4 TW, occurs for 1 μ s conduction at a load impedance of 1.7 Ω .

Fig. 6 shows the peak switch gap, D, derived from magnetic insulation arguments (critical current formula) for these shots plotted as a function of the load impedance at peak power^{6,7}. The data indicate that at least above the critical impedance the switch gap is fixed to 2.5-3 mm and is independent of conduction current. The voltage increases with conduction current because the larger magnetic field associated with larger conducted currents allows the fixed-gap POS to remain insulated at a higher voltage.

Current loss in the load limited regime is 100-150 kA, independent of conduction (or plasma density) for conduction currents over ~ 400 kA. Much of the loss could be ion loss in the switch. For example, the 100 kA, or 20% loss on the highest power shots (operating at the critical load impedance and 1 μ s conduction) is consistent with single species Child-Langmuir flow of C^{++} ions across a 2.5-3 mm gap. The additional current loss seen when operating above the critical impedance appears to be electron loss downstream of the switch near the load.

IV. Experimental Results with a 5 cm Diam Cathode

Hawk shot 366 with a 5 cm diam cathode in the standard configuration is shown in Fig. 7. The switch conducts for 0.7 μ s and opens quickly, delivering 80% of the current, 400 kA, to the load in 20 ns. The voltage generated on this shot is 1.2 MV, well above the ~ 900 kV maximum voltage with the 10 cm diam cathode. The load impedance rises from 0 Ω to about 3 Ω and the peak power is 0.5 TW. Optimum switch performance with this cathode occurs at 0.75 μ s conduction times with a ~ 1.5 μ s plasma delay, which is also the delay for best opening with the 10 cm diam cathode. For a given plasma density, the switch opens earlier for larger magnetic fields, a consequence of MHD-limited conduction^{6,8}. To conduct even slightly longer than 0.75 μ s with the 5 cm diam cathode requires a very large increase in plasma timing delay with associated poor switch/load performance (e.g. electrode plasmas may expand into the switch gap and enough plasma reaches the load to limit the load impedance at peak power). This inability to conduct longer may be a consequence of the switch becoming source-limited: the flashboards may not be producing significantly higher plasma densities as the delay is increased above ~ 1.5 μ s.

Voltages as high as 1.7 MV were generated with the 5 cm diam cathode, a factor of 2 higher than the best 10 cm diam cathode shots and 2.7 times higher than the Marx voltage. The data indicate switch opening rates up to 1 Ω /ns or gap opening rates up to 20 cm/ μ s.

The voltage dependence on the load impedance at peak power for numerous 5 cm diam cathode shots is shown in Fig. 8. Here, the critical load impedance is about 3.5 Ω . Below this value the voltage depends on impedance, above it the voltage is clamped for a given conduction current.

The calculated peak switch gap is shown in Fig. 9 as a function of the load impedance at peak power. The switch gap is limited to the same 2.5-3 mm. The larger magnetic field produced with this smaller radius cathode means a larger voltage can exist across the fixed gap at critical current with the current coupled into a diode operating at a higher impedance, 3.5 Ω . Again, a significant fraction of the current loss in the load limited regime, which is also usually 100-150 kA, could be ion loss in the switch and the additional current loss operating above the critical impedance electron loss near the load.

V. Experimental Results with a 2.5 cm Diam Cathode

Voltages up to 2 MV were generated with a 2.5 cm diam cathode (see ref. 4). The optimum switch performance here occurs for conduction times of 0.6 μ s with the same ~ 1.5 μ s plasma delay. Peak load power was 0.6 TW, at a load impedance of ~ 7 Ω , with a 15 ns load current risetime. Longer conduction requires the similarly large increase in plasma timing delay found with the 5 cm diam cathode, and the subsequent degradation in performance.

VI. Summary of Voltage Dependence on Magnetic Field

The voltages generated with the different cathode radii are shown in Fig. 10 as a function of the cathode magnetic field. The data show the improved switch performance (higher voltage) as the magnetic field increases. The field increases as the conduction current is increased or as the cathode radius is reduced. Also plotted is the calculated effective gap for magnetic insulation. The data suggest a limit to the gap size of about 3 mm. Data points

below the $D=2.5$ mm line are in the load-limited, lower voltage, regime with load impedance less than the critical impedance. Higher power could be achieved if the switch gap size can be increased, as suggested by the PFD data (discussed below).

VII. Tapered Cathodes

Cathode tapers, abrupt and gradual, were tried in the switch region and upstream and downstream of the switch. The cathode magnetic field is larger in the tapered region which can, in principle, better insulate the electron flow and produce higher load powers. Only tapering in the switch, specifically the axial region from the middle of the switch to the downstream end of the switch, had any effect on performance. Better switch performance resulted using a small radius cathode in this region.

In particular, with a gradual 10 to 2.5 cm diam taper through the 8 cm length switch (the 2.5 cm diam being at the load end of the switch) load power up to 0.7 TW (1.5 MV and 465 kA in Fig. 11) was produced and 55 kJ (20% energy efficiency) was delivered to the load. This taper served as a good compromise between the high voltage with the 2.5 cm diam cathode and the long conduction/high current associated with the 10 cm diam cathode.

VIII. Plasma-Filled Diodes

An independent PFD was made with plasma from a flashboard downstream of the diode injected into the diode gap through holes in the anode plate. The PFD was used with a 5 cm diam cathode and with a 10 to 5 cm diam switch taper which also included flaring the cathode at the diode out to a 9.5 cm diam on some shots.

Switch voltages up to 2.2 MV were generated with a PFD. Flaring the cathode at the diode was a convenient way of reducing the load impedance at peak power, operating closer to the critical impedance, and in this geometry load powers approaching 0.7 TW were produced with a PFD. This was about 15% higher than shots without the PFD. However, some switch plasma reached the load--the impedance rises from zero even with no independent PFD on these long conduction time shots--so there are no true vacuum diode shots for comparison.

For short conduction times, where switch plasma does not reach the load and the load with no PFD behaves as a vacuum diode, the enhancement in load power using the PFD was greater. Peak load power on shots with short 0.4 μ s POS conduction times was up to 70% higher with the PFD (for similar load impedances at peak power). Both voltage and load current were higher, particularly the current. A possible explanation for this is the tendency toward unsaturated electron flow with a rising load impedance and saturated, hence lossy, flow with a falling load impedance that is seen in simulations⁹. It appears that larger switch gaps, up to 5 mm in size, were produced on the short conduction time PFD shots (see Fig. 10).

IX. Summary

High power pulses have been generated on the Hawk generator using a microsecond conduction time POS. Load power of 0.7 TW with 20% energy efficiency was achieved. The data indicate that an effective gap of 2.5-3 mm was produced in the switch, independent of the load impedance (at least above the critical impedance), conduction current, and cathode radius. Maximum power is obtained at the critical impedance, the transition point from load- to switch-limited operation. The voltage increases with cathode magnetic field. Increasing the field--by conducting more current or decreasing the cathode radius--allows the fixed-gap POS to remain insulated at a higher voltage. Voltages of 2 MV were generated with a small (2.5 cm) diam cathode (cathode magnetic field \sim 70 kG). Load powers were up to 70% higher using a PFD in conjunction with a POS, possibly because of less lossy (unsaturated)

electron flow, for POS conduction times short enough that switch plasma does not reach the load. The derived switch gaps are larger than 3 mm on these PFD shots.

References

1. G. Cooperstein and P.F. Ottinger, Guest Editorial, IEEE Trans. Plasma Science, PS-15 (Dec. 1987).
2. J.R. Boller, R.J. Commisso, P.J. Goodrich, D.D. Hinshelwood, J.C. Kellogg, J.D. Shipman, Jr., B.V. Weber, and F.C. Young, NRL Memorandum Report 6748, January 1991.
3. P. Sincerny, D. Drury, J. Goyer, G. James, M. Krishnan, J. Levine, C. McDonald, and I. Roth, 7th IEEE Pulsed Power Conference, Monterey, CA 1989, IEEE Cat. No. 89CH2678-2, p. 275.
4. B.V. Weber, J.R. Boller, R.J. Commisso, P.J. Goodrich, J.M. Grossmann, D.D. Hinshelwood, J.C. Kellogg, P.F. Ottinger, and G. Cooperstein, these Proceedings.
5. D.D. Hinshelwood, B.V. Weber, R.J. Commisso, P.J. Goodrich, J.M. Grossmann, and J.C. Kellogg, these Proceedings.
6. R.J. Commisso, P.J. Goodrich, J.M. Grossmann, D.D. Hinshelwood, P.F. Ottinger, and B.V. Weber, to be published in Phys. Fluids B, July 1992.
7. P.J. Goodrich, J.R. Boller, R.J. Commisso, D.D. Hinshelwood, J.C. Kellogg, and B.V. Weber, 8th IEEE Pulsed Power Conference, San Diego, CA 1991, IEEE Cat. No. 91CH3052-8, p. 515.
8. B.V. Weber, R.J. Commisso, P.J. Goodrich, J.M. Grossmann, D.D. Hinshelwood, J.C. Kellogg, and P.F. Ottinger, IEEE Trans. Plasma Sci. 19, p. 757 (1991).
9. J.M. Grossmann, private communication.

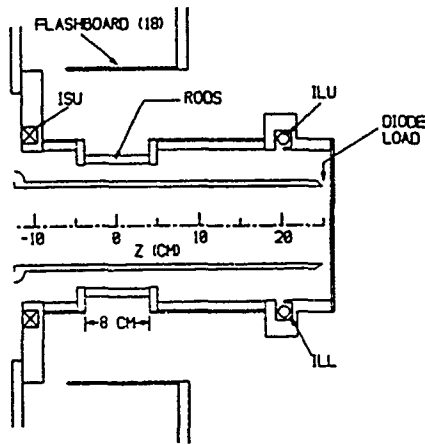


Fig. 1. Hawk switch/load vacuum section in the standard configuration.

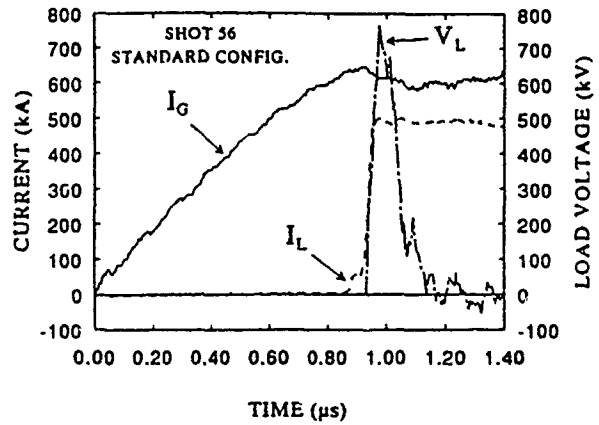


Fig. 2. Current and voltage data for a $0.9 \mu\text{s}$ conduction time POS shot with a 10 cm diam cathode.

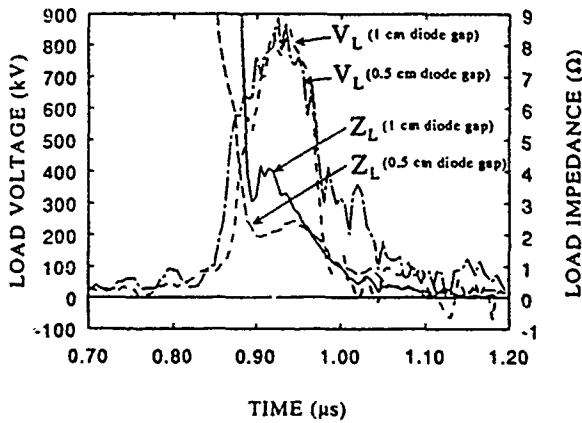


Fig. 3. Load data for two shots in the extended configuration. The diode looks like a vacuum diode with a falling impedance.

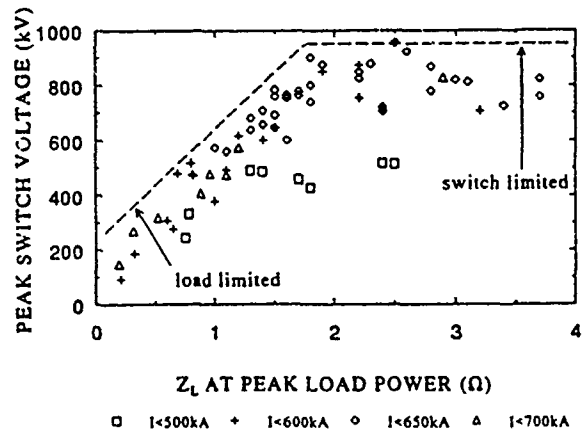


Fig. 4. Peak voltage as a function of load impedance with the 10 cm diam cathode. Above a critical impedance, $\sim 1.7 \Omega$, the voltage is constant for a given conduction current.

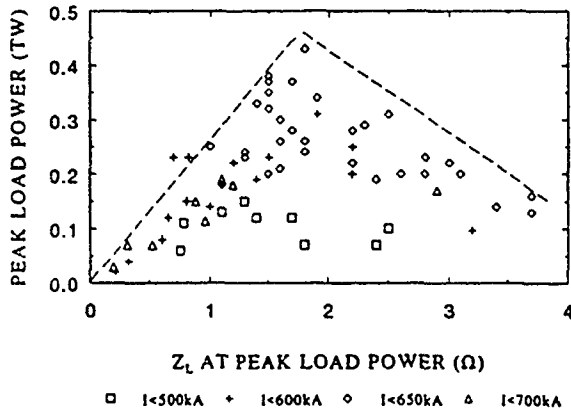


Fig. 5. Peak load power versus load impedance with the 10 cm diam cathode. Maximum power is delivered to a load operating at the critical impedance with $\sim 1 \mu\text{s}$ POS conduction times.

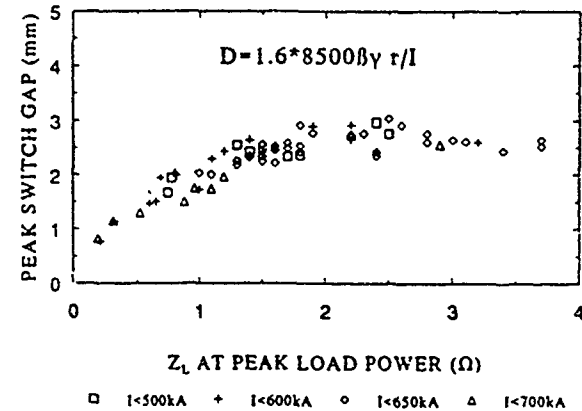


Fig. 6. Switch gap calculated at peak power, assuming the switch is at critical current, versus load impedance with the 10 cm diam cathode. The gap is independent of conduction current and, above the critical impedance, is fixed to 2.5-3 mm.

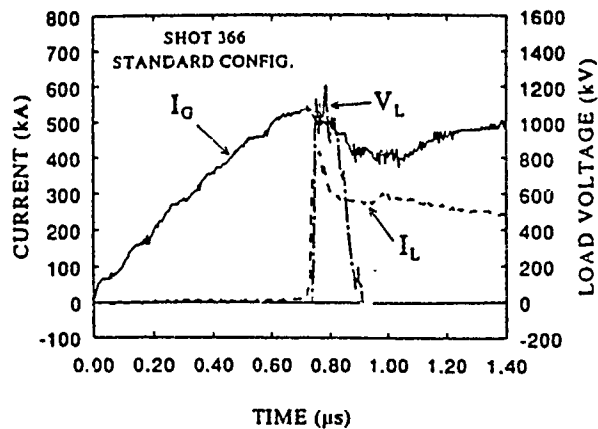


Fig. 7. Current and voltage data for a 0.7 μ s conduction time POS shot in the standard configuration with a 5 cm diam cathode.

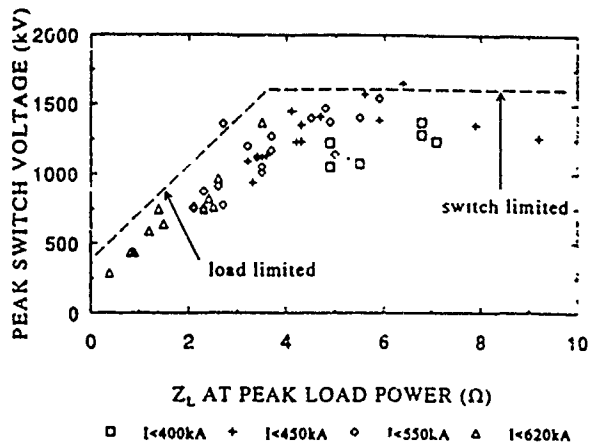


Fig. 8. Peak voltage as a function of load impedance with the 5 cm diam cathode. Above a critical impedance, $\sim 3.5 \Omega$, the voltage is constant for a given conduction current.

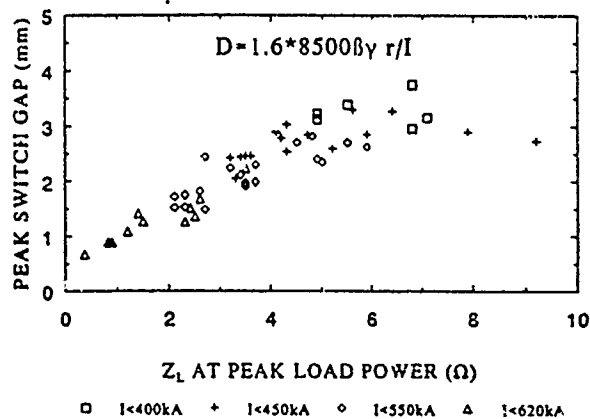


Fig. 9. Derived switch gap at peak power versus load impedance with the 5 cm diam cathode. The gap is also limited, above the critical impedance, to 2.5-3 mm.

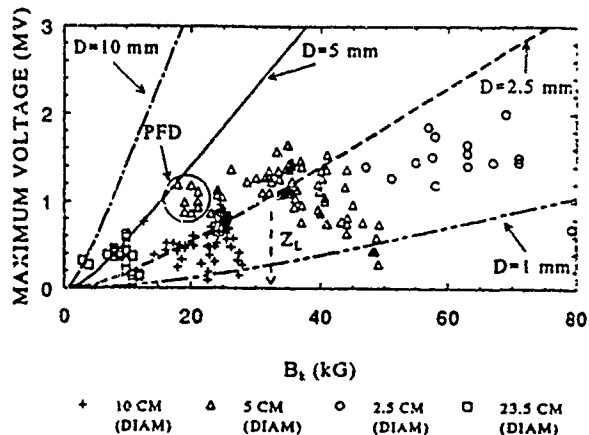


Fig. 10. Maximum voltage generated as a function of cathode magnetic field for different cathode diameters. Here the simple critical current model indicates the ways to increase the switch voltage.

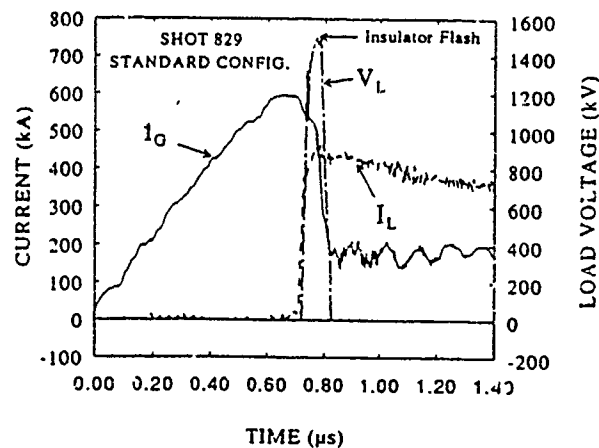


Fig. 11. On this shot with a 10 cm to 2.5 cm diam cathode taper in the switch region, load power was 0.7 TW (1.5 MV and 465 kA) and 55 kJ was delivered to the load.

11-43

HIGH POWER OPENING SWITCH OPERATION ON HAWK

P.J. Goodrich and D.D. Hinshelwood
Jaycor, Vienna, VA 22182-2270

R.J. Commisso, J.M. Grossmann, J.C. Kellogg, and B.V. Weber
Pulsed Power Physics Branch, Plasma Physics Division
Naval Research Laboratory, Washington D.C. 20375-5346

Abstract

The Hawk pulsed power generator is used in plasma opening switch (POS) experiments in the 1- μ s conduction time regime to study long conduction time switch physics. Recent experiments included modifying the POS electrode geometry, injecting plasma into the e-beam diode, gas gun plasma sources (with H₂, He, and Ar gases), and a helical cathode center conductor in the switch region to increase the total insulating magnetic field. Tapering the cathode over the 8 cm POS length from 10 cm to, typically, a 2.5 cm diam produced peak load powers of 0.7 TW with 55 kJ delivered to the diode--20% energy efficiency--with carbon-coated flashboards as the plasma source. Switch performance (voltage and power generated) with a straight 10 cm diam cathode deteriorated as the anode outer conductor just downstream of the switch, but at the same radius as the switch rods, was extended toward the load. Load power was up to 70% higher with a plasma-filled diode (PFD) used in conjunction with the POS for short POS conduction times (400 ns and less). Use of a helical center conductor resulted in dramatically degraded switch performance for >350 ns conduction times. Switch performance with gas guns was generally comparable to that with flashboards in a given switch/load configuration and was independent of the gas (H₂, He, and Ar) used.

Introduction

The Hawk generator¹ is a 600 nH, 1- μ F Marx bank² that stores 225 kJ at 80-kV charge to deliver up to 720 kA in 1.2 μ s to a plasma opening switch (POS). Past experiments and analyses³ have identified hydrodynamic plasma distortion as the dominant mechanism that controls much of the POS operation.⁴ A high density plasma is used to conduct the current pulse, while the opening phase is characterized by a rarefied plasma resulting from redistribution during the conduction phase. The maximum load power is determined by an effective gap for magnetic insulation in the POS. The data indicated that above a critical load impedance the final switch gap, as determined from magnetic insulation arguments, is limited to 3 mm. Above this critical impedance, called the switch-limited regime, current is shunted into the transition section between the switch and the load with the voltage remaining constant. At lower impedance values, the voltage decreases in proportion to the load impedance--called the load-limited regime. Maximum load power is obtained at this critical impedance. Increasing the cathode magnetic field (I/r)--by conducting more current or decreasing the cathode radius--allows the fixed-gap POS to remain insulated at a higher voltage. In this way peak load voltages up to 2 MV were achieved with a small 2.5 cm diam cathode, a factor of 2.8 higher than the Marx voltage.

In this paper, recent Hawk experiments with further modifications to the POS electrode geometry, plasma-filled diodes (PFD), and gas gun plasma sources are discussed.

Tapered Cathodes

Tapered cathodes, abrupt and gradual, were tried in the switch region and upstream and downstream of the switch. The cathode magnetic field is larger in tapered regions which can, in principle, better insulate the electron flow and produce higher load powers. Only tapering in the switch had an effect on performance with significantly improved performance using a taper like that shown in figure 1. This gradual 10 to 2.5 cm diam taper through the 8 cm length switch produced load powers up to 0.7 TW (1.5 MV and 465 kA in figure 2) and 55 kJ--20% energy efficiency--delivered to the load. Such a taper generated voltages close to those possible with a 2.5 cm diam cathode but with the longer conduction/higher currents associated with a 10 cm diam cathode, producing the high load powers. The importance of geometry on switch performance is illustrated by the fact that when the tapering starts just a few cm further downstream near the middle of the switch, instead of at the upstream end, performance becomes identical to a straight 10 cm diam cathode, i.e. 850 kV and 0.4 TW load power at 900 ns conduction.

Figure 3 shows the peak switch voltage as a function of load impedance at peak power for numerous shots with the taper in figure 1. Above $\sim 4 \Omega$ the voltage is roughly constant for a given conduction current--the switch-limited regime. Voltage increases with conduction current and is over 1.6 MV on the longest conduction (600 to 700 kA) switch-limited shots. The 4Ω impedance is the critical impedance for this geometry, producing 0.7 TW on 600-700 kA conduction shots.

The influence geometry can have on switch operation is further illustrated in figure 4 where two cathode taper shots with the same conduction time (same plasma conditions) are shown. In one case, the setup is the standard switch-to-load length in load-limited operation--good current transfer, relatively low voltage--because sufficient switch plasma reaches the load to limit the load impedance at peak power. (More switch plasma is accelerated to the load by $J \times B$ forces during conduction for small radius cathodes.) On the other shot (with the same diode gap) the transition section was extended, allowing high load impedance--switch-limited--operation with high voltage but modest current transfer.

Anode Modifications

Modest changes to the anode structure can, like the cathode, have a substantial affect on switch opening. Figure 5 shows a 6 cm long extension added to the anode just downstream of the switch at the same radius as the switch rods, providing a 2 cm radial gap in this region. The usual configuration is to expand out to a 4 cm radial gap immediately downstream of the switch rods. The extension was originally intended for experiments with a helical center conductor, serving as a flux conserving tube to produce a higher total magnetic field near the switch than is possible with a solid center conductor of the same nominal radius. Here the cathode is a solid 10 cm diam.

Figure 6 shows shots with 6 cm, 2 cm, and no extension for the same 950 ns conduction time. Switch opening with the 6 cm extension is very poor. Most of the current is lost over the last 3 cm length of the extension, with the location where the damage begins corresponding to the downstream edge of the switch at opening if the switch translates about half the switch length

during the conduction phase. Opening actually improved somewhat with shorter plasma delays--an atypical result. A 2 cm extension resulted in better switch opening, but still not as good as the no extension standard setup, where current transfer efficiency is 80% and voltages of 800 kV are produced.

Plasma-Filled Diodes

PFD experiments were done by injecting plasma from a flashboard downstream of the diode into the diode gap through holes in the anode strike plate. The PFD was used in three cathode configurations : a straight 5 cm diam cathode, a 10 to 5 cm diam switch taper, and a tapered cathode which was flared out to a 10 cm diam at the diode as shown in figure 7. Flaring the cathode at the diode was a convenient way of reducing the load impedance at peak power for a given diode gap, operating closer to the critical impedance. For long conduction time shots, peak load power was up to 30% higher with the PFD. However, some switch plasma reached the load--the impedance rises from zero even with no independent PFD on these long conduction shots--so there are no true vacuum diode shots for comparison.

For short conduction times, where switch plasma does not reach the load and the load with no PFD behaves as a vacuum diode, the enhancement in load power using the PFD was greater. Figure 8 shows peak load power on shots with 400 ns POS conduction times was up to 70% higher with the PFD (for similar load impedances at peak power). With the PFD, somewhat higher voltage is produced (larger switch gap) and more current reaches the load. This is consistent with the reduced vacuum electron flow with a PFD load that is seen in simulations.⁴ Also, the PFD shots showed strong on-axis beam pinching in the diode, evident from x-ray pinhole pictures and damage done to the anode plate. This is probably because the plasma is a source of ions necessary for pinching. (Shots with small radius cathodes at the diode--2.5 cm and 5 cm diam- without a PFD also show pinching.)

The control of load impedance provided by the PFD is illustrated in figure 9. This figure shows two PFD shots with the same POS conduction time and a large diode gap, but different PFD delays. In the upper plot, the PFD delay is short and performance is switch-limited: the load impedance at peak power and the voltage generated are high, current transfer is modest. In contrast, in the bottom plot the PFD delay is long and performance is load-limited: the impedance at peak power and the voltage generated are limited, while the current transfer efficiency is good. Note that the peak load power on these two shots is about the same.

Helical Center Conductor

A helical cathode center conductor with a pitch of four and a nominal 10 cm diam was used in the switch region as shown in figure 10. There are four slots in the helix. The helix is not centered under the flashboards/anode rods, but is displaced about 4 cm downstream. This was done so that the center-of-mass of the plasma, which may translate downstream about half the switch length or 4 cm during conduction, is at the center of the helix (where the field is highest) at opening. With the flux conserving tube in place as shown, the additional axial field increases the total insulating magnetic field over the middle 14 cm of the helix a factor of 2.3 above that from a solid cathode of the same diameter. Because of the detrimental effect of the anode extension

observed with solid cathodes, the helix experiments were done both with and without anode extensions for comparison (with no difference in performance seen).

Switch opening with the helix was generally very poor, although there appeared to be different "regimes" of operation. Conduction times for a particular plasma delay were typical of solid 10 cm diam cathodes. For long delays of $\geq 1 \mu\text{s}$ the switch conducts for $\sim 1 \mu\text{s}$, but with small load currents and low voltage generated upon opening with both short circuit and diode loads. Most of the current stays in the switch. With intermediate delays, from 0.5 to 1 μs , the switch did not open at all for both short circuit and diode loads. For short delays, less than 0.5 μs , with 350 ns conduction times or less and short circuit loads, switch opening was much improved and all the current reached the load. (No data exists with diode loads at these short conduction times.) Current appeared to be flowing in the helix ribs on the short plasma delay shots, because the ribs were deformed by magnetic forces during the pulse. This did not occur with the longer plasma delays and suggests that in this case current is carried in the plasma, not the helix, for the entire pulse. The fact that switch opening here is inferior to the solid cathode suggests that it is not simply a matter of the helical turns shorting out. Also, the B_z field decreases to zero at the ends of the helix and this may result in additional electron losses downstream of the switch. To retrap some of this flow, the cathode just downstream of the helix was reduced to 5 cm diameter on some shots, resulting in a slight improvement in performance.

Gas Gun Plasma Sources

Four gas guns,⁵ 90° apart, were also used as an opening switch plasma source with H_2 , He, and Ar gases. The gas, at 60 psig back pressure, was fed into the region between the coaxial electrodes, where the plasma discharge is initiated, through an automobile fuel injector used as the mechanical valve. Typically, the valve is pulsed at least several hundred microseconds before the discharge is initiated in the gun by a capacitor bank. This minimum gas puff delay is needed to initiate the gun discharge and involves the time it takes for the valve to start opening and the transit time of the gas from the valve to the location near the front of the gun where gas breakdown occurs. Best performance with H_2 and He gases occurred with gas puff delays of 400 to 450 μs . For Ar, gas puff delays of $\sim 500 \mu\text{s}$ resulted in best performance, consistent with its slower thermal velocity. The plasma produced by the guns typically has a slower velocity and is more localized than flashboard plasma.⁶

Figure 11 shows one of the configurations, a tapered cathode, used with the gas guns. The 10 cm and 2.5 cm diam cathodes were also used. The gun to cathode distance was varied from 3.5 to 10 cm. This figure shows two B-dot current monitors, ILU2 and ILL2, located behind the diode which were used on these gas gun shots in addition to the standard load current monitors, ILU and ILL, which are 5 cm upstream of the diode. In typical operation, these two sets of current monitors agree: little current is lost in the 5 cm distance from the standard current monitors to the load. Even in switch-limited operation, most of the current loss, which can be a substantial fraction of the total current, occurs near the load but upstream of the standard load current monitors ILU and ILL.

Switch performance with a 10 cm diam cathode was equivalent for the different gases. In addition, performance is very similar to flashboards: voltage and load power improve with conduction time and at 900 ns conduction switch voltage is $\sim 800 \text{ kV}$. Figure 12 shows peak switch voltage as a function of load impedance at peak power for shots with He gas. On the

longest conduction shots, the voltage is 800 kV at load impedances of $\sim 2 \Omega$ and above (similar to flashboards). The highest load power, about 0.4 TW, occurs at this 2Ω critical impedance, also comparable to flashboards.

Performance with a 2.5 cm diam cathode was, again, independent of the gas used. Voltage and load power improve with conduction time up to 600 ns, similar to flashboards. In figure 13, peak switch voltage is plotted versus load impedance at peak power for shots with H_2 gas. On the longest conduction shots, the voltage is still increasing with load impedance at 1.2 MV and 5.5Ω in this limited data set. Switch-limited operation may not have been reached and higher voltages may be possible if the load impedance can be increased above 5.5Ω . These shots were all taken with a 26 cm switch-to-load length, a configuration which for flashboards resulted in load-limited operation with the 2.5 cm diam cathode: sufficient switch plasma was accelerated to the load to limit the impedance at peak power. In the case of flashboards, the switch-to-load length was extended to produce the higher load impedances, $\sim 7 \Omega$, necessary for generating 1.5 to 2 MV switch voltages.

For the tapered cathode in figure 11 (with H_2 gas), voltage is 1.4 MV at the 4Ω critical impedance and above (figure 14 with H_2 gas). This is also similar to flashboards with tapered cathodes. However, in what is atypical behavior, the switch-limited voltage does not increase with conduction current, but is constant at 1.4 MV over a range of conduction currents from 350 to 550 kA.

Summary

Recent experiments on Hawk reiterate the importance of the electrode geometry on switch performance. Cathode and anode configurations can have a major impact on switch opening. Tapering the cathode over the 8 cm POS length from 10 cm diam to, typically, a 2.5 cm diam was a good compromise between the high voltage generated with a small radius cathode and the longer conduction/higher currents associated with the larger cathodes, producing load powers of 0.7 TW (1.6 MV and 450 kA load current) with 55 kJ--20% energy efficiency--delivered to the diode. There is a limit on the minimum radial gaps in the switch and downstream of the switch below which voltage and current transfer are reduced. For example, switch performance with a straight 10 cm diam cathode deteriorated as the anode outer conductor just downstream of the switch, but at the same radius as the switch rods, was extended toward the load.

Load power was up to 70% higher with a PFD used in conjunction with the POS for short conduction times (400 ns and less), where switch plasma does not reach the load. On longer conduction time shots, the effect was less pronounced, with about a 30% enhancement with the PFD. In this case, however, some switch plasma reached the load so there were no true vacuum diode shots for comparison.

A helical center conductor in the switch region, designed to increase the total insulating magnetic field for a given cathode radius, resulted in dramatically degraded switch opening (low voltage, poor current transfer) for >350 ns conduction times with both short circuit and diode loads. Opening was good for <350 ns conduction. Indications were that current was carried in the helix only on the short conduction time (low plasma density) shots, because the helical ribs were deformed by magnetic forces on these shots.

Switch/load performance with gas guns was generally comparable to that with flashboards in a given switch/load configuration. Performance was independent of the gas (H_2 , He, and Ar) used.

References

- [1] J.R. Boller, et. al., NRL Memorandum Report 6748, January 1991.
- [2] P. Sincerny, et. al., 7th IEEE Pulsed Power Conference, Monterey, CA, 1989, IEEE Cat. No. 89CH2678-2, p. 275.
- [3] P. J. Goodrich, et. al., 8th IEEE Pulsed Power Conference, San Diego, CA, 1991, IEEE Cat. No. 91CH3052-8, p. 515, also see P.J. Goodrich, et. al., Proceedings of the 9th International Conference on High Power Particle Beams, Washington D.C., 1992.
- [4]
- [5]
- [6]

PULSED POWER PHYSICS TECHNOTE 93-10

TITLE: POSITIVE POLARITY POS OPERATION ON HAWK

Author: D. Hinshelwood and R. Fisher

Date: May 4, 1993

Abstract: This note gives the results from a handfull of shots taken in June, 1992 where Hawk was operated in positive polarity. The conduction current as a function of generator delay was compared with that obtained in negative polarity using short circuit loads. A few shots were taken with a diode load. Conduction appears seen to be slightly greater in positive polarity. It is speculated that the apparent, longer conduction time may be related to a greater delay in establishing magnetic insulation between the switch and the load. This issue could be resolved with further experiments and PIC simulations, leading to an increase in our understanding of the POS.

Positive polarity POS operation was investigated with a small number of shots on Hawk in June, 1992. For these shots a 5-cm diam center conductor (anode) was used with a 4.5-cm radial gap in the switch region, i.e., the standard anode rod arrangement for the 10-cm diam center conductor was used. The standard-length configuration was used, with 13-cm-long anode rods connecting the load dB/dt collar to the switch anode rod assembly. Most of the run consisted of short circuit shots in alternate polarities. Only the usual machine electrical diagnostics were used. Reversing the polarity of Hawk is a simple procedure which requires only that the main and mini-Marx power supply leads be reversed. This run comprised shots 1009-1029 and the data is stored in [HAWK.PLUS].

The first five graphs on the page after next compare generator and load currents for both polarities, at five different generator delays. For each set of shots the delay was the same within the resolution of the data. With these delays the conduction current and time ranged from 250 kA at 300 ns to 670 kA at 1 μ s. The two load currents are averaged together in these graphs for clarity. Unless noted, both load dB/dt's agree fairly well with one another on these shots. At the earliest timing the switch appears to open at the same time on all three shots taken, although a small foot on the load currents in positive polarity causes opening to be delayed. At the next three timings, the switch appears to conduct slightly longer in positive polarity (on two of the positive polarity shots, shot 1024 at 1.6 μ s and shot 1014 at 2.1 μ s, the two load dB/dt signals differed by about 40%). The load currents in positive polarity also show a slight dip before opening, and this dip can almost be imagined to start when the load current begins in negative polarity. For these shots, the rise in switch voltage, associated with switching to the load inductance, also occurs later in positive polarity. At the latest timing, the load current starts at the same time in both polarities (on each shot one of the load dB/dt's lost it, so that the actual load currents were larger than shown). A polarity-dependent foot is also seen on both load current traces.

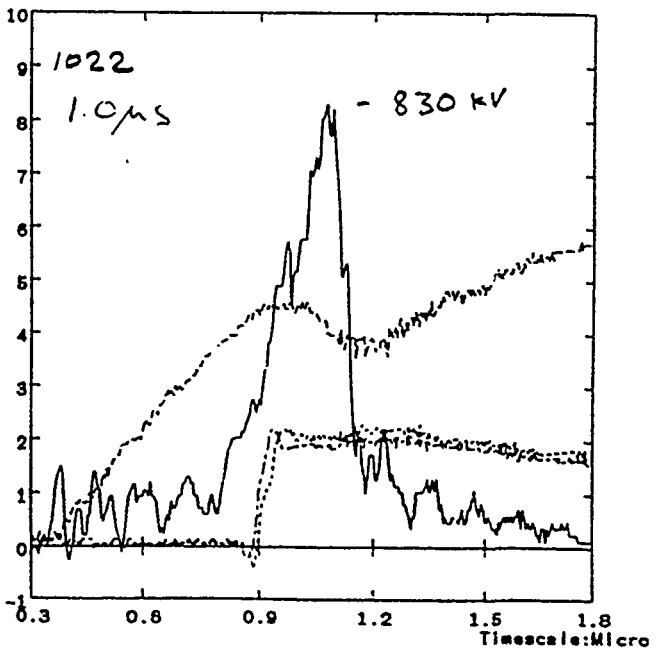
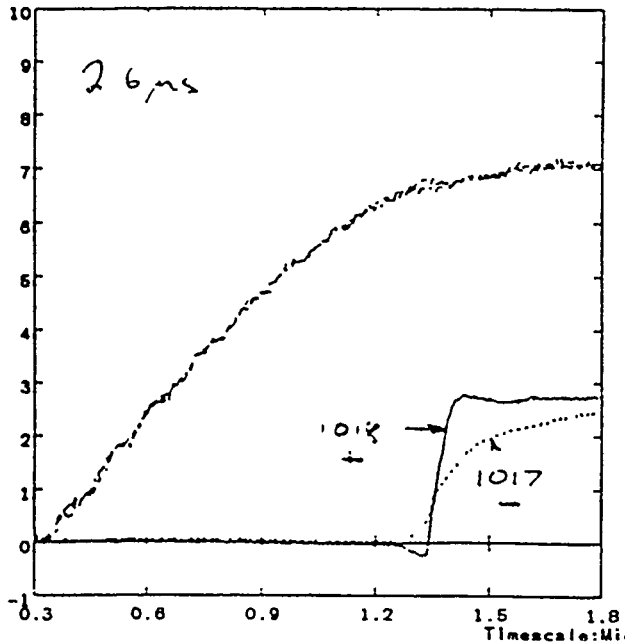
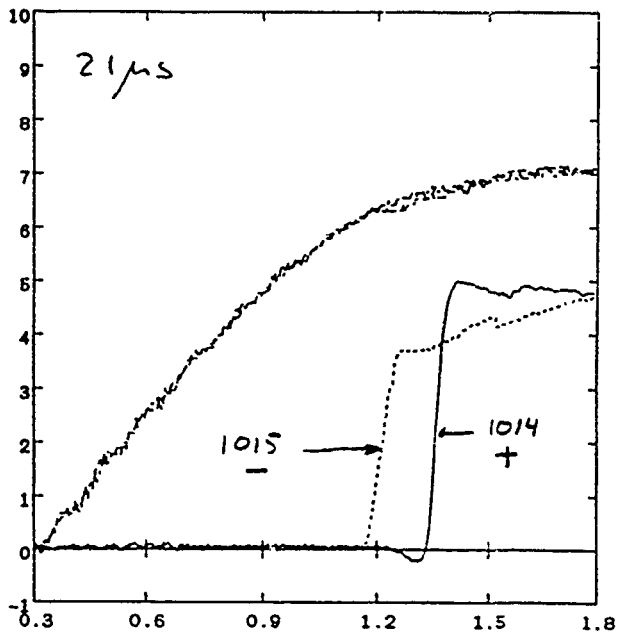
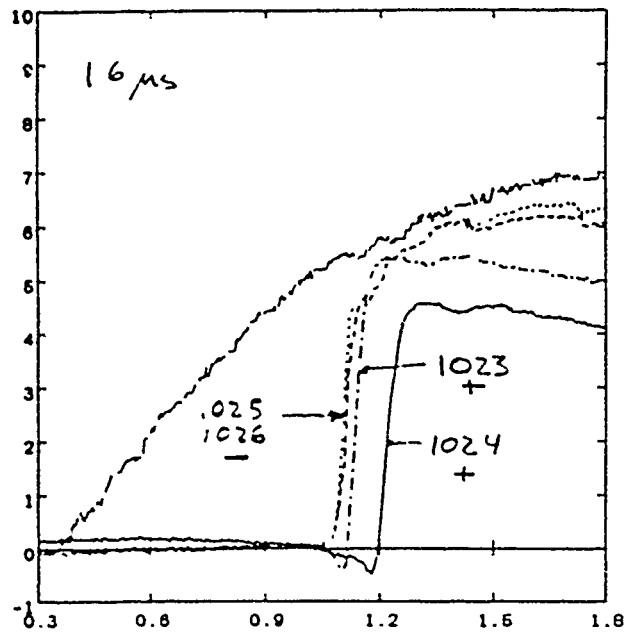
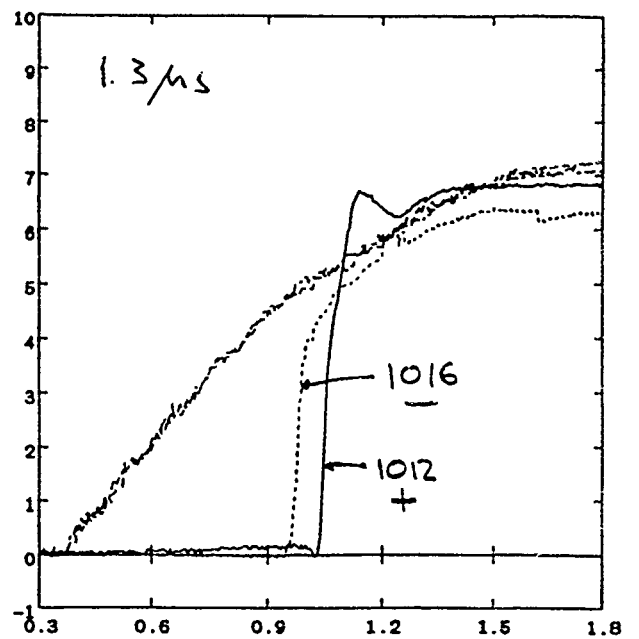
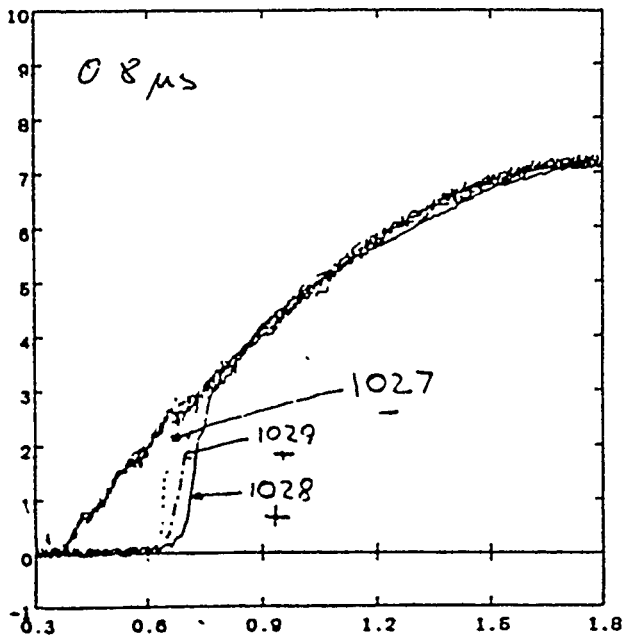
The last graph shows data from one of the few shots with a diode load. The center conductor was terminated in a butt end to form the anode, and another short section of 5-cm-diam hollow tube was installed in the short-circuit plate to form the cathode. The diode gap was about 1 cm. This shot was taken with a rather short delay; two other shots, taken at longer delays, exhibited much lower load impedance. The results from this shot are far from spectacular.

Interpretation of these results is complicated by the fact that in positive polarity the load current monitors are located on the cathode. The data Bruce is taking now show that both the anode and cathode load currents start at the same time. Therefore, the later load currents observed here for positive polarity shots are probably not the result of this monitor asymmetry. On the other hand, we would not expect switch opening in the MHD regime to be polarity dependent. A possible explanation is that in positive polarity there is a greater delay between switch opening and current transfer to the load. This delay is related to the establishment of magnetic insulation between the switch and the load and might well be polarity dependent in the cylindrical geometry of this experiment.

Since the total current into the diode load on shot 1022 was not measured, it is difficult to say whether the system was in the switch- or load-limited regime. Thus, the data here are insufficient to judge positive polarity operation of the switch into a diode

load. Like the dog on his hind legs, however, it is encouraging that the positive polarity switch works at all.

This polarity comparison should be continued with a limited number of shots as part of the current run on Hawk, where both anode and cathode monitors are installed, both immediately past the switch and at the load. If a polarity dependence is observed and can be attributed to phenomena beyond the switch, then the effect of polarity should be studied using PIC simulation. As a minimum, reproducing this effect with simulation would constitute a good benchmarking of the code, and may even lead to a greater understanding of POS operation.



PULSED POWER PHYSICS TECHNOTE NO. 90-31

TITLE: EYESS PEOS EXPERIMENT WITH NRL FLASHBOARDS

AUTHORS: B.V. Weber, R.J. Commisso, P.J. Goodrich, R. Fisher

DATE: December 13, 1990

ABSTRACT: A one-week PEOS experiment was performed on the PI Eyess generator involving NRL and PI personnel. The purpose of the experiment was to test the effects of using a different flashboard plasma source in the same configuration used in previous Eyess experiments. The flashboard used in these experiments was modified to generate a higher density at early time delays and was successfully tested on Pawn at NRL. On Eyess, these flashboards demonstrated the capability to conduct higher current than the flashboards used previously at PI, but the resulting load power was similar to previous results. Details of these experiments are included here. The results were presented at the Jan 1990 DNA opening switch workshop and at a Branch seminar.

THIS REPORT REPRESENTS
UNPUBLISHED INTERNAL
WORKING DOCUMENTS AND
SHOULD NOT BE REFERENCED
OR DISTRIBUTED

I. INTRODUCTION

A one-week PEOS experiment was performed on the PI Eyess¹ generator in November 1989 involving NRL and PI personnel. The NRL personnel who travelled to PI are: R. Commisso, R. Fisher, P. Goodrich and B. Weber. PI personnel who collaborated on this experiment are: J. Goyer, D. Kortbawi and G. Dealy. The purpose of the experiment was to increase the power generated by using different flashboard plasma sources in the same configuration used in previous Eyess experiments. The flashboards used in these experiments were modified to generate a higher density at early time delays and were successfully tested on Pawn at NRL. On Eyess, these flashboards demonstrated the capability to conduct higher current than the flashboards used previously at PI, but the resulting load power was similar to previous results. The details of these experiments are included here, including waveforms from chosen shots, tabulated parameters from all shots, comparisons of conduction currents for different situations, and density estimates based on hydro-limited conduction. These results were presented at the Jan 1990 DNA opening switch workshop and in a Branch seminar.

II. EYESS EXPERIMENT

A sketch of the experimental setup is shown in Figs. 1 and 2. Figure 1 is a sketch of the r-z cross section of the Eyess vacuum section showing the flashboard location, plasma injection aperture and diode load. Both short circuit and diode loads were used. This configuration is identical to experiments performed previously on Eyess using different flashboard plasma sources. The flashboards were positioned either 10 cm or 20 cm from the center conductor surface. The plasma injection aperture length was 5 cm for all the shots except three, where the length was increased to 14 cm. Figure 2 is a sketch of the r- ϕ cross section in the switch region.

Three flashboard variations are shown in Fig. 3. The first design (left hand side) was used in PEOS experiments on Gamble II, POP and Pawn at NRL. The flashboard gap array consists of 6 chains with 10 gaps each. These flashboards were given to PI and modified for Eyess experiments as shown on the right hand side in Fig. 3. At NRL, a new version² (center) with 6x20 gaps were constructed to generate higher density at the same delay time. These flashboards were tested on the Pawn generator. The driving current waveform is different for the three cases, as illustrated by the Peak I and quarter period (T/4) listed in the Figure. It became clear to us, by comparing results on Pawn and Eyess, that the 6x20 gap flashboards generate a far higher density at early time delays than the 3x8 gap flashboards. The following experiment was aimed at fielding these new plasma sources on Eyess with a goal of improved switch performance at conduction times approaching 1 μ s.

III. DISCUSSION OF RESULTS

Table I is a summary of the results from all the shots taken on Eyess using the 6x20 gap flashboards. Eighteen short circuit load shots were taken on the first day, followed by 18 diode load shots on the next two days. The parameters listed in Table I are described in the caption.

An example of generator and load current waveforms with short circuit loads is shown in Fig. 4. The conducted current increases with time delay (time between firing the flashboard bank and the Eyess bank). The conduction current is far higher using these flashboards compared to the 3x8 gap flashboards at the same time delay. Fast switching is achieved at full current using a time delay of about 2.2 μ s. This is an improvement in switching compared to results using the 3x8 gap flashboards.

Results using diode loads did not exhibit the improvement evident with short circuits. Waveforms for the highest power shot are shown in Fig. 5. The peak power, 0.34 TW, is similar to (but not greater than) the highest powers obtained on Eyess using the 3x8 gap flashboards. The voltage on this shot, 0.86 MV, is considerably less than the Eyess all-time record of \approx 1.5 MV. Waveforms for an Eyess shot using the 3x8 gap flashboards are shown for comparison in Fig. 6 (copied from the DNA Opening Switch Workshop presentation by J. Goyer in Jan, 1990). The load power is about the same on this shot as for the shot in Fig. 5, except at higher voltage and lower current.

The dependence of conduction current on parameters varied in this experiment are illustrated in Figs. 7-9. Fig. 7 compares the 6x20 gap flashboard conduction currents to those using 3x8 gap flashboards at the same distance (20 cm) and time delay. The conduction current (and conduction time) are over 2 times greater using the new flashboards. Fig. 8 shows the difference in conduction current for 10 and 20 cm distances between flashboards and center conductor. An additional 0.7 μ s is required to compensate for the additional 10 cm distance. Fig. 9 shows the small, but interesting sample of data on the effect of increased plasma injection length. The conducted current increases a noticeable amount (about 10%) when the injection length is increased from 5 cm to 14 cm. Increasing the injection length increases the plasma mass by some unknown factor, but the weak scaling of conduction current with length seen here is in the direction of (or beyond) hydro-limited conduction, where $I \propto l_0^{1/2}$. Measurements of the line density for 5 cm and 14 cm lengths would help resolve this scaling.

Figure 10 is a plot of a calculated plasma density based on finite hydrodynamic plasma displacement during conduction. The data in Table I (DII2 and Teff) are used to calculate a density so the plasma center-of-mass displacement is $l_0/2$. This calculation results in plasma densities in the 10^{15} cm⁻³ range, give or take a factor of 10. This calculation gives a lower bound on the plasma mass, unless the plasma displacement is larger than assumed, or unless plasma momentum is carried out of the system by fast ions crossing to the center conductor on a time scale shorter than the conduction time. Both of these effects are expected to be small in this experiment.

IV. THE BOTTOM LINE(S)

The bottom line of this experiment is these "new and improved" plasma sources did not improve the opening switch performance on Eyes in any important way, such as increased power, voltage, or faster switching. This in itself is an interesting result, suggesting that optimum switching does not require a fast plasma, contrary to our thinking for the short conduction time PEOS. A follow up analysis of the density- and length-scaling in this experiment could be done with test stand density measurements.

REFERENCES

1. P. Sincerney, et al., "A Microsecond Marx Bank for Driving High Current Electron Beams," 7th IEEE Pulsed Power Conf. Monterey, CA (1989), IEEE Cat. No. 89CH2678-2, p. 275.
2. R. Comisso, et al., "Experimental Study of Flashboard Variations," Pulsed Power Physics Branch Technote 89-34 (unpublished).

EYESS DATA USING NRL FLASHBOARDS

DATE	SHOT #	SEQ #	LOAD	FB-K (cm)	MASK (cm)	TIME (us)	ISW (kA)	VSW (kV)	XRD (V)	DII2 (C ⁻²)	Teff (ns)	neff (10 ⁻¹⁵)	PL (TW)
11/28/89	4773	1	short	10	5	0							
	4774	2	short	10	5	0							
	4775	3	short	10	5	0							
	4776	4	short	10	5	1.2	563	234		1.1E-02	645	0.91	
	4777	5	short	10	5	-	589	170		1.4E-02	696	1.16	
	4778	6	short	10	5	1.2	584	170		1.2E-02	650	0.99	
	4779	7	short	10	5	2.2	723	191		4.5E-02	1016	3.72	
	4780	8	short	10	5	3.2	790	80		1.3E-01	1581	10.74	
	4781	9	short	10	5	0.5	345	167		1.0E-03	318	0.08	
	4782	10	short	10	5	0.85	518	135		6.0E-03	518	0.50	
	4783	11	short	10	5	1.15	589	135		1.2E-02	644	0.99	
	4784	12	short	20	5	1.15	258	130		3.5E-04	251	0.03	
	4785	13	short	20	5	2.2	601	100		1.3E-02	657	1.07	
	4786	14	short	20	5	3.1	681	215		3.0E-02	896	2.48	
	4787	15	short	20	5	4.1	751	108		6.0E-02	1130	4.96	
11/29/89	4788	1	short	20	14	1.1	315	126		8.0E-04	311	0.01	
	4789	2	short	20	14	2.1	672	125		2.5E-02	815	0.26	
	4790	3	short	20	14	3.1	754	119		6.0E-02	1125	0.63	
	4791	1	diode	20	5	3.1	695	274	0.6	3.0E-02	863	2.48	0.04
	4792	-	diode	20	5	2.1	626	447	2.0	1.9E-02	763	1.57	0.18
	4793	3	diode	20	5	2.1	604	670	2.0	1.4E-02	679	1.16	0.24
	4794	1	diode	20	5	2.2	635	403	0.4	2.0E-02	771	1.65	0.15
	4795	2	diode	20	5	2.1	590	541	0.7	1.2E-02	643	0.99	0.20
	4796	3	diode	20	5	2.1	546	714	3.1	9.0E-03	502	0.74	0.20
	4797	4	diode	20	5	2.1	568	687	3.3	1.1E-02	640	0.91	0.28
	4798	5	diode	20	5	1.6	498	771	5.7	6.0E-03	539	0.50	0.23
	4799	6	diode	20	5	1.7	533	860	5.9	1.0E-02	650	0.83	0.34
	4800	7	diode	20	5	1.1	372	664	2.7	1.5E-03	361	0.12	0.19
	4801	8	diode	20	5	1.6	477	832	3.7	1.6E-02	767	1.32	0.24
	4802	9	diode	20	5	1.6	468	776	4.8	4.0E-03	468	0.33	0.19
11/30/89	4803	10	diode	20	5	1.6	407	877	7.5	2.5E-03	426	0.21	0.19
	4804	11	diode	20	5	2.1	477	1010	12.0	5.0E-03	514	0.41	0.26
	4805	12	diode	10	5	1.1	524	884	9.6	7.0E-03	553	0.58	0.25
	4806	13	diode	10	5	0.9	510	609	2.4	6.0E-03	526	0.50	0.23
	4807	1	diode	10	5	1.1	619	563	1.5	1.6E-02	613	1.32	0.12
	4809	3	diode	10	5	0	34	466	0.9	2.0E-02	763	0.00	0.09
	4810	4	diode	10	5	1.1	642	423	0.5	8.0E-03	575	1.65	0.17
4811	5	diode	10	5	0.7	539	470	0.6			0.66	0.16	

Table I. Summary of data taken on Eyess using NRL flashboards. SEQ # records the number of shots taken without opening the vacuum chamber. FB-K is the distance from the flashboards to the cathode surface. MASK is the axial aperture length. TIME is the delay from the flashboard driving current to the start of the Eyess generator current. Isw and Vsw are the peak switch current and voltage. XRD is the peak voltage on the x-ray detector. DII2 is double integral of I₂ during the conduction time. Teff is the conduction time of a linear ramp current with the same DII2 value. neff is the calculated density assuming the center of mass displacement is $l_0/2$ during conduction. PL is the peak load power.

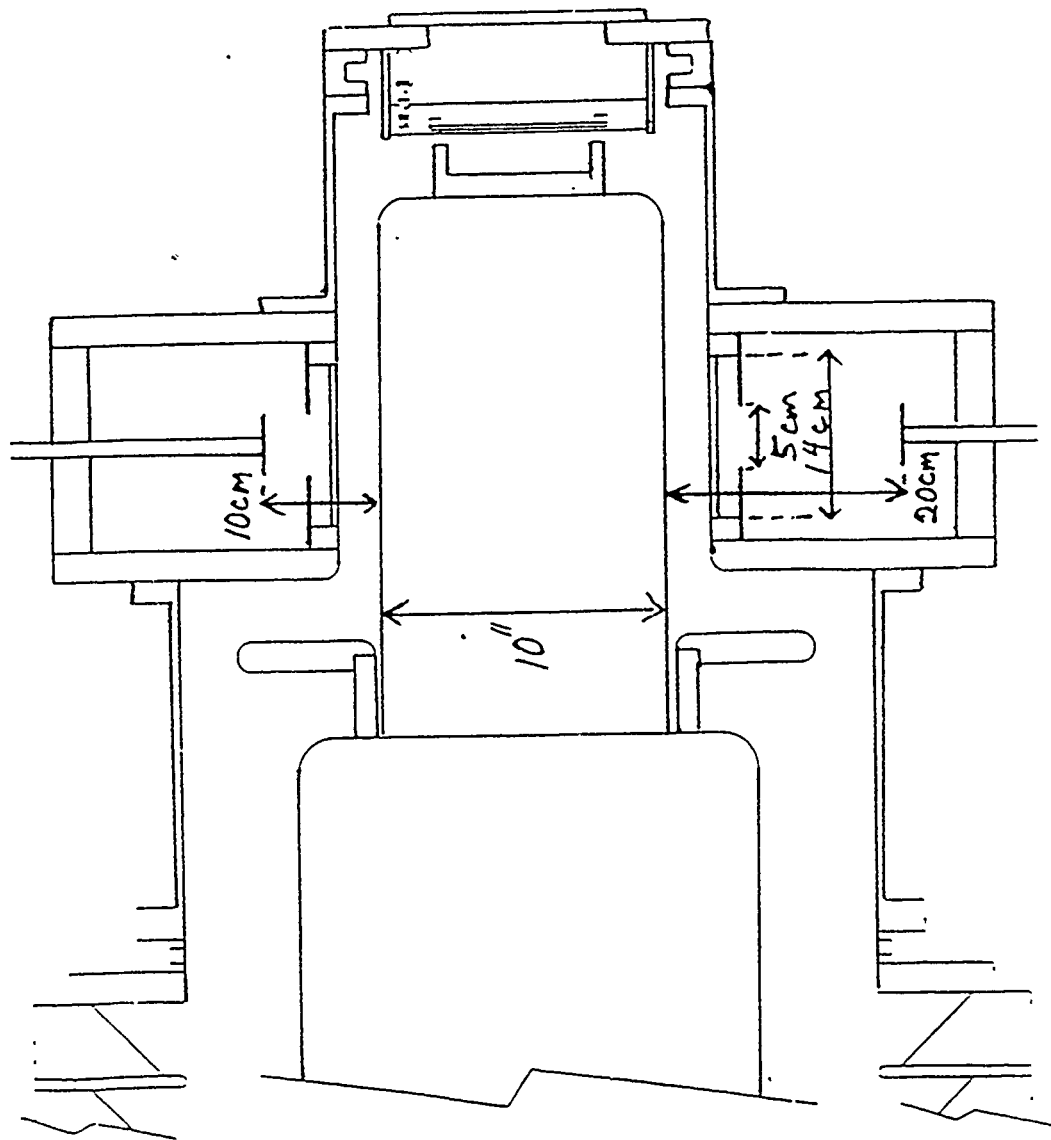


Figure 1. This experiment was done to test the use of different flashboards on the PI Eyes experiment. Two FB-cathode distances were used, 10cm and 20 cm. The injection aperture was limited to 5 cm for most of the shots. On some shots, this was increased to 14 cm. The center conductor diam is 10". The load was a short circuit or diode.

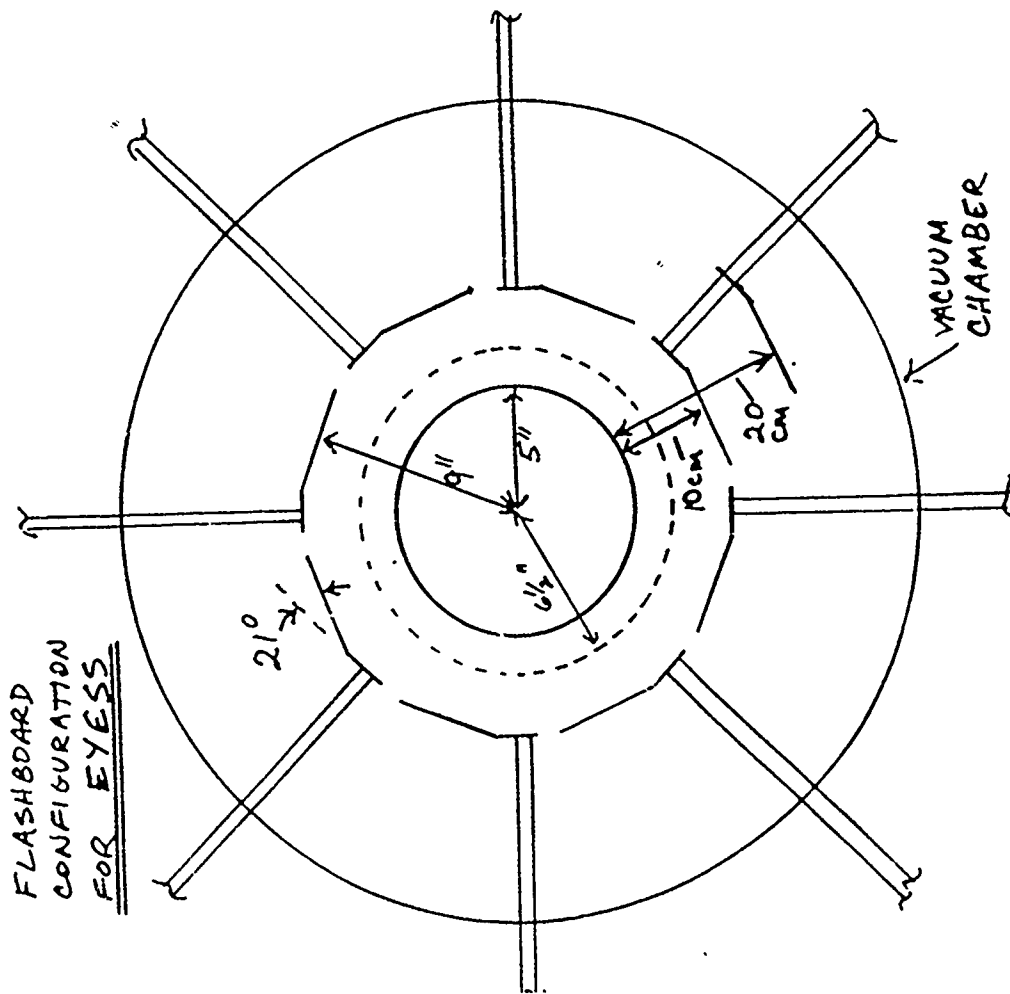


Figure 2. Eight flashboards are used to inject plasma into the switch region, as in previous Eyess experiments. The plasma-emitting surfaces on the flashboards are bent to direct plasma toward the axis. The transparent outer conductor (bird cage) is represented by the dashed circle.

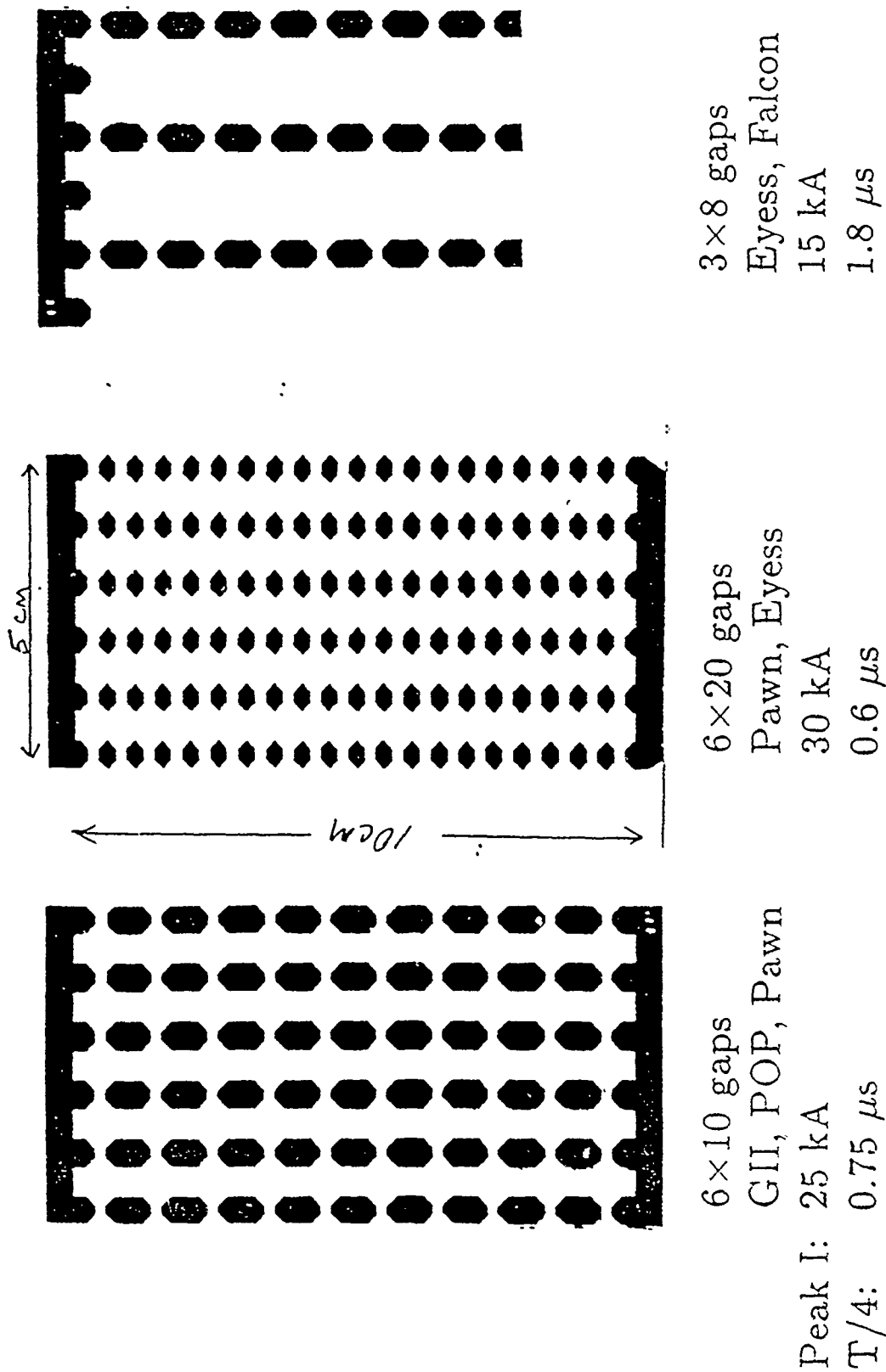


Figure 3. Three flashboard variations are shown that have been used in PEOS experiments at NRL and PI. The number of gaps, chains and the driving current waveforms are different in each case.

D=10CM, SHORT CIRCUIT SHOTS

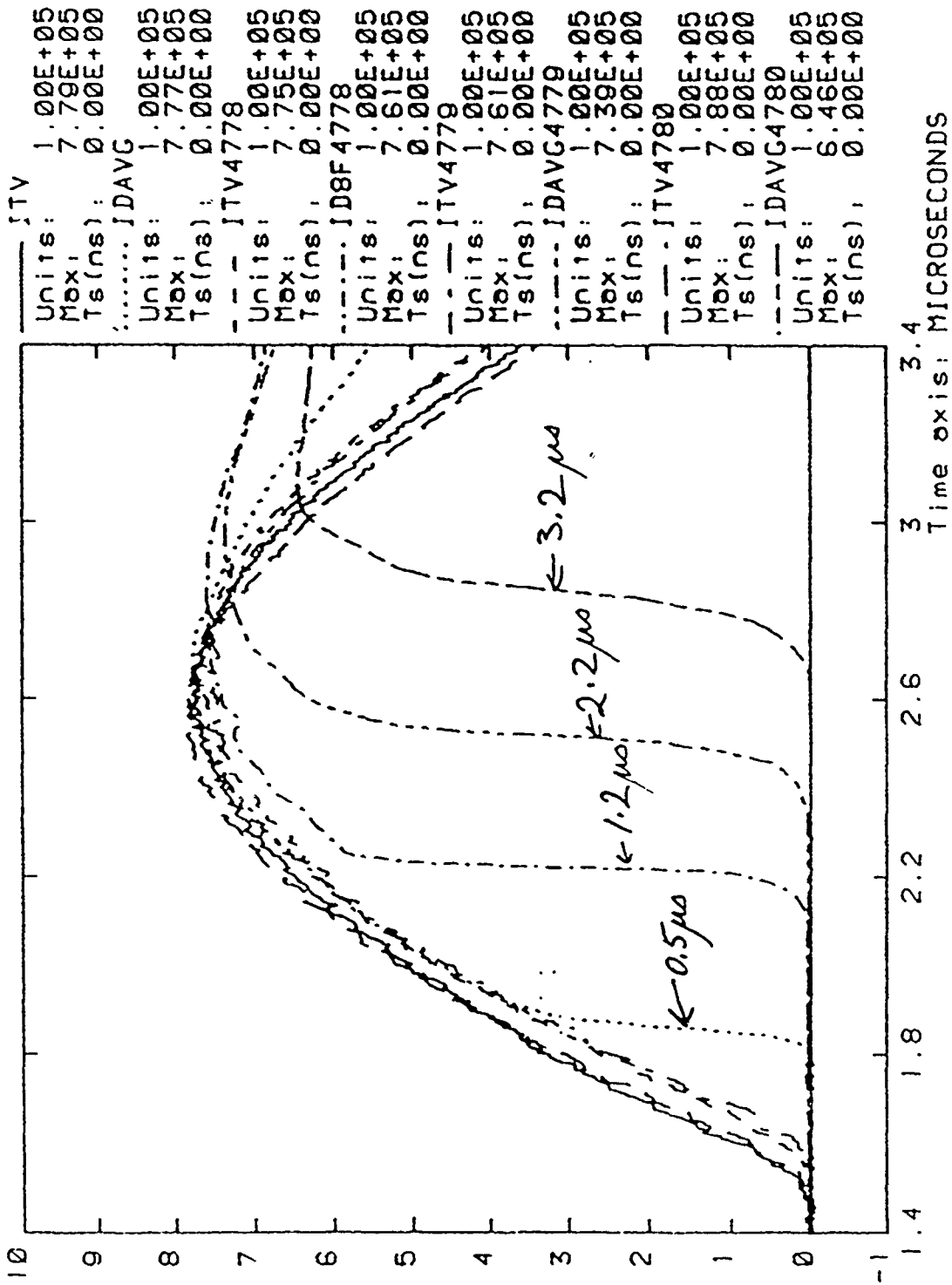


Figure 4. Generator and short circuit load currents for different time delays using a 10 cm F-K distance. The conduction currents are much higher than those obtained using the PI-modified FBs at the same timings.

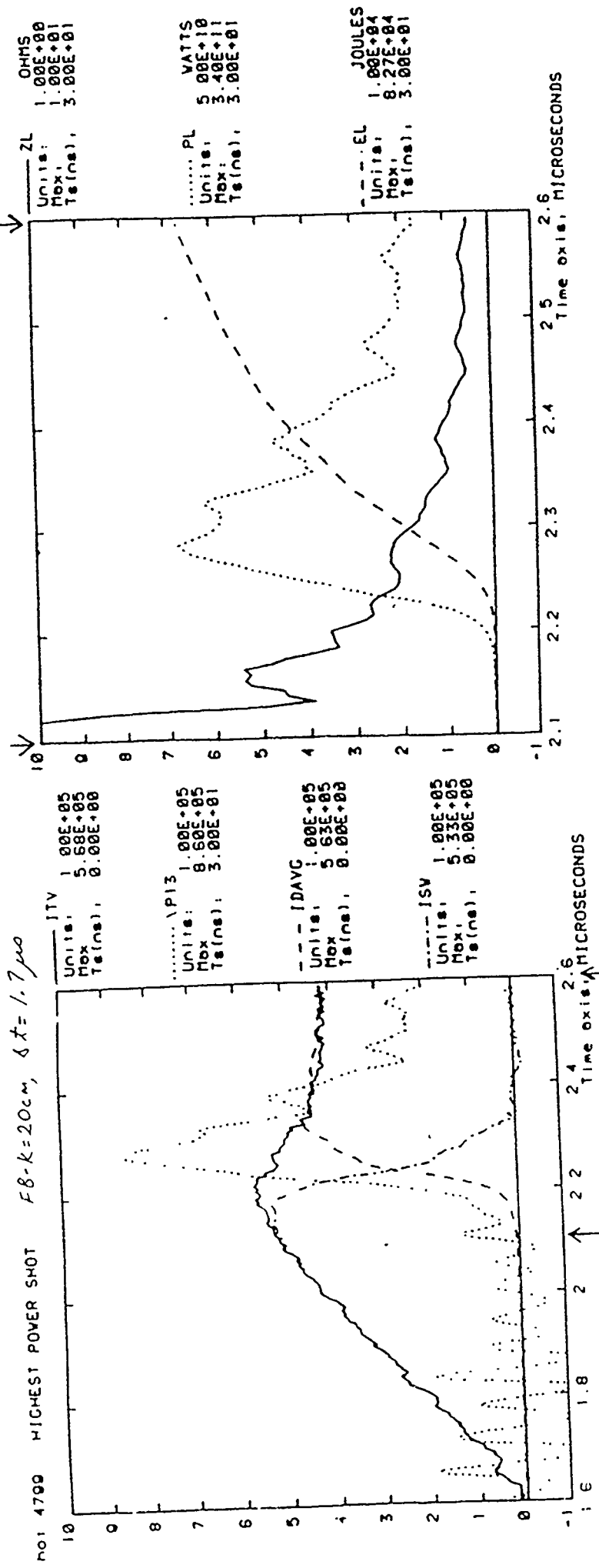
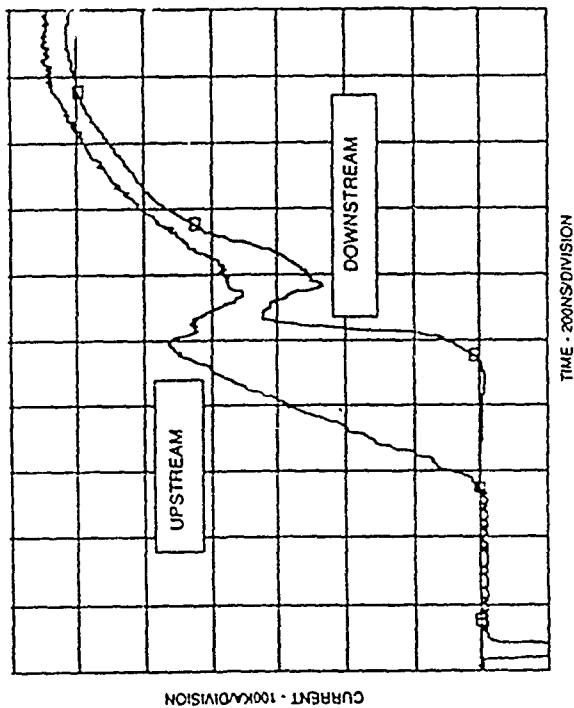


Figure 5. Waveforms for the highest power shot using a diode load. The FB-K distance is 20 cm, the time delay is 1.7 us and the aperture length is 5 cm. The peak load power is 0.34 TW, similar to (but not higher than) the highest powers obtained for previous Eyess shots. The peak load voltage is 0.86 MV, the switch current is 533 kA. These and other parameters are listed for all shots in Table I.

OLM

Typical Current Traces



OLM

Typical Diode Voltage Waveform

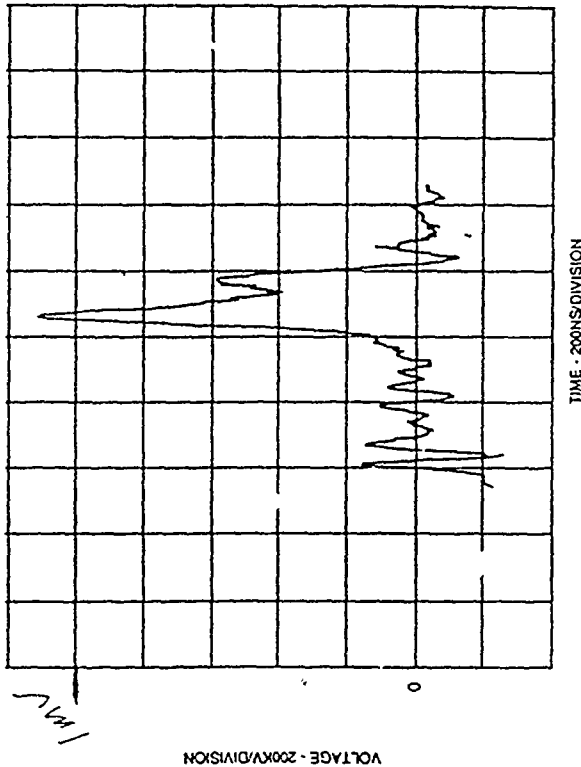


Figure 6. For comparison with Fig. 5, data from an Eyes shot using the 3x8 gap FBs is shown, copied from the presentation given by John Goyer at the Jan 1990 DNA Opening Switch Workshop. The load voltage is higher, and the load current lower, than the best results obtained using the 6x20 gap FBs.

Eyess conduction current
vs. delay time

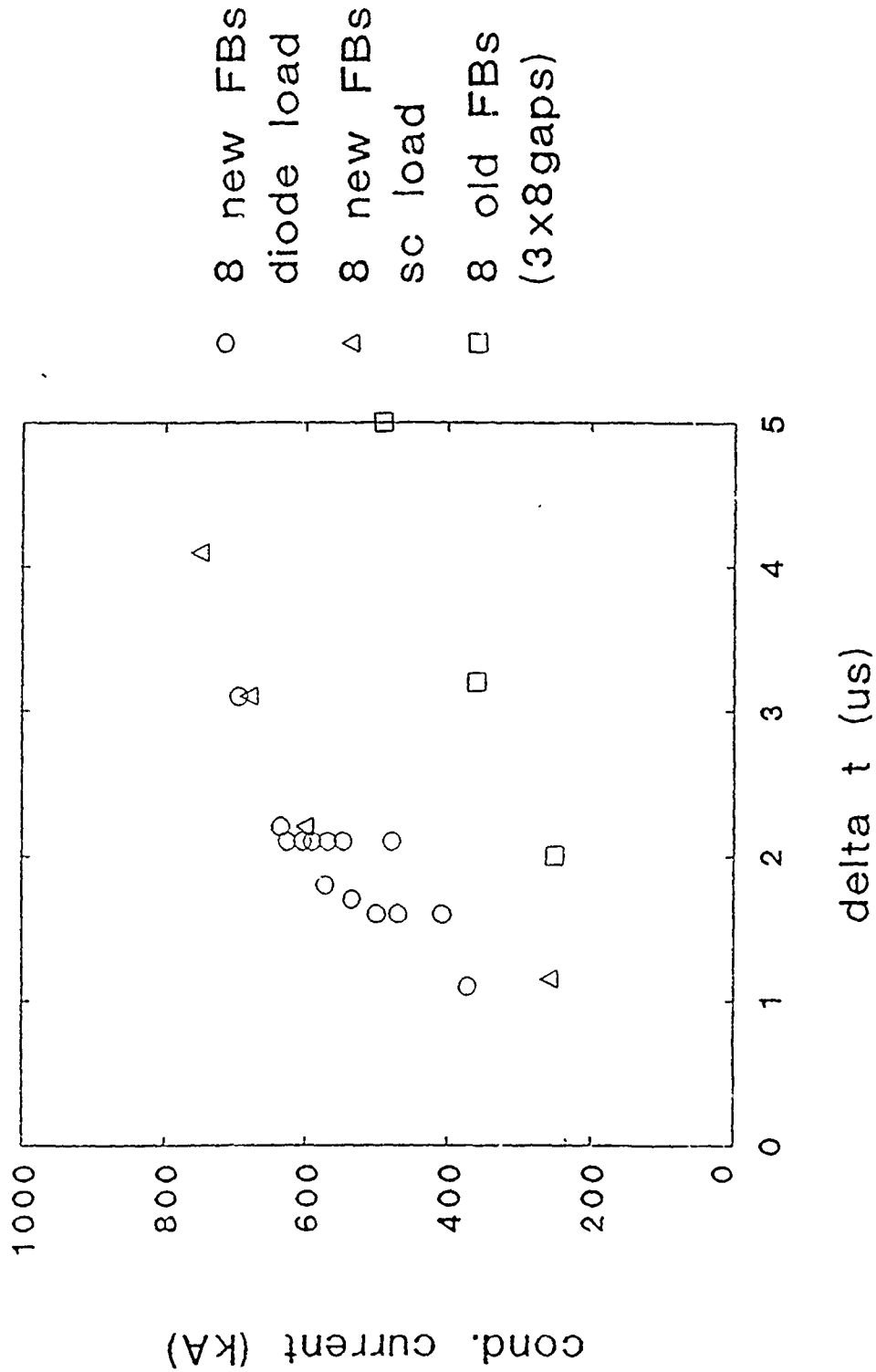


Figure 7. Comparison of peak switch currents for different flashboards. Using the 6x20 gap FBs, the conduction current and time are over 2 times higher than obtained using the 3x8 gap FBs at the same delay (delta t). The conduction current is the same for diode and short circuit loads (within the 10% scatter).

Eyess conduction current
vs. delay time

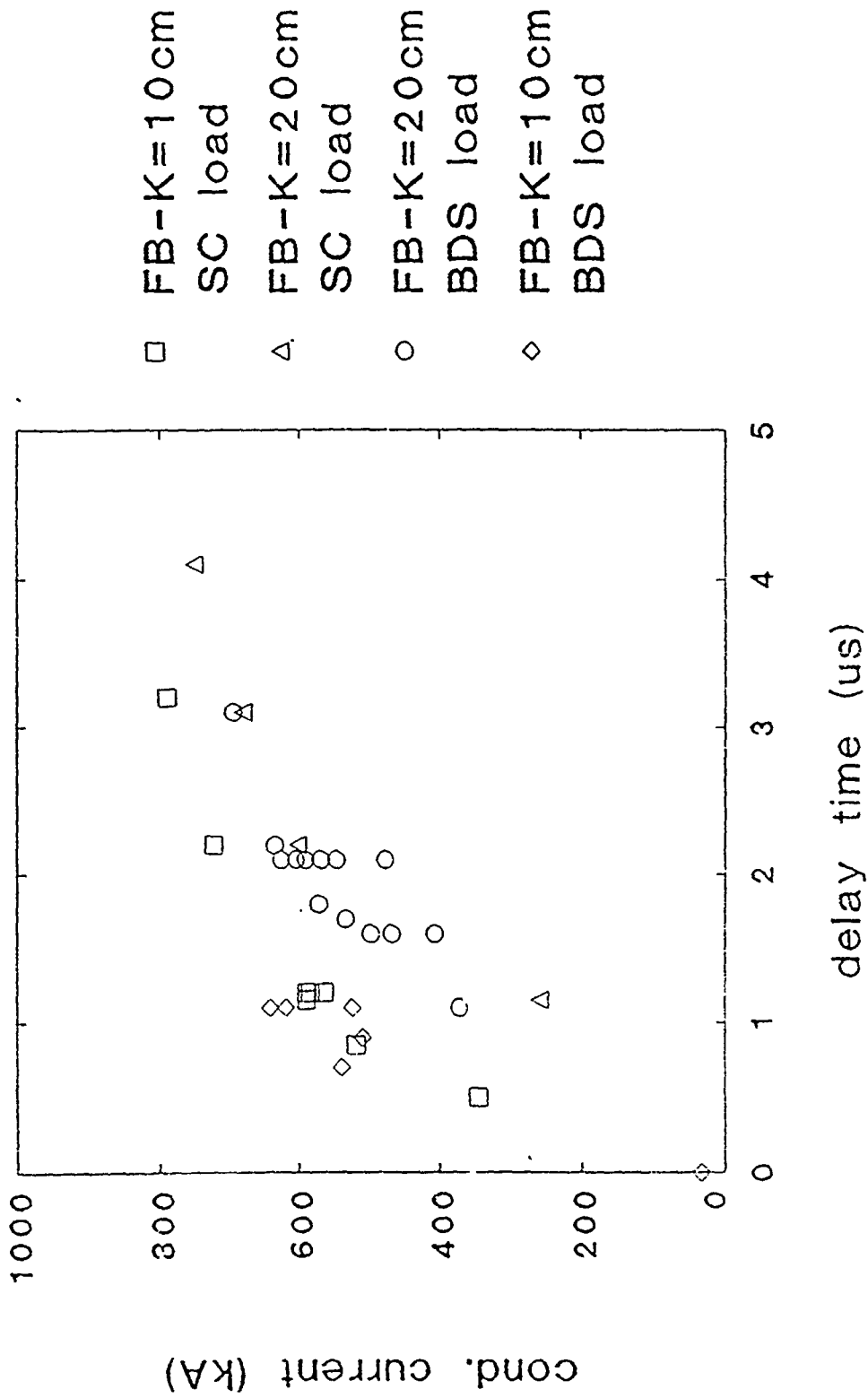


Figure 8. Comparison of conduction current for all shots using the 6x20 gap FBs and an aperture length of 5 cm. A time delay increase of about 0.7 us is required to compensate for the increased FB-K distance of 10 cm.

Eyess conduction current
vs. delay time

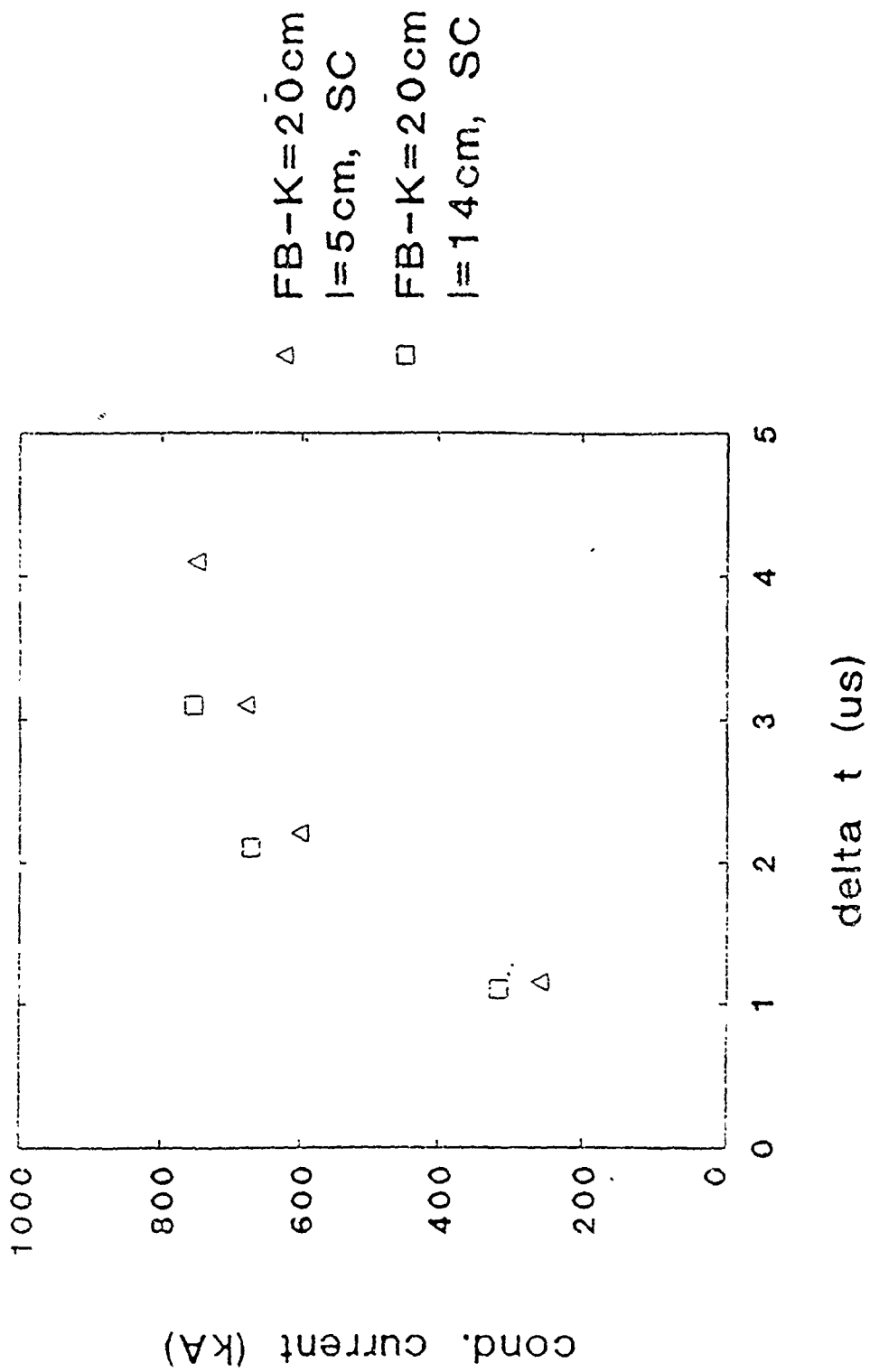


Figure 9. Comparison of conduction current using aperture lengths of 5 and 14 cm, with a FB-K distance of 20 cm and short circuit load. The conduction current (and time) increase by about 10% using the larger aperture length. Increasing the aperture length increases the injected plasma mass by some unknown factor between 1 and 14/5. The scaling of conduction current with length might be determined by a hydro limit, where I is proportional to $l^{1/2}$.

Calculated density
vs. delay time

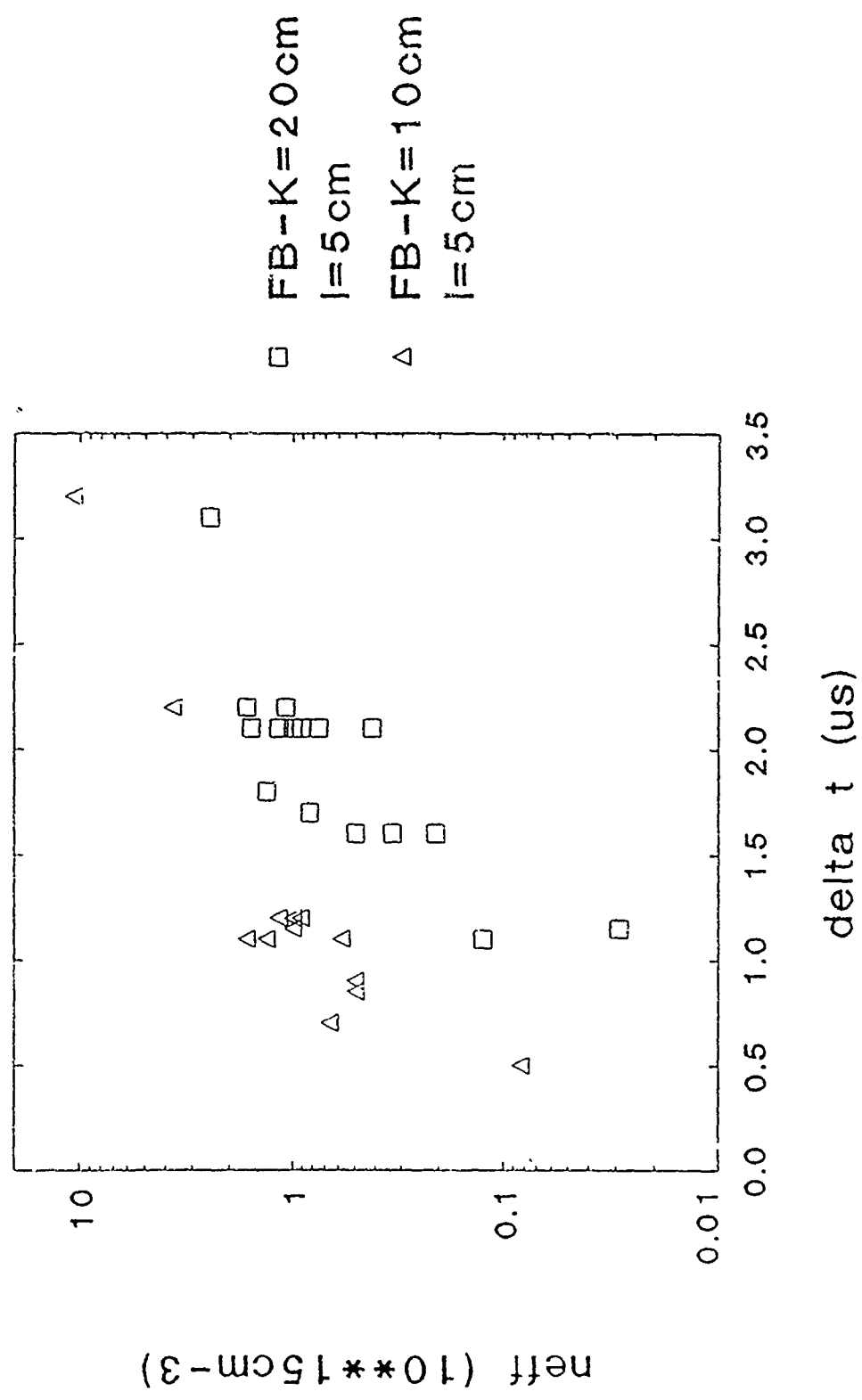


Figure 10. A plasma density is calculated assuming a hydro limit where the center of mass displacement during conduction is limited to $l_0/2$. The estimated density is in the range $n = 10^{14}-10^{16} \text{ cm}^{-3}$.

PULSED POWER PHYSICS BRANCH TECH-NOTE NO. 91-30

TITLE: GAS PUFF PEOS SOURCE ON HAWK

DATE: 10 September 1991

AUTHORS: D. Hinshelwood and R. Fisher

ABSTRACT: The first experiments with alternative PEOS plasma sources on Hawk have been performed. Two varieties of gas puff sources were examined, as a precursor to eventual gas puff/plasma gun sources. The sources used could easily conduct the entire generator pulse. However, switching performance was poor. This may be related to either the use of an initially neutral gas or to the injection geometry. Future experiments to resolve this are underway.

** THIS REPORT REPRESENTS
UNPUBLISHED INTERNAL WORKING
DOCUMENTS AND SHOULD NOT BE
REFERENCED OR DISTRIBUTED

Introduction

In our microsecond conduction time PEOS experiments we have tried many geometry variations in pursuit of optimum switch performance, with some success. For example, reducing the cathode radius and extending the switch-to-load distance has improved switching to diode loads. We are now attempting to further optimize the switch by investigating alternate plasma sources. This note describes the first work in developing a gas puff source. Typically, a puff of gas from a fast valve is ionized, and then current is driven through it on a microsecond timescale. The resulting plasma is $\vec{j} \times \vec{B}$ driven into the PEOS region. Such a source has several potential advantages over the standard flashboard sources. The plasma composition can be selected by simply changing the injected gas. Depending on the exact source design, the exposed hardware may well be more rugged than a flashboard. Higher localized plasma densities may be possible with this type of source. Switch performance with small radius cathodes has been limited by the density available at $\sim 1.5 \mu\text{s}$ delay times. At longer delays, performance degrades, possibly because the plasma is no longer localized. Finally, improved performance with gas puff sources has been observed by Krasik, et al, on the Double generator in Tomsk, RF, USSR.

In the present experiment, neutral gas was injected into the PEOS region, without any preionization or magnetic acceleration. The resulting switch performance was poor, but large currents could be conducted and the results give optimism for future gas puff plasma sources. Such sources are being designed presently.

Experiment

Details of the two variations studied are shown in Fig. 1. Gas was injected from the cathode toward the anode. This was done for two reasons: the manifold connections became much simpler, and gas which had crossed the electrode gap would leave the system, rather than stagnate against the cathode. Since diode loads were used, the gas had to be supplied through the machine and a transit time isolator was constructed for this purpose. This consists of about 7 turns of 3/4 in. copper refrigeration tubing, at roughly 30 cm diam and 3 cm interturn spacing. The calculated inductance was $10 \mu\text{H}$. The isolator contains 3, RG-223 cables and a line of poly gas tubing. No problems have been observed after hundreds of subsequent shots. One of our standard solenoid valves, originally developed by PI, was located in the cathode. It was driven by a 600 V, $1000 \mu\text{F}$ capacitor. The valve was fired several times after a new gas was used to clear the line.

In the first arrangement, shown at the top of Fig. 1, gas was supplied by six cylindrical brass nozzles. The exit diameter was 1 cm and throat diameters of 1.1, 2.2, and 4.5 mm were used on different shots. In the second arrangement, gas was supplied by a single radial nozzle. Four rods held the two cathode halves together. The exit aperture was 34 cm in circumference and 1.3 cm long. The throat was 3 cm in circumference. An adjusting screw controlled the throat length; it was set to 3 mm for these shots.

The cathode radius was 5.4 cm and the radial gap in the switch region was 1.7 cm for most shots. The radial gap outside of the switch region was 3.2 cm. The load was located 25 cm beyond the nozzle(s). For most shots, the anode rods in the switch region were surrounded by 50% transparent screen.

Gas characterization

A modified Penning gauge was used to characterize the initial gas distribution. The tube was placed in the chamber at various locations. The recorder output of a modified controller, with a larger capacitor, was monitored. The large capacitor was necessary to obtain fast time response: without it the signal is disrupted by fast spikes. Typical results are shown in Fig. 2. The top graph shows signals from the first nozzle configuration. The response of the Penning tube saturates at a few microns ($\sim 10^{14} \text{cm}^{-3}$), so that the chief utility of this tube is in showing where the gas is not. The solid curve in the graph was obtained with the tube located at the anode rods, immediately across from one of the nozzles. For the second curve, the tube was located at the anode, but azimuthally in between nozzles. In the last case the tube was located at the load. The initial baselines reflect the initial background pressure. The final saturated amplitude varied also and is probably not significant. Shots were typically fired at $t=0$ on this graph. The key point here is that at this time there is no gas at the load. Comparison of the other two curves indicates that the gas is well localized near the nozzles at this time.

The bottom graph shows data from the second nozzle, with the tube located across from the nozzle and at the load. Again, the gas is well localized at the time the generator is fired.

Results

On most shots, three flashboards were fired $1 \mu\text{s}$ before the generator to preionize the gas. The gas source conducted sufficient current, as shown in the top graph in

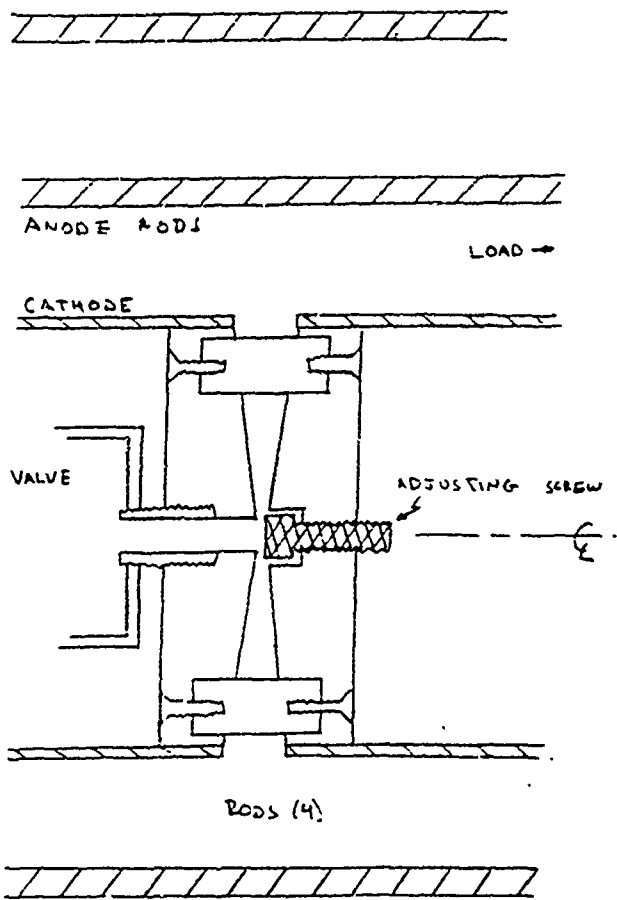
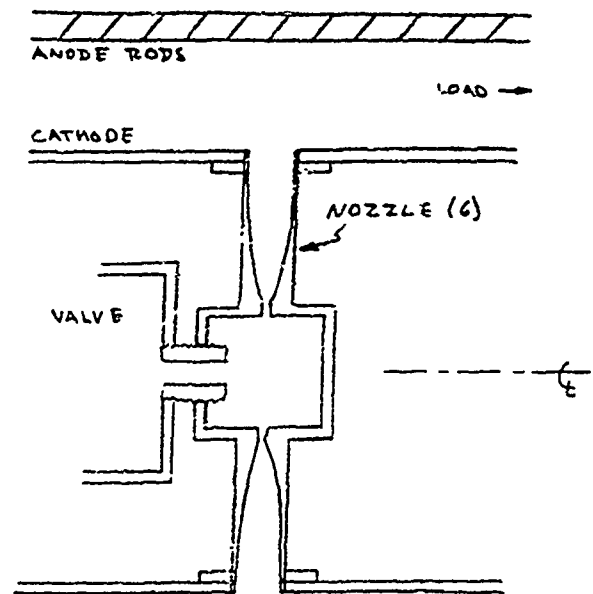
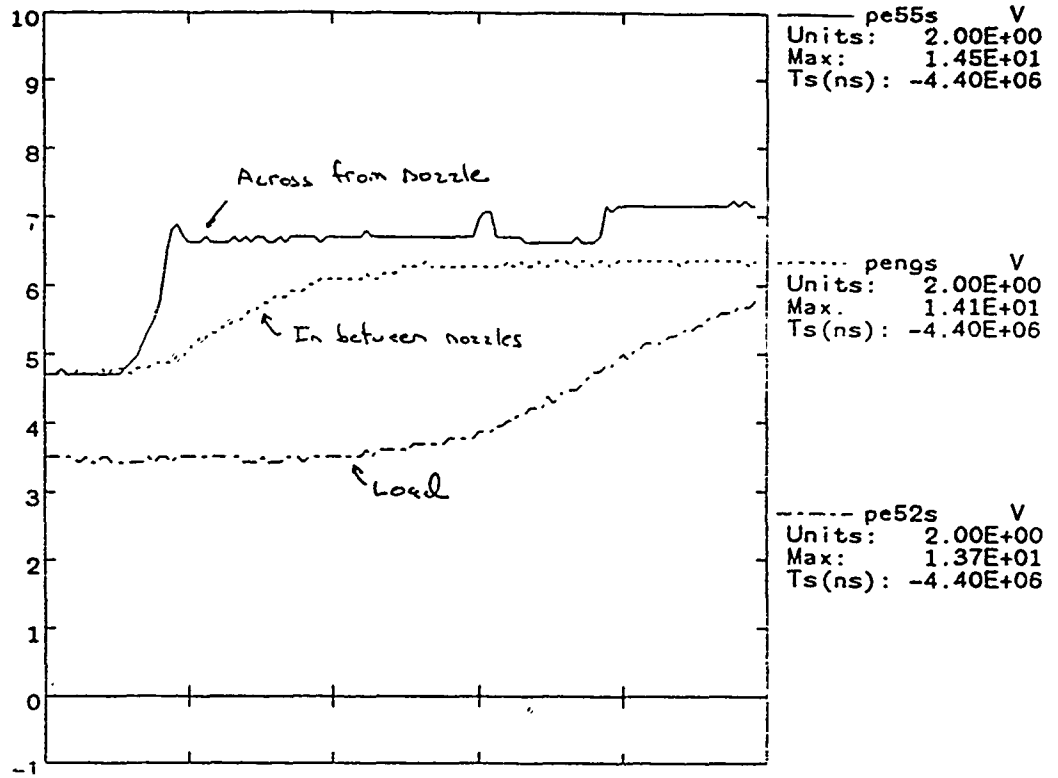


Fig. 1: Nozzle details: (The electrode gap is not to scale.) (top) Multiple nozzles. (bottom) Single radial nozzle.

Shot 0t54



Shot 0t60

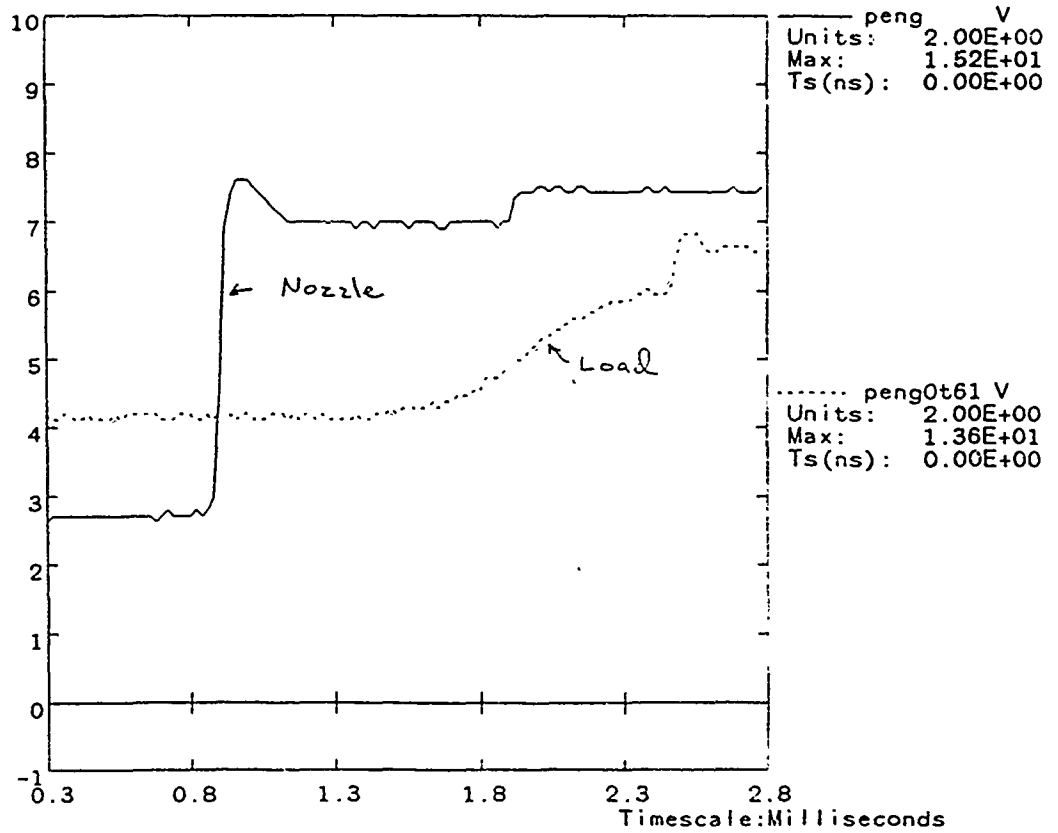


Fig. 2: Characterization of the initial gas distribution using a Penning gauge.

Fig. 3. In this case a short circuit load was used, and load currents are compared for shots with and without the gas puff. With flashboards alone only a tiny current is conducted before the switch opens. Later in time the switch begins to re-close and the re-opens. This is most likely due to a further inflow of flashboard plasma. With the puff added, the switch opens at 800 ns after conducting 600 kA. The current transfer is good, but the switching is noticeably worse than usual. On this shot, He at 50 PSIG back pressure was used.

The conduction time could be controlled by varying either the valve back pressure or the time delay, as shown in the bottom of Fig. 3 and the top of Fig. 4. Indeed, it was possible to conduct the entire generator current. These and all subsequent shots had nominal diode loads. The shots in Fig. 3 were taken with He gas. For all delays and back pressures used, current transfer was extremely poor. In addition, no resistive load voltage was observed. Next, Ar was tried. The shots in Fig. 4 used Ar, and the results were little better than with He. Load voltage was observed only for short conduction times, and even then the results were poor. Removing the screen behind the anode rods had no effect. The best load coupling obtained is shown at the bottom of Fig. 4. The diode vacuum gap was 2.1 cm, so the observed 2Ω impedance indicates the presence of plasma in the diode.

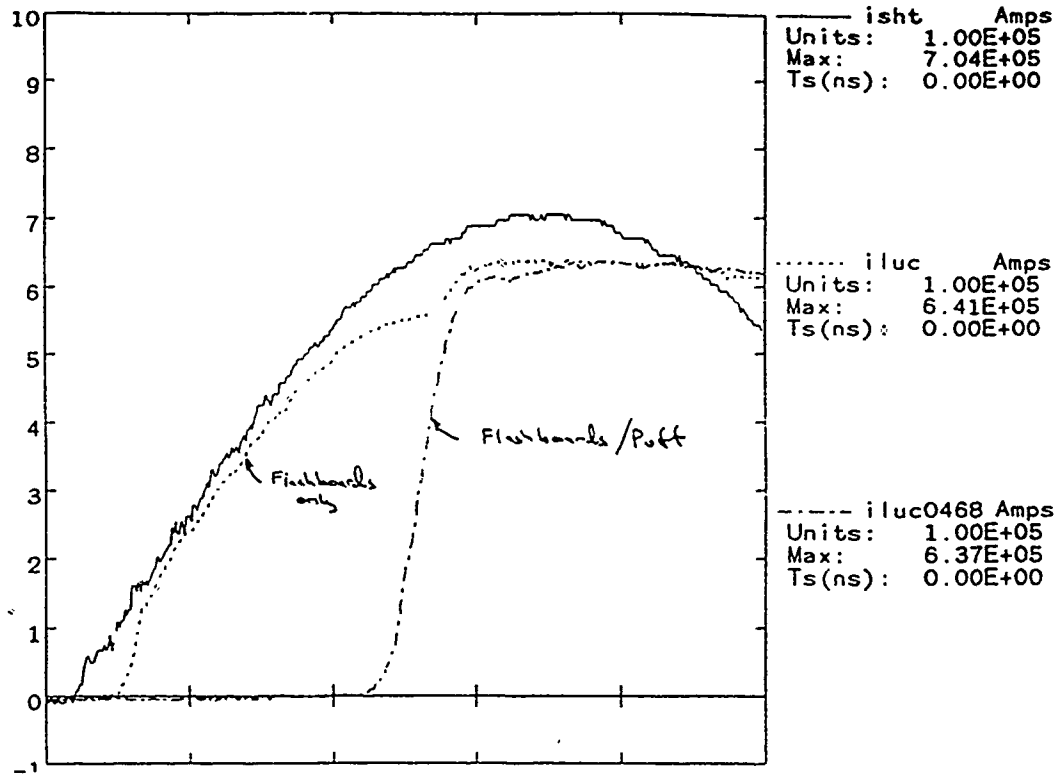
Results with the second nozzle were even worse. Typical data are shown in the top graph of Fig. 5. On this shot, no flashboards were used. Several shots without flashboards were taken during this experiment, and the results were similar to those with boards, so the boards were probably not necessary. This graph also shows the signal from a Faraday cup located in the anode at the load, looking back toward the switch.

At the end of the experiment three shots were taken with a 3.2 cm radial gap in the switch region. Current transfer was much better than with the smaller gap, and on one shot full transfer was observed, as shown in the bottom graph in Fig. 5. However, the resistive load voltage was still negligible. On the shot shown, no flashboards were used, and the gas is seen not to conduct at first. This was the only shot where such behavior was observed.

Summary

The poor performance of this source has two causes: current loss in the switch region resulting from an insufficient gap, and zero load impedance, evidently from plasma in the load region. Increasing the switch gap reduced the first problem and

Shot 0467



Shot 0478

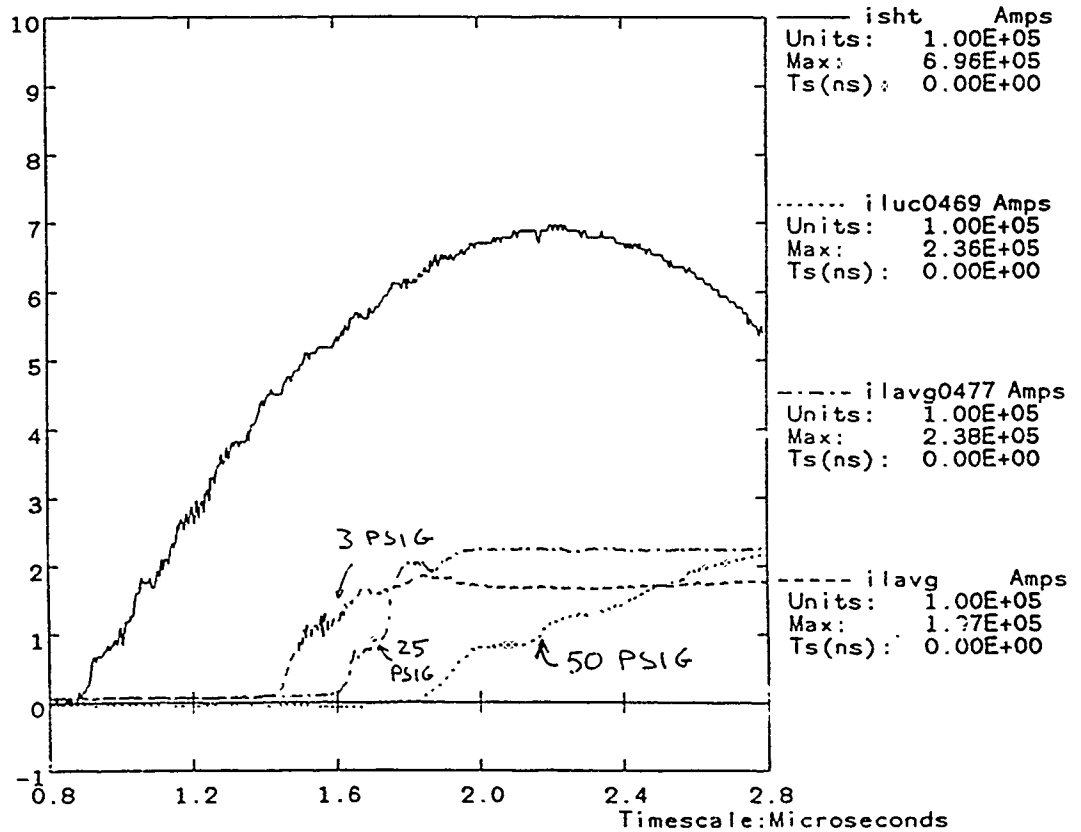
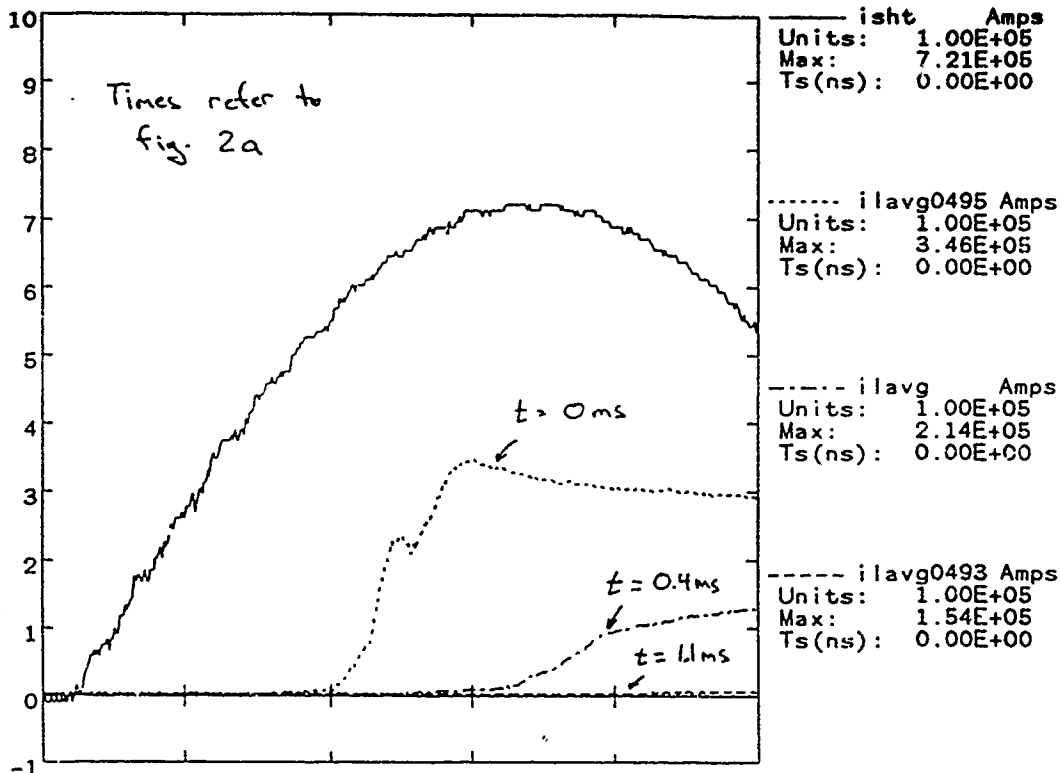


Fig. 3: Results with short circuit (top) and diode (bottom) loads. The gas was He in these shots.

Shot 0494



Shot 0500

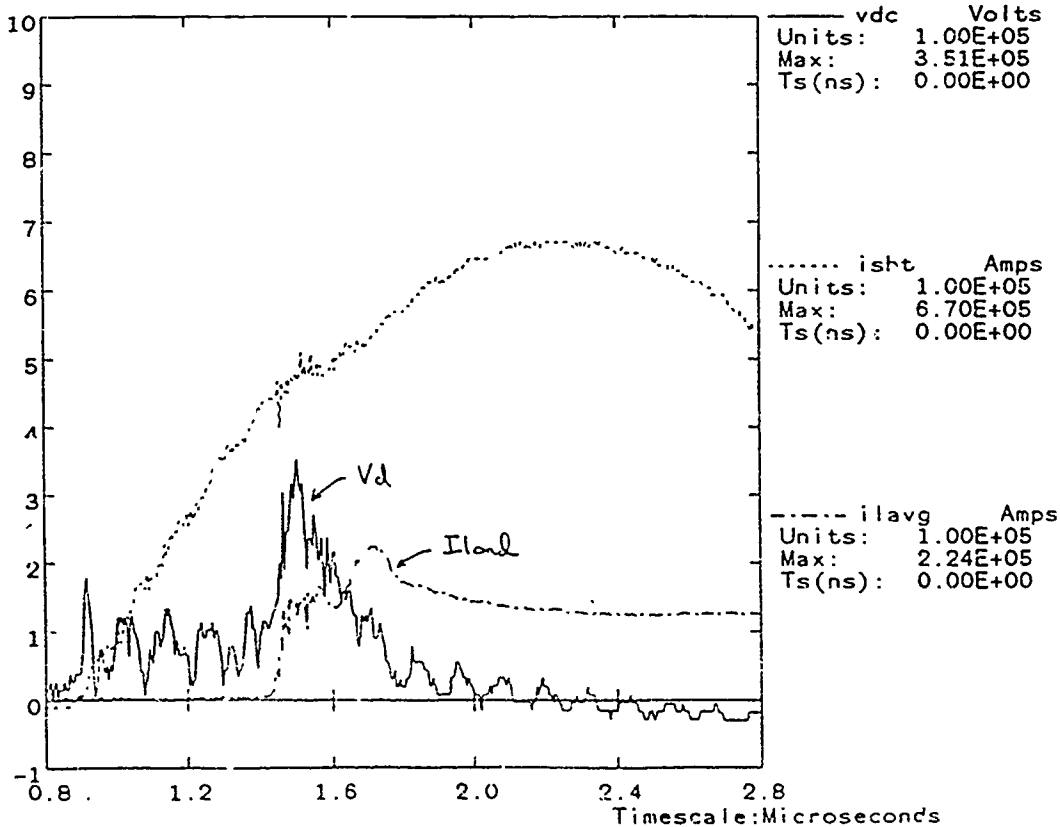
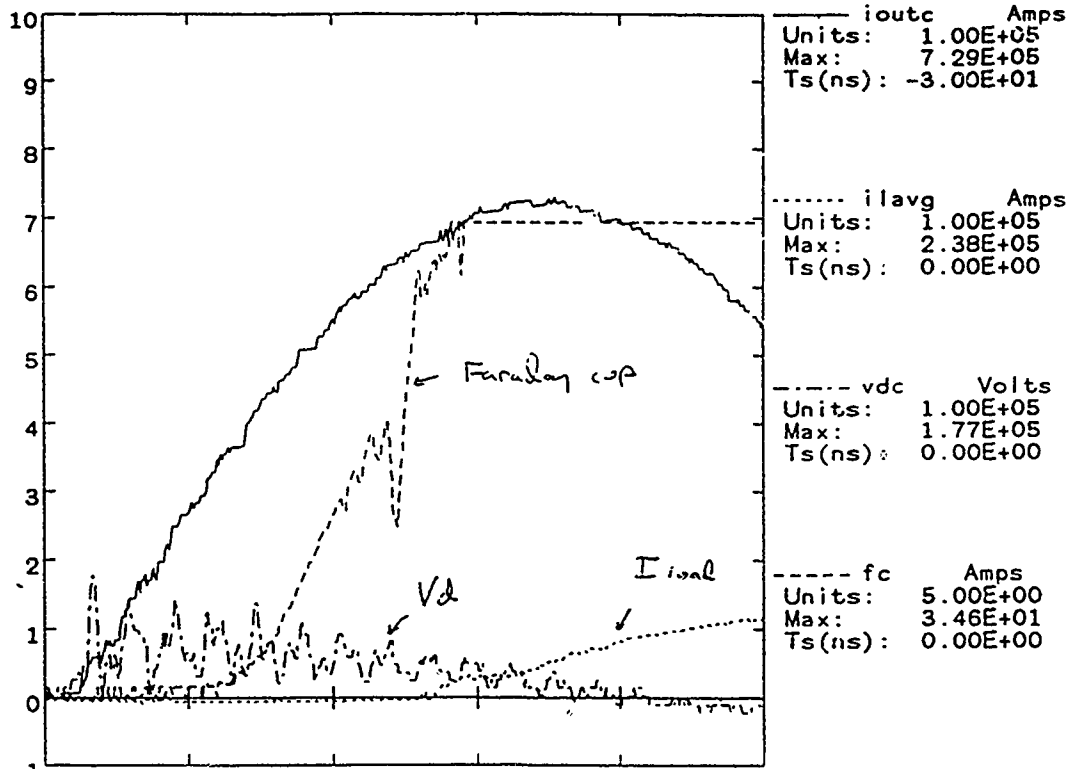


Fig. 4: (top) Results with Ar gas at different delays. (bottom) The best load results observed in this work. This shot had Ar at 50 PSIG back pressure.

Shot 0545



Shot 0550

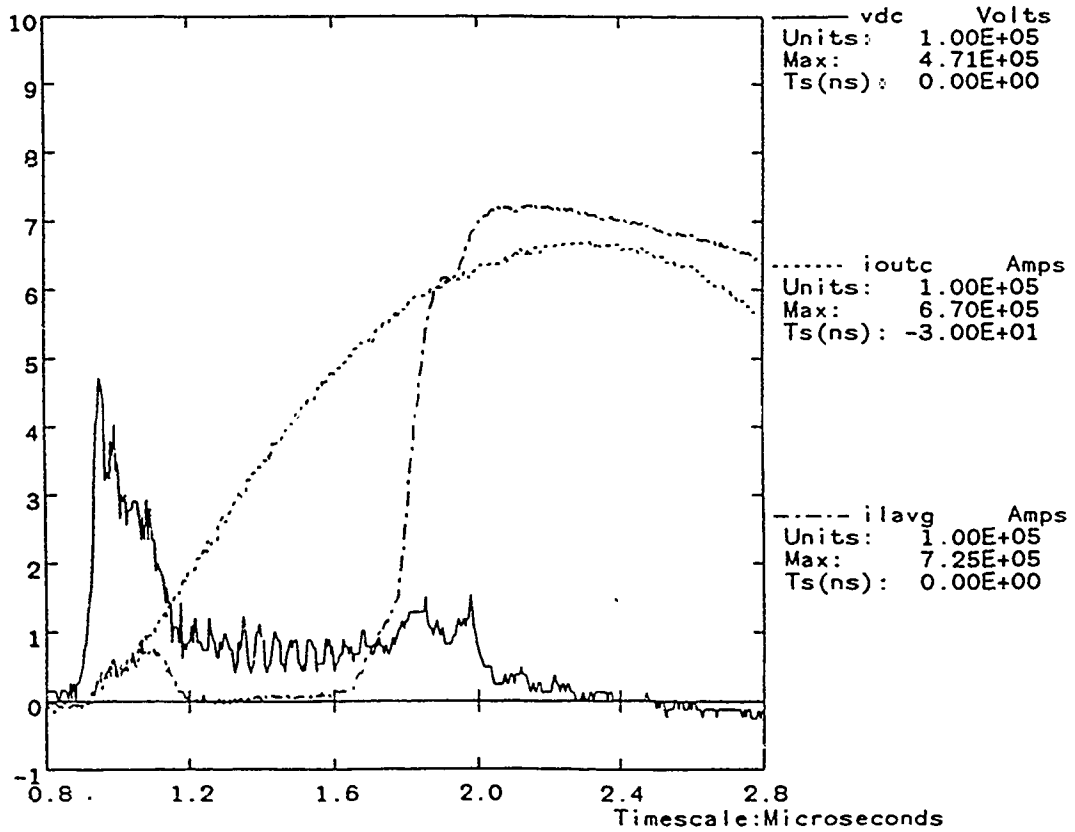


Fig. 5: (top) Typical results with the second nozzle, using Ar at 50 PSIG. (bottom) Results with an increased radial gap, also with the second nozzle and Ar at 50 PSIG.

in principle, a longer switch-to-load distance could solve the second. However, these problems did not occur, or were not as serious, with flashboards. The encouraging feature is that large currents, even the entire generator pulse, could be conducted with this source. The reason(s) for degraded switching with this source are not obvious because it differed from the flashboard source in three ways: the gas is initially neutral, the spatial distribution is different, and injection occurs from the cathode with negligible directed velocity. One possible explanation for the larger required radial gap might be that locating the nozzle exit right at the cathode produces a large density gradient across the radial gap, so that in order to have sufficient plasma at the anode, the density at the cathode is so large that the effective cathode radius is increased significantly. The increased plasma density in the load, as indicated by the low or zero load impedance, is more difficult to explain since the initial distribution seems to be as, or more localized than with flashboards. Future experiments, with different injection geometries and with driving currents, should clarify these issues, hopefully leading to an improved plasma source.

We are continuing gas source development by evaluating automobile fuel injectors rugged and inexpensive replacements for the solenoid valve. We will soon look at Marshall gun and eddy current driven injection schemes.

Conclusion

The first experiments with alternative plasma sources have been performed. The gas puff sources used led to poor switch performance. However, because of the large conduction currents possible, gas puff/plasma gun sources appear attractive for improving both switch performance and engineering reliability on Decade.

PULSED POWER PHYSICS TECHNOTE NO. 93-06

TITLE: INITIAL CABLE GUN POS EXPERIMENTS ON HAWK

AUTHORS: B. Weber, D. Hinshelwood, R. Commisso

DATE: 29 March 1993

ABSTRACT: Experiments have begun on Hawk using the cable gun plasma sources developed for use on DPM1 at PI. These plasma sources have resulted in impressive POS performance (high voltage and low jitter) on DPM1, and have been chosen as the probable plasma source for the Decade machine. The experimental objective on Hawk is to discover how the cable-gun POS operates, and how it is different from the flashboard POS. It is known, for example, that the cable gun plasma is about ten times slower than the flashboard plasma. This property may have beneficial effects, including: less secondary plasma at surfaces, reduced gap closure rate, and less plasma spreading away from the injection region.

This technote describes results using short circuit loads in the "standard" configuration ($r = 5$ cm, $l = 8$ cm, switch-load distance = 26 cm) with a He-Ne interferometer to measure the line-integrated electron density during shots. The density is measured at different radii for shots with conduction times of about 0.95 μ s. At all radii, the density increases during conduction above the level that would be measured by firing the sources alone. This is in contrast to the flashboard case, where the density follows the source-only density for the first part of the conduction phase, then decreases prior to opening (except near the conductors). The measured density is non-zero at all radii during opening; the trend suggests that opening actually occurs near the center conductor, closer than the 3 mm displacement of the laser beam. This is consistent with the expected MHD distortion of the approximately constant (initial) radial plasma distribution. The conduction time is longer for a given electron density than for flashboards, suggesting that the effective $M/Z = 10-14$, about a factor of two higher than for the flashboard plasma.

THIS REPORT REPRESENTS
UNPUBLISHED INTERNAL
WORKING DOCUMENTS AND
SHOULD NOT BE REFERENCED
OR DISTRIBUTED

I. Experimental Setup

The experimental arrangement on Hawk is shown in Fig. 1. The cable guns are constructed from 1/4" diam semi-rigid coax by drilling a 60° conical hole at the end. The gun is powered by a 0.6 μ F capacitor charged to 25 kV (the same as is typically used for a flashboard). The plasma composition may be somewhat different from flashboards because the flashover surface is Teflon (C_2F_4) instead of carbon-coated Kapton ($C_{22}H_{10}N_2O_5$). Twelve guns are arranged at the distance shown, 9 cm from the surface of the 5-cm radius center conductor. The plasma flows through the transparent rod region. The 8-cm long rods are located azimuthally between guns. The POS configuration is the same as for previous flashboard POS experiments using this "standard" configuration; that is, $l = 8$ cm, $r = 5$ cm, $\Delta r = 2$ cm in the plasma injection region, and the switch-load distance is 26 cm.

The He-Ne laser beam is indicated by the heavy dashed line in Fig. 1. The radial location of the beam can be changed shot to shot. The beam is located azimuthally under a gun. The line-integrated electron density is measured directly by this technique, and converted to an average density by dividing by the plasma injection length, 8 cm. For these experiments, the entire laser beam was recorded at the detector. This limits the spatial resolution of the measurement to the beam diameter in the plasma region, about 4-5 mm; This approach resulted in an excellent signal-to-noise ratio. The uncertainty in the average density is about 1×10^{14} cm^{-3} . A short circuit load is used to simplify the density measurement and to reduce debris and x rays.

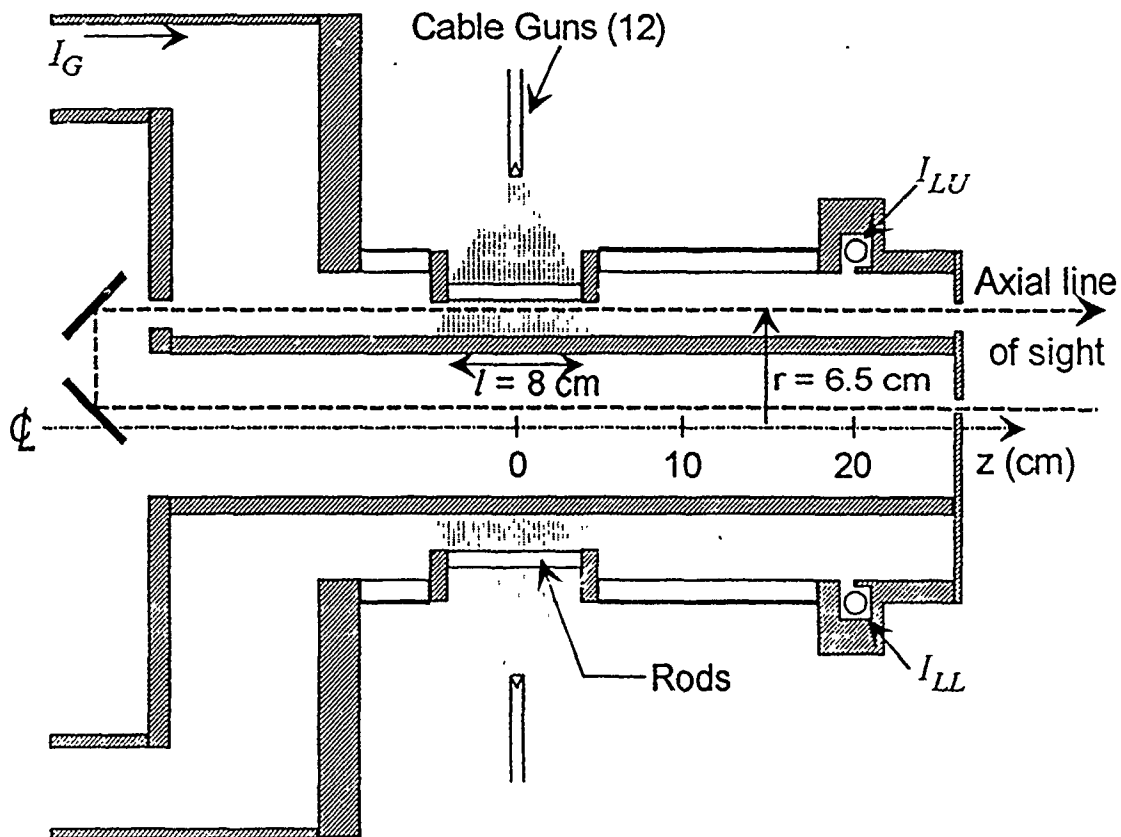


Figure 1. Cable Gun POS on Hawk

II. Radial Density Scan

POS shots were taken for the case of 0.95 μs conduction time. This required a delay time between firing the guns and firing Hawk of 3.7 μs . For comparison, the same conduction time using 18 flashboards 12.5 cm from the center conductor requires only a 1.5 μs time delay. The difference in required delay times is primarily the result of different flow velocities, and secondarily the result of different secondary plasma generation at the conductors. This conduction time was chosen for comparison with our published density data using flashboards (Phys. Rev. Lett. 68, 3567 (1992)), and because this conduction time results in maximum power with diode loads using flashboards.

Data taken at six different radial locations of the laser beam are shown in Fig. 2. For each beam location, the generator and load currents are plotted along with the average electron density measured during the shot and before the shot firing the guns alone. The radial location of the beam center is indicated in the upper left corner of each plot. The conduction time for all six shots is in the 0.9-0.95 μs range. The initial density is within 10% of $1 \times 10^{15} \text{ cm}^{-3}$ for all six shots. The load currents rise in about 50 ns to the full generator current. This set of shots is assumed to be reproducible enough to estimate the density distribution for comparison with the flashboard case.

At all six locations, the density increases during conduction. This differs from the flashboard case, where the density follows the flashboard-only density for the first part of the conduction phase, then decreases prior to opening at most locations in the cross section. The density increase with the cable guns could result from several sources. During conduction, $J \times B$ forces can move plasma in the radial direction, increasing the line-density at a given radius and decreasing it at others. Plasmas can evolve from the surfaces during conduction and increase the local density, and eventually contribute to the density in regions away from the conductors. Another possibility is ionization of plasma ions and neutrals during conduction. The density increase during conduction is a major difference between these cable gun experiments and flashboard experiments, and should be investigated further with more experiments and theoretical calculations.

The density decreases prior to opening beginning near the center conductor and propagating toward the outer conductor. Density cross plots for selected times are shown in Fig. 3. During the rise of the load current, the density is smallest close to the center conductor, but is still finite (a few times 10^{14} cm^{-3}). The density reaches zero (less than 10^{14} cm^{-3}) at the 6 mm, 9 mm, and 12 mm locations, but well after switching. (For the corresponding flashboard case, the density decreased essentially to zero at the 15 mm location at the onset of opening, and the density remained negligible at this location until 300 ns after opening.) For the cable guns, opening may begin close to the center conductor, assuming a vacuum gap is needed to explain the observed switching. The interferometer may not reveal a vacuum gap if it is smaller than the beam diameter (4-5 mm) or if it is not parallel to the beam.

The density distribution from the cable guns is relatively constant as a function of r . As current is conducted through this plasma, the magnetic forces will displace plasma near the center conductor farther in the axial direction. The distortion of the plasma would then allow radial magnetic forces to decrease the line density there. Opening could then begin in the rarefied plasma near the center conductor. The flashboard density distribution increases near the center conductor because of the surface interaction with the high velocity plasma. Opening (or at least

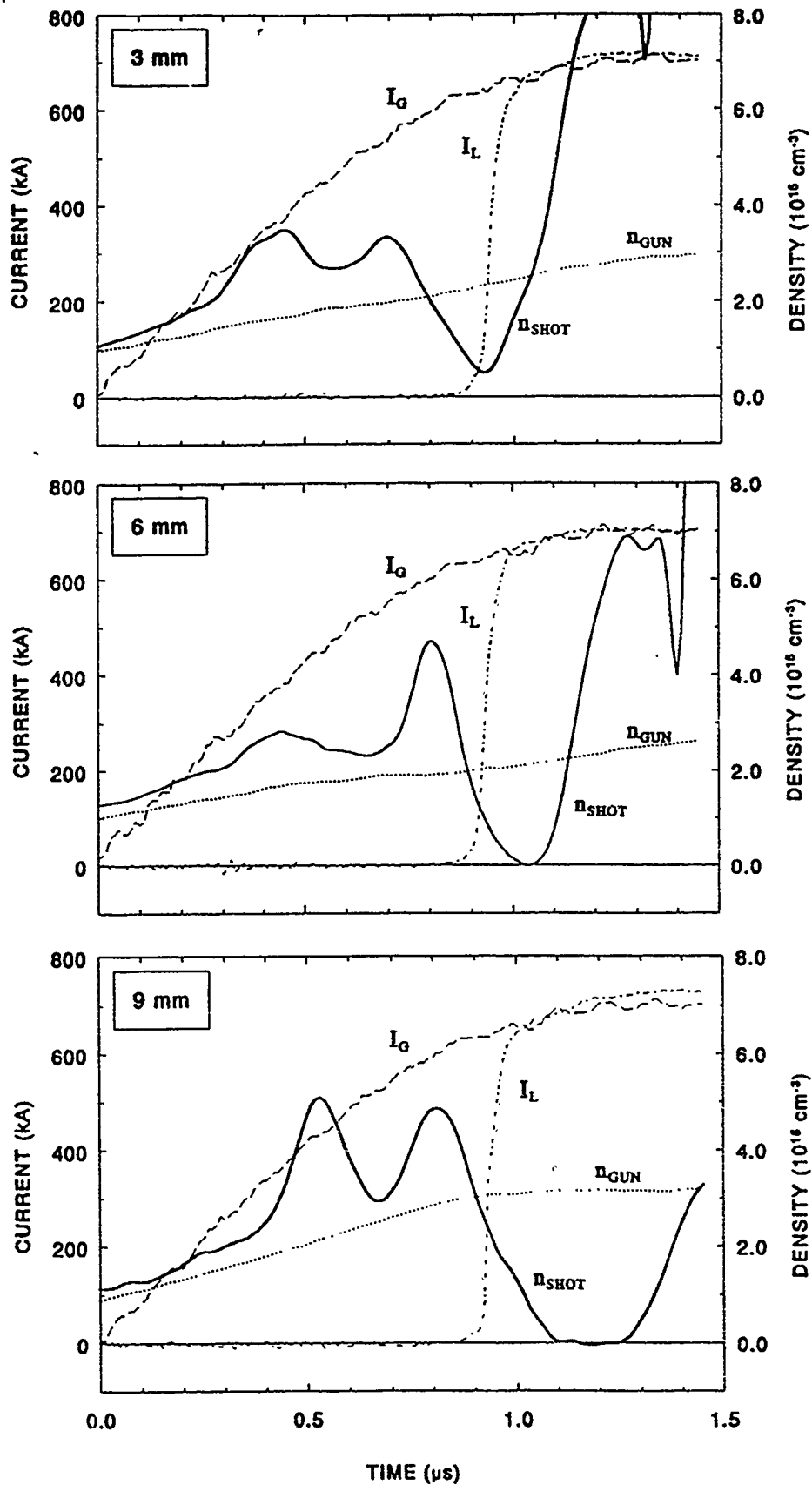


Figure 2 Density and current measurements on Hawk using cable guns.

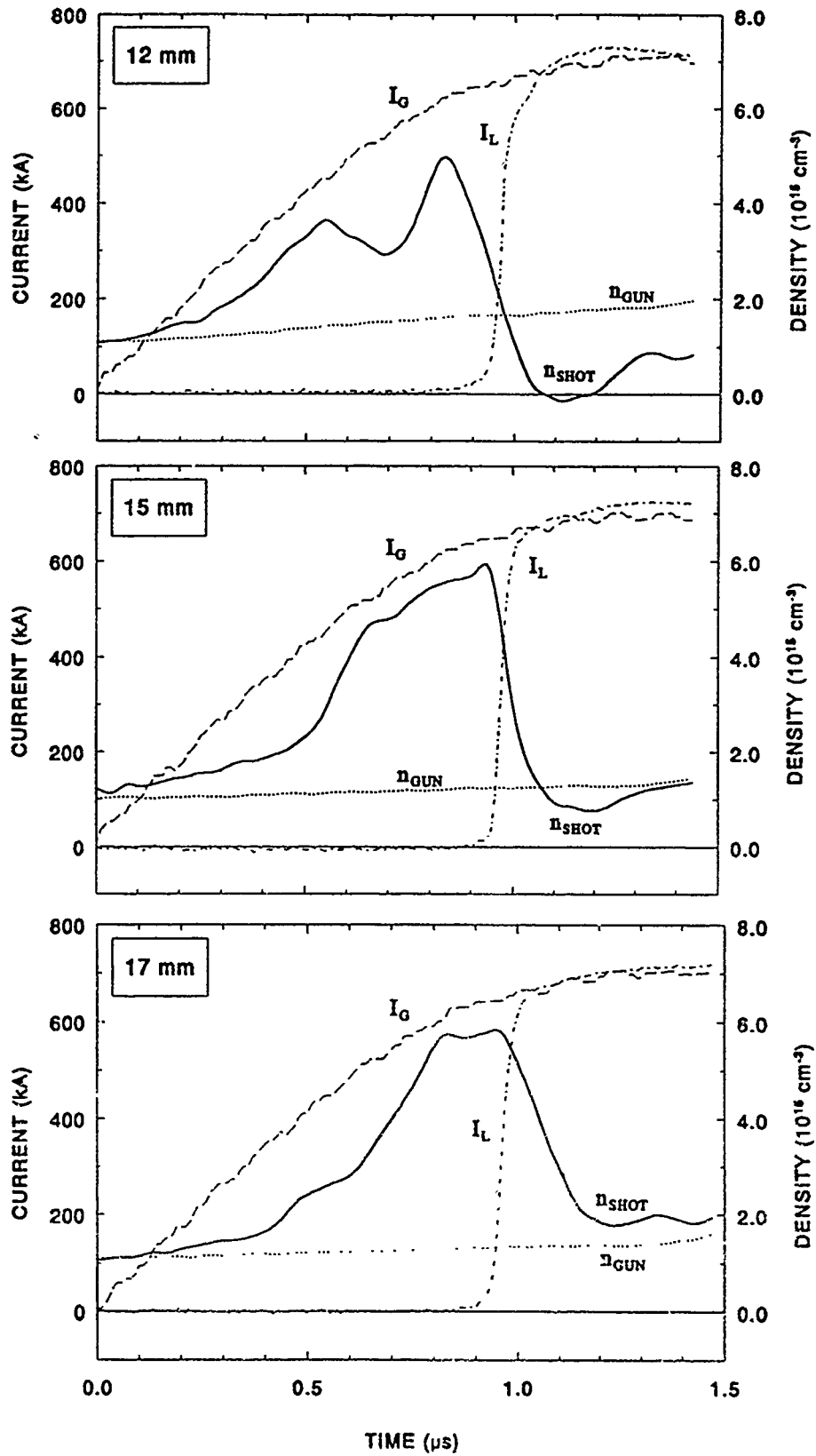


Figure 2 (continued)

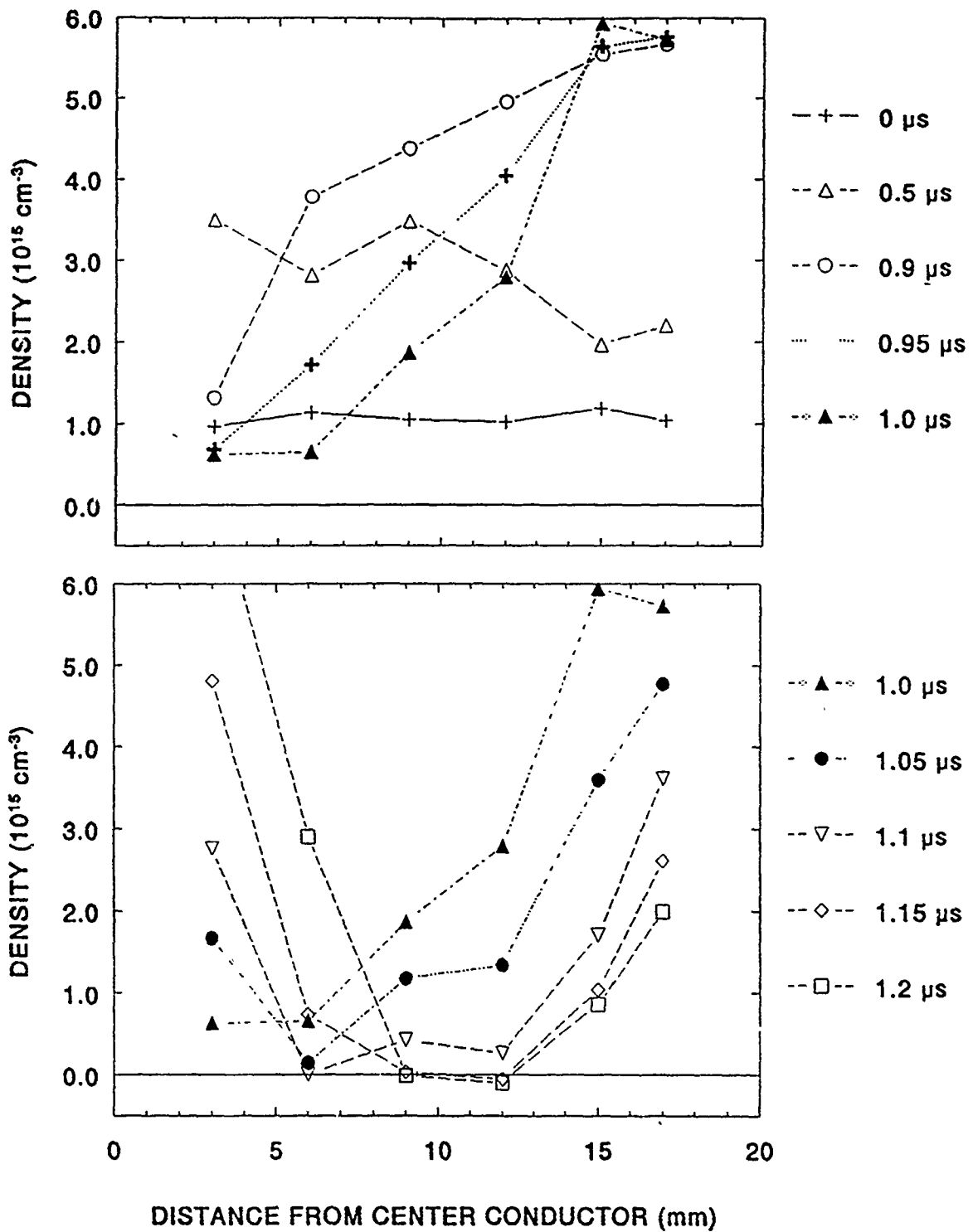


Figure 3. Cross plots of density for selected times: $t = 0 \mu\text{s}$ (start of conduction), $0.5 \mu\text{s}$ (during conduction), $0.9 \mu\text{s}$ (start of opening), $0.95\text{-}1.0 \mu\text{s}$ (during opening) and $1.05\text{-}1.2 \mu\text{s}$ (after opening)

density thinning) occurs 15 mm from the center conductor, in agreement with fluid calculations of the plasma distortion.

III. MHD Scaling

The plasma density required for conduction in this case can be estimated from the data in Fig. 2. Assuming opening begins near the center conductor and that the density increase during conduction contributes to the conduction time, the peak density during conduction at the 3 mm location, $3.5 \times 10^{15} \text{ cm}^{-3}$, will be taken to be "the density" for scaling purposes. The MHD conduction limit asserts that switching begins at the time the plasma center-of-mass is axially displaced by half the switch length (or equivalently, the time for a snowplow to reach the load end of the plasma). This model works remarkably well for Hawk flashboard experiments assuming a C^{++} plasma, for which $M_i/Zm_p = 6$. Applying the same argument to the cable gun data, and using as input the parameters: $r = 5 \text{ cm}$, $l = 8 \text{ cm}$, and $\iint I^2 dt^2 = 3-4 \times 10^{-2} \text{ C}^2$, a value of $M_i/Zm_p = 10-14$ is derived for the cable gun plasma. This is (very indirect) evidence that the cable gun plasma species is different from the flashboard plasma. For example, the cable guns may produce Fluorine (atomic weight 19) ions, more C^+ ions, and fewer protons than flashboards, increasing the effective M_i/Z .

If the cable gun plasma is filling only a fraction of the 8 cm injection aperture, then the calculated M_i/Z would be even greater by the factor $(8 \text{ cm}/l)$. Another source of uncertainty in these estimates is the actual plasma displacement, Δz , during conduction. If the displacement is different from $l/2$, the corresponding value of M_i/Z would change by a factor of $(l/2\Delta z)$.

IV. Conclusions

These initial experiments have shown several differences between flashboard and cable gun POSs that may be important for future work. For the specific case of $\sim 1 \mu\text{s}$ conduction on Hawk, the cable gun POS requires a longer delay time than the flashboard POS, consistent with the slower flow velocity of the cable gun plasma ($2-3 \text{ cm}/\mu\text{s}$ versus $15-30 \text{ cm}/\mu\text{s}$). Density measurements during shots show that the density increases during conduction, very different from the flashboard case. It is unclear what causes the density increase, but it is probably a combination of MHD displacement, plasmas evolving from surfaces, and ionization of the plasma ions and neutrals. During opening, the density is smallest near the center conductor. This is not unexpected based on the relatively constant radial density distribution and an MHD conduction limit. The measured density is finite at all radial locations during opening, possibly because a vacuum gap forms at a location closer to the center conductor, or because the gap is smaller than the beam or not parallel to the beam. In any case, the dynamics of the plasma are notable different from the flashboard case, where opening appears to happen at a large distance from the center conductor, 15 mm for the analogous flashboard case. Applying the MHD conduction limit argument to the cable gun POS, agreement between measurements and the simple theory requires the plasma species to have an M_i/Z value about two times higher than the flashboard plasma. This is indirect evidence that the plasma composition is different for the cable gun plasma, possibly including fewer protons, and more C^+ and F ions. Future experiments will examine

switching into loads and power flow between the POS and load to determine promising POS configurations that will then be examined using interferometry.

PULSED POWER PHYSICS TECHNOTE 93-09

TITLE: INTERFEROMETRIC STUDIES OF GAS GUN PLASMAS

Author: D. Hinshelwood

Date: April 28, 1993

Abstract: This is the first in a series of three technotes describing our work with gas guns. This note presents results from a few brief studies of the mechanical valve and of gas breakdown in the guns, and measurements of the electron density, obtained with our six-chord interferometer, both for the guns alone and during short circuit shots. The gas guns are seen to produce radial density profiles that range from similar to, to very different from, those produced by flashboard sources. Data taken during machine shots are consistent, both qualitatively and quantitatively, with what we would expect based on our MHD picture of conduction current limitation. Reproducibility is seen to be poor, and possible ways to improve it are discussed. The results of this work suggest improved ways of fielding these sources in the future. While further investigation of these sources is likely a low priority, with some changes in the source arrangement, these sources have the potential to allow further relevant physics experiments

INTRODUCTION

This is the first in a series of three technotes describing our work on gas gun plasma sources. Results from a few brief studies, of the mechanical valve and of gas breakdown in the guns, are presented first. Then, measurements of the electron density, obtained with our six-chord interferometer, both for the guns alone and during short circuit shots, are presented. The gas guns are seen to produce radial density profiles that range from similar to, to very different from, those produced by flashboard sources. Data taken during machine shots are compared both qualitatively and quantitatively with what we would expect based on our MHD picture of conduction current limitation. Reproducibility, and possible ways to improve it, is discussed. The results of this work suggest improved ways of fielding these sources in the future. Two companion technotes, presently under preparation, present the results of initial interferometric, test stand studies of the guns (Jim Kellogg) and the results of about 80 shots with diode loads (Phil Goodrich). So far, the use of gas gun plasma sources has not improved operation of the POS on Hawk. However, some useful physics information has been obtained and with some changes in the source arrangement, these sources have the potential to allow further, relevant physics experiments

GAS GUN DESIGN AND TESTING

A machine drawing of the gas gun we developed is shown at the top of Fig. 1. The gun geometry is based on the guns first used by Yasha Krasik in his work at Tomsk. Here, however, an automobile fuel injector is used as the mechanical valve. We learned of this technique from a paper by Michael Brown of Cal Tech (JAP 69, 6302 [1991]). Each valve is driven by a 200 μF , SCR-switched pulser built by Jim. For most of this work the pulsers were charged to 170 V. The plasma discharge itself is driven by two of our standard doghouses, with one, type-C cable connected to each of the six capacitors. Typically, the valve is pulsed several hundred microseconds before the doghouses are fired. Further details will be presented in Jim's note; in general the insulation and inductive isolation worked quite well and the guns were found to be quite reliable from this standpoint.

In the first test of the valves themselves, they were fired in vacuum toward, and at various distances from, a Penning gauge. This gauge can measure pressures up to a few microns ($\sim 10^{14} \text{ cm}^{-3}$) with a response time of about 50 μs , and so is sensitive to the first front of the expanding gas. With 100 V on the pulser and over a range of back pressures of air, the gas front moves at about 0.07 $\text{cm}/\mu\text{s}$, consistent with the mean thermal velocity of 0.05 $\text{cm}/\mu\text{s}$. Extrapolation of the data shows that the valve begins to open at 325 μs .

Next, mechanical operation of the valve was examined directly. A small sliver of paper was attached to the valve plunger in such a way that the paper blocked a HeNe beam from reaching a photodiode. Retraction of the plunger was measured by the increase in photodiode signal. The backing pressure, pulser voltage, and pulser capacitance were varied. The capacitance was seen to have a negligible effect on the initial signal rise so that similar results would be expected with the 200 μF used in Hawk experiments and the 100 μF used here. Typical data is shown in the center of Fig. 1. (The

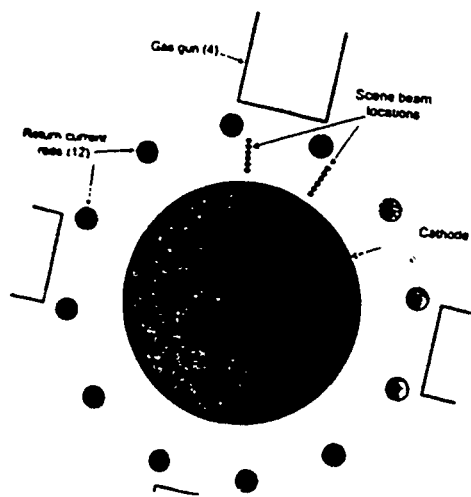
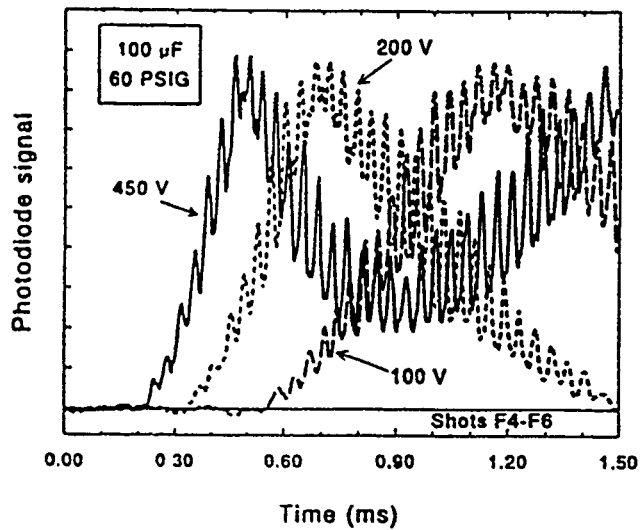
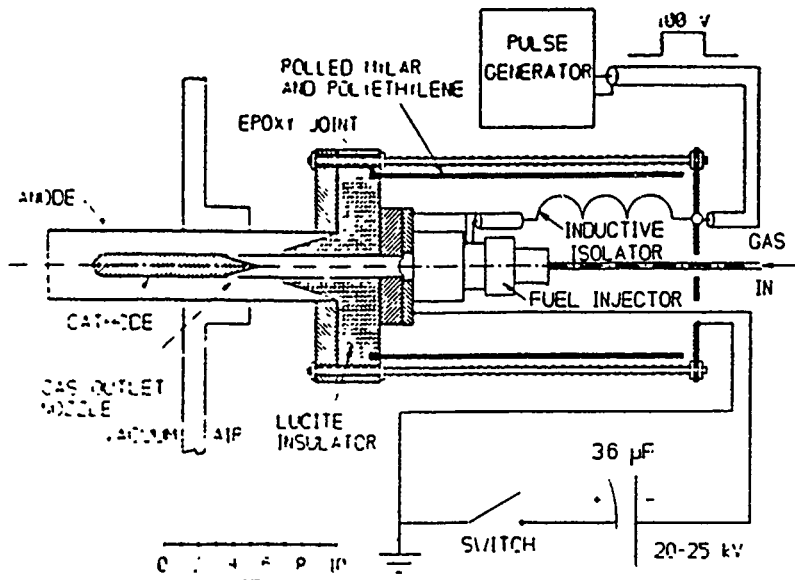


Figure 1: (top) Gas gun schematic; (middle) Measurement of the mechanical valve action; (bottom) Switch and scene beam arrangement.

fast oscillations on the signals do not occur in the absence of backing pressure and thus they are likely caused by a vibration of the plunger.) As the pulser voltage is raised, the valve opens sooner and more quickly. Unfortunately, this test was not set up to record the very first opening of the valve: for example at 100 V the valve begins to open at 325 μs but the motion is not noticeable here until 525 μs . By extrapolation of this data and that from the Penning measurements, at the 170 V used in the Hawk experiments the valve begins to open at about 250 μs and opens completely at 800 μs . This shows that the valves had only just begun to open at the timings used in the experiments. The limited data taken here show a good reproducibility in the mechanical action of one valve, but valve-to-valve reproducibility was not examined. The data here suggest that in the future the valves should be operated at higher voltages in order to sharpen the opening and hopefully reduce dispersion of gas in the guns prior to the discharge. They should also be operated with lower capacitance: reducing the capacitance does not change the initial rise but greatly reduces the duration of opening and thus reduces the pressure rise in the system after firing the guns.

Breakdown in the guns was diagnosed briefly using framing photography. A 4-mm wide slit was machined along the length of one gun barrel. The gun was operated with H_2 at 55 PSIG back pressure, using valve-to-discharge delays of 350-510 μs . These were the timings used on Hawk. For all delays, light is observed first at the location of the holes in the center conductor. The luminous region then expands toward the gun exit at roughly 5 $\text{cm}/\mu\text{s}$ for 430 μs delay and at 10 $\text{cm}/\mu\text{s}$ for 350 μs delay. By 1-2 μs , a slight difference in luminosity distribution is seen for different delays - for 350 μs the light is brighter near the center electrode tip while for 430 μs the light remains brighter near the holes.

INTERFEROMETRIC ARRANGEMENT

This experiment was the first to make use of our multichord interferometer. Briefly, two cylindrical lenses are used to expand in one direction the beam from a 35-mW HeNe laser (gracefully lent to us by John Thompson at MLI). The lens pair is located beyond the AOM so that both beams are expanded together. The resulting, roughly 2-cm-wide strip beams are directed along our usual interferometer arrangement. The combined output beam is observed by an array of six short fiber optic segments coupled to photodiodes. The experimental arrangement on Hawk, along with the scene beam locations in the switch region, is shown in the drawing at the bottom of Fig. 1. Four guns were used in the Hawk experiments and in most cases they were located very close to the anode rods as shown. This gives rise to a large azimuthal asymmetry when the 10-cm-diam cathode is used, which as a minimum complicates interpretation of the data. In future experiments they should probably be backed off. The 10-cm-diam cathode was used for all of the interferometric measurements.

The scene beams were located 0.24 cm apart in radius between 0.5 and 1.7 cm from the cathode. This setup did not have the beam-aligning paddle that was used in previous measurements, so that beam alignment could not be determined as accurately as before. There is probably a 0.1-0.15 cm uncertainty in the radial position of the beam

array in this work. Shots were taken with two locations of the gun collar, giving the two scene beam locations shown in the figure.

SOURCE-ONLY STUDIES

Figure 2 shows data taken using 430 μs valve-to-discharge delays with H_2 gas. Unless noted, a back pressure of 55-60 PSIG was used for all shots presented here. The top graph shows data taken with the scene beams under the gun (Fig. 1). The middle graph shows the same data on an expanded time scale. Note that in all of the graphs in this note the line-averaged electron density is given, because the axial length is less well determined than when flashboards were used. Also, in all graphs here time zero corresponds to the start of the gun discharge (doghouse) current. Density is observed first by the scene beam closest to the gun at 2.45 μs . This location is about 12 cm from the gas exit holes, giving an average velocity of 0.5 $\text{cm}/\mu\text{s}$ which is consistent with the framing photographic data. A sharp front is observed, moving at a faster velocity of about 10 $\text{cm}/\mu\text{s}$. Evidently the plasma observed here was either accelerated along the gun or originated later than the start of the discharge. A slight density decrease is seen behind the front. Shortly after the front reaches the cathode, a larger density increase is seen which propagates out from the cathode at 1-2 $\text{cm}/\mu\text{s}$. The last graph in Fig. 2 shows data taken with the scene beams offset from the gun. Here density is observed first close to the cathode, which is also closer to the gun as seen in Fig. 1. The later arrival time is consistent with the 10 $\text{cm}/\mu\text{s}$ front velocity. The initial density behavior at this timing, with its very large spatial and temporal gradients, differs greatly from that observed with flashboards. The later-time, secondary plasma is typical of flashboard data and may be unrelated in composition to that supplied from the guns. By varying the gun-to-generator time delay it is possible to vary greatly the initial radial profile of the electron density. For the first 400 ns the secondary plasma appears to be absent, so that during this time the plasma composition can be controlled. However, this is shorter than the typical conduction time. At much greater gun-to-cathode separations it may be possible to stretch out the early density behavior and allow more controllable physics experiments. During this time the density ranges from strongly peaked near the anode to evenly distributed. By moving the guns farther away and operating in parallel-plate geometry with different injection directions, it should be possible to study the effect of plasma species and profile on switch operation.

The minimum delay for which the discharge could be driven was about 340 μs . This time is consistent with the fact that the valve barely begins to open at 250 μs , and H_2 moving at the thermal speed of about 0.2 $\text{cm}/\mu\text{s}$ requires 50 μs to reach the holes in the gun center conductor. The top graph in Fig. 3 shows data taken for 350 μs discharge delays. At this timing the density behavior differs markedly from that seen in Fig. 2. Density is first observed at 1.7 μs , suggesting a faster plasma which is consistent with the framing photographic data. In this case, measurable density is seen simultaneously at all radial locations, and at both the center and offset azimuthal locations. After 1 μs the density is slightly larger both near the cathode and near the guns than it is in the middle of the gap. This is all indicative of a fast, low density plasma that impacts the cathode and

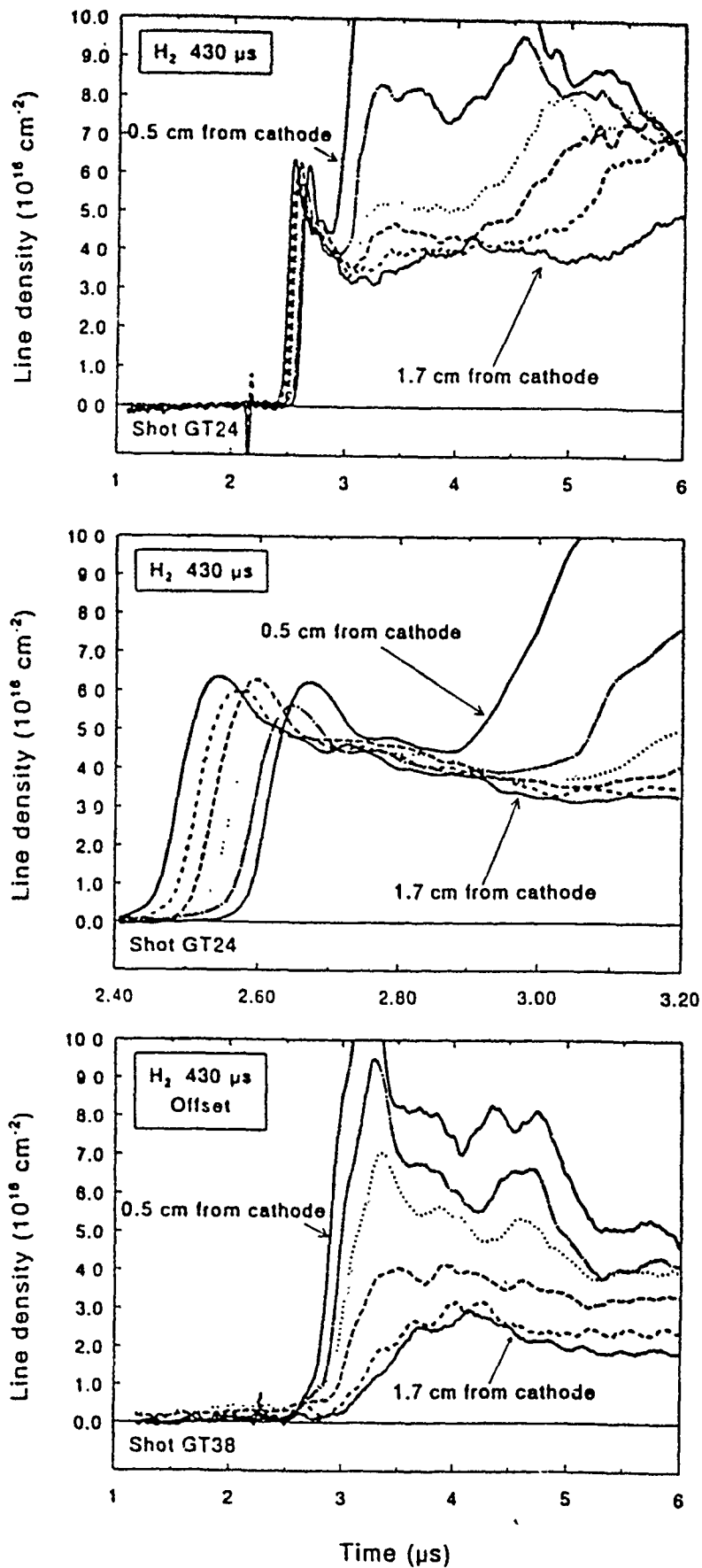


Figure 2: Density distributions from the sources alone.

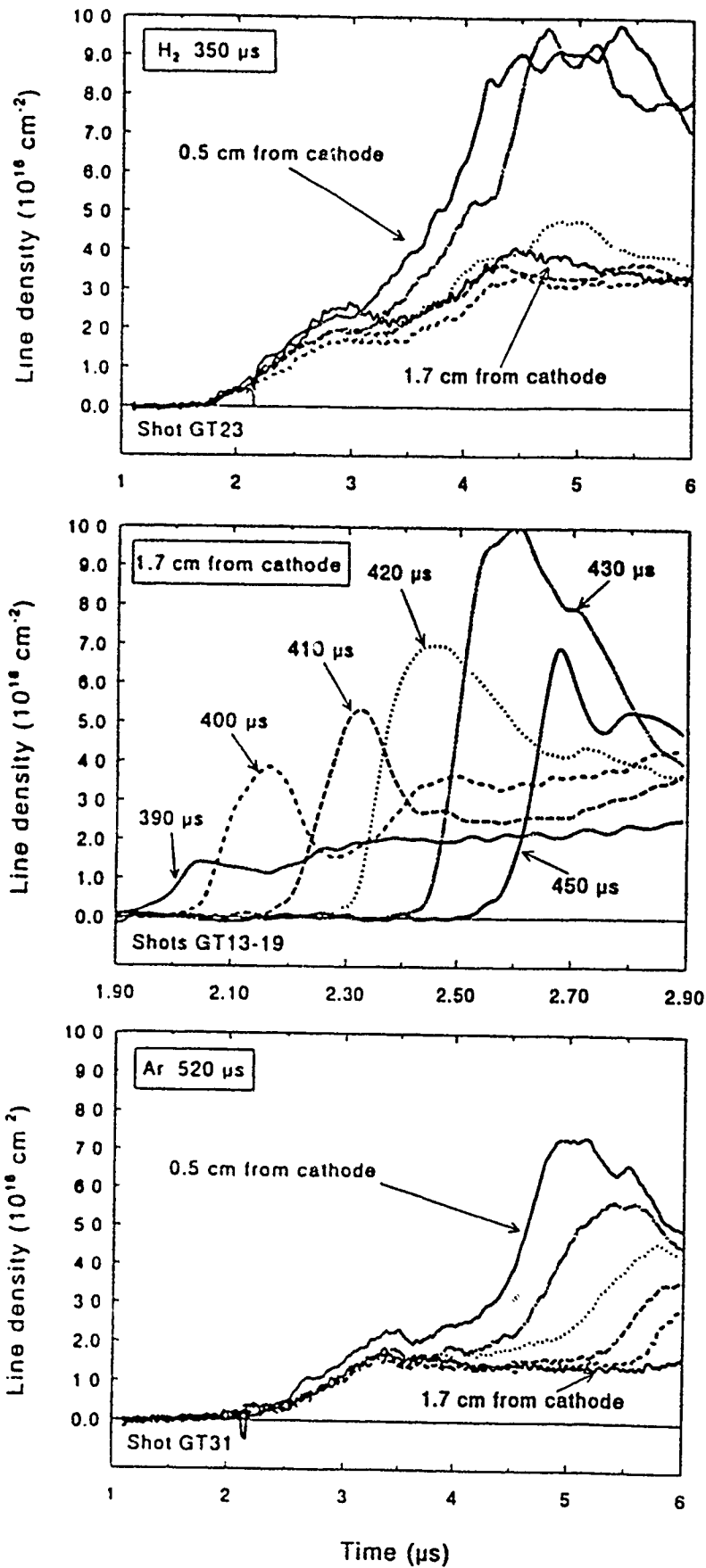


Figure 3. Density distributions from the sources alone.

bounces around, allowing the density to equilibrate within the switch region more rapidly than it increases with time. Later in time the profile is similar to that seen in Fig. 2.

At intermediate timings the density profile evolution varies smoothly between that shown here and that in Fig. 2. This is shown in the second graph in Fig. 3. Here data observed at 1.7 cm from the cathode is compared for a variety of timings. As the timing is increased beyond 430 μs , the steepness of the density front decreases.

The last graph in Fig. 3 shows density data for Ar gas. For Ar, 520 μs is about the minimum timing at which the discharge can be driven. With a thermal speed of roughly 0.04 cm/ μs , Ar should require 200 μs longer to transit from the valve to the holes than H_2 , so that this minimum time is consistent with that for H_2 . The density data are qualitatively similar to the early-timing data for H_2 shown in the top graph.

Reproducibility of these sources is discussed in the section after next.

MEASUREMENTS DURING MACHINE SHOTS

Interferometric measurements were performed during 11 machine shots with short circuit loads. Hydrogen gas was used for all shots with discharge delays of 430 μs . This timing was chosen because of the resulting initial density behavior. The graphs in Fig. 4 show data from shots with generator delays of 2.3 μs . Several interesting features are seen. On both shots the density at the start of conduction is very small. (Because of the weaker signals in this experiment, the noise-equivalent density is roughly a factor of two greater than in previous work.) Density increases during conduction as plasma flows into the switch region. On shot 1247 (top graph), opening appears to occur close to the cathode. Since the initial density is lowest there, this would be expected based on our MHD picture of conduction current limitation. On shot 1248, opening is a long, protracted process. This type of behavior was also observed on POP when the guns were placed very close to the cathode, and is believed to occur because the plasma influx increases rapidly over the conduction time. In this case, plasma can be supplied to the switch region as fast as it is distorted and/or eroded.

Figure 5 shows data from shots with 2.6- μs generator delays. Shot 1249 (top graph) shows a density profile evolution typical of that observed on shots with flashboards: the density decreases during conduction at all locations except close to the anode, where it increases. The density minimum is located at 1.5 cm from the cathode. Shot 1234, by comparison, shows different behavior. Here the density decreases to the measurement limit at all locations. It is not immediately obvious why this shot is different from shot 1249. On this shot the load current was not recorded and the time of opening is estimated from the switch voltage. Despite the encouraging, broad density reduction, the switch voltage does not indicate a rapid opening. (In fact, all of the short circuit shots in this run exhibit rather slow openings.) The last graph shows data taken with the scene beams at the offset location. Here also the density decreases at all observed radial locations during conduction. In this case the azimuthal asymmetry may cause azimuthal pinching of the switch plasma.

The top graph in Fig. 6 shows data from a shot with a 3 μs generator delay. At this time the secondary plasma density is much greater and opening appears to occur close

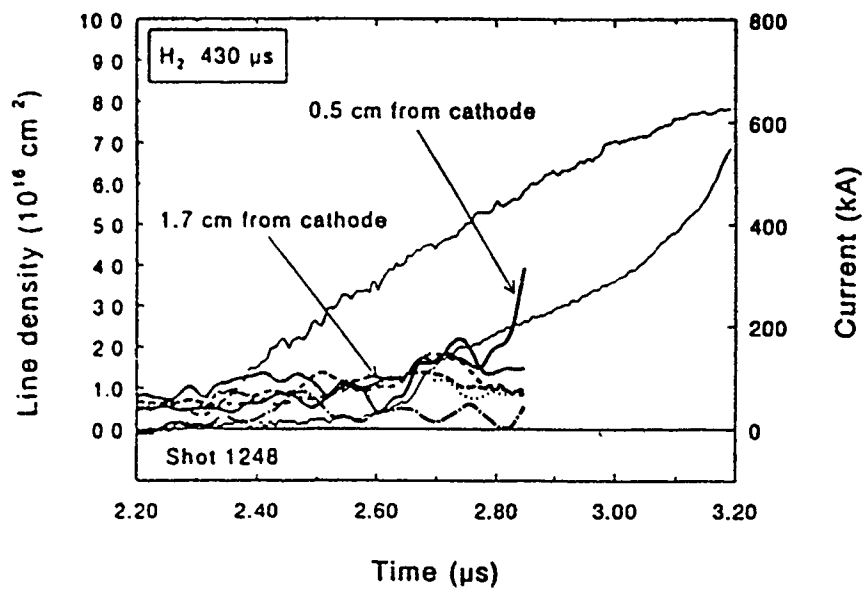
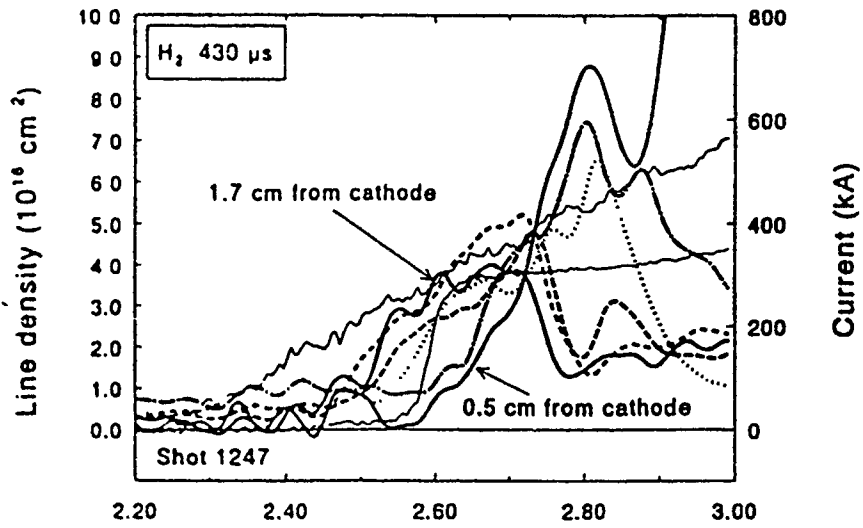


Figure 4: Density distributions from Hawk shots with early generator time delays.

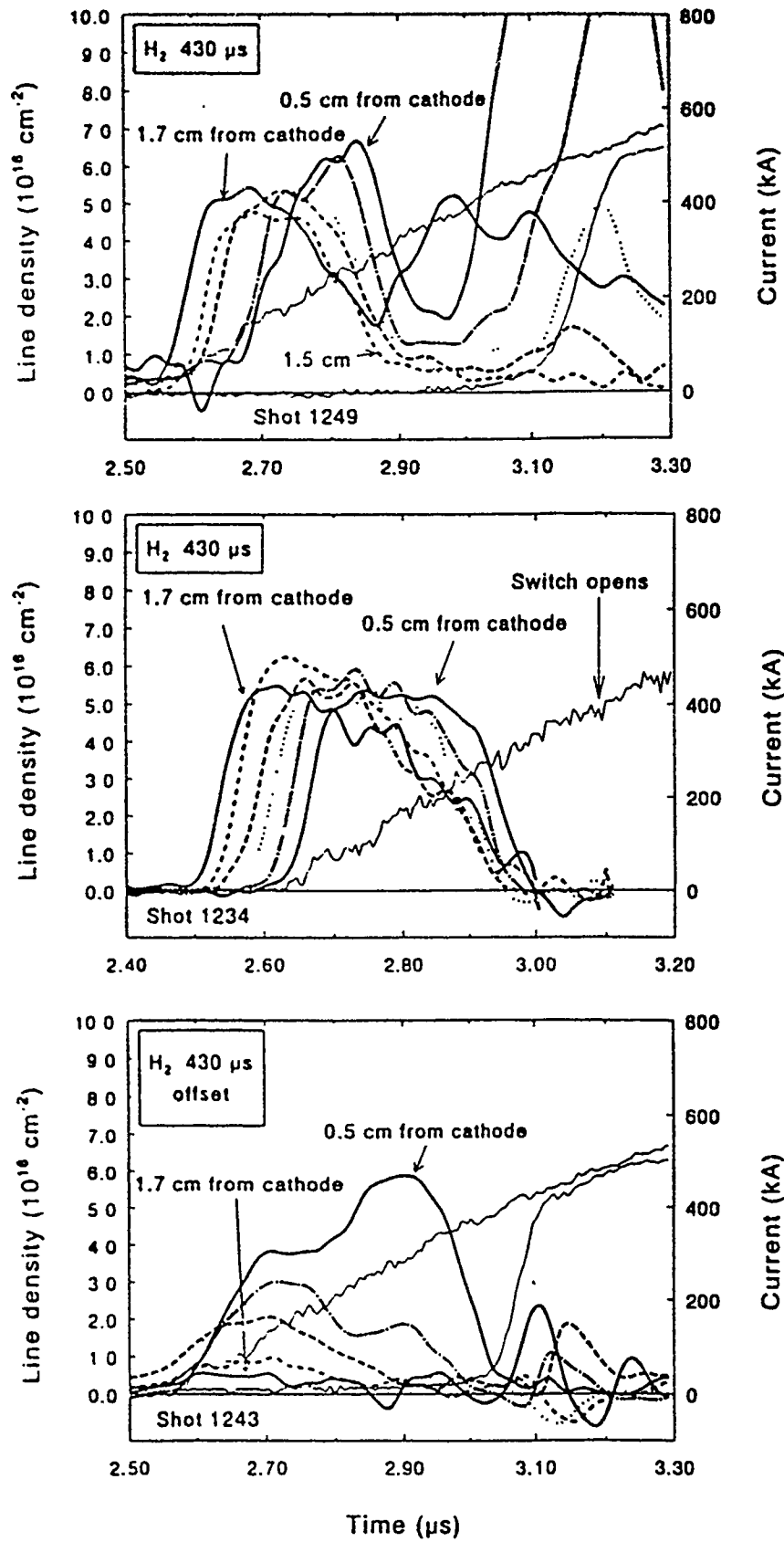


Figure 5: Density distributions from H₂wk shots with somewhat later generator time delays.

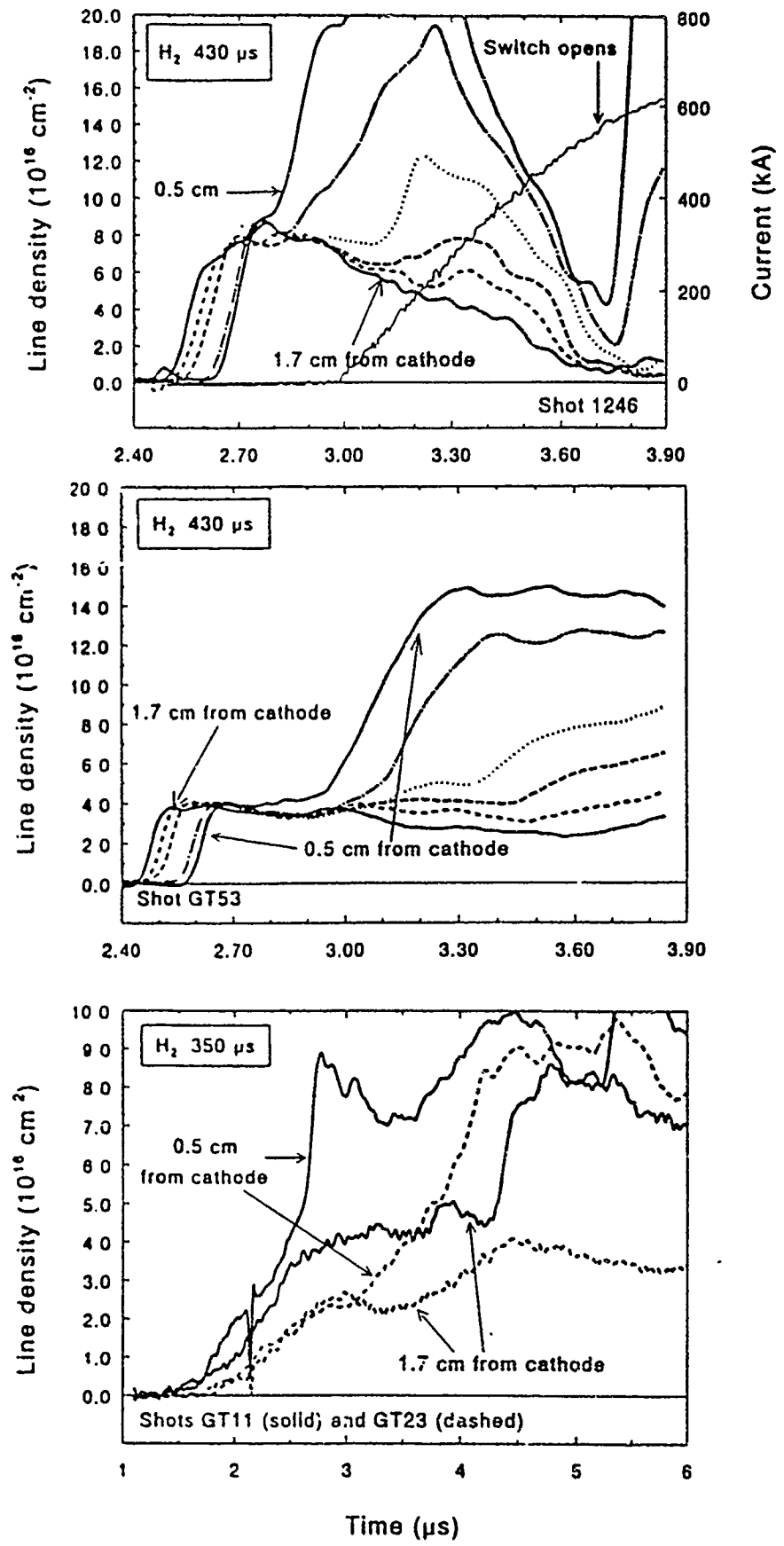


Figure 6: (top) Density distribution from a Hawk shot at a still later generator time delay; (middle) Distribution from the sources alone immediately prior to shot 1246; (bottom) Source irreproducibility.

to the anode. This would be expected based on our MHD picture because of the large radial density gradient away from the cathode.

REPRODUCIBILITY

In general, the data here show poor reproducibility, as illustrated in the last two graphs in Fig. 6. The middle graph shows data from the source-only shot immediately preceding shot 1246. The density profiles track well at first, but then become greatly different by the time generator current begins. With this irreproducibility it is not possible to compare directly shots with and without firing the generator, for example. The bottom graph compares data from two source-only shots taken with short discharge delays. Again, a large difference is exhibited. Such variation was not always observed, for example the data from the sequence of shots in Fig. 3 shows a smoothly-varying trend that is indicative of more reproducible behavior. Operation of these guns involves several processes which may vary shot-to-shot: action of the mechanical valve; gas breakdown and discharge initiation; interaction of the discharge with surfaces in the gun; and interaction of the injected plasma with the cathode surface. Some of the variation encountered may have resulted from incomplete purging and/or conditioning when the gas was changed or when the guns were brought up to air. The mechanical valves appear to be reliable and with further study, an operational/conditioning procedure could likely be developed that would allow reasonably reproducible operation of these guns.

COMPARISONS WITH OUR MHD PICTURE

As stated above, the results here are qualitatively consistent with our understanding of conduction current limitation. The switch is seen to open at the radial location of the density minimum (since the density gradients here dominate the weak magnetic field gradient): opening either at the cathode, at the anode, or in between, depending on the radial density profile.

The data are also quantitatively consistent. The diode shots Phil took with H₂ and Ar comprise mainly H₂ shots with 430 and 345 μ s discharge delays, and Ar shots with 520 μ s delays. For the early delay, the data here suggest that it is reasonable to assume azimuthal uniformity. In this case the measured density can be used to predict the conduction current. The diode shots at this early timing are found to have conduction currents that agree with those predicted, assuming a protonic plasma. Predictions for many of the H₂ shots at 430 μ s discharge delays are also consistent. However, in this case the rapid variation in density during conduction, and the observed azimuthal asymmetry complicate the interpretation. There are a few shots, such as shot 1247 in Fig. 4, for which the density is small-to-negligible at the start of the generator pulse. That conduction is observed indicates that either plasma flow into the switch region continues during conduction, or else new plasma is formed by ionization of neutrals that may be present along with the injected plasma. The Ar shots that Phil took also show conduction currents that are consistent with predictions assuming a doubly to triply ionized Ar plasma. In all of the above, the uncertainty in the density, azimuthal distribution, and composition have a relatively small effect on the predicted conduction current because of

its weak dependence on density in the MHD regime. By the same token, however, it is difficult to use the observed conduction current to deduce the plasma composition, or the existence of neutrals, etc.

RELEVANCE TO DIODE SHOTS

As discussed in Phil's Technote, switch performance with gas guns and diode loads was not very exciting. The data presented here indicate that at the generator delay times used in most of the diode shots taken with H_2 and Ar, either little current conduction occurred (as would have been expected), or the secondary plasma would have dominated, with a density profile similar to that on flashboard shots. Only a few shots with H_2 were taken under conditions corresponding to the rapidly varying density profile, and considering the lack of reproducibility it is not obvious what the exact density profiles were on these diode shots.

CONCLUSIONS

Considering the unexciting results with diode loads, further investigation of these sources would seem to be a relatively low priority within the POS program. However, they do have the potential of enlarging the available parameter space obtainable from POS plasma sources, and thus facilitating relevant physics experiments. If work on these sources were to continue, the first step should be a careful study of conditioning effects to improve the source reproducibility. As mentioned before, the valves should probably be driven with higher voltage, lower capacitance pulsers. The switch should be operated with more guns at a large distance from the cathode. Under these conditions, experiments could be performed that would add to our understanding of POS physics.

SECTION FIVE

SYSTEM STUDY FOR INDUCTIVE STORAGE GENERATOR

5.1 System Study for Inductive Storage Simulators

Decade is a multimodule pulsed power device designed as a NWES test facility. This device accelerates electron beams into high-atomic-number targets producing bremsstrahlung radiation in the x-ray region. These x-rays are then used for the testing of electronic components. During the design phase of the Decade facility, JAYCOR personnel carried out system studies to explore design options and find the optimum design criteria for Decade. The Decade designs employing inductive storage technology were analyzed with circuit modeling techniques. Realistic models for opening switches and diode loads were employed, and careful attention was paid to the stringent output requirements of the system. The Decade circuit model considered the storage inductance, capacitor bank voltage and capacitance, variable load and opening switch resistances (modeled), and a load inductance.

The results of the study included a number of design guidelines for maximizing the system efficiency. These included such detailed specifications as diode gap closure times (greater than 3 times the FWHM load pulse length), switch opening rates (maximize), and load inductance values (minimize). In addition, several general observations resulted from this study including the potential benefits of series diodes and longer conduction time opening switches.

5.2 List of Papers

5.2.1 "System Study for DECADE Using Inductive Storage Technology," P.F. Ottinger, J.M. Neri, R.J. Commisso, and D.V. Rose, J. Radiation Effects Research and Engineering 11, 143 (1993). Also, additional information can be found in NRL Memorandum Report 6733 (1990).

SYSTEM STUDY FOR DECADE USING INDUCTIVE STORAGE TECHNOLOGY*

Paul F. Ottinger, Jesse M. Neri, and Robert J. Comisso
 Naval Research Laboratory
 Plasma Physics Division
 Pulsed Power Physics Branch
 Washington, DC 20375

David V. Rose
 JAYCOR
 Vienna, VA 22182

Abstract

Designs for Decade using inductive storage combine the technologies of fast capacitor banks, vacuum opening switches, and advanced diode loads. Such designs require the choice of many system parameters, some of which are constrained by output requirements. However, the remaining parameters need to be chosen judiciously in order to optimize system performance and efficiency. Circuit analysis also suggests that elements of inductive generators are strongly interactive. Thus, realistic modeling of opening switches and the load are important for obtaining reliable results. A system study for Decade has been carried out with these concerns in mind. Results are presented, and advantages and disadvantages of various system options are discussed.

Introduction

Designs for Decade using inductive storage combine the technologies of fast capacitor banks, vacuum opening switches, and advanced diode loads.^{1,2} Such designs require the choice of many system parameters, some of which are constrained by output requirements. Typically, the peak load voltage V_L , the full-width at half-maximum (FWHM) of the load power τ_p , and the electrical energy delivered to the load E_L are specified. As in previous analyses,³ these three constraints can be viewed as fixing three system parameters. Here, the bank capacitance C , the storage inductance L , and the peak load resistance R_0 will be chosen as the three parameters that are determined by the output constraints. The remaining parameters need to be chosen judiciously in order to optimize system performance and efficiency.

Figure 1 shows a schematic of the Decade circuit. Initially, the capacitor bank is charged to a bank voltage V_b and no current is flowing. The capacitor bank is then discharged through the storage inductance L , which includes the inductance of the capacitor bank, the interface, and the vacuum region. The switch is assumed to remain closed and conduct current until a specified firing angle θ is reached. The conduction time of the switch τ_c is given by $\theta(LC)^{1/2}$, where $0 \leq \theta \leq \pi/2$. Once the switch begins to open, current is transferred to the load. The load resistance R_L overdamps the system [i.e., $(R_L/L)^2 \gg 4/LC$] so that the current decays exponentially as

$\exp(-tR_L/L)$ and the power is delivered to the load on a time scale much faster than τ_c . A finite-load inductance L_L is also included between the switch and the load.

Analysis suggests that elements of inductive generators are strongly interactive. Thus, realistic modeling for the opening switch resistance $R_{sw}(t)$ and the load resistance $R_L(t)$ are needed to obtain reliable results. In the absence of a physics model for the opening switch, the switch resistance is assumed to rise linearly in time, so that

$$R_{sw}(t) = \begin{cases} 0 & 0 \leq t \leq \tau_c \\ dR_{sw}/dt (t - \tau_c) & t > \tau_c \end{cases} \quad (1)$$

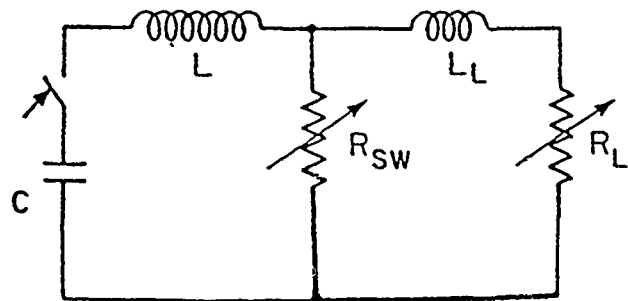


Figure 1. Schematic of single-stage inductive generator circuit.

* Work sponsored by Defense Nuclear Agency under MIPR #90-582NM.

It is also assumed that no voltage appears across the load until $t > \tau_c$, which agrees with most experiments. Once power is delivered to the load, it is assumed that the diode turns on instantaneously. Electrode plasmas, however, will expand across the anode-cathode gap and eventually short out the load. Gap closure occurs on a time scale of $\tau_g \sim D_0/v_c$, where D_0 is the initial gap spacing and v_c is the closure velocity. This effect is modeled by a linearly falling load resistance given by

$$R_L(t) = \begin{cases} R_0 & 0 \leq t \leq \tau_c \\ R_0 [1 - (t - \tau_c)/\tau_g] & \tau_c < t < \tau_c + \tau_g \end{cases} \quad (2)$$

This assumes that the diode current scales as the critical current. Although more sophisticated models will be used in the future, these models for R_{sw} and R_L are sufficient for the purposes of this study and provide considerable insight into the effects of switching rate and diode gap closure on system performance.

Many rough scaling relationships can be obtained from simple system considerations. The peak load power scales roughly as V_L^2/R_0 , so that, using $E_L \sim P_L \tau_p$ the peak load resistance scales as

$$R_0 \sim \frac{V_L^2 \tau_p}{E_L} \quad (3)$$

Similarly, the peak load current scales roughly as V_L/R_0 , so that

$$I_L \sim \frac{E_L}{V_L \tau_p} \quad (4)$$

For a fast opening switch, a negligible load inductance (i.e., $L_L \ll L$) and a load resistance that overdamps the system, the FWHM of the power pulse can be approximated by $\exp(-2\tau_p R_0/L) \sim 0.5$. Usually, the rise time of the load power is only a fraction of τ_p for the cases considered here, so that this provides a reasonable scaling under these circumstances. Using Equation 3, this yields

$$L \sim \frac{2 V_L^2 \tau_p^2}{E_L \ln(2)} \sim \frac{4 L_s}{\ln(2)} \quad (5)$$

where $L_s \equiv (V_L \tau_p)^2 / 2 E_L$ is the Shannon inductance.⁴ Note that the usual definition of the Shannon inductance is $L_s \equiv V_L^2 \tau_p / 2 P_L$. Since V_L , E_L , and τ_p are the specified parameters, $E_L \sim P_L \tau_p$ has been used to substitute for P_L in the definition of L_s that will be used here. The rough scaling in Equation 5 suggests that the storage inductance should be about 5.8 times L_s . However, the calculations that follow will show that the optimum L is about 2.3 times L_s . Inductances much larger than this optimum value will lead to a considerable efficiency penalty. Finite switching time and load inductance will also affect these scaling relationships and reduce efficiency.

The last rough scaling relationship is the condition for fast switching, which can be stated as $dR_{sw}/dt \gg R_0/\tau_p$. Again using Equation 3,

$$\frac{dR_{sw}}{dt} \sim \frac{V_L^2}{E_L} \quad (6)$$

Here, Equation 6 is meant to be a scaling relationship and not an equality. For example, if V_L is doubled the switch rate must be increased by a factor of four to obtain the same performance. These rough scaling relationships will be used to help explain the trends in the data. The results from the analysis will then be used to empirically find coefficients of proportionality to turn the scaling relationships in Equations 3 through 6 into approximate scaling equations.

Previous studies have investigated the effects of varying the storage inductance and firing angle on the system efficiency.⁴⁻⁶ The approach here is to determine the design for a system that satisfies the desired output specifications for V_L , τ_p , and E_L . The values of L , C , and R_0 , which result in an output pulse with peak voltage of V_L , FWHM of power of τ_p , and energy of E_L — no more and no less — will be called the "point-design" values for C , L , and R_0 . These point-design parameters C , L , and R_0 will be determined for a range of assumed values for θ , L_L , V_b , τ_g , and dR_{sw}/dt . Of these five variables, θ , L_L , and V_b are well defined and externally controllable, whereas τ_g and dR_{sw}/dt are controlled by physics. This algorithm will be repeated to investigate narrower power pulses and the use of series diodes⁷⁻¹² in order to address simulation fidelity concerns.

The efficiency of delivering energy from the capacitor bank to the load is very important, because it is directly related to the size and cost of the system. Consistent with the concept of finding the point design for a specified τ_p , E_L will be defined as the energy delivered to the load from $t - \tau_c = 0$ to $t_{1/2}$, the time (relative to the beginning of the power pulse) of half peak power on the falling part of the power pulse. Thus, the efficiency is defined as

$$\eta = \frac{\int_{\tau_c}^{\tau_c+T} I_L^2(t) R_L(t) dt}{CV_b^2/2} \quad (7)$$

where I_L is the load current and $T = t_{1/2}$ for the point-design parameter study. For an ideal switch (i.e., one that opens to $R_{sw} \gg R_L$ in a time much faster than τ_p) and an ideal load (i.e., $\tau_g \gg \tau_p$ so that $R_L \sim \text{constant}$) that overdamps the circuit [i.e., $(R_L/L)^2 \gg 4/LC$], this definition results in an efficiency of about 50 percent because about half the energy is still stored in L at $t = \tau_c + t_{1/2}$. Efficiencies much greater than 0.5 are not attainable because T is constrained to be $t_{1/2} \sim \tau_p$.

Aside from efficiency, the requirements on the opening switch performance are of particular importance and concern. For a given system, requirements on switch conduction time τ_c , conduction current I_0 , and opening rate dR_{sw}/dt must all be satisfied for proper system performance. As system parameters are varied, the switching requirements change. In many cases, values of τ_c , I_0 , and dR_{sw}/dt are required that are beyond the present limits of

switching capability. Thus, research to extend opening switch performance is required in order to consider the feasibility of some of the systems discussed in this study.

Also of concern is the efficiency penalty that results when the inductance is larger than the point-design value. Although the point-design parameter study will identify a value for L for the point design, such a value is not always physically realizable. Because of inherent inductance in the capacitor design, packing issues, voltage holdoff concerns, etc., a realistic inductance may be considerably larger than the point-design value. This issue of a physically realizable inductance will be referred to throughout as the inductance constraint. To evaluate the efficiency penalty that must be paid in cases where this inductance constraint plays a role, the effect of varying L about its point-design value is investigated. In this analysis, for each system with fixed capacitance C , the inductance is varied about the point-design value found in the previous analysis. Here, however, V_L is the only specified constraint and is assumed to fix R_o . Equation 3 is evaluated from $t - \tau_c = 0$ to a fixed time $t - \tau_c = T$. (Note for the efficiency penalty study, $T \neq t_{1/2}$.) E_L and τ_p are not fixed, but are calculated for each system. If L is larger than the point-design value, τ_p will exceed T , implying that the efficiency will drop and the simulation fidelity will be reduced. The efficiency penalty for using an inductance that is larger than the point-design value will be calculated and compared with those calculated previously.⁴⁻⁶

A number of design guidelines for maximizing the efficiency will be obtained from this study:

1. Firing angle θ should be $\sim 2\pi/5$
2. Load inductance L_L should be made as small as possible
3. Diode gap-closure time should be $> 3\tau_p$
4. Switch-opening rate should be as large as possible.

These conditions will be quantified. When all four of these conditions are satisfied, scaling equations can be written for the point-design parameters C , L , and R_o in terms of the three specified output parameters (V_L , E_L , and τ_p) and V_b . A number of other observations will also be made. Results from the point-design parameter study will show:

1. The only major difference between the design and performance of a lower voltage bank compared with a higher voltage bank is the longer switch conduction time
2. There are many advantages to using series diodes in terms of alleviating system constraints
3. To obtain a shorter power pulse width, inductance constraints and gap-closure concerns are further strained
4. Higher (lower) radiation production efficiency, and thus lower (higher) E_L , translates into a lower (higher) point-design value for C and a higher (lower) point-design value for L .

The results of the efficiency penalty study will provide quantitative information about the efficiency and fidelity penalties for using a storage inductance that is larger than the point-design inductance found in the point-design parameter study. For realistic values of L_L and dR_{sw}/dt , the efficiency can be significantly less than that derived from ideal circuit considerations. The dose will be commensurately less as well. All these results and their implications will be discussed in detail.

All analyses were carried out using a lumped-circuit approach, so that any important transit time effects were not investigated. In addition, the resistance of the capacitor bank and safety resistors were assumed negligible. It was also assumed that insulator flashover does not occur. If insulator flashover does occur, the energy stored in the bank inductance will be lost. This may be significant, depending on the detailed system design. All these effects tend to reduce the system efficiency and will be studied in the future.

Point-Design Parameter Study

Referring to Figure 1, the circuit analysis is broken into two parts: the conduction phase ($t < \tau_c$) and the opening phase ($t > \tau_c$). During the conduction phase, when $R_{sw} = 0$ and no current flows through the load, the circuit equation is written as

$$-\frac{Q}{C} + L \frac{dI}{dt} = 0 \quad (8)$$

In Equation 8, Q is the charge on C and $I = -dQ/dt$ is the current through L . Applying the initial conditions $Q(0) = CV_b$ and $I(0) = 0$, the solution is

$$I(t) = V_b \left(\frac{C}{L} \right)^{1/2} \sin \left[\frac{t}{(LC)^{1/2}} \right] \quad (9)$$

The argument of the sine function is commonly referred to as the firing angle θ . Choosing $\theta = \tau_c / (LC)^{1/2}$, the initial conditions for the opening phase become

$$Q_o = CV_b \cos \theta \quad (10a)$$

$$I_o = V_b \left(\frac{C}{L} \right)^{1/2} \sin \epsilon \quad (10b)$$

During the opening phase (i.e., for $t > \tau_c$), the circuit equations are:

$$-\frac{Q}{C} + L \frac{dI}{dt} + I_{sw} R_{sw} = 0 \quad (11a)$$

$$I_{sw} R_{sw} = L_L \frac{dI_L}{dt} + I_L R_L \quad (11b)$$

where $-dQ/dt = I = I_{sw} + I_L$, I_{sw} is the switch current, I_L is the load current, and $R_{sw}(t)$ and $R_L(t)$ are given in Equations 1 and 2, respectively. These equations can be rearranged to yield

$$\frac{dI_L}{dt} = (I_{sw} R_{sw} - I_L R_L) / L_L \quad (12a)$$

$$\frac{di_{sw}}{dt} = +\frac{Q}{LC} - \frac{i_{sw} R_{sw}}{L} - \frac{di_L}{dt}, \quad (12b)$$

$$\frac{dQ}{dt} = -(i_{sw} + i_L). \quad (12c)$$

These three coupled first-order differential equations are solved for $t \geq \tau_c$ with initial conditions $Q(\tau_c) = Q_0$, $i_{sw}(\tau_c) = i_0$, and $i_L(\tau_c) = 0$, where Q_0 and i_0 are defined in Equations 10a and 10b.

When solving Equations 12a through 12c for the point-design parameter study, L , C , and R_0 must be chosen so that the solution yields the specified values of V_L , E_L , and τ_p . To do this, a three-parameter shooting technique is used.^{13,14} Details of how this technique is applied to this problem are described in Reference 15. The code that was developed to carry out the design parameter study using this three-parameter shooting technique was benchmarked against analytic results obtained previously³ for the case with an ideal switch (i.e., $dR_{sw}/dt \rightarrow \infty$), $R_L = \text{constant}$, and $L_L \rightarrow 0$. In Reference 3, the firing angle θ and the bank voltage V_b were varied, and the output parameters were set at $V_L = 1.8$ MV, $E_L = 2.5$ MJ and $\tau_p = 85$ nsec. Analytic results for these cases can be found in Tables 1 and 2 of Reference 3. For the benchmarking code run, $dR_{sw}/dt = 1,000$ $\Omega/\mu\text{sec}$, $\tau_g = 1,000$ nsec, and $L_L = 0.5$ nH were used, and θ and V_b were varied. Agreement with the analytic results was obtained with rapid convergence.

The purpose of the point-design parameter study was to determine the design for a system for which the system parameters result in precisely the desired output specifications for V_L , τ_p , and E_L . The point-design parameters C , L , and R_0 were determined using the three-parameter shooting technique for a range of assumed values for V_b , θ , L_L , dR_{sw}/dt , and τ_g . Table 1 lists the values of the parameters for the seven computer runs that were made.

The output parameters, V_L , E_L , and τ_p , are chosen to match Decade bremsstrahlung radiation specifications. The peak load voltage V_L is a measure of the maximum or endpoint voltage of the radiation-producing electrons generated in the diode. Typically, 1.5 MV is the highest acceptable endpoint voltage. If a series diode is used to divide the generator voltage down to the desired endpoint voltage, then V_L can be higher. Runs 5 through 7 are meant to simulate the case where two diodes are used in series so that the peak load voltage, as seen by the generator, is 3 MV. To achieve the specified dose at an endpoint voltage of 1.5 MV, 2.5 MJ of electrical energy must be delivered to the load. $E_L = 2.5$ MJ is used for all the runs except Run 7. In this case, $E_L = 3$ MJ was used to investigate the effect of lower radiation production efficiency in series diodes. Initially, the specified radiation pulse width is 40 nsec. It is assumed that the dose rate associated with forward-directed bremsstrahlung scales as $IV^{2.8}$, so that for $P \sim IV \sim e^{-t/\tau_p}$, the radiation pulse width scales as $\tau_{rad} \sim \tau_p/1.9$. For $\tau_{rad} = 40$ nsec, $\tau_p = 76$ nsec. Eventually, Decade will require $\tau_{rad} = 20$ nsec or $\tau_p = 35$ nsec. Runs 6 and 7 investigate the impact on the design parameters of this shorter pulse option. If another scaling for the dose rate is used, then τ_p needs to be adjusted appropriately. For reference, column 5 in Table 1 shows $L_s = (V_L \tau_p)^2 / 2E_L$ for each run.

The other five parameters shown in Table 1, V_b , θ , L_L , dR_{sw}/dt , and τ_g , are variables. For each run, two parameters are varied over a range of values and the other three are set at fixed values. The symbol "v" in the table indicates which parameters are varied for each run. In Run 1, θ is varied between $\pi/4$ (45°) and $\pi/2$ (90°), and L_L is varied between $0.1 L_s$ and L_s to study their effects on the design parameters. In Run 2, τ_g is varied between 125 and 1,000 nsec to study the effect of gap closure on the system. In Run 5, dR_{sw}/dt is varied between 2 and 20 $\Omega/\mu\text{sec}$ to investigate the effect that switch-opening rate

Table 1. Parameters for computer runs.

Run #	Specified Output Parameters				Variable Values ^a				
	V_L (MV)	E_L (MJ)	τ_p (nsec)	L_s (nH)	V_b (kV)	θ (rads)	L_L (nH)	dR_{sw}/dt (W/msec)	τ_g (nsec)
1	1.5	2.5	76	2.6	750	v	v	4	1,000
2	1.5	2.5	76	2.6	750	v	$0.1 L_s$	4	v
3	1.5	2.5	76	2.6	750	v	$0.1 L_s$	v	1,000
4	1.5	2.5	76	2.6	v	$2\pi/5$	$0.1 L_s$	v	1,000
5	3.0	2.5	76	10.4	v	$2\pi/5$	$0.1 L_s$	v	1,000
6	3.0	2.5	38	2.6	v	$2\pi/5$	$0.1 L_s$	v	1,000
7	3.0	3.0	38	2.2	v	$2\pi/5$	$0.1 L_s$	v	1,000

Note:

^a The two parameters for each run that were varied over a range of values are indicated by the symbol "v."

has on system performance and design. The lower limit for this range of values is obtained by scaling presently demonstrated switch-opening rates (e.g., $\sim 125 \Omega/\mu\text{sec}$ at $I_o = 450 \text{ kA}$ on EYESS¹⁶) with the inverse of the conduction current [so that $dR_{sw}/dt \sim 125 \Omega/\mu\text{sec}$ ($0.45/25 \text{ MA}$) = $2.25 \Omega/\mu\text{sec}$]. This assumes that the voltage at the switch remains the same. V_b is varied between 0.25 and 1.25 MV in Run 4 to study system design requirements and performance for both high- and low-voltage banks. With $V_L = 3 \text{ MV}$, Run 5 considers the advantages and disadvantages of using series diodes. In Runs 5 through 7, dR_{sw}/dt is varied between 2 and $40 \Omega/\mu\text{sec}$. Run 6 investigates the difficulties of reducing the pulse width. Lastly, Run 7 studies the effect of increasing the required load energy if, for example, a series diode is less efficient in coupling electrical energy to radiation.

For each of the runs, data are presented in a set of curves plotting L , C , η , and τ_c as a function of one of the two variables with individual curves parameterized by the second variable. Surface plots, which provide better visualization of the trends in the data, are given in Reference 15. With the exception of Run 2, the third design parameter R_o only varies slightly over the range of variables studied. Thus, it is only plotted for Run 2 where the gap-closure time is varied.

Run 1, Varying θ and L_L

In Run 1, θ and L_L are varied to study their effects on the design parameters. A bank voltage of 750 kV is chosen to model the capacitor banks presently being studied for use in Decade. A large gap-closure time, $\tau_g = 1,000 \text{ nsec} \gg \tau_p$ is chosen so that gap-closure effects can be ignored for the moment. A switching rate of $dR_{sw}/dt = 4 \Omega/\mu\text{sec}$ was chosen. Figure 2 shows the data from this run. The peak load resistance was found to lie between 0.058 and 0.06 Ω for the range of variables studied for this run. The higher values of R_o occur at larger θ and larger L_L . The peak load current and load power vary only slightly with θ and L_L for this run and are found to be about 26.5 MA and 40 TW. These results all agree with the scaling relationships found for R_o , I_L , and P_L (i.e., Equations 3 and 4, and $P_L \sim E_L/\tau_p$) because these three quantities are all independent of both θ and L_L .

Figure 2c shows that the efficiency decreases linearly as L_L increases for all firing angles. Since E_L is fixed, C must increase with L_L as η decreases, as shown in Figure 2b. To understand this η scaling with L_L , consider the following: If at $t = \tau_c$, the current in L is I_o , and if at $t = \tau_c + t_{1/2}$ the load current is I_f , then from conservation of energy

$$\frac{1}{2} LI_o^2 = \frac{1}{2} LI_f^2 + \frac{1}{2} L_L I_f^2 + E_L + \Delta E \quad (13)$$

Here, ΔE is the energy dissipated in the switch minus (plus) any additional energy drawn from (returned to) the capacitor bank during the time from τ_c to $\tau_c + t_{1/2}$. For an overdamped system ($t_{1/2} \ll \tau_c$) and a fast opening switch

(peak load current $\sim I_o$, so that $I_f^2 \sim I_o^2/2$ at the half-power point), $\Delta E \sim 0$ and

$$\begin{aligned} \eta &= \frac{E_L}{\frac{1}{2} CV_b^2} \leq \frac{E_L}{\frac{1}{2} LI_o^2} = 1 - \left(1 + \frac{L_L}{L}\right) \frac{I_f^2}{I_o^2} \\ &= 0.5 - \frac{L_L}{2L} \end{aligned} \quad (14)$$

For $\theta = \pi/2$, $CV_b^2/2 = LI_o^2/2$ and, thus, $\eta \approx 0.5 - L_L/2L$. This same result can be obtained using flux conservation arguments. For $\theta < \pi/2$, η will be less because energy is still left in the capacitor bank (note: $\eta_{\text{max}} \sim 0.5$). Equation 14 provides insight into why η decreases linearly with L_L . Empirically scaling η with L_L from the data in Figure 2c yields

$$\eta = \eta(\theta, L_L = 0) - 0.2 \frac{L_L}{L_s} \quad (15)$$

where $\eta(\theta, L_L = 0)$ is the efficiency for firing angle θ when $L_L \ll L_s$. Equation 15 is scaled with L_s rather than L because Figure 2a or 3a shows that L varies with both θ and L_L . From the results displayed in Figure 2c and a comparison of Equations 14 and 15, it is concluded that $L = 2.3 L_s$ for the optimum system. This conclusion is also consistent with results from the other code runs of this study.

Other trends in the data seen in Figure 2 should also be noted. The efficiency peaks at a firing angle of about $2\pi/5$ (see Figure 2c). Note that τ_c is about 350 nsec for this value of θ . For θ larger than this value, some energy from L begins to recharge C during opening, and thus reduces η . The efficiency decreases as θ decreases below $2\pi/5$ because, as the switch opens earlier, a larger fraction of the energy is left in the capacitor bank (and is unavailable to drive the load for $\tau_p \ll \tau_c$). Since E_L is fixed, this also implies that C must be larger for smaller θ (see Figure 2b). However, if $\tau_c = \theta(LC)^{1/2}$ becomes small enough (compared with τ_p) as θ decreases, significant energy will pass from C through L to the load during τ_p . This allows for smaller L as θ decreases, since less energy has to be stored in the inductor (see Figure 2a). L also decreases as L_L increases to maintain the proper $(L + L_L)/R_L$ decay for the pulse width. L does not decrease linearly as expected from this argument because the rise time of the load power pulse also increases as L_L increases. This requires the proper decay rate to increase somewhat with L_L so that L does decrease, but not linearly with L_L (see Figure 2a). The conduction time τ_c ranges from about 200 nsec for $\theta = \pi/4$ to about 500 nsec for $\pi/2$ (see Figure 2d).

The results of Run 1 show that a firing angle of about $2\pi/5$ is optimum. It is also clear from Equation 15 that L_L should be made as small as possible compared with L_s to maximize efficiency.

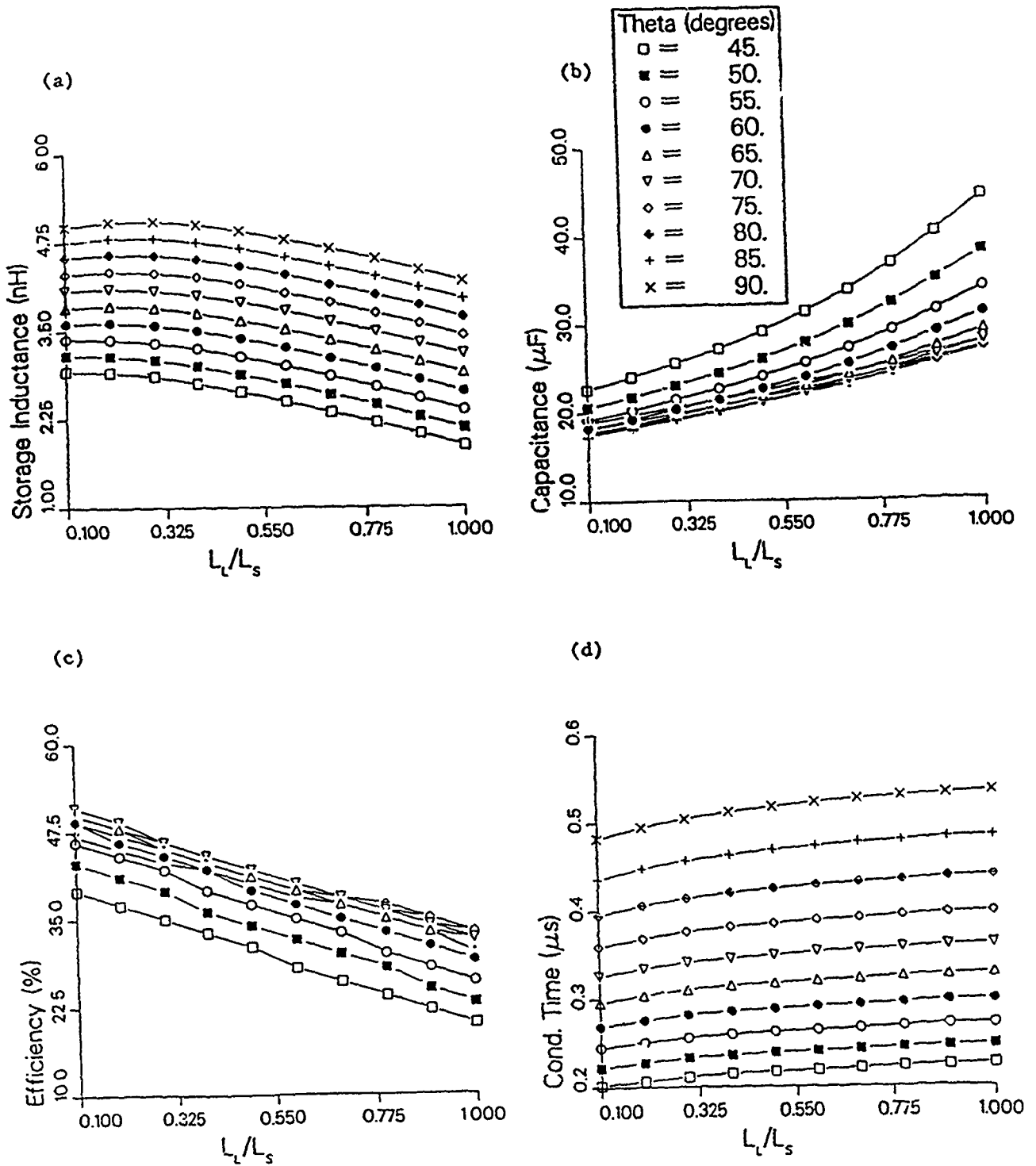


Figure 2. Run 1 plots of (a) $L(L_L)$, (b) $C(L_L)$, (c) $\eta(L_L)$, and (d) $\tau_c(L_L)$ with curves parameterized by θ .

Run 2, Varying τ_g and θ

In Run 2, τ_g is varied to study the effect of gap closure on the system. Figure 3 shows the data from this run. The peak load current and load power for this run are about 26.5 MA and 40 TW, and vary only slightly with θ and τ_g until τ_g drops below ~200 nsec where the load power begins to decrease as τ_g decreases. At $\tau_g = 125$ nsec, the peak load power is about 38.7 TW. Figure 3c shows that the efficiency drops dramatically for τ_g , less than about 200 nsec for this case with $\tau_p = 76$ nsec. Thus, to obtain high efficiency it is necessary to have

$$\tau_g \geq 3\tau_p \quad (16)$$

If Equation 16 is not satisfied, C increases as shown in Figure 3b in order to deliver the specified load energy at lower efficiency. Because $R_L(t)$ decreases in time, R_o increases as τ_g decreases to maintain the same fixed peak load voltage. Figure 3e shows the variation of R_o with τ_g . As shown in Figure 3a, L also increases as τ_g decreases so that the average L/R_L decay time of the load power is appropriate for the specified value of τ_p . Since both L and C increase nearly proportionately, neither I_o (see Equation 10b) nor I_L change significantly as τ_g decreases, but τ_c increases rapidly with decreasing τ_g (see Figure 3d).

The results of Run 2 show that gap closure can severely degrade efficiency if Equation 16 is not satisfied. For the small gaps associated with the low-impedance diodes required for Decade, this is a major concern. Although larger inductances can be tolerated as τ_g decreases, this advantage seems far outweighed by the loss in efficiency. A large fraction of the extra inductance that can be tolerated may, in fact, reside in the capacitor bank, since the bank inductance will also increase in a realistic system as C increases.

Run 3, Varying dR_{sw}/dt and θ

In Run 3, dR_{sw}/dt is varied to investigate the effect that switch-opening rate has on system performance and design. Figure 4 shows the data from this run. The peak load resistance was found to lie between 0.055 and 0.6 Ω for the range of variables studied in this run. The higher values occur for lower dR_{sw}/dt and there was little variation with θ . The peak load current and load power for this run range from about 26 MA and 39 TW to about 27.7 MA and 41.6 TW, with the higher values occurring at higher dR_{sw}/dt values. For fixed dR_{sw}/dt , the peak load current and load power are nearly constant over the range of θ . [Figure 8c shows, as expected, that the efficiency decreases as the switch-opening rate decreases. These results were used to determine the constant of proportionality for the scaling relationship in Equation 6.] Choosing the point where η rises to within 5 percent of its peak value (as $dR_{sw}/dt \rightarrow \infty$) yields

$$\frac{dR_{sw}}{dt} \geq \frac{6.5 V_L^2}{E_L} \quad (17)$$

For slower switch-opening rates, η drops significantly from its peak values for all θ . The efficiency drops because more energy is dissipated in the switch when the

opening rate is slower. Because of the increased competition for current between R_{sw} and R_L at slower switch-opening rates, the rise time of the load current is also slower. This requires a faster L/R_L decay once the current switches (i.e., peaks) to maintain a fixed τ_p . Thus, as seen in Figure 4a, L decreases as dR_{sw}/dt decreases. In addition, as the efficiency drops, C increases to maintain a fixed E_L . As dR_{sw}/dt decreases, L decreases slightly faster than C increases. Thus, as shown in Figure 4d, τ_c decreases slightly as dR_{sw}/dt decreases.

The results of Run 3 show that, as would be expected, efficiency increases as the switch-opening rate increases. Beyond the opening rate given in Equation 17, there is little additional efficiency benefit. However, an added advantage to achieving the highest possible dR_{sw}/dt is that the point-design value for L increases as dR_{sw}/dt increases.

Run 4, Varying V_b and dR_{sw}/dt

V_b is varied in Run 4 in order to study system design requirements and performance for both high- and low-voltage banks. Figure 5 shows the data from this run. The peak load resistance was found to lie between 0.055 and 0.06 Ω for the range of variables studied in this run. R_o is nearly constant over the range of V_b , with the higher values of R_o occurring at smaller dR_{sw}/dt . The peak load current and load power for this run range from about 26 MA and 39 TW to about 27.7 MA and 41.6 TW, with the higher values occurring at higher dR_{sw}/dt values. For fixed dR_{sw}/dt , the efficiency (see Figure 5c), peak load current, and peak load power are all nearly constant over the range of V_b . As previously, η decreases as the switch-opening rate decreases below the value given in Equation 17. Since η is nearly independent of V_b and E_L is fixed, C scales as V_b^{-2} . Figure 5b shows this scaling. Figure 5a shows that L is roughly independent of V_b , in agreement with the scaling in Equation 5. Thus, τ_c should scale as V_b^{-1} , as seen in Figure 5d.

The results of Run 4 show that ~50 percent efficiency is attainable over the entire range of V_b studied, for $dR_{sw}/dt > 5 \Omega/\mu\text{sec}$. However, at lower V_b , longer τ_c is required for the same dR_{sw}/dt . Experimentally, dR_{sw}/dt is found to decrease as τ_c increases. Staged switching may solve this problem if adequate single-stage switching is not attainable. Lower voltage banks have many advantages that could be utilized if switching requirements could be met. For example, capacitors are combined largely in parallel for low-voltage banks and in series for high-voltage banks, so that the bank inductance L_b scales roughly as V_b^2 . Thus, L_b can be significantly lower in a low-voltage bank than in a high-voltage bank, freeing more of the total system inductance for the vacuum feeds. Other advantages include design simplicity and less severe problems with high-voltage breakdown.

Run 5, Doubling V_L -Series Diodes

With $V_L = 3$ MV, Run 5 considers the advantages and disadvantages of using two diodes in series compared

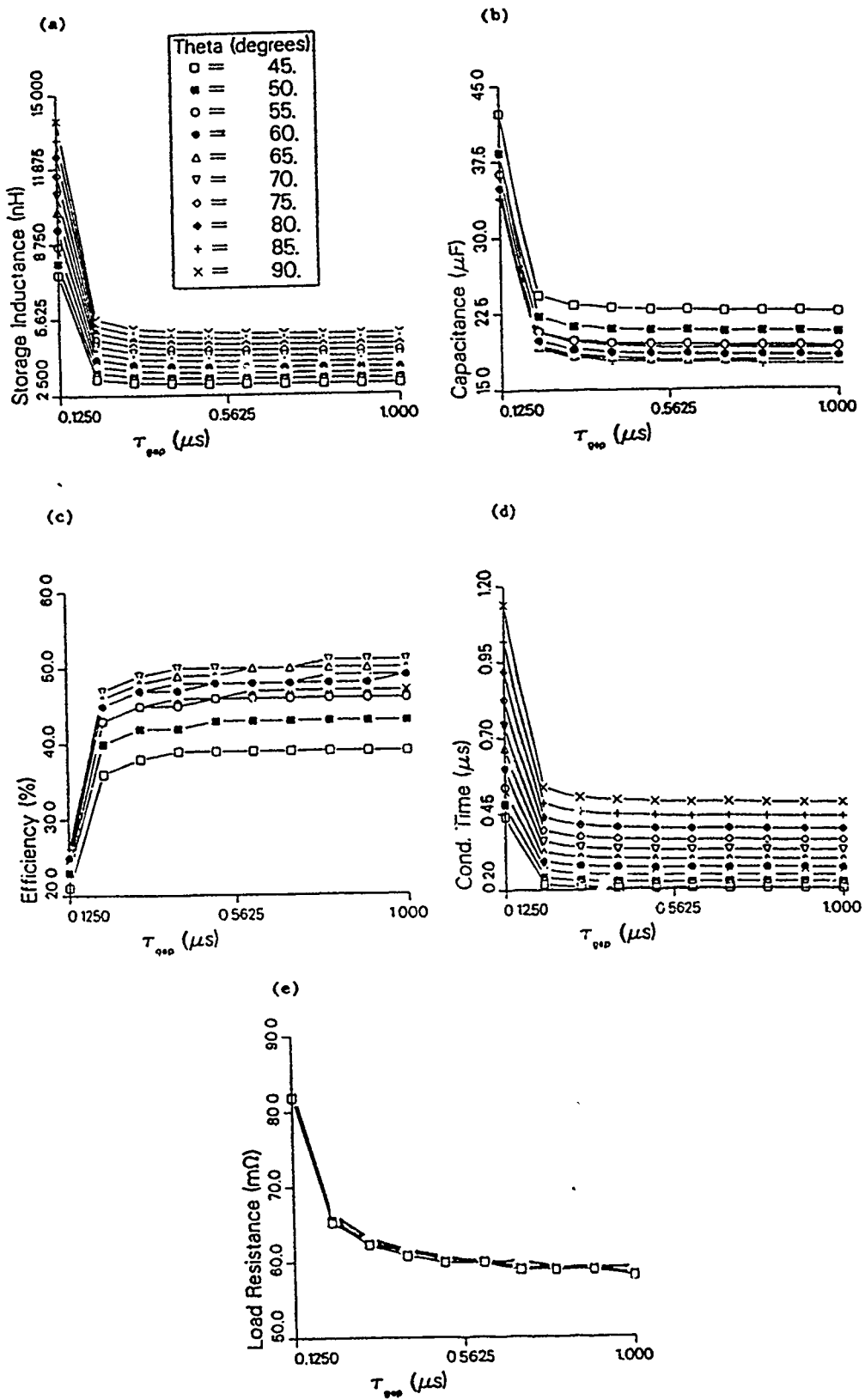


Figure 3. Run 2 plots of (a) $L(\tau_g)$, (b) $C(\tau_g)$, (c) $\eta(\tau_g)$, (d) $\tau_c(\tau_g)$, and (e) $R_L(\tau_g)$ with curves parameterized by θ .

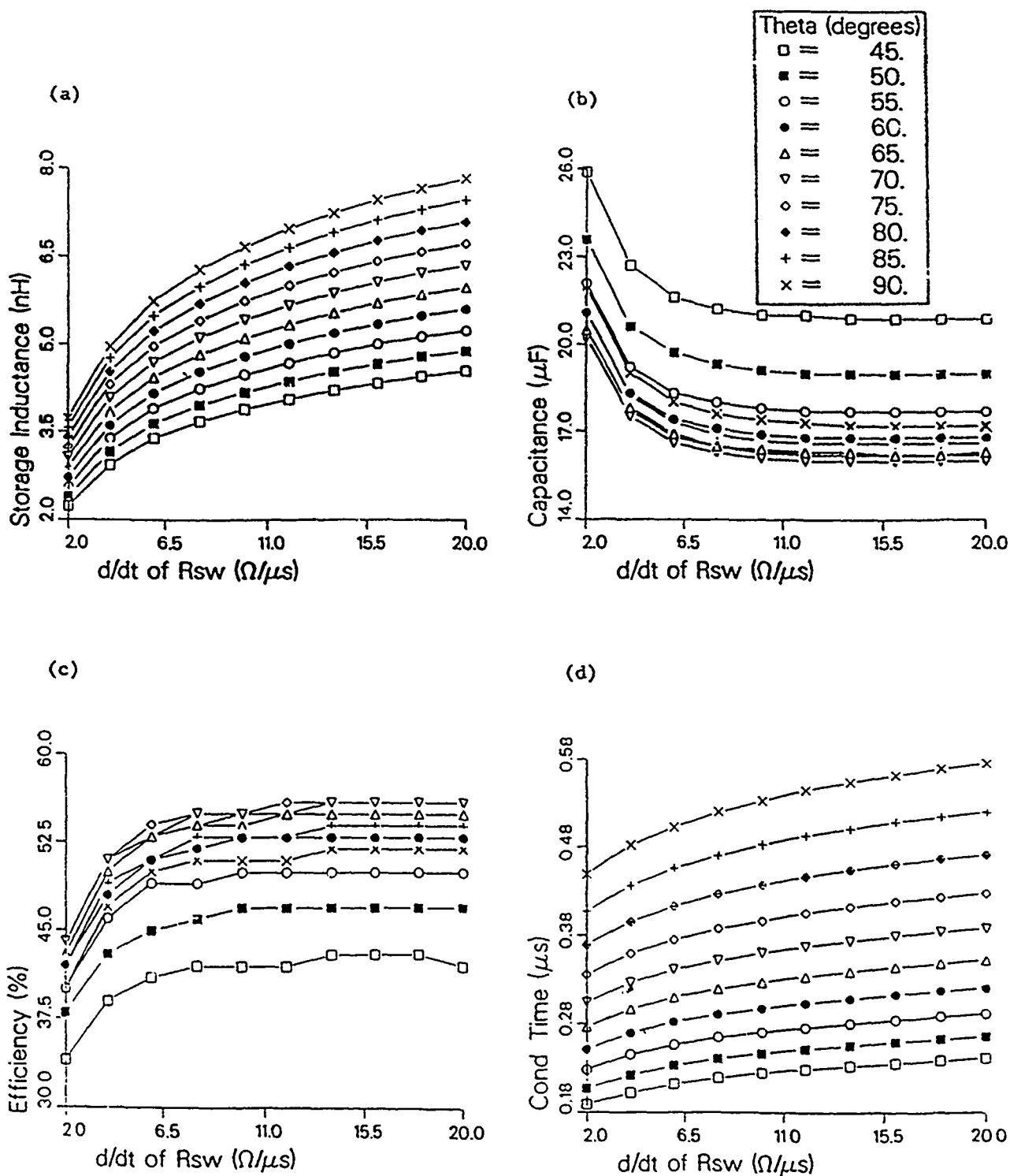


Figure 4. Run 3 plots of (a) $L(dR_{sw}/dt)$, (b) $C(dR_{sw}/dt)$, (c) $\eta(dR_{sw}/dt)$, and (d) $\tau_c(dR_{sw}/dt)$ with curves parameterized by θ .

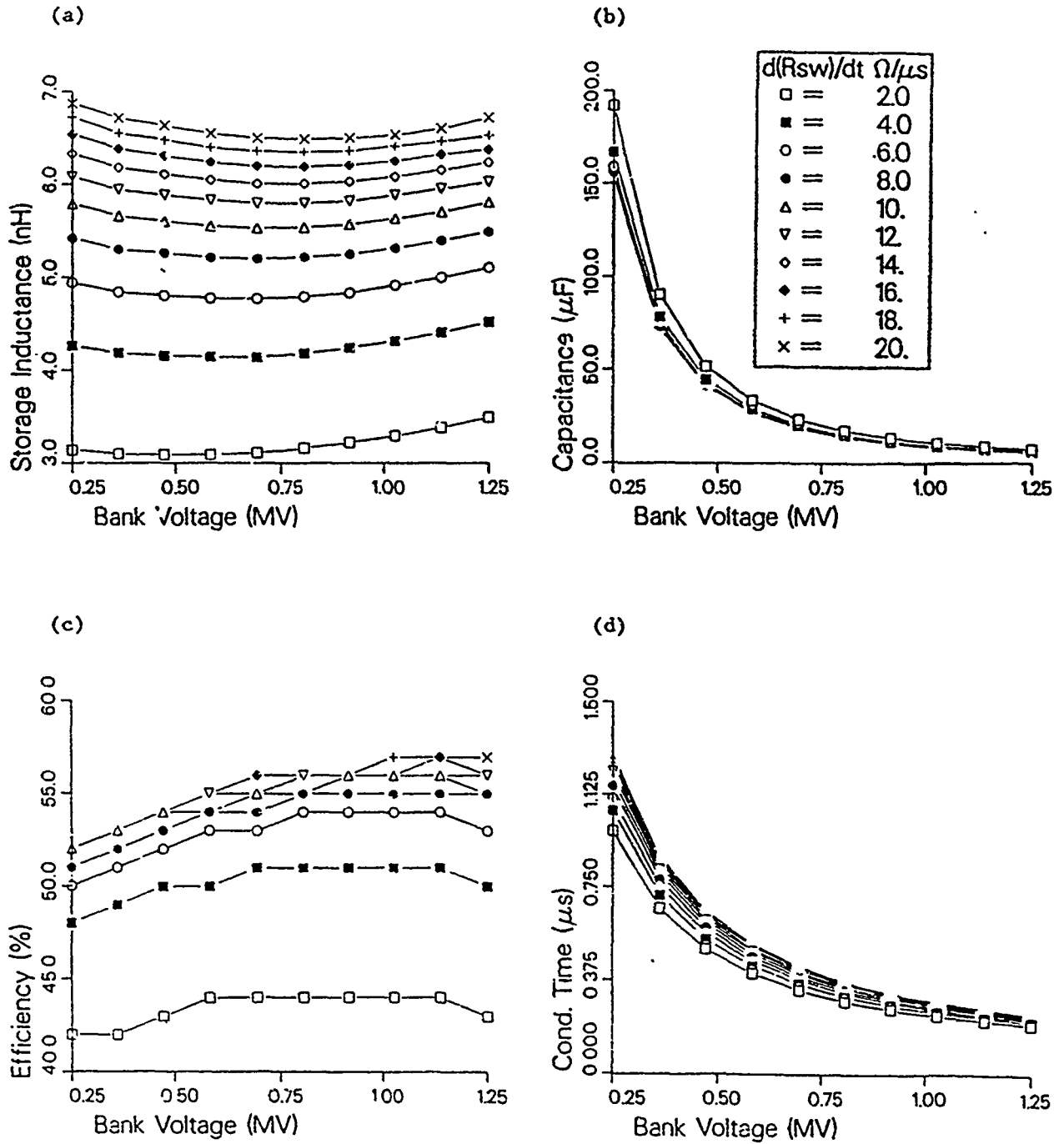


Figure 5. Run 4 plots of (a) $L(V_b)$, (b) $C(V_b)$, (c) $\eta(V_b)$, and (d) $\tau_c(V_b)$ with curves parameterized by dR_{sw}/dt .

with a single diode with $V_L = 1.5$ MV in Run 4. Figure 6 shows the data from this run. Note that the range of dR_{sw}/dt was increased to $40 \Omega/\mu\text{sec}$, since, as indicated by Equation 17, the required switch-opening rate for high efficiency is a factor of four higher at $V_L = 3$ MV than at 1.5 MV. The peak load resistance was found to lie between 0.225 and 0.25Ω for the range of variables studied in this run. This is a factor of four higher than for Run 4, which agrees with the scaling of Equation 3. Each of the two series diodes would have $R_o \sim 0.125 \Omega$, or about twice the resistance of the single diode in Run 4. Again, R_o is nearly constant over the range of V_b , with the higher values of R_o occurring at smaller dR_{sw}/dt . The peak load current and load power for this run range from about 12.6 MA and 37.8 TW to about 13.7 MA and 40.8 TW, with the higher values occurring at higher dR_{sw}/dt values. The peak power is about the same as in Run 4, while the peak current is down by a factor of two. For fixed dR_{sw}/dt , the peak load current and load power are nearly constant over the range of V_b . Since L_s increases by a factor of four when V_L is doubled, Equation 5 implies that L should be four times larger than in Run 4. This is confirmed by comparing the data in Figure 6a with those in Figure 5a. A four-times-larger L_L can also be tolerated without degrading efficiency. With C the same and L four times larger, τ_c is twice as large as in Run 4.

The results of Run 5 show that using series diodes has many advantages. Generalizing to N diodes in series, both L and L_L can be increased by N^2 , making the physical constraints on inductance more tolerable. In addition, the total load resistance increases by N^2 , so that each of the N diodes has a resistance N times higher (remember that I_L decreases by a factor of N). This will alleviate the gap-closure problem, because resistance scales roughly linearly with gap for a pinched-beam diode. These advantages are also gained without sacrificing dose rate. If the dose rate for an endpoint voltage of V_o scales as IV^α , then the dose rate from Run 4 would be $I_o V_o^\alpha$. For Run 5, the dose rate is $N(I_o/N)[(NV_o)/N]^\alpha$, which is equal to the dose rate for Run 4. Here, the leading N accounts for the N diodes in series, I_o/N is the current in each diode, and the expression in the square brackets is the voltage on each diode (i.e., the full voltage NV_o divided by the number of diodes in series). The major disadvantage with using series diodes is the required enhancement in switch performance; dR_{sw}/dt and τ_c are required to increase by a factor of N^2 and N , respectively. Other disadvantages include increased diode complexity and high-voltage power-flow concerns.

Run 6, Halving τ_p

Run 6 investigates the difficulties of reducing the pulse width. Since R_o , L , and L_L all scale unfavorably with τ_p , it is assumed here that a two-stage series diode will be used. Thus, V_L is set equal to 3 MV for this run. Figure 7 shows the data from this run. As expected, the scalings for R_o in Equation 3, for L in Equation 5, and for L_L in Equation 15 are all confirmed by the results. The peak load resistance was found to lie between 0.111 and

0.122Ω for the range of variables studied in this run. Once again, R_o is nearly constant over the range of V_b , with the higher values of R_o occurring at smaller dR_{sw}/dt . The value of R_o is a factor of two smaller than in Run 5. Smaller R_o makes the gap-closure problem more severe, but the shorter pulse alleviates the problem somewhat. The value of L is smaller by a factor of four than in Run 5. Without the two-stage series diode, L would be reduced another factor of four. The peak load current and load power for this run range from about 25.3 MA and 75.8 TW to about 27.2 MA and 81.6 TW, with the higher values occurring at higher dR_{sw}/dt values. The values for peak load power are twice as high as in previous runs, because E_L is fixed and τ_p is two times smaller. For fixed dR_{sw}/dt , the peak load current and load power are nearly constant over the range of V_b .

The results of this run show that to obtain a shorter power pulse width, inductance constraints and gap-closure concerns are further strained. Gap closure is more severe because R_o (and gap size) scales linearly with τ_p ; however, the shorter pulse itself reduces the gap-closure problem. Series diodes can be used to alleviate the problems associated with reduced τ_p , again at the expense of improved switch performance.

Run 7, Increasing E_L

Lastly, Run 7 studies the effect of increasing the required load energy if, for example, a series diode is less efficient in coupling electrical energy to radiation than a single diode. Figure 8 shows the data from this run. Results should be compared with Run 6, since the shorter 38-nsec power pulse width was used for this run. The peak load resistance was found to lie between 0.0925 and 0.102Ω for the range of variables studied in this run. The decrease in R_o from that found in Run 6 is in agreement with that predicted by Equation 3. As in previous runs, R_o is nearly constant over the range of V_b , with the higher values of R_o occurring at smaller dR_{sw}/dt . The peak load current and load power for this run range from about 30.3 MA and 91.2 TW to about 32.8 MA and 98.2 TW, with the higher values occurring at higher dR_{sw}/dt values. For fixed dR_{sw}/dt , the peak load current and load power are nearly constant over the range of V_b . From Equation 17, the required switch-opening rate for high efficiency is somewhat higher than in Run 6. The required C is proportionately higher for the higher E_L . Similarly, from Equation 5, L is proportionately lower. Thus, τ_c is unchanged from its value in Run 6.

The results of this run show that higher E_L requires higher C and lower L . As would be expected, this makes the capacitor bank larger and more expensive and the inductance constraint more severe. Conversely, if a diode design is more efficient at coupling electrical energy to radiation (and thus reducing the required E_L), then the point-design value for C will be lower and the point-design value for L will be higher. In this case, the capacitor bank will be smaller and less expensive, and the inductance constraint will be less severe.

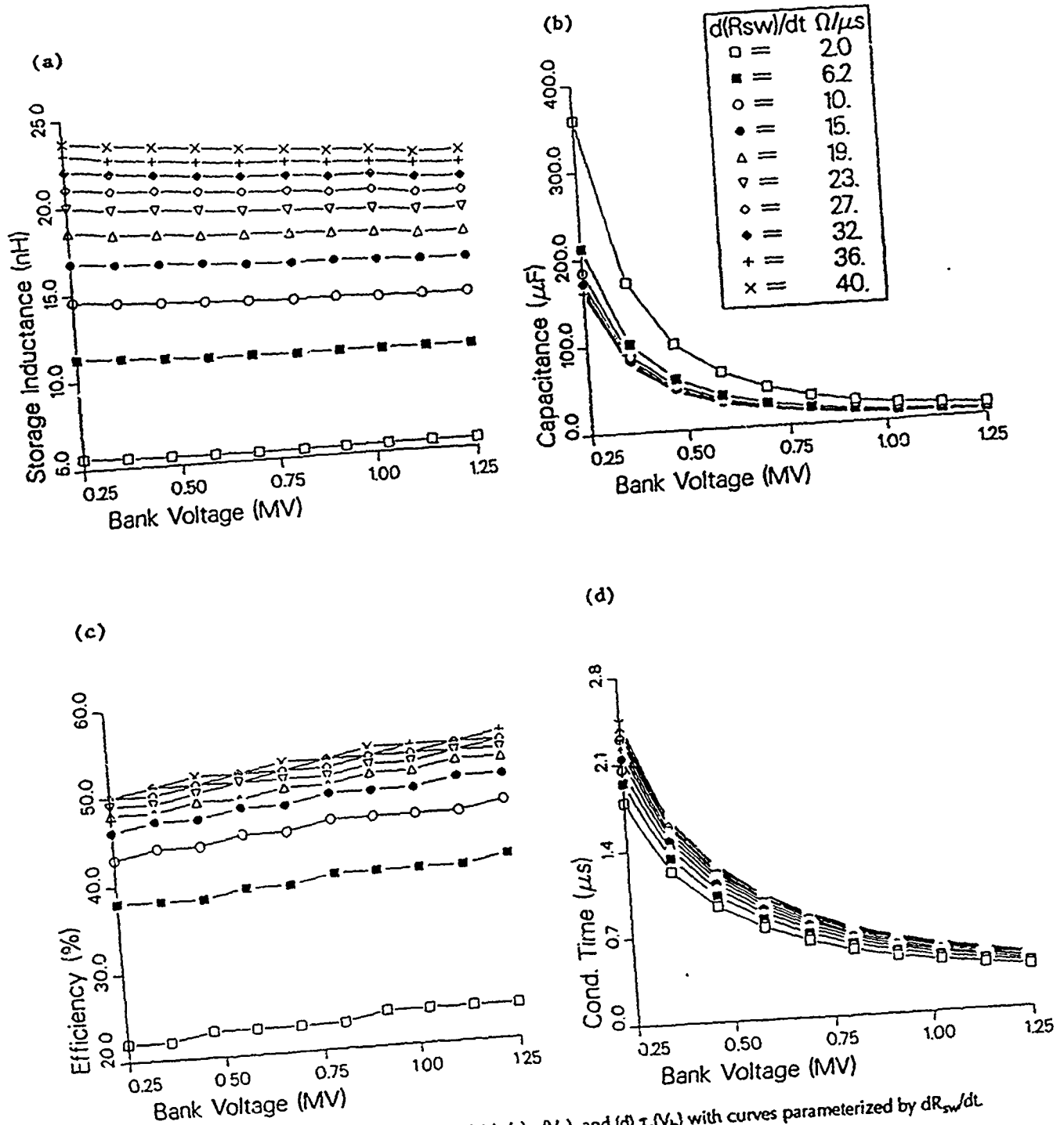


Figure 6. Run 5 plots of (a) $L(V_B)$, (b) $C(V_B)$, (c) $\eta(V_B)$, and (d) $\tau_c(V_B)$ with curves parameterized by dR_{sw}/dt .

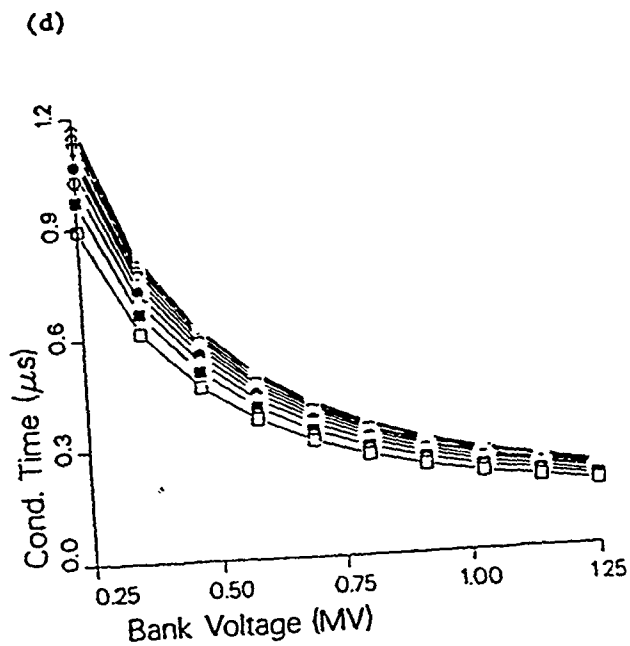
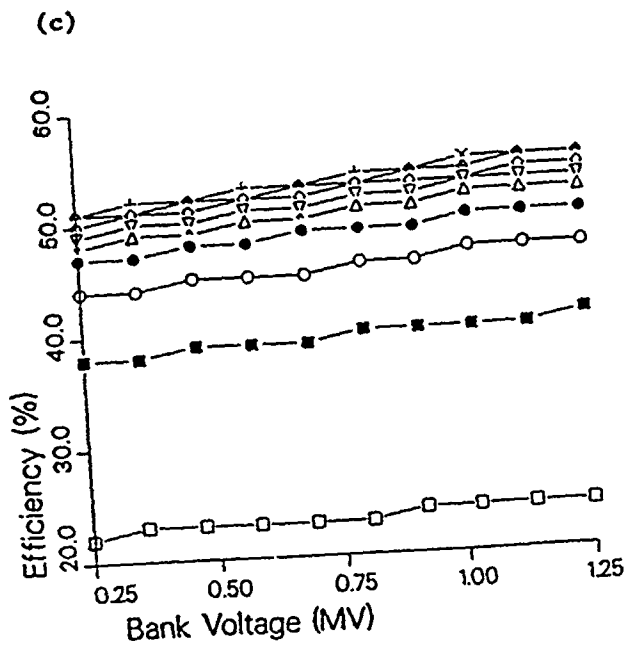
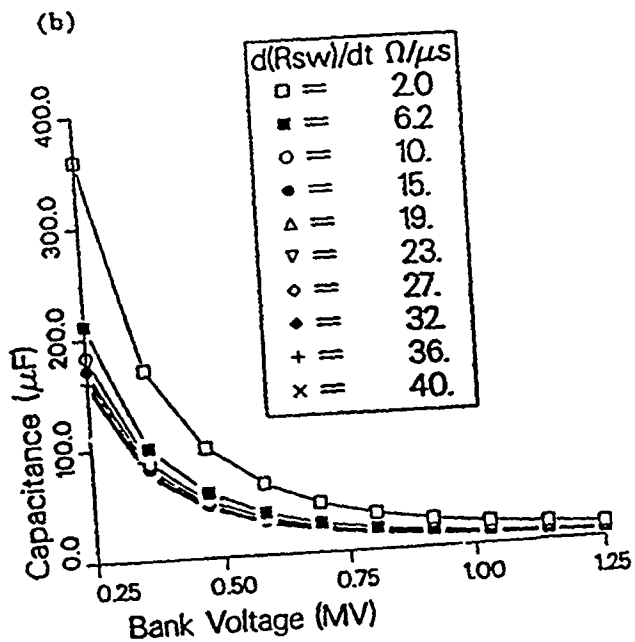
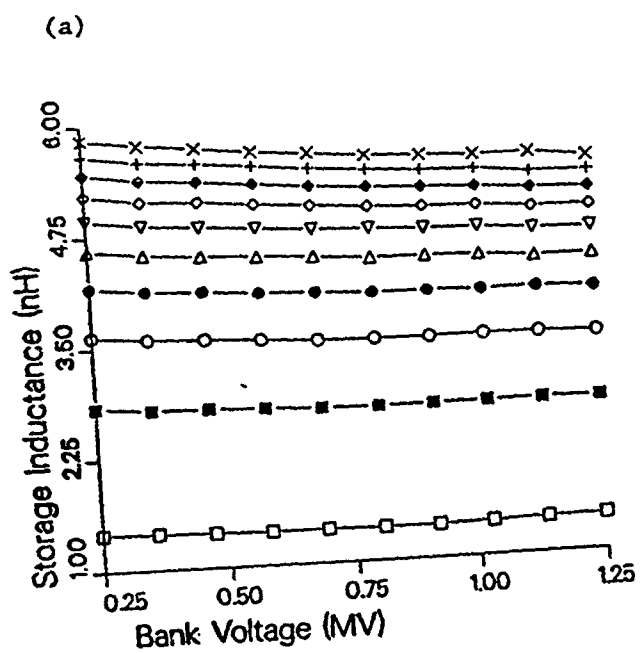


Figure 7. Run 6 plots of (a) $L(V_b)$, (b) $C(V_b)$, (c) $\eta(V_b)$, and (d) $\tau_c(V_b)$ with curves parameterized by dR_{sw}/dt .

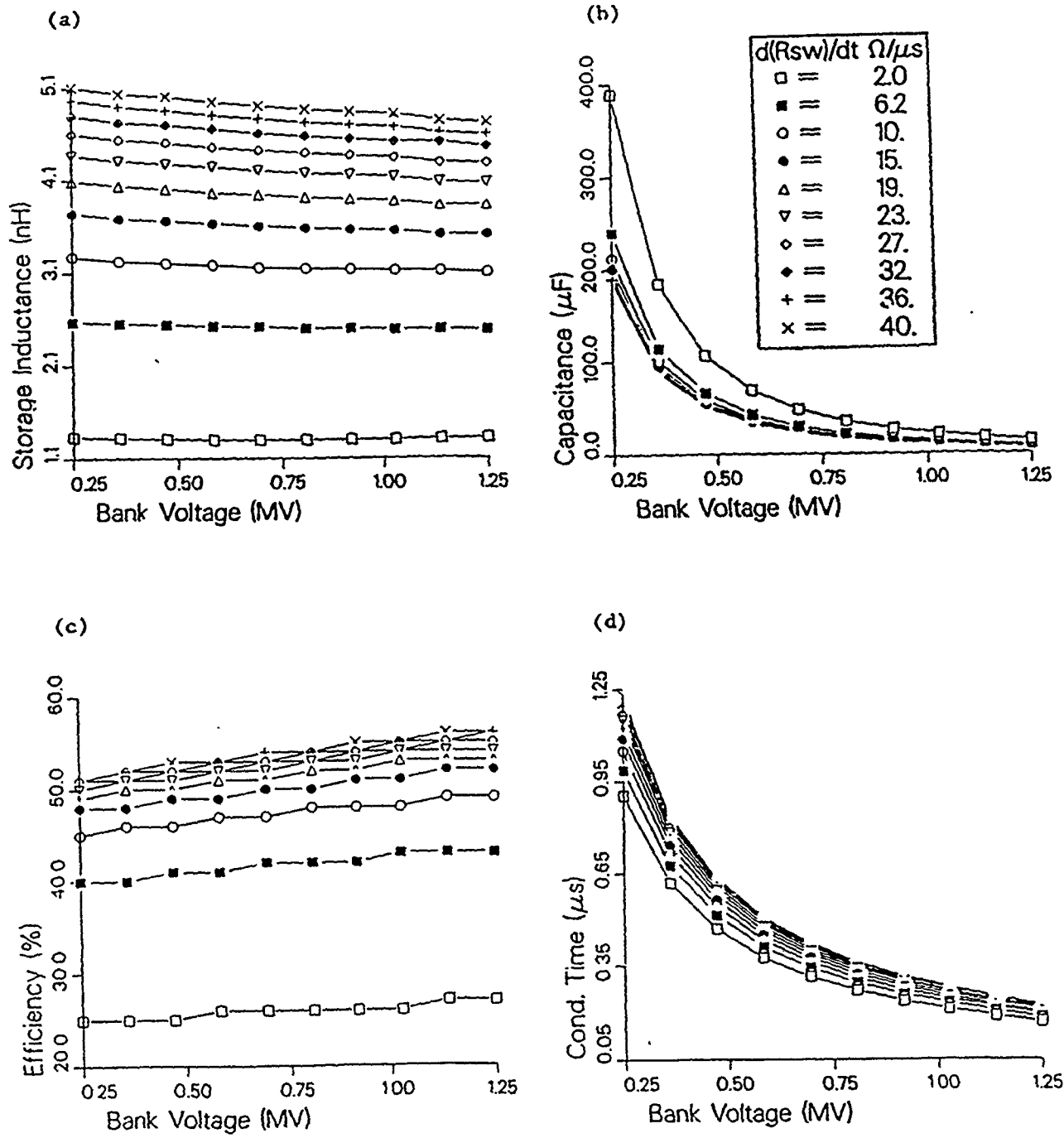


Figure 8. Run 7 plots of (a) $L(V_b)$, (b) $C(V_b)$, (c) $\eta(V_b)$, and (d) $\tau_c(V_b)$ with curves parameterized by dR_{sw}/dt .

Scaling Equations

The data from these runs can now be used with the scaling relationships developed earlier (Equations 3 and 4) to derive approximate scaling equations. In deriving these equations, it will be assumed that peak efficiency and point-design parameters are desired. Thus, these scaling equations assume that $L_L \gg L_s$, $\theta \sim 2\pi/5$, and that the conditions stated in Equations 16 and 17 for τ_g and dR_{sw}/dt are well satisfied. Data from Run 4 are most appropriate for this purpose, since $L_L = 0.1 L_s$, $\theta = 2\pi/5$, and $\tau_g = 1,000$ nsec. Data in the range of $dR_{sw}/dt = 16$ to $20 \Omega/\mu\text{sec}$ will be used in order to be well above the limit of $6 \Omega/\mu\text{sec}$ set by Equation 17. Since the power pulse is not a square wave, the coefficient of proportionality between P_L and E_L/τ_p must be adjusted for the wave shape. Empirically fitting this from the data yields

$$P_L = \frac{1.25 E_L}{\tau_p} \quad (18)$$

Using Equation 18 to rewrite Equations 3 and 4 yields

$$R_o = \frac{0.8 V_L^2 \tau_p}{E_L} \quad (19)$$

and

$$I_L = \frac{1.25 E_L}{V_L \tau_p} \quad (20)$$

Similarly, Equations 7 and 5 can be used to derive scaling equations for the point-design values of C and L . Since these equations are meant to apply for systems designed at peak efficiency, η will be ~ 0.5 . Fitting the equations to the data yields

$$C = \frac{4 E_L}{V_b^2} \quad (21)$$

and

$$L = 2.3 L_s = 2.3 \left(\frac{V_L^2 \tau_p^2}{2 E_L} \right) \quad (22)$$

Finally, a scaling equation for the conduction time, $\tau_c = \theta(LC)^{1/2}$, can be obtained using Equations 21 and 22. With $\theta = 2\pi/5$, this equation becomes:

$$\tau_c = \frac{2.7 V_L \tau_p}{V_b} \quad (23)$$

Using the definitions $G_v \equiv V_L/V_b$ and $G_t \equiv \tau_p/\tau_c$, Equation 23 can be rewritten as $G_v G_t = 1/2.7 = 0.37$, which agrees with previous results.³

Equations 19, 21, and 22 provide scaling equations for the point-design parameters for a Decade-like system assuming that $L_L \ll L_s$, $\theta \sim 2\pi/5$, and that conditions stated in Equations 16 and 17 for τ_g and dR_{sw}/dt are well

satisfied. Under these same conditions, $\eta \sim 0.5$, and Equations 18, 20, and 23 provide scaling equations for P_L , I_L , and τ_c . Note that these equations are written only in terms of the three specified output parameters (V_L , E_L , and τ_p) and V_b . If any of these conditions are violated, η will decrease and Equations 18 through 23 will no longer hold.

Efficiency Penalty Study

Although the point-design parameter study identified a point-design value for L , such a value is not always physically realizable. Because of inherent inductance in the capacitor design, packing issues, voltage holdoff concerns, etc., a realistic inductance may be considerably larger than the point-design value. The purpose of this efficiency penalty study is to evaluate the efficiency penalty that must be paid in cases where this inductance constraint plays a role. In addition to the efficiency penalty, there is also a fidelity penalty when L exceeds its point-design value. With C and V_b fixed for a particular bank design, the energy delivered to the load decreases when the efficiency decreases. Thus, a fidelity penalty in terms of a lower E_L (i.e., lower dose delivered during the desired radiation pulse width) results when the point-design inductance is exceeded. Some dose is also delivered at late times because of the longer-than-desired pulse width.

When solving Equations 12a through 12c for the efficiency penalty study, R_o must be chosen so that the solution yields the specified values of V_L . To do this, a one-parameter shooting technique is used.^{13,14} Again, details of how this technique is applied to this problem are described in Reference 15. In this analysis, for each system with fixed capacitance C , the inductance is varied about the point-design value found in the point-design parameter study. Parameters from Run 4 are used so that $\theta = 2\pi/5$, $L_L = 0.1 L_s$, and $\tau_g = 1,000$ nsec. V_b is varied and dR_{sw}/dt is set equal to a typical value of $4 \Omega/\mu\text{sec}$. (Note that this value of dR_{sw}/dt is somewhat less than the $\sim 6 \Omega/\mu\text{sec}$ required by Equation 17 for approaching peak efficiency.) $V_L = 1.5$ MV is the only specified constraint and is assumed to fix R_o . Equation 3 is evaluated from $t - \tau_c = 0$ to a fixed time $t - \tau_c = T$, where $T = 76$ nsec is chosen for this study to keep the radiation pulse width within the 40-nsec limit. E_L and τ_p are not fixed, but are calculated for each system. If L is larger than the point-design value found previously in Run 4, τ_p will exceed T and the efficiency will drop. E_L also drops as the efficiency drops. Note that the L_s , which is used to define L_L and scale the results in Figures 10 and 11, is the $L_s = 2.6$ nH calculated for the desired output specifications, with $E_L = 2.5$ MJ, $\tau_p = 76$ nsec, and $V_L = 1.5$ MV. This value of L_s will not vary with E_L or τ_p as L is varied about its point-design value.

Results of the study are shown in Figure 9. Figure 9c shows η as a function of V_b and L . The efficiency for the point-design value of L found in Run 4 is about 55 percent. The efficiency decreases for L greater than the point-design value and increases for L less than the

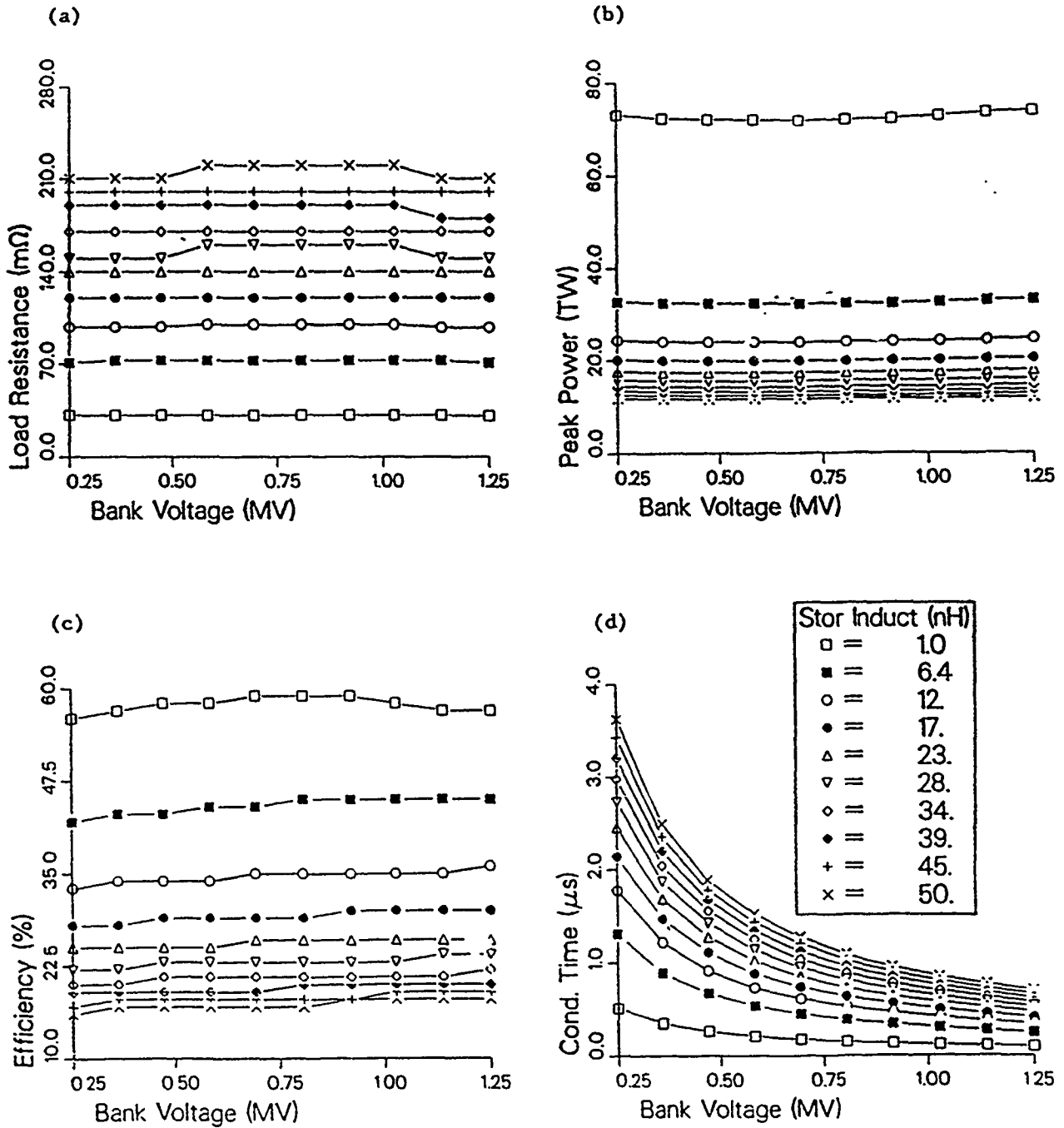


Figure 9. Efficiency penalty study plots of (a) $R_L(V_b)$, (b) $P_L(V_b)$, (c) $\eta(V_b)$, and (d) $\tau_c(V_b)$ with curves parameterized by L.

point-design value. However, the increase in η is limited by L_L . For the case displayed here with $L_L = 0.1 = 0.26$ nH, η begins to decrease for L less than about 0.5 nH. At $L = 0.5$ nH, η has already decreased from a peak value of about 60 percent to about 50 percent. Since the energy stored in the capacitor bank is fixed for a given V_b (remember C is fixed), as L increases the peak current will decrease. Thus, R_o will increase with L to maintain the specified peak load voltage. This is seen in Figure 9a. The peak load power also decreases as the current drops with increasing L . This is shown in Figure 9b. Finally, as would be expected, Figure 9d shows that $\tau_c = \theta(LC)^{1/2}$ increases as $L^{1/2}$ and scales as V_b^{-1} (see Equation 23). Because τ_c increases when L is larger than its point-design value, the switch must conduct for a longer time but still open at the same rate. Thus, in addition to the efficiency penalty, the switching requirements are also more severe when L is larger than its point-design value.

Previous analyses²⁻⁴ have shown that the efficiency for a circuit with an ideal switch (i.e., one with $dR_{sw}/dt = \infty$), $L_L = 0$, and constant load resistance (i.e., $\tau_g = \infty$) can be expressed as

$$\eta_i = \sin^2\theta [1 - \exp(-4 L_p/L)] \quad (24)$$

The L_s used in Equation 24 is also the value obtained from the desired output specifications, which again is 2.6 nH for the case considered here. Results from Figure 9c for η at $V_b = 750$ kV (with $dR_{sw}/dt = 4 \Omega/\mu\text{sec}$ and $L_L = 0.1 L_s$) are plotted against Equation 24 in Figures 10 and 11. Results from other runs with different values of dR_{sw}/dt and L_L are also displayed in Figures 10 and 11. For each set of parameters that defines a curve in Figure 10 (displayed in Figure 11), C is set equal to the point-design value found in Run 4 (Run 1). Thus, C is constant along any given curve in Figures 10 and 11, but varies from curve to curve. The point-design value for L also varies from curve to curve, and its value relative to L_s is

indicated by the solid dot in each curve. In all cases, $V_L = 1.5$ MV, $V_b = 750$ kV, $\theta = 2\pi/5$, and $\tau_g = 1,000$ nsec.

Equation 24 is compared with the calculated efficiency for three different values of dR_{sw}/dt in Figure 10 with $L_L = 0.1 L_s$ and for three different values of L_L in Figure 11 with $dR_{sw}/dt = 4 \Omega/\mu\text{sec}$. Results show that a significant efficiency penalty must be paid if L is larger than the point-design value (indicated by the solid dot). Enhanced efficiency for L less than the point-design value is limited by L_L . The efficiency derived from ideal circuit considerations (Equation 24) overestimates the efficiency for smaller values of L/L_s . The lower efficiency at small L/L_s found here results from energy lost to the switch resistance and load inductance. Figure 10 shows that the calculated efficiency decreases for all values of L/L_s as dR_{sw}/dt decreases. Figure 11 shows that the calculated efficiency decreases for all values of L/L_s as L_L increases, and that, for a given value of L_L , the efficiency peaks and begins to drop off rapidly for L less than about $2 L_L$.

For large L/L_s , the efficiency calculated here can be somewhat higher than that predicted by the ideal curve. Because of the finite rise time of the load current in the nonideal case (i.e., when dR_{sw}/dt is not infinite), the peak load current is less than in the ideal case (i.e., when dR_{sw}/dt is infinite). Consequently, for fixed peak load voltage, R_o must be larger for the nonideal case. For a given L , this allows energy to be dissipated in the load faster (i.e., L/R_o is smaller and the pulse is narrower) in the nonideal case; in some cases, slightly higher efficiency is obtained because of the shorter pulse width.

The results of this study provide quantitative information about the efficiency penalty for using a storage inductance that is larger than the point design inductance found in the point-design parameter study. The decrease in E_L , which translates into a fidelity penalty in terms of

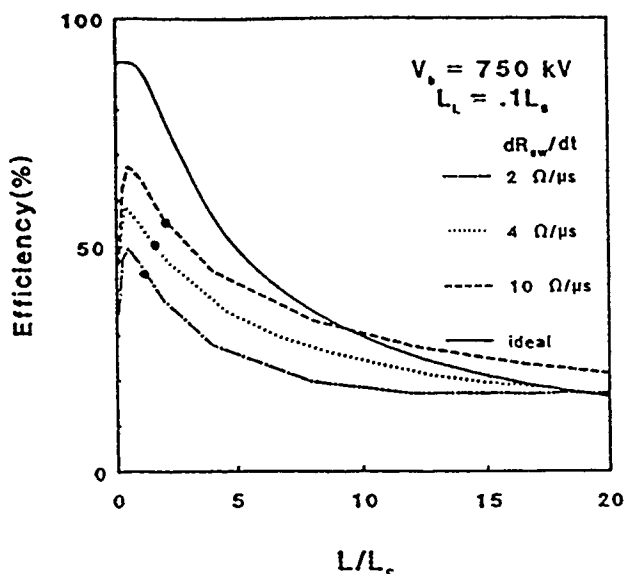


Figure 10. Efficiency penalty study plots of η versus L/L_s for various switch-opening rates (for reference, Equation 24 is plotted as the "ideal" curve).

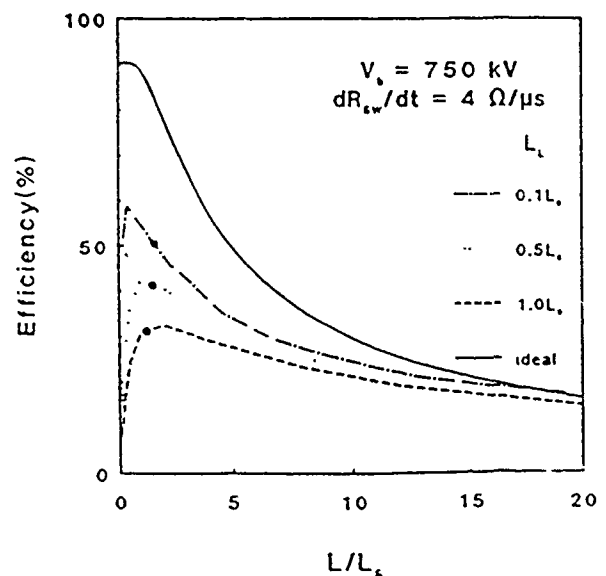


Figure 11. Efficiency penalty study plots of η versus L/L_s for various values of L_L (for reference, Equation 24 is plotted as the "ideal" curve).

a decrease in dose, can also be obtained by comparing the efficiency at any L (greater than the point-design L) with that at the point-design L (indicated by the point on each curve). The energy delivered to the load for that L will then be the desired $E_L = 2.5$ MJ reduced by the ratio of the efficiencies. For realistic values of L_L and dR_{sw}/dt , the efficiency can be significantly less than that derived in Equation 24 from ideal circuit considerations. However, efficiencies ~20 percent or larger are still theoretically achievable with these realistic values of L_L and dR_{sw}/dt for L/L_s as large as 10. In addition to the efficiency penalty, τ_c also increases as L is increased beyond the point-design inductance, making the switching requirements more severe.

Conclusions

The purpose of the point-design parameter study was to determine the design for a system that provided precisely the desired output specifications for V_L , τ_p , and E_L . The point-design parameters C , L , and R_o were determined using the three-parameter shooting technique for range of assumed values for θ , L_L , τ_c , dR_{sw}/dt , and V_b . The output parameters, V_L , E_L , and τ_p , were chosen to match Decade bremsstrahlung radiation specifications. A number of design guidelines for maximizing the efficiency were obtained from this study:

1. Firing angle θ should be $\sim 2\pi/5$
2. Load inductance L_L should be made as small as possible (Equation 15 quantifies the efficiency penalty for nonzero L_L)
3. As indicated by Equation 16, the diode gap-closure time should be $> 3\tau_p$
4. The switch-opening rate should be as large as possible.

The efficiency is within 5 percent of its peak value when Equation 17 is satisfied. When all four of these conditions are satisfied, Equations 19, 21, and 22 provide scaling equations for the point-design parameters C , L , and R_o for a Decade-like system. Under these same conditions, $\eta \approx 0.5$ and Equations 18, 20, and 23 provide scaling equations for P_L , I_L , and τ_c . All these scaling equations are written only in terms of the three specified output parameters (V_L , E_L , and τ_p) and V_b . If any of these four conditions are violated, η will decrease and these scaling equations will no longer strictly hold.

A number of other observations can be made:

1. Results show that the only major difference between the design and performance of a lower voltage bank compared with a higher voltage bank is the longer switch conduction time, which, from Equation 23, scales as V_b^{-1} . An efficiency of ~50 percent is attainable over the entire range of V_b studied, if dR_{sw}/dt can be maintained with increasing τ_c . Longer τ_c with the same dR_{sw}/dt is equivalent to requiring a higher voltage gain from the switch. Typically, however, dR_{sw}/dt is found experimentally to decrease as τ_c increases. Staged switching may solve this problem if adequate single-stage switching is not attainable. Lower

voltage banks have many advantages that could be utilized if the switching requirements can be met. For example, capacitors are combined largely in parallel for low-voltage banks and in series for high-voltage banks, so that the bank inductance L_b scales roughly as V_b^2 . Thus, L_b can be significantly lower in a low-voltage bank than in a high-voltage bank. This frees more of the total system inductance for the vacuum feeds, and reduces the voltage applied back onto the capacitor bank once the switches open. Other advantages include design simplicity and less severe problems with high-voltage breakdown.

2. Results show that there are many advantages to using series diodes. With N diodes in series, both L and L_L can be increased by N^2 , making the physical constraints on inductance considerably more tolerable. In addition, the total load resistance increases by N^2 , so that each of the N diodes has a resistance N times higher. This also alleviates the gap-closure problem, since resistance scales roughly linearly with gap for a pinched-beam diode. These advantages are all gained without sacrificing dose rate. The major disadvantage of using series diodes is the required enhancement in switch performance. dR_{sw}/dt and τ_c are required to increase by a factor of N^2 and N , respectively. Other disadvantages include increased diode complexity and high-voltage power-flow concerns.
3. Results show that to obtain a shorter power pulse width, inductance constraints and gap-closure concerns are further strained. Series diodes can be used to alleviate this problem, again at the expense of improved switch performance.
4. Results also show that lower radiation production efficiency and, thus, higher E_L requires higher C and lower L . As would be expected, this makes the capacitor bank larger and more expensive, and the inductance constraint more severe. Conversely, if a diode design is more efficient in coupling electrical energy to radiation so that the required E_L decreases, then the point-design value for C will be lower and the optimum value for L will be higher. In this case, the capacitor bank will be smaller and less expensive, and the inductance constraint will be less severe.

The results of the inductance penalty study provide quantitative information about the efficiency penalty for using a storage inductance that is larger than the point-design inductance found in the point-design parameter study. For realistic values of L_L and dR_{sw}/dt , the efficiency can be significantly less than that derived in Equation 24 from ideal circuit considerations. However, efficiencies ~20 percent or larger are still theoretically achievable with these realistic values of L_L and dR_{sw}/dt , even for L/L_s as large as ~10. The optimum value for L/L_s is typically approximately ≤ 2.3 . There is also a fidelity penalty when L exceeds its point-design value. With C and V_b fixed for a particular bank design, the energy delivered to the load decreases when the efficiency decreases. Thus, a fidelity penalty in terms of a lower E_L (i.e., lower dose) results when the point-design inductance is exceeded. With the efficiency at the point-design

value for L at ~ 50 percent, the energy delivered to the load at efficiencies of ~ 20 percent is ~ 1 MJ. In addition to the efficiency and fidelity penalties, τ_c also increases as L is increased beyond the point-design inductance, making the switching requirements more severe.

Aside from the obvious engineering goals of minimizing L_L and holding L down to a value as close as possible to its point-design value, it is clear from this analysis that there are three areas of research where advances would have a major impact on the design of inductive generators. These areas include opening switches, series diodes, and advanced bremsstrahlung diodes. Improvement in switch-opening rate will enhance efficiency, and extension of switch conduction time, while maintaining an adequate opening rate, will allow for the use of series diodes. Development of multiple-stage series bremsstrahlung diodes will alleviate both the inductance constraint and the gap-closure problem. And, more efficient radiation converters in advanced bremsstrahlung diode designs will reduce the size of the required capacitor bank and also alleviate the inductance constraint by reducing the required load energy. Research in all these areas will be essential to attain the goals of the Decade program and to move toward the goals of Century.

In the future, effects of finite transit time, bank resistance, safety resistors, and insulator flashover will be investigated. In addition, physics models for both the switch and the load will be incorporated into the analysis. Finally, staged switching will be considered, particularly in looking forward to Century design requirements.

Acknowledgments

This work was supported by the Defense Nuclear Agency. The authors would also like to thank G. Cooperstein for many useful conversations during the course of this work.

List of References

1. P. Sincemy, "DECADE Concept," *Proceedings of the Defense Nuclear Agency Advanced Pulse Power Conference* (Albuquerque, NM, July 31-August 3, 1990), DASIAC TR-90-006, p. 7-22 (U).
2. R. Miller, W. Rix, and A. Wilson, "MLI DECADE System Development," *Proceedings of the Defense Nuclear Agency Advanced Pulse Power Conference* (Albuquerque, NM, July 31-August 3, 1990), DASIAC TR-90-006, p. 7-29 (U).
3. J.M. Neri, *Modeling of Single Stage Inductive Storage Systems for x10 with Combined Switch/Load Models*, NRL MR 6502, 1990 (U).
4. J. Shannon, *Simulator Development Using Compact Marx Generators*, Maxwell Laboratories, MLR-3073, 1988 (U).
5. M. Krishnan and P. Sincemy, *The Inductive Store Simulator Development Program at Physics International Company*, Physics International PIIR 1-88 (U).
6. M. Krishnan, "Design Considerations for Inductive Store Simulators," *DNA Opening Switch Workshop* (Alexandria, VA, January 30 - February 2, 1990), unpublished (U).
7. J.R. Boller, S.J. Stephanakis, S.A. Goldstein, and G. Cooperstein, "Series Diode REB Experiments," *Bull. Am. Phys. Soc.*, Vol. 27, p. 991, 1982 (U).
8. I.D. Smith, L.J. Demeter, and K.E. Neilsen, U.S. Patent 4 359 660, 1982 (U).
9. G. Cooperstein, J.R. Boller, R.A. Meger, J.M. Neri, and S.J. Stephanakis, "Progress in Bremsstrahlung Diode Source Development," *Meeting Record — DNA Pulsed Power Review and SDIO Update* (Las Vegas, Nevada, 1986), E.E. Stobbs, R.J. Commisso, and J.M. Neri (eds.), pp. 654-664 (U).
10. J.M. Neri, "Bremsstrahlung Diode Source Development at NRL," *Meeting Record — DNA Pulsed Power Review and SDIO Update* (Las Vegas, Nevada, 1986), E.E. Stobbs, R.J. Commisso, and J.M. Neri (eds.), pp. 485-510 (U).
11. J.C. Riordan, J.S. Meachum, J.E. Faulkner, and M.J. Wiley, "Efficient Production of Soft Bremsstrahlung with Series Diodes," *Bull. Am. Phys. Soc.*, Vol. 34, p. 2102, 1989 (U).
12. V.J. Harper-Slaboszewic, J.R. Lee, M.A. Hedemann, G.T. Baldwin, J.W. Poukey, L.J. Lorence, Jr., G.A. Carlson, W.E. Fowler, D.L. Faucell, and C.O. Landron, "Operation of a Bidirectional Voltage-Dividing Bremsstrahlung Diode," *J. Appl. Phys.*, Vol. 67, pp. 3233-3242, 1990 (U).
13. S.M. Roberts and J.S. Shipman, *Two-Point Boundary Value Problems: Shooting Methods*, American Elsevier, New York, 1972 (U).
14. S.D. Conte and C. DeBoor, *Elementary Numerical Analysis: An Algorithmic Approach*, McGraw-Hill, New York, 1965 (U).
15. P.F. Ottinger, D.V. Rose, J.M. Neri, and R.J. Commisso, *System Study for Decad. Using Inductive Storage Technology*, NRL MR 6733, 1990 (U).
16. P. Sincemy and C. McDonald, "The Dependence of Pulsed Power Designs on Opening Switch Performance," *DNA Opening Switch Workshop* (Alexandria, VA, January 30 - February 2, 1990), unpublished (U).

